INSTITUTE OF FUNDAMENTAL TECHNOLOGICAL RESEARCH
POLISH ACADEMY OF SCIENCES

41ST SOLID MECHANICS CONFERENCE

BOOK OF ABSTRACTS

Editors: K. Wiśniewski, T. Burczyński

Co-editors: B. Błachowski, M. Nowak, P. Tauzowski

41st SolMech 2018

Warsaw, Poland

August 27-31, 2018

INSTITUTE OF FUNDAMENTAL TECHNOLOGICAL RESEARCH
POLISH ACADEMY OF SCIENCES

41st Solid Mechanics Conference

Book of Abstracts

Editors:
Krzysztof Wiśniewski
Tadeusz Burczyński

Co-editors:
Bartłomiej Błachowski
Marcin Nowak
Piotr Tauzowski

WARSZAWA 2018

ISBN 978-83-65550-13-2

Institute of Fundamental Technological Research PAN
02-106 Warszawa, ul. Pawińskiego 5B
www.ippt.pan.pl

Preface

This e-book contains abstracts of papers accepted for presentation at the 41st Solid Mechanics Conference (SOLMECH 2018). The conference was held in Warsaw, Poland, on August 27-31, 2018. More details can be found on the conference website: http://www.solmech2018.ippt.pan.pl

The Solid Mechanics Conferences are a series of biennial international conferences, which have been organized by the Institute of Fundamental Technological Research of the Polish Academy of Sciences (IPPT PAN) since 1953. This conference series aims at maintaining high scientific standards, while providing a friendly atmosphere that facilitates discussion of theoretical and applied research topics on solid mechanics. A set of plenary and keynote lectures is delivered by invited speakers of international recognition in their field of research.

This, the 41st edition of the conference series, was held at the Conference Center of Warsaw University, a quiet and pleasant vicinity close to the old town of Warsaw. The conference hosted 7 general lectures and 16 thematic sessions. 273 abstracts from 28 European and non-European countries (43% of them from outside Poland) were presented.

The solid mechanics of materials and structures is in itself an area of active and dynamic research, that also provides the foundation of numerous industrial applications that necessitate sophisticated computational models and methods. Naturally, the SOLMECH conference series encompass these research directions as well and this trend is clearly growing; and we foresee that it will continue to grow in the future.

Prof. K. Wiśniewski
Chairman of SOLMECH 2018

Prof. T. Burczyński
Director of IPPT PAN

41st SOLID MECHANICS CONFERENCE
AUGUST 27-31, 2018, WARSAW, POLAND
http://solmech2018.ippt.pan.pl

Organizers

The 41st Solid Mechanics Conferences is organized by the Institute of Fundamental Technological Research under the auspices of the Committee on Mechanics, both of the Polish Academy of Sciences.

International Advisory Board

Z.Bažant (*USA*)
D.Bigoni (*Italy*)
T.Inoue (*Japan*)
S.Kourkoulis (*Greece*)
P.Ladeveze (*France*)
W.K.Liu (*USA*)
E.Oñate (*Spain*)
I.Romero (*Spain*)
A.Rusinek (*France*)
H.Tobushi (*Japan*)
W.Wagner (*Germany*)
P.Wriggers (*Germany*)
R.Zaera (*Spain*)
Z.Zhuang (*China*)

Honorary Scientific Committee

R. Będziński
A. Borkowski
W. Gutkowski
J. Holnicki-Szulc
J. Kubik
M. Kleiber
Z. Mróz
A. Nowicki
W. Pietraszkiewicz
M. Pietrzyk
G. Szefer
A. Tylikowski

Scientific Committee

J. Awrejcewicz (*PŁ*)
J. Badur (*IMP*)
Cz. Bajer (*IPPT*)
M. Basista (*IPPT*)
T. Burczyński (*IPPT*)
J. Chróścielewski (*PG*)
P. Dłużewski (*IPPT*)
D. Gawin (*PŁ*)
T. Kapitaniak (*PŁ*)
Z. Kotulski (*PW*)
P. Kowalczyk (*IPPT*)
Z. Kowalewski (*IPPT*)
M. Kuczma (*PP*)
T. Lewiński (*PW*)
T. Łodygowski (*PP*)
E. Majchrzak (*PŚ*)
J. Pamin (*PK*)
H. Petryk (*IPPT*)
R. Pęcherski (*IPPT*)
E. Pieczyska (*IPPT*)
P. Pyrzanowski (*PW*)
J. Rojek (*IPPT*)
T. Sadowski (*PL*)
A. Seweryn (*PB*)
B. Skoczeń (*PK*)
S. Stupkiewicz (*IPPT*)
R. Śliwa (*PRz*)
J. Tejchman (*PG*)
J. Warmiński (*PL*)
K. Wilde (*PG*)
K. Wiśniewski (*IPPT*)

Organizing Committee

K. Wiśniewski - *Chairman of the Conference*
B. Błachowski - *Scientific Secretary*
M. Nowak - *Coordinator*
P. Tauzowski - *Webmaster, Email Coordinator*

Thematic Sessions and Their Organizers

S01: Elasticity, plasticity and phase transition

S. Forest (*MINES Paristech, CNRS, Paris*), H. Petryk (*IPPT PAN, Warsaw*)

S02: Micromechanics, interfaces and multiscale modelling

V. Kouznetsova (*Eindhoven UT*), A. Menzel (*TU Dortmund*), S. Stupkiewicz (*IPPT PAN, Warsaw*)

S03: Damage and fracture modelling of advanced materials

M. Basista (*IPPT PAN, Warsaw*), G. Bolzon (*Polit. di Milano*), Ch. Sommitsch (*TU Graz*)

S04: Plasticity, damage and fracture: microstructural aspects

K. Kowalczyk-Gajewska (*IPPT PAN, Warsaw*), S. Mercier (*Univ. of Lorraine, LEM3, Metz*), J. Rodriguez-Martinez (*Univ. Carlos III, Madrid*), G. Vadillo (*Univ. Carlos III, Madrid*)

S05: Computational aspects of solid mechanics

O. Allix (*LMT, ENS Cachan, France*), T. Burczyński (*IPPT PAN, Warsaw*), P. Kowalczyk (*IPPT PAN, Warsaw*)

S06: Discrete and multiscale modelling in solid mechanics

J. Rojek (*IPPT PAN, Warsaw*), M. Pietrzyk (*AGH Univ. of Science and Technology, Cracow*), R. Kačianauskas (*Vilnius Gediminas TU, Lithuania*), B. Peters (*Université du Luxembourg*)

S07: Coupled fields in nanostructures and continua

T. Łodygowski (*Poznan UT*), R. Pęcherski (*IPPT PAN, Warsaw*), H. M. Shodja (*Sharif UT, Iran*)

S09: Experimental mechanics

S. Kourkoulis (*National TU of Athens*), Z.L. Kowalewski (*IPPT PAN, Warsaw*)

S10: Geomechanics and multiscale modelling of materials

Z. Mróz (*IPPT PAN, Warsaw*), S. Pietruszczak (*McMaster University, Ontario*), R. Michalowski (*University of Michigan*), J. Tejchman (*Gdansk UT*)

S12: Biomechanics

R. Będziński (*TU Wroclaw*) , J-F. Ganghoffer (*Univ. of Lorraine, Nancy*), E. Majchrzak (*Silesian UT*), M. Nowak (*TU Poznan*)

S13: Smart materials and structures

E. A. Pieczyska (*IPPT PAN, Warsaw*), H. Tobushi (*Aichi IT, Toyota-city*), Q. P. Sun (*HKUST, Hong Kong*)

S14: Structural mechanics and optimization

M. Gilbert (*U Sheffield*), T. Lewiński (*Warsaw UT*), A. V. Pichugin (*Brunel U.,London*)

S15: Nonlinear and adaptive dynamical systems

P. Perlikowski (*Łódź UT*), S. Evangelou (*Imperial College, London*), Ł. Jankowski (*IPPT PAN, Warsaw*)

S16: Shells and plates

Dedicated to the anniversary of Prof. W. Pietraszkiewicz with the tribute speech by Prof. J. Badur (IMP PAN, Gdansk)

J. Chróścielewski (*Gdansk UT*), F. Gruttmann (*TU Darmstadt*), V. Eremeyev (*Rostov on Don, Gdansk UT*), K. Wiśniewski (*IPPT PAN, Warsaw*)

S17: Stochastic mechanics

Dedicated to the memory of the late Professor Kazimierz Sobczyk (1939-2017)

R. Iwankiewicz (*TU Hamburg*), Z. Kotulski (*Warsaw UT*)

S18: Composite Materials and Structures

B. Brank (*U Ljubljana*), J. Hohe (*IWM Freiburg*), I. Kreja (*Gdansk UT*)

Contents

Session S09: Experimental mechanics 253

Plenary lectures

MECHANICAL PROPERTIES OF SHAPE MEMORY ALLOYS, POLYMERS AND THEIR COMPOSITES

H. Tobushi[1]

[1]*Aichi Institute of Technology, 1247 Yachigusa, Yakusa-cho, Toyota, 470-0392, Japan*
e-mail: tobushi@aitech.ac.jp

1. Introduction

The functional subjects important to design the shape memory elements are the mechanical properties of the materials such as shape memory effect, superelasticity, shape recovery, shape fixity, fatigue, secondary shape forming etc. [1], [2]. These properties appear due to the phase transformation depending on variation in stress, strain and temperature. In the present paper, the main subjects discussed till now will be introduced for shape memory alloys (SMAs), polymers (SMPs) and their composites (SMCs). Following these mechanical properties of the materials, the advanced subjects in the mechanical properties of the materials will be discussed.

2. Deformation and fatigue properties of shape memory alloys

The important functions of SMAs in applications are the deformation and fatigue properties, which can be summarized as follows.

(1) The basic functional properties of the shape memory effect (SME) and superelasticity (SE) appear due to the martensitic transformation. With respect to the SME, not only the shape recovery but also the recovery stress are used in applications. The recovery stress of 400 MPa can be obtained by heating. The energy storage and dissipation are obtained in the SE.

(2) The cyclic deformation due to the R-phase transformation does not change during cycling. However, the upper stress plateau due to the martensitic transformation decreases during cyclic deformation.

(3)The return-point memory appears in the subloop loading under the low strain rate. However, the return-point memory does not appear in the stress-controlled subloop loading, and the transformation-induced creep and stress relaxation appear.

(4) The thin SMA tape can be easily twisted by simply grasping both ends. The simple rotary reciprocating actuators can be developed by using the torsional deformation of the SMA thin tape.

(5) The highelatic deformation with the almost linear stress-strain curve of the TiNi SMA can be obtained up to a stress of 1400 MPa and a strain of 4%.

(6) The relationship between strain amplitude and number of cycles in bending fatigue life can be expressed by a power function. The fatigue limit appears around a strain amplitude of 1%, which is in the R-phase transformation region. The bending fatigue life can be enhanced by the nitrogen ion implantation and the ultrasonic shot peening.

3. Deformation and long-time properties of shape memory polymers

The main mechanical properties of shape fixity and shape recovery of SMPs appears based on the glass transition of the materials. The important characteristics are as follows.

(1) The rigidity of SMPs is high and low at temperatures below and above the glass transition temperature, respectively. The deformed shape with high rigidity is obtained by cooling, shape fixity, and the original shape is recovered by heating, shape recovery.

(2) If the deformed shape is held at low temperature, it can be fixed under no-load for a long time and the original shape can be recovered by heating after that.

(3) If the deformed shape is held at high temperature, the original shape can't be recovered by heating and the irrecoverable strain appears, the secondary shape forming. If we use this property in applications, we can obtain the SMP elements with complex shape by the simple method without using metal molds.

4. Shape memory composites with SMA and SMP

The dependence of rigidity and yield stress on temperature is quite opposite between SMA and SMP. If the shape memory composite made of SMA and SMP is fabricated by using both materials, the novel functional materials, SMCs, can be developed. If we fabricate the SMCs by combing the SMA and SMP elements with different phase transformation temperatures and memorized shapes, the SMC actuator with three way motion during heating and cooling can be developed.

5. Advanced subjects of shape memory alloy and polymer

5.1 Functionally-graded shape memory material

(1) Functionally-graded shape memory alloy

The SME and SE appears due to the martensitic phase transformation. The elastic modulus and stress plateau vary depending on temperature. The phase transformation temperatures depend on the composition of SMAs. If the composition of SMA changes gradually in each position, the rigidity and yield stress change corresponding to the composition. The functionally-graded SMA therefore can be obtained by developing the fabrication method for changing the composition of SMA.

(2) Functionally-graded shape memory polymer

The polyurethane SMP has been used in the form of sheet, film and foam with various glass transition temperatures. In the case of foam, not only glass transition temperature but also density can be changed. Therefore, if we fabricate the laminated SMP with various glass transition temperatures and densities, the functionally-graded SMP can be developed. In the functionally-graded SMP, the deformation resistance varies in each layer and therefore the stepwise local deformation and recovery stress appear.

5.2 3D-printing of shape memory polymer

If we make a product with SMP using the 3D printer, the new device which is well suited to the individual complex shape can be developed without using expensive metal molds.The material used to fabricate the 3D-printing SMC belt was a SMP filament. The 3D-printed SMP belt was fabricated by the fused deposition modeling 3D printer. The shape fixity and shape recovery properties are obtained in the 3D-printed SMP as same as the SMP made by the general method. The thermomechanical properties of the 3D-printed SMP depend on the nozzle temperature, table temperature, printing rate and pattern of the each layer. These points are the future subjects.

6. Conclusions

The deformation and fatigue properties of SMA, SMP and SMC are important for the design of machine elements. The development of functionally-graded SMA and SMP and 3D-printed SMP is expected.

Acknowledgments The author acknowledges the financial support of research for AIT and IFTR by JSPS and PAS.

References

[1] H. Tobushi, R. Matsui, K. Takeda and E.A. Pieczyska, *Mechanical properties of shape memory materials*, Nova Science Pub., 2013.

[2] Q.P. Sun, R. Matsui, K. Takeda and E.A. Pieczyska, *Advances in shape memory materials – In commemoration of the retirement of Professor Hisaaki Tobushi* -, Springer, 2017.

NUMERICAL MODELING OF ADHESIVE WEAR ACROSS SCALES

J.F. Molinari[*1], R. Aghababei[2], L. Frérot[1], E. Milanese[1], T. Brink[1]

[1]*Department of Civil Engineering, Department of Materials Science*
Ecole Polytechnique Fédérale de Lausanne (EPFL), Switzerland
e-mail: jean-francois.molinari@epfl.ch
[2]*Department of Mechanical Engineering, Aarhus University, Denmark*

1. Introduction

Wear, the process of material loss when materials come into contact, takes various forms and is present in literally all engineering applications. It is experienced at disparate scales from single atom removal at the nanoscale, to the eraser of a student leaving rubber debris on paper, and the formation of gouge along a tectonic fault.

Around mid-twentieth century tremendous progress was made in Tribology, the science of interacting surfaces in relative motion. Scientific advances explained the intimate relationship between surface roughness, load, and the real contact area. Due to the complexity of wear mechanisms, scientific progress has arguably slowed down ever since, although there has been a rapid increase in the number of empirical models describing various forms of wear. Recently, with the advent of nanotribology, fundamental discoveries were made regarding friction mechanisms at nanoscale asperities. However, by and large, the dots remain unconnected and our macroscopic engineering-scale understanding of wear remains limited.

We present our recent attempts at developing a fundamental, mechanistic, across scales, understanding of adhesive wear.

2. Coarse-grained atomistic simulations

We begin by summarizing recent numerical simulation results, based on coarse-grained atomistic potentials [1, 2], that capture debris formation at a contact junction. The two mechanisms at play in our simple model are plastic shearing of contacting asperities, and (if enough elastic energy is available) crack propagation leading to debris creation. This ductile to brittle transition was shown to occur at a material-dependent critical contact-junction size [2]. We have shown that, in the simple situation of an isolated micro contact, the final debris size scales with the maximum junction size attained upon shear, and with the total shear-load mechanical work. This permits to draw analogies with Archard adhesive wear model [3], which states that the wear volume is proportional to the normal load, the sliding distance, while it is inversely proportional to the hardness of the softer material in contact.

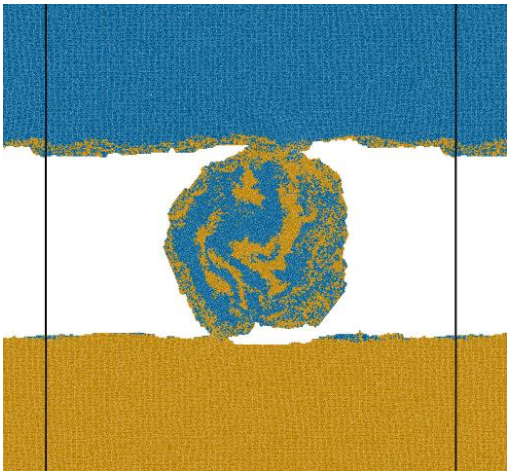

Figure 1: Debris particle rolling between two surfaces under a constant normal pressure. Colours show material particles origin: top material is blue, bottom material is yellow. Black vertical lines indicate periodic boundary conditions

We also discuss recent results regarding the long term evolution of surface roughness. Investigating different initial conditions, e.g. surface geometries, we reveal that after a sufficiently long wear process the initial conditions are forgotten, and the resulting worn surfaces are self-affine. The worn surfaces are characterized by a Hurst exponent between 0.6 and 0.8, suggesting that the process is not random. During the wear process, the debris particle that is formed

and wears the surfaces is also investigated (Figure 1). We show that its volume increases throughout the process, indicating that the mechanism of detaching material from the bulk is favoured over detaching material from the particle.

2. Mesoscale wear model

Next, we incorporate this single-asperity understanding in a novel mesoscale model [4], which aims at estimating from first principles the wear coefficient, a notoriously little understood parameter in wear models. We estimate the amount of volume of debris formed for a given applied load, using the probability density of micro-contact sizes. A crucial element of this mesoscale model is the distribution of surface heights, which should evolve as wear processes take place.

In order to obtain a realistic distribution of micro-contact sizes, we model the contact between solids with self-affine rough surfaces [5, 7]. We propose two interpretations of the wear coefficient that are applied to the contact model: one based on Archard's view of the wear coefficient as the probability of debris formation, and one stemming from up-scaling of single asperity wear considerations. Both are based on a Griffith-like criterion that leads to the emergence of a critical length scale governing wear particle formation [1]. These developments allow us to bring physical properties of the interface [1] as well as geometrical and mechanical information into the estimation of the wear coefficient [4], figure 2. This opens the path to many potential developments of this model, including elasto-plastic contact and surface roughness evolution.

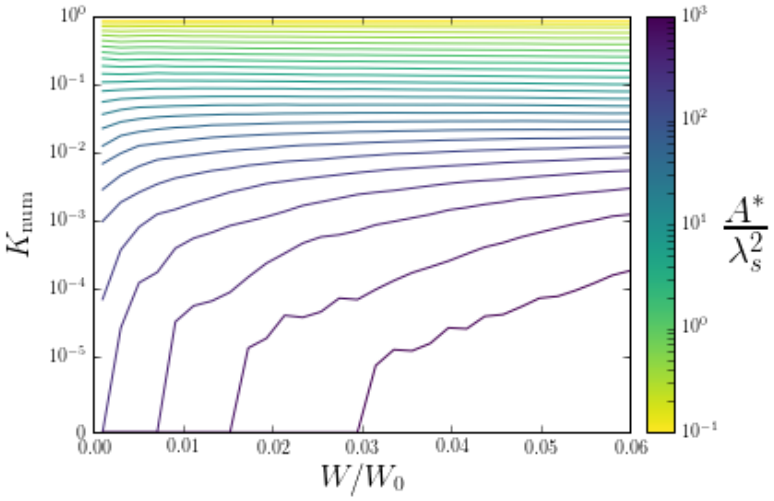

Figure 2: Wear coefficient as a function of the load, for different values of the critical micro-contact area A. The wear coefficient increases with the load up to a constant plateau, which is a characteristic feature of mild adhesive wear [6].*

Acknowledgments The authors acknowledge the financial support of Swiss National Science Foundation, through project 200021_162569.

References

[1] Aghababaei, R., Warner, D.H., Molinari, J.F., "On the debris-level origins of adhesive wear", PNAS, **114**(30), pp. 7935-7940 , 2017.

[2] Aghababaei, R., Warner, D.H., Molinari, J.F., "Critical length scale controls adhesive wear mechanisms", Nature Communications, 11816, 2016.

[3] Archard, J.F., "Contact and rubbing of flat surfaces", Journal of Applied Physics, **24**, 981, 1953.

[4] Frérot, L., Aghababaei, R., Molinari, J.F., "On understanding the wear coefficient: from single to multiple asperities contact", submitted to JMPS, 2017.

[5] Hu, Y.Z., and K. Tonder. "Simulation of 3-D Random Rough Surface by 2-D Digital Filter and Fourier Analysis." International Journal of Machine Tools and Manufacture, **32**, 83-90, 1992.

[6] Burwell, J. T., and C. D. Strang. "On the Empirical Law of Adhesive Wear." Journal of Applied Physics, **23**, 18-28, 1952.

[7] Stanley, H. M., and T. Kato. "An FFT-Based Method for Rough Surface Contact." Journal of Tribology, **119**, 481-85, 1997.

APPLICATION OF MULTIPHASE POROUS MEDIA MECHANICS FOR ASSESSMENT OF BUILDING MATERIALS DURABILITY

D. Gawin[1*], M. Koniorczyk[1], and F. Pesavento[2]

[1]*Department of Building Physics and Building Materials, Lodz University of Technology, Lodz, Poland*
[2]*Department of Civil, Environmental and Architectural Engineering, University of Padova, Padova, Italy*

e-mail: dariusz.gawin@p.lodz.pl

1. Modeling durability of building materials

Durability of building materials is of great practical importance. It may be analysed by means mechanics of multiphase porous media, non-equilibrium thermodynamics and damage mechanics. A general approach [1] to modelling various degradation processes in partially saturated porous building materials, due to combined action of variable chemical, hygro-thermal and mechanical loads, is presented. Kinetics of physico-chemical processes, like: salt crystallization/dissolution [2], calcium leaching [3], alkali silica reaction (ASR) [4], and water freezing/thawing [5], is described with evolution equations in order to take into account variable hygro-thermal conditions. The mathematical model consists of the mass-, energy- and momentum balances, the evolution equations describing chemical reactions/processes, as well as the constitutive and physical relations. The model state variables are capillary pressure, p^c, gas pressure, p^p, temperature, T, displacement vector, $\mathbf{u}$, and, if necessary, chemical species concentration, $c_{chem.}$ The internal variables of the model are mechanical damage parameter, d, chemical damage, V, and chemical process extent, Γ_{ch}. The most important mutual couplings between the chemical, hygral, thermal and deterioration processes are considered and discussed, both from the viewpoint of physicochemical mechanisms and mathematical modelling.

2. Kinetic model of chemical- and deterioration processes

Following linear non-equilibrium thermodynamics, the rate of chemical process, $\dot{\Gamma}_{ch}$ (e.g. salt crystallization – dissolution, calcium leaching, ASR progress, water freezing – ice thawing), is expressed in terms of the process affinity A_{ch} (i.e. the difference between chemical potentials of the actual state and equilibrium one) and the process constant k, which is dependent on the process characteristic time τ_{ch} and temperature T,

$$\dot{\Gamma}_{ch} = k \cdot A_{ch} . \tag{1}$$

Specific form of relationship (1) for a considered process is given in [2] for salt crystallization – dissolution, in [3] for non-isothermal calcium leaching, in [4] for alkali silica reaction, and in [5] for water freezing – thawing. Material deterioration may be directly dependent on the progress of chemical process, e.g. chemical damage for calcium leaching [3], or caused by material cracking due to expanding strains, e.g. for ASR [4], or crystallization pressure exerted on the skeleton, e.g. for water freezing [5] or salt crystallization [6]. The latter process is modelled by means of the delayed damage model, where the rate of mechanical damage, $\dot{d}$, is directly considered, as presented and discussed in [5, 6].

3. Numerical solution

The weak form of the model governing equations is obtained with Galerkin's method, and state variables are discretized in space by means finite element method and in time domain using implicit finite difference scheme, resulting in the following equation set [1],

$$\mathbf{C}_{i,j}\left(\mathbf{X}_j^{n+1}\right)\frac{\mathbf{X}_j^{n+1}-\mathbf{X}_j^{n}}{\Delta t}+\mathbf{K}_{i,j}\left(\mathbf{X}_j^{n+1}\right)\mathbf{X}_j^{n+1}-\mathbf{f}\left(\mathbf{X}_j^{n+1}\right)=\mathbf{0}, \tag{2}$$

where $\mathbf{X}_j^{n+1}$ is the vector of nodal values of state variables at time step *n+1*, $\mathbf{C}_{i,j}(\mathbf{X}_j^{n+1})$ and $\mathbf{K}_{i,j}(\mathbf{X}_j^{n+1})$ are the coupling matrices, and $\mathbf{f}(\mathbf{X}_j^{n+1})$ is the vector considering BCs and source terms, (*i,j= g, c, T, u_x, u_y*). The nonlinear equation set (2) is solved by means of a monolithic Newton-Raphson type iterative procedure [1]. At each iteration the discretized form of kinetic equation (1) is solved in all the Gauss points.

4. Application examples

Four examples of the model application for analysing transient chemo-hygro-thermo-mechanical processes in porous building materials are presented and discussed. The first example concerns the salt crystallization during drying of a wall made of concrete and ceramic brick, causing degradation of surface layer due to development of crystallization pressure. The second one deals with calcium leaching from a concrete structure due to chemical attack of pure water, exposed to gradients of temperature and pressure. The third one describes cracking of concrete element, caused by development of expanding products of ASR. The fourth example concerns freezing – thawing of a wet concrete wall in variable hygro-thermal conditions.

Some exemplary results of numerical simulations concerning moisture content, ASR progress and shape deformation in a retaining wall exposed for 2 years to external air with variable temperature and relative humidity from one side, and the other side and its footing being in direct contact with the ground, are presented in Fig. 1. The results showing calcium content distribution in a concrete column exposed to 20-years action of pure water having temperature of 25°C or 60°C, are presented in Fig. 2.

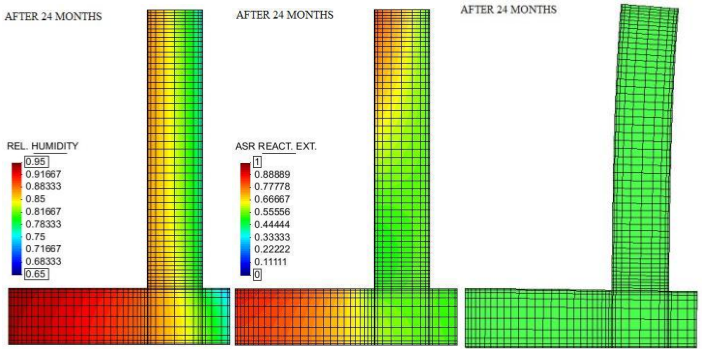

Figure 1: Results of simulations for a retaining concrete wall exposed to ASR for 24 months: relative humidity, reaction extent and deformed configuration (shown with factor 25x)

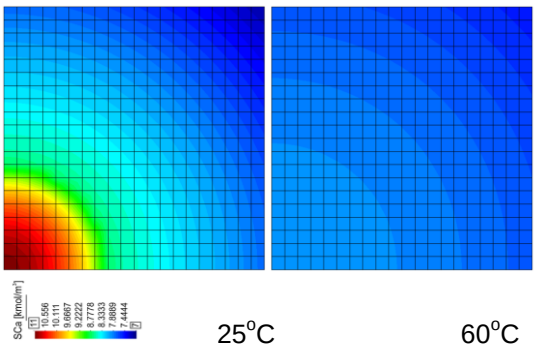

Figure 2: Calcium content in a concrete column exposed to calcium leaching for 20 years in pure water at temperature of 25°C and 60°C.

5. References

[1] D. Gawin, M. Koniorczyk and F. Pesavento. Modelling of hydro-thermo-chemo-mechanical phenomena in building materials. *Bull. Pol. Ac.: Tech.*, 61(1):51–63, 2013.

[2] M. Koniorczyk and D. Gawin. Modelling of salt crystallization in building materials with microstructure – poro-mechanical approach. *Construction and Building Materials*, 36:860–873, 2012.

[3] D. Gawin, F. Pesavento and B. A. Schrefler. Modeling deterioration of cementitious materials exposed to calcium leaching in non-isothermal conditions. *Comput. Methods Appl. Mech. Engrg.*, 198(37-40):3051–3083, 2009.

[4] F. Pesavento, D. Gawin, M. Wyrzykowski, B. A. Schrefler and L. Simoni. Modeling alkali-silica reaction in non-isothermal, partially saturated cement based materials. *Comput. Methods Appl. Mech. Engrg.*, 225-228:95–115, 2012

[5] M. Koniorczyk, D. Gawin and B. A. Schrefler. Modelling evolution of frost damage in fully saturated porous materials exposed to variable hygro-thermal conditions. *Comput. Methods Appl. Mech. Engrg.*, 297:38–61, 2015.

[6] M. Koniorczyk, D. Gawin and B. A. Schrefler. Multiphysics model for spalling prediction of brick due to in-pore salt crystallization. *Computers and Structures*, 196:233–245, 2018.

Acknowledgments The authors acknowledge the financial support of National Science Center – Poland, grant No. UMO-2014/15/B/ST8/02854.

A SIMPLE AND EFFICIENT GEOMETRIC NONLINEAR ROTATION-FREE TRIANGLE AND ITS APPLICATION IN DRAPE SIMULATION

K.Y. Sze[1], Y.X. Zhou[2]

[1]*Department of Mechanical Engineering, the University of Hong Kong, Pokfulam, Hong Kong, China.*
[2]*Faculty of Science, Harbin Institute of Technology (Shenzhen), Shenzhen, Guangdong, China.*

E-mail: [1]*kysze@hku.hk*

The idea of the rotation-free element that possesses no rotational dofs for thin shell analyses can be dated back to the 1970s. The rotation-free element does not follow the finite element format in the sense that its integration domain is smaller than its interpolation domain. Different methods including hinge-angle, polynomial interpolation, finite volume method, subdivision surface method, smoothed finite element method, etc. have been employed to quantify the curvature and, thus, the bending energy in the integration domain. Here, a simple and efficient geometric nonlinear rotation-free triangle is presented. With reference to Figure 1, a flat corotational strain-free configuration is set up with 5^C coincident with 5' and 4^c-5^c -6^c coplanar with 4'-5' -6'. Let **n** be the unit vector normal to 4^c-5^c-6^c, the deflection from 4^c-5^c -6^c to with 4'-5'-6' parallel to **n** is

$$w = \mathbf{n}^T(\mathbf{U} - \mathbf{U}^C) \tag{1}$$

where $\mathbf{U}^C$ is the rigid body motion that brings 1-to-6 to 1^c-to-6^c. When the radius of curvature is considerably larger than the integration domain and the inplane stretching is not significant, **n** and **U** - $\mathbf{U}^C$ are nearly parallel. Thus,

$$\mathbf{U} - \mathbf{U}^C = \mathbf{n}\mathbf{n}^T(\mathbf{U} - \mathbf{U}^C) \quad , \quad \mathbf{U}_{,pq} = \mathbf{n}\mathbf{n}^T\mathbf{U}_{,pq} \qquad \text{for} \qquad p, q = x, y. \tag{2}$$

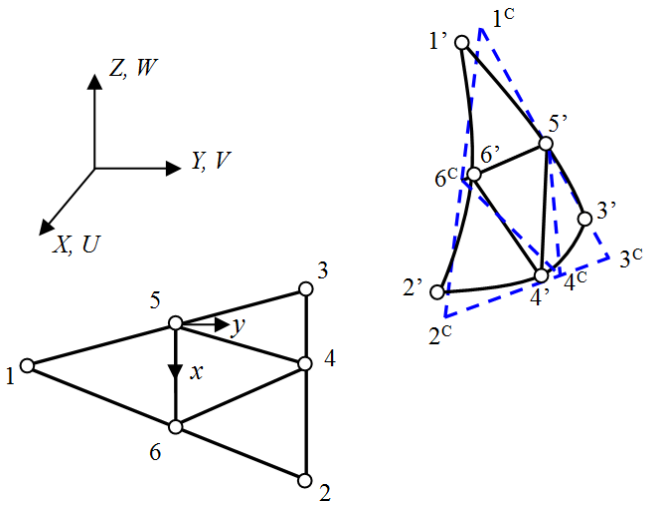

Figure 1. 1-to-6, 1'to-6' and 1^c-to-6^c show the initial, deformed and flat corotational configurations.

By virtue of the quadratic interpolation whose second order derivatives with respect to (x,y) are constant, $\mathbf{U}_{,pq}$ and the displacement vector of the element patch $\mathbf{U}_{1..6}$ is related by a constant matrix **B**. The bending energy can be expressed as

$$E^b = \frac{A}{2}\begin{Bmatrix} w_{,xx} \\ w_{,yy} \\ 2w_{,xy} \end{Bmatrix}^T \mathbf{D} \begin{Bmatrix} w_{,xx} \\ w_{,yy} \\ 2w_{,xy} \end{Bmatrix} = \frac{A}{2}\begin{Bmatrix} \mathbf{U}_{,xx} \\ \mathbf{U}_{,yy} \\ 2\mathbf{U}_{,xy} \end{Bmatrix}^T \begin{bmatrix} D_{11}\mathbf{I}_3 & D_{12}\mathbf{I}_3 & D_{13}\mathbf{I}_3 \\ D_{21}\mathbf{I}_3 & D_{22}\mathbf{I}_3 & D_{23}\mathbf{I}_3 \\ D_{31}\mathbf{I}_3 & D_{32}\mathbf{I}_3 & D_{33}\mathbf{I}_3 \end{bmatrix} \begin{Bmatrix} \mathbf{U}_{,xx} \\ \mathbf{U}_{,yy} \\ 2\mathbf{U}_{,xy} \end{Bmatrix} = \frac{A}{2}\mathbf{U}_{1..6}^T(\mathbf{B}^T\mathbf{D}\mathbf{B})\mathbf{U}_{1...6} \tag{3}$$

where A is the area of 4-5-6, $\mathbf{D} = [D_{ij}]$ is the bending rigidity matrix and **D** is self-defined. Consequently, the tangential bending stiffness matrix, which is the second derivative of E^b with respect to $\mathbf{U}_{1..6}$, is a contant matrix and needs not be updated in the iterative solution procedure. This feature renders the triangle

particularly simple and efficient [1]. The membrane energy can be considered by using the CST. Figure 2 shows the prediction of the triangle in a poupluar benchmark problem. It was latter noted that a spurious folding mode appear. The mode, however, can be suppressed effectively by deriving the membrane energy from a 6-node interpolation of displacement [2], see Figures 3a and 3b.

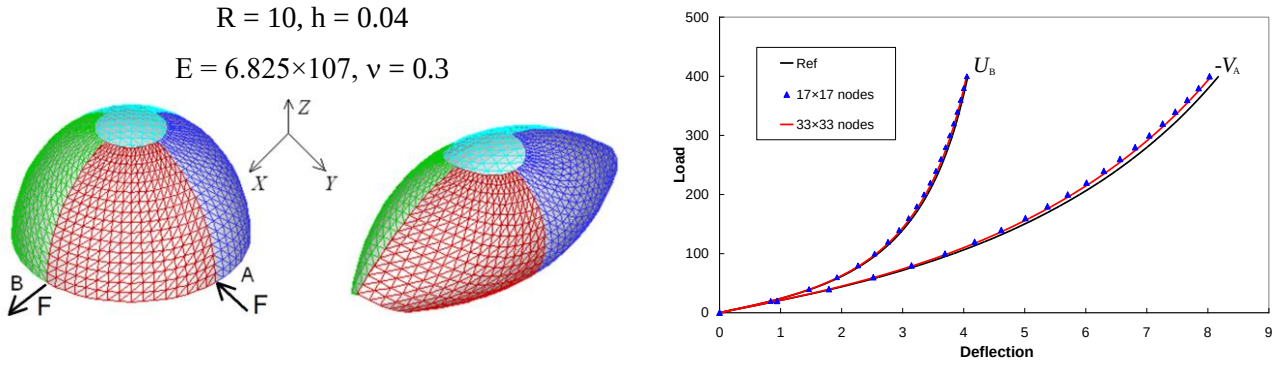

Figure 2. The undeformed and the predicted deformed geomtry in a popular elastic shell problem.

Drape simulation finds its applications in fashion design, e-commerce of clothing and production of animated movies. Fabric drapes are typical large displacement, large rotation and small strain problems. Compared with the conventional geometric non-linear shell analysis, computational drape analysis is particularly challenging due to the small bending to tensile rigidity ratio of most fabric. This presentation will discuss how the rotation-free triangle is applied to drape simulation which considers not only large displacement/rotation but also adaptive remeshing, dynamic, contact/collision and drape over moving manikin [2,3], see Figure 3c.

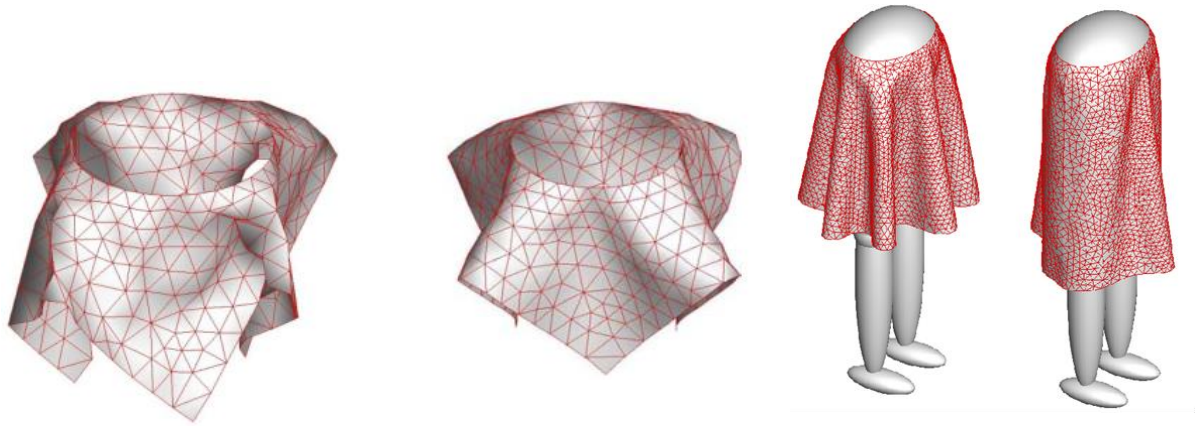

(a) (b) (c)

Figure 3. Non-physical sharp folds in (a) are eliminated in (b). (c) Skirts drape over manikins.

References

[1] Y.Z.Zhou, K.Y.Sze. A geometric nonlinear rotation-free triangle and its application to drape simulation. Inter.J. Numer.Methods Engrg. 89: 509-536, 2012.

[2] K.Y.Sze, Y.X.Zhou. An efficient rotation-free triangle for drape/cloth simulations - Part I: model improvement, dynamic simulation and adaptive remeshing. *Inter J Comput. Methods* 13(3): 1650021 (27 pages). DOI: 10.1142/S0219876216500213, 2016

[3] Y.X.Zhou, K.Y.Sze. An efficient rotation-free triangle for drape/cloth simulations - Part II: collision handling and drape over moving manikin. In preparation

RESTORING STONE MONUMENTS OF CULTURAL HERITAGE: CRITICAL ASPECTS FROM THE ENGINEERING POINT OF VIEW

S. K. Kourkoulis

Laboratory for Testing and Materials, Department of Mechanics, National Technical University of Athens, Theocaris Building, Zografou Campus, 157 73, Greece, e-mail: stakkour@central.ntua.gr

1. General

Restoration of monuments is a multi-disciplinary field demanding harmonious cooperation between archaeologists, architects and engineers and the decisions made arise, usually, as compromises between de facto conflicting approaches. From the engineering point of view, the key issue is the restoration of the structural integrity of the monument, keeping in mind that any intervention should be restricted to the minimum possible and, also, that it should be implemented according to a reversible approach. Moreover, any intervention should respect and protect the authentic structural elements while the materials used should be compatible (from both the mechanical and the physicochemical aspect) to the authentic building material. The extent of acceptable interventions is outlined in the "Venice Charter" [1]. In the present study attention is focused to the restoration of stone monuments of classical Cultural Heritage, taking advantage of the experience gathered from the restoration project of the monuments of the Acropolis of Athens and mainly from the Parthenon Temple.

2. Experience from the restoration of the Acropolis monuments: The Parthenon project

Ancient Greek temples were built using natural building stones quarried from the near vicinity of the place of the temple. Among the very few exceptions are the monuments of the Acropolis of Athens, which were built using marble quarried from mount Pentelicus, more than 30 km away from the Acropolis hill. It is a fine-grained white marble consisting of calcite (~98%) and very small amounts of muscovite, sericite, chlorite and quartz. It is a bimodular, slightly nonlinear, anisotropic material, usually, modelled as transversely isotropic [2].

Given that quite a few structural elements of the Acropolis monuments are damaged, an ambitious restoration project is in progress under the auspices of the "*Committee for the Conservation of the Acropolis Monuments*". The technique adopted for restoring fragmented members is based on the use of metallic reinforcements placed either in holes drilled in the marble body (threaded bars, Fig.1a) or in grooves sculptured on their surface (e.g., "I"-shaped beams, Fig.1b). Both holes and grooves are then filled with a cement-based material [3].

3. Modelling the response of restored structural elements. Detecting pre-failure indicators

The restoration technique described above generates a three-material-complex (marble-cement-titanium) with two "hidden" interfaces (i.e., marble-to-cement and cement-to-titanium). Given that damage mechanisms are firstly activated along these interfaces, any attempt to model the mechanical response of the restored elements necessitates data from these interfaces. Such data can be only obtained with the aid of novel sensing techniques,

Figure 1: (a) In-situ restoration of one of the longest epistyles of the Acropolis Propylaea using threaded titanium bars; (b) Inter-connecting epistyles of the Parthenon Temple using "I"-shaped titanium beams.

like, for example, Acoustic Emissions (AE), Pressure Stimulated Currents (PSCs) [4], Optical Fibers etc. In addition, the unique cultural value of these monuments renders continous Structural Health Monitoring (SHM) a pressing demand. The relative data required must be obtained with the aid of cheap, reliable and very small sensors, since they should not destroy the aesthetic splendor of the monuments. In the direction of providing some answers to the above open problems, various experimental protocols are implemented in the Laboratory for Testing and Materials of the National Technical University of Athens. Both traditional and innovative sensing techniques are used in a combined manner, for validation reasons and, also, in order to properly calibrate the outcomes of the novel techniques, which in most cases are of qualitative rather quantitative nature.

As an example, results of an ongoing project related to the response of the restored connection of marble epistyles are here discussed. The specimens consisted of two marble blocks, joined together by means of an "I"-shaped connector and suitable cementitious material. Loading/gripping were achieved by an in-situ improvised set-up assuring pure shear loading of the connection, a challenging task, taking into account the asymmetries of the specimens (Fig.2). The specimens were monitored by a system of eight R15α AE sensors, two electric sensors (recording the PSCs with the aid of sensitive electrometers) and a 3D-Digital Image Correlation (DIC) system. In parallel, traditional sensing tools (electrical strain gauges, LVDTs and dial gauges) were also used.

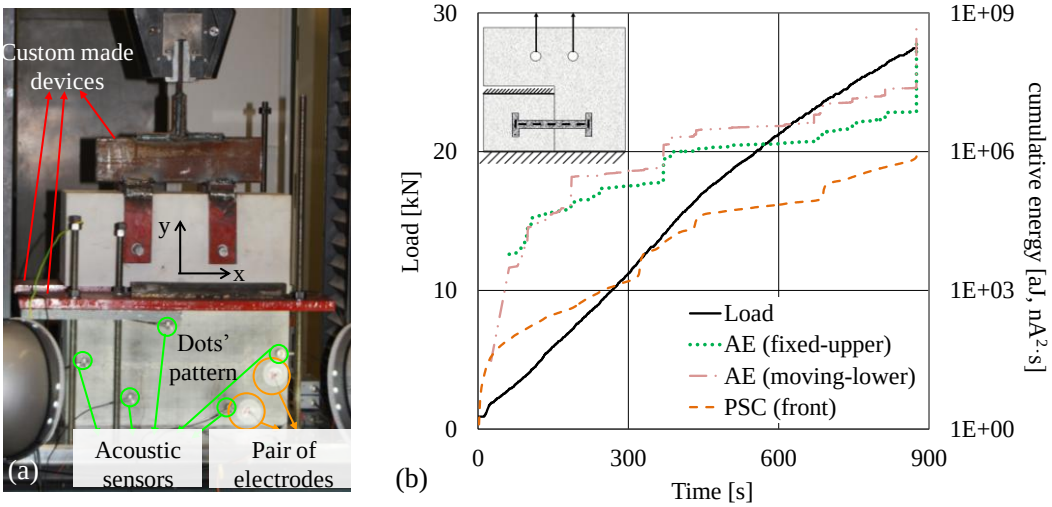

Figure 2: (a) The experimental set-up; (b) Time evolution of the load induced, in juxtaposition to that of the cumulative energy of the Acoustic Emissions and of the Pressure Stimulated Currents.

4. Some concluding remarks

The data gathered during the tests (see, for example, Fig.2b, in which the time evolution of the cumulative energy of the AE and the PSCs is plotted in juxtaposition to that of the load imposed) indicate that both the AE and PSC techniques "follow" the mechanical response of the restored epistyles according to a satisfactory manner. Moreover, both techniques provide early signs concerning the entrance of the system to its "critical stage", i.e., clearly distinguishable pre-failure indicators. Taking into account the low cost of the sensors of the PSC-technique and, also, their small size, it appears that this technique is an attractive alternative for SHM of restored elements of ancient monuments. The fact that the PSC data are in excellent accordance to those of the AE technique [5] provides a reliable calibration tool for the PSC technique (given that the AE technique is based on a well founded scientific basis and it is nowadays considered as a mature sensing system).

References

[1] ICOMOS. The Venice Charter. *2nd Int. Congress of Architects and Technicians of Historic Monuments*. Venice, 1964.
[2] S.K. Kourkoulis, G.E. Exadaktylos and I. Vardoulakis. U-notched Dionysos-Pentelicon marble in three point bending: The effect of nonlinearity, anisotropy and microstructure. *Int. J. Fracture*, 98(3-4):369-392, 1999.
[3] M. Korres and Ch. Bouras. *Study for the Parthenon's restoration (in Greek)*. Athens: Ministry of Culture, 1983.
[4] D. Triantis, I. Stavrakas, A. Kyriazopoulos, G. Hloupis and Z. Agioutantis. Pressure stimulated electrical emissions from cement mortar used as failure predictors. *Int. J. Fracture*, 175:53-61, 2012.
[5] S.K. Kourkoulis, E.D.Pasiou, I. Dakanali, I.Stavrakas and D.Triantis. Notched marble plates under tension: Detecting pre-failure indicators and predicting entrance to the critical stage. *Fatigue Fract. Eng. Mater. Struct.*, in press, 2018.

STRAIN GRADIENT AND COSSERAT CRYSTAL PLASTICITY WITH APPLICATION TO GRAIN BOUNDARY MIGRATION

Samuel Forest[1], Anna Ask[1], and Benoît Appolaire[2]

[1]*Centre des Matériaux, Mines ParisTech CNRS, Paris, France*
[2]*Institut Jean Lamour, Université de Lorraine, Nancy, France*

e-mail: samuel.forest@ensmp.fr

1. Stored energy by means of the dislocation density tensor in crystals

Internal stresses in crystalline solids are often induced by the development of non-homogeneous plastic deformation inside the grains of metallic polycrystals. The latter can be accounted for by means of the dislocation density tensor defined as the rotational part of the plastic deformation field. Energy is stored in that way and represented by appropriate terms in the Helmholtz free energy density function. Different forms of this potential will be discussed highlighting the various types of single crystal constitutive behaviour, especially under cyclic loading [6, 9].

Fig. 1 shows the response of a single crystal under shear with microhard boundary conditions inducing the pile-up of dislocations at grain boundaries. These non convex loops are obtained when the free energy density is proportional to the norm of the dislocation density tensor or to its logarithm. They correspond to the concept *first in–last out* for dislocations at grain boundaries [3].

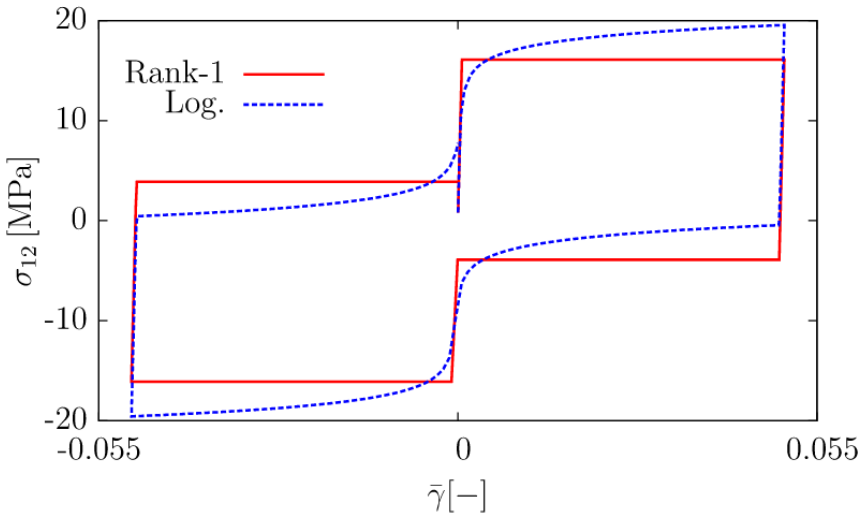

Figure 1: Non-convex cyclic loops in simple shear using two different free energy functions depending on the dislocation density tensor, after [9].

2. Cosserat crystal plasticity

The lattice curvature tensor can be seen as an approximation of the full dislocation density tensor. It has the advantage that it can be measured in a standard way by means of Electron Back-Scatter Diffraction, thus allowing for direct comparison between experiment and computations. The previous strain gradient plasticity model can be reduced to a Cosserat theory of crystal plasticity [5, 7]. Finite element simulations of the deformation of Cosserat and strain gradient polycrystalline aggregates will be presented.

3. Phase field modelling of grain boundary motion

This Cosserat theory of crystal plasticity is finally coupled to the phase field appoach to simulate the evolution of the polycrystalline microstructure. For that purpose, a phase field variable representing the crystal order is introduced, having minimal values inside diffuse grain boundaries of the polycrystal [1, 2, 8]. The gradient of stored energy serves as a driving force for grain boundary migration. Lattice rotation then has two origins: plasticity driven lattice rotation in the bulk of the grain, and lattice reorientation inside moving grain boundaries. The fully coupled Cosserat mechanical and phase field framework is used to simulate dynamic recrystallization at the mesoscale [4].

Fig. 2 shows the field of lattice orientation, cristallinity parameter and stored energy in deformed aluminium. The sweeping of some grain areas by grain boundaries is clearly visible on the right. Dynamic and static dislocation recovery takes place in the diffuse boundary.

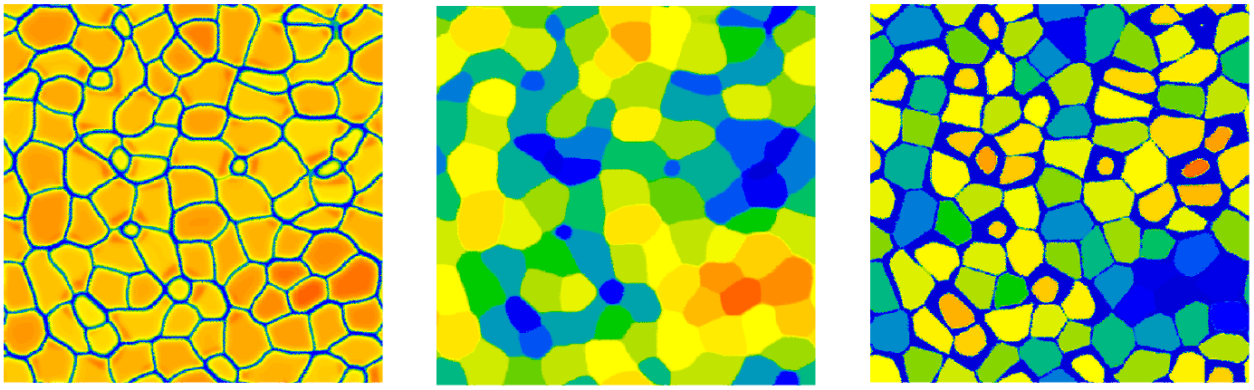

Figure 2: Phase field simulation of grain boundary migration in a deformed polycrystal, after [2]

References

[1] G. Abrivard, E.P. Busso, S. Forest, and B. Appolaire. Phase field modelling of grain boundary motion driven by curvature and stored energy gradients. part i: theory and numerical implementation. *Philosophical Magazine*, 92:3618–3642, 2012.

[2] G. Abrivard, E.P. Busso, S. Forest, and B. Appolaire. Phase field modelling of grain boundary motion driven by curvature and stored energy gradients. part ii: Application to recrystallisation. *Philosophical Magazine*, 92:3643–3664, 2012.

[3] R. J. Asaro. Elastic–plastic memory and kinematic hardening. *Acta Metallurgica*, 23:1255–1265, 1975.

[4] A. Ask, S. Forest, B. Appolaire, K. Ammar, and O. U. Salman. A cosserat crystal plasticity and phase field theory for grain boundary migration. *submitted*, 2018.

[5] S. Forest, G. Cailletaud, and R. Sievert. A Cosserat theory for elastoviscoplastic single crystals at finite deformation. *Archives of Mechanics*, 49:705–736, 1997.

[6] S. Forest and N. Guéninchault. Inspection of free energy functions in gradient crystal plasticity. *Acta Mechanica Sinica*, 29:763–772, 2013.

[7] J.R. Mayeur and D.L. McDowell. A comparison of gurtin type and micropolar theories of generalized single crystal plasticity. *International Journal of Plasticity*, 57:29–51, 2014.

[8] V. de Rancourt, B. Appolaire, S. Forest, and K. Ammar. Homogenization of viscoplastic constitutive laws within a phase field approach. *Journal of the Mechanics and Physics of Solids*, 88:35–48, 2016.

[9] S. Wulfinghoff, S. Forest, and T. Böhlke. Strain gradient plasticity modeling of the cyclic behavior of laminate microstructures. *Journal of the Mechanics and Physics of Solids*, 79:1–20, 2015.

ON OBJECTIVE DYNAMIC FAILURE PREDICTIONS USING LOCAL CONSTITUTIVE MODELS

O. Allix

LMT/ENS-Paris-Saclay/CNRS/ Université Paris-Saclay, Cachan, France

Institut Universitaire de France

e-mail: olivier.allix@ens-paris-saclay.fr

1. Context: the modelling and simulation of damage and failure

Today, realistic simulations of complex industrial problems including all their technological complexity require using legacy codes. In the case of the simulation of failure, two main difficulties arise. The first one concerns only quasi-static or slow dynamic problems. In this case, implicit schemes should be the dominant approaches. However the numerous instabilities associated with damage and cracking make the convergence problematic and sometimes impossible. Here, path following techniques are mandatory and are often used in combination with viscosity. In order to ensure convergence, explicit algorithms are therefore mainly used by industrials. In this case, mass and time scaling techniques allow for the increase of the critical time step to allow for quasi-static simulation. It is unclear though how the use of these techniques affects the prediction of failure.

The second difficulty is the occurrence of spurious mesh dependence in the failure prediction. A huge literature has been devoted to non-local model with variants from non-local integral approaches to explicit and implicit gradient approaches or Cosserat models [1-2]. Despite of all this studies the development of these approaches in an industrial context is still seldom. The main reason is probably the fact that non-locality implies many and non-obvious code developments, identification practices are also an issue.

2. Rate dependent model and localization

That is why we have sought for another, even if maybe less general, possibility, to overcome the difficulty, the use of rate dependent models. Needleman was possibly the first to discuss how, in statics, the use of viscosity can allows to conserve the elliptic property of a plastic negative hardening model and, thus should eliminate pathological mesh-sensitivity [3]. Several models have been proposed in order to control localization by viscosity, particularly for ductile materials with negative hardening [4]. Nevertheless, it has been observed that the crack growth behavior predicted by simulations based on a visco-plastic version of the GTN model is mesh sensitive [5]. Other experiences were also deceptive showing that spurious localization is not automatically circumvent when using viscous model.

3. Bounded rate model

That is why we have proposed in the concept of bounded damage rate model, which has been used, for dynamic loading as impact, to predict the failure of composite materials but also the one of metallic material in the case of ductile failure [5]. A physical interpretation of the model is that a continuous damage variable results from a complex averaging process of micro flaws each of which having a finite propagation velocity, leading thus to a bounded damage rate. The main limitation of such approaches, has can be seen so far, is that such model should be used in combination with dynamic analyses.

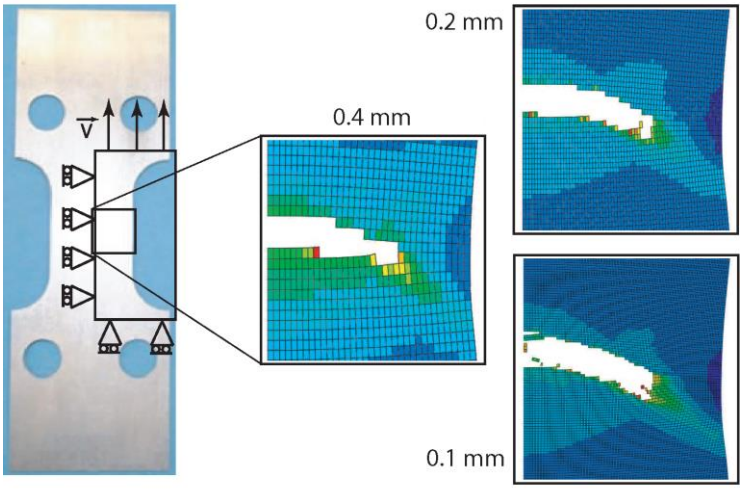

Figure 1: Mesh independent prediction in dynamics using a bounded rate ductile damage model [5]

4. Toward objective quasi-static failure prediction with bounded rate model

Recently we have tried to make use of such model for the quasi-static failure prediction of metallic materials. The proposed path is the combination of explicit simulations and bounded rate models using adapted scaling techniques aiming at performing mesh independent quasi-static simulations [6].
After an overview concerning the basis of bounded rate model illustrated on several examples the presentation explores its extension to quasi-static situations on examples relevant for turbo-machinery disks.

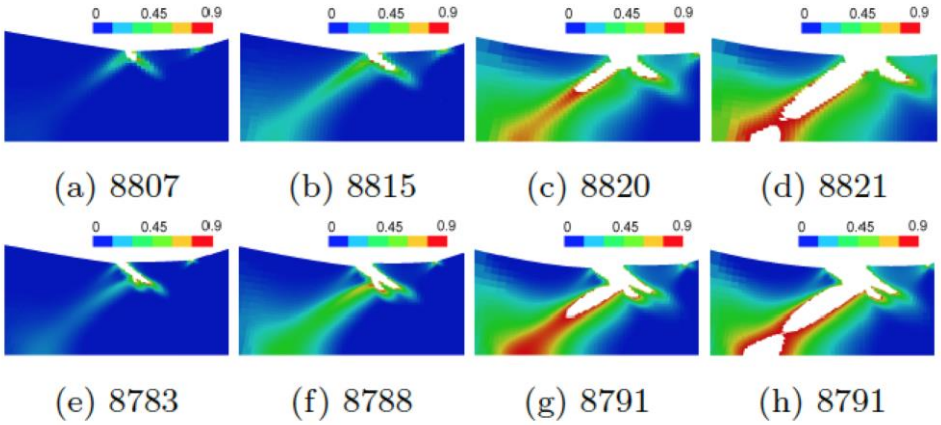

Figure 2: Comparison of the crack pattern of a 2D rotating disk at four (close) instants for two different meshes and different time scales for a scaled dependant damage rate model of Lemaitre type [6]

5. References

[1] J-J. Marigo, J-J, C. Maurini, P-K Khim, An overview of the modelling of fracture by gradient damage models, Meccanica, 51 (2016) 3107-3128, 2016
[2] Peerlings, R.H.J., Geers, M.G.D., De Borst, R., Brekelmans, W.A.M., 2001. A critical comparison of non-local, gradient enhanced softening continua. In: International Journal of Solids and Structures, 38, 7723-7746.
[3] Needleman, A., 1988. Material rate dependence, mesh sensitivity in localization problems. In: Computer Methods in Applied Mechanics and Engineering, 63, 69-85.
[4] Sluys LJ and De Borst R (1992) Wave propagation, localization in a rate-dependent cracked medium: model formulation, one dimensional examples. International Journal of Solids and Structures 29: 2945–2958.
[5] O. Allix, The bounded rate concept: a framework to deal with objective failure predictions in dynamic within a local constitutive model, International Journal of Damage Mechanics (2012)
[6] D. Lindner, O. Allix, O. Paulien-Camy, An attempt to use bounded-rate model for objective simulation of quasi-static failure in explicit dynamics: mastering of scaling techniques, to be submitted to Int. J. of Damage Mechanics

Session S01: Elasticity, plasticity and phase transition

Organizers: S. Forest (MINES Paristech, CNRS, Paris), H. Petryk (IPPT PAN, Warsaw)

RATE-INDEPENDENT DISSIPATION IN PHASE-FIELD MODELING OF EVOLVING MICROSTRUCTURE

K. Tůma[1], S. Stupkiewicz[2], and H. Petryk[2]

[1]*Mathematical Institute, Faculty of Mathematics and Physics, Charles University, Prague, Czech Republic*
[2]*Institute of Fundamental Technological Research, Polish Academy of Sciences, Warsaw, Poland*

e-mail: ktuma@karlin.mff.cuni.cz

1. Introduction and description of the model

Shape memory alloys (SMA) are known for the shape memory effect and pseudoelasticity that are associated with the martensitic phase transformation. The material can exist in different phases (austenite, martensite). During the phase transformation the interfaces are created and a part of the energy is stored into them.

Recently, we have developed a rate-dependent phase-field model for evolution of the microstructure. This model belongs to the class of usual viscous-type models, when one phase may transform into another with arbitrarily small thermodynamic driving force. However, experimental results show that for SMA some critical driving force has to be reached for the initiation of the transformation. This is related to the observations that the hysteresis, e.g. in the stress-strain response, does not tend to zero as the rate of loading tends to zero. Thus, the usual viscous models are not capable of describing rate-independent dissipative effects.

The current phase-field model [3] was modified such that it takes into account these phenomena by including a non-smooth mixed-type dissipation potential that combines the viscous and rate-independent contributions, see [4]. The finite element implementation of the model handles the physical constraints on the order parameter together with the non-smooth dissipation potential by a single Lagrange multiplier using the augmented Lagrangian method [2]. By employing this method the originally non-smooth minimization problem is transformed into a smooth saddle-point problem that is convenient to be solved numerically.

2. Results

The main purpose of the numerical examples is to show the differences between the usual viscous dissipation and the rate-independent dissipation. The first example shows the fundamental qualitative difference. Initially, at $t = 0$, a random distribution of two variants of martensite is prescribed in an unconstrained domain. Then, an evolution of the system is simulated until a steady state is attained. Figure 1 shows snapshots of microstructure evolution simulated for the viscous dissipation ($f_c = 0$) and mixed-type dissipation ($f_c = 1\,\mathrm{MPa}$), both starting from the same initial distribution. The system evolves such that the total free energy is decreasing, see Figure 2. For a viscous dissipation, the steady state is a pure single variant and the total free energy attains zero. For the mixed-type dissipation, microstructure evolution stops, the steady state is a non-trivial frozen microstructure and the free energy stays positive.

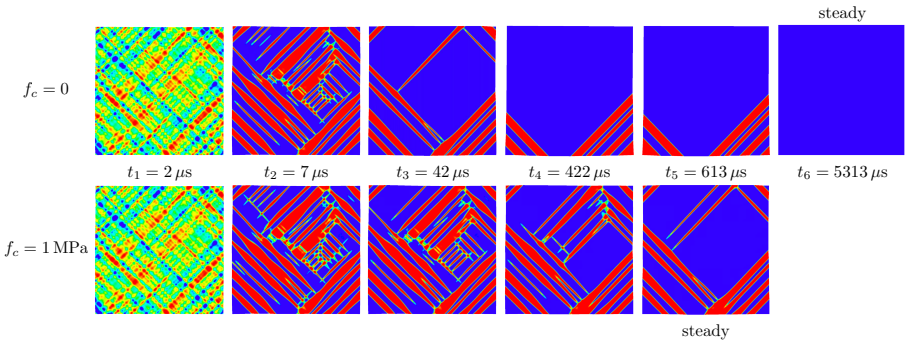

Figure 1: Qualitative difference in the microstructure evolution between the viscous dissipation (top) and mixed-type dissipation (bottom).

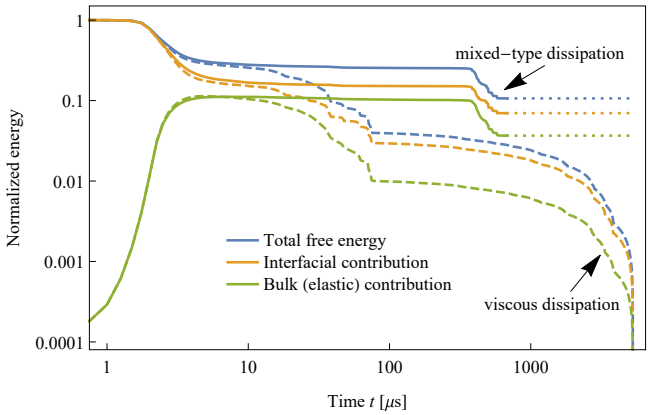

Figure 2: Dependence of free energy on time during microstructure evolution.

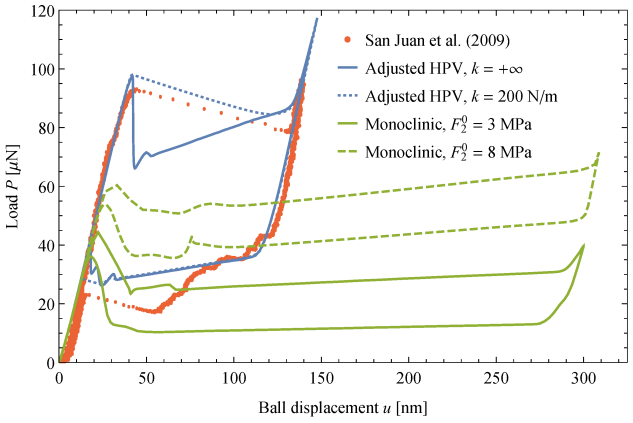

Figure 3: Hysteresis stress-strain curve recorded by San Juan et al. (2009) in the compression experiment.

The second example simulates the experiment by San Juan et al. (2009) in which the micro-pillar is compressed by a nano-indentation device, then released and the corresponding stress-strain curve is recorded, see red points in Figure 3. It shows that the hysteresis curve creates a non-zero area which can not be described by the viscous dissipation. Presented mixed-type dissipation captures the observed curve quite well. Initially, the micro-pillar is in austenite phase and during the compression is being transformed into martensite, see Figure 4.

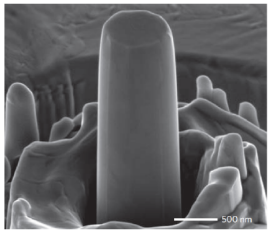

Reproduced from [1].

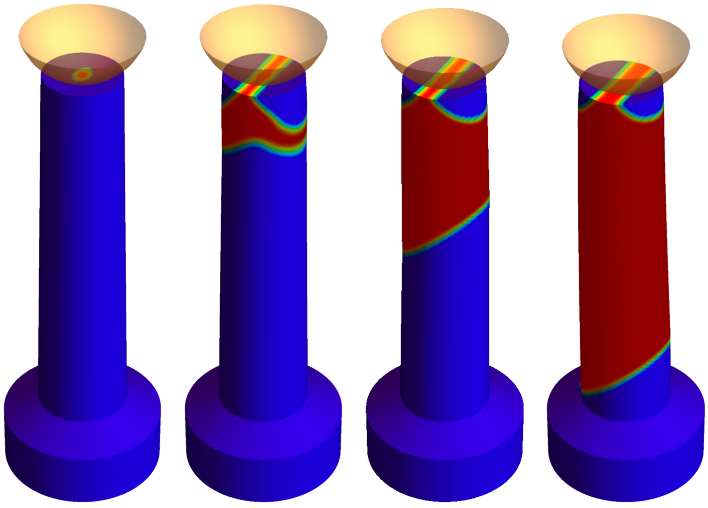

Figure 4: Snapshots of the transformation pattern during the micro-pillar compression (austenite is blue, martensite is red).

Acknowledgments This work has been partially supported by the National Science Center (NCN) in Poland through Grant No. 2015/17/B/ST8/03242.

References

[1] J. San Juan, M.L. Nó, and C.A. Schuh. Nanoscale shape-memory alloys for ultrahigh mechanical damping. *Nat. Nanotechnol.*, 4(7):415–419, 2009.

[2] S. Stupkiewicz and H. Petryk. A robust model of pseudoelasticity in shape memory alloys. *Int. J. Numer. Method. Eng.*, 93:747–769, 2013.

[3] K. Tůma, S. Stupkiewicz, and H. Petryk. Size effects in martensitic microstructures: finite-strain phase field model versus sharp-interface approach. *J. Mech. Phys. Solids*, 95:284–307, 2016.

[4] K. Tůma, S. Stupkiewicz, and H. Petryk. Rate-independent dissipation in phase-field modelling of displacive transformations. *J. Mech. Phys. Solids*, 114:117–142, 2018.

MODEL EQUATIONS OF DIFFUSIVE MICROSTRETCH THERMOELASTICITY WITH MICROTEMPERATURES AND MICROCONCENTRATIONS

A. Chirilă[1] and M. Marin[1]

[1]*Department of Mathematics and Computer Science, Transilvania University of Braşov, Braşov, Romania*

e-mail: adina.chirila@unitbv.ro

1. Motivation

This paper is dealing with the linear theory of microstretch thermoelasticity, a theory that is part of the mechanics of generalized continua and which accurately describes the behaviour of materials with microstructure. The concept of generalized continua was introduced by the Cosserat brothers in 1909, who considered a micropolar continuum to be a collection of interconnected particles in the form of small rigid bodies that have three additional rotational degrees of freedom besides the three translational degrees of freedom from classical continuum mechanics. Cosserat thermoelasticity was generalized to microstretch thermoelasticity by Eringen in 1990 [6] by including the effect of axial stretch during the rotation of molecules.

In this paper, we prove the well-posedness of the mathematical model introduced in [3] for the anisotropic case. The idea is to verify the assumptions from the Lumer-Phillips corollary to the Hille-Yosida theorem. As in [2], the theory we derived is closer to the realistic constitutive structure of solids since it describes thermal-diffusion interactions at the macroscopic and microscopic levels. Given the increasing interest in nanomaterials, it is important to take into consideration both the microtemperatures and the microconcentrations of the nanoparticles. The concept of microconcentrations is a novel one, introduced for the first time in the theory of thermoelasticity in [2] and for the first time in mechanics of generalized continua in [3].

2. Basic equations

The equations of diffusive microstretch thermoelasticity with microtemperatures and microconcentrations [3]

$$
\begin{array}{lll}
t_{ji,j}+\rho f_i=\rho\ddot{u}_i & \rho T_0\dot{S}=q_{i,i}+\rho s & \\
h_{k,k}+g+\rho l=J\ddot{\varphi} & \rho\dot{\varepsilon}_i=q_{ji,j}+q_i-Q_i+\rho G_i & \dot{C}=\eta_{i,i} \\
m_{ji,j}+\varepsilon_{irs}t_{rs}+\rho g_i=I_{ij}\ddot{\varphi}_j & \rho\dot{\omega}_i=\eta_{ji,j}+\eta_i-\tilde{\sigma}_i &
\end{array}
\tag{1}
$$

In the equations above, u_i is the displacement vector field, φ is the microdilatation function, φ_i is the microrotation vector, t_{ij} is the stress tensor, ρ is the reference mass density, f_i is the body force, h_j is the microstretch vector, g is the internal body force, l is the external microstretch body load, m_{ij} is the couple stress tensor, g_i is the body couple density, C is the concentration, η_i is the flux vector of mass diffusion, S is the microentropy. According to [3], the constitutive equations of the mathematical model for the anisotropic case are

$$
\begin{aligned}
t_{ij}&=A_{ijrs}e_{rs}+B_{ijrs}\kappa_{rs}+D_{ij}\varphi+F_{ijk}\zeta_k+L_{ijk}T_k-a_{ij}\theta+d_{ij}C\\
m_{ij}&=B_{rsij}e_{rs}+C_{ijrs}\kappa_{rs}+E_{ij}\varphi+G_{ijk}\zeta_k+M_{ijk}T_k-b_{ij}\theta+f_{ij}C\\
h_i&=F_{rsi}e_{rs}+G_{rsi}\kappa_{rs}+A_{ij}\zeta_j+B_i\varphi-N_{ij}T_j-d_i\theta+\tilde{f}_iC\\
g&=-D_{ij}e_{ij}-E_{ij}\kappa_{ij}-B_i\zeta_i-\xi\varphi-R_iT_i+F\theta-\tilde{g}_1C\\
\rho S&=a_{ij}e_{ij}+b_{ij}\kappa_{ij}+d_i\zeta_i+F\varphi+b_iT_i+a\theta+\varpi C\\
\rho\varepsilon_i&=L_{rsi}e_{rs}+M_{rsi}\kappa_{rs}-N_{ji}\zeta_j+R_i\varphi-B_{ij}T_j-b_i\theta-R_{ij}C_j\\
P&=d_{ij}e_{ij}+f_{ij}\kappa_{ij}+\tilde{f}_i\zeta_i+\tilde{g}_1\varphi-\varpi\theta+\varrho C\qquad \rho\omega_i=-C_{ij}C_j-R_{ji}T_j
\end{aligned}
\tag{2}
$$

Here, T_0 is the absolute temperature in the reference configuration, q_i is the heat flux vector, s is the heat supply per unit mass, ε_i is the first moment of energy vector, q_{ij} is the first heat flux moment tensor, Q_i is the microheat

flux average, G_i is the first heat supply moment vector, η_{ij} is the first mass diffusion flux moment tensor, $\tilde{\sigma}_i$ is the micromass diffusion flux average, P is the particle chemical potential, T is the absolute temperature, $\theta = T - T_0$, T_i are the microtemperatures, C_i are the microconcentrations and ε_{ijk} is the alternating symbol.

3. Well-posedness

We assume null boundary conditions. We introduce the notations $\dot{u}_i = v_i$, $\dot{\varphi}_i = \psi_i$ and $\dot{\varphi} = \psi$. Let $\mathcal{H} = \left\{(u_i, v_i, \varphi, \psi, \varphi_i, \psi_i, \theta, T_i, P, C_i) : u_i, \varphi_i \in \mathbb{W}_0^{1,2}(\Omega), v_i, \psi_i, T_i, C_i \in \mathbb{L}^2(\Omega), \psi, \theta, P \in L^2(\Omega), \varphi \in W_0^{1,2}(\Omega)\right\}$ where $W_0^{1,2}(\Omega)$, $L^2(\Omega)$ are the familiar Sobolev spaces and $\mathbb{W}_0^{1,2}(\Omega) = \left[W_0^{1,2}(\Omega)\right]^3, \mathbb{L}^2(\Omega) = \left[L^2(\Omega)\right]^3$. The boundary initial value problem can be transformed into the following equation in the Hilbert space $\mathcal{H}$

$$\frac{\mathrm{d}\mathcal{U}}{\mathrm{d}t} = \mathcal{A}\mathcal{U}(t) + \mathcal{F}(t) \qquad \mathcal{U}(0) = \mathcal{U}_0 \tag{3}$$

where $\mathcal{U} = (u_i, v_i, \varphi, \psi, \varphi_i, \psi_i, \theta, P, T_i, C_i)$, $\mathcal{U}_0 = \left(u_i^0, v_i^0, \varphi^0, \psi^0, \varphi_i^0, \psi_i^0, \theta^0, P^0, T_i^0, C_i^0\right)$ is the vector of initial conditions and $\mathcal{A}$ is a certain matrix operator on $\mathcal{H}$.

Lemma 3.1 *In the case of diffusive microstretch thermoelasticity with microtemperatures and microconcentrations and for every $\mathcal{U} \in \mathcal{D}(\mathcal{A})$, the operator $\mathcal{A}$ satisfies the inequality*

$$\langle \mathcal{A}\mathcal{U}, \mathcal{U} \rangle \leq 0 \tag{4}$$

in a suitably introduced inner product in $\mathcal{H}$.

Lemma 3.2 *In the case of diffusive microstretch thermoelasticity with microtemperatures and microconcentrations, and for Id the identity operator in $\mathcal{H}$, the operator $\mathcal{A}$ has the property that*

$$Range(Id - \mathcal{A}) = \mathcal{H} \tag{5}$$

Theorem 3.1 *The operator $\mathcal{A}$ generates a semigroup of contractions in $\mathcal{H}$.*

This result proves that in the motion following any sufficiently small change in the external system, the solution of the initial boundary value problem is everywhere arbitrary small in magnitude. Now that we proved that the mathematical model is well-posed by means of the semigroup of linear operator theory, the asymptotic behaviour of solutions and the effect of a concentrated heat source can be studied.

References

[1] M. Aouadi. Some theorems in the isotropic theory of microstretch thermoelasticity with microtemperatures. *Journal of Thermal Stresses*, 31(7):649-662, 2008.

[2] M. Aouadi, M. Ciarletta, and V. Tibullo. A thermoelastic diffusion theory with microtemperatures and microconcentrations. *Journal of Thermal Stresses*, 40(4):486-501, 2017.

[3] A. Chirilă and M. Marin. Diffusion in microstretch thermoelasticity with microtemperatures and microconcentrations. in *Springer book's series Studies in Systems, Decision and Control, Contributed Volume: Advanced Models and Theories in Social Systems*, accepted, 2018.

[4] A. Chirilă and M. Marin. The theory of generalized thermoelasticity with fractional order strain for dipolar materials with double porosity. *Journal of Materials Science*, 53(5):3470-3482, 2018.

[5] C. M. Dafermos. Contraction semigroups and trends to equilibrium in continuum mechanics. in P. German and B. Nayroles (eds.) *Applications of methods of functional analysis to problems in mechanics*, Springer Lecture Notes in Math., 503:295-306, Springer-Verlag, Berlin, 1976.

[6] A. C. Eringen. Theory of thermo-microstretch elastic solids. *International Journal of Engineering Science*, 28(12):1291-1301, 1990.

[7] M. Marin, I. Abbas, and R. Kumar. Relaxed Saint-Venant principle for thermoelastic micropolar diffusion. *Structural Engineering and Mechanics*, 51(4):651-662, 2014.

[8] M. Marin and S. Nicaise. Existence and stability results for thermoelastic dipolar bodies with double porosity. *Continuum Mechanics and Thermodynamics*, 28(6):1645-1657, 2016.

INITIAL BOUNDARY VALUE PROBLEM IN THE FRAMEWORK OF FRACTIONAL VISCOPLASTICITY

M. Szymczyk[1], W. Sumelka[1], and M. Nowak[2]

[1]*Poznan University of Technology, Institute of Structural Engineering, Piotrowo 5 street, 60-969 Poznan, Poland*
[2]*Institute of Fundamental Technological Research PAS, Pawinskiego 5B street, 02-106 Warsaw, Poland*

e-mail: michal.g.szymczyk@doctorate.put.poznan.pl

1. Introduction

The desirable goal of the consitutive modelling is to obtain a model that with a few material parameters is able to provide a good compatibility between the experimental and numerical results. Application of the fractional calculus to Perzyna type viscoplasticity presents a new approach for describing the inelastic behaviour of various materials. This may be useful especially in the case of materials that display rate-dependent properties and were subjected to dynamic loading. Fractional derivative introduces a new material parameters that comes from the non local character of this generalization. In several papers [3], [4], [5], [6] the fractional approach to classical plasticity was presented demonstrating a induced anisotropy and non-associated plastic flow.

2. Experimental background

The plastic deformation that leads to formation of instability bands in metal plates was discussed in [1]. Authors shown that in the process of achieving the maximum true stress one can observe a diffuse necking in the region where intersecting instability bands appear. As the deformation proceeds, the necking and the elongation of material concentrate in one of the bands (cf. Fig. 1) and in their area the rate of deformation increases. At this stage practically all of the plastic deformation is taking place within this band.

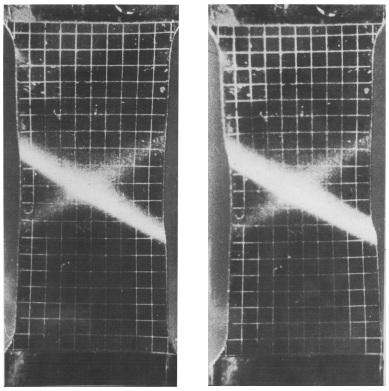

Figure 1: Development of instability bands and concentration of plastic deformation in predominant direction [1].

3. Fractional material model

The Theory of Thermo-Viscoplasticity was originally published by Perzyna in [2]. In the classical model the rate of inelastic strain is defined by a partial derivative of yield function F in the stress space. In the framework of fractional calculus this relation is reformulated to

$$\dot{\varepsilon}^p = \Lambda \mathbf{p} = \Lambda \, D^{\alpha} F \, ||D^{\alpha} F||^{-1}, \tag{1}$$

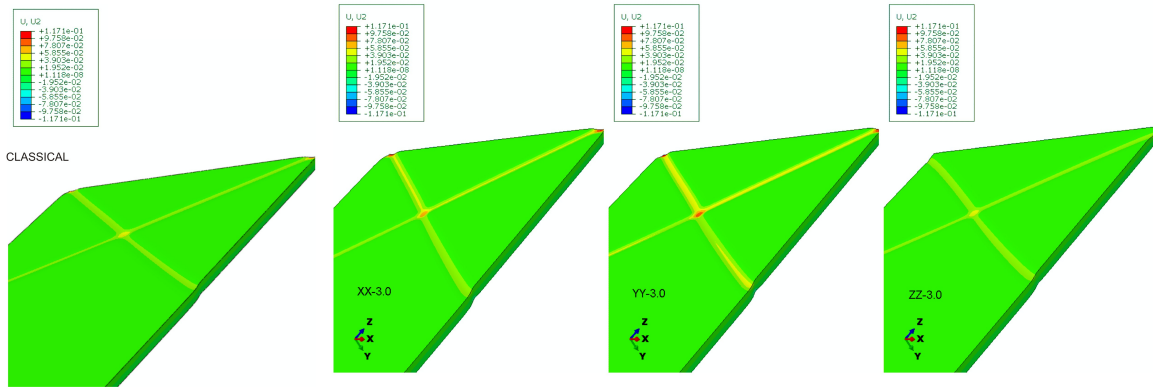

Figure 2: Necking achieved in numerical model for classical (leftmost) and fractional plasticity with different material parameters.

where Λ is a scalar multiplier and $D^{\alpha}F$ denotes the fractional operator. For the purpose of this paper the definition of the Riesz - Caputo (RC) derivative consisting of the left- and right-sided Caputo derivative is assumed

$$ {}_{a}^{RC}D_{b}^{\alpha}f\left(t\right)=\frac{1}{2}\left({}_{a}^{C}D_{t}^{\alpha}f\left(t\right)+\left(-1\right)^{n}{}_{t}^{C}D_{b}^{\alpha}f\left(t\right)\right), \tag{2} $$

where α denotes the order of the derivative $D(.)$ and whereas a, t, b are terminals describing the range on non-locality. Due to the limited number of analytical solution utilising fractional derivatives the Huber–Mises–Hencky (HMH) criterion was herein selected. The application of fractional operator results in new material parameters, namely the order of the derivative α and two six-dimensional vectors $\Delta^{L}_{(ij)}$ and $\Delta^{R}_{(ij)}$ that denotes the virtual neighborhood of a stress state. One of the advantages of this model is that it is possible to achieve the volume change, without any additional assumption, only through the modification of the new parameters. The built-in numerical VUMAT procedure for Abaqus/Explicit was used for numerical study of the aforementioned model. Simulations were conducted for a three-dimensional plates fixed at the one end while the other one was subjected to dynamic loading.

4. Results

The results were obtained for different velocities of the applied tension as well as for various material parameters α and Δ - Fig. 2. This type of examination allows to recognize how changes in parameters affect the localised viscoplastic deformation and exemplify the intensity of observed phenomena. This can be useful in the model's calibration process for a specific material. In future, a task of comparative analysis between experimental and numerical data will be considered.

References

[1] Amiya K. Chakrabarti and Joseph W. Spretnak. Instability of plastic flow in the directions of pure shear: I. theory. *Metallurgical Transactions A*, 6(4):733–736, apr 1975.

[2] P. Perzyna. The constitutive equations for rate sensitive plastic materials. *Quarterly of Applied Mathematics*, **20**:321–332, 1963.

[3] W. Sumelka. Application of fractional continuum mechanics to rate independent plasticity. *Acta Mechanica*, 255(11):3247–3264, 2014.

[4] W. Sumelka. Fractional viscoplasticity. *Mechanics Research Communications*, 56:31–36, 2014.

[5] W. Sumelka and M. Nowak. Non-normality and induced plastic anisotropy under fractional plastic flow rule: A numerical study. *International Journal for Numerical and Analytical Methods in Geomechanics*, 40:651–675, 2016.

[6] W. Sumelka and M. Nowak. On a general numerical scheme for the fractional plastic flow rule. *Mechanics of Materials*, DOI: 10.1016/j.mechmat.2017.02.005, 2017.

A STUDY ON THE PROPERTIES ESTIMATION OF HYPERELASTIC MATERIAL UNDER LOW TEMPERATURE CONDITIONS

Byoungjae Park[1], Kangsu Lee[1], Minsuk Ki[1], Doyoub Kim[1], and Hyun-Seok Kim[1]

[1]*Korea Research Institute of Ships & Ocean Engineering, Daejeon, Korea*
e-mail: byoungjae@kriso.re.kr

1. Introduction

Hyperelastic materials are used in various fields such as machinery, civil engineering and marine & offshore plants industries due to excellent vibration damping ability, energy absorption capacity and low noise characteristics. The behavior of the hyperelastic material is described using the strain energy density function and there are various nonlinear material models to express it. In general, for the analysis of hyperelastic materials, the material properties test is required to derive the coefficients of the nonlinear material model. In particular, the properties of hyperelastic materials is changed according to temperature, unlike ordinary steels. Therefore, in order to consider various temperature conditions, it is necessary to carry out the same number of tests as the number of conditions. In this study, tensile test was performed for four temperature conditions to analyse the behavior of hyperelastic material under low temperature condition. An algorithm for estimating properties of hyperelastic materials at specific temperatures was developed and verified.

2. Tensile test of hyperelastic material under low temperature conditions

The physical properties of the hyperelastic material under low temperature conditions were tested under hysteresis conditions in consideration of Mullin's effect. The specimens are made of natural rubber and the temperature conditions are -40°C, -20°C, 0°C, 23°C. The stress-strain curve of the tensile test result and nonlinear material models are shown in Fig.1. The material models considered are Ogden, Yeoh, and Mooney-Rivlin models, and are expressed as equation (1) - (3), respectively.[1][2]

(1) $$W = \sum_{i=1}^{N} \frac{u_i}{\alpha_i}\left(\bar{\lambda}_1^{\alpha_i} + \bar{\lambda}_2^{\alpha_i} + \bar{\lambda}_3^{\alpha_i} - 3\right) + \sum_{k=1}^{N} \frac{1}{d_k}(J-1)^{2k}$$ – Ogden Model

(2) $$W = \sum_{i=1}^{N} C_{i0}\,(\bar{I}_1 - 3)^i + \sum_{k=1}^{N} \frac{1}{d_k}(J-1)^{2k}$$ – Yeoh Model

(3) $$W = C_{10}(\bar{I}_1 - 3) + C_{01}(\bar{I}_2 - 3) + \frac{1}{d}(J-1)^2$$ – Mooney-Rivlin Model

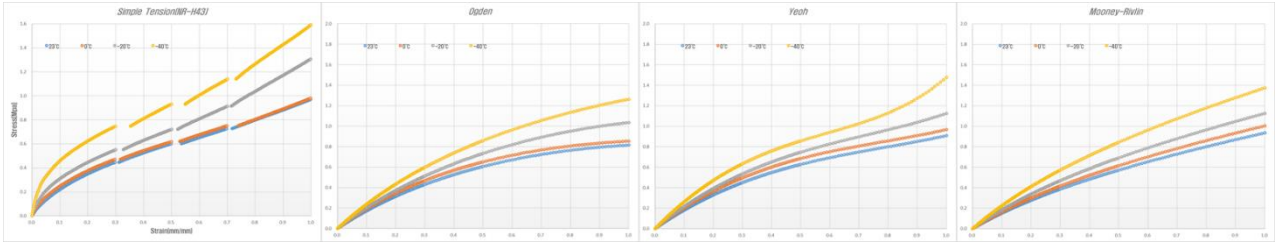

Figure 1 : Tensile test result and nonlinear material models under the low temperature condition

3. Estimation of mechanical properties of hyperelastic materials in low temperature condition

The algorithm for estimating the mechanical properties of the hyperelastic material at a specific temperature is formulated as shown in Equation (4) and the procedure is as follows:

(4) $stress_{temp.} = nU + \sum_{a}^{n-1} ay$

Where, n : range of temperature(between to max. temperature and min. temperature)
U : unit change value(change value per 1℃ between 0℃ and 23℃)
y : Change with temperature
a : Weight factor of temperature

Phase 1 : Draw the S-S curves of the nonlinear material model at 23 ° C, 0 ° C, and -40 ° C.
Phase 2 : Separate the S-S curve equally according to the strain
Phase 3 : Derive the stress value for the strain at the specific temperature through the formalized model.
Phase 4 : Draw the S-S curve and derive the material model coefficients

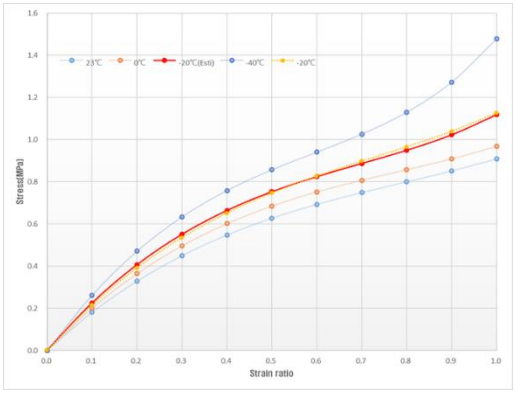

Figure 2 : Estimation of hyperelastic material properity at -20℃

Figure 2 show the estimation results at -20 ° C temperature condition. Yeoh model was used for this estimation. The results show up to about 5% error with the experimental results and it can be seen that the developed algorithm is well estimated

4. Conclusion

In this study, the behavior of hyperelastic material in low temperature condition was analyzed and an algorithm for estimating mechanical properties of hyperelastic material at specific temperature was developed.
1) The stiffness of hyperelastic material increases with decreasing temperature and the amount of change in stiffness are initially increases and then decreases
2) An algorithm for estimating properties of hyperelastic materials at specific temperature was developed and verified for applicability. This study is meaningful to confirm that it is possible to estimate properties of hyperelastic material which is a representative nonlinear material. This study is meaningful to confirm that it is possible to estimate properties of hyperelastic material which is a representative nonlinear material.
Further research will be carried out on generalization study of algorithms developed for various hyperelastic materials.

Acknowledgments This research was supported by a grant from Endowment Project of "Development of the Core Technology of Structural damage assessment based on ALS(Accident Limits State) for offshore plants (2/3)" funded by Korea Research Institute of Ships and Ocean engineering(PES9480).

References

[1] Ogden, R. W., Saccomandi, G. and Sgura, I., 2004, "Fitting hyperelastic Models to Experimental Data," Computational Mechanics, Vol. 34, No. 6, pp. 484~502.
[2] Rivlin, R. S. and saunders, D. W., 1951, "Large Elastic Deformations of Isotropic Materials - VII. Experiments on the deformation of Rubber" phlos. Trans. R. Soc.(A), Vol. 243, pp. 251~288

ANALYTICAL SOLUTION METHOD FOR RHEOLOGICAL PROBLEMS OF SOLIDS

T. Fülöp and M. Szücs

Budapest University of Technology and Economics, Department of Energy Engineering, Budapest, Hungary

e-mail: szucsmatyas@energia.bme.hu

A large variety of solid materials – like plastics, rocks, asphalt, biomaterials etc. – possess viscoelastic/rheological characteristics. Correspondingly, one can observe some kind of delayed and damped elastic behaviour. In a linear regime, rheology of solids can be expressed as a generalization of Hooke's law where elasticity coefficients are replaced by polynomials of the time derivative operator. Then time dependent boundary conditions, like those when gradually creating a hole, tunnel etc., induce time dependent processes, which also influence the elasticity originated space dependence.

Volterra's principle [1,2] is a long-known method to treat such problems. Here, we introduce and present another approach that is simpler to apply (no operator inverse is required to compute but only linear ordinary differential equations to solve). Our method starts with the elastic solution, replaces the elasticity coefficients with time dependent functions, derives differential equations on them, and determines the solution corresponding to the initial conditions.

More concretely, Hooke's law, written in the deviatoric–spherical decomposition

$$\boldsymbol{\sigma}^{\mathrm{dev}} = E^{\mathrm{dev}}\boldsymbol{\varepsilon}^{\mathrm{dev}}, \qquad \boldsymbol{\sigma}^{\mathrm{sph}} = E^{\mathrm{sph}}\boldsymbol{\varepsilon}^{\mathrm{sph}}, \qquad E^{\mathrm{dev}} = 2G, \quad E^{\mathrm{sph}} = 3K \tag{1}$$

with the spherical and deviatoric parts defined according to

$$\varepsilon^{\mathrm{sph}} = \frac{1}{3}(\mathrm{tr}\,\boldsymbol{\varepsilon}), \qquad \boldsymbol{\varepsilon}^{\mathrm{sph}} = \varepsilon^{\mathrm{sph}}\mathbf{1}, \qquad \boldsymbol{\varepsilon}^{\mathrm{dev}} = \boldsymbol{\varepsilon} - \boldsymbol{\varepsilon}^{\mathrm{sph}}, \tag{2}$$

is replaced by

$$\mathcal{S}^{\mathrm{dev}}\boldsymbol{\sigma}^{\mathrm{dev}} = \mathcal{E}^{\mathrm{dev}}\boldsymbol{\varepsilon}^{\mathrm{dev}}, \qquad \mathcal{S}^{\mathrm{sph}}\boldsymbol{\sigma}^{\mathrm{sph}} = \mathcal{E}^{\mathrm{sph}}\boldsymbol{\varepsilon}^{\mathrm{sph}} \tag{3}$$

with the operator polynomials

$$\mathcal{S}^{\mathrm{dev}} = 1 + \tau_1^{\mathrm{dev}}\frac{\partial}{\partial t} + \tau_2^{\mathrm{dev}}\frac{\partial^2}{\partial t^2} + \ldots, \qquad \mathcal{E}^{\mathrm{dev}} = E_0^{\mathrm{dev}} + E_1^{\mathrm{dev}}\frac{\partial}{\partial t} + E_2^{\mathrm{dev}}\frac{\partial^2}{\partial t^2} + \ldots, \tag{4}$$

$$\mathcal{S}^{\mathrm{sph}} = 1 + \tau_1^{\mathrm{sph}}\frac{\partial}{\partial t} + \tau_2^{\mathrm{sph}}\frac{\partial^2}{\partial t^2} + \ldots, \qquad \mathcal{E}^{\mathrm{sph}} = E_0^{\mathrm{sph}} + E_1^{\mathrm{sph}}\frac{\partial}{\partial t} + E_2^{\mathrm{sph}}\frac{\partial^2}{\partial t^2} + \ldots. \tag{5}$$

In our applications, we concentrate on the Kluitenberg–Verhás model family [3]

$$\boldsymbol{\sigma}^{\mathrm{dev}} + \tau^{\mathrm{dev}}\dot{\boldsymbol{\sigma}}^{\mathrm{dev}} = E_0^{\mathrm{dev}}\boldsymbol{\varepsilon}^{\mathrm{dev}} + E_1^{\mathrm{dev}}\dot{\boldsymbol{\varepsilon}}^{\mathrm{dev}} + E_2^{\mathrm{dev}}\ddot{\boldsymbol{\varepsilon}}^{\mathrm{dev}}, \tag{6}$$

$$\boldsymbol{\sigma}^{\mathrm{sph}} + \tau^{\mathrm{sph}}\dot{\boldsymbol{\sigma}}^{\mathrm{sph}} = E_0^{\mathrm{sph}}\boldsymbol{\varepsilon}^{\mathrm{sph}} + E_1^{\mathrm{sph}}\dot{\boldsymbol{\varepsilon}}^{\mathrm{sph}} + E_2^{\mathrm{sph}}\ddot{\boldsymbol{\varepsilon}}^{\mathrm{sph}}, \tag{7}$$

which is important from both theoretical [3] and experimental [4] aspects (overdot denoting time derivative).

We work in the small-strain region with the geometric compatibility equation

$$\overrightarrow{\nabla} \times \boldsymbol{\varepsilon} \times \overleftarrow{\nabla} = \mathbf{0} \tag{8}$$

for the strain tensor $\boldsymbol{\varepsilon}$, and take the mechanical equation of motion in the force equilibrial approximation (i.e., acceleration neglected)

$$\boldsymbol{\sigma} \cdot \overleftarrow{\nabla} = -\varrho\mathbf{g}, \tag{9}$$

where $\boldsymbol{\sigma}$ denotes the Cauchy stress tensor and $\varrho\mathbf{g}$ is the volumetric force density.

In the examples treated by us, a hole/tunnel in a pre-stressed medium is established progressively via switching on a stress-free boundary condition gradually, described by a smooth multiplying function

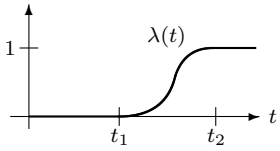

$$\lambda(t) = \begin{cases} 0 & \text{if} \quad t \le t_1, \\ 1 & \text{if} \quad t \ge t_2, \\ \text{smooth in between.} \end{cases} \tag{10}$$

The solution of the corresponding elastic problem (typically already known from sources like [5–7]) is assumed in finite sum form, then we replace the elasticity coefficients with time dependent functions, on which a set of ordinary differential equations is derived from (3), and for suitable switch-on functions $\lambda(t)$ the solution can be obtained analytically.

We present several examples solved via this new method, like tunnels and spherical hollows opened in various initial stress states, and pressurizing of thick-walled tubes and spherical tanks. These examples are useful for applications and, in parallel, are suitable for testing and validating numerical methods of various kinds.

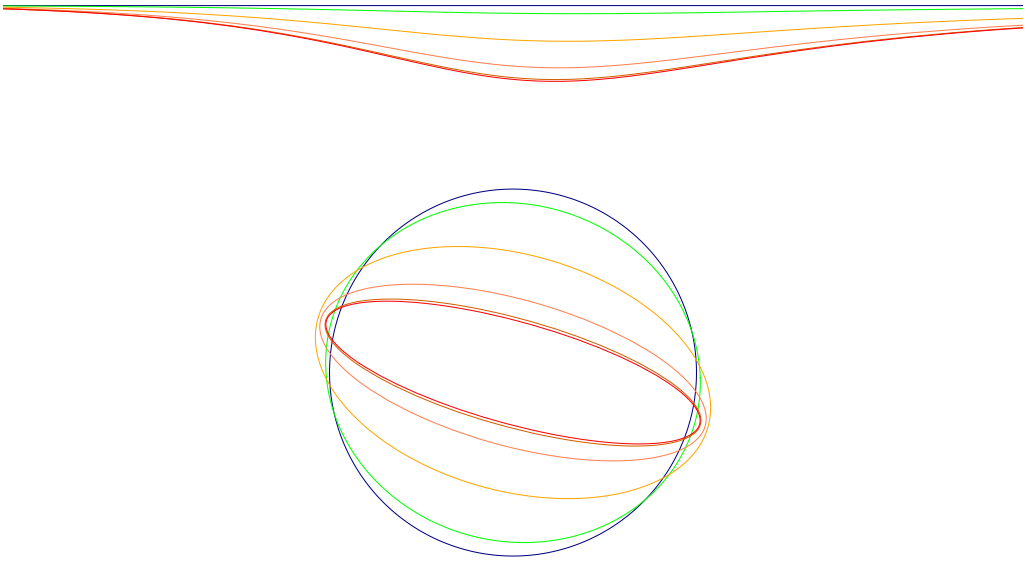

Figure 1: Time evolution of the displacement field when a cylindrical hole is opened in an anisotropically pre-stressed medium: change of the shape of the hole and of a nearby plane surface.

Acknowledgments The authors acknowledge financial support from contract NKFIH K116375.

References

[1] V. G. Gromov (1971). *On the mathematical content of Volterra's principle in the boundary value problem of viscoelasticity*, PMM 35, 869–878.
[2] Ju. N. Rabotnov (1980). *Elements of hereditary solid mechanics*, Mir Publishers, Moscow.
[3] Cs. Asszonyi and T. Fülöp and P. Ván (2015). Distinguished rheological models for solids in the framework of a thermodynamical internal variable theory, *Continuum Mechanics and Thermodynamics*, **27**, 971–986.
[4] Cs. Asszonyi and A. Csatár and T. Fülöp (2016). Elastic, thermal expansion, plastic and rheological processes – theory and experiment, *Periodica Polytechnica – Civil Engineering*, **60**, 591–601.
[5] R. D. Mindlin (1939). Stress distribution around a tunnel, *Proceedings of the American Society of Civil Engineering*, New York, 619–642.
[6] P. R. Papkovich (1939). *Elasticity theory*, Oborongiz, Moscow–Leningrad.
[7] G. N. Savin (1970). *Stress distribution around holes*, National Aeronautics and Space Administration, Washington, D. C.

EXPERIMENTS AND MODELING OF NATURAL AGING IN ZAMAK ALLOYS

M.A. Martinez Page[1] and S. Hartmann[1]

[1]*Institut of Applied Mechanics, Clausthal University of Technology, Clausthal-Zellerfeld, Germany*

e-mail: maria.angeles.martinez.page@tu-clausthal.de

Zinc die casting alloys are widely used in the production of components of cars and machines. Because of their low melting point and their ability to produce very accurate components, these alloys are considered to be the best castable of all commonly used alloys. This advantage is accompanied by a pronounced rate dependence, temperature dependence and aging [4].

Aging denotes the development of the material properties and the mechanical response due to microstructural changes over the course of time. These changes are associated with precipitation of alloying elements or phases with low solubility, phase decomposition, and changes in the crytallographic structure [5]. These microstructural changes influence the mechanical response of the material [3].

1. Experimental investigation

In order to characterize the temperature-dependent aging behavior, the experiments of [4] were extended to three additional aging times. In this previous work, tension, compression and torsion experiments with thin-walled tubes were carried out at different temperatures and strain rates. As exposed in [1] and [2], torsion tests in thin-walled cylinders offer the advantage of isolating the deviatoric behavior of the material, which simplifies the identification process.

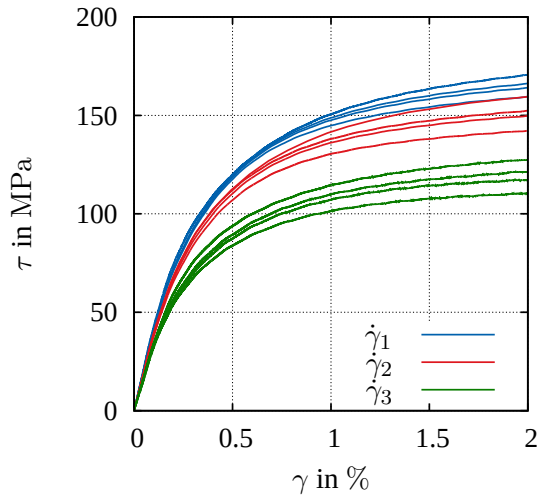

Figure 1: Torsion tests at a constant temperature of 20 °C for three different strain rates (different colors) and for every strain rate, four aging times. Higher aging times show a decreasing stress-strain curve at the same strain rate.

Moreover, other aging-dependent thermal properties such as the thermal conductivity and the shrinkage, were also experimentally characterized.

2. Modeling and identification

The modeling and identification steps are closely connected to each other, since the temperature and aging-dependent parameters are developed after some previous pre-identification steps. The constitutive model has a partitioned structure, in which the total stress is decomposed into an equilibrium and an overstress part

$$\mathbf{T} = \mathbf{T}_{\text{eq}} + \mathbf{T}_{\text{ov}}. \tag{1}$$

This decomposition of the total stress has also advantages in the identification step, since the parameters of the equilibrium stress can be identified independently of the other parameters with the help of the equilibrium hysteresis.

The aging is modeled with the help of an internal variable g

$$\dot{g} = f(\Theta, g). \tag{2}$$

This variable has a positive, growing value between 0 and 1. The value 0 corresponds to the initial, unaged stage and 1 to the completely aged stage. The aging rate is defined temperature-dependent in a way that higher temperatures result in a faster aging process. The influence of the aging in the model is introduced with the selection of aging-dependent parameters. Finally, the thermodynamical consistency of the model is ensured with the selection of the free energy.

3. Implementation of the model

The model is implemented in the in-house FE-code TASAFEM. In the case of small deformations, the internal variables of the model can be computed directly from the input variables of the stress algorithm, which means that in this model a local Newton-iteration is not necessary. This leads to shorter computation times.

4. Simulation example

The behavior of the model is shown with a simulation example using the finite element code TASAFEM.

Acknowledgments We would like to thank the German Research Foundation DFG for funding this research project with the project no. DFG HA2024-18/1.

References

[1] P. Haupt. *Continuum mechanics and theory of materials*. Springer, 2000.
[2] P. Haupt and A. Lion. Experimental identification and mathematical modelling of viscoplastic material behavior. *Journal of Continuum Mechanics and Thermodynamics*, 7:73–96, 1995.
[3] W. Leis and H. Lothar. Ageing of zink alloys. *International Foundry Research*, 64:2–23, 2011.
[4] M. A. Martinez Page and S. Hartmann. Experimental characterization, material modeling, identification and finite element simulation of the thermo-mechanical behavior of a zinc die-casting alloy. *International Journal of Plasticity*, 101:74–105, 2018.
[5] Y.H. Zhu. Phase transformations of eutectoid Zn-Al alloys. *Journal of Materials Science*, 36:3973–3980, 2001.

NOVEL ASPECTS IN DISLOCATION CONTINUUM THEORY: J-, M-, AND L-INTEGRALS

E. Agiasofitou*, and M. Lazar

Darmstadt University of Technology, Department of Physics

Hoshschulstr. 6, 64289, Darmstadt, Germany

e-mail: agiasofitou@mechanik.tu-darmstadt.de

1. Introduction

In this work, new aspects in dislocation continuum theory concerning the **J**-, M-, and **L**-integrals are presented within the framework of three-dimensional, linear, incompatible elasticity theory. First, the **J**-, M-, and **L**-integrals are derived for two straight (edge and screw) dislocations and second for a single (edge and screw) dislocation in isotropic materials. The results provide to the **J**-, M-, and **L**-integrals an important physical interpretation revealing their significance in dislocation continuum theory.

2. J-, M-, and L_3-integrals of straight dislocations

For two parallel edge dislocations with Burgers vectors in x-direction, the **J**-, M-, and L_3-integrals per unit dislocation length are given by [1]

$$\frac{J_1}{l_z} = 2K^e_{xx}\,\frac{\cos\varphi\cos 2\varphi}{\bar{r}}\,, \tag{1}$$

$$\frac{J_2}{l_z} = 2K^e_{xx}\,\frac{\sin\varphi(2+\cos 2\varphi)}{\bar{r}}\,, \tag{2}$$

$$\frac{M}{l_z} = K^e_{xx}\left[2-\ln\frac{\bar{r}}{L}-\sin^2\varphi\right], \tag{3}$$

$$\frac{L_3}{l_z} = K^e_{xx}\,\sin 2\varphi\,, \tag{4}$$

where

$$K^e_{xx}(b_x,b'_x) = \frac{\mu b_x b'_x}{4\pi(1-\nu)} \tag{5}$$

is the *pre-logarithmic energy factor* for edge dislocations with Burgers vectors in x-direction. Here, μ is the shear modulus, ν is the Poisson ratio, L is the size of the dislocated body (or outer cut-off radius), $\bar{r} = \sqrt{\bar{x}^2+\bar{y}^2}$ is the distance between the two dislocations, and φ is the location angle of the dislocation with Burgers vector $\mathbf{b}$.

The M-integral between two edge dislocations with Burgers vectors in x-direction can be written in terms of the corresponding interaction energy as follows

$$\frac{M}{l_z} = 2K^e_{xx} + \frac{1}{2}\frac{U_{\text{int}}}{l_z}\,, \tag{6}$$

where

$$\frac{U_{\text{int}}}{l_z} = -2K^e_{xx}\left[\ln\frac{\bar{r}}{L}+\sin^2\varphi\right]. \tag{7}$$

Eq. (6) states that the *M-integral of two parallel edge dislocations with Burgers vectors in x-direction per unit*

dislocation length is half the interaction energy between the two dislocations per unit length, plus twice the pre-logarithmic energy factor K^e_{xx}.

Important results are summarized as follows:

- The **J**-integral of dislocations is the Peach-Koehler force (interaction force) between two dislocations.
- Eq. (6) provides to the M-integral the physical interpretation of the interaction energy between the two straight dislocations.
- The configurational work produced by the Peach-Koehler force for straight dislocations (per unit dislocation length) is constant, and equals twice the corresponding pre-logarithmic energy factor.
- The L_3-integral of two straight dislocations is the z-component of the configurational vector moment or the rotational moment (torque) about the z-axis caused by the interaction of the two dislocations.
- Fundamental relations between the **J**-, L_3-, and M-integrals of straight dislocations have been found and they show that the **J**-, L_3-, and M-integrals are not independent. If the M-integral is given, then the J_1-, J_2-, J_r-, J_φ-, and L_3-integrals can be easily calculated from it. From that point of view, the M-integral is of primary importance.
- The translational energy-release $\mathcal{G}^T_k$ of straight dislocations is identical to the J_k-integral.
- The rotational energy-release $\mathcal{G}^R$ of straight dislocations equals twice the value of the L_3-integral.

3. J-, M-, and L_3-integrals of a single dislocation

For a single edge dislocation with Burgers vector b_x, the **J**-, M-, and L_3-integrals per unit dislocation length, are given respectively [2]

$$\frac{J_1}{l_z} = 2K^e_{xx}\,\frac{1}{\epsilon}\,, \qquad \frac{J_2}{l_z} = 0\,, \tag{8}$$

$$\frac{M}{l_z} = K^e_{xx}\Big[\ln\frac{L}{\epsilon} + 2\Big]\,, \qquad \frac{L_3}{l_z} = 0\,, \tag{9}$$

where

$$K^e_{xx}(b_x) = \frac{\mu b_x^2}{4\pi(1-\nu)} \tag{10}$$

is the *pre-logarithmic energy factor* for a single edge dislocation with Burgers vector in x-direction. Here, ϵ is the inner cut-off radius being proportional to the constant dislocation core radius.

An important outcome is that the *M-integral (per unit length) of a single dislocation represents the total energy U_{total} of the dislocation (per unit length) which consists of the self-energy (per unit length) plus the dislocation core energy (per unit length)*

$$M/l_z = U_{\text{s}}/l_z + U_{\text{core}}/l_z = U_{\text{total}}/l_z\,. \tag{11}$$

The dislocation core energy can be identified with the work done by the Peach-Koehler force. It is shown that the dislocation core energy (per unit length) is twice the corresponding pre-logarithmic energy factor.

References

[1] E. Agiasofitou and M. Lazar. Micromechanics of dislocations in solids: J-, M-, and L-integrals and their fundamental relations, *Int. J. Eng. Sci.*, 114, 16-40, 2017.

[2] M. Lazar and E. Agiasofitou. Eshelbian dislocation mechanics: J-, M-, and L-integrals of straight dislocations, *Mech. Res. Commun. (Special Issue G.A. Maugin)*, http://dx.doi.org/10.1016/j.mechrescomm.2017.09.001, 2017.

FROM GRADIENT ELASTICITY TO ANGSTRÖM-MECHANICS OF DISLOCATIONS

Markus Lazar*[1] and Giacomo Po[2]

[1]*Department of Physics, Darmstadt University of Technology, 64289 Darmstadt, Germany*
[2]*Department of Mechanical and Aerospace Engineering, University of California Los Angeles, Los Angeles, CA 90095, USA*

e-mail: lazar@fkp.tu-darmstadt.de

1. Introduction

In this work, a non-singular theory of three-dimensional dislocations in a particular version of Mindlin's anisotropic gradient elasticity with up to six length scale parameters is presented [1,2,3]. The theory is systematically developed as a generalization of the classical anisotropic theory in the framework of incompatible elasticity. The non-singular version of all key equations of anisotropic dislocation theory are derived as line integrals, including the Burgers displacement equation with isolated solid angle, the Peach-Koehler stress equation, the Mura-Willis equation for the elastic distortion, and the Peach-Koehler force. It is shown that all the elastic fields are non-singular, and that they converge to their classical counterparts a few characteristic lengths away from the dislocation core. In practice, the non-singular fields can be obtained from the classical ones by replacing the classical (singular) anisotropic Green tensor with the non-singular anisotropic Green tensor derived by [1,2]. The elastic solution is valid for arbitrary anisotropic media. In addition to the classical anisotropic elastic constants, the non-singular Green tensor depends on a second order symmetric tensor of length scale parameters modeling a weak non-locality, whose structure depends on the specific class of crystal symmetry. The anisotropic Helmholtz operator defined by such tensor admits a Green function which is used as the spreading function for the Burgers vector density. The anisotropic non-singular theory is shown to be in good agreement with molecular statics without fitting parameters, and unlike its singular counterpart, the sign of stress components does not show reversal as the core is approached. Compared to the isotropic solution, the difference in the energy density per unit length between edge and screw dislocations is more pronounced.

2. Non-singular dislocation key equations

In the considered version of anisotropic strain gradient elasticity theory, the strain energy density is given by

$$\mathcal{W} = \mathcal{W}(e_{ij}, \partial_k e_{ij}) = \frac{1}{2} C_{ijkl} e_{ij} e_{kl} + \frac{1}{2} D_{ijmkln} \partial_m e_{ij} \partial_n e_{kl} \tag{1}$$

with

$$D_{ijmkln} = C_{ijkl} \Lambda_{mn} \,, \tag{2}$$

where C_{ijkl} is the tensor of elastic moduli and Λ_{mn} is a (symmetric) length scale tensor containing up to six length scales and describes the shape of the dislocation core. Λ_{mn} gives the additional material parameters of gradient elasticity. Here $e_{ij} = (\beta_{ij} + \beta_{ji})/2$ is the elastic strain tensor, $\partial_k e_{ij}$ is the elastic strain gradient tensor (elastic double-strain), $\beta_{ij} = \partial_j u_i - \beta^P_{ij}$ is the elastic distortion tensor, u_i and β^P_{ij} denote the displacement vector and the plastic distortion tensor, respectively. Gradient elasticity is a continuum model of dislocations with core spreading and leads to non-singular elastic fields.

All the famous dislocation key-equations are non-singular in the used version of anisotropic strain gradient

elasticity and they read

$$u_i(\boldsymbol{x}) = -\frac{b_i\,\Omega(\boldsymbol{x})}{4\pi} - \oint_{\mathcal{L}} C_{mnpq}\epsilon_{jqr}b_p F_{jnim}(\boldsymbol{R})\,\mathrm{d}L'_r \tag{3}$$

(anisotropic Burgers equation)

$$\beta_{ij}(\boldsymbol{x}) = \oint_{\mathcal{L}} C_{mnpq}\epsilon_{jqr}G_{im,n}(\boldsymbol{R})\,b_p\,\mathrm{d}L'_r \tag{4}$$

(Mura-Willis equation)

$$\sigma_{ij}(\boldsymbol{x}) = \oint_{\mathcal{L}} C_{ijkl}C_{mnpq}\epsilon_{lqr}G_{km,n}(\boldsymbol{R})\,b_p\,\mathrm{d}L'_r \tag{5}$$

(anis. Peach-Koehler stress equation)

$$W_{AB} = \oint_{\mathcal{L}_A}\oint_{\mathcal{L}_B} \epsilon_{jkl}C_{ilmn}\epsilon_{npq}C_{rstp}F_{skmr}(\boldsymbol{R})\,b_t^A b_i^B\,dL_q^A\mathrm{d}L_j^B \tag{6}$$

(anisotropic Blin's formula)

$$\mathcal{F}_k = \oint_{\mathcal{L}} \epsilon_{kjm}\sigma_{ij}b_i\,\mathrm{d}L_m \tag{7}$$

(Peach-Koehler force)

where $\Omega(\boldsymbol{x})$ is a non-singular solid angle and b_p is the Burgers vector. They are given in terms of a non-singular Green tensor and a non-singular $\boldsymbol{F}$-tensor.

The results are summarized as follows:

- the theory of incompatible anisotropic strain gradient elasticity delivers a non-singular and parameter-free dislocation continuum theory,
- Green functions and their first derivatives are non-singular,
- the dislocation key-formulas are non-singular, since: singular Green tensor $\rightarrow$ non-singular Green tensor,
- weak anisotropic nonlocality is relevant in the dislocation core.

Moreover, anisotropic strain gradient elasticity contains

- a two-fold anisotropy: anisotropy of the material (bulk anisotropy, C_{ijkl}) and the anisotropy of the core (nonlocal anisotropy, Λ_{mn}),
- characteristic lengths which can be determined from atomistic calculations (DFT) and give the scale where nonlocality is relevant.

References

[1] M. Lazar, G. Po, The non-singular Green tensor of Mindlin's anisotropic gradient elasticity with separable weak non-locality, Physics Letters A 379 (2015), 1538–1543

[2] M. Lazar, G. Po, The non-singular Green tensor of gradient anisotropic elasticity of Helmholtz type, European Journal of Mechanics-A/Solids 50 (2015), 152–162

[3] G. Po, M. Lazar, N.C. Admal, N. Ghoniem, A non-singular theory of dislocations in anisotropic crystals, International Journal of Plasticity 103 (2018), 1–2

USE OF GRADIENT POLYCONVEXITY IN THE MODELING OF RATE-INDEPENDENT EVOLUTION OF DIFFUSED PHASE IN SHAPE MEMORY ALLOYS

M. Kružík[1], P. Pelech[1,2], and A. Schloemerkemper[3]

[1]*Institute of Information Theory and Automation, Czech Academy of Sciences, Prague, Czechia*
[2]*Mathematical Institute, Charles University, Prague, Czechia*
[3]*Institute for Mathematics, University of Wuerzburg, Wuerzburg, Germany*
e-mail: pelech@karlin.mff.cuni.cz

1. Motivation and Background

Shape-memory alloys (SMAs) belong to the class of so-called smart materials which have wide range of important applications, especially in aerospace or mechanical engineering and human medicine. SMAs exhibit specific hysteretic stress/stain/temperature response, which is called a shape-memory effect or pseudoelasticity. The mechanism behind this behavior is connected with the so-called martensitic phase transformation; the material can exist in different phases which are separeted by a thin transition layer which stores a specific amount of interfacial energy; see e.g. [4].

Many interesting applications call for finite-strain models of SMAs which brings, however, many mathematical difficulties not presented in the small-strain regime. In particular, the constrain of local non-interpenetration of matter that involves determinant of deformation gradient and hence excludes convex or quasiconvex energies. The concept of polyconvexity, that allows for satisfactory existence theory for many hyperelastic solids, does not apply, however, for SMAs due to the presence of multiple stable phases.

One possible solution, c.f [1,2], consists in regularizing via the second gradient of deformation in which the energy is convex. This option corresponds to including interfacial energy effect that penalizes rapid spatial oscillations of deformation gradient (i.e. oscillations of phases). The resulting model falls into the class of so-called non-simple materials that, in comparison with 1st-gradient theories, allow for a wider class of possible boundary conditions; see [6].

2. Results

We consider interfacial energy of a different form, based on the concept of gradient polyconvexity, recently introduced in the context of hyperelastic materials in [3]:
Definition (Gradient Polyconvexity)**.** *Let* $\hat{W}:\mathbb{R}^{3\times3}\times\mathbb{R}^{3\times3\times3}\times\mathbb{R}^3\to\mathbb{R}\cup\{+\infty\}$ *be a lower semicontinuous function. The functional*

$$I(y)=\int_\Omega \hat{W}(\nabla y,\nabla[\mathrm{Cof}\,\nabla y],\nabla[\det\nabla y])\,\mathrm{d}x, \tag{1}$$

defined for any measurable function $y:\Omega\to\mathbb{R}^3$ *for which the weak derivatives* ∇y, $\nabla[\mathrm{Cof}\,\nabla y]$, $\nabla[\det\nabla y]$ *exist and are integrable, is called* gradient polyconvex on a domain $\Omega\subset\mathbb{R}^3$ *(or* gradient polyconvex *for short) if the function* $\hat{W}(F,\cdot,\cdot)$ *is convex for every* $F\in\mathbb{R}^{3\times3}$.

Here $\hat{W}$ stands for stored energy density which is up to a multiplication by material density an isothermal restriction of Helmholtz free energy. Since determinant and cofactor measure the transformation of volumes and surfaces, respectively, the energy penalizes abrupt changes of these quantities. As opposed to the aforementioned approach that supposes coercivity of the energy in $|\nabla^2 y|^p$, for some $p\geq1$, here only coercivity in $|\nabla[\mathrm{Cof}\,\nabla y]|^q$, for proper q, is assumed. As a consequence, the deformation y needs not to lie in Sobolev space $W^{2,p}(\Omega,\mathbb{R}^3)$. Indeed, for any $p\geq1$ there exists a function (c.f. [3])

$$y\in W^{1,p}(\Omega;\mathbb{R}^3)\cap L^\infty(\Omega;\mathbb{R}^3)\setminus W^{2,1}(\Omega;\mathbb{R}^3)$$

such that

$$0 < \det \nabla y \in W^{1,\infty}(\Omega) \quad \text{and} \quad \operatorname{Cof} \nabla y \in W^{1,\infty}(\Omega; \mathbb{R}^{3\times 3}).$$

Hence, the gradient polyconvexity allows for existence theory with weaker regularity assumptions on deformation. Moreover, since $\operatorname{Cof} \nabla y \in W^{1,q}$, its boundary value (and therefore the outer normal in deformed configuration) is well defined . In addition, the regularity still suffice for proving physically desirable properties of deformation such as local invertibility ($\det \nabla y > 0$) or global injectivity. Besides, the integrability of $\det^2 \nabla y$ in a Sobolev space $W^{1,r}(\Omega)$ is obtained for an appropriate $r \geq 1$. Concerning the modeling aspect of view, this special energy's dependence on the second gradient of deformation leads to a different form of hyperstress, a generalized form of stress occurring in higher-order gradient theories.

In a forthcoming paper, we extend the previous result for static problems in hyperelasticity to inelastic, isothermal processes. We treat the phase transformation as a dissipative rate-independent process, which is a justified assumption for many situations; see e.g. [7, 8]. We prove existence of *Energetic-solution* (c.f. [5] for a definition) driven by the Gibbs-type stored-energy potential $\mathcal{E}$ and the Rayleigh-type dissipation-energy pseudopotential $\mathcal{R}$; i.e. the activation criterion for the phase-transformation is purely energetic. We suppose that the state of the system is described, besides deformation y, by so-called internal variable z, denoting the vector of volume fractions of individual phases. The vector is determined by deformation gradient via a continuous mapping $\lambda : \mathbb{R}^{3\times 3} \to \mathbb{R}^l$, where $l \in \mathbb{N}$ stands for the number of phases. The Gibbs-type potential is of the form

$$\mathcal{E}(t, y, z) = \begin{cases} I(y) - \langle \ell(t), y \rangle & \text{if } z = \lambda(\nabla y) \text{ a.e. in } \Omega, \\ +\infty & \text{otherwise,} \end{cases}$$

where t denotes time, I is as in (1) and $\ell(t)$ is a continuous linear functional of external forces at time t. Note that the functional depends on time only through loading $\ell(t)$, since we do not consider time-dependent Dirichlet data; nevertheless these can be effectively approximated by a penalty in Neumann boundary condition. The dissipation pseudopotential takes the form

$$\mathcal{R}(\dot{z}) = c \int_\Omega |\dot{z}| \, \mathrm{d}x,$$

where $c > 0$ is tightly related to the amount of energy dissipated by the phase change. This specific choice of potentials $\mathcal{E}$ and $\mathcal{R}$ is a straightforward modification of the model summarized e.g. in [5].

Acknowledgments The authors gratefully acknowledge the financial support by GAUK project No. 670218, Charles University Research program No. UNCE/SCI/023, GAČR project 17-04301S, GAČR project 18-03834S, and by GAČR-FWF project 16-34894L.

References

[1] J. M. Ball and E. C. M. Crooks. Local minimizers and planar interfaces in a phase-transition model with interfacial energy. *Calculus of Variations and Partial Differential Equations*, 40(3):501–538, Mar 2011.

[2] J. M. Ball and C. Mora-Corral. A variational model allowing both smooth and sharp phase boundaries in solids. *Communications on Pure & Applied Analysis*, 8(1):55–81, 2009.

[3] B. Benešová, M. Kružík, and A. Schloemerkemper. A note on locking materials and gradient polyconvexity. *Preprint arXiv:1706.04055*, 2018.

[4] K. Bhattacharya. *Microstructure of Martensite. Why it Forms and How it Gives Rise to the Shape-Memory Effect*. Oxford University Press, New York, 2003.

[5] A. Mielke and T. Roubíček. *Rate-Independent Systems: Theory and Application*. Springer-Verlag New York, 2015.

[6] P. Podio-Guidugli and M. Vianello. Hypertractions and hyperstresses convey the same mechanical information. *Continuum Mechanics and Thermodynamics*, 22(3):163–176, 2010.

[7] T. Roubíček. Models of microstructure evolution in shape memory alloys. In P. Ponte Castañeda, J. J. Telega, and B. Gambin, editors, *Nonlinear Homogenization and its Applications to Composites, Polycrystals and Smart Materials*, pages 269–304, Dordrecht, 2005. Springer Netherlands.

[8] S. Stupkiewicz and H. Petryk. Modelling of laminated microstructures in stress-induced martensitic transformations. *Journal of the Mechanics and Physics of Solids*, 50(11):2303 – 2331, 2002.

ISOGONAL AND ISOTOXAL HEXAGONS AS EXTREMAL YIELD FIGURES

H. Altenbach[1], P.L. Rosendahl[2], W. Becker[2], and V.A. Kolupaev[3]

[1]*Otto-von-Guericke-Universität Magdeburg, Universitätsplatz 2, D-39106 Magdeburg, Germany*
[2]*Technische Universität Darmstadt, Franziska-Braun-Straße 7, D-64287 Darmstadt, Germany*
[3]*Fraunhofer Institute for Structural Durability and System Reliability, Schloßgartenstr. 6, D-64289 Darmstadt, Germany*

e-mail: holm.altenbach@ovgu.de

1. Area of Interest

In the theory of plasticity the existence of the yield surface is assumed. In the past, several yield surfaces were formulated. However, choosing an appropriate surface for a particular material remains challenging. The extremal yield figures for isotropic material behavior will be generalized in this paper for universal practical application. Measured data for concrete will be approximated with the help of the proposed criterion.

2. Introduction

Yield criteria for isotropic material behavior are built up using invariants of the symmetric second-rank stress tensor. Three stress invariants – the trace (axiator) I_1 of the stress tensor and the invariants I_2', I_3' of the stress deviator expressed by principal stresses [1, 2] – are used here. The stress angle θ

$$\cos 3\theta = \frac{3\sqrt{3}}{2}\frac{I_3'}{(I_2')^{3/2}}, \qquad \theta \in \left[0,\, \frac{\pi}{3}\right] \tag{1}$$

is sometimes preferred over I_3' because it allows for a simple geometrical interpretation of the stress state. Yield criteria as function of the equivalent stress σ_{eq} are formulated according to

$$\Phi(I_1,\, I_2',\, I_3',\, \sigma_{\mathrm{eq}}) = 0 \qquad \text{or} \qquad \Phi(I_1,\, I_2',\, \theta,\, \sigma_{\mathrm{eq}}) = 0, \tag{2}$$

where the dependence on I_1 can be neglected for pressure-insensitive materials.

The criteria are subjected to special requirements. Among others, such so-called plausibility assumptions are the explicit resolvability of the criterion with respect to σ_{eq}, wide range of possible convex shapes in the π-plane, continuous differentiability except at the border, and no additional outer contours surrounding the physically reasonable shape of the surface. Fulfilling all of the above yields reliable criteria that are easy to handle. Unfortunately, criteria satisfying all requirements are not known.

3. Extremal Yield Figures

The lower and upper bounds of the convexity restriction for isotropic criteria give extremal yield figures of isotoxal and isogonal hexagons (Figs. 1 and 2). The polynomial formulations of these hexagons are known as CAPURSO and HAYTHORNTHWAITE criterion, respectively [2]. However, their polynomial forms feature intersections surrounding the physically reasonable shape of the surface and their application is intricate.

Isotoxal hexagons as function of stress angle (lower bound) can be described using the PODGÓRSKI criterion [3]. A criterion for isogonal hexagons (upper bound) as function of stress angle without case discrimination is missing. Both hexagons degenerate to the same equilateral triangles in border cases.

The present work aims at finding a universal yield criterion which contains the extremal yield figures and satisfies all plausibility assumptions.

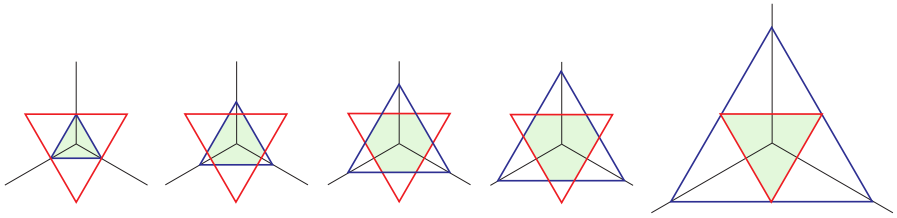

Figure 1: Isogonal hexagons (upper bound) consist of two intersecting triangles in the π-plane.

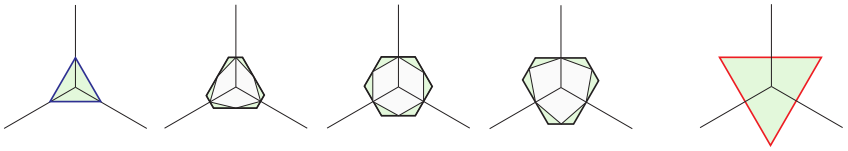

Figure 2: Isotoxal (lower bound) and isogonal hexagons in the π-plane.

4. Universal Yield Criterion

Consider the minimum function $\Omega = \min[\kappa, \lambda]$. In order to avoid case discrimination, the $\min$ operator may be replaced according to [4]:

$$\Omega = \frac{1}{2}\left[\kappa + \lambda + \sqrt{(\kappa - \lambda)^2}\right]. \tag{3}$$

Using the IVLEV [2] shape function

$$\kappa(\theta,\, \beta,\, \gamma) = \cos\left[\frac{1}{3}\left(\pi\,\beta - \arccos\left[\sin\left[\gamma\,\frac{\pi}{2}\right]\,\cos[3\,\theta]\right]\right)\right] \tag{4}$$

and the scaled MARIOTTE [2] shape function

$$\lambda(\theta,\, \alpha,\, \beta,\, \gamma) = \frac{1}{2}\,(3\,\alpha + 1)\,\cos\left[\frac{1}{3}\left(\pi\,\beta - \arccos\left[-\sin\left[\gamma\,\frac{\pi}{2}\right]\,\cos[3\,\theta]\right]\right)\right], \tag{5}$$

we obtain the universal yield function

$$\sigma_{\mathrm{eq}} = \sqrt{3\,I_2}\,\frac{\Omega(\theta,\, \alpha,\, \beta,\, \gamma)}{\Omega(0,\, \alpha,\, \beta,\, \gamma)}, \tag{6}$$

normalized with respect to the unidirectional tensile stress $\sigma_{\mathrm{eq}} = \sigma_+$. The parameters are restricted as follows:

$$\alpha \in [0, 1], \qquad \beta \in [0, 1], \qquad \gamma \in [0, 1]. \tag{7}$$

This yield function (6) contains the HAYTHORNTHWAITE criterion (isogonal hexagons) with $\alpha \in [0, 1]$, $\beta = 0$, and $\gamma = 1$, the CAPURSO criterion (isotoxal hexagons) with $\alpha \in \{0, 1\}$, $\beta \in [0, 1]$, and $\gamma = 1$, and the regular dodecagon in the π-plane according to SOKOLOVSKY [2] with $\alpha = 1/3$, $\beta = 1/6$, and $\gamma = 1$ without plane intersecting. The VON MISES criterion follows with $\alpha \in [0, 1]$, $\beta \in [0, 1]$, and $\gamma = 0$.

References

[1] H. Altenbach, J. Altenbach, and A. Zolochevsky. *Erweiterte Deformationsmodelle und Versagenskriterien der Werkstoffmechanik*. Deutscher Verlag für Grundstoffindustrie, Stuttgart, 1995.

[2] V. A. Kolupaev. *Equivalent Stress Concept for Limit State Analysis*. Springer, Cham, 2018.

[3] J. Podgórski. General failure criterion for isotropic media. *J. of Engineering Mechanics*, 111(2):188–201, 1985.

[4] H. Walser. Isogonal polygons (in German: Isogonale Vielecke). http://www.walser-h-m.ch, Frauenfeld, 2018.

A THERMOMECHANICAL FINITE ELEMENT FRAMEWORK FOR THE SIMULATION OF SELECTIVE LASER MELTING PROCESSES VIA PHASE TRANSFORMATION MODELS

I. Guschke[1], T. Bartel[1], and A. Menzel[1,2]

[1]*Institute of Mechanics, TU Dortmund, Dortmund, Germany*
[2]*Division of Solid Mechanics, Lund University, Lund, Sweden*

e-mail: isabelle.guschke@tu-dortmund.de

1. Introduction

Selective Laser Melting (SLM) is a technique belonging to additive manufacturing, a processing technique in contrast to the traditional material removal or casting technologies, which displays a great potential for industrial applications. Using the SLM process, a full dense metallic part with complex geometry can be produced directly and incrementally. The workpiece is manufactured using a high thermal energy source, e.g. a laser beam, to melt the metallic powder. Thus, the respective part undergoes a solid-liquid and subsequently a liquid-solid phase transformation which together result in high eigenstresses. To optimize the process parameters, the thermal, mechanical and metallurgical process has to be predicted. Thus, a finite element simulation using an appropriate model able to capture the constitutive material behaviour and the process itself is necessary. There are various models, as e.g. [6], which mostly focus on the temperature evolution, while using temperature-dependent material properties. In this contribution, the material modelling framework is adopted from solid-solid phase transformation simulation of shape memory alloys, cf. [1] and applied to the modelling of the different material states during the SLM process – powder, molten and re-solidified – as phase changes.

2. Thermomechanical framework

A fully coupled thermomechanical model is used to capture the temperature evolution and the process-induced eigenstresses. The linearised strain measure $\boldsymbol{\varepsilon}$ is applied, which is considered appropriate for the moderate strains occurring during SLM. The finite element simulation is based on the balance of linear momentum and the energy equation,

$$\nabla \cdot \boldsymbol{\sigma} + \boldsymbol{b} = 0 \,, \tag{1}$$

$$-\nabla \cdot \boldsymbol{q} + r + \mathcal{D}_{\mathrm{mech}} + \theta\, \partial_\theta [\, \boldsymbol{\sigma} : \dot{\boldsymbol{\varepsilon}} - \mathcal{D}_{\mathrm{mech}} \,] - \widetilde{c}\, \dot{\theta} = 0 \,. \tag{2}$$

In these equations, $\boldsymbol{\sigma}$ describes the stress tensor, $\boldsymbol{b}$ is the body force, $\boldsymbol{q}$ represents the heat flux vector, r denotes the externally supplied heat, $\mathcal{D}_{\mathrm{mech}}$ symbolizes the mechanical dissipation, θ is the temperature and $\widetilde{c} := -\,\theta\, \partial^2_{\theta\theta} \psi$ defines the effective specific heat capacity.

3. Constitutive framework

A mechanical material model based on fundamental constitutive models for each phase of the material, namely powder, molten and re-solidified, is used in this contribution. Adapting the framework provided in e.g. [1], the constitutive behaviour of each phase is modelled via phase energy densities ψ_i which consist of a mechanical and a caloric part. The constitutive model for the case of coexisting phases is obtained via a mixture rule

$$\bar{\psi} = \sum_{i=1}^{n_{\mathrm{ph}}} \xi_i\, \psi_i(\boldsymbol{\varepsilon}_i) \,, \tag{3}$$

where ξ_i describes the volume fraction and $\boldsymbol{\varepsilon}_i$ the total strain of the respective phase i. The range of the volume fractions is restricted by $\sum_{i=1}^{n} \xi_i = 1$ and $0 \leq \xi_i \leq 1$. An additive decomposition of elastic and inelastic strains is applied, where the only inelastic contribution considered is thermal strains in the re-solidified phase. With

this at hand, the temperature-induced change of the material's composition is obtained via energy minimisation of (3) resulting in

$$\psi^{\mathrm{rel}} = \min_{\boldsymbol{\varepsilon}_i, \xi_i} \left\{ \bar{\psi} \right\} \tag{4}$$

subject to

$$\boldsymbol{r}_{\boldsymbol{\varepsilon}} = \boldsymbol{\varepsilon} - \sum_{i=1}^{n} \xi_i \, \boldsymbol{\varepsilon}_i = \boldsymbol{0} \; . \tag{5}$$

Thus, the relaxed energy density is obtained by the minimisation of the averaged energy density w.r.t. the total strains in each phase and the volume fractions. With this at hand, an explicit formulation for the optimal strains within the respective phase can be calculated. An additional constraint $\dot{\xi}_{\mathrm{pow}} \leq 0$ needs to be taken into account, as the rate of the powder fraction $\dot{\xi}_{\mathrm{pow}}$ can only decrease. The minimisation problem with the inequality constraints is treated via the Karush-Kuhn-Tucker approach to calculate the respective volume fractions. Accordingly, the thermal model has to be adapted. A standard linear heat expansion model is used w.r.t. the irreversible strains in the re-solidified phase, whereas a classic isotropic Fourier ansatz is made for the heat conduction model. Thus, an averaged heat conduction and the effective specific heat capacity is used. Altogether, this establishes a physically well-motivated material model, where the different states of the material, namely powder, molten, and re-solidified, are captured as single phases with respective volume fractions.

4. Implementation and numerical examples

The constitutive framework is implemented into the commercial finite element software Abaqus. Here, the fully coupled thermal-stress analysis is used which is based on the weak forms of (1) and (2). Then, the previously explained constitutive material model is defined as an user material in the subroutine *UMAT*. For the implementation further numerical reformulations are necessary. The Karush-Kuhn-Tucker constraints are rewritten by the Fischer-Burmeister nonlinear complementarity functions as established in [3], see also [1], [5]. Thus, the determination of the volume fractions of the respective phases is possible via standard Newton-type algorithms. In addition to the update of the volume fractions which are saved as internal state variables, the algorithmic tangent and the stress update have to be defined within the routine. Finally, a model of the SLM process itself has to be developed. Therefore, a layer is built up with the help of (de-)activated elements which Abaqus enables by the interaction *Model Change*. This method has been established in [4] and is also used by e.g. [6]. Furthermore, an additional subroutine is applied to model a moving volumetric heat source representing the laser beam. For further information on Abaqus the interested reader is referred to [2]. In a final step, the commercial simulation software is used to generate representative small-scale examples using the aforementioned constitutive framework and process model. This allows the generation of – at the present state of investigation – qualitatively accurate predictions of the evolution of the material states and temperature, as well as the simulation of process-induced eigenstresses and the workpiece's final geometry.

References

[1] T. Bartel and K. Hackl. A micromechanical model for martensitic phase-transformations in shape-memory alloys based on energy-relaxation. *Journal of Applied Mathematics and Mechanics*, 89:792–809, 2009.

[2] Dassault Systèmes. Abaqus Documentation v2016, 2015.

[3] A. Fischer. A special newton-type optimization method. *Optimization*, 24:269–284, 1992.

[4] Z. Gan, H. W. Ng, and A. Devasenapathi. Deposition-induced residual stresses in plasma-sprayed coatings. *Surface & Coatings Technology*, 187:307–319, 2004.

[5] B. Kiefer, T. Bartel, and A. Menzel. Implementation of numerical integration schemes for the simulation of magnetic SMA constitutive response. *Smart Materials and Structures*, 21:094007, 2012.

[6] I. A. Roberts, C. J. Wang, R. Esterlein, M. Stanford, and D. J. Mynors. A three-dimensional finite element analysis of the temperature field during laser melting of metal powders in additive layer manufacturing. *International Journal of Machine Tools and Manufacture*, 49:916–923, 2009.

STEADY VIBRATIONS PROBLEMS IN THE THEORY OF THERMOELASTICITY FOR MATERIALS WITH TRIPLE VOIDS

M. Svanadze

Ilia State University, Tbilisi, Georgia

e-mail: svanadze@gmail.com

1. Introduction

The prediction of the thermomechanical properties of materials with single and multiple porosity has been one of hot topics of continuum mechanics for more than one hundred years. The mathematical models for materials with single and multiple voids have found applications in many branches of civil and geotechnical engineering, technology and biomechanics. In this connection, Cowin and Nunziato [1] presented the linear theory of elastic materials with single voids. Ieşan [2] extended this theory and developed a linear theory of thermoelastic materials with single voids. Nowadays, these mathematical theories are extensively investigated by several authors and the basic results may be found in the books of Ciarletta and Ieşan [3], Ieşan [4], Straughan [5] and references therein.

Further, Ieşan and Quintanilla [6] developed the theory of thermoelastic materials with double voids by using the mechanics of materials with voids. Moreover, in this new theory the independent variables are the displacement vector, the volume fractions of pores and fissures and the variation of temperature. The basic boundary value problems (BVPs) of equilibrium and steady vibrations in the theory of elasticity for materials with double voids are investigated by using the potential method by several authors (see [7]- [10]). Most recent results in the theories of materials with double voids are given in the new book of Straughan [11].

Recently, Svanadze [12] presented the linear equilibrium theory of elasticity for materials with triple voids structure by using the concept of the mechanics of materials with voids, and the uniqueness and existence theorems for regular (classical) solutions of the internal and external BVPs of equilibrium are proved by using the potential method.

In this work the mathematical model of the linear thermoelasticity for materials with triple voids (macro-, meso- and microporosity) structure is developed. In this model the independent variables are the displacement vector, the volume fractions of macro-, meso- and micropore networks and the variation of temperature. The BVPs of steady vibrations of this theory are investigated by using the potential method.

2. Basic Equations

Let $\mathbf{x} = (x_1, x_2, x_3)$ be a point of the Euclidean three-dimensional space $\mathbb{R}^3$. In what follows we consider an isotropic and homogeneous elastic material with triple porosity structure that occupies a region of $\mathbb{R}^3$; $\mathbf{u}(\mathbf{x})$ denote the displacement vector, $\mathbf{u} = (u_1, u_2, u_3)$; $\varphi_1(\mathbf{x})$, $\varphi_2(\mathbf{x})$ and $\varphi_3(\mathbf{x})$ are the changes of volume fractions from the reference configuration corresponding to macro-, meso- and micropore networks, respectively; θ is the temperature measured from the constant absolute temperature T_0 ($T_0 > 0$).

Within a dual porosity conceptual framework [6], the system of homogeneous equations of steady vibrations in the linear theory of thermoelasticity for materials with triple voids structure has the following form

$$
\begin{aligned}
&\mu\Delta\mathbf{u} + (\lambda+\mu)\nabla \operatorname{div}\mathbf{u} + b_j\nabla\varphi_j - \gamma_0\nabla\theta + \rho\omega^2\mathbf{u} = \mathbf{0},\\
&(\alpha_{lj}\,\Delta + \rho_{lj}\omega^2 - a_{lj})\,\varphi_j - b_l \operatorname{div}\mathbf{u} + \gamma_l\theta = 0,\\
&k\Delta\theta + i\omega T_0(a\,\theta + \gamma_0 \operatorname{div}\mathbf{u} + \gamma_j\varphi_j) = 0,
\end{aligned}
\tag{1}
$$

where Δ is the Laplacian operator, $l = 1, 2, 3$; ρ is the reference mass density, $\rho_{lj} = \delta_{lj}\rho_j$ (no sum), δ_{lj} is the Kronecker delta, ρ_1, ρ_2 and ρ_3 are the coefficients of the equilibrated inertia corresponding to macro-, meso- and

micropore networks, respectively, $\rho_j > 0$ $(j = 1, 2, 3)$; ω is the angular frequency; $a, a_{lj}, b_l, k, \alpha_{lj}, \gamma_0, \gamma_l, \lambda$ and μ are the constitutive coefficients and repeated indices are summed over the range (1,2,3). We assume that the internal energy of the isotropic and homogeneous thermoelastic materials with triple voids is positive definite.

3. Basic results

The following results in the considered theory are obtained:

(i) The governing field equations of the linear theory thermoelasticity for materials with triple voids is presented by using the mechanics of materials with multiple voids;

(ii) The fundamental solution of the system (1) is constructed explicitly by means of elementary functions and its basic properties are established;

(iii) The basic internal and external BVPs are formulated. Green's formulae and Sommerfeld-Kupradze type radiation conditions are established;

(iv) The uniqueness theorems for these BVPs are proved. The basic properties of the surface (single-layer and double-layer) and volume potentials and singular integral operators are established;

(v) The BVPs are reduced to the equivalent singular integral equations for which Fredholm's theorems are valid;

(vi) Finally, on the basis of the potential method and the theory of singular integral equations the existence theorems for the classical solutions of the BVPs of steady vibrations are proved.

References

[1] S.C. Cowin and J.W. Nunziato (1983). Linear elastic materials with voids, *J. Elasticity*, **13**, 125-147.

[2] D. Ieşan (1986). A theory of thermoelastic materials with voids, *Acta Mechanica*, **60**, 67-89.

[3] M. Ciarletta and D. Ieşan (1993). *Non-Classical Elastic Solids*. New York, NY, Harlow, Essex, UK: Longman Scientific and Technical, John Wiley & Sons, Inc.

[4] D. Ieşan (2004). *Thermoelastic Models of Continua*. London, UK: Kluwer Academic Publishers.

[5] B. Straughan (2008). *Stability and Wave Motion in Porous Media*. Springer, New York.

[6] D. Ieşan and R. Quintanilla (2014). On a theory of thermoelastic materials with a double porosity structure, *J. Thermal Stres.*, **37**, 1017-1036.

[7] D. Ieşan (2015). Method of potentials in elastostatics of solids with double porosity, *Int. J. Engng. Sci.*, **88**, 118-127.

[8] M. Svanadze, Plane waves, uniqueness theorems and existence of eigenfrequencies in the theory of rigid bodies with a double porosity structure. In: B. Albers and M. Kuczma (eds) (2016). *Continuous Media with Microstructure 2*. Springer Int. Publ. Switzerland, 287-306.

[9] M. Svanadze (2017). Boundary value problems of steady vibrations in the theory of thermoelasticity for materials with double porosity structure, *Arch. Mechanics* **69**, 347-370.

[10] M. Svanadze (2018). Steady vibrations problems in the theory of elasticity for materials with double voids, *Acta Mechanica*, DOI: 10.1007/s00707-017-2077-z (in press).

[11] B. Straughan (2017). *Mathematical Aspects of Multi-Porosity continua*, Springer Inter. Publ. AG.

[12] M. Svanadze (2018). On the linear equilibrium theory of elasticity for materials with triple voids, *Quart. J. Mech. Appl. Math.* (in press).

VISCO-PLASTIC EFFECTS DUE TO DEFORMATION ALONG CIRCULAR LOADING PATH

T. Szymczak[1], Z.L. Kowalewski[2]

[1] *Motor Transport Institute, Warsaw, Poland*
[2] *Institute of Fundamental Technological Research, Warsaw, Poland*

e-mail: zkowalew@ippt.pan.pl

1. Introduction

Cyclic circular loading path is classified as a non-proportional deformation. Experimentally it can be obtained by the use of two out-of-phase sinusoidal signals of strain or stress: axial and shear [1, 2]. The phase shift between the signals should be equal to 90 degrees. An influence of circular path on material behaviour is investigated by many research groups [1-4]. They analyse variations of stress state components versus time. The results enable analysis of a cyclic softening or hardening of materials [1, 2, 4], variations of principal strain directions [3], and effective strain evolution [2]. For better understanding of material behaviour under non-proportional cycles further systematic investigations are required.

2. Experimental procedure and results

All tests were carried out at room temperature using thin-walled tubular specimens and servo-hydraulic testing machine. The wall thickness and gauge length of the specimens were equal to 0.75 mm and 60 mm, respectively. The 2024 aluminium alloy, widely used in aircraft industry, was selected for investigations. Strain gauges, cemented on the specimen measurement length, were used to control the testing machine. Two strain signals: axial and shear were applied to create circular strain path, Fig 1. Four values of the effective strain amplitude were selected in the experimental programme: ±0.2, ±0.4, ±0.6 and ±0.8%. The frequency was constant (0.02Hz).

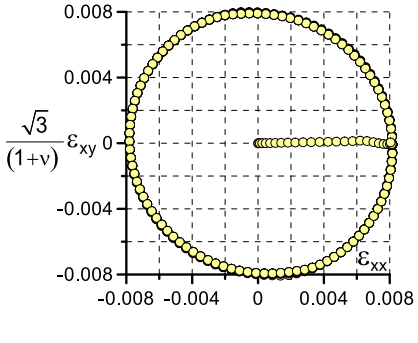

Fig. 1. Circular strain path for effective amplitude of ±0.8%

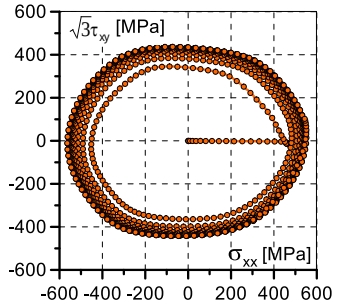

Fig. 2. Stress response into the programme shown in Fig. 1

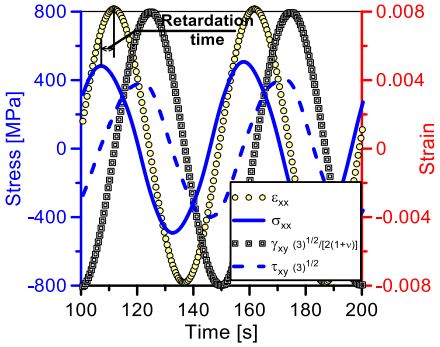

Fig. 3. Retardation time between strain and stress signals during cyclic deformation along circular strain path

Material behaviour during deformation along circular strain path was elaborated on the basis of: stress response (Fig. 2); retardation time and retardation angle (f) (Figs. 3, 4c); dynamic modulus (Fig. 4a); and modulus variation (Fig. 4b). For the strain amplitude of ±0.8% the stress response identifies material hardening, Fig. 2. A comparison of the stress and strain signals as a function of time makes it possible to determine a retardation time, Fig. 3. This phenomenon becomes more significant with increasing number of cycles and tends asymptotically to the constant level. Dynamic modulus (Fig. 4a) for axial and torsional directions can be expressed by the proportion of stress and strain amplitudes:

(1a, b)
$$E_{d\_xx} = \frac{\sigma_a}{\varepsilon_{xx\_a}}; \quad E_{d\_xy} = \frac{\tau_a}{\varepsilon_{xy\_a}}.$$

Stress and strain amplitudes, that are used for calculation of dynamic modulus increment (Fig. 4b) in both directions considered may be defined by the following equations:

(2a, b) $$E_{d1\_xx} = E_{d\_xx}\cos(\varphi); \quad E_{d2\_xx} = E_{d\_xx}\sin(\varphi);$$

(3a, b) $$E_{d1\_xy} = E_{d\_xy}\cos(\varphi); \quad E_{d2\_xy} = E_{d\_xy}\sin(\varphi).$$

Retardation angle can be represented by the following relationships:

(4a, b) $$\tan(\alpha)_{\_xx} = \frac{E_{d2\_xx}}{E_{d1\_xx}}; \quad \tan(\alpha)_{\_xy} = \frac{E_{d2\_xy}}{E_{d1\_xy}}.$$

It achieved the highest value at the beginning of cyclic loading, and finally took almost constant magnitude, Fig. 4c.

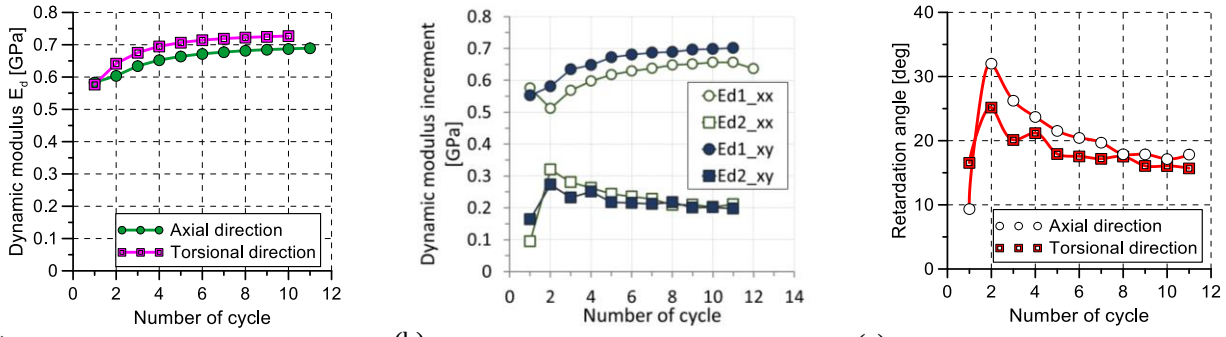

(a) (b) (c)

Fig. 4. Visco-plastic effects observed during deformation along circular strain path: (a) dynamic modulus; (b) dynamic modulus increment; (c) retardation angle

Gradual increase of dynamic modulus (E_d) versus number of cycles identifies the material hardening. For the final stage of cyclic loading it takes constant level, close to the Young's modulus of the aluminium alloy tested. The same effect is observed for the variations of E_{d1_xx} and E_{d1_xy}, Fig. 4b. The variations of E_{d2_xx} and E_{d1_xy} moduli represent an opposite tendency. In the case of the retardation angle one can notice lowering of its value up to 17° for both directions taken into account, Fig. 4c. It means that the phase shift between stress and strain signals did not vanish, however, the saturation state was achieved (Fig. 2 and 4c).

3. Summary

An influence of circular strain path on the material behaviour can be studied on the basis of: (a) variations of principal strain directions, phase shift and retardation angle between stress and strain signals; (b) increase of dynamic moduli.

References

[1] E. Tanaka, S. Murakami, M. Ooka, Effects of plastic strain amplitudes on non–proportional cyclic plasticity, *Acta Mech.*, 57, 167–182, 1985.

[2] S. Calloch, D. Marquis, Additional hardening due to tension–torsion loadings: influence of the loading path shape, Multiaxial Fatigue and Deformation Testing Techniques, *ASTM STP 1280*, 113-130, 1997.

[3] T. Szymczak, Z.L. Kowalewski, A. Rutecka, Material responses to the laboratory simulation of complex cyclic loadings, 34th European Congress Kones 2008, *Journal of Kones Powertrain and Transport*, 7-10 September 2008, Vol. 15, No. 3, 509-516.

[4] Z.L. Kowalewski, T. Szymczak, J. Maciejewski, 2014. Material effects during monotonic-cyclic loading, *Int. J. Solid and Structures*, 51, 3-4, 740-753.

ELLIPTICITY OF LARGE STRAIN THERMO-PLASTICITY: THEORY AND NUMERICAL ANALYSIS

J. Pamin[1], B. Wcisło[1], K. Kowalczyk-Gajewska[2], and A. Menzel[3,4]

[1]*Institute for Computational Civil Engineering, Cracow University of Technology, Cracow, Poland*
[2]*Institute of Fundamental Technological Research, Polish Academy of Sciences, Warsaw, Poland*
[3]*Institute of Mechanics, Technische Universitaet Dortmund, Dortmund, Germany*
[4]*Division of Solid Mechanics, Lund University, Lund, Sweden*

e-mail: JPamin@L5.pk.edu.pl

1. Introduction

When instability in a material occurs, for example due to material or thermal softening, the boundary-value problem loses its ellipticity and, as a consequence, becomes ill-posed. The theoretical solution of such problem leads to strain localization in a set of measure zero (for three-dimensional problem it is a surface), whereas the results of numerical simulations pathologically depend on discretization [4]: the size and the mesh orientation govern the width and the direction of the localized deformation band. Thus, if ellipticity is lost the problem requires some regularization.

The ellipticity conditions are well described for isothermal problems involving large strains or inelastic behaviour, see e.g. [6] or [5] However, in the case of thermo-mechanical coupling researchers usually assume some limitations, for example small strains, elasticity [1], or internal adiabaticity (lack of heat conduction) [3]. The aim of this paper is the analysis of the ellipticity condition for large strain thermo-plasticity.

2. Material model

The considered material model involves hyperelasticity and plasticity with the von Mises yield criterion and associative flow rule. Young's modulus and initial yield strength may depend on the change of temperature. The thermomechanical coupling includes thermal expansion and heat production in a plastic process. Following [7], the multiplicative split of the deformation gradient into reversible and plastic components is used, $\mathbf{F} = \mathbf{F}^r\mathbf{F}^p$, and the free energy function has the form

$$\psi(\mathbf{b}^r,\gamma,T) = \frac{K}{2}\left[\frac{1}{4}\left[\ln(J^{br})\right]^2 - 3\alpha_T(T-T_0)\ln(J^{br})\right] + \frac{G}{2}\left[\mathrm{tr}([J^{br}]^{-1/3}\mathbf{b}^r) - 3\right] + \psi^p(\gamma) + \psi^T(T) \tag{1}$$

where $\mathbf{b}^r = \mathbf{F}^r(\mathbf{F}^r)^{\mathrm{T}}$, γ is a measure of plastic strain, T is absolute temperature, K and G denote material parameters, $J^{br} = \det(\mathbf{b}^r)$, α_T is a thermal expansion coefficient and T_0 – referential temperature. The implementation of a similar large strain thermoplasticity model within *AceGen/FEM* packages is presented in [8].

3. Ellipticity verification

The condition of ellipticity loss can be derived in two ways. The first one is based on the examination of equilibrium on a discontinuity surface [3]. It is assumed that a jump of traction (and its rate) across discontinuity surface is zero

$$[\![\boldsymbol{\sigma}]\!]\mathbf{n} = \mathbf{0}, \qquad [\![\dot{\boldsymbol{\sigma}}]\!]\mathbf{n} = \mathbf{0} \tag{2}$$

where $\boldsymbol{\sigma}$ is Cauchy stress tensor and $\mathbf{n}$ is a normal to the discontinuity surface in the current configuration. For the thermomechanical coupling a zero jump of heat flux $\mathbf{q}$ and of its rate is also required

$$[\![\mathbf{q}]\!]\cdot\mathbf{n} = 0, \qquad [\![\dot{\mathbf{q}}]\!]\cdot\mathbf{n} = 0 \tag{3}$$

The second approach involves the analysis of the perturbation of a base state [1]. On the initially homogeneously deformed specimen with constant temperature distribution the following perturbations are imposed

$$\mathbf{u}^{pert}(\mathbf{x},t) = \exp(ik\,(\mathbf{n}\cdot\mathbf{x}+vt))\hat{\mathbf{u}}, \qquad T^{pert}(\mathbf{x},t) = \exp(ik\,(\mathbf{n}\cdot\mathbf{x}+vt))\hat{T} \tag{4}$$

where $\mathbf{x}$ is the particle current position, t is time, $\hat{\mathbf{u}}$ and $\hat{T}$ are constant amplitudes, v is wave speed, k – wave number and i – imaginary unit. Inserting definitions (4) into balance equations for linear momentum and energy, the set of equations for $\hat{\mathbf{u}}$ and $\hat{T}$ is obtained.

Both approaches might be formulated in the referential or current configuration. It can be noted that for the coupled thermomechanical problem both methods lead to a set of two equations. There are two special limit cases which are analysed: isothermal and adiabatic, for which singularity of isothermal and adiabatic acoustic tensors, respectively, indicates the loss of ellipticity. It is worth mentioning that an alternative approach involving the analysis of generalized eigenvectors is considered in [2].

The derived conditions are numerically tested for samples in tension, simulated within the finite element method using *AceGen/FEM* package. The crucial feature of the package is automatic differentiation which is efficiently applied for the calculation of material tangents required to obtain acoustic tensors. The ellipticity conditions are verified at selected Gauss points after converged load steps. The exemplary output of the ellipticity analysis is presented in Figure 1.

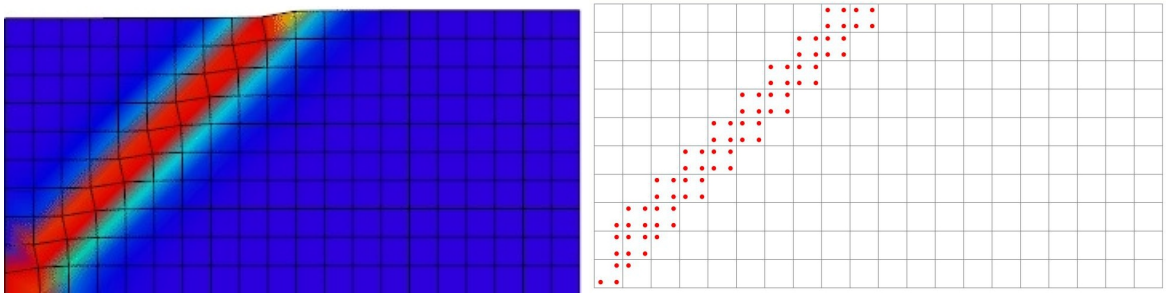

Figure 1: Deformed sample with plastic strain measure distribution (on the left) and Gauss points at which ellipticity is lost (on the right) – results for large strain elastoplasticity

References

[1] R. Abeyaratne and J. K. Knowles. On the stability of thermoelastic materials. *J. Elasticity*, 53:199–213, 1999.

[2] M. Arriaga, C. McAuliffe, and H. Waisman. Onset of shear band localization by a local generalized eigenvalue analysis. *Comput. Methods Appl. Mech. Engrg.*, (289):179–208, 2015.

[3] A. Benallal and D. Bigoni. Effects of temperature and thermo-mechanical couplings on material instabilities and strain localization of inelastic materials. *J. Mech. Phys. Solids*, 52:725–753, 2004.

[4] S. Forest and E. Lorentz. Localization phenomena and regularization methods. In J. Besson, editor, *Local approach to fracture*, pages 311–370. Les Presses de l'École des Mines, Paris, 2004.

[5] H. Petryk. Plastic instability: criteria and computational approaches. *Archives of Computational Methods in Engineering*, 4(2):111–151, 1997.

[6] J. R. Rice. The localization of plastic deformation. In W.T. Koiter, editor, *Proc. 14th Int. Cong. Theoretical and Applied Mechanics*, pages 207–220, Amsterdam, 1976. North-Holland Publishing Company.

[7] M. Ristinmaa. Thermodynamic formulation of plastic work hardening materials. *ASCE J. Eng. Mech.*, 125:152–155, 1999.

[8] B. Wcisło and J. Pamin. Local and non-local thermomechanical modeling of elastic-plastic materials undergoing large strains. *Int. J. Numer. Meth. Engng*, 109(1):102–124, 2017.

MODELLING OF WEDGE INDENTATION USING A GRADIENT-ENHANCED CRYSTAL-PLASTICITY MODEL

M.J. Lewandowski and S. Stupkiewicz

Institute of Fundamental Technological Research, Warsaw, Poland

e-mail: maclewan@ippt.pan.pl, sstupkie@ippt.pan.pl

1. Introduction

Size effects is metal plasticity attract a significant interest in the materials science and mechanics communities. This work is concerned with the modelling of the size effects induced by strain gradients, for instance, in micro-torsion, micro-bending, and micro/nano-indentation. The related hardening mechanism ('smaller is stronger') is associated with the geometrically necessary dislocations (GNDs) that accommodate the strain gradients [1].

Modelling of the indentation size effect is in most cases limited to isotropic plasticity, often based on a simplified geometric model, e.g. [2]. Simulations employing gradient crystal plasticity models are much more scarce. In this work, a recently developed gradient-enhanced crystal-plasticity model [3,4] is applied to predict the size effects in wedge indentation.

2. Minimal gradient enhancement of crystal plasticity

In the model of Petryk and Stupkiewicz [3], the classical framework of crystal plasticity is enhanced with slip-rate gradient effects by extending the usual anisotropic hardening law with a single isotropic term that represents the GND hardening. Unlike in the frequently used split of the total dislocation density into the densities of statistically stored dislocations (SSDs) and GNDs, e.g., [1, 2], such a split is applied in an incremental form only. The difference may seem minor, but it has a significant influence on the resulting model. The internal length scale ℓ,

$$\ell = \frac{a^2 \mu^2 b}{2\tau\theta}, \tag{1}$$

depends on the current flow stress τ and hardening rate θ, the remaining parameters being essentially known for a given material. The length scale ℓ has been shown to be closely related to the mean free path of dislocations and thus possesses a direct physical interpretation [3]. The resulting 'minimal' gradient enhancement of the hardening law is thus free of any fitting parameters. Specifically, the following gradient-enhanced hardening law for the critical resolved shear stresses $\dot{\tau}_\alpha^c$ has been derived,

$$\dot{\tau}_\alpha^c = \theta\bigg(\sum_\beta q_{\alpha\beta} |\dot{\gamma}_\beta| + \ell\dot{\chi} \bigg), \tag{2}$$

where the slip-rate gradient effects are introduced through the term $\ell\dot{\chi}$, and $\dot{\chi}$ is the effective slip-rate gradient. For $\ell\dot{\chi} = 0$, the usual hardening law is recovered with $q_{\alpha\beta}$ denoting the latent-hardening interaction matrix.

3. Simulation of wedge indentation into nickel single crystal

The model has been applied to simulate wedge indentation into a nickel single crystal [5]. The experimental results reported by Dahlberg et al. [6] and Sarac et al. [7] have been used for verification of the model in the range of relatively large indentation depths (about $200\,\mu$m) for which the gradient effects are expected to be negligible. A good agreement with the experiment has been obtained in terms of the indentation load–penetration depth curves for three wedge angles, as well as in terms of the distributions of lattice rotation,

GND density, and net Burgers vector. At the same time, the results obtained confirm that the effect of slip-rate gradients is indeed negligible for the indentation depth of 200 μm. Subsequently, the size effects have been studied by varying the maximum indentation depth in the range between 200 μm and 1 μm. In this range of indentation depths, the size effect manifests itself in the increase of hardness by the factor of approximately four with respect to the large penetration-depth limit. This is also accompanied by size-dependence of other features, including the residual imprint. Sample results are shown in Figs. 1 and 2.

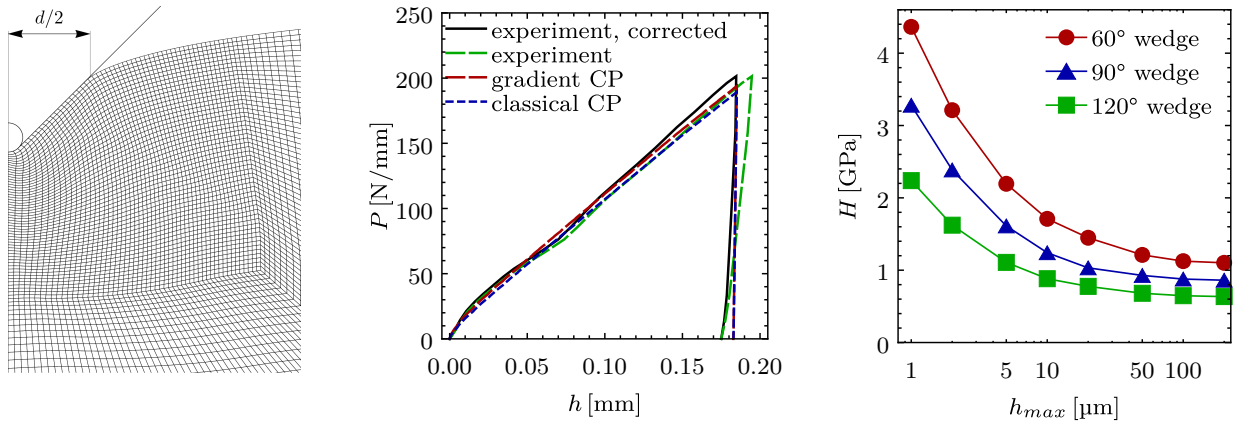

Figure 1: Wedge indentation into a nickel single crystal: deformed mesh in the vicinity of the indent (left), indentation load–penetration depth curve (middle), and the dependence of hardness on the maximum indentation depth (right).

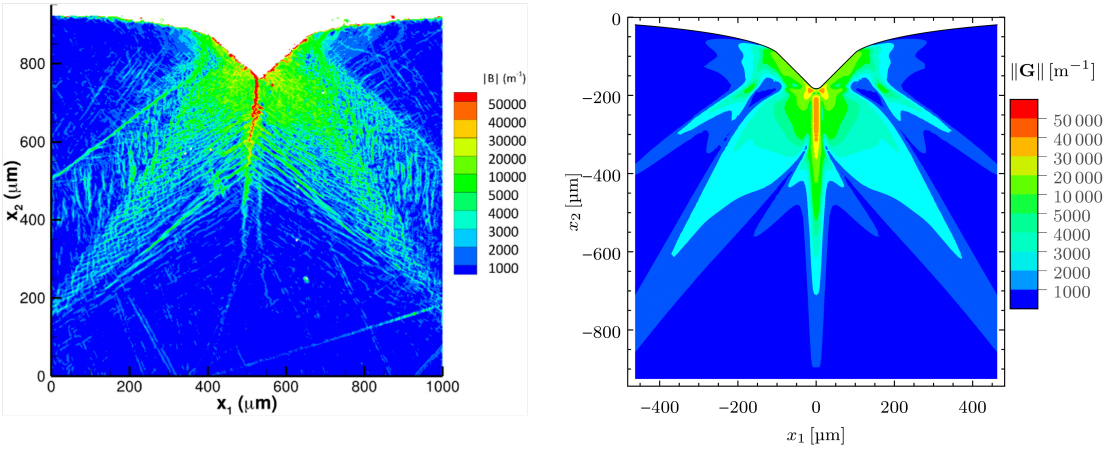

Figure 2: Distribution of GNDs near the indent: experiment [7] (left) and simulation (right).

References

[1] M.F. Ashby (1970). The deformation of plastically non-homogeneous materials, *Philosophical Magazine*, **21**, 399–424.

[2] W.D. Nix and H. Gao (1998). Indentation size effects in crystalline materials: a law for strain gradient plasticity, *Journal of the Mechanics and Physics of Solids*, **46**, 411–425.

[3] H. Petryk and S. Stupkiewicz (2016). A minimal gradient-enhancement of the classical continuum theory of crystal plasticity. Part I: The hardening law, *Archives of Mechanics*, **68**, 459–485.

[4] S. Stupkiewicz and H. Petryk (2016). A minimal gradient-enhancement of the classical continuum theory of crystal plasticity. Part II: Size effects, *Archives of Mechanics*, **68**, 487–513.

[5] M.J. Lewandowski and S. Stupkiewicz (2018). Size effects in wedge indentation predicted by a gradient-enhanced crystal-plasticity model, *International Journal of Plasticity*, doi: 10.1016/j.ijplas.2018.05.008.

[6] C.F.O. Dahlberg, Y. Saito, M.S. Oztop and J.W. Kysar (2016). Geometrically necessary dislocation density measurements associated with different angles of indentations, *International Journal of Plasticity*, **54**, 81–95.

[7] A. Sarac, M.S. Oztop, C.F.O. Dahlberg and J.W. Kysar (2016). Spatial distribution of the net Burgers vector density in a deformed single crystal, *International Journal of Plasticity*, **85**, 110–129.

Session S02: Micromechanics, interfaces and multiscale modelling

Organizers: V. Kouznetsova (Eindhoven UT), A. Menzel (TU Dortmund), S. Stupkiewicz (IPPT PAN, Warsaw)

APPLICATION OF THE FUZZY LATTICE BOLTZMANN METHOD FOR A NUMERICAL MODELLING OF 2D THIN METAL FILMS IRRADIATED BY ULTRASHORT LASER PULSES

A. Piasecka-Belkhayat, A. Korczak

Institute of Computational Mechanics and Engineering
Silesian University of Technology, Konarskiego 18A, 44-100 Gliwice, Poland
e-mail: alicja.piasecka-belkhayat@polsl.pl, anna.korczak@polsl.pl

1. Introduction

In the paper, the numerical modelling of heat transfer in two-dimensional metal films is considered. The fuzzy coupled lattice Boltzmann equations for electrons and phonons supplemented by the adequate boundary and initial conditions have been applied to analyse the thermal process proceeding in a thin metal film. The two-dimensional 9-speed model (D2Q9) with fuzzy trapezoidal values of relaxation times and boundary conditions is proposed. The problem considered is solved by the fuzzy lattice Boltzmann method using α-cuts and the rules of directed interval arithmetic [1]. The application of α-cuts allows one to avoid complicated arithmetical operations in the set of fuzzy numbers. In the final part of the paper the results of numerical computations are shown.

2. The fuzzy Boltzmann transport equation

The fuzzy Boltzmann transport equations for the 2D coupled model with two kinds of carriers (*e*-electrons and *ph*-phonons) can be written using the following formulas [2]

$$\frac{\partial \tilde{e}_e}{\partial t} + \mathbf{v}_e \cdot \nabla \tilde{e}_e = -\frac{\tilde{e}_e - \tilde{e}_e^0}{\tilde{\tau}_{re}} + \tilde{Q}_e \tag{1}$$

$$\frac{\partial \tilde{e}_{ph}}{\partial t} + \mathbf{v}_{ph} \cdot \nabla \tilde{e}_{ph} = -\frac{\tilde{e}_{ph} - \tilde{e}_{ph}^0}{\tilde{\tau}_{r\,ph}} + \tilde{Q}_{ph} \tag{2}$$

where $\tilde{e}_e, \tilde{e}_{ph}$ are the fuzzy energy densities, $\tilde{e}_e^0, \tilde{e}_{ph}^0$ are the equilibrium fuzzy energy densities, $\mathbf{v}_e, \mathbf{v}_{ph}$ are the frequency-dependent propagation speeds, $\tilde{\tau}_{re}, \tilde{\tau}_{r\,ph}$ are the fuzzy relaxation times, *t* denotes the time and $\tilde{Q}_e, \tilde{Q}_{ph}$ are the fuzzy energy sources related to a unit of volume for electrons and phonons respectively.

The fuzzy values of the electron and phonon energy densities at their equivalent nonequilibrium temperatures are given by the formulas

$$\tilde{e}_e(\tilde{T}_e) = \left(n_e \frac{\pi^2}{2} \frac{k_b^2}{\varepsilon_F} \right) \tilde{T}_e^{\,2} \tag{4}$$

$$\tilde{e}_{ph}(\tilde{T}_{ph}) = \left(\frac{9\eta_{ph} k_b}{\Theta_D^3} \int_0^{\Theta_D/\tilde{T}_{ph}} \frac{z^3}{\exp(z)-1}\,\mathrm{d}z \right) \tilde{T}_{ph}^4 \tag{5}$$

where Θ_D is the Debye temperature of the solid, k_b is the Boltzmann constant, ε_F is the Fermi energy, $\tilde{T}_e, \tilde{T}_{ph}$ are the fuzzy lattice temperatures for electrons and phonons respectively, while n_e is the electron density and η_{ph} is the phonon density.

The fuzzy electron and phonon energy sources are calculated using the following expressions [2]

$$\tilde{Q}_e = Q' - G(\tilde{T}_e - \tilde{T}_{ph}), \qquad \tilde{Q}_{ph} = G(\tilde{T}_e - \tilde{T}_{ph}) \tag{6}$$

where Q' is the power density deposited by the external source function and G is the electron-phonon coupling factor which characterizes the energy exchange between electrons and phonons. The equations (1) and (2) should be supplemented by the initial and boundary conditions [3]. The temporal variation of laser output pulse is treated as source term in the energy equation and may be approximated by the form of exponential function [3]

$$Q'(x,t) = I_0 \delta e^{-\delta y - \beta t} e^{-\frac{2x^2}{r^2}} \tag{7}$$

where I_0 is the peak power intensity of the laser pulse, δ is the absorption coefficient, β is the laser pulse parameter, r is the radius of the laser beam, *x* and *y* are the coordinates.

3. Results of computations

As a numerical example, the heat transport in a gold thin film of the dimensions 1000 nm × 200 nm has been analysed. The following input data have been introduced: $\tilde{q}_{b1} = \tilde{q}_{b2} = \tilde{q}_{b3} = \tilde{0}\,\mathrm{W/m^2}$, $\tilde{T}_{b4} = (285, 292.5, 307.5, 315)\,\mathrm{K}$, $T_0 = 3\ 0\ 0$ $\Delta t = 0.01\,\mathrm{ps}$, fuzzy relaxation times for phonons $\tilde{\tau}_{ph} = (\tau_{ph} - 0.05\tau_{ph}, \tau_{ph} - 0.025\tau_{ph}, \tau_{ph} + 0.025\tau_{ph}, \tau_{ph} + 0.05\tau_{ph})$ and electrons $\tilde{\tau}_e = (\tau_e - 0.05\tau_e,\ \tau_e - 0.025\tau_e,\ \tau_e + 0.025\tau_e, \tau_e + 0.05\tau_e)$, $r = 160\,\mathrm{nm}$, the other material and laser properties are defined in Table 1.

	τ_{ph} [ps]	τ_e [ps]	Θ_D [K]	$n_e(\times 10^{28})$ [1/m^3]	ε_F [eV]	$I_0(\times 10^{13})$ [W/m^2]	$\beta(\times 10^{13})$ [1/s]	$\delta(\times 10^{7})$ [1/m]
Au	0.8	0.04	170	5.9	5.53	2	0.5	7.55

Table 1: Material and laser properties.

Figure 1 illustrates the fuzzy electrons heating curves obtained for $\alpha = 0.5$ in the nodes: (100, 80) – 1, (100, 100) – 2 and (100,120) – 3.

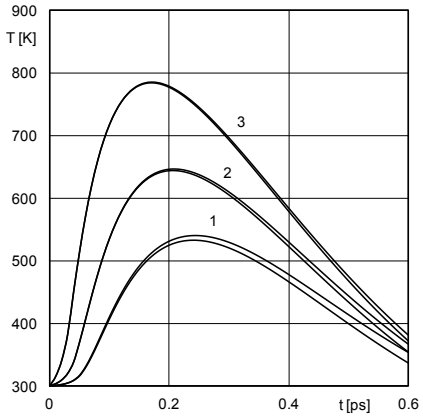

Fig. 1. Fuzzy electrons heating curves in chosen nodes.

Acknowledgments The research is funded from the projects Silesian University of Technology, Faculty of Mechanical Engineering.

References

[1] A. Piasecka-Belkhayat and A. Korczak, Numerical modelling of the transient heat transport in a thin gold film using the fuzzy lattice Boltzmann method with α-cuts. *J. of Appl. Math. and Comp. Mech.*, Vol. 15, 1, 123-135, 2016.

[2] S.S. Ghai, W.T. Kim and R.A. Escobar, et al., A novel heat transfer model and its application to information storage systems. *J. of Applied Physics*, Vol. 97, 10P703 1-3, 2005.

[3] J.K. Chen, D.Y. Tzou and J.E. Beraun, A semiclassical two-temperature model for ultrafast laser heating. *Int. J. of Heat and Mass Transfer*, Vol. 49, 307–316, 2006.

BOUNDARY LAYER EFFECT AT THE FREE EDGE OF COMPOSITE MATERIAL USING HOMOGENIZATION THEORY

S. Koley, P. M. Mohite, and C. S. Upadhyay

Department of Aerospace Engineering, Indian Institute of Technology Kanpur, India

e-mail: skoley@iitk.ac.in

1. Introduction

Many studies in the theory of composite materials are based on the homogenization approach, which consists of the substitution of the heterogeneous medium by a homogeneous one with certain effective properties [1,2]. These effective properties are obtained from internal asymptotics which excludes boundary layer effects. On considering the individual ply, at the boundary of the domain one can notice a disruption of periodic arrangement. This disruption leads to possible loss of periodicity, hence the asymptotic approach needs to be corrected [3]. Here, boundary layer study is a correction in the micro solution which accounts for the error in the boundary condition. This error gives rise to a boundary layer which decays very quickly when it travels to the interior of the domain.

2. Asymptotic homogenization for multiple scale analysis

Homogenization methods have proven to be powerful techniques for the study of heterogeneous media [4]. The existence of two length scales such as length scale of the microstructure ε and the length scale of the structure, L. The two scales x_i and y_i are spatial variables, where x_i is a macroscopic quantity and $y_i = x_i/\varepsilon$ is a microscopic one as y_i is associated with the length scale of the inclusions or heterogeneities. The solution u_i^ε are approximated with an asymptotic series representation in ε to admit the following ansatz

$$u_i^\varepsilon(\vec{x};\vec{y}) = u_i^{(o)}(\vec{x}) + \varepsilon\left(u_i^{(1)}(\vec{x};\vec{y}) + u_i^{(bl)}(\vec{x};\vec{y})\right) + \text{ h.o.t} \tag{1}$$

where each function $u_i(x,y)$ is Y-periodic function with respect to fast variable y, u_i^{bl} is a decaying function in direction normal to free edge and periodic in all other y_j directions.

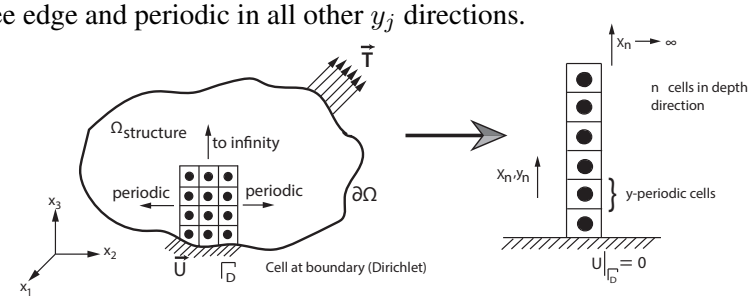

Figure 1: Elastic body with *Y* - periodic cells tends to infinity

The periodic micro correction to $u_1(y)$ can be obtained from each of the six fundamental macro-strains e_x^{ij}, by solving the periodic cell problem. From the equilibrium equation and the consistency condition we get,

$$\left[\frac{1}{V_{RVE}}\left(\int_{V_{RVE}}\left(C_{ijkl}\left(\delta_{km}\delta_{ln} + \chi_{klmn}\right)dv\right)\right)\right]\left(\bar{\varepsilon}_{mn}\right)_{,x_j} + f_i = 0 \tag{2}$$

The expression inside the square bracket is equal to $\bar{C}_{ijkl}$, which is the RVE volume averaged/effective global stiffness and it is a macro problem, where χ_{klmn} is the fully periodic solution.

3. Problems at the vicinity of the boundary

Due to the boundary layer phenomenon, this homogenized system depends in a non trivial way on the boundary [5]. Considering the cell at the boundary of the composite material, as shown in Figure 1 with homogeneous Dirichlet boundary condition, we get $u_i^\varepsilon|_{\Gamma_D} = u_i^0 + \varepsilon\left(u_i^1 + u_i^b l\right) = 0$. But $u_i^0|_{\Gamma_D} = 0$ which gives $u_i^{bl}|_{\Gamma_D} = -u_i^1|_{\Gamma_D}$ as displacement boundary condition for the boundary layer correction with the enforcement of $u_i^{(o)}(\vec{x}) = 0$ but $u_i^{(1)}(\vec{x};\vec{y}) \neq 0$. This is coupled with the consistency enforced equilibrium equation as

(3) $$\frac{\partial}{\partial y_i} C_{ijkl} \bar{\varepsilon}^{bl}_{kl} = 0$$

The above condition means that, u_i^{bl} is not required to be fully Y - periodic and therefore, one needs to solve u_i^{bl} for only one column of cells starting from Γ_D as shown in Figure 2.

4. Results

Selected results for the decay of the displacement fields for three different fibre orientations are shown in Figure 3. Variation of stress fields for both fully periodic and boundary layer problem are shown in Figure 4 for unit macro strain of ϵ_{zz}. Microstructural effects for different fibre orientation have been investigated according to the procedure described in [5].

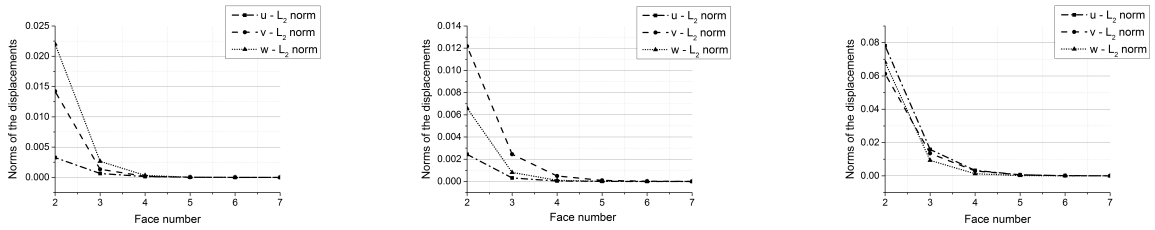

(a) (b) (c)

Figure 2: Decay of the displacement norms for unit macro strain (ϵ_{zz}) over the RVEs with fibre orientation at (a) 0 ° (b) 90 ° (c) 45 °

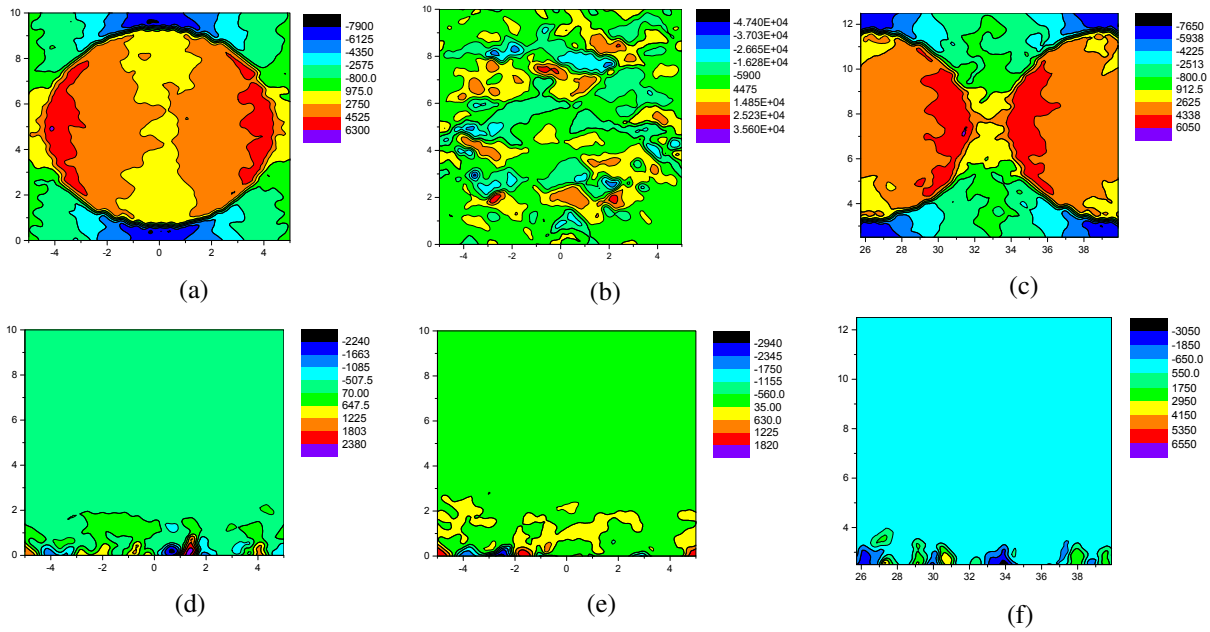

(a) (b) (c) (d) (e) (f)

Figure 3: Distribution of micro stress fields (σ_{zz}) due to unit macro strain (ϵ_{zz}) over the RVEs of (a) 0 ° (b) 90 ° (c) 45 ° - for fully periodic problem and (d) 0 ° (e) 90 ° (f) 45 ° - for boundary layer problem

References

[1] S. Nemat-Nasser, M. Hori, Micromechanics: Overall Properties of Heterogeneous Materials, (1993).

[2] J. Aboudi, S. M. Arnold, B. A. Bednarcyk, Micromechanics of Composite Materials: A Generalized Multiscale Analysis Approach, Butterworth-Heinemann, 2012.

[3] A. Bensoussan, J. L. Lions, G. Papanicolaou, Asymptotic Analysis for Periodic Structures, Vol. 374, American Mathematical Soc., 2011.

[4] N. Bakhvalov, G. Panasenko, Homogenisation: Averaging Processes in Periodic Media: Mathematical Problems in the Mechanics of Composite Materials, Vol. 36, Springer Science & Business Media, 2012.

[5] G. Allaire, M. Amar, Boundary layer tails in periodic homogenization, ESAIM: Control, Optimisation and Calculus of Variations 4 (1999) 209–243.

THE CASIMIR FORCE AS A DRIVER IN MICROMECHANICS

G. L. Klimchitskaya[1,2], V. M. Mostepanenko[1,2], and V. M. Petrov[3]

[1]*Central Astronomical Observatory at Pulkovo of the Russian Academy of Sciences, Saint Petersburg, 196140, Russia*
[2]*Institute of Physics, Nanotechnology and Telecommunications, Peter the Great Saint Petersburg Polytechnic University, Saint Petersburg, 195251, Russia*
[3]*Institute of Advanced Manufacturing Technologies, Peter the Great Saint Petersburg Polytechnic University, Saint Petersburg, 195251, Russia*

e-mail: vmostepa@gmail.com

1. Introduction

In modern practice, the micromechanical devices play a broad spectrum of roles and find expanding application in engineering and industry. With schrinking device dimensions to submicrometer level, in addition to mechanical and electric forces, the Casimir force induced by the electromagnetic fluctuations comes into play. This attractive force is of entirely quantum nature. It acts even between uncharged material surfaces and far exceeds typical electric forces for devices of size below a few hundred nanometers [1]. Experts in micromechanics have long been aware [2] that the Casimir force may play a detrimental role in the functionality of a micromechanical device leading to a jump of the moving part of it to a fixed piece. This phenomenon was called a *pull-in* or *stiction*. It was also demonstrated [3] that the Casimir force can be used for actuation of a micromechanical oscillator. This device was refined and found numerous applications in precise measurements of the Casimir interaction and in micromechanics [1, 4]. What is more, the possibility of frictionless transduction of mechanical motion through a vacuum gap using the lateral Casimir force [5, 6] was proposed [7].

2. Optical chopper driven by the Casimir force

It is well known that the standard mechanical choppers exploit the wheels of various shape which should have a highly stable rotating speed. Here, we demonstrate that it is possible to create the micromechanical optical chopper with no rotating wheels driven by the Casimir force. The key element of this device is the Fabry-Pérot microfilter schematically shown in Fig. 1. The length of its resonator cavity a should be made only slightly larger than the half wavelength $\lambda/2$ of the incidence laser beam $I_{\rm in}$. When the laser is switched off, the top of the right mirror, under an action of the attractive Casimir force $F(a)$ and mechanical electric force, will become for Δa closer to the top of the left mirror. The balance of both forces is given by

$$k\Delta a = \frac{1}{2}P(a)S, \tag{1}$$

where k is the spring constant of the 5 μm thick wall, $P(a) = F(a)/S$ is the Casimir pressure expressed by the Lifshitz formula [1], and $S = 50 \times 50\,\mu\text{m}^2$ is the common area of the wall and of the cube side. Note that detection of the mechanical deformation of a macroscopic object induced by the Casimir force can be observed by means of an adaptive holographic interferometer [8].

When the laser is switched on, the effective resonator length over an area of the light beam becomes equal to $\lambda/2$, i.e., the resonance condition is obeyed [9]. This leads to a cyclic process. First, the amplitude of a standing wave in the resonator will instantaneously increase resulting in a detection of relatively high intensity $I_{\rm tr}$ of the transmitted light. Then, the repulsive force due to the light pressure in the resonator will compensate the Casimir force and the right mirror will become vertical. This means that the effective resonator length becomes larger than $\lambda/2$ in violation of the resonance condition, and the wave amplitude in the gap falls down leading to an almost zero level in the transmitted light I_{tr}. Finally, the Casimir force, which is not balanced by the repulsive force due to the light pressure any more, will work against the mechanical elastic force and return the

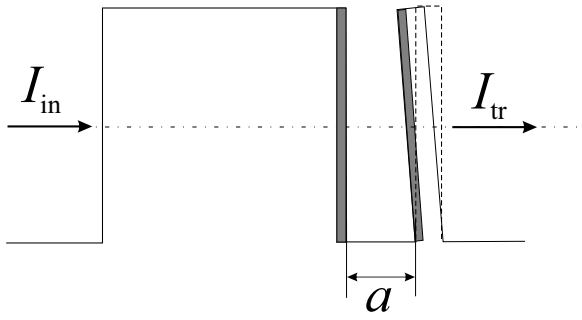

Figure 1: Two thin metallic mirrors marked by dark-grey deposited on the side of a SiO_2 cube and on a thin SiO_2 wall form a microresonator.

right mirror in its initial inclined position where the resonance condition is again obeyed. Thereafter, the next working cycle of a micromechanical chopper starts.

Detailed computations of the mechanical elastic, Casimir and light-pressure forces and their balance for the CW Nd-YAG laser (with $\lambda = 532.0\,\text{nm}$ and 7 mW power) and Ag mirrors of 1.175 nm thickness, presented in the talk, demonstrate feasibility of the proposed microdevice.

3. Conclusions

Various micromechanical devices are of considerable current use in both fundamental science and technological applications. We emphasize that in microdevices of next generations with sizes below a few hundred nanometers the role of a driver will be played by the fluctuation-induced Casimir force. One device of this type, an optical chopper, is proposed in this presentation.

References

[1] M. Bordag, G. L. Klimchitskaya, U. Mohideen, and V. M. Mostepanenko. *Advances in the Casimir Effect*. Oxford University Press, 2015.

[2] E. Buks and M. L. Roukes. Stiction, adhesion, and the Casimir effect in micromechanical systems. *Phys. Rev. B*, 63:033402, 2001.

[3] H. B. Chan, V. A. Aksyuk, R. N. Kleiman, D. J. Bishop, and F. Capasso. Quantum mechanical actuation of microelectromechanical system by the Casimir effect. *Science*, 291:1941, 2001.

[4] G. L. Klimchitskaya, U. Mohideen, and V. M. Mostepanenko. The Casimir force between real materials: Experiment and theory. *Rev. Mod. Phys.*, 81:1827, 2009.

[5] H.-C. Chiu, G. L. Klimchitskaya, V. N. Marachevsky, V. M. Mostepanenko, and U. Mohideen. Demonstration of the asymmetric lateral Casimir force between corrugated surfaces in nonadditive regime. *Phys. Rev. B*, 80:121402(R), 2009.

[6] H.-C. Chiu, G. L. Klimchitskaya, V. N. Marachevsky, V. M. Mostepanenko, and U. Mohideen. Lateral Casimir force between sinusoidally corrugated surfaces: Asymmetric profiles, deviations from the proximity force approximation, and comparison with exact theory. *Phys. Rev. B*, 81:115417, 2010.

[7] A. Ashourvan, M. Miri, and R. Golestanian. Noncontact rack and pinion powered by the lateral Casimir force. *Phys. Rev. Lett.*, 98:140801, 2007.

[8] V. M. Petrov, M. P. Petrov, V. V. Bryksin, J. Petter, and T. Tschudi. Optical detection of the Casimir force between macroscopic objects. *Optics Lett.*, 32:3167, 2006.

[9] M. Born and E. Wolf. *Principles of Optics*, Cambridge University Press, 1999.

MICROMORPHIC MODEL FOR SIMULATION OF LÜDERS-LIKEBANDS IN SMAs

M. Rezaee Hajidehi and S. Stupkiewicz

Institute of Fundamental Technological Research, Polish Academy of Sciences, Warsaw, Poland

e-mail: mrezaee@ippt.pan.pl, sstupkie@ippt.pan.pl

1. Introduction

Based on experimental observations, the stress-induced pseudoelastic response of shape memory alloys (SMAs), e.g. the uniaxial response of NiTi wire in tension, is often accompanied by strain localization and macroscopic phase front propagation. To simulate this phenomenon appropriately, a gradient-enhanced model and its micromorphic counterpart are developed [2]. The latter, which facilitates the computational treatment, is performed by adding an extra variable, the micromorphic peer of the volume fraction of martensite, into the model, see Maziére and Forest [1]. The resulting micromorphic model is then implemented into a finite-element framework based on an incremental energy approach combined with the augmented Lagrangian treatment, see Stupkiewicz and Petryk [3].

Finally, to study the effect of loading rate on the localization and fronts propagation, the micromorphic model is extended to a thermomechanically coupled version.

2. The thermomechanically coupled micromorphic model

In this study, the Helmholtz free energy function of SMA is adopted in the following form,

$$\phi(\varepsilon,\eta,T)=\phi_{chem}(\eta,T)+\phi_{el}(\varepsilon,\eta)+\phi_{int}(\eta) \qquad \text{with} \qquad \phi_{int}=\frac{1}{2}H\eta^2, \tag{1}$$

where $\phi_{chem}(\eta,T)$, $\phi_{el}(\varepsilon,\eta)$ and $\phi_{int}(\eta)$ are, respectively, the chemical, elastic and interaction energy contributions, η is the volume fraction of martensite, T is the temperature and H is the hardening/softening parameter.

Equation (1) is only applicable when $H>0$, i.e. for hardening behaviour. For $H<0$, a softening response is obtained and the loss of ellipticity of the governing differential equations occurs that makes the numerical results inadmissible.

One way to regularize the problem is to enhance the model with the gradient term $(1/2)\,G|\nabla\eta|^2$, where G is a positive parameter. However, the direct implementation of the gradient-enhanced model is not straightforward, because of the presence of the Laplacian of η. Thus, a micromorphic regularization is performed in which a new degree of freedom $\bar{\eta}$ is inserted into the local model (1), i.e. the free energy function is modified as,

$$\phi_\mu(\varepsilon,\eta,\bar{\eta},\nabla\bar{\eta},T)=\phi(\varepsilon,\eta,T)+\frac{1}{2}\chi(\eta-\bar{\eta})^2+\frac{1}{2}G|\nabla\bar{\eta}|^2, \qquad \text{with} \qquad \chi=\frac{G}{\ell^2}. \tag{2}$$

where ℓ is an internal length parameter.

In order to make the model thermomechanically coupled, first, the chemical part of the free energy $\phi_{chem}(\eta,T)$ is taken as a linear function of T and η to relate the pseudoelastic response of SMA to the temperature. Then, the latent heat of transformation together with the dissipated energy are considered as the local heat sources in the heat equation.

3. Numerical application

To demonstrate the suitability of the proposed micromorphic model, the uniaxial response of a NiTi wire in tension is studied [2]. To this end, the effect of loading rate on the force-displacement curve, the hysteresis

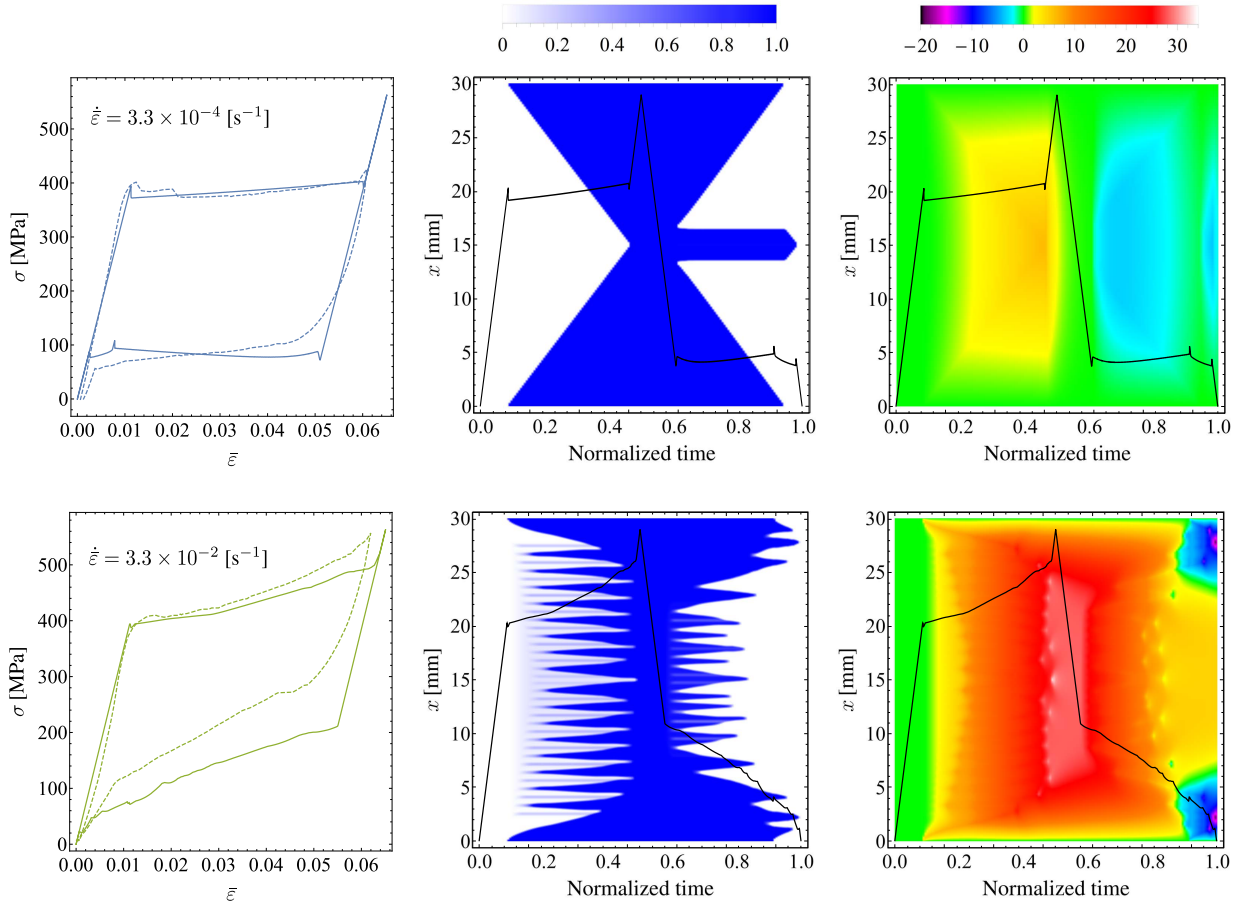

Figure 1: Detailed results corresponding to two loading rates $\dot{\bar{\varepsilon}}$: force-displacement curve (left), transformation pattern (middle), relative temperature field (right). The dashed lines in the force-displacement curves represent the experimental results of Zhang et al. [4]

area, the transformation pattern and the temperature field is studied. The numerical results are then compared with the experimental results obtained by Zhang et al. [4].

Figure 1 depicts the force-displacement curves, the transformation pattern, and the temperature field of the NiTi wire corresponding to two loading rates. The results demonstrate that for the low loading rate ($\dot{\bar{\varepsilon}} = 3.3 \times 10^{-4}$ s^{-1}) the effect of thermal hardening is insignificant. On the other hand, for the high loading rate ($\dot{\bar{\varepsilon}} = 3.3 \times 10^{-2}$ s^{-1}), a dominant thermal hardening is observable in the force-displacement curve.

Overall, despite the simplicity of the model, it is able to simulate the nucleation and transformation patterns induced by softening and its results show a good agreement with the experiment of Zhang et al. [4].

References

[1] M. Mazière and S. Forest. Strain gradient plasticity modeling and finite element simulation of Lüders band formation and propagation. *Continuum Mech. Thermodyn.*, 27:83–104, 2015.

[2] M. Rezaee Hajidehi and S. Stupkiewicz. Gradient-enhanced model and its micromorphic regularization for simulation of lüders-like bands in shape memory alloys. *Int. J. Solids Struct.*, 135(1):208–218, 2018.

[3] S. Stupkiewicz and H. Petryk. A robust model of pseudoelasticity in shape memory alloys. *Int. J. Numer. Meth. Eng.*, 93(7):747–769, 2013.

[4] X. Zhang, P. Feng, Y. He, T. Yu, and Q. P. Sun. Experimental study on rate dependence of macroscopic domain and stress hysteresis in NiTi shape memory alloy strips. *Int. J. Mech. Sci.*, 52(12):1660–1670, 2010.

INCLUSION SHAPE IN MEAN-FIELD MICROMECHANICAL MODELS

M. Majewski* and K. Kowalczyk-Gajewska

Institute of Fundamental Technological Research, Warsaw, Poland
e-mail: mmajew@ippt.pan.pl

1. Introduction

The shape of inhomogeneity in micromechanical approach, which uses an inclusion-matrix concept, is modelled by the concentration tensor. The tensor relates a local average of mechanical field with its macroscopic counterpart. The concentration tensors for the ellipsoidal inclusion shape are well examined in the literature. In [1], the authors have compared several strategies for non-ellipsoidal heterogeneity in the context of homogenization methods: analytical based on Eshelby's tensor decomposition into isotropic and anisotropic part, and the semi-analytical Mori-Tanaka method with replacement tensor approach (RMTM).

Incorporation of additional microstructural parameters such as particle packing, size of inclusions or properties of the area between phases (interphase), with simultaneous sustainment of simple formulations, is possible using the Morphology-based Representative Pattern (MRP) approach [2]. The MRP concept is based on the idea of the composite sphere introduced by Hashin in 1962. The MRP is formulated for an elastic and isotropic continuous matrix and isotropically dispersed spherical inclusions with equal radiuses.

The MRP takes into account the mean minimum distance between inclusions $\bar{\lambda}$ and, by introducing an additional phase t_{int} at the boundary of the composite components, the effect of the particle size. In the simplest example of two-pattern approach the microstructure of composite is simplified using two representative patterns (see Fig.1): the first one governed by the n-phase GSC scheme (4-GSC), and the second one described by the classical self-consistent scheme (SC). The first n-GSC pattern can be changed to e.g. the RMTM pattern in order to study influence of inclusion shape. To account for the size effect in the first pattern an interphase is introduced, having a thickness t_{int} independent of the particle radius R_i and different properties than the basic two phases. To describe the packing effect, the coating thickness in this pattern is specified by half the mean minimum distance between nearest-neighbour particles $\bar{\lambda}/2$ in the RVE.

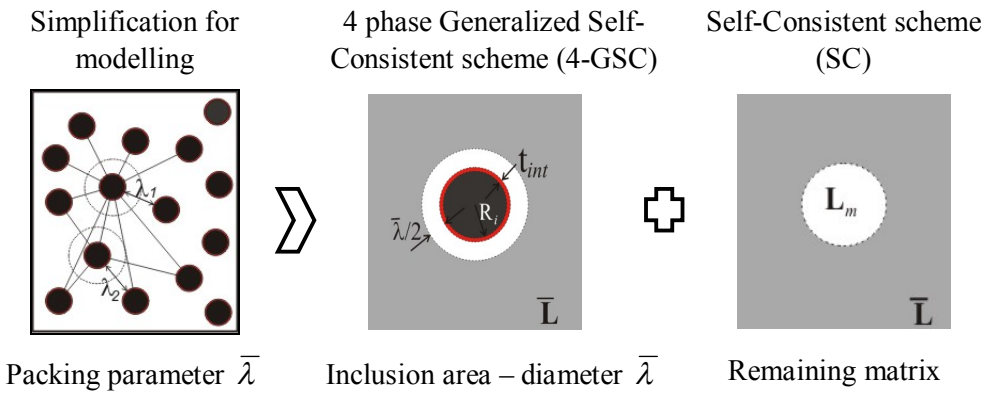

Fig.1 The idea of MRP approach. For the presented simplest case of MRP the mean radius R_i and the mean minimum distance $\bar{\lambda}$ between nearest-neighbour particles are calculated. The MRP is divided into two sub-problems: 4-GSC and SC, joint solution of these two sub-problems is final result of MRP model. GSC pattern describes an influence of local mechanical fields in the area of inclusion (spherical region of radius equal to $\bar{\lambda}/2$) on the macroscopic composite response and SC considers remaining matrix. The interphase, of different material parameter and thickness t_{int}, describes the size effect of inclusions.

2. Results

Analytical multi-scale models based on the inclusion-matrix concept, like MRP, take into account the shape of heterogeneity through a concentration tensor. Nogales and Böhm (2008) have extended the standard Mori-Tanaka scheme to inhomogeneities of non-ellipsoidal shapes by introducing the dilute "replacement" inhomogeneity strain concentration tensor $\mathbf{A}_{inc}^{FEM}$. For Mori-Tanaka method with replacement tensor approach (RMTM) the strain concentration tensor is

$$\mathbf{A}_{inc}^{RMTM} = [c_{inc}\mathbf{I} + c_m(\mathbf{A}_{inc}^{FEM})^{-1}]^{-1}$$

where $\mathbf{A}_{inc}^{FEM}$ for non-elliptical or non-ellipsoidal inhomogeneities has to be obtained numerically, e.g., from Finite Element (FE) simulations of a single inhomogeneity of appropriate shape and properties embedded into a large, but finite matrix region, see Fig.2b-d. The unit cells, Fig.2b-d, were exploited to determine the numerical concentration tensors for different inclusion shapes. The unit cells based on the microstructure photos obtained using Scanning Electron Microscope (SEM) and were modelled using FEM. The local stress and strain fields were computed at the Gauss points of FE for known macroscopic boundary conditions. Preliminary results concerning the effective Young modulus of polymer matrix composite reinforced with glass particles of different shape of inclusions are shown in Fig.2a. The numerical results are computed using numerical homogenization and FEM, the experimental results are adopted from [Kushvaha et al., 2014]. As the reinforcement volume increases, the stiffness of the composite increases, and the influence of the reinforcement shape is more visible.

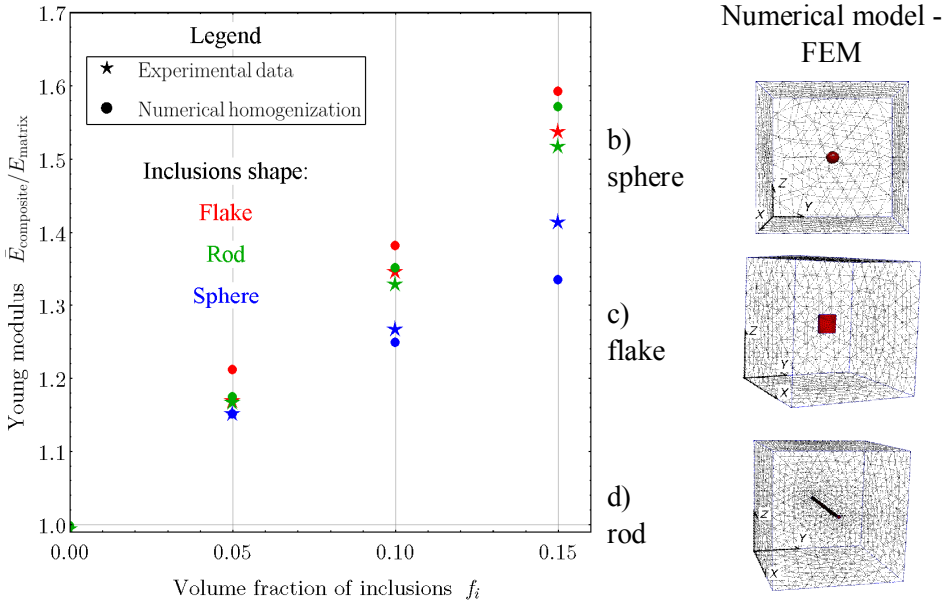

Fig.2 a) the macroscopic Young's modulus (composite/matrix) E_c/E_m vs. the volume fraction of inclusions f_i. The results of mechanical tests [Kushvaha et al., 2014] of polymer matrix composite reinforced with glass particles of various shapes: flake, rod and spherical is compared with the outcomes of numerical homogenization outcomes. b)-d) The unit cells set in FEM based on the microstructure SEM photos [Kushvaha et al., 2014].

Acknowledgments The research was partially supported by the project of the National Science Centre, Poland, granted by the decision No. DEC-2017/25/N/ST8/01968.

References

[1] B. Klusemann, H.J. Bhom, and B. Svendsen, Homogenization methods for multi-phase elastic composites with non-elliptical reinforcements: Comparisons and benchmarks, *Eur. J. Mech. A/Solids,* 34:21–37, 2012.
[2] M. Majewski, M. Kursa, P. Holobut and K. Kowalczyk-Gajewska, Micromechanical and numerical analysis of packing and size effects in elastic particulate composites, *Compos. B Eng.,* 124:158-174, 2017.

Hysteretic losses in lubricated sliding soft contacts

P. Sadowski and S. Stupkiewicz

Institute of Fundamental Technological Research, Warsaw, Poland

e-mail: psad@ippt.pan.pl, sstupkie@ippt.pan.pl

1. Introduction

The use of polymeric materials in various engineering applications, e.g., wipers, tyres, seals, has resulted in an increasing number of studies of their contact behaviour. The lubricated elastomeric contacts usually operate in special conditions which can be classified as the soft-elastohydrodynamic lubrication regime (soft-EHL). As one or both contacting bodies are highly compliant, relatively low contact pressures may lead to large deformations which in turn influence fluid flow. The soft-EHL regime is also characteristic for many biotrobological contacts, e.g., synovial joints, eye-eyelid contact, oral processing of food, which results in an increased interest in lubricated soft contacts.

Motivated by the applications mentioned above, we have performed a series of friction measurements using a home-made ball-on-disc tribometer [1]. NBR rubber and steel were used to produce elements of the tribo-pair. Three types of the ball-on-disc set-up, namely soft-on-hard (S/H), hard-on-soft (H/S) and soft-on-soft (S/S), have been examined. The friction coefficient has been investigated in lubricated contact conditions for varied sliding velocities and normal loads high enough to cause finite deformations, recently studied in soft-EHL [2].

2. Hysteretic friction coefficient

In our experimental set-up, the ball, fixed in a grip and loaded by a normal force, slides on a lubricated flat disc, and the friction force is measured. In the H/S and S/S configurations, the contact zone is moving with respect to the rubber disc. The disc is thus repeatedly deformed, and this is associated with hysteretic losses in the viscoelastic rubber material. Accordingly, the measured friction force comprises then two components: the interfacial friction force and the hysteretic friction force. In the S/H configuration, there is no hysteretic friction because the rubber ball, once loaded by a constant load, does not deform any more. To estimate the

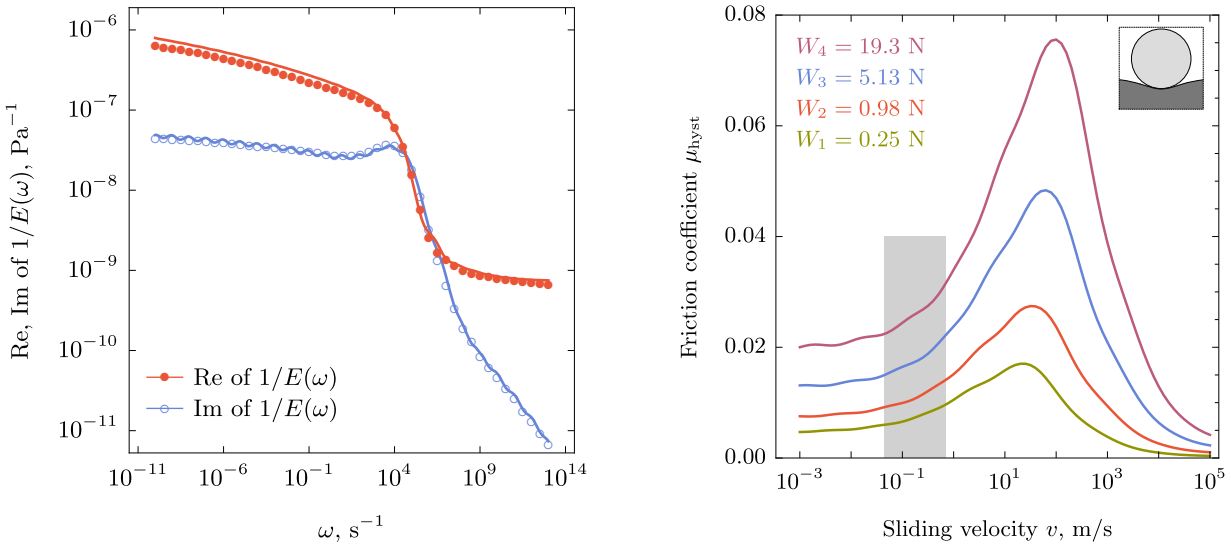

Figure 1: (a) Real and imaginary part of the complex function $1/E(\omega)$ for NBR rubber: transformed DMA measurements (markers) have been fitted by the Prony series (solid lines). (b) Hysteretic friction coefficient μ_{hyst} as a function of the sliding velocity v and load W for the H/S configuration.

hysteretic friction coefficient μ_{hyst}, NBR rubber has been characterized via DMA measurements, cf. Fig. 1a. After extrapolating the experimental data with use of the Prony series, the Persson's model [3], see also [4], has been used. Results of μ_{hyst} as a function of the sliding velocity v for the H/S configuration and all loads W used in the experiment are shown in Fig. 1b. In the whole range of sliding velocities, the hysteretic friction coefficient increases with increasing load.

3. Correction for the hysteretic losses

Results of friction measurements in lubricated contact conditions are usually visualized via so-called Stribeck curves, representing the dependence of the friction coefficient on $U\eta$, the product of the entrainment speed U and lubricant viscosity η. Fig. 2 shows the experimental data for all considered configurations and for the normal load $W = 5.13\,\mathrm{N}$. Transition from the full elastohydrodynamic to mixed lubrication regime is well captured. The estimated hysteretic friction coefficient characteristic for the H/S and S/S configurations has been used for extraction the interfacial friction, results of which are shown in Fig. 2 with filled markers. As a reference, the corresponding results for the S/H configuration are also included in Fig. 2. It can be seen that, upon correction for the hysteretic losses, the friction coefficient in the elastohydrodynamic regime (see the increasing branch corresponding to higher values of $U\eta$) does not depend on the configuration.

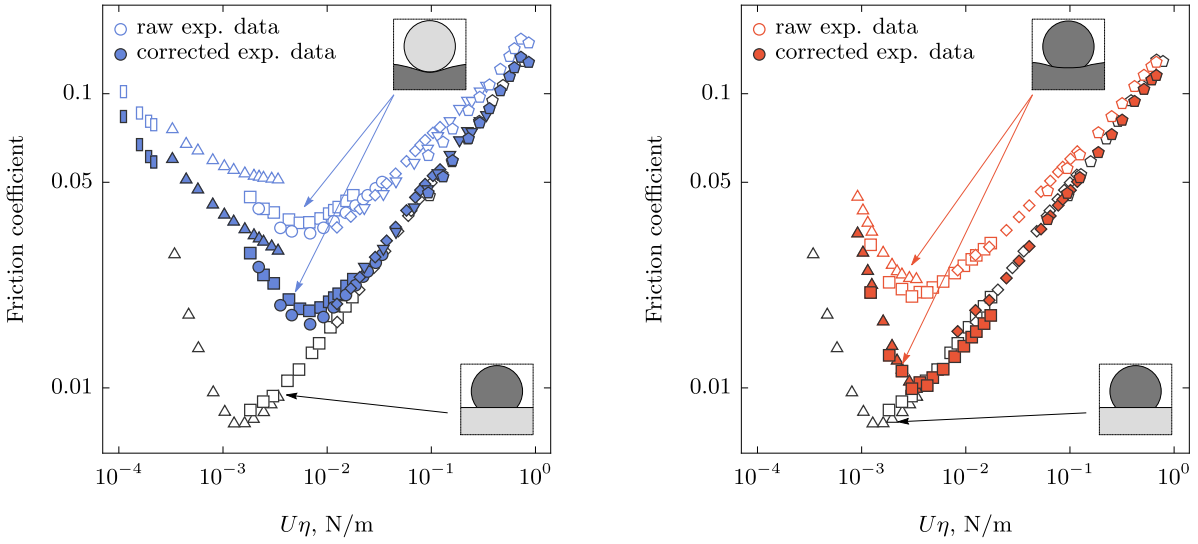

Figure 2: Friction coefficient as a function of $U\eta$: raw experimental data (empty markers) and friction coefficient corrected for hysteretic losses (filled markers) for the H/S configuration (a) and S/S configuration (b) for the load $W = 5.13\,\mathrm{N}$. Results corresponding to the S/H configuration are provided as a reference.

References

[1] P. Sadowski and S. Stupkiewicz. Friction in lubricated soft-on-hard, hard-on-soft and soft-on-soft sliding contacts, *in preparation*.

[2] S. Stupkiewicz, J. Lengiewicz, P. Sadowski and S. Kucharski (2016). Finite deformation effects in soft elastohydrodynamic lubrication problems, *Tribology International*, **93**, 511–522.

[3] B. N. J. Persson (2010). Rolling friction for hard cylinder and sphere on viscoelastic solid, *The European Physical Journal E*, **33**, 327–333.

[4] M. Scaraggi and B. N. J. Persson (2014). Rolling Friction: Comparison of Analytical Theory with Exact Numerical Results, *Tribology Letters*, **55**, 15–21.

HYSTERETIC BEHAVIOR OF RANDOM PARTICULATE COMPOSITES BY THE STOCHASTIC FINITE ELEMENT METHOD

D. Sokołowski[1] and M. Kamiński[1]

[1]*Department of Structural Mechanics, Łódź University of Technology*
Faculty of Civil Engineering, Architecture and Environmental Engineering
Al. Politechniki 6, 90-924 Łódź, Poland
e-mail: sokolowski.dmn@gmail.com, marcin.kaminski@p.lodz.pl

1. Introduction

The main purpose of this work is determination of the uncertainty level in the strain, dissipated and internal energies of particulate composite subjected to biaxial cyclic stretch. This is done for the hexagonal Representative Volume Element (RVE) of this hyper-elastic two-phase composite clearly demonstrating a hysteretic behavior. The first component – a spherical particle located centrally in the RVE – is linearly elastic and has material parameters equal to $E = 10GPa$ and $\mu = 0.3$; hyper-elastic polymeric matrix occupies 95% of the RVE. This RVE is presented in Fig. 1 and, except its initial and final configurations, it also includes the mesh. Uncertainty in this analysis results from the probabilistic constitutive model of the matrix having the given level of statistical dispersion in its stiffness resulting in different stress-strain curves. The minimum, mean and maximum values are presented in Fig. 2, where the stretching level of this RVE increases together with each of four stretch cycles and returns to zero in the end point of this analysis. Random output includes expected values, coefficients of variations, skewness and kurtosis of both elastic and dissipated energies. This analysis is a continuation of the previous considerations for an uncertainty in linear elastic particulate composites [1,2]; interested readers may refer also to Clément et al [3] or Ma et al [4], both concerning stochastic homogenization of composites.

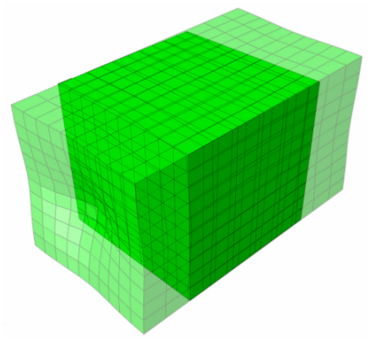

Figure 1: Discretization and deformation map of the composite RVE.

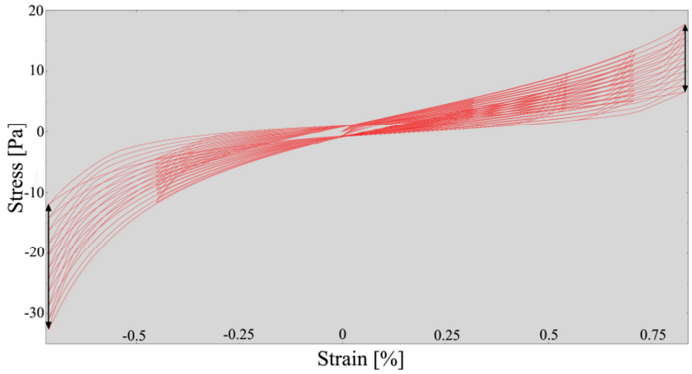

Figure 2: Hysteresis dispersion of the given composite.

2. Theory

Let us consider the unitary RVE with linearly elastic reinforcement and hyper-elastic matrix constituted below by the Van der Waals constitutive law

$$U = \mu\left\{-(\lambda_m^2 - 3)[ln(1-\eta)+\eta] - \frac{2}{3}a\left(\frac{\tilde{I}-3}{2}\right)\right\} + \frac{1}{D}\left(\frac{J_{el}^2-1}{2} - \ln(J_{el})\right), \tag{1}$$

where $\tilde{I} = (1-\beta)\bar{I_1} + \beta\bar{I_2}$, $\eta = \sqrt{\frac{\tilde{I}-3}{\lambda_m^2-3}}$ and $[I_1, I_2]$ are the first and second deviatoric strain invariants. The hysteretic behavior of this matrix is governed by the following equation:

$$\dot{\epsilon}_B^{cr} = A[\lambda_B^{cr} - 1 + E]^C(\sigma_B)^m, \tag{2}$$

where $\dot{\epsilon}_B^{cr}$ is the effective creep strain rate in network B, $\lambda_B^{cr} - 1$ is the nominal creep strain, and σ_B is the effective stress in this network. Statistical dispersion is considered for material parameters governing normal stiffness and Poisson ratio of this composite, i.e. μ and D, so that the resulting behavior of the entire composite is random and exhibits remarkable uncertainty in the stress-strain curve (see Fig. 2).

3. Results

The final results include the first four probabilistic characteristics of the maximum values of three different energies, i.e. elastic strain energy E_{el}, dissipation energy E_{cd} and the total internal energy E_i calculated for the entire RVE. This is done using three different probabilistic techniques, i.e. Iterative Stochastic Finite Element Method (ISFEM), crude Monte-Carlo simulation (MCS) and semi-analytical method (AM) with respect to the input coefficient of variation of constitutive model parameters, further denoted by c_p; these parameters are assumed to be uncorrelated and Gaussian. The expected value is presented in Fig. 3 and shows a moderate dependence on the $\alpha(c_p)$ with small decreases of all energies together with its increase. The internal energy is the largest one and is followed by the dissipated energy, while the elastic one is more than four times smaller. This is because of a cyclic stretch, where dissipated energy increases during each relaxation, while the elastic one depends on the stretch level only. The internal energy as a sum of these two is the largest during the last cycle for the ultimate strain of 0.8, where elastic strain energy is maximized. During comparison of the output coefficients of variation collected in Fig. 4 it is clearly seen that they are almost proportional and very close to the input uncertainty. The one for E_{el} is the largest, while variation of E_{cd} – exhibits minimum value; this difference increases together with an increase of $\alpha(c_p)$ and reaches approx. 30% for $\alpha(c_p) = 0.15$. Output of the three concurrent probabilistic methods shows a perfect agreement for the expected values and a little worse for the coefficients for variation, but the results are still very close to each other and within 5% tolerance.

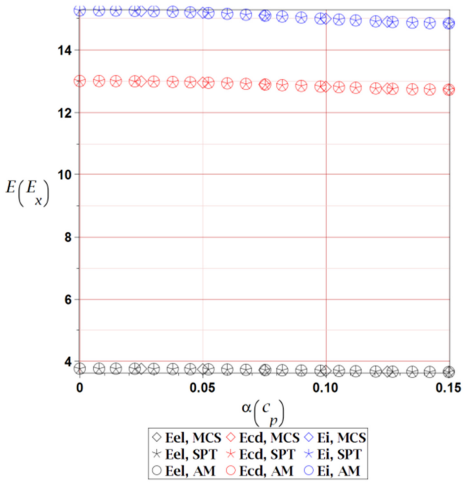

Figure 3: Expected value of the ultimate elastic strain E_{el}, dissipation E_{cd} and internal E_i energies in the RVE vs. $\alpha(c_p)$.

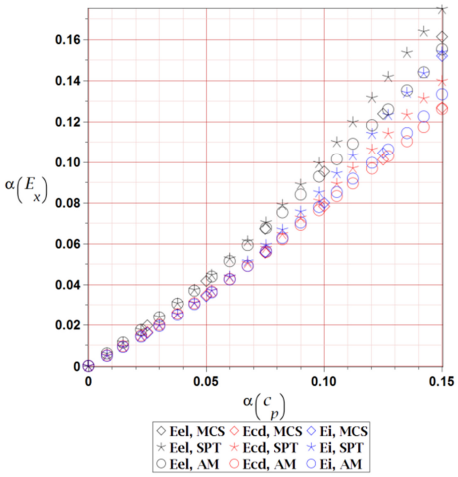

Figure 4: Coefficient of variation of ultimate elastic strain E_{el}, dissipation E_{cd} and internal E_i energies in the RVE vs. $\alpha(c_p)$.

4. Conclusions

Deformation energies in hyperelastic RVE of the composite subjected to a cyclic stretch have a certain level of uncertainty, which is almost the same as the one of the input constitutive law for the matrix. The analyzed expectations decrease a little bit together with an increase of an input uncertainty, the skewness as well as kurtosis differ both from zeros and demonstrate remarkable magnitudes.

Acknowledgments The first author would like to acknowledge the financial support of the grant 2016/21/N/ST8/01224 from the National Science Center in Cracow, Poland.

References

[1] D. Sokołowski and M. Kamiński. Computational homogenization of carbon/polymer composites with stochastic interface defects. *Compos. Struct.*, 183:434, 2018.

[2] M. Kamiński and D. Sokołowski. Dual probabilistic homogenization of the rubber-based composite with random carbon black particle reinforcement. *Compos. Struct.* 140:783, 2016.

[3] A. Clément, C. Soize, J. Yvonnet. Computational nonlinear stochastic homogenization using a nonconcurrent multiscale approach for hyperelastic heterogeneous microstructures analysis. *Int. J. Numer. Meth. Engng*, 91:799, 2012.

[4] J. Ma, S. Sahraee, P. Wriggers, L. De Lorenzis. Stochastic multiscale homogenization analysis of heterogeneous materials under finite deformations with full uncertainty in the microstructure. *Comput. Mech.*, 55:819, 2015.

A HYPOELASTIC CONSTITUTIVE MODEL FOR GRAPHENE AND CARBON NANOTUBES BASED ON INTERATOMIC INTERACTIONS

D. Jasińska

Institute of Structural Mechanics, Cracow University of Technology, Cracow, Poland

e-mail: djasinska@pk.edu.pl

1. Introduction

Several continuous hyperelastic theories have been proposed for the description of mechanical properties of graphene and carbon nanotubes, based on interatomic potentials [1], [2], [3] or calibrated from existing quantum data [4]. In the present paper the hypoelastic constititutive model is proposed for modeling of the mechanical behavior of graphene sheets and CNT under the assumption of large displacements but small strains. The model is based on the modified Cauchy-Borne rule with the introduction of inner relaxation, and directly incorporates potentials describing interatomic interactions accounting for the multi-body effects through terms depending on angles between bonds.

2. Materials and methods

Unlike the molecular dynamics simulations, where the motion of every atom is tracked, the continuum theories based on molecular statics represent the collective behavior of atoms through the constitutive model. Since graphene is a non-centrosymmetric atomic structure, the internal atom of the representative unit cell (Fig.1) doesn‘t follow the homogenous deformation of the cell edges. Hence the Cauchy_Borne hypothesis, bridging molecular and continuous scales, has to be augmented with an additional internal degree of freedom: the vector parameter describing this internal inhomogenity [1].

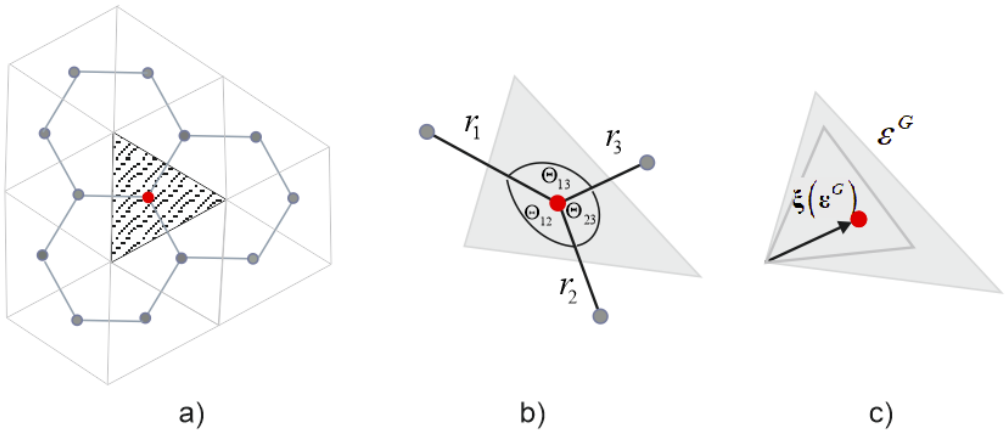

Fig.1 a) undeformed graphene lattice, b) deformed representative cell as function of intermolecular distances and angles, c) deformed representative cell as function of strain tensor and internal vector parameter

The internal energy of the representative cell U^a, depending on bond lengths and interbond angles, resulting from the applied atomistic multibody potential is equated to the strain energy of the equivalent hyperelastic continuum U^e depending on the Green strain tensor $\boldsymbol{\varepsilon}^G$ and the internal vector parameter $\boldsymbol{\xi}$.

(1) $$U^a\left(r_1, r_2, r_3, \Theta_{12}, \Theta_{13}, \Theta_{23}\right) = U^e(\boldsymbol{\varepsilon}^G, \boldsymbol{\xi})$$

For a given strain state, the internal degree of freedom is determined by minimizing the cell strain energy, which leads to a nonlinear implicit equation system which is solved numerically

(2) $$\frac{\partial U^e(\boldsymbol{\varepsilon}^G, \boldsymbol{\xi})}{\partial \boldsymbol{\xi}} = 0 \rightarrow \boldsymbol{\xi} = \boldsymbol{\xi}\left(\boldsymbol{\varepsilon}^G\right)$$

Restricting further analysis to small strains (while maintaining the large displacements assumption), allows for proposing the hypoelastic model, in which the rate of change of stress is defined as

$$d\sigma = D(\varepsilon) : d\varepsilon, \tag{3}$$

where $d\varepsilon$ is the rate of change of infinitesimal elastic strains and $D(\varepsilon)$ is the tangent stiffness matrix calculated as

$$D(\boldsymbol{\varepsilon}) = \frac{\partial^2 U^e(\boldsymbol{\varepsilon})}{\partial \boldsymbol{\varepsilon} \partial \boldsymbol{\varepsilon}} \tag{4}$$

The dependence of the elasticity tensor (4) on the deformation state is analyzed for two interatomic multibody potential types: Tersoff-Brenner and modified Morse.
The restriction placed upon the strain size, which obviously limits model applicability range, allows for proposing the hypoelastic orthotropic or even isotropic model. The elastic moduli can be expressed directly as functions of strain invariants in the tabular form. Such tables are compiled for both discussed interatomic potentials. The advantages of such a formulation are: the possibility of implementing this model in any advanced finite element code without the necessity of developing own numerical procedures describing material constitutive behavior, and a significant reduction of the computation time, since equation (2) can be approximated as the polynomial function of infinitesimal strains, and there is no need to solve it numerically for each consecutive deformation state in every finite element.

3. Results

The proposed hypoelastic model is applied to the FEM analysis of the behaviour of graphene sheets and CNT of different chiralities under stretching bending and torsion. The results are compared with those obtained by the atomic-scale finite element method [5] which is based directly on molecular mechanics, can handle discrete atoms and takes into account the multibody interactions. Calculations were performed by means of the FEM code Abaqus.

4. Conclusions

The results of numerical tests prove the effectiveness of the proposed model. The explicit tabular dependence of Young's modulus and Poisson's ratio on the strain invariants allows for its straightforward application in many standard FEM codes, for instance in numerical simulations of nanocomposites or multiscale analysis.

Acknowledgments The research was supported by Pl-grid Infrastructure.

References

[1] P.Zhang, H.Jiang,Y.Huang, P.H.Geubelle and K.C.Hwang. An atomistic-based continuum theory for carbon nanotubes: analysis of fracture nucleation. *J.Mech.Phys.Solids*, 52: 977,2004.
[2] M.Aroyo and T. Belytschko,, An atomistic-based finite deformation membrane for single layer crystalline films, *J.Mech.Phys.Solids*, 50:1941, 2002.
[3] Q. Dong, Z. Qingjin, R.S. Ruoff. Multiscale simulation of nanostructures based on spatial secant model: a discrete hyperelastic approach. Comput Mech, 42:557, 2008.
[4] R.Gharffari and R.A.Sauer. A new efficient hyperelastic finite element model for graphene and its application to carbon nanotubes and nanocones,arXiv:1802.09825v1, 2018
[5] B.Liu,Y.Huang,H. Jiang, S.Qu,K.C.Hwang. The Atomic Scale finite element method.*Comp.Methods App.Mech.Eng*, 193,17-20:1849, 2004.

PROPAGATION OF SURFACE WAVES IN FCC HALF-SPACES WITHIN SURFACE ELASTICITY

C. Enzevaee[1] and H.M. Shodja[1,2]

[1]*Department of Civil Engineering, Sharif University of Technology, P.O. Box 11155-9313, Tehran, Iran*
[2]*Institute for Nanoscience and Nanotechnology, Sharif University of Technology, P.O. Box 11155-9161, Tehran, Iran*

e-mail: cenzevaee@gmail.com

1. General

Surface wave propagation in solids with semi-infinite extent due to its broad encountering in such field of works as surface science, seismology, acoustoelectronics, and nondestructive evaluations has been of great interest to many researchers and engineers. The inadequacy of classical theory of elasticity in capturing all the propagating waves under certain situations and describing such a phenomenon as dispersion associated to a propagating wave with wavelength comparable to the intrinsic length of the medium of interest is well-known. A remedy to such dilemma is to employ such augmented theories as surface theory of elasticity which has been proposed by [2]. Using this theory, an analytical solution is presented for Love and Rayleigh surface wave propagations in a semi-infinite medium with face-centered cubic (fcc) single crystal structure. The anisotropic nature of the fcc half-spaces along its free surface and within its bulk are incorporated in the formulations accurately [1]. To show the effect of the crystallographic anisotropy and its orientation, two different crystallographic orientations with respect to the incident wave vector are examined: (a) the free surface of the half-space is (010) plane and the surface waves propagate in [100] direction as shown in Fig.1, (b) the free surface of the half-space is (110) plane and the surface waves propagate in [110] direction as shown in Fig.2.

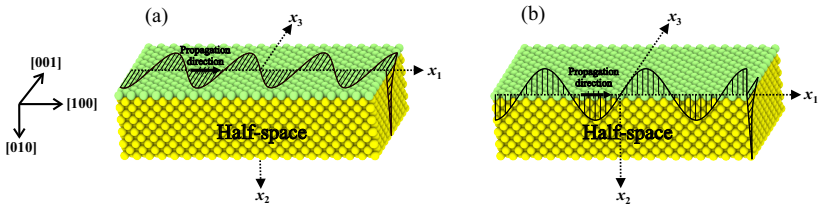

Figure 1: (a) Love and (b) Rayleigh Surface wave propagation in a half-space with (010) free surface.

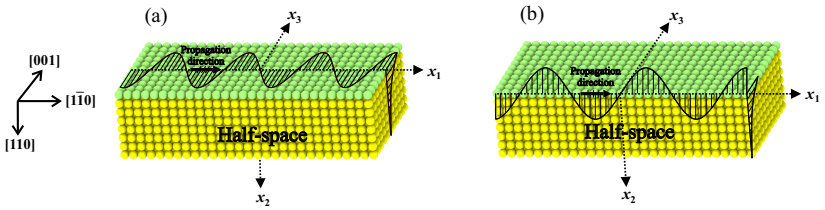

Figure 2: (a) Love and (b) Rayleigh Surface wave propagation in a half-space with (110) free surface.

2. Formulation

In the mathematical framework of surface elasticity presented by [2], surface is considered as a two-dimensional linearly elastic layer, governed by the following equation of motion:

$$\mathrm{div}_{s0}\mathbf{S}^s - \mathbf{S}.\mathbf{n} = \rho^s \ddot{\mathbf{u}}, \tag{1}$$

where $\mathbf{S}^s$ is the first Piola-Kirchhoff surface stress tensor, div_{s0} is the divergence with respect to the undeformed surface, $\mathbf{n}$ is the outward unit normal vector to the free surface, $\mathbf{S}$ is the continuous extension to the surface of the stress tensor in the bulk. Moreover, the constitutive relation for the surface is:

$$\mathbf{S}^s = \mathbf{I}.\mathbf{M} + \mathbf{I}.\mathbf{C}^s.\mathbf{E}^s + (\boldsymbol{\nabla}_{s0}\mathbf{u}).\mathbf{M}, \tag{2}$$

where $\mathbf{I}$ is the inclusion map from the tangent space of the surface (2D) onto the 3D space, $\mathbf{M}$ is the residual stress tensor, $\boldsymbol{\nabla}_{s0}\mathbf{u}$ is the surface gradient of the displacement field, and $\mathbf{E}^s = \frac{1}{2}\left(\mathbf{Du} + \mathbf{Du}^T\right)$ is the surface strain tensor, and $\mathbf{Du} = \mathbf{P}.(\boldsymbol{\nabla}_{s0}\mathbf{u})$ where $\mathbf{P} = \mathbf{I}^T$ is the perpendicular projection matrix from the 3D space onto the tangent space of the surface.

3. Numerical results

Contrary to the predictions based on classical theory, surface elasticity theory predicts Love waves can propagate in a homogeneous elastic fcc half-space and is dispersive which is depicted in 3(a) for Al, Cu, and Ni, and 3(b) for Ag, Au, and Pd. It can be seen that Love wave propagation in Ag, Al, Au, Cu, Ni, and Pd half-spaces associated to either free surface layers, (010) and (110) is normal dispersive.

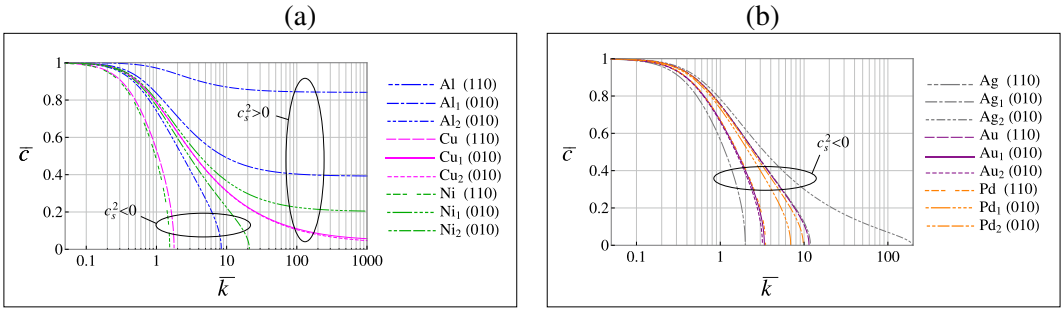

Figure 3: Variation of the normalized Love wave phase velocity, $\overline{c}$ with the normalized wave number $\overline{k}$, for several half-spaces made of different fcc single crystals, (a) Al, Cu, and Ni, and (b)Ag, Au, and Pd.

Rayleigh wave propagation in a homogeneous single crystalline fcc half-space is shown to be dispersive and its propagation in Al half-space with (110) plane as its free surface is anomalous dispersive, whereas in Ag, Au, Cu, Ni, and Pd half-space is normal dispersive.

References

[1] C Enzevaee and HM Shodja. Crystallography and surface effects on the propagation of love and rayleigh surface waves in fcc semi-infinite solids. *International Journal of Solids and Structures*, 2018.

[2] Morton E Gurtin and A Ian Murdoch. A continuum theory of elastic material surfaces. *Archive for Rational Mechanics and Analysis*, 57(4):291–323, 1975.

WEAKENED HILL-MANDEL CONDITION FOR COMPUTATIONAL HOMOGENISATION OF RANDOM MEDIA

M. Wojciechowski[1]

[1]*Faculty of Civil Engineering, Architecture and Environmental Engineering, Technical University of Łódź, , Al. Politechniki 6, 90-924 Łódź, Poland,*

e-mail: mwojc@p.lodz.pl

1. General definitions

One of the principles of the theory of computational homogenisation is the so called Hill-Mandel condition, which ensures energy preservation during scale transition [2]. This criterion, for the commonly known elasticity problems, is usually written as:

$$\Delta E = \Sigma_{ij}\mathcal{E}_{ij} - \frac{1}{\Omega}\int_{\Omega}\sigma_{ij}\varepsilon_{ij}d\Omega = 0, \tag{1}$$

where σ_{ij}, ε_{ij} are microscopic stress and strain fields, respectively, inside the representative volume element (RVE) of the volume Ω and Σ_{ij}, $\mathcal{E}_{ij}$ are averages of these quantities given by:

$$\Sigma_{ij} = \frac{1}{\Omega}\int_{\Omega}\sigma_{ij}d\Omega \tag{2}$$

$$\mathcal{E}_{ij} = \frac{1}{\Omega}\int_{\Omega}\varepsilon_{ij}d\Omega \tag{3}$$

In this short paper the weakened form of the Hill-Mandel criterion is postulated, i.e.:

$$\Delta E = \Sigma_{ij}\mathcal{E}_{ij} - \frac{1}{\Omega}\int_{\Omega}\sigma_{ij}\varepsilon_{ij}d\Omega \leq \epsilon, \tag{4}$$

where the maximum energetic discrepancy ϵ is defined as:

$$\epsilon = \frac{1}{4}(\Sigma^k_{ij} - \Sigma^s_{ij})\mathcal{E}_{ij}. \tag{5}$$

In the above, the $\Sigma^k_{ij}\mathcal{E}_{ij}$ and $\Sigma^s_{ij}\mathcal{E}_{ij}$ terms stand for upper and lower bounds of the macroscopic strain energy density, obtained when loading the RVE with linear kinematic and minimal kinematic boundary conditions, respectively (see eg. [1,3,4]).

2. Derivation of maximum energetic discrepancy

It is well known that the equation (1) is preserved, if the RVE is loaded with the macroscopic strain $\mathcal{E}_{ij}$ by means of linear kinematic, periodic (not considered here) or uniform traction boundary conditions (BCs). Linear kinematic BCs ensure that the perturbation of displacements vanishes at the RVE boundary and the *stiff* answer of the RVE is generated (upper bound). Using these BCs the following set of quantities is obtained as a solution: ε^k_{ij}, σ^k_{ij} and Σ^k_{ij}. Uniform traction BCs ensure in turn, that the perturbation of tractions is vanishing at boundary and the *soft* answer of the RVE is obtained (lower bound). These BCs provide the following solution set: ε^s_{ij}, σ^s_{ij} and Σ^s_{ij}. Let's assume now, that there exist a smooth, linear transition from one state of the material to the other and the following intermediate strain field can be defined:

$$\varepsilon^{\alpha}_{ij} = (1-\alpha)\varepsilon^k_{ij} + \alpha\varepsilon^s_{ij}, \qquad \alpha \in \langle 0,1\rangle \tag{6}$$

The above can be followed by the definitions of intermediate microscopic and macroscopic stresses:

$$\sigma_{ij}^{\alpha} = (1-\alpha)\sigma_{ij}^{k} + \alpha\sigma_{ij}^{s} \tag{7}$$

$$\Sigma_{ij}^{\alpha} = (1-\alpha)\Sigma_{ij}^{k} + \alpha\Sigma_{ij}^{s} \tag{8}$$

The assumption of smooth transition can be fully justified by the assumption of the continuity of the displacement field and the well behaving material properties (constants for example). Now, let's consider the discrepancy between the macroscopic and microscopic strain energy density for this intermediate state:

$$\Delta E^{\alpha} = \Sigma_{ij}^{\alpha}\mathcal{E}_{ij} - \frac{1}{\Omega}\int_{\Omega}\sigma_{ij}^{\alpha}\varepsilon_{ij}^{\alpha}d\Omega. \tag{9}$$

Inserting equations (6)-(8) into (9) the following is derived, after some transformations:

$$\Delta E^{\alpha} = \alpha(1-\alpha)(\Sigma_{ij}^{k} - \Sigma_{ij}^{s})\mathcal{E}_{ij}, \tag{10}$$

It is immediate to see that the above attains its maximum at $\alpha = 0.5$ and takes the value given by equation (5).

3. Boundary conditions for weakened Hill-Mandel principle

Note that for kinematic solution it can be written at the boundary: $\varepsilon_{ij}^{k} = \mathcal{E}_{ij}$, whereas for the static solution the following holds: $\varepsilon_{ij}^{s} = \mathcal{E}_{ij} + \tilde{\varepsilon}_{ij}^{s}$. The $\tilde{\varepsilon}_{ij}^{s}$ is the strain perturbation at static loading, which vanishes at boundary in the integral sense only. The strain perturbation at kinematic loading $\tilde{\varepsilon}_{ij}^{k}$ also exists, but it just vanishes strictly at boundary. From equation (6) it is then derived, that the intermediate state can be obtained by applying the at the RVE boundary:

$$\varepsilon_{ij}^{\alpha} = \mathcal{E}_{ij} + \alpha\tilde{\varepsilon}_{ij}^{s}. \tag{11}$$

which stand for the *statically perturbed boundary conditions* [4]. Note that the static solution ε_{ij}^{s} have to be known first, in order to apply these boundary conditions.

4. Conclusions and prospects

The weakened Hill-Mandel condition for homogenisation of disordered media is proposed which allows for discrepancy in macro- and microscopic energy density. The maximum discrepancy is derived from the assumption that the true answer of the macroscopic material is located in between the kinematic and static solutions taken from the representative volume element. Such definition opens new possibilities in computational homogenisation, especially it potentially allows for smaller volumes of the material which can serve as the RVE (see results reported in [4]).

References

[1] Wojciechowski, M., Lefik, M., On the Static Nature of Minimal Kinematic Boundary Conditions for Computational Homogenisation, *Engineering Transactions*, 64-4, pp. 581-587, 2016.

[2] Kouznetsova, V. G., Geers, M. G. D., & Brekelmans, W. A. M., Computational homogenisation for non-linear heterogeneous solids. Multiscale Modeling in Solid Mechanics. Computational Approaches, eds. U. Galvanetto and M. HF Aliabadi, 3, 1-42, 2009.

[3] Mesarovic, S. D., & Padbidri, J., Minimal kinematic boundary conditions for simulations of disordered microstructures. Philosophical Magazine, 85(1), 65-78, 2005.

[4] Wojciechowski, M., Statically perturbed kinematic boundary conditions for computational homogenisation of unstructured composites, CMM2017 - 22nd Computer Methods in Mechanics, Lublin, Poland, September 13th-16th, MS02-35(#263), 2017

VALIDATION OF MEAN-FIELD APPROACHES FOR THE DESCRIPTION OF ELASTIC-PLASTIC TWO-PHASE COMPOSITES

M. Kursa, K. Kowalczyk-Gajewska, M.J. Lewandowski, and H. Petryk

Institute of Fundamental Technological Research (IPPT PAN), Warsaw, Poland

e-mail: mkursa@ippt.pan.pl

1. Introduction

Multiscale analyses and multi-objective optimization of thermo-mechanical properties of composite materials, particularly in a non-linear regime, still need relevant and computationally efficient models. Micromechanical mean-field estimates of effective properties of composites can provide a tool for optimal designing, characterization of performance and techniques applied for processing of newly-developed materials. Analytical micromechanical estimates can be desirable for preliminary selection of an optimal two-phase composites for a specific future application [4]. This work presents a synthetic approach to estimating the effective properties of metal-matrix composites (MMC). Selected micromechanical schemes and finite element unit-cells estimates are analysed and verified. Both, micromechanical and FE estimates of effective elastic-plastic properties of two-phase composites are compared to each other and validated with respect to experimental data. Such comprehensive study of the three types of data for different MMC is hardly to be found in the literature. The validation with respect to experimental data is crucial for modelling nonlinear behaviour because the estimated overall properties of composites are strongly affected by the method applied [3].

2. Averaging schemes for a two-phase isotropic composite

Among the available micromechanical mean-field estimates the attention is focused on the Mori-Tanaka (MT), self-consistent (SC) and generalized self-consistent (GSC) methods. The incremental linearization is applied at each time step using so-called tangent ($\mathbf{L}^{\mathrm{t}}$) or secant ($\mathbf{L}^{\mathrm{s}}$) stiffness moduli for the matrix representing an elasto-plastic medium

$$\dot{\boldsymbol{\sigma}} = \mathbf{L}^{\mathrm{t}} \cdot \dot{\boldsymbol{\varepsilon}}\,, \quad \boldsymbol{\sigma} = \mathbf{L}^{\mathrm{s}} \cdot \boldsymbol{\varepsilon}\,. \tag{1}$$

It is assumed that the ceramic phase is linearly elastic and the metal matrix is elasto-plastic. The metal matrix is described by the standard Huber-von Mises yield function with an associated flow rule. Both phases are assumed to be isotropic. The resultant tangent elasto-plastic stiffness tensor of the metal matrix is anisotropic and can be isotropized in order to take the form [1]

$$\mathbf{L}_{\mathrm{m}}^{\mathrm{t(iso)}} = 3K_{\mathrm{m}}\mathbf{I}^{\mathrm{P}} + 2G_{\mathrm{m}}^{\mathrm{t}}(\varepsilon_{\mathrm{eq}}^{\mathrm{p}})\mathbf{I}^{\mathrm{D}}, \tag{2}$$

where the bulk modulus K_{m} is constant and the current shear modulus $G_{\mathrm{m}}^{\mathrm{t}}(\varepsilon_{\mathrm{eq}}^{\mathrm{p}})$ evolves with an accumulated plastic strain $\varepsilon_{\mathrm{eq}}^{\mathrm{p}}$. It has been assumed that ceramic inclusions have spherical shape.

3. Unit cell models

Finite element analysis is restricted to the simplified one-particle cells: spherical (FE-S) and cylindrical (FE-C), Fig. 1. The composite is subjected to the axially symmetric loading. The FE analyses have been performed in the AceFEM environment [2]. The problems have been calculated as two dimensional axi-symmetric ones using four node standard finite elements available in the program.

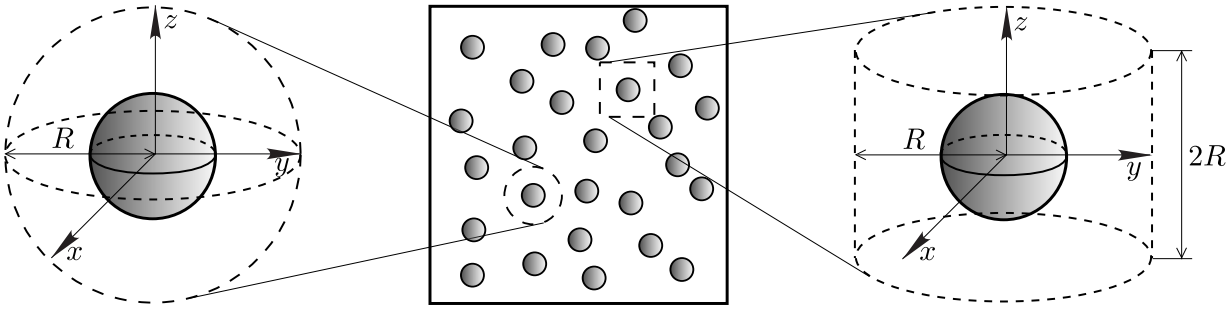

Figure 1: Spherical (FE-S) and cylindrical (FE-C) unit cells.

4. Results

All analytical mean-field averaging schemes have been implemented using a simple and universal algorithm of the incremental iterative procedure. Tension and compression tests have been modelled using those analytical schemes and the two FE unit cell models. The analysis of results has revealed that the generalized self-consistent (GSC) and Mori-Tanaka (MT) estimates provide very good agreement with FE results in the whole range of volume content of ceramic phase, Fig. 2. The mean-field estimates are computationally more efficient than FE analyses of the unit cells so that they can be applied when quick and robust assessment of overall composite properties in the non-linear elastic-plastic regime is needed.

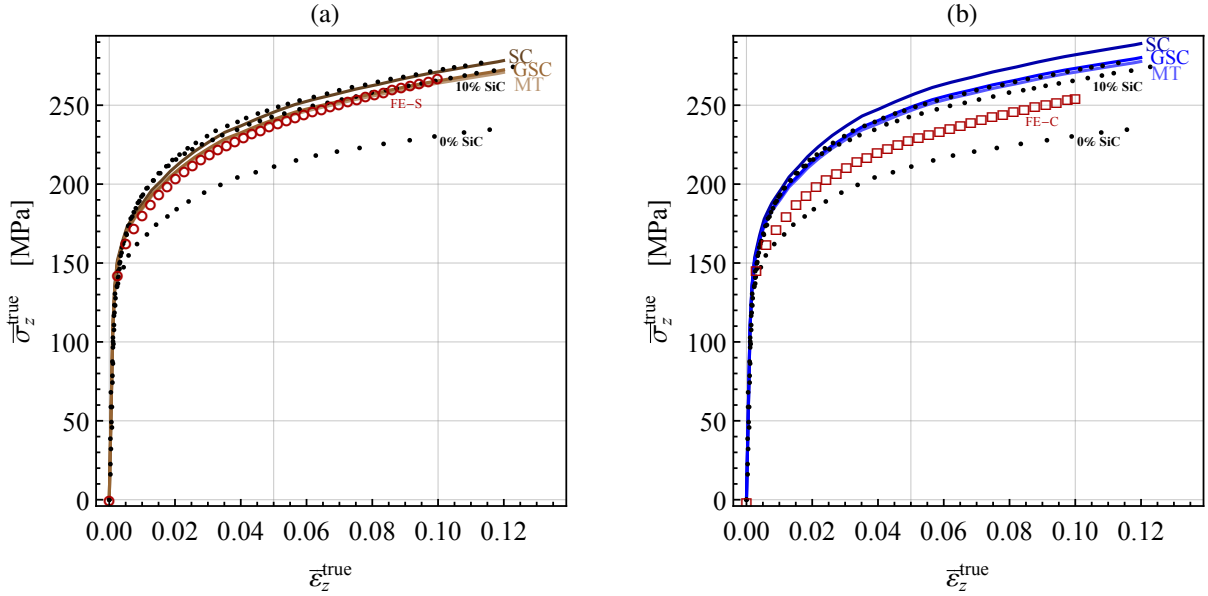

Figure 2: Comparison of stress-strain response in compression for AA6061-10%SiC composites obtained experimentally and with use of SC, GSC and MT averaging schemes using tangent (a) or secant (b) linearization, as well as the FE results of two unit cells, FE-S (a) and FE-C (b).

References

[1] J.L. Chaboche, P. Kanoute, A. Roos (2005). On the capabilities of mean-field approaches for the description of plasticity in metal-matrix composites, *Int. J. Plast.*, **21**, 1409–1434.

[2] J. Korelc (2002). Multi-language and multi-environment generation of nonlinear finite element codes, *Eng. Comput.*, **18**, 312–327.

[3] M. Kursa, K. Kowalczyk-Gajewska, M.J. Lewandowski, H. Petryk (2018). Elastic-plastic properties of metal matrix composites: Validation of mean-field approaches, *Eur. J. Mech. A. Solids*, **68**, 53–66.

[4] M. Kursa, K. Kowalczyk-Gajewska, H. Petryk (2014). Multi-objective optimization of thermo-mechanical properties of metal-ceramic composites, *Composites Part B*, **60**, 586–596.

PREDICTION OF LOCALIZED NECKING IN POLYCRYSTALLINE AGGREGATES BASED ON PERIODIC HOMOGENIZATION

J-C. Zhu[1], M. Ben Bettaieb[1,2*], and F. Abed-Meraim[1,2]

[1]*Arts et Métiers ParisTech, Université de Lorraine, CNRS, LEM3, F-57000 Metz, France.*
[2]*DAMAS, Laboratory of Excellence on Design of Alloy Metals for low-mAss Structures, Université de Lorraine, France.*
e-mail: Mohamed.BenBettaieb@ensam.eu

Ductile failure is the main mechanism that limits the formability of thin metal sheets during forming processes. In the current contribution, ductile failure is assumed to be solely induced by the occurrence of localized necking within the sheet metal. Hence, other failure scenarios such as damage evolution are excluded in this study. It is well known from a number of previously reported works that the onset of localized necking in thin sheets is strongly dependent on the microstructure-related parameters, such as initial and induced textures, grain morphology and crystallographic structure. To accurately understand and analyze this dependency, several micromechanical constitutive frameworks have been coupled in the literature with various localized necking criteria ([1]). The aim of the current investigation is to contribute to this effort by developing a powerful and efficient numerical tool to predict the onset of localized necking in polycrystalline aggregates, which are assumed to be representative of thin metal sheets. In this tool, the periodic homogenization multiscale scheme is used to accurately derive the mechanical behavior of polycrystalline aggregates from that of their microscopic constituents (the single crystals). Compared to other multiscale schemes, such as the Taylor model or the self-consistent approach, the periodic homogenization technique allows us to acurately consider some important aspects in the modeling of the polycristalline behavior (realistic description of the morphology of the grains, boundary conditions, grain boundaries...). The constitutive framework at the single crystal scale follows a finite strain formulation of rate-independent crystal plasticity. At this scale, the Schmid law is used to model the plastic flow and the hardening is defined by a non-linear power law relating the evolution of the critical shear stresses to the slip rates of the crystallographic slip systems. From a numerical point of view, the periodic homogenization problem is solved by using the finite element method. In the present study, we have used ABAQUS/Implicit finite element code, where the polycrystalline aggregate is discretized by 3D finite elements. Each grain is assigned to one finite element. The periodic boundary conditions as well as the macroscopic loading are applied on the polycrystalline aggregate by using the Homtools developed by Lejeunes and Bourgeois ([2]). As the developed model is used to study the ductility limit of thin sheets, the macroscopic plane stress condition (in the thickness direction of the sheet) is legitimately adopted ([3]). The single crystal constitutive equations are integrated by using a powerful and robust numerical implicit scheme belonging to the family of ultimate algorithms ([4]). This numerical scheme is implemented via a user material subroutine (UMAT) into Abaqus. To predict the incipience of localized necking in polycrystalline aggregates, the developed periodic homogenization scheme is coupled with the bifurcation approach ([5]). With this approach, the localization phenomenon is viewed as a consequence of instability in the constitutive description of uniform deformation. In other words, the occurrence of strain localization is a result of jump in the macroscopic velocity gradient of the deformed solid. It is noteworthy that, besides its sound theoretical foundations, the bifurcation approach does not need the calibration of any additional parameter, such as the geometric imperfection factor required when the M–K analysis is used ([6]). The use of the Schmid law at the single crystal scale allows predicting localized necking at realistic strain levels. To apply the bifurcation approach for the prediction of strain localization, the macroscopic tangent modulus should be determined. In the current work, this tangent modulus is derived by a condensation of the global stiffness matrix ([7]). This global stiffness matrix is determined by coupling a 3D user element (UEL), used to compute the element stiffness matrices, with a Python Script developed to assembly these matrices. We have also developed a set of Python Scripts to condense the global stiffness matrix and then to obtain the macroscopic tangent modulus. Compared to other numerical techniques, such as the fluctuation technique ([8]) and the perturbation technique ([9]), the condensation technique seems to be the most appropriate and the most robust to derive the macroscopic tangent modulus. The performance and accuracy of the proposed computational methods will be demonstrated for representative numerical problems dealing with polycrystals

with microstructures of FCC single crystals. The evolution of the macroscopic tangent modulus during the loading will be particularly analyzed and commented. A sensitivity study will be conducted in order to investigate the effect of some microstructure parameters (initial crystallogrpahic texture, initial morphology of the grains...) on the prediction of localized necking. In order to investigate the effect of the multiscale scheme on the predictions of strain localization, the results obtained with the current model will be compared with the results obtained with other multiscale schemes (the Taylor model and the self-consistent approach).

References

[1] H.K. Akpama, M. Ben Bettaieb, F. Abed-Meraim. Localized necking predictions based on rate-independent self-consistent polycrystal plasticity: Bifurcation analysis versus imperfection approach. *Int. J. Plasticity*, 91:205, 2017.

[2] S. Lejeunes, S. Bourgeois. Une Toolbox Abaqus pour le calcul de propriétés effectives de milieux hétérogènes. *10éme Colloque National en Calcul des Structures*. France. 2011.

[3] J.W. Hutchinson, K.W. Neale, A. Needleman. Sheet necking-I. Validity of plane stress assumptions of the long-wavelength approximation. *In: Koistinen, D.P., Wang, N.M. (Eds.), Mechanics of Sheet Metal Forming. Plenum*, 111, 1978.

[4] H.K. Akpama, M. Ben Bettaieb, F. Abed-Meraim. Numerical integration of rate-independent BCC single crystal plasticity models: comparative study of two classes of numerical algorithms. *Int. J. Num. Meth. Eng.* 108:363, 2016

[5] J.W. Rudnicki and J.R. Rice. Conditions for the localization of deformation in pressure-sensitive dilatant materials. *J. Mech. Phys. Solids*, 23:371, 1975.

[6] Z. Marciniak, K. Kuczynski. Limit strains in processes of stretch-forming sheet metal. *Int. J. Mech. Sci.* 9:609, 1967.

[7] C. Miehe. Computational micro-to-macro transitions for discretized micro-structures of heterogeneous materials at finite strains based on the minimization of averaged incremental energy. *Comput. Method Appl. M.* 192:559, 2003.

[8] C. Miehe, J. Schröder, M. Becker. Computational homogenization analysis in finite elasticity: material and structural instabilities on the micro- and macro-scales of periodic composites and their interaction. *Comput. Method Appl. M.* 191:4971, 2002.

[9] A. Javili, G. Chatzigeorgiou, P. Steinmann. Computational homogenization in magneto-mechanics. *Int. J. Solids Struct*. 50:4197, 2013.

MACROSCOPIC FRICTION OF MICROSCOPICALLY ROUGH SOFT CONTACTS

J. Lengiewicz[1], M.F. Leyva-Mendivil[2,3], G. Limbert[2,3,4], and S. Stupkiewicz[1]

[1]*Institute of Fundamental Technological Research, Polish Academy of Sciences, Warsaw, Poland*
[2]*Faculty of Engineering and the Environment, National Centre for Advanced Tribology at Southampton (nCATS), University of Southampton, Southampton SO17 1BJ, United Kingdom*
[3]*Faculty of Engineering and the Environment, Bioengineering Research Group, University of Southampton, Southampton SO17 1BJ, United Kingdom*
[4]*Faculty of Health Sciences, Laboratory of Biomechanics and Mechanobiology, Department of Human Biology, Division of Biomedical Engineering, University of Cape Town, Observatory 7935, South Africa*

e-mail: jleng@ippt.pan.pl

1. Introduction

One can distinguish a number of possible mechanisms and sources of dissipation at different length- and time scales, which can contribute to what manifests itself as the macroscopic frictional response. As such, rough contacts in sliding usually exhibit complex behavior, and their satisfactory description is still viewed as one of the frontiers of modeling in tribology [1]. In this work, we follow the multiscale approach to modeling, which provides us with methods allowing to gain deeper understanding of the analyzed contact systems and to effectively model friction.

We focus on a specific class of contact systems in which one or both bodies are soft and thus may undergo large deformations. These can be, for instance, rubber-like materials like elastomeric seals or biological tissues like the skin. For such systems, the viscoelastic dissipation induced by the moving contact roughness and the accompanying non-homogeneous fluctuation of contact forces is usually viewed as a dominant effect that is responsible for differences in frictional characteristics between the micro- and the macro scale [2, 3]. However, it turns out that one can also observe non-trivial frictional effects at the macro scale even if only purely elastic contacts and the simple Amonton-Coulomb friction model are considered at the micro scale [4–6]. The latter (purely-elastic) case is more deeply analyzed and discussed in this work.

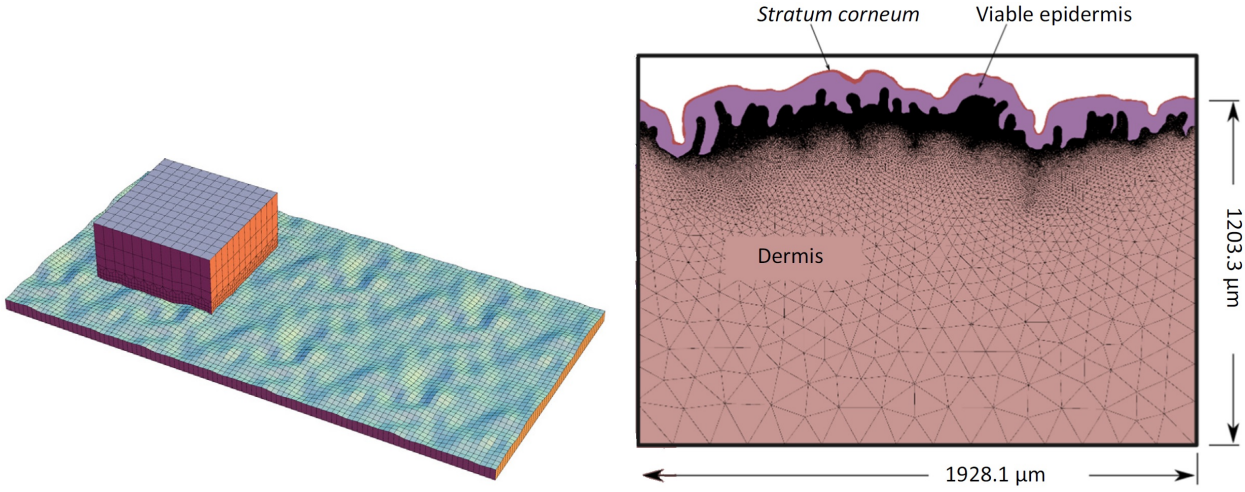

Figure 1: Two microscopically-rough contact systems: (a) randomly rough periodic surfaces, (b) 2D anatomically-based FE model of the skin to be in sliding contact with a rigid indenter.

2. Frictional response of microscopically rough soft elastic contacts

Two families of contact systems have been analyzed. The first family (further referred to as Case 1) is based on randomly generated rough periodic surfaces [4], see Figure 1a, and is characterized by relatively low asperities' heights and slopes' angles. The second family (Case 2) uses the geometry and material properties which correspond to a real anatomy of skin section. It features a complicated surface topography at the microscopic scale and a layered structure [5, 6], see Figure 1b. In Case 2, a simplified counter-surface has been considered, represented by isolated rigid cylinders (not shown in Figure 1b).

In both cases, FEM-based contact homogenization procedures have been used (different for each case) to analyze the frictional response. As expected, it was shown that the macroscopic friction coefficient can be in general different from the microscopic one. But it was also observed that it can substantially depend on the normal contact pressure. A further study of how the friction-pressure relationship depends on various problem parameters has been performed in both analyzed cases. In Case 1, for the Poisson's ratio $\nu \leq 0$, a counter-intuitive effect has been observed, in which the macroscopic friction coefficient drops below the microscopic one, see Figure 2a. In Case 2, the global-to-local friction coefficient ratio is higher than in the Case 1, and it possibly depends on asperities' radii on the counter-surface, see Figure 2b.

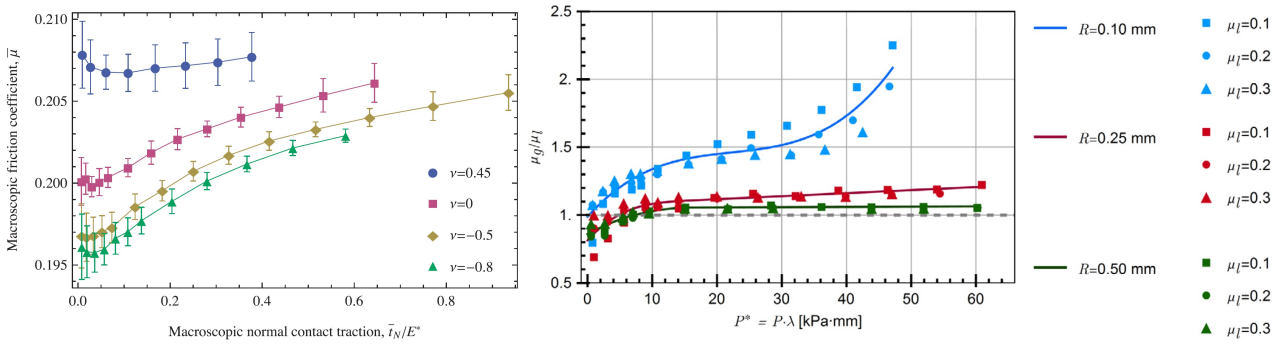

Figure 2: Friction-pressure relationship in macro scale: (a) in Case 1, [4], for different values of the Poisson's ratio ν and for the micro-scale friction coefficient $\mu_l = 0.2$, (b) in Case 2, [6], for different cylindrical indenter radii R and different micro-scale friction coefficients μ_l.

References

[1] R.W. Carpick, The contact sport of rough surfaces, *Science*, 359:38-38, 2018.

[2] P. Wagner, P. Wriggers, C. Klapproth, C. Prange, B. Wies, Multiscale FEM approach for hysteresis friction of rubber on rough surfaces, *Computer Methods in Applied Mechanics and Engineering*, 296:150-168, 2015.

[3] K.I. Kilic, I. Temizer, Tuning macroscopic sliding friction at soft contact interfaces: interaction of bulk and surface heterogeneities. *Tribol. Intern.*, 104:83âĂŞ97, 2016.

[4] S. Stupkiewicz, M. Lewandowski and J. Lengiewicz, Micromechanical analysis of friction anisotropy in rough elastic contacts, *Int. J. Solids Struct.*, 51:3931-3943, 2014.

[5] M.F. Leyva-Mendivil, J. Lengiewicz, A. Page, N.W. Bressloff and G. Limbert, Skin microstructure is a key contributor to its friction behaviour, *Tribol. Lett.*, 65:12, 2017.

[6] M.F. Leyva-Mendivil, J. Lengiewicz and G. Limbert, Skin friction under pressure. The role of micromechanics, *Surf. Topogr.: Metrol. Prop.*, 6:014001, 2018.

MODELLING KINEMATIC HARDENING FOR PROGRESSIVE MEAN STRESS RELAXATION IN PLASTICITY

E.R.F. de Souza Campos[1,2], R. Desmorat[1], and L. Malcher[2]

[1]*Laboratoire de Mécanique et Technologie- LMT, ENS Paris Saclay/CNRS/Univ Paris-Saclay, Cachan, France*
[2]*Department of Mechanical Engineering, Faculty of Technology, University of Brasília, Brasília, Brazil*

e-mail: estarle@lmt.ens-cachan.fr

Abstract

Several constitutive models for cyclic plasticity have been proposed over the last 40 years. Despite the progress made by most modern approaches, some difficulties still persist, specially regarding a precise descriptions of progressive mean stress relaxation and ratcheting. The present contribution proposes a non standard kinematic hardening model to handle complex loading conditions in low cycle fatigue. The model starts from a non-saturating power law for kinematic hardening in which a relative backstress term is introduced. Such formulation allows a good description of partial mean stress relaxation phenomena under complex loading conditions, at least in proportional cases, with the advantage of need few material parameters. An implicit numerical integration scheme is suggested and implemented to ensure robustness of calculations. The validation is realized considering experimental data available in literature for INCONEL-718DA alloy used in turbine high pressure discs.

1. introduction

The response of continuum damage and other approaches to predict fatigue life are directly dependent on a good description of plasticity phenomena. Nowadays, great efforts have been made to better describe the mean stress relaxation and ratcheting under cyclic multiaxial loadings in inelastic regimes. The mean stress effect in high cycle fatigue (HCF), well known and often satisfactorily represented in uniaxial stress cases by Goodman and Soderberg linear rules, becomes quiet complex in multiaxial solicitations, [8]. Criterion as Sines and Crossland cannot describe the full triaxiality range nor properly handle non-proportional loadings. In case of low cycle fatigue (LCF), even in uniaxial cases, standard models for kinematic hardening like [1] or based in variations of it, [3], predict a complete mean stress relaxation over few cycles. In [7] a model based in the kinematic hardening governed by a non-saturating law introduced by [2]. Such approach considers a calibration of the material parameter that governs the spring back term accordingly with the loading conditions. It provided some good results in uniaxial traction-compression tests predicting the mean stress relaxation progressively, but its extension to complex cases as variable strain ratio or multiaxial still a open question. Thus, the aim of this work is to propose a kinematic hardening formulation capable to better describe stress-strain amplitude in presence of mean stress. An implicit numerical integration scheme is suggested and some preliminary results are present to evaluate the methodology response. The study validation will consider the experimental campaign of [7] for INCONEL 718DA alloy.

2. Kinematic hardening and mean stress relaxation in plasticity

Kinematic hardening represents the phenomenon known as Bauschinger effect, i.e., the yield surface translation as a rigid body in stress space. A number of constitutive models has been proposed to describe ic behaviour under cyclic loading conditions [6], [1] [3], [4] [5], [2]. Considering the recent advances in the elastoplasticiy characterization, the more modern kinematic hardening laws take the general form:

$$\dot{\boldsymbol{X}} = \frac{2}{3} C \dot{\boldsymbol{\varepsilon}}^p - \mathfrak{B}(\boldsymbol{X}, p, \boldsymbol{\sigma}) \dot{\mathcal{P}}_k(\boldsymbol{X}, \boldsymbol{\sigma}, \dot{\boldsymbol{\varepsilon}}^p) \tag{1}$$

where C is a matrial parameter and the product $\mathfrak{B}\dot{\mathcal{P}}$ represents the springback term. Generally, the function $\dot{\mathcal{P}}$ has a proportional and linear dependency in relation to plastic strain rate such as $\dot{\mathcal{P}}_k(\boldsymbol{X}, \boldsymbol{\sigma}, a\dot{\boldsymbol{\varepsilon}}) = a\dot{\mathcal{P}}_k(\boldsymbol{X}, \boldsymbol{\sigma}, \dot{\boldsymbol{\varepsilon}}) \quad \forall a >= 0$. In order to achieve the concave shape of the stress strain curve, the tensorial function $\mathfrak{B}$ is commonly assumed heaving the same sign of $\boldsymbol{X}$and $\|\mathfrak{B}\|$ increasing with $\|\boldsymbol{\sigma}\|$.

2.1 . Alternative formulation for kinematic hardening

One considers the original Desmorat's formulation for kinematic hardening, [2], represented by:

$$\dot{\boldsymbol{X}} = \frac{2}{3} C\dot{\boldsymbol{\varepsilon}}^p - \Gamma X_{eq}^{M-2} \boldsymbol{X} \left\langle \dot{X}_{eq} \right\rangle \tag{2}$$

where C is the modulus of kinematic hardening, Γ is a material parameter of the springback term , M is an exponent to control the curvature of stress strain curve and X_{eq} is the von Mises norm of the back stress tensor $\boldsymbol{X}$.

To prevent the fast mean stress relaxation, the general idea is to define the instant when load reversals in plasticity, make $\mathfrak{B}\dot{\mathcal{P}}(\boldsymbol{X}_r) = \boldsymbol{0}$ on it, and maintain the general behaviour of a power law ($\|\mathfrak{B}\| \uparrow$ with $\|\boldsymbol{X}\| \uparrow$) at the subsequent instants. That will ensure $\Delta X_{(uncharge)} = \Delta X_{(charge)}$ for any loading, symmetrical or unsymmetrical, although the concavity due to spring back term holds at both situations.

Thus, it is proposed to change the initial condition in equation (2) at the instant $t = t^\star$ when $\dot{\boldsymbol{X}} : \boldsymbol{X} < 0$ from $\boldsymbol{X}(t^\star) = \boldsymbol{X}$ to $\boldsymbol{X}_r(t^\star) = \boldsymbol{X} - \boldsymbol{X}^\star$, where $\boldsymbol{X}^\star$ is the backstress tensor at infinitesimal of time before $\boldsymbol{X}^\star = \boldsymbol{X}(t^\star - \delta)$. Such modification implies that $\mathfrak{B}\dot{\mathcal{P}}(t^\star) = \boldsymbol{0}$, instant when $\dot{\boldsymbol{X}}$ takes the opposite direction of $\boldsymbol{X}$, and will ensure its growing in norm if $\dot{\boldsymbol{X}}$ holds the same direction (increases or decreases monotonically). Let us introduce the term $\boldsymbol{X}_r = \boldsymbol{X} - \boldsymbol{X}^\star$ and call it relative backstress, then substitute it into equation (2):

$$\dot{\boldsymbol{X}} = \frac{2}{3} C\dot{\boldsymbol{\varepsilon}}^p - \Gamma (X_r)_{eq}^{M-2} \left\langle (\dot{X}_r)_{eq} \right\rangle \boldsymbol{X}_r \tag{3}$$

After that, is necessary to stablish a precise (mathematical) definition of the reversion meaning in plastic strain rate and some important quantities to extend such ideas to multiaxial cases. More detailed informations about the model will be present at final version of the article.

References

[1] P. J. Armstrong and C. O. Frederick. A mathematical representation of the multiaxial bauschinger effect. *Report RD/B/N731*, 24:334, 1966.

[2] R. Desmorat. Non-saturating nonlinear kinematic hardening laws. *Comptes Rendus Mécanique*, 338(3):146 – 151, 2010.

[3] G. Cordier J.L. Chaboche, K. Dang-Van. Modelization of the strain memory effect on the cyclic hardening of 316 stainless steel. *In: SMIRT 5, Berlin*, 1979.

[4] Z. Mróz. On the description of anisotropic workhardening. *Journal of the Mechanics and Physics of Solids*, 15(3):163 – 175, 1967.

[5] N. Ohno and J.-D. Wang. Kinematic hardening rules with critical state of dynamic recovery, part i: formulation and basic features for ratchetting behavior. *International Journal of Plasticity*, 9(3):375 – 390, 1993.

[6] W. Prager. Recent developments in the mathematical theory of plasticity. *J. Appl. Phys.*, 20:235, 1949.

[7] V. I. Prisacari. Modelling of partial mean stress relaxation and biaxial mechanical testing of inco718da. *PhD thesis, Ecole Normale Supérieure Paris-Saclay*, 24:334, 2018.

[8] H. Cherouali P. Gomez P. Kanoute D. Pacou V. Bonnand, J.L. Chaboche. Experimental and theoretical comparison of some multiaxial fatigue design criteria in the context of life assessment of rotating parts in turbo-engines. *25th ICAF symposium on bridging the gap between theory and operational practice*, 24:743–764, 2009.

Session S03: Damage and fracture modelling of advanced materials

Organizers: M. Basista (IPPT PAN, Warsaw), G. Bolzon (Polit. di Milano), Ch. Sommitsch (TU Graz)

INTERACTION BETWEEN INCLUSIONS AND CRACKS IN SMART COMPOSITES

Chyanbin Hwu[1], Wei-Ren Chen[1],Ting-Hsiang Lo[1]

[1] *Institute of Aeronautics and Astronautics, National Cheng Kung University, Tainan, TAIWAN, R.O.C.*
e-mail: CHwu@mail.ncku.edu.tw

1. Introduction

Due to the ability of converting energy from one form (among mechanical, electric, and magnetic energies) to the other, piezoelectric and magneto-electro-elastic (MEE) materials are widely used as sensors and actuators in intelligent advanced structure design. Owing to the designable characteristics of composite laminates, a smart system constructed by composites with piezoelectric/MEE sensors and actuators is a common practical engineering design. If we treat sensors/actuators as inclusions, fracture analysis of such smart system can be studied via interaction between inclusions and cracks. With the nature of anisotropy, composite materials are usually modeled as anisotropic elastic solids. Thus, the simultaneous existence of anisotropic elastic, piezoelectric and MEE materials in the problems of inclusions and cracks is unavoidable.

In the literature, most of the inclusion problems were considered for a specific material type such as isotropic, anisotropic, piezoelectric, or MEE materials. Due to the difference of their mechanical behaviors, several different mathematical models and solution methods have been proposed. Thus, it is difficult to combine them together to deal with the possible situation that different types of materials appear simultaneously in the same structure. Among all the different methods, the Stroh formalism for two-dimensional anisotropic elasticity has been proved to preserve the same mathematical expressions for anisotropic, piezoelectric and MEE materials. By using Stroh formalism, some analytical solutions related to the inclusions, holes, or cracks in the piezoelectric or MEE materials have been shown to have the same mathematical matrix forms as their corresponding problems with anisotropic elastic materials [1].

If more than one inclusion is considered, the possibility of simultaneous existence of anisotropic, piezoelectric and MEE materials is raised. Although there are many studies on the problems with multiple inclusions, most of them still focus on a specific kind of materials. Similar situation occurs for the studies of interaction between inclusion and dislocation/crack/hole. With the special feature of preserving the same solution form by Stroh formalism, in this paper we develop an adaptable adjustment technique and apply it to the dislocation superimposed method (DSM) [2] and the boundary-based finite element method (BFEM) [3] to deal with fracture analysis of composites in which the piezoelectric and MEE inclusions may exist simultaneously. The proposed technique intends to adjust the matrix dimension of Stroh formalism to include the piezoelectric and/or magnetic effects from the ordinary elasticity matrices according to the real situation of the inclusion problem. To show the correctness of the proposed method, several examples are implemented by using the extended DSM or BFEM, and compared with the solutions calculated by the commercial finite element software ANSYS. Since ANSYS does not provide the function for the general MEE materials, for the purpose of comparison with ANSYS only special cases of MEE such as piezoelectric or piezomagnetic are calculated. The general cases of MEE are verified by the comparison between DSM and BFEM provided in this paper, or through its mechanical behavior.

2. Numerical examples

In order to study the interaction between an elliptical inclusion and a crack, we consider a fiber-reinforced composite with an elliptical MEE inclusion and an inclined crack subjected to a uniform tension $\sigma_{22}^{\infty}=1\text{MPa}$ at infinity (Figure 1) . The properties of composites are

$$E_1=181\text{GPa},\ E_2=10.3\text{GPa},\ G_{12}=7.17\text{GPa},\ \nu_{12}=0.28,$$

where the symbols *E*, *G* and ν denote, respectively, Young's modulus, shear modulus and Poisson's ratio, and the subscripts 1 and 2 denote, respectively, the fiber direction and the direction transverse to the fiber.

The MEE inclusion is made by mixing the fiber-reinforced composite with piezoelectric $BaTiO_3$ and piezomagnetic $CoFe_2O_4$, whose properties are

$$C_{11} = C_{33} = 166\text{GPa},\ C_{12} = C_{23} = 78\text{GPa},\ C_{13} = 77\text{GPa},$$
$$C_{22} = 161\text{GPa},\ C_{44} = C_{66} = 43\text{GPa},\ C_{55} = 44.5\text{GPa},$$
$$e_{21} = e_{23} = -4.4\text{C/m}^2,\ e_{22} = 18.6\text{C/m}^2,\ e_{16} = e_{34} = 11.6\text{C/m}^2,$$
$$\omega_{11} = \omega_{33} = 11.2\times10^{-9}\text{C/V},\ \omega_{22} = 12.6\times10^{-9}\text{C/V},$$
$$q_{21} = q_{23} = 580.3\text{N/Am},\ q_{22} = 699.7\text{N/Am},\ q_{16} = q_{34} = 550\text{N/Am},$$
$$m_{11} = m_{33} = 5\times10^{-12}\text{Ns/VC},\ m_{22} = 3\times10^{-12}\text{Ns/VC},$$
$$\xi_{11} = \xi_{33} = 5\times10^{-6}\text{Ns}^2/\text{C}^2,\ \xi_{22} = 10^{-5}\text{Ns}^2/\text{C}^2,$$

in which C_{ij}, e_{ij}, ω_{jk}, q_{ij}, m_{ij}, and ξ_{ij} are, respectively, the elastic constants, piezoelectric stress constants, dielectric permittivity constants, piezomagnetic constant, magneto-electric constant and permeability constant. Table 1 shows the normalized stress intensity factors, $K_I/\sigma_0\sqrt{\pi \mathrm{l}}$ and $K_{II}/\sigma_0\sqrt{\pi \mathrm{l}}$ where $\sigma_0 = \sigma_{22}^{\infty}$, of the crack tip *A* (Figure 1) with various *d* and α_c. From Table 1 we see that the results obtained by DSM and BFEM are quite close to each other. When the distance between inclusion and crack is larger, the values of stress intensity factors go to the ones for a crack in a homogeneous material, which are $K_I = \sigma_0 \cos^2\alpha_c\sqrt{\pi \mathrm{l}}$ and $K_{II} = \sigma_0 \sin\alpha_c \cos\alpha_c\sqrt{\pi \mathrm{l}}$. Moreover, the stress intensity factors decrease when the crack is closer to the inclusion (see for example the variation of K_I with *d* when $\alpha_c = 0^o$). It is now not easy to judge the consistency with the conclusion made for isotropic materials [4] – the presence of harder/softer inclusions will reduce/enhance the stress intensity of the crack. Thus, further examples and studies are necessary for smart composites.

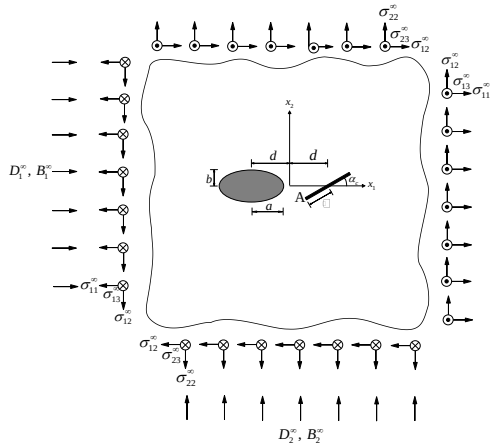

Figure 1. An infinite plate with an elliptical inclusion and a crack under uniform load at infinity. (*a*=2 m, *b*=1 m, l =1 m)

Inclusion	*d*/*a*	α_c(°)	$K_I/\sigma\sqrt{\pi l}$		$K_{II}/\sigma\sqrt{\pi l}$	
			DSM	BFEM	DSM	BFEM
MEE	6	0	0.9985	0.9974	0	0
		45	0.4969	0.4970	0.5014	0.5003
		60	0.2463	0.2469	0.4341	0.4331
	4	0	0.9962	0.9950	0	0
		45	0.4933	0.4933	0.5025	0.5012
		60	0.2425	0.2430	0.4348	0.4336
	2	0	0.9814	0.9797	0	0
		45	0.4801	0.4766	0.5011	0.5017
		60	0.2322	0.2313	0.4332	0.4310

Table1. Stress intensity factor of crack tip A

Acknowledgments The authors would like to thank Ministry of Science and Technology, TAIWAN, R.O.C for support through Grants MOST 104-2221-E-006-138-MY3.

References

[1] C. Hwu. *Anisotropic Elastic Plates*, Springer, 2010.
[2] C. Hwu, Y.K. Liang, and W.J. Yen. Interaction between inclusions and various types of cracks. *Int. J. Fract.*, 73(4):301-323, 1995.
[3] C. Hwu, S.T. Huang, and C. C. Li. Boundary-based finite element method for two-dimensional anisotropic elastic solids with multiple holes and cracks. *Eng. Anal. Bound. Elem.*, 79:13-22, 2017.
[4] C. Hwu and C.Y. Liao. A special boundary element for the problems of multi-holes, cracks and inclusions. *Computers and Structures*, 51(1): 23-31, 1994.

INVESTIGATING THE EFFECTS OF GEOMETRICAL PARAMETERS ON FRACTURE RESPONSE OF THE NOTCHED SMALL PUNCH TEST

B. Deliktas[1], I. C. Tumturk[2], and M. O. Yayli[1]

[1]*Uludag University, Department of Civil Engineering , Bursa, Turkey*
[2]*Meteksan Defence,Mechanical Design Departmant, Ankara, Turkey*

e-mail: bdeliktas@uludag.edu.tr

1. Introduction

The non-destructive techniques have the great advantage to evaluate the material properties in-situ, in particular the small punch test shows to be very attractive and promising as it relies on a small, but representative material volume of the component in-service and it has been successfully applied in other research fields. Therefore, the aim of this study is a numerical investigation of the effects of geometrical parameters of a predefined notch on fracture characteristics of small punch testing specimens. Taking the experimental research of notched specimens published by Turba et.al, finite element based study of small punch fracture specimens made of P91 steel, have been modeled in ABAQUS. Then, using this model as a departure point, geometrical parameters of the predefined notch (such as notch radius, placement, depth) have been varied and the effects of such geometrical changes on fracture response of the specimen is investigated numerically.

2. Theoretical Background

Theoretical framework is based on the thermo-mechanical finite strain coupled plasticity and continuum damage mechanics models. Cleavage failure in metallic materials is modled with the deterministic model by Ritchie-Knott-Rice [3], relies on a critical stress over the critical distance principle whereas whereas the ductile fracture is characterized by using the Gurson porous plasticity to model dilatational yielding and ductile rupture.([5], [2], and [1]. This model devises a hydrostatic stress dependent yield potential derived using homogenization over void-rigid plastic matrix and limit analysis

$$\begin{aligned} \phi^p &= \left[\frac{\overline{\overline{\sigma}}_{eq}}{\sigma_y}\right]^2 + 2q_1 f^* \cosh\left(\frac{q_2}{2\sigma_y}\mathrm{tr}\left[\overline{\overline{\sigma}}\right]\right) - \left[1 + \left[q_1 f^*\right]^2\right] = 0. \\ \overline{\overline{\sigma}}_{eq} &= \sqrt{\frac{3}{2}\left[\mathrm{dev}\overline{\overline{\sigma}} : \mathrm{dev}\overline{\overline{\sigma}}\right]} \end{aligned} \tag{1}$$

where f is the void volume fraction that evolves with plastic strains, σ_y is the current yield stress of material and $\overline{\overline{\sigma}}$ is the so-called *effective stress* [4]. Note that the proposed coupling with continuum damage mechanics formalism introduces dev $\left[\overline{\overline{\sigma}}\right]$ as the deviatoric part of the effective stress tensor at rotationally neutralized configuration in the yield potential ϕ^p, onto which both void-growth and micro-crack driven damage mechanisms are reflected in order to account for softening effects of ductile and brittle failure phenomena.

3. Numerical Analysis of Small Punch Test

Small Punch Testing is a recently developed mechanical testing method that allows the mechanical, fracture and creep characterization of tiny specimens. Axisymmetric finite elements with reduced integration and enhanced hourglassing controls (CAX4R) has been used. Small punch experiment has been modelled for 22° and −196C. The set of material parameters used to predict P91 behavior have been listed in the following table.

Table 1: Gurson-Tvergaard-Needleman model parameters for P91.

f_N	s_N	ε_N	q_1	q_2	$q_3 = 1/f_U$	f_0	k_w
0.005	0.1	0.03	1.5	1.0	2.25	0.0055	3.0

3.1. Effects of specimen geometry on fracture response of SPT

The geometrical parameters of the small punch experiment such as puncher radius and notch depth (Figure-**??**) have been varied and the effects of such geometrical changes on fracture response of the specimen is investigated numerically. The effects of the puncher radius on the fracture response of SPT, is investigated using various the puncher radius of the loading with the values of 2.25mm, 2.5mm and 2.75mm, respectively. The results of analyses are presented in Figure 1. As one can notice that reducing the puncher radius a too small

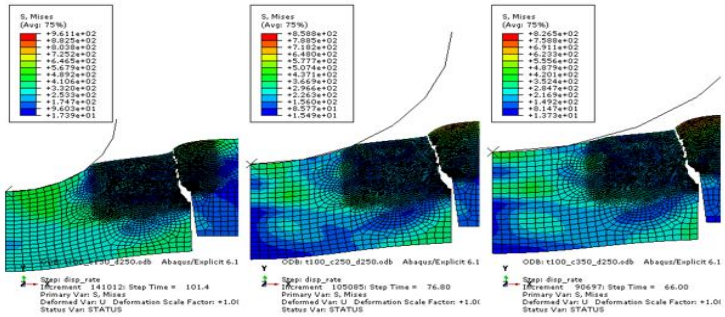

Figure 1: (a) Numerical prediction of effects of the puncher radius with 2.25mm, 2.5mm and 2.275mm on the notched specimen

value, more stress concentration occurs near by the underneath of the puncher region and also failure of the specimen is dominated by shear due to punching effect. Depth of the crack is one of the most important fracture parameter that causes the damage and fracture in the materials. Therefore, to investigate the effect of crack depth on the fracture response of the small punch test, three different crack depths, with length of of 0.44mm, 0.49mm, and 0.54mm, are used in numerical simulation. As the crack depth increases along the direction of the thickness of the specimen material becomes weaker and is much likely prone to damage and fracture. At the lower temperature $-196°$C for all crack lengths the material behaves completely brittle.

4. Conclusions

In the enclosed work, a coupled continuum damage mechanics and porous plasticity model on local scale has been presented. Constitutive modelling and small punch experiments have been performed for P91 steel. It has been found out that the proposed model precisely and conveniently predicts crack patterns within a relatively wide temperature range from 22°C to $-196°$C.

References

[1] L. Malcher, F.M. Andrade Pires, and J.M.A. Cesar de Sa. An assessment of isotropic constitutive models for ductile fracture under high and low stress triaxiality. *International Journal of Plasticity*, 30-31:81–115, 2012.

[2] K. Nahshon and Z. Xue. A modified gurson model and its applications to punch-out experiments. *Engineering Fracture Mechanics*, 76:997–1009, 2009.

[3] R.O. Ritchie, J.F. Knott, and J.R. Rice. On the relationship between critical tensile stress and fracture toughness in mild steel. *J. Mech. Phys. Solids*, 21:395–410, 1973.

[4] I.C. Turtuk and B. Deliktas. Coupled porous plasticity âĂŞ continuum damage mechanics approaches in modelling temperature driven ductile-to-brittle transition fracture in ferritic steels. *International Journal of Plasticity*, 2016.

[5] V. Tvergaard. On localization in ductile materials containing spherical voids. *Int J Fract*, 18:237–252, 1982a.

EXPERIMENTAL AND NUMERICAL SIMULATION OF MATERIAL AND DAMAGE BEHAVIOUR OF 3D PRINTED POLYMERS IN COMPARISON TO METALS

D. Schob[2] R. Roszak[1,2], H. Sparr[2], M. Ziegenhorn[2]

[1] Poznan University of Technology, Poland
[2] Brandenburg University of Technology Cottbus-Senftenberg, Germany

robert.roszak@put.poznan.pl
daniela.schob@b-tu.de
holger.sparr@b-tu.de
matthias.ziegenhorn@b-tu.de

1. Motivation

This paper describes the material and damage behaviour of new materials. In the recent years the new materials become more and more interesting in the field of construction materials. One of the main task in this field is the characterisation of these materials due to influence of manufacturing processes. In this sector, rapid prototyping is becoming increasingly important. Products can be produced faster and more cost-effectively using 3D printing. However, the innovative production methods also pose challenges. The new materials must withstand complex loadings, as metals have done so far. In this research project, material and damage behaviour of 3D printed polymers are investigate and compared to metals. For the description of the material behaviour, the viscoplastic model of Chaboche was used, which is already adapted for metals under thermomechanical loading. The Gurson model that is commonly used for cast-iron and steel, was selected to consider the damage behaviour of 3D printed polymers.

2. Material Model

The investigations carried out for 3D printed Polyamid12 (PA12). Specimens were produces by selective laser sintering and manufactured in accordance to DIN EN ISO 527-2 [1]. The material behaviour was characterized according to Haupt [2] with complex experiments. Viscoplastic material behaviour was identified. In this respect, the Chaboche model [3] selected for numerical simulation.

(1)
$$\dot{\boldsymbol{\sigma}} = \boldsymbol{E}(\dot{\boldsymbol{\varepsilon}}^{tot} - \dot{\boldsymbol{\varepsilon}}^{vp})$$

(2)
$$\dot{\boldsymbol{\varepsilon}}^{vp} = \sqrt{\frac{3}{2}} \left\langle \frac{\sqrt{\frac{3}{2}} \left\| \boldsymbol{\sigma}' - \sum_{j=1}^{n_{aa}} \boldsymbol{\alpha}_j \right\| - (y_0 + \sigma^M)}{K} \right\rangle^n \frac{\boldsymbol{\sigma}' - \sum_{j=1}^{n_{aa}} \boldsymbol{\alpha}_j}{\left\| \boldsymbol{\sigma}' - \sum_{j=1}^{n_{aa}} \boldsymbol{\alpha}_j \right\|}$$

This model contains parameters that are determined by different experiments (Eq. 1 and 2). Started with static tensile and relaxation test, followed by dynamic cyclic load tests. After determination of material behaviour and parameters, a microscopic analysis was carried out. Based on the detection of voids caused by the production process of 3D printing, a damage model was investigated.

3. Damage Model

A well-known ductile damage continuum model is the Gurson Tvergaard Needleman (GTN) model [4], [5] which is based on the concept of void nucleation, growth, and coalescence as being the mechanism responsible for damage and failure in ductile metals. Physically motivated by void induced failure process, the GTN model has been widely used to predict load deformation and fracture resistance behaviour of a range of ductile metallic materials such as steel, cast iron, copper, and aluminium. Numerical implementation of the GTN model to polymers is limited primarily because the void nucleation, growth, and coalescence process is not present in most polymers in the same way it is in metals. However, the GTN model (Eq. 3) is a continuum softening and failure model, so an appropriate selection of parameters could make the model applicable to failure of polymers like PA12.

(3)

$$\Phi = \left(\frac{\sigma_e}{\sigma_0}\right)^2 + 2q_1 f^* \cosh\left(q_2 \frac{3\sigma_m}{2\sigma_0}\right) - (1 + q_3 f^{*2}) = 0$$

Although generally good agreements have been reported between numerical and experimental results in the above-mentioned studies of polymers, there is no specific framework on how GTN [6] model parameters can be consistently determined from experiments on polymeric materials, or how a link between experiment and numerical analysis.

The papers presents the application of the GTN model for sheer test for polymeric materials. The study of the polymer material was compared to the results obtained from the study of basic materials such as aluminium. The material parameters for the GTN model were also estimated.

4. Conclusion

This research project has successfully addressed two main topics. On the one hand, it has been shown that the Chaboche model, which has so far been used for metals at high temperatures, can also be used for 3D printed polymers at room temperature and under complex loads. On the other hand, the numerical simulation of the damage behaviour using the GTN model under static loading has shown the same phenomena as in the experiment and revealed good similarities. In the continuing research, the influence of the damage under dynamic loads and a coupling of the material and damage model of Chaboche and GTN are investigated.

References

[1] DIN Deutsches Institut für Normung e.V.: DIN EN ISO 527-2. *Kunststoffe – Bestimmung der Zugeigenschaften. Teil 2: Prüfbedingungen für Form- und Extrusionsmassen*, 2012.

[2] Haupt, P. *Continuum Mechanics and Theory of Materials.* 2002.

[3] Chaboche, J.-L. *Viscoplastic Constitutive Equations for the Description of Cyclic and Anisotropic Behaviour of Metals. In: 17th Polish conference on mechanics of solids*. 1975.

[4] Gurson, A.L. *Continuum Theory of Ductile Rupture by Void Nucleation and Growth: Part I Yield Criteria and Flow Rules for Porous Ductile Media*, Journal of Engineering. Materials and Technology, 99: 2-15. 1977

[5] Tvergaard, V. and Needleman. *A. Analysis of the Cup-Cone Fracture in a Round Tensile Bar.* Acta Metallurgica, 32: 157-169. 1984

[6] Gatea S., Ou H., Lu B., McCartney G. *Modelling of ductile fracture in single point incremental forming using a modified GTN model.* Engineering Fracture Mechanics 186: 59–79, (2017)

DETERMINATION OF THERMAL RESIDUAL STRESSES IN ALUMINA REINFORCED WITH CHROMIUM – THE GRAIN SIZE EFFECT

W. Węglewski, M. Basista, M. Krajewski, and K. Bochenek
Institute of Fundamental Technological Research, Polish Academy of Sciences, Pawinskiego Street 5B, 02-106 Warsaw, Poland
e-mail: wweglew@ippt.pan.pl

1. Experimental determination of thermal residual stress in alumina matrix

In ceramic-metal composites thermal residual stresses (TRS) are inherently present mainly due to different coefficients of thermal expansion of the phase materials. Such stresses may trigger microcrack nucleation and growth especially in the ceramic phase. Therefore, determination of TRS is of continuing research interest both in experimental mechanics and materials modelling.

In this communication we present experimental measurements and numerical simulation of processing-induced thermal residual stresses (TRS) in aluminium oxide (alumina) matrix reinforced with chromium particles (60vol.%Al_2O_3/40vol.%Cr). This ceramic-metal composite was manufactured by powder metallurgy route comprising powder mixing in a planetary ball mill and consolidation by hot pressing (HP). Two different chromium powders (mean particle size of 5 μm and 45 μm) were used. The alumina particle mean size (1 μm) was kept constant in all experiments.

The average residual stresses in alumina matrix have been determined applying two optical methods: photoluminescence piezo-spectroscopy (PLPS) and Raman spectroscopy (RS). For comparison the TRS are also measured using two diffraction methods: neutron diffraction (ND) and X-ray diffraction (XRD) [1] and the results are shown in Fig. 1. These four experimental techniques reveal a size effect of chromium particles on the magnitude and sign of the average residual stress in the alumina matrix. When the fine chromium powder (5 μm) is used the average residual stress in the ceramic phase is tensile, whereas for the coarser chromium powder (45 μm) it becomes compressive (Fig.1).

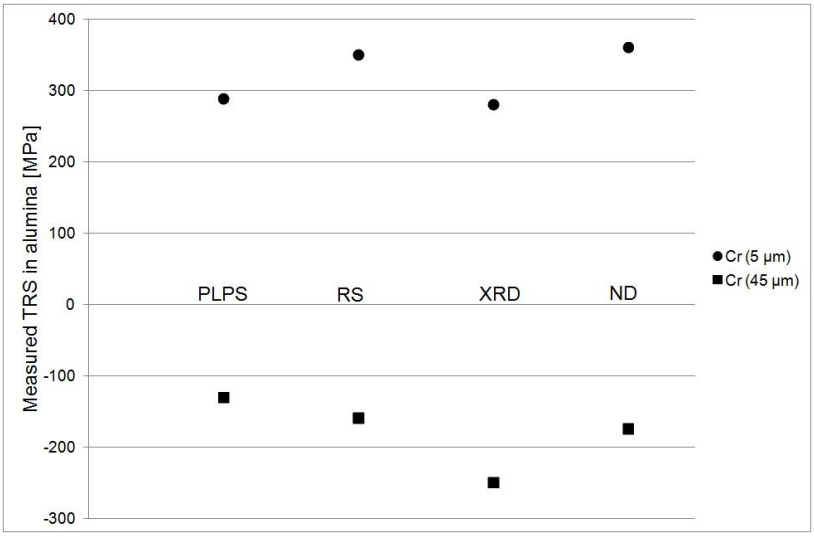

Fig. 1. Experimental measurements of average residual stress in the alumina matrix of 60vol.%Al_2O_3/40vol.%Cr composite as obtained by photoluminescence piezo-spectroscopy (PLPS), Raman spectroscopy (RS), neutron diffraction (ND) and X-ray diffraction (XRD).

2. Discussion of experimental results and modelling approach

The unexpected effect of the sign change of average TRS in the alumina matrix (Fig. 1) has been consistently detected by the four experimental methods and cannot, thus, be deemed as an artefact of any specific

measuring technique. Also, by a series of additional PLPS tests and by the neutron diffraction measurements we have ruled out a possibility that the TRS sign change is a surface effect. A plausible explanation of the influence of the size of metal particulates on the TRS in the alumina matrix has been sought using models based on the Eshelby solution of an inhomogeneous inclusion with eigenstrain embedded in an elastic matrix (e.g. [2]). These models allow for determination of the average stresses in ceramic matrix and metal particulates depending on the volume fraction of inclusions, the misfit strains stemming from CTE's difference, and elastic constants of matrix and inclusions. However, using the Taya et al. [2] solutions the average TRS in alumina is compressive, which contradicts our experimental data for 5 μm chromium powder. Apparently, such micromechanical models do not account for the fluctuating stresses caused by complex microstructure that could be a source of the TRS behaviour as shown in Fig. 1.

A more realistic approach seem to be offered by numerical models based on real material microstructures obtained from micro-CT [3], [4]. In such models the inclusions are not approximated by ellipsoids like in the Eshelby solution but micro-CT images of a composite microstructure reflecting the size and mutual position of metal reinforcing particulates are transformed into a finite element mesh using a dedicated software (cf. Fig. 2a). The TRS are then computed by the FEM solving the heat transfer problem of cooling from the high sintering temperature to room temperature (cf. Fig. 2b). This numerical model of TRS in alumina is now in progress. The results will be presented and compared with the experimental measurements.

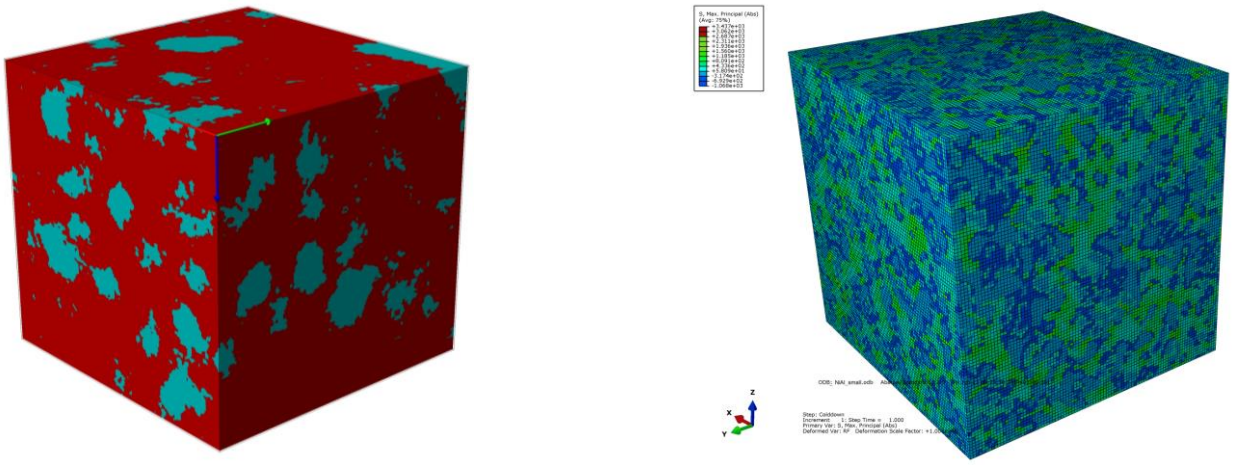

a) b)

Fig. 2. Micro-CT based FEM model for TRS in alumina-chromium composite: (a) FE mesh obtained from micro-CT images, (b) TRS distribution in ceramic matrix and metal reinforcement computed with Abaqus. .

3. Acknowledgment

This research was supported by Polish National Science Centre grant, Influence of Thermal Residual Stresses on Fracture Behaviour and Selected Mechanical Properties of Metal-Ceramic Composites: Experiments and Modeling (UMO-2014/15/B/ST8/ 04314).

4. References

[1] M. Krajewski, W. Węglewski, K. Bochenek, A. Wysmołek, M. Basista, Optical measurements of thermal residual stresses in alumina reinforced with chromium, *under preparation.*

[2]. M. Taya, S. Hayashi, A.S. Kobayashi, H. S. Yoon Toughening of a particulate-reinforced ceramic-matrix composite by thermal residual stress, J Am Ceram Soc., **73** 1382-1391, 1990

[3] M. Basista, W. Węglewski, K. Bochenek, Z. Poniżnik, Z. Nowak, Micro-CT Finite Element Analysis of Thermal Residual Stresses and Fracture in Metal-Ceramic Composites, Adv. Eng. Mat., **19**, 1600725, 2017

[4] W. Węglewski, M. Basista, A. Manescu, M. Chmielewski, K. Pietrzak, Th. Schubert, Effect of grain size on thermal residual stresses and damage in sintered chromium–alumina composites: Measurement and modeling", Composites Part B, **67**, 119–124, 2014

THE EVALUATION OF MICROSTRUCTURE OF CARBON STEEL SURFACE LAYER AFTER DIFFUSION CHROMIZING AND LASER HEAT TREATMENT

I. Bauer[1], M. Paczkowska[2]

[1] *University of Warmia and Mazury in Olsztyn, Faculty of Technical Science, Department of Materials and Machine Technology, Poland*
e-mail: iwona.bauer@uwm.edu.pl;
[2] *Poznan University of Technology, Institute of Machines and Motor Vehicles, Division of Motor Vehicles and Road Transport, Poland*
e-mail: marta.paczkowska@put.poznan.pl

1. Introduction

Damage and wear of machine components is a significant problem in many industries. Various technologies for producing surface layer in order to improve the surface properties are developed [1-4]. There is a growing demand for technology that improve the performance of machine and equipment parts to lower manufacturing costs. The attributes of chromized layers produced by powder methods are enhanced through the selection of optimal mixture components, carbon concentrations in steel and process parameters. The advantage of this process is the ability uphill diffusion of carbon, that activity is lowered in the presence of chromium atoms and carbon was migrated from the steel core to the diffusion layer. Modification of surface layers formation with the help of laser techniques has been dealt with in many scientific centers. The use of laser for surface heat treatment can be also applied on various metal alloys (mainly iron alloys), even with diffusion layers [5-8].
This paper is devoted to the evaluation of microstructure of C45 steel surface layer after diffusion chromizing and laser heat treatment. The influence of laser parameters on the microstructure of the modified layer were analyzed.

2. Investigated materials and methods

Samples of C45 steel were chromized by the powder-pack method and were placed in the powder mix in special boxes made of X6CrNiTi18-10 steel. To prevent sample oxidation, the boxes were covered with lids and sealed with vitreous enamel. The applied powder mixture to produce the chromized layer contained: Cr_2O_3 with an addition of Al, Al_2O_3 and an activator NH_4Cl. The process was carried out in a Labotherm LH15/14 furnace at 1050°C for 8 hours. Chromizing process was followed by laser heat treatment in two variants of laser beam parameters. Dual diode TRUDISK 1000 laser device has been used. Laser beam power density variant no 1: 678 E [W/mm^2] , variant no 2: 185 E [W/mm^2]. The structure of the analyzed layer was evaluated by an optical and scanning microscopes. The phase composition of a chromized layer and laser heat treatment was evaluated using a Panalytical Empyrean equipment with the CuKα radiation. The chemical composition of the diffusion layer and remelted zones was assessed by optical emission spectrometry. Vickers hardness tests were preformed on transverse microsections. The depth, width, hardness of remelted zone from the solid state case modified by laser heating were carried.

3. Results and discussion

Chromized layer on samples of C45 steel were clearly separated from the ferrite-perlite steel substrate with an estimated thickness of 30 μm. After laser heat treatment of the diffusion layer remelted zone was appeared. Chromized diffusion layer following after laser heat treatment on samples of C45 steel were characterized by higher surface roughness than chromized steel. The surface of C45 steel samples following diffusion chromizing viewed under the SEM is shown in Figure 1 and following diffusion chromizing after laser heat treatment is shown in Figure 2.

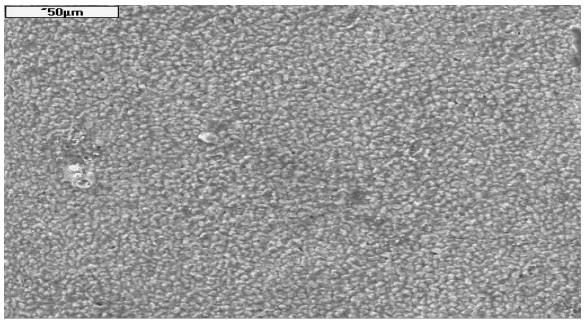

Fig.1. An example of the surface of C45 steel following diffusion chromizing, SEM

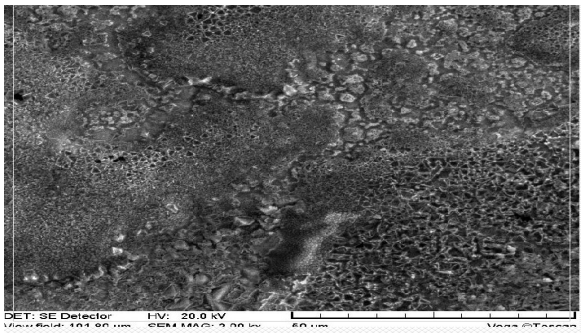

Fig.2. An example of the surface of C45 steel following diffusion chromizing and laser heat treatment, variant no 1, SEM

Microscopy observation revealed that, the microstructure of laser remelted zone was fine and homogenous in both treatment variants. Although, the size of the laser modified zone depended on laser beam parameters. It was also observed that chromium contracted in the layer after diffusing chromizing was dissolved in whole remelted zone as a result of laser heat treatment. Achieved zones were characterized by higher hardness than the core material of C45 steel. It is worthy emphasizing, that the presence of the hardened zone form the solid state under the remelted zone should additionally strengthen the whole surface layer. X-ray diffraction of chromized layer revealed the presence of: $(Cr, Fe)_{23}C_6$, Fe_2AlCr and $Cr_2(N,C)$ but chromized and laser heat treated layer: $(Cr, Fe)_{23}C_6$, Cr_2O_3, Fe_3O_4 in case of the first variant LHT and $(Cr, Fe)_{23}C_6$, $(Cr, Fe)_7C_3$ $Fe_{0,942}O$, Fe_2C, Cr_2O_3 in the second one. It could be the result of different conditions of microstructure creation resulted of different laser beam parameters in case of those two variants. It seems, that lower value of laser beam power density allowed to create additional type carbide $(Cr, Fe)_7C_3$.

4. Conclusions

The investigation have been carried out to analyze in details the diffusion chromizing process and laser heat treatment of C45 steel. Performed research showed, that it is possible to change the microstructure effectively of diffusion layer using the laser heating.The considered problem modification of microstructure after diffusion chromizing and laser heat treatment can be applied to gain some specific microstructure with grain refinement. The density of the laser beam exerts a significant influence on the structure of the chromium layer after laser heat treatment. The structure of the chromized layer after laser thermal treatment depended on the parameters laser beam power density applied.The presented research on modification of a chromized layer of medium carbon steel by laser heat treatment could find practical applications.

6. References

[1] B. Bogdański, E. Kasprzycka, J. Kacprzyńska-Gołacka. *Properties of carbide layers produced by means of the powder method at low presure.* Tribologia, 2, 17-24, 2017.

[2] I. Bauer. The *effect of microstructure on the tribocorrosive properties of chromosiliconized layers.* Physico-Chemical Mechanics of Materials, 7, 293-295, 2008.

[3] G. Moskal, L. Swadźba, W. Supernak., M. Mikuśkiewicz., A. Mościcki., M. Jabłońska, D. Niemiec, P. Kałamarz, M. Staszewski, A. Wrona, M .Osadnik. *Microstructural characterization of silicide coatings on Mo and TZM alloy.* Advanced Materials Research, 1036, 164-167, 2014.

[4] A. Kochmańska. *Microstructure of aluminide coatings on Ti6Al4V alloy produced by the slurry method with inorganic binder.* International Journal of Materials Research 109, 1-8, 2018.

[5] M. Paczkowska. *The evaluation of the influence of laser treatment parameters on the type of thermal effects in the surface layer microstructure of gray irons.* Optics and Laser Technology, 76, 143-148, 2016.

[6] M. Paczkowska. *The Importance of Operating Conditions and Parameters on Laser Alloying with Silicon during Surface Layer Modification of Nodular Iron*. Lasers in Engineering, 33, 4-6, 305-326, 2016.

A CRITICAL VIEW AT DIRECT APPLICABILITY OF THE STRAIN ENERGY RELEASE RATE DETERMINATION STANDARDS TO COUPLED COMPOSITE LAMINATES

S. Samborski

Department of Applied Mechanics, Faculty of Mechanical Engineering,
Lublin University of Technology, Lublin, Poland
e-mail: s.samborski@pollub.pl

1. Introduction

The field of applications of composite laminates in contemporary engineering could be broadened of the coupled layups. In the papers by York, ex. [1], thorough analysis of possible couplings was presented. The author of the current article continues his attempts to apply directly the standardized strain energy release rate (SERR) determination procedures (ASTM D5528, ISO 15024, ISO 15114, ASTM D7905) by introducing additional parameters for the data reduction schemes [2-4]. For this purpose the finite element (FE) simulations were led on the multidirectional continuous fiber reinforced polymer (CFRP) beam models to obtain the distributions of the SERR along the front of delamination. The FE simulations preceded the experiments led by the author's team [5] in order to plan the tests properly. The virtual crack closure technique (VCCT) was used in the simulations performed with the Abaqus code. For the sake of generality, the Reeder Law has been chosen as the fracture criterion [6]:

$$G_{\mathrm{I}}+G_{\mathrm{II}}+G_{\mathrm{III}} \geq G_{\mathrm{Ic}}+\left(G_{\mathrm{IIc}}-G_{\mathrm{Ic}}\right)\left(\frac{G_{\mathrm{II}}+G_{\mathrm{III}}}{G_{\mathrm{I}}+G_{\mathrm{II}}+G_{\mathrm{III}}}\right)^{\eta}+\left(G_{\mathrm{IIIc}}-G_{\mathrm{IIc}}\right)\left(\frac{G_{\mathrm{III}}}{G_{\mathrm{II}}+G_{\mathrm{III}}}\right)\left(\frac{G_{\mathrm{II}}+G_{\mathrm{III}}}{G_{\mathrm{I}}+G_{\mathrm{II}}+G_{\mathrm{III}}}\right)^{\eta}.$$

2. Results and discussion

The material data used in the simulations were taken from the literature [7] for the SEAL's Texipreg HS160RM carbon-epoxy prepreg laminate – see Table 1.

Young moduli	[GPa]	Shear moduli	[GPa]	Poisson coeff.	[-]	Fracture const.	[N/mm]
E_1	109.0	G_{12}	4.3	ν_{12}	0.34	G_{Ic}	0.4
E_2	8.8	G_{13}	4.3	ν_{13}	0.34	G_{IIc}	0.8
E_3	8.8	G_{23}	3.2	ν_{23}	0.38	G_{IIIc}	0.8

Table 1: Material data used in the FE simulations.

In Fig. 1 an excerpt from the FE simulation results is presented. The SERR distributions for the double cantilever beam (DCB) test configuration exhibiting non-symmetries induced by the bending-twisting (BT) coupling at different fiber orientation angles θ in the 18-ply BT sequence: $[\theta/0/\theta/\theta/0/-\theta/0/-\theta/-\theta/-\theta/-\theta/0/-\theta/\theta/0/0/\theta/\theta]$. The plots are either contracted or deviated – depending on the value of θ; these effects can be described well by additional measures of the SERR distribution defined in one of the previous papers [2].

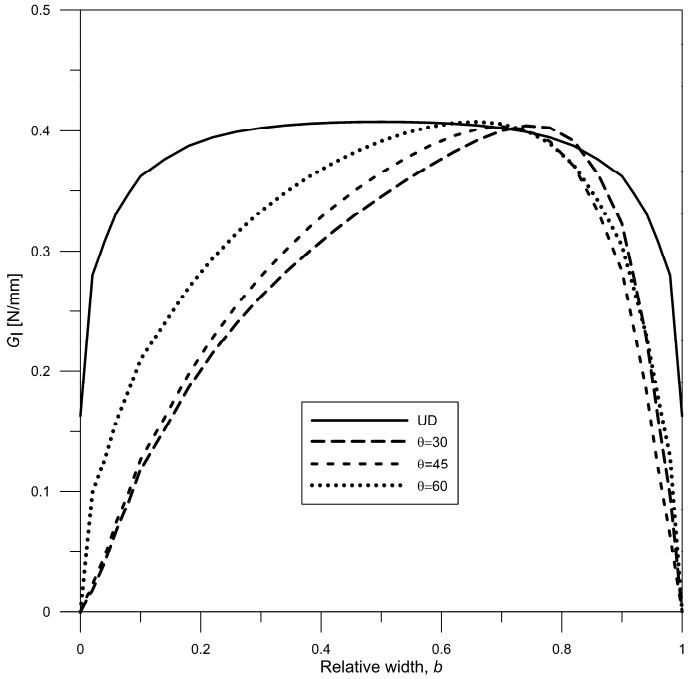

Figure 1: Skewness of the SERR plots induced by coupling.

5. Summary

The paper indicates possible difficulties in direct application of the standardized SERR determination methods. The presented results of the FEM simulations of delamination processes in laminated beams are a part of the study aimed at proper planning of the experiments on multidirectional layups. Additional parameters describing the distribution of SERR along delamination front were proposed in the previous stage of the study [2] in order to modify the data reduction schemes. The numerical outcomes are now being verified in laboratory tests with specimens of different couplings/delamination interfaces [5]. Further efforts to adjust the standards to the multidirectional laminates are being made [4].

Acknowledgments This paper was financially supported by the Ministerial Research Project No. DEC-2016/21/B/ST8/03160 financed by the Polish National Science Centre.

References

[1] C.B. York. Unified approach to the characterization of coupled composite laminates. Benchmark configurations and special cases. *J. Aerosp. Eng.*, 23(4):219, 2010.
[2] S. Samborski. Numerical analysis of the DCB test configuration applicability to mechanically coupled Fiber Reinforced Laminated Composite beams. Compos. Struct., 152:477, 2016.
[3] S. Samborski. Analysis of the end-notched flexure test configuration applicability for mechanically coupled fiber reinforced composite laminates. Compos. Struct., 163:342, 217.
[4] S. Samborski. Prediction of delamination front's advancement direction in the CFRP laminates with mechanical couplings subjected to different fracture toughness tests. Compos. Struct., (in press 2018).
[5] S. Samborski, J. Rzeczkowski. Numerical modeling and experimental testing of the DCB laminated composite beams with mechanical couplings. AIP Conference Proceedings1922, 2018.
[6] J. R. Reeder. NASA Report No. TM-1992-104210, 1992.
[7] M. F. de Moura, R. Campilho and J. Goncalves. de Moura M, Campilho R, Goncalves J. Crack equivalent concept applied to the fracture characterization of bonded joints under pure mode I loading. J. Compos. Sci. Technol., 68:2224, 2008.

DEVELOPMENT OF A CREEP CAVITY MODEL IN MOD. 9 Cr-Mo STEEL (MODEL & EXPERIMENT)

M.R. Ahmadi, M.C. Poletti, B. Sonderegger, C. Sommitsch

Institute of Materials Science, Joining and Forming, Graz University of Technology, Kopernikusgasse 24/I, 8010 Graz, Austria.

Email: mohammad.ahmadi@tugraz.at

Abstract

A model has been proposed to describe the nucleation and growth of creep cavities in crystalline material in service. In this work, the Becker-Döring (BD) nucleation model is applied for nucleation of cavities, while for the growth of pores, a vacancy flux model towards nucleated or existing pores is utilized. The model can describe nucleation and growth rates of pores in the matrix, at grain boundaries and at particles/inclusions. Nucleation and growth of pores in the creep process is determined to be a function of uniaxial or multiaxial external stress, internal stress due to the residual stresses, working temperature, local microstructure (nucleation and growth of particles), nucleation sites, interfacial energy of grain boundaries, phase boundary energies, diffusion rates in different paths and pore geometry, which are all considered in the present approach.

Systematic interrupted creep tests are performed under 66 MPa uniaxial creep loading at 650°C to track the pore evolution after 0, 2000, 4000, 5200 and 8000 hours for 9Cr-1Mo martensitic (ASME Gr.91) steels. The model results are then compared to experimental findings in terms of mean pore size and volume fraction. The comparison shows good agreement between experimental and simulation results [1].

Introduction

Nucleation sites of cavities

In this research, different nucleation sites of cavities in the bulk and at grain boundaries are considered and shown in Fig. 1. Fig. 1(a) shows less probable nucleation of a cavity in the bulk while Fig. 1(b) depicts vacancy condensation in a plane transverse to the external stress between two grains. Nucleation in this plane is more probable compared to the other ones displayed in Fig. 1 (c) and (d), because of larger nucleation sites [2]. Fig. 1(c) shows nucleation of a cavity at a triple line of boundaries (a line surrounded by three grains, which is called 3-grains) and Fig. 1(d) shows nucleation of a cavity at a point located in the intersection of four grains, which is called 4-grains. Other nucleation sites of cavities on precipitate's sidewall are also discussed.

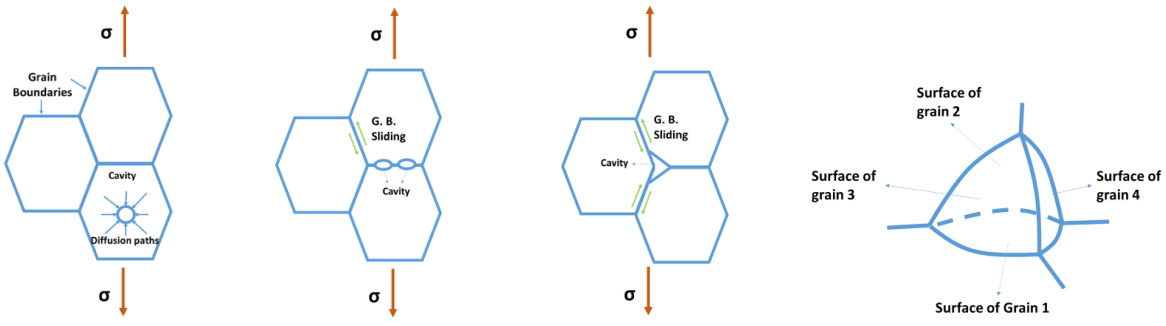

(a) (b) (c) (d)

Fig. 1. Different nucleus sites of cavities during creep, (a) in the bulk (b) in a plane between two grains (c) in a line enclosed by three grains (3-grains) and (d) in a point surrounded by four grains (4-grains).

Experimental results

Fig. 2 demonstrates SEM result of creep cavities after 8000 hours at 650°C under 66 MPa tensile stress, which are mostly formed on the pre-austenitic grain boundaries.

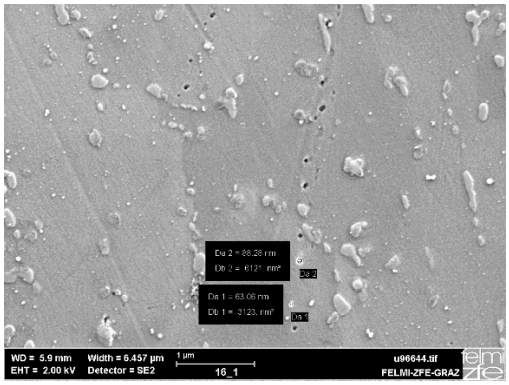

Fig. 2. Microstructure of the steel P91 after 8000 hours at 650°C under 66 MPa tensile stress.

Simulation results

In this work, the well-known model of Becker-Döring [3] is utilised for nucleation of cavities, and the proposed model of Svoboda et al. [4] is applied for the evaluation of cavity growth. Fig. 3 shows simulation results of number density and diameter of the formed pore in the matrix. As it is shown in this figure, the number density of cavities on grain boundaries is higher than 3- or 4- grains and they reach a mean diameter of 0.1 µm after 10,000 h creep.

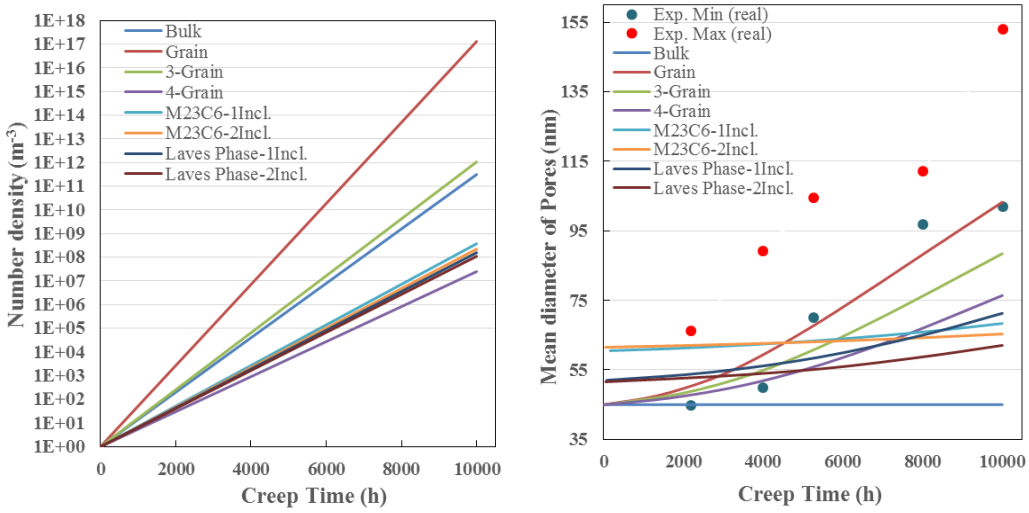

Fig. 3. Simulated results of (a) number density and (b) size of the formed pore in different regions of the crept material such as bulk, grain, 3-grain, 4-grain, $M_{23}C_6$ and Laves phase after 10,000 hours creep at 650°C and under 66 MPa tension.

[1] M.R. Ahmadi, B. Sonderegger, S. D. Yadav, M.C. Poletti, Modelling and simulation of diffusion driven pore formation in martensitic steels during creep, *Materials Science & Engineering A* 712 (2018) 466–477.
[2] E. Kozeschnik, in: K.G.F. Janssens, D. Raabe, E. Kozeschnik, M.A. Miodownik, B. Nestler (Eds.), *Computational Materials Engineering* – An Introduction to microstructure Evolution, Elsevier Academic Press, Burlington (2007), 179-217.
[3] R Becker and W Döring. Kinetische Behandlung der Keimbildung in übersättigten Dämpfern. *Ann. Phys.* (Leipzig) 24, 719-752 (1935).
[4] Svoboda J, Fischer F D, Fratzl P, Kozeschnik E, 2004 *Materials Science and Engineering A* 385 166–174.

ON THE SCREW DISLOCATION CONSIDERING SURFACE ENERGY: STRAIN-GRADIENT ELASTICITY VS. SURFACE ELASTICITY

V. A. Eremeyev[1,5] and E. C. Aifantis[2,3,4,5]

[1]*Gdańsk University of Technology, ul. Gabriela Narutowicza 11/12, 80-233 Gdańsk, Poland*
[2]*Aristotle University of Thessaloniki, Thessaloniki, 54124, Greece*
[3]*Michigan Technological University, Houghton, MI 49931, United States*
[4]*ITMO University, St. Petersburg, 197101, Russia*
[5]*Togliatti State University, Togliatti, 445020, Russia*

e-mail: eremeyev.victor@gmail.com; mom@mom.gen.auth.gr

1. Introduction

Nowadays it is well-known that the surface phenomena are almost responsible for the mechanical and physical properties of micro- and nanostructured materials. In particular, they are responsible for the size-effect observed at the nano-scale. Among the theories of continuum which can describe such surface-related behavior it is worth to mention the Gurtin-Murdoch surface elasticity model [5] and the first and second strain gradient elasticity presented by Toupin [11], Mindlin [7,8], see also [9,10], and Aifantis [1,2]. The characterization of the surface elasticity within the strain-gradient elasticity was performed in [4,6] considering anti-plane surface waves. Here we compare the both models considering stress concentration in the vicinity of the linear defect such as a screw dislocation. We analyze here a deformation of a hollow circular cylinder with a screw dislocation considering the both theories of strain-gradient elasticity and of surface elasticity.

2. Strain-gradient elasticity

In what follows we consider infinitesimal deformations of an elastic solid which are described by the displacement field $\mathbf{u} = \mathbf{u}(\mathbf{x})$, where $\mathbf{x}$ is the position vector. Strain energy density W is given by [7]

$$W = W_1 + W_2, \quad W_1 = \frac{1}{2}\mathbf{e} : \mathbf{C} : \mathbf{e}, \quad W_2 = \frac{1}{2}\nabla\mathbf{e}\dot{:}\mathbf{A}\dot{:}\nabla\mathbf{e}, \quad \mathbf{e} = \frac{1}{2}\left(\nabla\mathbf{u} + (\nabla\mathbf{u})^T\right), \tag{1}$$

where $\mathbf{C} = C_{ijkl}\mathbf{i}_i \otimes \mathbf{i}_j \otimes \mathbf{i}_k \otimes \mathbf{i}_l$ and Einstein's summation convention is used, $\mathbf{A} = A_{ijklmn}\mathbf{i}_i \otimes \mathbf{i}_j \otimes \mathbf{i}_k \otimes \mathbf{i}_l \otimes \mathbf{i}_m \otimes \mathbf{i}_n$ are the fourth- and six-order tensors of elastic moduli, respectively, $\mathbf{i}_k$, $k = 1, 2, 3$, are vectors of Cartesian orthonormal basis. For an isotropic strain gradient solid the elastic moduli tensors are given by [3]

$$C_{ijkl} = \lambda\delta_{ij}\delta_{kl} + \mu\left(\delta_{ik}\delta_{jl} + \delta_{il}\delta_{jk}\right), \tag{2}$$

$$\begin{aligned} A_{ijklmn} = {} & a_1\left(\delta_{ij}\delta_{kl}\delta_{mn} + \delta_{ij}\delta_{km}\delta_{ln} + \delta_{ij}\delta_{kn}\delta_{lm} + \delta_{in}\delta_{jk}\delta_{lm}\right) + a_2\left(\delta_{ij}\delta_{kn}\delta_{lm}\right), \\ & + a_3\left(\delta_{ik}\delta_{jl}\delta_{mn} + \delta_{ik}\delta_{jm}\delta_{ln} + \delta_{il}\delta_{jk}\delta_{mn} + \delta_{im}\delta_{jk}\delta_{ln}\right) + a_4\left(\delta_{il}\delta_{jm}\delta_{kn} + \delta_{im}\delta_{jl}\delta_{kn}\right), \\ & + a_5\left(\delta_{il}\delta_{jn}\delta_{km} + \delta_{im}\delta_{jn}\delta_{kl} + \delta_{in}\delta_{jl}\delta_{km} + \delta_{in}\delta_{jm}\delta_{kl}\right), \end{aligned} \tag{3}$$

where δ_{ij} is the Kronecker symbol, λ, μ, a_1, a_2, a_3, a_4, and a_5 are elastic moduli.

The equilibrium equation takes now the form

$$\nabla \cdot (\boldsymbol{\sigma} - \nabla \cdot \boldsymbol{\tau}) = \mathbf{0}, \tag{4}$$

where the tensors $\boldsymbol{\sigma}$ and $\boldsymbol{\tau}$ are defined by $\boldsymbol{\sigma} = \mathbf{C} : \mathbf{e}$, $\boldsymbol{\tau} = \mathbf{A}\dot{:}\nabla\mathbf{e}$, which are the second-order stress tensor and third-order hyperstress tensor, respectively. Aifantis' strain-gradient model [1,2] utilizes more simple constitutive equation with one additional length-scale parameter ℓ such that $\boldsymbol{\tau} = \ell^2\nabla\boldsymbol{\sigma}$. Eq. (4) should be complemented by proper boundary conditions which we omit here.

3. Surface elasticity

For an isotropic material the Gurtin-Murdoch model results in the classic constitutive equation in the bulk $W = W_1$ and an additional constitutive relation for the surface strain energy $\mathcal{W}_s$ [5]

$$\mathcal{W}_s = \mu_s \boldsymbol{\epsilon} : \boldsymbol{\epsilon} + \frac{1}{2}\lambda_s (\mathrm{tr}\boldsymbol{\epsilon})^2, \quad \boldsymbol{\epsilon} = \frac{1}{2}\left(\mathbf{P}\cdot(\nabla_s \mathbf{u}) + (\nabla_s \mathbf{u})^T \cdot \mathbf{P}\right), \quad \mathbf{P} \equiv \mathbf{I} - \mathbf{n}\otimes\mathbf{n}$$

where λ_s and μ_s are the surface Lamé moduli, tr is the trace operator, ∇_s is the surface nabla operator, $\mathbf{P}$ is the surface unit second-order tensor, $\mathbf{n}$ is the unit vector of outer normal. For a free surface the static boundary condition takes the following form

$$\mathbf{n}\cdot\boldsymbol{\sigma} = \nabla_s \cdot \mathbf{s}, \quad \mathbf{s} \equiv \frac{\partial \mathcal{W}_s}{\partial \boldsymbol{\epsilon}} = \mu_s \boldsymbol{\epsilon} + \lambda_s \mathbf{P}(\mathrm{tr}\boldsymbol{\epsilon}).$$

Here $\mathbf{s}$ is the surface stress tensor.

4. Screw dislocation

In order to compare the both theories we consider the hollow circular cylinder of radius a with a screw dislocation. It is known that the strain-gradient elasticity and surface stresses affect the singularity near defects. Using the semi-inverse approach the deformation of a cylinder with a screw dislocation is given as a mapping [12]

$$r = r(R), \quad \phi = \Phi, \quad z = \frac{b}{2\pi}\phi + Z, \tag{5}$$

where r, ϕ, z and R, Φ, Z are the polar coordinates in the actual and reference placements, respectively, and b is the magnitude of the Burgers vector. For small deformations mapping (5) gives an example of an antisymmetric deformations such as in [4]. We discuss the solutions behaviour for $a \to 0$. We demonstrate that the both theories give similar qualitative results for the displacement amplitudes. Nevertheless, there are some quantitative differences which will be discussed during SOLMECH2018 in all details.

Acknowledgments Authors gratefully acknowledge the support of the Ministry of Education and Science of Russian Federation under Mega Grant Project "Fabrication and Study of Advanced Multi-Functional Metallic Materials with Extremely High Density of Defects" (No.14.Z50.31.0039) to Togliatti State University.

References

[1] E. C. Aifantis. Update on a class of gradient theories. *Mech. Mater.*, 35(3–6):259–280, 2003.
[2] E. C. Aifantis. Gradient material mechanics: perspectives and prospects. *Acta Mech.*, 225(4-5):999–1012, 2014.
[3] F. dell'Isola, G. Sciarra, and S. Vidoli. Generalized Hooke's law for isotropic second gradient materials. *Proc. Roy. Soc. London A*, 465(2107):2177–2196, April 2009.
[4] V. A. Eremeyev, G. Rosi, and S. Naili. Comparison of anti-plane surface waves in strain-gradient materials and materials with surface stresses. *Math. Mech. Solids*, DOI: 10.1177/1081286518769960:1–10, 2018.
[5] M. E. Gurtin and A. I. Murdoch. A continuum theory of elastic material surfaces. *Arch. Ration. Mech. Anal.*, 57(4):291–323, 1975.
[6] F. Jia, Z. Zhang, H. Zhang, X.-Q. Feng, and B. Gu. Shear horizontal wave dispersion in nanolayers with surface effects and determination of surface elastic constants. *Thin Solid Films*, 645(Supplement C):134 – 138, 2018.
[7] R. D. Mindlin. Micro-structure in linear elasticity. *Arch. Ration. Mech. Anal.*, 16(1):51–78, 1964.
[8] R. D. Mindlin. Second gradient of strain and surface-tension in linear elasticity. *Int. J. Solids. Struct.*, 1(4):417–438, 1965.
[9] R. D. Mindlin and N. N. Eshel. On first strain-gradient theories in linear elasticity. *Int. J. Solids Struct.*, 4(1):109–124, 1968.
[10] R. D. Mindlin and H. F. Tiersten. Effects of couple-stresses in linear elasticity. *Arch. Ration. Mech. Anal.*, 11:415–448, 1962.
[11] R. A. Toupin. Elastic materials with couple-stresses. *Arch. Ration. Mech. Anal.*, 11(1):385–414, 1962.
[12] L. M. Zubov. *Nonlinear Theory of Dislocations and Disclinations in Elastic Bodies*. Springer, Berlin, 1997.

A COMPUTATIONAL FRAMEWORK FOR MODELING ELECTRIC BREAKDOWN IN ELECTROACTIVE POLYMERS

D. Bishara[1] and M. Jabareen[1]

[1] *Civil and Environmental Engineering, Technion-Israel Institute of Technology, Haifa, Israel*

e-mail: danabi@campus.technion.ac.il

1. Introduction

Electroactive polymers (EAPs) are considered a promising emerging class of smart materials, which have received an extensive consideration among researchers. EAPs are an active class of materials with the ability to undergo large deformations when they are subjected to external electric stimuli. Therefore, various applications have been proposed in the literature including artificial muscles, medical devices and soft biomemetic applications ([2],[1]).

A typical actuator consists of a thin film of dielectric elastomer, which on its major surfaces, two flexible electrodes are smeared, and an electric potential difference between the electrodes is applied. Despite the high-level of actuation performances enabled by EAPs, their extensive use is conditioned by a high driving electric fields. Thus, the applied electric field may cause an electric breakdown. As the electric breakdown in solid dielectrics takes place, tubular conductive channels evolve, and they do not recover when the voltage is discharged.

In this work, a computational model, which is able to predict possible electric breakdown while accounting for the electromechanical coupling is presented. Moreover, a finite element formulation with various nodal degrees of freedom is introduced.

2. Governing equations

In this paper, we consider a body, which occupies a $\mathcal{B}_0$ at reference configuration. The body is subjected to mechanical body forces, mechanical surface tractions on the boundary $\partial\mathcal{B}_0^{\mathbf{T}}$, and electric charges on the boundary $\partial\mathcal{B}_0^{\mathrm{Q}}$, as shown in Fig. 1.

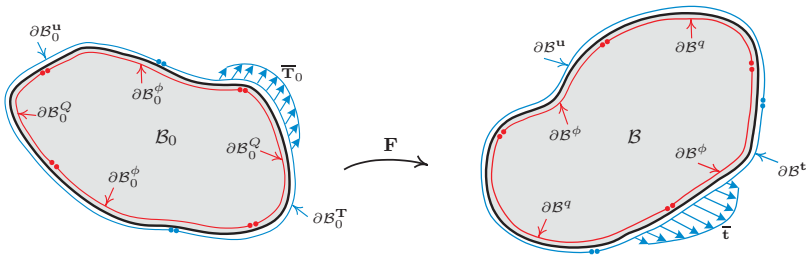

Figure 1: Sketch of the deforming body.

Let $\mathbf{X}$ denotes the location of a material point in the reference configuration, $\mathbf{x}$ denotes the location of the same material point in the present configuration, and $\mathbf{F} = \partial\mathbf{x}/\partial\mathbf{X}$ denotes the deformation gradient, which maps the reference configuration to present configuration with the constraint $J = \det(\mathbf{F}) > 0$. Also, let $\{\boldsymbol{E}, \boldsymbol{D}\}$ be the reference electric field vector and reference electric displacement vector, respectively. In the case of electrostatics and in the absence of free currents and free electric charges, Maxwell's balance equations become,

$$\mathrm{Div}\,(\boldsymbol{D}) = 0, \quad \mathrm{Curl}\,(\boldsymbol{E}) = \mathbf{0} \tag{1}$$

Next, the equilibrium equations, which are derived from the linear momentum balance in the local form for nonlinear electroelasticity are written in reference configuration such as

$$\text{Div}\,(\mathbf{FS}) + \mathbf{f} = \mathbf{0}, \tag{2}$$

with $\mathbf{S}$ being the total second Piola-Kirchhoff stress tensor consists of all contributions. $\mathbf{f}$ is the reference mechanical body forces (force by unit reference volume). In order to derive the constitutive laws, a strain energy function (per unit volume), is assumed. Specifically, the strain energy function reads

$$W\left(\mathbf{C},\, \boldsymbol{E},\, \mathbf{A}_1, ..., \mathbf{A}_n, s\right) = \rho_0 \psi\left(\mathbf{C},\, \boldsymbol{E},\, \mathbf{A}_1, ..., \mathbf{A}_n, s\right) - \frac{1}{2} J \varepsilon_0 \mathbf{C}^{-1} \colon \left(\boldsymbol{E} \otimes \boldsymbol{E}\right). \tag{3}$$

where $\{\mathbf{A}_1, ..., \mathbf{A}_n\}$ are the strain like internal variables, $\mathbf{C}$ is the right Cauchy-Green deformation tensor, n represents the number of the viscus Maxwell branches, ρ_0 is reference density, and ψ is free energy function. As well, $s\left(\mathbf{X}, t\right)$ is a phase scalar, which varies from $s = 0$ indicating the totally damaged state to $s = 1$ indicating the virgin state.

3. Finite element

For providing a numerical tool, a finite element formulation has been developed. The nodal degrees of freedom are the displacements in the three dimensional space, the electric potential, and the phase field scalar, as shown in Fig. 2.

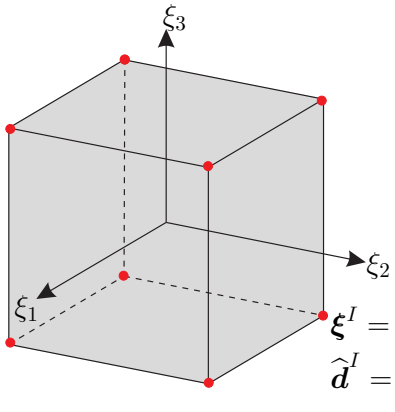

Shape functions:

$$N_I = \tfrac{1}{8}\left(1 - \xi_1\xi_1^I\right)\left(1 - \xi_2\xi_2^I\right)\left(1 - \xi_3\xi_3^I\right)$$

The fields interpolations:

$$\boldsymbol{d} = \sum_{I=1}^{8} N_I \widehat{\boldsymbol{d}}^I$$

Figure 2: Sketch of an element in the isoparametric space.

Acknowledgments Financial support for this work was provided by the Israel Science Foundation under grant 1713/13, which is gratefully acknowledged.

References

[1] Pelrine R., Kornbluh R., Eckerle J., Jeuck P., Oh S., Pei Q., and Stanford S. Dielectric Elastomers: Generator Mode Fundamentals and Applications. In *Smart Structures and Materials*, volume 4329, pages 148–156, 2001.

[2] Bar-Cohen Y. Biomimetics–using nature to inspire human innovation. *Bioinspiration and Biomimetics*, 1:P1, 2006.

ELASTOSTATIC PROBLEM OF TWO ASYMMETRICAL CRACKS ALONG THE INCLUSION-MATRIX INTERFACE UNDER A REMOTE UNIFORM LOAD

V.H.T. Le[1], S. Brisard[1], and A. Pouya[1]

[1] *Université Paris-Est, Laboratoire Navier, UMR 8205, CNRS, ENPC, IFSTTAR, F-77455 Marne-la-Vallée, France*

e-mail: vinh-hoang-tan.le@enpc.fr

1. Abstract

Heterogeneous geomaterials as well as composite industrial materials are widely studied because of their applications to engineering problems or use in industrial processes. In these materials, the interface plays a very important role in the mechanical behavior. It ensures the transmission of forces between the matrix and the inclusion during a solicitation. In fact, one of common failure modes in the composites is the rupture at the interface. Interfacial resistance largely influences the final properties of the composite like stiffness, strength and the fracture behavior. For these reasons, the study of the failure mechanism at the interface of composite materials relating to a imperfect inclusion-matrix interface (i.e a partial debonding at the interface) is essential.

This research focuses mainly on the plane problem of a circular disc shape inclusion in an infinite linear elastic matrix with two cracks which can be asymetrical on its boundary created by a far-field stress (see figure 1).

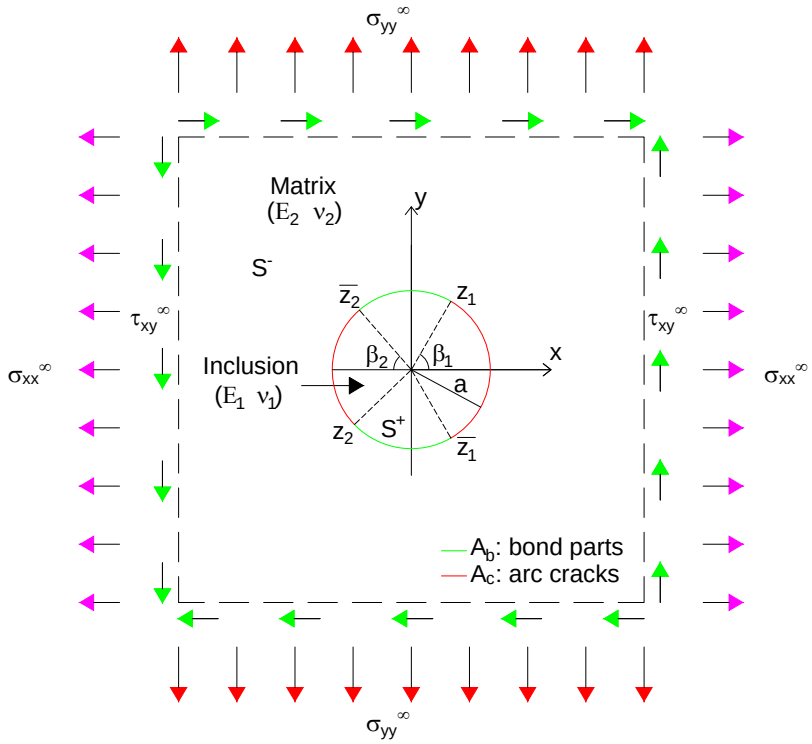

Figure 1: Two asymmetrical cracks at the inclusion-matrix interface under uniform stress at infinity

Among various mathematical methods to solve this problem, we find that the complex potential function method [2] is the more appropriate to take into account the presence of cracks. In this method, stresses and displacements are expressed in terms of analytic functions of complex variables. Significant contributions to this problem have been already reported in the literature. Some authors ([3], [7], [5] and [4]) used this method to study the problem of cracks lying along the interface of a circular inclusion embedded in an infinite solid. However these works have been either limited to a single crack arc or two symmetrical crack arcs. In fact, the

problem of interaction between two asymmetrical cracks at the inclusion-matrix interface is a general solution extending two special cases already studied in literature: A single crack (where one crack has null length) and a two symmetrical cracks (where two cracks have the same length).

The paper starts with the formulation and solution of the problem of two asymmetrical interface arc cracks around a circular elastic inclusion embedded in an infinite matrix subjected to a uniform far load, that is presented in section 2. In section 3, the expression of the complex stress intensity factors (SIFs) at a crack tip along an inclusion-matrix interface is presented. To verify the solution, in section 4, the analytical SIFs for various crack angles in the case of uniaxial tension in plane strain conditions were compared to solution obtained by the Displacement Extrapolation method [1, 6]. The calculation of the total energy release rate (ERR) for the interface crack is carried out in section 5. The conclusions are finally presented in section 6.

Acknowledgments This work has benefited from a French government grant managed by ANR within the frame of the national program Investments for the Future ANR-11-LABX-022-01

References

[1] Jakob Gager. *Numerical simulations of interface cracks in glued die-attach semiconductor devices*. PhD thesis, TU Wien, 2010.

[2] Nikola Ivanovich Muskhelishvili. *Some basic problems of the mathematical theory of elasticity*. Noordhoff, Groningen, The Netherlands, 1953.

[3] AB Perlman and GC Sih. Elastostatic problems of curvilinear cracks in bonded dissimilar materials. *International Journal of Engineering Science*, 5(11):845–867, 1967.

[4] PBN Prasad and KRY Simha. Interactions of interfacial arc cracks. *International Journal of Fracture*, 117(1):39–62, 2002.

[5] PBN Prasad and KRY Simha. Interface crack around circular inclusion: Sif, kinking, debonding energetics. *Engineering Fracture Mechanics*, 70(2):285–307, 2003.

[6] Yuuki Ryoji and Cho Sang-Bong. Efficient boundary element analysis of stress intensity factors for interface cracks in dissimilar materials. *Engineering Fracture Mechanics*, 34(1):179–188, 1989.

[7] M Toya. A crack along the interface of a circular inclusion embedded in an infinite solid. *Journal of the Mechanics and Physics of Solids*, 22(5):325–348, 1974.

Session S04: Plasticity, damage and fracture: microstructural aspects

Organizers: K. Kowalczyk-Gajewska (IPPT PAN, Warsaw), S. Mercier (Univ. of Lorraine, LEM3, Metz), J. Rodriguez-Martinez (Univ. Carlos III, Madrid), G. Vadillo (Univ. Carlos III, Madrid)

DYNAMIC STABILITY ANALYSIS IN NON-LOCAL FRACTIONAL THERMODYNAMICS

P. B. Béda[1]

[1] *Budapest University of Technology and Economics, Budapest, Hungary*

e-mail: bedap@kme.bme.hu

1. Introduction

In material instability problems, spatial non-locality plays an important role in nonlinear bifurcation (post-bifurcation) investigations. By using dynamical systems, stability analysis of thermo-mechanical continua can easily be studied, even when fractional derivatives are used. Such case may be obtained, when non-locality is described by a generalized, fractional strain. In constitutive formulation, two types of constitutive equations are used, thermodynamical constitutive equations should also be added to the classical (mechanical) constitutive equations. In such a way, a closed system of equations is obtained to determine the motion of the thermo-mechanical continuum.

2. Fractional thermo-mechanics

First, the basic equations for a solid body with thermal stresses should be formed. In addition to the basic equations of continuum mechanics, heat propagation should also be taken into account by using Vernotte-Cattaneo equation instead of Fourier law. The set of basic equations consists of the kinematic equation

$$\dot{\varepsilon} = \frac{\partial^\alpha v}{\partial x^\alpha}, \tag{1}$$

the equation of motion

$$\dot{v} = \frac{1}{\rho}\frac{\partial \sigma}{\partial x}, \tag{2}$$

and the constitutive equation, which in rate form reads

$$\dot{\sigma} = B(\dot{\varepsilon} - \theta\dot{\vartheta}) + \chi\dot{h}. \tag{3}$$

In equations (1), (2), and (3) the notations are: strain (for uniaxial small deformations) ε, velocity v, space coordinate x, mass density ρ, temperature ϑ. Overdot denotes derivative with respect to time t, B is the tangent stiffness, while χ is a material constant. In (1) a generalized strain is used, where $0 < \alpha < 1$ denotes the order of the fractional derivative. Such generalization of strain is generally used in fractional continuum mechanics.

Symbol $\frac{\partial^\alpha}{\partial x^\alpha}$ refers to all kinds of symmetric fractional derivatives. For example, it may denote symmetric Caputo's derivative from Atanackovic [1], where left and right Caputo derivatives are defined:

$${}^C D^\alpha_{a+} u(x) = \frac{1}{\Gamma(1-\alpha)}\frac{d}{dx}\left(\int_a^x \frac{u(\xi)-u(a)}{(x-\xi)^\alpha} d\xi\right)$$

and

$${}^C D^\alpha_{L-} u(x) = -\frac{1}{\Gamma(1-\alpha)}\frac{d}{dx}\left(\int_x^L \frac{u(\xi)-u(a)}{(\xi-x)^\alpha} d\xi\right).$$

Then a generalized strain is defined by the symmetric fractional derivative of the displacement field

$$\varepsilon = \frac{1}{2}\left({}^C D^\alpha_{a+} u(x) - {}^C D^\alpha_{L-} u(x)\right).$$

Several types of definitions are used for such derivatives [3], [4]. All of them use a fractional integral operator, which adds non-local effects to the formulation. A detailed overview of symmetric fractional derivatives applied in non-local mechanics can be found in [2].

In the following, symmetric fractional derivative will not be specified, a generalized formula is used instead. Instead of Fourier law, heat conduction is given by the Vernotte-Cattaneo equation

$$\tau\dot{h} + a\frac{\partial}{\partial x}\vartheta + h = 0, \tag{4}$$

where the relaxation time of heat flux is denoted by τ, the heat flux by h, and heat conductivity by a. The reason of such selection is that Fourier heat conduction equation results infinite wave speeds, which is a non-generic dynamic behavior. For the constitutive variables $\varepsilon, \sigma, \vartheta$, and h, two types of constitutive equations are given. The one in form (3) could be referred as mechanical constitutive equation, while the other

$$\Theta_1\dot{\sigma} + \Theta_2\dot{\varepsilon} + \Theta_3\dot{h} = \dot{\vartheta} \tag{5}$$

may be called the thermodynamic constitutive equation [9], with material constants $\Theta_1, \Theta_2, \Theta_3$. From (4)

$$\dot{h} = -\frac{a}{\tau}\frac{\partial}{\partial x}\vartheta - \frac{h}{\tau}. \tag{6}$$

By substituting (1) and (6) into the mechanical and thermodynamic constitutive equations (3) and (5), we have

$$\dot{\sigma} = c_1\frac{\partial^\alpha v}{\partial x^\alpha} + c_2\,\frac{a}{\tau}\frac{\partial}{\partial x}\vartheta + c_2\frac{h}{\tau}\ , \tag{7}$$

$$\dot{\vartheta} = d_1\frac{\partial^\alpha v}{\partial x^\alpha} - d_2\frac{a}{\tau}\frac{\partial}{\partial x}\vartheta - d_2\frac{h}{\tau}\ . \tag{8}$$

Now equations (2), (6), (7), and (8) for variables v, σ, ϑ, and h can be used to describe the motion of the thermodynamic continuum.

3. Stability and bifurcaton investigation

By using the system of equations presented in the previous part, a dynamical system can be defined and the requirements of generic static and dynamic bifurcations can be studied similarly to [5]. Unfortunately, in the general case, the evaluation of such conditions is a difficult problem and simplifications are necessary. When the investigation is restricted to homogeneous periodic perturbations, general necessary conditions are formulated for both static and dynamic bifurcations. For the conventional setting (small deformations, linearized constitutive equations, Vernotte-Cattaneo equation), no generic static bifurcations are found. For dynamic bifurcation, there are possibilities to have generic behavior. A general formula is derived for such case. Moreover, having done a few simplifying restrictions, conditions are presented for the material constants of the constitutive equations to ensure generic dynamic bifurcation.

References

[1] T. M. Atanackovic and B. Stankovic (2009). Generalized wave equation in nonlocal elasticity, *Acta Mech.*, **208**, 1–10

[2] W. Sumelka (2016). Fractional Calculus for Continuum Mechanics - anisotropic non-locality, *Bulletin of the Polish Academy of Sciences Technical Sciences*, **64**, 361–372

[3] C.S. Drapaca and S. Sivaloganathan (2012). A fractional model of continuum mechanics, *Journal of Elasticity*, **107**, 107–123

[4] K. A. Lazopoulos and A. K. Lazopoulos (2016) Fractional derivatives and strain gradient elasticity, *Acta Mech.*, **227**, 823–835

[5] P.B. Béda (2000). Dynamic systems, rate and gradient effects in material instability, *International Journal of Mechanical Sciences*, **42**, 2101–2114.

SIMULATIONS OF THE EQUAL CHANNEL ANGULAR PRESSING PROCESS USING CRYSTAL PLASTICITY FINITE ELEMENT METHOD WITH SOLUTION MAPPING

K. Frydrych[1], K. Kowalczyk-Gajewska[1], and A. Prakash[2]

[1]*Institute of Fundamental Technological Research, ul. Pawińskiego 5B, 02-106 Warszawa, Polska*
[2]*Department of Materials Science and Engineering, Institute I, Friedrich-Alexander-Universität Erlangen-Nürnberg, Martensstrasse 5, 91058 Erlangen, Germany*

e-mail: kfryd@ippt.pan.pl

1. Introduction

Simulations of equal channel angular pressing (ECAP) process using the crystal plasticity finite element method (CPFEM) are described in this paper. The ECAP process is a well known severe plastic deformation (SPD) process, in which the material deforms by shearing. To obtain considerable grain refinement, multiple passes through an angular channel need to be conducted. One approach that enables the understanding of mechanisms leading to texture evolution and grain refinement is to use CPFEM simulations. Modelling multiple passes using the finite element method formulated in the Lagrangian approach is however challenging due to strong element distortions. The possible solution is the application of remeshing and solution mapping. However, solution mapping of micro-mechanical variables that is consistent with the macroscopic response is not a trivial task. The crystallographic orientations and tensorial variables cannot be interpolated directly, because it would lead to spurious rotations. Instead, one can pass the orientations and tensorial variables from point to another point or one can make use of spherical linear interpolation algorithm (SLERP) [**?**] to deal with interpolating the variables. While the first approach will necessarily lead to less accurate results, in the second one there are additional difficulties. One arises from the fact that the SLERP algorithm deals only with interpolating between two points, and in general 3D case interpolation between four points is needed. The other question is how to properly interpolate points close to sharp orientation changes.

2. Modelling framework

In the CPFEM implementation used, the total Lagrangian setting together with the Euler backward integration scheme has been applied. The deformation gradient is multiplicatively decomposed into elastic and plastic parts. The plastic velocity gradient is the sum of shears on slip systems. Simulations reported in this paper have been conducted using the rate-independent formulation with a single yield surface [**?**, **?**]. The yield surface F is defined as follows [**?**, **?**]:

$$F = \left(\sum_r \left(\frac{\tau^r}{\tau_c^r} \right)^{2n} \right)^{1/(2n)} - 1 \,, \tag{1}$$

where τ^r is the resolved shear stress and τ_c^r is its critical value. Shear rates $\dot{\gamma}^r$ depend on the stress state by the associated flow rule, namely

$$\hat{\mathbf{L}}^p = \dot{\lambda} \frac{\partial F}{\partial \mathbf{M}_e} \rightarrow \dot{\gamma}^r = \dot{\lambda} \frac{1}{\tau_c^r} \left(\frac{\tau^r}{\tau_c^r} \right)^{2n-1} \,, \tag{2}$$

where $\dot{\lambda}$ is the plastic multiplier obtained from the Karush-Kuhn-Tucker conditions and $\mathbf{M}_e$ is the Mandel stress tensor obtained from hyper-elastic law from the anisotropic St. Venant-Kirchhoff hyperelastic law, cf. [**?**].

For a typical rate-independent formulation there is a problem of unique selection of active slip systems. Using a single yield surface (1) enables to avoid this problem, therefore the standard procedures of finite strain elasto-plasticity in the fully Lagrangian displacement-based formulation can be implemented [**?**]. Implementation of

the element code including crystal plasticity has been done with the use of a code generator AceGen, which joins the symbolic algebra capabilities of Wolfram Mathematica software with automatic differentiation and advanced optimization of expressions [**?**]. The finite element simulation itself has been performed using the AceFEM package. The proposed scheme for remeshing and solution mapping shares some key concepts with solution mapping applied for simulation of the accumulated roll bonding process [**?**].

3. Results

The simulations of two passes of the ECAP process have been carried out. The simulated textures were compared with available experimental data [**?**]. Satisfactory agreement has been obtained.

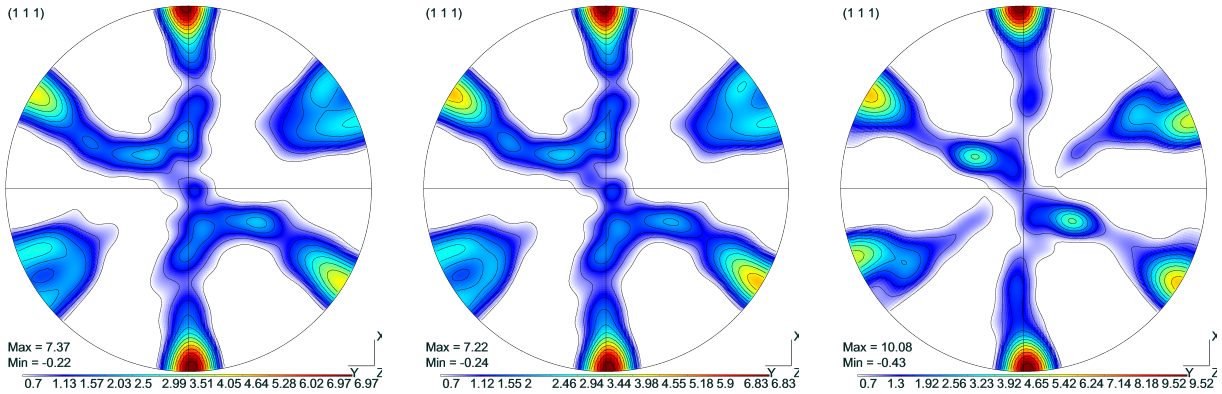

a) b) c)

Figure 1: Simulated {111} pole figures of copper subjected to ECAP process. a) After one pass, b) after one pass and remeshing, c) after two passes. JTEX software [**?**] was used to draw the pole figures.

4. Acknowledgement

The KMM-VIN Research Fellowship grant is gratefully acknowledged.

TEMPERATURE EFFECTS DURING IMPACT OF WC/Co COMPOSITES

E. Postek[1], T. Sadowski[2]

[1]*Institute of Fundamental Technological Research of the Polish Academy of Sciences, ul Pawińskiego 5B, 02-106 Warsaw, Poland*

[2]*Department of Solid Mechanics, Lublin University of Technology, Nadbystrzycka 40 str, 20-618 Lublin, Poland*

e-mail: epostek@ippt.pan.pl

1. Introduction

Generally, the papers on dynamic loading of composites more focus on the layered composites, for example [1]. High attention is paid to blast load. However, in our opinion, the process of impact a gap for analysis of WC/Co composite during impact conditions. During impact of WC/Co composite objects and the other composites with metallic binder heat of plastic work is generated. If the process is fast enough the problem can be treated as adiabatic. However, more common situation is slower process when the heat is generated in metallic interfaces and the neighbouring grains are heated due to conduction. The process should be rather considered as coupled [2]. We developed our model of WC/Co composite towards impact load, [3].

2. Problem statement

The thermal problem is described by the discretized finite element equation, as follows:

(1) $$\mathbf{KT} + \mathbf{C}\dot{\mathbf{T}} = \mathbf{F}$$

where **K** is the conductivity matrix, **C** is the heat capacity matrix, **T** is the nodal temperatures vector and **F** the thermal sources and fluxes vector**.** The contribution to the vector F due to plastic dissipation is given by the formula:

(2) $$\mathbf{f} = \chi \boldsymbol{\sigma} : \mathbf{e}^{pl}$$

where **f** is the rate of heat generation (heat flux), $\boldsymbol{\sigma}$ is the Cauchy stress tensor, $\mathbf{e}^{pl}$ is the rate of plastic deformation tensor and χ is the Taylor-Quinney coefficient that indicates fraction of plastic work converted into heat, [3].

There are two kinds of two-phase CM materials, Figure 1. In the given example below, we investigate the case in Figure 1 (a), i.e., the CM material with continuous interfaces.

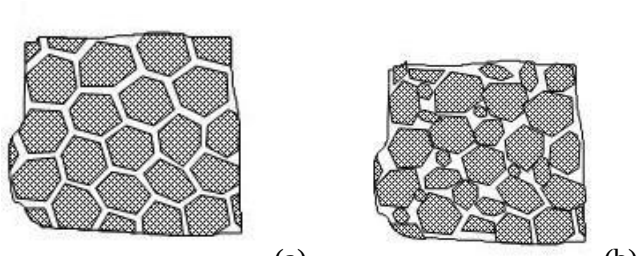

(a) (b)

Figure 1: Different types of two-phase CM internal structures having a small content of the second phase (up to 10%): a) with a small thickness and continuous interfaces, b) without continuous interfaces

3. Outline of numerical results

The physical model and the discretized system of thin binders is given in Figure 2 (a) and (b), respectively. We show the deformed shape of the composite plate in Figure 2 (c). The composite hits the rigid wall with velocity 100 m/s. The shape is presented at time instant 3.5 ns of the process.

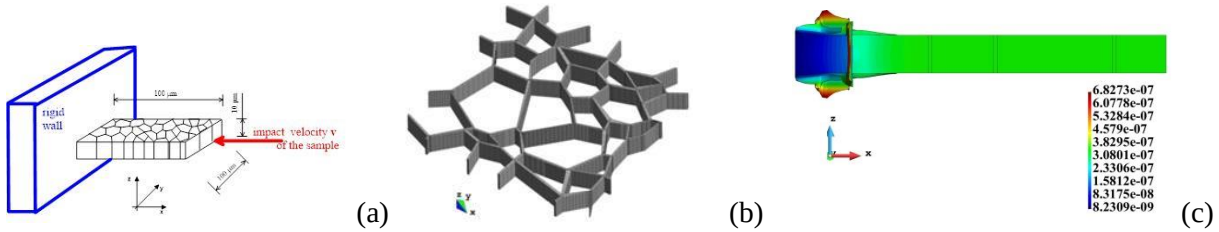

(a) (b) (c)

Figure 2: Physical model and boundary conditions (a) discretized system of interfaces (b) deformed structure (m) scaled 10 times at time instant 3.5 ns.

The effects of the impact are shown in Figure 3. We compare the adiabatic solution with the coupled thermo-mechanical solution. Obviously, temperature distribution for the adiabatic solution is exactly the same as plastic strains distribution, Figures 3 (a) and (b). In the case of the thermo-mechanical solution we note that even for the short duration of the process temperature varies in the neighbouring grains. Moreover, maximum increase of temperature in the adiabatic process is 200.73 deg, Figure 3 (b), while during the coupled solution the maximum increase of temperature is 65.93 deg, Figure 3 (c).

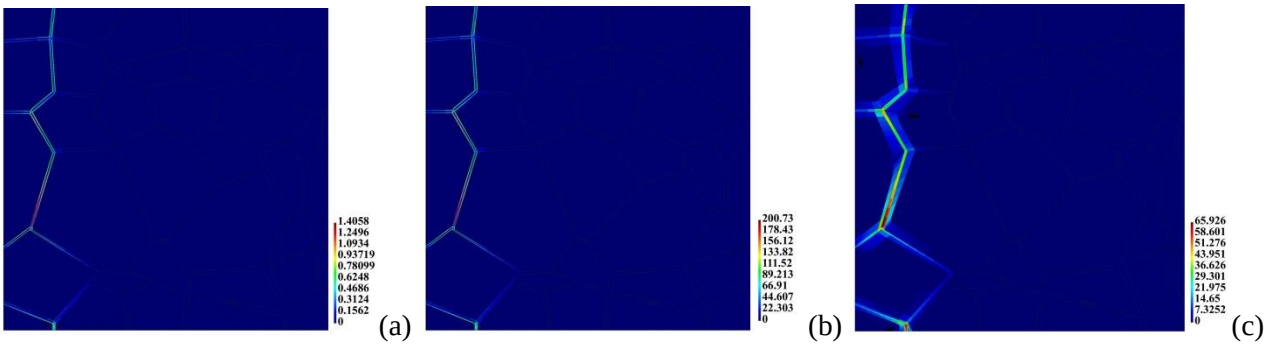

(a) (b) (c)

Figure 3: Time instant 3.5 ns; equivalent plastic strain field (a) adiabatic solution - temperature field (b) transient solution – temperature field (c).

4. Conclusions

We note that the calculated maximum temperatures during short duration of impact are significantly lower when the process is considered as coupled than while the process assumed to be adiabatic. The neighbouring grains are affected by the temperature increase immediately. During the analysis the effect of heat conduction should not be neglected.

Acknowledgments This work was financially supported by Ministry of Science and Higher Education (Poland) within the statutory research (IPPT PAN) and National Science Centre (Poland) project No 2016/21/B/ST8/01027 (Lublin University of Technology). The calculations were done at the Interdisciplinary Centre for Mathematical and Computational Modelling, University of Warsaw, Poland. The licenses for the MSC Patran and Abaqus programs were provided by Academic Computer Centre in Gdańsk, Poland.

References

[1] S. El Sayed, S. Sridharan, Predicting and tracking interlaminar crack growth in composites using a cohesive layer model, *Compos. Part B*. 32:545, 2001.
[2] P. Wriggers, C. Miehe, M. Kleiber, J.C. Simo, On the coupled thermomechanical treatment of necking problems via finite element methods, *Int. J. Num. Meth. Eng.* 33:869, 1992.
[3] T. Sadowski, S. Hardy, E. Postek, Prediction of the mechanical response of polycrystalline ceramics containing metallic intergranular layers under uniaxial tension, *Comput. Mat. Sci.* 34:46, 2005.

TOWARDS VERIFICATION OF A GRADIENT-ENHANCED DUCTILE DAMAGE MODEL

L. Sprave[1] and A. Menzel[1,2]

[1]*Institute of Mechanics, TU Dortmund, Leonhard-Euler-Str. 5, D-44227 Dortmund, Germany*
[2]*Division of Solid Mechanics, Lund University, P.O. Box 118, SE-221 00 Lund, Sweden*

e-mail: leon.sprave@tu-dortmund.de

1. Introduction

Processes in the metal forming industry involve large plastic deformations accompanied by ductile damage. In order to better predict the properties of the finished product as well as the behaviour during the process, more accurate simulations are necessary. Damage models require a regularisation to obtain mesh independent results. In the following a specific gradient-enhancement strategy is discussed.

2. Nonlocal damage model

An elegant way to include gradients into a model was suggested in [1, 4]. In this context, the free Helmholtz energy is split into a local and nonlocal contribution

$$\Psi = \Psi^{\mathrm{loc}}(\boldsymbol{F}, d, \boldsymbol{\mathcal{I}}^{\mathrm{p}}) + \Psi^{\mathrm{nl}}(\boldsymbol{F}, d, \phi, \nabla_{\boldsymbol{X}}\phi) \quad \text{with} \quad \Psi^{\mathrm{nl}} = \frac{c_d}{2}\|\nabla_{\boldsymbol{X}}\phi\|^2 + \frac{\beta_d}{2}\left[\phi - d\right]^2 ,$$

where the quantity ϕ, an additional field variable in the context of the finite element method, represents nonlocal damage and is linked in penalty type fashion to the local damage variable d. Since the gradient of the local damage $\nabla_{\boldsymbol{X}} d$ is not required, many already established local damage models can be incorporated into this framework. Successful implementations can be found in, e.g. [2, 3, 5].
The material model uses a multiplicative split of the deformation gradient $\boldsymbol{F} = \boldsymbol{F}^{\mathrm{e}} \cdot \boldsymbol{F}^{\mathrm{p}}$ and logarithmic strains $\boldsymbol{\varepsilon}^{\mathrm{e}}$ for the elastic free Helmholtz energy

$$\Psi^{\mathrm{loc}}\left(\boldsymbol{\varepsilon}^{\mathrm{e}}, d, \alpha\right) = \frac{K}{2} f^{\mathrm{vol}}(d) \left[\mathrm{tr}\left(\boldsymbol{\varepsilon}^{\mathrm{e}}\right)\right]^2 + \mu\, f^{\mathrm{iso}}(d)\, \boldsymbol{\varepsilon}^{\mathrm{e}} \colon \boldsymbol{\varepsilon}^{\mathrm{e}} + \Psi^{\mathrm{p}}\left(\alpha\right) .$$

The volumetric and isochoric contributions are each multiplied with damage functions $f^{\bullet}(d)$ defined as

$$f^{\bullet}(d) := \left\{\mathbb{R}_0^+ \to]0, 1]\right\} \quad \text{with} \quad f^{\bullet}(d) = \exp(-\eta_{\bullet}\, d) ,$$

such that the local damage d is positive but otherwise unbounded.
In this multisurface formulation the driving forces q, $\boldsymbol{m}$ and β have to lie in the elastic domain, which is bounded by a von Mises yield criterion including nonlinear isotropic hardening as well as a damage criterion with a variable damage threshold, i.e.

$$\Phi^{\mathrm{p}}(\boldsymbol{m}^{\mathrm{t}}, \beta, d) = \|\,\mathrm{dev}(\boldsymbol{m}^{\mathrm{t}}_{\mathrm{eff}})\| - \sqrt{\frac{2}{3}}\left[\sigma_{\mathrm{y}}^0 - h\,\alpha^{n_{\mathrm{p}}}\right] \quad \text{and} \quad \Phi^{\mathrm{d}}(q, d) = q_{\mathrm{eff}} - q_{\max}\left[1 - f^q(d)\right]^{n_{\mathrm{d}}} .$$

In both criterions effective driving forces are used to intensify the coupling — the spatial Mandel stresses $\boldsymbol{m}$ are divided by the damage function $f^{\boldsymbol{m}}$ and in an analogous way the damage driving force q is divided by an exponential function dependent on the hardening variable α.
Using standard thermodynamics and the postulate of maximum dissipation yields evolution equations which are transformed into an algorithmic update with an exponential scheme for the integration of $\boldsymbol{F}^{\mathrm{p}}$ and backward Euler integration for d. The resulting double set of Karush-Kuhn-Tucker conditions are solved using an active set scheme.

3. Parameter identification

The underlying experiment for the parameter identification (PI) is a tension test of a specimen cut from DP800 sheets, see Figure 2. The experiment was recorded by a suitable camera such that the inhomogeneous displacement field could be obtained from DIC software. The experimental displacement field components u_{tij}^{exp} at every point in time t, every point i and every dimension j considered together with the corresponding displacements from the simulation u_{tij}^{sim} enter the objective function

$$F = \sum_{t} \sum_{i=1}^{n_{\mathrm{np}}} \sum_{j=1}^{n_{\mathrm{dim}}} \left[\Delta u_{tij}^{\mathrm{exp}} - \Delta u_{tij}^{\mathrm{sim}} \right]^2 .$$

The objective function only consists of the squared error of relative displacements — the difference in displacement compared to neighbouring points — since the force measured in the experiment is directly applied as Neumann boundary condition in the finite element simulation. Relative displacements are chosen over the actual displacements to remove the influence of rigid body motions. After identifying the elastic parameters for DP800, a PI to determine the plastic parameters was carried out. The load displacement diagram shows a good agreement between experiment and simulation, see Figure 1. An additional simulation including unloading confirms the evolution of plastic strains. In future work the damage parameters shall be identified. The gradient parameter c_d will receive special focus in order to check its independence from geometry and specimen size.

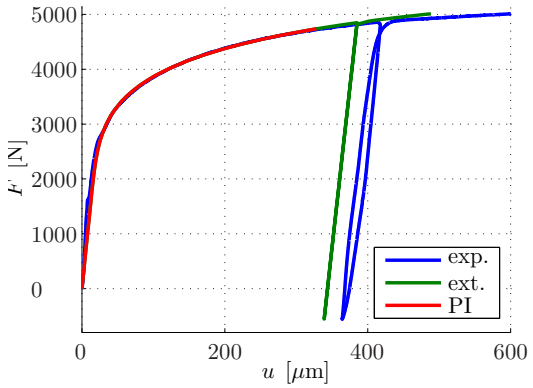

Figure 1: Load displacement diagram of the tension test including unloading underlying the PI. Experiment (blue), PI result (red) and simulation including the unloading (green).

Figure 2: Image of the specimen geometry. The specimens from 1.5 mm DP800 sheets are 50 mm long.

Acknowledgments The financial support of the German Research Foundation (DFG), Transregio 188 "Damage Controlled Forming Processes" (TRR 188) within project C2, is gratefully acknowledged.

References

[1] B. J. Dimitrijevic and K. Hackl. A method for gradient enhancement of continuum damage models. *Technische Mechanik*, 28(1):43–52, 2008.

[2] Bjoern Kiefer, Tobias Waffenschmidt, Leon Sprave, and Andreas Menzel. A gradient-enhanced damage model coupled to plasticity—multi-surface formulation and algorithmic concepts. *International Journal of Damage Mechanics*, 27(2):253–295, 2018.

[3] C. Polindara, T. Waffenschmidt, and A. Menzel. A computational framework for modelling damage-induced softening in fibre-reinforced materials – application to balloon angioplasty. *International Journal of Solids and Structures*, 118-119:235 – 256, 2017.

[4] P. Steinmann and E. Stein. A unifying treatise of variational principles for two types of micropolar continua. *Acta Mechanica*, 121(1-4):215–232, 1997.

[5] Tobias Waffenschmidt, César Polindara, Andreas Menzel, and Sergio Blanco. A gradient-enhanced large-deformation continuum damage model for fibre-reinforced materials. *Computer Methods in Applied Mechanics and Engineering*, 268:801–842, 2014.

FRACTION HYPERELASTIC DAMAGE MODEL FOR ROOF MEMBRANES MATERIALS

Bartosz Łuczak[1], Wojciech Sumelka[1], and George Z. Voyiadjis[2]

[1]*Institute of Structural Engineering, Poznan University of Technology, Piotrowo 5 street, 60-965, Poznan, Poland*
[2]*Boyd Professor, Department of Civil and Environmental Engineering, Louisiana State University, Baton Rouge, LA 70803, USA*

e-mail: {bartosz.luczak, wojciech.sumelka}@put.poznan.pl, voyiadjis@eng.lsu.edu

Roofing are an important constituent of each building structure. Due to their meaningful function the materials which are used to construct this element should meet very rigorous requirements, especially to manage extreme weather conditions like moisture penetration, high temperatures gradients, rainfalls, snowfalls or UV radiation. Therefore, the time in which this materials meet their requirements are relatively short in comparison to the life cycle of the whole building. This results in the need to make repairs and renovations which usually are expensive, hence even small elongation of the life time of these materials will cause significant savings.

To make the life time predictions of roofing materials possible the computer-aided engineering tools are needed. Hence, in this article the modelling of roof membranes in the framework of the hyperelastic fractional damage material model with memory presented by W. Sumelka and G.Z. Voyiadjis in [5] is applied. Furthermore, the extension of this model to include healing effects will be discussed [6]. In the model, the original idea of extension of the classical scalar hyperelastic damage model (energy equivalence formulation) utilizing fractional calculus [1, 3, 4] was postulated. The evolution of damage variable ϕ has obtained the fractional form

$$ {}^{C}_{t-l_t}D^{\alpha}_{t}\phi = \frac{1}{T^{\alpha}}\Phi\left\langle \frac{I_{\phi}}{\tau_{\phi}} - 1 \right\rangle, \tag{1} $$

where the bracket $\langle\ .\ \rangle$ defines the ramp function and the ${}^{C}D$ is the left-sided Caputo derivative

$$ {}^{C}_{a}D^{\alpha}_{t}f(t) \ = \ \frac{1}{\Gamma(n\ -\ \alpha)}\int_{a}^{t}\frac{f^{(n)}(\tau)}{(t\ -\ \tau)^{\alpha-n+1}}d\tau \qquad \text{for} \quad t\ >\ a, \tag{2} $$

where t denotes time variable, α is an order of derivative (order of fractional velocity), T stand for the characteristic time, Φ is the overstress function, I_{ϕ} is the stress intensity invariant, τ_{ϕ} is the threshold stress for damage evolution, Γ is the Euler gamma and $n = [\alpha] + 1$ function.

The investigations are divided into three parts. First one aimed to reconstruct the results presented in [5] utilizing software for symbolic mathematical calculations *Wolfram Mathematica*. Next, the implementation of the concept of hyperelastic fractional damage material model with memory in *AceFem* software is considered. The choice of *AceFem* software was dictated by its structure (the system combines symbolic and numeric approaches) and because its environment is designed to solve multi-physics and multi-field problems. Finally, the last step covers the preparation of a simple 3D model with "memory". Simulations, include a cubic geometry induced for basic deformation modes [2].

References

[1] A.A. Kilbas, H.M. Srivastava, and J.J. Trujillo. *Theory and Applications of Fractional Differential Equations*. Elsevier, Amsterdam, 2006.
[2] V. A. Kolupaev, M.-H. Yu, and H. Altenbach. Fitting of the strength hypotheses. *Acta Mechanica*, 227(6):1533–1556, Jun 2016.
[3] A.B. Malinowska, T. Odzijewicz, and D.F.M. Torres. *Advanced Methods in the Fractional Calculus of Variations*. SpringerBriefs in Applied Sciences and Technology. Springer, 2015.
[4] I. Podlubny. *Fractional Differential Equations*, volume 198 of *Mathematics in Science and Engineering*. Academin Press, 1999.

[5] W. Sumelka and Voyiadjis George Z. A hyperelastic fractional damage material model with memory. *International Journal of Solids and Structures*, 124:151–160, 2017.

[6] George Z Voyiadjis and Peter I Kattan. Healing and super healing in continuum damage mechanics. *International Journal of Damage Mechanics*, 23(2):245–260, 2014.

UNIAXIAL COMPRESSION BEHAVIOUR OF POROUS COPPER: EXPERIMENTS AND MODELLING

B. R. Bodapati[1,2], P. S. Phani[1], P.P. Bhattacharjee [2]
and G. Sundararajan [1,3]

[1]*International Advanced Research Center for Powder Metallurgy and New Materials (ARCI), Balapur (P.O), Hyderabad – 500 005, India*
[2] *Department of Materials Science and Metallurgical Engineering, Indian Institute of Technology (IITH) Hyderabad – 502 285*
[3] *Department of Metallurgical and Materials Engineering, Indian Institute of Technology (IITM) Chennai – 600 036, India*

The yielding behavior of porous metallic materials has been fairly well studied. However, the data on post-yield flow behavior is rather scarce. In the current study, porous copper samples with a wide range of porosity (2% - 25%) are prepared by suitably changing the process parameters of Spark Plasma Sintering (SPS) process. Uniaxial compression tests are performed on the porous samples with different initial porosities to experimentally determine the evolution of porosity and flow stress and thereby understand the post-yield hardening behavior. A simple analytical model is developed for evolution of porosity and flow stress during uniaxial compression based on the Gurson model. A unique linear relationship was observed for normalized porosity (porosity / initial porosity) with strain and normalized flow stress (flow stress / flow stress of matrix) with porosity as shown in Fig. 1. The model predictions are in good agreement with the experimental results and Finite Element Analysis (FEA) results over a wide range of porosity and strain.
Furthermore, a new model for strain hardening rate (θ) is developed which explains the significant strain hardening observed in the uniaxial compression tests as shown below.

$$\theta = \theta_M (1-q_1 f) + \sigma_M q_1 f_0 a$$

where, θ_M is strain hardening rate of the matrix, σ_M is the flow stress of the matrix, f is porosity, f_0 is initial porosity, q_1 and a are constants.
The observed strain hardening rate of the porous samples depends not only on the strain hardening rate of the matrix material but also on the extent of pore closure during compression. While the relative contribution of the strain hardening rate of the matrix largely dominates the observed response, the contribution due to pore closure is significant for samples with high initial porosity, especially at higher values of strain.

The Gurson model parameters for the current material system and porosity range will also be presented along with a discussion on the applicability of the Gurson model for the current range of porosity.

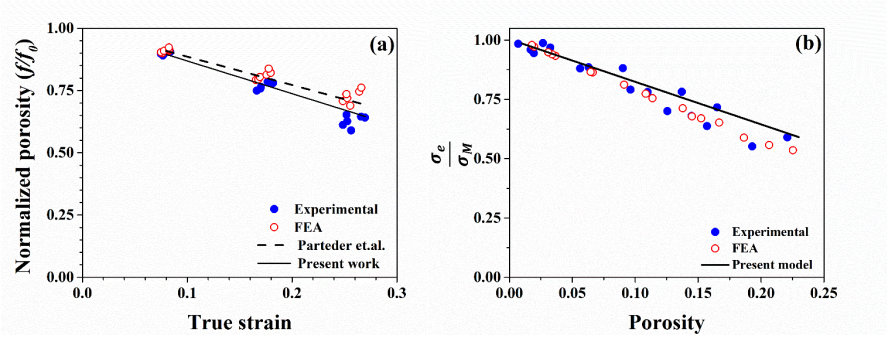

Fig. 1: (a) Comparison of experimental, FEA and theoretical results for normalized porosity (f/f_o) during compression (b) Variation in normalized flow stress (σ_e/σ_M) with porosity, comparison between experimental data, FEA predictions and theoretical analysis

DYNAMIC INTERACTION OF BRANCHED CRACKS

P. Fedelinski[1]

[1]*Institute of Computational Mechanics and Engineering, Silesian University of Technology, Poland*
e-mail: piotr.fedelinski@polsl.pl

1. Introduction

Branched cracks in materials exist as a result of technological processes, corrosion, loading conditions, etc. Fast running cracks subjected to high loadings can split into several branches. The stresses at crack tips of branched cracks are characterized by stress intensity factors (SIF). The values of static or dynamic SIF for a general geometry of the body and loading conditions are obtained by numerical methods.
Daux et al. [1] presented the extended finite element method (X-FEM) to analysis of cracks with multiple branches and cracks emanating from holes. A standard displacement approximation was enriched by incorporating additional discontinuous functions. The method allows the modelling of discontinuities independently of the mesh. Raffie et al. [2] investigated bifurcation and trifurcation of fast running cracks under various biaxial loading conditions. Arbitrary curvilinear crack propagations were analyzed by the time-domain BEM. Branching of cracks was controlled by the opening mode SIF and velocity and direction of crack growth by the maximum circumferencial stress at the crack tip. Numerical solutions were compared with experimental results. Fedelinski [3] applied the boundary element method to analysis of statically and dynamically loaded plates with branched and intersecting cracks. The dynamic problem was solved by using the Laplace transform method and the solution in the time domain was computed by the Durbin numerical inversion method. Numerical examples of a branched crack in a rectangular plate and a star-shaped crack in a square plate were presented. The influences of angles between branches of the crack and dimensions of the plate for the star-shaped crack on dynamic SIF were analyzed.
In the present work the boundary element method is applied to analysis of static and dynamic stress intensity factors of branched cracks in infinite plates. The infinite plates are analyzed to study interaction between the cracks and to avoid interaction with external boundaries of plates. The crack problem is solved by the dual BEM which was developed for dynamic loading by Fedelinski et al. [4]. An overview of different BEM approaches in dynamic fracture mechanics was presented by Fedelinski [5]. The present paper is an extension of the previous work [3] published by the author. In this work influence of distance between branched cracks, their orientation and direction of loading on static and dynamic SIF are analyzed.

2. Numerical example – two branched cracks in an infinite plate

Two branched cracks in an infinite plate are subjected to tensile loading, as shown in Fig. 1. The dimension of the crack branches is a=1 cm and the distance between crack centres is 2l and l/a=2. The angle between crack branches is $2\alpha=2/3\pi$. The material is isotropic and linear-elastic and the Young modulus is E=200 GPa, the Poisson ratio ν=0.3, mass density ρ=8000 kg/m^3 and the material is in plane strain conditions. The velocity of the longitudinal wave is c_1=5801 m/s and the velocity of the shear wave is c_2=3101 m/s. The tensile loading p with the Heaviside time-dependence is applied in the direction perpendicular to the line connecting crack centres. In order to model the infinite plate and avoid influence of reflection of waves from boundaries the rectangular plate of width 2w=30 cm and height 2h=20 cm is considered. The uniformly distributed tractions are applied along horizontal edges of the plate. The plate with the cracks is divided into 320 boundary elements (200 elements for the external boundary and 10 elements for each crack edge). The numerical solution is obtained using 50 Laplace parameters and the time step Δt=0.4 μs. The stress intensity factors are normalized with respect to $K_o = p\sqrt{\pi c}$, where 2c=3/2a is the width of the branched crack in the horizontal direction. The results for the static and dynamic loading are compared with the solution for the single crack in the centre of the plate. The normalized static SIF for double and single cracks are given in Table 1. The time dependence of dynamic SIF is presented in Fig. 2.
The static SIF for the interacting cracks are several percent larger than SIF for single cracks. The dynamic SIF are 0 up to about 16 μs when the longitudinal wave propagates from the loaded boundary to the crack tips. For the considered distance between cracks the influence of interaction on dynamic SIF is small.

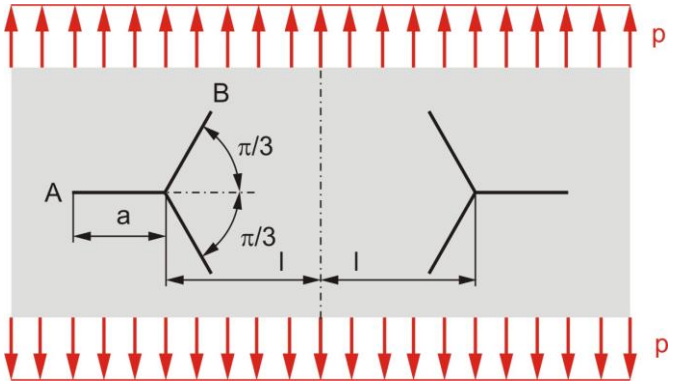

Fig. 1. Two branched cracks in an infinite plate

Branched cracks	$K_I(A)/K_o$	$K_I(B)/K_o$	$K_{II}(B)/K_o$
double	1.700	0.472	0.915
single	1.659	0.434	0.898

Table 1. Normalized static SIF for double and single branched cracks

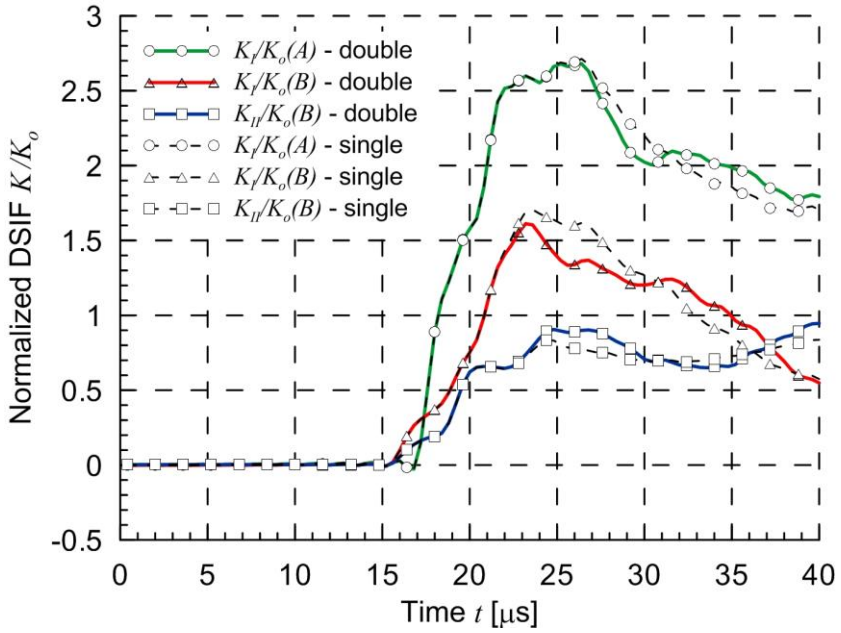

Fig. 2. Normalized dynamic SIF for double and single branched cracks

Acknowledgments The author acknowledge the financial support of the statutory project of Faculty of Mechanical Engineering, Silesian University of Technology BK 226/RMT4/2018 (10/040/BK_18/0066).

References

[1] Ch. Daux, N. Moes, J. Dolbow, N. Sukumar, T. Belytschko, Arbitrary branched and intersecting cracks with the extended finite element method. *Int. J. Numer. Meth. Eng.*, 48: 1741-1760, 2000.

[2] S .Raffie, Th. Seelig, D. Gross. Simulation of dynamic crack curving and branching under biaxial loading by a time domain boundary integral equation method. *Int. J. Frac.*, 120: 545-561, 2003.

[3] P. Fedelinski. Dynamically loaded branched and intersecting cracks. *J. Civil Eng., Envir. Arch.*, 34: 17-26, 2017.

[4] P. Fedelinski, M. H. Aliabadi, D.P Rooke. The Laplace transform DBEM method for mixed-mode dynamic crack analysis. *Comp. Struct.*, 59: 1021-1031, 1996.

[5] P. Fedelinski. *The boundary element method in dynamic analysis of deformable structures with cracks*. Publisher of the Silesian University of Technology, Mechanics, 137, Gliwice, 2000 (in Polish).

IRRADIATION CREEP DAMAGE IN NUCLEAR REACTOR COMPONENTS

A. Ustrzycka[1]

[1]*Institute of Fundamental Technological Research, Polish Academy of Sciences, Warsaw, Poland*
e-mail: austrzyc@ippt.pan.pl

The main mechanisms of failure in irradiated materials subjected to elevated temperature is mostly the result of the initiation, formation of voids, their coalescence and growth. The particle radiation in nuclear reactor components has crucial effect on the creep damage and final fracture. The flux of energetic particles significantly enhances particularly the creep process.

In order to investigate the irradiation creep problem the main processes that underlie the response of the irradiated material to stress are recognized. The processes of the defect formation and initial clustering as well as the interaction between point defects which are the basis of the creep theory are considered. The irradiation of metals by high energy particles leads to the interaction of energetic incident particles with lattice atoms [1]. The energetic particles transfer their kinetic energy to the lattice atoms creating primary knock on atom (PKA), which, in turn, leads to the displacement of next generation of target atoms, the process is called collision cascade. Collision cascade usually contains a vacancy-rich core surrounded by a halo of interstitial atoms. Displacement phase of the collision cascade usually lasts about 10^{-11} seconds, after about 10^{-10} seconds the cascade is thermalized. The pair of interstitial atom and vacancy in irradiated crystalline solids is known as the Frenkel defect. These phenomena such as Frenkel pairs formation are characteristic for irradiated materials and determine the physical effects, and with the application of stress, the mechanical effects of irradiation. These physical effects include numerous microstructural processes such as void formation growth, swelling, phase instability and radiation induced segregation [2]. After the end of the collisional phase of cascade evolution the point defects (vacancies and interstitials) may migrate in material leading to the formation of various forms of defect clusters: e.g. clusters of voids and helium bubbles. In this way, the process of damage initiation in the crystal structure is created.

Most of the energy deposited by high-energy particles is dissipated as the local heating of the crystal. Most of the Frenkel pairs created in collision cascade annihilate during the early phase of its evolution, the increase of the target temperature leads to additional recombination process of vacancies and interstitials at later stages. The origins of void swelling of metals are qualitatively understood. The collection of interstitial atoms as extra planes in the lattice causes the solid to swell. The consequences of radiation on material components structure include changes in shape and volume, increases in hardness, severe reduction in ductility and increased embrittlement, and susceptibility induced cracking.

The present work is concerned with the mechanical modeling of irradiation creep damage of metals applicable to structural analyses of metal components in nuclear reactor (Fig. 1). Multiscale model created to assess irradiation creep containing strong physical background related to the mechanism of generation of clusters of voids and helium bubbles in the irradiated solids has been built [3]. The irradiation creep was described by modifying Kachanov creep damage theory for brittle and Hoff creep damage theory for ductile materials by incorporating the effect of irradiation.

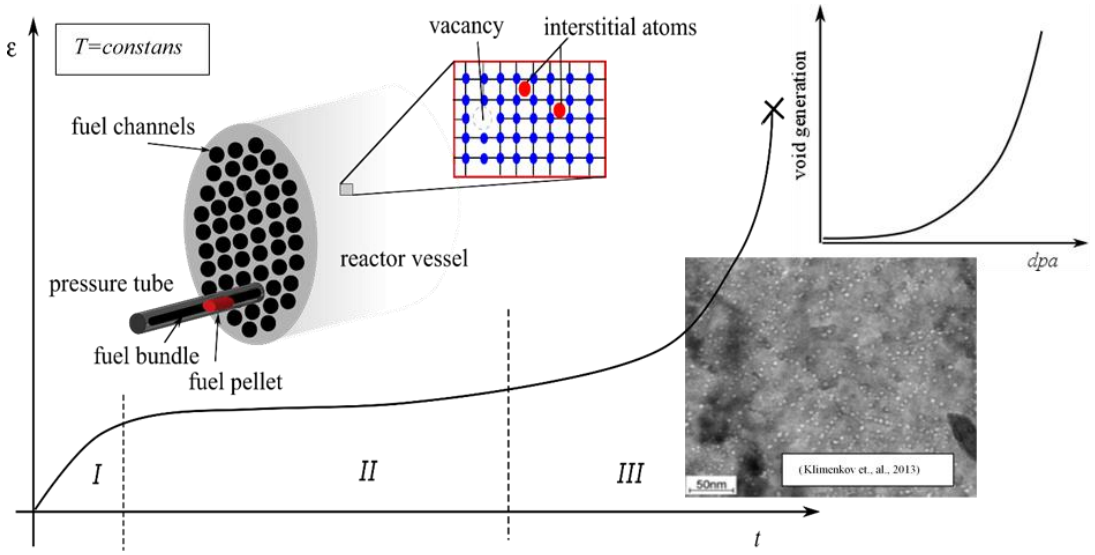

Fig. Degradation mechanisms of specific nuclear reactor structures

A bar tensioned with normal force constant in time serves as a model. It is assumed, that material is exposed in equal intervals of time to equal doses of irradiation. After each time interval, hence after accumulation of each irradiation burst, the sample is reanalyzed. Diminishing of effective cross-sectional area of the bar caused by particle flux is assumed relatively at the same level at each consecutive application of irradiation. However, at each emission of radiation (radiation burst) it acts on the cross section reduced, due to creep damage. All the irradiated creep process is thus divided into several steps. In a single cycle the material is subjected to flux of energetic particles (or irradiations pulses), which induce radiation defects in the material expressed in *dpa* [4]. Simultaneously, the material is subjected to thermo-mechanical loads at high temperature, which induce the deformation and cracking of material in creep range. The proposed model takes into account both; diminishing of the effective cross-sectional area caused by particle flux and geometrical changes resulting from creep deformation. At each emission of radiation it acts on the cross section reduced, due to creep damage. Consequently, the thermo-mechanical loads act on the cross section reduced due to radiation induced damage. In this way bilateral coupling of radiation and creep damage is performed.

As an application of the proposed equations, creep damage evolution in a metal component subjected to irradiation load was analyzed. The semi-analytical results and the special topics associated with irradiation creep modelling are discussed. The utility of the proposed constitutive equation was demonstrated by analyzing the irradiation creep and irradiation creep damage for different materials parameters. The experimental result confirm the mathematical analysis that the lifetime of irradiated components is significantly shorted [5].

References

[1] K. Nordlund, S. J. Zinkle, A.E. Sand, F. Granberg, R.S. Averback, R. Stoller, T. Suzudo, T. L. Malerba, F. Banhart, W. J. Weber, F. Willaime, S. L. Dudarev, D. Simeone. Improving atomic displacement andreplacement calculations with physically realistic damage models. *Nature Communications.* 9:1084 2018.
[2] G. Was. *Fundamentals of Radiation Materials Science*. Springer, 2007.
[3] A. Ustrzycka and K. Szuwalski. Modeling of the Bilateral Coupled Effect of Creep Damage and Radiation Damage, (under review).
[4] B. Skoczeń and A. Ustrzycka. Kinetics of evolution of radiation induced micro-damage in ductile materials subjected to time-dependent stresses. *IJP*, 80:86, 2016.
[5] S. J. Zinkle and G. S. Was. Materials challenges in nuclear energy *Acta Mater*., 61:735, 2013.

DYNAMIC RESPONSE OF DUCTILE MATERIALS CONTAINING CYLINDRICAL VOIDS : ANALYTICAL MODELING AND FINITE ELEMENT VALIDATION

Manoj Subramani[1], Christophe Czarnota[1] , Sébastien Mercier[1] and Alan Molinari[1]

[1]*Université de Lorraine, CNRS, Arts et Métiers ParisTech, LEM3, 7 rue Felix savart, 57073 Metz Cedex 03, France.*

email: Manoj.subramani@univ-lorraine.fr, christophe.czarnota@univ-lorraine.fr, sebastien.mercier@univ-lorraine.fr, lain.molinari@univ-lorraine.fr

Keywords: Dynamic homogenization, micro-inertia, length-scale effect, damage, porous material

1 Introduction

The fracture of ductile materials is often the result of the nucleation, growth and coalescence of microscopic voids. In the present talk, we mainly focus on the growth process of voids. In dynamic loading, micro-voids sustain an extremely rapid expansion which generates strong acceleration of particles in the vicinity of cavities. These micro-inertia effects are thought to play an important role in the development of dynamic damage. To account for these large accelerations in the constitutive behavior, a multi-scale approach has been proposed in [1] and it has been shown that the micro inertia contribution to the macro stress is significant when dynamic loading is considered. Here we are focusing on the description of the behavior of the porous material containing cylindrical voids under dynamic conditions.

2 Modelling and Results

To derive the constitutive model, a multiscale approach is adopted where the acceleration contribution is accounted for. Indeed, under dynamic loading, the static definition for the macrostress (as the volume average of the local stress) does not exist further. The overall macroscopic stress is the sum of two contributions: the static term (micro-inertia independent term) and the dynamic term (micro-inertia dependent term):

$$\Sigma = \Sigma^{stat} + \Sigma^{dyn}$$

In this work, we focused on the material response of porous medium with cylindrical voids. As a consequence, a cylindrical representative volume element for the porous material is considered, similar to the one proposed by Gurson [2]. The radius of the void is *a*, the length is *L*. The outer radius of the RVE is *b*, see Figure 1. The porosity *f* is therefore given by $f = \left(\frac{a}{b}\right)^2$. The RVE is subjected to transversely isotropic loading.

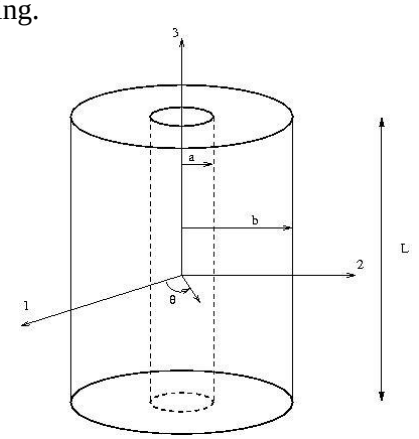

Fig 1: Representative volume element for a porous material containing cylindrical void.

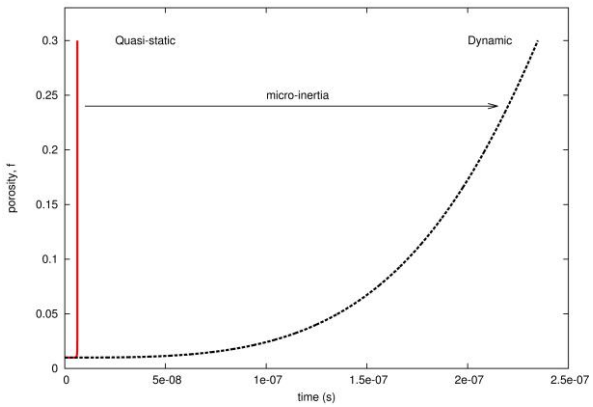

Fig 2: Evolution of the porosity during spherical loading. Quasi-static v/s dynamic results, the delay between dynamic and quasi-static predictions is due to micro-inertia effects.

The static term is derived from the visco-plastic yield function proposed by Gurson [2]. As a consequence, the present work is an extension to dynamic loading of the Gurson's model (cylindrical voids). The dynamic stress Σ^{dyn}needs to be evaluated analytically. Following the formalism proposed in [1], a trial velocity field is adopted to reproduce the velocity field which may prevail during the dynamic expansion of the RVE. Based on the Gurson's velocity field, it is shown, as for spherical voids, that the dynamic stress is scaled by the mass density, the size of the voids, the porosity, the strain rate tensor and the time derivative of the strain rate tensor. An important outcome of the model is the differential lengthscale effect which exists between in plane and out of plane components of the macrostress. Namely, it is observed that for the in plane stress components Σ_{11}^{dyn} and Σ_{22}^{dyn} are only related to the radius *a* while Σ_{33}^{dyn} is linked to the radius *a* and the length of the RVE *L*:

$$\Sigma_{11}^{dyn} = \rho a^2 F\left(f, D, \acute{D}\right) \Sigma_{22}^{dyn} = \rho a^2 G\left(f, D, \acute{D}\right) \wedge \Sigma_{33}^{dyn} = \rho a^2 H\left(f, D, \acute{D}\right) + \rho L^2 J\left(f, D, \acute{D}\right)$$

where D is the overall strain rate tensor.

In this talk, we will propose predictions of damage evolution when the RVE is subjected to spherical and axisymmetric plane strain loadings; here ramps at constant stress rate are considered. While for plane strain loading in quasi static condition, Σ_{33} is the half sum of the in plane components, in dynamic conditions, the inertia contribution reveals a difference. An important result of the proposed theory is the length effect of the RVE, which does not exist in quasi static conditions. A parametric study on the aspect ratio of the RVE will clarify this length scale effect. Next, the analytical model is validated based on comparisons with finite element calculations (Abaqus/Explicit) [3].

Acknowledgements : The research conducted in this work has received funding from the European Union's Horizon 2020 Programme (Excellent Science, Marie-Sklodowska-Curie Actions) under REA grant agreement 675602 (OUTCOME Project)

References :

[1] A. Molinari, S. Mercier, (2001). Micro-mechanical modeling of porous materials under dynamic loading. J. Mech. Phys. Solids, 49, 1497-1516.

[2] A.L. Gurson, (1977). Continuum theory of ductile rupture by void nucleation and growth : Part I - yield criteria and flow rules for porous ductile media. J. Eng. Mater. Technol., 99, 2–15.

[3] C.Sartori, S.Mercier, N.Jacques, A. Molinari (2014). Constitutive behavior of porous ductile materials accounting for micro-inertia and void shape. Mechanics of Materials, 324-339.

MULTISCALE MODEL OF HARDENING IN METASTABLE MATERIALS WITH RADIATION INDUCED POROSITY

B. Skoczeń

Institute of Applied Mechanics, Cracow University of Technology, Poland
e-mail: blazej.skoczen@pk.edu.pl

1. Introduction

Metastable materials, like stainless steels, are massively used in the construction of scientific instruments, operating at extremely low temperatures (e.g. superconducting particle accelerators). The components operating in the proximity of a source of primary or secondary particles are subjected to irradiation that induces an enhanced level of porosity, accompanied by the presence of inclusions of secondary phase resulting from the plastic strain induced phase transformation [1]. Therefore, the primary phase (austenitic matrix) contains two types of microstructural imperfections: the porosity in the form of clusters of micro-voids, and the inclusions of secondary phase. Both of them strongly affect hardening, in particular due to the Orowan mechanism of interaction between the dislocations and the lattice defects (voids, cavities, interstitials, inclusions, etc.). On the other hand, the presence of porosity affects the stiffness of two-phase continuum, leading to the material softening. Both mechanisms, hardening and softening, are contradictory and their multiscale description is essential for correct prediction of the behaviour and the lifetime of components operating at very low temperatures.

2. Irradiation induced porosity and softening

Exposure to irradiation (flux of particles) leads to creation of clusters of defects in the material [2]. The so-called atomic displacement damage process correlates with the evolution of porosity. Energy brought by the incident particles is dissipated mainly by the elastic collisions with the lattice atoms. These nuclear interactions lead to creation of atoms moving inside the lattice, and to the production of defects (interstitials and vacancies). The vacancies form clusters and grow into the so-called cavities, often filled with helium at high pressure. It is shown that the actual pressure is function of the overall strain, that leads to the evolution of size of the clusters according to the Rice-Tracey kinetics. The increase of porosity is expressed by the following formula:

$$\Delta\xi_p = \xi_{p_0}\left(e^{3C\Delta p} - 1\right)$$

where ξ_{p_0} is the initial porosity, C is function of triaxiality, and Δp denotes accumulated plastic strain. The pressurized cavities form spaces subjected to internal pressure and characterized by specific value of surface energy. The cavities form Eshelby type ellipsoidal entities that reduce the tangent stiffness of the matrix. As the porosity evolves with plastic strain, the resultant tangent stiffness is function of the increase in porosity.

3. Plastic strain induced fcc-bcc phase transformation

Plastic flow in the metastable alloys (e.g. stainless steels) is usually accompanied by dynamic evolution of the microstructure, resulting from the phase transformation. In the course of plastic strain induced phase transformation, that occurs in the LSFE materials at extremely low temperatures, the γ-austenite (fcc microstructure) is transformed into α'-martensite (bcc microstructure). The martensite platelets (lenticular martensite), embedded in the austenitic matrix, affect the surrounding fcc lattice and induce local distortions. Therefore, the plastic strain induced fcc-bcc phase transformation results in significant evolution of the material properties, and strong nonlinear hardening. The classical sigmoidal curve, representing the volume fraction of secondary phase, is essentially valid for wide range of temperatures. However, at extremely low

temperatures the phase transformation rate is less temperature dependent, and a simplified linearized kinetics can be applied:

$$\dot{\xi}_t = A\left(T, \underline{\underline{\sigma}}\right) \dot{p} H\left(\left(p - p_{\xi}\right)\left(\xi_{tL} - \xi_t\right)\right)$$

where ξ_t denotes volume fraction of secondary phase, and *H* is the Heaviside function.

4. RVE based multiscale model of irradiated metastable continuum

Formulation of the constitutive model of elastic-plastic continuum subjected to the plastic strain induced phase transformation in the presence of radiation induced porosity is based on multiscale approach. In particular, it takes into account the micromechanical phenomena such as the interactions of dislocations with the inclusions and the pressurized cavities (micro-level), or the influence of hard inclusions and "soft" cavities on the resultant tangent stiffness of two-phase continuum (meso-level). The model is defined on the mesoscopic level by means of the representative volume element (RVE), size of which should be large enough to contain representation of all microstructural phenomena (lattice defects and inhomogeneity), but small enough to justify the local approach. The final constitutive model, defined at the macroscopic level, comprises the model of mixed plastic hardening consisting of the kinematic hardening component, represented by the position of the centre of yield surface expressed by the second rank tensor $\underline{\underline{X}}$, and the isotropic hardening component, described by a scalar parameter *R*. The proportion between them is defined by the appropriate value of the Bauschinger parameter.

5. Hardening due to the evolution of secondary phase

When crossing a pair of inclusions or pressurized cavities of the average size *d*, much smaller than the average distance between them ($d<<l$), a dislocation driven by the enhanced shear stress leaves around each inclusion or cavity a closed loop (the Orowan mechanism). This mechanism, described by means of the micromechanical analysis, leads to substantial increase of hardening parameter. Moreover, the evolution of material micro-structure induces strain hardening related to the increase of the equivalent tangent stiffness as a result of evolving proportions between both phases, each characterised by different stiffness. The corresponding hardening model is based on the Hill concept (1965), supplemented by the Mori-Tanaka (1973) homogenisation algorithm. As soon as the phase transformation threshold is reached, combination of both the above described effects results in nonlinear hardening, that is only to some extent compensated by the softening related to the presence of pressurized cavities [3].

6. Closed form analytical solutions

The above presented new model takes into account two contradictory phenomena in metastable alloys: softening due to the presence of radiation induced porosity, and hardening due to the phase transformation. The model contains relatively small number of parameters and is suitable for the temperatures ranging from absolute zero to the room temperature. New closed form analytical solutions were obtained for the uniaxial cases, and the results were cross-checked directly with the available experiments.

Acknowledgments The author acknowledges the financial support of the National Science Centre.

References

[1] R. Ortwein, B. Skoczeń, and J.Ph. Tock. Micromechanics based constitutive modeling of martensitic transformation in metastable materials subjected to torsion at cryogenic temperatures. *Int. Journal of Plasticity,* 59, 152-179, 2014.
[2] B. Skoczeń, A. Ustrzycka. Kinetics of evolution of radiation induced micro-damage in ductile materials subjected to time-dependent stresses. *International Journal of Plasticity*, 80, 86-110, 2016.
[3] M. Ryś, B. Skoczeń. Coupled constitutive model of damage affected two-phase continuum. *Mechanics of Materials,* 115, 1-15, 2017.

DISCONTINUOUS PLASTIC FLOW IN THE LOW-TEMPERATURE SUPERCONDUCTORS

J. Tabin and B. Skoczeń

Institute of Applied Mechanics, Faculty of Mechanical Engineering, Cracow University of Technology, al. Jana Pawła II 37, 31-864 Cracow, Poland
e-mail: kubatabin@mech.pk.edu.pl

1. General

Low-temperature (LT) superconductors consisting of superconducting filaments embedded in the copper matrix are used in the applications where high current density can generate strong magnetic field. Primary applications of LT superconductors (e.g. Cu/NbTi, Cu/Nb3Sn) include: magnets for MRI, nuclear magnetic resonance (NMR), laboratory apparatus, particle accelerators, electric power conditioning, levitating trains and superconducting magnetic energy storage (SMES). The applied magnetic field, the temperature and the current density in such devices must be maintained below a critical surface in order to retain superconductivity. Therefore, any heat dissipation effects, such as energy dissipation during the discontinuous plastic flow (DPF), are undesired. Such effects may occur independently in the matrix and in the filaments during the plastic deformation at near 0K temperature. DPF is attributed to the mechanism of local catastrophic failure of lattice barriers (including Lomer–Cottrell locks), under the stress fields related to the accumulating edge dislocations. Failure of LC locks leads to massive motion of released dislocations, accompanied by step-wise increase of the strain rate (macroscopic slip), and a drastic drop of stress. Moreover, the plastic power dissipated in the slip band is partially converted to heat, which results in a drastic increase of temperature promoted by the thermodynamic instability (nearly adiabatic process). Thus, DPF is a potential factor leading to the loss of superconductivity in the magnet. Therefore, the experimental investigations and the constitutive modelling of DPF in the LT superconductors seem to be essential.

2. Tensile test results of LT superconductors at 4.2 K

In order to investigate the behaviour of LT superconductors at cryogenic temperatures, a custom built experimental set-up was used (Tabin et al., 2017). A cryostat equipped with tested specimen and the relevant transducers was mounted between traction machine grips. The cryogen (liquid helium, 4.2 K) was fed into the cryostat by means of a transfer line, until the specimen with the transducers was immersed in the bath. The level of the cryogen inside the cryostat was indicated by a dedicated thermistor.

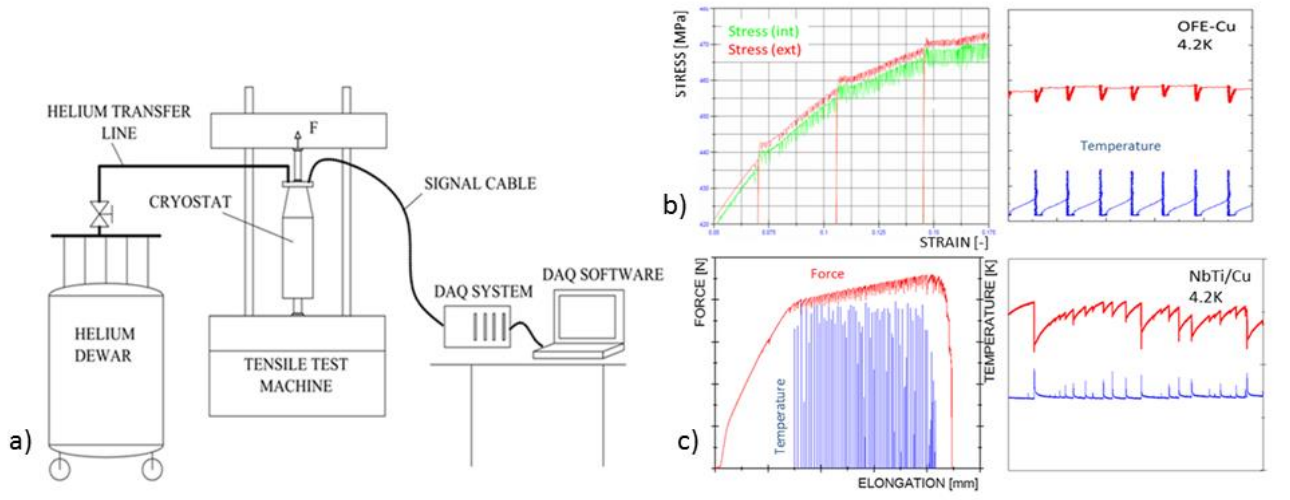

Fig. 1 a) The experimental set-up for uniaxial tests at 4.2K; b) the stress-strain curve (red and green) and the temperature-strain curve (blue) for OFE-Cu; c) the force-elongation curve (red) and the temperature-elongation curve (blue) for NbTi/Cu composite

The kinematically controlled tests were carried out. During each test, the elongation of the specimen was measured by means of the clip-on extensometers, whereas the applied force was measured by means of the piezoelectric transducer mounted above the specimen. The temperature of the specimen during plastic deformation was measured by means of the thermistor mounted in the middle of the gauge length. General scheme of the experimental set-up, as well as uniaxial tensile test results, are presented in Fig. 1.

3. Multiscale constitutive model of DPF

During the uniaxial tensile tests at 4.2K, the plastic flow instability (serrations) is observed independently in the Cu matrix and in the NbTi filaments (Fig. 1c). The DPF consists in the massive failure of lattice barriers associated with the increase of the resolved shear stress at the heads of the dislocations pile-ups, until the stresses reach the level of cohesive strength of the material (Skoczeń et al., 2010). The main function that reflects the number of internal lattice barriers per unit surface is the density B. The rate of production of dislocation pile-ups at the internal lattice barriers $\dot{B}$ is strictly related to the rate of the accumulated plastic strain $\dot{p}$. In general, the kinetics of DPF is expressed by:

$$\dot{B} = F_{LC}^{+}\left(\rho, T, \underline{\underline{\sigma}}\right)\dot{p}H\left(p - p_{LC}\right) \tag{1}$$

where F_{LC}^{+} is function of dislocations density ρ, temperature T, and stress σ, whereas p_{LC} represents the threshold above which the lattice barriers massively develop. $H(...)$ denotes the Heaviside function. The criterion of avalanche-like failure of lattice barriers is based on the interaction between B (the density of lattice barriers) and τ_e (the average shear stress at the head of dislocation pile-up). A combination of both parameters triggers the serration (drop of stress) (Skoczeń et al., 2008). A numerical model of DPF is provided for the transversely isotropic composite, consisting of the filaments in the copper matrix (Fig. 2).

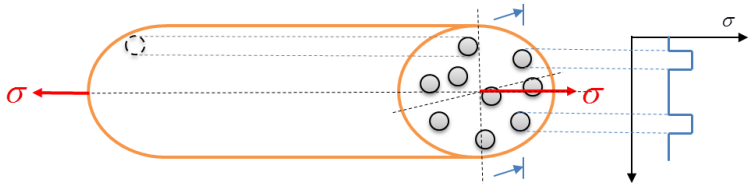

Fig. 2 Transversely isotropic composite consisting of filaments embedded in the copper matrix

It is assumed that during the kinematically controlled tensile test, the total strain is the same for the matrix and the filaments. Thus, the effective stress has following form:

$$\bar{\sigma} = \beta_m \sigma_1 + \beta_f \sigma_2 \tag{1}$$

where β_m, β_f denote the surface fraction of the matrix (OFE-Cu) and the filaments (NbTi), and σ_1, σ_2 denote the stress in the matrix and in the filaments, respectively. The above discussed constitutive model is physically based, and reflects all the important features of the DPF. Moreover, the model allows us to reproduce the observed serrations, which is crucial for its application in the design of components operating at extremely low temperatures.

Acknowledgments This work has been supported by the National Science Centre through the Grant No UMO-2016/21/N/ST8/02368.

References

[1] Skoczeń, B., 2008. Constitutive model of plastic strain induced phenomena at cryogenic temperatures. Journal of Theoretical and Applied Mechanics, 46, 4, pp. 949-971,
[2] Skoczeń, B., Bielski, J., Sgobba, S., Marcinek, D., 2010. Constitutive model of discontinuous plastic flow at cryogenic temperatures. International Journal of Plasticity 26, pp. 1659-1679.
[3] Tabin, J., Skoczen, B., Bielski, J., 2017. Damage affected discontinuous plastic flow (DPF). Mechanics of Materials 110, pp. 44-58.

NON-UNIFORM DISTRIBUTIONS OF INITIAL POROSITY IN METALLIC MATERIALS AFFECT THE GROWTH RATE OF NECKING INSTABILITIES IN FLAT TENSILE SAMPLES SUBJECTED TO DYNAMIC LOADING

K. E. N'souglo[1], J. A. Rodríguez-Martínez[1]

[1]*Department of Continuum Mechanics and Structural Analysis. University Carlos III of Madrid. Avda. de la Universidad, 30. 28911 Leganés, Madrid, Spain*

e-mail: jarmarti@ing.uc3m.es

Abstract

In this work we assess, using finite element calculations performed with ABAQUS/Explicit, the influence of porosity in the development of necking instabilities in flat metallic samples subjected to dynamic tension. The mechanical behaviour of the material is described with the Gurson—Tvergaard—Needleman [1-3] constitutive model pre-implemented in the finite element code. The novelty of our methodology is that we have included in the gauge of the specimen various non-uniform distributions of initial porosity which, in all cases, keep constant the average porosity in the whole sample. This has been carried out assigning random values of initial porosity (within specified bounds) to some nodes and zero to the others. Therefore, the larger the percentage of nodes with non-zero initial porosity, the smaller their initial value of porosity. The idea is to replicate the heterogeneous microstructure of (most) metals which have a finite number of voids non-uniformly distributed in the bulk. The key point of this work is that, following this methodology, we reproduce the experimentally-observed asymmetric-growth of the pair of necking bands which define the localization process in flat tensile samples subjected to dynamic loading [4].

Acknowledgments The research leading to these results has received funding from the European Union's Horizon2020 Programme (Excellent Science) under REA and ERCEA grant agreements 675602 and 758056 (Projects OUTCOME and PURPOSE).

References

[1] A. Gurson. Continuum theory of ductile rupture by void nucleation and growth. Part I: Yield criteria and flow rules for porous ductile media. *ASME Journal of Engineering Materials and Technology* 99, 2–15, 1977.

[2] V. Tvergaard. Influence of voids on shear band instabilities under plane strain conditions. *International Journal of Fracture* 17; 389–407, 1981.

[3] V. Tvergaard. On localization in ductile materials containing spherical voids. *International Journal of Fracture* 18, 237–252, 1982.

[4] A. Vaz-Romero, J. A. Rodríguez-Martínez, A. Arias. The deterministic nature of the fracture location in the dynamic tensile testing of steel sheets. *International Journal of Impact Engineering* 86, 318–335, 2015.

MICROMECHANICAL AND NUMERICAL MODELING OF POLYMER-METAL COMPOSITES IN LARGE STRAIN REGIME

M. Taraszewski[1] and K. Kowalczyk-Gajewska[2]

[1] *Warsaw University of Technology, Faculty of Production Engineering, Warsaw, Poland*
[2] *Institute of Fundamental Technological Research, Polish Academy of Sciences, Warsaw, Poland*

e-mail: Michal.Taraszewski@gmail.com

1. Introduction

The micromechanical model of two phase polymer-metal composite is developed in the large strain framework [3, 4]. The tangent linearization method [3] is used to adopt the Eshelby result for the inclusion in an infinite matrix undergoing large strains. A long-term goal of research is to extend the sequential averaging scheme [2] to elastic-(visco)plastic materials and large strain regime. The proposed framework will be validated by computational homogenization employing the finite element method (FEM) [5].

2. Results of FE analyses

In order to validate the performance of micromechanical model ANSYS Mechanical APDL R18.0 software [1] was used to perform FEM analysis. Following numerical simulations were conducted. A spherical inclusion centrally placed in a cubic unit cell was considered, see Fig. 1. The inclusion was varying in radius R corresponding to the volume fractions c: 0.42%, 3.35%, 11.31%, 17.96%, 22.09%, 26.81%. Additionally, each problem (in terms of a volume fraction) was calculated in two configurations: 1st when the matrix is made from steel and the inclusion from polymer, 2nd – exactly reverse. Two limit cases were also calculated when both the inclusion and the matrix were represented by the same material, steel and polymer, respectively. The polymer phase is described by the hyperelastic Yeoh model, while steel is elastic-plastic with the Kirchhoff type hyperelasticity and the J2 plasticity. A unit cell was subjected to isochoric extension in z direction. It is observed that due to a large contrast in the elastic stiffness, for the case of polymer matrix, strain in a steel inclusion is negligible as compared to the strain in polymer.

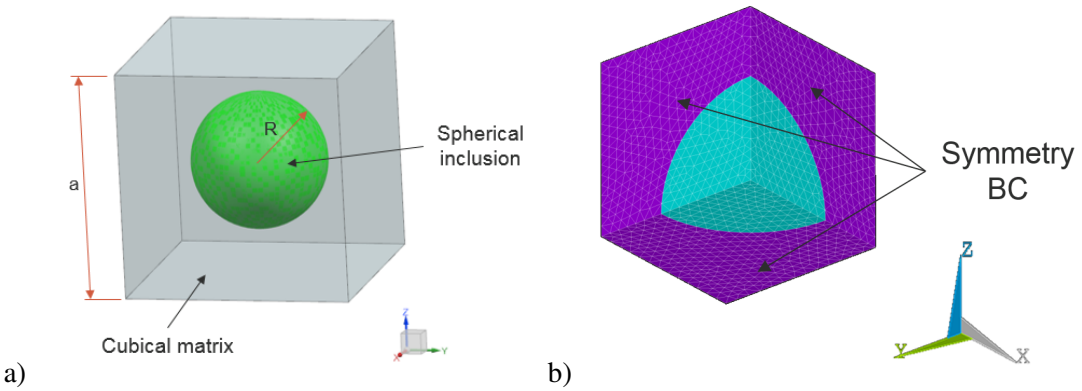

a) b)

Figure 1: A composite unit cell (a) and its computational model analyzed in ANSYS. (b)

Overall and per-phase responses were studied. For the composite with a steel matrix addition of polymer inclusions increases the specific tangent modulus (i.e. the current modulus divided by the composite density). Considering results shown in Fig. 2a, it can be said that above 0.12 of true strain all results are stabilized, monotonically decreasing and tend to converge with each other. For the stabilized part of the curve the value of specific modulus for composite cases is always higher than for a pure steel case. At the same strain level, the specific modulus first increases with the polymer volume content, reaching the highest value for $c = 3.35\%$, and then decreases.

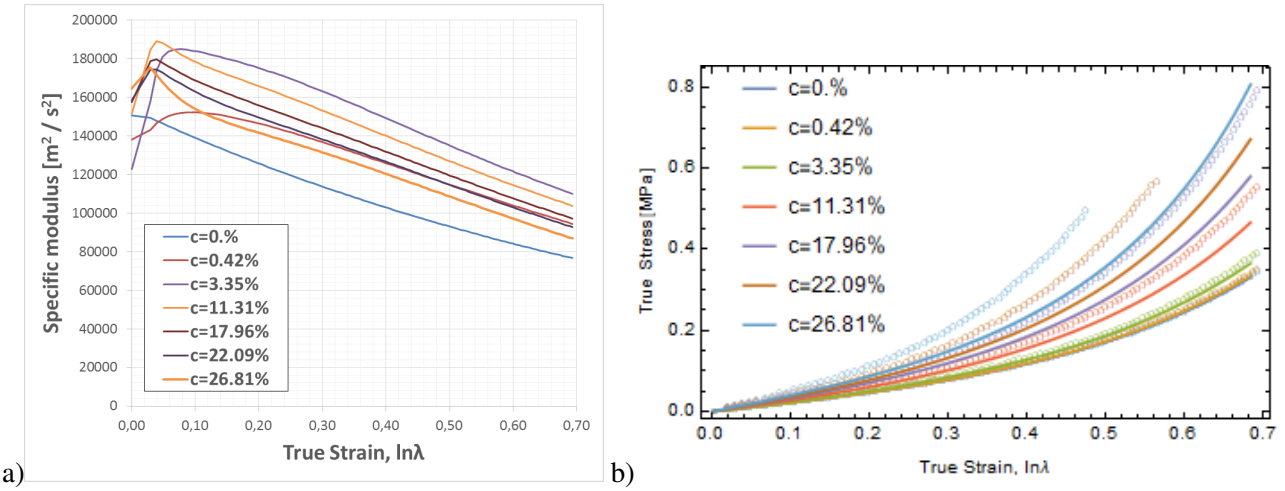

Figure 2: (a) Specific smodulus as a function of true strain for steel matrix configuration (only FE analysis) (b) Comparison of true strain-true stress curves obtained by FE analyses (circles) and using micromechanical model (continuous line) for polymer matrix configuration.

In the case of polymer matrix almost no strain is observed in the steel inclusions that behave as rigid. The overall true stress-true strain curves obtained for a different steel volume content c are demonstrated in Fig. 2b. For the same strain the stress level increases with c. Preliminary validation of the micromechanical scheme based on the incremental tangent linearization and the Mori-Tanaka averaging is also shown for this configuration. In the model the non-linear polymer behaviour (the Yeoh law) is linearized as follows

$$\mathbf{T}_m = f(\mathbf{F}_m) \rightarrow \dot{\mathbf{T}}_m = \mathbf{L}_m^{tg} \cdot \dot{\mathbf{F}}_m \quad \text{where} \quad \mathbf{L}_m^{tg} = \frac{\partial f(\mathbf{F}_m)}{\partial \mathbf{F}_m} \tag{1}$$

and the interaction law takes the form

$$\dot{\mathbf{T}}_i - \dot{\mathbf{T}}_m = -\mathbf{L}_*(\mathbf{L}_m^{tg}) \cdot (\dot{\mathbf{F}}_i - \dot{\mathbf{F}}_m)\,, \tag{2}$$

in which $\mathbf{F}_{m/i}$ and $\mathbf{T}_{m/i}$ are the deformation gradient and the first Piola-Kirchhoff stress in the matrix and inclusion, respectively, while $\mathbf{L}_*$ is the Hill tensor. Inclusions are assumed as rigid, therefore $\mathbf{F}_i = \mathbf{I}$ and $\mathbf{F}_m = 1/(1-c)(\bar{\mathbf{F}} - c\mathbf{I})$ ($\bar{\mathbf{F}}$ is the overall deformation gradient imposed in the analyses). It can be seen in Fig. 2b that the model agrees well with FE results for small volume content of steel inclusions, while for a higher c the stress level is under-predicted, especially for an increasing strain level.

Acknowledgments The research was supported by the project of the National Science Center (NCN) granted by the decision No. 2016/23/B/ST8/03418.

References

[1] ANSYS MECHANICAL APDL R18.0 HELP VIEWER. Theory Reference.

[2] K. Kowalczyk-Gajewska and H. Petryk. Sequential linearization method for viscous/elastic heterogeneous materials. *Eur. J. Mech. Solids/A*, 30:650–664, 2011.

[3] P. Ponte Castañeda and P. Suquet. Nonlinear composites. *Adv. Appl. Mech.*, 34:171–302, 1998.

[4] P. Ponte Castaneda and E. Tiberio. A second-order homogenization procedure in finite elasticity and applications to black-filled elastomers. *J. Mech. Phys. Solids*, 48:1389–1411, 2000.

[5] T. Zohdi and P. Wriggers. *Introduction to Computational Micromechanics*. Springer-Verlag, Berlin Heidelberg, 2005.

IMPACT OF MICROSTRUCTURE-INDUCED ANISOTROPY ON THE OVERALL RESPONSE OF ELASTIC-VISCOPLASTIC POLYCRYSTALLINE METALS

K. Kowalczyk-Gajewska

Institute of Fundamental Technological Research, Polish Academy of Sciences, Warsaw, Poland

e-mail: kkowalcz@ippt.pan.pl

1. Introduction

It is well known [1, 2] that the overall response of the polycrystalline material in the inelastic regime is strongly influenced by the anisotropy of the single crystal related to the presence of easy- and hard-to-initiate mechanisms of plastic deformation. Prediction of the effective properties of such materials by means of mean-field schemes is a challenging task. For the case of elastic-viscoplastic material response one can use either the schemes based on the Laplace-transform technique [4] or the approaches that employ the approximate linearization in a real time space, e.g. [3, 5]. Yet another possibility is offered by computational homogenization. In the present contribution the comparison of predictions offered by mean-field schemes and finite element RVE analyses are presented for TiAl-like crystals of varying viscoplastic anisotropy and strain rate sensitivity subjected to the inelastic deformation processes involving the strain path changes.

2. Methodology and results

Within the mean-field sequential scheme the response of the Maxwell-type elastic-viscoplastic polycrystal is established by solving at each strain increment two subproblems: creep-type one (purely viscoplastic) and instantaneous one (purely elastic). In the simplest version of the sequential self-consistent scheme, when the additional accommodation step is not necessary and the grains are of the spherical shape, two interaction equations corresponding to two mentioned subproblems take the form:

$$\dot{\boldsymbol{\varepsilon}}_g^v - \dot{\boldsymbol{\varepsilon}}_0^{\mathrm{Vg}} = -\bar{\mathbf{M}}_*^v \cdot (\boldsymbol{\sigma}_g - \boldsymbol{\Sigma}), \quad \dot{\boldsymbol{\varepsilon}}_g^e - \dot{\boldsymbol{\varepsilon}}_0^{\mathrm{E}g} = -\bar{\mathbf{M}}_*^e \cdot (\dot{\boldsymbol{\sigma}}_g - \dot{\boldsymbol{\Sigma}}) \tag{1}$$

where $\dot{\boldsymbol{\varepsilon}}_g^e + \dot{\boldsymbol{\varepsilon}}_g^v = \dot{\boldsymbol{\varepsilon}}_g$, $\dot{\boldsymbol{\varepsilon}}_0^{\mathrm{Vg}} + \dot{\boldsymbol{\varepsilon}}_0^{\mathrm{Eg}} = \dot{\mathbf{E}}$ and $\dot{\boldsymbol{\varepsilon}}_g^{v/e}$ and $\boldsymbol{\sigma}_g/\dot{\boldsymbol{\sigma}}_g$ are the viscoplastic/elastic strain rate and stress/stress rate in the grain g, while $\dot{\mathbf{E}}$ and $\bar{\boldsymbol{\Sigma}}$ the overall strain rate and the stress in the polycrystal, correspondingly. The tensors $\bar{\mathbf{M}}_*^{v/e}$ are the inverse Hill tensors for purely viscous and purely elastic problems obtained with use of the corresponding overall stiffness calculated according to the self-consistent procedure. In the case of non-linear viscoplastic polycrystals tangent or secant linearization of the local response is performed in order to use the Eshelby result.

At the level of single grain the standard formulation of rate-dependent crystal plasticity is used. The linear anisotropic Hooke's law is assumed for elasticity. Viscoplastic flow takes place by movement of dislocations on the crystallographic slip systems defined by the lattice geometry. For simplicity the Norton-type power law without hardening is assumed. It relates the slip rate and the resolved shear stress at a single slip system (for details look at [1]). FE calculations are performed using AceFEM software for the volume element of polycrystal of checkerboard distribution of randomly selected N grain orientations (Fig. 1(a)). Each grain is divided into M^3 elements. The macroscopic strain program is imposed using microperiodic boundary conditions.

Mean-field and finite element calculations are performed for a tetragonal γ-TiAl-like aggregate (L1 lattice geometry, 4 ordinary dislocations: $\{111\}\langle 1\bar{1}0]$, 8 super-dislocations $\{111\}\langle 10\bar{1}]$, with $\tau_c^{sup}/\tau_c^{ord} = \alpha > 1$, where α is an indicator of viscous anisotropy due to only 3 independent easy slip systems). Components of the elasticity tensors are assumed as reported in [1]. The exemplary results for a tension-compression and shear cyclic loading are shown in Fig. 1c,d. FE predictions lie between the results of the sequential method combined with the tangent and affine linearization of viscous response. For the presented example of polycrystal with

strong viscous anisotropy satisfactory agreement has been obtained when the modified tangent linearization with a tuning parameter $\beta = 3$ [6] is used in the purely viscous step.

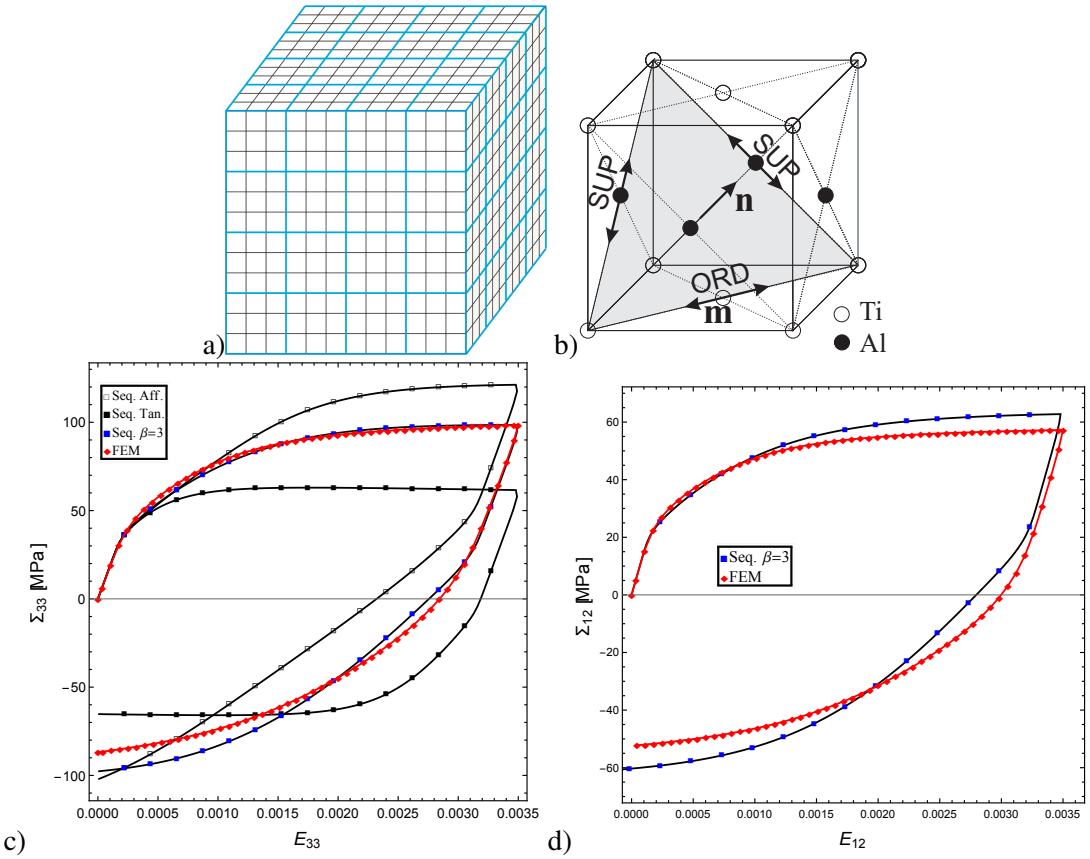

Figure 1: Example of RVE with FE mesh ($N = 64$, $M = 3$) (a); slip systems in γ-TiAl (ORD - ordinary dislocations, SUP - superdislocations) (b); overall response in tension-compression (c) and shear (d) cycle for γ-TiAl aggregate shown in (a) with exponent $n = 8$ in the local power law and an anisotropy factor $\alpha = 5$.

Acknowledgments The research was supported by the project of the National Science Center (NCN) granted by the decision No. 2016/23/B/ST8/03418.

References

[1] K. Kowalczyk-Gajewska. Micromechanical modelling of metals and alloys of high specific strength. *IFTR Reports 1/2011*, pages 1–299, 2011.

[2] K. Kowalczyk-Gajewska. Estimation of overall properties of random polycrystals with the use of invariant decompositions of Hooke's tensor. *Int. J. Solids Struct.*, 49:3022–3037, 2012.

[3] K. Kowalczyk-Gajewska and H. Petryk. Sequential linearization method for viscous/elastic heterogeneous materials. *Eur. J. Mech. Solids/A*, 30:650–664, 2011.

[4] R. Masson and A. Zaoui. Self-consistent estimates of the rate-dependent elasto-plastic behaviour of polycrystalline materials. *J. Mech. Phys. Solids*, 47:1543–1568, 1999.

[5] S. Mercier and A. Molinari. Homogenization of elastic-viscoplastic heterogeneous materials: Self-consistent and Mori-Tanaka schemes. *Int. J. Plast.*, 25:1024–1048, 2009.

[6] C. N. Tomé and R. A. Lebensohn. Manual for Code Visco-Plastic Self-Consistent (VPSC). Version 7b. Technical report, Los Alamos National Laboratory, May 2, 2007.

REGULARIZED LARGE STRAIN ELASTO-PLASTICITY: SIMULATION OF A PROPAGATIVE INSTABILITY

M. Mucha[1], B. Wcisło[1], and J. Pamin[1]

[1]*Institute for Computational Civil Engineering, Cracow University of Technology, Cracow, Poland*

e-mail: MMucha@L5.pk.edu.pl

1. Introduction

Softening of any kind (material, geometrical or thermal) can provoke the occurrence of a localized deformation mode in the form of a neck or a shear band. When a classical continuum description is employed this can involve an excessive mesh sensitivity of simulation results, which is caused by strains tending to localize in the smallest volume admitted by discretization. This pathological effect can be prevented by an upgrade of the constitutive description called regularization, involving either nonlocal averaging, spatial gradient dependence or time rate sensitivity.

The localization zones are often stationary and can lead to failure. On the other hand, one can encounter so-called propagative instabilities [1, 6], i.e. localized patterns which evolve in the loading process. One of such phenomena are Lueders bands, see for instance [3].

In this paper the thermal influences are neglected and attention is focused on phenomenological modelling. Two large strain elasto-plasticity models are used: the first one, presented for instance in [5], is extended towards viscoplasticity, the second one is based on [2] and gradient-dependent. Numerical analysis of a propagative instability of a Lueders type is performed for a two-dimensional configuration in plane strain conditions subjected to imposed tensile deformation [5].

2. Model description

The considered model is based on the multiplicative decomposition of the deformation gradient $\mathbf{F} = \mathbf{F}^e\mathbf{F}^p$. The state of the material is described by the Helmholtz free energy, decoupled additively in elastic and plastic hardening parts $\psi(\mathbf{b}^e, \gamma) = \psi^e(\mathbf{b^e}) + \psi^p(\gamma)$, where $\mathbf{b}^e$ is the elastic left Cauchy-Green tensor and γ is a scalar plastic strain measure.

The plastic process is governed by the yield condition $F_p(\boldsymbol{\tau}, \gamma) = f(\boldsymbol{\tau}) - \sqrt{2/3}\sigma_y(\gamma) \leq 0$. The equivalent stress function $f(\boldsymbol{\tau})$ is a Kirchhoff stress measure (e.g. J_2 Huber-von Mises type) and $\sigma_y(\gamma)$ denotes the yield strength which includes multi-linear strain hardening/softening. To regularize the model either a viscous term $\xi\dot{\gamma}$ is included in σ_y making the model rate-dependent (it is so-called consistency viscoplasticity [6] with viscosity parameter ξ) or isotropic degradation of plastic properties as in [2] is incorporated together with a gradient-enhancement.

3. Implementation and numerical tests

The numerical simulations are performed using symbolic-numerical packages *Ace* in *Wolfram Mathematica* environment [4]. Standard hexahedral elements with linear interpolation of all fields and *F-bar* modification are employed. Special attention is focused on the ability of the models to represent the propagative instability.

The adopted material model parameters are: Young's modulus E = 207 GPa, Poisson's ratio ν = 0.29, initial yield strength σ_{y0} = 450 MPa. For the yield strength softening is initially assumed with H_1=-0.01 E as the equivalent plastic strain grows from 0 to γ_1=0.15, then the yield strength is constant until γ_2=0.3, and hardening with H_2=0.005 E follows.

The dimensions of the plate are: L=0.1 m, S = 0.05 m, H=0.0025 m. To set the position of the incipient shear band a 10% reduction of the yield strength is assumed in one element at the lower left-hand corner of the configuration. The plate extension is specified by factor λ which scales the total imposed elongation of $0.4L$.

Figure 1 shows the diagrams of the sum of reactions versus the imposed elongation for the two regularized models. Figure 2 presents deformed meshes with the distributions of accumulated plastic strain γ. The left plots exhibit shear bands formed due to softening. The right ones show that they broaden and hardening induces a propagation of the plastic front while the plastic zone expands. The process is sensitive to the viscosity and weakly sensitive to the nonlocality present in the gradient model.

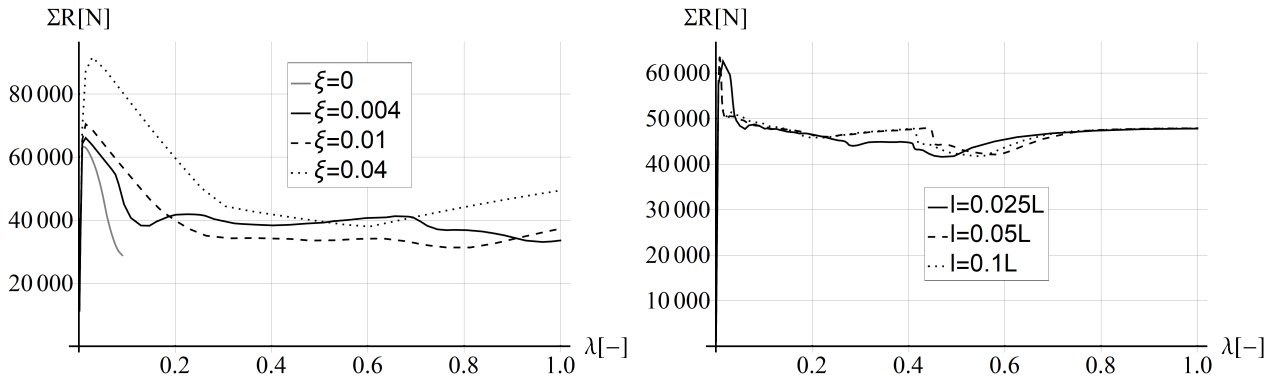

Figure 1: Force-extension diagrams for the viscoplastic model (left, different viscosities) and gradient-dependent model (right, different internal lengths)

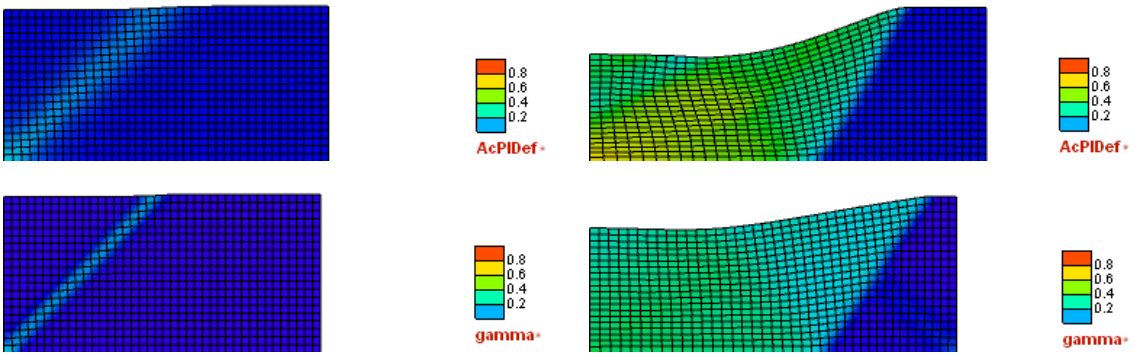

Figure 2: Distributions of equivalent plastic strain: first row - viscoplastic model with ξ=0.004 for two extension values λ = 0.08 (left) and λ = 0.66 (right); second row - gradient-enhanced model with internal length l = $0.1L$ for λ = 0.02 (left) and λ = 0.42 (right)

References

[1] Y. Estrin and L.P. Kubin. *Spatial coupling and propagative plastic instabilities*, chapter 12, pages 395–450. John Wiley & Sons, Chichester, 1995.

[2] M. G. D. Geers. Finite strain logarithmic hyperelasto-plasticity with softening: a strongly non-local implicit gradient framework. *Comput. Methods Appl. Mech. Engrg.*, 193:3377–3401, 2004.

[3] J.F. Hallai and S. Kyriakides. Underlying material response for Lüders-like instabilities. *Int. J. Plasticity*, 47:1–12, 2013.

[4] J. Korelc. Automation of primal and sensitivity analysis of transient coupled problems. *Computational Mechanics*, 44:631–649, 2009.

[5] M. Mucha, B. Wcisło, J. Pamin, and K. Kowalczyk-Gajewska. Instabilities in membrane tension: Parametric study for large strain thermoplasticity. *Arch. Civ. Mech. Eng.*, 18(4):1055–1067, 2018.

[6] W. M. Wang. *Stationary and propagative instabilities in metals - a computational point of view*. Ph.D. dissertation, Delft University of Technology, Delft, 1997.

ON THE INTERPLAY BETWEEN MACROSCOPIC LOCALIZATION AND VOID COALESCENCE FOR STRAIN RATE SENSITIVE MATERIALS

J. Reboul[1], G. Vadillo[1], A. Srivastava[2], S. Osovski [3]

[1]*Department of Continuum Mechanics and Structural Analysis, University Carlos III of Madrid, Leganés, Madrid, Spain*
[2] *Department of Materials Science and Engineering, Texas A&M University, College Station,TX, USA*
[3] *Faculty of Mechanical Engineering, Technion-Israel Institute of Technology, Haifa, Israel*

e-mail: gvadillo@ing.uc3m.es

Abstract

Significant progresses have been made in the last decades on the understanding and modelling of the micromechanics that govern the ductile fracture phenomena in porous metallic materials subjected to complex stress states. Two modes of plastic flow localization commonly occur in the failure of ductile materials. The first is the so-called "macroscopic localization" and occurs when the deformation becomes highly non-uniform and localizes into a thin band. The second one is the so-called coalescence and occurs when nearby microscopic voids interact and merge, leading to the formation of macroscopic cracks.

The question addressed in the present work is whether macroscopic localization occurs prior or after the void coalescence. For that purpose, we have developed an original numerical methodology, based on 3D unitary-cell computations in ABAQUS/Standard [1], to simulate the evolution of a spherical void subjected to complex stress states: predefined triaxiality and Lode parameters which remain fixed during loading. The key and original feature of our investigation, which is based on a previous work of Tekoglu et al. [2], is to consider the strain rate dependence on the flow behavior of the material. We have identified that the viscosity of the material plays a crucial role on both localization modes. Nevertheless, irrespective of the material properties considered, our numerical results have shown that "macroscopic localization" occurs always earlier than "coalescence". The implications and consequences of such behavior will be exposed and discussed.

Numerical results

As is shown in Fig.1, attention is focused to analize a parallelepiped unitary cell that initially contains a spherical void in its center with initial radius R_0.

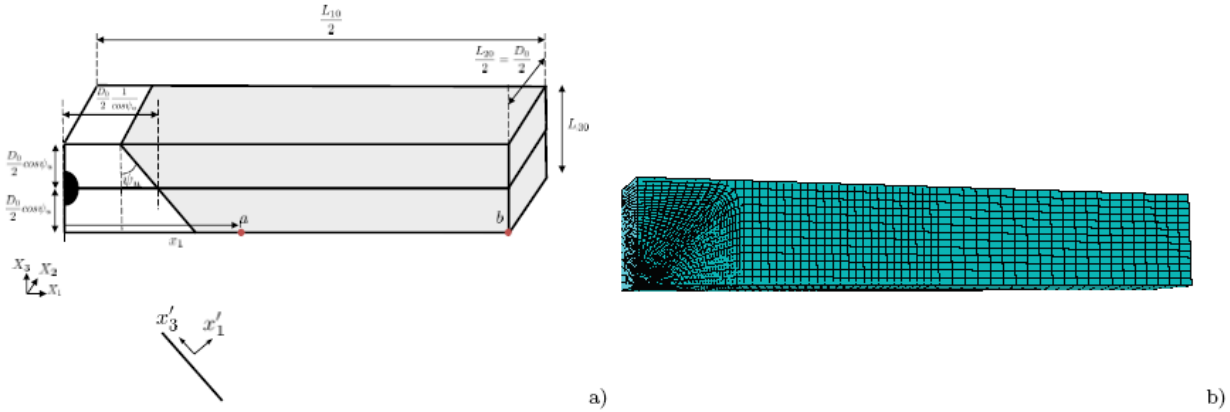

Fig. 1. Squeme of (a fourth) representative volume element used in the simulations. The initial orientation of the voided cell = Ψ^u and his characteristic length = L_0. b) Finite element mesh of the representative element for f0=0.001 and Ψu =0º

The representative volume element was numerically analyzed using the finite element software ABAQUS/Standard [1], wich employs a finite strain J_2 flow theory within and updated Lagrangian formulation to account for large deformations. The chosen material for the analysis follows a power-law type rate hardening formulation defined by:

$$\bar{\sigma} = \begin{cases} E\varepsilon & \varepsilon \leq \varepsilon_0 \\ \sigma_0 \left(1 + \left(\frac{\dot{\varepsilon}^p}{\dot{\varepsilon}_0}\right)^m\right) & \varepsilon > \varepsilon_0 \end{cases}$$

where σ_0 represents a reference yield stress, m the strain rate sensitivity parameter of the material, $\dot{\varepsilon_0}$ a reference strain rate, E the Young modulus and $\varepsilon_0 = \sigma_0/E$. The full set of constants employed in the simulations to define material properties are E=167 GPa, ν=0.3, σ_0=418 MPa, $\dot{\varepsilon_0}$ =1s^{-1} and ε_0= 0.0025. In order to study the relative contribution of the strain rate effect in localization and void colescence, numerical simulations are going to be carried out considering the strain rate parameter m varying within the range of values m=0-0.25.

To exemplify the influence of the strain rate parameter on localization and coalescence behavior, the macroscopic strain in the band E_{eq}^{cb} at the onset of localization and coalescence, are plot in Figs. 2 versus triaxiality T for the different m values considered. The prescribed Lode parameter is L = -1 and the initial porosity is f_0 = 0.001. As can be observed, macroscopic localization and coalescence are strongly affected by m parameter promoting, for every T value tested, a delay of the value of E_{eq}^{cb} where localization and coalescence take place.

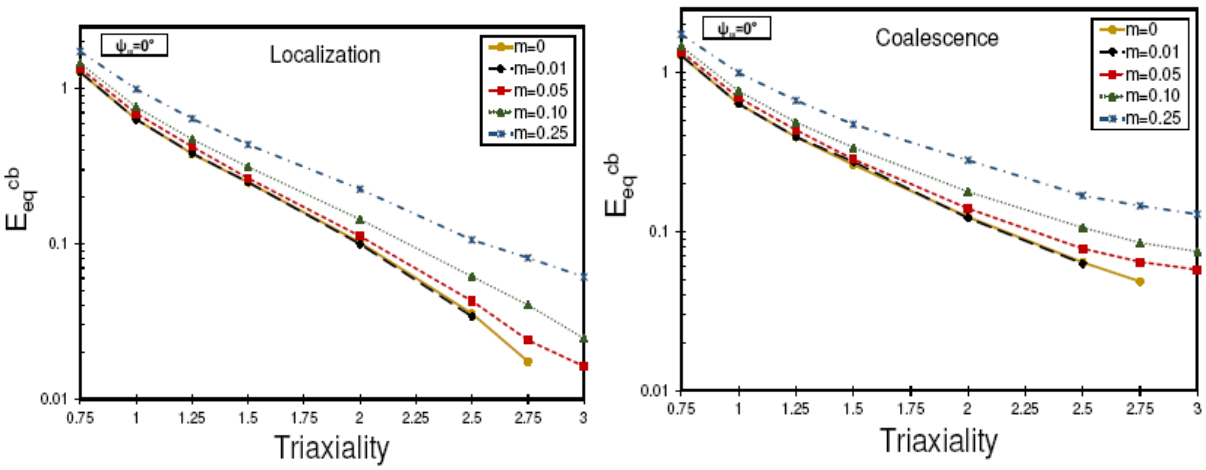

Fig. 2. Critical equivalent strain at the onset of localization and coalescence as a function of triaxiality for strain rate parameters *m* = 0, 0.01,0.05, 0.1 and 0.25.

Acknowledgments The research leading to these results has received funding from the European Union's Horizon2020 Programme (Excellent Science) under REA and ERCEA grant agreements 675602 and 758056 (Projects OUTCOME and PURPOSE).

References

[1] *ABAQUS. 2017 The Abaqus documentation collection, Version 6.17. Providence, RI: Dassault Systèmes*.
[2] Tekoğlu C, Hutchinson J, W,Pardoen T. On localization and void coalescence as a precursor to ductile fracture. Phil.

MODELING OF ANISOTROPIC HARDENING AND GRAIN SIZE EFFECTS BASED ON ADVANCED CRYSTAL PLASTICTIY MODELS

B. Berisha[1], S. Hirsiger[2], H. Hippke[2] and P. Hora[2]

[1]*inspire AG, Institute of Virtual Manufacturing (inspire-ivp), Tannenstrasse 3, Zurich, Switzerland*
[2]*ETH Zurich, Institute of Virtual Manufacturing (ivp), Tannenstrasse 3, Zurich, Switzerland*

e-mail: berisha@inspire.ethz.ch

1. Introduction

The quality of the optimization of metal forming processes strongly depends on material models used. In addition, determination of the model parameters is commonly the most time consuming part and can be very expensive, due to the needed experimental data. As the models are getting more and more complex, the number and complexity of the required experiments is increasing continuously as well. In the sheet metal forming context, these requirements are even more pronounced, because of the anisotropic behavior of the sheet materials. In general, tensile tests in at least three directions, biaxial tests and tension-compression or shear-reverse shear experiments are performed to determine the parameters of the macroscopic models, e.g. the HAH model [1]. Hence, determination of the macroscopic model parameters based on virtual experiments is a very promising strategy to overcome these difficulties and to reduce the number of real experiments to a minium. For this purpose, in the framework of this study, following topics are covered:

- Investigation of the influence of the grain size on the hardening behavior
- Modeling of the Bauschinger effect at the grain level
- Prediction of the anisotropic behavior (yield locus) based on crystal plasticity simulations

2. Material models and numerical modeling techniques

Modeling of the plastic behavior of metals based on crystal plasticity theory is a well-established methodology. However, in general, the computation time is very high and therefore, the computations are restricted to simplified microstructures as well as simple polycrystal models. In the presented work, an efficient coupling of a physically based phenomenological crystal plasticity model - including an implementation of the backstress and grain size effects - and the FFT-spectral solver of the code DAMASK [2] is proposed. For the aluminum alloy AA5356 the influence of the grain size on the yield stress is shown in Figure 1 (left).

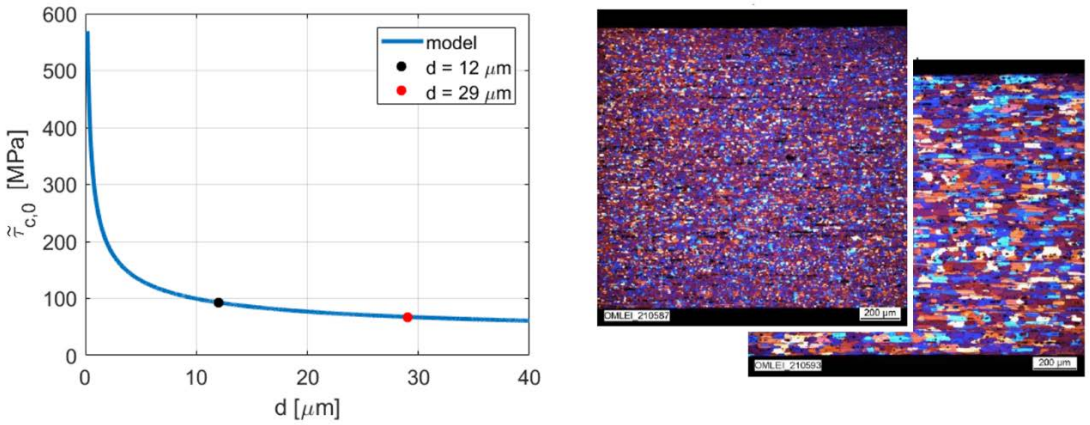

Figure 1: Yield stress as a function of the grain size (left); Micrographs for two different grain sizes: $12\mu m$ and $29\mu m$ (right).

The grain size effect is based on a Hall-Petch relationship. The initial critical resolved shear stress as well as the saturation stress are modified as follows:

(1) $$\tilde{\tau}_{c,0}^{\alpha} = \tau_{c,0}^{\alpha} + k_1 \frac{1}{\sqrt{d}}$$

(2) $$\tilde{\tau}_{sat}^{\alpha} = \tau_{sat}^{\alpha} + k_2 \frac{1}{\sqrt{d}}$$

where d is the grain size and k_1 and k_2 parameters fitted on tensile tests with grain sizes shown in Figure 1. A further aspect considered in this study is the Bauschinger effect. Similar to the macroscopic nonlinear Armstrong-Frederick type, a backstress model (see eq. 3 and 4) at the slip system level is implemented [4] in DAMASK. Predictive capabilities of the model for a tension-compression load case are shown in Figure 2.

(3) $$\dot{\tau}_b^{\alpha} = c\dot{\gamma}^{\alpha} - \eta\left|\dot{\gamma}^{\alpha}\right|\tau_b^{\alpha}$$

(4) $$\dot{\gamma}^{\alpha} = \dot{\gamma}_0^{\alpha}\left|\frac{\tau^{\alpha}-\tau_b^{\alpha}}{\tau_c^{\alpha}}\right|^{\frac{1}{n}} sgn(\tau^{\alpha} - \tau_b^{\alpha})$$

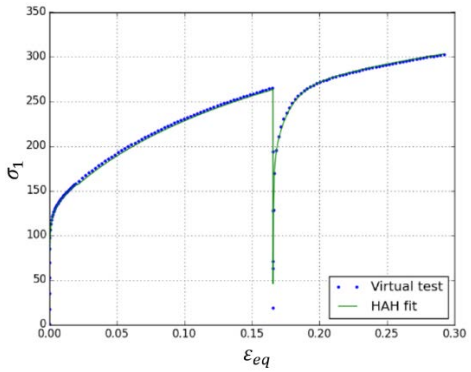

Figure 2: Modeling of the Bauschinger effect for the aluminium alloy AA5182.

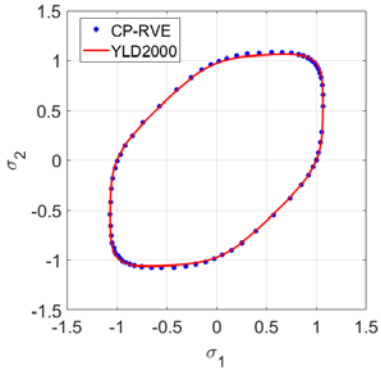

Figure 3: Comparison of the fitted YLD2000-2d model and CP-model prediction for AA6016-T4.

Modeling of the anisotropic behavior based on CP-simulations and the macroscopic model is shown in Figure 3 [4]. In this context it is worthwhile to mention that for the CP-simulations only the yield curve and the ODF has been used to predict the anisotropic behavior, whereas fitting of the YLD2000-2d model on experimental data requires three tensile tests at different directions as well as the equi-biaxial tension test.

3. Conclusions and Outlook

It can be concluded that an efficient coupling of crystal plasticity models and the FFT-spectral solver leads to a significant reduction of the amount of real experiments needed to calibrate macroscopic models. CP-modeling can be used to model anisotropic hardening more accurately by considering the backstress, similar to well-established macroscopic kinematic hardening models. Further, due to the time efficient spectral solver used in the computation of the RVE models, detailed modeling of the microstructure is possible. Performing of experiments with pre-strained material in tension and equi-biaxial stretching are subject of the ongoing work. These experiments will enable a validation of the CP-models for more general loading paths.

References

[1] F. Barlat, J. J. Gracio, M.-G. Lee, E. F. Rauch, and G. Vincze. An alternative to kinematic hardening in classical plasticity. *International Journal of Plasticity*, 27(9):1309-1327, 2011.
[2] F. Roters, P. Eisenlohr, C. Kords, D. Tjahjanto, M. Diehl and D. Raabe. Damask: the Düsseldorf advanced material simulation kit for studying crystal plasticity using an FE based or a spectral solver. *Proc. IUTAM.*, 3:3-10, 2012.
[3] S. Hirsiger, B. Berisha and P. Hora. *Internal report*. Institute of Virtual Manufacturing ETH Zurich, 2017.
[4] H. Zhou. *Master thesis*. Institute of Virtual Manufacturing ETH Zurich, 2016.

Session S05: Computational aspects of solid mechanics

Organizers: O. Allix (LMT, ENS Cachan, France), T. Burczyński (IPPT PAN, Warsaw), P. Kowalczyk (IPPT PAN, Warsaw)

VIBRATIONS OF A DOUBLE-BEAM SYSTEM WITH INTERMEDIATE ELASTIC RESTRAINTS DUE TO A MOVING FORCE

F. Zakęś[1], P. Śniady[1]
[1] *Wroclaw University of Environmental and Life Sciences, Wroclaw, Poland*
e-mail: filip.zakes@upwr.edu.pl, pawel.sniady@upwr.edu.pl

1. Mathematical model and governing equations

We investigate the dynamic behavior of a system of two beams with arbitrary boundary conditions, connected with a number of k elastic restraints of finite stiffness s (see figure 1). Beams can have different flexural rigidity EI, mass density m, damping coefficient c and length L. One of the beams is subjected to a point force of constant magnitude P moving with constant velocity v. Equations of motion describing flexural vibrations $w_I = w(x_I, t)$ and $w_{II} = w(x_{II}, t)$ of the beam I and II have the form:

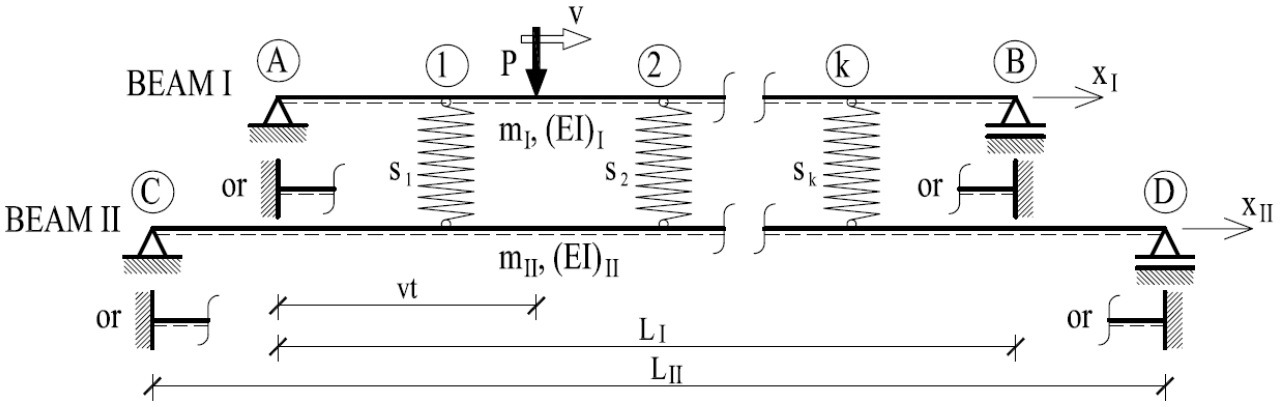

Fig 1. Double-beam system with multiple elastic restraints subjected to a moving force

$$(EI)_I w_I^{IV} + c_I \dot{w}_I + m_I \ddot{w}_I + \sum_{i=1}^{k} s_i [w_I - w_{II}] \delta(x_I - x_{I,i}) = P\delta(x_I - vt) \tag{1}$$

$$(EI)_{II} w_{II}^{IV} + c_{II} \dot{w}_{II} + m_{II} \ddot{w}_{II} + \sum_{i=1}^{k} s_i [w_{II} - w_I] \delta(x_{II} - x_{II,i}) = 0 \tag{2}$$

where roman numerals denote differentiation with respect to spatial coordinates x_I and x_{II} while dots ($\dot{}$) denote differentiation with respect to time t. Symbol $\delta(.)$ denotes the Dirac delta.

In the presented method we replace analyzed structure with two single-span beams. Vibrations of the upper beam can be described as $w_I = w_I^P + \sum_{i=1}^{k} w_I^{Xi}$ while vibrations of the unloaded lower beam are equal to $w_{II} = -\sum_{i=1}^{k} w_{II}^{Xi}$. Expression w_I^P denotes vibrations of the single-span beam due to the given moving force P while expressions w_I^{Xi} and w_{II}^{Xi} are vibrations of the I and II beam resulting from the force $X_i(t)$ in the „i" elastic restraint. Forces $X_i(t)$ can be determined from a set of compatibility equations:

$$w_I^P(x_{I,i}, t) + \sum_{i=1}^{k} w^{Xi}(x_{I,i}, t) + \sum_{i=1}^{k} w^{Xi}(x_{II,i}, t) + \frac{X_i(t)}{s_i} = 0 \tag{3}$$

If we assume that vibrations w_I^{Xi} and w_{II}^{Xi} are presented in the convolution form with use of Duhamel's integral, equation (3) will have the form of the Volterra integral equation of the second order which can be solved numerically applying methods described in [4].

2. Numerical example

Presented example is of a three-span double-beam system (see figure 1). Upper beam is simply supported while the lower beam is clamped on both ends. Beams have the same length $L = 12\ m$, flexural rigidity $EI = 4 \cdot 10^6\ Nm^2$and mass density $m = 25\ kg/m$ and are connected with two elastic restraints of stiffness $s_1 = s_2 = 1 \cdot 10^6\ N/m$. System is subjected to a point force of constant magnitude $P = 1000\ N$ moving on the upper beam with constant velocity $v = 30\ m/s$. In further calculations we analyze dynamic deflections of the middle points at the upper and lower beam (sections "a" and "b"). Results for the both sections are presented on the figure 3.

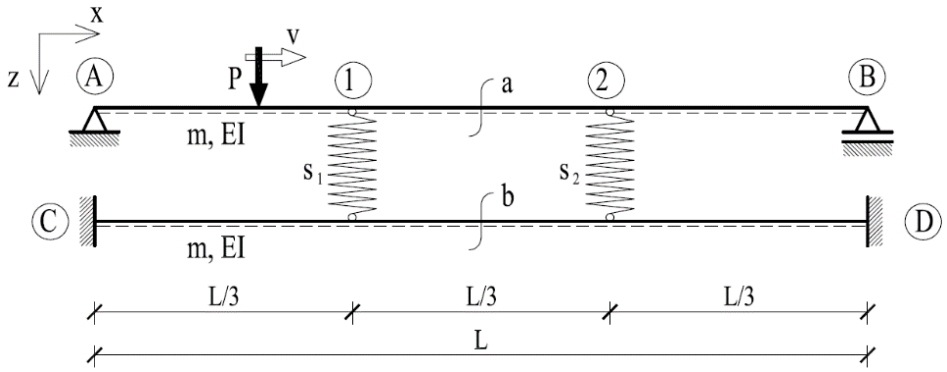

Fig 2. Double-beam system with two elastic restraints

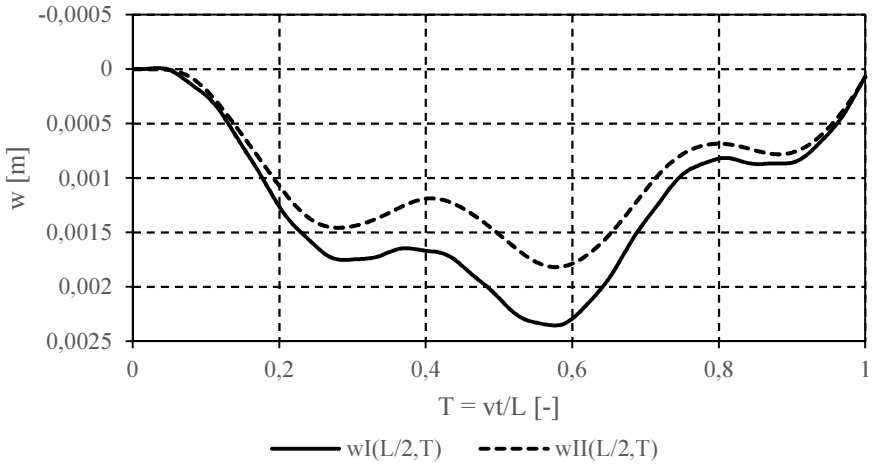

Fig 3. Dynamic deflections of the middle points at the upper and lower beam

3. References

[1] L. Fryba (1999). *Vibrations of solids and structures under moving load*, Telford, London.

[2] M. Abu-Hilal, (2006). Dynamic response of a double Euler-Bernoulli beam due to a moving constant load, *Journal of sound and vibration.*, **297**, 477-491.

[3] Z. Oniszczuk, (2003). Forced transverse vibrations of an elastically connected simply supported double-beam system, *Journal of sound and vibration.*, **264**, 273-286.

[4] F. Zakęś, P.Śniady (2016). Application of Volterra Integral Equations in Dynamics of Multispan Uniform Continuous Beams Subject to a Moving Load, *Shock and vibration*, 1-12.

APPLICATION OF THE MESHLESS MONTE CARLO METHOD WITH RANDOM WALK PROCEDURE TO SELECTED ELLIPTIC PROBLEMS OF MECHANICS

S. Milewski[1]

[1]*Institute for Computational Civil Engineering, Civil Engineering Department, Cracow University of Technology, Cracow, Poland*

e-mail: s.milewski@L5.pk.edu.pl

1. Introduction

This paper is focused on the development of the meshless Monte Carlo (MC) method with the random walk (RW) technique and its application to selected elliptic problems in mechanics. MC belongs to the wide class of probabilistic approaches and is commonly used in a variety of algebraic and differential problems. Its main concept is based upon the performance of series of simulations (trials) with properly defined success trial. Eventually, the number of success trials related to the total number of all trials, scaled by the dimension quantity (area, function value) may be treated as an unbiased estimator of the unknown solution to the considered problem. In this manner, MC combined with the RW technique, allows for a simple and effective estimation of the solution of the Laplace differential equation at selected point(s) of the domain, without a generation of a system of equation, combining all unknown function values [1]. However, the standard MC/RW approach is limited to an analysis of very simple elliptic problems, with essential boundary conditions and a regular mesh of nodes. In order to overcome those drawbacks, the original concept, proposed in this paper, is based upon the application of selected aspects of the meshless finite difference method (MFDM, [2]) to the MC/RW approach. Especially, the classification criteria of nodes into the FD stars as well as the local moving weighted least squares (MWLS, [2, 3]) approximation are taken into account. Therefore, an analysis of a wider class of problems, with more complex geometry, natural boundary conditions, non-homogeneous material and right-hand side functions as well as arbitrarily irregular clouds of nodes, is possible. The proposed meshless MC/RW approach is examined on selected 2D benchmark elliptic problems (torsion of a prismatic bar, stationary heat problem).

2. Standard Monte Carlo with random walk

When the Laplace equation is considered ($\nabla^2 F = 0$ in Ω with $F = \bar{F}$ on $\partial\Omega$), the following solution strategy may be adopted: 1. Select any arbitrary internal point $\mathbf{x}_k$ with unknown function value F_k, which belongs to the regular mesh of nodes (Fig.1a). 2. Randomly choose one of the four equally possible directions (north, east, south, west) and move to the closest node located there. 3. Proceed as long as the first boundary node is reached - note its function value $\bar{F}_i$ and increase its number of hits N_i (equal zero by default) by one. 4. Return to the point of interest $\mathbf{x}_k$ and repeat the entire procedure (1-3) until all N random walks are performed. 5. Estimate the function value F_k as

$$F_k \approx \frac{1}{N} \sum_{i \in \partial\Omega} \bar{F}_i N_i \tag{1}$$

The mathematical proof [1] for the convergence of (1) to the true solution of Laplace problem is based upon the similarity of the stochastic system of equations to the one obtained by the standard finite difference method (FDM).

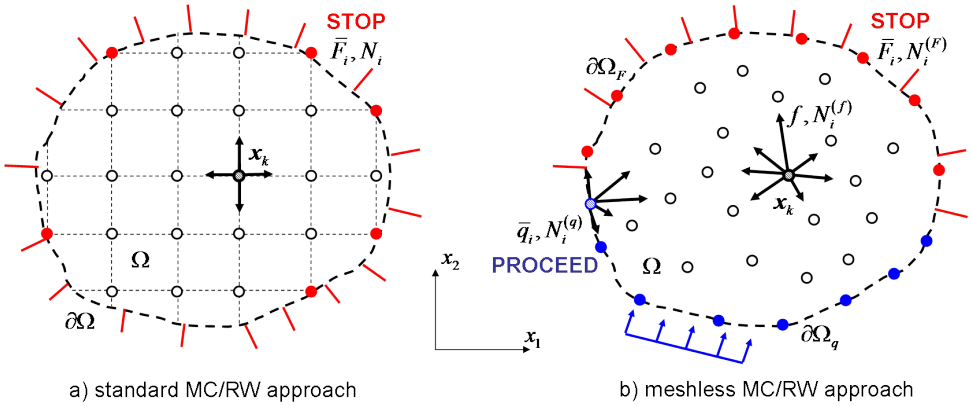

Figure 1: Comparison of the standard MC/RW (a) and the meshless MC/RW (b) concepts

3. Meshless Monte Carlo with random walk

More general elliptic equation is considered ($a\dfrac{\partial^2 F}{\partial x_1^2} + \dfrac{\partial^2 F}{\partial x_2^2} = f$ in Ω with $F = \bar{F}$ on $\partial\Omega_F$ and $\dfrac{\partial F}{\partial n} = \bar{q}$ on $\partial\Omega_q$). Moreover, if the domain Ω has a complex shape, an arbitrary irregular cloud of nodes has to be generated (Fig.1b). In such case, a directions of possible moves from the selected point $\mathbf{x}_k$ may be determined using meshless approach (e.g., FD stars with distance or cross criteria, [2]). Furthermore, selection probabilities depend on the distance between nodes in a FD star and the material function a value. They are found by means of the local MWLS technique [3], taking advantage from the information overload. The random walk terminates when the first boundary node $i \in \partial\Omega_F$ is reached. However, it continues for all internal and boundary nodes $i \in \partial\Omega_q$. The final meshless MC/RW formula combines all a-priori known information ($a, \bar{F}, f, \bar{q}$) as well as numbers of nodal hits N_i^F, N_i^f, N_i^q, determined in a stochastic manner, according to the MC concept.

4. Numerical examples

A variety of problems has been solved by the proposed MC/RW approach. Both regular meshes and strongly irregular clouds of nodes are investigated. Accuracy of solution and solution derivatives is taken into account. Solution convergence is terms of random walk number is examined. The most interesting up-to-date examples will be presented during the Conference.

5. Final remarks

Though obtained results are very promising, the method is still under current development. 2D+time (non-stationary), 3D as well as non-linear problems are planned as the following research stage. Additionally, the optimal balance between the number of walks N, and the number of nodes n needs to be determined.

Acknowledgments This research was supported by the National Science Centre, Poland, under the scientific project 2015/19/D/ST8/00816 (*Computational coupled FEM/meshless FDM analysis dedicated to engineering nonstationary thermo-elastic and thermoplastic problems*)

References

[1] J.F. Reynolds, A Proof of the Random-Walk Method for Solving Laplace's Equation in 2-D, The Mathematical Gazette, 49(370):416-420, Mathematical Association, 1965.

[2] S. Milewski, Meshless Finite Difference Method with Higher Order Approximation - Applications in Mechanics, Archives of Computational Methods in Engineering, 19(1):1-49, Springer, 2012.

[3] P. Lancaster, K. Salkauskas, Curve and surface fitting, Academic Press Inc, 1990.

A UNIFIED APPROACH TO ADAPTVE MODELLING AND SIMULATION IN COUPLED AND SOLID MECHANICS PROBLEMS

G. Zboiński[1,2]

[1]*Institute of Fluid Flow Machinery of the Polish Academy of Sciences, 14 Fiszera Street, Gdańsk, Poland*
[2]*Faculty of Technical Sciences of University of Warmia and Mazury, 10 Oczapowskiego Street, Olsztyn, Poland*

e-mail: zboi@imp.gda.pl

1. Introduction

The main goal of this paper is to present some compuational technology for the adaptive analysis of the problems of solid mechanics and the coupled problems as well. The adaptation concerns both the modelling and solution of the problems. The main feature of the presented methodology is its unifying character, which means that the same methods are applied to hierarchical modelling and hierarchical approximations of the problems under consideration. Furthermore, the analogous a priori error estimation methods, serving the same a posteriori error estimation algorithms and analogous adaptivity control schemes, are applied to the mentioned problems.

The presented methodology is assigned for complex problems in which three types of complexity are allowed. The physical complexity consists in the possibility to consider the coupled problems where the fields of various physical character are analysed together. The geometrical complexity lies in the possibility to apply structures or domains composed of different geometrical parts, i.e. solid parts, thin- or thick-walled symmetric-thickness members, and transition parts as well. Finally, the model complexity is related to the possible application of more than one mathematical model for the decription of the uncoupled physical phenomenon or coupled physical phenomena under consideration regardless of the division of the structure or domain into geometrical parts. In this paper the expemplification of the approach includes the uncoupled problems of elasticity and dielectricity and the coupled problem of piezoelectricity.

2. State-of-the-art issues

The 3D-based hierarchical models considered here conform to the primal displacement variational formulation. Such models were proposed first in the initiating work [3] concerning shell structures. The models were generalized in [11] for a wider class of 3D-based elastic theories. The a priori error estimation method for the modelling error is based on the general dimensional reduction method of [1,2], exemplified by the conventional shell models [6]. The a priori error estimation for the approximation error is based on the general considerations for the hp-approximations of the elliptic problems. The a posteriori error estimation takes advantage of the equilibrated residual method, elaborated for the approximation error in the uncoupled elliptic problems [8]. The method was applied to 3D-elasticity in [5] and the conventional hierarchical shell models in [7]. The method was also adopted for the 3D-based elastic models in [12]. The adaptivity control method uses the three-step strategy [4]. Such an adaptive strategy was used for the conventional plate- and shell-like structures in [7]. The method was extended to the 3D-based complex elastic structeres in [12].

Application of the above mentioned methods to dielectricity and piezoelectricty is less common. Hierarchical models of dielectrics and piezoelectrics were elaborated in [9] up to the fourth order for the case of the mixed variational formulation. The 3D-based models within the primal variational formulations were presented in [13, 14]. Therein, also the hierarchical approximations, analogous to the elasticity case, were proposed. The a priori modelling error estimation for the case of dielectricity were performed in the unpublished work of this author. The a priori approximation error estimation can be based on the general considerations concerning elliptic problems. The a posteriori error estimation and adaptivity control algorithms based on the equilibrated residual methods for the cases of dielectricity and piezoelectricity were introduced in [13, 14]. The same works include also the three-step adaptivity control algorithms for both the cases. The alternative way of adaptivity control for the case of piezoelectricity can be found in [10].

3. Findings and attainments of the research

The following novely elements are presented in the paper. The idea of the 3D-based hierarchy of models of linear elasticity, including 3D-elasticity, first- and higher-order hierarchical shell models, and solid-to-shell transition models, has been adopted for dielectricity. The hierarchy of 3D-based dielelectric models consists of the 3D-dielectricity model and the hierarchical symmetric-thickness models of dielectricty. In the case of the piezoelectricity, both hierachies are applied in such a way that any combination of the elastic and dielectric models is possible. As far as the hierachical hp-approximations are concerned, the same hierarchical shape functions, constrained approximations, and transition approximations as well, have been applied to the above elastic, dielectric and piezoelectric hierarchies of models. Furthermore, for any of three media, the hierachies of the corresponding models have been combined with the related hierarchical approximations. This way, three hierarchies of numerical models of elasticity, dielectricity, and piezoelectricity have been generated.

In the case of the a priori error estimation, the existing results for elasticity have been extended onto dielelectricty. The a posteriori error estimation methods, based on the equilibrated residual method applied earlier to both conventional and 3D-based models, have been applied to the 3D-based models of the uncoupled dielectricity and 3D-based models of the coupled piezoelectricity. The related algorithms for the splitting functions determination and for solution of the local problems have been elaborated and theoretically substantiated.

The methods of model- and hp-adaptivity control based on the three-step strategy have been extended to the complex problems where the physical, geometrical and model complexity may appear. The methods cover elastic, dielectric and piezoelectric problems, and their electro-mechanical combinations as well.

Acknowledgments The author acknowledges the partial financial support of the Scientific Research Commettee (now the National Science Center) under the research grant no. N N504 5153 040.

References

[1] M. Vogelius and I. Babuška (1981). On a dimensional-reduction method; I. The optimal selection of basis functions, *Math. Comput.*, **37**(155), 31-46.

[2] M. Vogelius and I. Babuška (1981). On a dimensional-reduction method; II. Some approximation-theoretic results, *Math. Comput.*, **37**(155), 47-68.

[3] B. A. Szabó and G. J. Sahrmann (1988). Hierarchic plate and shell models based on p-extension, *Int. J. Numer. Meth. Engng.*, **26**, 1855-1881.

[4] J. T. Oden (1993). Error estimation and control in computational fluid dynamics: The O. C. Zienkiewicz lecture. In: *Proc. Math. of Finite Elements (MAFELAP VIII)*. Brunel University, Uxbridge, 1-36.

[5] M. Ainsworth, J. T. Oden and W. Wu (1994). A posteriori error estimation for hp approximation in elastostatics, *Appl. Numer. Math.*, **14**, 23-55.

[6] J. R. Cho and J. T. Oden (1996). A posteriori modelling error estimates of hierarchical models for elasticity problems for plate- and shell-like structures, *Mathl. Comput. Modelling*, 23(10), 117-133.

[7] J. T. Oden and J. R. Cho (1996). Adaptive hpq finite element methods of hierarchical models for plate- and shell-like structures, *Comput. Methods Appl. Mech. Engrg.*, **136**, 317-345.

[8] M. Ainsworth, J. T. Oden (2000). *A posteriori error estimation in finite element analysis*, Wiley, New York.

[9] E. Carrera, M. Boscolo and A. Robaldo (2007). Hierarchic multilayered plate elements for coupled multifield problems of piezoelectric adaptive structures: Formulation and numerical assessment, *Arch. Comput. Methods Engng.*, **14**(4), 384-430.

[10] C. Vokas and M. Kasper (2010). Adaptation in coupled problems. *Int. J. Comput. Math. Electr. Electronic Engng.*, **29**(6), 1626-1641.

[11] G. Zboiński (2010). Adaptive hpq finite element methods for the analysis of 3D-based models of complex structures: Part 1. Hierarchical modeling and approximations, *Comput. Methods Appl. Mech. Engrg.*, **199**, 2913-2940.

[12] G. Zboiński (2013). Adaptive hpq finite element methods for the analysis of 3D-based models of complex structures: Part 2. A posteriori error estimation, *Comput. Methods Appl. Mech. Engrg.*, **267**, 531-565.

[13] G. Zboiński (2016). Problems of hierarchical modelling and hp-adaptive finite element analysis in elasticity, dielectricity and piezoelectricity. In: *Perusal of the Finite Element Method*, R. Petrova, ed., InTech, Rijeka, ch. 1, 1-29.

[14] G. Zboiński (2018). Adaptive modelling and simulation of elastic, dielectric and piezoelectric problems. In: *Finite Element Method – Simulation, Numerical Analysis and Solution Techniques*, R. Pacurar, ed., InTech, Rijeka, ch. 7, 157-192.

A CASE-BASED REASONING APPROACH FOR DESIGN OF TAILORED FORMING HYBRID MATERIAL COMPONENT

R. Siqueira[1], M. Bibani[1], R. Lachmayer[1] and I. Mozgova[1]

[1]*Intitute for Product Development, Leibniz University, Hannover, Germany*
e-mail: siqueira@ipeg.uni-hannover.de

1. Introduction

The development of new manufacturing technologies with new application possibilities requires components with properties more and more specific, being a challenge to design methodologies. One of these new technologies is Tailored Forming, which presents a process chain for the manufacture of hybrid components, aim of the Collaborative Research Project (CRC) 1153 established at the Leibniz University of Hannover [1]. This CRC has as main focus the study of the manufacturing process to join different metals, producing results that are mostly not optimal for the design point-of-view. Furthermore, the design stage has to consider all the strong manufacturing limitations involved at the same time that offers new optimized solutions. For that, an adaptive design process has to be developed, so that the manufacturing constraints are learned and new solutions are generated.

2. Method

The objective of the present study is to develop a systematic design method for Tailored Forming that can combine the manufacturing experience obtained with Computed Aided Engineering (CAE) approaches. The method here proposed is based on a Case-based Reasoning (CBR) [2]. However, two distinct features are implemented in the retrieve step: a parametric design and a geometry similarity analysis. In the first one, it is created a parametric analysis framework that generates a large simulated case-base. Here is where the best solution is searched based on user requirements. Since Tailored Forming is a technology still in research, the results collected in this first stage present also valuable information for the actual development course. The second part, the geometry similarity, is a comparison of this simulated case-base with a second case-base that consist on real results, manufactured and tested. The level of similarity performed in this step provides information about the manufacturability of the simulated geometries. Figure 1 presents the whole CBR cycle, showing the proposed model for the Retrieve phase.

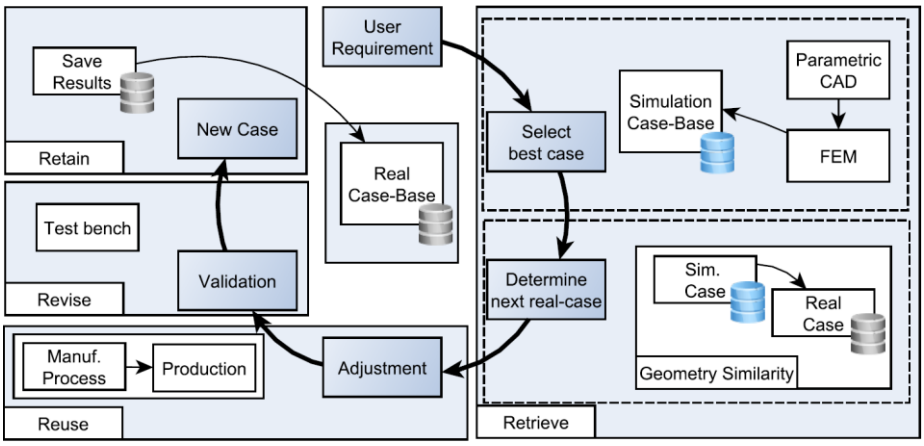

Figure 1. Diagram showing the proposed CBR.

To the end user, a mixed database is available, with simulated and real results. The best solutions are found according to user requirements in the simulated one, i.e. mechanical properties. Then, through the geometry similarity with the real cases, the results will be measured by the potential for manufacturing. So, by

selecting a certain degree of manufacturability, the user will be able to find new improved solutions that are not so different from the current ones, but present improved performance. With all this collected information, the manufacturing process properties can be adjusted and validated, in order to generate new improved solutions that will be saved as a new case in the real case-base. The present study, however, focus on the method in the retrieve step, not getting into details with the manufacturing and validation side of the process.

3. Application Example

As application example of the method we take a hybrid shaft that is made of Steel and Aluminium, which is one of the demonstrators of the CRC 1153. The parametric generation system was implemented using the softwares Autodesk Inventor (2017) and Abaqus CAE (2014). Since the focus here is the performance of the connection zone, only this zone was parametrized. The CAD files with variated parameters were then submitted to a FE analysis, saving all the results in our simulated case-base. The parametric description is a critical step in the process, since it has to cover a large solution space and include the current real geometries.

Parallel, the cases already manufactured were saved in the real case-base, with all manufacturing parameters. With that, the CBR was ready to be started by the user, which may select specific or minimal properties as requirements. In Figure 2, we present the results for a case where the user requirement is the minimization of the maximal stress at the joining zone. Firstly, the geometry with the best solution was found. Next, we use Euclidian distance to find the most similar real geometry. All this information is then forward to the manufacturing side of the process, where the CBR cycle continues.

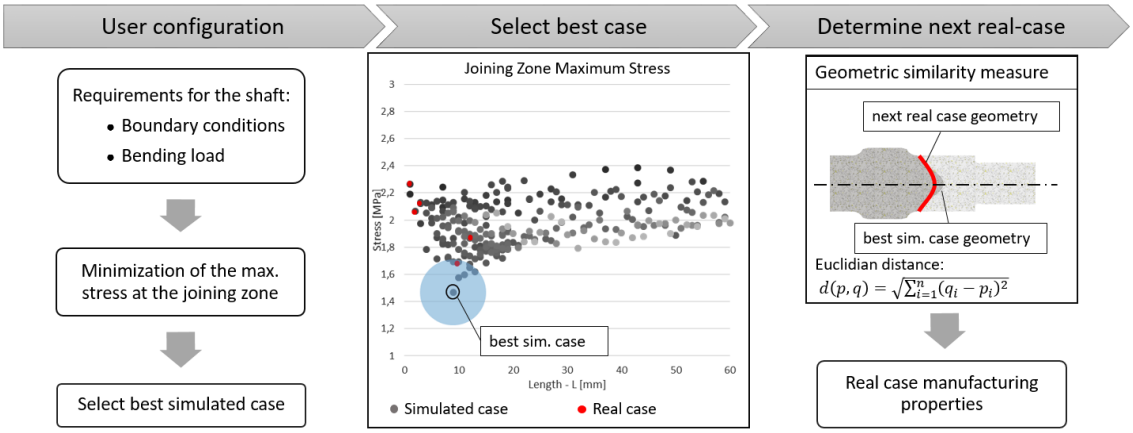

Figure 2: Implementation results until the retrieve phase for the hybrid shaft.

4. Conclusions

The method proposed in this study serve as tool not only for the current development of Tailored Forming, but also for industrial applications. The use of a simulated case-base has a positive impact on the initial research, since it measures the influence of each parameter on the design. The use of a real case-base in conjunction with the simulated one works as an efficient tool for the machine learning process. The proposed retrieve model is able to provide relevant knowledge for the next step of CBR, performed by the manufacturing side of the process. Thereby, the presented model can be here defined as a learning tool of the manufacturing restrictions, bringing new possibilities for the development of new technologies.

Acknowledgments The authors thank the German Research Foundation (DFG) and the CRC 1153 for its support.

References

[1] SFB 1153, Prozesskette zur Herstellung hybrider Hochleistungsbauteile durch Tailored Forming. [online] Leibniz Universität Hannover. Available at: https://www.sfb1153.uni-hannover.de/sfb1153.html (accessed 09.04.2018).
[2] Richter, Michael M., Weber, Rosina O., *Case-based reasoning*, Springer, 2016

THREE DIMENSIONAL REISSNER BEAM WITH NON-LINEAR CONTACT BETWEEN LAYERS

D. Lolić[1], M. Brojan[1], and D. Zupan[2]

[1] *University of Ljubljana, Faculty of Mechanical Engineering, Slovenia*
[2] *University of Ljubljana, Faculty of Civil and Geodetic Engineering, Slovenia*

e-mail: damjan.lolic@fs.uni-lj.si

1. Introduction

In this contribution, an initially curved composite Reissner beam is considered, [2]. The proposed numerical model enables simulations of arbitrary contact between laminae, modelled as a distributed load as a function of displacements. Delaminations of any size and direction can be simulated. We use quaternions for parametrization of rotations [4]. Rotation of an arbitrary vector using quaternion can be expressed as $\overline{a} = \hat{q} \circ \hat{a} \circ \hat{q}^* = \Phi_L(\hat{q})\, \Phi_R(\hat{q}^*)\hat{a} = Q(\hat{q})\hat{a}$. We use Q to denote the 4×4 rotational matrix.

2. Formulation

A three-dimensional beam element is uniquely described by the position vector $r_g(x)$ of the beam centroid axis and the orthonormal base vectors $G_1(x)$, $G_2(x)$, $G_3(x)$, where G_2 and G_3 span the plane of its cross-section and G_1 is its normal vector. Parameter $x \in [0, L]$ is the arc-length of elements centroid axis. We assume that the cross-sections are rigid and conserve their shape during deformation. Another set of fixed orthonormal vectors g_1, g_2, g_3 define physical space from reference point $\mathcal{O}$ of global coordinate system X, Y, Z, Figure 1.

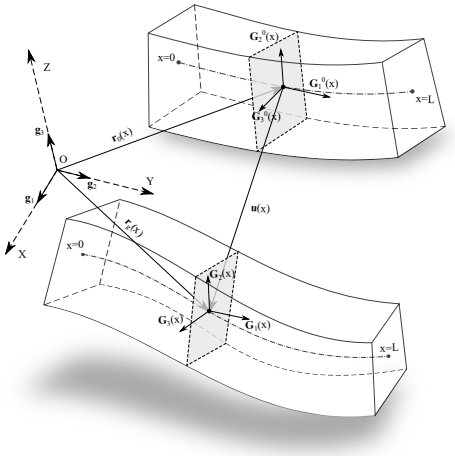

Figure 1: Undeformed and deformed arbitrary beam element in space.

The equilibrium equations of an element of a beam are given by the following set of differential equations:

$$N_g'(x) + n_g(x) - k\, r_g(x) = 0, \tag{1}$$

$$M_g'(x) + r_g'(x) \times N_g(x) + m_g(x) = 0. \tag{2}$$

The force $N_g(x)$ and the moment $M_g(x)$ stress resultants depend on the external distributed force and moment vectors $n_g(x)$ and $m_g(x)$, respectively, both measured per unit of the undeformed length of the axis. We add to this formulation a distributed contact force $k = \text{diag}\,[k_x, k_y, k_z]$ to model general nonlinear behavior between the beam and the foundation or bonds between adjacent layers in composite beams.

Constitutive equations describe a connection of stress resultants with strain vectors γ_G and κ_G. The translational strain vector γ_g is expressed with respect to global basis and rotational strain vector κ_G with respect to material basis. Both are assumed constant throughout the length of the finite element of the beam, as in Refs. [1], [3],

$$\gamma_g = [\hat{q} \circ \hat{\gamma}_G \circ \hat{q}^*] = r'_g + c_g, \tag{3}$$

$$\hat{\kappa}_G = 2\hat{q}^* \circ \hat{q}' + \hat{d}_G, \tag{4}$$

where c_G and d_G are constants, given in the initial configuration. System of equations is constructed with constitutive, equilibrium, kinematic equations and boundary conditions.

Solution of a linearized system $K^{[n]}\delta y = -f^{[n]}$ in each step results in a vector of corrections $\delta y = \left[\delta r_g^0, \delta\hat{q}^0, \delta r_g^L, \delta\hat{q}^L, \delta N_g^0, \delta M_g^0, \delta\gamma_g, \delta\kappa_g\right]^T$. Update procedure for rotational quaternions requires special attention. Calculated correction rotational quaternion $\delta\hat{q}$ will be used to obtain multiplicative incremental rotational quaternion $\Delta\hat{q}^p = \cos(\delta\hat{q}^p \circ \hat{q}^{*p}) + \frac{[\delta\hat{q}^p \circ \hat{q}^{*p}]_{\mathbb{R}^3}}{|\delta\hat{q}^p \circ \hat{q}^{*p}|}\sin(\delta\hat{q}^p \circ \hat{q}^{*p})$, that is combined with the current rotational quaternion as $\hat{q}^{p[n+1]} = \Delta\hat{q}^p \circ \hat{q}^{p[n]}$.

3. Numerical example

We solved several examples and compared results with other authors to confirm the accuracy of our procedure. Here, we present an example from an adhesive shear stiffness test.

Adhesive stiffness is described with hyperbolic tangent function of spatial distance between two FE. To simulate shear test, two beams are held together by an adhesive and then pulled apart while measuring the force. Sketch of the test and the stiffness function is shown in Figure 2. Simulation results are shown as a relation between force and displacement of both beams. It is evident how beams return to initial configuration after the bond breaks, since only elastic deformation is considered.

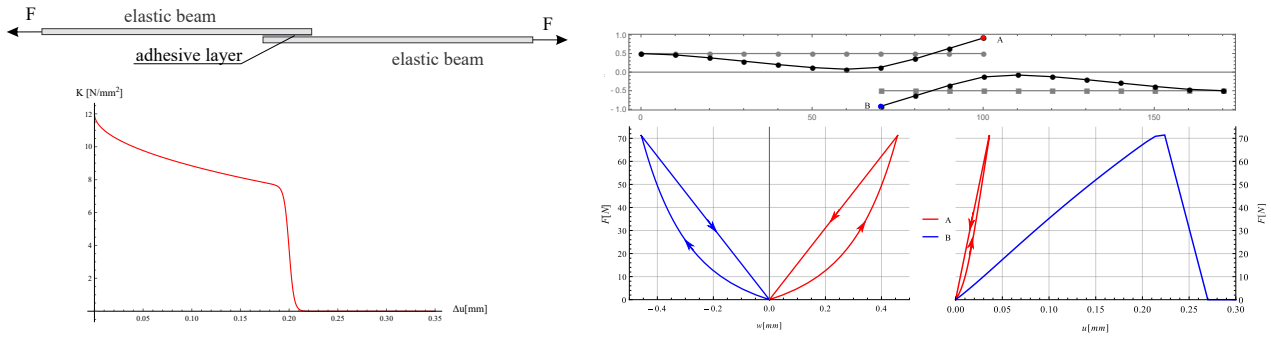

Figure 2: Shear test of two beams connected by adhesive with defined properties.

References

[1] P Češarek, M Saje, and D Zupan. Kinematically exact curved and twisted strain-based beam. *International Journal of Solids and Structures*, 49(13):1802–1817, 2012.

[2] Eric Reissner. On one-dimensional finite-strain beam theory: the plane problem. *Zeitschrift für angewandte Mathematik und Physik ZAMP*, 23(5):795–804, 1972.

[3] Dejan Zupan and Miran Saje. Finite-element formulation of geometrically exact three-dimensional beam theories based on interpolation of strain measures. *Computer Methods in Applied Mechanics and Engineering*, 192(49):5209–5248, 2003.

[4] Eva Zupan, Miran Saje, and Dejan Zupan. The quaternion-based three-dimensional beam theory. *Computer methods in applied mechanics and engineering*, 198(49):3944–3956, 2009.

PRELIMINARY EFFICIENCY ANALYSIS OF ANN MODELLING OF COMPRESSIVE BEHAVIOUR OF METAL SPONGES

A. M. Stręk[1], M. Dudzik[2], A. Kwiecień[1], K. Wańczyk[3], and B. Lipowska[4]

[1]*Cracow University of Technology, Faculty of Civil Engineering, Institute of Structural Mechanics, ul. Warszawska 24, 31-155 Krakow, Poland*

[2]*Cracow University of Technology, Faculty of Electrical and Computer Engineering, Department of Traction and Traffic Control, ul. Warszawska 24, 31-155 Krakow, Poland*

[3]*Foundry Research Institute, Center for Design and Prototyping, ul. Zakopiańska 73, 30-418 Krakow, Poland*

[4]*Institute of Ceramics and Building Materials, Refractory Materials Division in Gliwice, ul. Toszecka 99, 44-100 Gliwice, Poland*

e-mail: anna.strek@pk.edu.pl

1. General

Porous metallic materials are one of the most interesting class of modern engineering materials, which find applications in a wide range of fields, like: medicine (implants), transportation (plane coatings, car bumpers), energy industry (batteries) etc [1]. Depending on the type of porosity, they can be classified to different subgroups, e.g. open-cellulars, closed-cell metallic materials, gasars, sponges (open irregular porosity) and others [2]. The authors would like to present here a study on open-cell aluminium.

The material was produced in own laboratories and its properties were investigated in uniaxial compression experiments. An ANN analysis was performed in attempt to modelling of the compressive behaviour of own aluminium open-cell material.

2. The material and uniaxial compression tests

The material was not bought from an external supplier, but was self-produced [3]. The parameters of the production method were calibrated in course of the manufacturing, so there were two sample groups obtained: the prototype group (with some minor structural imperfections and generally larger relative densities) and the regular group (without structural mistakes, with smaller relative densities). Both groups were then subjected to uniaxial compression [3–5]. The experiments showed that compressive response was related to samples' density (Fig. 1).

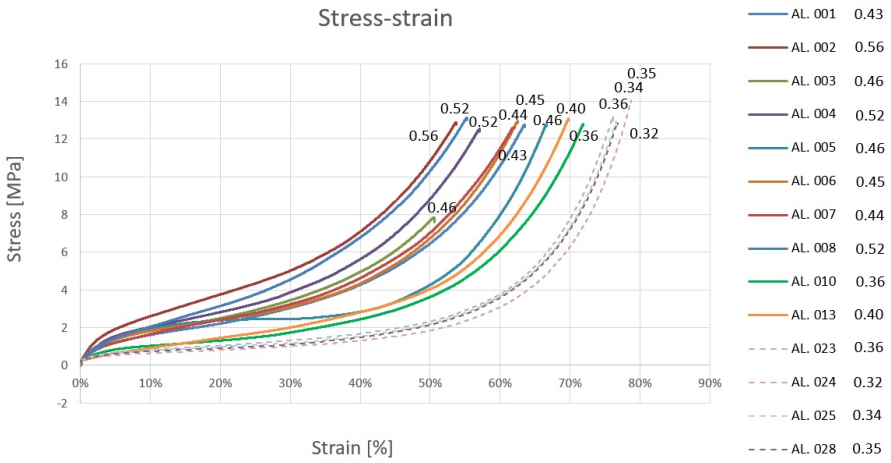

Figure 1: Stress-strain diagram for open-cell aluminium samples (the numbers by plots are relative densities in [g/cm^3]).

3. The ANN analysis

The computational analysis aimed at modelling of the aluminium sponge compressive response with relation to its density. The method chosen was an artificial neural network analysis [6, 7].

The calculations were performed using Matlab R2011B version. All data were taken from the conveyed uniaxial tests for all samples for the range $\sigma = 0 \div \sim 3$ [MPa]. The input data for the ANN analysis were in this case pairs of numbers for each sample: strain and density. The output was the stress. Measurement data processing was performed using a two-layer feedforward neural network implemented in Matlab environment. The first layer was the hidden layer, the second was the output layer. In detail, the ANN procedure consisted of training, validation and test.

Fig. 2 depicts the created neural network structure. It had one hidden layer consisting of 3 neurons; there were no delays implemented on the input for this layer. The activation function for the hidden layer was tangensoidal (tansig). The output layer had a linear activation function. The obtained results showed that the assumed neural network is capable of modelling of the compressive behaviour of the given material with relation to its density for the assumed stress range: the obtained regression for all data was R=0.966. The regression chart and the histogram error plot are presented below (Fig. 3).

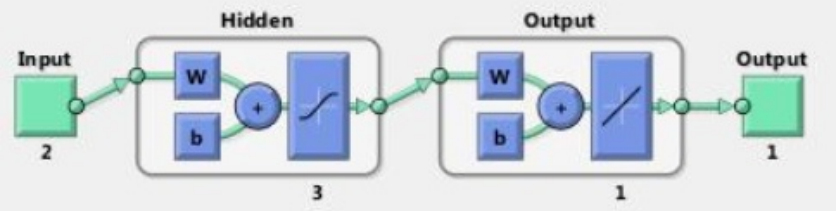

Figure 2: ANN structure.

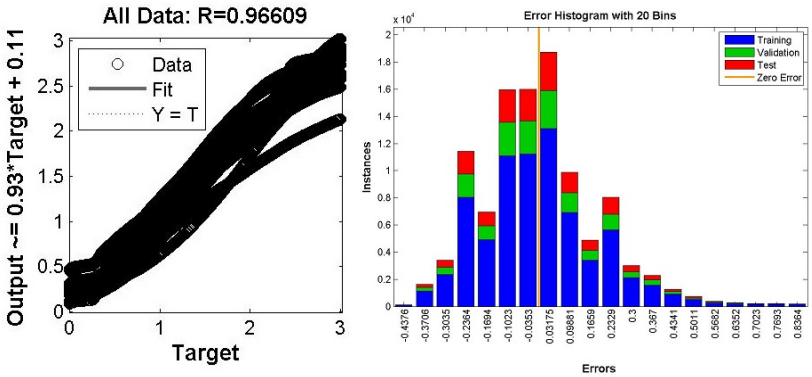

Figure 3: Regression and error histogram for the ANN.

References

[1] H. Degischer and B. Kriszt. *Handbook of cellular metals: production, processing, applications*. Wiley-VCH, 2002.
[2] J. Sobczak, A. Wojciechowski, L. Boyko, L. Drenchev, P. Darłak and P. Dudek. *Materiały wysokoporowate*. Instytut Odlewnictwa, Kraków, 2005.
[3] A. M. Stręk. *Ocena właściwości wytrzymałościowych i funkcjonalnych materiałów komórkowych*. Doctoral thesis, AGH, Kraków, 2017.
[4] ISO 13314:2011 *Mechanical testing of metals — Ductility testing -– Compression test for porous and cellular metals*.
[5] DIN 50134:2008-10 *Prüfung von metallischen Werkstoffen – Druckversuch an metallischen zellularen Werkstoffen*.
[6] R. Tadeusiewicz. *Sieci neuronowe*. Akademicka Oficyna Wydaw. RM, Kraków 1992.
[7] *Matlab documentation.*

A finite element formulation in boundary representation for the analysis of heterogeneous structures

S. Klinkel[1] and R. Reichel[1]

[1]*Chair of Structural Analysis and Dynamics, RWTH-Aachen University, Mies-van-der-Rohe-Str. 1, Aachen, Germany*

e-mail: klinkel@lbb.rwth-aachen.de

1. Introduction

The contribution is concerned with a numerical element formulation in boundary representation. It results in a polynomial element description with an arbitrary number of nodes on the boundary. Scaling the boundary description determines the interior domain. The scaling approach is adopted form the so-called scaled boundary finite element method (SB-FEM). The SB-FEM is a semi-analytical formulation to analyze problems in linear elasticity, see [1]. Within this method, the basic idea is to scale the boundary with respect to a scaling center. The boundary denoted as circumferential direction and the scaling direction span the parameter space. In the present approach, interpolations in scaling direction and circumferential direction are introduced. The interpolation in circumferential direction is independent of the scaling direction. The formulation is suitable to analyze problems in non-linear solid mechanics. The displacement degrees of freedom are located at the nodes on the boundary and in the interior element domain. The degrees of freedom located at the interior domain are eliminated by static condensation, which leads to a polygonal finite element formulation with an arbitrary number of nodes on the boundary. The element formulation allows per definition for Voronoi meshes and quadtree mesh generation, see [2]. The present approach considers a quadtree mesh to model the heterogeneous structure. The heterogeneous structure includes voids and inclusions located in the interior domain. Curved intersection boundaries are modeled by using a special trimming algorithm. It avoids also staircase approximation of curved boundaries. Numerical examples give rise to the performance of the present approach in comparison to other polygonal element formulations, like the virtual element method (VEM). Some benchmark tests show the capability of the element formulation and a comparison to standard and mixed element formulations is presented.

2. Numerical example

The example is concerned with an heterogenous version of the Cook's membrane. The membrane is bounded by the polygon with the (x,y) tuple: (0mm; 0mm); (48mm; 44mm); (48mm; 60mm); (0mm; 44mm), see Fig.1.

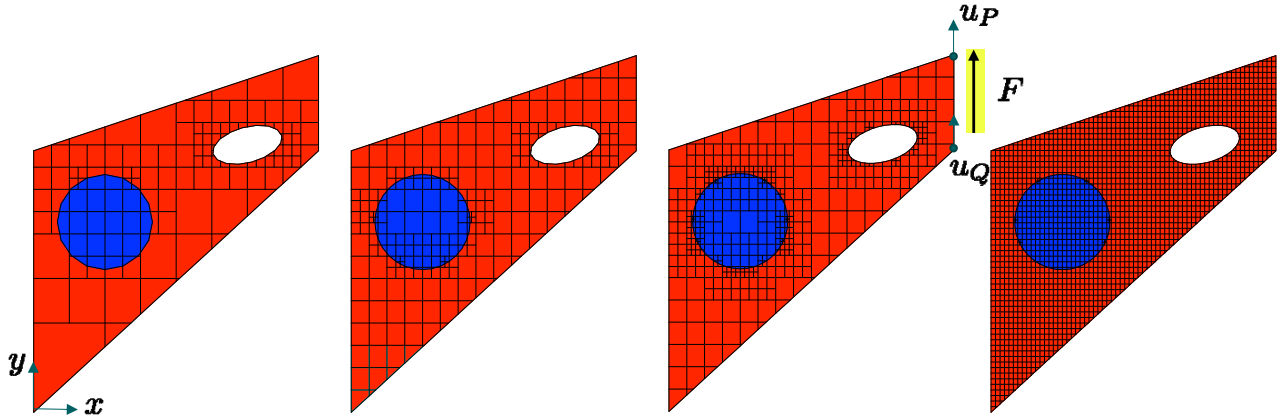

Figure 1: The Cook's membrane with an inclusion and a void. The color red denotes the Neo-Hooke material, blue the St. Venant-Kirchhoff material. The structure is modeled by different quadtree meshes.

The material is described by an Neo-Hook material model, defined with the strain energy function $\Psi = \frac{\mu}{2}(\mathrm{tr}\boldsymbol{F}^{\mathrm{T}}\boldsymbol{F} - 1) - \mu \ln(\mathrm{J}) + \frac{\Lambda}{4}(\mathrm{J}^2 - 1 - 2\ln(\mathrm{J}))$ with the Lame constants $\Lambda = 400889\mathrm{N/mm}^2$ and $\mu =$

80.1938N/mm^2. Here $\boldsymbol{F}$ denotes the deformation gradient and J is its determinant. The boundary of the inclusion is described by a circle with a radius of 8mm and a center point defined by the co-ordinates (12mm, 23mm). The material behavior of the inclusion is determined by the St. Venant-Kirchhoff material with the Young's modulus $E = 2400\text{N/mm}^2$ and the Poisson's ratio $\nu = 0.3$. The void is defined by an ellipse with a center located at (36mm, 45mm). The principal axis are rotated with 15 anticlockwise. The largest and smallest radii are defined by 8mm, 3mmm.

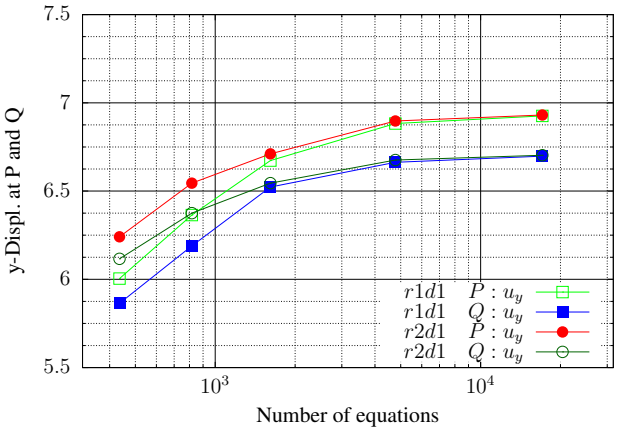

Figure 2: The deflection versus the number of equations (degrees of freedom) for the meshes shown in Fig. 1.

The left side of the membrane is clamped and a force of 100N is applied uniformly to the left hand side. The load is applied in ten steps. The vertical displacement of the upper right corner P and the lower right corner Q are calculated. Therefore the heterogeneous structure is modeled by the quadtree meshing. The meshes with four steps of refinement are shown in Fig.1. Fig.2 shows the deflection versus the number of equations. A nice convergence with mesh refinement is observed. The deformed structure at F=100N is depicted in Fig.3.

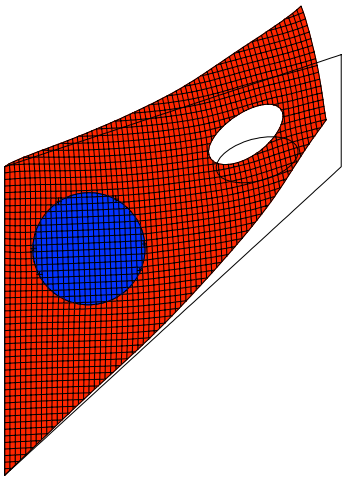

Figure 3: Deformed configuration at F=100N.

Acknowledgments The authors acknowledge the financial support of Exploratory Research Space by RWTH Aachen University.

References

[1] C. Song and J. P. Wolf. The scaled boundary finite-element method-alias consistent infinitesimal finite-element cell method-for elastodynamics. *Comput. Meth. Appl. Mech. Engrg.*, 147:329–355, 1997.

[2] M. Yerry and M. Shephard. A modified quadtree approach to finite element mesh generation. *IEEE Comput. Graph. Appl.*, 3(1):39–46, January 1983.

ANALYZING DEFORMATIONS OF 2D SOLID STRUCTURES USING ELASTIC MULTIPOLES

M. Čebron[1], S. Sarkar[2], A. Košmrlj[2], M. Brojan[1]

[1]*University of Ljubljana, Faculty of Mechanical Engineering, Laboratory for Nonlinear Mechanics, Ljubljana, Slovenia*
[2]*Princeton University, Department of Mechanical and Aerospace Engineering, Princeton, New Jersey, USA*

e-mail: matjaz.cebron@fs.uni-lj.si, miha.brojan@fs.uni-lj.si, ss33@princeton.edu, andrej@princeton.edu

1. Introduction

Recently we have seen an expansion of research on mechanical metamaterials, where the geometry of highly deformable structures is responsible for their unusual mechanical properties, such as negative Poisson's ratio [1], mechanical cloaking and tuneable phononic band gaps [2]. Understanding how such structures deform in response to applied external stresses/loads is crucial for designing novel mechanical metamaterials. Here we present a method for predicting deformations of 2D solid structures with holes and inclusions in the linear response regime by employing analogies with electrostatics.

Just like external electric field induces polarization (dipoles, quadrupoles, etc.) of conductive objects, external stress induces "elastic multipoles" inside holes. In structures with many holes, interactions between induced elastic multipoles are responsible for complex deformation patterns observed in experiments and finite element simulations. We demonstrate that our method can successfully predict deformation patterns in periodic as well as aperiodic structures with holes and inclusions of varying sizes.

2. Elastic multipole method

The elastic multipole method employs analogies between electrostatics and 2D linear elasticity to predict deformations in 2D elastic materials. Electrostatics problems can be formulated in terms of a scalar field, electric potential, whose gradient is the electric field. Similarly, in 2D elasticity a scalar field, named Airy stress function χ, can be defined such that spatial derivatives are normal and shear stresses. From mechanical equilibrium and compatibility conditions in 2D linear elasticity we obtain the governing equation $\Delta\Delta\chi = Y\rho$, where Y is the 2D Young's modulus and ρ is the elastic charge density. This equation is similar to Gauss's Law $\nabla^2 U = -\rho/\varepsilon$ in electrostatics and just like in electrostatics, we can define point charges/monopoles, dipoles and quadrupoles in 2D elasticity.

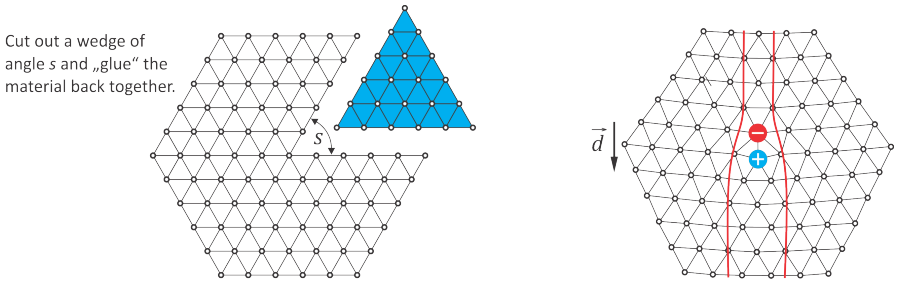

Figure 1: disclination defect (left) and a dislocation defect combining two opposite-sign disclinations.

When a wedge from a 2D elastic material is cut out and the two newly created boundaries of the remaining portion are glued back together, a disclination defect is formed, Fig. 1. The Airy stress function for a disclination defect (monopole), which is similar to a point charge in electrostatics, located at the origin of the coordinate system is given by $\Delta\Delta\chi = Ys\delta(\vec{x})$, which upon solving analytically gives:

$$\chi = s\chi_m = \frac{Ys}{8\pi}|\vec{x}|^2\left(\ln|\vec{x}| - 1/2\right).$$

Here the magnitude of the elastic "charge" s corresponds to the angle of the removed wedge. Two opposite disclinations that are adjacent to each other are referred to as dislocation/dipole, Fig. 1. The Airy stress

function in this case is $\chi_d = -\vec{d} \cdot \nabla \chi_m$. Similarly, the Airy stress function for a quadrupole can be derived. The general solution to the equation $\Delta\Delta\chi = 0$, except at the origin, in polar coordinates (r, φ) is given by an infinite series also known as the Michell solution [3]. All the elastic multipoles discussed above are included in this solution along with higher order multipoles. Some of these multipoles have to be omitted because their energy diverges with increasing size of the elastic material or they produce zero stress. The only terms from the Michell solution that we therefore need to consider are:

$$\chi = A_0 \ln r + A_1 r^{-1} \cos\varphi + C_1 r^{-1} \sin\varphi + \sum_{n=2}^{\infty} \left(A_n r^{-n} + B_n r^{-n+2}\right) \cos n\varphi + \sum_{n=2}^{\infty} \left(C_n r^{-n} + D_n r^{-n+2}\right) \sin n\varphi.$$

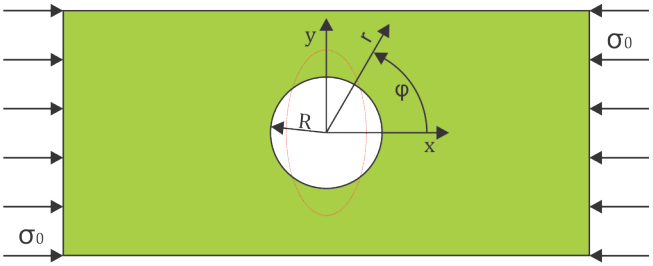

Figure 2: infinite sheet with a circular hole subjected to uniaxial stress.

As an example, we can look at the problem of an infinite 2D sheet with a circular hole of radius R at the center, Fig. 2. When this sheet is subjected to an external stress ($\sigma_{xx,ext} = -\sigma_0$), the resultant Airy stress function can be calculated analytically. From the expression given below in polar coordinates we can see that the external stress induces two types of quadrupoles and a higher order multipole inside the hole:

$$\chi = \underbrace{-\frac{\sigma_0 r^2}{4}\left(1 - \cos 2\varphi\right)}_{\text{External stress}} + \underbrace{\frac{\sigma_0 R^2}{2} \ln r}_{\text{Quadrupole P}} - \underbrace{\frac{\sigma_0 r^2}{2} \cos 2\varphi}_{\text{Quadrupole Q}} + \underbrace{\frac{\sigma_0 R^4}{4r^2} \cos 2\varphi}_{\text{Higher order multipole}}.$$

When more than one hole/inclusion is present in the elastic material, the external stress induces elastic multipoles in each hole, which then interact with each other. The strength of the elastic multipoles can be obtained by satisfying the appropriate boundary conditions at the boundary of each hole.

Results calculated using the elastic multipole method and linear FEM for the case of a hole placed near the edge of an infinite half-space, are presented below in Fig. 3. Finite element calculations were performed using commercial Finite Element code Ansys.

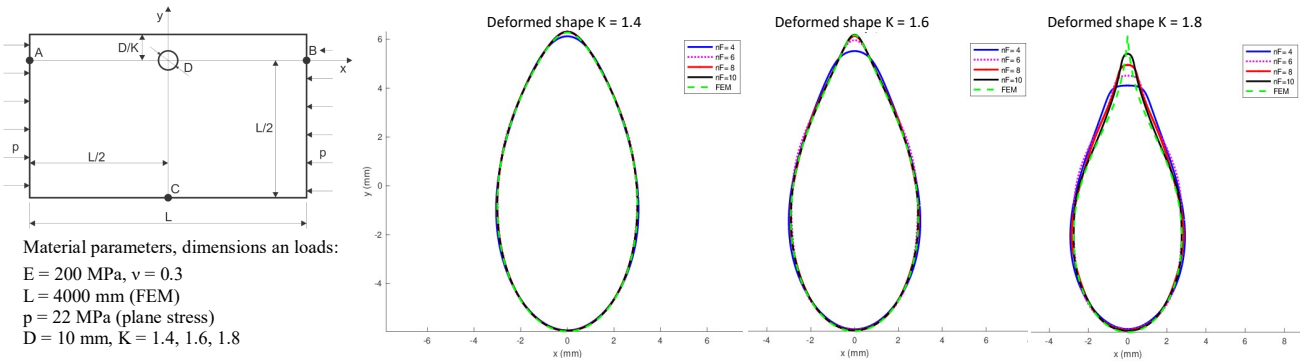

Figure 3: hole placed near the edge of a half-space, FEM and elastic multipole results.

References

[1] J. Shim, S. Shan, A. Košmrlj, S.H. Kang, E.R. Chen, J.C. Weaver and K. Bertoldi. Harnessing instabilities for design of soft reconfigurable auxetic/chiral materials. *Soft Matter*, 8198-8202, 2013.

[2] S. Shan, S. H. Kang, P. Wang, C. Qu , S. Shian, E.R. Chen and K. Bertoldi. Harnessing Multiple Folding Mechanisms in Soft Periodic Structures for Tunable Control of Elastic Waves. *Advanced Functional Materials*, 4935-4942, 2014.

[3] J.H. Michell. On the Direct Determination of Stress in an Elastic Solid, with application to the Theory of Plates. *Proceedings of the London Mathematical Society*, 100-124, 1899.

REFERENCE MAPPING: APPLICATION IN EULERIAN HYDROCODES

S. Ndanou[1], G. Dilts[2], and T. Masser[1]

[1]Los Alamos National Laboratory, *New Mexico, Los Alamos, Usa*
e-mail: sndanou@lanl.gov

Abstract

In the simulation of coupled high-rate solid and fluid mechanical processes, the Eulerian frame for hydrodynamics has an advantage over the Lagrangian in that large deformations, fracture, fragmentation and collision can be modeled without the disastrous degradations caused by mesh tangling. A major disadvantage is the diffusion of material properties as material flows through the mesh. Related are the ambiguities in material history caused by mixing materials with different properties or states, such as yield strength, damage characterization, etc. in a computational cell. Finally, there is the disrepect of advection schemes for material subtleties such as maintaining deviators on a yield surface. The reference mapping technique promises to remedy all of these deficiencies by evolving the material reference coordinate system on the Eulerian mesh by means of a simple advection equation. It was first described in 2009 by Kamrin and Nave [1] and in successive publications by Kamrin and coworkers [2] to treat hyperelasticity and fluid-structure interactions. Vitali and Benson [3] independently described it in 2012 to treat the diffusion of rapidly varying material properties. Using it, material properties at a late-time grid point can be looked up on the reference grid, where they can be evolved in the Lagrangian frame, and mapped back to the current grid. We will discuss the details of an implementation in a typical Eulerian code. The effectiveness of the algorithm will be tested on engineering examples.

Keywords

Eulerian Code, Shock waves, Numerical diffusion, Reference Map

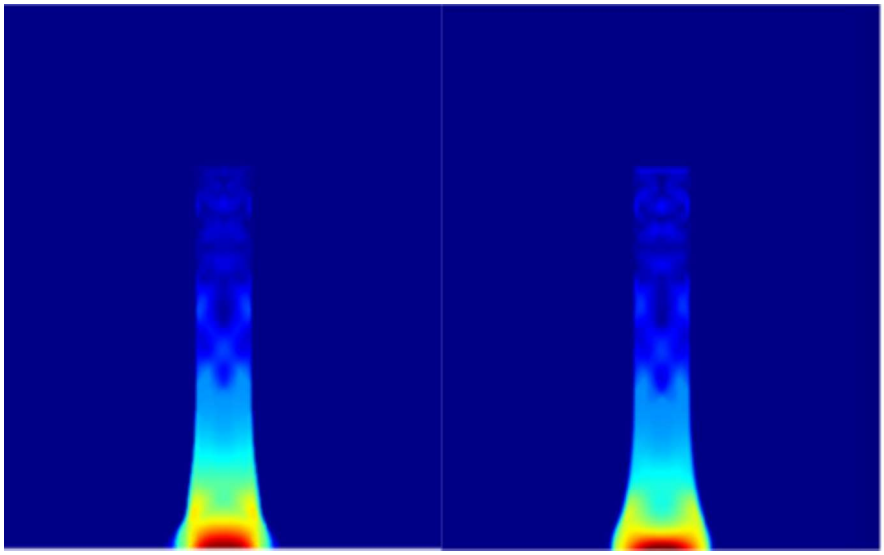

Figure 1: Comparison of the von Mises equivalent stress σ_v in a Taylor Anvil test. On the left the result with the reference map technique and on the right without the reference map. Observe the numerical diffusion near the bottom in the non-reference map result.

Acknowledgments Thank you to the U.S Departement of Energy for giving us its resources to carry out this work.

References:

[1] Ken Kamrin and Jean-Christophe Nave. An eulerian approach to the simulation of deformable solids: Application to finite-strain elasticity. http://arxiv.org/abs/0901.3799v2, 2009.
[2] K. Kamrin, C. H. Rycroft, and J-C Nave An eulerian approach to the simulation of deformable solids: Application to finite-strain elasticity. *Journal of the Mechanics and Physics of Solids*, 60:1952–1969, 2012.
[3] Efrem Vitali and David J. Benson. Modeling localized failure with arbitrary-lagrangian-eulerian methods. *Computational Mechanics*, 49:197–212, 2012.

OPTIMIZATION OF THERMAL MICROACTUATORS RELATED TO MULTIPLE CRITERIA

A. Długosz[1], P. Jarosz[2], and T. Schlieter[1]

[1] *Institute of Computational Mechanics and Engineering, Silesian University of Technology, Gliwice, Poland*
[2]*Institute of Computer Science, Faculty of Physics, Mathematics and Computer Science Cracow University of Technology, Cracow, Poland*

e-mail: adam.dlugosz@polsl.pl

1. Introduction

The problems of optimal design of MEMS (Micro Electro Mechanical Systems) structure attract more and more attention in the recent years. MEMS structures are mainly micro sensors and micro actuators, which are commonly used in telecommunication, automotive, aviation or medical industry. Many of them combines both measurements and actuation elements [3] [8]. Designer of such structures have to consider many technical aspects and restrictions. Among the various types of microactuators, most commonly used are: thermal, electrostatic and piezoelectric. For the first group as an material, polycrystalline silicon is used. It utilizes the Joule heating effect, due to the high value of electrical resistance of the silicone. The most commonly used in practice are: U-Beam microactuators (folded toggle) and V-Beam microactuators (shevron type). For such structures, deformation, maximum displacement, generated force or maximal value of equivalent stresses strongly depend on its geometry. Optimal design of complex structures such as microactuators, requires consideration of many criteria, which depends on the quantities like: the mass of the system, the distribution of stress, the temperature, the displacement, the dynamic characteristics, etc. In practice, this requires coupling of appropriate multi-criteria optimization methods and different numerical simulation techniques. The problems of optimal design of thermal actuators have been considered by many researches, e.g. [4] [5] [9]. In order to efficiently optimize such structures, proper optimization techniques have to be applied, especially when more criteria have to be taken into account [1]. Optimization taking into account one criterion with other criteria formulated as a restriction or weighting sum optimization method, can be found in vast of papers. The present paper proposes methodology of multiobjective optimization of thermal actuators which is more effective, when many criteria (more than three) are considered.

2. Multiobjective optimization algorithm

The metaphors of the game theory and immunology are used to solve the problems of multiobjective optimization using IMGAMO (Immune Game Theory Multi-Objective Algorithm). Each player has its own objective (a payoff function in the Nash equilibrium). The strategy for a particular player is the optimum solution for this player's problem remembering that other players also play their best strategies. The solution of the optimized problem consists of several parameters, each of which is assigned to one of the players. Each player optimizes only its parameters (its strategy) taking the rest of them as constant. The rest of the parameters are set by taking the best solutions from the other players. Solutions from all players should establish the solution of the problem. Then all players use the immune algorithm to optimize their objectives. IMGAMO algorithm was tested on several benchmark problems (ZDT and DTLZ problems). The results of multiobjective optimization are compared to the results obtained by NSGA2 nad SPEA2 algorithms [2] [11]. The metrices of general distance (GD) and spread of the Pareto optimal solutions (S) are used for comparison between algorithms. For the bi-objective optimization results obtained by IMGAMO and NSGA2 or SPEA2 algorithms are comparable, whereas for higher number of criteria (up to 7) IMGAMO gives significantly better results. Details of the algorithm have been described in [6].

3. Formulation of the problem

In order to simulate numerically electrothermal actuators, a coupled electrical, thermal, and mechanical analysis has to be solved. Such problem is described by the appropriate partial differential equations. The equations with arbitrary geometries and boundary conditions are solved by Finite Element Method [12]. This problem is weakly coupled and it requires solving electrical, thermal and mechanical analysis separately. The coupling is carried out by transferring loads between the considered analyses and by means of staggered procedures. FEM commercial software MSC Mentat/Marc is adapted to solve the coupled boundary-value problem.

Shevron-type microactuator is modelled and optimized. Several design variables are responsible for the shape of the beam. It concerns: shape of the beams (which are modelled by means of NURBS parametric curves), pre-bending angle, radii of connection between beams and anchors or central shafts.

Five different functionals are defined. Such functionals are related to the: mass of the structure, equivalent stress, maximum deflection of the actuator, total heat generated by the actuator and buckling safety factor.

Proposed approach allows to obtain a set of Pareto-optimal solutions as a result of a single optimization task run. Visualization of such a set, for two or three criteria is not a major problem, it leads to the form of curves or surfaces. Performing optimization task for larger number of criteria entails necessity of proper visualization of the results. One of the more popular methods is the projection of each pair of criteria and present them in the form of a matrix (Scater-plot matrix). For the large number of criteria this method of visualization can be ineffective. In present paper more convenient way to visualize the results of the optimization is the used - Self-Organizing Maps (SOM) [10]. This concept is based on Kohonen neural networks [6].These networks can also be used to visualize the vector of design variables for optimal solutions.

Acknownledegement The research is partially financed by research project no. 10/040/BK_18/0066

4. References

[1] Bui L., Alam S., Multi-objective Optimization in Computational Inteligence: Theory and Practice, Information Science Reference IGI Global, 2008
[2] Deb K., Pratap A., Agarwal S., Meyarivan T., A fast and elitist multiobjective genetic algorithm: NSGA-II, IEEE Transactions on Evolutionary Computation, vol. 26, Issue 2, pp. 182-197, 2002.
[3] Gad-el-Hak M., The MEMS Handbook, CRC Press LLC, 2002.
[4] Henneken V., Tichem M and Sarro P., Improved thermal U-beam actuators for micro-assembly, Sensors and Actuators, vol. 142, pp. 298–305, 2008.
[5] Jain N and Sharma A., K. S. Design and simulation of bidirectional in-plane chevron beam microtweezer. International Journal of Emerging Technologies in Computational and Applied Sciences, 43–49, 2012.
[6] Jarosz, P. and Burczyński T. (2011).Artificial immune system based on clonal selection and game theory priniciples for multiobjective optimization. Lecture Notes in Computer Science, 321–333.
[7] Kohonen T., Self-organized formation of topologically correct feature maps, Biological Cybernetics, vol. 43 (1), pp. 59-69, 1982.
[8] Maluf N., Williams K.: An Introduction to Microelectromechanical Systems Engineering, Artech House Publishers, London - Boston, 2004.
[9] Sigmund O., Design of multiphysics actuators using topology optimization, Comput. Methods Appl. Mech. Eng., 190, 6577-6604 ,2001.
[10] Takatsuka M., An application of the self-organizing maps and interactive 3-D visualization to geospatial data, Proc. in 6-th International Conference on GeoComputation, 2001.
[11] Zitzler E., Laumanns M., Thiele L., SPEA2: Improving the Strength Pareto Evolutionary Algorithm. Technical report 103, Computer Engineering and Networks Laboratory (TIK), ETH Zurich, Switzerland 2001.
[12] Zienkiewicz, O.C. and Taylor, R.L., The Finite Element Method, Vol. 1-3, Butterworth-Heinemann, Oxford, 2000.

APPLICATION OF EVOLUTIONARY ALGORITHMS IN IDENTIFICATION OF THERMAL PROPERTIES OF HARDENING CONCERTE

A. Dlugosz[1], I. Pokorska[2], M.A. Glinicki[3], R. Jaskulski

[1] *Faculty Mechanical Engineering , Silesian University of Technology, Gliwice, Poland*
[2] *Faculty of Civil Engineering, Czestochowa University of Technology, Czestochowa, Poland*
[3] *Institute of Fundamental Technological Research Polish Academy of Sciences, Warsaw, Poland*
[4] *Faculty of Civil Engineering, Mechanics and Petrochemistry, Plock, Poland*

e-mail: iwona.pokorska.pcz@gmail.com

1. Introduction

The proper determination of the thermal properties of hardening concrete plays a key role in the building the correct models of concrete structures. High temperature gradients associated with the exothermic chemical reactions of cement hydration may occur between the interior and the surface at the early age of concrete, when its strength is low. Cracks occur, when temperature gradients cause tensile stresses, which exceed the tensile strength of the young concrete. Thermal distortions have greater influence on stresses especially for massive structures [6].

Thermal characteristics of concretes described by: thermal conductivity, specific heat and heat of cement hydration, are evolving during hardening and depend on the maturity of concrete. Such parameters in practice can be determined by means of different experimental measurements, hot plate apparatus and several transient dynamic techniques. Thermal characteristics, identified in the paper, are performed on the basis of temperature measurements only [4,5].

In the paper [3] model of the hardened concrete sample specimen was considered as 2D. In present work axis symmetrical model is considered. The hardening of the concrete specimen is the long time process (up to 90 hours), so additionally, the heat losses have to be introduced in the model. In present paper appropriate the boundary conditions is introduced in the numerical model. The identification of the thermal properties is based on temperature measurements in the sensor points, which are located at the central axis of the thermally-isolated cylindrical mould. In order to solve identification task, an in-house implementation of the evolutionary algorithms (EAs) is used. EAs, as the global optimization technique for searching parameters, which describe thermal properties of hardening concrete are applied. Comparing to the use of conventional optimization methods, superiority of EAs manifest in many aspects, e.g. fitness function has not to be continuous, information about objective function gradient is not necessary, choice of the starting point may not influence the convergence of the method, regularization methods in no needed [1,2,3]

2. Formulation of the identification problem

From the mathematical point of view, the identification problem is expressed as the minimization of the functional. Following functional has been defined and implemented:

$$\min_{\mathbf{x}} \quad f(\mathbf{x}) = \sum_{i=1}^{n}\sum_{i=1}^{m}\left(T_{ij}(\mathbf{x}) - \hat{T}_{ij}(\mathbf{x})\right)^2 \tag{1}$$

where: n is a number of sensors, m is a number of time intervals, T_{ij} and $\hat{T}_{ij}$ represent computed and measured temperature values in particular point in time and space, respectively, $\mathbf{x}$ is a vector of design variables.

Measured values of the temperature (T_{ij}) has been taken from real experiment during the proces of hardening concrete specimen, while computed values ($\hat{T}_{ij}$) has been simulated numerically.

The vector of design variables $\mathbf{x}$ contains parameters, which define heat of hydration, specific heat and

thermal conductivity. The identification problem is solved by finding the vector of design variables **x**, by minimizing the functional (1). In-house implementation of EA, with the floating point gene representation is used (Fig. 1).

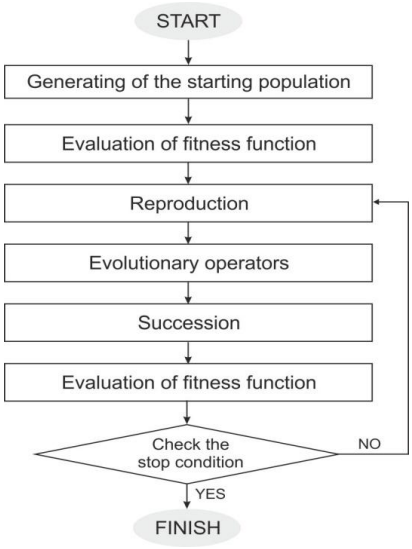

Figure 1: The flow chart of the applied Evolutionary Algorithm

In order to calculate temperature in time and space, unsteady heat conduction equation, including proper definition of internal heat sources is solved. Numerical model of the hardening concrete specimen was prepared and solved by means of the finite element method (FEM) [7].

The differentia equation of transient heat conduction problem in hardening concrete has following form:

$$\frac{\partial}{\partial x}\left(k\frac{\partial T}{\partial x}\right)+\frac{\partial}{\partial y}\left(k\frac{\partial T}{\partial y}\right)+\frac{\partial}{\partial z}\left(k\frac{\partial T}{\partial z}\right)+q=\rho c_p\frac{\partial T}{\partial t} \tag{2}$$

where: T - temperature of concrete $[^{\circ}\mathrm{C}]$, k - thermal conductivity, $[\mathrm{W/m\,K}]$, x, y, z – spatial coordinates, q- internal heat source $\left[\mathrm{W/m^3}\right]$, t- time [s], ρ – density of concrete $\left[kg/\mathrm{m^3}\right]$, c_p - specific heat of concrete $[\mathrm{J/kg\,K}]$.

Proposed identification algorithm was tested on an benchmark example, before it was used to identify thermophysical parameters on the basis of real experimental data. The identification tasks are performed for experimental data for different concrete mixtures.

References

[1] A. Długosz and T. Burczyński , Intelligent computing in optimization of coupled problems, *Proc in. Computational Methods for Coupled Problems in Science and Engineering*, pp.387-398, pp. 86-93, 2013.

[2] A. Długosz and T. Burczyński , Identification in multiscale thermoelastic problems, *Computer Assisted Mechanics and Engineering Sciences*, vol.20, No. 4, pp. 325-336, 2013.

[3] A. Długosz and I. Pokorska and M.A. Glinicki and R. Jaskulski, Idetification of thermal properties of hardening concrete by means of evolutionary algorithm, *Computer Assisted Methods in Engineering and Science*, 24(2), pp.101-111, 2017,

[4] M. A. Glinicki and R. Jaskulski and M. Dąbrowski and Z. Ranachowski, Determination of Thermal Properties of Hardening Concrete for Massive Nuclear Shielding Structures, SCMT4, *Proc. in 4th International Conference on Sustainable Construction Materials and Technologies*, pp.1-9, 2016.

[5] G. Knor and M. A. Glinicki and J. Holnicki-Szulc, Determination of thermal parameters of hardening concrete by means of inverse problem solution, *Roads and Bridges-Drogi i Mosty*, 11(4) 281-294, 2012.

[6] O. C. Zienkiewicz and R. C. Taylor, The finite element method, Vol. 1-3, 6th edition Elsevier, Oxford, United Kingdom, 2005.

[7] Lawrence, A., Tia, M., Ferraro, C., Bergin, M., Effect of early age strength on cracking in mass concrete containing different supplementary cementations materials: Experimental and Finite element investigation, *Journal of Materials in Civil Engineering*, 24 (4), pp.362-372, 2012.

ON FE MODELING OF A VIBRATING BODY CONTROLED BY SLIDING SOME OF ITS COMPONENTS

W. Szyszkowski[1], and E. Sharbati [2]

[1,2]*University of Saskatchewan, Saskatoon, Canada,*
e-mail: walerian.szyszkowski@usask.ca

1. Extended Abstract

A FE procedure to simulate a multibody system consisting of a main body and sliding small components is proposed. The procedure is suitable for control purposes since it allows imposing explicitly any relative motion of each component as input to obtain the response of the main body as output. In particular, attenuation effects in a vibrating main body can be generated by precisely synchronizing the current body configuration with relative motion of one or more of its components. Such effects are possible to obtain because the dynamic interaction between the main body and the sliding component triggers the Coriolis type forces that are generally capable of producing either attenuation or amplification in different phases of a cycle of the vibrating main body.

By maximizing these forces during attenuation phase and minimizing during amplification phase the reduction of the system's vibration in each cycle can be achieved [1]. It should be noted that handling such a task by the 'standard' FE approach (as used, for example, in vehicle-bridge or vehicle-rail tract simulations and involving typically only constant not controlled relative velocities) would be challenging mainly due to complexity of the geometrical constraints to be imposed between the sliding components and the main body.

In our procedure each component is forced to slide with an assumed $s(t)$ along a prescribed path (AB in Figure 1a) modeled by the beam elements (that represents a guiding beam, which can be real or fictitious) attached at nodes (see Figure 1b) to the main body meshed by any elements appropriate to simulating its vibrations. This way the sliding component interacts with the main body via the guiding beam in which only one currently traversed element (referred to as the composite element) is affected by the relative motion.

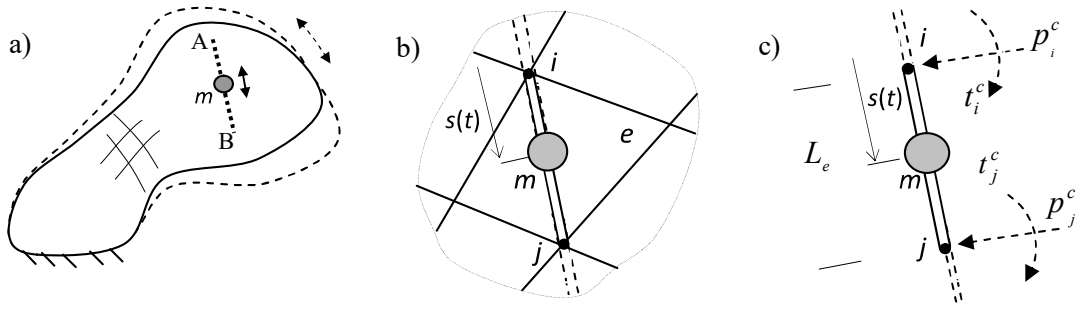

Figure 1: The vibrating system (a) the guiding beam (b), and the composite element (c)

This element has a time-dependent mass matrix, $\mathbf{M}_e(t)$ and, as it was shown in [2], the Coriolis forces generated in it can be explicitly identified in terms of the component's current position and velocity, which in turn permits relating directly these forces to assumed trajectories of the components and selecting the one resulting in 'best' attenuation. This is possible because the element equation for the composite element is derived in the following forms (in order to concentrate on the active attenuation any passive damping is omitted):

(1a,b) $\mathbf{M}_e(t)\ddot{\mathbf{u}}_e + \mathbf{C}_e\dot{\mathbf{u}}_e + \mathbf{K}_e\mathbf{u}_e = \mathbf{F}_e$ or $\mathbf{M}_e(t)\ddot{\mathbf{u}}_e + \mathbf{K}_e\mathbf{u}_e = \mathbf{F}_e - \mathbf{f}_e^c$

where $\mathbf{C}_e = \frac{d\mathbf{M}_e}{dt} = m\dot{s}\frac{\partial}{\partial s}(\mathbf{N}^T\mathbf{N})$ represent the Coriolis effects and can be treated as an 'instantaneous' damping matrix (where $\mathbf{N}=\mathbf{N}(s(t))$ are the values of the beam's shape functions matrix at the current mass location). The term $\mathbf{f}_e^c = \mathbf{C}_e\dot{\mathbf{u}}_e$ defines the 'Coriolis' force vector due to the relative motion (consisting of forces p^c and moments t^c as indicated in Figure 1c) that is assigned to the end nodes of the element. As can be seen the matrix $\mathbf{C}_e$ and vector $\mathbf{f}_e^e$ depend *explicitly* on the current relative velocity $\dot{s}$ of the mass and *implicitly* on its current position between the nodes of the element (the position is hidden in functions $\mathbf{N}$).

The first form, eq. (1a), indicates how the relative motion relates to periods of attenuation ($C_e^{ii} > 0$, if $\dot{s} > 0$) and to periods of amplification ($C_e^{ii} < 0$ if $\dot{s} < 0$), while the second form, eq. (1b), is more suitable for the practical simulation due to the fact that all the LHS terms can be routinely handled by typical FE software (in our case by ANSYS), while the values of $\mathbf{f}_e^e$ on the RHS can be easily calculated and added to forces at each time step of the integration procedure. The system's attenuation is achieved by controlling forces $\mathbf{f}_e^e$ (via properly choosing $s(t)$) that are to be maximized in the periods of attenuation and minimized in the periods of amplification.

The corresponding control schemes for the components' motion resulting in attenuation (active) of the main body will be presented. In fact these schemes generate 'inverse' self-excited vibrations that can be characterized by a positive damping coefficient. As illustration the test case of using relative motion of two small masses to attenuate vibrations of a frame is presented in Figure 2. For this particular case an effective active damping ratio of about 2.7% was obtained.

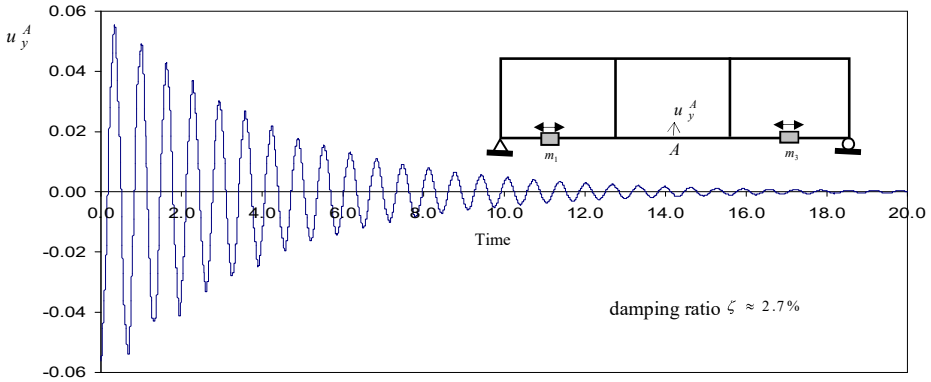

Figure 2: The response of vibrating frame controlled by motion of two masses.

The implementation and accuracy of the procedure, which may be particularly useful in providing a unique means for active reduction of vibrations in the systems for which internal/external passive damping is almost absent or not available, will be discussed in details.

2. References

[1] D.S.D. Stilling and W. Szyszkowski, Controlling angular oscillations through mass reconfiguration: a variable length pendulum case. *International Journal of Non-Linear Mechanics*, 37:89, 2002.
[2] W. Szyszkowski and E. Sharbati, On the FEM modeling of mechanical system controlled by relative motion of a member: A pendulum-mass interaction test case, *Finite Elements in Analysis and Design*, 45:730, 2009

NUMERICAL TREATMENT OF MATERIAL PARAMETER IDENTIFICATION USING FINITE ELEMENTS

R. R. Gilbert[1] and S. Hartmann[1]

[1]*Institute of Applied Mechanics, Clausthal University of Technology, Clausthal-Zellerfeld, Germany*

e-mail: rose.rogin.gilbert@tu-clausthal.de

1. Introduction

There are many materials having different properties and behaviors which are characterized in solid mechanics by constitutive models. These constitutive models have material parameters, which have to be calibrated to experiemental data in order to predict the material behavior within the range of application. This calibration is called *material parameter identification* or briefly *parameter identification*, see [2, 4].

Depending on the homogeneity of the deformation, the procedure of material parameter identification varies. If the deformation is inhomogeneous, the entire boundary-value problem need to be solved, commonly by using finite element method. The material parameter identification for inelastic materials using finite elements were discussed in [1, 5, 6]. In order to identify the material parameters, the sensitivities of the parameter needs to be calculated. The most common method to calculate these sensitivites is by using external numerical differentiation, see, for the terminology, [7]. However, for a constitutive model with inhomogeneous deformation having large number of parameters, the computational cost is high. In order to circumvent this issue, internal numerical differentiation is performed which reduces the computational time by a considerable amount.

In this presentation, initially the underlying problem is explained. This is followed by a brief description of the internal and external differentiation procedures. A couple of examples showing the difference between external and internal numerical differentiation is also provided to round off the presentation.

2. Problem statement

The most commonly used basis for parameter identification process is the least-square problem. The simulated results, $\boldsymbol{s} \in \mathbb{R}^{n_s^e}$ (n_s^e is the number of simulated data), from the finite-element program are compared with the experimental data, $\boldsymbol{d} \in \mathbb{R}^{n_d^e}$ (n_d^e is the number of experimental data from one or more experiments). The residual vector, $\tilde{\boldsymbol{r}}(\boldsymbol{\kappa}) = \boldsymbol{W}_j \{\boldsymbol{s}(\boldsymbol{\kappa}) - \boldsymbol{d}\}$, describes the difference between the experimental and the simulated data. In order to consider the different order of physical values (forces, displacements), weighting matrices, $[\boldsymbol{W}_j]$, are introduced. The so-called *objective function*, $f(\boldsymbol{\kappa}) = \frac{1}{2}\tilde{\boldsymbol{r}}^T\tilde{\boldsymbol{r}}$, is then minimized in a least-square sense using methods outlined in [3]. A trust-region reflective algorithm, provided in Matlab routine `lsqnonlin.m` is used to solve the problem. A necessary condition for a minimum at $\boldsymbol{\kappa} = \boldsymbol{\kappa}^*$ requires the derivative to be zero

$$\boldsymbol{F}(\boldsymbol{\kappa}^*) = \left.\frac{\mathrm{d}f}{\mathrm{d}\boldsymbol{\kappa}}\right|_{\boldsymbol{\kappa}=\boldsymbol{\kappa}^*} = \boldsymbol{D}^T(\boldsymbol{\kappa}^*)\{\boldsymbol{s}(\boldsymbol{\kappa}^*) - \boldsymbol{d}\} = \boldsymbol{0}, \tag{1}$$

with $\boldsymbol{D}(\boldsymbol{\kappa}) := \mathrm{d}\tilde{\boldsymbol{r}}(\boldsymbol{\kappa})/\mathrm{d}\boldsymbol{\kappa} = \mathrm{d}\boldsymbol{s}(\boldsymbol{\kappa})/\mathrm{d}\boldsymbol{\kappa}$, $\boldsymbol{D} \in \mathbb{R}^{n_\mathrm{D} \times n_\kappa}$. $\boldsymbol{D}(\boldsymbol{\kappa})$ represent the sensitivites and are calculated either by external differentiation or internal differentiation.

3. External Numerical Differentiation

It is more common to apply external differentiation schemes to approximate the sensitivites. Here, the entire finite element program has to be run $(n_\kappa + 1)$-times, for each iteration of the least-square solver. For each iteration, the material parameters are perturbed in order to obtain the sensitivites using a forward difference scheme. Therefore, the computational cost to calculate the sensitivities using external numerical differentiation is very high when the number of parameters to be identified are high. The details will be shown in the presentation.

4. Internal Numerical Differentiation

In the case of internal numerical differentiation, the entire time integration step is assumed to be dependent on the parameters $\boldsymbol{\kappa}$. The sensitivities are calculated based on Multilevel-Newton algorithm and are provided from the finite element program itself. These calculated sensitivities are then provided to the Matlab routine `lsqnonlin.m` to identify the material parameters. Since the sensivities are calculated internally using Acegen, the entire finite element program has to be run only once per iteration of the least-square solver. This reduces the computational cost considerably. However, there are storage requirements that need to be fulfilled. More details will be outlined in the presentation.

5. Examples

Examples showing the difference between external and internal differentiation will also be shown in the presentation. A particular focus lies on the storage requirements and the computational costs, where use is made of both models of hyperelasticity and models with internal variables.

References

[1] K. Andresen, S. Dannemeyer, H. Friebe, R. Mahnken, R. Ritter, and E. Stein. Parameteridentifikation für ein plastisches Stoffgesetz mit FE-Methoden und Rasterverfahren. *Bauingenieur*, 71:21–31, 1996.

[2] J. V. Beck and K. J. Arnold. *Parameter estimation in engineering science*. John Wiley & Sons, New York, 1st edition, 1977.

[3] J. E. Dennis and R. B. Schnabel. *Numerical methods for unconstrained optimization and nonlinear equations*, volume 16 of *Classics in Applied Mathematics*. SIAM Society for Industrial and Applied Mathematics, Philadelphia, 1996.

[4] S. Hartmann and R. R. Gilbert. Identifiability of material parameters in solid mechanics. *Archive of Applied Mechanics*, 88(1):3–26, 2018.

[5] R. Mahnken and E. Stein. A unified approach for parameter identification of inelastic material models in the frame of the finite element method. *Computer Methods in Applied Mechanics and Engineering*, 136:225–258, 1996.

[6] R. Mahnken and E. Stein. Parameter identification for finite deformation elasto-plasticity in principal directions. *Computer Methods in Applied Mechanics and Engineering*, 147:17–39, 1997.

[7] K. Schittkowski. *Numerical data fitting in dynamical systems*. Kluwer Academic Publ., Dordrecht, 2002.

NUMERICAL MODELING OF THE FSW JOINT USING AN ELASTO-PLASTIC MATERIAL MODEL

P. Nosal and A. Ganczarski

Institute of Applied Mechanics, Cracow University of Technology, Kraków, Poland

e-mail: nosal.przemyslaw@student.pk.edu.pl, artur.ganczarski@pk.edu.pl

Present work deals with numerical modeling of the material which contain the joint made by using the friction stir welding (FSW) technology. The consider material has a heterogeneous microstructure which determined its global response to the applied load. The thermodynamically consistent elastic-plastic model was introduced, additionally took the approach that assuming the construction of the joint as a composite material. Local mechanical properties were estimated based on numerical simulation determining the size of grains in the material, which are dependent on the temperature field accompanying the FSW process. The simulation results were then verified by comparing the results obtained experimentally.

1. Introduction

The FSW joint is characterized by a specific heterogeneous microstructure that affects directly on the mechanical properties of the weld [9]. Knowledge of the local constitutive relationships of individual weld zones allows to predicting its global response during loading based on the implementation of the appropriate numerical model for the MES software [3]. The omission of information about inhomogeneity of mechanical properties may be the cause of large discrepancies in numerical and experimental results [8]. However, the global behaviour of the material is not only determined by the mechanical properties of the weakest zone in the joint but also a combination of interactions of individual zones, their size, properties and geometry [9]. In order to understand these relationships, numerous simulations of the temperature distribution in the welding area and simulations of material flow around the tool are carried out, then these data are verified by experimental tests [9].

2. Experiments

Detailed results of the tensile tests of solid samples and a sample with an FSW joint were presented in the paper [5]. The base material was copper Cu-ETP in the state of R220 in the form of a sheet with a thickness of 5 mm. Based on the received tensile curves (Fig. 1) it can be concluded that the sample with FSW joint is characterized by a lower yield strength σ_{y} by approximately 60% and lower maximal strength σ_{m} by approximately 15% in compare to the base material.

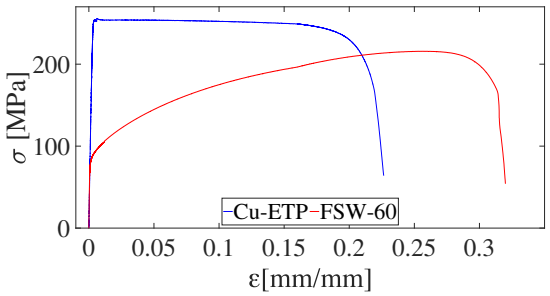

Fig. 1 Comparison of the tensile curves of a base material and a sample with an FSW joint [5].

3. Basic assumptions and equations

In this paper, in order to identify the local constitutive behaviour of individual joint zones, a 2-D simulation of the temperature distribution in the material which accompanies the process of FSW was carry out. This simulation, however, does not take into account plastic deformation, which is the second component of total thermal energy that is generated during the process [4]. The numerical model uses a non-stationary Fourier equation

$$\lambda(\theta_{,rr} + \theta_{,r}/r + \theta_{,zz}) + \dot{q}_{\mathrm{v}} = \rho c_{\mathrm{v}} \dot{\theta} \tag{1}$$

To determine the dependence of the yield strength on the grain size in the material, the description proposed by Hall and Petch is often used. However, in the case of nanostructures, this description is not very precise, the real values of σ_y are lower than it results from the H-P relationship. Therefore, another description was used to the limit of the beginning of plasticity, which was presented in the paper [2]. However, it does not have a physical explanation

$$\sigma_y = 104.9 + 111.8 \exp(d/10.3) + 54.9 \exp(d/135.6) + 235.6 \exp(d/0.13) \tag{2}$$

The constitutive model used in the paper was presented by Ottosen and Ristinmaa [6] and is based on the following assumptions: (1) elastic-plastic-damage material is considered, (2) small strains are assumed.

4. Numerical results

First simulation concern on the temperature distribution in the workpiece. Because this physical magnitude directly affects the value of the yield strength, it is also possible to observe its gradient within the welding area. Also when considering individual zones of joints, we must remember about their inhomogeneities (Fig. 2). The overall stress of the entire system was presented as the sum of stresses from individual joint zones using the composite material approach. The Reuss method was adopted as the mixing rule. In order to implement a constitutive model taking into account the local impact of individual joint zones on the global behaviour of the sample. A numerical predictor-corrector algorithm was adopted using the "return mapping" procedure [1]. Integration of the Euler backward type and the tangential matrix method called the Newton-Raphson method was used in this algorithm [7].

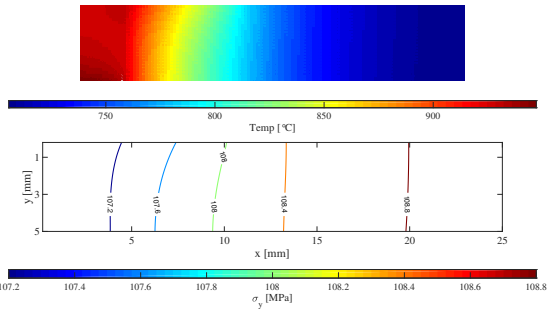

Fig. 2 The temperature field accompanying the FSW process on the cross section of the joint (1/2 of the sample) and its effect on yield strength of the copper.

References

[1] A. Ganczarski and J. Skrzypek (2009). *Plastyczność materiałów inżynierskich*, Wydawnictwo PK.
[2] V.Y. Gertsman, M. Hoffmann, H. Gleiter and R. Birringer (1994). The study of grain size dependence of yield stress of copper for a wide grain size range, *Acta metal. mater.*, 3539-3544.
[3] W.D. Lockwood, B. Tomaz and A.P. Reynolds (2002). Mechanical response of friction stir welded AA2024: experiment and modeling, *Materials Science and Engineering*, 348-353.
[4] P. Nosal and A. Ganczarski (2017). Modelling of the temperature field that accompanies Friction stir welding, *ITM Web of Conferences*, 1-5.
[5] P. Nosal, T. Machniewicz, M. Hebda and A. Korbel (2017). Wpływ parametrów procesu zgrzewania FSW na własności wytrzymałośsciowe połączeńn blach miedzianych, *XVI Krajowa Konferencja Mechaniki Pękania*, 321-328.
[6] N.S. Ottosen and M. Ristinmaa (2005). *The mechanics of constitutive modeling*, Elsevier.
[7] P. Sulich and W. Egner (2016). Algorytm numerycznej analizy termomechanicznych obciążeń niskocyklowych stali, *Episteme*, 135-148.
[8] L. Zhang, J. Min, B. Wang, J. Lin, F. Li and J. Liu (2016). Constitutive model of friction stir weld with consideration of its inhomogeneous mechanical properties, *Chinese Journal of Mechanical Engineering*, 357-364.
[9] Z.H. Zhang, W.Y. Li, J.L. Li and Y.J. Chao (2014). Effective predictions of ultimate tensile strength, peak temperature and grain size of friction stir welded AA2024 alloy joints, *Int. J. Adv. Manuf. Technol.*, 1213-1218.

SECOND-ORDER TWO-TEMPERATURE MODEL FOR THIN METAL FILM SUBJECTED TO THE ULTRASHORT LASER PULSE

E. Majchrzak and J. Dziatkiewicz

Institute of Computational Mechanics and Engineering, Silesian University of Technology, Gliwice, Poland

e-mail: ewa.majchrzak@polsl.pl, jolanta.dziatkiewicz@polsl.pl

1. Introduction

Thin metal film subjected to the ultra-short laser pulse is considered. Mathematical description of the process discussed is based on the system of four equations. Two of them describe the electrons and lattice temperature, while third and fourth equations represent the generalized Fourier law, it means the dependences between the electrons (lattice) heat flux and electrons (lattice) temperature gradient. Depending on the order of the generalized Fourier law expansion into the Taylor series, the first- and the second-order model can be obtained. In contrast to the commonly used first-order model, here the second-order two-temperature model is considered. The problem is solved using the explicit scheme of the finite difference method. The example of computations is also presented.

2. Governing equations

The two-temperature model describes the temporal and spatial evolution of the lattice and electrons temperatures (T_l and T_e) in the irradiated metal by two coupled nonlinear differential equations [1, 2] (1D problem)

$$C_e(T_e)\frac{\partial T_e(x,t)}{\partial t} = -\frac{\partial q_e(x,t)}{\partial x} - G(T_e)\left[T_e(x,t) - T_l(x,t)\right] + Q(x,t) \tag{1}$$

and

$$C_l(T_l)\frac{\partial T_l(x,t)}{\partial t} = -\frac{\partial q_l(x,t)}{\partial x} + G(T_e)\left[T_e(x,t) - T_l(x,t)\right] \tag{2}$$

where $T_e(x, t)$, $T_l(x, t)$ are the temperatures of electrons and lattice, respectively, $C_e(T_e)$, $C_l(T_l)$ are the volumetric specific heats, $G(T_e)$ is the electron-phonon coupling factor which characterizes the energy exchange between electrons and phonons [3], $Q(x, t)$ the source function associated with the irradiation.
In a place of the classical Fourier law the following formulas are introduced

$$q_e(x, t+\tau_e) = -\lambda_e(T_e, T_l)\frac{\partial T_e(x,t)}{\partial x} \tag{3}$$

and

$$q_l(x, t+\tau_l) = -\lambda_l(T_l)\frac{\partial T_l(x,t)}{\partial x} \tag{4}$$

where $\lambda_e(T_e, T_l)$, $\lambda_l(T_l)$ are the thermal conductivities of electrons and lattice, respectively, τ_e is the relaxation time of free electrons in metals, τ_l is the relaxation time in phonon collisions.
Using the second order Taylor expansion, the equations (3) and (4) can be written in the form

$$q_e(x,t) + \tau_e\frac{\partial q_e(x,t)}{\partial t} + \frac{\tau_e^2}{2}\frac{\partial^2 q_e(x,t)}{\partial t^2} = -\lambda_e(T_e, T_l)\frac{\partial T_e(x,t)}{\partial x} \tag{5}$$

and

$$q_l(x,t) + \tau_l\frac{\partial q_l(x,t)}{\partial t} + \frac{\tau_l^2}{2}\frac{\partial^2 q_l(x,t)}{\partial t^2} = -\lambda_l(T_l)\frac{\partial T_l(x,t)}{\partial x} \tag{6}$$

The source function $Q(x, t)$ is associated with the laser irradiation [3]

$$Q(x,t) = \sqrt{\frac{\beta}{\pi}}\frac{1-R}{t_p\delta}I_0\exp\left[-\frac{x}{\delta} - \beta\frac{(t-2t_p)^2}{t_p^2}\right] \tag{7}$$

where I_0 is the laser intensity, t_p is the characteristic time of laser pulse, δ is the optical penetration depth, R is the reflectivity of the irradiated surface and $\beta = 4\ln 2$.
For $x = 0$ and $x = L$ the non-flux conditions are assumed. The initial condition $T_e(x, 0) = T_l(x, 0) = T_p$ is also known.

3. Example of computations

The problem formulated is solved using the finite difference method with staggared grid (Figure 1). As an example of computations, the thin metal films of thickness 100 nm made of gold and copper are considered. The values of thermophysical parameters are taken from [1-4]. The laser parameters are the following: I_0 =10 J/m^2 and t_p =0.1 ps. In Figure 1 the electrons and lattice temperature histories at the irradiated surface are presented.

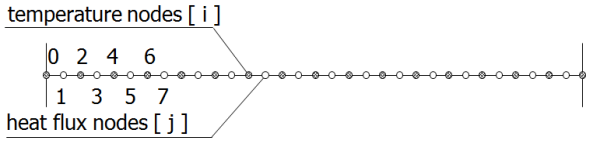

Fig. 1. Discretization

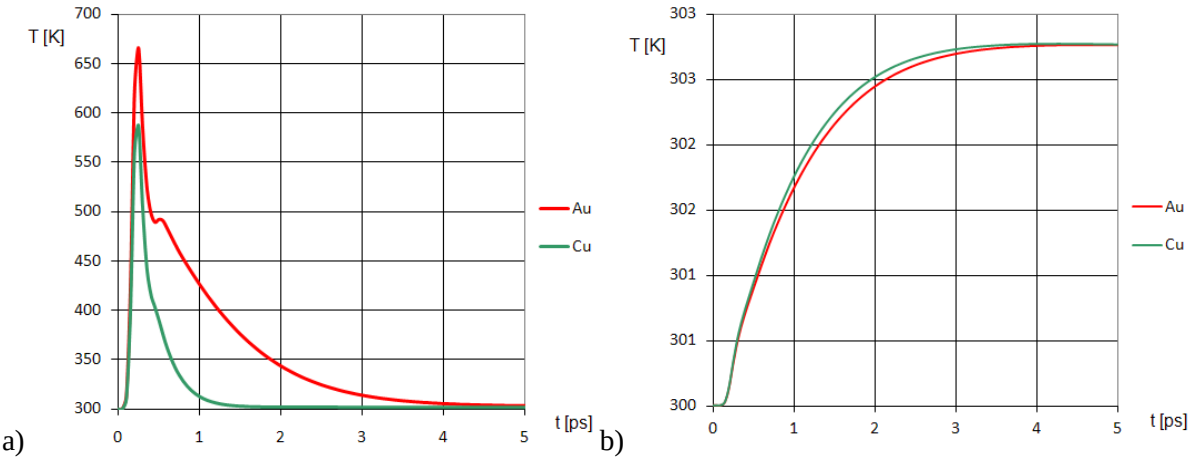

Fig. 1. Temperature history on the irradiated surface for Au and Cu: a) electrons, b) lattice

4. Conclusions

The second-order two-temperature model is considered. The comparison of the results obtained using the first- and second-order models will be shown in the full version of the paper. On this basis, the conclusions will be formulated, in particular for which laser parameters the first-order model is sufficient, and when the higher-order model should be used.

Acknowledgments The research is funded from the projects Silesian University of Technology, Faculty of Mechanical Engineering.

References

[1] Z.M. Zhang. *Nano/microscale heat transfer*, McGraw-Hill, 2007.
[2] Z. Lin, L.V. Zhigilei and V.Celli, Electron-phonon coupling and electron heat capacity of metals under conditions of strong electron-phonon nonequilibrium, Phys. Rev. B., 77:075133-1, 2008.
[3] J.K. Chen and J.E. Beraun. Numerical study of ultrashort laser pulse interactions with metal films, *Numer. Heat Tr A-Appl.*, 40:1, 2001.
[4] E.Majchrzak, J.Dziatkiewicz and Ł.Turchan. Analysis of thermal processes occuring in the microdomain subjected to the ultrashort laser pulse using the axisymmetric two-temperature model, *Int. J. Multiscale Comput. Eng.*, 15, 5: 395, 2017.

VALIDATION OF THERMAL IMAGING AND COMPUTER SIMULATIONS USING METHOD OF FUNDAMENTAL SOLUTIONS FOR CORNER WINDOW

A. Uściłowska[1] and M. Chudzicka-Adamczak[2]
[1] *Institute of Materials Technology, Poznan University of Technology, Poznan, Poland*
e-mail: anita.uscilowska@put.poznan.pl
[2] *Polytechnic Institute, Stanislaw Staszic University of Applied Sciences in Piła, Pila, Poland*
e-mail: mchudzicka@pwsz.pila.pl

1. Introduction

In this paper the validation of the Method of Fundamental Solutions (MFS) with the use of infrared thermovision images are presented. MFS is a meshless method that stands out with the simplicity of implementation. What is more, the preparation of data for calculations is not as time-consuming as in other numerical methods. This method allows to select parameters in a way that enables to obtain a solution with satisfactory, assumed and defined accuracy. The results are received in the form of continuous functions, which enables numerical analysis, e.g. determination of stresses and strains based on temperature change [4].

For the analysed object the results of the numerical method (obtained temperature fields) will be validated using thermovision temperature measurement. Infrared thermography is a very convenient method thanks to its main advantages, such as: simplicity and non-invasiveness. Thanks to these features tests using thermal imaging cameras are applicable in almost every field [1, 3, 6].

2. Measurement equipment and description of the test object

The Method of Fundamental Solutions is used to solve the boundary problem with the heat transfer equations for the window (barrier consisting of three layers with constant thermal conductivity coefficients of each layer). In this case the inverse problem is analysed, it means that the temperature is determined on the edge of the considered area. The obtained results are compared to the thermogram taken with the thermal imaging camera Testo thermal imager 875i with the following features: detector 160x120 pixels, resolution technology SuperResolution - up to 320x240 pixels, thermal sensitivity of <50 mK.

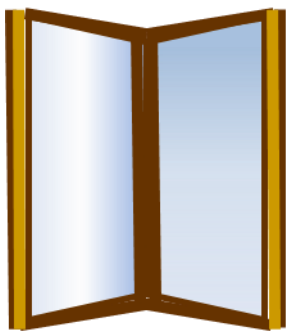

Fig. 1: Test object - corner window (the inside of the window)

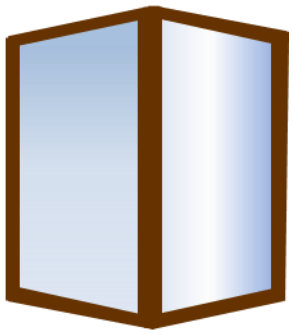

Fig. 2: Test object - corner window (the outside of the window)

Below, a temperature distribution (Figure 3) on the one side of the outside of the window with the outdoor temperature of 11° C is presented.

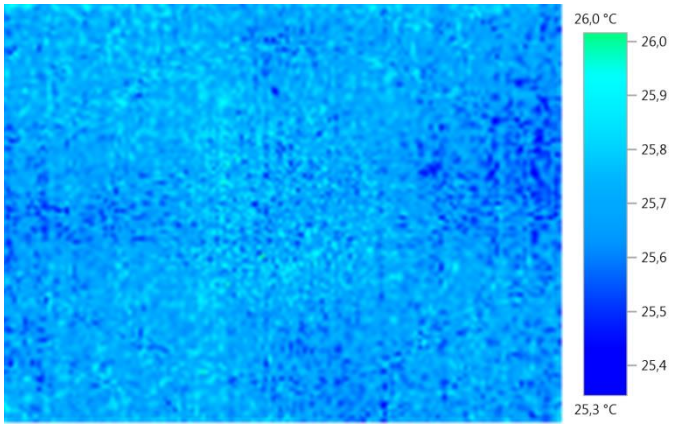

Fig. 3: Test object - corner window
(the teperature distribution on the outside of the window)

The above temperature distribution is a comparative model for the obtained results of computer simulation using MFS.

References

[1] J. Bauer, E. Dereń). Standardization of Infrared Thermal Imaging in Medicine and Physiotherapy (in Polish). *Acta Bio-Optica et Informatica Medica Inżynieria Biomedyczna*, **20**(1), 11-20, 2014.
[2] A. Derlatka and P. Lacki.Numerical analysis of temperature distribution in outside vertical compartment (in Polish). *Budownictwo o zoptymalizowanym potencjale energetycznym*, **1**(13), 22-27, 2014.
[3] R. J. Goldstein.Application of aerial infrared thermography to measurement of building heat loss. *ASHRAE Transactions*, **84**(1), 207-226, 1978.
[4]J. A. Kołodziej and A. Uscilowska. Application of MFS for determination of effective thermal conductivity of unidirectional composites with linearly temperature dependent conductivity of constituents. *Engineering Analysis with Boundary Elements*, **36**(3), 293-302, 2011.
[5]V. D. Kupradze and M. A. Aleksidze(1964). The method of functional equations for the approximate solution of certain boundary value problems. *USSR Comput. Meth. Math. Phys.***4**, 82-126,1964.
[6] H. Wiśniewski. Applications thermography in construction.
http://www.praze.pl/UserFiles/File/Pakiety/5/5.1/Zastosowanie%20termowizji%20w%20budownictwie%20-%20szkolenie%202.pdf [Access 20.03.2017]
[7]Collective work. *General construction*, Vol. 2, *Physics of Buildings.*Arkady, Warszawa, 2005.
[8] J. Dębowski, K. Firek. Technical condition of the elements of balconies in large panel system building (in Polish). *Przegląd budowlany***6**, 18-22, 1978.

AN ELASTIC-PLASTIC TORSION OF OPEN PROFILES MADE WITH FUNCTIONALLY GRADED MATERIAL - NUMERICAL EXPERIMENT BASED ON MESHLESS METHODS

A. Uscilowska

Poznan University of Technology, Poznan, Poland,

e-mail: anita.uscilowska@put.poznan.pl

1. Introduction

Elastic-plastic torsion of a bar is an important engineering problem, still discussed in literature. Special class of the bars is under considerations, i.e. we will consider prismatic bars and profiles with open cross-section. Moreover, it is assumed that the bars are made with functionally graded materials.
Twisting of prismatic bars made with homogeneous and isotropic materials have been undertaken by many authors [5; 10; 9; 11]. In the last time, the case of inhomogeneous and/or anisotropic material is more often discussed in literature [2; 3; 12]. It is related to the research of functionally graded materials (FGMs), designed for special engineering applications including aircraft,
aerospace, automobile industry and medicine. Functionally graded materials are characterized by the continuous changes of their properties at least in one direction and this feature distinguishes them from the conventional composite materials [8]. In fact the concept of FGMs is inspired with materials occurring in nature, such as: bones, skin and bamboo [4]. These materials have functionally graded and hierarchical structure and they also have different architecture that results in orthortropic behaviour [1].
In this work the elastic-plastic torsion problem of bars made with FGMs is investigated. In the recent years a number of numerical methods of solving this problem have been developed and improved. It is a more complex issue than problem of elastic bar torsion and proposed numerical methods use different approaches.

2. Model of phenomenum

This is a boundary value problem, described by partial differential equation of second order with variable coefficients and appropriate boundary conditions. The problem is formulated for the Prandtl's stress function. Generally, when the shear flexibility modulus is an arbitrary function of cross-sectional coordinates, the analytical solution is not available.
We consider a functionally graded bar of an arbitrary and uniform cross-section. The axis Oz is parallel to the longitudinal axis of the bar and the bar is twisted by two couples of forces acting on its ends. It is assumed that there are no body forces and the bar is free from external forces on its lateral surface. There are no normal stresses on the frontal cross-section.
In case of functionally graded material characteristic G in the torsion equation is a shear modulus in all direction axis on the plane whose is normal in direction Z. The G is a function of geometrical variables, i.e. G(x,y). It is assumed that the G(x,y) is the continuous and differentiable function depending on geometrical coordinates x and y.

The problem is formulated in terms of the Prandtl's stress function and it is described by the equation [7], which is Poisson-like equation. The equation consists of Laplace operator of Prandtl's stress function. In the elastic state the inhomogeneous part of equation is equal to -2. For plastic state the governing equation consists of Laplace operator and another additional non-linear differential operator of the Prandtl's function.
For the formulation the boundary condition has to described. The boundary condition says that the Prandtl's function is equal to zero on the whole boundary.

The stresses are defined as proper partial derivatives of Prandtl's stress function.
The state of each point of considered cross-section of the bar is estimated by von Misses (Huber) hipothesis, using the stresses given by Prandtl's function.
Moreover, the hardening of the material is takes into account. The hardening phenomenum is described by nonlinear analytical function.

3. Meshless methods

The proposal of this paper is to solve problem of elastic-plastic torsion of bar made with FGM using numerical procedure based on one of the meshless methods. The used method is the Fundamental Solution Method (see [6]) supported by approximation by Radial Basis Function. Moreover, the iterative algorithm is applied to tread nonlinearities of the differential equation.
The results of numerical calculation are presented in the paper. The parameters of proposed numerical algorithm are chosen by experiment.
The postprocessing analysis is made, i. e. the stresses and effective plastic stress, effective strain, material flow are calculated and plotted.
The influence of material characteristics and parameters on the torsion, range of plastic deformations are investigated and discussed.

References

[1] V. Birman and L. W. Byrd, Modeling and analysis of functionally graded materials and structures, *Applied Mechanics Reviews* 60:5, 195:216, 2007.
[2] T. Chen, A novel class of graded cylinders neutral to host shafts of arbitrary cross-sections under torsion, *Mechanics Research Communications* 38:1, 68–71, 2011.
[3] C. O. Horgan and A. M. Chan, Torsion of functionally graded isotropic linearly elastic bars, *J. Elasticity* 52:2, 181–199, 1998.
[4] D. K. Jha, T. Kant, and R. K. Singh, A critical review of recent research on functionally graded plates, *Composite Structures* 96, 833–849, 2013.
[5] J. A. Kołodziej and A. Fraska, Elastic torsion of bars possessing regular polygon in cross-section using BCM, *Computers & Structures* 84:1–2, 78–91, 2005.
[6] V. D. Kupradze and M. A. Aleksidze, The method of functional equations for the approximate solution of certain boundary value problems. *USSR Comput. Meth. Math. Phys.* **4**, 82:126, 1964.
[7] S. G. Lekhnitskii, Teori_ uprugosti anizotroinogo tela, 2nd ed., Nauka, Moscow, 1977. Translated as Theory of elasticity of an anisotropic body, *Mir*, Moscow, 1981.
[8] Y. Miyamoto, W. A. Kaysser, B. H. Rabin, A. Kawasaki, and R. G. Ford (editors), Functionally graded materials: design, processing and applications, *Materials Technology Series 5*, Springer, New York, 1999.
[9] A. K. Naghdi, “Torsion of rectangular bars with multiple cylindrical reinforcement or cavities”, *Journal of Applied Mechanics* 61:2, 483–487, 1994.
[10] W. Nowacki, Teoria sprezystosci, *Panstwowe Wydawnictwo Naukowe*, Warszawa, 1970.
[11] S. P. Timoshenko and J. N. Goodier, *Theory of elasticity*, 3rd ed., McGraw-Hill, New York, 1970.
[12] R. Xu, J. He, and W. Chen, Saint-Venant torsion of orthotropic bars with inhomogeneous rectangular cross section, *Composite Structures* 92:6, 1449–1457, 2010.

A MIXED FINITE ELEMENT FORMULATION FOR FINITE ELASTICITY WITH STIFF TWO FIBRE REINFORCEMENT

A. Zdunek[1] and W. Rachowicz[2]

[1]*HB BerRit, Solhelmsbackarna 73, SE-163 56 Spanga, Sweden*
[2]*Institute of Computer Science, Cracow University of Technology, Cracow, Poland*

e-mail: wrachowicz@pk.edu.pl

1. Introduction

A frequent source of anisotropy of elastic materials is the presence of reinforcing fibres which display strong stiffening properties accompanying their stretching. This phenomenon appears as near inextensibility and it is in some way similar to near incompressibility which is observed for the ruber-like materials. Numerical modeling of a nearly inextensible material by the Finite Element Method (FEM) may cause similar difficulties as approximation of a nearly incompressible solid body: unstable or oscilatory solutions. The remedy for incompressible mechanics is the well known splitting of the description of kinematics into the volumetric part (dilatation) θ and the unimodular deformation gradient. The mixed formulation with adequate approximation in the Q^p and P^{p-1} finite element spaces for the displacements $\boldsymbol{u}$ and the auxiliary variables θ and pressure p, respectively, allows one for effective modeling of the nearly incompressible solid [1]. In this work we propose analogous approach to approximation of elastic materials with two fibres reinforcement. One fibre case was studied in [2].

2. Description of kinematics and stresses

In this section we briefly present the main principles of constructing the mixed formulation for the materials reinforced with two families of fibres. We assume that the two preferred directions of reinforcement are given by two distinct fields of unit vectors $\boldsymbol{G}_A, A = 1, 2$ in the reference configuration. We augment them with the third direction $\boldsymbol{G}_3 := \boldsymbol{G}_1 \times \boldsymbol{G}_2/|\boldsymbol{G}_1 \times \boldsymbol{G}_2|$. We consider $\boldsymbol{G}_A$ a basis of the curvilinear system of coordinates corresponding to some parametrization $\boldsymbol{X} = \boldsymbol{X}(\xi^A), A = 1, 2, 3$, i.e. $\boldsymbol{G}_A = \partial \boldsymbol{X}/\partial \xi^A$. We consider also the basis $\underline{\boldsymbol{G}}^A$ of the adjoint space (of linear functionals) which is dual to $\boldsymbol{G}_A$: $\langle \underline{\boldsymbol{G}}^A, \boldsymbol{G}_B \rangle = \delta^A_B$. We use convective spatial coordinates, i.e. the spatial basis vectors are generated by the parametrization $\boldsymbol{x} = \boldsymbol{x}(\zeta^a)$, $\boldsymbol{g}_a = \partial \boldsymbol{x}/\partial \zeta^a$ for wich $\boldsymbol{\zeta} = \boldsymbol{\xi}$. It is known that the deformation gradient $\boldsymbol{F}$, its adjoint $\boldsymbol{F}^*$ and their inverses $\boldsymbol{F}^{-1}$ and $\boldsymbol{F}^{-*}$ take the form:

$$\boldsymbol{F} = \delta^a_A \boldsymbol{g}_a \otimes \underline{\boldsymbol{G}}^A, \quad \boldsymbol{F}^{-1} = \delta^A_a \boldsymbol{G}_A \otimes \underline{\boldsymbol{g}}^a, \quad \boldsymbol{F}^* = \delta^a_A \underline{\boldsymbol{G}}^A \otimes \boldsymbol{g}_a, \quad \boldsymbol{F}^{-*} = \delta^A_a \underline{\boldsymbol{g}}^a \otimes \boldsymbol{G}_A, \tag{2.1}$$

where $\underline{\boldsymbol{g}}^a$ denotes the adjoint basis dual to $\boldsymbol{g}_a$, i.e. satisfying the condition $\langle \underline{\boldsymbol{g}}^a, \boldsymbol{g}_b \rangle = \delta^a_b$. We also introduce the material and spatial metric tensors:

$$\boldsymbol{G} = G_{AB}\, \underline{\boldsymbol{G}}^A \otimes \underline{\boldsymbol{G}}^B \quad \text{and} \quad \boldsymbol{g} = g_{ab}\, \underline{\boldsymbol{g}}^a \otimes \underline{\boldsymbol{g}}^b, \tag{2.2}$$

where $G_{AB} := \boldsymbol{G}_A \cdot \boldsymbol{G}_B$ and $g_{ab} := \boldsymbol{g}_a \cdot \boldsymbol{g}_b$. The right Cauchy-Green deformation tensor takes the form:

$$\boldsymbol{C} = \boldsymbol{F}^* \boldsymbol{g} \boldsymbol{F}, \quad \boldsymbol{C} = \delta^a_A \delta^b_B g_{ab}\, \underline{\boldsymbol{G}}^A \otimes \underline{\boldsymbol{G}}^B. \tag{2.3}$$

We also introduce the structural tensors corresponding to the preferred directions of fibres:

$$\boldsymbol{A}_F := \boldsymbol{G}_F \otimes \boldsymbol{G}_F \quad \text{(no sum)}, \quad F = 1, 2. \tag{2.4}$$

The stretches λ_F of the directions $\boldsymbol{G}_F$ and the cosines between their images $\boldsymbol{g}_F$ can be found as follows:

$$\lambda_F = \langle \boldsymbol{C}, \boldsymbol{A}_F \rangle^{1/2}, \quad \alpha_{FG} = \boldsymbol{g}_F \cdot \boldsymbol{g}_G / (\lambda_F \lambda_G). \tag{2.5}$$

We express the Cauchy-Green deformation tensor in terms of these new variables applying the extra substitution $\lambda_F(\boldsymbol{C}) = \tilde{\lambda}_F,\ F = 1, 2$ reflecting the anticipated procedure of separate numerical approximation of stretches along fibres:

$$\tilde{\boldsymbol{C}} = \tilde{\boldsymbol{C}}(\boldsymbol{C}, \tilde{\lambda}_1, \tilde{\lambda}_2) = \begin{bmatrix} \tilde{\lambda}_1^2 & \alpha_{12}\tilde{\lambda}_1\tilde{\lambda}_2 & \alpha_{13}\tilde{\lambda}_1\lambda_3 \\ \bullet & \tilde{\lambda}_2^2 & \alpha_{23}\tilde{\lambda}_2\lambda_3 \\ \bullet & \bullet & \lambda_3^2 \end{bmatrix}_{AB} \underline{\boldsymbol{G}}^A \otimes \underline{\boldsymbol{G}}^B. \tag{2.6}$$

With these notions in mind we propose the ansatz for the strain energy function $\Psi = \Psi(\boldsymbol{C}; \boldsymbol{A}_1, \boldsymbol{A}_2)$ in the form taking into account that $\tilde{\boldsymbol{C}}$ is expressed by the dependent on deformation tensor $\boldsymbol{C}$ and separately approximated stretches $\tilde{\lambda}_F$:

$$\tilde{\Psi}(\tilde{\boldsymbol{C}}, \tilde{\lambda}_1, \tilde{\lambda}_2; \boldsymbol{A}_1, \boldsymbol{A}_2) = \Psi(\boldsymbol{C}; \boldsymbol{A}_1, \boldsymbol{A}_2). \tag{2.7}$$

Selecting separate approximation of stretches $\tilde{\lambda}_F$ suggests assuming the following augmented strain energy ansatz with the Lagrange multipliers $\tilde{\rho}^F$ corresponding to the constraints $\tilde{\lambda}_F = \lambda_F(\boldsymbol{C})$, F=1,2:

$$\Psi = \tilde{\Psi}(\tilde{\boldsymbol{C}}, \tilde{\lambda}_1, \tilde{\lambda}_2; \boldsymbol{A}_1, \boldsymbol{A}_2) - \textstyle\sum_{F=1}^{2} \tilde{\rho}^F [\tilde{\lambda}_F - \lambda_F(\boldsymbol{C})]. \tag{2.8}$$

The assumptions above and the Clausius-Plank inequality lead to the following constitutive equations for the 2nd Piola-Kirchhoff stress:

$$\begin{cases} \boldsymbol{S} = \sum_{F=1}^{2} \tilde{\rho}^F \lambda_F^{-1} \boldsymbol{A}_F + \tilde{\boldsymbol{S}}, \\ \tilde{\boldsymbol{S}} = \tilde{\mathbb{P}} \left[2 \dfrac{\partial \tilde{\Psi}}{\partial \tilde{\boldsymbol{C}}} \right], \ \text{with } \tilde{\mathbb{P}} := \left[\dfrac{\partial \tilde{\boldsymbol{C}}}{\partial \boldsymbol{C}} \right]^*, \\ \tilde{\rho}^F = \partial \tilde{\Psi} / \partial \tilde{\lambda}_F, \end{cases} \tag{2.9}$$

The mixed formulation for $(\boldsymbol{u}, \tilde{\rho}^F, \tilde{\lambda}_F)$ involves the principle of virtual work (expressing equilibrium), the identification $\tilde{\lambda}_F = \lambda_F(\boldsymbol{C})$ and the constitutive relation for $\tilde{\rho}^F$, and it takes the form: find $(\boldsymbol{u}, \tilde{\rho}^F, \tilde{\lambda}_F) \in (V + \boldsymbol{u}_0) \times Q^4$ such that:

$$\begin{cases} \displaystyle\int_\Omega \langle D_u \boldsymbol{E}(\boldsymbol{u})[\delta \boldsymbol{u}], \boldsymbol{S} \rangle dV = \int_\Omega \langle \boldsymbol{G} \delta \boldsymbol{u}, \bar{\boldsymbol{B}} \rangle dV + \int_{\Gamma_N} \langle \boldsymbol{G} \delta \boldsymbol{u}, \bar{\boldsymbol{P}} \rangle dA, \\ \displaystyle\int_\Omega \delta \tilde{\rho}^F \{ \lambda_F(\boldsymbol{C}) - \tilde{\lambda}_F \} dV = 0, \\ \displaystyle\int_\Omega \delta \tilde{\lambda}_F \{ \partial \tilde{\Psi} / \partial \tilde{\lambda}_F - \tilde{\rho}^F \} dV = 0, \end{cases} \tag{2.10}$$

for all $\delta \boldsymbol{u} \in V, \delta \tilde{\lambda}_F, \delta \tilde{\rho}^F \in Q$, $V = \{ \boldsymbol{v} \in H^1(\Omega) : \boldsymbol{v} = 0, \text{ on } \Gamma_D \}, Q = L^2(\Omega)$. In (2.10) $\bar{\boldsymbol{B}}$ denotes the volume forces, $\bar{\boldsymbol{P}}$ and $\boldsymbol{u}_0$ are the Neumann and Dirichlet data on Γ_N and Γ_D. In addition $\boldsymbol{E} = \frac{1}{2}(\boldsymbol{C} - \boldsymbol{I})$ and $D_u \boldsymbol{E}(\boldsymbol{u})[\delta \boldsymbol{u}] = \frac{1}{2}(\boldsymbol{F}^* \boldsymbol{\nabla} \delta \boldsymbol{u} + \boldsymbol{\nabla}^* \delta \boldsymbol{u} \boldsymbol{F})$. The FE approximation of (2.10) results in a system of nonlinear equations which is solved using the Newton-Raphson algorithm applied to linearization of (2.10).

Numerical tests confirm effectivity of the proposed formulation for strongly anisotropic materials.

References

[1] Simo, J., Taylor, R. and Pister, K., Variational and projection methods for volume constraint in finite deformation elasto-plasticity, *Comput. Methods Appl. Mech. Engng*, 51, pp. 177-208, 1985.

[2] Zdunek, A., Rachowicz, W. and Eriksson, T., A novel computational formulation for nearly incompressible and nearly inextensible finite hyperelasticity, *Comput. Methods Appl. Mech. Engng*, 281, pp. 220-249, 2014.

MESH-FREE AND MESH BASED FINITE VOLUME METHODS FOR THE SOLID MECHANICS ANALYSIS

N. Fallah

Faculty of Civil Engineering, Babol Noshirvani University of Technology, Babol, Iran
e-mail: fallah@nit.ac.ir

1. General

Although the Finite Volume Method (FVM) is a common numerical technique in the computational fluid dynamics, in the last two decades investigations and development of FVM have shown that the FVM can be a promising candidate for solid mechanics analysis. In FVM, the computational domain is discretized into a number of sub-domains, known as finite volumes, control volumes (CVs) or cells. Each sub-domain or control volume contains one computational point which is located in the control volume domain. The governing partial differential equation is forced to be satisfied corresponding to each CV in the integral sense over each finite volume. However, the distinctive feature of FVM is using boundary integral instead of domain integral for satisfying the governing partial differential equation.

According to the recent developments of the FVM, two main categories of FVM exist: mesh based FVM and Mesh-free Finite Volume (MFV) which are explained as follows. Depending on how the control volumes are generated, the mesh based FVM is divided in two groups: cell vertex and cell centred finite volume approaches. In the Cell Vertex Finite Volume (CV-FV), the domain is discretized by a mesh of isoparametric elements. Then, the sub-control volumes are constructed in the finite element mesh by connecting the element's centres to the midpoint of the element faces. Combining all the subcontrol volumes having common grid point, creates a polyhedra type cell that surrounds the common node of the subcontrol volumes. These cells are called as Control Volumes (CV). Figure 1 shows a two dimensional mesh consisting of triangular and quadrilateral elements with associated constructed control volume. In CV-FV, the grid point located in each CV is considered as the computational point where the unkown variables are associated with. The main feature of the CV-FV is that the unknown variables are approximated on faces of cells using the shape functions of the background isoparametric elements [1]. In the cell centred finite volume (CC-FV), a mesh of elements are used for the discretization of the domain and the unknown variables are associated with the computational points which are coincided on the centres of the elements. Different from the CV-FV, unknown variables and their derivatives are approximated based on the finite difference utilization [2]. Therefore, the accuracy of the CC-FV is independent of the order of the background elements mesh. Recently the finite volume capability has been enhanced by developing mesh-free finite volume methods where two mesh-free finite volume approaches are proposed. In both of the MFV approaches, a set of nodes with arbitrary numbers and places are distributed in the domain. In the first approach, non-overlapping CVs are formed around the filed nodes by applying Delaunay triangulation scheme or Voronoi tessellation method. In Delaunay triangulation, similar to the CV-FV scheme the subcontrol volumes are constructed in each triangle by connecting the triangle centre to the midpoint of the triangle faces. Combining all the

subcontrol volumes having common domain node, creates a polyhedra type cell that surrounds that domain node. These cells are called as control volumes (CV) which are non-overlapped. It should be emphasized that the field vaiables and their derivatives on cell faces are approximated by applying MLS technique which is independent of the background triangles geometry but depends to the node distribution [4,5]. It is clear that the distribution of nodes can be wisely performed according to the analyst's interest and based on the behavior of the unknown variable in the field domain. In the Voronoy approach, the nonoverlapping CVs are formed around the field nodes by using the Voronoi diagram technique. Again the field variables and their derivatives on cell faces are approximated by applying the MLS technique [5]. In the second type of MFV, overlapping CVs are formed around the field nodes and techniqes like MLS is used for the approximation of the field variables and their derivatives on cell faces. This type of construction of CVs provides a truly meshless formulation of FV which is also named as MLPG5 by Atluri and Shen [6]. This paper discusses the recent advancement achieved in the development of finite volume method.

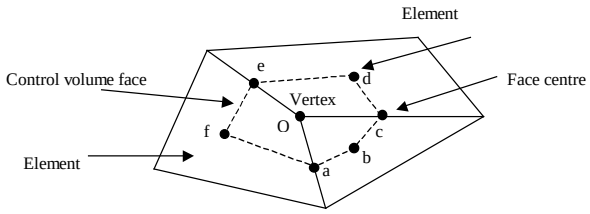

Figure 1. Construction of CVs in CV-FV method.

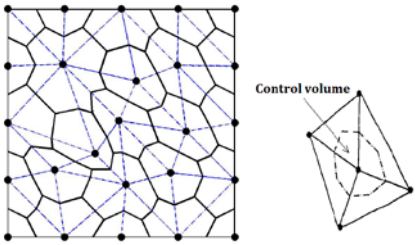

Figure 2. Delaunay triangulation around the distributed nodes and forming CVs.

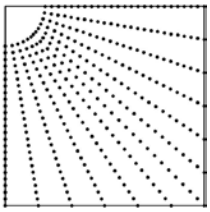

Figure 3. Wisely node distribution in meshless finite volume method.

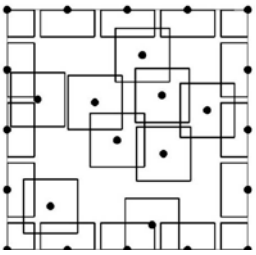

Figure 4. Overlapping CVs in meshless finite volume method.

References

[1] Bailey, C. and Cross, M. A finite volume procedure to solve elastic solid mechanics problems in three dimensions on an unstructured mesh. *Int. J. Numer. Methods Eng*., 38, 1757, 1995

[2] Demirdzic, I., Muzaferija, S. and Peric, M. Benchmark solutions of some structural analysis problems using finite volume method and multigrid acceleration. *Int. J. Numer. Methods Eng*., 40, 1893, 1997

[3] Ebrahimnejad, M., Fallah, N., Khoei, A. New approximation functions in the meshless finite volume method for 2D elasticity problems. *Eng Anal Bound Elem*, 46, 10, 2014.

[4] Fallah, N., Delzendeh, M. Free vibration analysis of laminated composite plates using meshless finite volume method. *Eng. Anal. Bound. Elem.*, 88, 132, 2018.

[5] A. Davoudi-kia, N. Fallah, Comparison of enriched meshless finite-volume and element-free Galerkin methods for the analysis of heterogeneous media, *Eng. Comput.*, DOI · 10.1007/s00366-017-0573-3.

[6] Atluri S. N. , Shen S. The meshless local Petrov-Galerkin (MLPG) method. a simple & less-costly alternative to the finite element and boundary element methods. *Comput. Model. Eng. Sci*., 3, 11, 2002.

A multilevel solver for Stokes equation with discontinuous viscosity

M. Wichrowski[1]

[1]*Institute of Fundamental Technological Research PAN, Pawinskiego 5B, Warsaw,Poland*

e-mail: mwichro@ippt.pan.pl

Introduction

The goal of this work is to develop an efficient scalable solver for the Stokes problem with a strongly discontinuous viscosity:

$$\begin{cases} (\mu \nabla v, \nabla \phi) + (p, \nabla \circ \phi) & = (g, \phi) \qquad \forall \phi \in \mathbb{V} \\ (q, \nabla \circ v) & = 0 \qquad \forall q \in \mathbb{Q} \end{cases} \tag{1}$$

in domain Ω. The domain Ω is partitioned into subdomains Ω_1 and Ω_2, the coefficient μ is strongly variable and subdomain-wise constant.

The main application of the presented solver are fluid-structure problems [5], where due to large difference of properties between fluid and solid, the apparent viscosity may vary by several orders of magnitude. Other important applications are simulation of viscoplastic fluids flows or composite materials in incompressible elasticy. Also mantle convection problems involve fluid models where viscosity may change by several orders of magnitude [3].

For the standard Stokes problem, there exist efficient linear solvers that also may work on high performance computers. The most popular are Krylov subspace methods combined with block preconditioners [4]. The idea behind block methods comes from dual decomposition of system matrix. It allows one to split the main problem into smaller ones. The sub-problems are easy to solve with well-known techniques such as multigrid or domain decomposition.

However, for the variable viscosity Stokes problem the resulting sub-problems are challenging. Especially, it is non-trivial to obtain the operator spectrally equivalent to the (1,1) block that could be inverted easily. The main problem is the dominating *grad-div* term.

Here we consider multigrid methods for saddle-point problems. The idea is to consider Stokes problem as a symmetric positive-definite problem in divergence-free subspace [1, 2]. Then, the constrained smoother may be constructed and used in the multigrid *V-cycle*. The constrained smoother requires computing projection od divergence-free subspace that is computationally demanding. This can be avioded by using approximate projection [7].

For the Laplace problem with discontinuous coefficient, the Krylov subspace solvers with multilevel preconditioners are robust with respect to the problem size and coefficient jump [6]. One may expect similar performance of GMRes method preconditioned by the constrained multigrid cycle.

The described method is here tested by numerical experiments. The results show uniform covergence with respect to both mesh size and coefficient jump.

Results

Numerical experiments were perfomed to study covergence of presented methods. Geometrical settings is showed on Figure 1. The viscosity on inner square was set to 10^6, on the outer ring viscosity was set to 1. The density $\rho = 1$ on the whole domain. Grids were uniformly refined and used for the test. The iteretive procedure was stopped after reducing residual by 10^{-8}.

Table 1. demostrates the obtained number of iterations. For structured and-semi structured grids, the number of iterations remains constant in all tests. The number of iterations in also comparable the constant coefficient

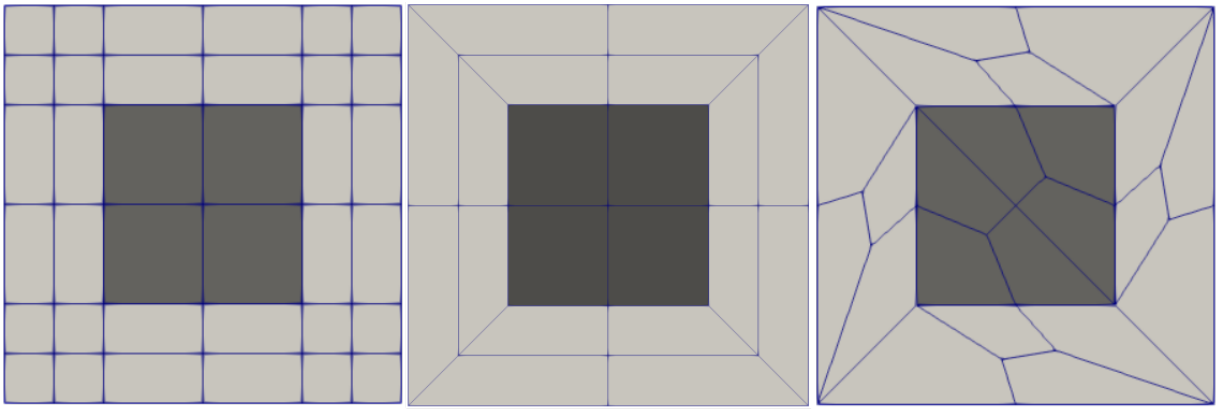

Figure 1: Benchmark problem with coarse grids used for testing the presented algorithm. The inner square is marked in darker grey. From left to right: structured grid, semi-structured grid and unstructured grid.

case. For the ustructured grid, the number of iteration grows slightly, resulting in nearly linear complexity. From the obtained result, one may expect that with increasing problem size the number of iterations may be bounded.

Refinements	Structured grid	Semi-structured grid	Unstructured grid
2	7	11	12
4	7	11	13
8	7	11	15
8, constant coefficient	5	10	13

Table 1: The number of the iterations of preconditioned GMRes method.

Acknowledgments Author would like to thank Prof. Stanisław Stupkiewicz and Dr. Piotr Krzyzanowski for their support. This work was supported by the National Science Centre (NCN) in Poland under grant No. 2015/19/N/ST8/03924.

References

[1] D. Braess and R. Sarazin. An efficient smoother for the stokes problem. *Applied Numerical Mathematics*, 23(1):3–19, 1997.

[2] Long Chen. Multigrid methods for saddle point systems using constrained smoothers. *Computers & Mathematics with Applications*, 70(12):2854–2866, 2015.

[3] Martin Kronbichler, Timo Heister, and Wolfgang Bangerth. High accuracy mantle convection simulation through modern numerical methods. *Geophysical Journal International*, 191(1):12–29, 2012.

[4] P. Krzyzanowski. Block preconditioners for saddle point problems resulting from discretizations of partial differential equations. *Efficient Preconditioned Solution Methods for Elliptic Partial Differential Equations*, page 44, 2011.

[5] J. Xu and K. Yang. Well-posedness and robust preconditioners for discretized fluid–structure interaction systems. *Computer Methods in Applied Mechanics and Engineering*, 292:69–91, 2015.

[6] J. Xu and Y. Zhu. Uniform convergent multigrid methods for elliptic problems with strongly discontinuous coefficients. *Mathematical Models and Methods in Applied Sciences*, 18(01):77–105, 2008.

[7] W. Zulehner. A class of smoothers for saddle point problems. *Computing*, 65(3):227–246, 2000.

NUMERICAL TREATMENT OF THE EPOXY CURING USING FINITE ELEMENTS

S. Hartmann[1] and C. Leistner[1]

[1]*Institute of Applied Mechanics, Clausthal University of Technology, Adolph-Roemer-Str. 2a, 38678 Clausthal-Zellerfeld, Germany*

e-mail: stefan.hartmann@tu-clausthal.de

1. Introduction

The production of polymers on the basis of curing processes of epoxy resins is connected to exothermal reactions. The estimation of the resulting temperatures is necessary since too high temperatures degrade the material and deflagration is initiated. Furthermore, shrinkage is connected to this process, so that a final part is connected to residual stresses. Thus, a precise estimation of the temporal temperature evolution is of particular interest.

First, a curing model is required, where it turns out that the classical Kamal-Sourour model, see [4], is over-parameterized. Thus, a new model with less material parameters is proposed, see [6]. Second, curing- and temperature-dependent heat capacity and heat conductivity are considered as well. Finally, the curing model has to be connected to the heat equation to study the spatial and temporal evolution of both the temperature and the curing state, see, as examples for the numerical treatment using finite elements, [1, 3, 5, 7].

2. Numerical Treatment using Finite Elements

The curing evolution is defined by an ordinary differential equation (ODE). It turns out that these models have a region, where the ODE is inherently unstable, i.e. local small errors increase with time. Thus, high-order time integration schemes have to be applied to minimize the increase of temperature. Since we are not interested in a high-order scheme on Gauss-point level, we draw on the high-order diagonally implicit Runge-Kutta methods (DIRK), where the Backward-Euler method is embedded as a special case. These high-order methods are applied to the space-discretized heat equation and the curing variables, which have to be evaluated at the spatial integration points (Gauss-points). Moreover, time-adaptivity is provided (for free) and does not require more computational effort, see [8]. Fig. 1 shows a comparison of the temperature and curing evolution within one

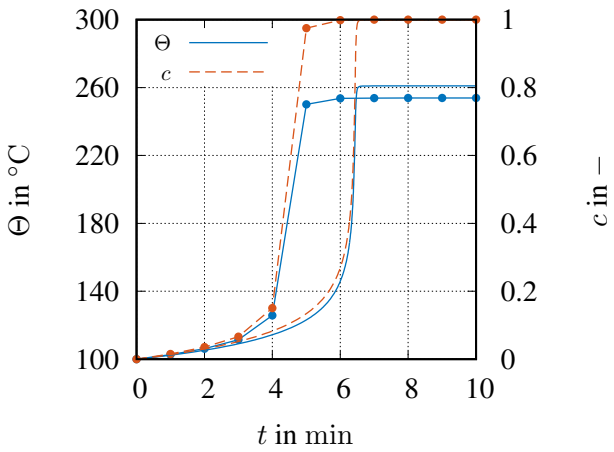

Figure 1: Stability investigation of the curing kinetics. Comparison of 10 time-steps using a Backward-Euler scheme and a time-adaptive, second order computation (dotted lines represent the Backward-Euler computations, whereas the undotted curves symbolize the time-adaptive computations).

element (adiabatic boundary conditions) of the Backward-Euler method with 10 time steps and a time-adaptive computation of Ellsiepen's method, see [2], which are applied to the heat equation and the curing equation.

A further misleading aspect is connected to the application of the non-linear solution scheme to solve the resulting coupled system of non-linear equations occurring after the time-discretization. It will be shown that the resulting space and time discretized coupled system is solved using the Multilevel-Newton algorithm (MLNA) proposed by [9] leading to the particular structure of solving on Gauss-point a non-linear equation to obtain within a global Newton-step the curing variable as well as the (consistent) tangent.

Finally, we apply the whole DIRK/MLNA concept to a validation example, where in an oil bath the temperature evolution of a curing epoxy resin is measured using thermographic measurements of the upper surface of a small cavity. These experiments are compared with the temperature evolution of the finite element computations.

3. Conclusions

On the basis of experimental data a new curing, heat capacity, and heat conductivity model is drawn on. This is implemented into a time-adaptive DIRK/MLNA finite element approach to compute the temperature evolution in a part, where it turns out that this is necessary due to the inherently instability of the curing ODE. The whole concept is compared to thermographic measurements of the temperature evolution of an cured epoxy resin.

Acknowledgments We would like to thank Professor Gerhard Ziegmann and Dr. Dilmurat Abliz for providing DSC measurements and helpful discussions. Furthermore, we would like to thank Marco Löffelholz for supporting the validation experiments.

References

[1] C. Brauner, S. Bauer, and A. S. Herrmann. Analysing process-induced deformation and stresses using a simulated manufacturing process for composite multispar flaps. *Journal of Composite Materials*, 49(4):387–402, 2015.

[2] P. Ellsiepen and S. Hartmann. Remarks on the interpretation of current non-linear finite-element-analyses as differential-algebraic equations. *International Journal for Numerical Methods in Engineering*, 51:679–707, 2001.

[3] M. Hossain and P. Steinmann. Continuum Physics of Materials with Time-Dependent Properties: Reviewing the Case of Polymer Curing. *Advances in Applied Mechanics*, 48:141–259, 2015.

[4] M. R. Kamal. Thermoset characterization for moldability analysis. *Polymer Engineering & Science*, 14(3):231–239, 1974.

[5] R. Landgraf. *Modellierung und Simulation der Aushärtung polymerer Werkstoffe*. PhD thesis, Technische Universität Chemnitz, 2015.

[6] C. Leistner, S. Hartmann, D. Abliz, and G. Ziegmann. Modeling and simulation of the curing process of epoxy resins using finite elements. *submitted to Continuum Mechanics and Thermodynamics*, 2018.

[7] C. Liebl, M. Johlitz, B. Yagimli, and A. Lion. Three-dimensional chemo-thermomechanically coupled simulation of curing adhesives including viscoplasticity and chemical shrinkage. *Computational Mechanics*, 49(5):603–615, 2012.

[8] K. J. Quint, S. Hartmann, S. Rothe, N. Saba, and K. Steinhoff. Experimental validation of high-order time-integration for non-linear heat transfer problems. *Computational Mechanics*, 48:81–96, 2011.

[9] N. B. G. Rabbat, A. L. Sangiovanni-Vincentelli, and H. Y. Hsieh. A multilevel Newton algorithm with macromodeling and latency for the analysis of large-scale nonlinear circuits in the time domain. *IEEE Transactions on Circuits and Systems*, 26:733–740, 1979.

EFFECTS OF MECHANICAL PROPERTIES ON WAVE PROPAGATION OF EXTENDED VISCOELASTIC EULER-BERNOULLI BEAM BY USING WAVELET SPECTRAL FINITE ELEMENT METHOD

M. Golmohammadi, S. Derakhshan, and M. Salehi

Amirkabir University of Technology, Tehran, Iran
e-mail: msalehi@aut.ac.ir

1. Introduction

Wave propagation analysis in structures is of much importance for its applications to problems like structural health monitoring (SHM) and non-destructive tests (NDT). Wave propagation problems deal with high frequency excitations and the FE modelling is not computationally viable as the element size has to be comparable to wavelengths, which are very small at higher frequencies. In the past decades, many different approaches have been published for signal processing like Fast Fourier Transform (FFT), Short Time Fourier Transform (STFT) and etc. These approaches mainly based on dividing time domain to constant fix window of time. Wavelet Transform (WT) is an efficient method for variant oscillations functions analysis like wave analysis. The advantage of WT over other methods is the use of wavelet and scaling functions. This makes variable time window due to oscillation of function in special domain, so, in this approach there is no noise in response in ideal condition.

Complex modulus is a property of viscoelastic materials. It is the ratio of stress to strain under vibratory conditions (calculated from data obtained from either free or forced vibration tests, in shear, compression, or tension). Complex variables can be used to express the moduli E^* and G^* follows:

$$E^* = E' + iE'' \qquad G^* = G' + iG'' \tag{1}$$

In present work, wavelet transform and spectral finite element used to temporal approximation and eigenvalue analysis respectively for Euler-Bernoulli beam formulation. Viscoelastic properties applied in the form of complex modulus time dependent properties. Response of beam (transient velocity) under impulse and tone burst loading extracted for SHM algorithm by studying the effect of mechanical properties of material.

2. Extended Euler-Bernoulli Beam equation

The Euler-Bernoulli Beam governing equation as follows:

$$E^* I \frac{\partial^4 w}{\partial x^4} + \rho A \frac{\partial^2 w}{\partial t^2} = 0, \quad E^* A \frac{\partial^2 u}{\partial x^2} = \rho A \frac{\partial^2 u}{\partial t^2} \tag{2}$$

Wavelet transformed equation is:

$$E^* \frac{d^2 \hat{u}_j}{dx^2} = -\frac{\rho}{\Delta t^2} \gamma_j^2 \hat{u}_j, \quad E^* I \frac{d^4 \hat{w}_j}{dx^4} = \frac{\rho A}{\Delta t^2} \gamma_j^2 \hat{w}_j \tag{3}$$

Where γ_j^2 is diagonal terms of connection coefficents of Daubechies compactly suppoerted wavelet[1]. Essential boundary condition must be transformed to wavelet space. This helps the model for applying arbitrary loading.

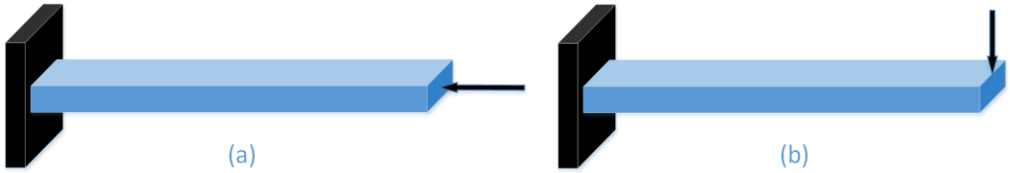

Figure 1.Applied (a)longitudinal (b)transverse loading

3. Problem Solution

Problem is solved by Matlab numerical code. Validation of problem is done with results in [3] with Aluminum material. For present propose PVC, VLDPE and HDPE viscoelastic polymer material properties considered based in [2]. Comparing transient velocity of this material based on properties effect helps to improve SHM algorithm.

4. Results

Response of longitudinal impulse loading applied at the free end by FEM and WSFEM compared in Figure 2. It is well seen that FEM does not provide an accurate response in this case. Comparison of viscoelastic and elastic ($E'' = 0$) of VLDPE behavior under impulse loading is shown in Figure 3.

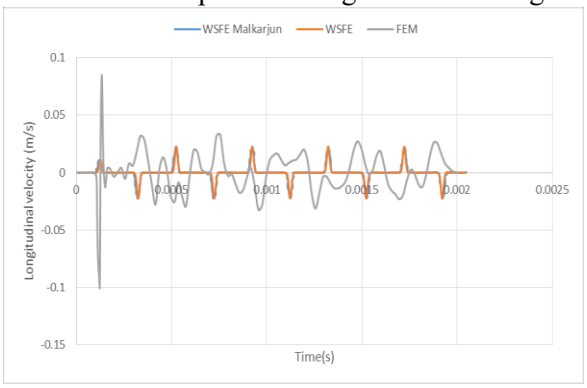

Figure 2. Longitudinal velocity at the free end of beam

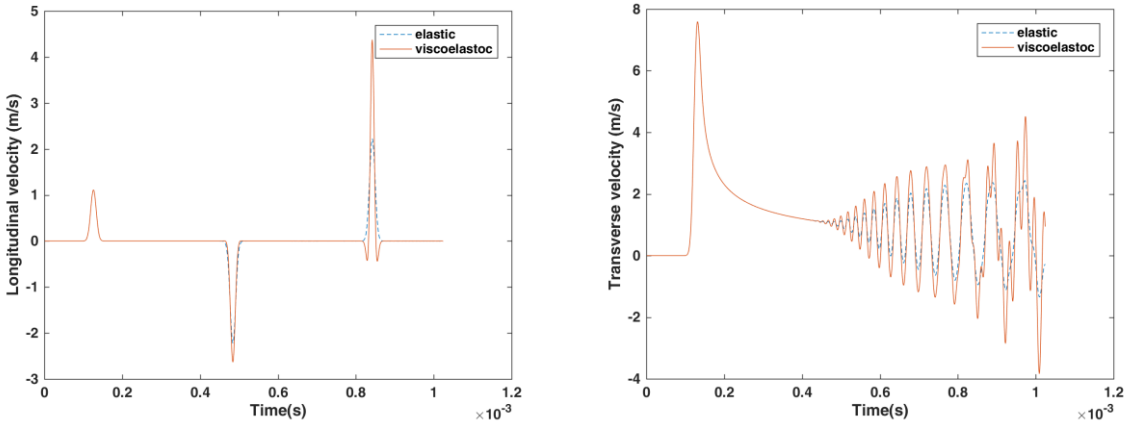

Figure 3. Response of VLDPE beam in elastic and viscoelastic properties under impulse load at the free end of beam

5. Conclusions

Wavelet spectral finite element is an efficient low cost method to wave propagation analysis. Viscoelastic properties of material have different response as compared to elastic properties that is so important because in viscoelastic properties stress may increase by 100%. It means that if only elastic properties are considered in polymer material, it can cause a high risk in design.

References

[1] Gopalakrishnan, Srinivasan; Mitra, Mira. *Wavelet methods for dynamical problems: with application to metallic, composite, and nano-composite structures*. CRC Press, 2010.
[2] Hay, J.; Herbert, E. Measuring the complex modulus of polymers by instrumented indentation testing. *Experimental Techniques*, 2013, 37.3: 55-61.
[3] B. Mallikarjun, "Response of extended Euler-Bernoluli beam under impulse load using wavelet spectral finite element method," National Institute of Technology, Rourkela, 2012.

COMPUTATIONAL ASPECTS OF CHEMO-ELASTIC PROBLEMS AND VEGARD'S LAW

P. Dłużewski

Institute of Fundamental Technological Research, Polish Academy of Sciences (IPPT PAN)
ul. Pawińskiego 5^B , 02-106 Warszawa, Poland

e-mail: pdluzew@ippt.pan.pl

Vegard's law states that the length of lattice vectors of a solid solution changes linearly with its chemical composition. In 1921, such a rule was observed for cubic crystals by Vegard [2]. Recently, this law is used widely for many other structures. In the case of low symmetry crystals, the shape of resultant unit cell (spanned on the lattice vectors) depends not only on three lattice parameters, a, b, c, but also on three crystallographic angles which are not determined uniquely by the classical (scalar) form of Vegard's law.

The problem is that for lattice structures of low symmetry (arbitrary chosen repère) the mentioned law can be generalized in a different way. In result, various generalizations were proposed in literature, see e.g. a discussion in [1].

In many computational problems the scalar weighting functions are used for averaging of elemental lattice vector bases (Vegard's law), for example:

1. Projection of nodal distortions to Gauss points in the finite element method (FEM),

2. Projection of lattice vectors to the interfacial zone in the phase field method (PFM),

3. Calculation of lattice vectors for solid solutions (the classical application of Vegard's law).

As a matter of fact, it can be proved that all generalizations of Vegard's law proposed as of yet do not determine uniquely the resultant size of unit cell for low symmetry solid solutions. For example, the use of Vegard's law for calculation of lattice vectors of a monoclinic binary system $Mg_yCu_{3-y}V_2O_8$ should not depend on the choice of the reference structure, $Mg_3V_2O_8$ vs $Cu_3V_2O_8$. From the stoichiometric point of view, the lattice (P 1 2_1/c 1) of $Mg_yCu_{3-y}V_2O_8$ and $Mg_{3-z}Cu_zV_2O_8$ for y = z = 1.5 means one and the same crystal structure $Mg_{1.5}Cu_{1.5}V_2O_8$.

In the case of the n-ary system the strain tensor generalization of Vegard's law can be rewritten in the following form

$$\mathbf{e}_j = \Big(\mathbf{1} + \sum_{i=1}^{n} x_i \boldsymbol{\varepsilon}_{i0}\Big)\mathbf{e}_{j_{cr_0}} \tag{1}$$

where $\mathbf{e}_j$, x_i, $\boldsymbol{\varepsilon}_{i0}$ and $\mathbf{e}_{j_{cr_0}}$ denote the resulting lattice vectors for the solid solution, the weighting function of the i-th chemical compound, its strain tensor, and the lattice vectors of a crystal phase chosen as the reference (the reference repère), respectively.

With respect to different definitions of strain tensors and different choice of the reference lattice, the many different generalizations of Vegard's law were published. Contrary to the previous generalizations, the generalized form of Vegard's law presented here is invariant with respect to the choice of the reference chemical composition. From the view point of the projection the nodal distortions to Gauss points, this form of Vegard's law provides the indifference of the Gauss point distortion with respect to the choice of the reference repère. From the viewpoint of the phase field method, the generalization proposed means that the resultant values of the lattice parameters in the interfacial zone are independent of the choice of the reference phase.

References

[1] L. Peters, K. Knorr, P. Schmid-Beurmann, and W. Depmeier. On the volume of solid solutions: an anisotropic approach. *Physics and Chemistry of Minerals*, 33(1):10–16, 2006.

[2] L. Vegard. Die konstitution der mischkristalle und die raumfüllung der atome. *Zeitschrift für Physik*, 5(1):17–26, Jan 1921.

Session S06: Discrete and multiscale modelling in solid mechanics

Organizers: J. Rojek (IPPT PAN, Warsaw), M. Pietrzyk (AGH Univ. of Science and Technology, Cracow), R. Kačianauskas (Vilnius Gediminas TU, Lithuania), B. Peters (Université du Luxembourg)

EFFECT OF TRIMODALITY ON STRUCTURAL AND MECHANICAL PROPERTIES OF GRANULAR PACKINGS WITH DIFFERENT PARTICLE SIZE RATIOS AND PARTICLE SIZE FRACTIONS

J. Wiącek

Institute of Agrophysics, Polish Academy of Sciences, Doswiadczalna 4, 20-190 Lublin, Poland

e-mail: jwiacek@ipan.lublin.pl

1. Introduction

Over the last few decades, a number of studies has been conducted to investigate the relation between the structural properties and the mechanical behavior of particulate assemblies with the particle size heterogeneity [1-3]. Although investigations were devoted to systems with various degree of polydispersity, a review of the literature shows that studies on properties of ternary granular packings with *PSD* uniform and nonuniform by number of particles are very limited. Since ternary mixtures are commonly used in many branches of industry (e.g., chemistry, pharmacy, and metallurgy) and exhibit interesting and unexplained behavior, an examination of their properties is very important and necessary. Therefore, this study focuses on the analysis of the effect of particle size ratio and the number fraction of mixtures composed of three grain size fractions on their structure and mechanical properties. Knowledge gained from presented project may lead to better understanding of real granular mixtures with more complex *PSD*s and may find application in industries dealing with granular materials.

2. System description and numerical procedures

The 3D simulations were conducted using the EDEM software, based on the Discrete Element Method [4]. A simplified viscous-elastic non-linear Hertz-Mindlin contact model was used. The input parameters for DEM simulations, corresponding to the mechanical parameters of steel rods and steel walls were used in this study.

A confined uniaxial compression test of granular packings was simulated, which is a standard laboratory test procedure to measure mechanical properties of granular materials. The spheres with random initial coordinates were generated inside the box with rectangular cross-section. Spheres settled down onto the bottom of the test chamber under gravity in a dispersed stream. Next, spheres were compressed through the top cover of the chamber that moved vertically downwards at a constant velocity until a maximum vertical pressure on the uppermost particles reached 100 kPa.

Simulations were carried out for samples composed of three particle size fractions. The samples were described by particle size ratio g, defined as a ratio between the diameter of the largest and the smallest spheres. The particle size ratio varied from 1.25 to 5. Samples had particle size distribution uniform by number of particles (*i.e.* an equal number of particles of different sizes) or nonuniform by number of particles (*i.e.* a different number of particles of different sizes). Mixtures with *PSD* nonuniform by number of particles were described by factor f which defined a percentage contribution of spheres representing different particle size fractions to total number of particles in mixture.

3. Results

The study included an effect of the particle size ratio and the number fraction on porosity, compression index, number of contacts, distribution of contact forces, pressure ratio and elastic modulus.

Figure 1a shows the evolution of the porosity of samples (Φ) with different values of g, subjected to compressive loads. An increase in value of g form 1.25 to 2.5 resulted in a substantial decrease in porosity, that was not observed for larger g values. In the entire range of compressive load, the differences between porosities of mixture with $g \geq 2.5$ fell within the range of scattering. The exceedance of $g=2.5$ did not change significantly volume of empty space between large particles providing approximate porosities.

Figure 1b shows the evolution of effective elastic modulus (E) with compressive loads in samples with different g values. No evident relation between the modulus of elasticity and particle size ratio was observed

and differences between E values calculated for different g lied within the range of scatter.

a) b)

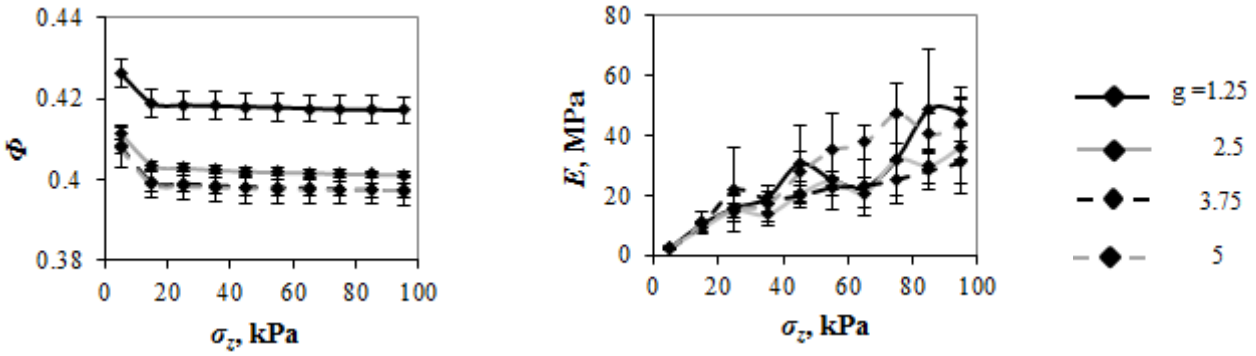

Fig. 1. Evolutions of porosity (a) and effective elastic modulus (b) of mixtures with various values of g with imposed compressive pressures.

Figure 2a shows the porosities of packings with various number fraction of particles with g=1.25 and g=3.75. Regardless of g value, the porosity increased with an increase in the number fraction of coarse spheres. The largest porosities were obtained for mixtures composed of the same number of coarse and medium spheres (f=442). Figure 2b presents the lateral-to-vertical pressure (k) ratio in mixtures with different g and f. Regardless of g value, the pressure ratio was greater in mixtures with f=424 as compared to samples with f=244, that increased by few percentage for samples with f=442. The k values were larger for smaller g indicating that, in mixtures with *PSD* non-uniform by number of particles, the pressure ratio is determined by both, geometric and statistic factors.

a) b)

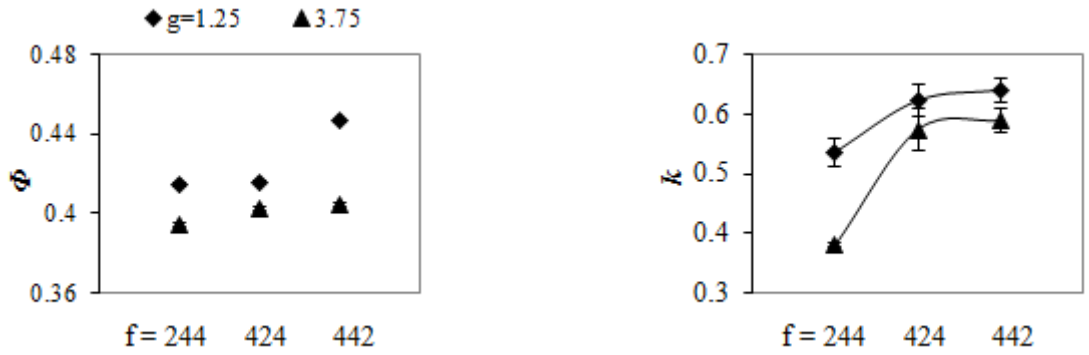

Fig. 2. Evolutions of porosity (a) and lateral-to-vertical pressure ratio (b) for mixtures with g=1.25 and g=3.75, and different number fraction of particles.

4. Conclusions

A study on the effect of the particle size ratio on the properties of ternary mixtures with *PSD* uniform by number of particles has shown that the g value significantly affected packing structure, while the mechanical properties were found to be negligibly influenced by the particle size ratio. An evident effect of the contribution of the particle size fractions in ternary packing on its porosity, coordination number, and pressure ratio was also observed, which increased with an increase in value of g.

References

[1] R.K. McGeary, Mechanical Packing of Spherical Particles, *J. Am. Ceram. Soc.*, 44: 513-523, 1961.
[2] F. Göncü, O. Durán and S. Luding, Constitutive relations for the isotropic deformation of frictionless packings of polydisperse spheres, *C.R. Mecanique*, 338: 570-586, 2010.
[3] J. Wiącek, M. Stasiak and P. Parafiniuk, Effective elastic properties and pressure distribution in bidisperse granular packings: DEM simulations and experiment, *Arch. Civ. Mech. Eng.*, 17: 271-280, 2017.
[4] P.A. Cundall and O.D. Strack, A discrete element model for granular assemblies, *Géotechnique*, 29: 47-65, 1979.

ASPHALT CONCRETE MODELING BY THE MULTISCALE FINITE ELEMENT METHOD

M. Klimczak and W. Cecot

Cracow University of Technology, Cracow, Poland

e-mail: mklimczak@L5.pk.edu.pl

1. Introduction

Asphalt concrete (AC) is a composite material consisting of a stone aggregate with irregularly shaped, randomly distributed and oriented grains, a bituminous binding agent, air voids as well as further specific additives (the binder mixed with a mineral filler of a very small diameter is called a mastic). In this study, we focus on the AC typical version comprising only the first three constituents. From the road engineer point of view, behavior of this composite is analyzed at the macro resolution. However, all of the phenomena occurring at lower scales should be incorporated in the macro scale analysis. A cumbersome fact is that above mentioned constituents of this heterogeneous compound can be described with different material models. A stone aggregate is typically analyzed as the elastic body [5,10,14], whereas the asphalt binder is usually assumed to behave viscoelastically [5,8,10–12,15] or viscoelastoplastically [2,9]. In complex studies, accumulating fracture damage due to thermal effects [2, 5, 14] is also investigated. Modeling of the mastic-aggregate interface is another demanding aspect [5, 8, 10].

Beside the phenomenological approach, which is costly and time consuming, numerical modeling of asphalt concrete is a very active research field. The developed methods allow to capture the effective response of this material under applied loads. This approach is justified specially in the context of the whole asphalt roadway analysis.

In this study, we focus on the efficient numerical modeling of the AC heterogeneity. Both the aggregate and binder phases are modeled as purely elastic. For the sake of simplicity, air voids and mastic-aggregate interfaces are also ignored. Our main objective is to present the upscaling method for AC taking into account both the randomness and non periodicity of its micro structure (c.f. [13]).

2. Methodology

In order to analyze the asphalt mix at the macro resolution, we use the multiscale finite element method (MsFEM). Its idea is based on a concept of special shape functions accounting for the material heterogeneity [3, 4] and neither periodicity nor scale separation are requested. Further contribution to the MsFEM was to accommodate it for higher order approximation [1, 7]. The algorithm of the MsFEM consists of three main steps. First, a coarse mesh is generated to discretize the analyzed domain. Subsequently, auxiliary problems (see [1] for details) are solved within every coarse element to assess modified shape functions resulting from the heterogeneity. This step leads to the computation of the effective stiffness matrices by fast algebraic operations without integration. Finally, the coarse mesh (generated at the first step) with these matrices is used to solve the problem of our interest.

The crucial part of this study is also the generation of the random AC micro structure. We propose a new algorithm based on a structured grid instead of the Voronoi diagram that is commonly employed for this purpose (c.f. [12, 13, 15]).

3. Results

We compared the results of the MsFEM and the fine mesh (an extremely refined mesh covering the material heterogeneity) computations. Significant reduction of the degrees of freedom number was observed without severe modeling error introduction.

4. Discussion

The present study is a part of the ongoing research aimed at the effective AC modeling. We demonstrated the applicability of the MsFEM to this scientific problem. The improved homogenization method is very efficient in the case of non periodic domain without a distinctive scale separation. In another paper [6], we presented the application of the MsFEM to non periodic viscoelastic materials with trivial inclusion shapes. Consequently, our further research effort is to verify the algorithm of the random AC generation for purely elastic cases and apply the MsFEM to real-life domains with nonlinear material models.

Acknowledgments The authors acknowledge the financial support of the National Science Center (NCN) under the grant no. UMO-2017/25/B/ST8/02752.

References

[1] W. Cecot and M. Oleksy (2015). High order FEM for multigrid homogenization, *Computers and Mathematics with Applications*, **70**(7), 1391-1400.

[2] A.C. Collop, A.T. Scarpas, C. Kasbergen and A. de Bondt (2003). Development and finite element implementation of a stress dependent elasto-visco-plastic constitutive model with damage for asphalt, *Journal of the Transportation Resarch Board*, **1832**, 96-104.

[3] Y. Efendiev and T.Y. Hou (2007). Multiscale finite element methods for porous media flows and their applications, *Appied Numerical Mathematics*, **57**, 577-596.

[4] T.Y. Hou and X.H. Wu (1997). A multiscale finite element method for elliptic problems in composite materials and porous media, *Journal of Computational Physics*, **134**, 169-189.

[5] YR. Kim, F.V. Souza and J.E.S.L. Teixeira (2013). A two-way coupled multiscale model for predicting damage-associated performance of asphaltic roadways, *Computational Mechanics*, **51**(2), 187-201.

[6] M. Klimczak and W. Cecot (2018). An adaptive MsFEM for nonperiodic viscoelastic composites, *International Journal for Numerical Methods in Engineering*, 1-21, https://doi.org/10.1002/nme.5768.

[7] M. Krówczyński and W. Cecot (2017). A fast three-level upscaling for short fiber reinforced composites, *International Journal for Multiscale Computational Engineering*, **15**(1), 19-34.

[8] P. Liu, J. Hu, D. Wang, M. Oeser, S. Alber, W. Ressel and G.C. Fala (2017). Modelling and evaluation of aggregate morphology on asphalt compression behavior, *Construction and Building Materials*, **133**, 196-208.

[9] K. Mitra, A. Das and S. Basu (2012). Mechanical behavior of asphalt mix: An experimental and numerical study, *Construction and Building Materials*, **27**(1), 545-552.

[10] L.T. Mo, M. Huurman, S.P. Wu and A.A.A. Molenaar (2008). 2D and 3D meso-scale finite element models for ravelling analysis of porous asphalt concrete, *Finite Elements in Analysis and Design*, **44**(4), 186-196.

[11] T. Schüller, R. Manke, R. Jänicke, M. Radenberg and H. Steeb (2016). Multi-scale modelling of elastic/viscoelastic compounds, *ZAMM - Journal of Applied Mathematics and Mechanics*, **93**, 126-137.

[12] T. Schüller, R. Jänicke and H. Steeb (2013). Nonlinear modeling and computational homogenization of asphalt concrete on the basis of XRCT scans, *Construction and Building Materials*, **109**, 96-108.

[13] J. Wimmer, B. Stier, J.-W. Simon and S. Reese (2016). Computational homogenisation from a 3D finite element model of asphalt concrete - linear elastic computations, *Finite Elements in Analysis and Design*, **110**, 43-57.

[14] T. You, R.K.A. Al-Rub, M.K. Darabi, E.A. Masad and D.N. Little (2012). Three-dimensional microstructural modeling of asphalt concrete using a unified viscoelasticŰviscoplasticŰviscodamage model, *Construction and Building Materials*, **28**(1), 531-548.

[15] V. Ziaei-Rad, N. Nouri, S. Ziaei-Rad and M. Abtahi (2012). A numerical study on mechanical performance of asphalt mixture using a meso-scale finite element model, *Finite Elements in Analysis and Design*, **57**, 81-91.

MULTI-SCALE MODELLING OF SNOW MECHANICS

B. KABORE[1], B. PETERS[1], C. WILLIBALD[2], T. THIELE[2], and M. SCHNEEBELI[2]

[1] *University of Luxembourg, Luxembourg, Luxembourg*
[2] *Institute for Snow and Avalanche Research SLF, Davos, Switzerland*

e-mail: bricewendlassida.kabore@uni.lu

1. Introduction

Dynamic and static behavior of snow are of great importance in some engineering applications: *impact on civil infrastructures, avalanches prediction and protection, tire-snow interactions, icing of aircrafts and machinery...* Beyond density, the microstructural parameters of snow have received increasing attention in recent years as the density alone could not accurately represent the mechanical behavior of snow. A realistic modeling of snow dynamics requires a multi-scale approach. This work adopts the following hierarchical modeling approach: first, a mathematical modeling of the grain scale response featuring most of relevant micro-mechanical processes; second, an investigation of meso-mechanical response of representative volumes from structures observed through x-ray computed tomography; Third, upscaling meso-mechanical properties for macro-mechanical behavior.

2. Method formulation

The complex underlying physics at grain scale includes friction, creep, pressure or frictional melting and re-freezing of contact interface creating a bonded structure and a high energy dissipation during macroscopic flow and deformation. Most of these processes are function of the thermodynamic state of the snow. Similar processes are observed in powder metallurgy and additive manufacturing where strengthening and porosity reduction through sintering is accelerated by pressure [3]. From numerical modeling viewpoint, the granular phase can be characterized with frictional interaction of discrete particles and hysteretic energy dissipation. The solid phase is a porous media composed of meso-scale structures with evolving geometries and fracture properties. The inherent mechanical behavior of such structures can be captured using bonded particles for which according to the stress state at the contact area occur: instantaneous bonding or re-bonding due to visco-plasticity and melt-freeze mechanism for compressive stress; elastic deformation and quasi-brittle fracture of the resulting structure under destructive torques, tensile and shear stress. The micro-structure evolution is represented by coupling discrete particle model for the first mechanism and a network of Euler-Bernoulli microbeam model with fracture for the later. Model parameters are calibrated using snow rheology and strength measurement of bond created between contacting ice spheres at different time scales [2] [4].

The snow is considered as a viscoelastic material with a memory effect [1]. For two contacting ice particles we consider the force displacement relation of burger material which includes rate dependence and loading history in the following equation:

$$f^c + [\frac{\eta_d}{k_d} + \eta_i(\frac{1}{k_d} + \frac{1}{k_i})]\dot{f^c} + \frac{\eta_d \eta_i}{k_d E_i}\ddot{f^c} = \eta_i \dot{u} + \frac{\eta_d \eta_i}{k_d}\ddot{u} \tag{1}$$

Where η_i and k_i are the instantaneous viscosity and stiffness constant, η_d and k_d the delayed viscosity and stiffness constant, $\dot{u}$ displacement rate, $\ddot{u}$ the acceleration.
The resulting bonding microbeam start thickening and the resistance force under tensile stress is calculated as follow :

$$f^b = \begin{cases} ku & \text{if } u < u_l \\ ku_l\Psi & \text{if } u_l \leq u \leq u_f \end{cases} \tag{2}$$

Where the bond stiffness k is function of the beam radius and length, u_l is the limit elastic displacement and Ψ is

a damping function for fracture energy dissipation, u_f is a displacement limit depending on the fracture energy. The shear force, bending and torsion torques are computed according to the Euler-Bernoulli beam theory with a quasi-brittle failure and fracture energy dissipation to explicitly account for phase change.

3. Results and remarks

The micro-scale model allowed us to carry out detailed analysis of high strain and rate-dependent behavior and microstructure based fracture parameters. The following images show created microbeam structure under an isotropic compression and the flow of a granular phase after failure of the microbeam structure under high strain rate uni-axial compression. The Fracture force is calculated by multiplying the area of the created bond to the ultimate tensile strength of ice. The solid phase is characterized by the presence of microbeam. Under high

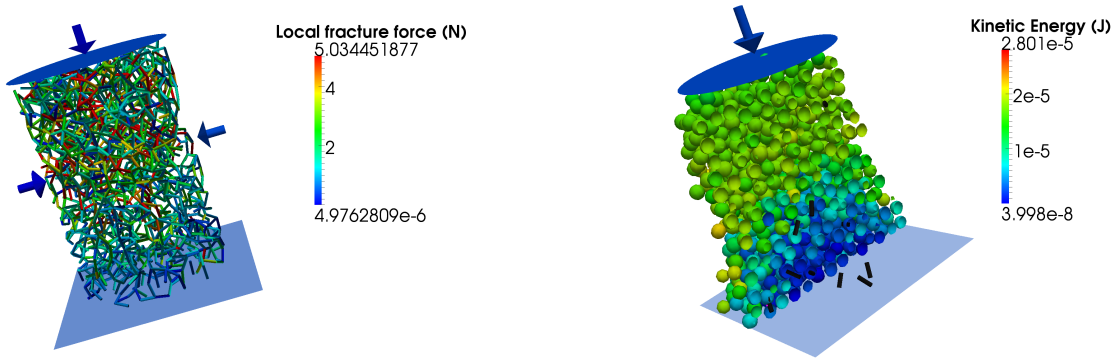

(a) (b)

Figure 1: *Tests at -5^oC a) Tensile force required to fracture local microbeam structure after a moderate strain rate isotropic compression; b) ongoing damage under high strain rate loading.*

strain rate the brittleness of snow and granular phase is characterized by fracture and low microbeams density.

4. Conclusion

In an effort to simulate the flow of granular snow and fracture behavior of packed snow during large deformations, a hierarchical approach consisting of micro-scale characterization, meso-mechanical and macro-mechanical modeling have been adopted. Based on creep tests and grains bonding strength measurements, calibration and validation of the grain scale mechanical model was performed and meso-scale fracture behavior was investigated. Also mechanical behavior under high strain and different strain rates and pressure sintering of snow have been investigated and modeled.

Acknowledgments This work received the financial support of the Luxembourg National Research Fund and the Swiss National Science Foundation. Simulations were carried out on the HPC facilities of the University of Luxembourg

References

[1] J. Desrues, F. Darve, E. Flavigny, and P. Navarre. An incremental formulation of constitutive equations for deposited snow. *Journal of Glaciology*, 1980.

[2] H. Gubler. Strength of Bonds between Ice Grains after Short Contact Times. *Journal of Glaciology*, 28(100):457–473, 1 1982.

[3] Szymon Nosewicz, Jerzy Rojek, Marcin Chmielewski, and Katarzyna Pietrzak. Discrete element modeling and experimental investigation of hot pressing of intermetallic NiAl powder. 2017.

[4] Denes Szabo and Martin Schneebeli. Subsecond sintering of ice. *Applied Physics Letters*, 2007.

ANALYSES OF SIZE EFFECT IN CONCRETE AT MESO-SCALE DURING SPLITTING TENSION TEST USING DEM

J. Suchorzewski[1] and J. Tejchman[1]

[1]*Gdańsk University of Technology, Narutowicza 11/12, Gdańsk, Poland*
e-mail: jansucho@pg.edu.pl

1. Introduction

The size effect is a fundamental phenomenon in concrete materials. It denotes that both the nominal structural strength and material ductility (ratio between the energy consumed during the loading process after and before the stress-strain peak) always decrease with increasing element size under tension [1]. Thus, concrete becomes ductile on a small scale and perfectly brittle on a sufficiently large scale. Two size effects are of a major importance: energetic (or deterministic) and statistical (or stochastic) one. In spite of the ample experimental evidence, the physically based size effect is not taken into account in practical design rules of engineering structures, assuring a specified safety factor with respect to the failure load. Instead, a purely empirical approach is sometimes considered in building codes which is doomed to yield an incorrect formula since physical foundations are lacking.

The objective of the present paper is to analyze numerically a quasi-static size effect in concrete at the meso-level during differing failure mechanisms (varying from quasi-brittle to very brittle with the snap-back instability) observed in quasi-static splitting tension tests for different specimen diameters.

2. Experiments

Own experiments on splitting tension were carried out with concrete specimens of the diameter D=74, 100, 150, 192 and 250 mm under the CMOD-control. The strength and ductility decreased with increasing specimen diameter. For large specimen diameters D>100 mm, a clear snap-back instability occurred. Advanced x-ray micro-tomography system Skyscan 117 was used to determine concrete meso-structure [2].

3. Simulations with Discrete Element Method (DEM)

The calculations were performed with the three-dimensional spherical discrete element model YADE, which was developed at University of Grenoble [3]. This 3D spherical discrete element method takes advantage of the so-called soft-particle approach (i.e. the model allows for particle deformation which is modelled as an overlap of particles). During the simulations, particles may overlap that can be interpreted as a local contact deformation. A linear normal contact model in compression was used. The interaction force vector representing the action between two spherical discrete elements in contact was decomposed into a normal and tangential vector, respectively. The normal forces acting on spheres were modelled by an elastic law with cohesion. Concrete was depicted as a four-phase composite material including aggregate, cement matrix, interfacial transitional zones (ITZs) and macro-voids [4]-[6]. The realistic description of the meso-structure with the presence of ITZs was necessary to faithfully reproduce the crack shape in concrete. The DEM calculations were performed with the concrete specimens of the different diameter used in experiments(Fig.1). ITZs were simulated for the sake of simplicity as contacts between aggregate and cement matrix grains. Thus they had not the physical width in contrast to experiments. The detailed calibration procedure was based on preliminary uniaxial compression laboratory tests.

The process of micro- and macro-cracking was studied in detail for various failure modes including the snap-back. The macroscopic stress-CMOD curves and shapes of cracks were directly compared with the test outcomes. In addition, the evolution of contact forces, crack displacements, number of broken contacts were analysed at the aggregate level. Internal energies were carefully studied in specimens of the different diameter with various failure modes. A satisfactory agreement between with experiments was obtained. The experimental size effect was realistically reproduced in numerical calculations at the aggregate level, i.e. the

concrete strength and ductility decreased with increasing concrete specimen diameter. The decreasing strength reached an asymptote with increasing specimen diameter.

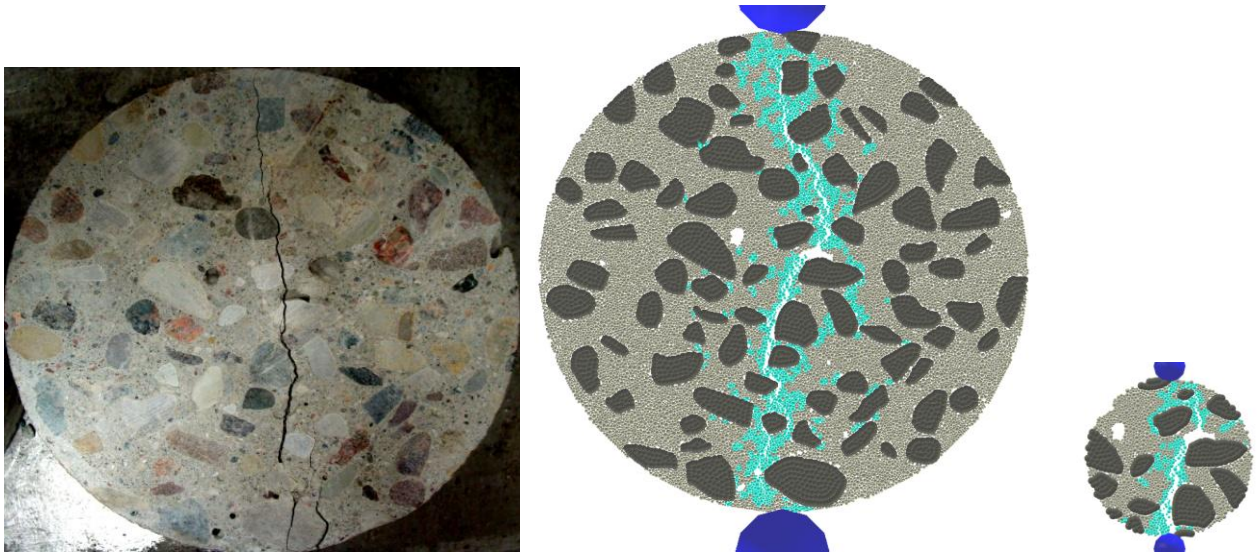

a) b) c)

Figure 1: Fracture in concrete specimen in splitting tensile test in a) experiment and DEM calculations with 2 different specimen diameters: b) D=0.15 m and c) D=0.05 m (black colour indicates aggregates, grey colour represents cement matrix, white colour shows macro-pores, cyan colour denotes area with broken contacts and blue colour shows supports

The relatively more contacts were broken before the peak load for the larger concrete specimen than for the smaller one (by 25%) and after the peak load for the smaller specimen than for the larger one (by 25%). Thus, during the snap-back behaviour relatively less contacts were damaged than during the quasi-brittle behaviour. The strong micro-cracking process mainly started in the smaller specimen slightly before the peak load and in the larger specimen clearly before the peak load (that contributed to the lower strength).

Acknowledgments Research was carried out within the project "Experimental and numerical analysis of coupled deterministic-statistical size effect in brittle materials" financed by the Polish National Science Centre NCN (UMO-2013/09/B/ST8/03598).

4. References

[1] J. Tejchman and J. Bobiński *Continuous and discontinuous modeling of fracture in concrete using FEM*. Spring Berlin-Heidelberg (eds. W. Wu and R. I. Borja), 2013.

[2] Skarżyński L. and Tejchman J. Experimental investigations of fracture process in concrete by means o f x-ray micro-computed tomography. *Strain* 52, 26-45, 2016.

[3] Kozicki J. and F.V. Donze F.V. A new open-source software developer for numerical simulations using discrete modeling methods. *Computer Methods in Applied Mechanics and Engineering* 197, 4429-4443, 2008.

[4] J. Suchorzewski, J. Tejchman, J. Nitka. DEM simulations of fracture in concrete under uniaxial compression based on its real internal structure. *Int. J. Damage Mechanics*, 27 (4) (2018), 578-607.

[5] J. Suchorzewski, J, Tejchman and M. Nitka Experimental and numerical investigations of concrete behaviour at meso-level during quasi-static splitting tension. *Theoretical and Applied Fracture Mechanics* 2017 10.1016/j.tafmec.2017.10.011.

[6] M. Nitka and J. Tejchman. A three-dimensional meso scale approach to concrete fracture based on combined DEM with X-ray μCT images. *Cement and Concrete Research*, 107: 11-29, 2018.

CONTACT TRANSFORMATIONS IN GRANULAR ASSEMBLIES OF 2D NON-CONVEX GRAINS

Krzysztof Szarf[1]

[1]*Chair of Geotechnics, Geology and Marine Civil Engineering, Faculty of Civil and Environmental Engineering, Gdansk University of Technology, Gdansk, Poland*
e-mail: krzszarf@pg.edu.pl

1. Context of the Study

Numerical modelling of granular materials as discrete particles becomes more common, especially with increasing computational power available. The default tactic of many researchers is to increase the overall complexity of the simulation but to save on computational power by oversimplifying important aspects of the medium itself, namely the form of the particles used. Most of Discrete Element Method simulations incorporate the simplest particle shapes possible: discs in 2D and spheres in 3D. The well-known pathological effects of such assemblies (e.g. low shear resistance, small changes of volume in shearing) are remediated with various numerical features, such as additional contact laws [4, 5], restrictions on degrees of freedom [2], etc. Such approaches, however effective, can be regarded as controversial because of dubious values of the multiple numerical parameters needed.
Other simulations incorporate complex particle shapes, but without full understanding of the underlying physics. Detailed studies focused on the grain shape influence have been performed [1, 3, 7], but the problem remains open to further investigations.

2. Overview of the Study

A family of non-convex 2D particles (clumps) with three axes of symmetry was chosen to form multiple polydisperse assemblies simulated in the framework of Molecular Dynamics in *PFC*^{2D}. The particles, each made of three discs, were described with a single low-order shape parameter α. The samples were carefully prepared so as to ensure homogeneity of the initial assemblies in terms of contact directions, spatial distribution of porosity, distribution of the coordination number, etc. The numerical parameters of the simulations were chosen with respect to certain dimensionless characteristic numbers [6] to assure quasi-static loading conditions. Each sample consisted of 5000 identical particles of different sizes, initially loaded isotropically in a square box, and later biaxially compressed ($\dot{\varepsilon}_1$= *const*; σ_3= *const*) up to a critical state, where $\frac{p}{q} = \frac{\sigma_1 - \sigma_3}{\sigma_1 + \sigma_3} \cong const$ and $\varepsilon_{vol} \cong const$. Four comparable but random samples of each particle shape type were prepared in parallel in order to enable statistical analysis of the results. Although the results of such simulations were investigated macroscopically in the past [8], their microscale studies leave a lot of room for further research.

Because of the complex shapes of the clumps, much more complicated contacts were possible between any two particles (contacts between two neighbouring clumps via two, three or four discs), unlike in assemblies made of separate discs, where only a singular point of contact is possible. The focus of this research was to observe the transitions of contact types in different phases of the biaxial compression test, contact point (area) transformations, location of certain contacts in the force chain network, and to examine the findings in the context of contact force magnitudes and the shapes of the particles.

Acknowledgments The author would like to express his gratitude to Gaël Combe and Pascal Villard of Laboratoire 3S-R in Grenoble, France for their invaluable input to this work.

References

[1] Emilien Azéma, Itthichai Preechawuttipong, and Farhang Radjai. Binary mixtures of disks and elongated particles: Texture and mechanical properties. *Physical Review E*, 94(4):042901, 2016.

[2] Francesco Calvetti, Fabrice Emeriault, et al. Interparticle forces distribution in granular materials: link with the macroscopic behaviour. *Mechanics of Cohesive-frictional Materials*, 4(3):247–279, 1999.

[3] Gaël Combe, Cécile Nouguier-Lehon, Émilien Azéma, Krzysztof Szarf, Baptiste Saint-Cyr, Marie Chaze, Farhang Radjai, Pascal Villard, Jean-Yves Delenne, Vincent Richefeu, et al. A benchmark for particle shape dependence. In *AIP Conference Proceedings*, volume 1542, pages 883–886. AIP, 2013.

[4] MJ Jiang, H-S Yu, and D Harris. A novel discrete model for granular material incorporating rolling resistance. *Computers and Geotechnics*, 32(5):340–357, 2005.

[5] Michał Nitka, Jacek Tejchman, and Jan Kozicki. Discrete modelling of micro-structural phenomena in granular shear zones. In *Bifurcation and Degradation of Geomaterials in the New Millennium*, pages 7–12. Springer, 2015.

[6] Jean-Noël Roux and François Chevoir. Discrete numerical simulation and the mechanical behavior of granular materials. *Bulletin des laboratoires des ponts et chaussées*, 254:109–138, 2005.

[7] Baptiste Saint-Cyr, Krzysztof Szarf, Charles Voivret, Emilien Azéma, Vincent Richefeu, J-Y Delenne, Gaël Combe, C Nouguier-Lehon, P Villard, P Sornay, et al. Particle shape dependence in 2D granular media. *EPL (Europhysics Letters)*, 98(4):44008, 2012.

[8] K. Szarf, G. Combe, and P. Villard. Polygons vs. clumps of discs: A numerical study of the influence of grain shape on the mechanical behaviour of granular materials. *Powder technology*, 208(2):279–288, 2011.

DEVELOPMENT OF THE MULTISCALE FINITE ELEMENT METHOD FOR THE ANALYSIS OF ADVANCED MATERIALS

M. Dryzek[1], W. Cecot[1]

[1]*Institute for Computational Civil Engineering, Cracow University of Technology, Kraków, Poland*
e-mail: mdryzek@l5.pk.edu.pl

1. Introduction

In recent years, we observe a significant development of new materials, particularly composites and metamaterial, as well as the technological advancements that these new materials have allowed. To reduce the cost of experimental testing during the design stage of those materials, digital modeling can be incorporated. In order to represent correctly the materials' global mechanical behavior, it is necessary to include certain features of the microscale when modeling. However, the complexity of the problem leads to a large number of degree of freedom (dof). Therefore, we propose an application of the Multiscale Finite Element Method (MsFEM) [1] to reduce the computational cost.

The MsFEM is a promising method used to model heterogeneous materials. It requires neither the assumption of scale separation nor the periodicity of the microstructure. Furthermore, the calculations can be easily parallelized, since the MsFEM special macroscale shape functions that capture microscale details are computed independently, in appropriate groups of elements.

The proposed multiscale modeling will contribute to development of efficient and reliable tools for a better understanding of the relationship between the additive manufacturing process, metamaterial microstructure, and the overall mechanical properties of 3D printed elements.

2. Problem formulation

We consider the linear elasticity problems formulated below for heterogeneous or porous materials.

Find field of displacements u(x) in a domain Ω such that:

(1) $$-\frac{\partial}{\partial x_j}\left(C^{\epsilon}_{ijkl}\frac{\partial u_k}{\partial x_l}\right) = f_i \qquad \forall \omega_s \subset \Omega$$

with kinematic ($\hat{a}$) and static ($\hat{t}$) boundary conditions specified on $\partial\Omega_D$ and $\partial\Omega_N$ respectively, where $\partial\Omega_D \cup \partial\Omega_N = \partial\Omega, \partial\Omega_D \cap \partial\Omega_N = \emptyset$ and continuity conditions at the interface between subdomains ω_s. The strong ellipticity and boundedness of the microscale material parameter tensor C^{ϵ} is assumed (i.e., $\exists \alpha,\beta \in R^{+}: \alpha\xi_{ij}\xi_{ij} \leq C^{\epsilon}_{ijkl}\xi_{ij}\xi_{kl} \leq \beta\xi_{ij}\xi_{ij}, \quad \forall \boldsymbol{\xi}_{ij} \in R^2$). The material parameters are differentiable (typically constant) in each ω_s, and f_i denotes a body force component.

The discrete counterpart of problem (1) may be written in the following matrix form

(2) $$\boldsymbol{K}^h\boldsymbol{u}^h = \boldsymbol{f}^h$$

where $\boldsymbol{u}^h$ is the vector dof and $\boldsymbol{K}^h$, $\boldsymbol{f}^h$ denote the assembled matrix and vector, respectively.

The MsFEM uses two meshes of finite elements. A coarse mesh is generated at the macroscale and is locally refined, for each coarse element node. This creates a set of fine meshes for every element (see example in Fig. 1). The most important issue of the MsFEM is an approximation of solutions of the following auxiliary problems to determine special shape functions

Given Ψ_m, find Φ_m such that:

$$(3)\qquad \begin{cases} \dfrac{\partial}{\partial x_j} C_{ijkl} \dfrac{\partial (\Phi_m)_k}{\partial x_l} = \dfrac{\partial}{\partial x_j} C^0_{ijkl} \dfrac{\partial (\Psi_m)_k}{\partial x_l} & \forall\, i = 1,2 \quad x \in L_H \\ \Phi_m = \hat{\varphi}_m & \text{on } \partial L_H \end{cases}$$

In other words, problem (3) defines the interpolation operator that transfers M coarse element dof into N fine mesh dof. Such a mapping is represented by a matrix $I_{N\times M}$ and is used to compute the coarse element matrix $\boldsymbol{K}^H$, vector $\boldsymbol{f}^H$ of fine mesh.

$$(2)\qquad \boldsymbol{K}^H = \boldsymbol{I}^T \boldsymbol{K}^h \boldsymbol{I}, \qquad \boldsymbol{f}^H = \boldsymbol{I}^T \boldsymbol{f}^h .$$

Assembling such a matrixes and vectors leads to a system of macroscale algebraic equations with relatively small number of dof.

3. Preliminary results

Below, we present a study of convergence of the method for on exemplary 2D problem (see Fig. 1).

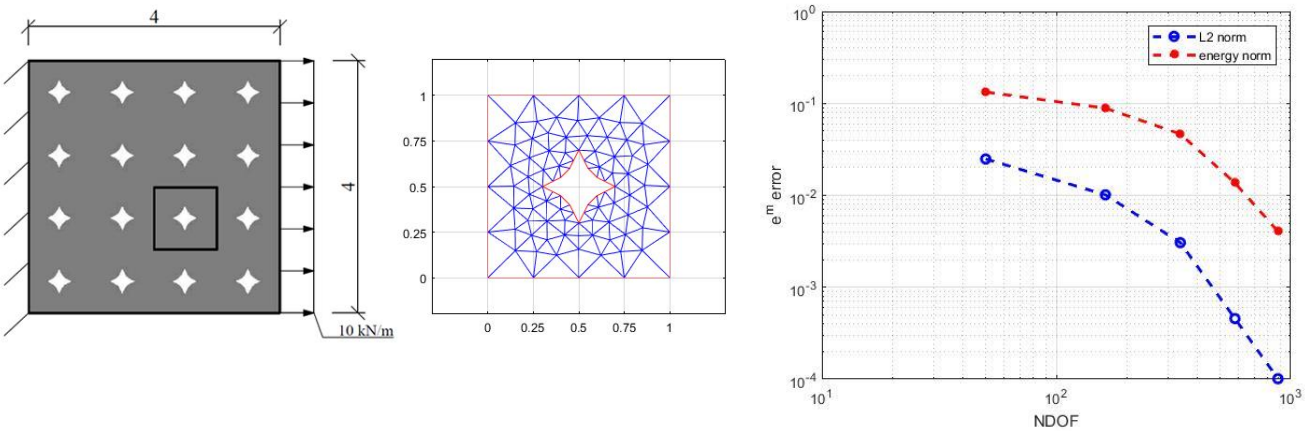

Fig. 1: Numerical example: the problem scheme and 4 × 4 element coarse mesh (left), fine mesh used for one coarse element (center), p-convergence of the error in L_2 and energy norms (right).

4. Concluding remarks

The results presented in the previous section as well as some other examples known from both literature and other research [2] indicate that MsFEM with higher order application is an efficient method for modeling of advanced materials. An experimental validation of the approach is conducted and its results will be discussed at the conference.

References

[1] T. Hou and X. Wu. *A multiscale finite element method for elliptic problems in composite materials and porous media*. J. of Comp. Phys., 134:169–189, 1997.
[2] W. Cecot and M. Oleksy. *High order FEM for multigrid homogenization*. Comp. and Math. with App., 70(7):1370–1390, 2015.

RESPONSE SURFACES IN THE NUMERICAL HOMOGENIZATION OF NON-LINEAR POROUS MATERIALS

W. Beluch[1] and M. Hatłas[1]

[1] *Institute of Computational Mechanics and Engineering*
Silesian University of Technology, Gliwice, Poland
e-mail: witold.beluch@polsl.pl

1. Introduction

Numerical homogenization methods are widely applied to the calculation of the equivalent properties of microscopically inhomogeneous media. Their direct application to non-linear materials usually leads to very high computational effort. Nowadays, the solution of such a task requires the use of computational clusters or supercomputers and cannot be effectively used in engineering simulation.
One of techniques which allows reducing computational time is the response surfaces attitude. The use of the response surfaces allows rapid approximate determination of homogenised material properties.
The aim of the paper is to obtain a reliable range of the equivalent material properties values of a non-linear porous material by means of the numerical homogenization and response surfaces methodology. The boundary-value problem has been solved by means of the finite element method (FEM) ANSYS software in both considered scales.

2. Numerical homogenization of non-linear materials

Numerical homogenization, belonging to the group of homogenization methods, is an efficient numerical procedure which allows obtaining a medium macroscopically equivalent to a medium micro-scale inhomogeneous one. It is usually assumed that a representative volume element (RVE) represents the whole structure (global periodicity) or its part (local periodicity) [1]. If the material is non-linear, the number of the required RVE calculations is usually extremely high as it is necessary to solve the boundary-value problem(s) for each integration point in each iteration for the global model. Different attitudes to non-linearities in multi-scale analysis of heterogeneous media are presented e.g. in [2] and [3].
In the present paper an attitude with the use of response surfaces is proposed. The response surface methodology allows obtaining an approximate input-output relation if the true relationship is not known or hard to obtain [4]. The advantages of response surface approach are almost instantaneous output parameters evaluation and several design point calculations requirement to obtain high accuracy (for most cases).
In the present paper the response surface methodology with an artificial neural network (ANN) implemented in the ANSYS Workbench software has been used.

3. Numerical example

A RVE made of porous Ti-6AL-4V alloy with 64 uniformly distributed spherical pores has been created (Fig. 1a). It is assumed that the material is an elastoplastic with bilinear isotropic hardening one with the parameters collected in Table 1.

Parameter	Young modulus E	Poisson's ratio ν	Density ρ	Yield strength R_e	Tangent modulus E_t
value	105.66 GPa	0.342	4430 kg/m^3	1.09 GPa	0.85 GPa

Table 1: Parameters of Ti-6Al-4V elastoplastic alloy.

Tensile tests for 9 different porosity values p=0.01-0.8 regulated by pores' diameter has been performed to calculate the dependence between equivalent stresses and strains. The results have been used to construct the response surface by means of the Kriging method (Fig. 1 b).

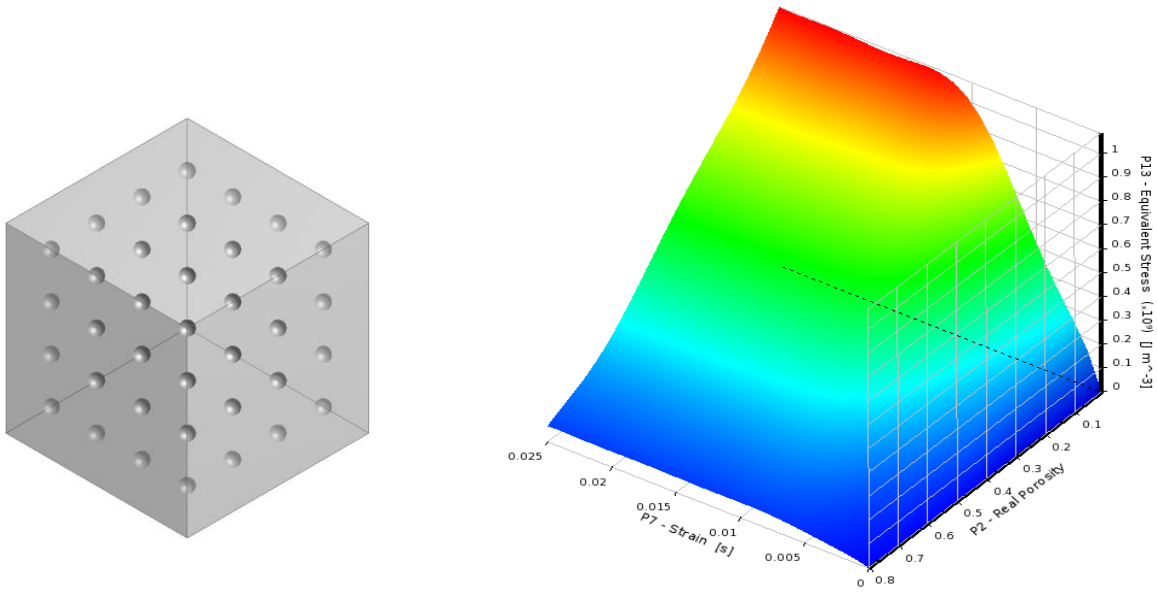

a) b)

Figure 1: Non-linear homogenization: a) RVE and pores location b) obtained response surface.

The response surface has been used to calculate stresses and strains of the two-point supported beam of the same non-linear material with porosity p=0.2. The beam has been divided into 1250 hexahedral finite elements, which represent RVE models. A feed-forward ANN of 2-5-1 topology has been used to determine non-linear behaviour of each finite element. The obtained results have been compared to a macroscopic model with 1250x64 pores and discretized by fine tetrahedral mesh. The maximum deflection evaluation error between applied approaches was lower than 4%. A calculation time in the response surface approach was about 1350 times lower than in the macroscopic model approach.

4. Conclusions

The application of the response surfaces idea to the numerical homogenization of non-linear porous materials has been presented. Such attitude allows obtaining satisfactory results dramatically reducing the number of RVE calculations, comparing with classical attitude. The presented methodology may be applied to different non-homogeneous media with material nonlinearities, e.g. composites.

Acknowledgments The research was partially financed from the Polish science budget resources as the project 10/040/BK_18/0066.

References

[1] V. G. Kouznietsova. *Computational homogenization for the multi-scale analysis of multiphase materials.* Ph.D. thesis, TU Eindhoven, 2002.
[2] K. Terada and N. Kikuchi. A class of general algorithms for multi-scale analyses of heterogeneous media. *Comput. Methods Appl. Mech Engrg.*, 190:5427, 2001.
[3] S. Marfia and E. Sacco. Multiscale technique for nonlinear analysis of elastoplastic and viscoplastic composites. *Composites Part B.* 136:241, 2018.
[4] G. E. P. Box and N.R. Draper. *Empirical Model-Building and Response Surfaces*. Wiley, 1987.

MODELLING OF THE THERMOCHEMICAL PROCESSES IN POROUS MEDIA WITH PHASE TRANSITION USING XDEM AND FVM METHODS

I. Wardach-Święcicka[1], D. Kardaś[1], and B. Peters[2]

[1]*The Szewalski Institute of Fluid-Flow Machinery Polish Academy of Sciences, Gdańsk, Poland*
[2]*University of Luxembourg, Luxembourg*

e-mail: izabela.wardach@imp.gda.pl, dariusz.kardas@imp.gda.pl, bernhard.peters@uni.lu

1. Introduction

The fluid flow through the porous media with phase transition is an important technical issue that is common in the power industry, and is also an interesting research problem. The task described and analyzed in the following work is derived directly from the thermal conversion of solid fuel. It refers for example to a process of gasification/combustion in the packed bed or even the conversion of single fuel particles. Thermal conversion of solid fuels plays an important role in energy generation. In Poland still over 80% of electrical energy is produced from coal. The combustion of fossil fuels gives Poland high energy independence, while providing relatively low cost of the electricity and heat produced from coal. Unfortunately, the combustion of coal, mostly in small scale old domestic boilers, causes high concentration of PM2.5 in the surrounding air and the highest level of benzopyrene in the European Union [1] which is one of the most toxic components of smog. Therefore, an analysis of thermal conversion of solid fuels has a practical meaning. Moreover flow through a porous packed bed of solid particles with mass loss phenomenon is interesting from research reasons.

The main goal of this work is to investigate the possibility of different numerical methods (eXtended Discrete Element Method - XDEM, Finite Volume Method - FVM) to simulate the behavior of solid fuel particles during the gasification process that is performed in the Institute of Fluid-Flow Machinery PASci (IMP).

2. Thermochemical processes in packed bed and single fuel particle

The XDEM method aims at resolving the particulate phase with its various processes attached to the particles [3]. The main assumption of numerical modelling is that each particle undergoes a sequence of thermodynamic processes that are described by a set of one-dimensional and transient conservation equations for mass, momentum and energy using Discrete Particle Method (DPM) [2]. XDEM practically extends the dynamics of particles described by the classic DEM. In the analyzed solid fuel conversion problem the simplified geometry of the IMP "INKA" reactor was used. In Figure 1 the XDEM/CFD numerical results are presented. The propagation of the heating front and the moisture content in each particle can be observed. As can be seen, the hot gas flows into the cylinder from the top wall to the bottom wall. Due to the heat transfer from hot air to cold biomass, the central temperature of each particle is increasing.

For comparison the numerical analysis of single particle heating obtained from 1D in-house code is presented (Figure 2). The numerical code is based on the finite volume method (FVM) and includes the mass, momentum and energy balance equations with the source terms. Main assumption is the structure of the solid particle which consists of the solid, gas and water phase and has an ideal spherical shape. Additional simplification is that the thermochemical properties may change only in the radial direction, what gives simpler form of the partial differential equations. The cold particle is heated by the stream of hot nitrogen. Due to the heat transfer from the surrounding gases, the structure of particle is changing and the moisture and volatiles are released. The mass source terms for moisture and volatiles, the porosity change and the particle thermophysical properties variation were implemented basing on the appropriate temperature relationships [4].

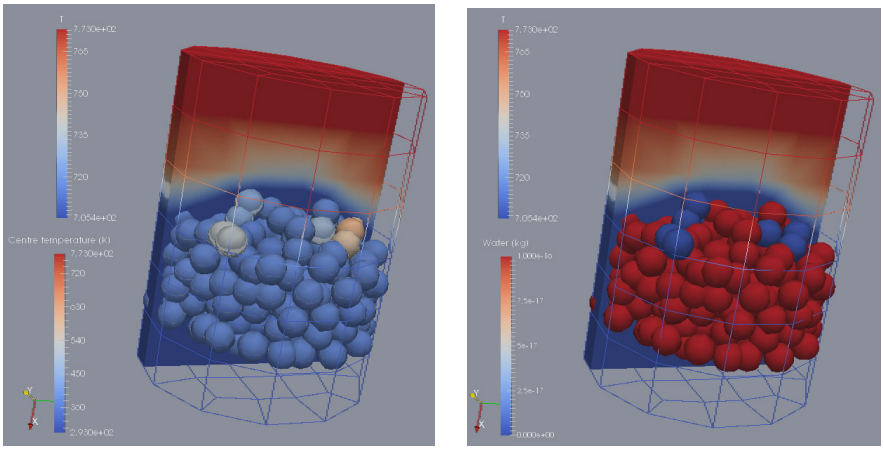

Figure 1: Temperature distribution and particle water content in a simplified reactor geometry

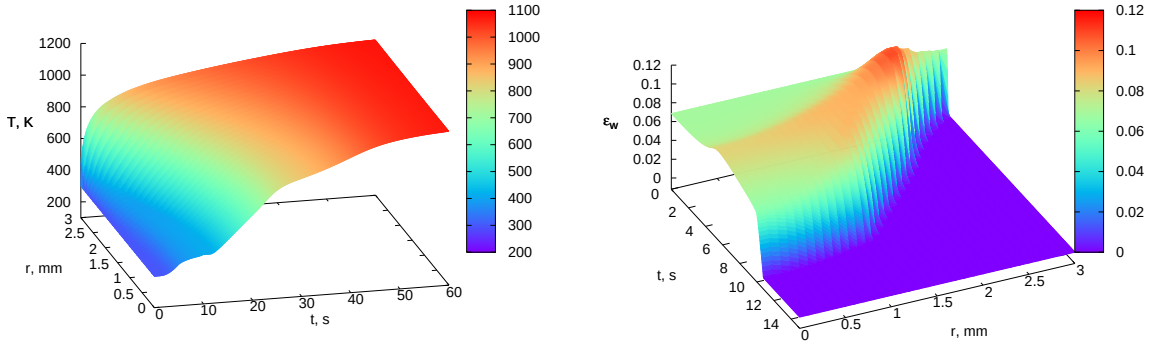

Figure 2: Temperature distribution and particle water volume content in the solid single fuel

3. Conclusions

The main goal of this work was to investigate the possibility of the XDEM/1D FVM programs to simulate the behavior of the solid fuel particles during the thermochemical conversion process that was performed in the real gasifier called "INKA" (IMP). Basing on the test case calculations of the analyzed reactor, the following conclusions can be made: (I) the XDEM method can be used to simulate heat and mass transfer processes in the packed bed reactors, (II) the numerical results obtained using both programs show propagation of the heating front and the change of the moisture content in particles, (III) the time of conversion depends on the type of the fuel, its structure, size and physical parameters.

References

[1] Polycyclic aromatic hydrocarbons air pollution at urban background stations in 2016 - in Polish. *Główny Inspektorat Ochrony Środowiska, Warszawa*, 2017.

[2] A. A. Estupinan Donoso and B. Peters. XDEM used for predicting tungsten-oxide reduction. *CAPE Forum 2015, Computer Aided Process Engineering, University of Paderborn, April 27-29, Paderborn, Germany*, 2015.

[3] B. Peters, X. Besseron, A. Estupinan, F. Hoffmann, M. Michael, and A. Mahmoudi. Enhanced thermal process engineering by the extended discrete element method (XDEM). *Univ. J. Eng. Sc.*, 1(4):139–145, 2013.

[4] I. Wardach-Święcicka. *Modelling of physicochemical processes in a solid fuel particle in a stream of hot gases, PhD Thesis - in Polish.* IMP, Gdańsk, 2016.

A NOVEL TREATMENT FOR THE DEFORMABILITY OF DISCRETE ELEMENTS

J. Rojek [1], A. Zubelewicz[2], N. Madan[1], S. Nosewicz[1], and D. Lumelskyj[1]

[1]*Institute of Fundamental Technological Research, Polish Academy of Sciences, Pawinskiego 5B, 02-106 Warsaw, PL*
[2]*University of New Mexico, USA*

e-mail: jrojek@ippt.pan.pl

1. Introduction

Correct representation of macroscopic properties using standard DEM models is still a challenge. Even the so-called *soft-contact* [1] approach of contact treatment which allows a small particle overlap equivalent to particle deformation at contact is not always sufficient to obtain a required deformation behaviour [5]. Different approaches reported in the literature to incorporate particle deformability within DEM include the use of finite elements to discretize particles [4] and adding deformation modes to a rigid motion for polygonal or polyhedral elements [7]. Works considering the deformability of circular elements with soft contact approach are rather very few. For example, Haustein et al. [2] presented a simple approach purely based on geometrical assumptions. This paper presents a novel treatment for the deformability of the circular discrete elements consisting in adding a global deformation mode induced by an average stress tensor derived from the contact forces acting on each particle. An interesting feature of our novel method is that by using appropriate model parameters, we can recover the finite element solution of the problem. Our new formulation is termed as deformable discrete element method or DDEM and an overview of its formulation is presented further. For a detailed discussion on DDEM see [6].

2. Formulation of the novel concept for treating particle deformability

The idea of our novel concept for treating particle deformability is shown in Fig. 1. Under the uniform stress assumption, the internal particle stress is obtained from contact forces as volume average stress using the formula [3]:

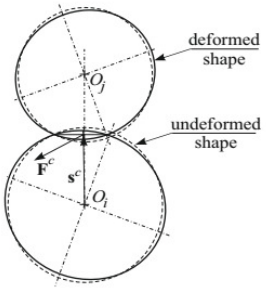

Figure 1: The idea of the deformable discrete element method

$$\tilde{\boldsymbol{\sigma}}_p = \frac{1}{V_p} \sum_{c=1}^{n_{pc}} \frac{1}{2} \left(\mathbf{s}^c \otimes \mathbf{F}^c + \mathbf{F}^c \otimes \mathbf{s}^c \right) \tag{1}$$

where V_p – particle volume, n_{pc} – no. of elements in contact, $\mathbf{s}^c$ is vector connecting particle center with contact point, $\mathbf{F}^c$ – contact force and symbol $\otimes$ – outer tensor product. An inverse constitutive relationship is used to obtain particles strains,

$$\epsilon_p = \mathbf{D} : \boldsymbol{\sigma}_\mathbf{p} \tag{2}$$

where $\mathbf{D}$ is elastic compliance tensor for plane strain. These strains elicit new contacts and concurrently lead to change in local particle overlap in our soft contact model due to deformation of a circular disk into an ellipse with axis aligned along principal strain directions (cf. Fig(1)). Hence, the deformability of discrete elements invokes interdependency of contacts, similar to that of a non-local contact model. This is the distinct characteristic of our new formulation as compared to standard DEM. It will be shown that in-fact we can retrieve a FEM solution from a DDEM model using suitable parameters. A numerical example will be presented for its verification.

3. Numerical example

The equivalence between finite element solution and deformable discrete element method is verified numerically by simulating uniaxial compression of a 2D rectangular sample. The DEM sample which is assumed to represent an elastic solid is discretized with 180 bonded disk elements of radii $r = 1$ mm. Equivalent FEM model has been obtained by taking porosity of the DEM sample into account. Figure 2 shows the displacement contours in x and y directions for DDEM model (a) and b)) and an equivalent FEM model (c) and d)). From the results presented in Fig. 2, it can be observed that in-fact, our novel method to treat deformability of discrete elements allows us to obtain a solution equivalent to the FEM one, and which captures correctly the Poisson's effect which in this case would be impossible with the standard DEM model.

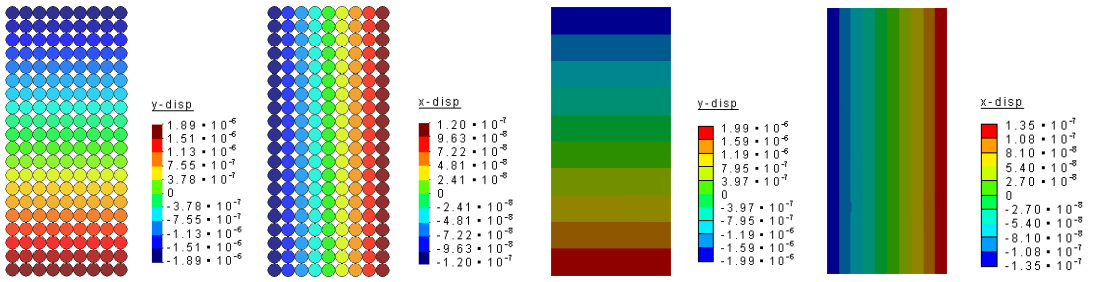

a) b) c) d)

Figure 2: Displacement contours – simulation results obtained with: new DEM formulation – contours of displacements along a) the y-axis, b) the x-axis; equivalent FEM model – contours of displacements along c) the y-axis, d) the x-axis; [6]

Acknowledgments This work has been financed from the funds of Polish National Science Centre (NCN) awarded by the decision number DEC-2015/19/B/ST8/03983.

References

[1] P.A. Cundall and O.D.L. Strack. A discrete numerical method for granular assemblies. *Geotechnique*, 29:47–65, 1979.

[2] M. Haustein, A. Gladkyy, and R. Schwarze. Discrete element modeling of deformable particles in yade. *SoftwareX*, 6:118 – 123, 2017.

[3] S. Luding. Micro-macro transition for anisotropic, aperiodic, granular materials. *International Journal of Solids and Structures*, 41:5821–5836, 2004.

[4] A. Munjiza. *The Combined Finite–Discrete Element Method*. Wiley, 2004.

[5] C. O'Sullivan, J.D. Bray, and L. Cui. Experimental validation of particle-based discrete element methods. In *Proceedings of the GeoCongress, Georgia, Atlanta*, 2006.

[6] J. Rojek, A. Zubelewicz, N. Madan, and S. Nosewicz. The discrete element method with deformable particles. *International Journal for Numerical Methods in Engineering*, 0(0):1–33, 2018.

[7] J.R. Williams and G.W. Mustoe. Modal methods for the analysis of discrete systems. *Computers and Geotechnics*, 4:1–19, 1987.

CONVERGENCE LIMIT OF A DEFORMABLE DISCRETE ELEMENT MODEL

N. Madan[1], J. Rojek [1], A. Zubelewicz[2], and S. Nosewicz[1]

[1]*Institute of Fundamental Technological Research, Polish Academy of Sciences, Pawinskiego 5B, 02-106 Warsaw, PL*
[2]*University of New Mexico, USA*

e-mail: nmadan@ippt.pan.pl

1. Problem statement

Despite successful use of discrete element method or DEM over a wide variety of engineering problems, the rigidity of particles assumed in classical formulation of DEM leads to incorrect behaviour in applications such as powder compaction at higher relative densities [1]. In our previous work [3], we have proposed an original formulation of DEM for deformable particles which we term as deformable discrete element method or DDEM. In-fact we have proven that the modelling capabilities of standard DEM can be enhanced by taking proper account of particle deformation. In order to incorporate deformability in discrete elements, the iterative scheme of our novel formulation results in an implicit relationship between contact forces and particle displacements. In presented work, the convergence limit for this implicit relationship is obtained analytically and verified numerically. The idea of DDEM is explained further.

2. Basic formulation of the deformable discrete element method

Referring to Fig.1 idea of DDEM can be explained as follows, under the uniform stress assumption a global deformation mode is introduced in particles which in-turn establishes new contact interaction due to reshaping of the particle and invokes force redistribution. Simultaneously, the modification in particle shape also leads to change in local interaction and hence alters the particle overlap from say, h to h_c (cf. Fig. 1). In this way, due to particle deformation, the contact in one point influences the contact interaction at other points and thus a non-local contact model evolves. This is the distinctive feature of DDEM formulation with respect to standard DEM where contacts are independent and do not influence each other. Considering the global deformation mode to deduce particle overlap and consequently the contact force gives an implicit relationship of the form,

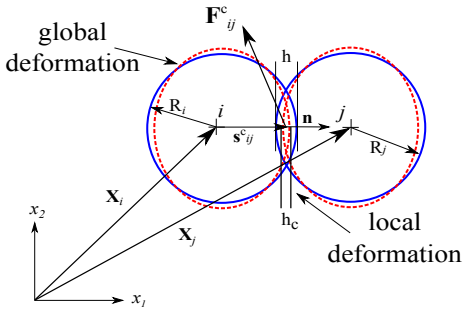

Figure 1: The idea of the deformable discrete element method (DDEM)

$$\mathbf{F}_c^{(n)} = \mathbf{F}_c(\mathbf{u}^{(n)}, \boldsymbol{\epsilon}_p(\mathbf{F}_c^{(n)})) \tag{1}$$

where, the superscript n denotes the current time step and $\boldsymbol{\epsilon}_p$ indicate the strains instigated in particles due to contact force at current time step, $\mathbf{F}_c{}^{(n)}$. It will be shown that the implicit relationship of Eqn. (1) can be solved iteratively and corresponding relationship for the successive differences can be formulated as:

$$\mathbf{F}_c^{(n,k+1)} - \mathbf{F}_c^{(n,k)} = \mathbf{B}\,(\mathbf{F}_c^{(n,k)} - \mathbf{F}_c^{(n,k-1)})\,, \quad k >= 1\,. \tag{2}$$

where, $\mathbf{B}$ is certain matrix and $k-1$, k, $k+1$ represent the consecutive iterations for a given time step n. It must be noted though that the iterative solution may not always converge. In general, the convergence requires that for a certain matrix norm $\|\cdot\|$ we have, cf. [2]:

$$\|\mathbf{B}\| < 1 \tag{3}$$

The norm of matrix $\mathbf{B}$, cf. Eqn. (3) can be small in some norms and large in others, therefore a more stringent condition based on spectral radius, ρ of matrix, $\mathbf{B}$ i.e. $\rho(\mathbf{B}) < 1$ [2] is used in our work.

3. Numerical example

A 2D rectangular sample of equal sized particles (cf. Fig 2) has been used to numerically verify the convergence criterion defined by Eqn. (3). The discrete model consisting of 180 bonded disks of radii $r = 1$ mm and normal contact stiffness $k_n = 7 \cdot 10^{10}$ N/m was simulated under unconfined uniaxial compression mode. It will be shown that the specific form of convergence criterion (cf. Eqn. (3)) for the rectangular sample is given as,

$$\frac{4k_n(1+\nu_p)}{\pi E_p l} < 1 \tag{4}$$

where, k_n is normal contact stiffness, ν_p is particle Poisson's ratio and E_p is particle Young's modulus. A substantial number of simulations have been done for the particle Poisson's ratio ν_p ranging between 0.05 to 0.45 and a comparison between numerical and analytical convergence limit is presented.

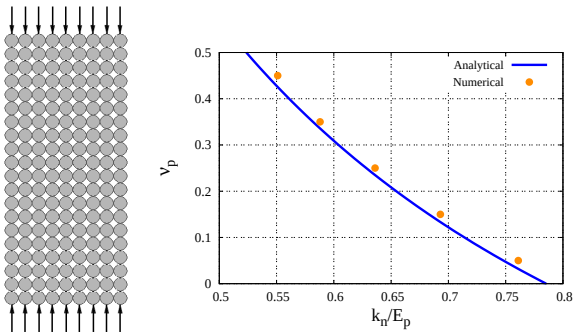

Figure 2: Verification of convergence criteria for an rectangular discrete sample of equal size particles

It can be seen from Fig. 2, that indeed we can predict the convergence limit of a DDEM model analytically and hence select the microscopic elastic parameters suitably to obtain a convergent solution using DDEM model.

Acknowledgments This work has been financed from the funds of Polish National Science Centre (NCN) awarded by the decision number DEC-2015/19/B/ST8/03983.

References

[1] B. Harthong, J.-F. Jérier, P. Dorémus, D. Imbault, and F.-V. Donzé. Modeling of high-density compaction of granular materials by the Discrete Element Method. *Int. J. Solids and Structures*, 46:3357–3364, 2009.
[2] C.T. Kelly. *Iterative Methods for Linear and Nonlinear Equations*. SIAM, Philadelphia, 1995.
[3] J. Rojek, A. Zubelewicz, N. Madan, and S. Nosewicz. The discrete element method with deformable particles. *International Journal for Numerical Methods in Engineering*, 0(0):1–33, 2018.

DISCRETE ELEMENT SIMULATION OF DAMAGE AND FRACTURE OF CONRETE AT INTERFACE ON GPU

R. Pacevič[1,2], ***R. Kačianauskas***[2], ***A. Kačeniauskas***[2] and ***R. Barauskas***[1]

[1]*Kaunas University of Technology, K. Donelaičio 73, Kaunas, Lithuania*
[2]*Vilnius Gediminas Technical University, Saulėtekio 11, Vilnius, Lithuania*

e-mail: ruslan.pacevic@ktu.lt

1. Introduction

Numerical simulation on a microscopic scale to predict macroscopic properties is becoming conventional approach applied in mechanics of materials. The discrete element method (DEM) suggested in the original work of Cundall and Strack [1] is developed further into powerful simulation tool recognised as suitable technique. Recently, the DEM is extended to various types of continuous and discontinuous solid, macroscopic properties of which are predefined by microscopic structure of bonded particles [2]. Ability to describe discrete nature and inter-particle damage and cracking as a real discontinuity among the particles presents the main advantage of this method. Moreover, the fracture analysis [2] and visualisation [3] at the level of particles has the disadvantage of making DEM computationally very expensive. To increase speed-up, the graphical processing units (GPUs) has been applied in the DEM [4]. The present work was carried out to develop the fast DEM code on GPU for fracture analysis of concrete reinforced interface.

2. Methods

The standard DEM is applied for simulation of behaviour of cohesive visco-elastic particles. The solution domain is covered by the face-centred cubic lattice. The materials properties assigned to the nodes of the lattice. These nodes are considered as discrete spherical particles undergoing translational motion during deformation. The normal and tangential component of the contact force comprises elastic and viscous ingredients represented by a composition of the linear spring-dashpot model. The bonds described by springs can break when the external loading exceeds the strength of bonds, leading to crack formation directly between two particles. The equations of motion are solved by using the 5th–order Gear predictor-corrector scheme. The fast GPU-based DEM code is developed to increase computational efficiency of large-scale simulation of fracture, involving millions of particles.

3. Problem description

The reinforces concrete sample under central tension is considered (Fig.1(a)). The sample provide to phase composite. Interface surface between concrete and steel reinforcement formed by ribs has complicated shape.

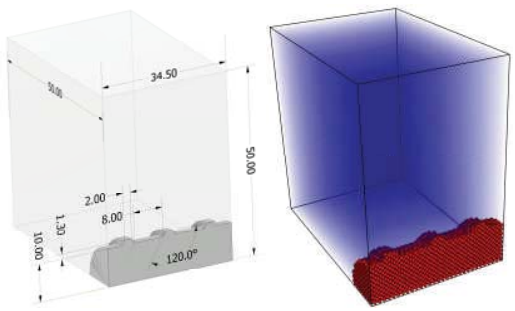

a) b)

Figure 1: a) problem description; b) discretization of space using spherical particles.

The singularities of interface lead to local concentration of stresses and finally to local damage occurring on a small scale. To describe the fracture pattern very fine discretization is necessary. For modelling this problem, the million number of discrete particles may be needed. Therefore code running on GPUs is necessary for solving such type of problem to increase the performance of DEM computations. One quarter and three ribs of the real specimen is simulated. The simulated system (Fig 1(b)) consists of 232320 particles, with the radius of 0.4 mm and 1357548 springs.

5. Results and conclusions

Selected numerical results of simulation are presented in Fig. 2. The constitutive relationship shown in Fig. 2(a) corresponds to analytical prediction and is confirmed by physical experiment. It is obvious that cracks starts to form at first rib at strain 0.00011. Cracks extracted by using the cell centre-based technique in a 3D domain are shown in Fig. 2(b). The crack surfaces [3] are coloured in red colour, while the edges of the faces are represented by green tubes.

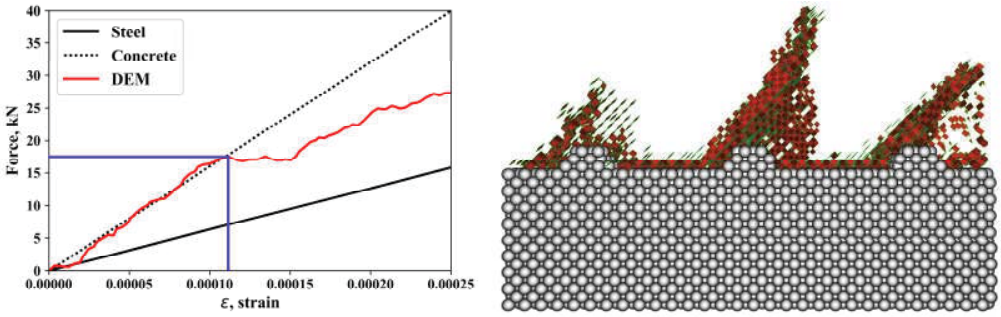

a) b)

Figure 1: a) force and strain relationship; b) fracture visualization.

All double-precision computations are performed on the NVIDIA® Tesla™ P100 GPU Computing Accelerator. The same OpenCL code optimized for multi-thread shared-memory architectures is executed on the desktop PC to evaluate the speedup ratio of GPU to CPU. Speedup values up to 10.5 are obtained in spite of intensive usage of advanced vector extensions by OpenCL on CPU. Higher differences become obvious in case of larger numbers of particles. On single GPU attained performance was higher than that reported in the literature in spite of the implemented complex physical model.

Acknowledgments

The research performed by R. Pacevič, research project No. 09.3.3-LMT-K-712-02-0131, funded under the European Social Fund measure „Strengthening the Skills and Capacities of Public Sector Researchers for Engaging in High Level R&D Activities", administered by the Research Council of Lithuania.

References

[1] P. A. Cundall and O. D. L. Strack. A discrete numerical model for granular assemblies. *Géotechnique*, 29:47, 1979.
[2] R. Rezakhani, X. Zhou, G. Cusatis. Adaptive Multiscale Homogenization of the Lattice Discrete Particle Model for the Analysis of Damage and Fracture in Concrete. *Int J Solids Struct*, 125:50, 2017.
[3] R. Pacevič, A. Kačeniauskas, D. Markauskas. Visualization of cracks by using the local Voronoi decompositions and distributed software. *Adv Eng Softw*, 84:85, 2015.
[4] M. Durand, P. Marin, F. Faure, B. Raffin. DEM based simulation of concrete structures on GPU. *Eur J Environ Civ* En, 16:1102, 2012.

DEM MODELING OF VACUUM PACKED PARTICLES DAMPERS

P. Chodkiewicz[1], R. Zalewski[1], and J. Lengiewicz[2]

[1]*Faculty of Automotive and Construction Machinery Engineering, Warsaw University of Technology,Warsaw, Poland*
[2]*Institute of Fundamental Technological Research, Polish Academy of Sciences, Warsaw, Poland*

e-mail: pawel@chodkiewicz.com.pl

1. Introduction

We present a method based on Discrete Element Method (DEM) to modeling the Vacuum Packed Particles (VPP)—a class of smart materials/smart structures. Mechanical properties of VPP can be simply adjusted by controlling the underpressure, which makes the structures very interesting from practical point of view, giving raise to numerous applications, including smart grippers [2], dampers [1, 6] or medical tools [5].

VPP are made of loose granular material encapsulated in a hermetic wrappnig. When the pressure inside the structure is equal or higher than the pressure outside, the VPP structure has mechanical properties like a baggy bulk. When the pressure inside is lower than outside, the whole structure behaves more like a solid material. Those special properties of VPP, together with the fact that they are in general cheaper and more eco-friendly than electro- or magnetorheological materials of similar characteristics, make them potentially very promising engineering structures. One of such structures—VPP dampers—are analyzed in this work.

In our previous works, VPP dampers were mostly described by using macroscopic rheological models [7, 8]. This kind of modeling usually requires relatively large number of parameters to be identified even for simple damper designs. Moreover, those parameters are not general and need to be individually adjusted to each design. In the present work we will pursue our earlier attempts, [3], to focus more on understanding how VPP dissipate energy under an oscillatory excitation (see Fig. 1a), which can possibly suggest ideas for a more accurate model. Such model could then be used to describe and analyze not only VPP dampers but possibly also other VPP structures.

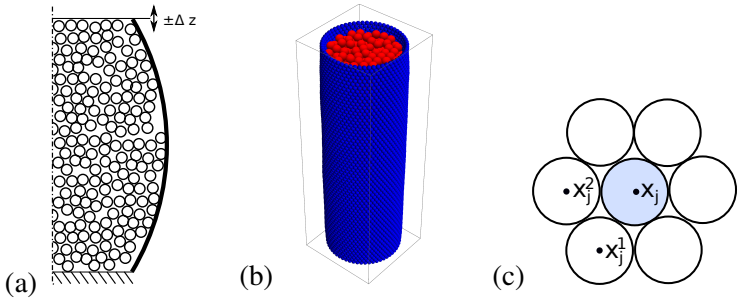

Figure 1: VPP damper: schematics (a), DEM model (b), geometry of an elementary surface element of the warp (c).

2. DEM model of VPP damper

We use open-source Yade DEM software, [4], to model VPP dampers. The granular media is directly represented by spherical discrete particles, and the surrounding foil warp is represented by an array of smaller spherical particles, interconnected by cohesive bonds, see Fig. 1b. Frictional model is assumed for granule-granule and granule-foil contact.

In order to provide the special pressure boundary conditions, which are characteristic to VPP structures, the standard Yade DEM model for foil-warp material has been extended as follows. For each elementary segment j of the warp (which is made of 7 spheres—one in the center with 6 neighbors, see Fig. 1c) we apply the force

$$F_j = A_j \cdot p \tag{1}$$

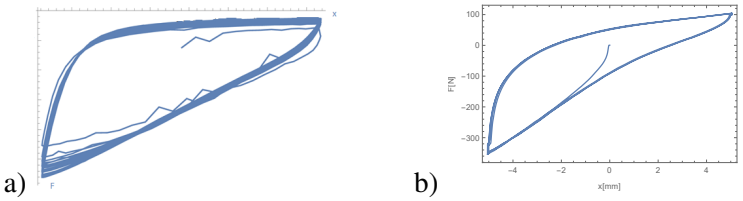

Figure 2: Force-displacement hysteresis loops: DEM results (a), and experimental results (b).

acting on the central sphere of the segment. Here, p is the applied pressure difference, and A_j is the tributary surface area vector,

$$A_j = \frac{1}{6}\sum_{i=1}^{6} s_i, \qquad s_i = (\mathbf{x}_j^i - \mathbf{x}_j) \times (\mathbf{x}_j^{1+(i\%6)} - \mathbf{x}_j), \tag{2}$$

where $\mathbf{x}_j$ is the current position of j-th module of the warp, and $\mathbf{x}_j^i$ is the current position of its i-th neighbor, cf. Fig. 1c.

3. Preliminary results

The performed DEM simulations of cycling loading of VPP damper consists of three steps: (i) the granulate is inserted into the foil warp, (ii) the warp is sealed from the top, (iii) the oscillatory motion of the sealing plane and the top ring of the warp is applied, and the reaction force from the top clamping is acquired. The analysis was performed in the quasi-static regime.

The preliminary results, Fig. 2, prove that DEM model is able to qualitatively capture the, experimentally observed, dissipative effects of VPP dampers. However, the most important advantage of the presented discrete element modeling is the ability to retrieve the individual inter-granular dissipative interactions, observe them along the process, and identify the dissipation patterns in the structure. This is a subject of our ongoing research.

References

[1] Jacek Mateusz Bajkowski, Czesław Bajer, and Bartłomiej Dyniewicz. Smart control in vibrations of structures. In *6th World Conf. of the International Association for Structural Control and Monitoring (IACSM)*, 2014.

[2] Eric Brown, Nicholas Rodenberg, John Amend, Annan Mozeika, Erik Steltz, Mitchell R Zakin, Hod Lipson, and Heinrich M Jaeger. Universal robotic gripper based on the jamming of granular material. *Proceedings of the National Academy of Sciences*, 107(44):18809–18814, 2010.

[3] Paweł Chodkiewicz, Jakub Lengiewicz, and Robert Zalewski. Discrete element method approach to modelling VPP dampers. In *MATEC Web of Conferences*, volume 157, 2018.

[4] J Kozicki and FV Donzé. Yade-open dem: an open-source software using a discrete element method to simulate granular material. *Engineering Computations*, 26(7):786–805, 2009.

[5] Arjo J Loeve, Oscar S van de Ven, Johan G Vogel, Paul Breedveld, and Jenny Dankelman. Vacuum packed particles as flexible endoscope guides with controllable rigidity. *Granular matter*, 12(6):543–554, 2010.

[6] Robert Zalewski. *Modelowanie i badania wpływu podciśnienia na właściwości mechaniczne specjalnych struktur granulowanych*. Wydawnictwo Komunikacji i Łączności, 2013.

[7] Robert Zalewski and Paweł Chodkiewicz. Gubanov model for vacuum packed particles. In *Mechatronics 2013*, pages 57–63. Springer, 2014.

[8] Robert Zalewski, Paweł Chodkiewicz, and Mariusz Pyrz. Modeling of complex properties of vacuum packed particles using evolutionary algorithms. In *New Contributions in Information Systems and Technologies*, pages 267–276. Springer, 2015.

TWO-SCALE MODELLING OF POWDER SINTERING

S. Nosewicz[1], J. Rojek [1], G. Maciejewski[2], M. Maździarz [1], and M. Chmielewski[3]

[1]*Institute of Fundamental Technological Research, Polish Academy of Sciences, Pawinskiego 5B, 02-106 Warsaw, PL*
[2]*Institute of Aviation, Al. Krakowska 110/114, 02-256 Warsaw, PL*
[3]*Institute of Electronic Materials Technology, Wólczyńska 133, 01-919 Warsaw, PL*

e-mail: snosew@ippt.pan.pl

1. Introduction

Sintering is a manufacturing process in which loose or weakly bonded metal or ceramic powders are consolidated into a solid compact body by heat treatment which can be combined with mechanical pressure. Macroscopically during sintering, one can observe changes of the bulk material volume (shrinkage) and, associated with this, densification and decrease of porosity. The macroscopic phenomena result from processes undergoing at the microscopic level. The microstructure during sintering undergoes an evolution characterized by grain rearrangement and increase of grain compaction. In the initial stage, cohesive bonds (necks) are formed between powder particles. When the sintering process is continued the necks between particle grow due to mass transport. Surface and grain boundary diffusion are normally dominant mechanisms of mass transport in sintering.

This paper will present a two-scale framework for numerical modelling of sintering phenomena. The proposed approach bridges simulations performed at the atomistic and microscopic scales. The two-scale model has been validated using the results of own experimental studies of pressure-sintering of NiAl powder.

2. Atomistic modelling

The atomistic modelling has been carried out using the molecular dynamics (MD). The methodology to estimate parameters of a microscopic sintering model by MD simulations has been developed in [1]. The parameters include temperature dependent diffusion parameters, surface energy and linear thermal expansion. These parameters define material behavior during sintering and are used in the microscopic model of sintering.

3. Microscopic model of sintering

The authors' own original viscoelastic model [2] developed within the framework of the discrete element model have been used for simulation of the powder sintering process at the microscopic level. The discrete element models consider the powder as a collection of spherical particles (discrete elements) interacting with one another by contact forces. The two-particle model of sintering is derived considering diffusion as the main mechanism of sintering.

$$F_{\mathrm{n}} = \frac{\pi a^4}{8 D_{\mathrm{eff}}} v_{\mathrm{rn}} + \pi \gamma_S \left[4r \left(1 - \cos \frac{\Psi}{2} \right) + a \sin \frac{\Psi}{2} \right] \tag{1}$$

where F_{n} is the normal force between two particles, v_{rn} – the normal relative velocity, r – the particle radius, a – the radius of the interparticle boundary, Ψ – the dihedral angle, γ_{S} – the surface energy.

The value of diffusion parameter directly depends on certain diffusion mechanism, which is considered at the constitutive model of sintering. Assuming that the grain boundary diffusion is a dominant mechanism in the neck growth and shrinkage of the system the effective grain boundary diffusion coefficient D_{eff} is given by the following formula:

$$D_{\mathrm{eff}} = \frac{D_{\mathrm{gb}} \delta \Omega}{\mathrm{k_B T}} \tag{2}$$

where D_{gb} is the grain boundary diffusion coefficient with the width δ, Ω is the atomic volume, $\mathrm{k_B}$ is the Boltzmann constant and T is the temperature.

4. Numerical results

Pressure assisted sintering of an intermetallic NiAl powder has been simulated using the methodology described above. First, the molecular dynamics simulations have been carried out to derive sintering parameters from an atomic scale level. The simulations have been performed with LAMMPS program [3] using the embedded-atom method (EAM) potential developed for Ni-Al system [4]. The MD model for grain boundary diffusion simulation is shown in Figure 1a. The GB diffusion coefficient D_{gb} has been extracted from the Einstein relation $\langle x^2 \rangle = 2D_{\mathrm{gb}}t$, where $\langle x^2 \rangle$ is a mean-squared displacements of atoms within the GB core region.

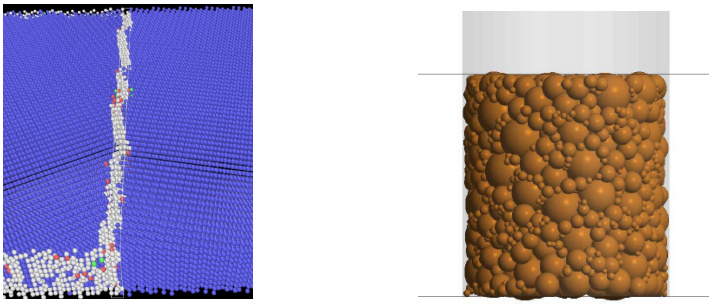

a) b)

Figure 1: Numerical models: a) MD model for grain boundary diffusion simulation, b) DEM model of powder sintering process

The parameters estimated in the MD simulations have been used in the microscopic DEM model of sintering. The DEM model of sintering is presented in Figure 1b. The evolution of the relative density obtained numerically has been compared with the experimental data. in Figure 2. A good agreement can be observed, which demonstrates a good performance of the presented two-scale model of powder sintering.

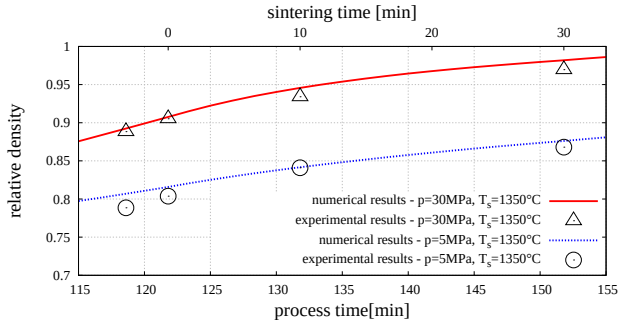

Figure 2: Comparison of experimental and numerical results – density evolution during sintering.

Acknowledgments This work has been financed from the funds of Polish National Science Centre (NCN) awarded by the decision number DEC-2013/11/B/ST8/03287.

References

[1] M. Maździarz, J. Rojek, and S. Nosewicz. Estimation of micromechanical NiAl sintering model parameters from the molecular simulations. *International Journal for Multiscale Computational Engineering*, 15:343–358, 2017.

[2] S. Nosewicz, J. Rojek, K. Pietrzak, and M. Chmielewski. Viscoelastic discrete element model of powder sintering. *Powder Technology*, 246:157–168, 2013.

[3] S. Plimpton. Fast parallel algorithms for short-range molecular dynamics. *J. Comp. Physics*, 117:1–19, 1995.

[4] G.P. Purja Pun and Y. Mishin. Development of an interatomic potential for the Ni-Al system. *Philosophical Magazine*, 89:3245–3267, 2009.

IDENTIFICATION OF THE MULTISCALE MATERIAL MODEL BASED ON AN INTERNAL VARIABLE

D. Szeliga, Ł. Rauch, M. Pietrzyk

[1]*GU University of Science and Technology, al. Mickiewicza 30, 30-059 Kraków, Poland*
e-mail: szeliga@agh.edu.pl

1. Introduction

Internal variable method (IVM) is an alternative for conventional models describing processing of materials. When the latter are used the history of the process is not accounted for. Fast change of the process conditions moves the model to a new equation of state without delay, which is observed in experiments. When external variables are replaced by internal ones, this disadvantage is eliminated. An approach, which uses dislocation density as the independent variable, was considered in the paper. This approach based on works [1,2] proved its extensive predictive capabilities. Difficulties with identification of this model limit its wide practical approach. Inverse approach to identification of the IVM was the main objective of the present work

2. Inverse approach for IVM

In the IVM differential equation describing evolution of dislocation populations (ρ) is solved:

(1) $$\frac{d\rho(t)}{dt} = A - B\rho(t) - C\rho(t - t_{cr}).$$

(2) $$A = \frac{a_1 Z^{a_3}}{b} \qquad B = a_2 \dot{\varepsilon}^{-a_9} \exp\left(\frac{a_3}{RT}\right) \qquad C = \begin{cases} 0 & \text{for } t \le t_{cr} \\ a_4 \exp\left(\frac{a_5}{RT}\right) \rho(t)^{a_8} \rho(t - t_{cr}) & \text{for } t \le t_{cr} \end{cases}.$$

where: b – length of the Burger vector, Z – Zener-Hollomon parameter, T – temperature in K, R – universal gas constant, t_{cr} – time at which critical dislocation density $\rho_{cr} = a_{11} - a_{12} Z^{a10}$ is reached, $a_1 - a_{13}$ - coefficients. External variable models can be easily identified on the basis of simple experiments, separately for the flow stress and for the static recrystallization (SRX). Since IVM uses the same equation for DRX and SRX, identification of this model is complex. Result of identification based on the flow curves only is shown in Figure 1. From one side, the model proved its capability to reproduce qualitatively the response of the material involving oscillations, which is characteristic for copper. On the other side quantitative agreement with the experiment is poor. Therefore, two-step compression was used as an experiment in this work. By changing the time between deformations it is possible to obtain data for identification of the SRX model.

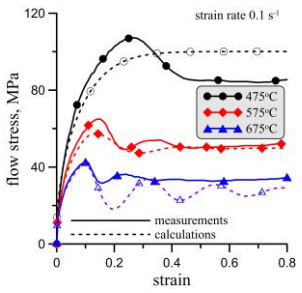

Figure 1: Measured and calculated flow stress for copper.

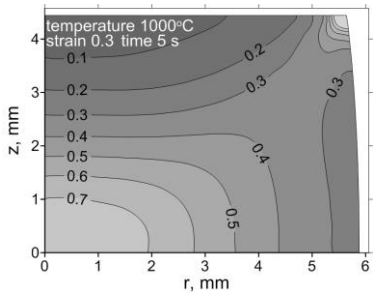

Figure 2: Distribution of the RX volume fraction at the sample cross section after 5 s interpass times.

The 2-step test involves strong inhomogeneity of strains and temperatures [3]. Inhomogeneity of deformation is well seen in Figure 1, where distribution of the RX volume fraction in 5 s after the first deformation is plotted. Therefore, inverse analysis was applied to identification of coefficients **a** in the model. Finite

element (FE) code was used to simulate two-step compression test. Equation (1) was solved in each Gauss integration point of the FE model (Figure 3). The objective function was defined as a square root error between calculated and measured force in the second step.

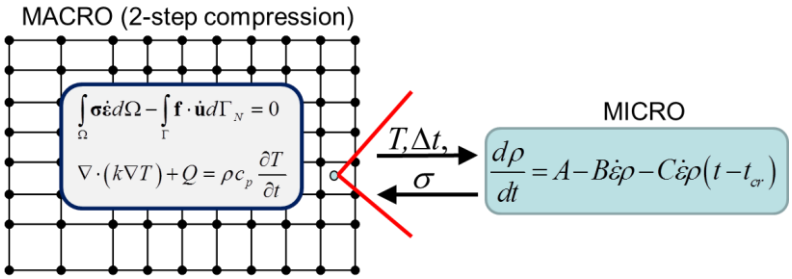

Figure 3: Schematic illustration of the multiscale model of the 2-step compression.

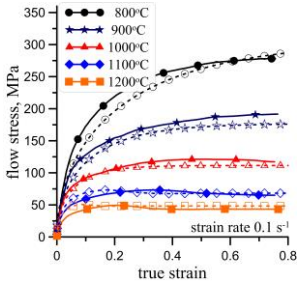

Figure 4: Measured and calculated (IVM model) flow stress.

3. Results

Identification was performed for a DP600 steel (steel A in [3]) and coefficients **a** in equations (1) and (2) were determined. Selected result of comparison of measured flow stress and calculated using optimal model is shown in Figure 4. Good agreement was obtained for all strain rates. Due to multiscale approach it is possible to follow distributions of all parameters in the test. Figure 5 shows distribution of dislocation density multiplied by 10^{-10} at the sample cross section of the sample in 4 s after the end of deformation, strain $\varepsilon = 0.4$, strain rate $\dot{\varepsilon} = 0.1\ s^{-1}$ and temperature $T = 900^oC$. Due to symmetry a quarter of the cross section is shown. Figure 6a shows changes of the dislocation density in the centre of the sample during 2-step test. Figure 6b shows flow stress for the 2-step tests with different interpass times.

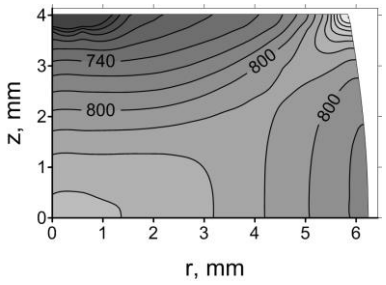

Figure 5: Distribution of the dislocation density at the cross section of the sample in 4 s after deformation.

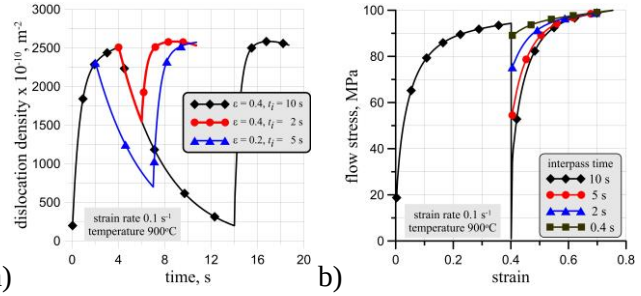

a) b)

Figure 6: Changes of the dislocation density in the centre of the sample during 2-step test (a) and flow stress for different interpass times (b), first strain $\varepsilon_1 = 0.4$.

4. Conclusions

Multiscale model with FE in macro scale and IVM in micro scale was identified on the basis of the 2-step compression. Numerical tests confirmed extensive predictive capabilities of the model as far as far as prediction of metallurgical phenomena is considered.

Acknowledgments Financial support of the NCN, project no. 2017/25/B/ST8/01823, is acknowledged.

References

[1] Estrin, Y., Mecking, H., A unified phenomenological description of work hardening and creep based on one-parameter models, *Acta Metall.*, 32:57, 1984.
[2] Sandstrom R., Lagneborg R., A model for hot working occurring by recrystallization, *Acta Metall.*, 23:387, 1975.
[3] Szeliga D., Kuziak R., Kopp R., Smyk G., Pietrzyk M., Accounting for the inhomogeneity of deformation in identification of microstructure evolution model, *Arch. Metall. Mater.*, 60:3087, 2015.

Session S07: Coupled fields in nanostructures and continua

Organizers: T. Łodygowski (Poznan UT), R. Pęcherski (IPPT PAN, Warsaw), H. M. Shodja (Sharif UT, Iran)

ANALYSIS OF STATIC AND DYNAMICAL THREE-DIMENSIONAL MODELS OF THERMOELASTIC PIEZOELECTRIC SOLIDS

***G. Avalishvili*[1] *and M. Avalishvili*[2]**

[1]*Iv. Javakhishvili Tbilisi State University, Faculty of Exact and Natural Sciences, Tbilisi, Georgia*
[2]*University of Georgia, School of Informatics, Engineering and Mathematics, Tbilisi, Georgia*

e-mail: gavalish@yahoo.com, mavalish@yahoo.com

Modern complex engineering constructions and technological processes are controlled by using sensors and actuators, which gather information and facilitate the adequate adjustment of construction or process. The need of construction of sensors and actuators with the appropriate physical characteristics stimulate the analysis of interaction between various physical fields, such as elastic, thermal, electric and magnetic. Mathematical models of continuum mechanics, in which processes of interaction of several physical fields are considered, are described by boundary or initial-boundary value problems for quite complicated systems of partial differential equations on three-dimensional domains. Consequently, investigation of the problems of continuum mechanics of this type is of crucial importance from practical as well as theoretical point of view. Piezoelectric materials are one of the most common materials currently being used and investigated for smart structures applications due to their direct and converse piezoelectric effects, which permit them to be utilized as both actuators and sensors. The wide area of application of them is aerospace engineering, where most structures operate in changing thermal environments. Therefore, due to their possible applications in the fabrication of smart and adaptive material systems, the study of mechanics and physics of thermo-electro-magneto-elastic materials has attracted increasing attention.

One of the first rigorous theoretical model of piezoelectricity describing the interaction between elastic, electric and thermal properties of thermoelastic body was constructed by W. Voigt [1]. Later on, W. Cady [2] treated the physical properties of piezoelectric crystals as well as their practical applications. H. Tiersten [3] studied problems of vibration of piezoelectric plates. A three-dimensional model of piezoelectric body taking into account thermal properties of the constituting material was derived by R. Mindlin [4] applying variational principle. Further, W. Nowacki [5] developed some general theorems for thermoelastic piezoelectric materials. R. Dhaliwal and J. Wang [6] proved uniqueness theorem for linear three-dimensional model of the theory of thermo-piezoelectricity, which was generalized by J. Li in the paper [7], where a generalization of the reciprocity theorem of W. Nowacki [8] was also obtained. Applying the potential method and the theory of integral equations D. Natroshvili [9] studied the problems of statics and pseudo-oscillations with basic and crack type boundary conditions.

Note that the three-dimensional boundary and initial-boundary value problems with general mixed boundary conditions for mechanical displacement, electric and magnetic potentials, and temperature corresponding to the linear static and dynamical models of inhomogeneous anisotropic thermoelastic piezoelectric bodies with regard to the magnetic field have not been well investigated. The well-posedness results are mainly obtained for thermoelastic piezoelectric bodies consisting of homogeneous materials.

The present paper is devoted to the investigation of the linear three-dimensional boundary and initial-boundary value problems with mixed boundary conditions corresponding to the linear static and dynamical three-dimensional models of piezoelectric solid taking into account magnetic and thermal properties of the material. We consider thermoelastic piezoelectric body consisting of inhomogeneous anisotropic material, when on certain parts of the boundary density of surface force, and normal components of electric displacement, magnetic induction and heat flux vectors are given, and on the remaining parts of the boundary mechanical displacement, temperature, electric and magnetic potentials vanish. We investigate boundary and initial-boundary value problems for coupled systems of partial differential equations corresponding to the static and dynamical three-dimensional models of thermoelastic piezoelectric bodies with regard to magnetic field, which consist of the linearized equations of motion or static equilibrium, equation of the entropy balance and quasi-static equations for electro-magnetic fields, where the rate of change of magnetic field is small, i.e. electric field is curl free, and there is no electric current, i.e. magnetic field is curl free. In the case of thermoelastic piezoelectric bodies, which consist of several subdomains with piecewise continuous parameters characterizing elastic, thermal, electric and magnetic properties of the body, the partial differential equations corresponding to the static or dynamical three-dimensional models are given in the

subdomains and along the common interfaces between the subdomains rigid contact conditions are fulfilled, i.e. mechanical displacement and stress vectors, temperature, electric and magnetic potentials, and normal components of the heat flux, electric displacement and magnetic induction are continuous. From the differential formulations of the boundary and initial-boundary value problems we obtain integral equations, which are equivalent to the original problems in the spaces of smooth enough functions, but require less regularity of the unknown functions than in the differential formulations. On the basis of the obtained integral equations we present variational formulations of the static and dynamical three-dimensional problems in the corresponding function spaces, which are Sobolev spaces for static problem, and spaces of vector-valued distributions with respect to the time variable with values in Sobolev spaces for dynamical problem. In the static case we determine the structure of the set of solutions of the homogeneous boundary value problem, when the density of surface force, and normal components of electric displacement, magnetic induction and heat flux vectors vanish. In the dynamical case we consider the set of solutions of the homogeneous equations corresponding to electric and magnetic fields, when the density of electric charges, normal components of electric displacement and magnetic induction, mechanical displacement and temperature vanish. By applying the sets of solutions of the corresponding homogeneous problems we define the factor spaces of suitable Sobolev spaces, which we use for investigation of the well-posedness of the three-dimensional problems. By using variational formulation and Lax-Milgram lemma [10] with non-symmetric bilinear form we obtain the well-posedness result for the boundary value problem corresponding to the linear static three-dimensional model of thermoelastic piezoelectric bodies in suitable factor-spaces of Sobolev spaces. By applying Faedo-Galerkin method [11], suitable a-priori estimates and compactness arguments we prove new existence result for the initial-boundary value problem corresponding to the linear dynamical three-dimensional model of thermoelastic piezoelectric solids in the corresponding spaces of vector-valued distributions with values in suitable factor spaces of Sobolev spaces. Furthermore, an energy equality is obtained, which permits us to prove the uniqueness result and continuous dependence of the solution on the given data in suitable function spaces. If mechanical displacement, temperature, electric and magnetic potentials vanish on the parts of the boundary with positive areas, then the corresponding homogeneous boundary value problems possess only trivial solutions and we obtain existence and uniqueness results in suitable Sobolev spaces. Note, that the proof of the existence of solution of the initial-boundary value problem gives an algorithm for approximation of the solution of the three-dimensional dynamical problem by a sequence of solutions of linear finite-dimensional systems of ordinary differential equations. The methodology outlined in this paper can be used for investigation of various coupled problems in the continuum mechanics and the construction of algorithms of their solution.

Acknowledgments. This work was supported by Shota Rustaveli National Science Foundation (SRNSF) [Grant number 217596, Construction and investigation of hierarchical models for thermoelastic piezoelectric structures].

References

[1] W. Voigt. Piëzo- und Pyroelectricität, diëlectrische Influenz und Electrostriction bei Krystallen ohne Symmetriecentrum, *Abh. der Königlichen Gesellschaft der Wissenschaft zu Göttingen*, 40:343-372, 1894.
[2] W.G. Cady. *Piezoelectricity*. Dover, 1964.
[3] H.F. Tiersten. *Linear piezoelectric plate vibrations*. Plenum, 1964.
[4] R.D. Mindlin. Equations of high frequency vibrations of thermopiezoelectric crystal plates. *Int. J. Solids Struct.*, 10: 625-637, 1974.
[5] W. Nowacki. Some general theorems of thermopiezoelectricity. *J. Thermal Stresses*, 1:171-182, 1978.
[6] R.S. Dhaliwal and J. Wang. A uniqueness theorem for linear theory of thermopiezoelectricity. *Z. Angew. Math. Mech.*, 74:558-560, 1991.
[7] J.Y. Li. Uniqueness and reciprocity theorems for linear thermo-electro-magnetoelasticity. *Quart. J. Mech. Appl. Math.*, 56, 1:35-43, 2003.
[8] W. Nowacki. A reciprocity theorem for coupled mechanical and thermoelectric fields in piezo-electric crystals. *Proc. Vibr. Prob.*, 1: 3-11, 1965.
[9] D. Natroshvili. *Mathematical problems of thermo-electro-magneto-elasticity*. Lecture Notes of TICMI, 12, Tbilisi State University Press, 2011.
[10] W. McLean. *Strongly elliptic systems and boundary integral equations*. Cambridge University Press, 2000.
[11] R. Dautray and J.-L. Lions. *Mathematical analysis and numerical methods for science and technology, Vol. 5: Evolution problems* I. Springer-Verlag, 2000.

CRYSTALLIZATION KINETICS OF POLYAMIDE 2200 IN THE MODELING OF ADDITIVE MANUFACTURING PROCESSES BY FE ANALYSES

P. Bajerski[1], R.B. Pęcherski[2], D. Chudy[2], L. Jarecki[3]

[1)] *ABB Sp. z o.o. Corporate Research Center, Krakow, Poland*
[2)] *Faculty of Mechanical Engineering and Robotics, AGH University of Science and Technology, Krakow, Poland*
[3)] *Institute of Fundamental Technological Research, Polish Academy of Sciences, Warsaw, Poland*
e-mail: pawel.bajerski@pl.abb.com

1. Introduction

Additive Manufacturing (AM) process is a very fast and promising technique to build various very complex prototypes and components directly in the industry. One can choose different techniques of AM like Selective Laser Sintering (SLS), Fused Filament Fabrication (FFF) dedicated for thermoplastic materials or Direct Laser Metal Sintering (DMLS) for powder metals, or Stereolitography Apparatus (SLA) for thermosets. One of the most common techniques in AM are SLS and FFF for thermoplastic materials. The complexity of the processes and the behaviour of the materials in specific environment have a strong influence on the quality, strength and warpage of the obtained structures. The state of the art of the studies indicates that morphology of the material and the crystallization processes influence the aforementioned characteristics of the created components. The knowledge on the crystallization kinetics of polymers is known since many years but it is still developing in order to get an adequate description of the behaviour of the materials in isothermal and non-isothermal conditions. Furthermore, it is needed to predict the warpage of manufactured components based on the virtual AM process in order to decrease the costs. The available tools dedicated for FE analyses allow to increase functionality and implementation of own material models and techniques to perform the customize simulations. Based on the theory and Differential Scanning Calorimetry (DSC) results it is possible to predict the behaviour of the materials and start working on simulation of the virtual AM process [1-4]. The extracted curves of the velocity of material crystallization in temperature domain with different cooling rate obtained in FE simulations are shown in Fig. 1. The simulated curves are confronted with the DSC experimental results.

2. Theoretical and experimental background

The crystallization kinetics theory describes the evolution of the degree of crystallization $\alpha(t)$ as a function of time t and time-dependent temperature $T(t)$. The models of crystallinity evolution include information on the crystal nucleation and growth kinetics in the bulk of material. The general Avrami equation for the isothermal crystallization reads [1].

$$\alpha(t) = 1 - \exp(-k(T)t^n) \tag{1}$$

The Avrami exponent n is equal to the growth dimensionality in the case of heterogeneous nucleation or to the dimensionality increased by unity in the case of sporadic homogeneous nucleation, $k(T)$ is the isothermal crystallization rate constant dependent on temperature and the geometry of crystal growth [1-3]. Nakamura expanded the isothermal Avrami equation for non-isothermal crystallization [2, 3].

$$\alpha(t) = 1 - \exp\left[-\left(\int_0^t K\big(T(\tau)\big) d\tau \right)^n \right] \tag{2}$$

Where $K(T)$ is a crystallization rate function. The Nakamura and Avrami theories can be directly related to the crystallization half time $t_{1/2}$ expressed by the Hoffman-Lauritzen theory [5]. The material parameters needed to be implemented in the crystallization model, such as the constants present in the function $K(T)$, glass transition and equilibrium melting temperatures, specific heat of melting, heat capacity and other are determined from the DSC tests.

Based on the theoretical and empirical models of the crystallization kinetics and DSC results one can implement the crystallization process of each of the analysed materials in the FE approach. The method is the first step to predict structure formation during the AM process. The example of the curves of the velocity of

crystallization obtained for the considered Polyamide 2200 at several constant cooling rates in FE simulations is presented in Figure 1.

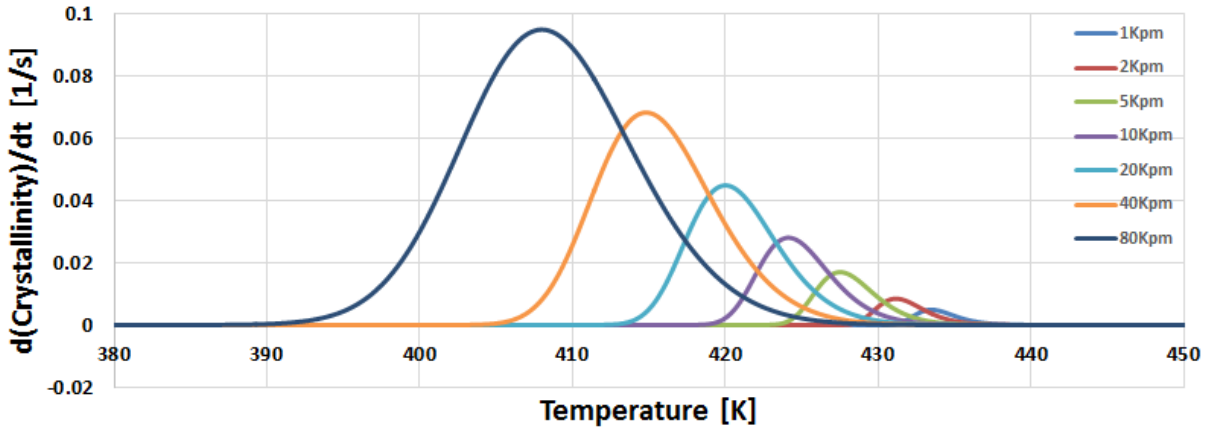

Figure 1: The simulated numerically curves of the velocity of crystallization of Polyamide 2200 at several constant cooling rates.

3. Implementation of polymer crystallization in the FE method

Available commercial finite element (FE) tools like Abaqus/SIMULIA offer to perform customization by expanding the solver. The user-subroutines can be written and implemented to standard analysis in order to calculate non-standard cases. The software dedicated to the prediction of the residual stresses and temperature distributions is available on the market but it is limited to metallic materials. The user-subroutines in Abaqus system offer good alternative and allow to create models for various non-metallic materials used in simulations of the AM processes.
In order to model the AM process for polymers and predict the progress of crystallization, the following evolution equation proposed by Nakamura for non-isothermal crystallization [2, 3] is used.

$$\frac{d\alpha}{dt} = nK(T(t))(1-\alpha)\left[\ln\left(\frac{1}{1-\alpha}\right)\right]^{\frac{n-1}{n}} \tag{3}$$

4. Further investigations

Crystallization of polymers has a strong influence on the strength and warpage structure obtained at the AM process. Furthermore, the complexity of the material behaviour at crystallization under non-isothermal conditions causes that the AM process is difficult to control and optimize. One has also to underline that after addition of new layers during the component manufacturing, the last built layer is partially melted in order to merge a new layer. It causes locally the change of material properties. The implementation of the crystallization process in the FE computations makes the first step in the analyses of the residual stresses and strength of the structures obtained during the technological tests.

5. References

[1] G. H Michler, F. J. Balta-Calleja. *Mechanical Properties of Polymers Based on Nanostructure and Morphology.* CRC Press, 2005.
[2] J. M. Schultz. *Polymer Crystallization. The Development of Crystalline order in Thermoplastic Polymers.* Oxford University Press, 2001.
[3] A. Amado, K. Wegener, M. Schmid, G. Levy. Characterization and modelling of non-isothermal crystallization of Polyamide 12 and co-Polypropylene during the SLS process. *5th International Polymers & Moulds Innovations Conference, Ghent;* 2012.
[4] L. Jarecki, R. B. Pęcherski, Kinetics of oriented crystallization of polymers in the linear stress-orientation range in the series expansion approach, *EXPRESS POLYMER LETTERS*, **12**, No.4, pp. 330-348, 2018.
[5] J. D. Hoffman., G. T. Davis, J. I. Jr. Lauritzen. The rate of crystallization of linear polymers with chain folding. *Treatise on Solid State Chemistry*, vol. 3 (ed.: Hannay N. B.) Plenum, New York, 1976.

VIRTUAL ADDITIVE MANUFACTURING BASED ON SEMICRYTSALLINE POLYMER POLYETHERETHERCETONE (PEEK)

P. Bajerski[1], R. Pęcherski[2], D. Chudy[3]

[1]*ABB Sp. z o.o. Corporate Research Center, Krakow, Poland*
[2]*Faculty of Mechanical Engineering and Robotics, AGH University of Science and Technology, Krakow, Poland*
[3]*Faculty of Mechanical Engineering and Robotics, AGH University of Science and Technology, Krakow, Poland*

e-mail: pawel.bajerski@pl.abb.com

1. **Introduction**

Additive Manufacturing process is the most appropriate technique for fast creating mechanical components and it allows for building complex parts which could not be created in traditional technology like injection molding process. Many available tools allow to perform simulations of the Additive Manufacturing process but based on these tools user can perform analysis regarding with process for metals, thermosets or polymers. The analyses usually give information about the paths of created parts, temperature distribution and residual stress for simple material models. Empirical investigations indicate that for semi-crystalline polymers the crystallization kinetic has a strong influence on viscoelastic behaviour and consequently residual stresses and warpage of the obtained built components.
The present investigation describes the dual crystallization kinetics model for considered thermoplastic material PEEK and implementation whole process in Abaqus/SIMULIA software. The innovation of the proposed approach is to interpreting G-Code, which is an input for real machines dedicated to AM. The path and time of particular steps for process are extracted from the G-Code and they are included as one of inputs for simulation. Extended programming using user subroutines will help for perform simulation of real process of the additive manufacturing in order to optimize model before real production [1].

2. Dual crystallization kinetics model

The crystallization in polymers consists basically from nucleation and growth. Overall crystallization for non-isothermal conditions is described by the Velisaris & Seferis in 1986 who expanded Avrami Model for isothermal crystallization of polymers. Dual crystallization kinetics model quite good fits to experiments. Volume crystallinity is presented in equation (1) which represents two connected crystallization processes with respectively factors. The summation of the factors should be equal to 1 (2). Parameters from one curve of the process corresponds to homogeneous crystallization, the second one corresponds to heterogeneous crystallization. Each of the expressed process is described as (3). The proposed model describes non-isothermal conditions for high temperature polymers like PEEK [2], [3].

(1) $$X_{\upsilon c} = X_{\upsilon c\infty}(w_1 * F_{\upsilon c1} + w_2 * F_{\upsilon c2})$$

(2) $$w_1 + w_1 = 1$$

(3) $$\mathrm{F}_{\upsilon \mathrm{c,i}} = 1 - \exp\left[- \mathrm{C}\int_0^{\mathrm{t}} \mathrm{T} \times \exp\left\{ \frac{-\mathrm{C}_{\mathrm{i2}}}{\mathrm{T} - \mathrm{T}_{\mathrm{g}} + T_{add,i}} - \frac{-\mathrm{C}_{\mathrm{i3}}}{\mathrm{T}(\mathrm{T}_{\mathrm{m,i}} - T)^2} \right\} n_i t^{n_i - 1} dt, i = 1,2 \right]$$

3. Implementation of the printing process in Abaqus/SIMULIA

The implementation presented material model dedicated for PEEK was presented using Abaqus/SIMULIA software. Dual crystallization model was presented in incremental version to better description in FEM. Additionally, melting material model was implemented to simulate real behavior of the structure during the adding new layer of the material on partially crystallized material. Basic information about printing process is included in "G-Code" format file. Information from the G-Code file is translated to binary file where input is source for written subroutine UMATHT and subroutine UEPActivationVol in Abaqus. The simulation is performed according to real process (see Figure 1).

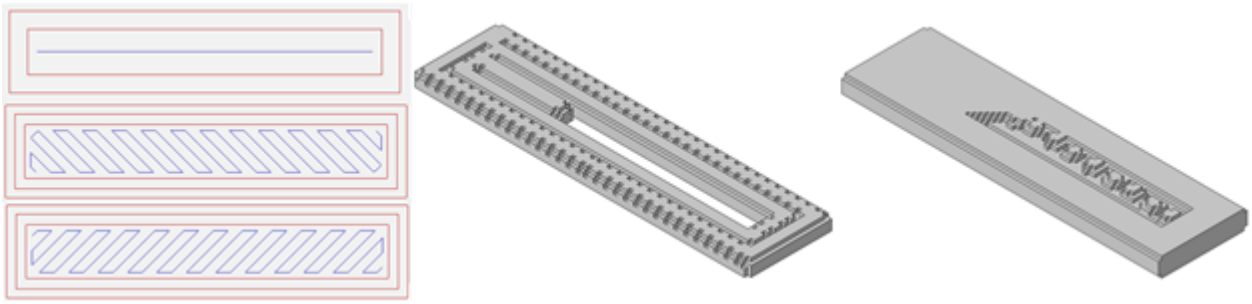

Figure 1: Additive Manufacturing simulation based on paths generated from G-Code

The results are extracted from analyses in different cooling rate (see Figure 2).

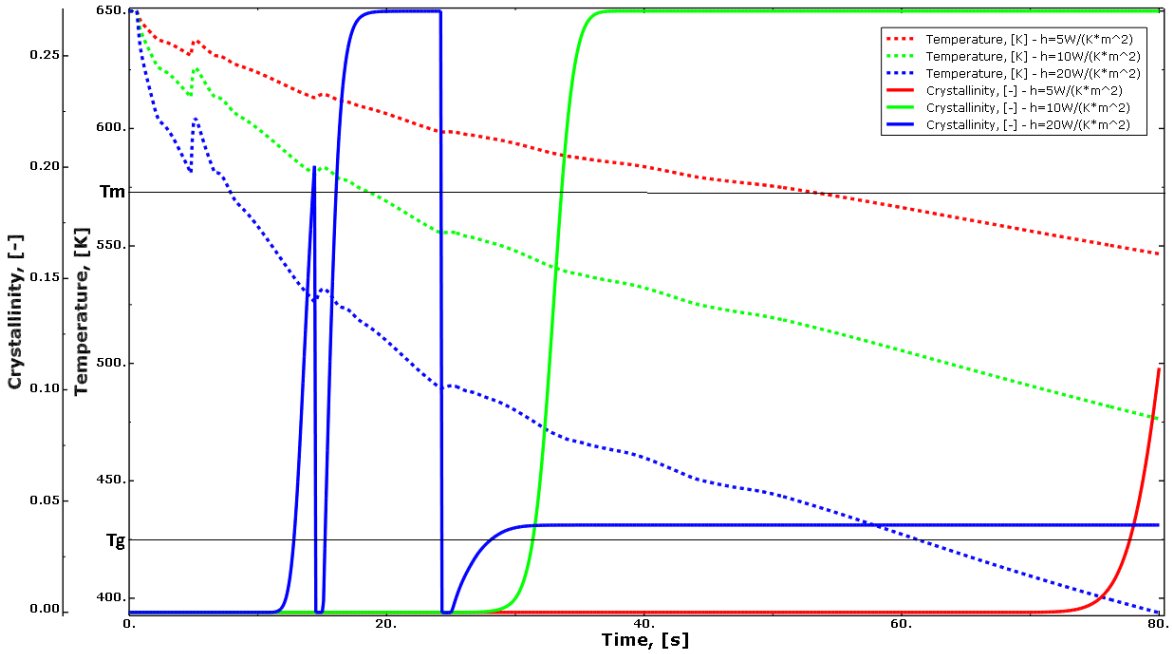

Figure 2: Temperature distribution (K) and crystallinity (-) with different heat of transfer measured at the specific node.

4. Conclusions and further investigations

The investigations presents fundamental information about the crystallization of the polymers in non-isothermal conditions and implementation in CAE softwares. The approach to the interpreting G-Code file which is the same in real Additive manufacturing process is described. Based on the conduction of the same process in simulation as in real indicates to optimize process parameters and orientation part in the chamber in order to obtain part with required conditions. The presented simulations are the first step to calculate warpage and residual stresses analysed structures and compare with real tests. Prepared approach will allow performing mechanical simulations and improve quality manufactured structures made from polymers.

6. References

[1] B. Brenken, E. Barocio, A. J. Favaloro and R. Byron Pipes. Simulation of Semi-Crystalline Composites in the Extrusion Deposition Additve Manufacturing Process. *Science in the Age of Experience*, Chicago, IL 2017

[2] A. J. Favaloro, B. Brenken, E. Barocio, and R. Byron Pipes. Simulation of Polymeric Composites Additive Manufacturing using Abaqus. *Science in the Age of Experience*, Chicago, IL 2017

[3] J. M. Schultz. *Polymer Crystallization. The Development of Crystalline order in Thermoplastic Polymers.* Oxford Unversuty Press, 2001

[4] A. Amado, K. Wegener, M. Schmid, G. Levy. Characterization and modelling of non-isothermal crystallization of Polyamide 12 and co-Polypropylene during the SLS process. *5th International Polymers & Moulds Innovations Conference*, Ghent; 2012

MATERIAL MODELLING FOR CYCLIC LOADING - A THERMO-MECHANICAL APPROACH

H. Sparr[1], D. Schob[1], R. Roszak[1,2], and M. Ziegenhorn[1]

[1]*Brandenburg University of Technology Cottbus-Senftenberg, Germany*
[2]*Poznan University of Technology, Poland*

e-mail: holger.sparr@b-tu.de

1. Motivation

The mechanical properties of reinforced plastics in conventional or additive manufacturing are dominated by the properties of the matrix material. These materials exhibit a rate-dependent behaviour. An accepted material classification scheme depicts the rate-dependency in an equilibrium hysteresis when subjected to a relaxation process on the load path [5]. This statement holds for various other classes of materials and can be weighted as increasingly important for high-perfomance structural components under cyclic loading.

Secondly, a temperature evolution in specimens or components under cyclic loading is observed. An increased temperature in the specimen can be attributed to external or internal heat sources or, which is the main subject in this work, to dissipative phenomena in the material itself. The dissipative phenomena are basically related to viscoplastic deformations.

As a matter of course in common loading regimes, the dissipation amount per cycle is small compared to the stored total free energy. Nonetheless, the dissipated energy is transferred into heat, the dissipation process accumulates and leads to a characteristic temperature evolution field. By including a temperature field measurement in the procedure of material characterisation, we can exploit quantitative observations to improve and refine the material model. Therefore a thermo-mechanically coupled analysis based on general principles from continuum mechanics is introduced to study the effect of deformation mechanisms of different material classes.

The complexity in terms of low- and high-cycle fatigue of metals incorporating viscoplasticity has been widely studied (e.g. [2]) and is nowadays transferred to new material classes like additive manufactured plastics. To cover the different micro-mechanical phenomena the applied material models and the experimental procedures to establish the set of material parameters need to be adapted. Additionally through the application of thermography, the consideration of an evolving temperature field opens an opportunity to verify the chosen modelling approach and creates further possibilities for proof [3, 4, 6].

2. Governing principles and equations

General material models are represented by simple networks of basic material properties related to spring, friction or damper elements. A more differentiated network can always be reduced to one of the four main classes outlined by HAUPT (see [5]). More importantly, the network representation gives hold of a main principle - the additive decomposition of physical entities.

To incorporate an evolving temperature due to mechanical loading we start with the two fundamental laws of thermodynamics. Eq. (1) shows the CLAUSIUS-DUHEM inequality for the one-dimensional case.

$$\delta = \frac{1}{\varrho}\sigma\dot{\varepsilon} - \dot{e} + \theta\dot{s} - \frac{1}{\varrho\theta}q\frac{\partial\theta}{\partial x} \geq 0 \tag{1}$$

By the introduction of the HELMHOLTZ free energy ψ and the straightforward additive split in terms of stress, strain and energies (see eq. (2)) according to the assumed network the implementation point of experimentally motivated material models is achieved.

$$\psi = \psi_{th} + \psi_{el} + \psi_{iso} + \psi_{kin} + \dots \tag{2}$$

Then the summands of the internal dissipation in eq. (3) are associated with network members as well.

$$\delta_{mech} = \delta_{vis} + \delta_{iso} + \delta_{kin} + \dots \tag{3}$$

Taking the yield condition and the flow rule for viscoplasticity into account, we need to solve a system of evolutionary equations in a PERZYNA type formulation.

For a specific metal alloy under simple loading condition a deep theoretical quantitative discussion was published in [1], whereas YU *et.al.* [7] apply this methodology to PA6 for up to 1 000 cycles and show a reasonable agreement with experimental data.

3. Parametric study for experimental setup

With the presented study, the setup for our experimental investigations for different material classes and loading definition are prepared. Suitable sensitivity analyses with respect to material parameters influencing the amount of internal dissipation result in a better understanding for appropriate material models as depicted in Fig. 1.

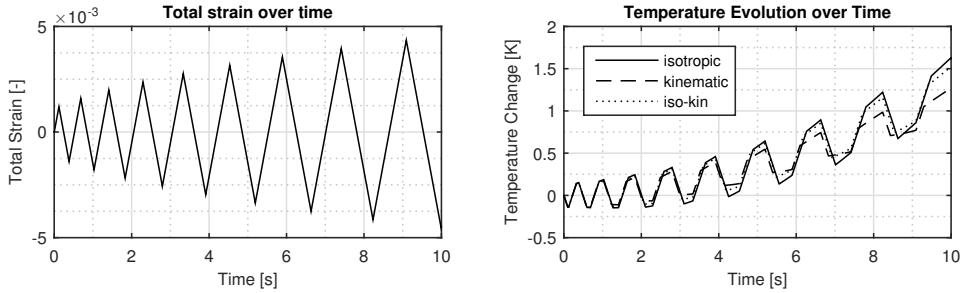

Figure 1: Sample temperature evolution for a viscoplastic material with hardening

Conclusions to the required IR-camera resolution will be drawn by discussing upper and lower bounds based on idealized thermal boundary conditions. Strategies to identify the enlarged number of material parameters are outlined.

The usage of a modern servo-hydraulic testing machine with climate chamber brings likewise an optimized loading regime (e.g. load amplitude, load frequency or intermediate relaxation time) into focus.

4. References

Acknowledgments The authors acknowledge the financial support in a ZIM project through the Federal Ministry for Economic Affairs and Energy of Germany.

References

[1] C. Bröcker and A. Matzenmiller. An enhanced concept of rheological models to represent nonlinear thermoviscoplasticity and its energy storage behavior. *Continuum Mechanics and Thermodynamics*, 25(6):749–778, Nov 2013.

[2] J. L. Chaboche. Constitutive equations for cyclic plasticity and cyclic viscoplasticity. *International Journal of Plasticity*, 5:247–302, 1989.

[3] A. Chrysochoos. Infrared thermography applied to the analysis of material behavior: a brief overview. *Quantitative InfraRed Thermography Journal*, 9(2):193–208, 2012.

[4] R. Guzmán, J. Meléndez, J. Zahr, and J. L. Pérez-Castellanos. Determination of the constitutive relation parameters of a metallic material by measurement of temperature increment in compressive dynamic tests. *Experimental Mechanics*, 50(3):389–397, 2010.

[5] P. Haupt. *Continuum Mechanics and Theory of Materials*. Springer-Verlag, 2nd edition, 2002.

[6] P. Knysh and Y. P. Korkolis. Determination of the fraction of plastic work converted into heat in metals. *Mechanics of Materials*, 86:71 – 80, 2015.

[7] Ch. Yu, G. Kang, and K. Chen. A hygro-thermo-mechanical coupled cyclic constitutive model for polymers with considering glass transition. *International Journal of Plasticity*, 89:29–65, 2017.

KINETIC MODEL OF POLYMER CTYSTALLIZATION UNDER HIGH TENSILE STRESS OR MOLECULAR ORIENTATION

B. Misztal-Faraj, L. Jarecki and R. B. Pęcherski

Institute of Fundamental Technological Research, Pawińskiego 5B, Warsaw, Poland
e-mail: bfaraj@ippt.pan.pl

1. General

Molecular deformation and orientation in the amorphous phase subjected to tensile stresses strongly accelerates crystallization of polymers by orders of the magnitude. Closed-form analytical formula is derived for the crystallization rate under high tensile stresses in the entire range of crystallization temperature and the temperature rates. Such formula, lacking in the literature, is needed for modelling of the dynamics of crystallizing polymers processing and predicting structure development in obtaining highly oriented materials of enhanced tensile modulus and tenacity. Rapid online crystallization strongly influences the rheological behaviour during the processing and introduces coupling of crystallization with the processing dynamics. Tensile stress affects the crystallization rate mainly by influencing the configurational entropy of the chain macromolecules in amorphous phase. In our earlier publication [1], a series expansion approach of the crystallization rate over the amorphous orientation factor has been considered basing on the Gaussian statistics of configurations of linear flexible chains, limited to low tensile stresses and orientation. None of the actually available models are capable to account for the effects of high molecular orientation in the crystallization kinetics.

In the present approach, non-Gaussian chain statistics is considered to account for finite extensibility of real macromolecules in the amorphous phase under high tensile stresses which results in non-linear effects in the model. The Hoffman-Lauritzen model of crystallization kinetics is extended to account for free energy of deformation of the amorphous component under uniaxial molecular orientation produced by the tensile stresses. The crystallization rate is considered as controlled by predetermined and sporadic nucleation present in real systems. The involvement of both nucleation mechanisms in the crystallization kinetics varies strongly with the level of tensile stress and amorphous orientation, with domination of sporadic nucleation at high orientations. The closed-form analytical formulas are validated by computations. Example numerical calculations illustrate influence of amorphous orientation on the crystallization free energy and the crystallization rate function involving both nucleation mechanisms.

2. The model formulations

The progress of crystallization $X(t)$ is controlled by nucleation followed by crystal growth, both driven by the crystallization free energy affected by the tensile stress and orientation in the entire crystallization temperature range. We use the crystallization rate formula in the quasi-static approximation extended for the transformations under variable amorphous orientation factor $f_a(t)$ and temperature $T(t)$

$$\frac{dX}{dt} = nK\left[T(t), f_a(t)\right]\left(1-X\right)\left[\ln\left(1-X\right)\right]^{-(n-1)/n}$$

where temperature- and orientation-dependent function $K(T, f_a)$ represents the rate of crystallization and is inversely proportional to the crystallization half-time. f_a characterizes orientation of the chain segments in the amorphous phase and varies from zero at no orientation and unity at full uniaxial chain alignment, n is the Avrami exponent. For the transformation controlled by predetermined nucleation, the $K(T, f_a)$ function expresses by the linear growth rate of crystals, while for the processes controlled by sporadic, homogeneous nucleation – by the product of the nucleation and the crystal growth rates. The orientation-dependent free energy of crystallization $\Delta g(T, f_a)$ increases with increasing f_a, and the thermodynamic barriers of nucleation

and crystal growth are reduced the more, the higher is the orientation. The largest contribution of the orientation, or the orienting stress, to the thermodynamic driving force of crystallization comes from the decrease of the configurational entropy, $\delta s_a(f_a) < 0$, of ν amorphous macromolecules per unit volume

$$\Delta g(T, f_a) \cong \Delta g^0(T) + T\delta s_a(f_a)$$

where $\delta s_a = \nu N k \left[\left\langle \int_0^{h/Na} \mathrm{L}^{-1}(x)dx \right\rangle_{W(\mathbf{h},t)} - \left\langle \int_0^{h/Na} \mathrm{L}^{-1}(x)dx \right\rangle_0 \right]$ is the difference of the molecular entropies averaged over the distributions of the chain end-to-end vectors **h** under the stress at the instant of time *t* and at the isotropic relaxed state, respectively, *N* is the number of statistical segments of length *a* in the macromolecule, $\mathrm{L}^{-1}(x)$ - the inverse Langevin function, *k* – the Boltzmann constant.

The orientation factor f_a and deformation entropy δs_a are calculated for distribution of chain macromolecules in the fluid subjected to uniaxial elongational flow. Effectivity of the tensile stress on the orientation and the deformation entropy in the flow is determined by the product $\dot{q}\tau$ of the elongation rate and a molecular stretch relaxation time. Time-evolution of the molecular deformation is described by the coupled equations for the chain extension coefficients λ and $\lambda_\perp$ along and perpendicular to the flow axis, respectively [2]

$$\frac{d\lambda^2}{d(t/\tau)} + \left[E(\lambda,\lambda_\perp) - 2\dot{q}\tau\right]\lambda^2 - 1 = 0\,, \qquad \frac{d\lambda_\perp^2}{d(t/\tau)} + \left[E(\lambda,\lambda_\perp) + \dot{q}\tau\right]\lambda_\perp^2 - 1 = 0$$

where E is the Peterlin modulus of non-linear elasticity of the system dependent on the average chain extension coefficients which varies between unity at zero tensile stress and infinity at full extension of the macromolecules. Analytical formulas are derived for the dependence of the orientation factor f_a and the deformation entropy δs_a on the coefficients λ and $\lambda_\perp$ during the deformation time, t/τ. The inverse Langevin function is approximated by a series expansion with the first non-Gaussian term, $\mathrm{L}^{-1}(x) = 3x+9x^3/5$, and by a Padé approximation, $\mathrm{L}^{-1}(x) = x(3-x^2)/(1-x^2)$, valid in the entire range of the chain extensions. The values of the deformation entropy δs_a vs. orientation factor f_a coincide in a single master plot formula $\delta s_a(f_a)$, independently on the elongation rate $\dot{q}\tau$ and the time t/τ, but affected by the inverse Langevin function approximations.

3. The main results

For the Padé approximation, the master plot $\delta s_a(f_a)$ is predicted for the entire range of the orientation factor f_a between zero and unity. In the range of low f_a values, the master relation based on the first non-Gaussian term approximation shows slightly better formula than that obtained basing on the Padé approximation, and approaches the Gaussian limit at zero orientation. The closed-form analytical formulas approximate the $\delta s_a(f_a)$ master relation, one in the range of small and intermediate orientations (basing on the first non-Gaussian term approximation) and second one for high orientations (basing on the Padé approximation). The analytical formulas are very well validated by the exact computations of f_a and δs_a at various elongation rates and the deformation times. The master relation can be expressed also in terms of the tensile stress, Δp, with the use of the stress-orientation formula presented in ref. [3] for both molecular statistics. With the $\delta s_a(f_a)$ or $\delta s_a(\Delta p)$ relations the rate functions $K(T, f_a)$ based on the Hoffman-Lauritzen model of crystallization kinetics express in terms of f_a, or Δp, for predetermined, as well as for sporadic nucleation. Conditions for equal contribution of both nucleation mechanisms in terms of f_a or Δp are defined.

References

[1] L. Jarecki andR. B. Pęcherski. Kinetics of orientedcrystallization of polymers in the linear stress-orientation range in the series expansion approach. *Express Polymer Lett.*,12:330, 2018.

[2] A.Schoene,A.Ziabicki andL. Jarecki. Transient uniaxial orientation of flexible polymer chains in a wide range of elongation rates.*Polymer*, 46:3927, 2005.

[3] L.Jarecki and B. Misztal-Faraj. Non-linear stress-orientation behavior of flexible-chain polymers under fast elongational flow.*Eur. Polymer J.*, 95:36, 2017.

IMPACT RESISTANCE OF CRUSHABLE FOAM SKELETON

E. Postek, Z. Nowak and R. B. Pęcherski

[1]*Institute of Fundamental Technological Research of the Polish Academy of Sciences,*
Pawinskiego 5b, 02-106 Warsaw, Poland
e-mail: epostek@ippt.pan.pl

1. Introduction

The analyses of the modern cellular materials due to complexity of their internal structure require efficient computer methods and codes. The new method that has been developed mostly in the last 10 years is peridynamics [1, 2]. The developments resulted in highly parallelized code [3] that we use in our analysis.
The subject of the study are alumina foams produced by gelcasting method. The results of microtomography of alumina foams are used to create the numerical model reconstructing the structure of foam skeleton. The numerical simulations of failure strength under compression for alumina foams are performed. The calculations with use of the numerical model are time consuming. Therefore, the simplified method of the assessment of failure strength is proposed. The 3D model of the foam structure is created. The detailed description of the model generation is presented in Nowak *et al.* [5].
The numerical models of real Al_2O_3 foam with porosity 96 %, and discussion of theirs mechanical properties have been presented. The method of the assessment of failure strength of real alumina foam produced by the gelcasting is proposed.
We attempt to present the mechanism of damaging of a crushable foam under impact.

2. Material model of solid alumina

We analyse a skeleton of a 3D ceramic foam that impacts a stiff wall with velocities 50 m/s and 100 m/s, Figure 1 and Figure 2, respectively. The velocities are directed down along the Figures.
One of the most important aspects in numerical simulation of the material is to formulate constitutive material model. The elastic part of deformation for solid alumina describes isotropic Hooke's law.
In terms of small deformations and when the stress level is much smaller than the elastic limit, the Hooke's model is a good way to describe the behaviour of solid alumina.
Concerning the assumption that the damage is isotropic, the maximum reduced stress can be expressed as follows, [4]

$$\sigma_{\max}^{D} = \sigma_{\max}\left(1 - D\right) \tag{1}$$

where the reduced stress is related to the non-dimensional damage variable $D=A/A_o$ where A is the damaged area, and A_o is the initial area. The variable D varies between 0 and 1.

3. Numerical results

We assume Young's modules 370 GPa and Poisson's ratio 0.22 and density 3.92g/cm3, see Nowak et al. [6]. The foam is discretized with 585897 points. The critical strain is 0.0005. We note gradual damage in the samples in both Figures 1 and 2. An interesting observation is done in Figures 1 (c) and 2(a). We find that the maximum values of damage variable that are close to 1, form islands in the entire structure, far from the attacking edge. It can be interpreted that stress wave phenomena play a role during this kind of process.

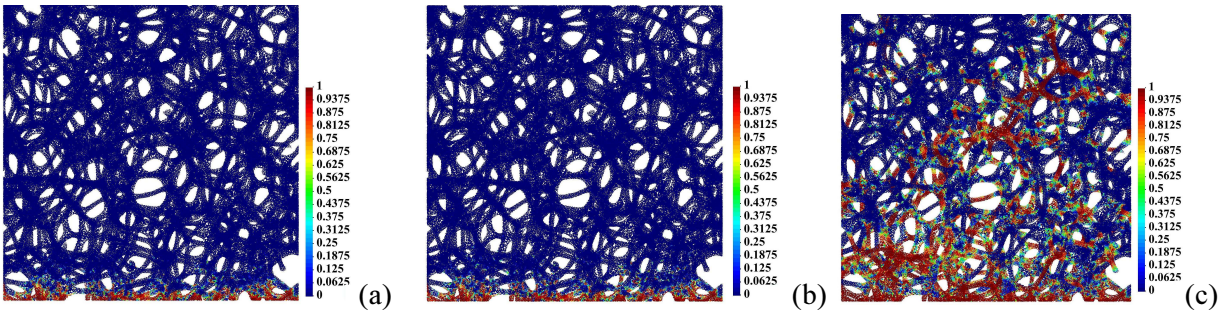

Figure 1. Damage advancement, impact velocity 50 m/s: (a) time instant 11.51E-08 s; (b) time instant 21.74E-08 s; (c) time instant 26.85E-08 s

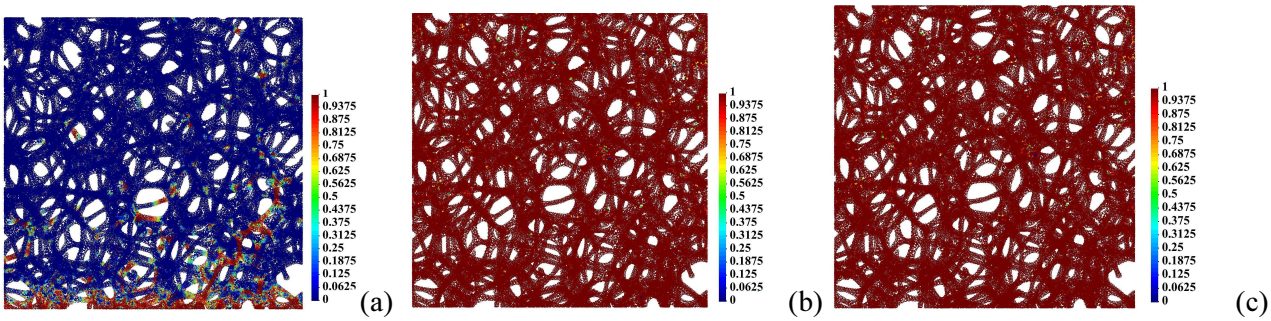

Figure 2. Damage advancement, impact velocity 100 m/s: (a) time instant 11.51E-08 s; (b) time instant 21.74E-08 s; (c) time instant 26.85E-08 s

5. Final Remarks

A numerical model for the open-cell ceramic foam structures is presented.
The increase of localized stresses and the brittle nature of ceramics cause the failure of some struts of ceramic foam. For this reason the understanding of stress state in ceramic foam is necessary.
Several numerical simulations have been performed to analyze the influence of applied velocity on the compressive strength of the considered alumina foam. The peridynamic modelling is applied to investigate its dynamic damage process under axial compression. The results show that, it is the alumina ceramic phase that makes the dominant contribution to the model's damage due to its intrinsic brittleness.

Acknowledgments The calculations were done on CRAY XC40 system at the Interdisciplinary Centre for Mathematical and Computational Modelling, University of Warsaw, Poland. The license for the MSC Patran was provided by Academic Computer Centre in Gdańsk, Poland.

References

[1] S. A. Silling. Reformulation of elasticity theory for discontinuities and long range forces, *J. Mech. Phys. Solids*, 48:175, 2000.
[2] A. Silling, M. Epton, O. Weckner,J. Xu, and E. Askari, Peridynamic states and constitutive modeling, *J. Elasticity,* 88:151, 2007.
[3] M. L. Parks, D. J. Littlewood, J. A. Mitchell, and S. A. Silling, *Peridigm Users' Guide, Tech. Report SAND2012-7800*, Sandia National Laboratories, 2012.
[4] L. M. Kachanov, *Introduction to Continuum Damage Mechanics,* Martinun Nijhoff Publishers, Dordrecht, 1986.
[5] M. Nowak, Z. Nowak, R.B. Pęcherski, M. Potoczek and R.E. Śliwa, On the reconstruction method of ceramic foam structures and the methodology of Young modulus determination, *Archives of Metallurgy and Materials*, 58:1219, 2013.
[6] Z. Nowak, M. Nowak, R.B. Pęcherski, M. Potoczek and R.E. Śliwa, Mechanical properties of the ceramic open-cell foams of variable cell sizes, *Archives of Metallurgy And Materials*, 60:1957, 2015.

TEMPERATURE SENSITIVE BRITTLE COATING (TSBC) – AS A PERFECT EXAMPLE ON THE SYMBIOSIS BETWEEN THEORY AND PRACTICE

Andras Szekeres[1], Md Tanweer Raza[1]

[1]*Dept. Applied Mechanics*
Budapest University of Technology and Economics (BUTE)
email: szekeres@mm.bme.hu

According to the title and the purpose of the conference we will display a possible tool to analyse structures, mainly mechanical engineering ones. Being at a university, by the way, one of the oldest and most famous one in Europe, let us mention also the clear scientific aspects of the problem:

- to develop the paint (coating),
- to work out the (mechanical) measurement method,
- to prepare the evaluating software of the problem.

There are three main trends in the up-to-date development of the solid mechanics, namely

- theoretical one,
- practical one,
- the effect of the new tools.

The TSBC in both sense, i.e. as a procedure and as a tool unites the above-mentioned trends, purposes. On the other side, there are multi-lateral interactions among them. The theoretical basis is the coupled fields, or generally the interdisciplinary. The practical ones are the

- new materials and
- fast(er) processes, i.e. impossible to neglect the coupling in both sense
- objects: heat & moisture,
- mode: conduction and convection.

The effects of the new tools are the following:

- numerical (IT, e.g. FEM, CAD, etc.),
- experimental (video, electrical analogy, etc.),
- there are interactions among these:
- experiments -> numeric, e.g. analogy -> calculations,
- FEM -> experiments.

Returning to the scientific basis, i.e. to the fast processes of the thermomechanics (TM), it is clear that a well elaborated theory (fast TM as a part of the thermo-hygro-mechanics [THM]) makes possible the practical application and the latter one needs further theoretical basis. It is a really exceptional example of the symbiosis between theory and practice, in other words research and engineering.

The paper deals with the above-mentioned problems based mainly on the following references:

References

[1] Szekeres, A: Thermo-Hygro-Elasticity (THE), *Encyclopedia of Thermal Stresses*, pp. 5918-924, Springer, 2013
[2] Szekeres, A: Cross-Coupled Heat and Moisture Transport:Part 1 - Theory, *Journal of Thermal Stresses*, 35:248-268, 2012.
[3] Szekeres, A; Fekete, B: Cross-Coupled Heat and Moisture Transport: Part 2/1 – Applications in Mechanics (Electrical Analogy - Analytical Solution - Experiments), *Journal of Thermal Stresses* (Being prepared).
[4] Farkas, I; Szekeres, A: Application of the Modified Law of Heat Conduction and State Equation to Dynamical Problems of Thermoelasticity, *Periodica Polytechnica*, Mech.Eng., 28: Nos. 2-3, 163-170, 1984.
[5] Szalontay, M; Szekeres, A: Experiments on Thermal Shock of Long Bars, *Periodica Polytechnica*, Mech. Eng., 24: No.3,243-251, 1980.
[6,7] Janco, R; Ecsi, L; Elesztos, P: FSW Numerical Simulation of Aluminium Plates by Sysweld - Parts 1-2, *Journal of Mechanical Engineering*, 66: No. 2, 47-52, 2016.
[8] Fekete, B; Szekeres, A: Investigation on Partition of Plastic Work Converted to Heat During Plastic Deformation for Reactor Steels Based on Inverse Experimental- Computational Method, *European Journal of Mechanics - A/Solids*, 53: 175-186, 2015.
[9] Petrov N, Szekeres A (2008) New approach to the non-classical heat conduction. *J Theor Appl Mech*, Sofia 38(3):61-70.
[10] A Szekeres, D Jyoti, K Ahervar, Md T Raza, D Raport, SK Tomar: THM from different aspects. Pres. *14th Joint European Thermodynamics Conference*, Budapest, Hungary, 21-25 May, 2017.

SURFACE EFFECTS IN SHEAR STRESS ENHANCEMENT DUE TO MICRO OR NANOFLOWS AS ANALOGY FOR INCREASED RATE OF REACTION DUE TO CATALYTIC PROPERTIES IN NI_3AL

P. Ziółkowski[1], J. Badur[1], M. Stajnke[1], P. Jóźwik[2] and Z. Bojar[2]

[1]*Energy Conversion Department, Institute of Fluid-Flow Machinery Polish Academy of Sciences, 80-231 Gdańsk, Fiszera 14, Poland*

[2]*Department of Advanced Materials and Technologies, Faculty of Advanced Technologies and Chemistry, Military University of Technology, Kaliskiego 2 Str., 00-908 Warszawa, Poland*

e-mail: pziolkowski@imp.gda.pl

1. Introduction

The presence of walls has naturally influence on the flow of fluid. Within the fluid layer, located in direct vicinity of the solid wall (called the wall layer), significant gradient of velocity, species and temperature are found. Together with the increase of the turbulent kinetic energy or rate of catalytic reaction, related to the Reynolds stresses and large gradients of the mean fluid velocity, the flow becomes more turbulent and the variety of different "jump" phenomena like slipping, rolling, spin-slipping, surface mobility, surface friction, thermo-porosis, etc. can occurs [1,2,3]. However, in some special applications, for example, in microfluidic and nanofluidic devices, where the surface-to-volume ratio is huge, the slip velocity behaviour obtain visible influence, and therefore a sort of "slip" hydrodynamic boundary condition should be used [4,5]. Regardless the slip physical mechanism, the degree of slip is normally quantified through the slip length, the slip velocity, the temperature jump, concentration jump, and other typical for the specific phenomena [1,2].

This work is focused on the theoretical presentation of fluid-solid interaction model with surface friction forces on of those surprising phenomena that is surface effect in shear stress enhancement due to micro or nanoflows. Some kind analogy for increased rate of reaction due to catalytic properties should be considered. As well analytical as numerical analysis can be conducted to find enhancement of mass flow rate and to find others effects important in vicinity of surface. The main assumption of this paper is that this phenomenon is completely governed by a contact interface between a solid surface and gas. Thus, from a viewpoint of mathematical modelling, the friction forces should be understood as some kind of "boundary conditions" problem. Similar consideration should be introduced into surface chemical reaction, because solid body is treated as catalyst, for example: thin foils of alloys based on intermetallic phase Ni_3Al [3].

2. Navier-Stokes boundary condition

One of the methods to model the wall layer is the use of a „wall function", which omits calculations of the viscous sublayer where the influence of the viscosity is the greatest and only half-empirically approximates the phenomena occurring between the wall and the fully turbulent layer. However, in microscale and nanoscale, there should be assumed that classical linear (laminar) models of friction forces should be enhancement by adding adherence part and non-linear (turbulent) part of friction. Therefore, the friction force possesses three known contributions: Duhem, Navier and du Buat [1,5]:

$$\mathbf{f}_r = \nu_D\,(p-\omega)\mathbf{e}_f + \nu(\mathbf{v}-\mathbf{v}_{wall}) + \nu_B(\mathbf{v}-\mathbf{v}_{wall})^2\mathbf{e}_f \tag{1}$$

where: the internal (Euler) and the external (Stokes) pressures p and ω, respectively; the slip versor is defined as: $\mathbf{e}_f = (\mathbf{v}-\mathbf{v}_{wall})/|\mathbf{v}-\mathbf{v}_{wall}|$ and ν_D, ν, ν_B are three friction coefficients [Duhem, Navier, du Buat, respectively] which are dependent simultaneously on the materials of the fluid and solid surface. The skin friction force $\mathbf{f}_r$ appearing between contacting fluid and solid materials is some additive function of powers of

the slip [relative] velocity: $\mathbf{v}_s = \mathbf{v} - \mathbf{v}_{wall}$. Therefore, force of isotropic friction is a composition of three parts: the adherence dry friction, the Navier linear friction ν and the kinetic friction. However, the most important is the Navier friction force $\mathbf{f}_r = \mathbf{f}_N = \nu\mathbf{v}_s$ which is a parallel to the slip velocity $\mathbf{v}_s$. The coefficient ν is called the "external viscosity".

From mechanical point of view, the boundary conditions related to the bulk equation of fluid motion [linear momentum balance], becomes "the surface layer equation of motion". In a solid-fluid surface the separate equation of motion appears. Besides the classical 'bulk' behaviour, wall stress also appears to introduce new quantities such as surface friction force, surface mobility force, surface flux of momentum, etc. [3,4]. In the literature concerning the force boundary condition there are founded by hypothesis of Young asserts that there is no any external friction between a fluid and a solid wall then in a contacting point :

$$\boldsymbol{\tau}_{w|fluid} = \boldsymbol{\tau}_{w|solid} \tag{2}$$

Non-standard wall function is connected with the boundary condition therefore consistencies of boundary condition could be simply recognized if we compare the internal and external coefficients that appear in the model:

$$\boldsymbol{\tau}_{w|fluid} = \mathbf{pn} = (\mu_0\mathbf{I} + \mu\mathbf{d} + \mu_2\mathbf{d}^2)\mathbf{n} = \nu_D\,(p-\omega)\mathbf{e}_f + \nu(\mathbf{v}-\mathbf{v}_{wall}) + \nu_B(\mathbf{v}-\mathbf{v}_{wall})^2\mathbf{e}_f\,. \tag{3}$$

where: $\mathbf{d} = \frac{1}{2}(\text{grad}\,\mathbf{v} + \text{grad}^T\,\mathbf{v})$ - the rate of deformation, the adherence part $\mu_0\mathbf{I}$, the Navier linear or nonlinear dynamic viscosity μ and the turbulent viscosity μ_2. Additionally, it should be mention that $\mathbf{n}$ is the unit normal vector on the boundary surface and **I** means unit tensor (Gibbs' idemfactor). The proper definition of $\boldsymbol{\tau}_{w|solid}$ is to be defined.

3. Summary

The consistency of presented model can even be extended on chemical reaction cases with enhanced properties of the solid surface for example in case on intermetallic phase Ni_3Al. The flow of a fluid mixture is characterized by an effect of concentration jump, which occurs particularly when the reacting mixture is considered, and channel walls have catalytic properties. Therefore the discontinuity of concentration may take place in the direction normal to the boundary, similar to the velocity slip. The model for the concentration boundary condition proposed by Lewis can be implemented in analogy to surface effects in shear stress enhancement due to micro or nanoflows.

Acknowledgments The authors acknowledge the financial support of the National Research and Development Centre in the project PBS 3 ID 246201 entitled: "The development of innovative technology, thin foils of alloys based on intermetallic phase Ni_3Al with high activity thermocatalytic in the field of purification of air from harmful substances or controlled decomposition of hydrocarbons".

References

[1] J.Badur, M. Karcz, M. Lemański and L. Nastałek. Enhancement TransportPhenomena in the Navier-Stokes Shell-like Slip Layer. *CMES*,73:299–310, 2011.

[2] J. Badur et.al. Enhanced energy conversion as a result of fluid-solidinteraction in micro-and nanoscale.*Journal of Theoreticaland AppliedMechanics*,56(1):329-332, 2018.

[3] P. Jóźwik, J. Badur and M. Karcz. Numerical modelling of a microreactor for thermocatalytic decomposition of toxic compounds. *Chemical and Process Engineering*, 32 (3):215-227, 2011.

[4] T.A. Kowalewski, P. Nakielski, F. Pierini, K. Zembrzycki S. Pawłowska.*Micro and nanofluid mechanics*, [in]: Advances in Mechanics: theoretical, computational and interdisciplinary issues, Edt. Kleiber et al., 27-34, 2016.

[5] P. Ziółkowski, J. Badur.A theoretical, numerical and experimental verification of the Reynolds thermal transpiration law.*International Journal of Numerical Methods for Heat and Fluid Flow*, 28(1):64-80, 2018.

NATANSON'S NONLINEAR EXTENDED THERMODYNAMICS

J. Badur[1], P. Ziółkowski[1], D. Sławiński[1]

[1]*Energy Conversion Department, Institute of Fluid-Flow Machinery Polish Academy of Sciences, 80-231 Gdańsk, Fiszera 14, Poland*
e-mail: jb@imp.gda.pl; pziolkowski@imp.gda.pl

1. Introduction

Here we present the previously underrepresented contributions of Ladislavus Natanson to the field of thermodynamics. We focus on the mathematical reconstruction of a few of his principal ideas that until now have been neglected by the literature. To set these ideas in proper epistemological order, we thought it would be valuable to first revalue and reconstruct some missing parts of the proceedings process by Natanson constructed their thermodynamics. We also aimed to present Natanson's achievements against the background of modern continuum mechanics, exemplifying old but still relevant approaches. We propose that Natanson's ideas were ahead of their time by about one century. Give that scientist was educated in the scientific royal way: chemistry, through mechanic of solid and fluid, thermodynamics, electro-chemistry, electrodynamics, early quantum and relativistic mechanics, we can closely compare their conceptions and solutions. Natanson was in strong opposition with Newtonian mechanisms, the Maupertuis least action principle formed the basis of his activities, which they were developing as a sum of elementary quantum actions.

2. Natanson's nonlinear extended thermodynamics

Ladislavus Natanson initial interests were focused on the Maxwell kinetic theory of gases, which was the subject of his doctoral theses [1] prepared at Dorpat under the supervisor of professor Arthur von Oettingen. In 1890, Natanson (now 26-years-old) and living in Warsaw produced his first book, entitled "Introduction to Theoretical Physics" [2]. This book was wholly original and the few last chapters were completely novel, containing an introduction to extended thermodynamics in a fully three-dimensional framework. According to Maxwell, Natanson introduced the use of two kinds of velocity vectors: molar $\mathbf{u}$ and molecular $\mathbf{c}$ [3]:

$$\mathbf{u}+\mathbf{c}=\left(u\,\mathbf{e}_x+v\,\mathbf{e}_y+w\,\mathbf{e}_z\right)+\left(\xi\,\mathbf{e}_x+\eta\,\mathbf{e}_y+\zeta\,\mathbf{e}_z\right) \tag{1}$$

Taking into account the body force $\mathbf{f}$ Natanson, repeating Maxwell's original reasoning [4], was able to extended Maxwell fundamental equation [2]:

$$\frac{d}{dt}\left(\overline{Q}n\right)+\operatorname{div}\left(n\overline{\mathbf{c}\otimes Q}\right)+\operatorname{div}\left(\mathbf{u}\right)\overline{Q}n=\frac{\delta}{\delta t}\left(\overline{Q}n\right)+n\overline{\left(\mathbf{f}\cdot\frac{\delta Q}{\delta\mathbf{u}}\right)} \tag{2}$$

That is now the well-known starting point for the kinetic theory of gases. By repeating extending Maxwell's reasoning, step-wise, Natanson obtained a set of evolution equations for different balanced quantities Q (topological charges). By firstly taking $Q=m$ and the following identities [5] :

$$\overline{\mathbf{c}\otimes Q}=\overline{m\,\mathbf{c}}=0,\quad \overline{Q}n=\rho,\quad \overline{Q}=m,\quad \frac{\overline{\delta Q}}{\delta\mathbf{u}}=0 \tag{3}$$

Next, by setting (3) into (2), a non-conservative form of the fundamental equation was obtained [6,§1,eq.5]:

$$\rho\frac{d}{dt}\overline{Q}+\operatorname{div}\left(\rho\overline{\mathbf{c}\otimes Q}\right)=\rho\frac{\delta}{\delta t}\overline{Q}+\rho\overline{\left(\mathbf{f}\cdot\frac{\delta Q}{\delta\mathbf{u}}\right)} \tag{4}$$

where the d'Alembert-Euler material derivative is defined as: $\frac{d}{dt}\left(\cdot\right)_{X=\text{const}}=\frac{\partial}{\partial t}\left(\cdot\right)_{x=\text{const}}+\operatorname{grad}\left(\cdot\right)\mathbf{u}$

In order to identify a source of irreversibility at Nature, Natanson introduced the concept of Coertia, which is similar to inertia. Natanson's Coertia is a fundamental property of space that is responsible for every irreversible phenomena in matter, as well as in the electromagnetic and gravitational fields. Owing to this concept, the irreversible changes proposed in the Maxwell procedure can be described with appropriate relaxation times as [7]:

$$\frac{\delta}{\delta t}\mathbf{q} = -\frac{\mathbf{q}}{\tau_q} \quad , \quad \frac{\delta}{\delta t}\mathbf{p} = -\frac{\mathbf{p}}{\tau_P} \quad , \quad \frac{\delta}{\delta t}\mathbf{j} = -\frac{\mathbf{j}}{\tau_j} \tag{5}$$

where τ_q, τ_p, τ_j are relaxation times for heat, momentum and mass fluxes.

By looking at the Maxwell procedure of finding moments of the fundamental equation, Natanson quickly realized the necessity for cutting of the moment, hereby setting appropriate closure equations. He proposed the following logical structure: taking Q as a balanced quantity and the $\mathbf{f}_Q$ flux of Q and $\mathbf{F}_Q$ as a super-flux of $\mathbf{f}_Q$, the set of equations were determined [6]:

- Balance equation

$$\frac{\partial}{\partial t}\overline{Q} + \operatorname{div}\mathbf{f}_Q = 0 \tag{6}$$

- Evolution equation $\mathbf{f}_Q$

$$\frac{\partial}{\partial t}\mathbf{f}_Q + \frac{1}{\tau_\mathbf{f}}\mathbf{f}_Q + \operatorname{div}\mathbf{F}_Q = 0 \tag{7}$$

- Algebraic clousure for $\mathbf{F}_Q$

$$\mathbf{F}_Q = a^2 \operatorname{grad}\overline{Q} \tag{8}$$

- Resulting equation for Q

$$\frac{\partial^2}{\partial t^2}\overline{Q} + \frac{1}{\tau_\mathbf{f}}\frac{\partial}{\partial t}\overline{Q} - a^2 \operatorname{div}\left(\operatorname{grad}\overline{Q}\right) = 0 \tag{9}$$

In Natanson's opinion, the above governing equation describes a whole real phenomena of nature, where reversibility is entangled with irreversibility by the relaxation time only. Thus, if $\tau_\mathbf{f} = \infty$ (inertia), it is a case of reversible, while if $\tau_\mathbf{f} = 0$ (coertia) it is an irreversible phenomenon. More information about Natanson's nonlinear extended thermodynamics can be found in works [8-10].

References

[1] L. Natanson. Űber die kinetische Theorie der Joule'schen Erscheinung. Doktorschrift, Dorpat,1888.
[2] L. (Władysław) Natanson. Wstęp do Fizyki Teoretycznej, Wyd. Prac Matematyczno-Fizycznych, Warszawa, 1890
[3] L. Natanson. On the probability of molecular configuration. *Phil. Mag.*, 34, 51-54, 1892.
[4] J. Maxwell. On the dynamical theory of gases. *Phil. Trans. Royal Soc. London.*,57, 49-88, 1866.
[5] L. Natanson. Sur l'interprétation cinétique de la fonction de dissipation.Rozpr. Wydz. Mat.-Przyr. PAU Kraków 1894, 27, 171-180 ; Bull Int. de l'Acad de Cracove 1893,338-357 ; C.R. 1893, 117, 539-542; Phil. Mag. 1895, 39, 455-460.
[6] L. Natanson. Sur le lois de la visconsité, Rozpr. Wydz. Mat.-Przyr. PAU Kraków1901, 41, 223-240; Bull Int. de l'Acad de Cracove1901, 95-111; Zf. F. Phys. Chem. 1901, 38, 640-704; Phil. Mag. 1901, 2, 342-356.
[7] L. Natanson. Inertia and Coercion. The Journal of Physical Chemistry 1903, 7, 118-135.
[8] K. Gumiński. On the Natanson Principle of Irreversible Processes. Acta Physica Polonica 1980 vol. A 58,501-507.
[9] J. Badur. Rozwój pojęcia energii. Gadńsk, Wyd. IMP PAN, 2009.
[10] J. Badur, P. Ziółkowski, D. Sławiński. Duhem i Natanson – dwie mechaniki. Biuletyn Polskiego Towarzystwa Mechaniki Teoretycznej i Stosowanej, Rok 2015, 127-162.

THERMAL STRESSES AND TWO TEMPERATURE HEAT TRANSFER

Włodzimerz Bielski[1], Piotr Kowalczyk[2], and Ryszard Wojnar[3]

[1]*Institute of Geophysics PAS, Warszawa, Poland*
[2]*Institute of Applied Mathematics and Mechanics, University of Warsaw, Warszawa, Poland*
[3]*Institute of Fundamental Technological Research PAS*

e-mail: wbielski@igf.edu.pl

1. Introduction

For description of thermal behaviour of metal films exposed to ultrashort laser pulses a two-temperature heat theory was introduced, cf. [1] - [4]. The theory involves the electron temperature $T_{\rm e}$ and the lattice temperature $T_{\rm a}$. The energy transferred by electrons to lattice per unit volume of the crystal per unit time is proportional to the difference $T_{\rm e} - T_{\rm a}$. Mathematical properties of the theory were discussed in [5] and [6]. The problem has analogies in the diffusion theory (two-level diffusion of enzymes) and in viscous flow through non-homogeneous porous media with components of different porosity, [7].

2. Basic heat equations

Consider an elastic solid body B (a crystal, in particular a metal) irradiated by a laser pulse. Emerging of equilibrium between electrons and lattice in a crystal is realized by a relaxation process. During the relaxation processes crystal must be looked upon as a two-temperature system. The heat energy transferred by electrons to lattice per unit volume of the crystal per unit time is

$$\alpha(T_{\rm e} - T_{\rm a}) \quad \text{with} \quad \alpha \propto \frac{s^2}{\tau_{\rm e}\, T_{\rm e}} \tag{1}$$

where $T_{\rm e} = T_{\rm e}(x,t)$ is the electron temperature and $T_{\rm a} = T_{\rm a}(x,t)$ - the lattice temperature, both being functions of the position $\boldsymbol{x}$ and time t. Moreover, s denotes the velocity of sound, and $\tau_{\rm e}$ is the electron relaxation time, which can be regarded as a function of the electron temperature $T_{\rm e}$. The expressions (1) are valid, when the temperatures $T_{\rm e}$ and $T_{\rm a}$ are much greater than Debye's temperature. Since, in this case $\tau_{\rm e} \propto 1/T_{\rm e}$, the heat transfer coefficient α is independent of the temperature.

Estimates based on the electrical conductivity of metals give values of α of the order 10^{10} J/(cm^3 s K). If the specific heat of the lattice is $c_{\rm a}$, the relaxation time for the phonon temperature is of the order of $c_a/\alpha \approx 10^{-10}$s. For laser pulses of shorter duration, the violation of equilibrium between the electrons and lattice becomes important.

The heat energy balance equations for the metal absorbing the laser pulse has the form

$$\begin{aligned} c_{\rm e}(T_{\rm e})\frac{\partial T_{\rm e}}{\partial t} &= \lambda_{\rm e}\,\Delta T_{\rm e} - \alpha\,(T_{\rm e} - T_{\rm a}) + r(\boldsymbol{x},t) \\ c_{\rm a}(T_{\rm a})\frac{\partial T_{\rm a}}{\partial t} &= \lambda_{\rm a}\,\Delta T_{\rm a} + \alpha\,(T_{\rm e} - T_{\rm a}) \end{aligned} \tag{2}$$

where λ denotes the heat conductivity coefficient, and the function $r(\boldsymbol{x},t)$ describes the energy brought by the laser pulse. The symbol Δ denotes Laplacian.

3. Thermal deformations and stresses

We shall regard as the non-deformed state the state of the body before applying the heat source and consider deformations which accompany changes in the temperature of the body $T_{\rm a} - T_0$. The stress tensor is, cf. [8].

$$\sigma_{ij} = 2\mu\, u_{ij} + \left(K - \frac{2}{3}\mu\right) u_{ll}\, \delta_{ij} - \gamma(T_{\rm a} - T_0)\delta_{ij} \quad \text{with} \quad u_{ij} = \frac{1}{2}(u_{i,j} + u_{j,i}) \tag{3}$$

and $(u_i) = \boldsymbol{u}$ is the displacement in the elastic body. Moreover, K is the bulk modulus (modulus of hydrostatic compression) and μ is the shear modulus (modulus of rigidity). The coefficient $\gamma = 3K\alpha_{\rm T}$, and $\alpha_{\rm T}$ is the thermal expansion coefficient of the body. The equation of motion reads

$$\rho\frac{\partial^2 \boldsymbol{u}}{\partial t^2} = 2\mu\,\Delta\boldsymbol{u} + \left(K + \frac{1}{3}\mu\right)\nabla(\nabla\cdot\boldsymbol{u}) - \gamma\nabla T_{\rm a} \tag{4}$$

and ∇ stands for the gradient operator.

In this study we solve a Danilovskaya problem for the new heat procedure, when the thermoelastic phenomenon is induced by a radiation pulse by two step action, $T_{\rm e} \rightarrow T_{\rm a} \rightarrow$ the stress, cf. [9, 10].

4. Applications

Description of laser - matter interaction may be useful in industrial applications, such as cutting, welding, material heat treatment.
In spectral analysis, arisen by the photothermal mechanism, the photoacoustic signal is useful in measuring the light absorption spectrum, particularly for transparent samples where the light absorption is very small.

Acknowledgments This work was partially supported within statutory activities No 3841/E-41/S/2017 of the Ministry of Science and Higher Education of Poland.

References

[1] S. I. Anisimov, B. L. Kapeliovich, T. L. Perelman, Electron emission from metal surfaces exposed to ultrashort laser pulses, *Sov. Phys. JETP* **39** 375–377 (1974).
[2] D. K. Ilnitsky, V. A. Khokhlov, N. A. Inogamov, V. V. Zhakhovsky, Yu. V. Petrov, K. V. Khishchenko, K. P. Migdal and S. I. Anisimov, Two-temperature hydrodynamics of laser-generated ultrashort shock waves in elasto-plastic solids *Journal of Physics: Conference Series* **500** 032021 (2014).
[3] Yu. V. Petrov, K. P. Migdal, N. A. Inogamov, V. V. Zhakhovsky, Two-temperature equation of state for aluminium and gold with electrons excited by an ultrashort laser pulse, *Applied Physics* B **119** (3) 401–411 (2015).
[4] K. P. Migdal, N. A. Inogamov, Yu. V. Petrov, V. V. Zhakhovsky, Two-temperature equations of state for d-band metals irradiated by femtosecond laser pulses, arXiv:1702.00825v3 [cond-mat.mtrl-sci] 11 Jul 2017.
[5] J. Ignaczak, The second law of thermodynamics for a two-temperature model of heat transport in metal films, *Journal of Thermal Stresses* **28** (9) 929–942 (2005).
[6] W. Bielski, P. Kowalczyk, R. Wojnar, Two-temperature heat transfer in metal films, in: *Conference Proceedings of the Numerical Heat Transfer* 2015 - Eurotherm Seminar No. 109, edited by Andrzej J. Nowak, Jerzy Banaszek, Božidar Šarler, Institute of Thermal Technology Silesian University of Technology, Institute of Heat Engineering Warsaw University of Technology, Gliwice - Warszawa 2015.
[7] W. R. Bielski, R. Wojnar, Nonstationary flow through porous piezoelectric body with two scale structure, in: *Solmech - Polish Conference of Solid Mechanics*, Kraków, 4-8 September 2006.
[8] L. D. Landau and E. M. Lifshitz, *Theory of elasticity*, Volume 7 of Course of Theoretical Physics, transl. from the Russian by J. B. Sykes and W. H. Reid, 3rd edition, Pergamon Press, Oxford - New York - Toronto - Sydney - Paris - Braunschweig 1970.
[9] V. I. Danilovskaya, Thermal stresses in an elastic semi-space due to a sudden heating of its boundary, *Prik. Mat. Mekh.* **14** (3) 316–318 (1950).
[10] A. Gałka, R. Wojnar, One-dimensional dynamic thermal stresses generated in an elastic half-space by laser pulses, *Journal of Thermal Stresses* **18** (2) 113–140 (1995).

Coupled-field theory for grade 2 piezoelectric media: application to quantum dots

H.M. Shodja, S.S. Marashi, and E. Rashidinejad

Department of civil engineering, Sharif university of technology, Tehran, Iran

e-mail: shodja.hossein@gmail.com

1. General

Quantum dots (QDs) are often grown with a periodic distribution within a piezoelectric matrix (barrier). An example of such quantum structures (QSs) is shown in Figure 1. The initial misfit strains within the embedded quantum dots stemming from the lattice mismatch between the QDs and the surrounding matrix result in the electro-elastic fields within both the QDs and the barrier. The lattice mismatch provides the needed driving force for the generation of the self-organized QDs during Stranski-Krastanov growth mode via molecular beam epitaxy (MBE). This intrinsic strain field, which affects the interatomic distances and consequently alters the energy level and the bonding electrons, influences the electronic and optical properties of semiconductor crystalline QDs [2]. Therefore, an accurate determination of the strain field associated with QSs is beneficial for predicting the creation and evolution of semiconductor QSs as well as the design of optoelectronic and microelectronic devices. It is well-known that, if the principal feature of interest is to model the nanoscopic variation of field variables within solids, the size independent classical theory cease to hold. For enhancing the solution, the employed theory must be capable of capturing not only the size effect, but also resolve the strain gradient across the interfaces with sufficient accuracy. To this end, a mathematical framework for the calculation of the electromechanical fields associated to electro-elastic inclusions with an arbitrary distribution of eigenfields - eigenstrain field, $\boldsymbol{\epsilon}^*(\boldsymbol{x})$, eigenstrain gradient field, $\boldsymbol{\eta}^*(\boldsymbol{x})$, eigenelectric field, $\mathbf{E}^*(\boldsymbol{x})$, and eigenelectric gradient field, $\boldsymbol{\zeta}^*(\boldsymbol{x})$- in grade 2 piezoelectric media is developed.

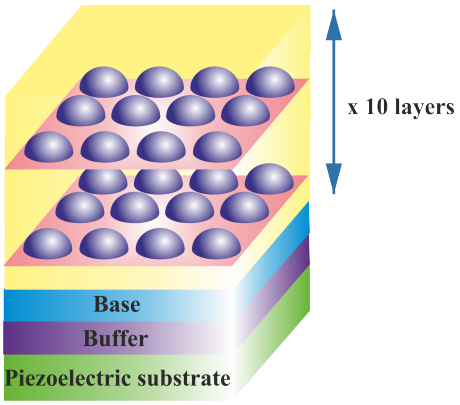

Figure 1: A sample of periodic distribution of semi spherical inclusions within a piezoelectric barrier in solar cells.

2. Formulation

In the absence of body forces and electric charge density, the equilibrium equations and charge equation of electrostatics are given as [1], [3]

(1a) $$(t_{ij} - \mu_{ijk,k})_{,j} = 0,$$

(1b) $$D_{i,i} = 0.$$

Respectively, where **t** is Cauchy stress tensor, **μ** is the double stress tensor, and **D** is the grade 2 electric displacement tensor. The presence of a given distribution of eigenfields is conveyed to the above equations through the field quantities **t**, **μ**, and **D**.

3. Numerical results

For illustration, consider a periodic distribution of spherical inclusions within a piezoelectric barrier. Assume that the direction of polarization coincides with the x_3 axis. Let the spheres have radius, R= 3 nm and period of distribution 12 nm in x_1-, x_2-, and x_3- directions. For convenience, suppose that the elastic behavior of the medium is isotropic, while it is transversely isotropic with respect to its piezoelectric properties. Moreover, let $\epsilon^*_{ij}(\boldsymbol{x}) = \delta_{ij}$ inside each sphere and $\epsilon^*_{ij}(\boldsymbol{x}) = 0$ outside the sphere. Under the above mentioned assumptions, the strain component $\epsilon_{33}(0, 0, x_3)$ has been calculated and plotted as a function of x_3 in Fig. 2. In this figure, l_1 is a characteristic length of the piezoelectric medium. The case of $l_1 = 0$ corresponds to classical piezoelectric material. Figure 2 shows that the gradient effects in grade 2 piezoelectricity are more notable near the boundaries and the jump of $\epsilon_{33}(0, 0, x_3)$ is decreases by increasing the gradient effects (l_1).

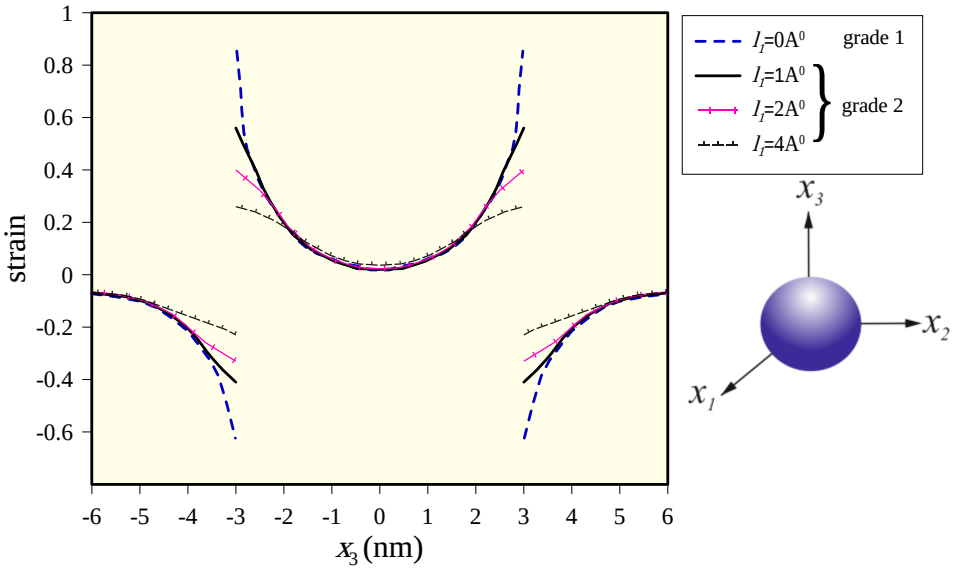

Figure 2: Variation of $\epsilon_{33}(0, 0, x_3)$ versus x_3 associated with the spherical QDs.

References

[1] R.D. Mindlin. Micro-structure in linear elasticity. *Archive for Rational Mechanics and Analysis*, 16(1):51–78, 1964.

[2] H. M. Shodja and E. Rashidinejad. Interacting functionally graded quantum wires/quantum dots with arbitrary shapes and general anisotropy within a distinct piezoelectric matrix. *Journal of the Mechanical Behavior of Materials*, 23(1-2):1–14, 2014.

[3] Y.M. Yue, K.Y. Xu, and E.C. Aifantis. Microscale size effects on the electromechanical coupling in piezoelectric material for anti-plane problem. *Smart Materials and Structures*, 23(12):125043, 2014.

THE EFFECT OF STRENGTH DIFFERENTIAL ON MATERIAL EFFORT OF STEAM TURBINE ROTORS UNDER THERMO-MECHANICAL LOAD

M. Banaszkiewicz[1], W. Dudda[2], and J. Badur[1]

[1]*The Szewalski Institute of Fluid-Flow Machinery Polish Academy of Sciences, Gdańsk, Poland*
[2]*University of Warmia and Mazury, Olsztyn, Poland*

e-mail: mbanaszkiewicz@imp.gda.pl

1. Introduction

A bulk of mechanical integrity analyses of machinery components employ the classical Huber-Mises-Hencky plasticity theory to define the equivalent stress and describe the plastic response of materials [1]. This theory assumes that the mean stress has no effect on plastic flow and the material is incompressible in the plastic regime. The classical definition of equivalent stress based on the second invariant of the deviatoric stress tensor J_2 neglects the strength differential effect, i.e. the difference of yield stresses in tension and compression, which was experimentally found in many materials [2]. For materials exhibiting this effect, a better match of theoretical predictions with experimental stress-strain curves was found when Burzyński yield condition was applied. According to the Burzyński hypothesis, the measure of material effort defining the limit of elastic range is a sum of the density of distortion elastic energy and a part of density of dilation elastic energy [3]. The first contribution is related with the Huber-Mises-Hencky (HMH) equivalent stress, while the second part is mean stress dependent. The resulting definition of equivalent stress σ_B explicitly includes the yield stress in compression σ_y^C and tension σ_y^T by their ratio $k = \sigma_y^C/\sigma_y^T$ and reads [4]

$$\sigma_B = \frac{1}{2k}\left[3(k-1)\sigma_m + \sqrt{9(k-1)^2\sigma_m^2 + 4k\sigma_e^2}\right], \tag{1}$$

where σ_m is the mean stress and σ_e is the Huber-Mises-Hencky equivalent stress.

2. Experimental investigations of 2CrMoV steel

High-temperature rotors operating at temperature below 540°C are usually made of 2CrMoV creep-resistant steel of martensitic microstructure. Round specimens made from this steel were used in uniaxial tensile and compression tests conducted at room temperature. Tensile tests were performed on 6 specimens having gauge length L_0 = 35 mm and diameter d_0 = 7 mm. For compression tests also 6 specimens of gauge height h_0 = 18 mm and diameter d_0 = 12 mm were prepared. Average stress-strain curves at tension and compression obtained from the tests are presented in Fig. 1 which clearly shows significant differences between the two curves in plastic conditions. The measured yield stress at tension was σ_y^T = 727 MPa, while at compression reached σ_y^C = 798 MPa, which results in their ratio k = 1.1.

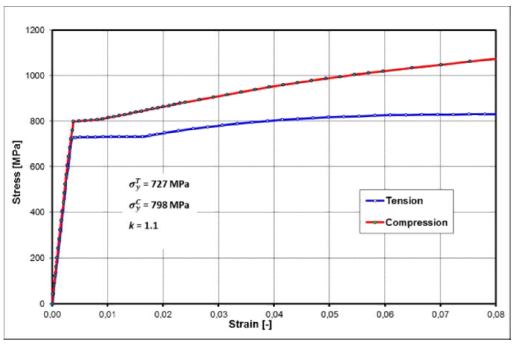

Fig. 1. Stress-strain curves of 2CrMoV steel at tension and compression.

3. Numerical analysis of steam turbine rotor

The material effort of a steam turbine rotor subject to thermo-mechanical loading was investigated by performing transient finite element analysis. Linear elastic material model was adopted together with temperature-dependent material properties and nonlinear thermal boundary conditions. Variations in time of the mean stress and the equivalent stresses evaluated at the circumferential U-groove using both hypotheses are shown in Fig. 2. The Burzyński stress was calculated assuming constant yield stress ratio k = 1.1. For most of the time, the Huber-Mises-Hencky stress is visibly higher than that obtained with Burzyński hypothesis and their ratio attains 1.16. In this phase, the mean stress is negative and lower than $1/3\sigma_e$, but when it exceeds this limit, the Burzyński stress becomes slightly higher and the stress ratio does not drop below 0.97. The operation phase when the mean stresses are negative corresponds to the rotor heating-up, while the positive mean stresses are present in steady-state and during cooling down phase. Thus, high compressive stress states reduce the material effort and due to the strength differential effect allow for higher HMH stresses during heating-up without adversly affecting the rotor material effort and damage. This is of high practical importance as the rotor heating-up takes place during turbine start-up and more accurate determination of the equivalent stress can allow for better utilization of material strength and result in a reduction of start-up time.

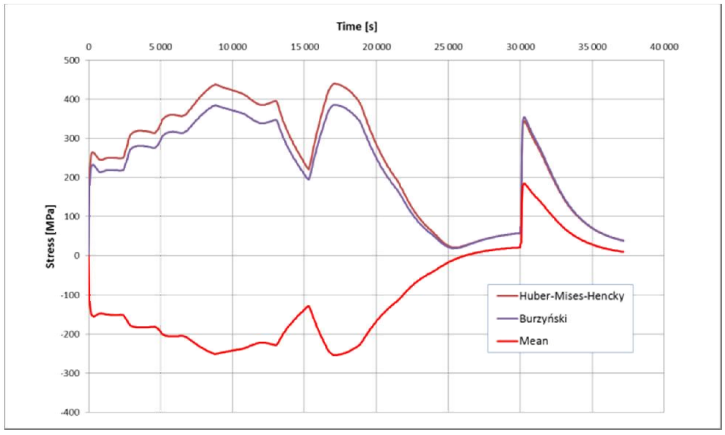

Fig. 2. Variations of equivalent stress evaluated using Huber-Mises-Hencky and Burzyński hypotheses.

5. Summary

The existence of strength differential effect in 2CrMoV rotor steel was prooved experimentaly and its positive effect on the material effort was shown by numerical simulations of the rotor during transient operating conditions. The measured magnitude of strength differential k = 1.1 results in the equivalent stress ratio reaching a maximum of 1.16 at the circumferential U-groove during the compressive phase of the cycle. Thus, the use of Burzyński hypothesis allows for better utilization of material strength provided that the strength differential effect is experimentally confirmed.

References

[1] G. Vadillo, J. Fernandez-Saez, R.B. Pęcherski. Some applications of Burzynski yield condition in metal plasticity. Materials and Design, 32:628-635, 2011.
[2] T. Frąś, Z. Kowalewski, R.B. Pęcherski, A. Rusinek. Applications of Burzynski failure criteria – I. Isotropic materials with asymmetry of elastic range. Engineering Transactions, 58:1-10, 2010.
[3] W. Burzyński. Theoretical foundations of the hypotheses of material effort. Czasopismo Techniczne, 47:1-41, 1929.
[4] K. Banaś, J. Badur. Influence of strength differential effect on material effort of a turbine guide vane based on a thermoelastoplastic analysis. Journal of Thermal Stresses, 40:1368-1385, 2017.

LOVE WAVES PROPAGATION IN ELASTIC WAVEGUIDES LOADED BY VISCOELASTIC MEDIA

Piotr Kielczynski, Marek Szalewski, Andrzej Balcerzak and Krzysztof Wieja

Institute of Fundamental Technological Research,
Polish Academy of Sciences, Pawińskiego 5B, 02-106 Warsaw, Poland
pkielczy@ippt.gov.pl

1. Introduction

It is very important from a practical point of view, to develop new and accurate methods of measuring the rheological parameters (viscosity η, elasticity μ and density ρ) of plastics and polymers. New materials require new methods of measuring their rheological parameters. To evaluate the rheological parameters of plastics so far mechanical methods are used. These methods are cumbersome, outdated and destructive. The use of SH (Shear Horizontal) surface Love waves, to evaluate rheological parameters of polymers, does not possess these disadvantages. The objective of this work is to establish a mathematical model of propagation of Love waves in layered elastic waveguides covered on their surface with viscoelastic materials described by different viscoelastic models, i.e., Kelvin-Voigt, Newton and Maxwell models. To this end, we developed a complex dispersion equation for Love waves propagating in loaded waveguides and performed numerical calculations.

2. Physical model

Dispersion curves of the Love wave, i.e., the dependence of the phase velocity and attenuation on frequency, result from solution of the boundary value problem (called the direct Sturm-Liouville problem). Love waves propagate in layered structures, e.g., in elastic waveguides composed of an elastic surface layer rigidly bonded to an elastic substrate. The top of the surface layer $x_2 = -D$ is loaded with a viscoelastic medium, see Fig.1. Love waves, propagating in isotropic waveguides, have only one SH (Shear Horizontal) component of vibrations u_3, polarized along the axis x_3 that is perpendicular to the direction of propagation x_1.

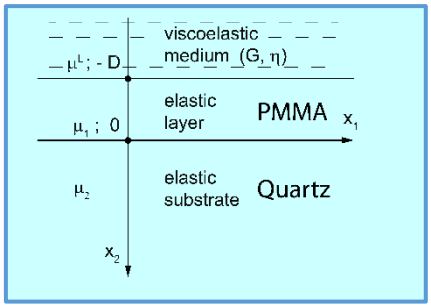

Fig.1. Lossless (elastic) Love wave waveguide (surface layer plus substrate) loaded at the surface $x_2 = -D$ with a lossy viscoelastic medium of the shear modulus G and viscosity η.

3. Rheological models of viscoelastic media

We chose 3 models for the viscoelastic media, i.e., Newton, Kelvin-Voigt, and Maxwell models, that load the surface of the Love wave waveguide. For time-harmonic waves, using constitutive equations for the 3 visco-elastic media considered, we obtain the following 3 formulas for the complex shear moduli c_{44}^L of elasticity:

a) Newton model: (1) $c_{44}^L = -j\omega\eta$; where: η is the viscosity of the viscoelastic medium,

b) Kelvin-Voigt model: (2) $c_{44}^L = G - j\omega\eta = G(1 - jtan\delta)$; where: G is the elastic shear modulus, and η is the viscosity of a viscoelastic medium, $tan\delta = \omega\eta/G$, and

c) Maxwell model: (3) $c_{44}^L = G\frac{(\omega\tau)^2}{1+(\omega\tau)^2} - jG\frac{\omega\tau}{1+(\omega\tau)^2}$; where: $\tau = \eta/G$ is the relaxation time.

4. Complex Dispersion Equation for Love Waves

The complex dispersion equation for Love waves that propagate in the waveguide structure from Fig.1 is:

$$\sin(qD)\cdot\{(\mu_1)^2\cdot q^2-\mu_2\cdot b\cdot\lambda_1\cdot c_{44}^L\}-\cos(qD)\cdot\mu_1\cdot q\cdot\{\mu_2\cdot b+\lambda_1\cdot c_{44}^L\}=0 \tag{4}$$

where: complex pairs of quantities (μ_2, b), $(\mu_1, q), and\ (\lambda_1, c_{44}^L)$ correspond to the substrate, surface layer and the loading material, respectively, and $j=(-1)^{1/2}$. The above equation is a nonlinear transcendental algebraic equation for the complex propagation constant $k=k_0+j\alpha$ as unknown. Solving equation 4 (the solution is a pair $(k_0,\ \alpha)$) allows for determination of the phase velocity of the Love wave $v=\omega/k_0$ and the imaginary part α of the complex wavenumber k that represents the attenuation in Np/m of the Love wave per unit length.

5. Dispersion Curves of Love Waves

Numerical calculations were performed for the waveguide structure shown in Fig.1. The substrate is Quartz (ST-cut 90º X) and the surface layer is PMMA poly(methyl methacrylate). The frequency of the Love wave varied from 1 to 1000 MHz. Thickness D of the surface layer equaled 0.1 mm. Losses in the PMMA layer and Quartz substrate were neglected. The only source of losses is the viscosity of the viscoelastic medium.

Attenuation Curves

In Figure 2 the attenuation of Love waves, in the range of frequencies; from 0 to 1000 MHz is presented.

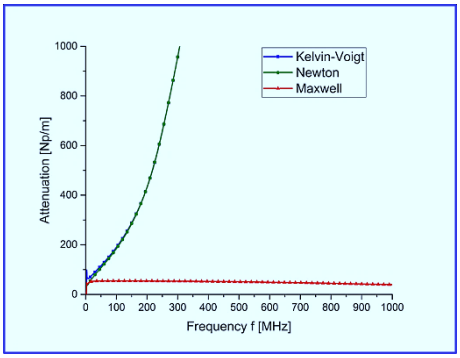

Fig.2. Attenuation of the Love surface wave, propagating in a lossless elastic waveguide, loaded with 3 different types of lossy viscoelastic materials, i.e., Kelvin-Voigt, Newton and Maxwell. Low, medium and high frequency limits: $tan\delta\in[0.127-127]$, $G=5\cdot10^4 Pa,\ \eta=1\ mPas$.

6. Conclusions

The theoretical analysis and the results of numerical calculations presented in this paper reveal that the attenuation of the Love wave reflects directly the viscoelastic properties of the loading material described by Kelvin-Voigt, Newton and Maxwell models. Namely:

a) in the low frequency limit $tan\delta \ll 1$ the attenuation of the Love wave due to the Maxwellian liquid and that due to the Newtonian liquid are almost the same (see Fig.2)

b) in the high frequency limit $tan\delta \gg 1$ the attenuation of the Love wave due to the Kelvin-Voigt material and that due to the Newtonian liquid are almost identical (see Fig.2).

The results of this study should be useful for designers and scientists working in geophysics, microelectronics (MEMS, biosensors, chemosensors), mechanics of materials and biomechanics.

Acknowledgment: The project was funded by the National Science Centre (Poland), granted on the basis of Decision No. 2016/21/B/ST8/02437.

STRATEGY FOR CREATING BIO-COMPOSITES WITH UNIQUE MECHANICAL PROPERTIES

K. Nalepka[1], K. Berent[2], M. Bieda[3], M. Strąg[3] P. Nalepka[1], and K. Sztwiertnia[3]

[1] *Faculty of Mechanical Engineering and Robotics, AGH University of Science and Technology, Kraków, Poland*
[2] *Academic Centre for Materials and Nanotechnology, AGH University of Science and Technology, Kraków, Poland*
[3] *Institute of Metallurgy and Materials Science Polish Academy of Sciences, Kraków, Poland*

e-mail: knalepka@agh.edu.pl

1. Introduction

The dynamic development of technology and civilization requires constant search for new materials with appropriate functional and mechanical properties. Meanwhile, the key problem of material engineering remains the solution to the conflict between high strength and fracture toughness [1]. A need to improve the first property lowers the latter. It is worth looking at how Nature solved this issue. One of the more interesting example are shells of molluscs. On the path of evolution lasting millions of years, these animals have produced material not only of significant strength and fracture toughness, but also light and functional. This result all the more deserves attention because the components used for construction, calcium carbonate (calcite and aragonite) and proteins, are weak. The source of unique mechanical properties lies in a hierarchically complex structure. The most of molluscs, about 90% species, prefer crossed lamellar structure. Usually, it is constructed on three levels. The first order structural unit is a lamella with dimensions of a few millimetres. Inside it, there are parallel stacked laths (2-nd order lamellae). These, in turn, consist of parallel fibres with a thickness of less than 1 micron (3–rd order lamellae). It turns out that the successive first order lamella, adjacent to the consider one, is built analogically, but the fibres are rotated by 90 degrees. In this way, the 0°/90°/0° cross system is obtained. The above described structure is embedded in organic matrix. Thus, the shell is not built in a chaotic manner, but carefully thought out, in accordance with the design of Nature. The question arises what mechanisms to improve mechanical properties are included at the lower scale levels: micro and nanometric one. Despite many works on this subject, a complete answer is still missing [2]. The solution to the formulated problem is important because it can be a biomimetic basis for creation of new materials exhibiting unique mechanical and functional properties. The purpose of the present work is to identify and analyse the mutual orientation (disorientation) of crystallites in calcite layers of shells of two molluscan species *Pinctada margaritifera* and *Pinna nobilis*. The obtained results shed new light on the mechanical response of the shell subjected to an external load.

2. Experiment and analysis

The investigation of shell microstructures is performed by means of electron backscatter diffraction (EBSD) method. It turns out that the considered species of molluscs prefer a strictly defined set of disorientations. They are defined by means of an axis around which the rotation by a certain angle generates the crystallite adjacent to the considered one. Among disorientations with high frequencies (Fig. 1 and Fig. 2), there are twins typical for the synthetic calcite (T_1, T_2, T_3) [3], as well as two others of which one (T'_3) is new and has not been shown in the literature so far.

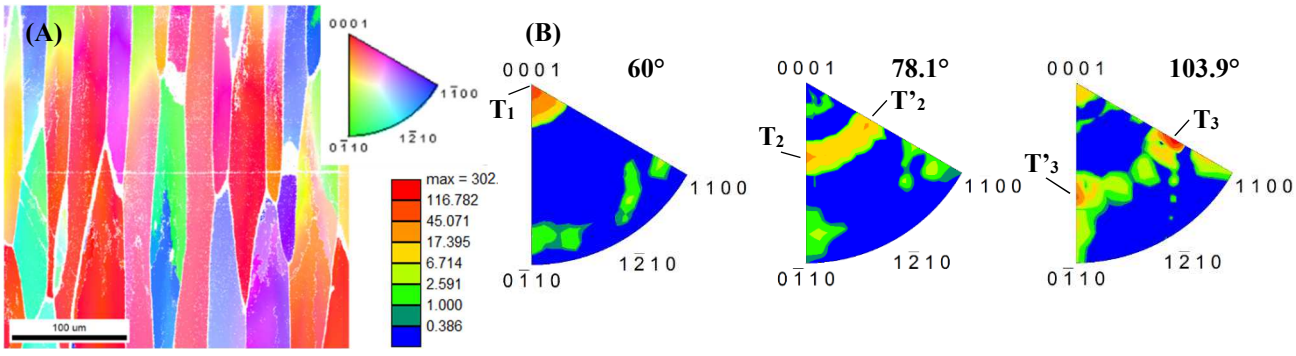

Figure 1 Inverse pole figure (*IPF*) map (A) and axis/angle misorientation distribution function (B) of the *Pinctada margaritifera.*

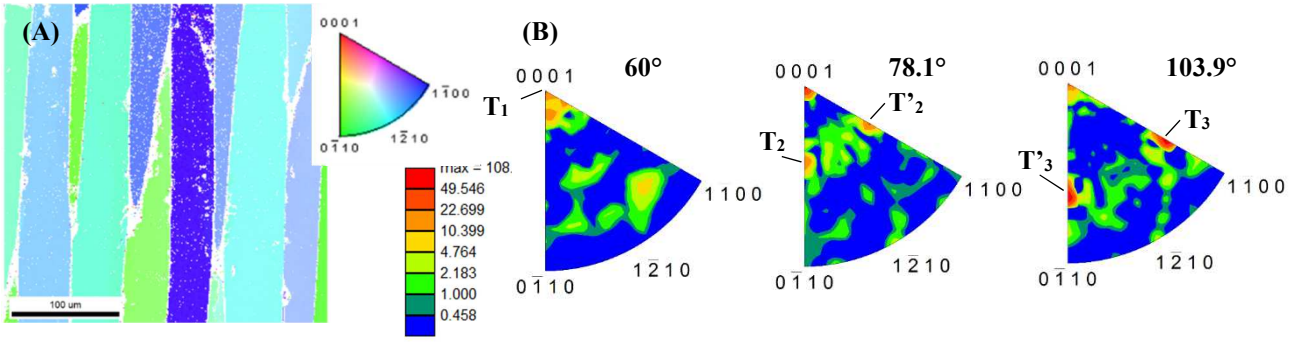

Figure 2 Inverse pole figure (*IPF*) map (A) and axis/angle misorientation distribution function (B) of the *Pinna nobilis.*

To explain the observed regularities, we have examined how the energy of the phase boundary calcite/ calcite changes when one of the crystallites is rotating. The exact determination of this quantity for a large, representative number of disorientations is very difficult and computationally expensive, due to the complex interatomic interactions at the boundary [4]. Therefore, the approximate approach proposed by Gautam and How [5] is used. According to their method, the interfacial energy decreases with the increasing total intensity *I* contained in the overlapping regions diffraction reflections from two phases [6]. Calculations carried out for the calcite / calcite phase boundary show a very interesting distribution of the total overlap intensity *I* (Fig. 3) There are clearly visible energetically favourable disorientations, i.e. those for which the interface energy achieves local minima. It turns out that the distinguished mutual orientations of crystallites are pairs of twins generated by means of two-fold axes related to each other by a mirror plane (1 0 -1 0). As a result, we get two disorientation groups. One of them are twins characteristic of the synthetic calcite, and the latter one are their counterparts with higher interface energy. The identified disorientations are strongly preferred by the studied molluscan species.

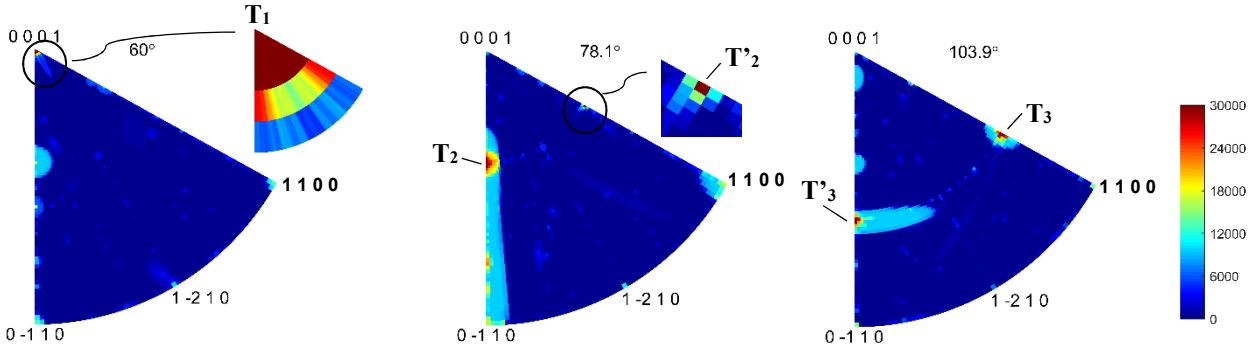

Figure 3 Total overlap intensity as a measure of the interfacial energy

3. Conclusions

The bio-composite structure of molluscan shells is highly ordered not only at the macro level, but also micro and nanometric. It has been shown that crystallites of calcite layers are not randomly oriented but in such a way that form low energy boundaries. As a result, there arise twins typical of calcite and their counterparts with slightly higher energies. The formation of this second group of twins is a deliberate effort of Nature. The external load applied to the shell causes crystallite rotation. As a result, the boundaries with higher energies transform into those with lower energies. This process enables dissipation of energy and thus becomes one of the mechanisms that Nature has invented to increase fracture toughness.

Acknowledgments This work was supported within the framework of the statutory research No. 11.11.130.375

References

[1] R. O. Ritchie. *Nat. Mater.* 10, 817, 2011.
[2] X. W. Li et al., *J. Mech. Behav. Biomed. Mater.* 74, 54, 2017.
[3] B. Pokroy et al., PNAS, 104, 7337, 2007.
[4] K. Nalepka, *Eur. Phys. J. B.,* 85, 45, 2012.
[5] A.R.S. Gautam J.M. Howe, *Phil. Mag.* 91, 3203, 2011.
[6] K. Nalepka, K. Sztwiertnia, P. Nalepka, *Acta Mater.* 104, 156, 2016.

ROLE OF NONLINEARITY OF THE PHONON DISPERSION RELATION IN THE WAVE-TYPE PHONON HEAT TRANSPORT

W. Larecki

Institute of Fundamental Technological Research of the Polish Academy of Sciences,
Pawińskiego 5B,02-106 Warsaw, Poland
e-mail: wlarecki@ippt.pan.pl

Abstract.

The heat transport in non-metallic micro- and nanostructures is predominantly due to phonon processes, and therefore it can be analysed in terms of a flow of a phonon gas. Phonons are quantized lattice vibrations characterized by wave-vectors $\boldsymbol{k}$ from the first Brillouin zone and by the $\boldsymbol{k}$ dependent frequency ω. For simplicity, a single-branch phonon model is adopted, and consequently phonon polarizations are neglected. The dispersion relation $\omega(\boldsymbol{k})$ together with the relaxation times associated with normal and resistive phonon scattering processes determine the behaviour of a phonon gas.

According to [1, 2, 3], the commonly used linear isotropic approximation of the phonon dispersion relation $\omega(\boldsymbol{k}) = c\,|\boldsymbol{k}|$ employed in the phonon gas hydrodynamics leads to the constant speeds of thermal waves propagating into the region in thermal equilibrium. This contradicts the experimental results on the second sound propagation in solids. The dependence of the second sound wave speed on the sample temperature has been analysed in [4].

The nonlinearity of the phonon dispersion relation significantly influences the thermal properties of micro- and nanostructures. Several forms of the nonlinear phonon dispersion relation $\omega(\boldsymbol{k})$ have been suggested for various structures and substrates in the literature, motivated either by empirical data or by the first-principle calculations. In micro- and nanostructures, the wave-type heat transport has been observed at low and elevated temperatures with temperature dependent propagation speeds. Hence, the phonon gas hydrodynamics employing the linear isotropic approximation of phonon dispersion relation seems to be inadequate in such cases.

The four-moment phonon gas hydrodynamics involving a nonlinear isotropic phonon dispersion relation $\omega(\boldsymbol{k}) = \omega(|\boldsymbol{k}|)$ and the maximum entropy phonon distribution function has been proposed in [1], and further developed in [5]. The governing conservation equations for energy and the quasi-momentum (understood as a vector internal state variable) are determined by the entropy function and by the additional scalar potential. Both, the entropy function and the additional potential are given by integral formulae involving the nonlinear isotropic phonon dispersion relation. Approximation of the finite domain of phonon wave-vectors by whole space R^3 eliminates the additional potential and simplifies the form of conservation equations. For this approximation, the propagation of the waves of weak discontinuity into the region in thermal equilibrium has been analysed in [6], and the dependence of the wave speeds on the temperature in a region ahead the wave front has been determined.

In order to compare predictions of the theory derived in [5, 6] with the second sound experimental data [4], the nonlinear isotropic phonon dispersion relation $|\boldsymbol{k}| = \omega\, c^{-1}\, (1+b\,\omega^2)$ proposed in [7] is adopted. For the values of the parameters c and b for NaF and Bi given in [7, 8, 9, 10], the dependence of the speed of weak discontinuity wave on the temperature ahead the wave front has been calculated and compared with the experimentally measured second sound velocity as a function of the sample temperature [4], and with the calculations based on the alternative second sound theory given in [11, 12]. Our results are in good agreement with the experimental data as well as with the predictions of [11, 12], and show that the nonlinearity of the phonon dispersion relation plays the crucial role in the effect of temperature dependence of thermal wave speeds.

In the same way, other nonlinear isotropic phonon dispersion relations proposed in the literature for specific

nanostructures can be used in the phonon gas hydrodynamics given in [5, 6]. Moreover, this hydrodynamics can be easily reformulated for two-dimensional non-metallic materials.

References

[1] W. Larecki.Symmetric conservative form of low-temperature phonon gas hydrodynamics. II. Equationsof heat transport and thermal waves in the case of linear isotropic approximation of phonon frequency spectrum. *Nuovo Cimento, D,*14:141, 1992

[2] Z.Banach and W. Larecki, Nine-moment phonon hydrodynamics based on the maximum entropy closure: one dimensional flow. *J.Phys. A:Math. Gen.,*38: 8781, 2005

[3] Z.Banach and W. Larecki, Nine-moment phonon hydrodynamics based on the modified Grad-type approach: hyperbolicity of the one-dimensional flow. *J.Phys. A:Math. Gen.,*37: 11053, 2004

[4] B. D. Coleman and D. C. Newman, Implications of nonlinearity in the theory of second sound in solids. *Phys. Rev.B,* 37:1492, 1988

[5] W. Larecki and Z. Banach, Consistency of the phenomenological theories of wave-type heat transport with the hydrodynamics of a phonon gas. *J.Phys. A:Math. Theor.,*43: 385501, 2010

[6] W. Larecki and Z. Banach,Influence of nonlinearity of the phonon dispersion relation on wavevelocities in the four-moment maximum entropy phonon hydrodynamics. *Physica D –Nonlinear Phenomena,* 49:65, 2016

[7] K. S. Dubey, Lattice thermal conductivity of NaF in the temperature range (2-100)K. *Phys. Rev.B,*7: 2876, 1976

[8] J. T. Lewis, A. Lehoczky and C. V.Briscoe, Elastic constants of the alkali halides at 4.2K. *Phys. Rev.*161: 877, 1967

[9] S. Epstein and A. P. deBreteville Jr.. Elastic constants and wave propagation in antimony and bismuth. *Phys. Rev.*138: A771, 1965

[10] A. M. Karo and R. J. Hardy, Lattice dynamics of NaF. *Phys. Rev.*181: 1272, 1969

[11] R. J. Hardy, Phonon Boltzmann equation and second sound in solids. *Phys. Rev.B,*2: 1193, 1970

[12] R. J. Hardy and S. S. Jaswal, Velocity of second sound in NaF. *Phys. Rev.B,*3:4385, 1971

STACKING FAULTS IN HEXAGONAL TI ALLOYS – LOCAL INSTABILITY OF CRYSTAL LATTICE AND ITS EFFECT ON SOLUTION STRENGTHENING

P. Kwasniak[1], J. Mizera[1], R.B. Pęcherski[2]

[1] *Materials Design Division, Faculty of Materials Science and Engineering, Warsaw University of Technology, Woloska 141, 02-507, Warsaw, Poland*

[2] *Institute of Fundamental Technological Research, Polish Academy of Sciences, Pawinskiego 5B, 02-106 Warsaw, Poland*

e-mail:piotr.kwasniak@inmat.pw.edu.pl

1. Introduction

Stacking faults are the special regions of the crystal structure that exhibit non-uniform structure and diversified stability. Energy of this defects determines configurations of dislocation cores and type of predominant plastic deformation mechanism. In this study we focus on the generalised stacking fault energy computations of multi-slip-system hexagonal Ti alloys in the context of solution strengthening effect and the atomic as well as electronic structure identification of the analysed planar defects.The far reaching goal is to provide the physical basis and theoretical infrastructure to answer the still unresolved question concerning the initiation of a micro-shear band in metallic solids.

2. General

The solid solution strengthening of α-Ti was investigated in respect of dislocation nucleation and dissociation in all four active glide modes. A series of Ti+X alloys (X = Al, Sn, V, Zr and O) was selected to analyse the impact of solute valence structure (Al, Sn - p type elements, V, Zr - d type elements) and lattice site (interstitial O) on the mechanisms responsible for variation of mechanical properties. The computational procedure relied on the generalized stacking fault energy (GSFE) concept combined with the nudged elastic band method that enables full atomic relaxation and determination of the true, minimum energy GSFE path [1]. Additionally, various concentrations of solutes and their distance to the glide plane were considered as well. Our study revealed a strong, nonlinear influence of X position on GSFE and migration of O atoms during the crystal slip. These new phenomena allowed one to determine three solution strengthening mechanisms:

(I) hindrance of <a> prismatic dislocation emission and reconfiguration of 1/3 <1120> screw dislocation cores (p type solutes),

(II) hindrance of <a> prismatic dislocation emission (V) and SFE reduction in other modes (both d type solutes),

(III) suppression of dislocation nucleation in all modes caused by O [2,3,4].

We found that the stacking faults formed by the single partial dislocations have a thickness of few atomic layers and exhibit a highly non-uniform structure. Their ability to accommodate the lattice deformation introduced by solute elements greatly affects the stacking fault energies of the α-Ti alloys.

3. Graphical presentation of computational results

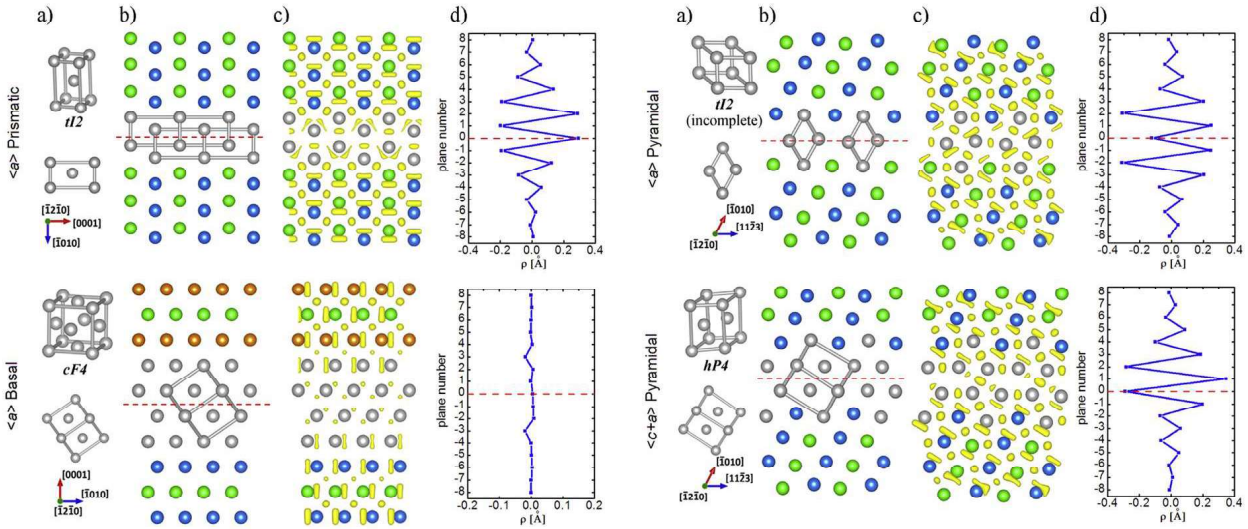

Fig. 1. Hexagonal Ti stacking faults: unit cell, Pearson number and orientation relative to host crystal (a), SFs structure arrangement (b), atomic bond patterns (yellow zones indicate electron-localization-function ELF isosurfaces) (c) and interplanar distance distortion plots (d). The gray spheres depict atoms belonging to SF regions while blue, green and orange ones denote A, B and C sequence of basal planes in unaltered sections of the crystal. Slip planes are marked by the red dashed lines. The ELF isosurface level is equal to 0.7 in all cases [5].

4. Conclusions

Conclusion of this study can be useful not only in terms of analysis of the line defects core geometries but also for phenomena influencing instability of plastic deformation i.e. nucleation and configuration of slip bands boundaries. The understanding of slip phenomena that appear in the active zone of initiating and propagating micro-shear band can be helpful in the formulation of theoretical description of plastic deformation accounting for multiscale shear banding processes [6].

5. References

1. P. Kwasniak, P. Śpiewak, H. Garbacz, Plasticity of hexagonal systems: split slip modes and inverse Peierls relation in α-Ti, *Physical Review*, B 89:144105, 2014.
2. P. Kwasniak, H. Garbacz, Screw dislocation mediated solution strengthening of substitutional α-Ti alloys – First principles investigation, *Acta Materialia*, 141:405, 2017.
3. Q. Yu, L. Qi, T. Tsuru, R. Traylor, D. Rugg, J.W. Morris, M. Asta, D.C. Chrzan, A.M. Minor, Origin of dramatic oxygen solute strengthening effect in titanium, *Science*, 347:635-639, 2015.
4. E. Clouet, D. Caillard, N. Chaari, F. Onimus, D. Rodney, Dislocation locking versus easy glide in titanium and zirconium, *Nature Materials,* 14:931, 2015.
5. P. Kwasniak, H. Garbacz, K.J. Kurzydlowski, Solid solution strengthening of hexagonal titanium alloys: Restoring forces and stacking faults calculated from first principles, *Acta Materialia,* 102:304, 2016.
6. R.B. Pęcherski, Macroscopic measure of the rate of deformation produced by micro-shear banding, *Arch. Mech.*, 49:385, 1997.

Solid solution strengthening of hexagonal Ti alloys: structures, energies and Peierls barriers of <*a*> type screw dislocations calculated from first principles

P. Kwasniak[1], J. Mizera[1], R.B. Pęcherski[2]

[1] *Materials Design Division, Faculty of Materials Science and Engineering, Warsaw University of Technology, Woloska 141, 02-507, Warsaw, Poland*

[2] *Institute of Fundamental Technological Research, Polish Academy of Sciences, Pawinskiego 5B, 02-106 Warsaw, Poland*

e-mail:piotr.kwasniak@inmat.pw.edu.pl

1. Introduction

Due to their finely balanced strength and density, hexagonal close-packed (hcp) metals such as Ti and Mg are perceived as potential prime elements for the production of new light, and strong alloys essential for the sustainable development of green technologies oriented towards a reduction in mass in all transport sectors. Nevertheless, the conscious design of materials requires information on the relationship between alloy elements and individual deformation mode activity. Such complex knowledge in the context of hcp systems remains a challenge, seriously hampering our ability to anticipate the strength and ductility of new materials developed. In general, hcp metals and alloys suffer from limited cold workability arising from reduced crystal symmetry (compared to cubic crystals) and from the geometrical relations between their dislocation glide planes [1]. On the other hand, the unique properties of single phase hcp materials, such as great strength and reasonable ductility of α-Ti+O solutions [2,3] and a pronounced solution softening of α-Mg+Y alloys [4,5], demonstrate the great potential of this groups of materials. All these aspects provide incentive for exploring the physics of plastic deformation and solution strengthening theories.

2. General

The mechanical properties of hexagonal Ti alloys depend substantially on the glide of <*a*> type screw dislocations. The configurations and stabilities of these line defects are, however, known only in pure Ti [6] and Ti + O solutions [7], where the locking-unlocking mechanism and a strong pinning effect control their activity. In this study, we investigated the unclear, screw dislocation mediated solution strengthening of substitutional α-Ti alloys. To this end, a first principle computational scheme was used to determine the structures and energies of the considered line defects during planar and cross-slip processes in the vicinity of the solute element. Two phenomena were determined that are crucial in terms of plastic deformation: (i) enhanced polymorphism of the dislocation cores leading to multiple new core configurations, and (ii) relatively large positive and negative interaction energies between the solutes and the line defects. Both these effects are strongly affected by the valence configuration of the alloying elements. Due to their pronounced structure and energy variations, dislocation planar and cross slip processes can occur under different scenarios, through diverse non-planar core geometries. The calculations performed also indicate In as a potential alloy element for improving both the strength and ductility of Ti by stabilizing a special, compact core geometry able to spread on an arbitrary glide plane with a low energy barrier. All of the above effects are discussed in terms of the physical factors (solute size misfit, stacking fault energy and electronic structure) that affect the energy and geometry of dislocation cores.

3. Graphical presentation of computational results

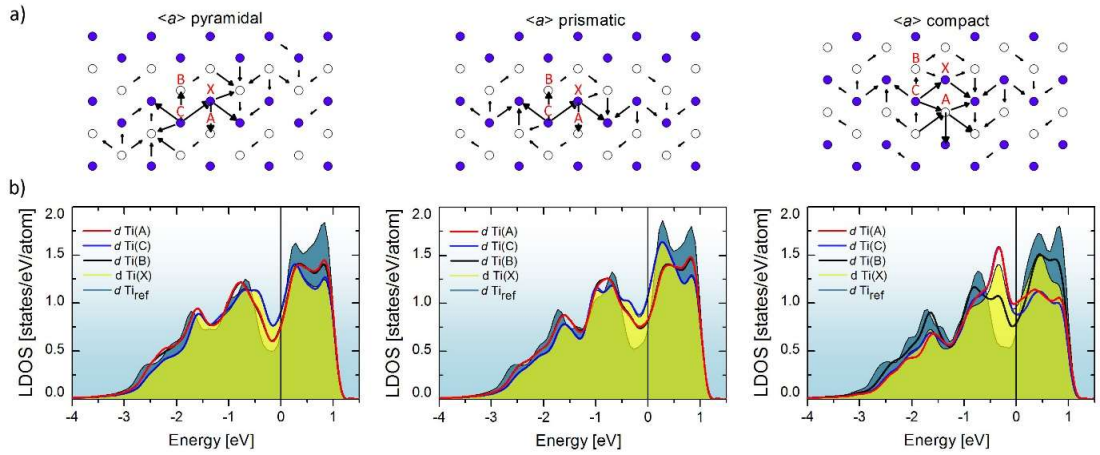

Fig. 1. Detailed structures of selected <a> type screw dislocation cores (a) and local density of states plots determined for X, C, B and A atomic position (b) [8]

4. Conclusions

This article describes the impact of substitutional solutes on α-Ti screw dislocation geometry, energy and motion. The alloying elements used in this study belong to two groups: simple (Sn, Ga, In) and transition (V, Zr) metals; this makes it possible to study the effect of solute valence structure on line defect behaviour. All calculations were performed within an ab initio framework, utilizing the full periodic boundary condition approach of dislocation modelling. The determined interaction energies between the substitutional solutes and <a> type screw dislocations are relatively large, even a few times greater than the Peierls barrier of high energy pyramidal glide in pure α-Ti – which shows the significant impact of substitutional solutes on screw dislocation mobility. Moreover, transition metals reduce the energy of the considered line defects, stabilizing its position and impeding further glide. Simple metals also introduce high energy dislocation states (dislocation repulsion), which improves the overall solution strengthening effect.

5. References

1. J.P. Hirth and J. Lothe, Theory of Dislocations, 2nd edn. (1992), Wiley, New York.
2. B. Sun, S. Li, H. IMAI, J. Umeda, K. Kondoh, Fabrication of high-strength Ti materials by in-process solid solution strengthening of oxygen via P/M methods, *Mater. Sci. Eng. A* 563 (2013) 95-100.
3. T. Lones, K. Kondoh, T. Mimoto, N. Nakanishi, J. Umeda, The Development of a Ti-6Al-4V Alloy via Oxygen Solid Solution Strengthening for Aerospace & Defense Applications, *Key. Eng. Mat.* 551 (2013) 118-126.
4. S. Sandlobes, Z. Pei, M. Friak, L.-F. Zhu, F. Wang, S. Zaefferer, D. Raabe, J. Neugebauer, Ductility improvement of Mg alloys by solid solution: Ab initio modeling, synthesis and mechanical properties, *Acta Mater.* 70 (2014) 92-104.
5. F. Wang, S. Sandlobes, M. Diehl, L. Sharma, F. Roters, D. Raabe, Collective grainscale mechanics in Mg and Mg–rare earth alloys, *Acta Mater.* 80 (2014) 77-93.
6. E. Clouet, D. Caillard, N. Chaari, F. Onimus, D. Rodney, Dislocation locking versus easy glide in titanium and zirconium, *Nat. Mater.* 14 (2015) 931.
7. Q. Yu, L. Qi, T. Tsuru, R. Traylor, D. Rugg, J.W. Morris, M. Asta, D.C. Chrzan, A.M. Minor, Origin of dramatic oxygen solute strengthening effect in titanium, *Science* 347 (2015) 635-639.
8. P. Kwasniak, H. Garbacz, Screw dislocation mediated solution strengthening of substitutional α-Ti alloys – First principles investigation, *Acta Mater.* 141 (2017) 405-408

MOVEMENT OF COINCIDENCE GRAIN BOUNDARIES WITH SIGMA = 7, 13, 19,$\cdots, 49, \cdots, 91, \cdots$: FROM ISOTROPY TO ANISOTROPY

R. Wojnar[1]

[1]*Institute of Fundamental Technological Research Polish Academy of Sciences, Warszawa, Poland*

e-mail: rwojnar@ippt.pan.pl

1. Isotropy

Isotropy means having the same properties in all directions (1856). The word is derived from the Greek, *isos* (equal) and *tropos* (way). The exact definitions depend on the field in which this concept is used. The opposite of isotropy is anisotropy. The term isotropy is associated with geometry and the concept of direction, while the term of homogeneity is associated with the concept of density. Simple chemical reaction and removal of a substrate by an acid or a solvent or is often close to isotropic. The kinetic theory of gases is also an example of description of the isotropic medium, cf. [1]. In Statistical Physics, for the system of N particles, the two-particle distribution function $n_2 = n_2(\boldsymbol{r}_1, \boldsymbol{r}_2)$ is defined as $n_2(\boldsymbol{r}_1, \boldsymbol{r}_2) = N(N-1)P_2(\boldsymbol{r}_1, \boldsymbol{r}_2)$, where $P_2(\boldsymbol{r}_1, \boldsymbol{r}_2)$ is the probability density to find particle nr 1 at $\boldsymbol{r}_1$ and nr 2 at $\boldsymbol{r}_2$. For isotropic system $n_2(\boldsymbol{r}_1, \boldsymbol{r}_2) = n_2(r_{12})$, cf. [2]. In Chemistry, the electron clouds described by s-orbitals are isotropic, and by other orbitals - anisotropic, cf. [3]. In Economics and Geography, an isotropic region is a region that has the same properties everywhere. The Big Bang theory of the evolution of the observable universe assumes that space is isotropic. It also assumes that space is homogeneous. These two assumptions are known as the Cosmological Principle, [4, 5].

Amorphous substances are isotropic, although they do not have to be homogeneous. Polycrystalline bodies may also be isotropic. If the individual crystallites are oriented completely at random, a large enough volume of polycrystalline material will be approximately isotropic. In hydrodynamics, we observe with the increasing velocity the passage from the laminar flow (anisotropic) to turbulent (isotropic) flow, cf. [6].

2. Isotropy and anisotropy in geometry and mechanics

Carl F. Gauss proved that the highest average density in close-packing of equal spheres is equal to $\pi/(3\sqrt{2}) \simeq 0.74048$ in 3D, and $\pi/(2\sqrt{3}) \simeq 0.9069$ in 2D. The Kepler conjecture, recently proved states that this is the highest density that can be achieved by any arrangement of spheres, either regular or irregular, cf. [7–9].

A hexagonal 2D crystal is anisotropic and has three symmetry axes. A deformation in the plane is determined by only two moduli of elasticity, as for an isotropic body, cf. [10]. A symmetric tensor of rank two, such as the termal conductivity or the termal expansion tensors have only one component, again as in isotropic medium.

Conversely, an isotropic medium subject to stress acquires anisotropic properties, behaves like a crystal and exhibits the birefringence, [11]. Similarly, the isotropic suspension of magnetic particles (in micrometer or nanometer scale spheres) sitributed randomly becomes in the magnetic field an anisotropic solid, [12].

3. Coincidence site lattice

A grain boundary is the interface between two kinds of grains, or crystallites, in a polycrystalline material. The boundary consists of structural units which in the 2-D system depend on the misorientation of the two neighbouring grains. The misorietation angle is given by

$$\alpha = \arccos \frac{d^2 + n^2 - m^2}{2\,d\,n} \quad \text{where} \quad d^2 = m^2 + n^2 + m\,n$$

and m, n are integers. The types of structural unit are described by the concept of the coincidence site lattice (CSL), in which repeated units are formed from points at which the two misoriented lattices happen to coincide.

The degree of fit (Σ) between the lattices of the two grains is described by the reciprocal of the ratio of coincidence sites to the total number of sites

$$\Sigma \equiv \frac{\text{surface of the CSL unit cell}}{\text{surface of the lattice unit cell}}$$

It is possible to draw the lattice for the 2 grains and count the number of atoms that are shared (coincidence sites), and the total number of atoms on the boundary (total number of site). For example, when $\Sigma = 7$ there will be one atom each 7 that will be shared between the two lattices. The misorientation angle $\alpha = 19.1066^{\text{o}}$ for $\Sigma = 7$, as in this case $m = 1, n = 2, d = \sqrt{7}$.

4. From isotropy to anisotropy

We are considering a 2-D system of point particles subject to periodic boundary conditions. To ensure uniform homogeneous density of the initial arrangement, we distribute the particles on the honey-comb lattice. In each cell of this lattice we randomly put 7 particles . In such a way the isotropic initial system is created.

Next, all the particles of the system are subjected to the Centroidal Voronoi iterations. One of the 7 particles in each honey-comb cell after a few iterations approaches to the very center of the cell. In this way, a coincidence point appears in the center of each honey-comb cell. After just a few iterations, the system begins to crystallize in two phases of different directions. During the further crystallization convexities and concavities of the grain boundaries are reduced and the grain boundaries straighten.

Thus, the consecutive iterations result in increasing the anisotropy by disappearing some pentagons-heptagons (5-7) pairs. As a result, the percentage of hexagons increases and in consequence the anisotropy is growing. The same procesure could be done for $\Sigma = 13, 19, \cdots$ and in general $\Sigma = 6\,k + 1$, $k = 4, 5, 6, \cdots$. After each iteration we examine the number of hexagons created. The increase in their number is a measure of the departure from isotropy. Finally, we observe the creation of a bicrystal formed by grains ofr only two kinds. Two phases are separated by the boundary of 5-7-pairs. It is important that contrary to the widespread opinion that the 5-7 pairs are symmetric, these 5-7 pairs do not lie on the boundaries in a symmetrical manner.

If other (not coincident) integer numbers are put in the honey-comb lattice cells, we get polycrystals. But, if $\Sigma = 49 = 7 \times 7$ and $\Sigma = 91 = 7 \times 13$ it is possible to build up interesting tricrystals.

References

[1] L. D. Landau and E. M. Lifshitz (2011). *Statistical Physics*, Volume 5 (Course of Theoretical Physics), transl. from the Russian J. B. Sykes and M. J. Kearsley, 3rd edit., Butterworth-Heinemann, Oxford OX.

[2] J. Stecki, *Termodynamika statystyczna*, PWN, Warszawa 1971.

[3] W. Kołos, *Chemia kwantowa*, PWN, Warszawa 1978.

[4] C. M. Will (1986) *Was Einstein Right? - Putting General Relativity to the Test*, Basic Books, New York.

[5] P. J. E. Peebles, D. N. Schramm, E. L. Turner & R. G. Kron (1994). The Evolution of the Universe, *Scientific American* **271** 29–33.

[6] L. D. Landau and E. M. Lifshitz, *Fluid mechanics*, Volume 6 of Course of Theoretical Physics, transl. from the Russian by J. B. Sykes and W. H. Reid, Second edition, Pergamon Press, Oxford - New York - Beijing 1987.

[7] T. C. Hales (1998). An overview of the Kepler conjecture, arXiv:math/9811071v2 Mathematics: does the proof stack up?, *Nature* **424**, 12–13.

[8] H. Cohn, A. Kumar, S. D. Miller, D. Radchenko, M. Viazovska (2017). The sphere packing problem in dimension 24, *Annals of Mathematics* **185** (3) 1017–1033. arXiv:1603.06518

[9] J. H. Conway, N. J. A. Sloane, E. Bannai (1999). *Sphere packings, lattices, and groups*, Springer Science+Business Media, New York.

[10] L. D. Landau and E. M. Lifshitz (1970). *Theory of Elasticity*, Volume 7 of Course of Theoretical Physics, transl. from the Russian by J. B. Sykes and W. H. Reid, 3rd edition, Pergamon Press, Oxford - New York - Toronto - Sydney.

[11] J. F. Nye (1957) *Physical Properties of Crystals: Their Representation by Tensors and Matrices*, Oxford University Press.

[12] L. J. Frąś, R. B. Pęcherski (2018). Modified split Hopkinson pressure bar for the investigations of dynamic behaviour of magnetorheological materials, *Journal of Theoretical and Applied Mechanics* **56** (1) 323–328.

Session S09: Experimental mechanics

Organizers: S. Kourkoulis (National TU of Athens), Z.L. Kowalewski (IPPT PAN, Warsaw)

EXPERIMENTAL RESEARCH OF THE INFLUENCE OF SELECTED SBM PROCESS PARAMETERS ON THE PET CONTAINERS PROPERTIES AND ANALYSIS OF THE PET MULTI-PHASE MICROSTRUCTURE

P. Wawrzyniak[1] and W. Karaszewski[2]

[1]*Warsaw University of Technology, Plac Politechniki 1, 00-661 Warsaw, Poland*
[2] *Gdańsk University of Technology, Gabriela Narutowicza 11/12, 80-233 Gdańsk, Poland*

e-mail: pwawrzyniak@poczta.simr.pw.edu.pl

1. Stretch Blow Molding process (SBM process)

The production of containers for beverages made of PET material with viscosity IV = 0.76 - 0.85 dl/g takes place in a so-called "Two-stage manufacturing process" (ISBM process). In the first step it is made a semi-finished product by injection molding, the so-called "preform", and in the second step by the blow molding with the simultaneous stretching (stretch blow molding process - SBM process) this preform is being shaped into the finished product (defined by the shape of the cooled blow mold). A detailed description of the ISBM process was presented in other author's works [1,2].

The properties of the bottle manufactured in the SBM process are influenced by thermodynamic, mechanical and physico-chemical phenomena. Thermodynamic effects are associated with heating the preform, rapid cooling of the blown bottle by the walls of the blow mold (and in part by a stretching rod), and with the heat exchange between the blown preform and the blow air. Mechanical phenomena and fluid mechanics are related to the speed of the stretching rod, the air pressure of the pre-blow and main blow, the flow rate of the air through the blow valves and exhaust flow rate of air trapped between the blown preform and the wall of the blow mold through the channels drilled in the blow mold. Physicochemical phenomena are associated with phase changes occurring in the PET material during the SBM process. All these phenomena affect in a coupled and nonlinear manner affecting the properties of the bottles PET material.

2. PET multi-phase microstructure model

It is very difficult to describe the whole issue of the SBM process in the terms of describing the influence of SBM process parameters on the microstructural properties of the PET material. The problem is that the amorphous phase itself occurs in 5 forms: the mobile unoriented amorphous phase, the rigid unoriented amorphous phase, the oriented amorphous phase, and this occurs in form of the nematic, smectic type C and smectic type A [3]. The crystalline phase occurs in two forms: a temperature-induced crystalline phase, and a strain induced one.

Simplifying the problem of behavior of PET in the SBM process, in the preform individual polymer chains usually form unordered amorphous entanglement, where individual chains influence the behavior of the material over a large area. This effect is due to the fact that individual macromolecules form entanglement with other macromolecules. Moreover, if there is a stress field (e.g. by deformation or elevation of temperature) the entanglement of macromolecules may disappear. These entanglements are randomly arranged, and from a macroscopic point of view, a polymeric material containing only an amorphous unoriented phase behaves like an isotropic material. The behavior of the chains relative to each other is determined by the stress field, which depends on the external extortion (deformation, temperature), but also on the interaction between the individual chains. In the SBM process, the deformation is so large that the polymer chains are orientated towards the deformation causing a change in the material structure, and consequently its mechanical properties - the unoriented amorphous phase is transformed locally into an oriented amorphous phase. As a consequence, the material exhibits anisotropy characteristics. Moreover, the

oriented amorphous phase can form nucleation of crystallization, which can lead to the transformation of the oriented amorphous structure into the crystalline phase - this is called strain induced crystallization.

In addition, individual areas can be subjected to several microstructural changes. The oriented amorphous region can be transformed into a crystalline region (if a stable nucleation of crystallization is formed) or it can be transformed into an initial form (amorphous unoriented) and later can be transformed into an oriented amorphous phase (and possibly further to the crystalline phase). In turn, the formed crystalline phase may break into a rigid amorphous unoriented phase. It differs in properties from the mobile unoriented amorphous phase, because it is predominantly composed of trans conformation whereas in the mobile amorphous phase, the probability of trans and gauche conformation is comparable (the crystalline phase contains only trans-conformations). In theory, it is assumed that at temperatures lower than the glass transition temperature, it is possible to convert between the oriented amorphous phase and the unoriented amorphous phase, but it is impossible to create a crystalline phase.

3. Experimental research

The purpose of the research results described in the paper is to determine, by means of ANOVA, the existence of qualitative and quantitative influence of selected SBM process parameters (factors) on the macroscopic characteristics of bottles, i.e. the thickness profile and pressure resistance of bottles. Main effects and cross-effects were analyzed. In addition, the results of macroscopic features of bottles were explained on the basis of multi-phase polymer structure theory, and the given interpretation was supported by literature data.

In terms of the influence on the thickness profile were examined the speed of the stretching rod (1), pre-blow air pressure (2) and WSR parameter (3). In terms of influence on pressure resistance were examined the speed of the stretching rod (1), pre-blow air pressure (2), WSR parameter (3) and preform temperature (4). The effect of factors 1, 2 and 3 on the thickness profile and pressure resistance were tested on the basis of a complete divalent three-factor plan (three-factor MANOVA). On the other hand, the influence of preform temperature on pressure resistance was tested on the basis of a divalent one-factor plan. The stretching rod speed varied from 0.72 m/s to 1.2 m/s, pre-blow pressure from 6 bar to 9 bar, and WSR parameter from 120 mm to 160 mm. The influence of preform heating by the heating furnaces on the preform temperature was measured by two pyrometers just before preform was being put into the blow molds. The average temperature of the preforms was 123°C for lower heating power and 132°C for higher heating powers.

The presented analysis showed that the changes in macroscopic features can be explained on the basis of the currently functioning theory of multi-phase PET material microstructure.

References

[1] P. Wawrzyniak and J. Datta. Charakterystyka faz rozdmuchu preform z poli(tereftalanu etylenu) w procesie rozdmuchiwania z jednoczesnym ich rozciąganiem. *Przem Chem*., 94:1114, 2015.
[2] P. Wawrzyniak and J. Datta. Maszyny rozdmuchowe stosowane do wytwarzaniu butelek z PET. *Przem Chem*., 94:1110, 2015.
[3] D. Kawakami, D. S. Hsiao, C. Burger and others. Deformation-Induced Phase Transition and Superstructure Formation in Poly(ethylene terephthalate). *Macromolecules*, 38:91, 2005.

CORROSION BEHAVIORS OF MAGNESIUM FILM COATED WITH BIOCOMPATIBLE MATERIALS UNDER PSEUDO-BIOLOGICAL ENVIRONMENT

S. Manzaki[1], T. Kojima[1], and M. Notomi[1]

[1]*Meiji University, 1-1-1 Higashimita, Tama-ku, Kawasaki, Japan*
e-mail: notomim@meiji.ac.jp

1. Introduction

Biomaterials are used to be embedded in the human body and classified by a period of using [1]; (a) Semi-permanently using such as the artificial heart, (b) Temporarily using such as a bone plate, and (c) Disposable using such as injection. The temporarily used biomaterials have to be removed with surgery after the complete recovery and it imposes expensive surgery and physical and mental pains to the patients. Recently, the application of magnesium (Mg) for bio-implant material has been interested because of its biodegradable, mechanical strength as much as bone and low cytotoxicity. On the other hand, the corrosion resistance of Mg is less to sustain the strength until the recovery of the affected part. There is some research for solving the problem of the corrosion resistance with Mg [1-3]. Figure 1 shows the strength degrading for corrosion under a pseudo-biological environment. The black and red curves mean the strength at corrosion times of virtual and ideal biodegradable material and pure Mg, respectively. The strength of pure Mg gradually degrades for excretion in the body. The ideal corrosion behaviors have two regions, Existing period and Dissolving period. The material keeps in the body for sustaining the mechanical strength in the Existing period and then that is promptly excreted from the body in Dissolving one. This study is to develop the biocompatible material coating Mg film and evaluate the corrosion behaviors of the Mg film under the pseudo-biological environment.

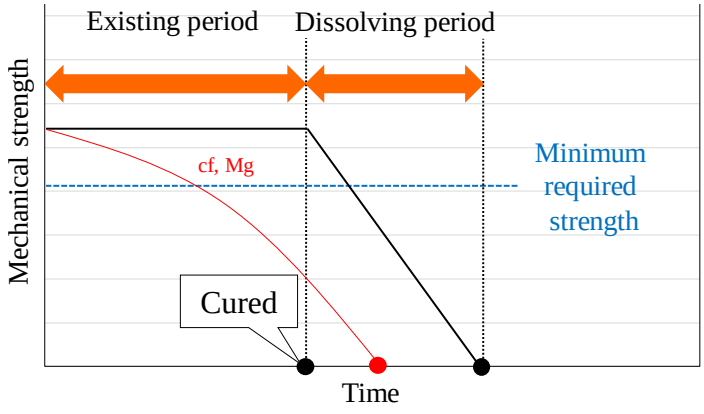

Figure 1: Mechanical strength of pure Mg and ideal biodegradable materials at corrosion times.

2. Experimental methods

The corrosion test was conducted with the Mg ribbonlike film manufactured by Nilaco Corporation. The specimen was cut from the film to a rectangular shape; 50×3.2×0.24 mm and layered with two kinds of materials, one for holding the existence of the specimen and the other for promoting the dissolution. The former material is Polylactic acid (PLA) and the latter Titanium (Ti). PLA, which has biodegradability and low

cytotoxicity, was available to control the degree of the Mg film corrosion. We coated PLA provided by Unitika Corporation on the surface of the Mg film with injection molding at 513K. Ti is also a biocompatible material and its galvanic corrosion between Ti and Mg promotes the dissolution and then reduces the Dissolving period. We deposed Ti on the surface of the specimens with a heat resistance vacuum deposition method. The three kinds of the specimens were prepared and called “As-received”, “Mg/PLA”, and “Mg/Ti”. We conducted the corrosion test to the specimens with the conditions as shown in Table 1. Then we evaluated the corrosion states with tensile test and X-ray diffractions (XRD). The tensile tests were carried out at room temperature at 0.5 mm/min. and evaluated one at before and after the corrosion test. XRDs were performed on a MiniFlex600 manufactured by Rigaku Corporation (Cu target, 40kV 15mA) with a step size 0.005° (2θ).

Hold temperature [K]	Solution	Corrosion time [h]		
310	Saline (0.9 wt% NaCl solution)	24	72	120

Table 1: Corrosion conditions.

3. Results & Discussion

In Fig.3 It was shown that the decrease of the weight of As-received and Mg/Ti (Fig.3(a)), an image of corroded Mg/Ti (Fig.3(b)), and the stress-strain curve of As-received before and after the corrosion test (Fig.3(c)). The decrease of the weight of 72h was 2.49 mg more than that of 24h. The decreased weight with 120h was 0.66 mg and less than that of 72h. We confirmed the specimen had Na on its surface according to XRD analysis, which was included in the solution, i.e., Saline. It seemed that component of the solution was coated during the corrosion progress. This Na might suppress the loss of the weight even though the corrosion. On the other hand, Mg/Ti completely dissolved after 24h due to the corrosion (Fig.3(b)). The corrosion potential between Mg and Ti is 1.6V [4] and that caused the dissolution of Mg and Ti. In the mechanical test, Fig.3(c) indicates that the stress and strain of As-received decreased 21.5 MPa and 0.311 ε with corrosion, respectively.

Figure 3: (a) The decrease of weight of As-received,(b) Corroded Mg/Ti, (c) The stress-strain curve of As-received.

4. Conclusion

Even though the mechanical strength decreased with corrosion, the corrosion products, Na suppressed the decrease of the weight of the specimen under the pseudo-biological environment. This effect might be available for controlling the times of Existing and Dissolving period.

References

[1] S. hiromoto. Corrosion Behaviour of Magnesium Alloys for Biomedical Use. *Zairyo to kankyo*, 63:6, 2014.
[2] M. Takamatsu. Application of magnesium to biomaterials for hand-tissue. *Keikinzoku*, 50:7, 2000.
[3] R. Yamamoto. Biomedical application of magnesium alloys. *Keikinzoku*, 58:11, 2008
[4] Japan Welding Society. *Keikinzoku yousetsu,* 47:3, 2009

DATA MINING IN FIELD TESTING OF SOIL: NEURAL NETWORKS APPLIED TO RCPTU INTERPRETATION

Stanisław Puakowski[1,2], Rafał Ossowski[1], and Krzysztof Szarf[1]

[1] *Chair of Geotechnics, Geology and Marine Civil Engineering, Faculty of Civil and Environmental Engineering, Gdańsk University of Technology (GUT), Gdańsk, Poland*
[2] *Norwegian University of Science and Technology (NTNU), Trondheim, Norway*

e-mail: krzszarf@pg.edu.pl

Context of the Study

Field testing of soil is a thriving branch of geomechanics, widely present in both scientific research and practical applications. The problem of measuring certain quantities in the natural environment and translating them into specific information about the granular material is far from trivial. Even the basic question of recognising the type of soil and its spatial location with a satisfying degree of probability remains largely unanswered.
Quick clay is a peculiar glacial marine sediment native to some parts of the Northern Hemisphere (Scandinavia, North America, Siberia) which, while being fairly resistant to loading, is prone to rapid liquefaction once disturbed [6, 7]. Due to several catastrophic events related to failure in quick clay deposits [1], a lot of work is being done to detect areas where quick clays may be found, e.g. the "Mapping of Quick Clay" project by the Swedish Geotechnical Institute [4].

One common method of soil field investigation involves Undrained Cone Penetration Tests (CPTU), where a probe continuously measures three basic parameters while being statically pushed into the soil: cone resistance $q_c\,[Pa]$, sleeve friction $f_s\,[Pa]$ and pore water pressure $u\,[Pa]$. CPTU can be enhanced with additional sensors to measure a fourth quantity: electrical resistivity of soil $R\,[\Omega m]$ (hence RCPTU) – an important parameter for marine sediments [2].

In a single RCPTU test, these four parameters are measured at each depth, up to several dozen meters deep. At each given level, the values of the measured parameters combined together can be used to establish the soil type and its mechanical properties. Such a large quantity of data is difficult to analyze by hand. Until recently, analysis of CPTU tests was mainly based on the experience of researchers supported with classification charts [3, 5], necessarily complemented with physical testing of soil samples collected from certain depths. In this study, a different approach was chosen – to use a data mining technique, namely artificial neural networks [8], to train automata to recognise quick clay layers in RCPTU and CPTU tests. Due to a rigorous training and testing protocol, as well as high quality of the input datasets, this approach proved to be successful.

Scope of the Study

Three tests sites around Trondheim, Norway were investigated with RCPTU and CPTU probings, as well as traditional drilling and laboratory testing. The results of the laboratory tests were treated as a benchmark, and the RCPTU sounding data from each test site were used to train several generations of neural networks. The trained networks were subsequently tested against each other with an objective to correctly classify soil profiles from sites which had not been used in their training. Some of the networks proved to be more flexible than others, managing to properly recognise soils in each of the three test sites.

In the final phase of the study, the well trained and tested neural networks were applied to a real-case scenario: an imperfect CPTU database with no additional information from laboratory testing. The performance of the neural networks was assessed against the classical approaches incorporating classification charts. The neural networks turned out to be at least on a par with the classical approaches,

but also surpassing them in some respects. It is an integral result of neural network operation that the network's performance in a given task, in this case recognising quick clay, is expressed in percentages of certainty. The shapes of these certainty curves give additional insight into the soil structure. The neural networks also skillfully captured transitional zones between different soil types, which are of high importance but are often disregarded in the classical approaches.

Summary of the Study

Data mining techniques are more and more often used in many fields of research. Their great versatility makes it possible to use them in almost any problem with significant amounts of data. But at the same time, without a thought-out course of investigation and with no scientific rigour, the results obtained might be worthless. In this paper, we present a simple, yet extensive, protocol of training, testing and applying neural networks, which assures high quality of the findings. A similar approach can be followed in other problems, using different computational software or data mining techniques.

References

[1] M. Geertsema, J. J. Clague, J. W. Schwab, and S. G. Evans. An overview of recent large catastrophic landslides in northern British Columbia, canada. *Engineering Geology*, 83(1-3):120–143, 2006.

[2] M. Long, S. Donohue, J.-S. L'Heureux, I.-L. Solberg, J. S. Rønning, R. Limacher, P. O'Connor, G. Sauvin, M. Rømoen, and I. Lecomte. Relationship between electrical resistivity and basic geotechnical parameters for marine clays. *Canadian Geotechnical Journal*, 49(10):1158–1168, 2012.

[3] T. Lunne, J. J. M. Powell, P. K. Robertson, et al. *Cone penetration testing in geotechnical practice*. CRC Press, 2014.

[4] K. Rankka, Y. Andersson-Sköld, C. Hultén, R. Larsson, V. Leroux, and T. Dahlin. Quick clay in Sweden, Swedish Geotechnical Institute, Linköping Report 65, 2004.

[5] P. K. Robertson. Soil classification using the cone penetration test. *Canadian Geotechnical Journal*, 27(1):151–158, 1990.

[6] I. T. Rosenqvist. Considerations on the sensitivity of Norwegian quick-clays. *Geotechnique*, 3(5):195–200, 1953.

[7] V. Thakur, S. Nordal, G. Viggiani, and P. Charrier. Shear bands in undrained plane strain compression of norwegian quick clays. *Canadian Geotechnical Journal*, 55(1):45–56, 2017.

[8] I. H. Witten, E. Frank, M. A. Hall, and C. J. Pal. *Data Mining: Practical machine learning tools and techniques*. Morgan Kaufmann, 2016.

THE ANALYSIS OF ACTUAL SURFACE AREAS IN ROLLING-SLIDING CONTACT FOR REAL OPERATIONAL CONDITIONS BY MEANS OF FEM AND PROFILOGRAFOMETRIC TESTS

A. John[1], H. Bąkowski[2]

[1]*Faculty of Mechanical Engineeringn, Silesian University of Technology, Gliwice, Poland*
[2]*Faculty of Trasnport, Silesian University of Technology, Katowice, Poland*

e-mail: henryk.bakowski@polsl.pl

1. Introduction

In real working conditions of the wheel-rail system, there are stresses and slips affecting the processes occurring in this important areas in the place of contact. The contact surface is permanently changed depending on many factors, both construction and operation. As a result of the overlap of these factors, the problem of durability of the surface layer, especially the running surface of railway rails, remains unsolved. Currently, the biggest problem is the balance between abrasive wear (vertical and lateral wear - present in railway rails) and fatigue wear, which occurs in the form of contact-fatigue damages leading to cracks on the surface and even crosswise cracks. In addition, tribological processes, occurring on the surface and just below it, in the rail are very similar to those that are formed in the railway wheel.

The phenomenon of wear occurring in a rolling-sliding contact always has the form of flaky wear products, the size and shape of which is determined by variable operating factors, type of treatment (thermal or plastic) and condition and properties of the surface layer of the material. However, in order to fully correlate the relationship between wear and durability, all the different types of stresses that occur in the rail under the influence of variable interactions should be considered [1].

2. Test procedure

Nowadays, FEM is the basic method of carrying out computer aided engineering calculations (CAE). The manufacturing process can also be made much simpler while designing and servicing the combustion engines. The reason of damages found in the selected subassemblies may be justified more easily by constructing the model of the analyzed object and performing the calculations by the Finite Elements Method. In order to reconstruct the real object and its real operational conditions as well as properly interpret the obtained calculation results it is necessary to apply the knowledge of mechanics, physics, machine and device operation and finally tribology.

Complementing the metallographic and simulation studies are geometric structure tests of the surface made on the TalySurf Series 2 profilographometer by Taylor Hobson. The calculations of stereometric parameters and isometric images of the surface in a photographic (3D) approach were developed using the TalyMap Universal program. This allowed to confirm the obtained results from simulation tests, which testifying to the type of wear process [2].

3. Numerical simulation

Appropriate models of the analyzed machine parts have to be built if FEM is to be effectively applied. Therefore the user should undertake the following activities:

- define the model of construction geometry,
- chose the type of element,
- build the finite elements mesh,
- define the material properties,
- define the elements properties,
- verify the quality of finite elements mesh,
- introduce load and boundary conditions,
- specify the type of required analysis,
- define the requirements regarding the number and kind of results,
- interpret the obtained results.

The above stages of preparation of the 3D model of the friction surface were preceded by the determination of the real friction surface on the nanotomograph - Nanotome S (Fig. 1).

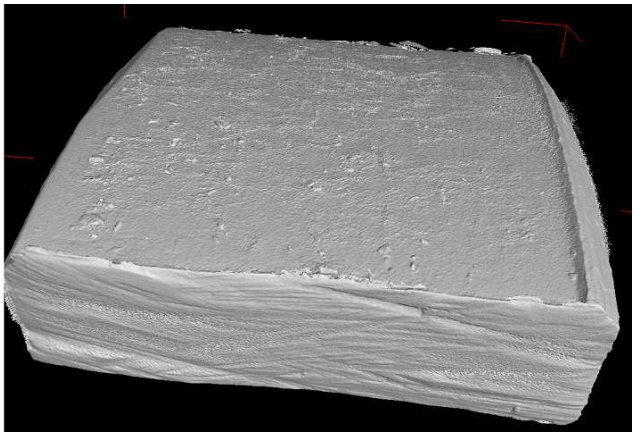

Fig 1. The real surface layer obtain in laboratory test by Computed Tomography (Nanotom S)

The subject of simulation tests is determination of stresses and deformations in the wheel-rail system for the redl contact surface in the following test sets:

a) analysis of friction surface after cooperation (both worn surfaces),
b) analysis of the friction surface after cooperation and the ideal surface (deformable),
c) analysis of the friction surface after cooperation and the ideal surface (rigid).

4. Conclusions

Numerical analysis allow to determine local stress values which are essential for understanding the wear mechanisms of the analyzed contact. The obtained results of operational investigations prove that cracks and spallings of the micro and macro scale appear in areas with maximum stress and deformation. On the basis of the conducted simulation tests, FEM was found to be the right tool used to identify the areas of special wear hazard. The method also helps to explain the wear mechanisms. FEM analysis helped to recognize and explain the wear mechanisms in depend of the selected operational conditions. The determination strains of the local stresses value of allowed the prediction of wear initiating places.

The main objective of the research was to determine the actual contact area and the relationship between the analyzed friction surface and its susceptibility to mechanical damage. This is of particular importance as the analyzed wear processes form differently on the actual contact surface than is the case for analyzes of ideal surfaces with isotropic material properties. An important part of the research is the attempt to locate the most vulnerable places depending on various operating conditions and to identify the basic mechanisms of wear.

References

[1] Dongchan L., Yoonhwan W., Sangho L., Changsoo H. Design consideration of the nonlinear specifications in the automotive body. *Finite Elements in Analysis and Design* p.851–861, 44, 2008.

[2] H. Bąkowski. Wear mechanism of spheroidal cast iron piston ring-aluminum matrix composite cylinder liner contact. *Arch. Metall. Mater*. p.481-490, 1:63 2018.

THE FRACTURE MODE OF A GLASS PLATE STUCK WITH THIN FILM UNDER A LOW-VELOCITY IMPACT

T. Kojima[1], K. Utakawa[2], and M. Notomi[1]

[1]*Meiji University, 1-1-1, Higashimita, Tama-ku, Kawasaki-shi, Kanagawa, Japan*
[2]*FUJITSU GENERAL, 3-3-17, Suenaga, Takatsu-ku, Kawasaki-shi, Kanagawa, Japan*

e-mail: kojimat@meiji.ac.jp

1. Introduction

The impact resistance improvement is important for glass members to protect people from injury. Although it was reported that sticking a thin polymeric film on the glass plate is an effective way to easily reinforce the glass plates against impact loads [1], the reinforcing mechanism is still unclear. We should understand the fracture characteristic of the glass plate with the two modes, bending mode fracture and Hertzian type fracture [2] for recognizing the mechanism. In this study, impact fracture behavior was investigated experimentally with a glass plate stuck with thin polymeric film.

2. Method

An impact experiment was conducted using the drop ball test. Figure 1 presents the schematic of the experimental apparatus used in the study. Impact loads were applied to the glass specimen through the impact bar of SUS304. The tip of the impact bar was rounded with 5 mm in radius. By using the impact bar, the applied impact load can be measured with stress wave analysis in the bar. The glass specimen was a 130×130×6 mm float glass plate stuck with 0.19 mm thick polymeric film (ULTRA S600, 3M Japan Ltd.) at the non-impact face. The specimen was cramped by the steel plates and rubber plates with a 40 mm hole in the center of it. The dropped ball was made of a steel, SUJ2 in Japanese standard, and its diameter was 82.5 mm. The drop height was 1 m above the top of the impact bar. During the experiment, impact load was estimated from the strain gauge output at the impact bar. The stress distribution and fracture behavior of the specimen were recorded by the high-speed video camera (Phantom VEO-710, Vision Research Inc.) with the photoelastic method in 5800,000 fps. The experiment was conducted in three times in the same condition.

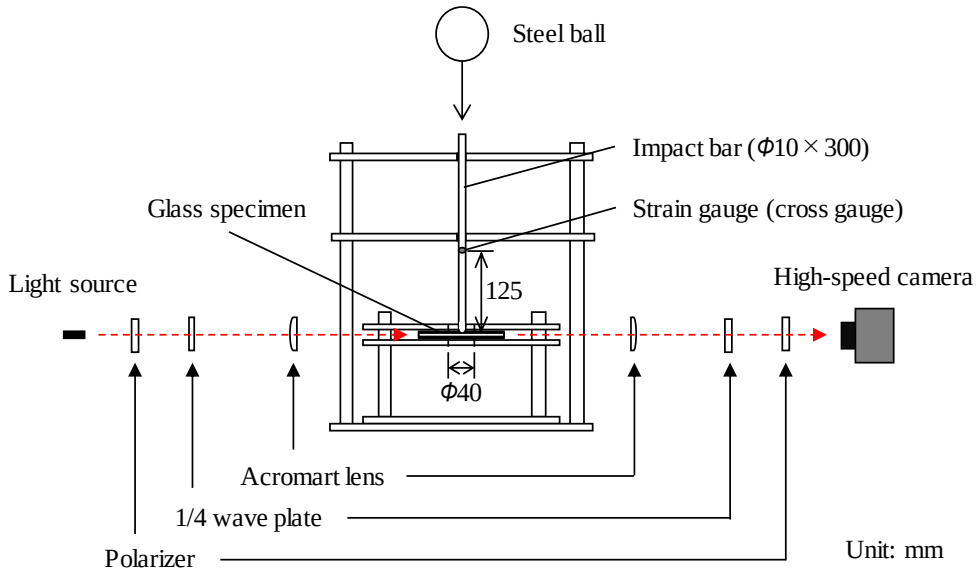

Figure 1: Schematic of the experimental apparatus used in the study.

3. Results and discussion

Figure 2 shows the representative data of the impact load history obtained at the impact bar. The history until about 0.2 ms is the load applied to the impact bar before fracturing of the specimen. The images in Figure 3 present the fracture initiation of the specimen and show the crack initiated from the bottom (non-impact face) and propagated to the horizontal directions in the specimen. This crack propagation indicates the occurring of the bending fracture and the trapezoidal crack appeared above the initial crack after 0.191 ms. This trapezoidal crack shape signifying that the crack propagated along with the tensile stress distribution from the impact point which can be explained by Hertz's contact theory. Therefore, it may have a similar characteristic with Hertzian type fracture. In this way, it was clarified the glass plate was fractured in a mixed mode of the bending fracture and Hertzian fracture in the impact condition at the velocity, i.e., a low-velocity impact. In addition, it appears that the bending fracture was dominant in the present experiment. Sticking the film to glass plate seemed to delay the fracture initiation without affecting the fracture mode.

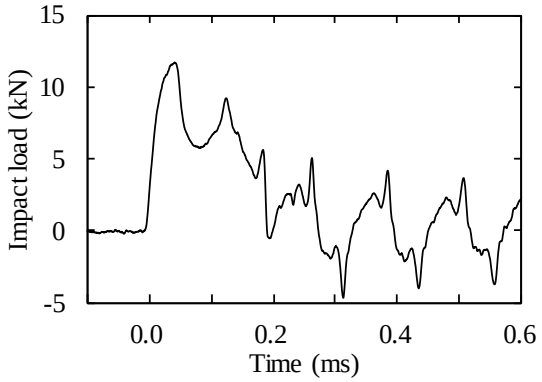

Figure 2: Impact load history.

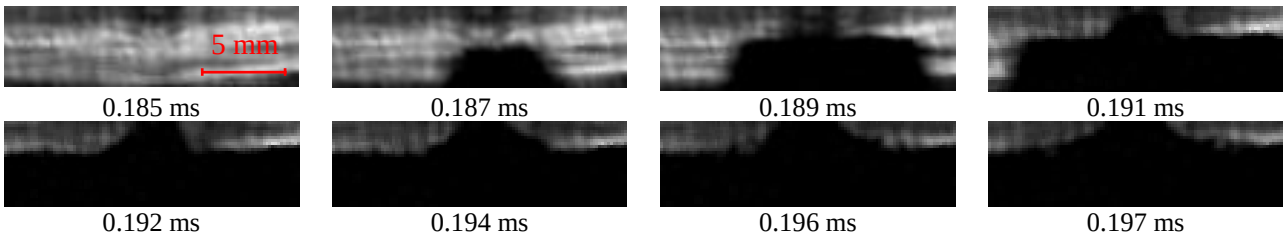

Figure 3: Stress concentration and crack propagation in the glass plate after the impact.

4. Conclusion

An experimental investigation was conducted for the impact fracture mode of a glass plate stuck with thin film. It was clarified the glass plate was fractured in a mixed mode of the bending fracture and Hertzian fracture and the former was dominant in the present experiment. Further study is needed to clarify the condition for a transition of the fracture mode and its relation with the impact resistance of the glass plate.

Acknowledgment

We thank H. Aoki and K. Aoki of SOUSHOW Co., Ltd. for their support on this research.

References

[1] Y. Yasumoto et al. Dynamic Finite Element Method for Impact Fracture of a Glass Installed Polymer Film. *Proc. of the 10th Intl. Conf. on Fracture and Strength of Solids (FEOFS2016).*, 1, 2016.

[2] R. C. Bradt and R. E. Tressler. *Fractography of Glass*. Springer US, 1994.

DETERMINATION OF THE STRENGTH OF INTERFACE IN PRINTED CIRCUIT BOARDS (PCBs): PEELING TEST AND ROLE OF PLASTICITY

E. Simlissi[1,2], M. Martiny[1], S. Mercier[1], S. Bahi[1], F. Lechleiter[2], L. Bodin[2]

[1]*Université de Lorraine, CNRS, Arts et Métiers Paris Tech, LEM3,*
7 Rue Felix Savart, 57073 Metz Cedex 03, France.
[2]*CIMULEC, Rue Charles Picard, 57365 Ennery, France.*
e-mail: essossinam.simlissi@univ-lorraine.fr, slim.bahi@univ-lorraine.fr, marion.martiny@univ-lorraine.fr, sebastien.mercier@univ-lorraine.fr, flechleiter@cimulecgroup.com, lbodin@cimulecgroup.com.

Keyword: Printed circuit boards, peel tests, cohesive elements, thin film, copper, plasticity.

1 Introduction

A printed circuit board (PCB) is a multi-layered material, made of dielectric materials and copper. For aerospace applications, the number of copper layers is large (over 10 to 20) and the reliability of the boards must be ensured during decades to make the electronic devices operating (in satellites or other equipments). During the qualification process, aero-mil standard must be fulfilled. For example, the PCB is subjected to thermal cycles in the range [-55°C, +125°C]. It is important to check that the copper traces are not presenting damage and that the interfaces remain safe. In the present talk, we discuss only the interface issue.

The structure of the board design for specific applications can mix various dielectric materials having very different mechanical properties. In the present work, we concentrate on the interface between a woven composite (glass fibers and epoxy resin) and a thin foil of copper.

The present talk will have two distinct parts: an experimental part for the characterization of the behavior of the interfaces and a numerical part. The goal of experiments is to feed numerical simulations with real data measured in laboratory. The ultimate goal of this work is to anticipate problem in advanced design so as to provide accurate predictions which can explain observed failures on specific printed circuits.

2 Experiments

For the experimental part, we have prepared samples which are representative of materials used in the real applications. For that purpose, pre-preg of epoxy glass fibers laminate and copper have been processed according to the industrial standard. Curing of the pre-preg materials at elevated temperature ensures the adhesion of copper. Secondly, strips of copper (10 mm) are etched on the surface of the sample, Figure 1. Note that the bonding of the copper is realized only on 2/3 of the total length of the sample so that the strip can be fixed in the grip of the peeling device, see Fig2. The peel test is carried out at a fixed crosshead velocity and the steady force for the peel force is recorded during the test, Fig3. For a given peel angle, tests have been carried out several times, providing the same stationary peel force, see Fig3. In our configuration, the copper film is thin (thickness 35µm). Three different peel angles (45, 90, 135 degrees) have been considered. It has been shown in this present work that the peel force decreases when peel angle increases as reported in Williams and Kauzlarich [1].

Fig. 1: Sample used for the peel test. The copper film has the following dimensions: 200mm length and 10mm width.

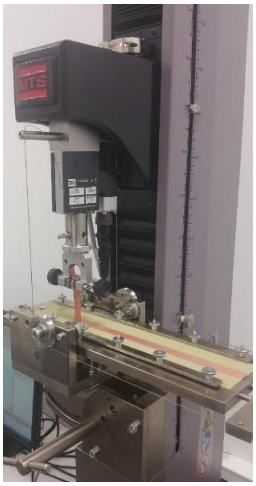

Fig. 2: Experimental peeling device. The film is pulled at constant velocity.

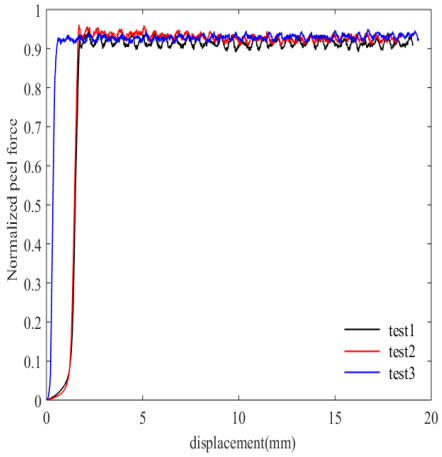

Fig.3: Evolution of the normalized peel force measured during a 90° peel test. After a few millimeters of crosshead displacement, a steady state is established.

3 Modeling

In an attempt to model the peel force evolution with the peel angle, the theory of elastic peeling test has been first adopted [2] and it has been shown, as already mentioned in the literature, that an elastic theory is not able to explain the trend when a thin metallic foil is considered. To understand the role of plasticity of copper during peeling, a numerical model has been developed with the finite element software ABAQUS. From the simulations, we have observed two zones where plasticity is cumulated: a first bending zone at the tip of the interface and a reverse plastic bending latter in the free arm. Those results are consistent with the work of Wei and Hutchinson [3]. Usually, in the literature, the behavior of the metallic thin film is not often known. In our work, the elastic-plastic behavior of copper thin film has been identified based on a uni-axial tensile test. In addition, the elastic behavior of the substrate has been identified in our laboratory. Cohesive elements (traction separation law) have been adopted to model the interface between copper and the substrate. Parameters of the cohesive elements have been estimated to mimic the experimental results. In the present talk, the effect of plasticity in the peel test will be quantified based on the energy balance. In the present configuration, it will be shown that the peel force does not provide a direct measurement of the interface energy. Additional work must be addressed to extract from the peel force, the surface energy.

Acknowledgements: The authors thank the ANR for their support through the Labcom program ANR-14-LAB7-0003-01 and the creation of the Labcom LEMCI. The research conducted in this thesis has received financial support from the European program ITN H2020 (European Union's Horizon2020 Program, Excellent Science, Marie-Sklodowska-Curie Actions) under approval number: REA grant agreement 675602 (OUTCOME Project). The authors thank the support of Région Grand Est and FEDER (Fonds européen de développement économique et regional).

References

[1] J. A. Williams and J.J Kauzlarich, The influence of peel angle on the mechanics of peeling flexible adherends with arbitrary load-extension characteristics. Tribology International 38 (951-958) 2005

[2] K. Kendall, Thin film peeling: the elastic term. J Phys D Appl Phys 8 (1449-1452) 1975

[3] Y. Wei et J.W. Hutchinson. Interface strength, work of adhesion and plasticity in the peel test. Int Journal of Fracture 93: (315-333) 1998.

APPLICATION OF ROTATION RATE SENSORS IN STIFFNESS "RECONSTRUCTIONS" OF STRUCTURAL SYSTEMS

Z. Zembaty[1], P. Bońkowski[1], P. Bobra[1] S. Kokot[1] and J. Kuś[1]

[1]*Faculty of Civil Engineering and Architecture, Opole University of Technology, Opole, Poland*
e-mail: z.zembaty@po.opole.pl

1. Introduction

In some areas of Structural Health Monitoring (SHM) e.g. for civil engineering structures (reinforced concrete (r/c) beams, frames or masonry structures), it is not possible to localize damages in form of simple 'cuts' and localized stiffness losses as it is usually assumed in SHM. Instead more difficult tasks have to be undertaken, aiming at formal "reconstructions" of spatially distributed stiffness variations (e.g. [1]). The problem of such "reconstructions" is particularly complicated for r/c structures due to the presence of multiple cracks even during their normal exploitation and under regular service loads. Recently, techniques of directly measuring angle variations have emerged [2] and matured to achieve angular resolution of 10^{-3} degrees. Thus, in addition to transversal accelerations, it is now possible to measure angle variations along the bar axis during vibrations of the structures. This way, the changes in curvature of the axes of the bars of the structures can be obtained almost directly. Numerical simulations demonstrated many potential advantages for these new angular measurements [3, 4]. The key advantage of rotational measurements for r/c structures is the ability to infer strain from rotation. Another particular advantage is the possibility to monitor plastic hinge development during seismic vibrations using two rotation rate sensors, as shown in Figure 1.

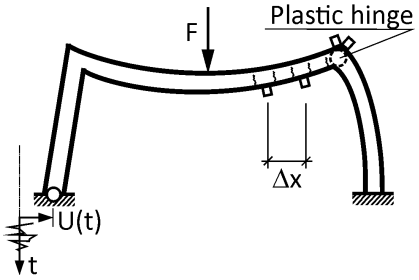

Figure 1: R/c frame with 2 rotation sensors measuring strain and other 2 to monitor plastic hinge

Before full scale, 'in situ' dynamic experiments one should carry on small scale laboratory tests. For this purpose, the Horizon HZ1 100-100 rotation rate sensors were chosen. Our presentation for the 41st SolMech will report results of experiments carried out using the Horizon sensors and plexiglass models of beams. In what follows a short description of the experiments is presented. Details of the methodology are given in paper [4], while the experiments are reported in the reference [5] and a very recent paper (see ref: [6]).

2. Description of the experimental set up

Consider vibrations of a cantilever beam under kinematic excitations, $u(t)$, (Figure 2). The vertical motion $u(t)$ of the plexi beam support was obtained by its kinematic movement using an actuator acting in the vertical direction on a 6 m, steel beam bearing, in the middle, the plexi model. The model beam dimensions were: h=1.45cm, b=11.45cm, L=80cm, Young modulus E=3.427·10^{9}N/m^2 and mass density 1203kg/m^3.

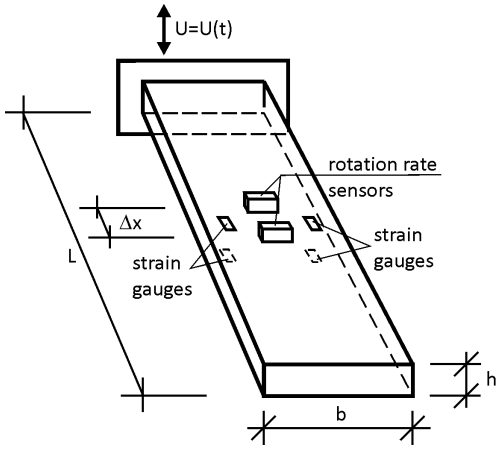

Figure 2: Sketch showing experimental set-up to measure direct strain and rotations of a beam

3. Indirect strain sensing

During this experiment, a seismic signal $u(t)$ drove vertical motion of the beam while the strains $\varepsilon(t)$ and rotations $\vartheta_1(t)$, $\vartheta_2(t)$ were simultaneously measured. Comparison of direct strains and strains derived from rotation difference $\Delta\vartheta$ using simple formula $\varepsilon(t)= h\Delta\vartheta/(2\Delta x)$ led to an accuracy of about 3% for Δx =10cm

4. Local stiffness modification

During this experiment, two measurements were carried out using the setup of Figure 2. The first experiment was done for an intact beam, the same as in previous experiment. Before the second experiment, a 20% stiffness drop was introduced to the beam by drilling holes in the plexiglass beam between the sensors, of Figure 2. The measured rotation rate differences of the intact and weakened cross section were integrated to obtain $\Delta\vartheta(t)$ and compared. A value of 9.6% maximum difference was obtained. Measuring such the stiffness drops could model early stages of plastic hinge development during e.g. seismic excitations (Figure 1).

5. Stiffness "reconstruction" using sets of translational and rotational sensors

During this experiment, the intact beam was excited by small, diagnostic, vertical, kinematic harmonic excitations $u(t)=u_0\sin(2\pi ft)$. Next, along the beam, starting from its support, three equally long sections of 15%, 30% and 45% cumulated stiffness drops were produced to mimic distributed structural "damage" similar to typical flexural stiffness losses of r/c beams. Respective mass losses were compensated by gluing additional ballasts to the beam. Calculations of the stiffness losses based on the changes in dynamic responses were done by measuring the amplitudes of the harmonic vibrations of the "damaged" beam and using special inverse problem algorithms [4]. Application of only translational sensors failed to "reconstruct" the bending stiffness loss distributions, while application of rotation rate sensors made the "reconstruction" successful with reconstructed stiffness drops 14%, 33% and 46% (see [5] for details).

References

[1] Liu G.R., Chen S.C., A Novel Technique for Inverse Identification of Distributed Stiffness Factor in Structures, *Journal of Sound and Vibration*, vol. 254, 2002, pp.823-835
[2] Meydan T. Recent trends in linear and angular accelerometers, *Sensors and Actuators A: Physical* 1997; 59: 43–50.
[3] Abdo M.A.-B. Hori M. A numerical study of structural damage detection using changes in the rotation of mode shapes, *Journal of Sound Vibration* 2002; 251: 227–239.
[4] Kokot S., Zembaty Z. Vibration based stiffness reconstruction of beams and frames by observing their rotations under harmonic excitations — Numerical analysis, *Engineering Structures* 2009; 31: 1581–1588.
[5] Zembaty Z., Kokot S., Bobra P. Application of rotation rate sensors in an experiment of stiffness 'reconstruction,' *Smart Materials and Structures* 2013; 22: 077001, DOI:10.1088/0964-1726/22/7/077001
[6] Zembaty Z., Bobra P., Bońkowski P., Kokot S., Kuś J. Strain sensing of beams in flexural vibrations using rotation rate sensors, *Sensors and Actuators A: Physical* 2018; 269: 322-330, DOI:10.1016/j.sna.2017.11.051.

APPLICATION OF MINIATURE SPECIMEN TESTING TO LIFETIME ASSESSMENT OF STEAM TURBINE ROTORS

M. Banaszkiewicz[1], A. Rehmus-Forc[1], W. Radulski[1] and K. Dominiczak[1]

[1]*GE Power Ltd, Elblag, Poland*
e-mail: mariusz.banaszkiewicz@ge.com

1. Introduction

The residual lifetime assessment and potential of failure of steam turbine components is a critical issue in the safety and reliability analysis of power plants. The bulk of lifetime assessment studies of high-temperature components is based on theoretical damage calculations, non-destructive tests and metallographic investigations [1]. Components' residual lifetime, and, in particular steam turbine rotors, can be rarely evaluated with the traditional mechanical test techniques, because there is usually insufficient material to sample non-invasively from the component [2]. Instead of these well-standardized techniques, various innovative techniques based on miniaturized specimens can be effectively employed for determining material properties and assessing residual lifetime. Among these, a small punch test (SPT) technique significantly developed over the last years, is an efficient and cost-effective method suitable for industrial applications.

The paper presents a case study of a steam turbine lifetime assessment where the small punch test technique was applied and supported a more accurate residual lifetime determination.

2. Small punch testing of the rotor

Lifetime assessment study performed for the high-temperature rotor of a 55 MW steam turbine revealed a high level of creep damage in the first stage disc. The damage was evaluated using the time fraction method assuming minimum creep rupture strengths for determining the time to rupture [1]. Crack initiation life was exhausted at the bottom of the disc, but non-destructive tests did not reveal any cracks or advanced microstructural damage. The creep damage was close to the permissible limit at the disc periphery in the blade groove which was not accessible for non-destructive examination. In order to determine tensile and fracture toughness properties of the rotor after long-term operation, small punch tests were performed [3]. Five material samples were taken from disc 1, which was found to be life-limiting, and for reference, also five samples were taken from disc 19 which operates at low temperature and is not subject to creep damage (Fig. 1). The extracted material samples were used for determination of chemical composition, metallographic examination and manufacture of disc-shaped punch test specimens of 8 mm diameter and 0.5 mm thickness. The following mechanical properties were estimated by SPT: yield stress, tensile strength, elongation, FATT and fracture toughness.

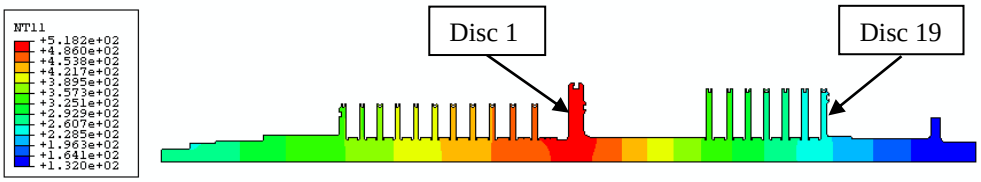

Figure 1: Rotor temperature distribution with indicated areas for SPT.

The chemical analysis confirmed the rotor steel composition to agree with the material standard requirements, while the metallographic examination confirmed the correct microstructure - tempered bainite. Comparison of tensile properties shown in Table 1 reveals no significant differences in the properties of the two discs and confirms compliance with the material standard requirements.

Source	Yield stress [MPa]	Tensile strength [MPa]	Elongation [%]
Disc 1	545	678	29-31
Disc 19	528	708	27-32
Standard	440	640	16

Table 1: Mechanical properties measured by SPT and required by the applicable standard.

The fracture appearance transition temperature evaluated by SPT is FATT = -3.7°C and the lower bound fracture toughness at room temperature corresponding to FATT is K_{Ic} = 121 MPa·m$^{1/2}$. The low value of FATT and high value of K_{Ic} confirm good fracture resistance and no visible degradation of the rotor material due to long-term operation at high temperature under creep conditions.

3. Residual lifetime assessment

Residual lifetime of the rotor was assessed by assuming the existence of small cracks in critical areas, not detectable by NDT, and calculating their growth until the critical size. For critical crack size estimation, the real fracture properties obtained from SPT were adopted, among others. As high fracture toughness was estimated by SPT, it could not be excluded that brittle fracture will not be the main failure mechanism, and due to this also ductile failure was taken into account by estimating the critical crack size. Crack growth due to creep, fatigue and their interaction was calculated assuming real operating conditions of the rotor. Based on the calculated crack propagation rate, the residual life of the rotor was estimated at approximately 200 000 hours and limited by the creep damage in disc 1.

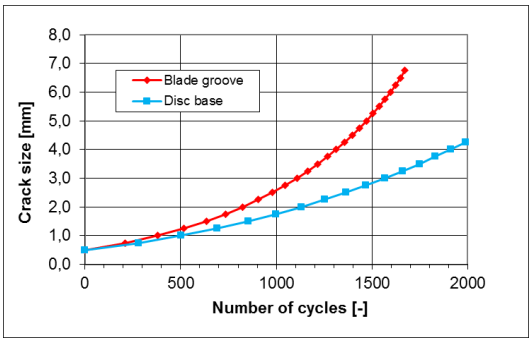

Figure 2: Crack propagation in disc 1.

6. Summary

The lifetime assessment performed using conventional methods showed complete lifetime exhaustion of the rotor. The use of SPT enabled determining the real material properties and performing more accurate residual lifetime assessment with the help of fracture mechanics methods. The performed comprehensive investigations allowed for significant lifetime extension of the rotor with a controlled risk of failure.

References

[1] M. Banaszkiewicz. Multilevel approach to lifetime assessment of steam turbine components. *Int. J. Fatigue*, 73:39, 2015.
[2] R.C. Hurst and K. Matocha. A renaissance in the use of the small punch testing technique. *Transactions SMIRT-23*, Manchester, August 10-14, 2015.
[3] K. Matocha, M. Filip, J. Purmensky, O. Balon, L. Kander, M. Miczkova and I. Nogol. Measurement of tensile and fracture toughness properties of material samples taken from steam turbine rotor in Lodz Power Plant using small punch test. Report No T-24/2006. VITKOVICE Research and Development Ltd.

DAMAGE ASSESSMENT OF EXPLOITED TURBINE BLADES USING BARKHAUSEN NOISE PARAMETERS

K. Makowska[1], Z. Kowalewski[1,2], W. Dudda[3] , P. Ziółkowski[4] and J. Badur[4]

[1] *Motor Transport Institute, 03-301 Warsaw, 80 Jagiellońska, Poland*

[2] *Institute of Fundamental Technological Research, 02-106 Warsaw, 5b Pawińskiego, Poland*

[3]*Department of Mechanics and Machine Design, University of Warmia and Mazury in Olsztyn, Poland*

[4]*Energy Conversion Department, Institute of Fluid-Flow Machinery Polish Academy of Sciences, 80-231 Gdańsk, Fiszera 14, Poland*

e-mail: katarzyna.makowska@its.waw.pl

1. General

A degradation level developing in the turbine blade material was analyzed experimentally using the magnetic method. A relationship between the exploitation time of turbine blade and selected parameters of the Barkhausen noise signal was identified. The results coming from the leading edge area of blade and the trailing edge area were compared. An influence of the blade deformation resulting from damage development on the Barkhausen noise level was also taken into account. Another issues taken into account theoretical background treated equation of oxygen level as an interface. Processes with oxygen layer can be considered such as the enhancement transport phenomena in the Navier-Stokes shell-like slip layer presented in earlier works [1-3].

2. Experimental results of the Barkhausen noise parameters

Exploitation time of the turbine blade material was analyzed experimentally using the magnetic Barkhausen noise method [4], [5]. A relationship between the exploitation time of turbine blade and selected parameters of the Barkhausen noise signal was identified. The results coming from the blades with and without oxidized layer were compared. An influence of the blade deformation resulting from damage development on the Barkhausen noise level was also taken into account. Table 1 presents notations of turbine blades investigated.

The number of turbine blade	Exploitation time [h]
A1, A2, A3	26 400
B1, B2, B3	36 100
C1, C2, C3	39 800
D1, D2, D3	60 800

Table 1: Exploitation time of the selected turbine blades

The diagrams presented in the Fig. 1 show comparison of amplitude of the Barkhausen noise amplitude measured without and with oxidized layer for the selected exemplary turbine blades. It is seen that the Barkhausen parameter measured on leading edge with removed oxidized layer increases slightly with exploitation time to 39 800 h and then decreases (Fig. 1b). Such relationship was not found for the areas close to the trailing edge of to turbine blade due to deformations introduced to the material as a result of turbine disassembly.

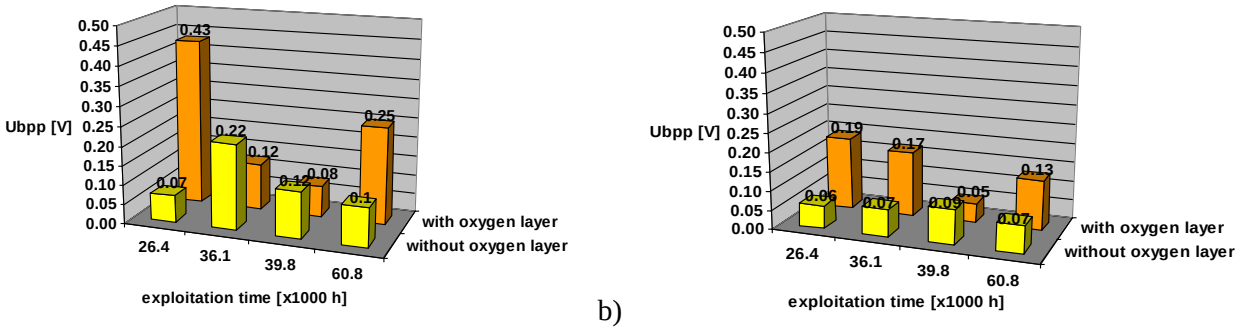

Fig. 1. The Barkhausen noise results coming from trailing edge a), leading edge; b) of turbine blades

3. Theoretical background

The generalized form of the boundary condition including phenomena of oxygen layer, can be expressed in the following way

$$\partial_t(\rho_z \mathbf{v}_z) + \mathrm{div}_s\left(\rho_z \mathbf{v}_z \otimes \mathbf{v}_{z|}\right) - \omega_n \mathbf{I}_s \rho_z \mathbf{v}_z + \mathrm{div}_s(\mathbf{p}_z) + \frac{\partial}{\partial n}(\mathbf{p}_z \mathbf{n}) + (\mathbf{t}_1 \mathbf{n}_1 + \mathbf{f}_1) + (\mathbf{t}_2 \mathbf{n}_2 + \mathbf{f}_2) = \rho_z \mathbf{b}_z + \dot{m}_z \mathbf{v}_z \quad (1)$$

where $\rho_z \mathbf{v}_z$ is the surface momentum density vectors, ρ_z is the oxygen layer density on the boundary. Thus it has been defined an excess of boundary density ρ_z [mass per unit of area; kg/m^2], the slip velocity between oxygen layer and original solid body $\mathbf{v}_z$ [m/s], and the surface momentum density vector $\rho_z \mathbf{v}_z$ ($\rho_z \mathbf{v}_z$ is just scalar multiplication). Next, $\mathbf{p}_z$ is the surface flux of momentum, $\mathbf{n}$ is the unit normal vector on the boundary surface, $\mathbf{f}$ is the boundary force, $\mathbf{b}_z$ is the body forces on the boundary, $\dot{m}_z$ is the oxygen layer mass influxes and ω_n normal pressure of fluid acting on the mill scale. Additionally, $\mathbf{p}_z$ in the boundary layer is usual spherical pressure tensor changes into but can be changed into an ellipsoidal pressure tensor due to Stokes normal surface pressure.

It should be added, that surface divergence div_s is defined as a right contraction of surface gradient: $\mathrm{grad}_s(.) = \mathrm{grad}(.)\mathbf{I}_s$. Tangent to surface component of the slip velocity is $\mathbf{v}_{z|} = \mathbf{v}_z \mathbf{I}_s$ where the surface Gibbs identity is defined to be: $\mathbf{I}_s = \mathbf{I} - \mathbf{n} \otimes \mathbf{n}$. In this approach it is postulated that the boundary force, responsible for a so-called generalized slip, can be separated by two components: $\mathbf{f}_1$ and $\mathbf{f}_2$ in two bodies. Both forces are the subject of constitutive modelling. Additionally, the bulk flux of momentum $\mathbf{t}_1$ and $\mathbf{t}_2$ have to be multiplied by proper unit normal vectors $\mathbf{n}_1$ and $\mathbf{n}_2$, respectively.

4. Summary

Equation (1) may help at least to decrease a number of experimental attempts to find the proper program of an experimental to find influence of oxygen layer on Barkhausen noise.

References

[1] J. Badur, M. Karcz, M. Lemański and L. Nastałek. Enhancement Transport Phenomena in the Navier-Stokes Shell-like Slip Layer. *CMES*, 73:299–310, 2011.

[2] J. Badur et. al. Enhanced energy conversion as a result of fluid-solid interaction in micro- and nanoscale. *Journal of Theoretical and Applied Mechanics*, 56(1):329-332, 2018.

[3] P. Ziółkowski, J. Badur. A theoretical, numerical and experimental verification of the Reynolds thermal transpiration law. International Journal of Numerical Methods for Heat and Fluid Flow, 28(1): 64-80, 2018.

[4] D.J. Buttle, G.A.D. Briggs, J.P. Jakubovics, E.A. Little and C.S. Scruby (1986) Magnetoacoustic and Barkhausen emission in ferromagnetic materials. *Phil. Trans. R. Soc. Land*. A320, pp. 363-378

[5] K. Makowska, Z.L. Kowalewski, B. Augustyniak and L. Piotrowski (2014). Determination of mechanical properties of P91 steel by means of magnetic Barkhausen emission. *Journal of Theoretical and Applied Mechanics (JTAM)*, vol. 52, no. 1, pp. 181-188

ANALYSIS OF FATIGUE CRACK INITIATION CAUSED BY CYCLIC MICROPLASTICITY

A. Ustrzycka[1], Z. Mróz[1], S. Kucharski[1], Z. L. Kowalewski[1]

[1]*Institute of Fundamental Technological Research, Polish Academy of Sciences, Warsaw, Poland*
e-mail: austrzyc@ippt.pan.pl, zmroz@ippt.pan.pl, skuchar@ippt.pan.pl, zkowalew@ippt.pan.pl

The present paper concerns the fatigue crack initiation and evolution for metals subjected to loading at stress level below the conventional yield stress. The stress-strain curve exhibiting the hysteresis loops obtained during selected cycles with different stress amplitudes σ_{ai} below the yield stress σ_y highlighting the regime of micro-plasticity are presented in Fig. 1.

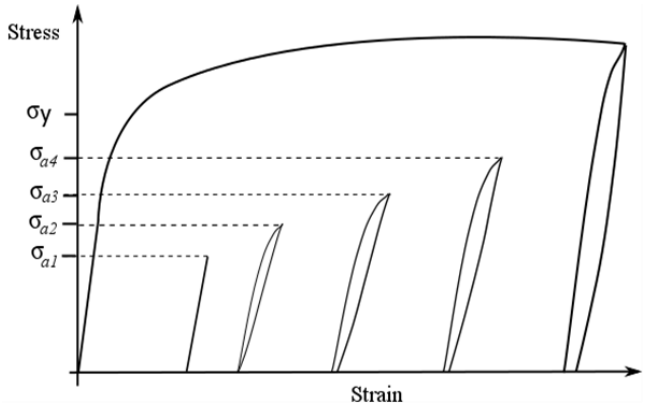

Fig. 1. Schematic stress-strain curve and the hysteresis loops showing the regime of micro-plasticity

The usual approach is based on averaged stress or strain amplitudes, with numerous fatigue conditions formulated for uniaxial or multiaxial stress states. However, the process of fatigue damage growth is of local nature and the account for stress fluctuations should be included [1]. Using the potential offered by the novel experimental techniques, it is possible to identify physical phenomena and to describe the mechanisms of degradation and fatigue damage development in modern structural materials [2]. In the present work the analysis of strain localization preceding crack initiation was performed by means of the optical method ESPI, namely the Electronic Speckle Pattern Interferometry apparatus using the coherent laser light (Fig.2).

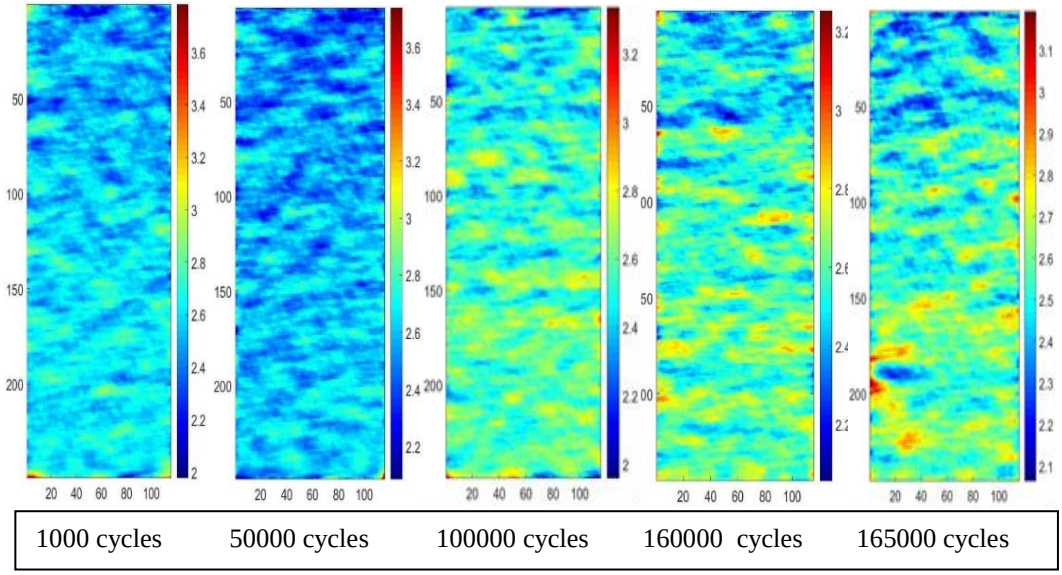

Fig. 2. Strain distribution maps on the plane specimen surface using ESPI for different stages of the fatigue process

The local stress-strain response in damage zones is analyzed by applying nano-indentation tests. The microindentation tests is a well established tool that enable to estimate local mechanical properties of macro-samples [3]. The load penetration curves are presented in Fig. 3.

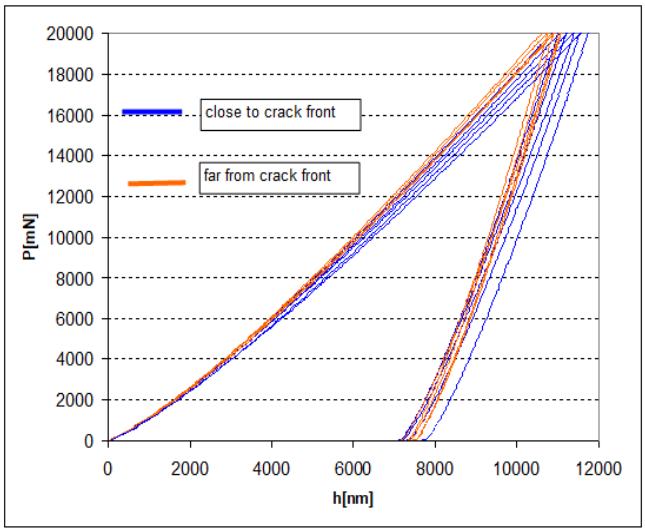

Fig. 3. Micro-indentation diagram close and distant to the crack front

It has been observed that the inclination of unloading curves far from crack front is lower than that measured close to the front end however, the residual penetration depth is practically the same. On can conclude that the elastic modulus is 10-12% lower in the regions of strain localization, while the hardness, that is a measure of plastic properties is practically the same in all regions. The micro tomographic analysis provides more detailed characterization of the damage state.

The mathematical model is formulated and applied to study damage evolution under cyclic tension. The proposed mathematical description of fatigue damage growth and crack initiation is based on the concept of critical plane. The condition of damage accumulation is formulated after Mróz et al., [4]

$$dD = A\left(\frac{\sigma_n - \sigma_0^*}{\sigma_c - \sigma_0}\right)^n \frac{d\sigma_n}{\sigma_c^* - \sigma_0^*} \tag{1}$$

The damage growth on the material plane is related to evolution of surface tractions. It is assumed that, when the critical stress condition is achieved on the material plane, a damage zone is generated. Afterwards, a growth of damage zone can be described. In the steady state the process of cyclic loading is described for the period of stress variation. It was noted that the local stress fluctuations occur at grain boundaries and on structure boundary components and their influence on the damage evolution and crack initiation is significant. The functions describing the grain and boundary fluctuations are proposed. The proposed model was applied to study damage evolution under cyclic tension, with its parameters calibrated by the experimental data.

Acknowledgments This work has been supported by the National Science Centre through the Grant No 2014/15/B/ST8/04368.

References

[1] R. Maass and P. M. Derlet. Micro-plasticity and recent insights from intermittent and small-scale plasticity. *Acta Materialia* 143: 338, 2018.

[2] M. D. Sangid. The physics of fatigue crack initiation. *International Journal of Fatigue* 57:58, 2013.

[3] S. Kucharski and Z. Mróz. Identification of yield stress and plastic hardening parameters from a spherical indentation test. *International Journal of Mechanical Sciences* 49:1238, 2007

[4] A. Ustrzycka, Z. Mróz, Z.L. Kowalewski. Experimental analysis and modelling of fatigue crack initiation mechanisms. *Journal of Theoretical and Applied Mechanics* 55:1443, 2017.

MINI-COMPACT TENSION SPECIMENS FOR FRACTURE TOUGHNESS EVALUATION

T. Szymczak[1], Z.L. Kowalewski[2], and A. Brodecki[1]

[1]*Motor Transport Institute, Warsaw, Poland*
[2] *Institute of Fundamental Technological Research of PAS, Warsaw, Poland*

e-mail: zkowalew@ippt.pan.pl

1. Introduction

Typical mechanical parameters such as the Young's modulus, yield point, ultimate tensile strength as well as fatigue limit are commonly used to indicate a possible applications of engineering materials. These parameters are required to carry out successfully all necessary static, dynamic or fatigue analyses. It has to be mentioned, that they are insufficient for investigations of crack growing. Therefore, the fracture toughness tests, that capture Stress Intensity Factor (SIF) [1] or Crack Tip Opening Displacement (CTOD) [2], are usually performed. They are carried out under plane strain state conditions [1, 2] using such parameters as Stress Intensity Factor and yield point i.e. $B \geq 2.5\,(K_{IC}/R^{0.2})^{0.5}$. When the SIF value cannot be calculated, then a proportion of the yield point to Young's modulus must be determined. Usually, it takes values starting from 0.0050 (for B equal to 7.5 mm) to 0.01 (for B equal to 0.65 mm) [1]. Various types of specimens can be used for such tests, e.g. arc, beam or compact [3, 4, 5]. Their thickness is usually equal to 13 mm [3]. In the case of smaller specimens it should be reduced up to 8 mm for mini-specimens [4], and 2 mm for micro-specimens [5]. Nowadays, many efforts of research groups are focused on modern material manufacturing and an effective failure reasons evaluation. Therefore, the main aim of the paper is to check an applicability of the mini-compact tension specimens for fracture toughness determination.

2. Details of experimental procedure

Two variants of mini-compact tension specimens were examined, Fig. 1a, d. The first one had a width, high and thickness equal to 32.5 mm, 31.2 mm and 6.5 mm, respectively, Fig. 1a, whereas the second one had all these dimensions 1.6 smaller, Fig. 1d.

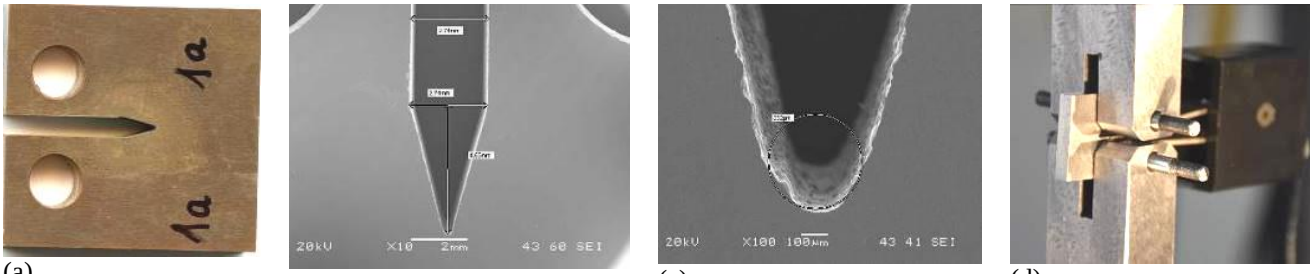

(a) (b) (c) (d)

Fig. 1. Details of the mini-compact tension specimen; (a) general view (Cu+20% Al_2O_3 (fibres)); (b) and (c) the notch dimensions for SEM analysis; (d) grips, micro-specimen and extensometer mounted in the testing machine

Dimensions of the mini-specimens (Fig. 1a) were checked using Light and SEM microscopic techniques, Fig. 1b, c. Miniaturized gripping system was used to mount specimens in the testing machine, Fig. 1d. CTOD was determined using extensometer of 5 mm nominal gauge length and travel for axial strain equal to 2 mm. The miniaturized specimens made of the Mo-40%Al_2O_3+5Re composite, Ti-6A1-4V alloy, and titanium alloy were tested. The fatigue pre-cracking was conducted under cyclic force control. A length of the fatigue pre-crack was checked after final stage of the test by means of microscopic measurements carried out at five points uniformly distributed along the specimen width, i.e. 0; 25; 50; 75 and 100%. These results were subsequently used in the procedure of specimen quality assessment according to the required standards.

3. Results

Experimental data from tests of the mini-compact specimens for all materials in question were analysed on the basis of force variations versus COD (Fig. 2), and features of fracture zones, Fig. 3. A quasi-linear relationship can be observed for the Mo–40%Al_2O_3+5Re composite, Fig. 2. However, calculation of the SIF value was not possible for this material. In the case of the 44200 aluminium alloy with Saffil fibres a brittle cracking was obtained, Fig. 3b. The critical value of SIF was equal to 12.2 MPa $m^{1/2}$. In the case of Ti-6Al-4V alloy tested in the parent and weld material zones (Figs. 2, 3c, d) variations of force versus COD represented plastic behaviour. The CTOD values determined for those zones were equal to: 0.0703 mm; 0.0872 mm, respectively. An inspection of the fatigue zone dimensions of the CT specimen representing weld region enabled identification of the unstable grow of the crack, Fig. 3d.

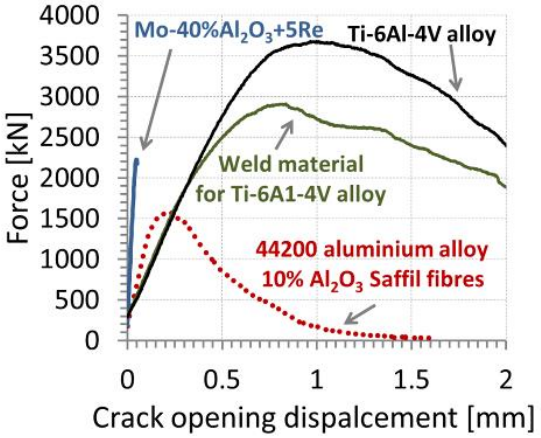

Fig. 2. Force versus crack opening displacement

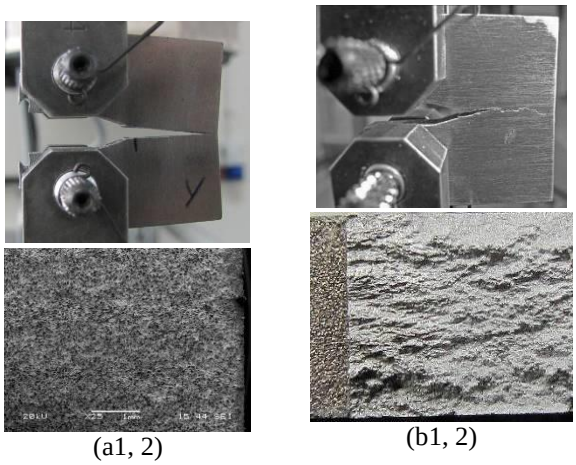

(a1, 2) (b1, 2)

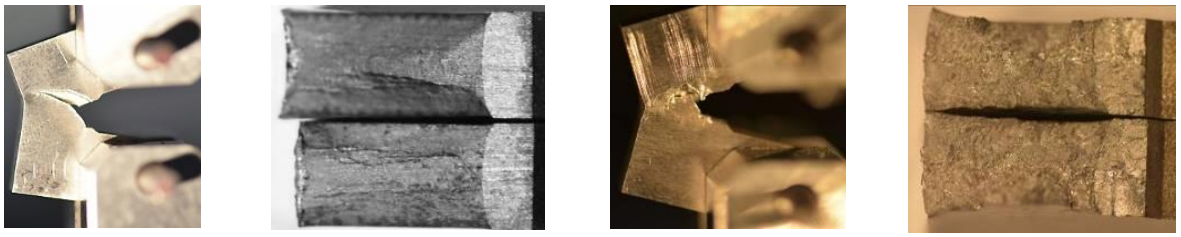

(c1, 2) (d1, 2)

Fig. 3. Mini-compact specimens: (a) Mo–40%Al_2O_3+5Re; (b) 44200 aluminium alloy 20% Al_2O3 Saffil fibres respectively; (c) Ti-6A1-4V alloy; (d) weld zone for the titanium alloy

4. Summary

The paper presents the results showing that besides of the classical compact specimens also application of the mini-compact specimens enables reasonable determination of the Stress Intensity Factor and Crack Tip Opening Displacement for various engineering materials.

References

[1] ASTM E-399, *Standard Test Method for Plane-Strain Fracture Toughness of Metallic Materials*.
[2] ASTM E 1290, *Standard Test Method for Crack-Tip Opening Displacement Fracture Toughness Measurement*.
[3] Kalluri S., Telesman J., Characterization of fatigue crack initiation and propagation in Ti-6A1-4V with electrical potential drop technique, *NASA Technical Memorandum 100877*, July 1998, 25 pages.
[4] Golerthan S., Herberg D., Baruj A., Eggeler G., Compact tension testing of martensitic/pseudoplastic NiTi shape memory alloys, *Materials Science Engineering*, 481-482, 156-159, 2008.
[5] Bajaj D., Sundaram N., Arola D., Striations resulting from fatigue crack growth in dentin, *Fractography of Glasses and Ceramics V: Ceramic Transactions*, James R. Varner, George D. Quinn, Marlene Wightman, 199, 2007.

LABORATORY TESTS AND NUMERICAL SIMULATIONS OF CARPENTRY CORNER LOG JOINTS

A. Pestka[1], and P. Kłosowski[2]

[1,2]*Gdańsk University of Technology, Gdańsk, Poland*

e-mail: [1]*annmlecz@pg.edu.pl,* [2]*klosow@pg.edu.pl*

1. Introduction

Wood is one of the most important building materials and nowadays is very popular. The advantages of wood that cause its popularity are: good strength parameters, weight (wood is much lighter than steel), facility in woodworking and assembling, good thermal and electric insulation. Wood is a natural material and hence it has some disadvantages such as: heterogeneity of the material [1-3] and its sensitivity to moisture, temperature and biological damage [4-7]. Despite numerous disadvantages, the wood is still widely used in civil engineering.

The development of the wooden constructions was mainly related to good strength parameters of wood and its wide availability. The most important role in the wooden structures constructions are carpentry joints. The carpentry connections combine the structure into a whole, transfer the forces and testify highly developed carpentry technique. The paper refers to the corner wall connections. In the historic wooden objects, the most popular were the crowned construction of walls [8]. Two types of joints connecting crowned walls at their corners: short-corner dovetail connection (without protrusion) and saddle notch corner joint (with protrusion) have been analysed in the paper. The carpentry corner log joints are shaped connections, which fulfil the purposes such as transferring the loads and ensuring proper position in relation to each other [8]. The geometry of the joints depends on the place and period of time, where they were used [8-11]. Despite the popularity of the carpentry corner log joints in the historic wooden structures, it is difficult to find research on these carpentry connections (see [12-13]). The knowledge of the behaviour of the carpentry corner log joints is very important due to maintenance, renovation and strengthening of existing elements in preserved historic wooden objects [8, 14].

2. Material and geometry

All the analysed carpentry corner joints models consists of five logs. Each log of the short-corner dovetail connection is 700 mm long. In turn, each log of the saddle notch corner joint is 775 mm long. The cross-section dimensions of both connections are approximately 75 × 135 mm. Due to experimental equipment possibilities, these dimensions are in scale 1:2 to the logs occurring in the real wooden structures [11]. The geometries of the short-corner dovetail connection and the saddle notch corner joint have been presented in Figure 1. All the carpentry connections have been made of the pine wood and most of mechanical properties have been determined during special small scale experiments before the main tests.

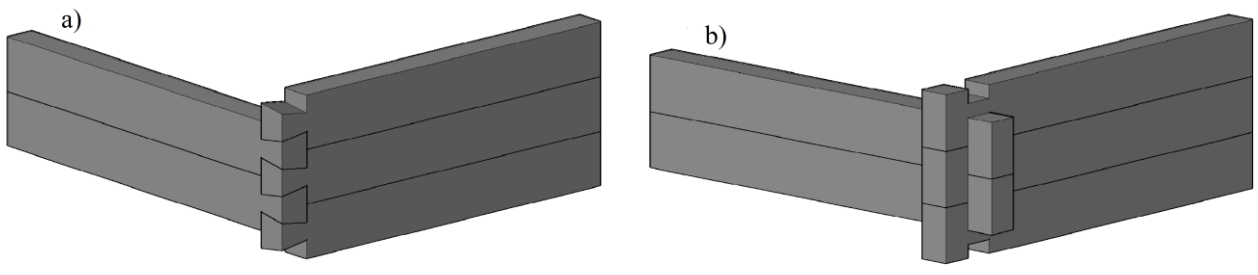

Figure 1: Geometry of carpentry joints: a) short-corner dovetail connection, b) saddle notch corner joint

3. Experimentation and numerical calculation

The laboratory tests have been performed for the short-corner dovetail connection and the saddle notch corner joint. Three tests for both carpentry connections have been carried out using biaxial testing machine. Before testing, each log of a join has been weighted and the wood moisture has been tested using a hygrometer. The displacements of the four joint's points selected at the logs surface have been recorded with an optical extensometer to better describe the connection's deformation.

In order to verify the obtained experimental results, the numerical calculations have been performed. They have been carried out using MSC.Marc software. Both the short-corner dovetail connection and the saddle notch corner joint have been modelled using solid elements. Between logs of the carpentry joints, the contact phenomenon with the proper friction coefficient has been defined. The finite element mesh is more dense in the connections' corners than in the rest of analysed joint to improve the accuracy of stress distribution. The results of experiments and the simulations have been compared and the regions of the potential damages have been established.

More details on conducting experiments and numerical analysis will be presented during the conference.

Acknowledgments
This work has been partially supported by the National Science Centre, Poland (grant No. 2015/17/B/ST8/03260) and by the subsidy for development of young scientists given by the Faculty of Civil and Environmental Engineering, Gdańsk University of Technology.

References

[1] D. W. Green, J. E. Winandy and D. E. Kretschmann. *Wood handbook – Wood as an Engineering Material.* Madison, 1999.
[2] J. Kotwica. *Wooden structures in traditional construction* (in Polish). Publisher Arkady, 2011.
[3] R. Kimbar. *Wood defects* (in Polish). Publisher Robert Kimbar, 2011.
[4] T. P. Nowak, J. Jasieńsko and K. Hamrol-Bielecka. In situ assessment of structural timber using the resistance drilling method – Evaluation of usefulness. *Construction and Building Materials*, 102: 403-415, 2016.
[5] W. Michniewicz. *Wooden construction* (in Polish). Publisher Arkady, 1958.
[6] P. Kozakiewicz. *Effects of temperature and moisture on the compressive strength along fibres selected types of wood of varying density and anatomical structure* (in Polish). Publisher SGGW, 2010.
[7] J. Ważny, J. Karyś et al. *Buildings protection against biological corrosion* (in Polish). Publisher Arkady, 2001.
[8] J. Jasieńko, T. Nowak and A. Karolak. Historical carpentry joints. *Journal of Heritage Conservation,* 40: 58-82, 2014.
[9] R. Cielątkowska. *Translocatio transfer of wooden temples of the three religions* (in Polish). Department of Architecture of Gdańsk University of Technology, 2014.
[10] H. Phleps. *Holzbaukunst der Blockbau*. Karlsruhe, 1942.
[11] F. Kopkowicz. *Polish carpentry* (in Polish). Publisher Arkady, 1958.
[12] A. Klein and M. Grabner. Analysis of Construction Timber in Rural Austria: Wooden Log Walls. *International Journal of Architectural Heritage*, 9: 553-563, 2015.
[13] P. Grossi, T. Sartori, I. Giongo and R. Tomasi. Analysis of timber log-house construction system via experimental testing and analytical modelling. *Construction and Building Materials*, 102: 1127-1144, 2016.
[14] T. P. Nowak, J. Jasieńsko and D. Czepizak. Experimental tests and numerical analysis of historic bent timber elements reinforced with CFRP strips. *Construction and Building Materials*, 40: 197-206, 2013.

QUALITATIVE CORRELATION BETWEEN ACOUSTIC AND ELECTRIC ACTIVITIES IN BRITTLE MATERIALS

Dimos Triantis[1], Ilias Stavrakas[1] and Stavros K. Kourkoulis[2]

(1) Laboratory of Electronic Devices & Materials, University of West Attica, Greece
(2) Laboratory for Testing and Materials, School of Applied Mathematical and Physical Sciences, Department of Mechanics, National Technical University of Athens, 157 73, Athens, Greece

1. Introduction

Low-level electric signals, generated during mechanical loading of specimens made of quasi-brittle materials, provide valuable information about internal damage processes. These signals are the result of formation and growth of micro-cracks [1], which are the origin of electric charges, constituting either electric dipoles or even more complicated electrically charged systems. Indeed, during cracking ionic bonds break, polarising the newly created crack edges, thus creating electric dipoles. These dipoles produce an electric potential across the crack allowing an electric current to flow. This current, denoted as Pressure Stimulated Current (PSC) [2] can be detected and recorded by means of ultra-sensitive electrometers using sensors in the form of pairs of golden electrodes attached on the specimens. In this study an attempt is described to qualitatively correlate the PSC signals with the data provided by another sensing technique, i.e., the Acoustic Emissions (AE) technique, which is worldwide considered as a mature tool for understanding the mechanisms activated before and during failure processes, and also as an efficient Structural Health Monitoring tool [3].

2. The experimental protocol

Prismatic specimens of square cross section, made of either Dionysos marble or cement mortar were subjected to uni-axial compression. The dimensions of their cross section were 50 x 50 mm^2 and their length equal to 100 mm. The experiments were quasi-static under load-control mode. The load was imposed monotonically, until fracture of the specimens, at a constant rate (for the whole duration of each experiment) equal to about 0.35 MPa/s.

During loading, the axial force, the axial strain, the PSC signal and the AE data (of amplitude equal or higher of 45 dB) were recorded as functions of time.

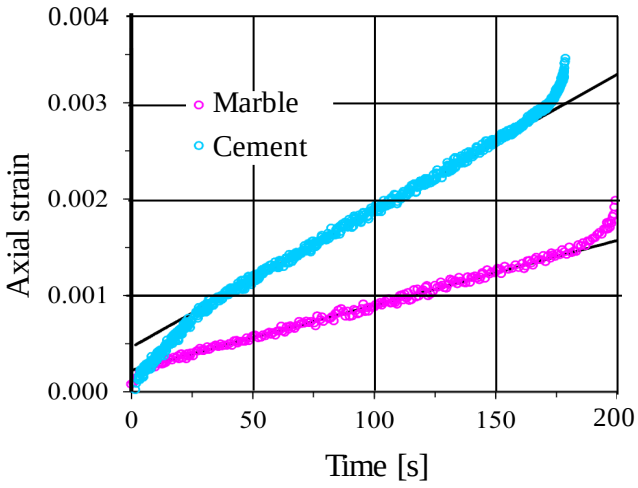

Figure 1: Axial strain vs. time for marble and cement specimens.

In Fig.1 the time evolution of the axial strain for two typical tests is shown. Given that the experiments are load-controlled, these graphs correspond to the stress-strain ones. As it is expected for very brittle materials, both graphs are characterized by almost perfect linearity (excluding an initial region, where bedding errors prevail, and the region very close to the fracture stress, where some non-linearities are expected). The moduli of elasticity determined are equal to about 70 GPa for marble and 20 GPa for cement mortar.

3. Acoustic versus electric activity - The F-function

An alternative method for representing the acoustic emission activity is adopted in the present study, in terms of the F-function, corresponding to the mean frequency of occurrence of AE hits in a time interval, in which n successive hits are recorded. F-function is plotted taking advantage of the interevent times of a sufficient number n of successive hits (it is here assumed that n=50). Each value of the F-function is paired to an average time instant τ of the time instants of the n successive hits used to calculate the specific value of F-function.

The time variation of the F-function and the PSC is plotted in Fig.2, for two characteristic experiments, one for marble (Fig.2a) and one for cement (Fig.2b). The plots are realized against the (t_f -τ) or the (t_f -τ) parameters (where t_f is the time instant of final fracture of the specimens) in logarithmic scales, in an attempt to better enlighten processes at the very last loading steps before the specimens' fracture. In the same figures, the respective time variation of the axial strain is plotted, together with its linear fit.

The overall qualitative similarity between the time evolution of the PSC signal and the F-function is quite striking for both materials. Moreover, it is worth mentioning, that after the time instant t_y, at which the materials enter the non-linear portion of the respective constitutive law (indicated by the dotted red line in Figs.2(a,b)), the plots of both the PSC and the F-function are perfectly described by a power law of the following form:

$$\text{(1)} \qquad \text{PSC or } F = A\left(t_f - \tau\right)^m$$

where A and m are numerically determined constants. The values of the constant m, representing the slope of the fitting lines in Figs.2(a,b), vary in a rather narrow interval (from -0.71 s to -0.84 s for marble and from -1.04 s to -1.20 s for cement).

Finally, it is to be mentioned that, for both the PSC signal and the F-function, the time evolution exhibits a clear maximum value, which is attained a few seconds before the final collapse of the specimens.

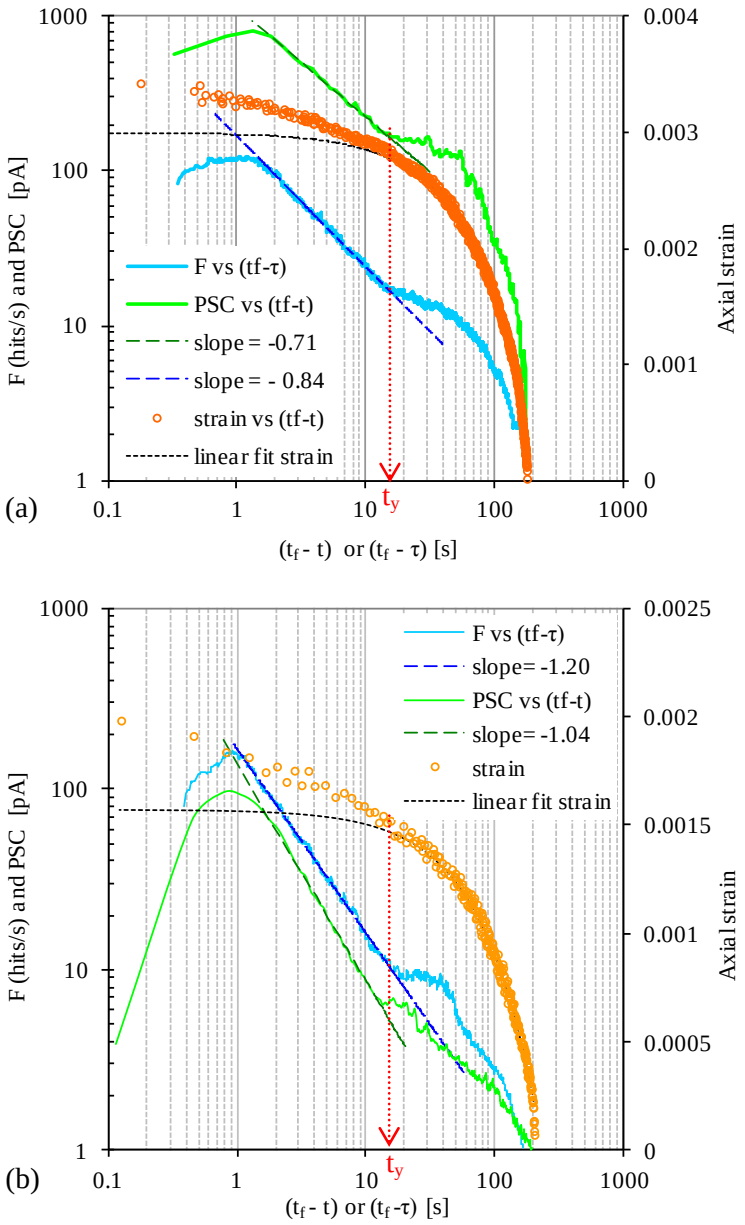

Figure 2: The PSC and the F-function against the (t_f -t) or (t_f -τ) or parameters, in juxtaposition to the respective variation of the axial strain, for marble (a) and cement (b).

4. Concluding remarks

The time evolution of the PSC recorded during compression of brittle materials and the respective one of the acoustic activity, expressed in terms of the F-function, exhibit common qualitative characteristics. Moreover, they provide clear indications that either the materials abandon linearity, exhibiting increased rate of damage (designated by a power law dependence of PSC and F-function on the (t_f-τ) parameter) or that fracture is approaching (designated by the attainment of a maximum value a little while before the specimens' collapse).

References

[1] F. Vallianatos, D. Triantis, A. Tzanis, C. Anastasiadis and I. Stavrakas. Electric earthquake precursors: From laboratory results to field observations, *Phys Chem Earth*, 29:339, 2004.

[2] I. Stavrakas, D. Triantis, Z. Agioutantis, S. Maurigiannakis, V. Saltas, and F. Vallianatos, Pressure stimulated currents in rocks and their correlation with mechanical properties, *Nat Hazard Earth Sys*, 4:563, 2004.

[3] D. Adams, *Health monitoring of structural materials and components. Methods with applications*", John Wiley, 2007.

THERMOMECHANICAL BEHAVIOR OF BEAMS COVERED WITH VISCOELASTIC PATCHES

Asma WERHANI [1, a)], Ali EL HAFIDI[1], Béatrice LAY[1] and Bruno MARTIN[1]

[1]DRIVE EA 1859, Université Bourgogne Franche-Comté, 49 Rue Mademoiselle Bourgeois, 58027 Nevers, France

[a)] e-mail:asma.werhani@u-bourgogne.fr

Keywords: Infrared thermography, thermomechanical study, viscoelastic patches, temperature measurement.

1. Summary

Infrared thermography is a non-destructive test method based on infrared measurement that provides a luminance map of the thermal scene observed, converting to temperature. The thermographic study allows a surface observation of the thermal effects in order to display the result as a film of the temperature distribution [1].

The present study focuses on the detection of volumetric energy sources in beams covered by viscoelastic patches. The objective is to establish a relationship between the mechanical energy dissipated by patches and the temperature elevation, which occurs in areas of high deformations and appears on the surface by thermal conduction [2].

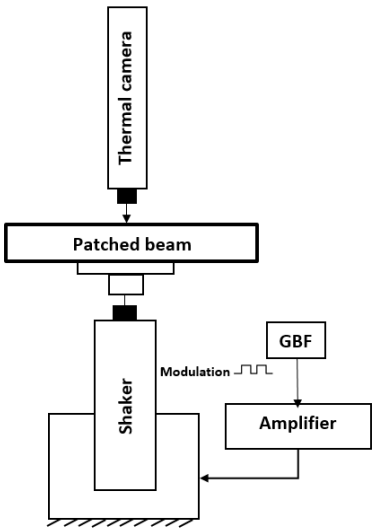

Figure 1: Experimental device

The experimental device is composed of a thermal camera, an aluminum patched beam, a shaker, a generator and a power amplifier.

During the experimental study, an infrared thermal camera was used to obtain a thermal field of the beam surface covered with the patch, without direct contact with the equipment. The aluminum beam (200 x 16 x 1 mm^3) is covered with a black paint of high emissivity.

The viscoelastic patch consists of two layers: a first layer of thickness 0.5 mm, consisting of a viscoelastic material and a second aluminum layer of thickness 0.2 mm. The viscoelastic material has a density of 1190 kg / m^3, a Poisson's ratio of 0.45 and a Young's modulus of 10 MPa.

This energy study was conducted successively at a frequency near the first and the second mode of the patched beam, because more energy is stored in lower order (frequency) modes.

These modes, whose frequency around 20 Hz and 155 Hz, have been identified by a vibration test using an accelerometer and a laser doppler vibrometer (ldv) [3]. The excitation signal was a sine modulated by rectangular signal whose period is around ten seconds. The purpose is to measure the evolution of the surface temperature of the beam, as a function of time.

These tests were performed to observe the response of the viscoelastic material to the stresses appearing in it according to the vibrations undergone. The temperature measurements are made on several zones of 20x20 pixels (corresponding to approximately about 1cm^2) along the beam.

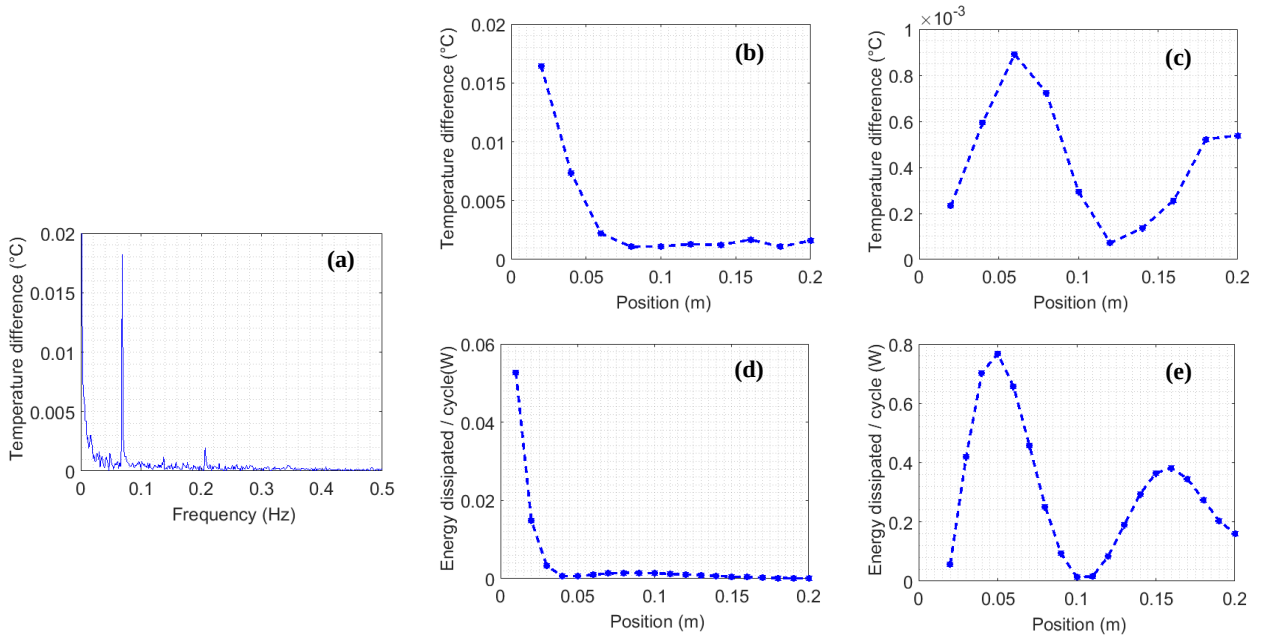

Figure 2: (a) Module of Fourier transform of temperature, Temperature evolution vs position: (b) first mode and (c) second mode, Energy dissipated per cycle: (d) first mode and (e) second mode, calculated with the software Actran.

Because of small temperature differences, and to minimize random noise, averages were calculated on each zone. Fourier transform calculation allows to highlight these differences in temperature, dependent on the modulation frequency (Figure 2a).

Several measurements were conducted along the beam to correlate the temperature difference (Figure 2b and 2c) and the dissipated mechanical volumetric energy generation in the viscoelastic patch (Figure 2d and 2e). Depending on the position of the treatment zones, it is observed that the temperature decreases and the beam dissipates less energy (Figure 2b and 2c). Therefore, we can say that, for the first two modes of vibration, the temperature and the energy have approximately the same profile.

By a reverse method, it is possible, depending on the surface temperature field, to obtain the location of the power density [4]. Therefore, the areas of high mechanical stress in the viscoelastic patch can be localized.

These experimental tests provide information to better understand the behavior of viscoelastic patches according to the mode of the studied structure and especially to verify by a non-contact measurement the efficiency of patch position.

Such studies based on experiment and numerical modeling could be useful, in future work, to optimize positions and dimensions of viscoelastic patches and to locate sticking problems of patches on different structures.

Acknowledgments

We thank the Bourgogne-Franche-Comte region and Nevers agglomeration for their financial support.

References

[1] Usamentiaga, Rubén, et al. "Infrared thermography for temperature measurement and non-destructive testing." Sensors14.7 (2014): 12305-12348.

[2] Moreira, R., and J. Dias Rodrigues. "Constrained damping layer treatments: Finite element modeling." Modal Analysis 10.4 (2004): 575-595.

[3] Montanini, Roberto, and Fabrizio Freni. "Correlation between vibrational mode shapes and viscoelastic heat generation in vibrothermography." NDT & E International 58 (2013): 43-48.

[4] Talai, S. M., D. A. Desai, and P. S. Heyns. "Application of frictional heat signatures for prediction of structural vibrational characteristics." Heat Transfer XIV: Simulation and Experiments in Heat Transfer and its Applications 106 (2016): 65.

EXPERIMENTAL AND NUMERICAL INVESTIGATION ON LASER-ASSISTED BENDING OF PRE-LOADED INCONEL 718 BEAMS

Z. Nowak[1], M. Nowak[1], J. Widlaszewski[1], and P. Kurp[1]

[1]*Institute of Fundamental Technological Research, Polish Academy of Sciences, Pawinskiego 5b, 02-106 Warsaw, Poland*
[2]*Department of Industrial Laser Systems, Kielce University of Technology al. Tysiąclecia Państwa Polskiego 7 , 25-314 Kielce, Poland*

e-mail: znowak@ippt.pan.pl, nowakm@ippt.pan.pl, jwidl@ippt.pan.pl, pkurp@tu.kielce.pl

1. Introduction

The polycrystalline nickel-based superalloys are typically used in components that work at elevated temperature in aggressive media. The key feature of these alloys is that they are able to keep their mechanical properties at relatively high temperatures. This makes them ideal candidates to manufacture aircraft engine components such as casings, diffusers or blades. The operating temperatures of turbine casings generally range from 400 °C to 800 °C. Increase of working temperature leads to the reduction of deformation resistance. The aim of this paper is to present experimental investigation and numerical simulation of laser-assisted bending of Inconel 718 alloy. The research is directed towards applications of hybrid thermal-mechanical forming in manufacturing of thin-walled components of aircraft engines [1], [2]. A good understanding of deformation behavior of Inconel 718 sheet metal within wide range of temperatures is a prerequisite for reliable numerical simulation of laser-assisted bending process and for processing parameters optimization.

2. Material and experiment

The chemical composition of the used Inconel 718 alloy (wt%) is the following: 52.9 Ni, 19.83 Cr, 3.12 Mo, 4.83 Nb, 0.05 Co, 0.29 Mn, 0.14 Si, >17.1 Fe, 0.60 Al, 1.04 Ti. A commercial Inconel 718 sheet blank in the as-received state, with an average initial grain size of 17.5 μm, was used in this work. The 1.0 mm thick and 20 mm wide specimens tested in the present investigation were laser-cut from the rolled sheet metal.

The experimental setup for laser-assisted bending of thin beams under mechanical load and heating with a moving laser beam is presented in Fig. 1 (left) (1 - sample, 2- laser beam, 3 - holder of the weights, 4 - auxiliary plate, 5 - the optical displacement sensor).

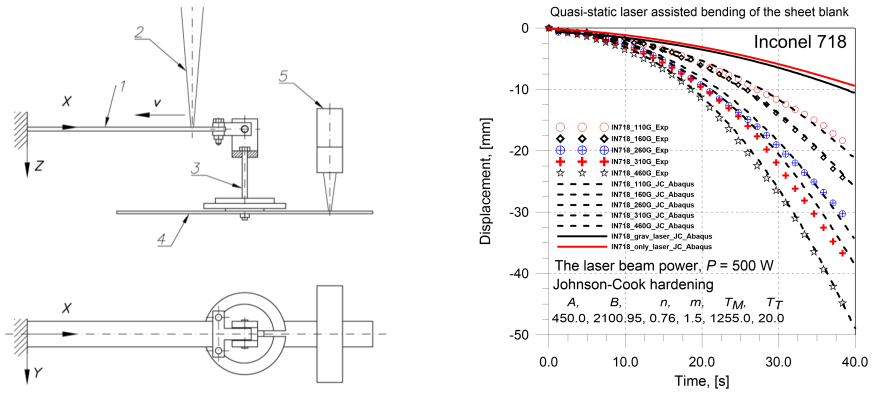

Figure 1: The scheme of laser-assisted bending of thin beams under mechanical load and heated with a moving laser beam (left) and a comparison of the free-end deflection U as a function of time, measured in experiments and calculated numerically for different mechanical loads.

In experiments of laser-assisted bending a CO_2 TRUMPF TruFlow6000 laser operating in the continuous wave (CW) mode and emitting radiation of 10.6 micrometres wavelength was used. The applied optical head produced approximately rectangular 20 x 2 mm laser spot on the material surface. The laser spot covered the whole

width of the laser-treated specimen. Laser beam of power 200 W had velocity 200 mm/min (3.33 mm/s) with respect to the specimen. In order to increase coupling of laser power, each specimen was coated with a black paint. The laser processing parameters were chosen so as to obtain the highest material temperature of 750 °C.

Deformation of the specimen was measured using an optical displacement sensor MicroEpsilon LLT1700. The gravitational load of the sample originated from its own weight and from the weights (external load Q) attached to its free end, at a distance of 175 mm from the fixture. A series of experiments was conducted with different values of the external load Q in the range from 1.1 N to 4.5 N (110 to 460 G). After the specimen had been loaded mechanically by its own weight and the external load Q (gravitational load), it was heated with a laser beam moving along longitudinal axis x, starting from the position x = 150 mm towards the fixed end of sample (x = 0).

3. Numerical simulations and results

In order to study the behavior of the Inconel 718 alloy during laser-assisted bending under static mechanical load, a series of computer simulations was performed. Different constitutive models were used in the simulations. It was concluded that for the process of hybrid thermal-mechanical bending a good agreement between calculations and experimental results is obtained using the isotropic strain hardening model with the Huber-Mises-Hencky yield criterion and the flow stress (σ) described by the Johnson-Cook model [3], which is defined as a function of plastic strain (ε^{pl}), the strain rate (here $\dot{\varepsilon} = 0.003\ 1/s$) and temperature ($T$) in the form $\sigma = (A + B \cdot (\varepsilon^{pl})^n)(1 + C{\cdot}ln(\frac{\dot{\varepsilon}}{\dot{\varepsilon}_0}))(1 - (T^*)^m)$, where $\dot{\varepsilon}_0$ (0.001 s^{-1} in this work) is the reference strain rate, $T^* = (T - T_r)/(T_m - T_r)$, T_m is the melting temperature (1250 °C in this work) and the reference temperature T_r is determined as 20 °C in this work. The values of A, B, n, C and m are obtained from the fitting based on experimental data, and are as following: A=450 MPa, B=2100.95 MPa, n=0.76, C=0.02 and m=1.5.

Numerical simulations were conducted using the commercial finite element method program ABAQUS. The influence of the plastic deformation on material temperature and thermal effects due to microstructural changes were neglected for the considered nickel-based superalloy. The thermal-mechanical sequentially coupled quasi-static analysis was conducted in two separate steps: (1) determination of temperature field under prescribed heat load and boundary conditions, and (2) elastic-plastic incremental analysis of stress and strain due to the mechanical load and thermal load, using the calculated temperature field. Symmetry condition in the thermal problem was accounted for by considering the plane of symmetry as adiabatic, whereas heat convection and radiation was allowed on all other surfaces of the model. The DC3D8 elements for the thermal problem, and compatible elements C3D8 for mechanical analysis were used. A comparison of the free-end of sample deflection U as measured in experiments and calculated numerically as a function of time for mechanical loads Q 110 G (1.08 N), 160 G (1.57 N), 260 G (2.55 N), 310 G (3.04 N) and 460 G (4.51 N) is presented in Fig. 1 (right).

Experimental study and numerical simulations showed that forming performance of Inconel 718 plates can be significantly improved by laser heating under mechanical pre-loading. With the identified model of the constitutive response of Inconel 718 sheet blanks various forming processes with similar conditions can be studied.

Acknowledgments The research reported herein was supported by a grant from the National Centre for Research and Development (No. PBS3/A5/47/2015).

References

[1] Z. Mucha and J. Widłaszewski and P. Kurp and K. Mulczyk (2016). Mechanically assisted laser forming of thin beams, *Proc. SPIE, doi:10.1117/12.2262114*, **10159**, 1-10.

[2] J. Widłaszewski and M. Nowak and Z. Nowak and P. Kurp (2017). Laser-assisted forming of thin-walled profiles, *Metal Forming*, **XXVIII (3)**, 183-198.

[3] G.R. Johnson and W.H. Cook (1985). Fracture characteristics of three metals subjected to various strains, strain rates, temperatures and pressures, *Engineering Fracture Mechanics*, **21**, 31-48.

Session S10: Geomechanics and multiscale modelling of materials

Organizers: Z. Mróz (IPPT PAN, Warsaw), S. Pietruszczak (McMaster University, Ontario), R. Michalowski (University of Michigan), J. Tejchman (Gdansk UT)

COUPLED APPROACH DEM/CFD FOR MODELLING HYDRAULIC FRACKING PROCESS IN ROCKS

M. Krzaczek[1], J. Kozicki[1] and J. Tejchman[1]

Gdańsk University of Technology, Gdańsk, Poland

mkrzacze@pg.edu.pl, jkozicki@pg.edu.pl, tejchmk@pg.edu.pl

1. General

Hydraulic fracking is a well stimulation technique to increase the productivity of petroleum reservoirs in which rocks are fractured by a pressurized liquid. The process involves the high-pressure injection of fluid (primarily water, containing sand or other proppants suspended with the aid of thickening agents) into a wellbore to create cracks in the deep-rock formations through which natural gas and petroleum will flow more freely. When the hydraulic pressure is removed from the well, small grains of hydraulic fracturing proppants hold the fractures open. The modelling of the fluid-driven fracture propagation into rocks comprises the coupling of different physical mechanisms, including deformation of the solid skeleton induced by the fluid pressure on fracture surfaces, flow of the pore fluid along new fractures and through the region of surrounding existing fractures and pronounced heat changes.

There are two main approaches for modelling the propagation of hydraulically driven complex fracture patterns: continuum-based models and discontinuous meso-scale models at the grain level. The continuum-based meso-scale models are obviously unable to fully render meso-scale coupled thermal-hydraulic-mechanical effects. As compared with conventional continuum mechanics methodologies used in most of existing numerical studies, discontinuous meso-scale models at the grain level (such as the discrete element method (DEM)) are more realistic since they allow for a direct simulation of meso-structure and are very useful for studies of the mechanism of the initiation, growth and formation of fractures [1], [2]. The commonly used approach to describe fluid flow and predict interaction mechanisms between flowing fluid and particles is the pore-network modelling, assuming that fluid flows through channels connecting pores that accumulate pressure. In this approach, a simplified laminar viscous Poiseuille flow [3] or Stokes flow [4] are usually assumed. The pore network model is built through a weighted Delaunay triangulation over the discrete element packing. The finite volume method is usually applied to solve the governing equations of motion. [3]. The model may describe incompressible [5] or compressible fluids [6].

Most of coupled DEM/CFD approaches meet the following simplified assumptions [3]: isothermal conditions, single phase flow, laminar fluid flow in pores and fractures and small grains displacements in rocks. In the paper, a significant extension of the pore-network model is proposed (called virtual pore network (VPN)).

2. Fluid flow model and coupled DEM/CFD simulations

The VPN model accurately reproduces grains and voids geometry (pores and fractures). The voids and fractures (fluid domain) are discretized with the aid of triangular (in 2D) or tetrahedral (in 3D) control volumes (called the virtual pores). Similarly as in the pore-network method, the virtual pores are connected by channels that connect their gravity centres The virtual pores are connected by channels that connect their gravity centres. Fluid flows in channels while virtual pores accumulate pressure and volume fraction of phases. The Poiseuille flow model is assumed in channels. To model multiphase flow of compressible fluid, the fluid volume (VOF) model [7] was implemented. VOF is a surface-tracking technique applied to a fixed

Eulerian mesh and can simulate two or more immiscible fluids by solving a single set of equations. Hence, the Poiseuille flow equation can be expressed for 3D problems and secondary-phase fluids as:

$$\frac{\partial}{\partial t}\left(\alpha_q \rho f_q h\right) = \frac{\partial}{\partial x}\left(\frac{\alpha_q \rho_q h^3}{12\mu_q}\frac{\partial P}{\partial x}\right) + \frac{\partial}{\partial z}\left(\frac{\alpha_q \rho_q h^3}{12\mu_q}\frac{\partial P}{\partial z}\right), \quad (1)$$

where index q denotes the liquid phase, α_q is the volume fraction, ρ_q is the density, h is the hydraulic channel aperture, μ_q is the dynamic viscosity and P denotes the pressure. Equation 1 is not solved for the gas phase that is computed based on the following constraint $\sum_{q=1}^{2} \alpha_q = 1$. In order to capture large grain displacements in rocks, a special transformation algorithm was applied, based on the assumption that mass is a topological invariant. This algorithm transforms simulation results computed for the old grid into the new grid that may be significantly geometrically deformed. It enables to investigate fluid flow in topologically variable pores and fractures (i.e. some pores and fractures may vanish and new ones may appear).

The mesoscopic mechanical constants for rocks were calibrated with preliminary DEM simulations of uniaxial compression and splitting tension [2]. The rock material was described as a 3-4-phase material. VPN was calibrated by simulating permeability tests. The series of numerical coupled DEM/CFD analyses were performed to study the process of filling pores and fractures with the fracturing fluid in rock specimens. The influence of the fluid pressure, fluid velocity, initial rock porosity, location and number of existing discontinuities (faults, joints, bedding layers) on the initiation and propagation of hydraulic fractures was carefully investigated. The numerical results were qualitatively in agreement with the experiments with respect to the fracture pattern.

3. Conclusions

In contrast to commonly used pore-network approaches, VPN reproduces more realistically fluid flow in pores and fractures in rocks and enables also to investigate multi-phase fluid flow. A strong relationship between the initial fraction of the liquid phase in pores and fractures and the propagation speed of the hydro-fracking process was observed in coupled DEM/CFD analyzes. The impact of initially existing discontinuities in rocks on the hydraulic fracture geometry was pronounced.

4. References

[1] M. Nitka and J. Tejchman, J. A three-dimensional meso scale approach to concrete fracture based on combined DEM with X-ray μCT images. *Cement and Concrete Research*, 107: 11-29, 2018.

[2] J. Suchorzewski, J. Tejchman and M. Nitka, M. Experimental and numerical investigations of concrete behaviour at meso-level during quasi-static splitting tension. *Theoretical and Applied Fracture Mechanics*, doi: 10.1016/j.tafmec.2017.10.011, 2017.

[3] J. S. Yoon, A. Zang and O. Stephansson, O. Numerical investigation on optimized stimulation of intact and naturally fractured deep geothermal reservoirs using hydro-mechanical coupled discrete particles joints model. *Geothermics*, 52: 165-184, 2014.

[4] A. T. Tong, E. Catalano and B. Chareyre, B. Pore-Scale Flow Simulations: Model Predictions Compared with Experiments on Bi-Dispersed Granular Assemblies. Oil & Gas Science and Technology – Rev. *IFP Energies Nouvelles*, 67(5), 743-752, 2012.

[5] B. Chareyre, A. Cortis, E. Catalano and E. Barthélémy. Pore-scale modeling of viscous flow and induced forces in dense sphere packings. *Transport in Porous Media*, 94(2): 595-615, 2012.

[6] L. Scholtès and F. Donzé. Modelling progressive failure in fractured rock masses using a 3D discrete element method. *I. Journal of Rock Mechanics and Mining Sciences*, 52, 18-30, 2012.

[7] C. W. Hirt and B. D. Nichols. Volume of fluid (VOF) method for the dynamics of free boundaries. *Journal of Computational Physics*, 39(1), 201-225, 1981.

MODELLING OF SEA-ICE PACK THERMODYNAMICS BY THE SMOOTHED PARTICLE HYDRODYNAMICS METHOD

Ryszard Staroszczyk

Institute of Hydro-Engineering, Polish Academy of Sciences, ul. Kościerska 7, Gdańsk, Poland

e-mail: rstar@ibwpan.gda.pl

1. Introduction

A typical sea-ice pack is a complex thermodynamic system comprising a multitude of floes of different size and geometry, driven by wind and water drag stresses, and subject to surface and basal freezing and melting in response to current local mechanical and thermal forcing. As individual floes move about and interact, in either ductile or brittle manner, they break, merge and override one another, giving rise to large variations in local ice thickness and ice area fraction (concentration). Since broken ice cover cannot carry tensile stresses, the mechanical behaviour of an ice pack in converging flow is remarkably different from that in diverging flow. The consequence of this is the development and subsequent propagation of interfaces that separate converging and diverging regions in sea ice, often leading to the fragmentation of an initially coherent pack domain. An important feature is also a significant change of the planar geometry of a domain occupied by the ice pack, associated with large displacements of boundaries between the coherent ice and the open sea. All these physical mechanisms are difficult to treat both mathematically and numerically, and significantly increase the complexity of numerical algorithms and the cost of calculations.

The equations describing the thermodynamic behaviour of sea ice have been derived by treating the problem as a two-dimensional on the 'horizontal' surface (the free surface of the ocean), and by integrating the mass, momentum and energy balances of the ice and lead water through the ice pack thickness (Gray and Morland [1]). The fundamental variables involved in the description are the local mean ice thickness, the ice concentration and two components of the velocity field. Sea ice is commonly treated as a viscous-plastic material (Hibler [2]), and its rheology is described by a constitutive law that relates the depth-integrated stresses to the two-dimensional deformation-rate. Since the strength of ice in tension is zero, the behaviour of an ice pack dramatically depends on whether the flow is locally converging or diverging. As a consequence, the structure of equations changes across interfaces separating converging and diverging flow regions, which can give rise to instabilities (Schulkes et al. [3], Guba et al. [4]) when solving the sea-ice flow equations by a numerical method.

In the present work, the sea-ice flow problem is solved by applying a mesh-free approach known as the Smoothed Particle Hydrodynamics (SPH). The SPH method is used to construct a numerical model which is applied to simulate the evolution of a coherent ice pack driven by wind stresses and subject to the mechanisms of ice grow or decay due to the phase changes (freezing of water and melting of ice). The thermodynamic processes resulting in the changes in ice mass are modelled in a simplified manner, by expressing the ice growth-rates by means of a single function of two arguments: local air temperature and current ice thickness. The latter function approximates the sea ice behaviour observed during a typical Arctic winter [2]. The ice is treated as a viscous-plastic material, and its rheology is described by a viscous fluid flow law, with two viscosity parameters bounded by an elliptic yield curve [2].

2. Smoothed particle hydrodynamics method

The Smoothed Particle Hydrodynamics (SPH) method was invented in 1977 by Lucy [5] and Gingold and Monaghan [6], but for nearly two subsequent decades its use was solely restricted to the field of astrophysics. Only in the mid 1990s some attractive features of the SPH method brought attention of the solid mechanics community, and ever since the interest in the method has been steadily growing and it has found applications in many branches of physics, applied mechanics and engineering, see Monaghan [7, 8]. The SPH method is fully Lagrangian and mesh-free, and owing to the fact that no connectivity between the particles is needed, the method has a natural capability of dealing with problems in which large deformations occur and surfaces of material discontinuity develop and subsequently propagate through the medium. Therefore, it seems that

the SPH approach is particularly well suited to solving the sea-ice pack flow problems, in which the application of conventional mesh-based discrete methods (such as the finite-difference or finite-element techniques, see Morland and Staroszczyk [9]) is difficult or entails significant numerical problems.

3. Sea-ice pack flow simulations

The SPH model has been implemented to simulate the evolution of a large sea-ice pack (of horizontal dimensions measured in tens or hundreds of kilometres) subject to the action of wind. First, the thermodynamic effects are ignored, and the model predictions for the viscous-plastic ice rheology are compared with those previously obtained for a non-linearly viscous rheology (Staroszczyk [10]), for an ice field under the action of wind of constant speed and direction. By the analogy with previously investigated problems solved by the finite-element method [3,9], an idealized, initially rectangular, geometry of the ice pack has been adopted, with two or three adjacent sides of the rectangle at solid boundaries (representing sea coasts), and the remaining two or one side(s) at open sea boundary. Then, the thermodynamic effects are included in the simulations, and a flow problem of an ice pack, initially of a uniform thickness and ice concentration, is solved. The pack is driven by a vortex geostrophic wind field, acting over at least several days, with the wind vortex centre located at the open sea off the initially rectangular ice cover. It seems that such a boundary value problem contains all the essential features which occur in realistic sea ice flows, and thus can serve as a test case for assessing the stability and performance of the applied mesh-free discrete model. The results of simulations illustrate the effects of the two rheological theories on the evolution of the ice pack, including the variations of the ice thickness and the ice area fraction in space and time. Further, the effects of different boundary conditions (free-slip and no-slip) assumed at the coast–ice interface are explored. Of particular interest are the changes in the position of an open sea boundary, as the tracking of the coherent sea-ice pack extent under given weather conditions is of practical importance to the navigation and the oil industry in the Arctic.

4. References

[1] J. M. N. T. Gray and L. W. Morland (1994). A two-dimensional model for the dynamics of sea ice. *Phil. Trans. R. Soc. Lond. A*, **347**, 219–290.

[2] W. D. Hibler (1979). A dynamic thermodynamic sea ice model. *J. Phys. Ocean*, **9**, 815-845.

[3] R. M. S. M. Schulkes, L. W. Morland and R. Staroszczyk (1998). A finite element treatment of sea ice dynamics for different ice rheologies. *Int. J. Num. Anal. Meth. Geomech.*, **22** (3), 153–174.

[4] O. Guba, J. Lorenz and D. Sulsky (2013). On well-posedness of the viscous-plastic sea ice model. *J. Phys. Oceanogr*., **43**, 2185–2199

[5] L. B. Lucy (1977). A numerical approach to the testing of the fission hypothesis. *Astron. J.*, **82** (12), 1013–1024.

[6] R. A. Gingold and J. J. Monaghan (1977). Smoothed particle hydrodynamics: theory and application to non-spherical stars. *Mon. Not. R. Astron. Soc.*, **181**, 375–389.

[7] J. J. Monaghan (1992). Smoothed particle hydrodynamics. *Annu. Rev. Astron. Astrophys.*, **30**, 543–574.

[8] J. J. Monaghan (2012). Smoothed particle hydrodynamics and its diverse applications. *Annu. Rev. Fluid Mech.*, **44**, 323–346.

[9] L. W. Morland and R. Staroszczyk (1998). A material coordinate treatment of the sea-ice dynamics equations. *Proc. R. Soc. Lond. A*, **454**, 2819–2857.

[10] R. Staroszczyk (2017). SPH modelling of sea-ice pack dynamics. *Arch. Hydro-Eng. Environ. Mech*., **64** (2), 115–137.

COMPARISON BETWEEN NUMERICAL ANALYSIS AND ACTUAL RESULTS FOR A PULL-OUT TEST

J. Gontarz[1], J. Podgórski[1], Józef Jonak[2], Marek Kalita[3], Michał Siegmund[3]

[1]*Faculty of Civil Engineering and Architecture, Lublin University of Technology, Nadbystrzycka 40, Lublin, Poland*

[2]*Faculty of Mechanical Engineering, Lublin University of Technology, Nadbystrzycka 36, Lublin, Poland*

[3]*KOMAG Institute of Mining Technology, Pszczynska 37, Gliwice, Poland*

e-mail: j.gontarz@pollub.pl, j.podgorski@pollub.pl, j.jonak@pollub.pl

1. Introduction

The authors of this paper attended to analyze the pull-out test in which a pre-set self-undercut anchor is pulled out of a stone surface. The research consisted in finding the parameters of the selected material - sandstone from the Braciszów quarry. Next, a pull-out test was modeled in the Abaqus program and computer analysis was performed using X-FEM elements, which are elements simulating the crack independent of the finite element mesh [1]. The results obtained in the calculations were compared with the pull-out tests performed on actual rock. The aim of the described research is to find a way to calculate the force of pulling out the anchor for any material and for any length of anchoring.

The HILTI HDA-P M20x250/100 anchor was adopted for pull-out tests. To mount this anchor, it is placed in a prepared hole in a rock surface, and then the anchor is pressed. Then while drilling it undercuts itself with deflecting elements. Scheme of mounting the anchor is shown in Figure 1a.

2. Description of the computer model

The pull-out test was modeled in 2D stress state as an axially symmetrical task. The computational models is presented in Figure 1b, where h is the length of the anchor. The load was simulated by the y-direction displacement. The boundary conditions were modeled on the right and bottom edge. The size of the model was assumed to be large enough so that the boundary conditions did not affect the result.

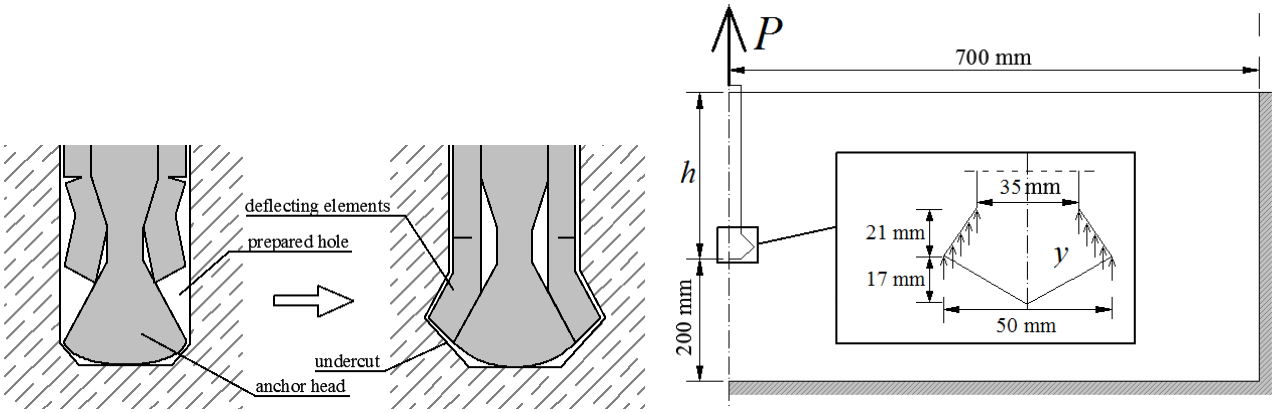

a) b)

Figure 1: a) Scheme of mounting the anchor, b) Scheme of the task.

3. Material parameters

Several laboratory tests on the described sandstone were performed. Compressive strength tests were carried out with uniaxial compression. The Young modulus and the Poisson ratio were obtained with the help of reading the vertical and horizontal strains in the samples. Tensile strength was also obtained using a modified Brazilian test. The exact tensile strength was obtained based on the analysis of the stress field in the Abaqus

code and on the author's previous work [2]. Critical strain energy release rate in mode I was also obtained from the test of three-point bending of beams with notches. This value was calculated with the Bower equation [3]. The results of the experiments gave the following values: compressive strength f_c = 202.7 MPa, tensile strength f_t = 7.945 MPa, Young modulus E = 15.984 GPa, Poisson ratio ν = 0.275, Critical strain energy release rate G_{Ic} = 0.257 N/mm.

4. Computer simulation and actual pull-out test

The above material parameters were used to model the test in Abaqus for an 8 cm anchoring. The view of the damaged model is shown in Figure 2a. As it can be seen, the crack starts to propagate horizontally near the upper edge. For various program settings and different mesh, it was not possible to cause the crack to go through to the end, probably that there is a stress state with which the Abaqus program can't cope. The pulling-out force at the beginning grows and then decrease after reaching the radius of the pulling-out fragment of about 8 cm (Figure 2b), where the expected radius of the broken cone is 18.5 cm, basing on the crack angle. The maximum force was about 132 kN. Tests in the quarry were also made on the same stone and for the same depth of the anchor (Figure 2c). For three successful tests, the average pulling-out force is 162 kN. Inspection of the damaged stones allowed to state that the shape of the broken fragment is very similar to that in the computer simulation.

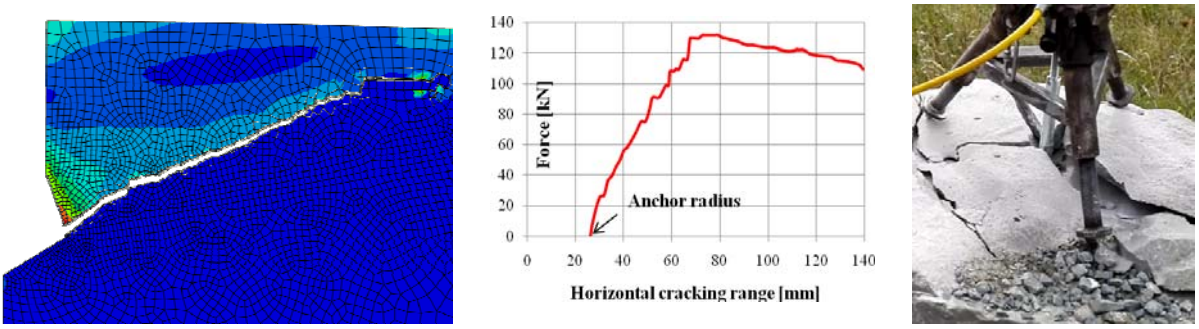

a) b) c)

Figure 2: Pull-out test. a) crack path obtained by computer simulation with Abaqus code, b) dependence of force on the crack's range, c) view of the detached fragment of the actual rock.

5. Summary

As it can be seen, the above results are similar. However, the results depend on many factors. The tested material is very heterogeneous because the test results were very different. For example, the tensile strength results fluctuated from 5.3 MPa to 10.6 MPa. Similarly, the pull-out test on actual rocks gave a result between 112 kN and 212 kN. Therefore, it can't be concluded that the X-FEM method in Abaqus, and in particular the given parameters, allow to obtain the correct result. It is therefore necessary to perform more pull-out tests on the actual rock. It is possible that it will be necessary to re-analyze all for a more homogeneous material.

Acknowledgments This research was sponsored by the Lublin University of Technology Statutory Funds S16/2017 and co-financed by the Polish National Science Center, project RODEST nr 2015/19/B/ST10/02817.

References

[1] S. Mohammadi, Extended Finite Element Method: Extended Finite Element Method: for Fracture Analysis of Structures, Wiley-Blackwell, 2007.
[2] J. Podgórski and J. Gontarz, Explanation of the mechanism of destruction of the cylindrical sample in the Brazilian test. *Advances in Mechanics: Theoretical, Computational and Interdisciplinary Issues*., CRC Press, 2016.
[3] A. F. Bower, Applied mechanics of solids, CRC Press, 2009.

FUNDAMENTALS OF GEOMETRICAL AND PHYSICAL CONCEPT OF PORE SPACE TORTUOSITY

M. Cieszko,

Institute of Mechanics and Applied Computer Science,
Kazimierz Wielki University, Bydgoszcz, Poland

e-mail: cieszko@ukw.edu.pl

Abstract

Parameter of the pore tortuosity together with the volume porosity and permeability form a set of basic parameters characterizing macroscopic pore space structure of permeable porous materials. This parameter plays important role in all transport processes taking place in porous materials. This concerns among others the flow of fluids, electrical current, and also diffusion and heat conduction. The importance of general description of the pore space structure is determined by the fact that engineering of transport processes in porous media is directly related with engineering of pore structure. In spite of the fundamental character of the tortuosity parameter and great number of publications devoted to its definition, analysis of the physical and geometrical meaning and the methods of determination (e.g. [1-3]), there is still no commonly accepted general definition of this macroscopic notion and its relation with microscopic pore structure. This problem becomes even more complicated in materials with anisotropic pore space structure.

The aim of the paper is to present the general solution of the problem of macroscopic description of the anisotropic pore space structure, which allows precise and consistent formulation of definitions of macroscopic parameters of pore space structure: pore tortuosity and surface porosity, and also their natural introduction into macroscopic description of processes occurring in porous materials. The general character of these definitions is also a necessary condition for formulation of general representation of these parameters by quantities characterizing microscopic pore structure.

Considerations have been based on the model assumptions presented in papers [4] and [5]. It was assumed that at the macroscopic point of view interconnected pores in permeable porous materials form anisotropic space the structure of which is determined by its metric and this space is modelled as Minkowski metric space. Such approach to this problem raises a number of consequences: a) modelling of the pore space structure is a primary problem in comparison to the modelling of processes occurring in the pore space; b) parameters of the pore space structure are defined by the metric of the space; c) pore structure parameters codetermine the course of each process occurring in the pore space and are independent of them.

Application of the concept of Minkowski metric space as a model of anisotropic pore space enables precise and consistent definition of macroscopic measures of distance, surface and volume in this space, and as a consequence, also definition of macroscopic parameters of pore space structure: pore tortuosity and surface porosity, directly related to these measures. It was shown that these parameters and their tensor characteristics are directly defined by the metric tensor of the pore space. This means that character of these parameters is purely geometrical.

Definitions of the pore structure parameters formulated based on the concept of Minkowski metric space are also the basis for precise determination of their relation with quantities characterising microscopic pore structure. General form of such relation for surface porosity and pore tortuosity have been obtained requiring the full representation of macroscopic density of fluid kinetic energy in the potential flow, by microscopic velocity field.

It was shown that such approach is directly related with the variational problem of minimization of scalar field inhomogeneity defined in the pore region the measure of which is the integral of square of gradient of this scalar field, called Dirichlet integral or Dirichlet energy. Euler equation for this problem takes form of the Laplace equation that is the basic equation describing various types of potential transport. This equation do not contain any material characteristics, and due to the pure geometrical character of the variational problem, its solutions are contingent also upon geometry of the region on which it is defined. In the case of potential flow of fluid, the variational problem means minimization of kinetic energy of fluid in the considered pore region.

The obtained microscopic representations of the macroscopic parameters of pore tortuosity and surface porosity have been applied for determination of these parameters in the exemplary pore space structures of simple pore space geometry. This allows one to demonstrate the influence of microscopic parameters of pore geometry on the pore tortuosity and surface porosity.

References

[1] Carman P., *Fluid Flow through Granular Beds*, Trans. Inst. Chem. Engng, 15, 150-166, 1937.
[2] Lorentz P. B., *Tortuosity in Porous Media*, Nature, 189, 386-387, 1961.
[3] Clennel M., *Tortuosity: A Guide through the Maze*, in Developments in Petrophysics, eds Lovell M.A. & Harvey P.K., Geological Society London Special Publication No 122: 299-344, 1997.
[4] Cieszko M., *Fluid Mechanics in Anisotropic Pore Space of Permeable Materials. Application of Minkowski Metric Space* (in polish), Wyd. Uniwersytetu Kazimierza Wielkiego, Bydgoszcz 2001.
[5] Cieszko M., *Description of Anisotropic Pore Space Structure of Permeable Materials Based on Minkowski Metric Space*, Archives of Mechanics, 61, 6 (425-444), 2009.

THE VISCOUS RELATION FOR THE INITIAL ISOTROPIC RESPONSE OF ICE IN ICE-SHEET FLOW

L. W. Morland[1] and R. Staroszczyk[2]

[1]*School of Mathematice, University of East Anglia, Norwich NR4 7TJ, UK.*
[2]*Institute of Hydroengineering, Polish Academy of Sciences, ul. Warynskiego 17, 71-310 Szczecin,Poland.*

Abstract

On the large time-scales of ice-sheet ow, the ice is assumed to be incompressible and commonly to obey a non-linearly viscous fluid constitutive law for the shear response, neglecting the shorter time-scale viscoelastic effects. That is, at constant temperature, the deviatoric stress depends only on the strain-rate. The pressure is a workless constraint, not given by any constitutive law, but determined by the momentum balances and boundary conditions. Such a viscous law, necessarily isotropic by material frame indifference, has a general quadratic representation, with alternative, but equivalent, stress and strain-rate formulations. However, it is still common practice to ignore the quadratic term and adopt a simple relation in which the deviatoric stress is co-axial with the strain-rate, and which depends on only one of the two stress (or strain-rate) invariants. Standard single stress component tests, uniaxial compression or simple shear, are not sufficient to determine the general form, but either can determine the response coefficient dependence on one invariant in the simple co-axial form. Early experiments showed that uniaxial compression and combined compression and shear data yielded different response coefficient dependences, but this has been ignored and the uniaxial correlation has been adopted. Here we show that it is necessary to include a quadratic term to correlate with independent uniaxial and shear data, but dependence on one invariant is sufficient. The stress and strain-rate configurations in combined uniaxial stress and simple shear experiments is analysed to derive a universal relation independent of the actual response coefficients in a general viscous relation, which is examined for the data determined by a set of such experiments, showing inconsistencies. Such data cannot then be applied to test the consistency of any viscous relation.

EFFECT OF SOIL CONSOLIDATION ON THE STRESS AND DEFORMATION OF PIPELINE IN MUSKEG

X.S. Zheng[1], M.L. Rodriguez[1], K. Zhang[2], and L.P. Li[1]

[1]*Department of Mechanical & Manufacturing Engineering, University of Calgary, Calgary, Canada*
[2]*Stress Engineering Services Canada, Calgary, Canada*

e-mail: Leping.Li@ucalgary.ca

1. Introduction

Pipeline stress response to mechanical loading is typically intricate when crossing soft soil. The pipelines in muskeg are subjected to unstable loadings due to seasonal water table variation, fluid pressure change, and soil consolidation. These loading can alter the mode of large deformation, which sometimes results in stability issues, e.g. global buckling. In addition, settlement due to soil consolidation for liquid pipelines may result in sustained stress concerns. Pipe-soil analysis typically involves finite element method with beam elements and discrete soil-springs. However, the soil-spring calculation methods, e.g. as suggested by The American Lifeline Alliance or The Pipeline Research Council International, are not considered applicable for peat/muskeg soil. Three-dimensional continuum modeling thus become necessary to better understand effects of unstable soil loadings on pipeline stress. The objective of the present study is to determine the stress and deformation due to soil settlement as a function of time for pipelines buried in soft soils.

2. Methods

The model consists of a 20-m long pipe buried in a soil that is 12.5-m deep and 4-m wide. The overburden is 2-m thick. The outer diameter of the pipe is 0.508m (20 inches). The chosen dimensions are found to be sufficient to minimize the boundary effect on the pipe stress analysis.

Three-dimensional parametrical pipe-soil interaction models were built in ABAQUS finite element package with 8-node brick elements for the pipe. It was assumed that the pipe was supported at both ends with solid foundation such as concrete. The soil was meshed with 20-node hexahedral pore pressure elements. Large sliding between the pipe and soil was modeled with the surface-surface contact in ABAQUS. Large pipe deformation was also modeled. Different scenarios were considered: frozen muskeg, soft clay and water-filled soft clay; internal oil pressures were included in some of these cases. Soil settlement due to consolidation was simulated to show the pipe stress and displacement as functions of time.

The modulus and Poisson's ratio of pipe steel are 207 GPa and 0.3 respectively. The default modulus and Poisson's ratio of soil are 5 MPa and 0.2 respectively unless otherwise used for comparison.

3. Results

Pipe deformation and stress are sensitive to soil properties with very soft soil such as muskeg, but insensitive after soil stiffness reaches a level of magnitude (Fig. 1). It takes more than one month for the pipe settlement to complete and the stress increased to the maximum if a pipe is laid in a frozen muskeg that is suddenly defrosted (Fig. 2). Soil consolidation could produce much larger stresses than any other factors alone.

4. Discussion

In contrast to commonly used soil-spring elements in the oil and gas industry to account for the soil support, only continuum elements were used in the present study. The pipe-soil interaction is thus more realistically modelled leading to interesting and potentially more accurate results.

Energy pipelines in muskeg in northern Canada are always built in the winter when the frozen muskeg makes the construction possible. Our results indicate that the pipe only experiences up to a few millimetres deflection at the time of construction, but hundreds of millimetres (Fig. 1) with over 2 times stress (Fig. 2) when the muskeg is defrosted in the summer. If we further consider the thermal expansion (study in progress) during operation, these additional deflection and stress could be a significant integrity concern.

Both pore fluid pressure and soil consolidation produce significant differences in pipe stress, which indicates that, in soft soil where seasonal fluid pressure changes, soil consolidation and soil particle flow is not uncommon, this additional loading needs to be considered in pipe stress and stability analysis to ensure pipeline safe operation. The study has suggested that an initial soil consolidation stage needs to be considered when calculating the springs that are to be used for conventional beam element analysis for pipe design. The study has also provided a range of settlement values for various soil consolidation conditions.

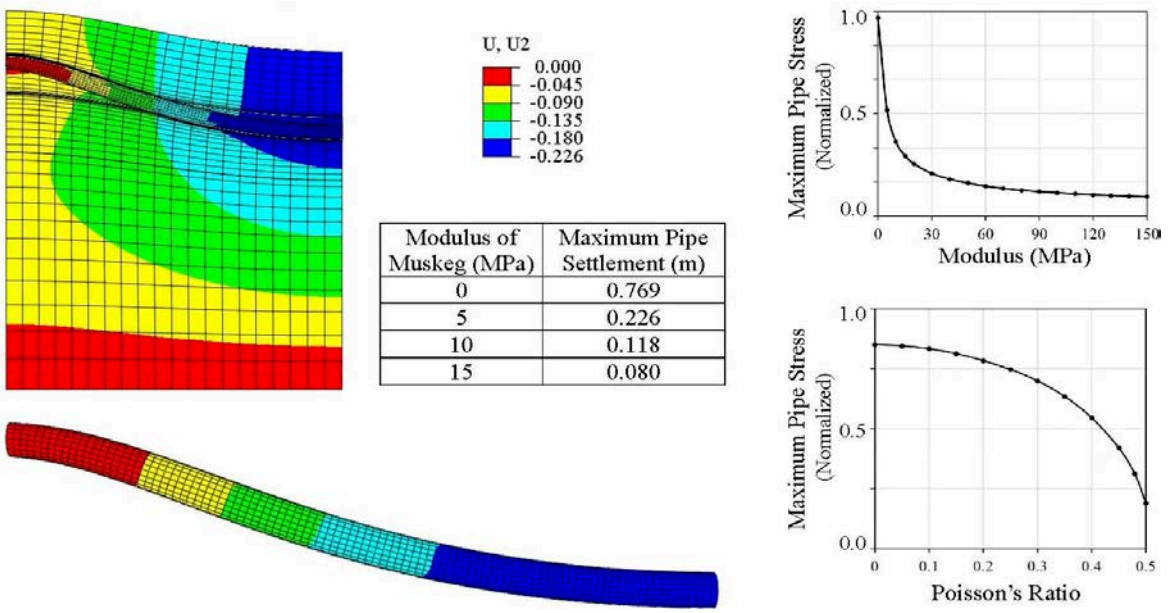

Modulus of Muskeg (MPa)	Maximum Pipe Settlement (m)
0	0.769
5	0.226
10	0.118
15	0.080

Figure 1: Final settlement of the pipe and soil (left), and normalized maximum pipe stress as a function of soil modulus (upper right) and of Poisson's ratio of the soil (lower right). The pipe is full with bitumen (900 kg/m^3). The modulus and Poisson's ratio of soil are 5 MPa and 0.2 respectively unless noted otherwise.

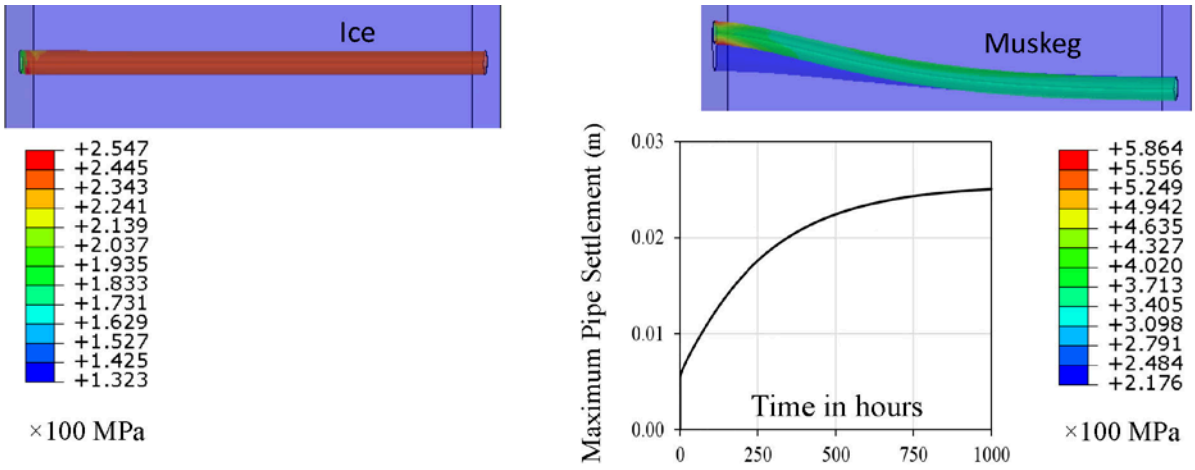

Figure 2: von Mises stress of pipe in ice (left) and settled muskeg (right), and the maximum pipe settlement as a function of time (inset).

Acknowledgments The authors acknowledge the financial support from the Natural Sciences and Engineering Research Council of Canada.

A NUMERICAL MODEL OF SINTERING PROCESSES AT MACROSCOPIC LEVEL

K. Wawrzyk, P. Kowalczyk, J. Rojek, and S. Nosewicz

Institute of Fundamental Technological Research, Polish Academy of Sciences
Pawińskiego 5B, 02-106 Warsaw, Poland

e-mail: kwawrzyk@ippt.pan.pl

1. Introduction

This paper presents modelling of double-phase powder sintering processes at the macroscopic level. In particular, its constitutive formulation, numerical implementation and numerical simulations are described. Numerical tests were carried out for a cylindrical specimen under uniaxial pressure and are compared against the microscopic model results. The model has been developed within the framework of a MUSINT project which is carried on in Institute of Fundamental Technological Research, Warsaw, Poland. The overall objective of the MUSINT (Multiscale numerical modelling of sintering processes) is development of numerical models allowing us to analyse at various scales manufacturing processes employing sintering as the main technological stage.

2. Constitutive model of single- and double-phase sintering

Sintered material is treated as continuous medium at the macro scale. Its constitutive model is tightly related to observations done at the micro scale (single grain level) and fully consistent with the model describing the microscopic mechanical phenomena of the sintering process. Such a model, proposed by Nosewicz [5], is schematically depicted in Fig.1 and is introduced as an author's original extension of viscous model. The rheological model of sintering presented in Fig.1 is enriched by adding elastic and thermal component to the standard viscous model [3] [2] [1]. By analysis of mass transport and stresses at the grain boundary between two sintered particles the following equation for the particle interaction during sintering is obtained [4]:

$$F_n = \frac{\pi a^4}{8 D_{eff}} v_{rn} + \pi \gamma_s \left[4r \left(1 - \cos \frac{\Psi}{2} \right) + a \sin \frac{\Psi}{2} \right] \tag{1}$$

where F_n is the normal force between two particles, v_{rn} - the normal relative velocity, r - the particle radius, a - the radius of the interparticle boundary, Ψ- the dihedral angle, γ_s - the surface energy.

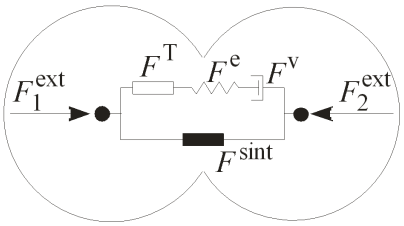

Figure 1: Rheological scheme of thermo-viscoelastic model [5]

At the macro scale sintered material is treated as continuous medium. Its constitutive model is tightly related to observations made at the micro scale (single grain level) and fully consistent with microscopic mechanical model described in the above section. The macroscopic model is derived with the use of methodology known from works of e.g. Zhang [6]. The total strain rate is a sum of three parts: thermal, elastic and viscous, as follows:

$$\dot{\boldsymbol{\varepsilon}} = \dot{\boldsymbol{\varepsilon}}^{th} + \dot{\boldsymbol{\varepsilon}}^{e} + \dot{\boldsymbol{\varepsilon}}^{visc} \tag{2}$$

Thus, the constitutive equation has the form:

$$\dot{\boldsymbol{\sigma}} = \mathbf{D}\left(\dot{\boldsymbol{\varepsilon}} - \dot{\boldsymbol{\varepsilon}}^{th} - \dot{\boldsymbol{\varepsilon}}^{visc}\right) + \dot{\boldsymbol{\sigma}}^{s} \tag{3}$$

where thermal strain, viscous strain rate, sintering stress is given as follows:

$$\boldsymbol{\varepsilon}^{th} = \alpha T \mathbf{I} \tag{4}$$

$$\dot{\boldsymbol{\varepsilon}}^{visc} = \frac{\boldsymbol{\sigma}'}{2\eta_s} + \frac{tr(\boldsymbol{\sigma}) - 3\sigma_s}{9\eta_b}\mathbf{I} \tag{5}$$

$$\boldsymbol{\sigma}^{s} = \sigma_s \mathbf{I} \tag{6}$$

$$\sigma_s = \frac{\beta\gamma_s\rho^2}{r_0}, \rho = \hat{\rho}e^{-(\varepsilon_x+\varepsilon_y+\varepsilon_z)} \tag{7}$$

All parameters in the above equations — viscosity η_s, η_b, initial relative density $\hat{\rho}$, surface energy γ_s etc. — are related to microscopic material properties. Some modifications of the material model parameters are required to simulate the sintering process of two-phase powder. The model of sintering of the two-phase powder NiAl-Al_2O_3 is based on the mixture theory which is used to predict behaviour of multiphase systems and the basic assumption is that, at any instant of time, all phases are present at every material point. In general, for some material properties it provides theoretical upper and lowerbounds on properties - Voigt and Reuss model, respectively. Formulas for parameter W by Voigt and Reuss model is presented in Eqs. (8) and (9) respectively:

$$W = V_1 W_1 + V_2 W_2 \tag{8}$$

$$W = \left(\frac{V_1}{W_1} + \frac{V_2}{W_2}\right)^{-1} \tag{9}$$

where: V_i and W_i are the volume fraction and material property of i-th constituent, respectively. In this work, theoretical upper and lowerbound were used to predict surface energy γ_s and shear or bulk viscosity η_s and η_b. The last two parameters are subject to investigations in our research and will be presented with the numerical results at the confference.

3. References

Acknowledgments This work has been financed from the funds of Polish National Science Centre (NCN) awarded by decision no. DEC-2013/11/B/ST8/03287.

References

[1] R.L. Coble. Sintering of crystalline solids. intermediate and final state diffusion models. *Journal of Applied Physics*, 32:787–792, 1961.

[2] D.L. Johnson. New method of obtaining volume, grain boundary, and surface diffusion coefficients from sintering data. *Acta Metallurgica*, 36:223–229, 1998.

[3] L.C. De Jonghe and M.N. Rahaman. Sintering stress of homogeneous and heterogeneous powder compacts. *Acta Metallurgica*, 36:223–229, 1998.

[4] S. Nosewicz, J. Rojek, K. Pietrzak, and M. Chmielewski. Viscoelastic discrete element model of powder sintering. *Powder Technology*, 246:157–168, 2013.

[5] S. Nosewicz, J. Rojek, K. Pietrzak, and M. Chmielewski. Discrete element modeling and experimental investigation of hot pressing of intermetallic nial powder. *Advanced Powder Technology*, 28:1745–1759, 2017.

[6] R. Zhang. *Numerical simulation of solid state sintering of metal powder compact dominated by grain boundary diffusion*. The Pennsylvania State Univeristy, 1998.

HOW WELL CAN WE MEASURE THE EVOLUTION OF SAND MICRO-STRUCTURE?

G. Viggiani[1], M. Wiebicke[2], E. Andò[1] and I. Herle[2]

[1]*Univ. Grenoble Alpes, CNRS, Grenoble INP, 3SR, F-38000 Grenoble, France*

[2]*Institute of Geotechnical Engineering, Technische Universität Dresden, D-01062 Dresden, Germany*

e-mail: cino.viggiani@3sr-grenoble.fr

1. Introduction

Fabric of granular materials plays a fundamental role in its macroscopic behaviour. However, due to technical limitations, measurement of fabric remained inaccessible in real experiments until recently, with the advent of x-ray tomography. In this work, triaxial compression experiments on natural sands are chosen to investigate the evolution of fabric. Two different subsets of the specimen are chosen for the contact fabric analysis: one inside and another one outside a shear band. Individual contact orientations are measured using advanced image analysis approaches within these subsets. The fabric is then statistically captured using a second order tensor and the evolution of its anisotropy is related to the macroscopic behaviour.

2. X-ray micro tomography

With x-ray micro tomography (x-ray μCT) it is now possible to acquire 3D full-field measurements of granular materials at suitable resolutions. In the first applications of x-ray CT to soil mechanics, the distribution of porosity was investigated with the aim of analysing the development of localisation phenomena in the soil specimen [1, 2]. Existing image analysis tools were either modified for the use in soil mechanics or new tools were developed in order to study the kinematics of the soil specimen. Digital Image Correlation (DIC) has been used to determine the deformations in a continuum framework [3, 4]. Particle tracking approaches, such as ID-Track [5], enable the determination of grain kinematics, *i.e.,* displacements and rotations of individual grains. Both approaches have provided a deep insight into the micro-mechanics of the processes governing the overall behaviour of granular materials.

3. Metrology of inter-particle contacts

In our previous work [6], the metrology of inter-particle contacts from images was studied intensively, pointing out the main problems of standard image analysis, quantifying its accuracy and developing strategies to tackle the identified problems. Two major problems in determining contact orientations were identified: contacts are systematically over-detected, mainly due to the partial volume effect, and depending on the chosen segmentation algorithm the determined orientations can be biased and experience significant errors to an extent where a quantitative analysis seems questionable.

In this contribution, these results and approaches are used to extract the contact fabric from images of triaxial compression tests on two different soils. These experiments were already analysed in [7, 8] determining the kinematics throughout the loading with a special focus on the evolution of shear bands. One of the main findings was the importance of grain rotations inside shear bands. In the present study we start from the same images and extract subsets inside and outside the forming shear bands in order to determine what happens to the contact fabric within these regions of the specimen. As stated in [8], “A full micro-mechanical description of the kinematics occurring at the grain scale needs to go beyond grain kinematics", meaning the structure of the contact network, particle orientations and possibly other fabric entities.

4. Main results and conclusions

Fabric is analysed in terms of individual inter-particle contact orientations as well as using a second order fabric tensor [9]. A scalar anisotropy factor [10] is chosen to describe the evolution of fabric throughout the experiments. Before the onset of the localisation process, the contact fabric behaves similarly in both subsets: the anisotropy increases and the orientations start to align with the direction of major principal stress. After the onset of strain localisation, contact fabric in both subsets takes different evolutions as expected. The anisotropy inside the shear band further increases until a peak and decreases afterwards to reach what could be a residual state. The orientations further align with the major stress direction. The anisotropy outside of the shear band decreases close to its initial value after the onset of localisation and presumably oscillates around that value. Both evolutions are expected from the micro-mechanical analysis of the kinematics in [8], where the main changes, especially rotations of grains, were detected inside the shear band, with comparably much smaller and random kinematics happening outside the shear band. These results are mainly similar for the two materials considered, Hostun sand and Caicos ooids. The two evolutions exhibit similar characteristics compared to the corresponding macroscopic stress response. The main differences being the speed at which fabric reacts to the macroscopic loading, and the range of the anisotropy, which is larger for the rounded Caicos ooids. This can be linked to the different shapes of the grains and the inter-particle friction of the two different materials.
Although these findings are striking and crucial for a full micro-mechanical description, they have to be regarded with care. The determination of contact properties in Hostun sand is still problematic, as pointed out in [6]. Further advances on the metrology of contacts in angular granular materials are still needed. Nevertheless, these applications on small subsets open the door to further analyses, *e.g.*, the analysis of a complete specimen rather than subsets, and the investigation of different loading cases, such as cyclic loading, and oedometer or isotropic loading.

Acknowledgments The research leading to these results has received funding from the German Research Foundation (DFG) n° HE2933/8-1 and from the European Research Council under the European Union's 7th Framework Program FP7-ERC-IDEAS Advanced Grant Agreement n° 290963 (SOMEF). Laboratoire 3SR is part of the LabEx Tec 21 (Investissements d'Avenir - grant agreement nANR-11-LABX-0030). We thank the Center for Information Services and High Performance Computing (ZIH) at TU Dresden for generous allocations of computational resources.

References

[1] J. Desrues, R. Chambon, M. Mokni, and F. Mazerolle. Void ratio evolution inside shear bands in triaxial sand specimens studied by computed tomography. *Géotechnique*, 46:3, 1996.
[2] M. Oda, T. Takemura, and M. Takashi. Microstructure in shear band observed by microfocus X-ray computed tomography. *Géotechnique*, 54:8, 2004.
[3] S.A. Hall, M. Bornert, J. Desrues, Y. Pannier, N. Lenoir, G. Viggiani, and P. Bésuelle. Discrete and continuum analysisof localised deformation in sand using x-ray mCT and volumetric digital image correlation. *Géotechnique*, 60:5, 2010.
[4] E. Tudisco, E. Andò, R. Cailletaud, and S.A. Hall. TomoWarp2: a local digital volume correlation code. *SoftwareX*, 6, 2017.
[5] E. Andò, S.A. Hall, G. Viggiani, J. Desrues, and P. Bésuelle. Grain-scale experimental investigation of localised deformation in sand: a discrete particle tracking approach. *Acta Geotechnica*, 7:1, 2012.
[6] M. Wiebicke, E. Andò, I. Herle, and G. Viggiani. On the metrology of interparticle contacts in sand from x-ray tomography images. *Measurement Science and Technology*, 28:12, 2017.
[7] E. Andò, S.A. Hall, and G. Viggiani. Experimental micromechanics: grain-scale observation of sand deformation. *Géotechnique Letters*, 2, 2012.
[8] E. Andò, G. Viggiani, S.A. Hall, and J. Desrues. Experimental micro-mechanics of granular media studied by x-ray tomography: recent results and challenges. *Géotechnique Letters*, 3, 2013.
[9] K.I. Kanatani. Distribution of directional data and fabric tensors. *Int. Journal of Engineering Science*, 22:2, 1984.
[10] X. Gu, J. Hu, and M. Huang. Anisotropy of elasticity and fabric of granular soils, *Granular Matter*, 19:2, 2017.

Session S12: Biomechanics

Organizers: R. Będziński (TU Wroclaw), J-F. Ganghoffer (Univ. of Lorraine, Nancy), E. Majchrzak (Silesian UT), M. Nowak (TU Poznan)

MODELLING OF THERMAL DAMAGE IN LASER IRRADIATED TISSUE WITH EMBEDDED NANOPARTICLES

M. Jasiński

Institute of Computational Mechanics and Engineering, Silesian University of Technology, Gliwice, Poland
e-mail: marek.jasinski@polsl.pl

1. Formulation of the problem

The purpose of this paper is to analyze the phenomena occurring in the laser-treated soft tissue wherein the cloud of nanoparticles is placed. The 2D domain of homogeneous biological tissue subjected to the laser action (Fig.1) is considered. The analysis is based on the Pennes bioheat transfer equation in the form [1]

$$\mathbf{x} \in \Omega: \quad c\dot{T} = \lambda \nabla^2 T + Q_{perf} + Q_{las} + Q_{met} \tag{1}$$

where λ [$\mathrm{Wm^{-1}K^{-1}}$] is the thermal conductivity, c [$\mathrm{Jm^{-3}K^{-1}}$] is the volumetric specific heat, Q_{perf}, Q_{met} and Q_{las} [$\mathrm{Wm^{-3}}$] are the heat sources connected with the perfusion, metabolism and laser radiation, respectively, while $T = T(\mathbf{x}, t)$ is the temperature. Equation (1) is supplemented by appropriate boundary conditions: Robin condition on the external tissue surface Γ_0 and no-flux condition on the internal tissue surface Γ_c. The initial distribution of temperature is also known.

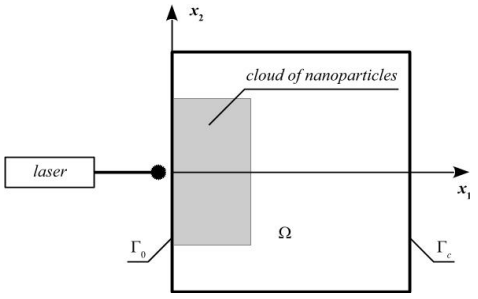

Figures 1: The domain considered.

In order to determine the internal heat source concerning information about laser irradiation the collimated and diffuse part of fluence rate must be determined. The diffuse fluence rate ϕ_d is calculated on the base of the steady-state optical diffusion equation [2,3]

$$\mathbf{x} \in \Omega: \quad D\nabla^2 \phi_d(\mathbf{x}) - \mu_a \phi_d(\mathbf{x}) + \mu_s' \phi_c(\mathbf{x}) = 0 \tag{2}$$

while the collimated fluence rate ϕ_c is given as [1]

$$\phi_c(\mathbf{x}) = \phi_0 \exp\left(-\frac{2x_2^2}{r^2}\right) \exp(-\mu_t' x_1) \tag{3}$$

where D [m] is the diffusion coefficient, μ_a, μ'_s and μ'_t [$\mathrm{m^{-1}}$] are the absorption, effective scattering and effective attenuation coefficient of tissue, respectively, ϕ_0 [$\mathrm{Wm^{-2}}$] is the surface irradiance of laser, r is the radius of laser beam.
The final form of the source function connected with the laser heating is described by the formula

$$Q_{las}(\mathbf{x}, t) = \mu_a \phi(\mathbf{x}) p(t) \tag{4}$$

where $\phi(\mathbf{x})$ [$\mathrm{Wm^{-2}}$] is the sum of collimated and diffuse parts of fluence rate and and $p(t)$ is the function equal to 1 when the laser is *on* and equal to 0 when the laser is *off*.

Damage of biological tissue resulting from temperature elevation is modelled by Arrhenius injury integral, defined as [2]

$$\Psi(\mathbf{x},t^F)=\int_0^{t^F} P\exp\left[-\frac{E}{RT(\mathbf{x},t)}\right]\mathrm{d}t \tag{5}$$

where R [J mole^{-1}K^{-1}] is the universal gas constant, E [J mole^{-1}] is the activation energy and P [s^{-1}] is the pre-exponential factor. The criterion for tissue necrosis is $\Psi(\mathbf{x}) \geq 1$.

2. Results of computations

As was mention previously the 2D domain of homogeneous biological tissue subjected to the laser action was considered. Two simulations were carried out – with and without the cloud of nanoparticles which was situated near the external surface of the tissue (Fig. 1). It should be pointed out that optical properties of tissue with nanoparticles were calculated on the basis of formulas [2,3]

$$\mu_{ap}=\mu_a+0.75\,f_v\frac{Q_a}{a},\quad \mu_{sp}=\mu_s+0.75\,f_v\frac{Q_s}{a} \tag{6}$$

where Q_a and Q_s are the dimensionless efficiency factor of absorption and scattering for single particles, respectively, f_v is the volume fraction of nanoparticles while a is the particle radius.
The bioheat problem (1) has been solved using the 1st scheme of the BEM for 2D transient heat diffusion while the optical diffusion equation (2) has been solved by the finite difference method.

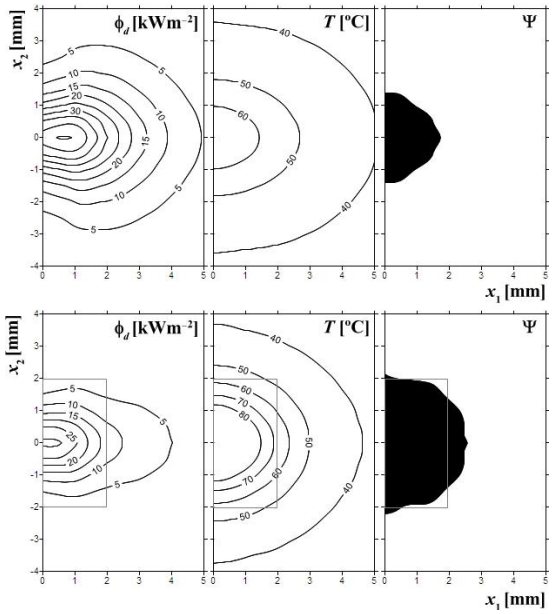

Figures 2: Distribution of diffuse fluence rate ϕ_d, temperature and Arrhenius integral after 10 s.

Acknowledgments The research is funded from the projects Silesian University of Technology, Faculty of Mechanical Engineering.

References

[1] F. Fanjul-Vélez, O.G. Romanov, J.L. Arce-Diego. Efficient 3D numerical approach for temperature prediction in laser irradiated biological tissues. *Comput. Biol. Med.*, 39:810, 2009.
[2] L.A. Dombrovsky, V. Timchenko, M. Jackson. Indirect heating strategy for laser induced hyperthermia: An advanced thermal model. *Int. J. Heat Mass Transfer*, 55: 4688, 2012.
[3] Y. Bayazitoglu, S. Kheradmand, T.K. Tullius. An overview of nanoparticle assisted laser therapy. *Int. J. Heat Mass Transfer*, 67: 469, 2013.

NUMERICAL AND EXPERIMENTAL TESTS OF INVERSE HONEYCOMB STRUCTURE USED IN THE EXOSKELETON FOR A CHILD

A. John[1] and M. John[2]

[1] *Institute of Computational Mechanics and Engineering, Silesian University of Technology, Gliwice, Poland*
[2] *Institute of Fundamentals of Machinery Design, Silesian University of Technology, Gliwice, Poland*

e-mail: antoni.john@polsl.pl, malgorzata.john@polsl.pl

1. Introduction

Very often when designing some devices, the important factors are the weight of the whole structures and the level of stiffening of its individual elements. It seems to us that one of such devices is an exoskeleton designed for children. We do not have such rigorous lifting requirements as in the case of exoskeletons for firefighters or army. In the case of an exoskeleton for a child, it is important that the whole structure does not weigh too much for a small patient. Sometimes the main task of the device is to correct movements made by the child. The exoskeleton forces natural, proper movement of the limbs, in order to eliminate pathological behaviors. The structure proposed by us is manufactured using a 3D printer. This facilitates the personalization of external coatings in a significant way. The structure will remain the same, its properties will not change, and a pattern will be applied to the outer coat that can make the treatment process more pleasant for the little patient. This is also a very important aspect, because in the case of rehabilitation, treatment is also important for the patient's attitude. Children are quickly discouraged. When we give them a device with which they could contribute, we will influence their psychological comfort.

2. The models preparation

Initially, the model adopted the classic honeycomb structure. Along with the subsequent numerical tests, based on the obtained results, some changes were introduced in the structure. Among other things, the thickness of the cell walls, the dimensions of the basic cell, and the building material of the structure were modified [1, 2]. Based on literature research and the obtained results of simulation of the numerical three-point bending test, changes in the geometry of the sample, and more specifically the empty spaces, were proposed. In the place of a rapid transition between the larger and smaller cells there were stress accumulation, as well as the direction of the crack propagation. They accumulated on combining two layers of cells. Combining it was also another layer of melted ABS material in the FDM 3D printing method. This change consisted of adding a transitional layer between the void layers.
The basic model with empty spaces was modeled so that changes in cell size introduced in one cell would automatically take place in the other cells. This significantly facilitated the introduction of changes and significantly reduced the time of modeling subsequent models. Therefore, modeling in the array was used. Due to the specificity of the base structure - honeycomb type - and bandwidth reshaping, it was impossible to model all cells with one pattern. In the final version there are two rectangular constructions in one larger formation. The same principle was adopted for models with a transition.

3. The experimental research

The experimental study was carried out on a MTS Insight 10 testing machine specially prepared for this study. The stand had to be adapted to the tested samples of small dimensions and forces used. The tests were carried out on samples made with the FDM rapid prototyping technique.. Due to limitations imposed by the manufacturing technique, the samples had to be scaled. They were enlarged three times, which gave analogously 12x12x120mm values. The head from standard to smaller has also been changed. Thanks to this change it was possible to create modeled samples on an available 3D printer - Prusa i3 MK2. The changes introduced in the numerical model, and due to the phenomenon of notch, were also beneficial from the technological point of view. The printer has managed to produce earlier samples. However, we were not able to check the print quality at critical locations because they were inside the sample. Knowing the capabilities

of a printer, we are able to say that it coped better with creating samples with a "transition". Six series of trials were carried out with five samples in each. They differed in the dimensions of smaller and larger cells. As a result, they had different volume and mass. Depending on the type of the sample, there was another crack propagation (Figures 1, 2). As a result of the tests carried out on the strength machine, the following average values presented in Table 1 were obtained for subsequent samples. Most of the samples did not break. Only in the case of 23a sample series each was broken. In the case of these samples, the greatest force was observed, the mean displacement being the highest.

Model	Peak Load [N]	Deflection [mm]
10a	248,575	4,92
16a	151,257	3,58
17a	155,093	3,78
18a	155,735	4,46
22a	288,895	4,16
23a	312,047	5,04

Table 1. The average values of load and deflection in experiment

Figure 1. The crack propagation in sample 16a

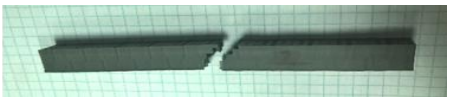

Figure 2. The crack propagation in sample 23a

4. Numerical simulation

In the next step numerical simulation of three-point bending test was performed. All numerically tested samples have the same dimensions as a previous tested samples prepared from ABS. The samples with a length of 120 mm, a height of 12 mm and 12 mm wide were modeled for each experimentally tested models. The models prepared in CAD system were imported to MSC.Software and before meshing material parameters were assumed. For ABS assumed Young modulus equals 1600MPa and Poisson's ratio 0.38. Boundary condition (support and load) assumed as typical during tree-point bending test. The spacing of supports is 100mm (due to experiment). The acting force assumed as maximal force for each test respectively (Table 1). Discretization of the models was carried out with tetrahedral elements of the Tet4 type with a linear shape function. The average distance between nodes was taken equal to 1mm. The developed models are composed of approximately 400,000 elements and have approximately 120,000 degrees of freedom. Vertical displacements (Y), reduced stresses (von Mises) and normal stresses along the longitudinal axis of the sample (Z) were selected as the representative results.

5. Conclusions

The research carried out was aimed at developing a lightweight structure and at the same time durable. An additional important limitation is the possibility of creating a structure in incremental 3D printing technology. The results obtained from numerical simulation well illustrates the mechanism of fracturing the samples observed in the experiment. However obtained distributions and values of stresses confirm the results obtained in experimental studies the deflection obtained in the numerical tests are smaller than in the experiment. It is observed that during manufacturing process the material properties change and may differ from those given for filament. This requires further research and "tuning" of the model. Also nonlinear analysis should be performed.

Acknowledgments The research is financed by project no. BK-226/RMT-4/2018 (10/040/BK_18/0066).

References

[1] M. He and W. Hu. A study on composite honeycomb sandwich panel structure. *Mat. and Design* 29, 709:713, 2008.
[2] M. John; A. John and W. Skarka. The influence of the geometrical parameters on the mechanical properties of honeycomb structure. *Mechanika, Vol. 23, No. 3,* 359:364, 2017.

Homogenized strain gradient remodeling model for trabecular bone microstructures

Zineeddine Louna[1], Ibrahim Goda[2,3], Jean-François Ganghoffer[4]

[1]LMFTA, Faculté de physique, USTHB, BP 32 El Alia 16111 Bab Ezzouar Algiers, Algeria
[2]LPMT, Université de Haute-Alsace, 11 rue Alfred Werner, 68093 Mulhouse Cedex, France
[3]Department of Industrial Engineering, Faculty of Engineering, Fayoum University, Fayoum 63514, Egypt.
[4]LEM3– Université de Lorraine, CNRS. 7, rue Félix Savart. 57073 Metz, France

Bone continuously adjusts its mass, architecture and properties to variations in its mechanical environment due to internal and external remodeling. Internal remodeling refers to the resorption or reinforcement of bone material, accompanied by the removal and densification of the architecture of cancellous bone, but no change in its overall shape. To the contrary, external or surface remodeling refers to the resorption or deposition of bone material on the external surface of the bone, resulting in a change of the external shape of the overall bone structure. Since these processes have a tremendous impact on the overall behavior and health of the entire body, bone remodeling simulations are of great importance, especially in applications dealing with bone adaptivity, such as bone implants and scaffold design, and furthermore to predict the outcome of dental or orthodontic treatment. We construct constitutive models for bone remodeling based on micromechanical analyses at the scale of a representative volume element (RVE) consisting of individual trabeculae defining the representative unit cell [1,2,3]. On the microscale, trabeculae undergo apposition of new bone modeled by a surface growth velocity field driven by a mechanical stimulus identified to the surface divergence of an Eshelby like tensor. The static and evolutive effective properties of a periodic network of bone trabeculae are evaluated by combining a methodology for the evaluation of the average kinematic and static variables over a unit cell and numerical simulations with controlled kinematics. The viscoplastic type constitutive model for growing bone is identified relying on the framework of the thermodynamics of irreversible processes. The obtained results quantify the strength and importance of the strain and strain gradient effects applied over the RVE on the overall bone remodeling process (Fig. 1).

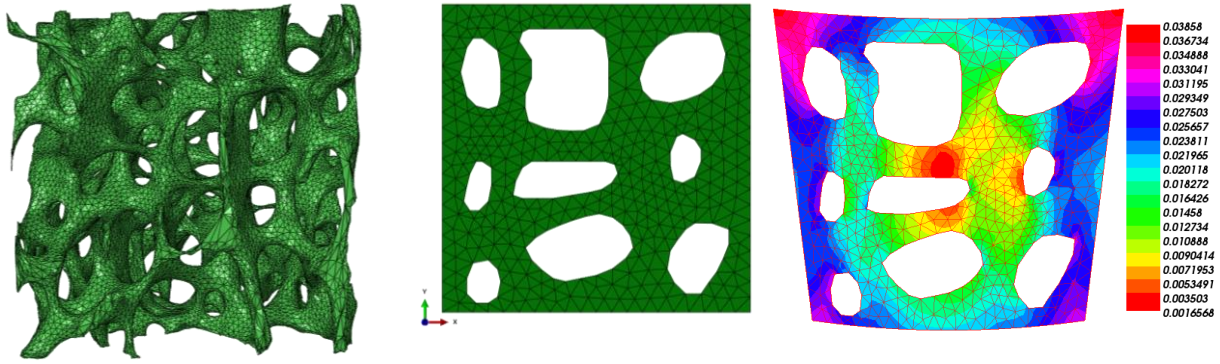

Figure 1: (a) Scan of the original 3D trabecular bone sample, (b) 2D section, and c) Distribution of equivalent strain due to in-plane bending.

References

[1] Louna, Z., Goda, I. Ganghoffer, J.F., Benhadid, S., 2017. Formulation of an effective growth response of trabecular bone based on micromechanical analyses at the trabecular level. Archive of Applied Mech. 87(3), 457-477.

[2] Goda, I. Ganghoffer, J.F., Maurice, G., 2016. Combined bone internal and external remodeling based on Eshelby stress. Int. J. Solids Struct., 94–95, 138–157.

[3] Ganghoffer, J.F., 2010. Mechanical modeling of growth considering domain variation – Part II: volumetric and surface growth involving Eshelby tensors. J. Mech. Phys. Solids 58 (9), 1434–1459.

CASCADE OF BOOSTED CLASSIFIERS AND ACTIVE APPEARANCE MODEL FOR SPINE ELEMENTS LOCALIZATION AND SEGMENTATION

D. Gaweł[1], M. Nowak[1], K. Łyduch[1], P. Główka[2] and T. Kotwicki[2]

[1]*Chair of Virtual Engineering, Poznan University of Technology, Poznan, Poland*
[2]*Department of Spine Disorders and Pediatric Orthopedics, University of Medical Sciences, Poznan, Poland*

1. Introduction

Magnetic Resonance Imaging (MRI) is a medical imaging technique widely used for visualization of internal body structures. The popularity of this method grows every year, because of its non-harmfulness, as opposed to Computed Tomography (CT). Usage of advanced computer science techniques including Machine Learning and Active Appearance Model gives an opportunity of automatic image interpretation. Presented solution was developed by specialists form Poznan University of Technology in cooperation with University of Medical Sciences and Rehasport Clinic and can be an answer for increasing needs for visualization in medicine.

2. Materials and Methods

Presented method is based on Machining Learning (ML) [1] and Active Appearance Model (AAM) [2] techniques. For the research purposes almost 50 MRI examinations were used. The data was provided by Rehasport Clinic. At the beginning DICOM images are read. Due to low quality of the images (low resolution, intensity inhomogeneity and high noise) the initial filtration algorithm is introduced.

Afterwards, to extract each vertebra from the images, Machine Learning technique based on Cascade of Boosted Classifiers [3] and extended set of Haar-like features is used. The process consists of two major stages: training the classifier and vertebrae localization.

In the next stage the tissue segmentation is performed. The process uses the Active Appearance Model (AAM) technique that combines Statistical Shape Model with gray-level Appearance Model. The method focuses on recognizing predefined characteristic features from vertebrae images. The detected features are afterwards used for defining the tissue boundaries.

3. Results

The method was tested on a set of 50 previously unseen vertebrae images. The spine tissue was manually segmented by experts and compared with Machine Learning Results. For the numerical evaluation three measures were used [4]: True Positive Fraction (TPF), False Negative Fraction (FNF) and False Fraction (FF). False Fraction (FF) is the most important measure as it combines information both about over- and under-segmentation. The table (see Table 1) presents segmentation results obtained by experts and introduced segmentation method. The difference between the average FF value for experts (91.32%) and presented method (90.19%) is less than 2%.

4. Conclusions

Statistical analysis of obtained segmentation results confirmed a good segmentation performance and possible application for spine elements extraction, however the procedure for full automation needs further work related to implementation of additional algorithms including, but not limited to, exchange of information between different stages and initialization of characteristic features localization.

In the future automatic segmentation could be used for creation of discrete (Figure 1) and continuous (Figure 2) 3D spine models, allowing better understanding of the pathology by the physicians and patients.

	TPF	FNF	FF	σ_{TPF}	σ_{FNF}	σ_{FF}
Computer segmentation	92.28±0.95	7.72±0.95	90.19±1.01	3.42	3.42	3.64
Expert segmentation #1	96.17±0.92	3.83±0.92	91.67±1.27	3.32	3.32	4.58
Expert segmentation #2	95.13±0.83	4.87±0.83	92.11±1.00	2.98	2.98	3.60
Expert segmentation #3	97.74±0.43	2.26±0.43	91.09±1.33	1.56	1.56	4.78
Expert segmentation #4	97.56±0.37	2.44±0.37	91.49±1.47	1.33	1.33	5.32
Expert segmentation #5	92.46±1.33	7.54±1.33	90.22±1.31	4.81	4.81	4.74

Table 1: Comparison (percentage) of True Positive Fraction, False Negative Fraction and False Fraction for data segmented using presented method and manually segmented by experts (significance level α=0.05). To achieve reliable results a mean value obtained from 100 procedure passes with 25 algorithm iterations each is presented. σ_{TPF} – standard deviation for True Positive Fraction, σ_{FNF} - standard deviation for False Negative Fraction, σ_{FF} - standard deviation for False Fraction.

Figure 1. Discrete STL 3D model created manually from characteristic features. The pathology of vertebrae and intervertebral disc is clearly visible.

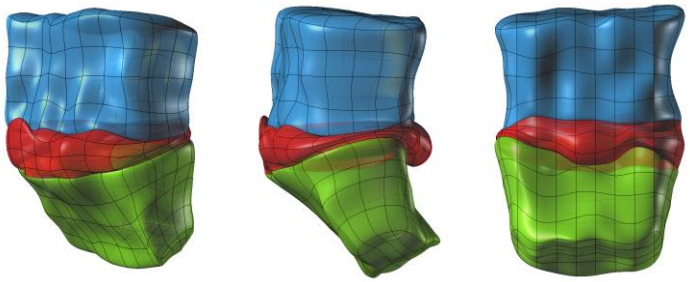

Figure 2. Continuous NURBS model created manually from characteristic features, easily convertible to Finite Element mesh. The pathology of vertebrae and intervertebral disc is clearly visible.

Acknowledgments This work was supported by The National Centre for Research and Development under the grant – decision no. DZP/PBS3/2296/2014.

References

[1] Sergios Theodoridis. *Machine learning: a Bayesian and optimization perspective*. Academic Press, 2015.
[2] Gareth J Edwards, Christopher J Taylor, and Timothy F Cootes. Interpreting face images using active appearance models. In *Automatic Face and Gesture Recognition, 1998. Proceedings. Third IEEE International Conference on*, pages *300*-305. IEEE, 1998.
[3] Paul Viola and Michael Jones. Rapid object detection using a boosted cascade of simple features. In *Computer Vision and Pattern Recognition, 2001. CVPR 2001. Proceedings of the 2001 IEEE Computer Society Conference on*, volume 1, pages I-I. IEEE, 2001.
[4] Tom Fawcett. An introduction to roc analysis. *Pattern recognition letters*, 27(8):861-874, 2006.

FEM BASED FRACTURE RISK ASSESSMENT IN PATIENT SPECIFIC OSTEOPOROTIC LUMBAR VERTEBRA L1

A. Maknickas[1], V. Alekna[2], O. Ardatov[1], D. Zabulionis[1], M. Tamulaitienė[2], and R. Kačianauskas[1]

[1]*Institute of Mechanics, Vilnius Gediminas Technical University, Vilnius, Lithuania*
[2]*Faculty of Medicine, Vilnius University, Vilnius, Lithuania*

e-mail: algirdas.maknickas@vgtu.lt

1. Introduction

The ability of fracture risk assessment is a useful diagnostic tool for analysing the state of osteoporotic bone. There are several developed methods which employ bone mineral density (BMD) in order to predict the long-term fracture risk. BMD is usually assessed by dual energy X-ray absorptiometry (DXA) and some studies have shown that decrease of standard deviation in BMD is associated with a higher risk for future fracture [1–3]. Modern techniques of medical diagnostics also dispose computer-based algorithms, such as FRAX [4], which calculate fracture probability from obtainable clinical risk factors like age, body mass index(BMI), and dichotomized risk factors comprising prior fragility fracture, parental history of hip fracture, current tobacco smoking, long-term oral glucocorticoid use, rheumatoid arthritis, other causes of secondary osteoporosis, alcohol consumption and others [5]. On the other hand, these methods don't verify the complexed relation between such important parameters as trabecular bone score (TBS), thickness of cortical shell and the value of external load.

The finite element method (FEM) based continuum models can supply the additional patient specific data in order to define the risk of fracture by additionally applying the reliability theory. This work proposes the new method of fracture risk calculation, based on statistically processed results obtained by numerical investigation of strength properties of lumbar vertebral L1 body with various grades of osteoporotic degradation.

2. Methods and Materials

Bone tissue model. The bone tissue is modelled as elastoplastic continuum, so the Maxwell-Huber-Hencky-von Mises criterion is chosen to predict the fracture of the model. The selection of this criterion is based on mechanical properties of bone, which seems to behave as a ductile material [6]. The inhomogeneous lumbar vertebral body consists of two basic structural members - outer cortical shell fulfilled by inner bone tissue. In this study, the DICOM data of human CT was used for development of initial anatomical geometry of vertebral body. The geometry of trabecular tissue was obtained by boolean cut operation of initial anatomical geometry model of vertebra by regular shifted cylinder system. The Maxwell-Huber-Hencky-von Mises yield criterion is applied on research of stresses, which occur on cortical shell and on trabecular tissue of the model. The Ramberg-Osgood equation mathematical model of the stress σ strain rate ε behaviour of bone was applied [7]. Finally, the model was meshed with tetrahedral grid due to its curvature and finite element method was applied for solving differential momentum equation of motion.

Model fitting. In risk evaluations we have used three degrees of freedom: external load P, cortical shell thickness of lumbar vertebra Δ and bone volume to total volume ratio β_{BVTV} which was obtained from trabecular bone score (TBS) interdependence. On other hand, TBS was obtained from 2D vertebra CT scan. These variables were used for solving finite element method for above proposed mechanical model strength of lumbar vertebra. Finally, the obtained set of points values for different combination of free variables were used for least square fitting by quadratic polynomial as follow

$$\sigma_s = \sum_{i,j,k=0}^{2} a_{ijk} \beta_{BVTV}^{i} \Delta^{j} P^{k} \tag{1}$$

Risk evaluation. Fracture risk of lumbar vertebra can by expressed in term of reliability $R = P(Z \leq 0)$, where $Z = X_\sigma - Y_{\sigma_Y}$ has the following CDF

$$R = P(Z \leq 0) = \int_{-\infty}^{0} \int_{-\infty}^{\infty} f_{X_\sigma}(\sigma + z) f_{Y_{\sigma_Y}}(\sigma) d\sigma dz \tag{2}$$

where f_{X_σ} and $f_{Y_{\sigma_Y}}$ are PDFs of the normal random variables X_σ and Y_{σ_Y} of the maximum stress caused by the external load P and the strength, respectively.

3. Numeric Results and Conclusion

The static failure reliability R, see Fig. 1, is evalueted by the Monte Carlo method. Our results show that the fracture risk is substantially higher at relatively low levels of apparent BV/TV ratio, and critical due to thinner cortical shell, and it suggests the high levels even during daily activities of typical distribution of external loads. In addition, this model could be used for determining of fracture risk of individual patient by applying of peculiar anatomical properties of lumbar vertebrae. The proposed method of fracture risk assessment based on cancellous bone and cortical shell in-silico finite element modelling includes basic principles of evaluation of fracture risk of mechanical system and should be used as supplementary method with other known fracture risk evaluation methods.

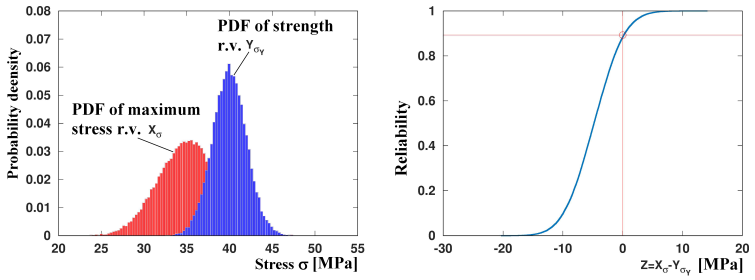

Figure 1: PDFs of the stress ($\mu = 35$ MPa) and the strength ($\mu = 40$ MPa) (left) and the reliability R (right).

4. References

References

[1] J.A. Kanis, A. Oden, O. Johnell, H. Johansson, C. De Laet, J. Brown et al (2007), *The use of clinical risk factors enhances the performance of BMD in the prediction of hip and osteoporotic fractures in men and women*, Osteoporosis International, 18, 1033–46.

[2] D. Marshall, O. Johnell and H. Wedel (1996), *Meta-analysis of how well measures of bone mineral density predict occurrence of osteoporotic fractures*, BMJ, 312, 1254–9.

[3] B. C. Taylor, P. J. Schreiner, K. L. Stone , et al. (2004), *Long-term prediction of incident hip fracture risk in elderly white women: study of osteoporotic fractures*, Journal of the American Geriatrics Society, 52(9), 1479–86.

[4] J.A. Kanis, A. Oden, H. Johansson, F. Borgstrom, O. Strom and E. McCloskey (2009, *FRAX and its applications to clinical practice*, Bone, 44(5), 734–43.

[5] J.A. Kanis, O. Johnell, A. Oden, H. Johansson and E. McCloskey (2008), *FRAX and the assessment of fracture probability in men and women from the UK*, Osteoporosis International, 19, 385–97.

[6] M. Dreischarf, T. Zander, a. Shirazi-Adl, C.M. Puttlitz, C.J. Adam, C.S. Chen, et al. (2014) Comparison of eight published static finite element models of the intact lumbar spine: Predictive power of models improves when combined together, *J. Biomech.* **47** 1757–1766. doi:10.1016/j.jbiomech.2014.04.002.

[7] Timothy, H.K. and Brandeau J.F. (1983) Mathematical modeling of the stress strain-strain rate behavior of bone using the Ramberg-Osgood equation. *J. Biomech*. **16**(6), 445–450.

NUMERICAL MODELS OF THE URETHRAL LOWER DUCT

M. Malinowski[1], A. Kaczmarek-Pawelska[1], A. Mackiewicz[1], R. Rudyk[1],
A. Noszczyk-Nowak[2], J. Madej[2] and J. Skonieczna[2], R. Będziński[1]

[1]*University of Zielona Gora, Faculty of Mechanical Engineering, Zielona Gora, Poland*

[2]*Wroclaw University of Environmental and Life Sciences, Wroclaw, Poland,*

1. Introduction

Most lower urinary tract pathologies, such as hyperplasia, stricture or urinary incontinence are treated using medical device that strongly interact with the urethra. Knowledge of its mechanical behaviour can improve the design of new devices and development of bioresorbable stents made of polymeric materials. Rabbit urethra tssue is similar to human urethra (histomorphometric features). In this paper male New Zealand (NZ) white rabbit urethra was investigated. The horses urethra was investigated by Natali et al [1]. Male human urethral tissues were tested and modeled in paper [2] and the rabbit tissues [3]. The present investigation entails histological, experimental and numerical results (mechanical behaviour) for a proximal and distal regions of the urethra.

2. Materials and methods

Mechanical parameters of tissues were determined for 7 urethra resected from male NZ white rabbits and all the animals were intact and clinically health. Each urethra was divided into 2 sections (proximal, distal regions of the length 8mm). Tensile tests on tubular urethra samples were performed (closed ring). Stress-strain curves were developed and regression was performed. The mechanical properties are defined by the Ogden 2 parameters isotropic hyperelastic model (homogenized mechanical properties). Compared to the other material models (Mooney-Rivlin, Neo-Hookean, Polynominal form), the Ogden option usually provides the best approximation to a solution at larger strain levels. The applicable strain level can be up to 700 percent. Non-linear least squares problem was solved and material constants were appointed (Proximal section: μ_1=0.0005, α_1=6.4191, μ_2=61.984, α_2=6.421x10^{-5}; Distal section: μ_1=-0.4036, α_1=-0.0041, μ_2=-0.4036, α_2=-0.0041). The urethra section is defined from histological image with particular regard to the lumen section. The geometrical model is imported into the finite element software ANSYS Mechanical APDL 16.2. An example of a proximal section of the intact urethra is presented in Fig.1. A two-dimensional solid model of the urethra was discretized with the use of PLANE182 element. It is defined by four nodes having two translations at each nodes. Plane stress element behaviour is assumed. Numerical analyses simulating inflation state are performed for proximal and distal urethras sections. Maximum intraluminal pressure for the rabbit urethra equals 4kPa [3].

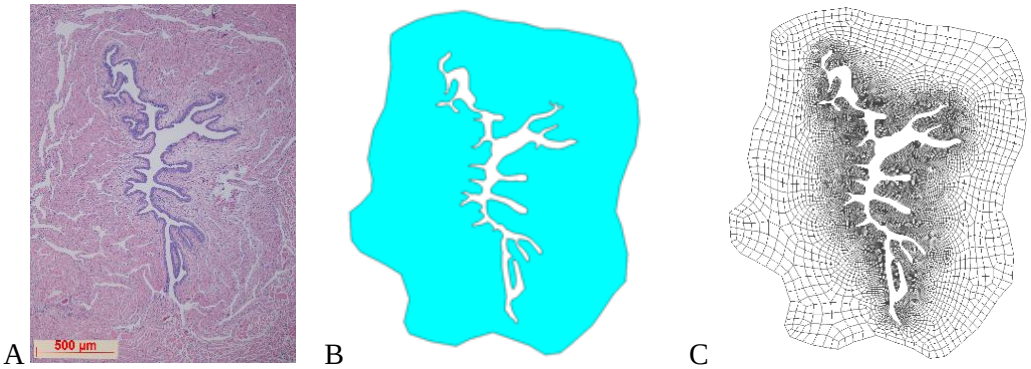

Figure 1: Rabbit proximal urethra-transverse section: (A) trichrome histological section (magnification x40), (B) geometrical model, (C) two-dimensional finite element model.

3. Numerical results

The strains field (Cauchy strain tensor) was calculated for the internal pressure in the range 0-4kPa. The numerical analysis of inflation tests allows evaluating the urethras mechanical behaviour in intraluminal state. The first Cauchy strain ε_1 is presented in Fig.2A. Tensor components versus pressure are reported in Fig.2B. Measurement of strains was made at the point marked with an arrow. For the maximum pressure the first maximum Cauchy strain equals 117%. The second Cauchy strain equals -54%.

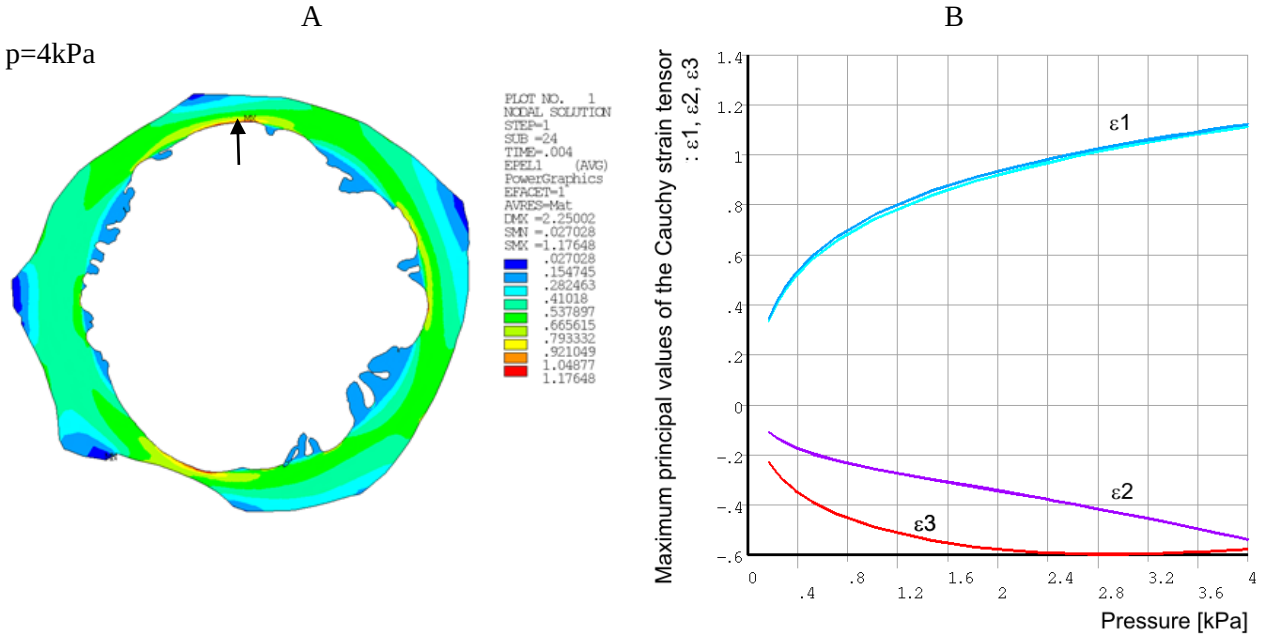

Figure 2: Numerical results of intraluminal pressure test: (A) contours strain field ε_1 for p=4kPa, (B) maximum principal values of the Cauchy strain tensor.

4. Conclusions

Evaluation of histological and mechanical properties of the urethra in animal models enables preliminary assessment of the change of deformation field values. Large strains have been identified in the tissue, which change non-linearly as a function of intraluminal pressure. The luminal cross-section area (CSA) increased several times. The interaction between the highly deformable tissue and a potential polymeric material (stent) is the goal of further works. The next steps of researches will numerical modeling of a urethra stricture and inflammation state and interaction with polymeric materials.

Acknowledgments The authors acknowledge the financial support of National Science Centre, Poland. Project OPUS11, DEC-2016/21/B/ST8/1972

References

[1] A. N. Natali, E. L. Carniel, C. G. Fontanella, A. Frigo, S. Todros, A. Rubini, G. M. De Benedictis, M. A. Cerruto and W. Artibani. Mechanics of the urethral duct: tissue constitutive formulation and structural modeling for the investigation of lumen occlusion. *Biomech. Model Mechanobiol.*, 16: 439-447, 2017.

[2] C. Masri, G. Chagnon, D. Favier, H. Sartelet and E. Girard. Experimental characterization and constitutive modeling of the biomechanical behavior of male human urethral tissues validated by histological observations. *Biomech. and Modeling in Mechanobiol.*, 1-12, 2018, https://doi.org/10.1007/s10237-018-1003-1.

[3] H. L. Andersen, B. U. Duch, H. Gregersen, J. B. Nielsen and H. Ørskov. The effect of the somatostatin analogue lanreotide on the prevention of urethral strictures in a rabbit model. *Urol. Res.*, 31: 25-31, 2003.

NUMERICAL ANALYSIS OF FRACTURE MECHANISM OF PELVIC RING DURING SIDE IMPACT LOAD

T. Klekiel[1], K. Arkusz[1] and R. Będziński[1]

[1]*Biomedical Engineering Division, Faculty of Mechanical Engineering, University of Zielona Gora, Licealna 9 Street, 65-547 Zielona Gora, Poland*

e-mail: t.klekiel@ibem.uz.zgora.pl

1. Introduction

Authors present the problem of a safety of a occupants in the car during a side impact. The mechanism of these fractures remains unclear and this makes the development of effective crash protection more difficult. The mechanism of a side-impact crash results in the energy transfer through the elements of a vehicle's construction onto the side of a passenger's [1] and causes pelvic fractures and injuries within the hip joint due to pressure of the femur head on the acetabulum. According to the contemporary knowledge, the influence of impulse loads on the passenger's body during a traffic accident depends on the velocity of a vehicle during the collision [2] distribution of passengers in the vehicle [3] type of the vehicle, as well as age, height, and weight of the passengers [4-5].

The objective of this work was to analyze the mechanism of multiple pelvis fractures in side-impact car crashes. The elaborated numerical model of the lumbo-pelvic complex includes the most important details responsible for its rigidity and strength including pelvic, hip, and the sacral bones and also soft tissues such as ligaments and cartilages.

2. Material and Methods

A geometric model of the lumbo-pelvic complex (LPC) including elements of skeletal, muscular and ligament structure stabilizing the pelvis was elaborated on the computed tomography images of 25-year-old patient. The fractures threshold were established by applying the impactor simulating the mass, velocity and energy similar to situation during side impact of the car with tree.

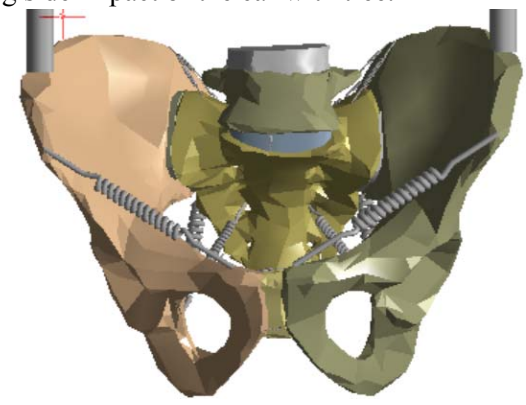

Fig.1. The model of Pelvic ring

LPC model included the following bones: hip, public, sacral with the coccygeal, femoral and the adjacent ligaments. Bone structures were meshed with 8-node tetrahedral finite elements. Cancellous and cortical bones were considered as isotropic material and its mechanical properties were defined using the literature data and original studies by Bedzinski et al. [6-7].

The ligaments were integrated into the model: ligaments responsible for supporting the weight of the torso

and upper limbs preventing herniation of the sacrum with the coccygeal bone in-between pelvic bones thus reducing the vibrations transferred from pelvis to the spine: the anterior sacroiliac ligament and the posterior sacroiliac. Additional ligaments responsible for: preventing backwards tilting of the sacrum's tip: sacrotuberous and sacrospinous ligaments were also studied.

3. Results

The obtained results were compared with the clinical data concerning a 25-year-old patient injured in a road accident (side collision), diagnosed with the fractures of the stem of the left pubic bone, the left superior pubic ramus, the left ischium ramus, and the left lateral mass of the sacrum.
Additionally, it was assumed that the fracture occurs within the layer of cortical bone. This assumption was applied since the analysis of parameters of cortical and cancellous bone revealed that stress concentrates on the surface on which the fractures has been diagnosed by clinical test.

4. Conclusions

The results suggested the mechanism of creating fractures during impact load. In result of the high impact the damages getting in calculations were formulated similar to clinical case as the multi-fractures concentrated around the lateral part of the sacrum and around the ischium. The obtained results explained the relation between the level of the fracture and stiffness of the all ring. The strength of the pelvic ring has influence on the safety of the internal organs and the breaking of the ring continuity is very important and dangerous.
Apart of them the proposed model gave the opportunity to predicted behaviour of the pelvis in some different boundary conditions among which the most likely were selected.

References

1. Lopez-Valdes FJ, Lau SH, Riley PO, Lessley DJ, Arbogast KB, Seacrist T, Balasubramanian S, Maltese M, Kent, R. The Six Degrees of Freedom Motion of the Human Head, Spine, and Pelvis in a Frontal Impact. Traffic Inj Prev. 2014;15(3):294-301.
2. Klekiel T. Biomechanical analysis of lower limb of soldiers in vehicle under high dynamic load from blast event. Series on Biomechanics. 2015;29(2-3):1430.
3. Klekiel T, Bedzinski R. Finite element analysis of large deformation of articular cartilage in upper ankle joint of occupant in military vehicles during explosion. Arch Metall Mater. 2015;60(3):2115-2121.
4. Rowe AS. Pelvic ring fractures: Implications of vehicle design, crash type, and occupant characteristic. Surgery. 2004;136(4):842-847.
5. Arkusz K, Klekiel T, Niezgoda MN, Będziński R. The influence of osteoporotic bone structures of the pelvic-hip complex on stress distribution under impact load. Acta Bioeng Biomech. 2018;20(1):29-38.
6. Bedzinski R, Nikodem AM., Scigala K, Dragan S. Mechanical and structural anisotropy of human cancellous femur bone, J Vibroeng. 2009;11(3):571-576.
7. Bedzinski R, Wysocki M, Kobus K, Szotek S, Kobielarz M, Kuropka P. Biomechanical effect of rapid mucoperiosteal palatal tissue expansion with the use of osmotic expanders, J Biomech. 2011;44(7)1313-1320.

FINITE ELEMENT MODELING OF TRANSAPICAL MITRAL VALVE REPAIR

***Gediminas Gaidulis*[1], *Rimantas Kačianauskas*[2], *Audrius Aidietis*[3]**

[1] *Vilnius Gediminas Technical University, Faculty of Mechanics, Department of Biomechanical Engineering*
[2] *Vilnius Gediminas Technical University, Faculty of Mechanics, Institute of Mechanics*
[3] *Vilnius University, Faculty of Medicine, Department of Cardiovascular Medicine*

1. Introduction

The mitral valve (MV) presents a biological membrane consisting of two leaflets anchored to the papillary muscles (PMs) by the chordae tendineae, a group of cord-like tendons. From the mechanical point of view, these leaflets play the role of the valve which opens and closes during the cardiac cycle and ensures unidirectional blood flow. MV prolapse is one of the most common valvular abnormalities, affecting 2-3% of the general population **[1]**. It is a condition in which MV does not close smoothly during heart contraction. In some cases, the prolapsed MV lets a small amount of blood flow backward. This abnormal reversal flow of blood is called mitral regurgitation (MR), which, if untreated, can lead to a life-threatening condition, such as heart failure. Both MV prolapse and MR are usually caused by the rupture of chordae tendineae. Due to different heart and valvular diseases, mechanical properties of chordae can change, and rupture of one or more chordae occurs.

MR caused by chordae tendineae rupture is typically corrected by the chordae replacement with expanded polytetrafluoroethylene (ePTFE) sutures **[2]**. Transapical off-pump MV repair with neochordae implantation is a novel surgical technique, allowing to correct MR without stopping the heart **[3]**. The procedure is performed under the guidance of echocardiography, therefore, the exact neochordal length to eliminate prolapse while preventing additional restriction of the leaflet can only be assumed **[4]**. For this reason, finite element modeling is proposed to evaluate the effects of neochordal length on the post-repair MV function.

2. Materials and Methods

The MV was modeled as thin-walled structure fixed to moving supports by elastic connectors. Geometry was reconstructed from echocardiographic data using custom platform developed in MATLAB (Mathworks) by Biomechanics Research Group of Politecnico di Milano (Italy) **[5]**. Positions of MV leaflets and PM tips were traced during the closure of the valve, i.e. the time frame between end-diastole, when MV can be assumed as approximately unloaded, and peak systole, when the transvalvular pressure reaches its maximum. The geometry of MV leaflets with a branched network of chordae tendineae connecting PM tips and valve leaflets was then created. Mechanical behavior of MV leaflets was assumed non-linear and anisotropic, and described through a constitutive model, proposed by Lee *et al.* **[6]** Mechanical behavior of the chordae tendineae was assumed non-linear and isotropic, and different types of chordae were modeled as 2nd order polynomial and 5th order Ogden hyperelastic materials.

Prolapse of MV was simulated by removing chordae inserted into the middle segment of posterior leaflet (PL). In order to evaluate the effect of neochordal length on post-repair MV function, a total of four virtual repairs using 4 neochordae of different length were performed. The annular contraction was applied as nodal displacements to MV annulus and a time-dependent physiologic transvalvular pressure curve increasing from 0 to 119 mmHg was applied on the ventricular surface of the leaflets. MV leaflets were meshed into 3-node shell elements, while chordae tendineae was modeled as truss elements (Fig 1a). The function of MV before and after virtual repairs for the time frame between end-diastole and peak systole was simulated in Abaqus/Explicit (Dassault Systèmes).

3. Results

All virtual repair procedures eliminated prolapse and significantly increased the coaptation area. However, while virtual repair restored the different level of coaptation length on the septal-lateral diameter of MV, this

length was insufficient (less than 5 mm **[7]**) after implantation of the shortest and the longest neochordae (Fig. 1b). After virtual repair with the shortest neochordae movement of PL was partially restricted, preventing leaflet apposition, while the implantation of the longest neochordae caused the opposite effect – the movement of the PL was not restricted enough and MV prolapse remained.

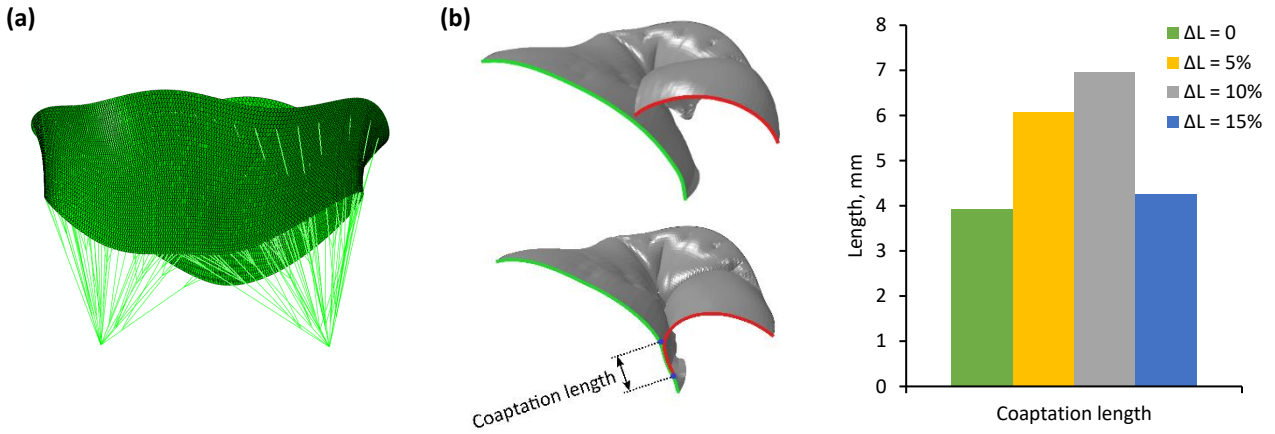

Figure 1. Finite element model of MV leaflets and chordae tendineae **(a)**; evaluation of virtual MV repair in terms of coaptation length **(b)**

4. Conclusions

In the present study, finite element modeling of the outcomes of transapical MV repair with neochordae implantation was introduced. The evaluation of the effect of neochordal length on post-repair MV function showed that the length of implanted neochordae has a significant impact on the correction of MR caused by chordae tendineae rupture.

5. Acknowledgments

We express our appreciation to the research fellows from Biomechanics Research Group of Politecnico di Milano (Italy) for the opportunity to carry out the internship and for the contribution to this work.

References

[1] E. Hayek, C. N. Gring, B. P. Griffin. Mitral valve prolapse. *Lancet.*, 365:507, 2005.
[2] M. Ibrahim, C. Rao, M. Savvopoulou, R. Casula, T. Athanasiou. Outcomes of mitral valve repair using artificial chordae. *Eur. J. Cardiothorac. Surg.*, 45:593, 2014.
[3] D. R. Merk, A. Aidietis, J. Seeburger. Off-pump transapical neo-chordae implantation. *Ann. Cardiothorac. Surg.*, 4:293, 2015.
[4] J. Seeburger, S. Leontjev, M. Neumuth, *et al.* Trans-apical beating-heart implantation of neo-chordae to mitral valve leaflets: results of an acute animal study. *Eur. J. Cardiothorac. Surg.*, 41:173, 2012.
[5] F. Sturla, A. Redaelli, G. Puppini, F. Onorati, G. Faggian, E. Votta. Functional and biomechanical effects of the edge-to-edge repair in the setting of mitral regurgitation: consolidated knowledge and novel tools to gain insight into its percutaneous implementation. *Cardiovasc. Eng. Tech.*, 6:117, 2015.
[6] C. H. Lee, R. Amini, R. C. Gorman, J. H. Gorman 3rd, M. S. Sacks. An inverse modeling approach for stress estimation in mitral valve anterior leaflet valvuloplasty for in-vivo valvular biomaterial assessment. *J. Biomech.*, 47:2055, 2014.
[7] J. J. Silbiger, R. Bazaz. Contemporary insights into the functional anatomy of the mitral valve. *Am. Heart. J.*, 158:887, 2009.
[8] Y. Rim, S. T. Laing, D. D. McPherson, H. Kim. Mitral valve repair using ePTFE sutures for ruptured mitral chordae tendineae: a computational simulation study. *Ann. Biomed. Eng.*, 42:139, 2014.

THE ROLE OF THE BONE STRENGTH ON THE CYST GROWTH IN THE MANDIBLE

J.Miodowska[1], J.Bielski[1], and M.Kromka-Szydek[1]

[1] *Cracow University of Technology, Institute of Applied Mechanics, Cracow, Poland*

e-mail: justyna.miodowska@pk.edu.pl

1. Introduction

Regarding the etiology of bone cysts, different theories have been proposed in order to describe the growth mechanism. One of them states that pressurized fluid enters the bone through a rupture and fractures trabeculae, thereby causing an area of disappearance of bone tissue (osteolysis). Although there is not much evidence indicating that fluid collecting inside the cyst fractures trabeculae, loading conditions of the surrounding bone may indeed cause decreasing of bone density and therefore bone loss. This may be described by a mechanoregulated bone adaptation theory [6]. According to another theory, pressurized fluid may decrease perfusion and oxygen supply for tissue, thereby leading to osteocytes death and further osteolysis. The basic assumption for both hypotheses is that pressurized fluid plays a crucial role in the development of bone cysts. Intracystic pressure may change during the cyst growth, as it is regulated by various factors such as osmotic tension of the fluid, the elasticity of the cyst wall, the permeability and the blood pressure of the capillaries in the cystic wall [2]. In this study we use a computational bone remodelling model to evaluate load conditions during the cyst growth.

2. Method

The computational model is linked to the remodelling model [4,5] that describes the change in the bone density in relation to remodelling stimulus based on the strain energy density as well as mass density of a tissue.

$$\frac{d\rho}{dt} = \begin{cases} B(\psi - K_{min}), & \psi < K_{min} \\ 0, & K_{min} \leq \psi \leq K_{max} \\ D(\psi - K_{over})^2 + K_w, & \psi > K_{max} \end{cases}$$

We mainly focus on the situation when stimulus exceeds the threshold value K_d indicating bone loss due to overload. We use the finite element model (Fig.1) to predict cyst growth and bone architecture changes in response to pressure induced by the presence of the fluid. The model consists of two materials of different properties, namely inner trabecular and outer cortical bone assumed as linear, isotropic and homogenous. It is noted that there are various relations between density and bone Young's modulus E available in the literature. In this paper, following equation is adopted: $E = c\,\rho^3$ [3], where c is a constant and equals 3790 [MPa·cm^9/g^3]. At each element of the FE model the value of the stimulus is calculated as a strain energy density divided by bone mass density. If the stimulus exceeds threshold value, the element is removed from the mesh.

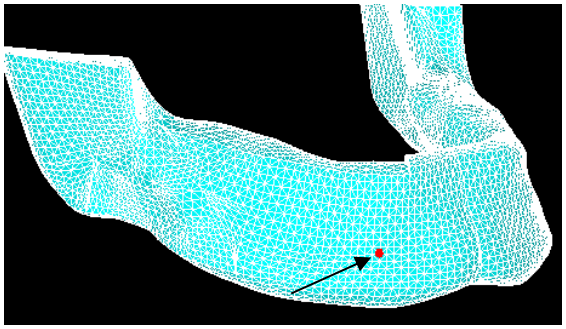

Fig.1. Finite element model of the mandible with the cyst.

With this volume change the boundary load conditions are updated to spread the pressure action over newly created areas. The surface of the cyst is loaded statically with normal pressure [1]. This resorption initiating value depends strongly on the bone elastic modulus. The stronger the bone is, the higher value of the pressure is necessary to start the process of cyst growth strictly connected with bone resorption. The choice of the applied load is not straightforward, since reported cancellous bone density and thus Young's modulus values cover a wide range. However, in this study the exact applied load values are not that important since, the results are evaluated qualitatively and not quantitatively.

3. Results

Bone resorption in response to pressure inside the cyst leads to growth of the cavity, which takes an irregular shape (Fig.2). The cyst growth and it shape depend on the Young modulus of the surrounding bone. After the initial stage, decreasing pressure maintains further expansion of the cyst in the mandible. However, the regulatory mechanisms of intracystic pressure and growth of cyst under lower pressure are unclear and remain speculative. Further studies are required to clarify them.

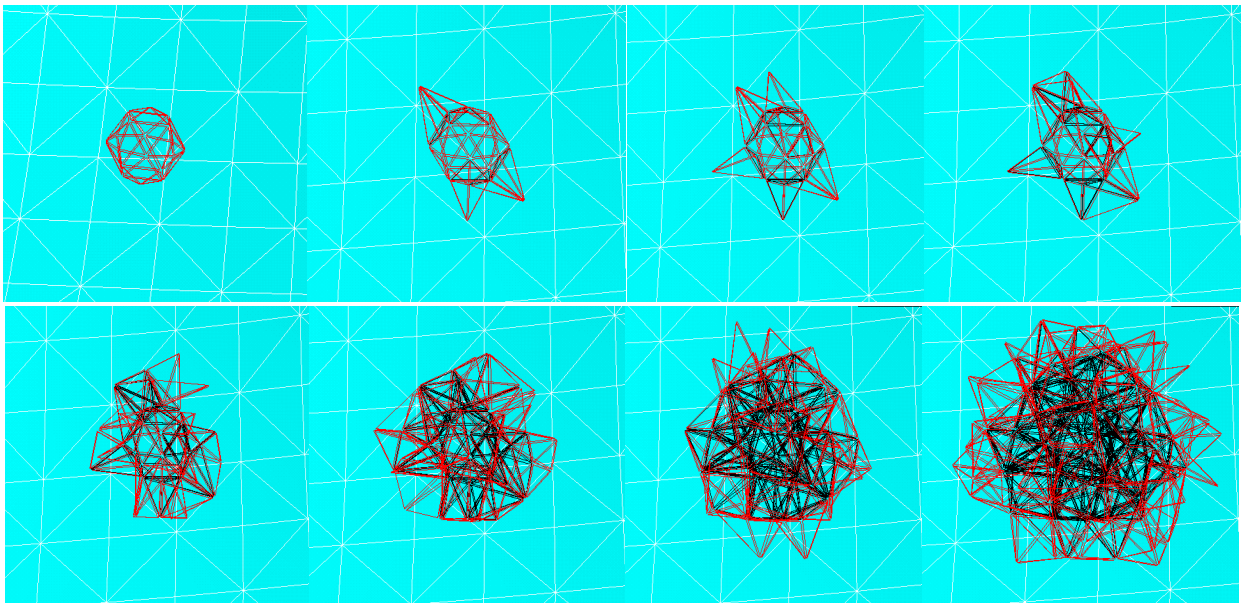

Fig.2. Subsequent stages of the cyst growth.

4. References

[1] L.G.E. Cox, et al. The role of pressurized fluid in subchondral bone cyst growth. *Bone*, 49, 762-768, 2011.

[2] Y. Kubota, T. Yamashiro, S. Oka. Relation between size of odontogenic jaw cysts and the pressure of fluid within. *British Journal of Oral and Maxillofacial Surgery*, 42, 391-395, 2004.

[3] L.C. Lin et al. Multi-factorial analysis of variables influencing the bone loss of an implant placed in the maxilla: Prediction using FEA and SED bone remodeling algorithm. *Journal of Biomechanics*, 43, 644-641, 2010.

[4] J. Miodowska, J. Bielski, M. Kromka-Szydek. Callus remodelling model. *AIP Conference Proceedings*, Vol. 1922, 070003, doi: 10.1063/1.5019070, 2018.

[5] J. Miodowska, J. Bielski, M. Kromka-Szydek. A new model of bone remodelling. *Engineering Transactions*, 64(4), 610-611, 2016

[6] H. Weinans, R. Huiskes and H.J. Grootenboer. The behavior of adaptive bone-remodeling simulation models. *Journal of Biomechanics*, 25, 1425-1441, 1992.

NUMERICAL MODELLING OF HEAT TRANSFER IN BIOLOGICAL TISSUE DOMAIN USING INTERVAL ANALYSIS

A. Piasecka-Belkhayat[1], B. Mochnacki[2]

[1]*Institute of Computational Mechanics and Engineering, Silesian University of Technology, Gliwice, Poland*
[2]*University of Occupational Safety Management in Katowice, Katowice, Poland*
e-mail: alicja.piasecka-belkhayat@polsl.pl, bmochnacki@wszop.edu.pl

1. Introduction

In the paper, the numerical analysis of heat transfer process proceeding in the non-homogeneous biological tissue domain subjected to external heat source is presented. In particular, the two-dimensional (axially symmetrical) model with uncertainly defined parameters is considered. The base of mathematical model is given by a set of the Pennes interval equations supplemented by the boundary and initial conditions. The problem discussed has been solved using the interval finite difference method with the rules of directed interval arithmetic [1]. A similar analysis has been done using extended gradual interval arithmetic as the combination of the gradual numbers and Kaucher arithmetic where subtraction and division operators are respectively the inverse operators of the addition and the multiplication [2]. In the final part of the paper the numerical computations obtained for both methods are shown.

2. Interval governing equations

Thermal processes proceeding in the axially symmetrical heterogeneous skin tissue domain can be described by the following system of interval energy equations

$$\left[c_e^-, c_e^+\right]\frac{\partial T_e(r, z, t)}{\partial t} = \left[\lambda_e^-, \lambda_e^+\right]\nabla^2 T_e\,(r, z, t) + \left[Q_e^-(r, z, t), Q_e^+(r, z, t)\right] \tag{1}$$

where e = 1, 2, 3 corresponds to the successive layers of skin (epidermis, dermis, subcutaneous region), $\left[\lambda_e^-, \lambda_e^+\right]$ is the interval thermal conductivity, $\left[c_e^-, c_e^+\right]$ is the interval volumetric specific heat, $\left[Q_e^-(x,t), Q_e^+(x,t)\right]$ is the capacity of interval internal heat sources, $T(r, z, t)$, t is the time, r and z denote the cylindrical coordinates. The interval capacity of internal heat sources is a sum of two components

$$\left[Q_e^-(x,t), Q_e^+(x,t)\right] = \left[G_{Be}^-, G_{Be}^+\right]c_{Be}\left[T_B - T_e\,(x, t)\right] + \left[Q_{me}^-, Q_{me}^+\right] \tag{2}$$

where $\left[G_{Be}^-, G_{Be}^+\right]$ is the interval perfusion coefficient, c_B is the volumetric specific heat of blood, T_B is the arterial blood temperature, $\left[Q_{me}^-, Q_{me}^+\right]$ is the interval metabolic heat source.

The mathematical model should be supplemented by the boundary and initial conditions.
The skin surface is subjected is subjected to an external heat source assumed in the form (see Figure 1)

$$t \le t_p: \quad q_b\left(r,0,t\right) = q_0 \exp\left[-\frac{r^2}{2\left(R/3\right)^2}\right] \tag{3}$$

where t_p is the exposure time, q_0 is heat flux corresponding to r = 0 and R is the radius of the cylinder. For the others parts of the boundary the no-flux conditions are taken into account (the significant dimensions of R and Z allow to consider such a condition). The initial tissue temperature is also known.

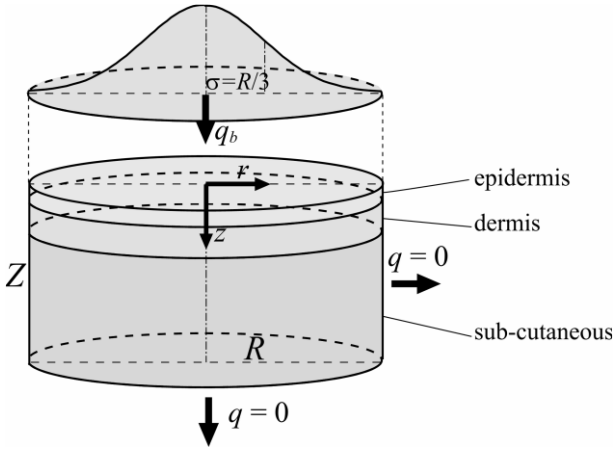

Fig. 1. Domain considered

3. Results of computations

At the stage of numerical computations a three-layered cylindrical skin tissue domain of dimension Z = 12.1 mm and R = 20 mm has been considered. In the first numerical example the thermophysical parameters $\overline{\lambda}_e = \left[\lambda_e - 0.05\lambda_e,\ \lambda_e + 0.05\lambda_e\right]$ and $\overline{c}_e = \left[c_e - 0.05c_e,\ c_e + 0.05c_e\right]$ have been assumed as interval numbers (for e = 1, 2, 3), the time of external heat source exposition is 5.21 s. The other input data are taken from [1]. The numerical model of the problem discussed is based on the finite differential method in the version adapted for the uncertain thermophysical parametrs. All numerical computations has been made using the rules of interval arithmetic, of course. Figure 2 illustrates the heating and cooling curves at the nodes 1 $\left(L_1, 0\right)$, 2 $\left(L_1, r/4\right)$ and 3 $\left(L_1, r/2\right)$ for $q_0 = 5 \cdot 10^3$ W/m^2. The results obtained have been compared to the results of the second example, where the theory of the extended gradual interval arithmetic has been applied. In the full version of the paper, the details of numerical algorithm and also the comparison and discussion of the results obtained will be presented.

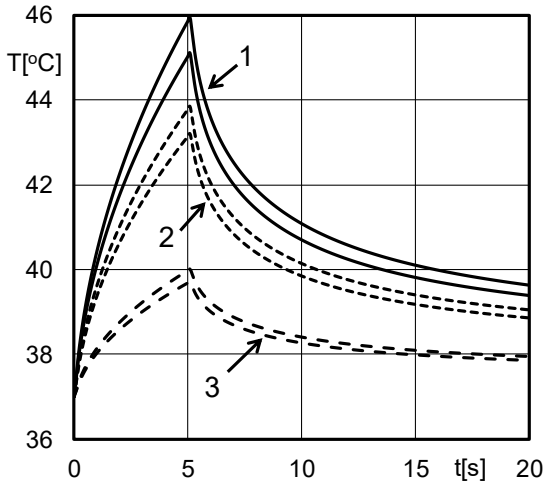

Fig. 2. Solution for directed interval arithmetic.

References

[1] B. Mochnacki and A. Piasecka-Belkhayat, Numerical modeling of skin tissue heating using the interval finite difference method, MCB: Mol. Cell. Biomech., 10, 3, 233-244, 2013.

[2] R. Boukezzoula, S. Galichet, L. Foulloy and M. Elmasry, Extended gradual interval (EGI) arithmetic and its application gradual weighted averages, *Fuzzy Sets and Systems 257*, 67-84, 2014.

BEHAVIOR OF THE PERIODONTIUM UNDER LOADING USING A KINETIC MODEL OF THE MASTICATORY SYSTEM

S. E. Martinez Choy[1], K. Schweizerhof[1], J. Lenz[1], and H. J. Schindler[2]

[1]*Research Group Biomechanics, Institute of Mechanics, Karlsruhe Institute of Technology (KIT), Karlsruhe, Germany*
[2]*Department of Prosthodontics, Dental School, University of Würzburg, Würzburg, Germany*

e-mail: Simon.choy@kit.edu

1. Introduction

The periodontal ligament (PDL) is a binding tissue that attaches the teeth to the alveolar bone and governs short-term tooth mobility. It is composed of bundles of connective tissue fibers, specific cells, vasculature, nerves and ground substance [2]. Occlusal forces are absorbed by the oblique fibers, which cover most of the surface of the tooth. The vasculature of the PDL has an essential role with respect to its functional properties. As the teeth are loaded, fluids inside in the PDL (blood vessels and ground substance) will flow to the alveolar bone (the rich vascular supply of the PDL penetrates the alveolar bone), granting the tissue dissipation properties. Once fluid flow can no longer take place, the PDL becomes essentially incompressible, and hydraulic pressure distribution occurs [4].

Currently, discrepancies found in the literature relating to the mechanical properties of the PDL complicate the interpretation of results obtained with simplified numerical models [3]. Additionally, unrealistic loading conditions of the masticatory system with forces not reproducing realistic chewing forces are often employed.

In this work, the behavior of the PDL is compared between two different material models, which are —though also simplified— able to reproduce the results from experimental tests [5], during realistic kinetic chewing tasks. Loading on the teeth and subsequently in the PDL are determined during common motor tasks of incisive biting and unilateral molar biting. These tasks are simulated under kinetic conditions by means of a complete model of the masticatory system which encompasses all essential components of the masticatory system, i.e. the mandible, maxilla, temporomandibular joints (TMJ), periodontal ligament, muscles and the teeth (Figure 1).

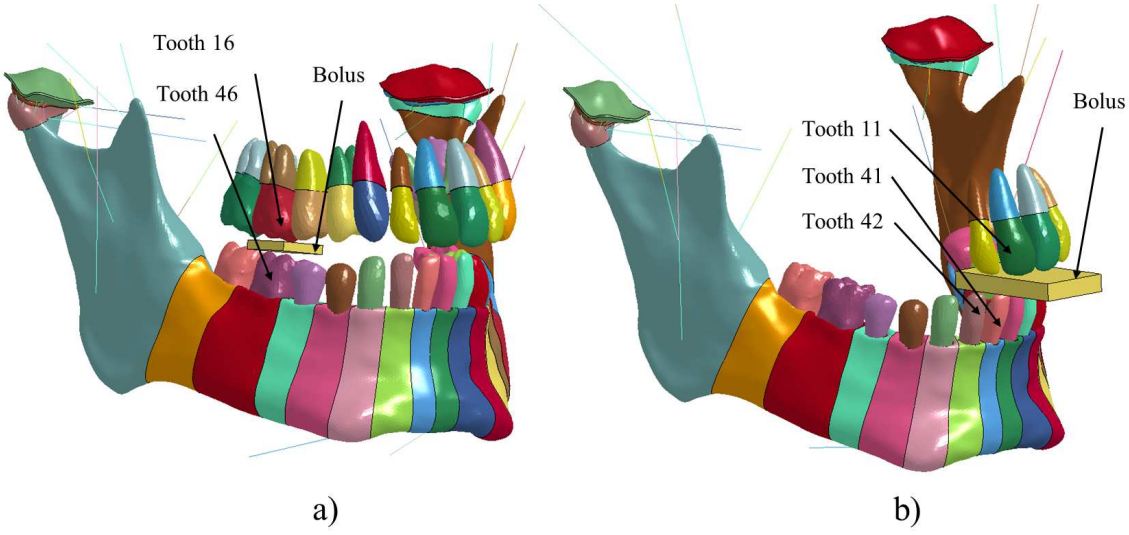

Figure 1: A finite element model that encompasses the majority of the components of the masticatory system is employed to recreate a unilateral molar biting task (a), and an incisive biting task (b)

2. Materials and Methods

A finite element (FE) model comprising all essential components of the stomatognathic system was employed to load the teeth by biting on a deformable bolus. The model is explained in detail in a previous work [1]. Two hyperelastic material models are used for the PDL, a first order Ogden model and a model in polynomial form that follows the work of Su et al. [6]. The strain energy function for the Ogden material model is defined as

$$W = \sum_{i=1}^{3} \sum_{j=1}^{n} \frac{\mu_j}{\alpha_j} (\lambda_i^{\alpha_i} - 1) + K(J-1)^2 \,. \tag{1}$$

where W is the strain energy potential, λ_i the deviatoric principal stretches, μ_j and α_j material parameters, J the determinant of the elastic deformation gradient, and K the bulk modulus. The employed material parameters can be found in Martinez et al. [1]. On the other hand, the strain energy function in polynomial form proposed by Su et al. [6] is given by

$$W = C_{10}(\bar{I}_1 - 3) + C_{20}(\bar{I}_1 - 3)^2 + C_{30}(\bar{I}_1 - 3)^3 + \frac{1}{D_1}(J-1)^2 + \frac{1}{D_2}(J-1)^4 + \frac{1}{D_3}(J-1)^6 \tag{2}$$

where C_{10}, C_{20}, C_{30}, D_1, D_2, D_3 are material parameters, $\bar{I}_1$ the first invariant of the right Cauchy strain tensor with the volumetric component removed, and J the determinant of the deformation gradient. The used material parameters are identical with those proposed in [6] for the volumetric finite strain viscoelastic model.

3. Results

Displacements occurring in the teeth, as well as stresses in the PDL estimated by the two material models are presented and compared during different biting tasks. Both material models are able to reproduce displacements of the teeth that are inside the range observed in experimental tests. However, in the case of very small forces, displacements are smaller than those in the experimental range. The material parameters could be modified to produce better results at this range, but with a significant increase of computational effort, as the non-linear behavior of the material model would increase as well. Stresses predicted by the materials are significantly different from each other, with the polynomial form showing predominantly compressive stresses to handle the loads on the teeth. In both material models, significant stress concentration is observed due to their exponential response to strain. The magnitude and orientation of the resulting forces on the teeth, as well as their respective application points are shown, which can be employed in simplified models where only the teeth and the PDL are modeled.

References

[1] S.E. Martinez Choy, J. Lenz, K. Schweizerhof, M. Schmitter, and H.J. Schindler. Realistic kinetic loading of the jaw system during single chewing cycles: a finite element study. *Journal of Oral Rehabilitation*, 44(5):375–384, 2017.

[2] H. Feneis. Anatomy and physiology of the normal gingiva. *Deutsche Zähnarztliche Zeitschrift*, 7(8):467–476, 1952.

[3] T.S Fill, R.W. Toogood, P.W. Major, and J.P Carey. Analytically determined mechanical properties of, and models for the periodontal ligament: Critical review of literature. *Journal of Biomechanics*, 45(1):9–16, 2012.

[4] A.B. Kristiansen and K.J. Heyeraas. Micropuncture measurements of interstitial fluid pressure in the rat periodontal ligament. *Proceedings of the Finnish Dental Society*, 85(4-5):295–300, 1989.

[5] G.J. Parfitt. Measurement of the physiological mobility of individual teeth in an axial direction. *Journal of Dental Research*, 39(3):608–618, 1960.

[6] Ming-Zen Su, Hao-Hueng Chang, Yu-Chih Chiang, Jung-Ho Cheng, Lih-Jyh Fuh, Chen-Ying Wang, and Chun-Pin Lin. Modeling viscoelastic behavior of periodontal ligament with nonlinear finite element analysis. *Journal of Dental Sciences*, 8:121–128, 2013.

EXPERIMENTAL VALIDATION OF FINITE ELEMENT MODELING OF CREEP BEHAVIOR OF HUMAN KNEE JOINT

M.L. Rodriguez[1], S. Uzuner[2], and L.P. Li[1]

[1]*Department of Mechanical & Manufacturing Engineering, University of Calgary, Calgary, Canada*
[2]*Duzce University, Duzce, Turkey*

E-mail: Leping.Li@ucalgary.ca

1. Introduction

The human knee joint primarily performs mechanical functions during daily life activities. The contact mechanics of the joint is predominantly influenced by the mechanical properties of articular cartilages and menisci that exhibit strong creep and relaxation behaviors, which must be understood in order to discover the mechanism of cartilage mechanobiology, joint injury and disease. While past studies investigated either the poromechanics of individual tissues or the elasticity of the whole joint, we are interested in the poromechanics of the intact knee joint. The joint functions may be better appreciated when the fluid pressure/flow and anatomically accurate knee structure are considered simultaneously. We have first developed a fibril-reinforced model of articular cartilage using multiple experimental validations. This tissue model highlights the interplay between the collagen fibril-reinforcement and fluid pressurization in the tissues. We have then implemented the constitutive model in a patient-specific knee joint model using 3-Tesla magnetic resonance imaging (MRI) in order to determine the creep, relaxation and contact mechanics of the knee joint modulated by the fluid pressurization in the tissues. This joint model was found to be able to predict the load support of the knee joint and load share between cartilages and menisci that cannot be described with an elastic model of the knee joint. The objective of the present study is to further validate and refine the previous model with dual fluoroscopic (DF) measurement of human participants (Fig. 1).

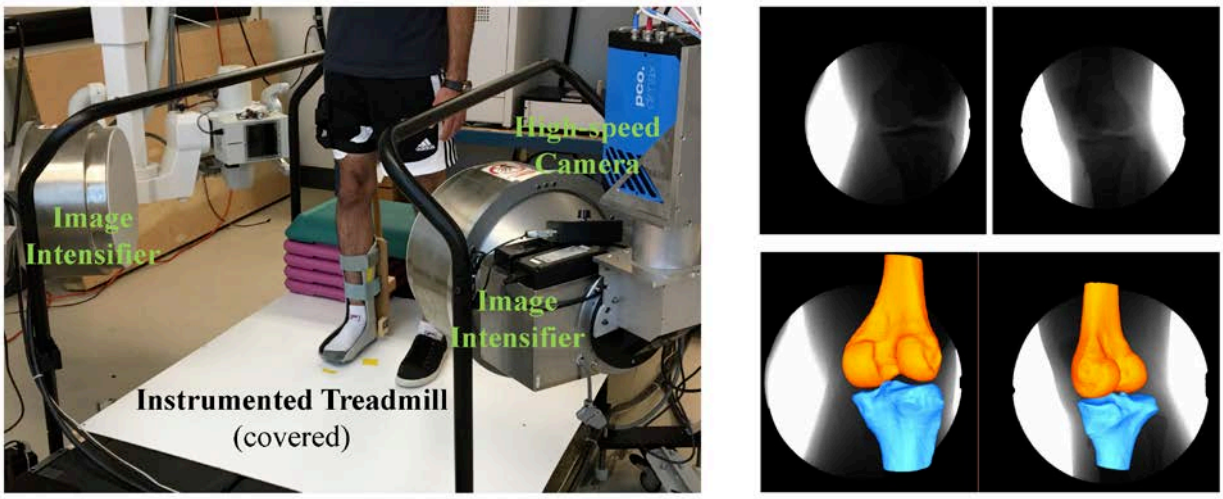

Figure 1: Experimental setup (left) and images from the two cameras of different angles (right).

2. Methods

We have so far performed 2 healthy adult knee measurements with 1 female and 1 male. Tests were done in early morning to minimize residual tissue deformation. The participants were given car rides from home and moved in wheelchairs to the test facility. The subjects further remained seated in an MRI compatible wheelchair for 30 minutes, before 3-Tesla MR images (Fiesta with GE MR750) were obtained from the unloaded knee. Afterwards, the right knee was imaged with biplanar DF while half body weight was gradually applied to the leg in approximately 5 seconds, followed by a 10-minute creep. Images were

acquired from two cameras at a frame rate of 6Hz, continuously for the first minute and at 6Hz for 2 s intermittently with 30-second breaks for the rest nine minutes. The measurement was calibrated and image distortion corrected. A 2D-3D image registration approach was used to align the DF images with 3D MRI based model of the joint in order to determine the bone displacement. The ground reaction was simultaneously recorded with a Bertec instrumented treadmill. The 3D MRI model was also used for finite element analysis, whose procedure has been previously developed.

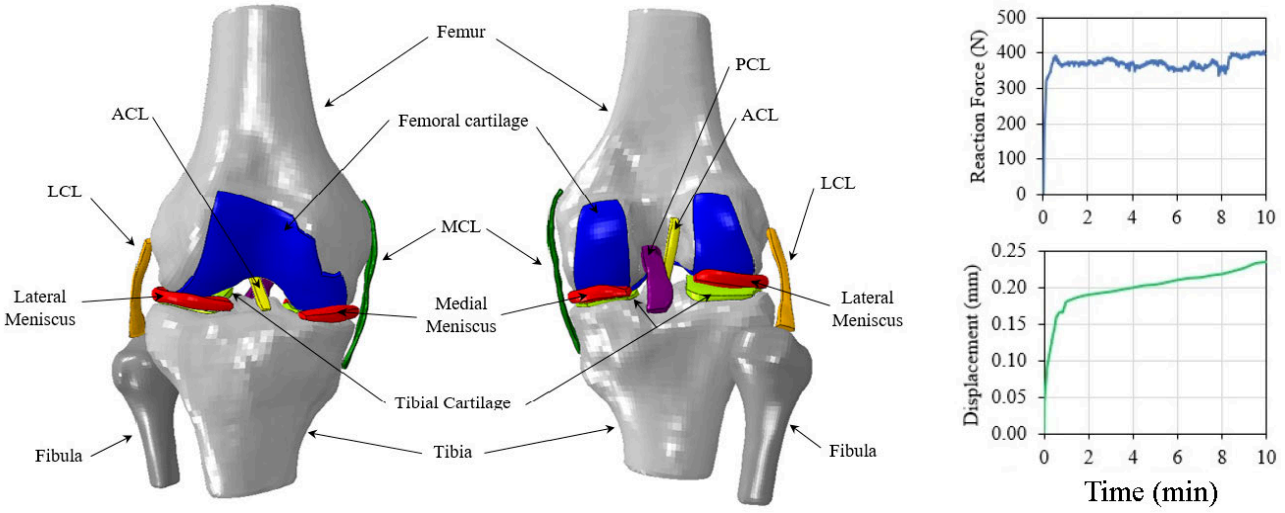

Figure 2: Knee joint model reconstructed from MRI in anterior (left) and posterior (middle) views (patellar not included), showing also the vertical reaction force measured by a force plate (upper right) and knee compression determined from DF images (lower right).

3. Results

Although there was no lab control on the weight applied on the knee in observation, a creep loading was followed pretty well in both measurements; only small fluctuations were observed (Fig. 2). The displacement found in the vertical direction of distal femur and proximal tibia indicates a nearly standard creep deformation in the joint (Fig. 2), although 3D displacement/rotation actually occurred with a maximum rotation of 4º and a maximum horizontal displacement of 1.5mm. A preliminary finite element analysis on the first measurement indicated a stiffer than expected knee. The data processing and modeling on the second measurement are still ongoing.

4. Discussion

The human knee measurements indeed demonstrated creep response, as predicted in our finite element modeling, and comparable with our lab tests of fresh porcine joint specimens. In particular, significant creep deformation can be developed in a minute, which indicates the necessity of considering creep response in the joint modeling that has not drawn sufficient attention in the area.

Live human measurement appears to be complicated, but a creep loading protocol can still be performed with satisfaction. In addition to model validation, our combined measurement and modelling approach will further determine the stress and pressure in the joint using measured displacements, which may be used to evaluate cartilage health state in vivo.

Acknowledgments The authors appreciate the use of Dr. Janet Ronsky lab and great help from her team. We also acknowledge the financial support of the Natural Sciences and Engineering Research Council of Canada. Human measurements were performed with research ethics REB15-1165_REN3 at the University of Calgary.

Session S13: Smart materials and structures

Organizers: E. A. Pieczyska (IPPT PAN, Warsaw), H. Tobushi (Aichi IT, Toyota-city), Q. P. Sun (HKUST, Hong Kong)

AN ESTIMATION ON AXIAL STRENGTH OF JOINT MADE OF FE-28MN-6SI-5CR SHAPE MEMORY ALLOY AT VARIOUS DEFORMATION RATE

Bo Cao[1] and Takeshi Iwamoto[2]

[1]*Graduate School of Engineering, Hiroshima University, 1-4-1 Kagamiyama, Higashi-Hiroshima, 739-8527, Japan*
[2]*Academy of Science and Technology, Hiroshima University, 1-4-1 Kagamiyama, Higashi-Hiroshima, 739-8527, Japan*

e-mail: iwamoto@mec.hiroshima-u.ac.jp

1. Introduction

Fe-based shape memory alloy (Fe-SMA) is attempted to be applied to large structural members such as the dampers to reduce vibration for the high-rise building structure [1] as well as the joint for the curved pipes in the underground. When applying this alloy to a smaller-scale member, it is difficult to fasten it sufficiently because its maximum recoverable strain so far is only about 4%. In addition, it can be realized that the pipe joint is loaded at various deformation rate such as earthquake or strong wind. Therefore, it is important to examine axial strength of the joint at various deformation rate especially at much higher deformation rate.

In the previous study, the joint strength is basically estimated by pull-out test based on the tensile test and the strength is defined as maximum force [2]. However, it is difficult to use this kind of the specimen to the impact testing machine because it has a quite complicated structure. On the other hand, a compression-shear test by pushing out only the joint has a simple method in comparison with the pull-out test. Therefore, it will be possible to expand the range of deformation rate for the test.

Fujita et al. [3] performed the three-point bending test of the joint at various deformation rate and estimated its rate sensitivity of bending strength. They define the strength at the fracture of the joint as force when the circumferential strain on the surface of the joint starts decreasing. As a result, it is revealed that the strength decreases with an increase in deformation rate. Following this viewpoint, Yamamoto et al. [4] also attempted to evaluate the axial deformation behavior by performing compression-shear test at various deformation rate by using two different testing apparatuses such as a conventional material testing machine under quasi-static condition and drop-weight testing machine under impact condition.

In the present research work, the axial deformation behavior of the joint is examined by the compression-shear test. Following the previous studies [3, 4], a specimen which consists of the expanded joint made of Fe-28Mn-6Si-5Cr alloy and bar made of SUS304 is heated to tighten. Next, the axial deformation behavior is estimated by performing the compression-shear test at various deformation rate. As a result, it is attempted that the rate sensitivity of maximum force and axial strength is discussed.

2. Experimental procedure

After machining joint and bar, they are heat-treated as same as the previous research works presented [3, 4]. On the other hand, diameter of the previously-mentioned joint is expanded by a tapered bar made of die steel. After inserting the bar made of SUS304, it is tightened by the joint because of its recovery behavior through the heat treatment. Two rosette gauges are glued at two positions on the surface of the joint. More details of the diameter expansion and fastening processes of joints can be also seen in Ref. [3, 4].

In the quasi-static test, the compression-shear test is performed by using a material testing machine (Shimadzu AG-250kNX). For the impact test, the compression-shear tests are performed by using a drop-weight test machine. The details of the compression-shear test conducted by using the material testing machine and drop-weight test are provided in the previous research work presented [4]. In order to investigate the axial strength of joint at various deformation rate including much higher deformation rate, compression-shear tests at room temperature are also carried out by using split Hopkinson pressure bar (SHPB) technique.

3. Results and discussions

Figure 1 shows the force and circumferential strain vs displacement obtained by the quasi-static test at 0.083mm/s. From this figure, both force and the circumferential strain become almost constant after reaching the maximum value. Before circumferential strain at upper side indicates its maximum value, a sudden change in a slope of the curve can be seen. Here, the axial strength of the joint can be defined as force when the slope of the curve on the circumferential strain changes as similar to the previous research works [3, 4].

On the other hand, for higher deformation rate, Fig. 2 shows the input, output and average force and circumferential strain vs displacement obtained by the SHPB technique at 3884mm/s. As shown in this figure, the circumferential strain at the upper and lower sides of the joint is consistent in the beginning of deformation. However, it can be seen that the difference begins to occur at the displacement of 0.1mm. Here, it is different from the above-mentioned mechanism of fracture, the axial strength at higher deformation rate can be defined as force at the point where the circumferential strain at the upper and lower sides of the joint start being different. In addition, compared with the maximum force and axial strength at lower deformation rate for the quasi-static test, it is possible to observe the value of both the maximum force and axial strength at higher deformation rate become higher.

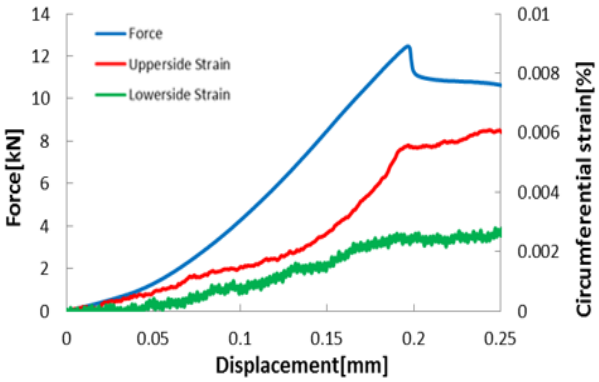

Fig. 1. Force and circumferential strain vs displacement obtained by the quasi-static test

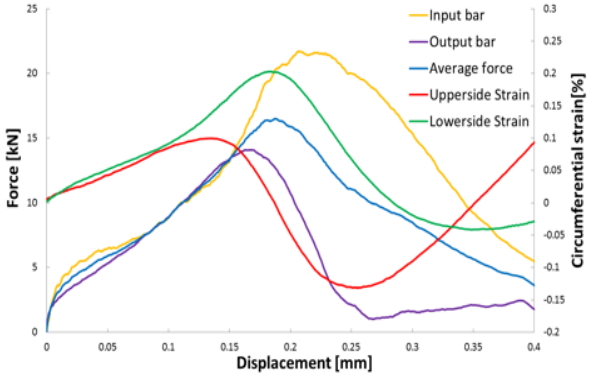

Fig. 2. Force and circumferential strain vs displacement obtained by the SHPB technique

4. Summary

For the bar made of Fe-SMA, the compression-shear test was carried out at various deformation rate. At the same time, the behavior of circumferential strain of the joint was measured. Other details will be discussed at the conference.

Acknowledgments We gratefully acknowledge financial supports from THE AMADA FOUNDATION and the 26th ISIJ Research Promotion Grant, Japan. We also wish to thank Mr. Yasuhiro Yamamoto of Nisshin Koki for his assistance with the experimental investigation.

References

[1] http://www.takenaka.co.jp/news/2014/05/01/index.html.
[2] W. Wada, H. Naoi and T. Maruyama. Shape recovery characteristics and strength of pipe joint made of ferrous shape memory alloy.
Proc. CAMP-ISIJ., 17:1044, 2004. (in Japanese)
[3] K. Fujita, K. Nishikori and T. Iwamoto. An assessment on strength of pipe joint made of Fe-shape memory alloy by three-point bending test in the wide range of deflection rate.
Proc. Plasticity., 139, 2015.
[4] Y. Yamamoto, K. Fujita and T. Iwamoto. An experimental study on axial joint strength made of Fe- 28Mn-6Si- 5Cr shape memory alloy at various deformation speeds.
Key. Eng. Mater., 725:99, 2016.

CORROSION FATIGUE STRENGTH OF THERMAL NITRIDED TINI SHAPE MEMORY ALLOY WIRE

R. Matsui [1], K. Yamada [2], and M. Okumura [3]

[1] Aichi Institute of Technology, 1247 Yachigusa, Yakusa-cho, Toyota, Aichi, 470-0392 Japan
[2] NIPPON THOMPSON Co. Ltd., 2-7-17 Shiba, Minato-ku, Tokyo, 105-0014 Japan
[3] Graduate School of Aichi Institute of Technology, 1247 Yachigusa, Yakusa-cho, Toyota, Aichi, 470-0392 Japan

e-mail: r_matsui@aitech.ac.jp

1. Introduction

A TiNi shape memory alloy (SMA) has some advantages compare to other series of SMAs such as large recovery strain, long fatigue life, better biocompatibility, etc. Therefore, the TiNi SMA is commonly used as actuators and medical devices. In the case of practical use of the TiNi SMA into these devices, it is important to grasp a corrosion resistance and corrosion fatigue strength of the material. A few researchers have investigated how to improve the corrosion resistance of the material [1], however, no study has revealed the fatigue properties of the TiNi SMA in severe conditions, such as in seawater or blood, yet. In this study, we attempt to clarify the corrosion fatigue life of the TiNi SMA and enhance it by means of a thermal nitridation (TN) treatment which is able to produce a thin passive layer on the surface of the material.

2. Experimental conditions and procedures

The material used in the study is a 0.7 mm diameter TiNi SMA wire (Ti-49.7 at% Ni) manufactured by Furukawa Techno Material Co., Ltd. We carried out the following procedure for TN treatment as shown in Fig. 1. First, the as-received (as-drawn) material was mechanically polished to remove a surface oxide film by abrasive wheels and a buffing compound. Second, the polished material was degreased by an ultrasonic washer. Then the degreased material was heat-treated in a gas substitution electrical furnace filled with pure N_2 gas for 1 h at 673 K at a gauge pressure of 0.1 MPa. The material was then allowed to cool inside the furnace. We also prepared a heat-treated (HT) material that was produced by only conventional shape memory heat treatment in air under the same condition as the TN process except for the atmosphere and a material that was removed the film generated via the HT. The material produced by this process is hereafter referred to as the HT-P material.

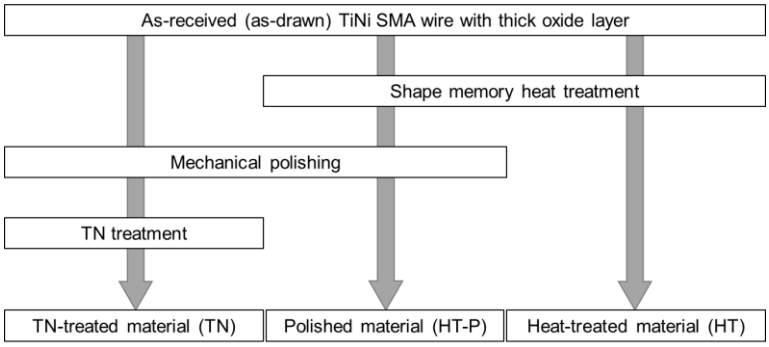

Fig. 1 Fabrication process of each material

We assessed the corrosion resistance of the materials by anodic polarization curves. In the experiment, we used a counter electrode made of platinum and a saturated calomel electrode as a reference. The anodic polarization curves were obtained by an automatic polarization system (HSV-110, Hokuto Denko Corporation), which can apply electrical potential at a scanning rate of 10 mV/min. A 3%-NaCl water solution was used as the electrolyte.
We also investigated the corrosion fatigue life of each material by rotating bending fatigue tests in 10%-NaCl water solution under a frequency of 100 cpm at room temperature.

3. Results and discussion

Figure 2 shows the anodic polarization curves of the materials. This figure includes results of pure Ti and 316L stainless steel which are common materials as medical devices. It is clearly found that the potential of the TN material is much higher than that of the HT-P, 316L, and HT material especially in the early stage of the corrosion. Not only that, the TN material has the corrosion resistance comparable to the pure Ti. Obviously, this high resistance is the effect of the passive layer consisted of Ti nitride generated by the TN process.
Fatigue life curves of the TN, HT-P, and HT materials obtained by the rotating bending fatigue tests in the 10%-NaCl water solution are shown in Fig. 3. The fatigue lives of the TN and HT-P materials are higher than that of the HT material because the surface roughness of these materials is much lower compare with that of the HT material owing to the mechanical polishing. In the low strain region (the strain range of above 1.5%), the TN material shows the long fatigue life even in the severe environment. Although we presume that such long fatigue life of the TN material is achieved by the presence of the thin passive layer, clarifying the influence of the passive layer on the corrosion fatigue life for the TiNi SMA is our future task.

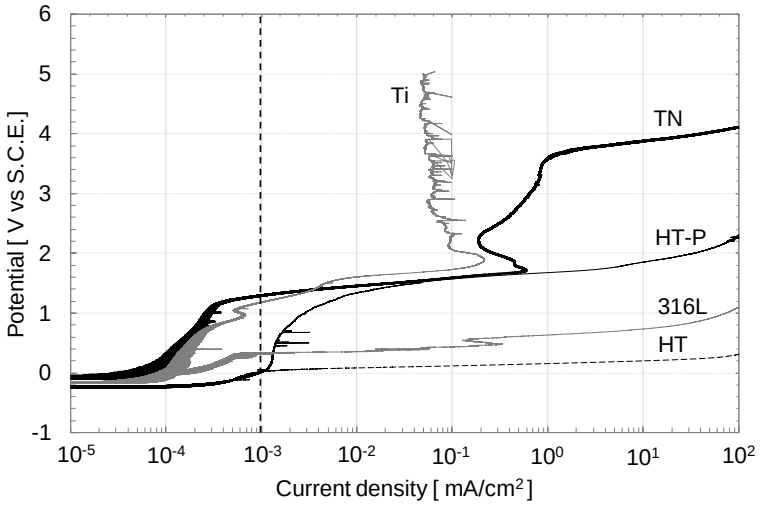

Fig. 2 Anodic polarization curves for each material

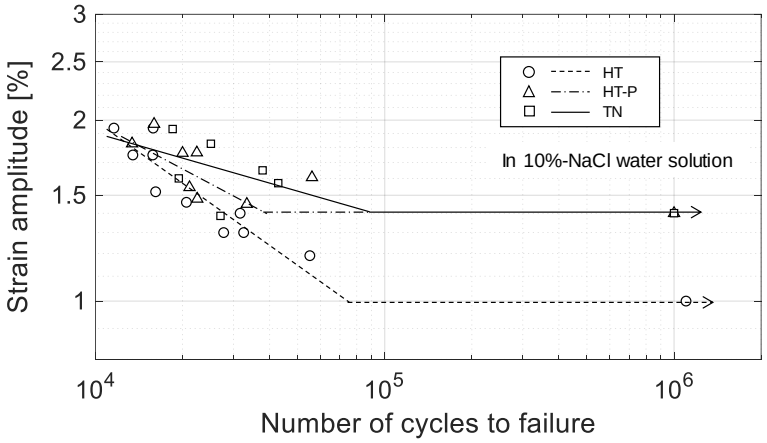

Fig. 3 Fatigue life curves for each material

Acknowledgments The authors acknowledge the financial support of The Science Research Promotion Fund.

References

[1] Ray W.Y. Poona, Joan P.Y. Hoa, X. Liua, C.Y. Chunga, Paul K. Chua, Kelvin W.K. Yeungb, William W. Lub, Kenneth M.C. Cheung. Anti-corrosion performance of oxidized and oxygen plasma-implanted NiTi alloys, *Mater. Sci. Eng. A*, 390:444, 2005.

DEVELOPMENT OF TWO-WAY ROTARY DRIVING ELEMENT USING TORSIONAL DEFORMATION OF TINI SHAPE MEMORY ALLOY THIN TAPE

Y. Furukawa [1], R. Matsui [2], and H. Tobushi [2]

[1] *Graduate School of Aichi Institute of Technology, 1247 Yachigusa, Yakusa-cho, Toyota, Aichi, 470-0392 Japan*
[2] *Aichi Institute of Technology, 1247 Yachigusa, Yakusa-cho, Toyota, Aichi, 470-0392 Japan*

E-mail: p17721pp@aitech.ac.jp, r_matsui@aitech.ac.jp, tobushi@aitech.ac.jp

1. Introduction

Intelligent materials are attracting attention as materials having functions such as detection and judgment. One such intelligent material is TiNi shape memory alloy (SMA) [1]. The TiNi SMA has higher recoverable strain and stress owing to the shape memory effect and superelasticity. Therefore, it is being used to drive elements of heat engines or actuators [2]. If a TiNi SMA thin tape is used as a rotary driving element, we can easily achieve a large rotating angle with high recovery torque. Hence, herein, we propose a two-way rotary driving element consisting of a combination of a thin tape of TiNi SMA and a superelastic alloy (SEA). We investigate the fundamental torsional deformation properties of the SMA tape at various temperatures and those of the SEA tape at room temperature. In addition, we propose a design chart for the two-way rotary driving element based on the results of the torsion test. Furthermore, we develop a model by using the two-way rotary driving element and investigate its operating characteristics under heating and cooling of the SMA tape.

2. Two-way rotary driving actuation using SMA and SEA tape

Figure 1 shows an outline of the structure of the two-way rotary driving element. The element is composed of SMA and SEA tapes, which are memorized flat shapes, and these tapes are connected in series through a center shaft. The SMA tape is twisted to the designated angle of twist and attached to the shaft, and the flattened SEA tape is fixed to the opposite side of the shaft.
If the twisted SMA tape is heated, recovery torque is generated because of the tendency of the tape to return to the memorized flat shape, resulting in rotary motion of the shaft. This motion stops when the torque of the SEA tape is balanced with the recovery torque of the SMA tape. If the SMA tape is cooled, the recovery torque decreases, and the shaft turns to the opposite direction owing to the superelasticity of the SEA tape. This is the mechanism of the two-way rotary driving element, which can move by heating and cooling of the SMA tape.

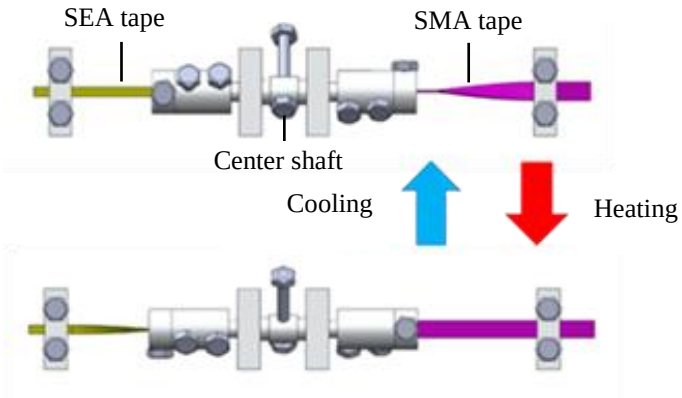

Fig. 1 Schematic of two-way rotary driving actuation using SMA and SEA tapes

3. Torsional deformation properties of thin strip of shape memory and superelastic alloys

To design the two-way rotary driving element, it is necessary to clarify its fundamental torsional deformation properties at temperatures considered to be useful in practical applications. Hence, we performed torsion tests to obtain the relationship between torque and angle of torsion for the SMA tape at various temperatures. Furthermore, we have proposed a design chart for the two-way rotary driving element by using the abovementioned relationships shown in the previous section.

The thickness, width, and length of the SMA tape were 0.35, 5.9, and 70 mm, respectively. Similarly, the dimensions of the SEA tape were 0.66 mm in thickness, 3.1 mm in width, and 70 mm in length. The torsion test was performed at the temperatures T = 293, 313, 333, 353, and 373 K for the SMA tape and 293 K for the SEA tape. The maximum twist angle per unit length θ_{max} was 78.5 rad/m (which corresponded to 180°). After these tapes were twisted to the maximum angle, they were unloaded.

Figure 2 shows the relationship between torque and angle of twist per unit length. Although Fig. 2 includes the loading curve of the SEA tape as well, it is inverted to correspond to the curve of the two-way rotary driving element proposed in this study. From this figure, the maximum torque of the SMA tape increases with T. This is caused by the fundamental deformation property of the material. The starting stress of martensitic transformation increases with increasing temperature. In the case that T of the SMA tape is higher than the finishing temperature of austenitic transformation A_f = 338 K or around this temperature, the material shows superelasticity. We confirmed that the SMA tape shows the shape memory effect after unloading at T = 293 and 313 K. In this figure, the difference between the intersection point of an unloading curve of the SMA tape (e.g., T = 373 K) and loading curve of the SEA tape and the origin of the loading curve of the SEA tape is considered to correspond to the rotating angle of the two-way rotary driving element when it is heated from 293 to 373 K. Based on this assumption, we predicted that the rotating angle of the two-way rotating driving element is 25.2 rad/m in the case of a fixed angle, and the temperature change is the same as that shown in Fig. 2.

In further experimental investigation, we found that the two-way rotating angle of the shaft in the element can be predicted almost precisely from the corresponding design chart, as shown in Fig. 2.

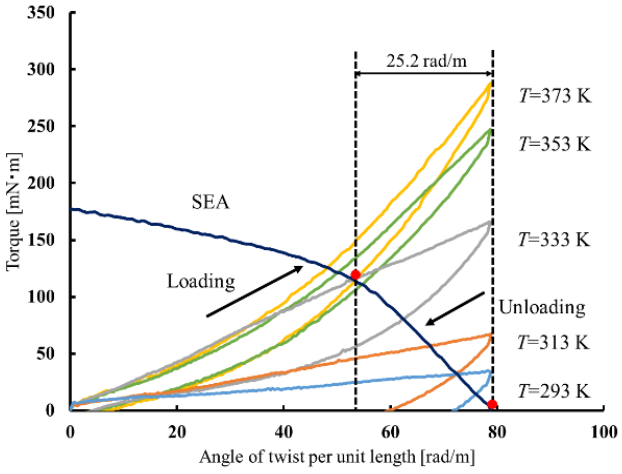

Fig. 2 Design chart of two-way rotary driving element for θ_{max} = 78.5 rad/m

Acknowledgments The authors acknowledge the financial support of JSPS KAKENHI Grant Number JP15K21477.

References

[1] Q.P. Sun, R. Matsui, K. Takeda and E.A. Pieczyska (Eds.). *Advances in Shape Memory Materials*, Springer, 2017.

[2] J.M. Jani, M. Leary, A. Subic and M.A. Gibson. A Review of Shape Memory Alloy Research, Applications and Opportunities, *Materials & Design*, 56:1078, 2014.

ENHANCEMENT OF FATIGUE PROPERTY OF TINI SHAPE MEMORY ALLOY WIRE BY ULTRASONIC SHOT PEENING

K. Takeda[1], D. Uemura[2] and K. Hattori[3]

[1]*Aichi Institute of Technology, 1247 Yachigusa, Yakusa-cho, Toyota, Japan*
[2]*Sinfonia Technology Co., Ltd., Shiba NBF Tower, 1-30, Shibadaimon 1-chome, Minato-ku, Tokyo, Japan*
[3]*Toyo Seiko Co., Ltd., 3-195-1 Umaganji, Yatomi, Japan*

e-mail: k-takeda@aitech.ac.jp

1. Introduction

In the practical applications using the shape memory alloy (SMA), the fatigue property is one of the most important subjects in view of evaluating functional characteristics of SMA elements. In a general way, the fatigue life can be enhanced by the ultrasonic-shot peening (USP). This USP process does not depend on the material shape. The fatigue life can be improved by USP due to induce the compressive residual stress on the surface layer and modify the surface properties. In this study, the rotating-bending fatigue life, the compressive residual stress and the fracture surface of TiNi SMA wire treated by USP was investigated.

2. Rotating-bending fatigue life

The relationships between bending strain amplitude ε_a and number of cycle to failure N_f obtained by the rotating-bending fatigue test under a constant frequency f = 150 cpm at room temperature are shown in Fig 1. The bending strain amplitude ε_a was obtained from the bending strain on the surface of the specimen at the fracture point. As can be seen in Fig. 1, the smaller the bending strain amplitude, the longer the fatigue life is. The effect of the USP to the fatigue life of SMA is large in the small strain and slight in the large strain. The fatigue life with the coverage of 1000% is longer than that of 2000% and 4000%.

3. Compressive residual stress

The distributions of compressive residual stress of as-received and USP-treated SMA wire in the surface layer are shown in Fig. 2. As can be seen in Fig. 2, in the USP-treated wire, the larger the depth from the surface, the smaller the compressive residual stress is. In the same depth from the surface, the larger the coverage, the larger the compressive residual stress is. In the case of the USP-treated wire with coverage of 2000% and 4000%, the compressive residual stress cannot be measured around the surface. The structure on the surface may become the amorphous.

4. Fracture surface

SEM photographs of a fracture surface for the USP-treated wire with coverage of 2000% and 200% are shown in Fig. 3 (a) and (b), respectively. As can be seen in Fig. 3 (a) and (b), the initiation point of the fatigue crack occurs both on the surface and at the inside with USP-treated wire. In the USP-treated wire with coverage of 200%, the initial fatigue crack appears at the surface in the all specimen. The percentages of the initiation point of the fatigue crack on the fracture surface of as-received and USP-treated wires are shown in Table 1. The larger the coverage, the larger the percentage in the case of the surface is.

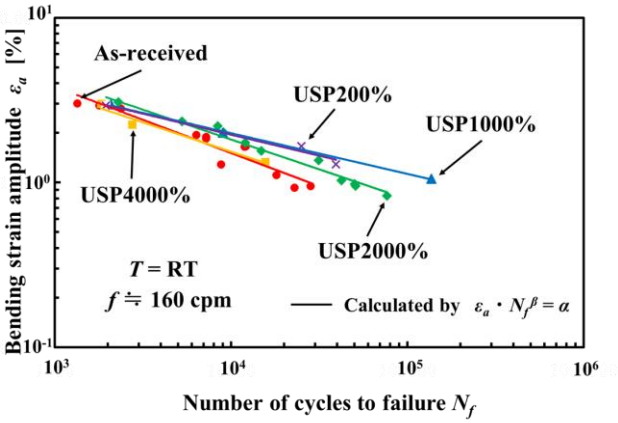

Fig. 1 Relationship between bending strain amplitude ε_a and the number of cycle to failure N_f obtained by the rotaing-bending fatigue test

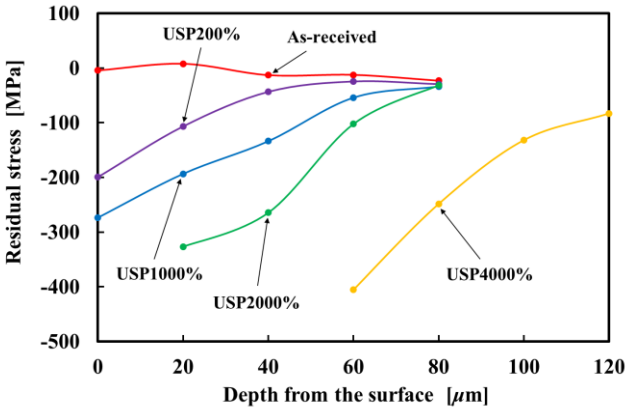

Fig. 2 Distributions of the compressive residual stress around the surface of as-recieved and USP-treated SMA wire

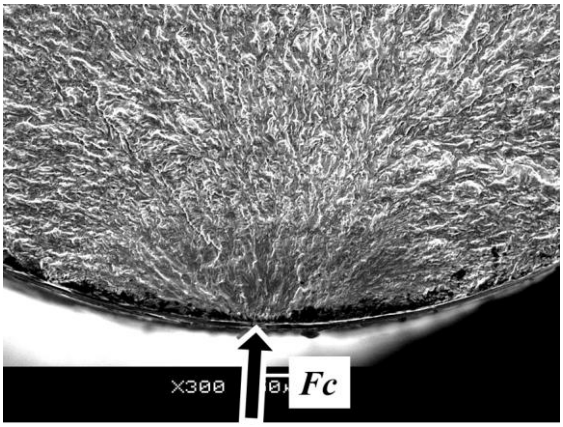

(a) USP-treated with coverage of 2000%

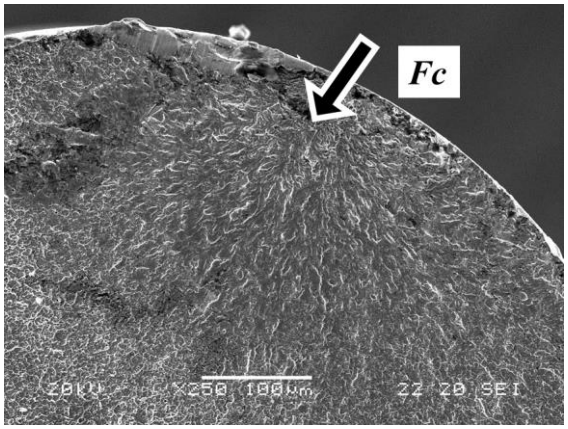

(b) USP-treated with coverage of 200%

Fig. 3 The initiation point of the fatigue crack of the USP-treated wires

Table 1 Percentages of the initiation point of the fatigue crack

Coverage conditions	Surface	Inside
As-received	100%	0%
USP200%	0%	100%
USP1000%	33%	67%
USP2000%	50%	50%
USP4000%	67%	33%

5. Conclusions

The influence of USP to the rotating-bending fatigue life and the initiation point of the fatigue crack of SMA wire was investigated. The effect of the compressive residual stress to the fatigue life of USP-treated SMA wire was discussed. The results obtained are summarized as follows.

(1) The effect of the USP to the fatigue life of SMA is large in the small strain and slight in the large strain.
(2) In the case of the USP-treated wire with coverage of 2000% and 4000%, the compressive residual stress cannot be measured around the surface. The structure on the surface may become the amorphous.
(3) In the initiation point of the fatigue crack, the larger the coverage, the larger the percentage in the case of the surface is.

ESTIMATION OF ENERGY STORAGE AND DISSIPATION IN SHAPE MEMORY POLYMER DURING ITS DEFORMATION

M. Staszczak[1], E.A. Pieczyska[1], R. Matsui[2], and K. Takeda[2]

[1]*Institute of Fundamental Technological Research, PAS, Pawińskiego 5B, 02-106, Warsaw, Poland*
[2]*Aichi Institute of Technology, 1247 Yachigusa, Yakusa-cho, Toyota-city, 470-0392, Japan*

1. Introduction

Shape memory polymer (SMP) is a class of stimuli-responsive material with high application potential which can rapidly change its shape under the influence of external stimulus. Among these materials, shape memory polyurethane has attracted worldwide attention. Shape memory properties of shape memory polyurethanes often are triggered by temperature. The temperature at which the polymer returns to the original shape is usually its glass transition temperature T_g [1].

During deformation some part of external mechanical energy is dissipated, while the other part is remained in the material after unloading as stored energy E_s. The stored energy denotes a change in internal energy of deformed materials and can be determined as difference between the energy of inelastic deformation W_{in} and dissipated energy W_d during the process of deformation. The transformation of the mechanical work into heat, its dissipation and the stored energy contribute to better understanding of the mechanisms of material deformation [2]. To the best the authors knowledge, the results on energy investigation of shape memory polymers, especially shape memory polyurethane, has not been reported in literature so far. Therefore, the goal of the paper is to estimate energy during shape memory polyurethane loading and deformation.

2. Materials and experimental details

Shape memory polyurethane PU-SMP with glass transition temperature $T_g \approx 25$°C, manufactured by *SMP Technologies Inc.*, Japan, was investigated. The tension tests were performed on MTS 858 testing machine at room temperature. The fast and sensitive infrared camera ThermaCam Phoenix was used in order to determine in contactless manner the temperature distributions on the SMP surface and to obtain temperature changes. The energy estimation was performed during PU-SMP loading with two strain rates of $2 \cdot 10^{-1}$ s^{-1} and $2 \cdot 10^{0}$ s^{-1}, for which the process conditions could be considered as adiabatic. The investigation was conducted for two strain ranges 0.6 and 1.18, where the deformation was macroscopically homogeneous.

3. Results and discussion

Scheme of the methodology for estimation of energy during loading of PU-SMP with $T_g \approx 25$°C used in the research is presented in Fig.1. Force F in function of displacement Δl obtained for strain rate of $2 \cdot 10^{-1}$ s^{-1} is shown in Fig. 1a, whereas for the strain rate of $2 \cdot 10^{0}$ s^{-1} in Fig.1b, respectively.

The external mechanical energy W_{ext} (*OAB*) delivered to the gauge part of the sample during deformation can be decomposed into a recoverable energy W_{rec} (*DAB*) and an inelastic one W_{in} (*OAD*) [3]. In the case of shape memory materials W_{rec} consists of the elastic energy W_e (*CAB*) and the energy required for the shape memory effect W_{SM} (*DAC*). Whereas W_{in} can be decomposed into the dissipated energy W_d and the energy stored in the material E_s. In this analysis, the heat exchange with the environment, as well as heat losses resulting from the conductivity to the grips of the testing machine, were neglected. The deformation process was assumed as adiabatic and the dissipated energy denoted as Q was equal to the sample temperature change ΔT multiplied by the specific heat value c_v. Assuming that the process is adiabatic, the energy balance includes an additional energy component E_{th}, associated with the drop in temperature (thermoelastic effect), which accompanies the elastic loading and unloading of the material.

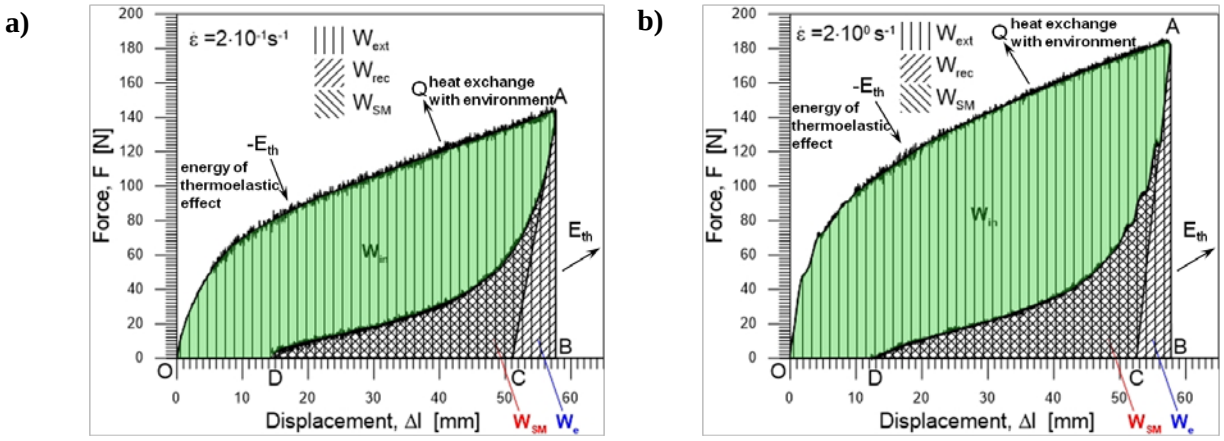

Figure 1: Scheme of energy estimation during PU-SMP loading-unloading cycle: a) $2 \cdot 10^{-1}\ s^{-1}$; b) $2 \cdot 10^{0}\ s^{-1}$.

The estimated energies for the SMP during the tension loading-unloading process are plotted in Fig. 2.

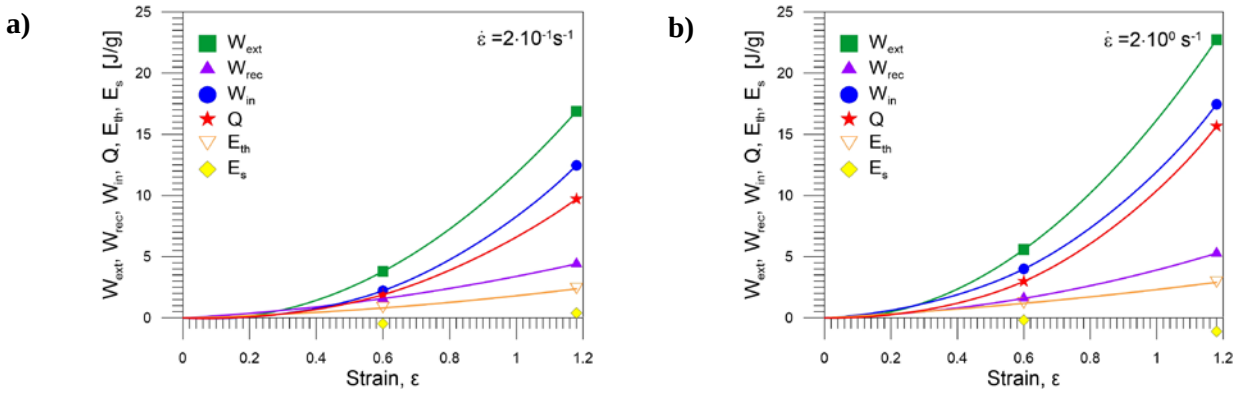

Figure 2: Comparison of estimated W_{ext}, W_{rec}, W_{in}, Q, E_{th}, E_s vs. strain for strain rates: a) $2 \cdot 10^{-1}\ s^{-1}$; b) $2 \cdot 10^{0} s^{-1}$.

4. Conclusions

A quantitative energy estimation was performed for polyurethane shape memory polymer ($T_g \approx 25°C$) loading with two strain rates under room conditions.

It was found that the mechanical energy W_{ext} provided to the sample during the deformation process, the inelastic energy W_{in} , as well as the dissipated energy Q, depend on the strain rate applied. The higher strain rate, the higher energy values were obtained. However, the values of recoverable energy W_{rec} and the energy of thermoelastic effect E_{th} almost did not depend on the strain rate. The estimated values of the stored energy E_s for both two strain rates and two strain ranges were close to zero. Therefore, it can be conclude that the energy was not stored in this polymer during the deformation process, but it was only dissipated, i.e. totally converted into heat. It should be also noted that as a result of the structural investigation, the crystalline phase was not found in the SMP in the examined strain range, considered as macroscopically homogeneous.

Acknowledgments The research has been carried out with support of the Polish National Center of Science under Grant 2014/13/B/ST8/04280. The authors are grateful to H.Tobushi for many helpful comments, to L.Urbański and M.Maj for obtaining mechanical and thermal data, as well as to S.Hayashi, SMP Technologies Inc., Japan, for providing PU-SMP.

References

[1] E.A. Pieczyska, M. Maj, K. Kowalczyk-Gajewska, M. Staszczak, A. Gradys, M. Majewski, M. Cristea, H. Tobushi, S. Hayashi, Thermomechanical properties of polyurethane shape memory polymer - experiment and modeling, *Smart Mater. Struct.*, 24:045043-16, 2015.

[2] M.B. Bever, D.L. Holt, A.L. Titchener. The Stored Energy of Cold Work. *Prog. Mater. Sci.*, 17:5-177, 1973.

[3] A. Chrysochoos, O.G.. Martin. Tensile test microcalorimetry for thermomechanical behaviour law analysis. *Mat. Sci. Eng. A*, 108:25-32, 1989.

EFFECT OF FIBER ORIENTATION ON MECHANICAL PROPERTY OF CFRP FABRICATED BY AM

T. Tanaka[1], T. Tateno[1,2] , and T. Kojima[2]

[1]*Graduate School of Science and Technology, Meiji University*
1-1-1 Higashimita, Tama-ku, Kanagawa 214-8571, Japan
[2]*Department of Mechanical Engineering Informatics, Meiji University*
1-1-1 Higashimita, Tama-ku, Kanagawa 214-8571, Japan

e-mail: ce172047@meiji.ac.jp

1. Introduction

Additive Manufacturing (AM) known as a layered fabrication method is a technique of laminating thin layers based on 3D model data and shaping an object. In recent years, due to the development of this technology, it has become possible to produce complicated shapes that were difficult in the past. There are various shaping methods in AM. Among them, Fused Filament Manufacturing (FFM), which melts an elongated resin material known as Fused Deposition Manufacturing (FDM) and extrudes it from a nozzle by heat, is known as a method for manufacturing practical parts at low cost.

However, In general, FFM uses plastic resins such as ABS and PLA, and it is said that its strength is limited. In recent years, attention has been paid to the application of carbon fiber in order to improve the strength. However, since FFM stacks layered materials, there is a difference in strength depending on the alignment of the additive process due to the influence of the adhesive surface. Conventional CFRP prevents anisotropy on strength by weaving fiber, but FFM can't weave between layers. For this reason, it is expected that the anisotropy is controled by the process alignment in FFM.

In this work, the effect of fiber orientation in FFM process on tensile strength of CFRP. Several specimens, which have different orientation of the fiber in each layer, are prepared. Tensile strength and Young's modulus were measured through tensile tests. Furthermore, by observing the broken part and considering from the stress-strain curve, the effective alignment pattern was discussed. Finally, as an application of FFM with CFRP, a high strength cell structure for shock absorption is proposed. The cell structure is devised considering process alignment from two points of view, which are easy for FFM and large capacity of energy absorption.

2.1. Tensile test specimen

The shape model of the specimen was formed by using a FFM modeler (Mark Two, Markforged, Inc.) and the orientation of the carbon fiber was set with a dedicated slicer (Eiger). The materials, which are fused nylon and carbon fiber, are extruded from a nozzle and allocated with nozzle motion. As a result, it is possible to incorporate carbon fibers in the nylon model. Orientation angle of fiber in one layer can be set by 15 degree (15n: n=0~6) so that the carbon fiber in each layer of the specimen in each layer is aligned with respect to the loading direction. The size of the specimen was unified with a length of 15 mm, a width of 150 mm, and a thickness of 0.75 mm.

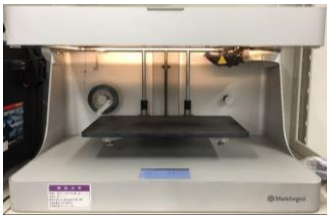

Fig 1: AM machine used in the experiment

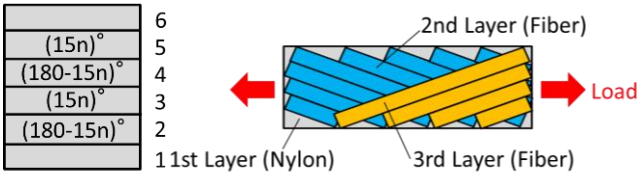

Fig 2: Cross-sectional view and top view of test specimen

2.2. Result of tensile test

The results of the tensile test are shown in Tables 2 and 3 below. When the fiber orientation angle is near perpendicular to the load direction, the tensile strength decreases. In addition, for the test piece with the fiber angle of 60 degree or more, the tensile strength was lower than that of the test piece without carbon fiber. The reason for this was thought that peeling between inter-layer surfaces was occurred prior to breaking of the fiber. Furthermore, the fracture factors were classified into the following three loading condition modes by considering the stress-strain curve and the broken part of the test piece.

i) Most of the nylon is under load.

ii) Both nylon and carbon fiber are under load.

iii) Most of the carbon fiber is under load.

Fiber angle [deg]	0,180	15,165	30,150	45,135	60,120	75,105	90,90	No fiber
Tensile strength [MPa]	346	254	79	71	27	23	17	43

Table 1: Result of tensile strength.

Fiber angle [deg]	0,180	15,165	30,150	45,135	60,120	75,105	90,90	No fiber
Young’s modulus [GPa]	20	17	4.3	2.9	1.7	1.8	1.8	0.2

Table 2: Result of Young’s modulus.

3. Proposal of shock absorbing structure

FFM realizes to fabricate the internal structure, which was difficult to do with the conventional processing method. Here, we propose a high strength cell structure for shock absorbing by using AM of CFRP material. The orientation of carbon fiber in each layer is not straight but bended along the honeycomb structure. The structure is designed to have space for elongation and for efficient reinforcement. The fiber orientation was specified for each layer, and the fiber alignment pattern is applied in vertical between the even layer and the odd layer. Furthermore, the shape of the cell structure itself was also examined. We designed a general auxetic structure, which can be transformed to a honeycomb structure with a positive Poisson's ratio and a special auxetic with a pseudo negative Poisson's ratio.

4. Conclusions

Tensile test of CFRP fabricated by FFM was carried out in different condition of carbon fiber orientation. It was confirmed that even if carbon fiber was applied to the shaped object, there was orientation condition that is not effective for reinforcement. Therefore, it is necessary to consider the fiber orientation which can be efficiently strengthened in the design stage. Considering the test results, a structure for shock absorbing parts was designed.

References

[1] Li Yang, Ola Harrysson, Harvey West and Denis Cormier. Mechanical properties of 3D re-entrant honeycomb auxetic structures realized via additive manufacturing. International Journal of Solids and Structures. 69-70, 2015, 475-490.

[2] A. Sohouli, M. Yildiz and A. Suleman. Design optimization of thin-walled composite strucrures based on material and fiber orientation. Compsite Structures. 176, 2017, 1081-1095.

HOW LOADING TYPE AFFECTS VISCOELASTIC RESPONSE IN POLYURETHANE STRUCTURES

M. Cristea[1], D. Ionita[1], S. Oprea[1] and E. A. Pieczyska[2]
[1]*"Petru Poni" Institute of Macromolecular Chemistry, Iasi, Romania*
[2]*Institute of Fundamental Technological Research, Warsaw, Poland*

1. Introduction

Specialists in polymers have a good understanding of the structure-property relation. They can choose the reactants, modify the synthesis conditions or the processing parameters in order to obtain polymeric materials with appropriate characteristics. However, all the characteristics of the polymeric materials are obtained in quasi-ideal conditions, i.e. the measured parameters are confined in a range wherein they obey some laws. When polymers are materials used in applications, the approaching of their properties should be done in a larger context. Among shape-memory materials, polymers provide a large variety of structures and applications. Polyurethanes are excellent candidates for shape-memory materials due to their segregated structures, with hard and soft domains [1]. The hard domain consists of hydrogen-bonding physical crosslinks that are responsible for the permanent shape structure. The amorphous soft domains represent the temporary shape. Mostly, polyurethanes are glass transition-type shape memory polymers [2]. This means that the variation of the storage modulus during the glass transition (determined by dynamic mechanical analysis-DMA) is the basis for the shape memory effect [3]. The glass transition temperature is regarded as a fingerprint of a polymer. Nevertheless, the analysis of the relation structure-properties only on the basis of a temperature value is not quite compelling [4]. The presentation intends to present the viscoelastic behaviour of polyurethane structures with the same glass transition temperature. The use of different fixtures in the DMA experiment helps in getting information on the structure-property correlation.

2. Experimental procedure, discussion

The DMA experiments were conducted on a Perkin Elmer DMA, in tension, shear and bending (Figure 1, a, b and c).

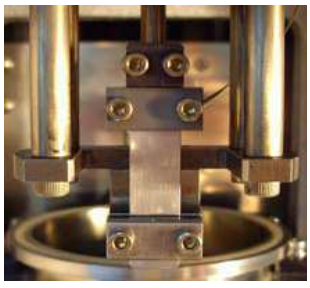
a)

b)

c)

Figure 1. Fixtures used in the DMA experiments: tension (a), shear (b), bending (c).

It should be mentioned that the characteristics of the samples (stiffness, dimensions) allow for the use of all three loading modes. The single-frequency temperature scanning experiment was run by increasing the temperature in ramp mode with 2 ^{o}C/min, at 1 Hz, starting from -150 ^{o}C. Also, multifrequency experiments were performed to establish the nature of some processes.

In the glassy region, all the samples are rigid, with storage modulus higher than 10^9 Pa. Due to structural specificities the order of rigidity is reversed during the glass transition. The multifrequency experiment indicates the unpacking of some polyurethane networks. Each loading mode features a specific phenomenon.
The tension mode stabilized the sample in the rubbery region, due to stress-induced orientation.
The bending mode revealed the strong effect of melting/crystallization on the stability of the samples.
The shear mode draw attention to enthalpic relaxation phenomena.

Acknowledgments The authors acknowledge the financial support of Romanian Academy.

References

[1] E. A. Pieczyska, M. Staszczak, K. Kowalczyk-Gajewska, M. Maj, K. Golasiński, M. Cristea, H. Tobushi and S. Hayashi. Investigation of thermomechanical couplings, strain localization and shape memory properties in a shape-memory polymer subjected to loading at various strain rates. *Smart Mat. Struct.* 25:085002, 2016.
[2] M. D. Hager, S. Bode, C. Weber and U. S. Schubert. Shape memory polymers: Past, present and future developments. Prog. Polym. Sci. 49-50:3, 2015.
[3] R. P. Chartoff, J. D. Menczel and S. H. Dillman, Dynamic mechanical analysis, in *Thermal analysis of polymers. Fundamentals and applications*, 387-495. Hoboken, New Jersey: Wiley, 2009.
[4] M. Cristea. Dynamic mechanical analysis in polymeric multiphase systems, in *Multphase polymer systems*, CRC Press, 173-192, 2016.

BUCKLING OF THIN-WALLED STRUCTURES WITH SHAPE MEMORY EFFECT UNDER THERMOELASTIC PHASE TRANSITIONS

S. I. Zhavoronok[1] and D. V. Nushtaev[2]

[1]*Institute of Applied Mechanics of Russian Academy of Sciences, Moscow, Russia*
[2]*TESIS Ltd., Moscow, Russia*

e-mail: Zhavoronok@iam.ras.ru

1. Introduction

It was shown in [1] that NiTi columns cooled homogeneously down to the austenite-to-martensite phase transition buckles under the compression dead load of 10%-15% of the Eulerian force corresponding to the minimum modulus even though the pure martensite is not reached. Thus, the traditional buckling analysis fails, and the dropping of elastic moduli cannot be interpreted as a main buckling cause for SMAs, moreover the same phenomenon is observed during the martensite-to-austenite transition following by raising moduli. Consistent critical load estimates for systems with phase transitions must be based only on coupled models [3]. The corresponding buckling concepts of von Kàrmàn's and Shenley's types were proposed in [4]; the good correlation with the test data was obtained. Here the free of concepts 3D numerical solutions for buckling and postbuckling of thin-walled SMA elements are presented, and their correlation with various analytical estimates [4] is shown.

2. Coupled model of thermoelastic SMA behavior

First, the dependence of the martensite volume ratio q on the dimensionless temperature t is given by (1) [2,5]:

$$(1)\quad \begin{gathered} q = \tfrac{1}{2}\left(1-\cos\pi t\right), \quad t\in[0,1]; \quad t\leqslant 0 \;\Rightarrow\; q=0; \quad t\geqslant 1 \;\Rightarrow\; q=1; \\ A\to M:\; t=\left(M_s-M_f\right)^{-1}\left(M_s-T_\sigma\right); \quad M\to A: \quad t=1-\left(A_s-A_f\right)^{-1}\left(A_s-T_\sigma\right). \end{gathered}$$

M_s, M_f are the start and finish temperatures of the $A\to M$ transition and A_s, A_f are the corresponding temperatures for $M\to A$ in unstressed state. The stress effect is accounted by the reduced temperature T_σ (2):

$$(2)\quad T_\sigma = T-\Delta S^{-1}\left[\omega_{ij}s^{ij}+Z(\sigma^{ij})+\varepsilon_0\varepsilon_k^k\right], \quad Z(\sigma^{ij})=\tfrac{1}{2}(\sigma_k^k)^2\left(K_M^{-1}-K_A^{-1}\right)+\tfrac{1}{6}\sigma_i^2\left(G_M^{-1}-G_A^{-1}\right);$$

$s^{ij}=\sigma^{ij}-\frac{1}{3}g^{ij}\sigma_k^k$, ΔS is the volumetric entropy density drop between A and M at a reference temperature, ε_0 is the $A\to M$ volumetric effect, and G_M, G_A, K_M, K_A are shear and bulk moduli of pure M and A phases,

$$(3)\qquad A\to M: \quad \omega_{ij}=(2+q)^{-1}\left[3\rho_D s_{ij}\sigma_i^{-1}\varphi_1(\sigma_i)+e_{ij}^{(1)}\right]; \qquad M\to A: \quad \omega_{ij}=q^{-1}e_{ij}^{(1)}.$$

The strain superposition is assumed, thus, $\varepsilon_{ij}=\varepsilon_{ij}^{(0)}+\varepsilon_{ij}^{(1)}$, where $\varepsilon_{ij}^{(0)}$ is the elastic strain given by (4) [2,5]:

$$(4)\quad \begin{gathered} \varepsilon_{ij}^{(0)}=\tfrac{1}{2}G^{-1}\sigma_{ij}-\left(\tfrac{1}{6}G^{-1}-\tfrac{1}{9}K^{-1}\right)\varepsilon_k^k g_{ij}+\alpha T g_{ij}; \\ G^{-1}=qG_M^{-1}+(1-q)G_A^{-1}; \quad K^{-1}=qK_M^{-1}+(1-q)K_A^{-1}; \quad \alpha=q\alpha_M+(1-q)\,\alpha_A, \end{gathered}$$

The increment of the phase and structure strain deviator $e_{ij}^{(1)}=\varepsilon_{ij}^{(1)}-\frac{1}{3}g_{ij}g^{kl}\varepsilon_{kl}^{(1)}$ can be defined as follows (5):

$$(5)\qquad A\to M: \quad de_{ij}^{(1)}=\omega_{ij}dq+\tfrac{3}{2}\rho_D s_{ij}\sigma_i^{-1}q\psi_2(\sigma_i)d\sigma_i; \qquad M\to A: \quad de_{ij}^{(1)}=\omega_{ij}dq;$$

ρ_D is the maximum strain intensity of the $A\to M$ [2]. The increments $dq(d\sigma^{kl},dT)$, $d\varepsilon_{ij}(d\sigma^{kl},dT)$ can be formulated hence, therefore we obtain $R_{ijkl}=\partial\varepsilon_{ij}/\partial\sigma^{kl}$ and $\alpha_{ij}=\partial\varepsilon_{ij}/\partial T$ allowing the tangent stiffness C^{ijkl} computing at a step of any algorithm, i. e. the model (1-5) can be implemented into finite element codes.

3. Buckling of SMA elements undergoing thermally induced martensite transitions

Let us consider a SMA solid with an initial configuration $G \in \mathbb{R}^3$, $\partial G = S_\sigma \oplus S_r$ defined by a vector radius $\mathbf{r}(M)$ with kinematical constraints $\mathbf{r}(M \in S_r) = \mathbf{r}_\star$ and loads $\mathbf{p}(M \in S_\sigma)$, and let it be entirely austenite: $q = 0$, $T_\sigma \geqslant M_s$. The further cooling is assumed to be sufficiently slow to neglect the heat conduction. Let us apply the perturbation $\delta\mathbf{r}$, $\delta\mathbf{r}(M \in S_r) = 0$; the stable and unstable configurations can be defined by (6), (7):

$$\forall\varepsilon > 0 \quad \exists\delta(\varepsilon) > 0 : \quad \forall\|\delta\mathbf{r}\| < \delta \quad \|\mathbf{u}(\delta\mathbf{r}, \tau, \mathbf{p})\| < \varepsilon; \tag{6}$$

$$\exists\tau^\star(\mathbf{p}) : \quad \forall\tau > \tau^\star \quad \|\mathbf{u}(\delta\mathbf{r}, \tau, \mathbf{p})\| \geqslant \varepsilon^\star, \tag{7}$$

where $\varepsilon^\star$ is the representative displacement value and the bifurcation point $\tau^\star$ can be found by analyzing the equilibrium curve or as the kinetic energy maximum point corresponding to the quick equilibrium state change:

$$\mathrm{T}(\tau^\star) = \tfrac{1}{2}\rho\dot{u}^i(\tau^\star)\dot{u}_i(\tau^\star) = \mathrm{T}_{\max}, \quad T_\star = T(\tau^\star). \tag{8}$$

here $T_\star$ is the critical temperature. This approach corresponds to the assumed "supplementary phase transform occurring everywhere", i. e. Shenley's concept. On the other hand, instantaneous applying of $\delta\mathbf{r}$ under fixed temperature $T \leqslant T_0$ and fixed load $\mathbf{p}$ should be close to the "fixed load assumption", or von Kàrmàn's concept.

4. Results and conclusions

Several finite element simulations for NiTi beams and plates were performed on the bsis of the SMA model (1–5) and the buckling defined by (6–8). The buckling forces obtained for the clamped-clamped prismatic NiTi beam of 0.01 m length and with 0.002×0.001 m cross-section are compared with the traditional Euler estimate P_{Cr} corresponding to the minimum elastic modulus of the martensite $E_{\mathrm{M}} = 30$ GPa for thermally induced and superelastic $A \to M$ transforms (table 1). The phase transition regime depends on the initial temperature T_0.

$P_{\mathrm{Cr}}(E_{\mathrm{M}})$, N	Thermally induced:	$P(\tau^\star)$, N	T_0, K	Superelasticity:	$P(\tau^\star)$, N	T_0, K
1974		220	343.15		375	323.15

Table 1: Buckling forces for the clamped-clamped prismatic NiTi beam of 0.01 m length: Euler's estimate based on minimum elastic modulus, E_{M}; thermally induced $A \to M$ transition; superelastic $A \to M$ transition.

The computed loads $P(\tau^\star)$ are about $10\ldots15\%$ of Euler's ones $P_{\mathrm{Cr}}(E_{\mathrm{M}})$, are consistent with the test data [1] and analytical solutions corresponding to the extended Shenley concept [4], and the buckling forces for the thermally induced $A \to M$ transform are about only 60% of the critical forces for the superelasticity regime. Thus, the buckling danger for SMA elements undergoing thermally induced phase transitions is underestimated, and the traditional bifurcation analysis fails whereas the approach [3, 4] allows one to obtain adequate results.

Acknowledgments This investigation is the part of the State Task for Basic Researches GP 14 (0050-2017-0001), the state register number AAAA-A17-117032010136-3, and partially supported by the RFBR under grant No. 16-01-00751-a.

References

[1] A. A. Movchan and S. A. Kazarina. Experimental investigation of the buckling resulted by thermoelastic phase transforms under compressive stresses. *J. Machinery Manufacture and Reliability*, 31(6):82–89, 2002.

[2] A. A. Movchan, I. A. Movchan, and L. G. Silchenko. Micromechanical model of nonlinear deformation of shape memory alloys under phase and structure transforms. *Mechanics of Solids*, 45(3):406–416, 2010.

[3] A. A. Movchan and L. G. Silchenko. Stability of the Shenley column under creep or under straight thermoelastic martensite transformation. *The J. of Mekhanika Kompozitsionnykh Materialov i Konstruktsii*, 6(1):89–103, 2000.

[4] A. A. Movchan and L. G. Silchenko. Buckling of a rod undergoing direct or reverse martensite transformation under compressive stresses. *J. of Applied Mechanics and Technical Physics*, 44(3):442–449, 2003.

[5] A. A. Movchan, L. G. Silchenko, and T. L. Silchenko. Taking account of the martensite inelasticity in the reverse phase transformation in shape memory alloys. *Mechanics of Solids*, 46(2):194–203, 2011.

ON THE EFFECTIVE PROPERTIES OF THE OCTET-TRUSS LATTICE

A. Czekanski[1] and M. Abdelhamid[1]

[1]*York University, Mechanical Engineering Department, Toronto, Canada*
e-mail: alex.czekanski@lassonde.yorku.ca

1. Architectural Materials

In the last few decades there has been a growing interest in lightweight load-bearing structures. Inspiration from nature can be found in natural cellular materials like wood, honeycomb, butterfly wings and foam-like structures such as trabecular bones and sponge [1]. Architectural cellular materials have been used to create mechanically-efficient engineering structures such as the Eiffel Tower and the Garabit Viaduct. This class of materials combines the benefits of low density as it only occupies a fraction of the monolithic bulk solid, and strength by arranging its elements efficiently to carry the loads. Previous studies have shown that the macroscopic mechanical properties of cellular materials depend on three parameters: the constituent material properties, the deformation mechanism, and the relative density $\overline{\rho}$ (defined as the solid volume within the unit cell divided by the volume of the unit cell). Cellular-solids theory predicts scaling relationships between the macroscopic stiffness and strength vs. the relative density, namely $E_s \, \alpha \, \overline{\rho}^m$ and $\sigma_y \, \alpha \, \overline{\rho}^n$ respectively, where the dimensionless parameters m and n depend on the unit cell geometry [2].

For a 3D structure to be rigid (i.e. statically and kinematically determinate), a minimum nodal connectivity of $Z = 6$ is required. A connectivity of $Z = 12$ categorizes the structure as stretching-dominated where the lattice members deform by tension/compression. Bending-dominated structures that deform through the bending of their members, has a connectivity of $6 \leq Z < 12$ [3]. For stretching-dominated structures such as the octet-truss lattice, these scaling relationships are linear. On the other hand, for bending-dominated structures such as honeycombs or the octahedral lattice, they are quadratic or stronger [4].

When the dimensions of the lattice members are scaled down below the micron length scale, they exhibit different mechanical behaviour. Examples of these size-dependent changes include strengthening in single crystalline metals and transition from brittle to ductile behaviour in metallic glasses and ceramics [5], [6]. Recent advances in additive manufacturing techniques have made it possible to manufacture lattice structures with more geometrical and dimensional freedom. Certain AM techniques like self-propagating photopolymer waveguides [7], projection micro stereolithography [1], and two-photon lithography have been utilized to produce micro and nanolattices within the length scales required to activate material size effects. This is in addition to the structural effects activated by changing the various geometric parameters of the lattice unit cell [8].

2. Constitutive Modelling of the Octet-truss

Continuum constitutive models have been developed to describe the effective mechanical properties of the octet-truss lattice structure. A common assumption amongst these models is that the lattice members are pin-jointed at all nodes, hence the contribution from the bending resistance of the members and nodes can be neglected compared to the axial tensile/compressive stiffness of the members. Deshpande et al. (2001) checked the accuracy of the pin-jointed assumption by comparing FE calculations of rigid-jointed structures against analytical values of pin-jointed models for relative densities $\bar{\rho}$ ranging 0.01 to 0.5, the results showed excellent agreement between the FE and analytical values proving the validity of this assumption [3]. Generally, symmetry considerations could be employed to deduce the number of independent constants in the macroscopic stiffness tensor. Following the pin-jointed assumption, these elastic constants are determined by averaging the contribution from each element to the macroscopic stiffness, which is achieved through 3D coordinate transformations.

Nayfeh and Hefzy (1978) derived a first order approximation of the relative density of the octet-truss lattice by dividing the solid volume within the unit cell by the total volume of the unit cell. They employed 3D coordinate transformation and volume averaging in order to obtain the macroscopic stiffness matrix. Lake

(1992) constructed a strength tensor by converting applied stresses to strains for each parallel group of members using the macroscopic compliance matrix. Failure would occur in a member if its axial strain exceeded a critical value based on an elastic buckling limit. The choice of elastic buckling over plastic yielding is somehow justified given that space structures, the typical application of lattice structures at that time, usually compose of slender members. Lake's strength tensor could easily accommodate multiaxial loading as well as different loading directions through coordinate transformation. The author also developed a 3D plot of the uniaxial compression strength in cartesian coordinates, from which he concluded the direction and value of the maximum strength of the octet-truss lattice for the case of cubic symmetry where the lattice angle θ equals $45°$ (the angle between the individual members and the horizontal midplane). Deshpande et al. (2001) investigated the effective properties of the octet-truss lattice structure both theoretically and experimentally [3]. They validated the analytically-predicted elastic modulus and strength using FEM and experimental uniaxial compression of octet-truss lattice made from a casting aluminium alloy.

It is important to note that the previous studies were performed only for the case of cubic symmetry. At this angle, the octet-truss is considered to be at the highest attainable level of symmetry. However, potential applications of metamaterials (e.g. thin-walled pressure vessels) necessitates the use of anisotropic lattice structures in order to achieve the optimal combination of low density and high load-carrying capacity.

3. Methodology and Results

The purpose of the present research is to investigate the effect of the lattice angle on the effective properties of the octet-truss lattice structure, namely the effective stiffness. The appropriate steps are followed to develop a continuum-based analytical model of the octet-truss lattice while including the lattice angle parameter θ. The output of these analytical derivations are the stiffness/compliance tensors. Isotropic and homogenous properties are assumed for the constituent material. The pin-jointed nodes assumption is assumed to simplify the derivations, where we only consider the axial compressive/tensile stiffness of the truss members and ignored the nodes and members bending resistance. This assumption aligns with the stretching-dominated behaviour of the octet-truss. General expressions for the effective elastic moduli of the octet-truss for a general lattice angle are obtained using two consecutive stiffness tensor transformations. Tri-dimensional polar representations of effective the elastic modulus for different lattice angles show that the loading direction of the maximum elastic modulus always lies in a plane perpendicular to the $x-y$ plane at $\varphi = 45°$. As θ increases, this direction moves closer to the z axis. As θ decreases, it moves closer to the $x-y$ plane. A Lattice angles less than $45°$ produce higher overall effective specific elastic moduli, specifically in the $x-y$ plane. A plot of the maximum and minimum specific stiffness against the lattice angle describes the anisotropic behaviour of the octet-truss lattice.

References

[1] X. Zheng, H. Lee, T. H. Weisgraber, M. Shusteff, J. DeOtte, E. B. Duoss, J. D. Kuntz, M. M. Biener, Q. Ge, J. a Jackson, S. O. Kucheyev, N. X. Fang, and C. M. Spadaccini, "Ultralight, ultrastiff mechanical metamaterials.," *Science*, vol. 344, no. 6190, pp. 1373–7, 2014.

[2] L. J. Gibson and M. F. Ashby, *Cellular solids: structure and properties*, Second. Cambridge: Cambridge University Press, 1997.

[3] V. S. Deshpande, N. A. Fleck, and M. F. Ashby, "Effective properties of the octet-truss lattice material," *J. Mech. Phys. Solids*, vol. 49, no. 8, pp. 1747–1769, Aug. 2001.

[4] N. A. Fleck, V. S. Deshpande, and M. F. Ashby, "Micro-architectured materials: past, present and future," *Proc. R. Soc. A Math. Phys. Eng. Sci.*, vol. 466, no. 2121, pp. 2495–2516, Jun. 2010.

[5] D. Jang, L. R. Meza, F. Greer, and J. R. Greer, "Fabrication and deformation of three-dimensional hollow ceramic nanostructures.," *Nat. Mater.*, vol. 12, no. 10, pp. 893–8, Oct. 2013.

[6] J. Wang, J. Lian, J. R. Greer, W. D. Nix, and K.-S. Kim, "Size effect in contact compression of nano- and microscale pyramid structures," *Acta Mater.*, vol. 54, no. 15, pp. 3973–3982, 2006.

[7] T. A. Schaedler, A. J. Jacobsen, A. Torrents, A. E. Sorensen, J. Lian, J. R. Greer, L. Valdevit, and W. B. Carter, "Ultralight Metallic Microlattices," *Science (80-.).*, vol. 334, no. 6058, pp. 962–965, Nov. 2011.

[8] L. C. Montemayor and J. R. Greer, "Mechanical response of hollow metallic nanolattices: combining structural and material size effects," *J. Appl. Mech.*, vol. 82, no. July, pp. 1–10, 2015.

AN INERTIAL PIEZOELECTRIC ROTARY MOTOR BASED ON THIN SQUARE TYPE FRAME

A.Čeponis[1,*], D.Mažeika[2] and P.Vasiljev[3]

[1,2] *Department of Information Systems, Faculty of Fundamental Sciences, Vilnius Gediminas Technical University, Sauletekio avn. 11, Vilnius, Lithuania.*

[3]*Ultrasonic Mechanisms Research Group, Institute For Scientific Research, Lithuanian University of Educational Sciences, Studentų Str. 39, Vilnius, Lithuania*

e-mail: andrius.ceponis@vgtu.lt

1. Abstract

Results of numerical and experimental investigations of a thin inertial piezoelectric rotary motor based on a square type frame is presented in the paper. The objective of investigations was to validate operation principle of the actuator and to analyse dynamic characteristics of the motor. The motor has small size and a simple design. It consist of a square type hollowed steel frame with four straight cantilevers used to move the rotor. Piezo ceramic plates are glued on the both sides of the stator and are used to excite the second in – plane bending mode of the beam. Excitation of the stator can be carried out by two saw-tooth signals with the phases shifted by π. The thickness of the stator is 1.3mm. Therefore it can be used for applications where space and mounting volume are critical parameters. Numerical and experimental investigations were performed to analyse vibration modes, resonant frequencies and to investigate dynamical and electrical characteristics of the actuator. A prototype of the motor was made and measurements of the mechanical and electrical characteristics were performed.

2. Introduction

An inertial piezoelectric motors are widely used in modern mechatronic systems and devices. These type of motors are used for the precise positioning, focus control in optical systems, scanning tunnelling microscopy and etc [1]. Wide applications of inertial piezoelectric motors are caused by the following advantages such as short response time, high resolution, self – locking, magnetic field free operation and small displacement step [2].

Inertial piezoelectric motors can be classified into two groups based on operation principle i.e. stick – slip and slip – slip [3]. In general, these operation principles of an inertial piezoelectric motors are based on different phases of acceleration at the contact point between stator and rotor. The difference of acceleration phases is caused by non – harmonic excitation signals. The most common signals used to excite an inertial piezoelectric motors are saw – tooth and square type waves [4].

The linear inertial piezoelectric motors are widely analysed and numerous different designs of these motors are presented in the literature [5, 6]. On the other hand, much less designs of the rotary inertial piezoelectric motors can be found, however demand of these motors in the market is quite high. The main advantage of inertial piezoelectric rotary motors is- a high angular resolution [7]. In most cases, inertial rotary motor operates at stick – slip.

3. Design and operation principle of the motor

Proposed inertial piezoelectric motor consist of a stator, rotor, shaft, preloading spring and clamping cylinder (Fig.1a). Stator of the motor has square shape frame with the four straight cantilevers pointed to the center of the frame. The L is defined as length and width of the stator and is equal to 25 mm (Fig. 1a). Thickness of the stator H is equal to 1.3 mm. The frame of the stator is made from DIN 1.4301 stainless steel. Sixteen lead zirconate titanate (PZT) plates are glued on the top and bottom surface of the stator. Electrodes of the PZT plates are divided into two equal sections. Polarization is of PZT plates are pointed along thickness. Plates are glued on the top and bottom surface have opposite polarization direction. Dimensions of each PZT plate is 8 x 4 mm.

Small alumina ceramic plates are glued at the end of each cantilever in order to increase contact friction between the stator and rotor. Double conical shaped rotor is placed in the centre of the stator. (Fig.1a). Spring is used to preload rotor to the stator. Adjustment of the preloading force of the spring is made by clamping cylinder that can be moved and fixed in the proper position on the shaft. M1.2 screw is used to fix clamping cylinder on the shaft.

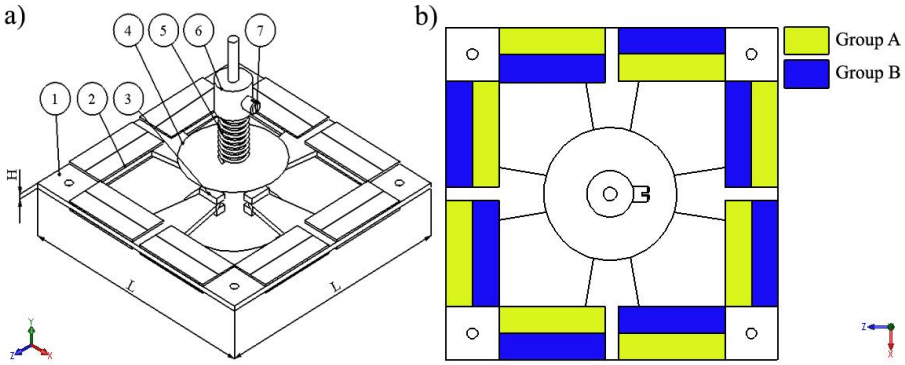

Figure 1. Principle design of the motor: a - Isometric view of the motor; 1 – stator; 2 – piezo ceramic plates; 3 – alumina ceramic plates; 4 - double conical rotor; 5 – spring; 6 – clamping cylinder; 7 – fixing screw; b – excitation scheme of the stator.

Operation of the motor is based on excitation of the 2nd in-plane bending mode of the frame. Electrodes of piezo ceramic plates were divided into two groups A and B respectively as shown in Fig.1b. Non-symmetric excitation signal with phase difference by π is applied on different groups of the electrodes. Excitation of group A expands stator while plates of group B shrinks stator. Transverse deformations of stator are obtained that excite second in-plane vibrati[illegible]

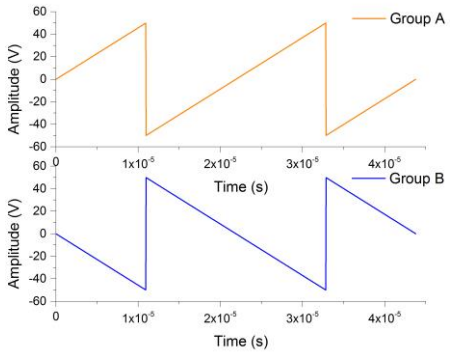

Figure 1 Shape of excitation signal

Stick – slip interaction between stator and rotor is achieved applying saw tooth excitation signal (Fig. 2). Timing of the stick - slip interaction is directly related to the shape of the excitation signal. Expansion and contraction of piezo ceramic plates is slow at the first step of excitation. Slow signal rising causes that friction force between stator and rotor is greater than inertial force of the rotor, so rotation of the rotor can be observed. However, then signals suddenly changes state inertial force becomes grater than friction force and cantilevers slips through surface of the rotor and motion is not transferred. Similar operation of the motor can be observed during its excitation by pulse shape signals.

Acknowledgments This research was supported by the Research Council of Lithuania under the project No. S-MIP-17-51.

References

[1] K. Spanner, B. Koc, Actuators 5, 6; doi:10.3390/act5010006 (2016)
[2] M. Hunstig, Actuators 6, 7; doi:10.3390/act6010007 (2017)
[3] M. Hunstig, T. Hemsel, W. Sextro, Sensors and Actuators A, 200, 90– 100 doi.org/10.1016/j.sna.2012.11.012 (2013)
[4] M. Hunstig, T. Hemsel, W. Sextro, Sensors and Actuators A, Sensors and Actuators A, 200 79– 89, doi: 10.1016/j.sna.2012.11.043
[5] T. Morita, T. Nishimura, R.Yoshida, H. Hosaka, Jpn. J. Appl. Phys. 52 07HE05, doi: 10.7567/JJAP.52.07HE05 (2013)
[6] W. X. Han, Q. Zhang, Y. T. Ma, C. L. Pan, and Z. H. Feng, Review of Scientific Instruments 80:1 doi: 10.1063/1.3053166 (2009)
[7] J. Xing, L. Xu, The ScientificWorld Journal, 2013, 854126, doi: 10.1155/2013/854126 (2013)

STRESS RELAXATION EFFECTS IN TiNi SMA

E.A. Pieczyska[1], V. Dunić[2], R. Slavkovic[2] and Z. Kowalewski[1]

[1] *Institute of Fundamental Technological Research, Polish Academy of Sciences, Warsaw, Poland*

[2] *University of Kragujevac, Faculty of Engineering, Kragujevac, Serbia*

e-mail: epiecz@ippt.pan.pl

1. Introduction

Experimental and numerical results of thermomechanical effects related to phenomena of stress relaxation investigated in TiNi SMA subjected to modified program of strain-controlled tensile loading at room temperature are analyzed. More details related to thermo-mechanical coupling approach can be find in [1, 2].

2. Experimental procedure

The experiments were carried out on belt type specimens cut off from TiNi SMA strip. The specimens were subjected to displacement-controlled tension with strain rate $5\times10^{-2}s^{-1}$. The loading and unloading processes were executed in two following way: loading up to strain equal to 4%; maintaining the strain value during 3 minutes; reloading up to the strain of 7% and unloading to zero stress. In the experiment, a monotonic stress drop of 170 MPa and specimen temperature increase of cca. 15 K were observed.

3. Thermo-mechanically coupled SMA constitutive model and numerical modeling

Details of the SMA phenomenological model [3], implemented into the software for structural analysis PAK based on Finite Element Method (FEM) were given in the previous paper of the authors [1, 2]. To realize the thermo-mechanical coupling [2] in the partitioned approach [4], the FEM programs for structural (PAKS) and heat transfer analysis (PAKT) were connected using the Component Template Library (CTL), developed by Niekamp [5]. The heat transfer program PAKT enabled computation of a temperature change in solids. The elementary dissipative energy q_{dis} of the martensitic phase transformation can be expressed as [2, 3]:

$$q_{dis} = \eta\left(\Pi - \rho\Delta s_0 T\right)\dot{\xi},$$

where η denotes the dissipative factor, Π is the thermodynamic force, $\rho\Delta s_0$ describes the stress sensitivity coefficient, $\dot{\xi}$ is the rate of martensitic volume fraction and T is the SMA temperature [3]. The TiNi belt type specimen has been modeled by the FEM 3D elements [1, 6]. It was assumed that the specimen ends have the same and constant temperature, because the grips of the testing machine are very large in comparison to the specimen thickness. The rest of the specimen model enabled free convection.

4. Results and conclusions

Comparison of the experimental and numerical results in the form of the stress and average temperature variations vs. strain is shown in Fig 1 for the TiNi SMA subjected to the loading program described above.

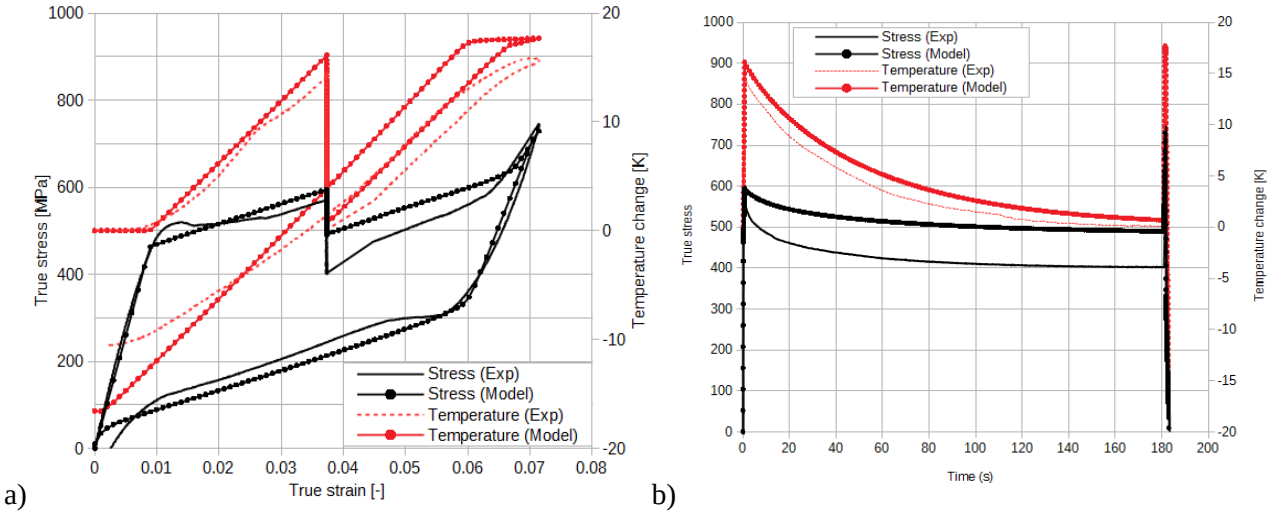

Figure 1. TiNi tension at strain rate of $5\times10^{-2}s^{-1}$ with 3 min loading break induced at advanced stage of martensite transformation - experiment and model. Stress and temperature variations vs.: strain (a); time (b).

The numerical approach proposed confirmed decrease of the stress when the strain was kept constant during the SMA loading (Fig. 1). A monotonic stress and the temperature drops were observed. Large stress relaxation reduction was observed for the strain rate applied. After the relaxation stage was completed, the transformation processes develop in typical manner. The exothermic character of the martensitic forward transformation was demonstrated, as well as decrease of the specimens temperature during the reverse transformation. Even a temperature decline below the initial level was confirmed by the model.

Acknowledgements

The research was supported by the Polish National Centre of Science- 2014/13/B/ST8/04280 and 2014/15/B/ST8/04368 and the Ministry of Education, Science and Technological Development, Serbia - TR32036 and III41007.

References

[1] Dunić V, Pieczyska E, Tobushi H, Staszczak M, Slavković R. Experimental and numerical thermo-mechanical analysis of shape memory alloy subjected to tension with various stress and strain rates. Smart Mater Struct. 23(5):055026, 2014.

[2] Dunić V, Busarac N, Slavković V, Rosić B, Niekamp R, Matthies H, Slavković R, Živković M. A thermomechanically coupled finite strain model considering inelastic heat generation. Contin Mech Thermodyn. 28:993, 2016.

[3] Lagoudas D. Shape Memory Alloys: Modeling and Engineering Applications. Springer, 2006.

[4] Matthies H, Niekamp R, Steindorf J. Algorithms for strong coupling procedures. Comput Methods Appl Mech Eng. 195(17-18):2028, 2006.

[5] Niekamp R. CTL Manual for Linux/Unix for the Usage with C++. Institut fur Wissenschaftliches Rechnen TU Braunschweig, Germany, 2005.

[6] Pieczyska EA, Staszczak M, Dunić V, Slavković R, Tobushi H, Takeda K. Development of Stress-Induced Martensitic Transformation in TiNi Shape Memory Alloy. J Mater Eng Perform. 23(7):2505, 2014..

MECHANICAL ANISOTROPY OF GUM METAL ANALYZED BY ULTRASONIC MEASUREMENTS AND DIGITAL IMAGE CORRELATION

E. Pieczyska[1], K. Golasiński[1], M. Maj[1], S. Mackiewicz[1], M. Staszczak[1], M. Zubko[2] and N. Takesue[3]

[1] *Institute of Fundamental Technological Research, Polish Academy of Sciences, Warsaw, Poland*
[2] *Institute of Materials Science, University of Silesia, Chorzów, Poland*
[3] *Department of Applied Physics, Fukuoka University, Japan*

e-mail: epiecz@ippt.pan.pl

1. Abstract

Experimental investigation of mechanical anisotropy in a multifunctional beta titanium alloy Gum Metal under compression is reported. Non-destructive and destructive techniques were used to analyze unique mechanical behavior of the alloy. Structural characterization showed a strong <110> texture of Gum Metal, which is a result of cold-swaging applied during its fabrication [1]. Due to this kind of texture Gum Metal can be treated as transversally isotropic solid. Ultrasonic measurements determined elastic constants with high accuracy. A significant difference between Young's moduli of the alloy calculated for parallel and perpendicular directions to the alloy swaging direction was demonstrated. Compression of Gum Metal cube samples with two orientations was conducted on a testing machine. Two perpendicular walls of each sample were monitored by two visible range cameras during the deformation process for further 2-dimensional digital image correlation (DIC) analysis. Strong mechanical anisotropy of Gum Metal was confirmed by a detailed analysis of the stress vs. strain curves and strain distributions.

2. Material and specimens- determination of Gum Metal elastic constants using ultrasonic test

Elastic constants and Young's moduli of the Gum Metal were determined using a non-destructive approach based on measurements of ultrasonic wave propagation. For the measurements of ultrasonic velocities in the sample the pulse-echo contact technique was used [2]. In order to determine all five independent elements of the elastic constants matrix for transversally isotropic solid at least five different values of velocities of ultrasonic waves propagating in different directions and/or with different polarizations must be measured in the material. For this purpose, two samples, denoted as U1 and U2, were cut out from the pre-machined Gum Metal rod in the way shown in Fig. 1. Sample U2 was cut out from the rod at an angle of 45° to the axis 3.

Figure 1: Configuration and orientation of the samples cut out from a Gum Metal rod for ultrasonic test.

Based on the established elastic constants, the Young's moduli of the Gum Metal in cold-swaging direction (3) E_3 = 60.7 GPa and in perpendicular direction (1 or 2) $E_{1/2}$ = 68.5 GPa were calculated. The obtained results are listed in Table 1.

Relation to direction of swaging	Parallel	Perpendicular
Young's modulus [GPa]	60.7	68.5

Table 1: Young's moduli of polycrystalline Gum Metal in relation to its technological texture.

Different values of the Young moduli in two perpendicular directions indicate considerable elastic anisotropy of the Gum Metal. For the compression Gum Metal cuboidal samples with sizes of ≈2.85 mm x 2.85 mm x 3.55 mm were cut out from the Gum Metal cold-swaged bar using electro-erosion machining.

3. Mechanical anisotropy of Gum Metal under compression

A scheme of the experiment set-up used for evaluation of mechanical anisotropy in Gum Metal under compressive loading along (II) and perpendicular (⊥) to its technological texture is shown in Fig. 2a, whereas force vs. crosshead displacement curves obtained from a testing machine is presented in Fig. 2b. In the case of the Gum Metal loading perpendicular to the swaging axis, the maximal force and stress demonstrated higher values around yielding in comparison to loading of the sample cut off along the swaging (Fig. 2b).

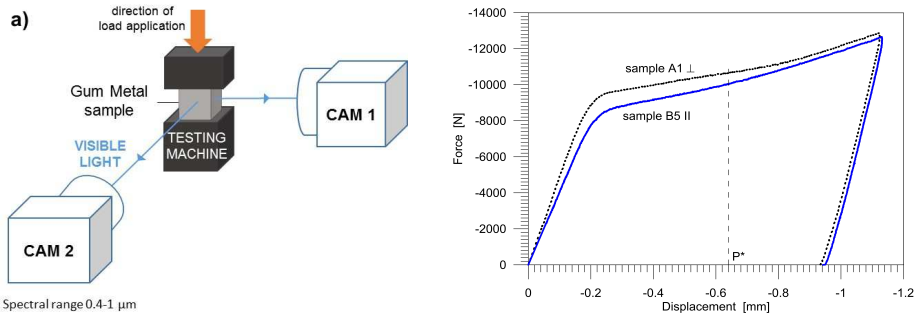

Figure 2: a) Scheme showing Gum Metal sample under compression monitored by two cameras; b) Force vs. crosshead displacement curves for the compression along (II) and perpendicular (⊥) to swaging axis.

Tendency to grow for the values of stresses related to yield limit noticed in Fig. 2b was also observed on the stress-strain curves, calculated by DIC algorithm [3] setting a virtual extensometer with 3 mm gauge length. However, a significant discrepancy between the strains for both curves was observed (Fig. 3a). Strain distributions E_{yy} determined for an advanced plastic deformation stage, denoted by "P" in Fig. 2b, for two perpendicular walls of two loading orientations are shown in Fig. 3b. The average strain discrepancy was mainly caused by shear deformation in the case of loading in perpendicular direction, as observed by camera CAM 2 for sample A1.

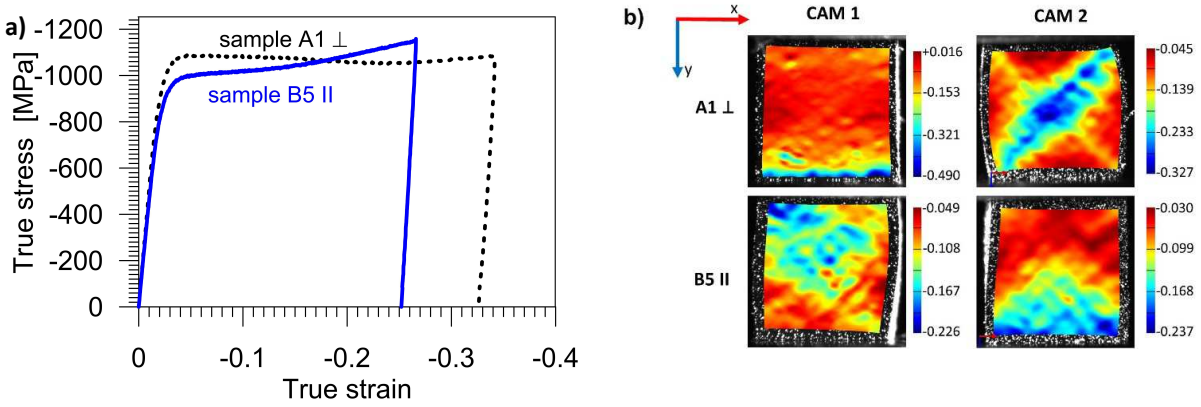

Figure 3: a) Stress vs. strain curves and b) strain distributions (E_{yy}) for Gum Metal under compression along (II) and perpendicular (⊥) to its <110> texture observed by two cameras (CAM 1 and CAM 2).

Such a significant difference between the deformation behavior of Gum Metal under compression along and perpendicular to the swaging direction and its <110> texture, confirmed its strong anisotropy.

Acknowledgements
The research was supported by the National Science Centre, Poland; 2014/13/B/ST8/04280 and 2016/23/N/ST8/03688.

References

[1] M. Hara, Y. Shimizu, T. Yano, N. Takesue, T. Furuta, S. Kuramoto, *Int. J. Mat. Res.*, 100:3, 2009.
[2] B.A. Auld, *Acoustic Fields and Waves in Solids*, Malabar FL, 1990.
[3] E.A. Pieczyska, M. Maj, K. Golasiński, M. Staszczak, T. Furuta, S. Kuramoto, *Materials*, 11:567, 2018.

Session S14: Structural mechanics and optimization

Organizers: M. Gilbert (U Sheffield), T. Lewiński (Warsaw UT), A. V. Pichugin (Brunel U.,London)

ANALYSIS OF TWO CONTACT SHAPE OPTIMIZATION PROBLEMS

I. Páczelt[1], Z. Mróz[2] and A. Baksa[1]

[1]*Institute of Applied Mechanics, University of Miskolc, Miskolc, Hungary*
[2]*Institute of Fundamental Technological Research, Warsaw, Poland*

e-mail: paczelt@freemail.hu

1. Introduction

The first problem relates to control of a point displacement of a loaded structure by applying the interacting punch loading. As at the same point both the displacement and the force are prescribed, a new type of optimization problem is formulated. The solution method of this problem can be used for design of robot clippers and gardening or plantation tools for mechanical processing.

In the second problem the steady wear state of the drum brake is analysed. Minimizing the wear dissipation power, the contact pressure distributions of the leading and trailing shoes are determined. The maximal pressure value is usually higher on the leading shoe. Next, the optimization problem is considered by maximizing the braking torque in the steady wear state and determining the optimal pin position.

2. First problem: displacement control of a loaded structure

2.1 Consider a cantilever beam clamped at its end *A* and loaded at point *Q* by the force F_Q, Fig.1. To control the deflection at *Q*, the lateral stamp action is applied by inducing the resultant load F_0 by a set of grippers or by a continuous contact interaction. The stamp form is defined by a given distribution of contact stresses between the stamp and beam with constraints that the displacement u_n^* and force F_Q at the point *Q* of the beam are prescribed.

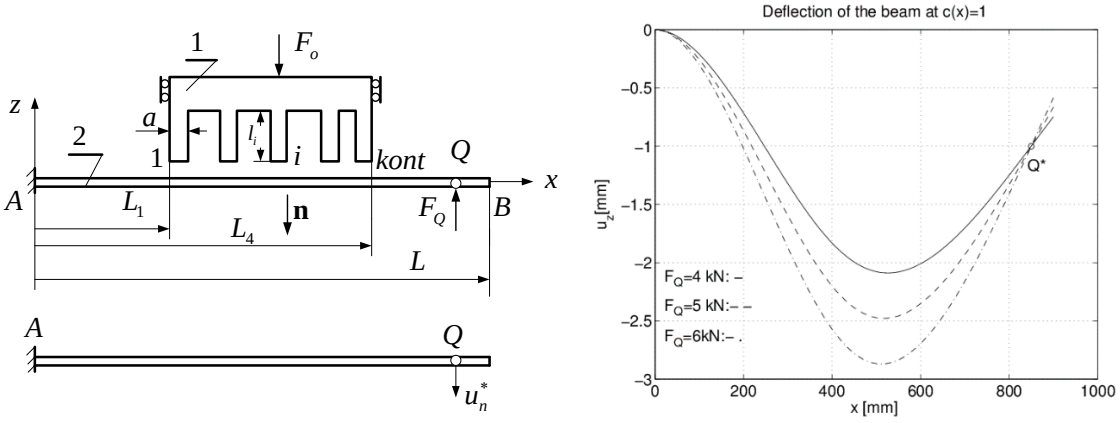

a) b)

Fig. 1a. Beam system for transmission of the stamp load F_0 the vertical displacement u_n^*.
1b) numerical results for different values of F_Q.

Assume first that the stamp action is executed by a set of grippers of the cross section area $A = ab$ and varying length l_i, cf. Fig. 1a. The forces between the stamp and beam are prescribed by the control function $c(\mathbf{x})$

(1) $$P_j = Ac(x_j)p_{\max} \quad , j=1,\ldots,kont$$

where $p_{\max}$ is the maximum of the contact pressure.

Using the Green function for the beam $H^{(2)}(x,s)$, the vertical displacement (in the direction *–z, in the* direction ***n***) at the point Q is expressed as follows

(2) $$u_n^* = \sum_{j=1}^{kont} H^{(2)}(x_Q, x_j) P_J + u_{n,load}^{(2)}$$

where $u_{n,load}^{(2)} < 0$ is the vertical displacement at point Q resulting from the specified force F_Q.
Using (1) and (2) we have

(3) $$p_{\max} = \frac{u_n^* - u_{n,load}^{(2)}}{\sum_{j=1}^{kont} H^{(2)}(x_Q, x_j) c(x_j) A}$$

After calculation of $p_{\max}$, from geometrical contact conditions we can determinate the shape of the stamp [1,2] The results in Fig.1b correspond to the beam cross section area $A_b = bh = 20 \cdot 50\ mm^2$, Young modulus $E = 2 \cdot 10^5\ MPa$, and other geometrical parameters $L_1 = 350, L_4 = 550, x_Q = 850, L = 900\ mm$, $kont = 5$.

2.2 A mechanical system has also been analysed when the beam is allowed to execute the rigid body vertical displacement $\lambda_F^{(2)}$. In this case, the large displacement u_n^* at Q can be assumed. In the solution of the optimization problem, first the value of $\lambda_F^{(2)}$ is calculated and from contact conditions between the punch and beam the rigid body displacement $\lambda_F^{(1)}$ is specified for punch, which may used in the mechanical technological process. The prescribed displacement u_n^* can be reached only by the vertical motion of the punch at the calculated rigid body displacement $\lambda_F^{(1)}$.
In the example of variant 2.2 the beam cross section area was different: $A_b = bh = 20 \cdot 75\ mm^2$, because the original area corresponds to a flexible beam with too large displacement.

3. Second problem: maximizing the torque of drum brake

In the previous paper [3] the formulae of the contact pressure distribution in the steady wear state for drum brake system were derived. The contact pressure distributions on the leading and trailing shoes were found to be different and larger on the leading shoe. Using these contact pressure distributions, it is easy way to calculate the braking torque. Assuming the varying position of the shoe pin, the optimization problem can be formulated by requiring the optimal pin position corresponding to maximal braking torque. The steady wear states and optimal designs were specified for both shoes. The elastic displacements of the drum brake at the optimal contact pressure distribution is calculated by the finite element system ABAQUS.

Acknowledgements The present research was partially supported by the Hungarian Academy of Sciences, by the program TÁMOP 4.2.1.B-10/2/KONV-2010-0001, by the grant National Research, Development and Innovation Office – NKFIH: K115701.

References

[1] I. Páczelt. Iterative methods for solution of contact optimization problems, *Arch. Mech*., 52, 4-5, 685-711, 2000.
[2] I. Páczelt, A. Baksa and Z. Contact optimization problems for stationary and sliding conditions, Springer International Publishing Switzerland 2016, P. Neittaanmaki et al. (eds.), *Mathematical Modelling and Optimization of Complex Structures, Computational Methods in Applied Sciences 40*, 281-312, DOI 10.1007/978-3-319-23564-6_16.
[3] I. Páczelt and Z. Mróz. On the analysis of steady sliding wear process, *Tribology International*, 42: 275-283, 2009.

ON THE FREE MATERIAL DESIGN FOR THE MULTIPLE LOADING CONDITIONS

S. Czarnecki, R. Czubacki and T. Lewiński

Warsaw University of Technology, Faculty of Civil Engineering, Warsaw, Poland
e-mail: t.lewinski@il.pw.edu.pl

1. The stress-based versions of the free material design: AMD, CMD, IMD and YMD

The free material design method (FMD) is one of the methods of optimum design of structural topology. The present paper discusses three variants of FMD.

In the AMD method (*anisotropy material design*, see [1], [2]) all components C_{ijkl} of Hooke's tensor $\mathbf{C}$ are design variables; $\operatorname{tr}\mathbf{C}=C_{ijij}$ represents the unit cost of the design within the given spatial design domain Ω.

In the CMD method (*cubic material design*, [3]) the principal elastic moduli *a,b,c* and the triplet of unit vectors **n**, **m**, **p** (the notation of Walpole [4] being used) are design variables. The unit cost is assumed as $\operatorname{tr}\mathbf{C}=a+3b+2c$.

In the IMD method (*isotropic material design*, see [5,6,7]) the bulk modulus *k* and the shear modulus μ are design variables; the unit cost is assumed as $\operatorname{tr}\mathbf{C}=3k+10\mu$.

In the YMD (*Young modulus design*, see [8]) the Young modulus is the only design variable, the Poisson ratio being kept fixed. The unit cost is proportional to the Young modulus.

Consider *n* variants of traction loads. The values of linear forms $f^{\alpha}(\mathbf{v})$, $\alpha=1,...,n$, on a virtual displacement field **v** represent the values of the virtual work of the loads for the subsequent load variants. Let $\mathbf{u}^{\alpha}$ represent the displacement field caused by the α th load. In order to construct the Pareto front we consider the problem of minimization of the functional

$$\wp_{\eta}=\eta_1 f^1(\mathbf{u}^1)+...+\eta_n f^n(\mathbf{u}^n),\quad \eta_1+...+\eta_n=1 \tag{1}$$

being a convex combination of the compliances corresponding to the subsequent load variants. The aim of the methods AMD, CMD, IMD and YMD is minimization of the functional (1) over the design variables satisfying the cost condition: the integral of the unit cost is predefined and equals Λ. Each of the optimization methods discussed leads to an auxiliary problem of the form

$$\min\left\{\int_{\Omega}\rho\left(\sqrt{\eta_1}\boldsymbol{\tau}^1,...,\sqrt{\eta_n}\boldsymbol{\tau}^n\right)dx \;\middle|\; \boldsymbol{\tau}^{\alpha}\in\Sigma_{\alpha}(\Omega),\ \alpha=1,...,n\right\} \tag{2}$$

where $\Sigma_{\alpha}(\Omega)$ is the set of statically admissible stress fields $\boldsymbol{\tau}^{\alpha}=(\tau_{ij}^{\alpha})$ corresponding to the α th load variant, while $\rho(\boldsymbol{\sigma}^1,...,\boldsymbol{\sigma}^n)$ is a *gauge function* of *n* stress fields, characteristic for the AMD, CMD, IMD and YMD methods, respectively. These gauge functions corresponding to the optimization methods discussed are norms and in general the minimizer of (2) is a Radon measure, see [9], where similar problems are discussed. Having found the minimizer of (2) one can determine the optimal moduli. Within the approaches: AMD, IMD and YMD we have at our disposal explicit formulae for making this computation efficiently. The formulae for the optimal moduli of cubic symmetry are known only for *n*=1, see [3]. One of the aims of the present paper is to derive the formulae of the method CMD for *n*>1.

2. The kinematic approach

The auxiliary problem (2) can be rearranged to its dual form involving virtual (or adjoint) displacements:

$$\max\left\{ f^1\left(\sqrt{\eta_1}\mathbf{v}^1\right)+...+ f^n\left(\sqrt{\eta_n}\mathbf{v}^n\right) \;\middle|\; \mathbf{v}^\alpha \in V(\Omega) \text{ and } \rho^*\left(\boldsymbol{\varepsilon}(\mathbf{v}^1),...,\boldsymbol{\varepsilon}(\mathbf{v}^n)\right)\le 1 \text{ a.e. in } \Omega\right\} \qquad (3)$$

where $\boldsymbol{\varepsilon}(\mathbf{v})$ is the symmetric part of the gradient of the field $\mathbf{v}$. For the methods: IMD and YMD the dual norms $\rho^*(.)$ have been derived in [7,8]. The aim of the present paper is to write down (3) in an explicit form for the AMD and CMD settings.

The main property of the dual pair of problems (2), (3) is that the solutions may vanish on an essential part of the design domain. The effective domain of the solutions determines the material subdomain where the structure emerges, capable of transmitting the given loads to the given supporting edge.

3. Final remarks

In the case of a single load condition the free material design methods in its anisotropic version AMD leads to the optimal, but highly degenerated Hooke tensor characterized by a single non-vanishing eigenvalue, hence the zero eigenvalue is characterized by the multiplicity 5. The CMD method leads to the less degenerated Hooke tensor in which the zero eigenvalue has multiplicity 3. By admitting more than one load condition the optimum designs may become non-singular, if the load variants are appropriately chosen. In case of the AMD method at least six load conditions are necessary to make the Hooke tensor positive definite. The aim of the paper is to clear up this question in the context of CMD.

Acknowledgments The paper has been prepared within the statutory project: *Optimum design and computer aided detailing of structures and materials.*

References

[1] M.P. Bendsøe, A.R. Diaz, R. Lipton, J.E. Taylor. Optimal design of material properties and material distribution for multiple loading conditions. *Int. J. Numer. Meth. Eng*. 38:1149–1170, 1995.
[2] S. Czarnecki and T. Lewiński. A stress-based formulation of the free material design problem with the trace constraint and multiple load conditions. *Structural and Multidisciplinary Optimization* 49: 707–731, 2014.
[3] R. Czubacki and T. Lewiński. Topology optimization of spatial continuum structures made of non-homogeneous material of cubic symmetry, *Journal of Mechanics of Materials and Structures*. 10: 519-535, 2015.
[4] L.J.Walpole. Fourth-rank tensors of the thirty-two crystal classes: multiplication tables. *Proc.Roy.Soc.Lond*. A 391: 149-179, 1984.
[5] S. Czarnecki. Isotropic material design. *Computational Methods in Science and Technology*. vol.21: 49-64, 2015.
[6] S. Czarnecki and P. Wawruch. The emergence of auxetic material as a result of optimal isotropic design, *Physica Status Solidi (B): Basic Solids State Physics* 252: 1-11, 2015.
[7] S.Czarnecki, T.Lewiński. Pareto optimal design of non-homogeneous isotropic material properties for the multiple loading conditions, *Physica Status Solidi B: Basic Solids State Physics*. 254, 1600821, 1-14, 2017.
[8] S. Czarnecki and T. Lewiński. On material design by the optimal choice of Young's modulus distribution. *International Journal of Solids and Structures*, vol. 110-111: 315-331, 2017.
[9] G. Bouchitté and I. Fragala. Optimality conditions for mass design problems and applications to thin plates, *Arch.Rat.Mech.Anal.* 184, 257-284, 2007.

THE LEAST GRADIENT PROBLEM IN THE FREE MATERIAL DESIGN

W. Górny, P. Rybka, and A. Sabra

Institute of Applied Mathematics & Mechanics, the University of Warsaw, Warsaw, Poland

e-mail: rybka@mimuw.edu.pl

Stating the least gradient problem

A version of the Free Material Design maybe stated as follows: given region $\Omega \subset \mathbb{R}^d$, $d = 2, 3$ a load at the boundary consistent with the equilibrium, i.e. $\int_{\partial\Omega} g\, dS = 0$ find the optimal distribution p of the material. By optimality we mean that

$$\int_\Omega |p| = \inf\{\int_\Omega |q| : \ q \in L^1(\Omega, \mathbb{R}^d),\ \operatorname{div} q = 0,\ q \cdot \nu|_{\partial\Omega} = g\}. \tag{1}$$

Here, ν is the outer normal to $\partial\Omega$. It obvious from the statement of (1) that one should expect to find a solution in the space of Radon measures, $\mathcal{M}$, on Ω.

One can look for a dimension reduction of (1), which is simple, when $d = 2$. We notice that (1) is equivalent to

$$\int_\Omega |Du| = \inf\{\int_\Omega |Dv| : \ v \in BV(\Omega),\ v|_{\partial\Omega} = f\}, \tag{2}$$

where $BV(\Omega)$ is space of functions with bounded total variation and $\frac{\partial f}{\partial \tau} = g$ and τ is a tangent vector to $\partial\Omega$. The equivalence is given by the mapping $BV(\Omega) \ni u \mapsto QDu \in \mathcal{M}$, where Q is the rotation by $\frac{\pi}{2}$, for details see [3].

Existence of solution in strictly convex domains for different boundary conditions

It is well-known fact that if $f \in C(\partial\Omega)$ and $\Omega \subset \mathbb{R}^2$ is strictly convex, then there exists a unique solution to (2), see [5]. For more general data neither existence, nor uniqueness is obvious. A part of the problem is that the problem (2) is ill-posed, because the following functional $\Phi : L^2(\Omega) \to \mathbb{R} \cup \{+\infty\}$, given by $\Phi(u) = \int_\Omega |Du|$, if and only if $u \in BV(\Omega)$ and $u|_{\partial\Omega} = f$, otherwise $\Phi(u) = +\infty$, is not lower semicontinuous. Nonetheless, we can show

Theorem 1. (see [2], [3])
If $\Omega \subset \mathbb{R}^2$ is strictly convex, $f \in BV(\partial\Omega)$, then problem (2) has at least one solution. □

Here is an **Example** of a solution, [3]. If $\partial\Omega$ is parametrized by arclength, $[0, L) \ni s \mapsto x(s) \in \partial\Omega$, then we take $f = (\alpha_1 + \alpha_2)\chi_{[s_2, s_2)} + \chi_{[s_2, L)}$, $s \in [s_2, L)$. The solution, u, takes three values, 0, α_1, $\alpha_1 + \alpha_2$ and it is depicted on Fig. 1.

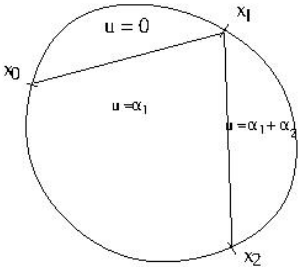

Fig. 1

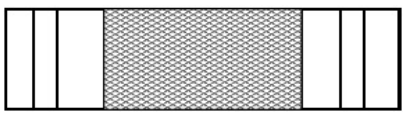

Fig. 2

By modifying the method of [5] we can show existence of solution to (2) when continuous data are specified only on $\Gamma \subsetneq \Omega$.

Theorem 2. (see [3])
If $\Omega \subset \mathbb{R}^2$ is strictly convex, $\Gamma \subsetneq \Omega$ is a smooth arc, $f \in C(\bar{\Gamma})$, then problem (2), when $u|_\Gamma = f$ is in place of $u|_{\partial\Omega} = f$, has at least one solution. □

Existence of solutions in convex but not strictly convex domains

The main problem for existence is presence of nontrivial line segments ℓ in the boundary of Ω, we call them *flat parts*. We shall say that a continuous function $f \in C(\partial\Omega)$ *satisfies the admissibility condition #1* on a flat part ℓ iff f restricted to ℓ is monotone.

We associate with f on a flat piece of the boundary, ℓ, a family of closed intervals $\{I_i\}_{i\in\mathcal{I}}$ such that $I_i = [a_i, b_i]$ is contained in the interior of ℓ relative to $\partial\Omega$. On each I_i function f attains a local maximum or minimum on each ℓ and each I_i is maximal with this property. We also set $e_i = f(I_i)$, $i \in \mathcal{I}$. For the sake of making the notation concise we will call I_i a *hump*.

After this preparation we state the admissibility condition for non-monotone functions. A continuous function f, which is not monotone on a flat part ℓ, *satisfies the admissibility condition #2* iff for each hump $I_i = [a_i, b_i] \subset \ell$ and $e_i := f([a_i, b_i])$, $i \in \mathcal{I}$ the following inequality holds,

$$\operatorname{dist}(a_i, f^{-1}(e_i) \cap (\partial\Omega \setminus I_i)) + \operatorname{dist}(b_i, f^{-1}(e_i) \cap (\partial\Omega \setminus I_i)) < |a_i - b_i|. \tag{3}$$

Theorem 3. (see [4])
Let us suppose that Ω is convex and $f \in C(\partial\Omega)$. In addition, $\partial\Omega$ has a finite number of flat parts $\{\ell_k\}_{k=1}^N$. If f satisfies the admissibility conditions #1 or #2 on each flat part $\{\ell_k\}_{k=1}^N$ of $\partial\Omega$, then there is a continuous solution to the least gradient problem. □

We can extend this result also to the case $f \in BV(\partial\Omega)$ or an infinite number of flat parts of $\partial\Omega$.

Example
We define $\Omega = (-L, L) \times (-1, 1)$, $L > 2$. We take, $f_i \in C(\partial\Omega)$, $i = 1, 2$ given by $f_1(x, y) = \cos(\frac{\pi}{2}y)$ and $f_2(x, y) = \cos(\frac{\pi}{2}\frac{x}{L})\chi_{|x|>L-2}(x) + \chi_{|x|\leq L-2}(x)$. For f_1 problem (2) has no solution, while for f_2 there is a unique solution whose level sets are shown on Fig. 2. The shaded area is a level set of positive Lebesgue measure.

We also discuss the lack of uniqueness of solutions. We show that non-uniqueness of solutions to (2) is related to level sets of u with positive 2-d Lebesgue measure and discontinuities of f. This is done in [1].

Acknowledgments The work of AS was supported by the Research Grant 2015/19/P/ST1/02618 financed by the National Science Centre, European Union's Horizon 2020 research and innovation program under the Marie Curie grant agreement No 665778. PR was in part supported by the National Science Centre Research Grants no 2013/11/B/ST8/04436 and 2015/19/P/ST1/02618.

References

[1] W. Górny, (Non)uniqueness of minimizers in the least gradient problem, arxiv:1709.02185.
[2] W. Górny, Planar least gradient problem: existence, regularity and anisotropic case, arxiv:1608.02617.
[3] W. Górny, P.Rybka, A.Sabra, Special cases of the planar least gradient problem, *Nonlinear Analysis*, **151** (2017), 66-95.
[4] P.Rybka, A.Sabra, The planar Least Gradient problem in convex domains, arxiv:1712.07150.
[5] P.Sternberg, G.Williams, W.P.Ziemer, Existence, uniqueness, and regularity for functions of least gradient, *J. Reine Angew. Math.*, **430** (1992) 35-60.

THE DEFORMATION OF THE HELICAL TYPE WIRE STRUCTURES

A. Danilin[1,2], S. Zavoronok[1,2]

[1]*Institute of Applied Mechanics, RAS, 125040, Leningradsky av., 7, Moscow, Russia*
[2]*Moscow Aviation Institute, 125993, Volokolamskoe shosse, 4, Moscow, Russia*

e-mail: andanilin@yandex.ru

Analysis of power transmission lines (PTL) involves the calculations of static states and vibrations of conductors (and cables) together with spiral accessories, vibration dampers and other devices attached on them. Many of these problems can be properly solved only by taking into consideration the internal structure of the conductors, the design of which is formed by wire layers wound on each other at different angles relative to the longitudinal axis. For example, such reference is required in the design of the systems of power safety and reliability of information-telecommunication supply of aerodromes, aircraft and rocket systems, overhead transmission lines, subject to intense wind, especially in icing conditions.

Due to the complex design of the wire structures the known issues arise in the estimates of their deformations, stiffnesses, bearing capacity, etc. For example, the bending stiffness of the conductor can sufficiently vary as its deformation, since the wire layers may slip relative to each other, and a separate wire is movable within the wire layer. Consequently, the values of stiffnesses can be varied both along the conductor axis and in time.

The work proposes a new deformation model of wires structures which are similar to PTL conductors. These structures include not only conductors and cables, but spiral clamps intended for tension, suspension, joints, protection and repair of conductors.

On the basis of energy averaging, each wire layer is considered as an elastically equivalent anisotropic cylindrical shell, thus a conductor or a spiral clamp are modeled as a system of cylindrical shells nested into each other and interacting by the forces of pressure and friction. Following this approach the formulae for the flexibility and stiffness matrices of spiral structures have been obtained.

The problem of interaction of a tension clamp with the external wire layer of a conductor has been formulated and solved. The mechanism of the force transfer from the clamp on the conductor has been investigated.

Acknowledgments. The work was financially supported by the Russian Ministry of Education and Science (Federal Programme no.14.604.21.0188, ID RFMEFI60417X0188).

References

[1] Dubois H., Lilien J.L., Dal Maso F. A new theory for frequencies computation of overhead lines with bundle conductors. *Rev. AIM – Liege*. No. 1. 1991. 46–62.

[2] Papailiou K.O. On the bending stiffness of transmission line conductors. *IEEE Transactions on Power Delivery*. 12-4.1997. 1576–1588.

[3] Rawlins C.B. Analytical Elements of Overhead Conductor Fabrication. *Fultus Corporation*. – 2005.

[4] Shalashilin V.I., Danilin A.N., Volkov-Bogorodskiy D.B. Model of overhead line conductor with interaction of layers. *Proc. 6th International Symposium on Cable Dynamics. Charleston (U.S.A).* 19–22 Sept. 2005. 371–377.

[5] Rawlins C.B. Flexural self-damping in overhead electrical transmission conductors. *J. of Sound and Vib*. 323-(1–2). 2009. 232–256.

BENCHMARK PROBLEM FOR STRUCTURAL OPTIMIZATION WITH MULTIPLE LOAD CONDITIONS IN 3-D

M. Nowak[1]

[1]*Chair of Virtual Engineering, Poznan University of Technology, Poland*

e-mail: Michal.Nowak@put.poznan.pl

1. Introduction

The trabecular bone adapts its form to mechanical loads and is able to form structures that are both lightweight and very stiff. In this sense, it is a problem (for the nature or living entities) similar to the structural optimization, especially the topology optimization. The presented structural topology optimization method is based on the trabecular bone remodeling phenomenon. The developed biomimetic topology optimization method allows shape modification using shape derivative without volume constraint [1]. Instead of imposing volume constraint shapes are parameterized by the assumed strain energy density on the structural surface.

2. Multiple load conditions

From an engineer's point of view, the single load case problem is rather rare. A more common problem, but also more valuable in terms of mechanical design, is the one of structural optimization under multiple loads. The biomimetic optimization method should be useful as, in real life, multiple independent loads are always present. Using he developed biomimetic topology optimization method also the problem of compliance optimization for multiple load cases can be efficiently solved.

3. Benchmark problem for structural optimization with multiple load conditions in 3-D

In the paper by Rozvany [2] the popular benchmarks problems in topology optimization were considered. All presented benchmarks were 2-D. The benchmark problem for structural optimization with multiple load conditions in 3-D is proposed here to allow comparison of different optimization methods. The benchmark box design domain with vertical bending and horizontal bending forces is depicted on Fig. 1.

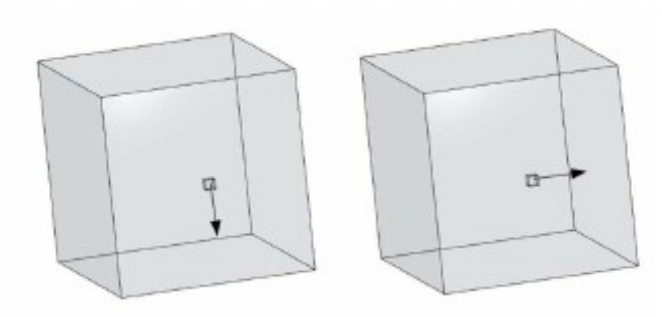

Figure 1: The box design domain: left – the vertical bending force; right – the horizontal bending force.

4. Optimization results for the benchmark problem in 3-D

Due to unique features of the presented biomimetic optimization method it is possible to find the solution, the stiffest structural configuration directly for the multiple load cases problem. The stiffest design is obtained by adding or removal material on the structural surface in the virtual space. The assumed value of the strain energy density on the part of the boundary subjected to modification is related to the material properties. The result of the 3D structural topology optimization for multiple load cases using the biomimetic approach is presented on Fig. 2.

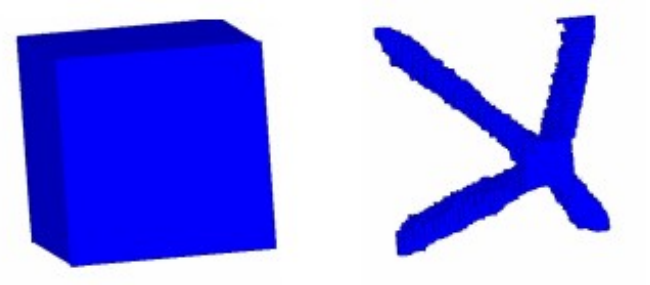

Figure 2: The box starting domain (left) and the final result of the optimization procedure for the multiple load cases for 3-D problem.

5. Conclusions

In the paper at hand, the new formulation of biomimetic optimization based on the trabecular bone remodeling applied to the multiple load problem was presented. The structural evolution is based on the shape gradient approximation by the speed method, and it is separated from the finite element method computations. The important advantage of the presented approach is that the optimization results are in the form of functional configuration. Accordingly, the assumed value of the strain energy density on the part of the boundary subject to modification could be related to the material properties. The 3-D example result shows the configuration for the real material. In view of the above, the 3-D example results with the assumed two perpendicular bending forces as multiple loads could be a good benchmark for testing other approaches to multiple load optimization problem.

6. Acknowledgments

This work was supported by the Polish National Centre for Research and Development under the grant - decision no. TANGO 1/266483/NCBR/2015 and the computational grant no. 362 Biomimetic approach to compliance optimization and multiple load cases of Poznan Supercomputing and Networking Center *(*PCSS), Poznan, Poland.

7. References

[1] M. Nowak, J. Sokołowski and A. Żochowski, Justification of a certain algorithm for shape optimization in 3D elasticity, *Structural and Multidisciplinary Optimization* 57/2:721–734, 2018.
[2] G. Rozvany, Exact analytical solutions for some popuar benchmark problems in topology optimization, *Structural optimization* 15: 42-48, 1998.

A MULTI-MATERIAL OPTIMIZATION METHOD WITH MANUFACTURING CONSTRAINTS FOR TAILORED FORMING

R. Siqueira[1], R. Lachmayer[1] and I. Mozgova[1]

[1]*Intitute for Product Development, Leibniz University, Hannover, Germany*
e-mail: siqueira@ipeg.uni-hannover.de

1. Introduction

New mechanical design approaches must be constantly developed to attend the specific requirements of new manufacturing technologies. Tailored Forming is a process chain with the objective of creating hybrid solid components by using semi-finished workpieces, theme of a collaborative research CRC 1153 [1]. With this technique, a new class of high performance parts can be constructed, aiming load-adjusted behaviour, lightweight or specific local properties. The objective of this paper is to find the optimal material distribution for its design, including the joining zone geometry, taking the specific manufacturing constraints of the process into consideration to bring the potential of Tailored Forming use to the maximum.
For that, Topology Optimization techniques were here reviewed, focusing on the progress made on the multi-material field, manufacturing constrained implementations and stress-based methods, since the forces at the joining zone are here a concern. Thereby, a new method was developed in [2], called Interfacial Zone Evolutionary Optimization (IZEO). This method is based on Evolutionary Algorithms methodology to solve optimization problems and has as objective function the minimization of weight, with stress constraints. The concept of it goes around an update process that happens only at the material interfacial zone, with predetermined steps of shape adjustment that gives a bi-directional ability to the algorithm (Figure 1).

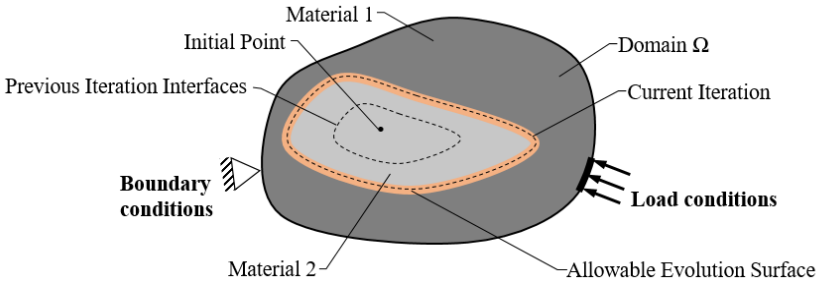

Figure 1: Representation model about the evolution process of IZEO.

The choice of such an approach was made based on advantages that evolutionary algorithms provide to follow-up the process and to make implementations through observations. It is shown that this interfacial limitation facilitates a gradual implementation of manufacturing constraints, which has been always a sensitive topic in the optimization field. Therefore, some of the geometric restrictions found in Tailored Forming were here applied through a flexible process, in order to generate useful results. Finally, an example is presented, where IZEO was able to generate a first dual-material high-performance design that can be manufactured today through the available technology.

2. Manufacturing Constraints

A key factor of the method is the possibility to implement a variety of manufacturing constraints. Following the same concept proposed in [3], the manufacturing constraints can be described as a combination of different geometric restrictions. The implementation of a set of different geometric restrictions allows the system to be flexible, which is an important characteristic when dealing with the process chain of Tailored Forming. The geometric constraints here implemented were the following: Symmetry; Minimum Member Size; Directional Placement; Continuous Phases limitation; and Outer Contour. These restrictions are

implemented by allowing only certain elements to change in the evolutionary process. Therefore, the translation of manufacturing constraints into geometric restrictions is here an important step. Each restriction must be implemented in a very specific way and has a big influence in the final result.

3. Results

The algorithm for IZEO is implemented in MATLAB and here performed for 2D problems. As example of its implementation we take one of the demonstrators of the CRC 1153, which is a hybrid shaft made of steel and aluminium. This shaft is manufactured through the following process chain: laser or friction welding of the semi-finished workpieces, impact extrusion or cross wedge rolling, machining and heat treatment.
The description of these manufacturing restrictions is not simple, due to the different processes involved and its requirements. The shaft has to be designed with a serial configuration, having one side made of steel and the other of aluminium. Due to the properties of the materials, the process requires that at the joining zone, the aluminium must be in the outer side and the steel in the inner side (Figure 2).

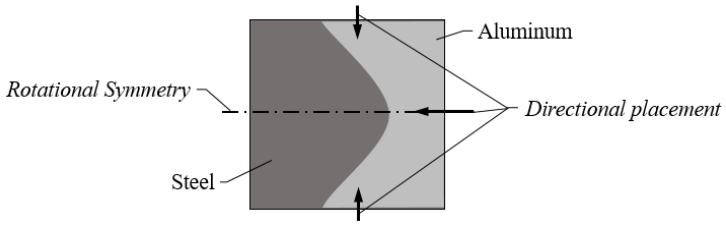

Figure 2: Representation of the geometric restrictions found in the manufacture of the hybrid shaft.

For the optimization process, the objective is to have a light component, meaning the most use of aluminium and a restricted safety factor. Since this shaft has a fixed geometry, this geometry is here our design domain and the initial point of the evolution for the aluminium is the extreme side where the aluminium is intended to be in the serial manufacture. The result of the optimization process is presented in Figure 3, where the load conditions of the simulation is also represented.

Figure 3: Optimized result for the hybrid shaft under bending with IZEO and manufacturing constraints.

4. Conclusions

The present study presented a method for generating optimized designs with the strong manufacturing constraints of Tailored Forming. The final result is highly dependent on the description of this restrictions, as expected. The 2D description is a current limitation, but it allows already a useful analysis of the method in this initial stage. Despite the method being heuristic, the results generated were realistic and simply to implement, showing that the method has a potential for further development and future applications.

Acknowledgments The authors thank the German Research Foundation (DFG) and the CRC 1153 for its support.

References

[1] SFB 1153, Prozesskette zur Herstellung hybrider Hochleistungsbauteile durch Tailored Forming. [online] Leibniz Universität Hannover. Available at: https://www.sfb1153.uni-hannover.de/sfb1153.html (accessed 09.04.2018).
[2] R. Siqueira, R. Lachmayer, I. Mozgova. Development of a Topology Optimization Method for Tailored Forming Multi-material Design, *COBEM Proceedings*, Curitiba, 2017
[3] S.L. Vatanabe, T.N. Lippi, C.R. de Lima, G.H. Paulino and E.C. Silva. Topology Optimization with Manufacturing Constraints: A unified Projection-based Approach, *Advances in Engineering Software*, Vol. 100, pp. 97–112. 2016

FIXED OFFSHORE PLATFORM DESIGN AND STRUCTURAL STRENGTH EVALUATION CONSIDERING SEA BED CONDITION

Doyoub Kim[1], Kangsu Lee[1], Byoung Wan Kim[1], Byoungjae Park[1], and Hyun-Seok Kim[1]

[1]*Offshore Plant Research Department, Korea Research Institute of Ships & Ocean Engineering, Daejeon, Korea*
e-mail: kimdy@kriso.re.kr

1. Introduction

In this study, structural design and strength evaluation of the platform structure, which is a typical fixed offshore platform, was performed as part of the structural design study for acquiring the structural safety evaluation technology of the offshore plant. The basic geometry of the platform structure is designed in accordance with the classification rules and general platform design guidelines. General guidelines for designing steel offshore structures are given in ANSI/AISC [1] and Euro Code 3 [2]. The detailed guidelines for the design of steel offshore structures are applied in the API RP 2A WSD [3]. For the designed platform, the structural strength was evaluated by performing the in-place analysis. The sea bed boundary condition suitable for the platform design and strength evaluation was proposed by analysing the effect of the platform structural strength and deformation according to the sea bed boundary condition of the pile fixed platform.

2. Platform structure design

The platform installation target sea is set to 130m water depth in the South China Sea near Malaysia. The platform with 20,000 ton superstructure was designed by rule scantling technique. The 8-leg type platform was selected considering the size of the superstructure and the spacing of the coupling part between superstructure and platform leg. The specific dimensions of legs and members of the platform were designed to meet material strength standards such as slenderness, buckling, and hydrostatic pressure collapse. The slenderness ratio of 80 on the U.S. coastal standard was applied to ensure sufficient safety. The ratio of diameter to thickness (D/t ratio) was less than 60 to prevent local buckling, and finally the designed platform weighed 5,300 tons.

3. Global structural analysis

The in-place analysis of platform was carried out using SACS (v.11.0), a structural analysis software for offshore structures. The extreme environmental condition (100-year repetition period) was applied to the platform load condition and the pinned joints were applied to the boundary condition between the platform and the sea bed. The platform had the highest stress in the beam sea condition, and the unity check ratio of 0.995 at the lowermost leg was caused by the self-weight of the superstructure and the bending moment due to the horizontal marine environment loads (Fig. 1). Unity check ratio was measured to be less than 1 to ensure structural integrity of the designed platform. And analytical results were verified by obtaining almost the same strength results through structural analysis using the in-house code based on the beam element.

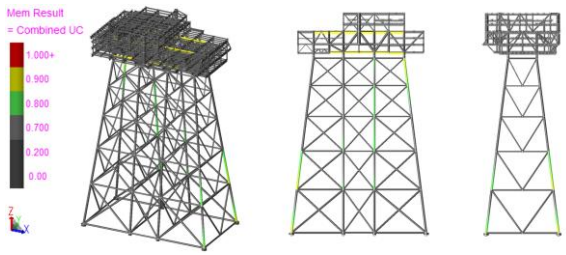

Figure 1: Analysis results of platform model (Combined unity check).

4. Sea bed boundary condition effect

The effect of sea bed boundary conditions between the bottom pile member of the platform and the sea bed was analysed. When the fixed boundary condition was applied to the bottom pile joints, the +y moment due to the horizontal environment loads occurred at the lowermost leg as the rotational deformation of the pile was constrained. In the case of the pinned boundary condition where horizontal displacement of the platform influences the rotational deformation of the pile, the –y axis moment due to the pile member rotational deformation occurred at the lowermost leg (Fig. 2). The axial stress of the leg due to weight of the superstructure is almost the same in both cases, but the moment due to the horizontal loads is opposite to the direction and the magnitude of the stress is quite different (Table 1). Fixed joint is not suitable sea bed boundary condition for platform global structural analysis because leg stress can be underestimated for it predicts deformation behaviour of piles differently from actual behaviour.

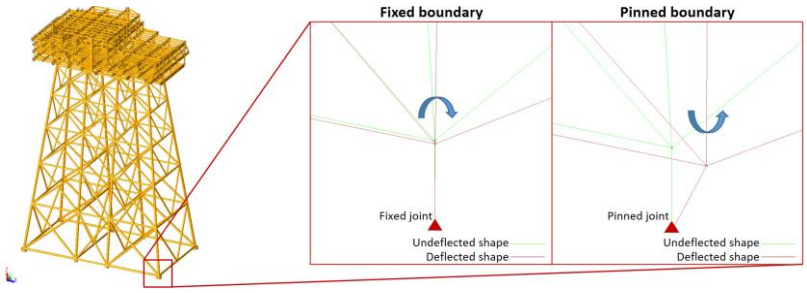

Figure 2: Structural deformation results of platform by sea bed boundary condition.

Joint condition	Unity check ratio				Applied stress (N/mm^2)			
	Max. U.C.	Axial U.C.	Bend-Y U.C.	Bend-Z U.C.	Axial stress	Bending Y-Y	Bending Z-Z	Com. Stress
Pinned	0.995	0.696	0.258	0.040	-114.01	-55.34	21.76	-173.47
Fixed	0.759	0.702	0.019	0.039	-114.88	6.50	-9.46	-126.35

Table 1: Comparison of U.C. ratio and stress of the lowermost leg (Pinned vs. Fixed).

5. Conclusions

A 5,300 ton platform structure satisfying the related design guidelines was designed and the structural integrity of the platform was evaluated for environmental loads and superstructure loads. The maximum stress occurred at the lowermost leg and was evaluated as U.C. ratio of 0.995, confirming the structural integrity. Prior to the Pile-Soil interaction analysis including the actual sea bed geological property, pinned boundary condition was found to be suitable for platform global structural analysis by analysing platform behaviour and stress characteristics according to boundary conditions at the end of piles.

Acknowledgments This research was supported by a grant from Endowment Project of "Study on the Core Technology of Structural Design, Engineering and Test for Establishment of Structural Evaluation System for Offshore Structure(2/3)" funded by Korea Research Institute of Ships and Ocean engineering(PES9470). This research was supported by a grant from Endowment Project of "Development of the Core Technology of Structural damage assessment based on ALS(Accident Limits State) for offshore plants(2/3)" funded by Korea Research Institute of Ships and Ocean engineering(PES9480).

References

[1] ANSI/AISC 303-16. *Code of Standard Practice for Steel Buildings and Bridges*, American Institute of Steel Construction, Chicago, IL, 2016.

[2] European Standard EN 1993-1-1 Eurocode 3. *Design of Steel Structures: General rules and rules for buildings*, European Committee for Standardization, Brussels, Belgium, 2005.

[3] API. *Recommended Practice for Planning, Designing and Constructing Fixed Offshore Platforms—Working Stress Design (RP 2A-WSD)*, American Petroleum Institute, Washington, DC, 2000.

NUMERICAL OPTIMIZATION OF DEPLOYABLE SCISSORS STRUCTURE WITH REINFORCING CHORD MEMBERS

Y. Chikahiro[1], I. Ario[2], P. Pawlowski[3], C. Graczykowski[3], and S. Shimizu[1]

[1]*Department of Water Environmental and Civil Engineering, Shinshu University, Nagano, Japan*
[2]*Institute of Engineering, Hiroshima University, Higashi-Hiroshima, Japan*
[3]*Institute of Fundamental Technological Research, Polish Academy of Science, Warsaw, Poland*

e-mail: chikahiro@shinshu-u.ac.jp

1. Introduction

A scissor structure is one of the well-known and most widely used deployable structure in the field of engineering. This type of structure enables to transform its configuration from the compact form to a large-size deployed state by extending in two or three directions [1], [2]. Generally, we can find applications of the scissor structures in architecture or space engineering. Very often they are used as light-weight temporary structures. The authors have proposed a scissors-type deployable bridge - Mobile Bridge$^{\mathrm{TM}}$ (MB) - based on the concept of the Multi-Folding Micro-structures [3] - [5]. The design concept of the MB enables to reduce the construction time on site by deploying the structure directly over a damaged bridge or a road without the need for any heavy machinery.

Our previous research was aimed at describing the fundamental mechanical properties of the MB. Several analytical methods were proposed based on the beam theory and equilibrium equations. At the current stage of the project, we have developed the full-scale experimental MB described in [6]. After successful initial tests we have concluded that in order to provide even higher level of safety in the disaster area, an effective reinforcing method and/or optimal bridge design should also be discussed. In this paper, we present the technique of reinforcement by the introduction of additional members, which can be added after the complete deployment of the bridge. Its optimal layout is evaluated by the combination of the FEM and the Differential Evolution (DE) optimization algorithm based on [7]. The optimal solution by weight minimization problem improves the performance of the bridge by selection of cross-sections of the scissor and reinforcing members.

2. Optimization methodology

This paper deals with the problem of minimization of the weight W, subject to the constraints imposed on the effective stress σ and the characteristic displacement δ, i.e

$$\begin{aligned} &\text{Minimize} && W, \\ &\text{s. t.} && \sigma_{\max} < \sigma_{\mathrm{y}},\ \delta_{\mathrm{c}} < \delta_{\mathrm{y}} \end{aligned} \tag{1}$$

where $\sigma_{\max}$ and δ_{c} are maximum stress and maximal allowable displacement in the center of the model. The problem is solved by changing each sectional area of the scissor and reinforcing components satisfying the constraint conditions based on the authors' previous paper [7].

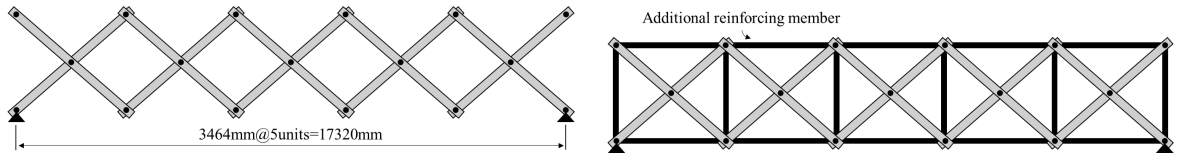

(a) (b)

Figure 1: Outline of the numerical model. (a) The model without any reinforcing members, (b) The model with reinforcing members.

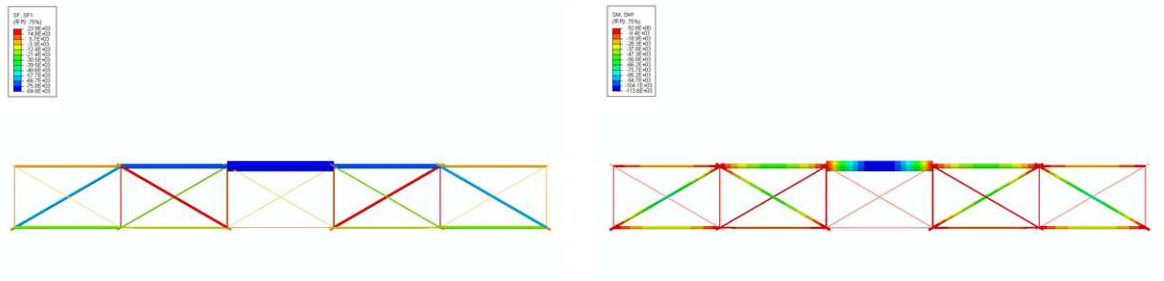

(a) (b)

Figure 2: Numerical results obtained for the operational state of the bridge. (a) Axial force distribution, (b) Bending moment distribution.

3. Numerical example

A simple 2D model of the mobile bridge implemented in ABAQUS 6.12 is shown in **Fig. 1**. After full expansion of the bridge, the total length of the span L is 17.3 m and the height η is 2.0 m. The bridge is analyzed in the operational conditions when simple supports are located on both sides of the lower span. The initial geometrical properties of all members of scissor structure and all reinforcing members are the same and equal: A = 28.0 cm^2, I = 1146.3 cm^4. The characteristics of the material are assumed to be linear elastic with Young's modulus E = 62.5 GPa and density ρ = 2.7 g/cm^3. The scaling of the geometry of the cross-sections required in the optimization procedure is conducted by introducing the coefficient factor γ. In the optimization procedure the scaling factor is assumed to be in the range from 0.01 to 2.0. The constraints imposed on yielding stress value σ_y and yielding deflection of the structure δ_y are assumed to be equal 180.0 MPa and L/500=34.6 mm, respectively. The applied loading includes both the dead weight and live load. The live load is caused by weight of the vehicle and is reflected in the numerical model by the point loads of 7.5 kN applied to the nodes located below the deck.

The conducted numerical simulations had revealed that initial design of the bridge is prone to large deformation due to large bending moment in the middle of the span. The optimized topology of the bridge is presented in **Fig. 2**. In the optimized topology the members of large cross-sections are present at the centre of the upper span, which corresponds to high compressive forces in this part of the structure. The top central part of increased thickness is supported by skew members such that the entire load bearing system of the bridge has the form of an arch. The presence of optimally sized reinforcing members causes that the bending moment in the scissor components is significantly reduced and deformation of the structure is considerably diminished.

Acknowledgments This research was partially supported by Encouraging prize from Society for the Promotion of Construction Engineering in 2017 and Grant-in-Aid for Young Scientists (18K13818) in 2018 - 2020.

References

[1] Z. You, and S. Pellegrino, Foldable bar structures, International Journal of Solids and Structures, 34(15), 1825-1847, 1997.
[2] C. Hoberman, Reversibly expandable doubly-curved truss structures, United States Patent 4,942,700, 1990.
[3] J. Holnicki-Szulc, P. Pawlowski, and M. Wiklo, High-performance impact absorbing materials - the concept, design tools and applications, Smart Mater. Struct., Vol. 12, No. 3, 2003.
[4] I. Ario, Structure with the expanding and folding equipment as a patent (No.2006-037668), 2006.
[5] I. Ario, M. Nakazawa, Y. Tanaka, I. Tanikura, S. Ono, Development of a prototype deployable bridge based on origami skill, Automation in Construction, Vol. 32, pp. 104-111, 2013.
[6] Y. Chikahiro, I. Ario, and M. Nakazawa, Theory and Design Study of a Full-Scale Scissors-Type Bridge, J. Bridge Eng., 2016. doi:10.1061/(ASCE)BE.1943-5592.0000913
[7] Y. Chikahiro, I. Ario, J. Holnicki-Szulc, P. Pawlowski, and C. Graczykowski, Numerical study on reinforcement and optimization of a scissors structure, Proc. of 40th Solid Mechanics conference, 2pages, 2016.

APPLICATION OF EQUILIBRIUM-BASED FINITE ELEMENT METHOD IN TOPOLOGY OPTIMIZATION PROBLEMS

Z. Więckowski[1] and M. Piątek[1]

[1]*Department of Mechanics of Materials, Łódź University of Technology, Łódź, Poland*

e-mail: zwi@p.lodz.pl

1. Introduction

The displacement-based finite element method (FEM) is usually utilized as a computational tool for solving topology optimization problems. Such an approach has been described e.g. in [2,1,3]. In the present work, the equilibrium problem has been solved by use of the stress-based FEM which follows from the principle of complementary work or – alternatively – from the principle of minimum of the complementary energy functional. As mentioned in [2], the topology optimization problem can be formulated as the following compliance minimization problem:

$$\min_{D\in \mathsf{E}_{\rm ad}} \min_{\boldsymbol{\tau}\in Y_{b,t}} \left\{ \frac{1}{2}\, b(\boldsymbol{\tau},\boldsymbol{\tau}) \right\} \qquad \text{with} \quad b(\boldsymbol{\sigma},\boldsymbol{\tau}) = \int_\Omega C_{ijkl}\, \sigma_{ij}\, \tau_{kl}\, \mathrm{d}x \tag{1}$$

where $\mathsf{D}_{\rm ad}$ denotes a set of admissible elasticity tensors D_{ijkl}, $C_{ijkl} \equiv D^{-1}_{ijkl}$, and $Y_{b,t}$ is the set of statically admissible fields of stress tensors

$$Y_{b,t} = \left\{ \tau_{ij} \in L^2(\Omega) : \tau_{ij} = \tau_{ji},\ \tau_{ji,j} + b_i = 0 \text{ in } \Omega,\ \tau_{ji}\, n_j = t_i \text{ on } \Gamma_\sigma \right\}. \tag{2}$$

Let us consider continuous distribution of the material described by a density function $\varrho(\boldsymbol{x})$, so the elasticity and compliance tensors can be expressed as follows (SIMP method, e.g. [2,1]):

$$D_{ijkl}(\boldsymbol{x}) = [\varrho(\boldsymbol{x})]^p\, D^0_{ijkl}, \quad C_{ijkl}(\boldsymbol{x}) = [\varrho(\boldsymbol{x})]^{-p}\, C^0_{ijkl}, \quad C^0_{ijkl} = (D^0_{ijkl})^{-1} \qquad \text{with } p > 3. \tag{3}$$

After using Eq. (3), the problem (1) can be written as the minimization problem:

$$\min_{\varrho(\boldsymbol{x})} b(\boldsymbol{\sigma},\boldsymbol{\sigma}) \tag{4}$$

provided that

$$b(\boldsymbol{\sigma},\boldsymbol{\tau}) = 0 \quad \forall \boldsymbol{\tau} \in Y_{0,0}, \quad \boldsymbol{\sigma} \in Y_{b,t}, \tag{5}$$

$$C_{ijkl}(\boldsymbol{x}) = [\varrho(\boldsymbol{x})]^{-p}\, C^0_{ijkl}, \tag{6}$$

$$\int_\Omega \varrho(\boldsymbol{x})\, \mathrm{d}x \le V, \qquad 0 < \varrho_{\min} \le \varrho \le 1 \tag{7}$$

where $Y_{0,0} = Y_{b,t}|_{b_i=0,\, t_i=0}$ and V is the given volume of the structure.

2. Stress-based finite element solution

The plane stress problem has been analyzed in the present work. To solve the equation of complementary work (5), the stress fields satisfying the equilibrium equations inside domain Ω have been constructed by means of the Airy stress function which has been interpolated with the help of rectangular hermitian element with 16 degrees of freedom. The equilibrium conditions given on the boundary of the design domain Γ_σ have a form of linear constraints and have been satisfied by use of the Lagrange multiplier method. To make the application

of this approach easier, additional elements have been implemented on edges of element located on Γ_σ. The detailed description of the stress-based approach can be found in [4].

3. Example

A rectangular design domain with ratio 6:1 has been considered. The vertical load distributed locally along a short segment has been assumed in the middle of the upper edge of the design region. The structure is considered to be simply supported at the central points of the vertical edges of the region.

The optimum solution has been found by use of two rectangular element grids: 150×50 and 300×100 elements to dicretize the right half of the design area. The same numbers of rectangular elements with 8 degrees of freedom have been utilized to find the solution based on the displacements method in order to compare the proposed approach with the well known method described in [1].

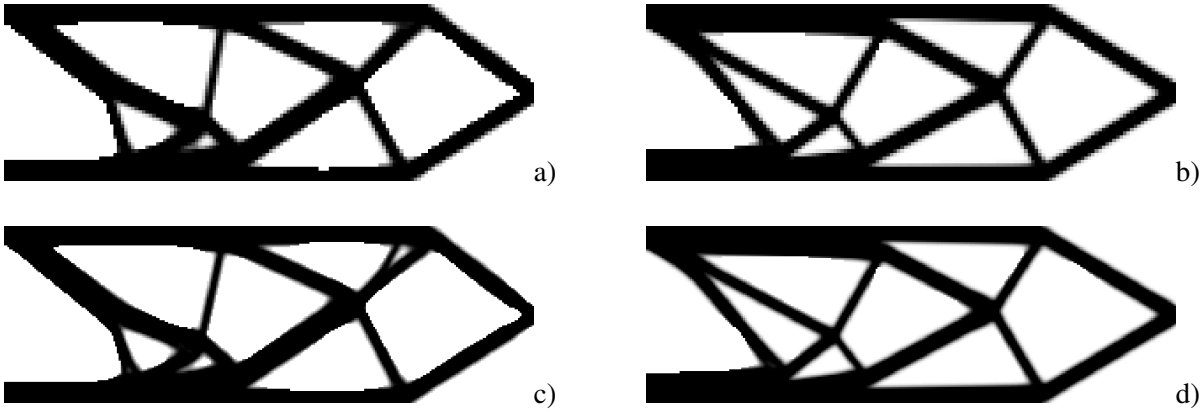

Figure 1: Optimized solution obtained by: a) stress-based approach, 150×50 elements; b) displacement-based approach, 150×50 elements; c) stress-based approach, 300×100 elements; d) displacement-based approach, 300×100 elements. Calculations made with volume fraction $V = 0.4$.

Although both the solutions, the stress and displacement ones, look similar, some differences related to the nature of the two approaches can be noticed. The image of the stress-based solution seems to be sharper a little than that obtained by the displacement approach. The stress-based approach has appeared to be more time consuming that the displacement-based one as expected. However, the proposed method has required much smaller number of iterations to satisfy the assumed tolerance.

Mesh resolution	Number of iterations		Execution time [s]	
	Stress method	Displacement method	Stress method	Displacement method
150×50	64	145	209	23.1
300×100	67	325	1409	224

Table 1: Comparison of efficiency of two applied methods.

References

[1] E. Andreassen, A. Clausen, M. Schevenels, B.S. Lazarov, O. Sigmund. Efficient topology optimization in MATLAB using 88 lines of code, *Struct. and Multidisc. Optim.*, 43, 1–16, 2011.

[2] M.P. Bendsøe, O. Sigmund. *Topology Optimization. Theory, Methods, and Applications*, Springer Verlag, Berlin, 2003.

[3] O. Sigmund. A 99 line topology optimization code written in Matlab. *Struct. and Multidisc. Optim.* 21, 120–127, 2001.

[4] Z. Więckowski, S.K. Youn, B.S. Moon (1999). Stress-based finite element analysis of plane plasticity problems, *Int. J. Numer. Meth. Eng.*, 44, 1505–1525.

ON IMPLEMENTATION OF SUBDOMAIN ORIENTED TOPOLOGY OPTIMIZATION INTO STRUCTURE RETROFITTING

K. Tajs-Zielińska, B. Bochenek

Institute of Applied Mechanics, Cracow University of Technology, Cracow,Poland
e-mail: katarzyna.tajs-zielinska@pk.edu.pl

1. Motivation

Nowadays, restoration processes have ability to enjoy the benefits of all innovations proposed in science and engineering. In what follows up-to-date retrofit designs can be obtained based on efficient numerical methods, including optimization ones. This paper is focused on one of the new concepts, namely implementation of topology optimization into retrofitting of structures suffering from the effects of structural damage and material degradation. Topology optimization allows to obtain stiffer, lighter and cheaper constructions preserving their aesthetic value by developing new, original shapes of strengthening.

2. Problem

Some important aspects of retrofitting and strengthening of existing structures have been reported in literature and the books [1], [2] may serve here as examples. This paper considers a new point of view, namely adaptation of topology optimization techniques to searching for the optimal layout of strengthening elements to be implemented into damaged and/or weakened structures. The idea is to implement a random stiffness information of the original structure into the optimization process. It can be done, by modelling design-passive regions with randomly distributed values of material data. The randomized stiffness distribution within weakened structure is modelled in order to include effects of material degradation. As a result, the new layout of strengthened structure of maximum stiffness for which the assumed volume fraction is preserved can be obtained. This approach allows to reduce a mass of strengthening elements, but what is essential, the complete and detailed information about the material degradation level of the original structure is not required to perform the optimization process.

In the problem formulated in this paper, two possible interpretations of objective function are taken into account. Firstly, it can be interpreted as a minimization of a compliance of the construction as a whole, where the design domain is only a part of the structure. Second way is to interpret the objective function as a compliance calculated only for the domain where the optimization process is performed. This approach is understood as a subdomain oriented topology optimization.

As the efficient topology generator the algorithm based on Cellular Automata concept developed by the Authors [3] has been used.

3. Results

In order to illustrate the above proposed approach, the subdomain oriented topology optimization of the bridge structure shown in figure 1 has been performed.

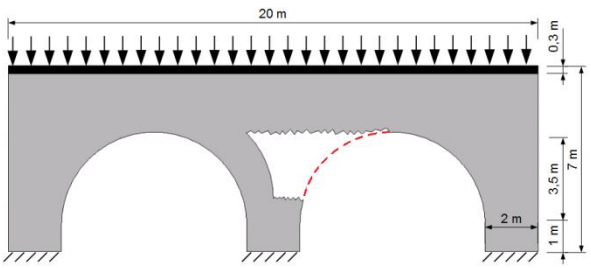

Figure 1: Damaged bridge structure with applied loads and supports.

It has been assumed that the bridge has been weakened by both structural damage and by the effect of material degradation. The upper part plotted in black colour is representing a road, this part is excluded from optimization. The Young modulus of the original material equals E =27 10^9 Pa.

Two models of a weakened material are considered. The first one it is uniformly distributed material of decreased, as compared with the original structure, value of the Young modulus. The constant value of 0.9 E has been selected. In the second model of the weakened material the Young modulus values are randomly selected from the interval: 0.8 E – E. The material degradation is illustrated in the figure 2a by randomly distributed green/grey regions. Performing optimization process within the selected design domain results in creating a topology of strengthening which minimizes the total structure compliance. In the figure 2b a visualization of expected optimization result is presented.

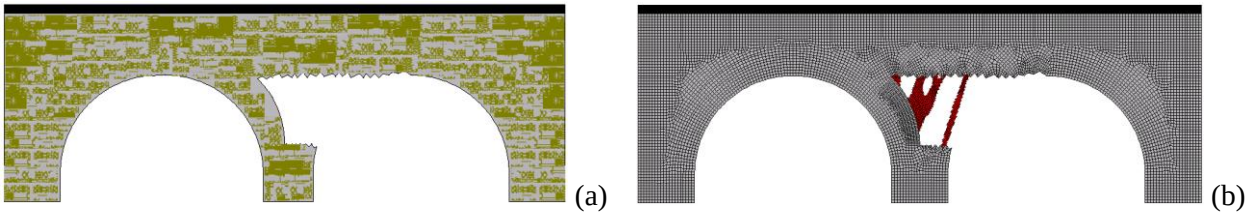

Figure 2: Randomly distributed weakened material (a), strengthened structure (b).

As the first task, the topology optimization has been performed for the damaged structure with uniformly weakened material. The Young modulus of a material in the domain selected for optimization equals E. The value of distributed load is 1000 N/m whereas assumed volume fraction of material for resultant, optimized topology within design domain equals 0.25. It is worth noting that structural damage caused significant increase of compliance from 0.01426 Nm calculated for original perfect structure to 0.03007 Nm. The further increase of compliance to 0.03322 Nm results from material degradation towards 0.9 E. In the figure 3 the obtained topology optimization results are presented. The total compliance has been reduced to 0.01871 Nm (a) and to 0.02031 Nm (b), respectively.

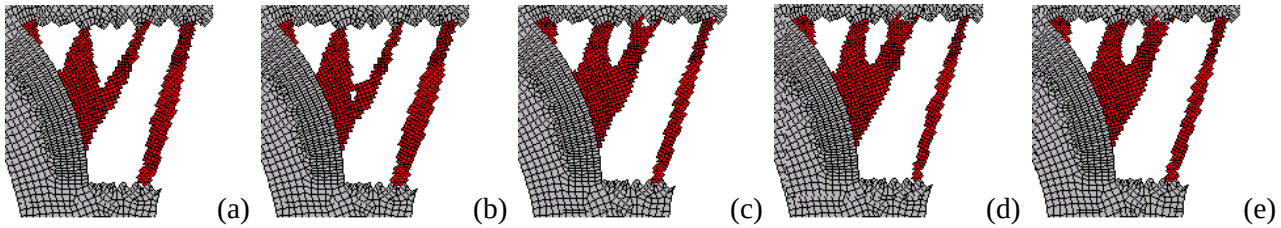

Figure 3: Topologies of strengthening: (a) uniformly distributed original material E, (b) uniformly distributed weakened material 0.9 E, (c)-(e) randomized distribution of weakened material 0.8 E – E.

The topology optimization procedure has been applied next to three different cases of random distribution of a weakened material (0.8 E – E) to check to what extent randomized values of the Young modulus influence final designs. Figure 3 presents topologies generated for all three cases for which compliance values are: (a) 0.02051, (b) 0.02112 and (c) 0.02061 Nm. It is worth noting that the results obtained for different randomizations are very similar, which means that there may exist a representative topology for the proposed random model of weakened material. To conclude, in all discussed cases the implemented retrofitting procedure allowed for a significant reduction of structure compliance what confirms the efficiency of the presented approach. It can be treated as a basis for developing novel design techniques for strengthening of existing structures suffering from the effects of structural damage and material weakening.

References

[1] S. Syngellakis, editor, *Retrofitting of Heritage Structures. Design and evaluation of strengthening technique*, WIT Transactions on State-of-the-art in Science and Engng, 62, 2016.
[2] A. Costa, A. Arêde and H. Varum, editors, *Strengthening and Retrofitting of Existing Structures*, Springer, 2018.
[3] B. Bochenek and K. Tajs-Zielińska. Novel local rules of Cellular Automata applied to topology and size optimization. *Eng. Opt.*, 44(1), 23-35, 2012.

TOPOLOGY OPTIMIZATION OF OFFSHORE PLATFORM STRUCTURE PANEL AND EXPERIMENTAL VALIDATION

H.-S. Kim[1], K. Lee[1], B. Park[1], and D. Kim[1]

[1]*Korea Research Institute of Ships and Ocean Engineering (KRISO), Daejeon, Republic of Korea*
e-mail: hskim85@kriso.re.kr

1. Introduction

Generally, the design of offshore platform structures is strictly guided by recognized codes and standards (RCS). The series of procedure on offshore structure design is called rule scantling. These regulations and guidelines are mostly empirical and are based on some old-fashioned but reliable safety factor approaches such as working stress design (WSD) or allowable stress design (ASD). Although these codes and standards provide a firm layout of offshore structure, it often result in over conservative design which causes millions of dollars of extra construction cost. In this research, to enhance the structural performance and to suggest a new novel design of offshore structures, we performed a topology optimization [1] based on solid isotropic material with penalization method (SIMP) on a designing process of an offshore platform structure panel. A volume constraint is applied in the optimization problem to utilize same material compared to the rule scantling offshore platform panel design. Since Bendsøe and Kikuchi [2] introduced concept of topology optimization based on the homogenization method, topology optimization has been widely utilized to obtain an optimal structural connectivity to satisfy the required performances. However, optimal design obtained as a result of topology optimization have limitations to apply directly to the design of offshore structures. Inherently, since it relies on the mesh of analysis method, optimal design from topology optimization has a non-smooth stair-wise boundary which is unable to manufacture and lacks usability. To overcome the difficulties we adopted the morphology concept to convert the optimal design into CAD (Computer Aided Design) data and utilized spline fitting based on NURBS (Non-Uniform Rational B-Spline) to enhance the manufacturability and applicability on the design of offshore structure. Later, the smoothed optimal design is manufacture by metal 3-D printing and experimentally validated by comparing the structural performance with the rule scantling based design under compression test with universal testing machine (UTM).

2. Topology optimization of offshore platform structure panel

To find optimal layout of offshore platform panel which maximize the structural stiffness, topology optimization is performed to minimize the structural compliance with a volume constraint to use same material as the rule scantling based design, Figure 1 (a). Design domain is considered with the corresponding displacement boundary condition of the rule scantling design as Figure 1 (b) and the optimal layout obtained from the topology optimization is shown in Figure 1 (c).

(1) $$\text{minimize } C = \sum_{i=1}^{NE} f_i u_i \,.$$

(2) $$\text{subject to } \sum_{i=1}^{NE} \rho_i V_i \le V_0 \,.$$

3. Smoothing the boundary of optimal design with morphology and spline fitting

To alleviate the stair-wise boundary of topology optimization, we applied morphology concept and spline fitting. First, morphology concept with dilatation method is utilized to topology optimization result to convert it into CAD data. Later, spline fitting with NURBS is employed to fit two geometric points located on the middle of the boundary of CAD converted optimal design while satisfying the volume constraint stated in the optimization problem (Figure 2).

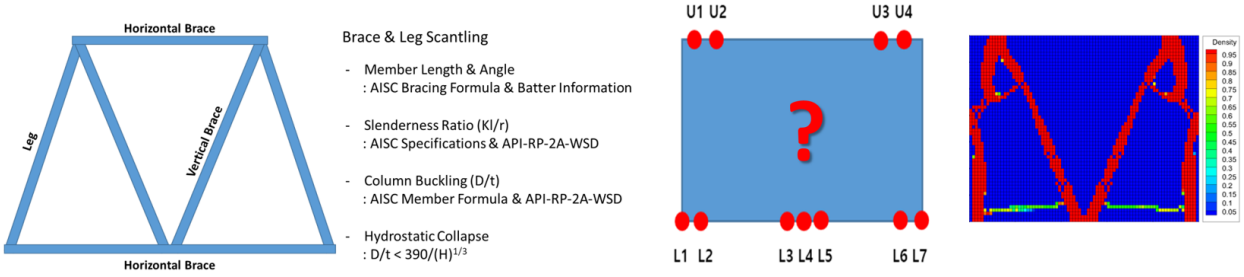

(a) Rule scantling of offshore jacket structure panel (b) Design domain (c) Optimal design

Figure 1: Offshore platform structure panel and topology optimization

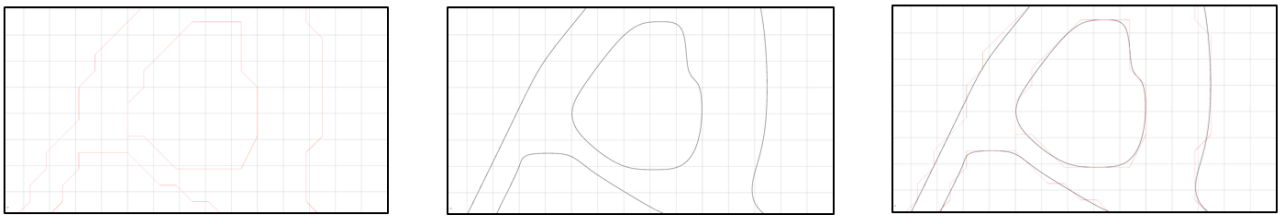

(a) Initial geometry from topology optimization (b) Geometry from spline fitting (c) Overlay of initial geometry and spline fitting

Figure 2: Boundary smoothing procedure by spline fitting

4. Experimental validation

Obtained optimal design of offshore platform structure panel with smoothed boundary is experimentally validated utilizing UTM under compression load by comparing the structural performance with the rule scantling design. As shown in Figure 3 (b), the proposed optimal offshore platform structure panel design has less deformation under same compressive load compared to the original design. The structural performance has been enhanced about 28% from the initial rule scantling design in the elastic region.

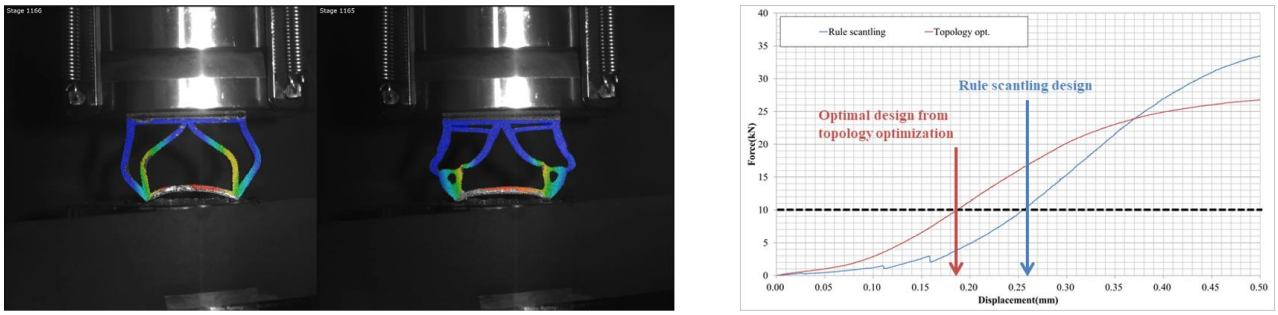

(a) Compression test with UTM (b) Displacement comparison under compression

Figure 3: Experimental validation of proposed optimal design of offshore platform structure panel

Acknowledgments This research was supported by a grant from Endowment Project of "Study on the Core Technology of Structural Design, Engineering and Test for Establishment of Structural Evaluation System for Offshore Structure(2/3)" funded by Korea Research Institute of Ships and Ocean engineering(PES9470).

References

[1] M.P. Bendsøe, *Optimization of Structural Topology, Shape and Material*, Springer, 1995.
[2] M.P. Bendsøe and N. Kikuchi, Generating optimal topologies in structural design using a homogenization method. *Comput. Methods Appl. Engrg.*, 71:197, 1988.

STRUCTURAL OPTIMIZATION PROBLEM USING MICROTRUSS METHOD

Y. Yokotani[1] and I. Ario[1]

[1]*Hiroshima University, Kagamiyama1-4-1, Higashihiroshima, Japan*

e-mail: m185931@hiroshima-u.ac.jp

1. Abstract

Typically, the design of the structure is determined by conditions imposed on maximal stresses and characteristic displacement. However, in case of larger structures, the amount and cost of applied material becomes more important. Thus, it is necessary to optimize structure topology in order to obtain fully stressed design of minimal weight. The examples of optimal designs are *Michell's structures* such as structure transferring vertical load into two pinned supports, schematically presented in Figure 1. However, *the structures* are characterized by infinitely dense distribution of members and thus they are not directly applicable in engineering practice. On the other hand, the optimal layouts can be obtained by relaxation of the problem of two-material design with the use of homogenization methods. However, the obtained designs are often characterized by checkerboard phenomenon, which significantly hampers their manufacturing and practical realization. The purpose of this research is to propose a novel method for optimal design of skeletal structures, which is deprived of the above mentioned drawbacks. The introduced method provides forming the optimum morphology by discretizing the design domain with micro-trusses and by gradual modification of the layout in order to obtain minimal weight design.

2. Optimal structural form of Michell

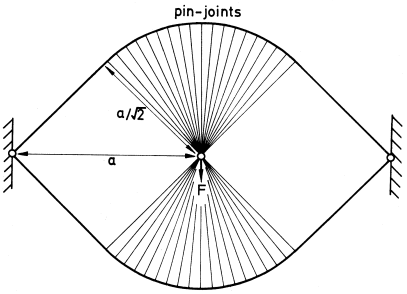

Figure 1: Approximation of Michell's truss by structure of finite number of members

We consider the inverse analytical problem to create an efficient structural form which has given the design conditions of materials, loads and boundary. It had been suggested that the optimum structure of this problem bases on the principle stress line on his theoretic approach (Figure 1). This classical problem is paid attention recently to create the digital design as the model of bench mark in the field of computing mechanics. It is well-known that this problem is as the Michell's optimum truss [1].

3. OPTIMISATION STRATEGY [2]

3.1. Optimum structural form using microtruss

We represent the design domain Ω of a continuum by micro-truss $\Delta\Omega^{(m)}$, (1). The discretisation is diagrammatically represented in Figure 2, where an example of a continuum Figure 2(a) is discretised as Figure 2(b). It is proposed that the behaviour of the domain Ω can be adequately modelled by microtrusses for large number of unit cells, M, where each microtruss member represents a pin-jointed linear extensional spring.

$$\Omega = \int \mathrm{d}\Omega = \lim_{\mathrm{d}\Omega \to 0} \lim_{n \to \infty} \sum_{m=1}^{n} \mathrm{d}\Omega^{(m)} \approx \sum_{m}^{M} \Delta\Omega^{(m)} \tag{1}$$

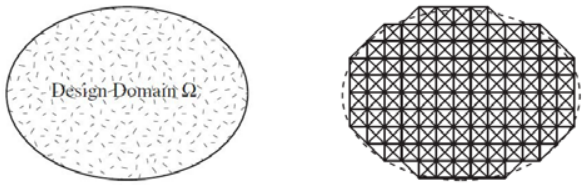

(a) Continuum, Ω (b) FEM of microtruss, $\sum \Delta\Omega$

Figure 2: Discretisation of a Continuum

3.2. Method of optimal morphogenesis

The design variable is the cross-sectional area of the microtruss members, $\boldsymbol{x} \in \boldsymbol{R}^N$ of $\Delta\Omega$ and therefore the linear equilibrium equation can be rewritten as (2).

$$\boldsymbol{F}(\boldsymbol{u}, f, \boldsymbol{p}, \boldsymbol{x}) = K(\boldsymbol{x})\boldsymbol{u} - f\boldsymbol{p} = \boldsymbol{0} \tag{2}$$

where $\boldsymbol{u} \in \boldsymbol{R}^N$ is a displacement vector, $f \in \boldsymbol{R}$ is a load parameter and $\boldsymbol{p} \in \boldsymbol{R}^N$ is a load vector.

The goal of optimization is a minimum weight design, represented as (3) in a discrete form. Since the density and the member length are constant, a more optimum form can be formed by changing only the cross-sectional area of each member.

$$\begin{aligned} &\text{Minimize : } \sum_{m=1}^{M} W^{(m)} = \sum_{m=1}^{M} \rho A_{(\nu)}^{(m)} \ell^{(m)} \\ &\text{subject to : } \boldsymbol{F}(\boldsymbol{u}, f, \boldsymbol{p}, \boldsymbol{x}) = \boldsymbol{0} \\ &\qquad A_{(\nu)}^{(m)} \leq A_{max}, \quad \sigma_{(\nu)}^{(m)} \leq \sigma_a \end{aligned} \tag{3}$$

where $W^{(m)}$ is the weight of each member, ρ is the density, $\ell^{(m)}$ is the member length, A_{max} is the maximum cross-sectional area and σ_a is the allowable stress. The design modification is based on the ratio of the member stress and the average stress $\overline{\sigma}_{(\nu)}$, where the stiffness of a member is updated at each load step according to (4).

$$\boldsymbol{x}_{(\nu+1)} = \mathcal{F}(\boldsymbol{x}_{(\nu)}) = \gamma \left(\frac{\sigma_{(\nu)}^{(m)}}{\overline{\sigma}_{(\nu)}} \right)^2 \boldsymbol{x}_{(\nu)} \tag{4}$$

where $\overline{\sigma}_{(\nu)} = \frac{1}{M} \sqrt{\sum_{m=1}^{M} \left(\sigma_{(\nu)}^{(m)} \right)^2}$, $\quad \nu = 1, 2, \cdots,$ $\quad \gamma$ is optimization rate constant.

4. CONCLUDING REMARKS

In this research, we have constructed a presented optimization method using microtruss method and addressed the problem of structure optimization using coat hanging problem and simple beam model as an example. It is the greatest result of this presented method that the layout of the skeleton structure with the minimum weight is obtained by placing the microtruss in the design area and applying the load and the boundary condition.

References

[1] A. G. M. Michell. The limits of economy of material in framed structures, Phil. Mag. (Series 6), 8, 589-597, 1904.
[2] I. Ario, M. Nakazawa, Y. Tanaka, I. Tanikura, S. Ono. Development of a prototype deployable bridge based on origami skill, Automation in Construction, Vol.32, 104-111, 2013.

SEISMIC BEHAVIOUR OF A CONCRETE-FILLED STEEL TUBE WITH DIAPHRAGM

S. Zenzai[1], S. Shimizu[1], C. Chikahiro[1], and T. Ohkami[1]

[1]*Shinshu university, Department civil engineering, Nagano, Japan*
e-mail: 16st403c@shinshu-u.ac.jp

1. Introduction

Concrete-filled steel tubes (CFST) have good strength and ductility performances compared to hollow columns. They are often utilized as the pier of the motorway viaducts. Japan road association recommends that the diaphragm is to be installed on the top of the filled-in concrete to fix the concrete in the steel tube [1]. However, Shimaguchi reported ductility performance of the CFST may become smaller by installing the diaphragm [2]. Therefore, it is necessary to clear the influence of the diaphragm on various CFST behaviour. In this study, authors make the dynamic analysis of CFST with diaphragm focusing on the diameter-thickness ratio D/t, the filling ratio L_c/L, and the concrete strength f_c. Within above results, we discuss the influence of the diaphragm on CFST behaviour.

2. Analytial model

Figure 1 shows the outline of the numerical model with the analytical conditions. Within Figure 1(a), D indicates the diameter, t is tube thickness, L is tube depth, and L_c is concrete height. In this study, we assume the CFST having the various parameters to investigate the effect on the CFST behaviour. Figure 1(b) show the analytical conditions. The bottom part of the CFST is fixed. At the top of the CFST, the mass M was considered to correspond to the superstructure of the viaduct, and the dead load Mg (g = 9.8m/s^2) and the three direction (North-South, East-West, and Up-Down) seismic load a were applied. As the seismic load a, the seismic load observed in the Kobe earthquake was utilized as shown in Figure 2. This earthquake occurred in 1995, and many structures were suffered the serious damage. This earthquake has the major tremor between 2 to 5 seconds, and the maximum acceleration is -8.2 m/s at 2.77 s.

At the interface of the steel tube and the concrete, they repeat separating, contacting, and slipping under the seismic load. These behaviours are modelled as the contact problem as same as the before author's studies [3-4].

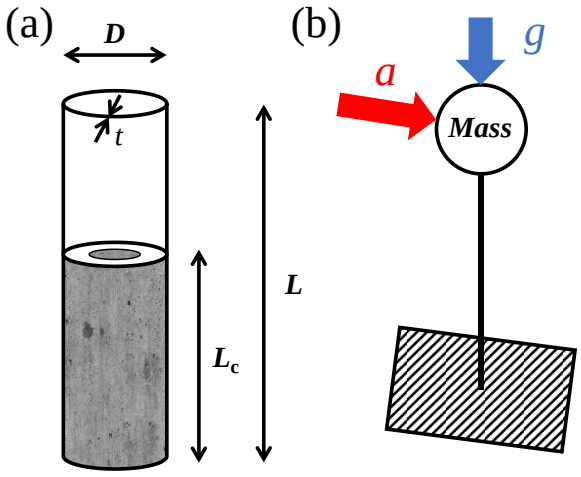

(a) outline of the model, (b) analytical conditions.
Figure 1: Numerical model and analysis conditions.

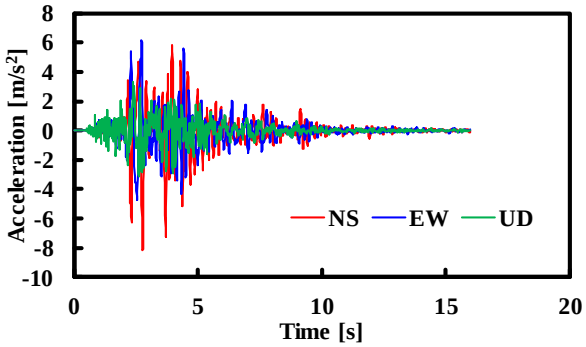

Figure 2: Kobe earthquake.

3. Result

We indicate the behaviours of CFST with difference filling ratio $L/L_{C.}$ Figure 3 shows the displacement hysteresis at the top of CFST. In this figure, the red line indicates the CFST having the concrete height accounts for 50 % of the tube depth, and the blue line the CFST having the concrete height accounts for 30 %. It can be seen that the large displacement arises on the model of L/L_c = 30%. Figure 4 shows the final stage deformation shapes of the CFST. In this figure, the buckling deformation is observed at the bottom part of the model of L/L_c = 50% of the tube depth. On the other hand, model of L/L_c = 30% has the buckling deformation just above the concrete (see black line at Figure 4(b)). These results imply that the large damage arises on the CFST with insufficient L/L_c.

The detail results and discussion will be shown during the Symposium.

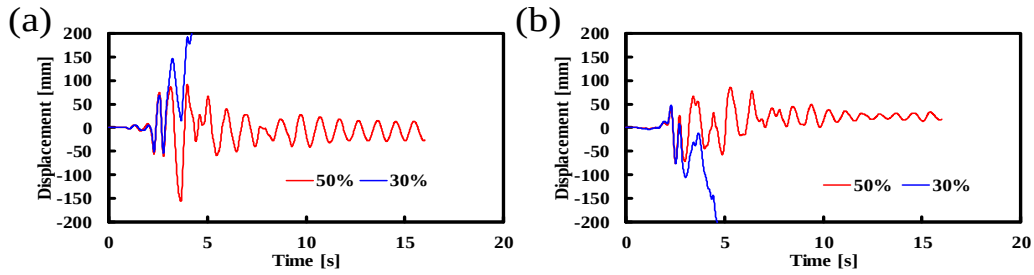

(a) North-South, (b) East-West.

Figure 3: Displacement hysteresis.

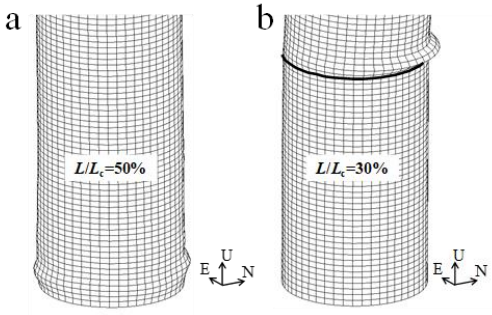

(a) L/L_c = 50%, (b) L/L_c = 30%.

Figure 4: Final stage deformation shapes.

References

[1] Japan road association. Specifications for highway bridges, Part V; Seismic design, 2017. (in Japanese)
[2] Y. Shimaguchi and M. Suzuki. Seismic performance evaluation of circular steel bridge piers which have damage and concrete filled repair. Journal of structural engineering, Vol. 61A, 292-301, 2015. (in Japanese)
[3] S. Shimizu. Behaviour of steel columns under 3-D seismic load. Thin-Walled Structures, Vol. 49, 544-553, 2011.
[4] S. Zenzai, S. Shimizu, and Y. Chikahiro. Behavior of a concrete filled steel box column with considering detachment under the seismic load. Thin-Walled Structures, Vol. 124, 98-106, 2016

OPTIMAL DESIGN OF AEROFOIL SYSTEMS FOR MANY CRITERIA

T. Schlieter[1] and A. Długosz[2]

[1, 2]*Institute of Computational Mechanics and Engineering*
Faculty of Mechanical Engineering
Silesian University of Technology, Gliwice, Poland
e-mail: [1]tomasz.schlieter@polsl.pl, [2]adam.dlugosz@polsl.pl

1. Introduction

The problem of optimal design of mechanical systems for more than 3 criteria attract more and more attention in the recent years. Such problems require efficient optimization algorithms as multiple numerical computation of objective functions for the mechanical problems is often extremely time consuming. The aim of this research is to develop an algorithm with improved convergence for a large number of criteria, employing an idea to couple game theory elements with differential evolution algorithm. Game theory elements are used to compare solutions, each player to represent a single objective. Differential Evolution is a population based evolutionary optimizer which in many variants found application in a range of engineering and scientific problems. The developed, coupled algorithm can be be useful in a wide range of real world multiobjective problems, including optimization of composite, thermoelastic, electrostatic and piezoelectric structures. Aerofoil design optimization problem was presented as a numerical example of application of designed algorithm in mechanical systems and finited element method software was used to determine values of objectives considered during the course of optimization.

2. Differential Evolution

Differential Evolution (DE) as a single objective optimizer was introduced by Price and Storn in 1997 [1] and is acclaimed for its simple structure, ease of use, speed and robustness. The algorithm utilises selection and mutation as exploration and exploitation mechanisms. Initial population is a set of parameter vectors usually chosen randomly from the solution space. During the course of optimization a weighted difference between two population members is calculated and then added to a third one to create a new design variables vector. If the resulting vector yields an improved objective value it replaces the former one.

3. Elements of game theory

In the multiobjective optimization problems a set of Pareto optimal (non-dominated) solutions is searched. The idea behind coupling DE and elements of game theory comes down to treating objectives as players, playing a cooperative game, trying to improve their respective objectives with the resources given and sharing the information with each other, iteratively looking for a Nash equilibrium. Each player is given a part of design variable vector at random as their resources, while the rest of the vector is fixed and determined by other players' choices. To assure diversification of solutions after each player makes his move, using a single objective DE optimizer to find a proposed solution, the assignment of resources is changed in a way each design variable is modified by one and only one player. Such an approach is used instead of traditional comparison methods based on dominance rank, depth or count, which encounter difficulties when solving tasks with more criteria since there is too many non-dominated solutions which can't be effectively compared.

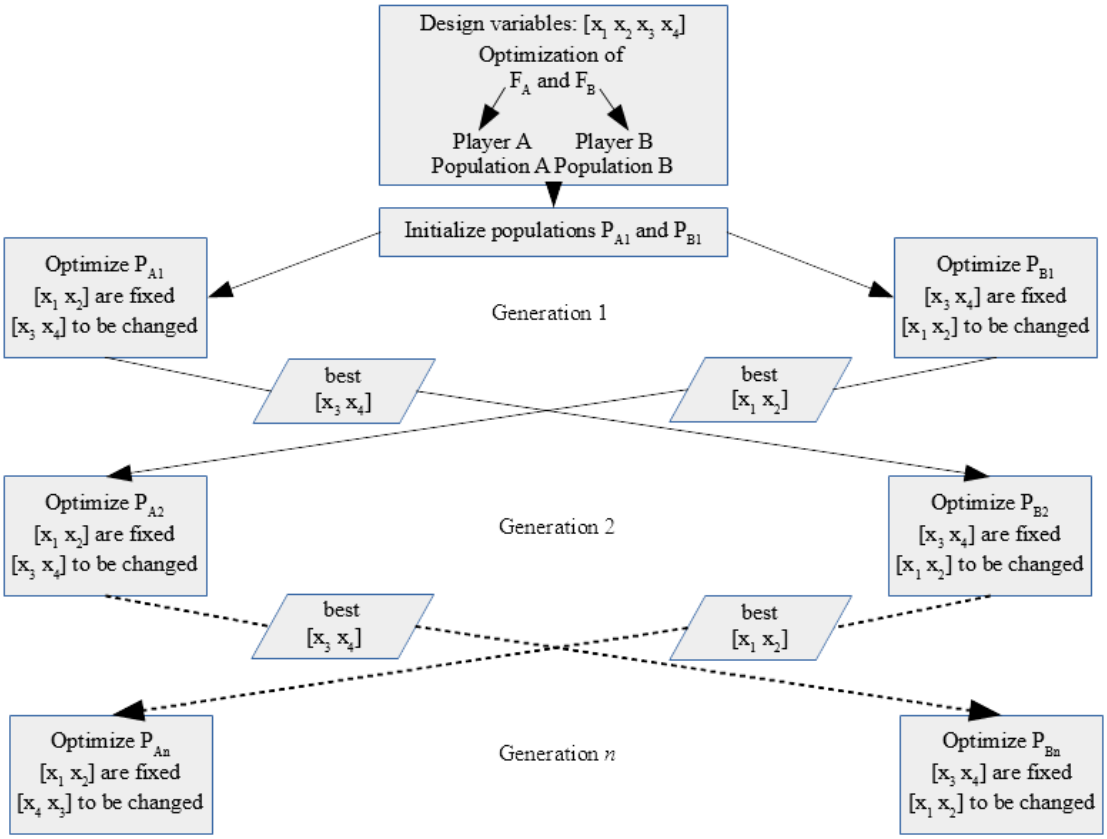

Figure 1: Coupled differential evolution and game theory multiobjective optimization algorithm.

4. Aerofoil design

Aerofoil systems are used to develop an aerodynamic force when moving through the fluids. When designing the optimal shape of an aerofoil many contradictory criteria have to be taken into consideration to provide the system with the desired properties, such as high endurance, low weight and high lifting force. Considered Aerofoil design consists of polyurethane foam and composite materials reinforced with carbon and glass fabric.

5. Objectives and design variables

Objectives in the optimization problem are devoted to minimization of maximal equivalent stresses, minimization of maximal displacements, minimization of total mass of the model and maximization of difference between values of modal frequency of a system and a given frequency – these are the examples of conditions required of aerofoil systems, although other criteria based on specific needs can be formulated. Values of functionals used as objectives are computed using FEM simulations. Boundary conditions and material properties are fixed during the optimization course and geometry of the model, described by design variables is changed to fit the declared needs, formally described by aforementioned functionals.

Acknowledgments The research was co-financed from the statutory subsidy of the Faculty of Mechanical Engineering of the Silesian University of Technology in 2018.

References

[1] J.-P. Blaizot and G. Ripka. *Quantum theory of finite systems*. MIT Press, 1985.
[2] O. C. Zienkiewicz and J. Z. Zu. A simple error estimator and adaptive procedure for practical engineering analysis. *Int. J. Num. Meth. Eng.*, 24:334, 1987.

ARE MICHELL STRUCTURES AND OPTIMUM GRILLAGES EQUIVALENT TO FRAMEWORKS COMPOSED OF INFINITE NUMBER OF STRAIGHT MEMBERS?

K. Bołbotowski[1]

[1]*Faculty of Civil Engineering, Warsaw University of Technology, Warsaw, Poland*

e-mail: k.bolbotowski@il.pw.edu.pl

A classical engineering problem is that of finding within a plane, convex design domain $\bar{\Omega}$ a truss form that optimally transfers a finite, self-equilibirated system of point-loads F. Since the dawn of the 20th century it has been established that, in general, an optimal truss consisting of finite number of bars does not exist – adding new members proves efficient and the process continues to infinity. The limit framework, called Michell structure, combines two types of media: a continuum-like fibrous domains and cables of finite cross-section area, possibly curved. The aim of this paper is to consider viewing mathematically the Michell structures as trusses made of infinitely many straight bars. The same question will be then readdressed for optimum grillages being a plate-like counterpart of Michell frameworks. We begin by revisiting the well-established description of Michell structures together with the most efficient numerical technique.

The continuum facet of the Michell structures enforces introducing a stress field σ, rather than operating with member forces. The presence of the finitely thick cables, however, rules out the possibility of viewing σ as a function, e.g. belonging to a L^p space; hence σ must be sought in a space of tensor-valued measures $\mathcal{M}\left(\bar{\Omega};\mathcal{S}^{2\times 2}\right)$. The stress formulation of the Michell problem can readily be posed as:

$$\inf\left\{\int_{\bar{\Omega}}\left(|\sigma_{\mathrm{I}}|+|\sigma_{\mathrm{II}}|\right):\sigma\in\mathcal{M}\left(\bar{\Omega};\mathcal{S}^{2\times 2}\right),\operatorname{div}\sigma+F=0\right\}, \tag{1}$$

where $\sigma_{\mathrm{I,II}}$ are eigenvalues of the stress tensor σ evaluated pointwise. The first, mathematically rigorous treatment of the problem (1) may be found in [2]; in their work authors proved that such variational form attains a solution $\hat{\sigma}$, i.e. the infimum is, in fact, a minimum. The extension of the searched space to measures turns out essential for this result, which validates the physical motivation for capturing the cable part of the structure.

The stress-posed problem (1) admits its dual, displacement-based variational form which was derived by Michell himself in 1904; the functional maximized is a virtual work of the loading system F on a vector-valued displacement function u:

$$\sup\left\{\int_{\bar{\Omega}}u\cdot F:u\in C^1\left(\bar{\Omega};\mathbb{R}^2\right),\max\left\{|\varepsilon_{\mathrm{I}}(x)|,|\varepsilon_{\mathrm{II}}(x)|\right\}\leq 1\text{ for a.e. }x\in\bar{\Omega},\varepsilon=1/2\left(\nabla u+\nabla^{\mathrm{T}}u\right)\right\}. \tag{2}$$

The pointwise constraint bounds all the eigenvalues $\varepsilon_{\mathrm{I,II}}$ of the strain tensor ε. After relaxing the condition $u\in C^1\left(\bar{\Omega};\mathbb{R}^2\right)$ the problem (2) also has a solution $\hat{u}$.

To this day the most efficient and commonly used method for numerical approximation of Michell structures was first developed in the '60s; it employs the so called *ground structure*. The construction of the ground structure starts by populating the design domain $\bar{\Omega}$ with a finite and fixed set $X\subset\bar{\Omega}$ of evenly spaced m nodes. Next, each pair of nodes in X is connected by a bar, thus generating a dense truss counting $n=m(m-1)/2$ members. The volume minimization problem for the ground structure reduces to a pair of finite-dimensional, mutually dual LP problems:

$$\min\left\{\sum_{i=1}^{n}l_i\,|S_i|:\mathbf{S}\in\mathbb{R}^n,\ \mathbf{B}^{\mathrm{T}}\mathbf{S}=\mathbf{F}\right\}, \tag{3}$$

$$\max\left\{\mathbf{u}\cdot\mathbf{F}:\mathbf{u}\in\mathbb{R}^{2m},\ \max_i\frac{|\Delta_i|}{l_i}\leq 1,\ \boldsymbol{\Delta}=\mathbf{B}\mathbf{u}\right\}, \tag{4}$$

where l_i, Δ_i and S_i are, respectively, length, virtual elongation and axial force of the i-th member; $\mathbf{u}$ is a vector of virtual nodal displacements. The geometric matrix $\mathbf{B}$ by definition gives the linear relation between the elongation and displacement vectors $\boldsymbol{\Delta}$ and $\mathbf{u}$. Together with recently developed adaptive algorithms, for the nodal set X sufficiently "dense", the ground structure approach delivers highly precise numerical representations of

the Michell structures with the optimum volume of several significant figures accuracy.

The successful strategy, stemming from the ground structure concept, encourages to pose problems analogical to (3,4) for an infinite nodal set X; we shall consider $X = \bar{\Omega}$. In this setting every pair of points $x \neq y \in \bar{\Omega}$ becomes a potential bar; the ground structure is thus equinumerous to the Cartesian product $\bar{\Omega} \times \bar{\Omega}$, excluding its diagonal. Consequently, instead of operating with finite vectors $\mathbf{\Delta}, \mathbf{S}$, the two-argument functions $\Delta, \lambda : \bar{\Omega} \times \bar{\Omega} \to \mathbb{R}$ must be considered. Unlike perhaps the stress-based problem (3), the kinematic problem (4) can be easily brought (at least formally) to infinite dimensional setting:

$$\sup \left\{ \int_{\bar{\Omega}} u \cdot F : u \in C\left(\bar{\Omega}; \mathbb{R}^2\right), \ \sup_{(x,y)\in\bar{\Omega}\times\bar{\Omega}} \frac{|\Delta(x,y)|}{|x-y|} \leq 1, \ \Delta = Bu \right\}, \tag{5}$$

where the linear operator B is an infinite dimensional counterpart of the matrix $\mathbf{B}$. This problem was thoroughly examined in [2] and was proven to be equivalent to the relaxed problem (2); hence both problems share the same solution $\hat{u}$. The duality argument yields the stress version of the problem:

$$\inf \left\{ \int_{\bar{\Omega}\times\bar{\Omega}} |x-y| \, |\lambda(x,y)| : \lambda \in \mathcal{M}\left(\bar{\Omega} \times \bar{\Omega}; \mathbb{R}\right), \ B^*\lambda = F \right\}. \tag{6}$$

The member forces λ again, and from the physical point of view precisely for the same reason as σ in (1), must be sought among certain measures instead of functions. Analogies between the forms (3) and (6) are clear; the linear operator B^* is a conjugate of B and, similarly as $\mathbf{B}^{\mathrm{T}}$, should be viewed as an equilibrium operator.

All the aforementioned problems except for (6) are established to have a solution; moreover all the duality gaps are proven to vanish. Therefore, the question of existence of a minimizer $\hat{\lambda}$ of (6) can be interpreted as follows: is there an optimum truss consisting of infinite number of straight bars? A positive answer would render Michell structures as infinite trusses in a strict mathematical sense. The minimizing solution, however, in general fails to exist, which can be intuitively explained: the Michell structures may contain curved bars and no curve is a union (finite or infinite) of straight segments which do not degenerate to points. This settles that Michell structures cannot be identified with infinite trusses.

In the early '70s an intensive research began on the problem of optimum grillages, i.e. horizontal frameworks that transfer the load through beams by means of bending (see e.g. [3]). The continuous setting of the optimization problem reduces to a pair of mutually dual forms analogical (up to second-order differentiation in grillages) to Michell problems (1) and (2). Through numerous, analytically derived optimum grillage layouts a feature that distinguishes them from Michell structures was discerned: for a sufficiently large design domain $\bar{\Omega}$ (in particular when $\bar{\Omega} = \mathbb{R}^2$) the optimum grillage does not contain curved beams. Recently the ground structure approach was successfully employed for the grillage problem, i.e. the analogues of (3) and (4) served as a numerical tool for approximating the exact optimum layouts, see [1]. Finally, the existence of solution of problem (6) posed for grillages remains open; the remarkable absence of curved beams in optimum layouts makes the attempt of proving this result worthwhile – unlike the Michell structures, the optimum grillage would turn out to be true straight-member frameworks.

Acknowledgments The paper was prepared within the Research Grant no 2015/19/N/ST8/00474 financed by the National Science Centre (Poland), entitled: Topology optimization of thin elastic shells - a method synthesizing shape and free material design.

References

[1] Karol Bolbotowski, Linwei He, and Matthew Gilbert. Design of optimum grillages using layout optimization. *Structural and Multidisciplinary Optimization*, 2018. doi: 10.1007/s00158-018-1930-6.

[2] Guy Bouchitté, Wilfrid Gangbo, and Pierre Seppecher. Michell trusses and lines of principal action. *Mathematical Models and Methods in Applied Sciences*, 18(09):1571–1603, 2008.

[3] W. Prager and G. I. N. Rozvany. Optimal layout of grillages. *J Struct Mech*, 5:1–18, 1977.

MICHELL CANTILEVER ON CIRCULAR SUPPORT FOR UNEQUAL PERMISSIBLE STRESSES IN TENSION AND COMPRESSION

T. Sokół[1] and T. Lewiński[1]

[1]*Warsaw University of Technology, Faculty of Civil Engineering, Warsaw, Poland*

e-mail: t.sokol@il.pw.edu.pl

1. Introduction

In his pioneering work, Michell [1] derived optimality criteria of least-volume trusses and showed that the optimal truss is immersed in an appropriate field of virtual displacements. Michell started his investigation from Maxwell theorem [2] and deduced that the layout of the optimal truss can be determined by solving the simplified problem with equal permissible stresses in tension and compression $\sigma_T = \sigma_C$. This conclusion, however, is valid only for Maxwell class of problems, when all external loads together with reaction forces, if any, are known and fixed. This restriction of truss theory proposed originally by Michell was noticed by Prager [3] and Hemp [5,6], who independently derived more general optimality criteria for trusses with different properties of material in tension and compression and supported in any way (including the case of unknown reaction forces). This topic was studied later by Rozvany [7], who has shown that for unequal permissible stresses Michell's optimality criteria are valid only for a highly restricted class of support conditions. Rozvany indicated that Michell's solution of his very first example, involving a point load and a circular support seems to be incorrect for $\sigma_T \neq \sigma_C$ and would need to be revised. The aim of the present paper is to provide an exact analytical solution to this particular problem.

2. Some preliminary analytical and numerical results

The considered problem consists in finding the lightest truss (more precisely Michell structure) transmitting a point load to a circular support, see Fig. 1. Here we assume that: i) the force is applied outside the circle ($r > r_0$) and is oriented circumferentially, ii) the design domain is the exterior of the circle, iii) the maximum allowable tensile and compressive stresses in a structure are σ_T and σ_C, respectively.

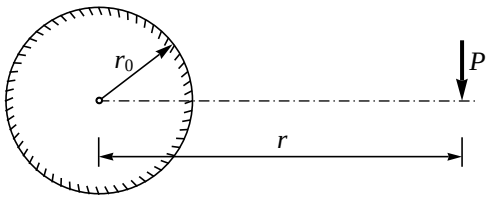

Figure 1. The problem setting.

The solution derived by Michell [1] is shown in Fig. 2a, and leads to the volume

$$V = P\,r\left(\frac{1}{\sigma_T}+\frac{1}{\sigma_C}\right)\log\frac{r}{r_0} \tag{1}$$

The layout consists of logarithmic spirals with a constant angle 45° between spirals and rays (or circles). It cannot satisfy kinematic boundary conditions derived by Hemp [6] for $\sigma_T \neq \sigma_C$. For example, if $\sigma_T = 3\sigma_C$ then the bars should intersect the supporting circle with angles 30° and 60° for tensile and compressive bars, respectively. This condition is satisfied in the improved solution proposed by Dewhurst and Srithongchai [8], see Fig. 2b. Here the layout consists again of logarithmic spirals but with different inclination angles of bars in tension and compression. It is interesting that the volume derived in [9] is identical with formula (1).

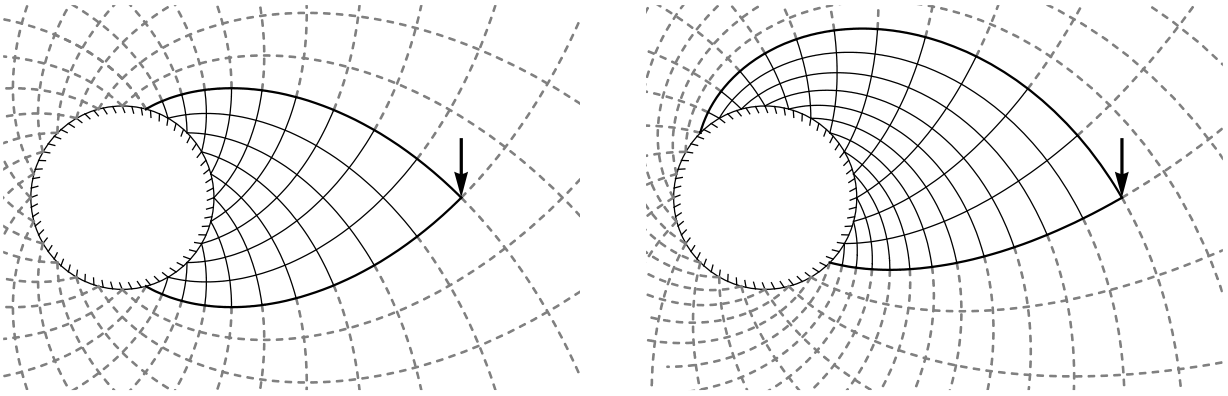

Figure 2. Suboptimal layouts of Michell structure for $\sigma_T/\sigma_C = 3$; solutions provided by a) Michell [1] and b) Dewhurst and Srithongchai [8].

Numerical tests performed with using adaptive ground structure method (see [9]) clearly indicate that both solutions of Fig. 2 are not optimal. A selected numerical solution for $r = 4r_0$, $\sigma_T = 2\sigma_0$, and $\sigma_C = (2/3)\sigma_0$ is presented in Fig. 3. It can be observed that the optimal layout is more complex because the inclination angles of bars are not constant and depend of the radius r. Moreover, the volume of the structure presented in Fig. 3 is smaller than the volume given by the formula (1). For assumed data the volume defined in (1) is equal to $8 \log 4\, V_0 \approx 11.090354\, V_0$, where $V_0 = Pr_0/\sigma_0$, while the volume of numerical solution is equal to $10.8405\, V_0$, which is about 2% smaller. It means that formula (1) is wrong because the discretized truss approximation cannot be better than the exact analytical solution including infinite number of bars.

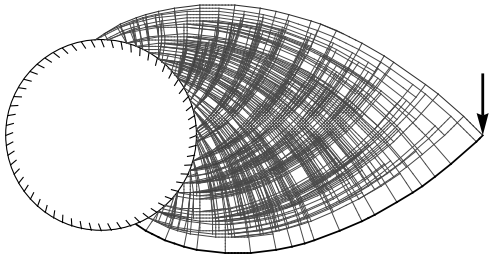

Figure 3. Numerical solution of Michell cantilever for $\sigma_T/\sigma_C = 3$; $r = 4r_0$.

3. Final remarks

The analytical solution of the considered problem is still not known but authors believe they can find and present it during the conference and in a full-length paper.

References

[1] A.G.M. Michell. The limit of economy of material in frame structures. *Philosophical Magazine*, 8(47):589, 1904.
[2] C. Maxwell. On Reciprocal Figures, Frames, and Diagrams of Forces. *Edinb Roy Soc Proc* 7:160, 1870.
[3] W. Prager. A problem of optimal design. *Proc. of the Union of Theoretical and Applied Mechanics*, Warsaw, 1958.
[5] W.S. Hemp. *Theory of the structural design. Report No. 115*. The College of Aeronautics, Cranfield, August 1958.
[6] W.S. Hemp. *Optimum structures*. Clarendon Press, Oxford, 1973.
[7] G.I.N. Rozvany. Some shortcomings in Michell's truss theory. *Structural Optimization*, 12:244, 1996.
[8] P. Dewhurst and S. Srithongchai. An Investigaton of Minimum-Weight Dual-Material Symmetrically Loaded Wheels and Torsion Arms. *ASME. J. Appl. Mech.*, 72(2):196, 2005.
[9] T. Sokół. On the Numerical Approximation of Michell Trusses and the Improved Ground Structure Method. In: Schumacher A., Vietor T., Fiebig S., Bletzinger KU., Maute K. (eds) *Advances in Structural and Multidisciplinary Optimization. WCSMO 2017*. pp. 1411-1417, Springer, 2018.

DETERMINATION OF STOCHASTIC FIELD OF YOUNG MODULUS FROM STRAIN MEASUREMENTS

N. A. Batalha[1], L. C. M. Vieira Jr[1], and S. Szyniszewski[2]

[1]*University of Campinas, Campinas, Brazil*
[2]*University of Surrey, Guildford, England*

nathalia_batalha@hotmail.com, luizvieirajr@gmail.com, s.szyniszewski@gmail.com

1. Introduction

This paper aims to present a method for computing the spatial distribution of stochastic material properties from known values of the strain field. Mechanical properties are usually defined by uniaxial compression and tension, bending, torsion or similar laboratory experiments. In all these cases, the material properties are calculated considering only global loading, measured strain, and, more recently, strain field through Digital Image Correlation (DIC) techniques. The determination of a specimen strain field is important to define mechanical-material properties throughout a non-homogeneous specimen, such as rocks and cellular structures. Neglecting the spatial variability of material properties can lead to inaccurate results when evaluating a solid behaviour and elastic properties, such as Young's modulus and Poisson ratio, which are conventionally assumed homogeneous throughout a sample. The proposed method attempted to compute the actual, spatial distribution of the material properties. The method was shown to converge to an accurate spatial distribution of Young modulus and Poisson ratio rapidly.

2. Digital Image Correlation (DIC) and the proposed algorithm

Digital Image Correlation (DIC) is an optical technique used to measure displacements and strains. The technique can be used to estimate the solid heterogeneity, from a set of measured strain observations in a selected domain. We have shown that an iterative approach to solving the systems of linear equations combined with the DIC measurements and a commercial finite element analysis (FEA) software such as Abaqus [1] can be used to compute the spatial distribution of the material properties within a sample. The approach developed herein leads to the determination of the field of mechanical-material properties – Young's modulus, E, and Poisson ratio, ν – based only on the spatial distribution of strains and the global loading and boundary conditions. The diagram below depicts the iterative process to determine the spatial distributions of E and ν.

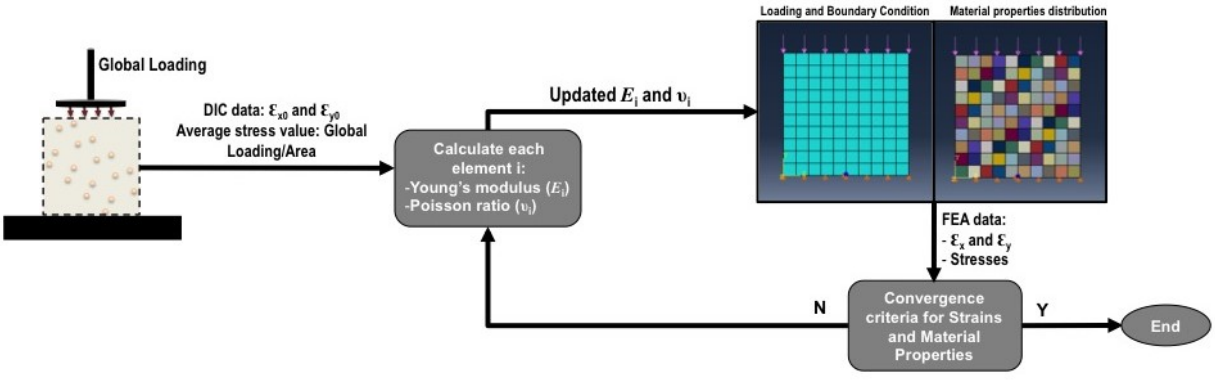

Figure 1: Iterative approach algorithm

In order to verify the proposed algorithm, a virtual experiment was considered. The virtual experiment was a plane stress problem, 10 by 10 elements (50 mm x 50 mm each). Each element had a different value of

Young's modulus and Poisson ratio generated based on normal random distributions, with mean 29269 MPa and 0.203, respectively, and standard deviation of 10% of the mean values. E and ν were not correlated, and were independent variables. Strain field was used as an input into our proposed iterative algorithm to mimic DIC strain measurements of a thin plate loaded parallel to its plane by a uniform loading of 19.5 MPa. The measured strain field data and the information about the global loading, from the virtual experiment, were used to compute the spatial distribution of Young's modulus using the proposed iterative approach. The convergence of Young Modulus and Poisson ratio using the proposed method is shown in Figure 2.

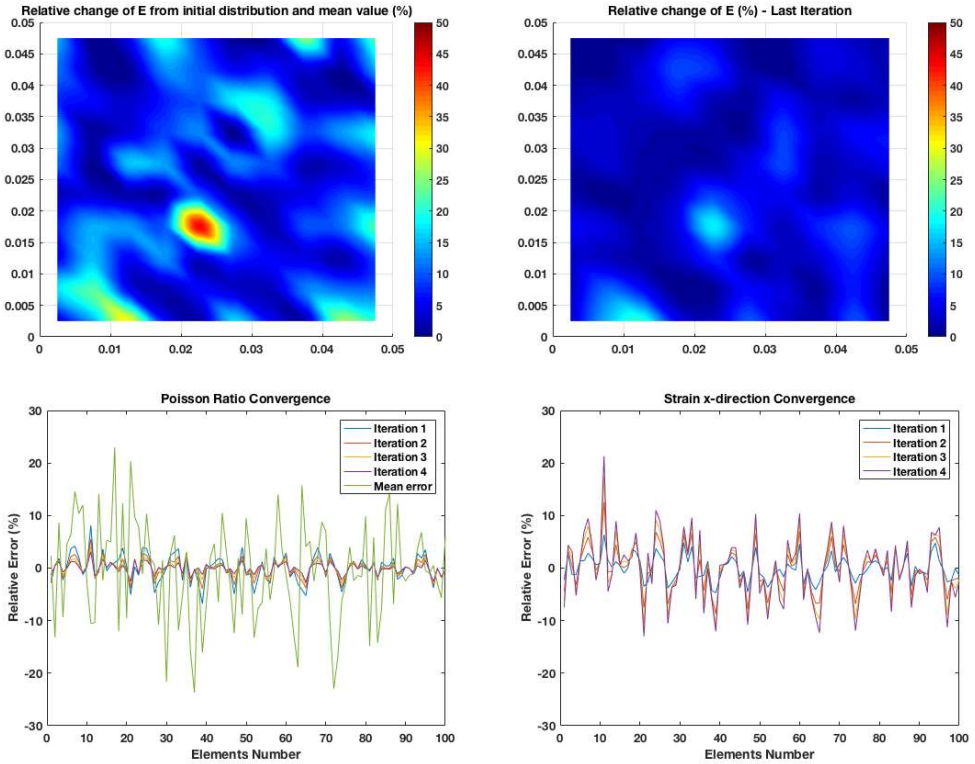

Figure 2: Relative change between iterations has been decreasing, hinging at the convergence of the algorithm as shown for Poisson ratio, axial strains. Colour maps show the convergence of the Young modulus.

5. Conclusion

The algorithm quickly converged to a spatial distribution of Young's modulus. The computed values of Young's modulus were within 1% accuracy when compared to the reference values in the FEA 'virtual experiment'. Poisson ratio and strains also presented fair convergence. The results demonstrated the ability of the model to compute a spatial distribution of material properties from the given strain field and the global loading information only. Convergence criteria need further work such that one can determine if the given problem is going to converge and the solution can be found at the beginning of the computations.

Acknowledgments The authors are indebted to Brazilian Petroleum Corporation - Petrobras, Grant: 5149, for funding this research project. Any opinions, findings, and conclusions or recommendations expressed in this material are those of the authors only and do not necessarily reflect the views of the sponsors, or affiliates.

References

[1] Abaqus 2016 Student Edition.

USING PRIMAL-DUAL INTERIOR POINT METHOD TO DETERMINE LEAST-WEIGHT TRUSS LAYOUTS

J. Gondzio[1] and A.G. Weldeyesus[1]

[1]*School of Mathematics The University of Edinburgh , Edinburgh EH9 3JZ, United Kingdom*

e-mail: J.Gondzio@ed.ac.uk, A.Weldeyesus@ed.ac.uk

1. Abstract

We are concerned with finding the least-weight truss layouts and consider two variations of such problems: a basic one which is cast as a potentially very large scale linear programming problem and a more elaborate one which involves stability constraints and therefore leads to a semidefinite programming problem. We address computational optimization techniques which allow to solve both problems in an efficient way. We demonstrate that a specialized primal-dual interior point methods handle large instances of such problems and, in acceptable time, deliver accurate solutions to practical layout optimization problems.

2. The problems

Let a_i, $i = 1, ..., n$ denote the cross-sectional areas of the member bars and let $m(\approx Nd$, where N is the dimension of the design domain and d is the number of nodes in the design domain) be the number of the non-fixed degrees of freedom, $f_\ell \in \mathcal{R}^m, \ell \in \{1, \ldots, n_L\}$ be a set of external forces applied to the structure, and $q_\ell \in \mathcal{R}^n$ be the associated tensile and compressive forces of the bars. Then, the classical multiple-load case least-weight truss layout optimization problem can be cast as the following linear program

$$
\begin{aligned}
\underset{a,q_\ell}{\text{minimize}} \quad & l^T a \\
\text{subject to} \quad & Bq_\ell = f_\ell, \qquad\qquad \ell = 1, \cdots, n_L \\
& -\sigma^- a \le q_\ell \le \sigma^+ a, \quad \ell = 1, \cdots, n_L \\
& a \ge 0,
\end{aligned}
\tag{1}
$$

where $l \in \mathcal{R}^n$ is a vector of bar lengths, and $\sigma^- > 0$ and $\sigma^+ > 0$ are the material's yield stresses in compression and tension, respectively. For each load case $\ell = 1, \cdots, n_L$, the equation $Bq_\ell = f_\ell$ states the nodal equilibrium with $B \in \mathcal{R}^{m \times n}$ the reduced geometry matrix.

Next, we consider the truss problem with global stability constraints based on linear buckling. This leads to the following semidefinite programming formulation

$$
\begin{aligned}
\underset{a,q}{\text{minimize}} \quad & l^T a \\
\text{subject to} \quad & Bq = f \\
& -\sigma^- a \le q \le \sigma^+ a \\
& K(a) + \tau G(q) \succeq 0 \\
& a \ge 0,
\end{aligned}
\tag{2}
$$

where the stiffness matrix K and the geometry stiffness matrix G are given by

$$
K(a) = \sum_{j=1}^{n} a_j K_j, \text{ with } K_j = \frac{E_j}{l_j} \gamma_j \gamma_j^T \quad \text{and} \quad G(q) = \sum_{j=1}^{n} q_j G_j, \text{ with } G_j = \frac{1}{l_j}(\delta_j \delta_j^T + \eta_i \eta_j^T).
$$

E denotes the Young's modulus and directions $(\delta_j, \gamma_j, \eta_j)$ are mutually orthogonal ($\eta = 0$ for 2D problems).

3. The method and example applications

The challenge when solving both these problems originates from very large number of bars and consequently very large dimensions (number of variables and constraints) in the resulting optimization problems. Therefore to tackle the problems we apply interior point methods [2] which are known to excel on large scale problems. In both cases, we incorporate the *member adding technique* [1] which translates the column generation principle [3] into engineering applications. Namely, we start with a structure constituting a minimum connectivity and gradually append those missing bars which violate dual feasibility constraints. The member adding process terminates when there are no such bars. The procedure allows to keep the size of underlying optimization problems small enough to reach optimal solutions of otherwise untractable design instances. Additionally, we specialize the linear algebra solver inside the interior point algorithm to take into account particular graph structure of the reduced geometry matrix. The linear system is reduced to a significantly smaller one and solved with a preconditioned conjugate gradient method. A specially designed preconditioner exploits the sparsity pattern and particular numerical properties of the reduced geometry matrix. The preconditioner improves the clustering of eigenvalues in the linear system and delivers fast convergence of the conjugate gradients method.

The application of the method to the multiple-load case truss layout optimization problems (1) is described in detail in [4] and its application is discussed in [5]. An extension to problems with global stability constraints based on linear buckling (2) is now being developed.

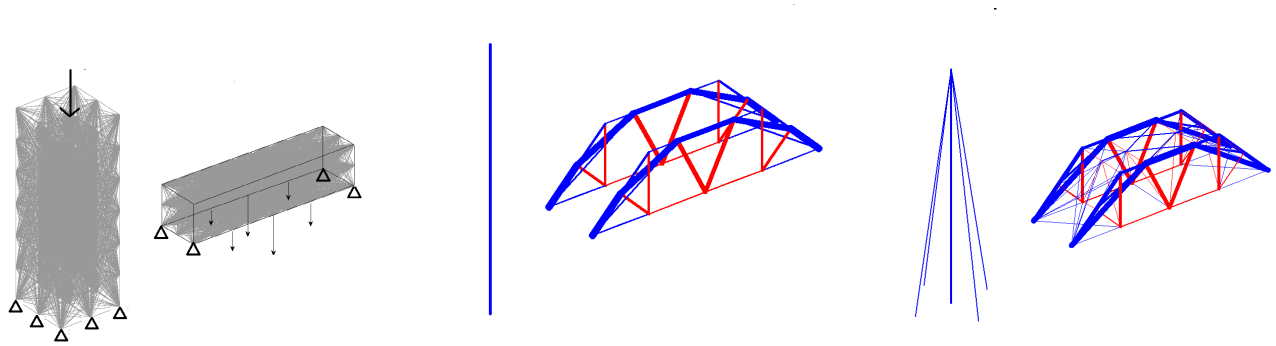

Domains and loads No stability constraints With stability constraints

We illustrate our findings on two small 3D examples presented in a figure above: a rectangular three-dimensional body clamped at its lower surface with a single load applied on top of it and a bridge with loads distributed at two edges on the bottom of it. Formulations (1) without stability constraints produce a solution of a single bar without any bracing for the clamped body and two independent planar trusses for the bridge. When stability constraints (2) are added, an extra bracing for the single bar of the clamped body appears and extra connections between planar trusses of the bridge are present.

Acknowledgments Supported by EPSRC grant EP/N019652/1.

References

[1] Matthew Gilbert and Andrew Tyas. Layout optimization of large-scale pin-jointed frames. *Engineering Computations*, 20(8):1044–1064, 2003.

[2] J. Gondzio. Interior point methods 25 years later. *European Journal of Operational Research*, 218(3):587–601, 2012.

[3] J. Gondzio, P. González-Brevis, and P. Munari. New developments in the primal-dual column generation technique. *European Journal of Operational Research*, 224(1):41–51, 2013.

[4] A. Weldeyesus and J. Gondzio. A specialized primal-dual interior point method for truss layout optimization problems. Technical Report ERGO 17-012, School of Mathematics, University of Edinburgh, November 2017.

[5] J. Ye, P. Shepherd, L. He, M. Gilbert, A. Tyas B. Davison, J. Gondzio, A. G. Weldeyesus, and H. Fairclough. Computational layout design optimization of frame structures. In *Proceedings of the IASS Annual Symposium 2017*.

LAYOUT OPTIMIZATION OF TRUSSES WITH MANUFACTURING CONSTRAINTS

M. Gilbert[1], L. He[1], H. Fairclough[1], and A. Tyas[1]

[1]*Faculty of Engineering, University of Sheffield, Sheffield, UK*

e-mail: m.gilbert@sheffield.ac.uk

1. Introduction

Computational layout optimization procedures, first developed for trusses over half a century ago [1], have been the subject of increasing interest in recent years. In a computational layout optimization problem the design domain is discretized using a grid of nodes which are interconnected with discrete line elements, forming a 'ground structure'. Linear optimization can then be used to identify the subset of elements forming the minimum volume structure required to carry the applied loading, with adaptive solution techniques ensuring solutions can be obtained rapidly [2]. Geometry optimization, which involves adjusting the positions of the nodes using a non-linear optimization step, can subsequently be undertaken to simplify and/or improve on the solution (Figure 1) [3].

However, when accurate solutions are required, fine nodal grids must be employed. This often leads to solutions that are complex in form, largely due to the nature of the optimal solutions being sought. Although rapidly developing additive manufacturing (AM, or '3D printing') techniques can be used to fabricate truss designs which are considerably more complex than can be fabricated using conventional techniques, limitations still exist, requiring manufacturing constraints to be considered in the optimization process. The nature of these constraints depends on the manufacturing process involved.

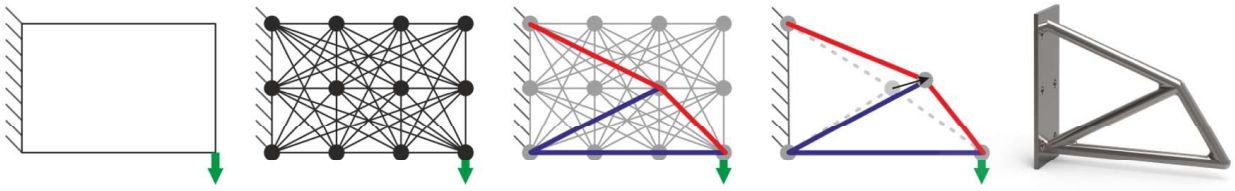

Figure 1: Stages in the truss layout optimisation process: (a) design domain, loads & supports; (b) nodes distributed across the design domain & potential truss element connections; (c) resulting minimum volume truss; (d) positions of nodes modified using geometry optimisation to further improve the result; (e) truss elements replaced with solid elements (e.g. cylinders) and joints added to create a watertight (for AM component design)

2. Manufacturing constraints

Two types of trusses are considered here: (i) trusses forming components to be produced via AM; (ii) trusses used to form large structures, such as those in canopy roofs or building frames.

Considering first the design of AM components: layout optimization is useful when the degree of design freedom is high, as truss-like forms are typically found to be very structurally efficient. Simple rules can be used to automatically transform a line element layout into a 3D continuum ready for AM [4], as indicated in Figure 1(e).

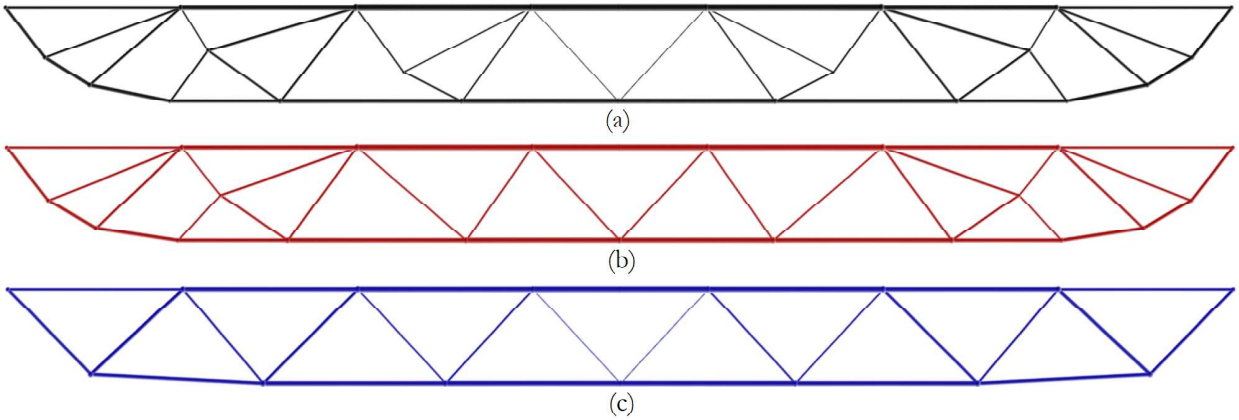

Figure 2: Sample optimized layouts for simply supported transfer truss: (a) obtained using layout and geometry optimization; (b) with MILP constraint on minimum cross-sectional area; (c) with MILP constraint on maximum number of joints.

However, with many AM processes elements inclined at shallow angles to the horizontal are difficult to fabricate without support structures. This issue can be addressed via introduction of hard and soft constraints, as will be described in this contribution.

Considering next the design of trusses used to form large structures: in this case there is a need to minimise the number and complexity of joints, and to e.g. avoid excessively thin structural members. Various means of addressing this will be outlined, from vertex enumeration and Mixed Integer Linear Programming (MILP) formulations for small and medium sized problems, to heuristic methods for larger problems. Figure 2 shows sample MILP solutions for a 21m span, 1.8m high, simply supported transfer truss carrying 6 equally spaced loads from intersecting beams.

3. Conclusions

Computational layout optimization is a powerful technique that can readily be adapted to take account of manufacturing constraints. In this contribution constraints relevant for the design of small-scale AM components and the design of large-scale structural frames are both considered.

Acknowledgements The authors acknowledge the financial support of EPSRC under grant reference EP/N023471/1.

References

[1] W.S. Dorn, R.E. Gomory, and H.J. Greenberg. Automatic design of optimal structures. *J. de Mechanique*, 3(25-52), 1964.

[2] M. Gilbert and A. Tyas. Layout optimisation of large-scale pin-jointed frames. *Engineering Computations*, 20(8):1044–1064, 2003.

[3] L He and M Gilbert. Rationalization of trusses generated via layout optimization. *Structural and Multidisciplinary Optimization*, 52(4):677–694, 2015.

[4] CJ Smith, M Gilbert, I Todd, and F Derguti. Application of layout optimization to the design of additively manufactured metallic components. *Structural and Multidisciplinary Optimization*, 54(5):1297–1313, 2016.

APPROXIMATION OF THE PARALLEL ROBOT WORKING AREA USING THE METHOD OF NONUNIFORM COVERING

Posypkin M.[1], Usov A.[1], Rybak L. [2], and Malyshev D.[2]

[1] Dorodnicyn Computing Centre, FRC CSC RAS, Moscow, Russian Federation
[2]Belgorod State Technological University named after V.G. Shukhov, Belgorod, Russian Federation
e-mail: rl_bgtu@intbel.ru

An important task, solved in the design of robots, is to determine its working area, i.e. set of points, which can reach tool, driven by a robot. The size of the working area is the key characteristic of the robot. The working area itself serves as the basis for laying the trajectory of the working tool. This article discusses two approaches to defining the working area of a robot.This article discusses two approaches to defining the working area of a robot DexTar [1]. One approach is based on the direct use of the system of kinematic equations of the coordinates of the output links along the lengths and angles of rotation of the links. The second approach is to bring a system of equations for links to a quadratic equation and verifying that the discriminant of the quadratic equation must not be less than zero.

Consider a flat RRRRR parallel robot DexTar (fig. 1a, b). The case is considered when the engines are located above the working area plane and not have on its influence.

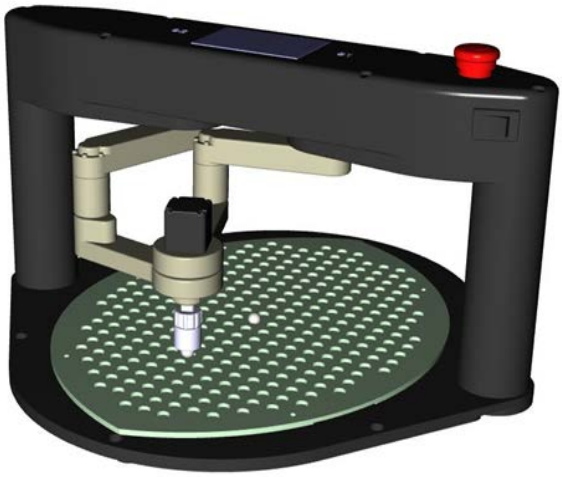

Fig. 1a. Robot RRRRR

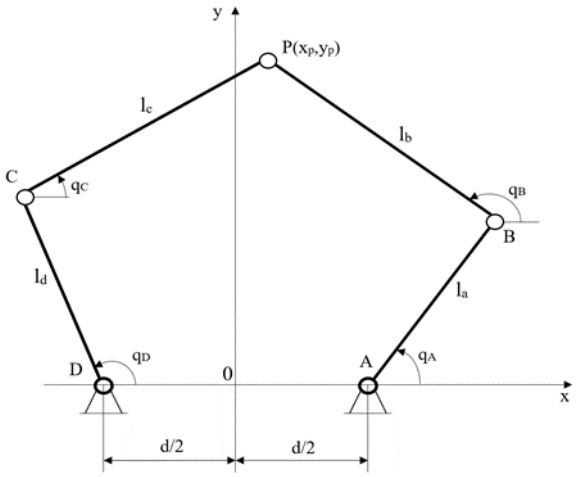

Fig. 1b. Diagram of the robot RRRRR

We write down the equations that determine the coordinate of the point $P(x_{p,}y_p)$:

$$(1)\qquad \begin{cases} x_p = l_b \cdot \cos q_3 + l_a \cdot \cos q_1 + \frac{d}{2}, \\ x_p = -\frac{d}{2} + l_d \cdot \cos q_2 + l_c \cdot \cos q_4, \\ y_p = l_a \cdot \sin q_1 + l_b \cdot \sin q_3, \\ y_p = l_d \cdot \sin q_2 + l_c \cdot \sin q_4. \end{cases}$$

These equations are the equations of connection of the robot under consideration and are formulas for computing the coordinates *x* and *y* according to the given geometric characteristics of the robot and angles of rotation of the links.

Consider two approaches for building a workspace using the method of uneven coatings. The first approach is based on the use of the system of equations (1). The algorithm works with two lists of six-dimensional parallelepipeds $\mathbb{P}$ and $\mathbb{P}_E$. Each of the axes of the six-dimensional space corresponds to changing parameters in the system of equations: coordinates x_p, y_p and angles of rotation of links q_i. The first step of the list $\mathbb{P}$ algorithm consists of only one parallelepiped P, which includes the entire range of angles $-\pi \le q_i \le \pi$ and ranges $-(l_a + l_b + d) \le x_p \le l_a + l_b + d$ and $-(l_a + l_b + d) \le y_p \le l_a + l_b + d$. Then the following actions are performed in the loop: A parallelepiped $P_i, i \in 1, n,$ is extracted from the list $\mathbb{P}$, where *n*

is the number of parallelepipeds which determines the accuracy of the approximation. For him is consistently determined minimum and maximum of the equations functions $q_i, i \in 1,4$ from the following system, obtained from the solutions of the direct kinematics problem:

$$\begin{cases} x_p - l_b \cdot \cos q_3 - l_a \cdot \cos q_1 - \frac{d}{2} = 0, \\ x_p + \frac{d}{2} - l_d \cdot \cos q_2 - l_c \cdot \cos q_4 = 0, \\ y_p - l_a \cdot \sin q_1 - l_b \cdot \sin q_3 = 0, \\ y_p - l_d \cdot \sin q_2 - l_c \cdot \sin q_4 = 0. \end{cases} \quad (2)$$

If at least one of the equations q_i satisfies at least one of the conditions ($\min g_i > 0$) or ($\max g_i < 0$), consequently, the parallelepiped does not contain a combination of variables, which are solutions of the equation and are excluded from further consideration, falling into the list $\mathbb{P}_E$.

The second approach is based on the formula for calculating the discriminant of a quadratic function. In this approach, the algorithm works with three lists of two-dimensional parallelepipeds $\mathbb{P}, \mathbb{P}_I$ and $\mathbb{P}_E$. Each of the axes of a two-dimensional space corresponds to coordinates x_p and y_p. In the first step of the algorithm, the list P also consists of only one parallelepiped P, including ranges $-(l_a + l_b + d) \le x_p \le l_a + l_b + d$ and $-(l_a + l_b + d) \le y_p \le l_a + l_b + d$.

We write the conditions, taking into account that $x'_{P1} = x_p - d/2$ and $x'_{P2} = x_p + d/2$:

$$\begin{cases} (2\left(-\frac{x_p - d/2}{y_p}\right)\left(\frac{(x_p - d/2)^2}{2y_p} + \frac{y_p}{2} + \frac{A^2 - B^2}{2y_p}\right))^2 - 4(1 + \frac{(x_p - d/2)^2}{y_p^2})((\frac{(x_p - d/2)^2}{2y_p} \\ \qquad + \frac{y_p}{2} + \frac{A^2 - B^2}{2y_p})^2 - A^2) >= 0 \\ \left(2\left(-\frac{x_p + d/2}{y_p}\right)\left(\frac{(x_p + d/2)^2}{2y_p} + \frac{y_p}{2} + \frac{A^2 - B^2}{2y_p}\right)\right)^2 - 4(1 + \frac{x_p + d/2)^2}{y_p^2} \\ \qquad + \frac{y_p}{2} + \frac{A^2 - B^2}{2y_p})^2 - A^2) >= 0 \end{cases} \quad (3)$$

From the list $\mathbb{P}$ has extracted a parallelepiped $P_i, i \in 1, n$. For him to consistently define the minimum and maximum of the function g_i of the systems of inequality (3). If for both functions condition ($\min g_i \ge 0$), then it completely satisfies the conditions and is added to the list $\mathbb{P}_I$. If at least one function meets a condition ($\max g_i < 0$), then consequently, parallelepiped does not meet the requirements and is excluded from consideration, falling into the list $\mathbb{P}_E$. In other cases, the parallelepiped is divided into two equal parallelepipeds on a method similar to the first approach - along the rib with the longest length. These parallelepipeds are entered at the end of the list $\mathbb{P}$. The loop is executed *n* times which is specified when the program is started. Determination of the minimum and maximum of functions in both cases was carried out by the method of uniform search by grid search and interval analysis method. The algorithm is implemented in C ++ using the Snowgoose library. The simulation revealed inaccuracies in determining the maximum and minimum for the second approach by the interval analysis method as a result of the occurrence of one variable in the calculations several times. Compensate for this error to ensure the accuracy of the work area ± 0*;* 2 can first divide the work area into 16,777,216 parallelepipeds. In addition, using the method of uniform search for the first approach, it takes a lot of time to compute, considerably exceeding the time of calculation by the method of interval analysis, with a high degree of evaluation of more than 10 times. Based on the foregoing, it is found that the most effective use of the method interval analysis for the first approach, based on the system of equations (1), uniform grid search method for the second approach, based on the system of equations (3).

This work was supported by the Russian Science Foundation, the agreement number 16-19-00148.

[1] Sergiu-Dan Stan Vistrian Maties, Balan Radu. *Optimization of a 2 dof micro parallel robot using genetic algorithms*. Frontiers in Evolutionary Robotics. 2008. P. 465–490.

KEY ISSUES OF DESIGN AND NUMERICAL INVESTIGATIONS OF REGULAR CELLULAR STRUCTURES MANUFACTURED ADDITIVELY OF Ti6Al4V

Paweł Płatek[1], Jacek Janiszewski[1], Paweł Baranowski[2], Jerzy Małachowski[2], Tomasz Czujko[3], Anna Antolak-Dudka[3], Tomasz Durejko[3],

[1]*Faculty of Mechatronics and Aviation, Military University of Technology, Warsaw,*
[2] *Faculty of Mechanical Engineering, Military University of Technology, Warsaw,*
[3]*Faculty of Advanced Technologies and Chemistry, Military University of Technology, Warsaw,*
e-mail: pawel.platek@wat.edu.pl

1. Introduction

Regular cellular structures are a new prospective group of multifunctional materials [1, 2]. Low density, high mechanical strength, as well as thermal, acoustic and vibration insulation make them attractive for many demanding branches of industry [3]. This group of materials is on interest of automotive, aviation, railway, chemical and civil engineering. Moreover, regular cellular structures could be potentially implemented in many military applications, especially in development of passive protective systems. Contemporary, a progress in the area of material science and a growing potential of additive manufacturing methods cause an increasing development of advanced engineering and functional cellular structure materials [4, 5].

The aim of the paper is to present the main issues related to designing and numerical investigation on a deformation process of 2D regular cellular structures produced of Ti6Al4V using LENS (Laser Engineering Net Shaping) additive manufacturing technique.

2. Key issues of numerical simulations of structure deformation process

The main idea of the conducted numerical investigation was directed to define a relationship between structure topology, relative density versus absorption energy. Typical honeycomb and re-entrant honeycomb structure samples made of Ti6Al4V were used during experimental investigations. They were tested under static and dynamic loading boundary conditions. The outcomes of the conducted experimental tests were used to validate a numerical model describing a structure deformation process. Unfortunately, the obtained results of the preliminary computer simulations were in disagreement to the experimental data. Based on the additional attempts to conducted numerical investigations, the authors have found certain key issues which should be included during preparation of numerical models (Fig. 1).

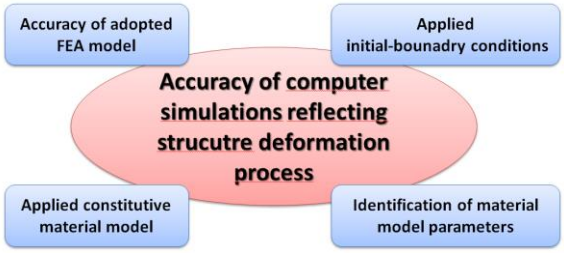

Fig. 1. Main issues influenced accuracy of a computer simulation structure deformation process

Owing to the above mentioned issues it is possible to increase the accuracy of numerical outcomes. The first issue is accuracy of the adopted FE model. Application of LENS system and a contouring procedure in the structure samples manufacturing process require CAD model with a thin wall thickness (0.01 mm). Due to technological limitation of LENS system, the wall thickness of a real structure sample was defined based on a single contour. The authors have noticed a considerable dimensional deviation between the assumed and the real value of the structure wall thickness. Additional measurements (3D scanning, computer tomography) and a quality control procedure must be adopted in order to define the correct value of wall thickness of a structure FE model (Fig. 2).

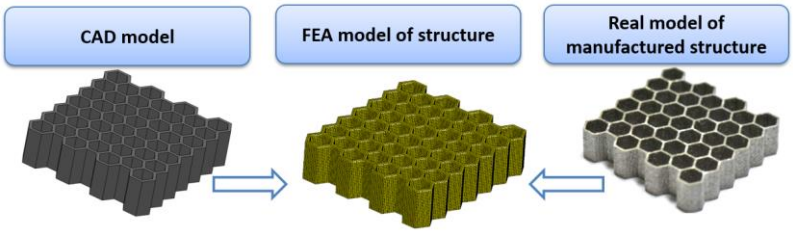

Fig. 2. Scheme of FEA model preparation including dimensional deviation of real structure

The other important issue which should be considered during numerical investigation of the structure deformation process is the applied definition of initial-boundary conditions. The restrain and loading conditions adopted in computer simulations need to be identical as in the experimental tests. Moreover, a contact definition strongly affects the obtained results. A constitutive material model is the further issue necessary to be considered. The authors of the paper have tested a few of the most popular constitutive material models available in LS-DYNA software (PLASTIC_KINEMATIC, PICEWISE LINEAR PLASTICITY, SIMPLIFIED JOHNSON-COOK, JOHNSON-COOK WITH FAILURE CRITERIA). Based on the obtained results it was noticed that material models without failure criteria present different results in comparison to the experimental data. The last point which, in authors' opinion is also crucial is a proper identification of the material model parameters. Structures manufactured additively by LENS indicate sensitivity to technological parameters. The samples used to determine the material model parameters should be produced in the same technological process as the structures. Moreover, they ought to be subjected the same heat treatment operations.

Acknowledgments The research was supported by the National Science Centre under research grant no. 2015/17/B/ST8/00825 and the Interdisciplinary Centre for Mathematical and Computational Modeling (ICM), University of Warsaw, under grant no GB65-19.

3. References

[1] Gibson RF. A review of recent research on mechanics of multifunctional composite materials and structures. Composite Structures..92.793:810. 2010.
[2] Ferreira, A. D. B. L., Nóvoa, P. R. O., Marques, A. T. Multifunctional Material Systems: A state-of-the-art review. *Composite Structures*. 151. 3:35, 2016.
[3] Yang, L., Harrysson, O., West, H., & Cormier, D. Mechanical properties of 3D re-entrant honeycomb auxetic structures realized via additive manufacturing. *International Journal of Solids and Structures*, 69–70. 475:490. 2014.
[4] Gao, W., Zhang, Y., Ramanujan, D., Ramani, K., Chen, Y., Williams, et al. The status, challenges, and future of additive manufacturing in engineering. *Computer-Aided Design*.65:89, 2015.
[5] Kucewicz M, Baranowski P, Małachowski J, Popławski A, Płatek P. Modelling, and characterization of 3D printed cellular structures. Materials and Design. 2018;142.

ON FUNICULARS AND ARCHGRIDS OF MINIMAL WEIGHT

R. Czubacki , G. Dzierżanowski , and T. Lewiński

Institute of Building Engineering, Warsaw University of Technology, Warsaw, Poland

e-mail: t.lewinski@il.pw.edu.pl

1. Introduction

The paper discusses the problem of optimum design of roofs and canopies of minimum weight, stressed up to a given limit σ_c, where σ_c is the permissible stress in compression. The structure is subject to a vertically transmissible load and is designed over a plane domain Ω. The structure is designed as a gridwork composed of two families of arches. Its projection on the plane of Ω forms an orthogonal net which can be identified with the parametric lines $x =$ const or $y =$ const of the Cartesian coordinate system. In general, the domain Ω may be composed of subdomains where the nets are chosen differently. The paper is aimed at an optimal choice of nets to attain the least weight structures. The paper is based on the concept of archgrids proposed by Rozvany and Prager [1].

2. The design algorithm

Assume that the coordinates (x, y) of points of the domain Ω satisfy:

$$x_1(y) \le x \le x_2(y),\ c \le y \le d \quad ; \quad a \le x \le b,\ y_1(x) \le y \le y_2(x) \tag{1}$$

let $l_1(y) = x_2(y) - x_1(y);\ l_2(x) = y_2(x) - y_1(x)$.

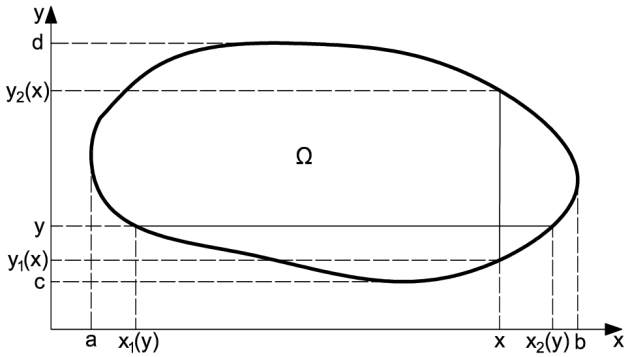

Figure 1: The design domain Ω over which the archgrid is formed.

The elevation function $z = z(x, y)$ of the roof determines the arch-like slopes of the sections:

- in the section $y =$ const the arch curve $z = z(x, y)$ links the pin supports at $A_y = (x_1(y), y)$, $B_y = (x_2(y), y)$, where the horizontal reactions are denoted by $H_x(y)$;

-in the section $x =$ const the arch curve $z = z(x, y)$ links the supports at $C_x = (x, y_1(x))$, $D_x = (x, y_2(x))$ where the horizontal reactions are $H_y(x)$.

The vertical load of intensity $q(x, y)$ is decomposed into two directions: $q_x = \frac{1}{2}q + p$, $q_y = \frac{1}{2}q - p$; $|p| \le \frac{1}{2}q$, where $p = p(x, y)$ is arbitrary at this stage of calculations. We solve the problems of statics of simply supported beams A_yB_y, C_xD_x subject to q_x, q_y, respectively, see [2], [3] . There appear transverse shear forces $\widehat{Q}_x$, $\widehat{Q}_y$ and bending moments $\widehat{M}_x$, $\widehat{M}_y$. The horizontal reactions are expressed by:

$$H_x(y) = \left[\frac{1}{l_1(y)} \int_{x_1(y)}^{x_2(y)} \left(\widehat{Q}_x\right)^2 \mathrm{dx}\right]^{1/2} \tag{2}$$

and $H_y(x)$ is given in a similar way. These forces become the coefficients of the elliptic equation:

$$H_x(y)\frac{\partial^2 z}{\partial x^2} + H_y(x)\frac{\partial^2 z}{\partial y^2} + q = 0 \tag{3}$$

posed in Ω. The elevation function $z = z(x, y)$ solves (3) with Dirichlet condition $z = 0$ along the contour of Ω. The volume of the structure is given by $V = 2V_1/\sigma_c$ with

$$V_1 = \int_a^b l_2(x)H_y(x)\mathrm{dx} + \int_c^d l_1(y)H_x(y)\mathrm{dy} \tag{4}$$

Since $p(x, y)$ was chosen arbitrary it may not be optimal in a sense that it may not lead to the minimal value of V. Let us introduce a new method for which minimum of V will be obtained.

Let us substitute $H_x(y), H_y(x)$ defined by (2) into (4) and denote r.h.s of such equation by $J(\widehat{\mathbf{Q}})$. Note that $J(\widehat{\mathbf{Q}})$ is a positively homogeneous function of degree 1, since $J(\lambda\widehat{\mathbf{Q}})$=$\lambda J(\widehat{\mathbf{Q}})$ if $\lambda \geq 0$. Moreover,

$$J(\mathbf{Q}+\mathbf{P}) \leq J(\mathbf{Q}) + J(\mathbf{P}) \qquad \forall\, \mathbf{P} = (P_x, P_y)\,,\ \mathbf{Q} = (Q_x, Q_y) \tag{5}$$

and, consequently, J satisfies Jensen's inequality and J is convex. The optimization problem reduces to

$$\min\left\{J(\widehat{\mathbf{Q}}) \mid \mathrm{div}\widehat{\mathbf{Q}} + q = 0\right\} \tag{6}$$

If augmented with regularity assumptions, the problem above may be well posed since the functional is convex and the set of admissible $\widehat{\mathbf{Q}}$ is non-empty. Assume that $\widehat{\mathbf{Q}}^*$ = $(\widehat{Q}_x^*, \widehat{Q}_y^*)$ is a minimizer of (6). Then we can compute H_x, H_y by (2) and construct z by solving (3). The function z thus constructed satisfies the mean square slope conditions.

3. Final Remarks

In its original formulation of archgrids of minimal weight proposed by Rozvany and Prager [1] the decomposition of the vertical load q, at each point of the design domain Ω, into two orthogonal directions is arbitrary. At first the load is decomposed and then for such decomposition the archgrid is constructed. In this paper distribution of the load is not fixed. The minimization over statically admissible shear forces $\widehat{Q}_x, \widehat{Q}_y$ is conducted in order to determine the optimal distribution of the load into two families of perpendicular arches. The numerical algorithm which solves such optimization problem is based on the numerical approach proposed by Czarnecki and Lewiński in [4] in order to solve Free Material Design problem.

Acknowledgments The paper has been prepared within the statutory project: Optimum design and computer aided detailing of structures and materials.

References

[1] G.I.N. Rozvany and W. Prager (1979). A new class of structural optimization problems: optimal archgrids, *Comp. Meth. Appl. Mech. Eng.*, **19**, 127-150.

[2] K. Hetmański and T. Lewiński (2007).Shaping the plane frames and arches for avoiding bending (in Polish), In: *Theoretical Foundations of Civil Engineering-XV.* Ed. by W. Szcześniak, pp. 231-246, Polish-Ukrainian-Lithuanian Transactions Oficyna Wydawnicza PW, Warszawa 2007.

[3] G.I.N. Rozvany, H. Nakamura and B.T. Kuhnell (1980). Optimal arch grids: allowance for selfweight, *Comp. Meth. Appl. Mech. Eng.*, **24**, 287-304.

[4] S. Czarnecki and T. Lewiński (2012). A stress-based formulation of the free material design problem with the trace constraint and single loading condition, *Bull. Polish Ac. Sciences. Tech. Sci.*, **60**, 191-204.

Session S15: Nonlinear and adaptive dynamical systems

Organizers: P. Perlikowski (Łódź UT), S. Evangelou (Imperial College, London), Ł. Jankowski (IPPT PAN, Warsaw)

NONLINEAR VIBRATIONS AND GALLOPING OF TRANSMISSION LINES' CONDUCTORS

A. Danilin[1,2], S. Zavoronok[1,2]

[1]*Institute of Applied Mechanics, RAS, 125040, Leningradsky av., 7, Moscow, Russia*
[2]*Moscow Aviation Institute, 125993, Volokolamskoe shosse, 4, Moscow, Russia*

e-mail: andanilin@yandex.ru

Nonlinear problem of spatial aeroelastic vibrations of iced conductors is considered. Mathematical model is formulated on the finite element method, taking into account finite deformations and the nonlinearity of the inertial forces.
Each finite element is associated with a local coordinate system for which the displacements, angles of rotation, the translational and rotational speed are considered strictly.

The tensile strain of the finite element is determined by quadratic approximation in dependence on its transverse displacements.

The displacements and twisting angles of the finite element at its ends as well as the coefficients of the expansions of these functions in sine series with integer number of loops per span are considered as generalized coordinates. The aerodynamic loads acting on the vibrating iced conductor are determined using the conventional quasi-steady formulas for the lift, drag and moment in dependence on the disturbed angle of attack.

The dynamic equations are obtained using d'Alembert-Lagrange principle. It is considered that the generalized coordinates are subjected to the linear relations relative to the generalized velocities. These relations are introduced to account for the interphase spacers and antigalloping dampers.

Variation of the problem functional, for which we seek steady-state value, is transformed by the addition of the constraint equations, multiplied by the undefined Lagrange multipliers. A variational problem for the transformed functional is solved as a free. The stationarity conditions, together with the differential equations of constraints, determine the desired values of generalized coordinates.

Nonlinear dynamic equations are integrated numerically using the integral curve length parameter as a problem argument.

Acknowledgments. The work was carried out within the framework of the state task (ID theme AAAAA 17-117032010144-8) and with partial financial support of RFBR (ID: 17-08-01461, 18-08-00778).

References

[1] Wang L., Lilien J.-L. Overhead Electrical Transmission Line Galloping. *IEEE Trans. On Power Delivery*., 13:3, 1998, p.909-916.

[2] Keutgen R. *Galloping Phenomena. A Finite Element Approach.* Ph.D. Thesis. Collection des publiciations de la Faculté des Sciences. Appliuées de l'Université de Liège. No. 191. 1999, 202 p.

[3] CIGRE. 2007. *State of the art of conductor galloping*. Technical Brochure 322. Task Force B2.11.06. 322. June 2007. Convenor Lilien, Jean-Louis.

[4] Danilin A.N., Shalashilin A.D. Hysteresis Modelling of Mechanical Systems at Nonstationary Vibrations. *Mathematical Problems in Engineering*, 2018, Article ID 7102796, 15 pages.

COMPUTATIONAL METHOD FOR SHAPING THE VIBRO-ISOLATION PROPERTIES OF SEMI-ACTIVE AND ACTIVE SYSTEMS

I. Maciejewski[1] and T. Krzyzynski[1]

[1]*Department of Mechatronics and Applied Mechanics, Faculty of Technology and Education, Koszalin University of Technology, Sniadeckich 2, 75-453 Koszalin, Poland*

e-mail: igor.maciejewski@tu.koszalin.pl, tomasz.krzyzynski@tu.koszalin.pl

1. Introduction

Passive vibration isolators are typically constructed using the inertial and visco-elastic elements. Although the dissipation of a substantial part of the vibration energy is provided at sufficiently high frequencies, the low-frequency vibration are usually amplified due to the resonance effect [1]. As a consequence, it is difficult to achieve an effective vibration reduction in the whole frequency range by means of passive systems [2]. However, the increased vibration damping effectiveness can be obtained by applying semi-active or active systems [3]. In this paper an original methodology of shaping the vibro-isolation properties of semi-active and active systems is presented for the purpose of improving the suspension dynamics and thus effectively reduce the vibrations transmitted to the human body.

2. Formulation of the overall method

The block diagram of the overall method for shaping vibro-isolation properties of semi-active and active systems is presented in Fig. 1. If the vibration exposure in typical working machines is simulated by means of random input signals, then the vibro-isolation properties have to be evaluated using simulation model of the vibration reduction system. Spectral characteristics of the input vibrations are specified in such a way that the generated excitation signals are representative for different types of working machines. Output signals of the simulation model should be used for determination and evaluation of risks from exposure to whole-body vibration. The desired vibro-isolation properties of semi-active or active system can be achieved by an appropriate selection of the controller settings that are calculated with the use of multi-criteria optimisation.

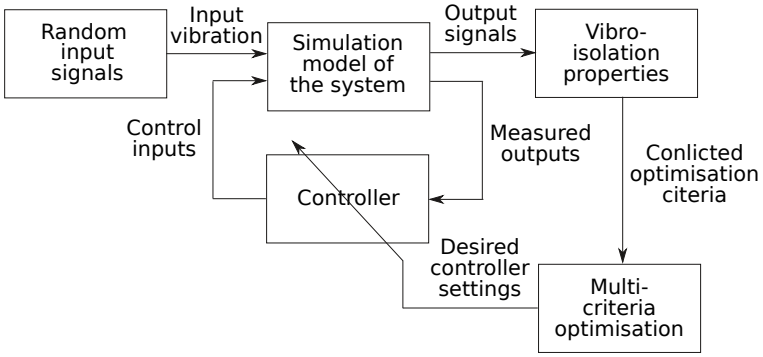

Figure 1: Block diagram of the overall method for shaping vibro-isolation properties

3. Simulation model of the semi-active and active systems

Simulation model of the semi-active of active vibration isolator should allow to predict the system performance under various input vibrations. If a model is a precise representation of the system dynamics then an analysis of the control strategy can be successfully conducted by using numerical simulation. The system modelling equations and control algorithm have to be combined into one model in order to simulate the closed-loop system

behavior for different values of the controller settings. The block diagram representing a general simulation model of the semi-active or active vibration reduction system is presented in Fig. 2.

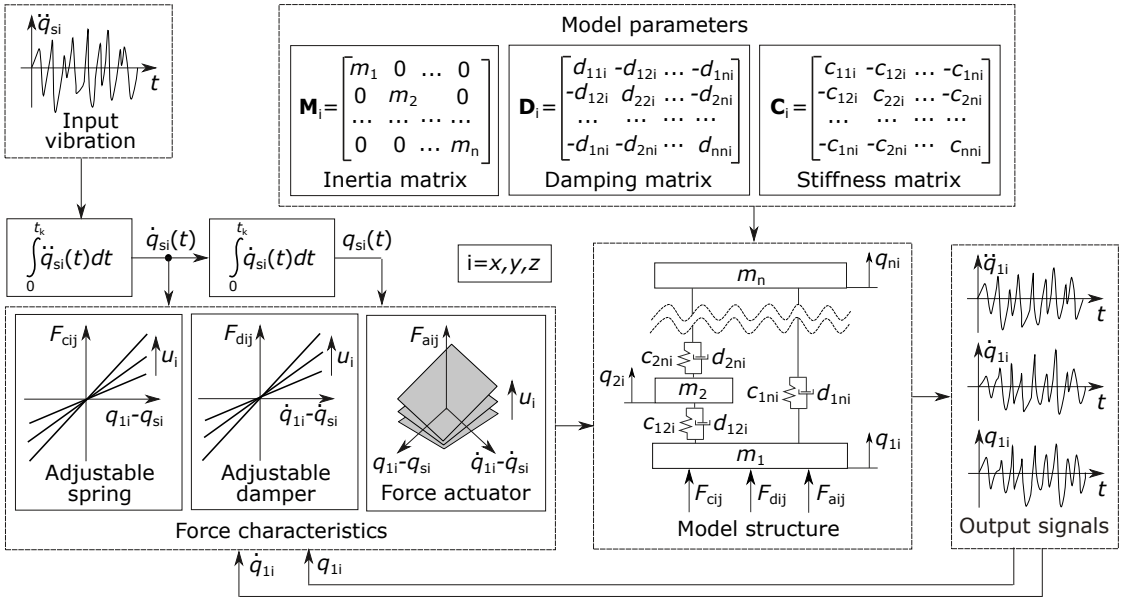

Figure 2: Block diagram for numerical simulation of the dynamic behaviour of vibration reduction systems

Since human response to vibration shall be investigated for different spectral classes of the excitation signals therefore the input vibration block (Fig. 2) is used to generate the random acceleration $\ddot{q}_{\mathrm{si}}(t)$ for different directions of the vibration exposure ($\mathrm{i} = x, y, z$). Then a double integration with respect to time t is applied in order to obtain the velocity $\dot{q}_{\mathrm{si}}(t)$ and displacement $q_{\mathrm{si}}(t)$ as input signals to the model. The applied force of adjustable spring F_{cij}, adjustable damper F_{dij} or force actuator F_{aij} is employed to compensate harmful vibrations affecting the human body. Their non-linear characteristics are described as functions of the input signal u_{i} and the system relative displacement $q_{1\mathrm{i}} - q_{\mathrm{si}}$ and/or relative velocity $\dot{q}_{1\mathrm{i}} - \dot{q}_{\mathrm{si}}$. The force characteristics must be evaluated for the components used in a specific type of the semi-active or active suspension system.

4. Conclusions

In this paper a generalised methodology of shaping the vibro-isolation properties of semi-active and active vibration reduction systems is discussed. Selecting their dynamic characteristics can be successfully employed for different excitation signals that are representative for vibrations affecting the machine operators at work. A general model of the vibration isolation system is elaborated therefore its dynamic characteristics can be selected using the multi-criteria optimisation in respect to reliable vibro-isolation criteria. Using the proposed optimisation procedure it is possible to adjust the vibro-isolation properties of semi-active and active vibration reduction systems by changing the controller settings.

Acknowledgments The paper is a part of the research project "Methods and procedures of selecting vibro-isolation properties of vibration reduction systems" founded by the National Science Center of Poland under the contract No. UMO-2013/11/B/ST8/03881.

References

[1] Maciejewski I., Meyer L., Krzyzynski T., *Modelling and multi-criteria optimisation of passive seat suspension vibro-isolating properties*, Journal of Sound and Vibration 324 (2009), pp. 520-538.

[2] Ibrahim R.A., *Recent advances in nonlinear passive vibration isolators*, Journal of Sound and Vibration 314 (2008), pp. 371-452.

[3] Yan B. , Brennan M.J., Elliott S.J., Ferguson N.S., *Active vibration isolation of a system with a distributed parameter isolator using absolute velocity feedback control*, Journal of Sound and Vibration 329(2010), pp. 1601-1614

EFFECTS OF NONLINEARITIES IN INERTER ON THE PERFORMANCE OF TUNED MASS DAMPER

P. Brzeski[1] and P. Perlikowski[2]

[1]*Division of Dynamics, Lodz University of Technology, Stefanowskiego1/15, 90-924 Lodz, Poland*

e-mail: przemyslaw.perlikowski@p.lodz.pl

1. Introduction

Tuned mass dampers (TMD) are widely used for damping of unwanted oscillations of mechanical and structural systems. In this paper we investigate the effects of adding an inerter to the TMD taking into account the influence of inerter nonlinearites of different types. Inerter has been introduced in early 2000s by Smith [1] and it is a two terminal element which has the property that the force generated at its ends is proportional to the relative acceleration of its terminals.

2. Model of the system

Model consists of the base oscillator that can move in vertical direction and the TMD connected to its top (see Fig. 1). The base oscillator has the mass M and is connected with the support via the spring of stiffness K and a viscous damper described by the damping coefficient C. It is excited by a harmonic force of amplitude F and frequency ω. The TMD is used to mitigate the vibrations of the base structure. The TMD has the mass m and is connected with the main body via four links: spring of stiffness k, viscous damper with damping coefficient c, element that corresponds to dry friction described by parameter d_f and the last one is the inerter. We use the model of inerter with play that is described by four parameters: inertance I, stiffness k_i, viscous damping coefficient c_i and dimension of the backlash gap ε.

The motion of the system is described by four generalized coordinates two of which are used to describe the dynamics of inerter with play. The vertical displacement of the base oscillator is given by coordinate x. To describe the position of the TMD we use coordinate y. The model of play uses coordinates r and u, where r describes the distance between the two nodes of inerter while u defines the actual gap in the system.

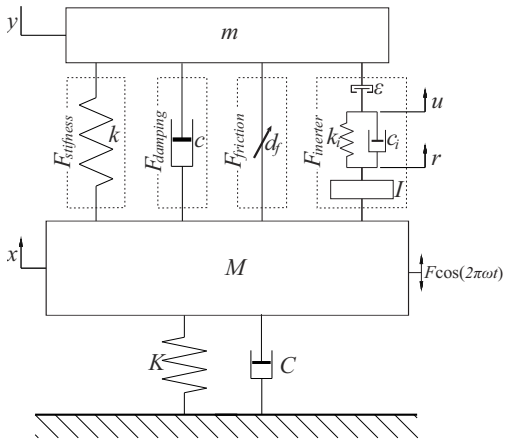

Figure 1: The model of the considered system and notation of system's parameters.

Using Lagrange equations of the second type we obtain the system's equations of motion:

$$M\ddot{x} + Kx + C\dot{x} + F_{stiffness} + F_{damping} + F_{friction} + F_{inerter} = F\cos(\omega t), \tag{1}$$

$$m\ddot{y} - F_{stiffness} - F_{damping} - F_{friction} - F_{inerter} = 0, \tag{2}$$

3. Full model of TMD with inerter

We compare the effects introduced by each element and investigate how they changes in the presence of the others. Results are presented in Figure 2 are calculated for $I_{ratio} = 0.1$). In Figure 2 (a) we show 5 FRC curves calculated for the following conditions: (1) $c = 0\,[\frac{Ns}{m}]$, $d_f = 0\,[N]$, $\varepsilon = 0\,[m]$, $k_i \to \infty\,[\frac{N}{m}]$, $c_i = 0\,[\frac{Ns}{m}]$ - (black line marked as "1"). (2) $c = 0\,[\frac{Ns}{m}]$, $d_f = 0\,[N]$, $\varepsilon = 0.0001\,[m]$, $k_i = 2 \cdot 10^7\,[\frac{N}{m}]$, $c_i = 0.01\,[\frac{Ns}{m}]$ - (yellow line marked as "2" (overlapped by the black line)). (3) $c = 10\,[\frac{Ns}{m}]$, $d_f = 0\,[N]$, $\varepsilon = 0\,[m]$, $k_i \to \infty\,[\frac{N}{m}]$, $c_i = 0\,[\frac{Ns}{m}]$ - (blue line marked as "3"). (4) $c = 0\,[\frac{Ns}{m}]$, $d_f = 10\,[N]$, $\varepsilon = 0\,[m]$, $k_i \to \infty\,[\frac{N}{m}]$, $c_i = 0\,[\frac{Ns}{m}]$ - (red line marked as 4) (5) $c = 10\,[\frac{Ns}{m}]$, $d_f = 10\,[N]$, $\varepsilon = 0.0001\,[m]$, $k_i = 2 \cdot 10^7\,[\frac{N}{m}]$, $c_i = 0.01\,[\frac{Ns}{m}]$ (green line marked as 5).

Comparing the FRCs from Figure 2 (a) we see that the effects caused by viscous damping and dry friction are qualitatively the same while the play itself does not cause macroscopic changes to the shape of FRC. In literature authors often use simple model of TMD with viscous damper because it is simple and mathematically convenient. Our results prove that such model can also well simulate the behaviour of TMDs with inerters but only when viscous damping coefficient and dry friction parameters are relatively small (see previous sections). Practically this means that simplified model is sufficient to model the device without additional damper (TMD which consists only of mass connected with the main body via spring and inerter.

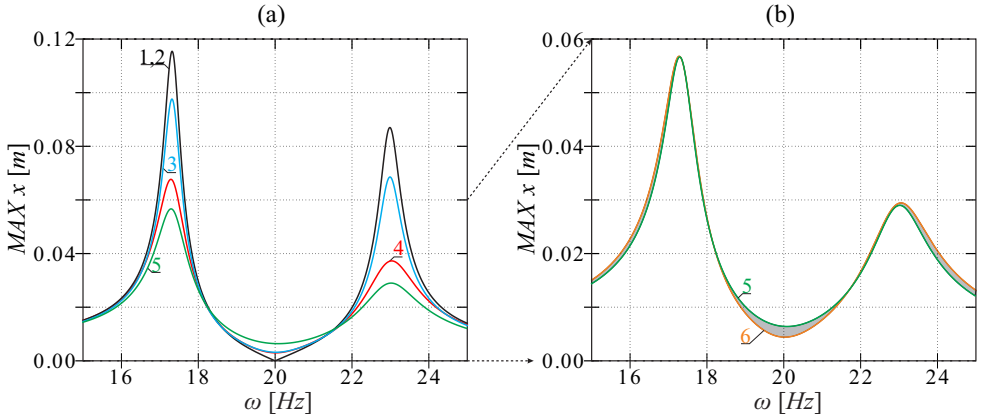

Figure 2: Comparison between the effects caused by four investigated elements. In subplots (a) we present FRC calculated for models with each investigated factor and the full model that contains all of them. In subplots (b) we magnify and compare the results obtained for the full model (green curves) and the simplified model (orange curves).

4. Conclusions

We analyzed the full model of TMD that contains all four factors. For the investigation we pick parameter values that corresponds to TMD with typical inerter. So we assume relatively small energy dissipation via viscous damping and dry friction, and reference play gap. After comparing the results we can say that the effects introduced by viscous damping and dry friction are qualitatively comparable while play has not macroscopic influence on the system's dynamics. For details see full paper [2]

Acknowledgements

This work has been supported by National Science Centre, Poland - project No. 2015/17/B/ST8/03325.

References

[1] M.C. Smith. Synthesis of mechanical networks, the inerter. *Automatic Control, IEEE Transactions on*, 47(10), 1648–1662 (2002).

[2] P. Brzeski, P. Perlikowski. Effects of play and inerter nonlinearities on the performance of tuned mass damper. *Nonlinear Dynamics 88 (2), 1027-1041 (2017).*

SEMI-ACTIVE CONTROL OF MECHANICAL ENERGY TRANSFER BETWEEN VIBRATIONAL MODES

M. Ostrowski, B. Błachowski, Ł. Jankowski, D. Pisarski

Institute of Fundamental Technological Research of the Polish Academy of Sciences, Pawińskiego 5B, 02-106 Warsaw, Poland
e-mail: bblach@ippt.pan.pl

1. Introduction

The vibration attenuation problem has been solved using many different methods, some of which involve the use of advanced control algorithms [1]. The topic of harvesting the energy of structural vibrations is less explored [2]. For that reason, this contribution studies the problem of conversion of mechanical energy of vibrations. The paper presents a method of semi-active control, which is applied to dynamically transfer the vibration energy into a selected vibration mode. The target mode is selected in such a way that the amount of energy that can be recovered during the vibration process is maximized. In other words, switching between two modes is not intended to dissipate the energy of vibrations, but rather to maximize the energy-harvesting potential of the overall system. The concept will be illustrated using an example of a simple frame structure, in which semi-actively controlled lockable joints modify the modal properties of the structure [3, 4].

2. Mathematical formulation

We consider a linear discretized undamped system with the following equation of motion:

(1) $$\mathbf{M}\ddot{\mathbf{q}} + \mathbf{K}\mathbf{q} = \mathbf{0} \quad ,$$

where $\mathbf{M}$ is the mass matrix, $\mathbf{K}$ is the stiffness matrix, and $\mathbf{q}$ denotes the vector of configuration coordinates (displacements and rotations of nodes). In the above equation all nodes are unlocked. When a selected node is locked then the corresponding degree of freedom (Dof) becomes constrained and effectively lost, and the matrices $\mathbf{M}$ and $\mathbf{K}$ change. Instead of adjusting the number of Dofs, we introduce a damping matrix $\mathbf{C}(\mathbf{u})$ with very large damping factors. Here $\mathbf{u}$ is the vector of the control signals (one signal for each lockable node). The damping factors and the zeros are distributed in the matrix in such a way that there is a negligible difference of angular velocities of beam ends connected at the locked node (as in a rigid connection). Each node can be controlled independently of other nodes. The state equation derived from equation (1), including the controlled damping matrix, is as follows:

(2) $$\dot{\mathbf{x}} = \begin{bmatrix} \mathbf{0} & \mathbf{I} \\ -\mathbf{M}^{-1}\mathbf{K} & -\mathbf{M}^{-1}\mathbf{C}(\mathbf{u}) \end{bmatrix} \mathbf{x} \quad ,$$

where $\mathbf{x}$ is the vector of state variables, $\mathbf{I}$ denotes the identity matrix.
Our control aim is to stabilize the system (2) while transferring the energy to selected modes. For that purpose, we define the energy of the *p*-th mode corresponding to its amplitude

(3) $$V_p = a_p^2 + \frac{1}{\omega_p^2}\dot{a}_p^2 \quad .$$

Here a_p is the amplitude of the *p*-th mode and ω_p is the *p*-th natural frequency. The total energy V of the system is given by $\sum_p V_p$. In order to transfer the system's energy to a selected mode *p*, we aim to increase the corresponding energy V_p. The proposed control maximizes the derivative of V_p

(4) $$\mathbf{u}^* = \arg\max_{\mathbf{u}\in U} \dot{V}_p \quad .$$

The existence of the solution to (4) is ensured by the compactness of the set of admissible controls $U = [0, u_{max}]^m$ (m – number of control inputs). Note that for $u = 0$ the node is unlocked and for u_{max} it is jammed. In addition to (4) we require $\dot{V} \leq 0$ which for (2) guarantees stability.

3. Numerical example

As an example we present a simple frame structure with two lockable nodes and five degrees of freedom. There are five modes of vibration when all nodes are unlocked. The example initial condition is that the third, fourth and fifth modal amplitudes have respectively the values of {1, -1, 1}, while the initial amplitudes of the first and the second modes are equal to zero. The first mode is chosen for maximization of its participation in vibrations. This is shown in figure 1a). The results of numerical simulations are presented in figures 1b) and c) which correspond to, respectively, the modal amplitudes and the energies. The mode shapes are not normalized with respect to the mass matrix **M**.

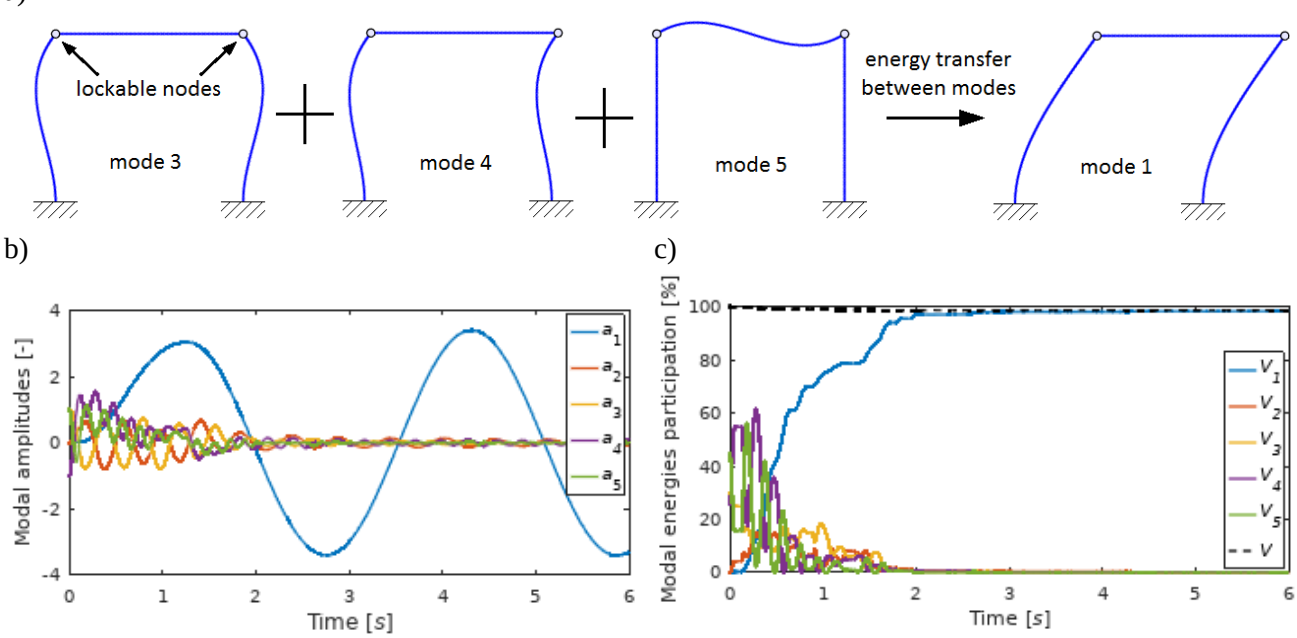

Fig. 1 Numerical example: a) visualization of initial modes and modes chosen for maximization, b) Time history of modal amplitudes, c) Time history of mode mechanical energies

4. Conclusion and further research

It is possible to dynamically switch between vibrational modes while keeping the system non-asymptotically stable. Non asymptotic stability is desired here, because it results in conservation of energy for an energy-harvester. The presented approach can be applied to structures excited by a short force impulse. After transferring the energy to a mode suitable for the installed energy-harvester, the mechanical energy can be extracted. In further research we will analyse more complex structures, use a model of the energy harvester, and test other control algorithms.

Acknowledgments The authors acknowledge the support of the National Science Centre, Poland, granted through the project Re-Con (DEC-2017/25/B/ST8/01800).

References

[1] A. Dhanda and G.-F. Franklin. *Optimal Control Formulations of Vibration Reduction Problems*. IEEE Transactions on Automatic Control, 55(2), February 2010.

[2] C. Wei and X. Jing. *A comprehensive review on vibration energy harvesting: Modelling and realization*. Renewable and Sustainable Energy Reviews, 74:1-18, July 2017.

[3] B. Popławski, G. Mikułowski, A. Mróz and Ł. Jankowski. *Decentralized semi-active damping of free structural vibrations by means of structural nodes with an on/off ability to transmit moments*. Mechanical Systems and Signal Processing, 100: 926–939, 2018.

[4] D. Pisarski, *Decentralized stabilization of semi-active vibrating structures*, Mechanical Systems and Signal Processing, 100: 694-705, 2018.

SEMI-ACTIVE MITIGATION OF EXTERNALLY INDUCED VIBRATIONS

B. Poplawski, G. Mikułowski, R. Wiszowaty, and Ł. Jankowski

Institute of Fundamental Technological Research, Polish Academy of Sciences, Warsaw, Poland

e-mail: bpop@ippt.pan.pl

1. Introduction

Almost all man-made structures are exposed to vibration. Regardless of whether these are large structures such as bridges or skyscrapers, machines with rotating parts such as engine shafts, frame structures or vehicle suspensions, excessive vibrations can be very harmful. From the perspective of their effects they can be seen as very spectacular (e.g., a collapse of a bridge) or not worth much attention (e.g., a failure of a motor shaft), but in each of these cases, the effect is the destruction of the structure and a negative impact on the users of these devices.

Several approaches can be used by the designers to overcome this phenomenon. The most basic, but often sufficient, method is to introduce changes in the mechanical parameters of the system affecting the severity of vibration in operational conditions, i.e., its mass or stiffness. If such design changes cannot be realized, or if vibration problems are detected after the system is manufactured, or if a vibration suppression system must be used for other reasons, one of the three basic types of such systems can be used [1].

The primary choice is usually a *passive vibration damping* system. These are relatively simple systems whose mode of operation is the passive dissipation of the energy of structural vibrations. Their design and simple functionality ensures that they are highly reliable, but their simplicity is reflected, unfortunately, in their limited efficiency. Their flexibility may be also considered as insufficient: once configured, even a small change in the specific operating conditions can result in a drastic loss of performance. This indicates a rather narrow spectrum (frequency range) of correct system operation.

Active systems constitute a much more effective damping approach. In this case, vibration attenuation is achieved not by means of dampers, but by actuators integrated into the structure. This approach allows to achieve very good results of vibration mitigation over a wide range of excitation frequencies. High efficiency, however, is burdened with a much higher degree of complexity of such a system as compared to the passive systems. In order to develop such a system, it is necessary to design the controller and install actuators that implement the control algorithm. During the vibration suppression, the actuators themselves require a large energy supply, which can be troublesome in some cases.

The compromise between these damping systems are *semi-active systems*, where the actuators are used to affect structural properties instead of exerting large external forces. In terms of reliability, semi-active systems can be compared with passive systems, while in terms of the efficiency of damping with active ones. They also do not require large amounts of electric energy to implement the control algorithm. Despite being a relatively new research area with less established design and development procedures, their advantages seem to be large enough to attract a growing number of scientists and engineers.

This contribution presents a strategy for semi-active reduction of forced vibrations in frame structures. Analogous damping technique proved to be effective in damping of free vibrations [2, 5]. The control strategy is based on the Prestress Accumulation–Release (PAR) concept and uses specially designed semi-active rotational nodes [4]. Successive decentralization of the damping system demonstrates that apart from the global mechanism of the energy dissipation based on the PAR, it is also possible to disperse it locally to individual beams that are separate elements of the damping system.

2. Control method

The equation of motion of the structure in which the proposed semi-active vibration damping system has been applied is as follows:

$$\mathbf{M}\ddot{\mathbf{x}}(t) + \left(\mathbf{C} + \sum\nolimits_i \gamma_i(t)\mathbf{C_i}\right)\dot{\mathbf{x}}(t) + \mathbf{K}\mathbf{x}(t) = \mathbf{f}(t) \tag{1}$$

where $\mathbf{M}$, $\mathbf{C}$ and $\mathbf{K}$ refer to the mass, damping and stiffness matrices, and $\gamma_i(t) \geq 0$ is the control function. The matrix $\mathbf{C_i}$ couples overlapping rotational degrees of freedom (Dofs) belonging to the ith node. It is used to effectively block the relative rotations of the involved rotational Dofs, which amounts to imposing a structural constraint in the form of $\dot{\theta}_1 = \dot{\theta}_2$. The vector $\mathbf{f}$ represents the excitation force, which is harmonic here.

Utilization of the Pontryagin minimum principle [3] with the control objective function formulated in the form of an integral of the global structural energy

$$J = \frac{1}{2}\int_{T_s}^{T_f} \left(\dot{\mathbf{x}}^{\mathrm{T}}\mathbf{M}\dot{\mathbf{x}} + \mathbf{x}^{\mathrm{T}}\mathbf{K}\mathbf{x}\right) \mathrm{d}t \tag{2}$$

results in the optimal control strategy of a bang-bang type: the control function switches between $\gamma_i = 0$ and $\gamma_i = \gamma_i^{\max}$. The proposed decentralized control algorithm incorporates this approach, and the switching points are selected quasi-heuristically to correspond to the maxima of the local energy.

3. Numerical example

The investigated structure is a 2D frame with the dimensions shown in Figure 1. Two semi-active nodes are used to implement the control strategy.

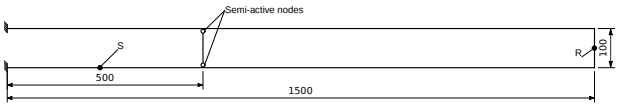

Figure 1: Considered 2D frame model equipped with two semi-active nodes

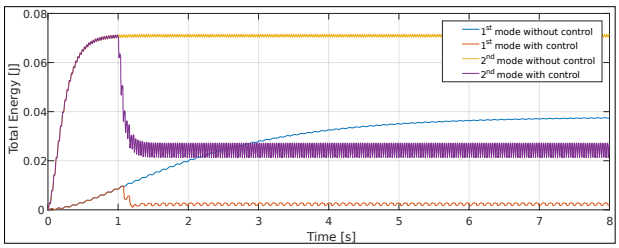

Figure 2: Comparison of the total energy of the structure: controlled and uncontrolled case

Figure 2 shows the comparison of the total structural energy of the considered frame for the excitation applied in point R with the frequency of the first and the second eigenfrequencies of the structure. The results confirm the excellent efficiency of the proposed control algorithm in dissipating the structural energy. The energy reduction in the first vibration mode is more than ten times, while in the second mode it is almost threefold.

Acknowledgments The authors acknowledge the support of the National Science Centre, Poland, granted through the project Re-Con (DEC-2017/25/B/ST8/01800).

References

[1] B. Basu, O.S. Bursi *et al.* A European Association for the Control of Structures joint perspective. Recent studies in civil structural control across Europe. *Structural Control and Health Monitoring*, 21(12):1414–1436, 2014.

[2] B.Poplawski, G.Mikułowski, A.Mróz, and Ł.Jankowski. Decentralized semi-active damping of free structural vibrations by means of structural nodes with an on/off ability to transmit moments. *Mech Syst Sig Process*, 100, 2018.

[3] D.E. Kirk. Optimal Control Theory: An Introduction (republication). Dover Publications, 2004.

[4] A. Mroz, A. Orlowska, and J. Holnicki-Szulc. Semi-active damping of vibrations. Prestress Accumulation-Release strategy development. *Shock and Vibration*, 17(2):123–136, 2010.

[5] B. Poplawski, G. Mikułowski, A. Mróz, K. Sekuła, and Ł. Jankowski. A decentralized strategy of structural reconfiguration in mitigation of vibrations. In *Procedia Engineering*, volume 199, 2017.

DYNAMICAL BEHAVIOUR OF NONLINEAR STRUCTURES UNDER VARYING LOAD

B. Dyniewicz and C.I. Bajer

Institute of Fundamental Technological Research, Polish Academy of Sciences, Warsaw, Poland

e-mail: bdynie@ippt.pan.pl, cbajer@ippt.pan.pl

1. Introduction

The problem is demonstrated on the example of a system that includes the so-called 'Gao beam,' which is modelled by a nonlinear beam equation. This study is motivated, in part, by the previous works on railway systems, see, e.g., [1, 2]. First, the track was subjected to a set of massless forces applied with more or less complex oscillators. Moreover, the dynamic properties and responses were not influenced by the additional inertia of the wheel-sets, which are invariably present in transportation applications. Indeed, their mass is about 750 kg per wheel and, thus, cannot be neglected. Second, the axial forces in rails were too simple. Moreover, the temperature of the rails can vary by more than 40 °C during a day and more than 70 °C during a year. Such variations in the temperature cause significant changes in the stresses and the mathematical models for the structures must take these processes into account. Here, we address the first item, while the issue of inclusion of thermal effects will be studies in the future. Such problems are of fundamental interest in railway transportation Models for a Gao beam were derived and simulated in [3], see also the references therein. They were investigated mathematically and computationally in [4].

2. Formulation and solution

We describe a model for the motion of a point-mass on a rail that is assumed to be a Gao beam, which has been constructed in [5]

$$\rho w_{tt} + k w_{xxxx} + \gamma w_{txxxx} + (\overline{\nu} p - a w_x^2) w_{xx} = \rho f, \tag{1}$$

where here and below, the subscripts x and t denote partial derivatives, f is the density of applied distributed force (per unit mass), ρ is the material density (mass per unit cross-sectional area), $k = 2h^3 E_Y/3(1-\tilde{\nu}^2)$, $\overline{\nu} = (1+\tilde{\nu})$, and $a = 3h\, E_Y$; $\tilde{\nu}$ and E_Y are the Poisson ratio and the Young modulus, respectively. Also, for mathematical reasons, we added a viscosity term γw_{txxxx}, with viscosity coefficient $\gamma > 0$, assumed to be small. We consider the moving mass m and the external force $f = f(x,t)$ subjecting a beam, with the traction $p = p(t)$ and the point load $P = P(t)$. The mass position is $\xi = \xi(t)$ the velocity $v = v(t)$, and the initial data w_0 and v_0; find the displacement field $w = w(x,t)$ for $x \in (0,1)$ and $t \in [0,T]$, such that

$$\begin{gathered} \rho w_{tt} + \delta(x-\xi) m w_{tt}(\xi,t) + k w_{xxxx} + \gamma w_{txxxx} - (a w_x^2 - \overline{\nu} p) w_{xx} = \rho f + \delta(x-\xi) P, \\ w(0,t) = w_x(0,t) = 0, \quad w(L,t) = w_x(L,t) = 0, \quad w(x,0) = w_0(x), \quad w_t(x,0) = v_0(x). \end{gathered} \tag{2}$$

3. Results

Let us compare the load trajectory in the case of increasing p factor (Figure 1). First we assume low values of p to keep the structure in the bending range with a relatively low contribution of string vibration. We expect gradual change of traces during the first passage and we look for a significant change in successive passages. The first diagram (Figure 1a) depicts curves for p upto 1.0, while the second one exhibit traces for p upto 100.0. We notice that for low ranges of p the bending is the main phenomenon that occurs. For higher ranges the wave phenomenon that appear in a string or in an axially loaded bar dominates. At moderate p the process starts to elevate the follower point. This fact is visualized better in Figure 2. The second passage gives more

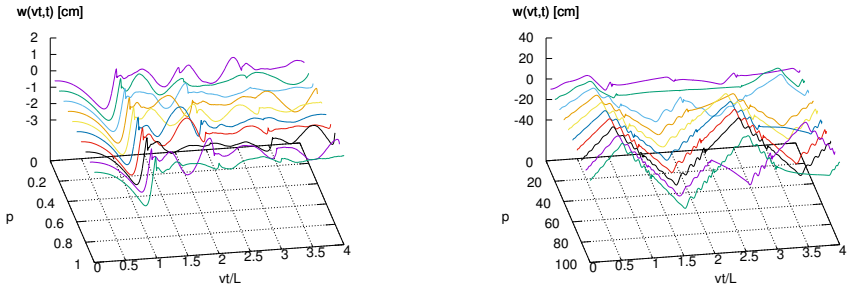

Figure 1: Load trajectories for various ranges of p.

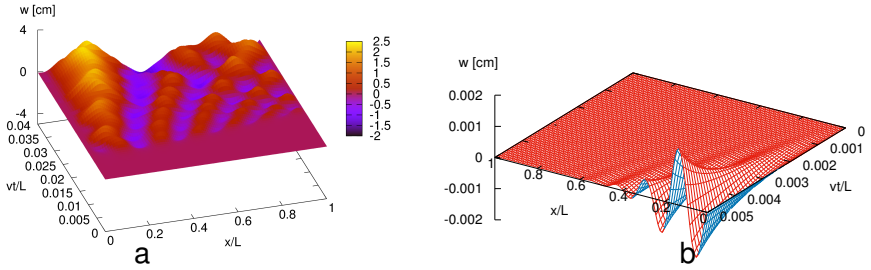

Figure 2: Displacement w in time (a) and displacement $w(x)$ at first steps of the process (b) (p=85).

flat surface in the diagram. Figure 2a shows the first stage of the passage through the span by the first load. The wave propagation from the loaded point is visible. At the beginning the beam is waved according to spatial parabolic terms of the differential equation. Wave effects are visible as well, especially as a reflection of waves from the end x=L. In such a case presence of the nonlinear Gao term strongly influences the response. The next Figure 2b is more contributing for better understanding the process. It shows the very early stage of the passage through the span by the first load. The lifted part of the beam at x/L=0.45 and 0.55 is noticeable. Wave crests have higher amplitudes than troughs. Moreover, careful sight at the beam axis at vt/L=0.0005 allows to notice small positive deflection of the segment 0.6<x/L<1.

4. Conclusions

The numerical simulations indicate that choosing the rail to be described by the Gao beam may be a better description if one is interested in the rail oscillations. First, for beams with a low bending stiffness the Gao beam is much more rigid than the Bernoulli-Euler beam. Second, a soft Bernoulli-Euler beam is characteristic of lower eigenfrequency than a rigid one. In the case of the Gao beam this relation is reversed. Third, higher external load increases the Gao beam features and strongly influences the frequency of the dynamic response.

Acknowledgments The research has been supported within the project 2017/26/E/ST8/00532 funded by the National Science Centre, which is gratefully acknowledged by the author.

References

[1] T. Dahlberg. Track issues. In Simon Iwnicki, editor, *Handbook of Railway Vehicle Dynamics*, pages 143–180. CRC Press, 2006.

[2] C. I. Bajer and R. Bogacz. Propagation of perturbances generated in classic track, and track with Y-type sleepers. *Arch. Appl. Mech.*, 74:754–761, 2005.

[3] D.Y. Gao. Finite deformation beam models and triality theory in dynamical post-buckling analysis. *Intl. J. Non-Linear Mechanics*, 35:103–131, 2000.

[4] K.T. Andrews, M.F. M'Bengue, and M. Shillor. Vibrations of a nonlinear dynamic beam between two stops. *Discrete and Continuous Dynamical System (DCDS-B)*, 12(1):23–38, 2009.

[5] C.I. Bajer, B. Dyniewicz, and M. Shillor. A gao beam subjected to a moving inertial point load. *Mathematics and Mechanics of Solids*, 23(3):461–472, 2018. DOI: 10.1177/1081286517718229.

INVESTIGATIONS ON SHOCK-ABSORBERS FOR SMALL AIRDROP SYSTEMS

R. Faraj[1], C. Graczykowski[1], J. Holnicki-Szulc[1]

[1]*Institute of Fundamental Technological Research Polish Academy of Sciences, Warsaw, Poland.*
e-mail: rfaraj@ippt.pan.pl

1. Introduction

The problem of efficient and robust impact mitigation is still an attractive field of research and industrial development. Numerous examples of shock-absorbers can be found, e.g. landing gears, suspensions of vehicles, bumpers of trains or cars, road barriers, etc. A passive solution is still the most appropriate for some applications from the economic point of view and the requirement of high system reliability. Nevertheless, a current significant progress in the field of sensors and smart materials allows to design more effective semi-active and active devices. Practical implementation of smart absorbers is becoming more and more common. The paper is aimed at discussion of various impact absorption techniques developed within a research project "Innovative systems for safe airdrop DROPs". The work is based on a number of innovative devices elaborated in order to ensure extremely high performance of impact mitigation during touchdown of small cargo dropped from the aircraft.

2. In search of shock-absorber for small airdrop system

The comparison of shock-absorbers based on completely different operation principles can be very difficult and some measureable quality indices have to be defined, e.g. specific energy being the ratio of dissipated energy to the absorber mass [1]. Objective evaluation of the best solution for implementation in the small airdrop system, first requires optimization of the considered absorbers. Mathematical formulation of the corresponding optimal impact mitigation problem takes the form:

$$\begin{cases} \max\limits_{\mathbf{u}(t)} (F_{abs}(t) - F_{ext}(t)) = \min \\ \int_d \mathbf{F_{abs}} d\mathbf{s} = E_{init} + \int_d \mathbf{F_{ext}} d\mathbf{s} \end{cases} \tag{1}$$

where $\mathbf{u}$ is the control vector (control variables depends on the device type), $\mathbf{F_{abs}}$ is the absorber reaction force, $\mathbf{F_{ext}}$ is the external force acting on the excited system, d is the absorber stroke and E_{init} is the initial kinetic energy of the object amortized by the shock-absorber.

Within conducted research various adaptation strategies have been elaborated and two different types of systems have been distinguished:

- adaptable absorbers, which are automatically adjusted to predicted loading conditions at the beginning of impact absorption and they are not controlled during remaining part of the process, e.g. Safe-Pack [2], pneumatic absorber Soft-Drop [3],
- adaptive absorbers, which requires on-line control but instead they are capable of re-adaptation during entire impact absorption process, e.g. pneumatic absorber with piezo-electric valve [4], hydraulic absorber with magneto-rheological fluid [5] or smart inertial shock-absorber [6].

Developed and analysed systems are shown in Fig. 1. One of the considered concepts is the Safe-Pack device equipped with a number of gears driven by racks during cargo touchdown. Decentralization of the damping forces and lengthening the displacement on which energy is dissipated increases the energy dissipation capabilities of the system. Similar concept of linear move conversion into rotation was applied in the so-called

Spin-Man shock-absorber. Nevertheless, in contrast to the first device in which the desired inertia of rotating parts should be minimal, the inertia of the Spin-Man's components should be relatively high. The device can be easily adapted by the control of energy conversion from translation to rotation and activation or deactivation of damping interface between rotating components of the absorber. Unfortunately, technological issues cause that the device is hard to be miniaturized. The promising alternative is the Soft-Drop pneumatic shock-absorber, which ensures efficient and reliable impact absorption by single reconfiguration of the release valve. The concept of Soft-Drop was proved by both the numerical simulations and the experimental tests [3].

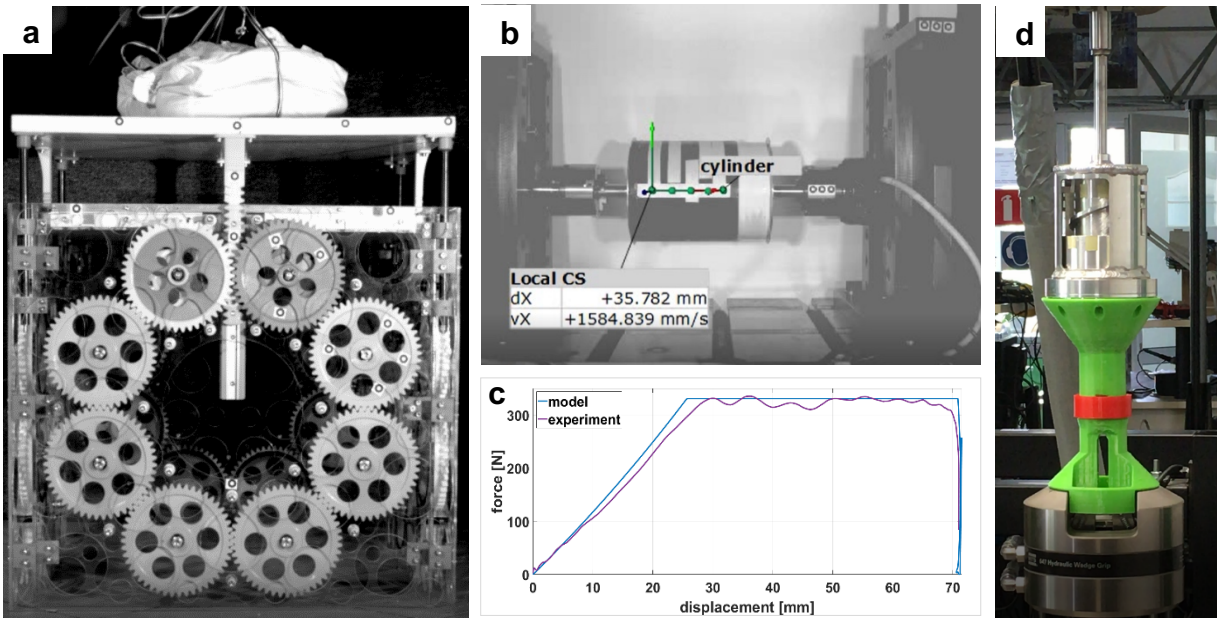

Figure 1. a) fast-camera image taken during drop test of Safe-Pack demonstrator, b) fast-camera image taken laboratory test of Soft-Drop shock-absorber, c) comparison of model and demonstrator response of the Soft-Drop system, d) demonstrator of the Spin-Man inertial shock-absorber tested at the MTS stand.

3. Conclusions

The conducted research was devoted to elaboration of efficient shock-absorbers for small airdrop systems. Simultaneously, control methods and adaptation techniques were developed in order to ensure optimal impact absorption in case of different excitations and unknown loading conditions. Numerical models were used for design of demonstrators and comparisons of experimental measurements with modelling results were conducted. The main challenges during shock-absorbers design and possible applications are indicated.

Acknowledgments
The scientific work was funded from the budget for education in the years 2015–2019 as a research project within the program under the name 'Diamond Grant'.

References

[1] C. Graczykowski, G. Mikułowski, J. Holnicki-Szulc, Adaptive impact absorption – a benchmark and an example absorber, *5th ECCOMAS Thematic Conference on Smart Structures and Materials*, Saarbrucken (DE), pp.663-668, 2011.
[2] J. Holnicki-Szulc, R. Faraj, A. Mróz, Shocks absorbing packaging, *Polish Patent PAT.225398*, granted 21.10.2016.
[3] R. Faraj, C. Graczykowski, Adaptable pneumatic shock absorber, *Journal of Vibration and Control*, in review.
[4] G. Mikułowski, R. Wiszowaty, Pneumatic Adaptive Absorber: Mathematical Modelling with Experimental Verification, *Math. Probl. Eng*, Vol. 2016, 7074206-1-14, 2016.
[5] Q.H. Nguyen, S.B. Choi, Optimal design of MR shock absorber and application to vehicle suspension, *Smart Mater. and Struct.*, Vol. 18, 035012, 2009.
[6] R. Faraj, J. Holnicki-Szulc, L. Knap, J. Seńko, Adaptive inertial shock-absorber, *Smart Mater. Struct.*, 25(3), 035031, 2016.

DEVELOPMENT OF ADAPTIVE AIRBAGS FOR EMERGENCY LANDING OF SMALL UAV

T. Kowalski[1], R. Faraj[2], C. Graczykowski[2], K. Hinc[2], G. Mikułowski[2], P. Pawłowski[2] and Z. Wołejsza[2]

[1]*Adaptronica Sp. z o. o., Łomianki, Poland*
[2]*Institute of Fundamental Technological Research Polish Academy of Sciences, Warsaw, Poland.*
e-mail: biuro@adaptronica.pl

1. Introduction

Currently, drones are used in a variety of applications and they are often equipped with expensive, specialized devices including e.g. high-resolution cameras, radars and LIDARs. Failures of avionic system, its sensors or engines as well as damages of other components of the UAV occur, what is the motivation for development of emergency landing system. In the case of possible crash with the ground, in addition to reducing drone destruction the emergency system should limit damages of objects on the ground or injuries of people around. One of the possible solutions is the use of parachute rescue systems. Unfortunately, such systems require relatively long time for deployment and increase of drag force which decelerates the falling UAV. As a result, the minimal altitude ensuring successful protection of drone after its failure reaches at least 10-15 m. In order to provide reliable solution, which will be efficient in case of low altitude failures, we propose the adaptive airbag system, further called Ad-Bag.

2. System development

The design of Ad-Bag system is a compromise between performance of the adaptive airbag, reliability of entire emergency system and costs of its production. In consequence, both adaptive as well as adaptable solutions are considered. The example of adaptive option can be real-time control of internal pressure with the use of precise gas release. Similarly, the application of optimal gas control for impact absorption was previously considered in reference to general concept of adaptive inflatable structures [1]. The main challenge in practical implementation of such solution is very short time of the impact absorption process and the corresponding requirement for very fast sensing and actuation. The adaptable alternative can be realized by activation of the proper release vents selected from the set of vents prepared for different crash scenarios. Selection of proper release vents should be based on actually predicted impact conditions. Similar technique was successfully implemented in the pneumatic shock-absorber designed for airdrop system [2].
In order to obtain high reliability, the Ad-Bag system is independent of main avionic system of drone and it includes two main subsystems:

- the electronic control system which is equipped with dedicated microprocessor system and a number of sensors used for detection of drone failure, prediction of impact condition and detection of the airbag contact with the ground,
- the mechanical executive system composed of airbag inflation subsystem and release vents activation system, which is responsible for proper adaptation of the system to actual impact conditions.

As a part of the project devoted to elaboration of the Ad-Bag system we have developed a dedicated airbag design method which includes application of simplified analytical models for optimization purposes, fully nonlinear dynamic FEM models solved by explicit solver LS-Dyna for precise airbag design (Fig. 1b) and procedures of experimental testing. The conducted simulations were validated and tuned during experimental drop tests. For this purpose, a drop test stand with the maximal drop height of 20 m was prepared. The stand

is composed of a vertical guiding system based on steel wires, remote control responsible for release of suspended object, and a base plate with piezoelectric force transducers for measurement of total dynamic vertical loads during the impact. The data acquisition system is based on LMS SCADAS platform and Vision Research Phantom v611 high speed camera. Video frame from exemplary drop test is shown in Fig. 1a.

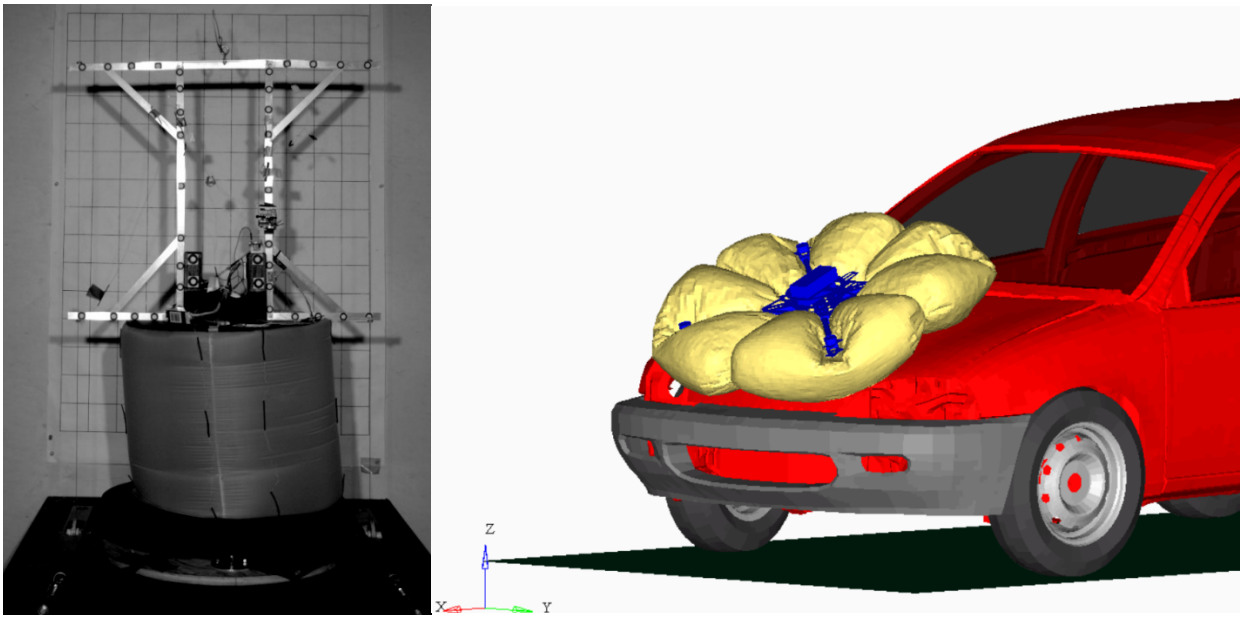

Figure 1. a) fast-camera image taken during drop test of exemplary airbag design, b) visualization of the numerical simulation used for airbag design with the use of Geo Metro detailed FE model.

3. Conclusions

As a response to limited application capabilities of emergency parachute systems the adaptive airbag system has been proposed in order to ensure safe emergency landing in case of low altitude failures of drones. The R&D activities have included design of the airbag, simulation of its operation, as well as experimental testing of the Ad-Bag emergency landing system.

Acknowledgments

The article was prepared with the support of the project: "Adaptive airbags for unmanned aerial vehicles emergency landing (ADBAG)" co-financed from the European Regional Development Fund wihin the Operational Programme Smart Growth 2014-2020, Measure 1.2. Sectoral R&D Programs. Contract No .: POIR.01.02.00-00-0083 / 16. The period of the project implementation: 01.01.2017-30.06.2019.

FE Model of the car: This model has been developed by The National Crash Analysis Center (NCAC) of The George Washington University under a contract with the FHWA and NHTSA of the US DOT. Authors would like to thank Mr. Jan Całka for his help with manufacturing of system components and preparation of testing stand.

References

[1] C. Graczykowski, J. Holnicki-Szulc, Crashworthiness of inflatable thin-walled structures for impact absorption, *Math. Probl. Eng.*, Vol. 2015, 830471, 2015.

[2] R. Faraj, C. Graczykowski, Adaptable pneumatic shock absorber, *Journal of Vibration and Control*, in review.

IDENTIFICATION OF A LOAD MOVING ON A PLATE USING THE ℓ_1 NORM MINIMIZATION

M. Gawlicki[a)] and Ł. Jankowski[b)]

Institute of Fundamental Technological Research, Polish Academy of Sciences
Pawińskiego 5B, 02-106 Warsaw, Poland
[a)]*mgawlic@ippt.pan.pl*
[b)]*ljank@ippt.pan.pl*

1. Introduction

There are two fundamental inverse problems in the field of structural health monitoring (SHM): identification of damages and identification of loads. Effectiveness of the related computational methods is crucial for maintaining integrity of the monitored structures. This contribution considers identification of unknown loads based on measurements of structural response. It is a relatively extensively researched problem: reviews of techniques used for off-line load identification can be found in [1,2], while techniques for online identification are reviewed in [3].

If the aim is to identify independent force histories in each of the excited degrees of freedom (Dofs), the uniqueness of the solution can be possible only if there are at least as many sensors (equations) as the excited Dofs (unknowns). Such a requirement can be satisfied in case of a few unknown stationary loads, but it becomes problematic if the unknown load is (even single but) moving in an unknown way across the structure. In such a case, a very large number of Dofs can be potentially excited and a limited number of sensors are available to measure the response. As a result, the naïve direct formulation of the inverse problem is underdetermined, and the solution is not unique.

This contribution is devoted to indirect identification of a single moving load that excites a 2D structure (plate). To attain the uniqueness, the solution space needs to be significantly constrained. However, instead of assuming a known trajectory of the load and identifying its value, the aim is to identify the trajectory only. Such a problem is important, e.g., in traffic monitoring and control [4,5]. Effectively, the approach is based on the assumption of sparsity of the excitation, which seems to suit the practice: even if the location of the load is unknown, at each time instant only a single (or a limited number of) Dofs is excited. Such an approach follows the methodology of compressed sensing [6], which includes such SHM-related applications as identification of impact load position [7]. The assumption of sparsity is usually expressed as a requirement of a bounded l1 norm of the solution [8].

The approach has already been verified numerically and experimentally using a flexible 1D structure (a beam) excited with a moving mass [9]. The cases considered there included single or multiple passes of the mass across the beam. The assumption of sparsity allowed the space-time trajectory of the load to be identified. Here, the goal is to test the approach in a much more complex problem that involves a 2D structure, e.g., a plate, subjected to a single moving load. In the fully dynamic case the task is computationally very demanding, thus we focus here on the quasi-static case. This abstract describes briefly the method and the experimental stand. Detailed results will be presented during the conference.

2. Load identification based on sparsity

The considered plate structure is assumed to respond in the linear range. In the quasi-static analysis, the response is decoupled with respect to time and can be expressed as

$$\mathbf{e}_t = \mathbf{B}\mathbf{x}_t, \tag{1}$$

where t indexes the time instants, the vector $\mathbf{e}_t$ collects the structural response measured in time t, $\mathbf{B}$ is the compliance matrix, and $\mathbf{x}_t$ collects the excitations in time t in all Dofs exposed to the moving load. If the length of the unknown excitation vector $\mathbf{x}_t$ is larger than the length of the measurement vector $\mathbf{e}_t$, there are

infinitely many solutions. To obtain a unique solution, an additional knowledge about the load has to be used to constrain the solution space. Here, we use the assumption of sparsity, which is expressed through the l_1 norm as the task of minimization of the following weighted objective function:

(2) $$F_t(\mathbf{x}) = \|\mathbf{e}_t - \mathbf{B}\mathbf{x}\|^2 + \alpha\|\mathbf{x}\|_1,$$

subject to the natural nonnegativity constraints $\mathbf{x} \geq \mathbf{0}$. Notice that (1) can be minimized independently for each time instant t. Alternatively, any desired time-dependent load evolution pattern can be promoted by performing a single minimization of a weighted sum of $\sum_t F_t(\mathbf{x_t})$ and a term that penalizes the deviations from the pattern.

3. Experimental stand

The experimental stand is designed for identification of a mass moving in a 2D space. The main part is a steel plate (0,0005m x 0.97m x 1m), see Fig. 1. One edge is fully fixed and there are 6 supporting points which restrain the plate in the vertical direction and which are realized by a set screw with a tapered end. The plate is loaded in a vertical direction by the mass of a line follower robot. The robot follows the black thick line painted on the top of the plate. The blue thin lines generate a grid that defines the load identification points. There are 81 equally spaced points. In order to measure the plate response, 7 strain gauges are installed on the bottom side of the plate. The directions and pattern is shown in the draft. There are 6 single strain gauges and one 2-element rosette with 90º stacked grid layout. Detailed results will be presented during the conference.

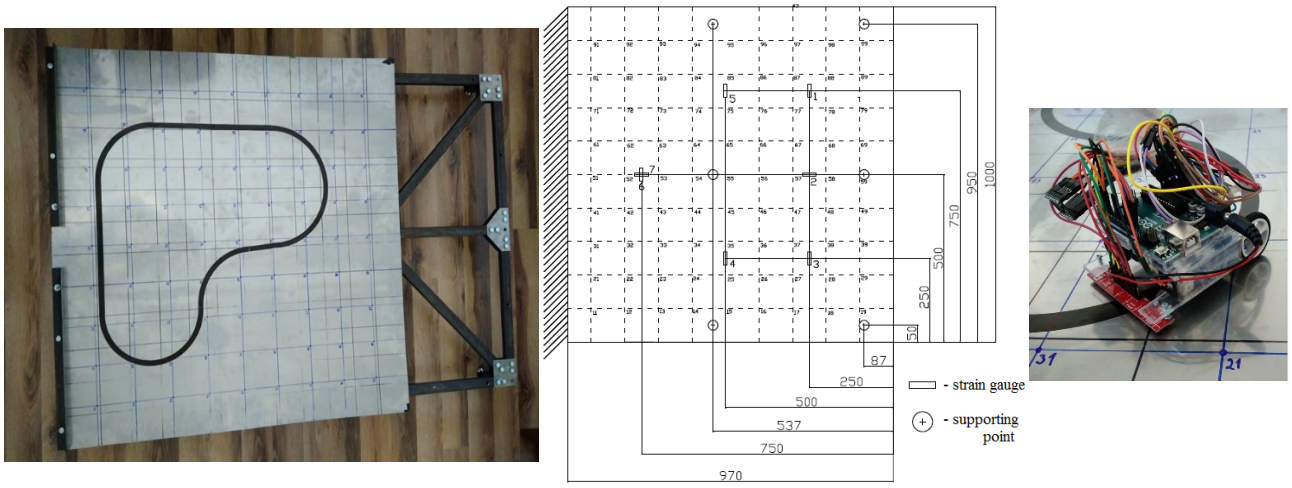

Figure 1: Photographs and a draft of the experimental stand.

Acknowledgments Support of the National Science Centre, Poland, granted through the project Ad-DAMP (DEC-2014/15/B/ST8/04363), is gratefully acknowledged.

References

[1] H. Inoue, J.J. Harrigan and S.R. Reid. Review of inverse analysis for indirect measurement of impact force. *Appl. Mech. Rev.*, 54(6): 503–524, 2001.
[2] T. Uhl. The inverse identification problem and its technical application. *Arch. Appl. Mech.*, 77(5):325–337, 2007.
[3] M. Klinkov and C.P. Fritzen. An updated comparison of the force reconstruction methods, *Key Eng. Mat.*, 347:461–466, 2007.
[4] X.Q. Zhu and S.S. Law. Recent developments in inverse problems of vehicle–bridge interaction dynamics, *J. Civil Struct. Health Monit.*, 6:107–128, 2016.
[5] Y. Yu, C.S. Cai and L. Deng. State-of-the-art review on bridge weigh-in-motion technology. *Adv. Struct. Eng.* 19:1514, 2016.
[6] D. Donoho. Compressed sensing, *IEEE T. Inform. Theory* 52:1289-1302, 2006.
[7] B. Qiao, X. Zhang, J. Gao and X. Chen. Impact-force sparse reconstruction from highly incomplete and inaccurate measurements. *J. Sound Vib.* 376: 72–94, 2016.
[8] R. Tibshirani. Regression shrinkage and selection via the lasso: a retrospective. *J. R. Stat. Soc. Ser. B-Stat. Methodol.* 73:273–282, 2011.
[9] M. Gawlicki and Ł. Jankowski. Identification of moving loads using l1 norm minimization, *API Conf. Proc.*, 1922:100007, 2018.

DETERMINATION OF PROPERTIES OF A TUNED MASS ABSORBERS USING A BASIN STABILITY METHOD

K. Mnich, P. Brzeski, M. Lazarek, P. Perlikowski

Division of Dynamics, Lodz University of Technology, 90-924 Lodz, Poland

e-mail: konrad.mnich@edu.p.lodz.pl

1. Introduction

In mechanical and structural systems the knowledge of all possible solutions is crucial for safety and reliability. Due to nonlinearity, for the same set of parameters more then one stable solution may exist [**?**, **?**]. This phenomenon is called multistability. As an example, we point out the classical tuned mass absorber [**?**]. This device is well known and widely used to absorb energy and mitigate unwanted vibrations. However, the best damping ability is achieved in the neighbourhood of the multistability zone [**?**, **?**]. Among all coexisting solutions only one mitigates oscillations effectively. Practically, in nonlinear dynamical systems with more then one degree of freedom it is impossible to find all existing solutions without huge effort and using classical methods of analytical and numerical investigation. That is why we use here a new method basing on the idea of basin stability [**?**].

2. Model of systems and resuluts

The example is a system with a Duffing oscillator and a tuned mass absorber presented in Figure **??**. The main body consists of mass M fixed to the ground with nonlinear spring (hardening characteristic $k_1 + k_2y^2$) and a viscous damper (damping coefficient c_1). The main mass is forced externally by a harmonic excitation with amplitude F and frequency ω. The absorber is modelled as a mathematical pendulum with length l and mass m. A small viscous damping is present in the pivot of the pendulum.

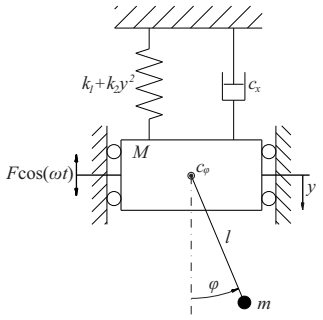

Figure 1: The model of the first considered system.

The dimensionless equations are as follows:

$$\begin{aligned} &\ddot{x} - ab\ddot{\gamma}\sin\gamma - ab\dot{\gamma}^2\cos\gamma + x + \alpha x^3 + d_1\dot{x} = f\cos\mu\tau, \\ &\ddot{\gamma} - \tfrac{1}{b}\ddot{x}\sin\gamma + \sin\gamma + d_2\dot{\gamma} = 0, \end{aligned} \tag{1}$$

where μ is the frequency of the external forcing and we consider it as controlling parameter. The dimensionless parameters have the following values: $f = 0.5$, $a = 0.091$, $b = 3.33$, $\alpha = 0.031$, $d_1 = 0.132$ and $d_2 = 0.02$.

We focus on three solutions. First is $2:1$ periodic oscilations, second is solution where pendulum is in hanging down postion (HDP) and third is $1:1$ rotations (for details see [**?**, **?**]). In Figure **??** we show the probability

of reaching the three aforementioned solutions obtained using basin stability method. The initial conditions are random numbers drawn from the following ranges: $x_0 \in [-2,\ 2]$, $\dot{x}_0 \in [-2,\ 2]$, $\gamma_0 \in [-\pi,\ \pi]$ and $\dot{\gamma}_0 \in [-2.0,\ 2.0]$. The frequency of excitation is within a range $\mu \in [0,\ 3.0]$. We take 15 equally spaced subsets of μ and in each subset we calculate the probability of reaching a given solution. For each subset we calculate 1000 trials each time drawing initial conditions of the system and a value of μ from the appropriate range. Then we plot the dot in the middle of the subset which indicate the probability of reaching a given solution in each considered range. Lines that connect the dots are shown just to emphasize the tendency.

In Figure **??** we mark the probability of reaching the $2:1$ resonance using blue dots. As we expected, for $\mu < 1.4$ and $\mu > 2.2$ the solution does not exist for details see [**?**]). In the range $\mu \in [1.4,\ 2.2]$ the maximum value of probability $p(2:1) = 0.971$ is reached in the subset $\mu \in [1.8,\ 2.0]$ and outside that range the probability decreases. A similar analysis is performed for HDP. The values of probability is indicated by the red dots. As one can see for $\mu < 0.8$, $\mu \in [1.2,\ 1.4]$ and $\mu \in [2.6,\ 2.8]$, the HDP is the only existing solution. The rapid decrease close to $\mu \approx 1.0$ indicates the $1:1$ resonance and the presence of other coexisting solutions in this range (see [**?**]). In the range $\mu \in [1.2,\ 1.4]$ the probability $p(\mathrm{HDP}) = 1.0$ which corresponds to a border between solutions born from $1:1$ and $2:1$ resonance. Hence, up to $\mu = 2.0$ the probability of the HDP solution is a mirror refection of $p(2:1)$. Finally, for $\mu > 2.0$ the third considered solution comes in and we start to observe an increase of probability of the rotating solution $S(\mu,\ \mathrm{HDP})$ as shown in Figure **??**(b). However, the chance of reaching the rotating solution remains small and never exceeds $p(1:1) = 8 \times 10^{-2}$.

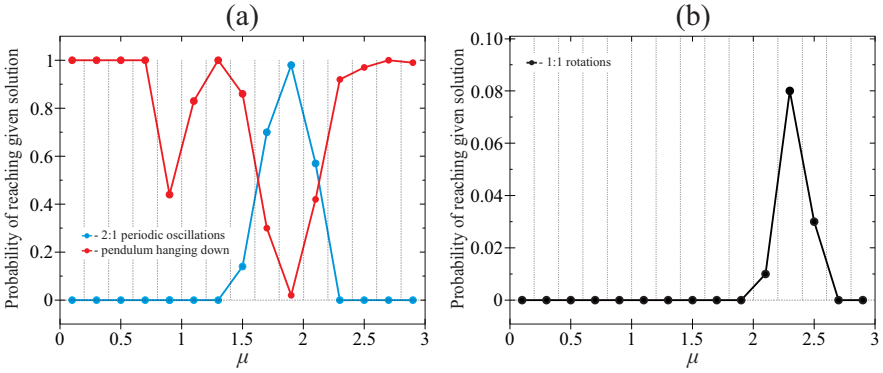

Figure 2: Probability of reaching given solutions in system giben by Eq. (1).

3. Conclusions

The presented method let us detect solutions in nonlinear dynamical systems. It is robust and can be used not only for mechanical and structural systems but also for any system given by differential equations where the knowledge about existing solutions is crucial.

Acknowledgement

This work is funded by the National Science Center Poland based on the decision number 2015/17/B/ST8/03325.

References

[1] P. Brzeski, P. Perlikowski, S. Yanchuk, and T. Kapitaniak. The dynamics of the pendulum suspended on the forced duffing oscillator. *Journal of Sound and Vibration*, 331:5347–5357, 2012.

[2] P. Brzeski, M. Lazarek, J. Kurths, and T. Kapitaniak and P. Perlikowski Basin stability approach for quantifying responses of multistable systems with parameters mismatch. *Meccanica*, 51:2713-2726, 2016.

[3] P. J. Menck, J. Heitzig, N. Marwan, and J. Kurths. How basin stability complements the linear-stability paradigm. *Nature Physics*, 9(2):89–92, 2013.

INERTER WITH CONTINUOUSLY VARIABLE TRANSMISSION FOR TUNED MASS DAMPER APPLICATION

Mateusz Lazarek[1], Piotr Brzeski[1], Przemysław Perlikowski[1]

[1]*Division of Dynamics, Lodz University of Technology, Stefanowskiego 1/15, 90-924 Lodz, Poland*

Abstract

The mitigation of vibrations is one of the crucial problems in engineering. In civil engineering the main source of hazardous vibrations are earthquakes and strong winds. In mechanical engineering the oscillations may appear from rotations of bodies with eccentricity, dry friction or likewise in vehicles form bumpy roads. Focusing on large structures like i.e. buildings, bridges the most common solution involves tuned mass dampers (TMD). Historically, the first solution of TMD was proposed by Frahm in 1909 [1]. The device is a mass on a spring and its natural frequency is tuned to a natural frequency of a damped body. One of the main disadvantage of the TMD is narrow range of frequencies where it works efficiently. It is most effective in close neighborhood of resonance and outside this range it increases the amplitude of vibrations of main body. Den Hartog [2] added dash-pot between the TMD and damped structure which causes significant increase of TMD efficiency range. Another approaches leads to usage of nonlinear spring and multiple TMDs. Recently, a novel concept of the varying natural frequency of the tuned mass damper has been applied using inerter with variable inertia [3, 4].

We focus on inerter equipped with a prototype continuously variable transmission (CVT) designed for the novel tuned mass damper. Inerter enables stepless changes of inertance via varying transmission ratio of the CVT. The main difference from classical inerter is addition of CVT. We present its design and properties in details (see Fig. 1).

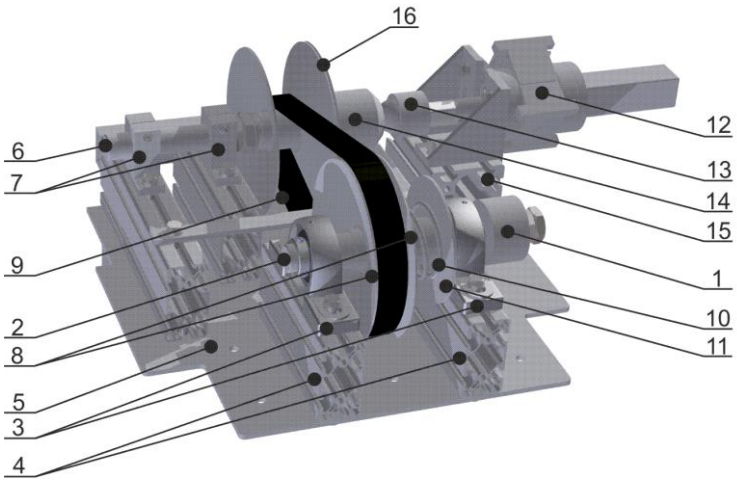

Figure 1 Isometric view of the CVT. Parts presented in the scheme: 1 - Gear, 2 - drive shaft, 3 - Bearing units, 4 - Aluminium profiles, 5 - CVT mounting plate, 6 - Stationary driven shaft, 7 - Shaft supports, 8 - Pulley plates, 9 - Belt, 10 - Spring, 11 - Spring retainer plate, 12 - Screw mechanism, 13 - Ball transfer unit, 14 - Brass sleeve, 15 - Control system base, 16 - Flywheel.

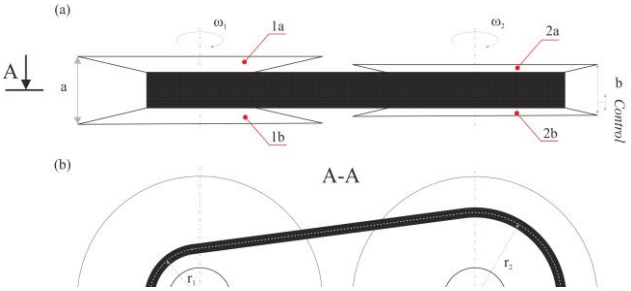

Figure 2 Schematic model of the CVT.

We derive the mathematical model of the system that include dissipation function. Schematically, it is presented in Fig. 2. The equation.
of motion is a second order ordinary differential equation (ODE):

$$I_{eq}\ddot{\varphi} + c_r\dot{\varphi} + d\ sign(\dot{\varphi}) = M_{ext}.$$

Where $I_{eq} = I_1 + i^2 I_2$ and I_1, I_2 are inertias of input and output shafts respectively. Parameter c_r is the viscous friction coefficient, d is a dry friction torque. Equivalent inertia I_{eq} of the CVT can be recalculated to obtain the value of inertance of inerter: $I_{iner} = \frac{4}{{d_p}^2}(I_1 + i^2 I_2) = \frac{4}{{d_p}^2} I_{eq}$, where d_p is the pitch diameter of the pinion that cooperates with the gear rack. Important to point, is a fact that in distinction form variators used in ATVs the ratio of our CVT is controlled by the screw mechanism which adjusts radius r_2. The radius r_1 adapt itself due to the presence of the spring.

We analyse the actual transmission ratio, internal motion resistances and identify the inertia of CVT components using energy conservation method. The important aspect of the study is that this transmission is a part of inerter mounted in the TMD designed to mitigate vibrations of structures. It implies that the motion of inerter and the CVT itself is oscillatory. Hence it changes the directionof rotations on regular basis. Hence, we apply actual working conditions and compare the experimental and numerical exciting torques of the CVT. We obtain good agreement between them, hence the proposed model is robust and gives reliable results (refer to Fig 3).

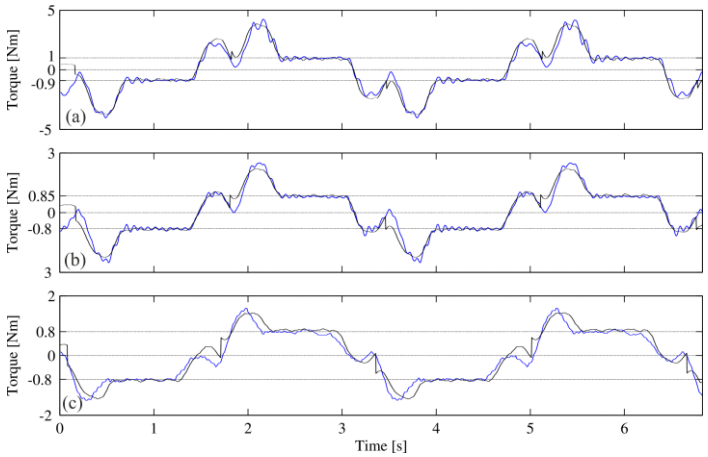

Figure 3 Torque-time graphs of the designed CVT in oscillatory motion test. Blue curves represents experimental data while black corresponds to simulation results. Tests are performed with ratio equal: i=1.76 [-] (a), i=1.17 [-] (b) and i=0.58 [-] (c).

This work has been supported by National Science Centre, Poland - Project No. 2015/17/B/ST8/03325.

References

[1] H. Frahm. Device for damping vibrations of bodies, 1909.

[2] J. P Den Hartog. Mechanical Vibrations. McGraw-Hill, New York, 1934.

[3] Michael ZQ Chen, Yinlong Hu, Chanying Li, and Guanrong Chen. Semi-active suspension with semi-active inerter and semi-active damper. IFAC Proceedings Volumes, 47(3): 11225–11230, 2014.

[4] P. Brzeski, P. Perlikowski, T. Kapitaniak, Novel type of tuned mass damper with inerter which enables changes of inertance. *Journal of Sound and Vibration*, 349: 56-66, 2015.

Session S16: Shells and plates

Organizers: J. Chróścielewski (Gdansk UT), F. Gruttmann (TU Darmstadt), V. Eremeyev (Rostov on Don, Gdansk UT), K. Wiśniewski (IPPT PAN, Warsaw)

Dedicated to the anniversary of Prof. W. Pietraszkiewicz with the tribute speech by Prof. J. Badur (IMP PAN, Gdansk)

NONLINEAR ANALYSIS OF REINFORCED CONCRETE CONSTRUCTION'S FRAGMENTS IN SCAD SOFTWARE

S. Fialko[1] and V. Karpilovskyi[2]

[1]*Cracow University of Technology, Warszawska, 24, Krakow, Poland*

[2]*IT Company SCAD Soft*[3]*, Osvity 3a of. 1, 2, Kiev, Ukraine*

e-mail: sergiy.falko@gmail.com

1. Introduction

The objective of our research is the development of software for analysing the stress-strain state and bearing capacity of structural fragments, rather than individual structural elements - plates, walls, columns, beams, etc., because the stress-strain state of an individual beam or slab in many cases considerably differs from the stress-strain state of the same structural element, which works in conjunction with its neighbours. We conne ourselves to the consideration of structures consisting of thin-walled plates and shells, and also from spatial bars for which the Kirchhoff-Clebsch hypothesis is satisfied. Quadrilateral and triangular finite elements, taking into account the plasticity both in concrete and in reinforcement, and also taking into account the degradation of the concrete of the stretched zone during the appearance and propagation of cracks, are presented. The quadrilateral finite element (FE) was described in [1], triangular FE - in [2]. In presented paper we focus our attention on the consideration of the behaviour of entire fragments consisted on presented above shell finite elements as well as two-node finite elements of the spatial frame (***Bar***3D) [3].

2. Problem formulation

Concrete is considered as an isotropic material, described by the relations of both the deformation theory of plasticity, formulated in terms of residual strains, and the relations of the plastic flow theory using the Drucker-Prager and Geniyev yield criteria [2], [3]. The degradation of the concrete in stretched zone due to appearing of cracks is modelled by the descending branch in the diagram $\sigma - \varepsilon$ (the deformation theory of plasticity) and by compression and translation of the yield surface, determined by the decrease of strength of concrete on tension σ_t during the increase of plastic deformations (plastic flow theory) [3]. In the compressed zone, softening is also taken into account after reaching the strength of concrete on compression σ_t.

The reinforcement is considered as the rods working on tension-compression and on transverse shear. For shell elements, the reinforcing rods are smeared in the plane of the given reinforcing layer, however, the reinforcing layers are taken into account discreetly along the thickness of the shell. Each reinforcement layer consists of rods of the same direction, located with the same step, and the direction of the reinforcing bars can be arbitrary with respect to the axes of the local coordinate system of the finite element. For the ***Bar***3D finite element, each reinforcing rod of the longitudinal reinforcement is taken into account discretely. For rebar, we use both the deformation theory of plasticity, formulated in terms of residual strains, and the theory of the plastic flow with von Mises yield criterion.

For the shell finite elements, the Mindlin-Reissner theory is used, and for the ***Bar***3D finite element, the S. P. Timoshenko shear model is applied. To eliminate the shear locking effect, the MITC approach for shell finite elements and the approximation of shear deformations at the midpoint for ***Bar***3D finite element is used. The governing relationships are obtained using the principle of virtual works, the formulation of which for the ***Bar***3D finite element is follows:

[3]SCAD Soft is an IT company, developer of SCAD FEA software, one of the most popular software in civil engineering in CIS countries, certicated according to regional building code.

.

(1) $$\iiint_V \delta\boldsymbol{\varepsilon}^T\boldsymbol{\sigma}dV + \sum_S A_S \int_0^a \boldsymbol{\varepsilon}_s^T dx\,\delta A = 0,$$

where $\boldsymbol{\varepsilon}, \boldsymbol{\sigma}$ are the strain and stress tensors for the ***Bar***3D finite element with taking into account of statical hypothesis of the Kirchhoff-Clebsch theory, $\boldsymbol{\varepsilon}_s$ and $\boldsymbol{\sigma}_s$are the strain and stress tensors for the s-th rebar rod, $A_s$is its cross-section area and δA is a virtual work of external forces. The linear shape functions are applied. To calculate the integrals over the volume of the finite element, triangulation of the cross-section domain is performed. We calculate the integrand expressions at the centers of gravity of the triangles, and at the midpoint along the length of the finite element.

3. Numeric results

Figure 1 shows a fragment of a multistorey building, the design model of which is taken from the collection of SCAD Soft problems. The walls are loaded by the weight of above-located floors. In addition, the evenly distributed pressure is applied to the floors. All loads vary in proportion to a single parameter. The curve 1 corresponds to deformation theory of plasticity and curves 2 and 3 - to plastic flow theory, where we use the Drucker-Prager yield criterion for floors and beams and the Geniyev yield criterion for walls. The Geniyev yield criterion presents a non-circular paraboloid in the space of principal stresses \cite{third}. The parameter $\alpha \in (0.532, 0.577]$, where $\alpha = 0.532$ corresponds to maximal deviation of paraboloid from circular shape and $\alpha = 0.577$ corresponds to circular paraboloid.

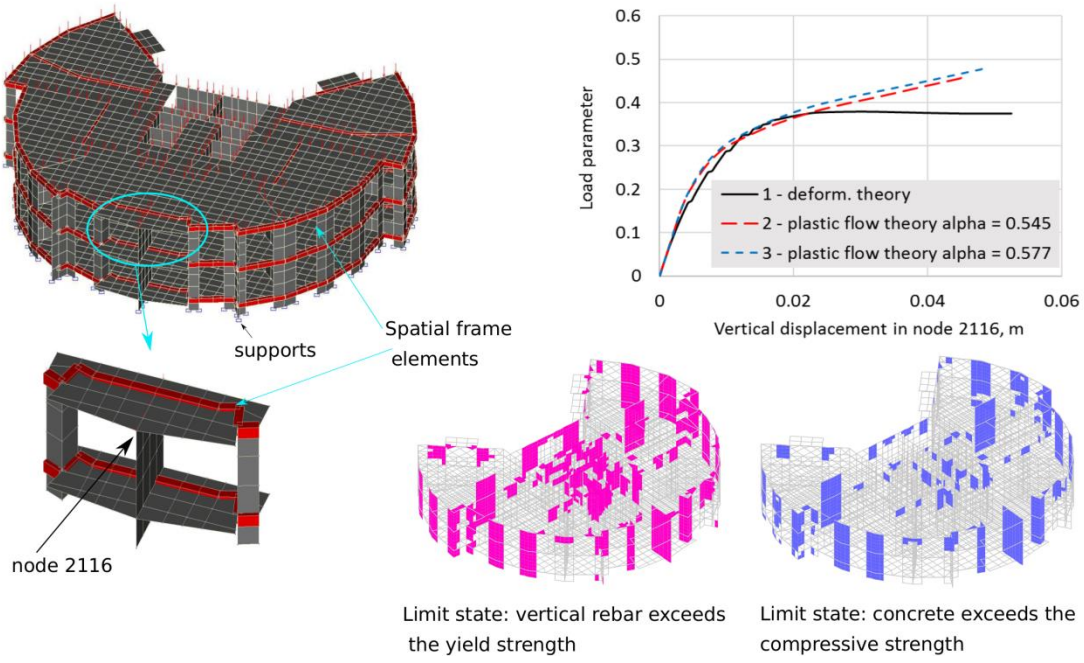

Figure 1 Fragment of multi-storey building

References

[1] S.Yu. Fialko. Quadrilateral finite element for analysis of reinforced concrete floor slabs and foundation plates, *Applied Mechanics and Materials*, 725 - 726, 820 835.

[2] S. Yu. Fialko and V. S. Karpilowskyi (2018). Triangular and quadrilateral at shell finite elements for nonlinear analysis of thin-walled reinforced concrete structures in SCAD software. In: Petraszkiewicz and Witkowski (eds). *Shell Structures: Theory and Applications* Volume 4., Taylor and Francis Group, London, 367-370.

[3] С. Ю. Фиалко Применение метода конечных элементов к анализу прочности и несущей способности тонкостенных железобетонных конструкций с учетом физической нелинейности, *СКАД СОФТ и АСВ*, Москва, 2018 (in Russian).

THEORY AND FINITE ELEMENT FORMULATIONS FOR LAYERED COMPOSITE SHELLS

F. Gruttmann[1] and G. Knust[1]

[1]*Chair of Solid Mechanics, Darmstadt University of Technology, Germany*

e-mail: gruttmann@mechanik.tu-darmstadt.de

1. Introduction

Shell elements which account for the layer sequence of a laminated structure are able to accurately predict the deformation behaviour of the reference surface, a sufficiently refined mesh presupposed. This holds also for the shape of the in–plane stresses, if the shell is not too thick. In contrast to that only averaged transverse shear strains through the thickness are obtained within the Reissner-Mindlin theory. As a consequence only the average of the transverse shear stresses is accurate. Neither the shape of the stresses is correct nor the boundary conditions at the outer surfaces are fulfilled. In a standard version the thickness normal stresses are neglected.

In several papers the equilibrium equations are exploited within a post–processing procedure to obtain the interlaminar stresses. The essential restriction of the approach is the fact that these stresses are not embedded in the variational formulation and an extension to geometrical and physical nonlinearity is not possible.

Higher order plate and shell formulations and layerwise approaches represent a wide class of advanced models. These theories are associated with global layerwise degrees of freedom which makes the general handling complicated for practical problems, e.g. when structures with intersections occur [1].

The use of brick elements or so-called solid shell elements represents a computationally expensive approach. For a sufficient accurate evaluation of the interlaminar stresses each layer must be discretized with several elements ($\approx 4-10$) in thickness direction. Especially for nonlinear large scale problems with a multiplicity of load steps and several iterations in each load step this is not a feasible approach [2].

An alternative to fully 3D computations is a multiscale formulation applying the so-called FE^2 approach. At the integration points of the macro scale representative volume elements (RVEs) are introduced. In case of thin structures the RVEs usually extend through the total thickness of the shell [3]. In comparison to one-scale computations using standard shell elements the computing times prove to be very high.

The discussion shows, that there is a need for further research in this range. Based on above arguments we propose a shell theory and associated finite element formulation which is characterized by the following features.

(i) The underlying nonlinear shell theory is based on Reissner–Mindlin kinematic assumptions. This leads in a basic version to averaged transverse shear strains and vanishing transverse normal strains when exploiting the Green–Lagrangian strain tensor. Subsequently the displacement field is enriched by warping displacements and thickness changes using layerwise interpolation functions. Thereby an interface to arbitrary three–dimensional material laws with restriction to small strains is created.

(ii) The weak form of the boundary value problem is derived using the equilibrium equations for the stress resultants and stress couple resultants, the local equilibrium equations in terms of stresses, the geometric field equations, the constitutive equations and a constraint which enforces the correct shape of the displacement fluctuations through the thickness.

(iii) Static condensation is applied to eliminate a set of parameters on element level. The resultant quadrilateral shell element possesses the usual 5 or 6 nodal degrees of freedom. This is an essential feature since standard geometrical boundary conditions can be applied and the element is applicable also to shell intersection problems. In comparison to fully 3D computations and to FE^2 computations present formulation needs only a fractional amount of computing time.

2. FE formulation for layered shells

Layered shells of thickness h are considered in this contribution. With ξ^i we denote a convected coordinate system of the body, where for the thickness coordinate $h^- \leq \xi^3 \leq h^+$ holds. Thus, the reference surface Ω can arbitrarily be chosen related to the outer surfaces. The coordinate on the boundary $\Gamma = \Gamma_u \cup \Gamma_\sigma$ is denoted by s. The shell is loaded statically by surface loads $\bar{\mathbf{p}}$ in Ω and by boundary forces $\bar{\mathbf{t}}$ on Γ_σ. Inserting the kinematic assumptions according to Reissner and Mindlin into the Green–Lagrangian strain tensor one obtains well-known expressions for the shell strains. The membrane strains, curvatures and transverse shear strains are summarized in the vector $\boldsymbol{\varepsilon}_g$.

A displacement field $\tilde{\mathbf{u}}$ is superposed on the displacement shape of the Reissner-Mindlin theory. Its components $\tilde{u}_i$ refer to a constant element basis system, where $\tilde{u}_1, \tilde{u}_2$ denote out of plane warping displacements and $\tilde{u}_3$ thickness changes. The shape of $\tilde{\mathbf{u}}$ through the thickness is chosen as in [4]

$$\tilde{\mathbf{u}}(\xi^3) = \boldsymbol{\Phi}(\xi^3)\,\boldsymbol{\alpha}\,. \tag{1}$$

The vector $\boldsymbol{\alpha}$ is element-wise constant and contains displacements at nodes in thickness direction of the laminate. For N layers this leads to $M = 9 \cdot N + 3$ components in $\boldsymbol{\alpha}$. The interpolation matrix $\boldsymbol{\Phi}(\xi^3)$ is formulated with cubic hierarchic functions

$$\begin{aligned} &\boldsymbol{\Phi}(\xi^3) = \left[\ \phi_1\,\mathbf{1}_3 \quad \phi_2\,\mathbf{1}_3 \quad \phi_3\,\mathbf{1}_3 \quad \phi_4\,\mathbf{1}_3\ \right]\,\mathbf{a}^i \\ &\phi_1 = \frac{1}{2}\,(1-\zeta) \qquad \phi_2 = 1-\zeta^2 \qquad \phi_3 = \frac{8}{3}\,\zeta\,(1-\zeta^2) \qquad \phi_4 = \frac{1}{2}\,(1+\zeta)\,, \end{aligned} \tag{2}$$

where $-1 \leq \zeta \leq 1$ is a normalized thickness coordinate of layer i. Furthermore, $\mathbf{a}^i$ is an assembly matrix, which relates the 12 degrees of freedom of layer i to the M components of $\boldsymbol{\alpha}$.

Using admissible variations for the independent mechanical fields the variational equation as basis for the FE formulation reads

$$\int_\Omega \delta\boldsymbol{\varepsilon}_g^T\boldsymbol{\sigma} + \delta\boldsymbol{\sigma}^T(\boldsymbol{\varepsilon}_g - \boldsymbol{\varepsilon}) + \delta\boldsymbol{\vartheta}^T\boldsymbol{\psi}\,\mathrm{d}A - \int_\Omega \delta\mathbf{u}^T\bar{\mathbf{p}}\,\mathrm{d}A - \int_{\Gamma_\sigma} \delta\mathbf{u}^T\,\bar{\mathbf{t}}\,\mathrm{d}s = 0\,. \tag{3}$$

Here, $\boldsymbol{\sigma}$ denotes the vector of independent stress resultants and $\boldsymbol{\varepsilon}$ denote physical shell strains, which enter into the material law. The vector $\boldsymbol{\psi}$ summarizes the material law, the equilibrium of higher order stress resultants and a constraint. The work conjugate vector $\boldsymbol{\vartheta} = [\boldsymbol{\varepsilon}, \boldsymbol{\alpha}, \boldsymbol{\lambda}]^T$ contains besides $\boldsymbol{\varepsilon}$ and $\boldsymbol{\alpha}$ the vector of Lagrange parameters $\boldsymbol{\lambda}$. Integration by parts and using standard arguments of variational calculus yields the associated Euler-Lagrange equations. One obtains the equilibrium of stress resultants, the geometric field equations, the local equilibrium in terms of stresses, a constraint and the static boundary conditions. The interpolation functions for the independent quantities are specified in detail in Ref. [5]. Several linear and nonlinear test examples show the effectiveness of the proposed model.

References

[1] F. Gruttmann and W. Wagner (1994). On the numerical analysis of local effects in composite structures, *Composite Struct*, **2**9, 1–12.

[2] S. Klinkel, F. Gruttmann and W. Wagner (1999). A continuum based 3D–shell element for laminated structures, *Computers & Structures*, **7**1, 43–62.

[3] F. Gruttmann and W. Wagner (2013). A coupled two-scale shell model with applications to layered structures, *Int. J. Num. Meth. Eng.*, **94**, 1233–1254.

[4] F. Gruttmann, W. Wagner and G. Knust (2016). A coupled global-local shell model with continuous interlaminar shear stresses, *Comp. Mech.*, **5**7 (2), 237–255.

[5] F. Gruttmann, G. Knust and W. Wagner (2017). Theory and numerics of layered shells with variationally embedded interlaminar stresses, *Comp. Meth. Appl. Mech. Engrg.*, **326**, 713-738.

KIRCHHOFF'S PLATE BENDING ANALYSIS BY EQUILIBRIUM FINITE ELEMENT METHOD

P. Świątkiewicz[1] and Z. Więckowski[1]

[1]*Department of Mechanics of Materials, Łódź University of Technology, Łódź, Poland*

e-mail: Paulina.Swiatkiewicz@p.lodz.pl, Zdzislaw.Wieckowski@p.lodz.pl

1. Introduction

The equilibrium approach of the finite element method, despite of some difficulties arising in construction of statically admissible stress field, provides an interesting alternative to the displacement method. This paper presents the application of the equilibrium finite element method to the static problem of Kirchhoff's plate bending. The statically admissible fields of stresses have been constructed with use of the Southwell vector stress function. The possibility of employing this function for seeking the approximate solution for structural analysis of plates was indicated by Zienkiewicz and Fraeijs de Veubeke in [3]. The utilization of this function was proposed by Morley in [4] and Elias in [2].

2. Formulation of the problem

The flat plate bending problem is governed by three types of equations, which will be presented in this paper with use of the indicial notation. Firstly, the differential equilibrium equations

$$M_{\alpha\beta,\beta} - Q_\alpha = 0, \quad Q_{\alpha,\alpha} + q = 0 \tag{1}$$

where $\alpha, \beta = 1, 2$, and $M_{\alpha\beta}$ is the tensor of bending and twisting moments, Q_α the vector of transverse forces and q the transverse distributed load. Next, the geometric relations:

$$\kappa_{\alpha\beta} = -w_{,\alpha\beta} \tag{2}$$

where $\kappa_{\alpha\beta}$ denotes the tensor of curvature and w a function of deflection of plate's middle surface. Finally, the constitutive relation which takes form of the generalized Hooke's law:

$$\kappa_{\alpha\beta} = C_{\alpha\beta\gamma\delta}\, M_{\gamma\delta} \tag{3}$$

where $C_{\alpha\beta\gamma\delta}$ indicates a compliance tensor. Equations (1) – (3) should be supplemented with boundary conditions which may be of kinematic, static or mixed nature. The strong form of the problem presented above may also be set in the variational form as the complementary work principle which can be obtained by multiplication of geometric relation by variation of tensor of bending and twisting moments and integration of it over the plate area. This also corresponds to minimization of the complementary energy functional

$$\Pi_\sigma = \frac{1}{2}\int_\Omega M_{\alpha\beta}\, C_{\alpha\beta\gamma\delta}\, M_{\gamma\delta}\, \mathrm{d}x - \int_{\Gamma_\varphi} M_n\, \bar{\varphi}_n\, \mathrm{d}s - \int_{\Gamma_w} (Q_n + M_{ns,s})\, \bar{w}\, \mathrm{d}s \tag{4}$$

on the following set of statically admissible moment fields

$$Y = \left\{ M_{\alpha\beta} \in L^2(\Omega) : M_{\alpha\beta,\alpha\beta} + q = 0 \text{ in } \Omega, \;\; M_n = M_0 \;\&\; Q_n + M_{ns,s} = Q_0 \text{ on } \Gamma_\sigma \right\}.$$

where $\bar{\varphi}_n$ and $\bar{w}$ are the angle and deflection functions given on boundaries Γ_φ and Γ_w, respectively, and symbol L^2 denotes the space of square integrable functions.

3. Equilibrium approach

The equilibrium equations are satisfied in internal points of plate's area Ω by virtue of Southwell's vector stress function [5], with components U_α. The equilibrium equations will be identically met provided that the bending and twisting moments are determined by Southwell's function's components as follows:

$$M_{\alpha\beta} = \frac{1}{2}\left(\epsilon_{\alpha\gamma}\epsilon_{\beta\delta}U_{\gamma,\delta} + \epsilon_{\alpha\gamma}\epsilon_{\beta\delta}U_{\delta,\gamma}\right) - \delta_{\alpha\beta}P_0. \tag{5}$$

where P_0 is the solution of the Poisson equilibrium equation $(1)_2$, which may be either arbitrary presupposed in an analytic form or found numerically. The Southwell stress functions have been approximated with shape functions of class C_0 by use of triangular elements. The solution is found by minimization of the complementary energy and the boundary conditions have been satisfied by use of Lagrange's multiplier method.

4. Numerical example

A square uniformly loaded plate with the bottom edge free and remaining three edges clamped has been considered. The results have been compared with the ones received by means of the Hsieh-Clough-Tocher macro-element, e.g. [1], by the displacement approach. It is shown (see Figure 1) that both methods lead to similar results, but the fact worth highlighting is that the equilibrium approach allows one to find the upper bound of the strain energy when only external forces are prescribed, whereas the displacement method leads to the lower bound. The convergence rate is similar for each of these two elements. With use of both the methods the relative error of approximate solution has been calculated on basis of Synge's hypercycle method. It reaches small values and in the case of the densest mesh barely exceeds 1%.

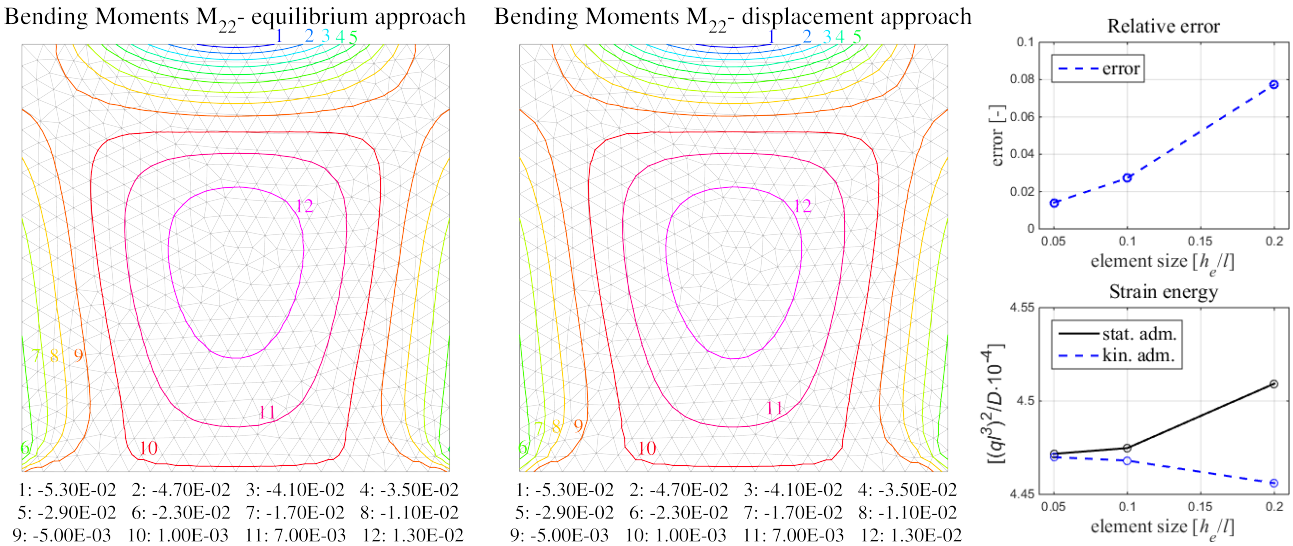

Figure 1: Statically and kinematically admissible solutions (M_{22}), relative error of solution and strain energy

References

[1] P. Ciarlet. *The Finite Element Method for Elliptic Problems*, North-Holland Publ. Co., 1978.

[2] Z.M. Elias. Duality in finite element method. *Proc. ASCE, J. Eng. Mech. Div*, EM4:931, 1968.

[3] B. Fraeijs De Veubeke, O. C. Zienkiewicz. Strain energy bounds in finite-element analysis by slab analogy. *The Journal of Strain Analysis for Engineering Design*, 2:265, 1967.

[4] L.C.D. Morley. The triangular equilibrium element in the solution of plate bending problems. *Aero.Q.*,19:149, 1968.

[5] R. V. Southwell. On the analogues relating flexure and extention of flat plates. *The Quaterly Journal of Mechanics & Applied Mathematics*, 3:257, 1950.

EXISTENCE AND UNIQUENESS THEOREMS FOR CUSPED POROUS ELASTIC PRISMATIC SHELLS IN THE ZERO APPROXIMATION OF THE HIERARCHICAL MODELS

N. Chinchaladze[1]

[1]*I.Vekua Institute of Applied Mathematics & Faculty of Exact and Natural Sciences of I. Javakhishvili Tbilisi State University, Tbilisi, Georgia*

e-mail: natalia.chinchaladze@tsu.ge

In [1] hierarchical models for porous elastic and viscoelastic Kelvin-Voigt prismatic shells on the basis of linear theories is constructed. Using I. Vekuas dimension reduction method ([2,3]), governing systems are derived and in the Nth approximation boundary value problems are set. The ways of investigation of boundary value problems (BVPs), including the case of cusped prismatic shells, are indicated and some preliminary results are presented.

Let us consider prismatic shells occupying 3D domain Ω with the projection ω (on the plane $x_3 = 0$) and the face surfaces

$$x_3 = \overset{(+)}{h}(x_1, x_2) \in C^2(\omega) \cap C(\overline{\omega}) \ \text{ and } \ x_3 = \overset{(-)}{h}(x_1, x_2) \in C^2(\omega) \cap C(\overline{\omega}), \ \ (x_1, x_2) \in \omega.$$

In what follows we assume that

$$2h(x_1, x_2) := \overset{(+)}{h}(x_1, x_2) - \overset{(-)}{h}(x_1, x_2) = \begin{cases} > 0, & \text{for } (x_1, x_2) \in \omega, \\ \geq 0, & \text{for } (x_1, x_2) \in \partial\omega \end{cases}$$

is the thickness of the prismatic shell. Prismatic shells are called cusped shells if a set γ_0, consisting of $(x_1, x_2) \in \partial\omega$ for which $2h(x_1, x_2) = 0$, is not empty (see, e.g., Figures 1, 2).

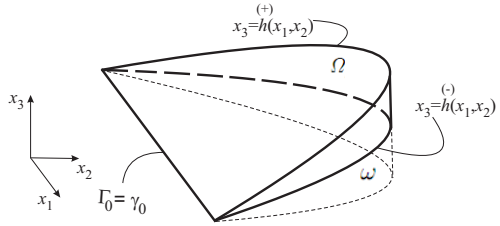

Figure 1: A sharp cusped prismatic shell with a semicircle projection. $\partial\Omega$ is a Lipschitz boundary

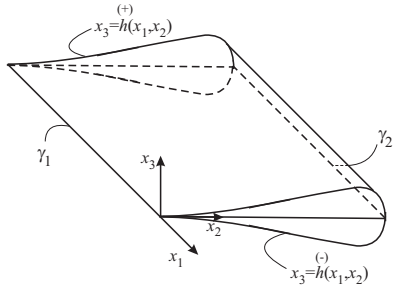

Figure 2: A cusped plate with sharp γ_1 and blunt γ_2 edges, $\gamma_0 = \gamma_1 \cup \gamma_2$. $\partial\Omega$ is a non-Lipschitz boundary

The governing system of porous elastic prismatic shells in case of zero approximation has the following form (see [1])

$$(\mu h v_{\alpha 0,\beta})_{,\alpha} + (\mu h v_{\beta 0,\alpha})_{,\alpha} + (\lambda h v_{\gamma 0,\gamma})_{,\beta} + (bh\psi_0)_{,\beta} + \overset{0}{X}_{\beta} = \rho h \ddot{v}_{\beta 0}, \quad \beta = 1, 2; \tag{1}$$

$$(\mu h v_{30,\alpha})_{,\alpha} + \overset{0}{X}_3 = \rho h \ddot{v}_{30}; \tag{2}$$

$$(\tilde{\alpha} h \psi_{0,\alpha})_{,\alpha} - bh v_{\gamma 0,\gamma} - \xi h \psi_0 + \overset{0}{H} = \rho \ddot{\varphi}_0 - \mathcal{F}_0, \tag{3}$$

where λ, μ, $\tilde{\alpha}$, b, ξ are the constitutive coefficients, ρ is the reference mass density, $v_{i0} := \dfrac{u_{i0}}{h}$ $(i = 1, 2, 3)$, $\psi_0 := \dfrac{\varphi_0}{h}$, u_{i0} and φ_0 are the zero moments of the displacements vector components and of the changes of the volume fraction from the matrix reference volume fraction, correspondingly, $\overset{0}{X}_i$ $(i = 1, 2, 3)$, $\overset{0}{H}$, F_0 are

given functions (see [1]). The points as superscripts mean differentiation with respect to the time, and Einsteins summation convention is used; indices after comma mean differentiation with respect to the corresponding variables of the Cartesian frame $Ox_1x_2x_3$.

Let the thickness is given by the following expression

$$2h(x_1,x_2)=h_0x_2^{\kappa},\quad x_2\in[0,l]\quad h_0,\ \kappa,l=const>0.$$

In case of harmonic vibration with the oscillation frequency ϑ system (1)-(3) can be rewritten as follows

$$\begin{aligned}
&-\mu\Big[(h\overset{\circ}{u}_{\alpha,\beta})_{,\alpha}+(h\overset{\circ}{u}_{\beta,\alpha})_{,\alpha}\Big]-\lambda(h\overset{\circ}{u}_{\gamma,\gamma})_{,\beta}-b(h\overset{\circ}{u}_4)_{,\beta}-\rho h\vartheta^2\overset{\circ}{u}_{\beta}=F_{\beta},\quad \beta=1,2,\\
&-\mu(h\overset{\circ}{u}_{3,\alpha})_{,\alpha}-\rho h\vartheta^2\overset{\circ}{u}_{30}=F_3,\\
&-\tilde{\alpha}(h\overset{\circ}{u}_{4,\alpha})_{,\alpha}+bh\overset{\circ}{u}_{\gamma,\gamma}+\xi h\overset{\circ}{u}_4-\rho h\vartheta^2\overset{\circ}{u}_4=F_4,
\end{aligned}\tag{4}$$

where

$$\overset{\circ}{u}_i:=\overset{\circ}{v}_{i0},\quad \overset{\circ}{u}_4:=\overset{\circ}{\psi}_0,\quad F_i:=\overset{\circ}{X}_i,\quad F_4:=\overset{\circ}{H}+\mathcal{F}_0,$$

$$\overset{\circ}{H}+\mathcal{F}_0=e^{\iota\vartheta t}F(x_1,x_2),\quad \overset{\circ}{X}_3=e^{\iota\vartheta t}\overset{\circ}{X^0}_3(x_1,x_2),\quad v_{30}=e^{\iota\vartheta t}\overset{\circ}{v}_{30}(x_1,x_2),\quad \psi_0=e^{\iota\vartheta t}\overset{\circ}{\psi}_0(x_1,x_2).$$

BCs for the weighted displacements and the weighted volume fraction are nonclassical in the case of cusped prismatic shells. Namely, we are not always able prescribe them at cusped edges.

For the particular case of deformation when

$$\overset{\circ}{u}_{\alpha}\equiv 0,\quad \alpha=1,2;\quad \overset{\circ}{u}_3,\ \overset{\circ}{u}_4\not\equiv 0$$

the following theorem can be proved

Theorem. *If*

$$\xi-\rho\vartheta^2\geq 0,$$

(i) $\kappa<1$, the Dirichlet problem (find $\overset{\circ}{u}_3,\ \overset{\circ}{u}_4\in C^2(\omega)\cap C(\bar{\omega})$ by their values prescribed on $\partial\omega$) is well-posed;

(ii) if $\kappa\geq 1$, the Keldysh problem (find bounded $\overset{\circ}{u}_3,\ \overset{\circ}{u}_4\in C^2(\omega)\cap C(\omega\cup(\partial\omega\setminus\overline{\gamma}_0))$ by their values prescribed only on the arc $\partial\omega\setminus\overline{\gamma}_0$) is well-posed.

The talk is devoted to the homogeneous Dirichlet problem for the general system (4). The classical and weak setting of the problem are formulated. For arbitrary $\kappa\geq 0$, we introduce appropriate function spaces X^{κ} , which are crucial in our analysis. We show coerciveness of the corresponding bilinear form and prove uniqueness and existence results for the variational problem. We describe in detail the structure of the spaces X^{κ} and establish their connection with weighted Sobolev spaces. Moreover, we give some sufficient conditions for a linear functional arising in the right-hand side of the variational equation to be bounded.

Acknowledgments This work is supported by Shota Rustaveli National Science Foundation [217596, Construction and investigation of hierarchical models for thermoelastic piezoelectric structures].

References

[1] G. Jaiani (2017). *Hierarchical Models for Viscoelastic Kelvin-Voigt Prismatic Shells with Voids*, Bulletin of TICMI, 21 (1), 33-44.

[2] I. Vekua (1985). Shell theory: general methods of construction, *Pitman Advanced Publishing Program, Boston-London-Melbourne*.

[3] G. Jaiani (2011). Cusped Shell-like Structures, *Springer Briefs in Applied Science and Technology, Springer-Heidelberg-Dordrecht-London-New York*.

DETERMINATION OF VIBRATIONS IN AN ELASTIC MEDIUM AFTER THE PASSAGE OF A SPHERICAL WAVE THROUGH A VIBRATION-ABSORBING PLATE

N.A. Lokteva[1], D.V. Tarlakovskii[2]

[1]*Moscow Aviation Institute (National Research University), Moscow, 125993, A-80, GSP -3, Volokolamskoye shosse 4, Russia*

[2] *Institute of Mechanics Lomonosov Moscow State University, Moscow 119192, Michurinski prospekt 1, Russia*

Introduction

In current times buildings and facilities are exposed to various external negative effects arising from utility equipment, industrial machinery, as well as transportation means (such as shallow-depth city railroad systems, heavy trucks, railway trains, trams) that cause huge dynamic loads [1]. Vibration-absorbing barriers placed between the vibration source and the object to be protected is one of the ways of protection of foundations against ground vibrations [2, 3].

This paper is intended to study vibration-absorbing properties of a plate exposed to subsurface spherical harmonic waves. In practice, such situation may correspond to vibrations caused by a point source situated nearby the barrier.

1. Statement of problem

Let us consider an elastic plate surrounded from both sides by half-spaces “1” and “2” filled with the ground. The coordinate system $Oxyz$ is of Cartesian type. It is assumed that the plane Oxy for the plate is a median one and limited along axes Ox and Oy, having the length of l. The beginning of the coordinates is assumed to be situated in the upper right corner of the plate.

When undisturbed, the ground is considered to be undeformed. The obstacle is overrun by a harmonic tensile wave of an normal stress amplitude p_* at the front and frequency ω, coming from the negative Oz-axis. The normal vector towards the front of the wave is in the plane Oxy.

The main purpose of this study is finding the resultant vector field of acceleration **a** (vibration accelerations) in the second half-space as a function of the frequency ω and spatial coordinates x, y and z depending on the parameters of the plate. The stated purpose of the problem solution is refined as follows. It is necessary to find the coordinates of the vibration acceleration field

$$a_x = -\omega^2 u_1^{(2)},\ a_y = -\omega^2 u_2^{(2)}, a_z = -\omega^2 w^{(2)}, \tag{1}$$

and the module

$$a = \sqrt{a_x^2 + a_y^2 + a_z^2}\ , \tag{2}$$

where $u_1^{(2)}, u_2^{(2)}$ are displacements of the medium “2” by coordinates x, y; $w^{(2)}$ is the normal displacement of the second medium.

The mathematical statement of the problem includes setting the ingoing wave, equations of displacements of the ground and plate, boundary conditions for the plate and ground, condition for infinity, as well as a condition of the ground-to-obstacle contact where the adhesion of the plate with the ground is ignored.

2. Equations of displacements of sandwich plate

The displacement of the plate is described by a system of Paymushin V.N. equations [4]. Two bearing layers are of elastic isotropic type with the modulus of elasticity E, Poisson’s ratio ν, and thickness of $2t$. The filler is orthotropic of a honeycomb configuration with the elasticity modulus E_z, the Poisson’s ratio ν_z, and thickness of $2h$. The bearing layers are affected by normal outer stress loads p_1 and p_2. Tangential

displacements are indicated by $u_1^{(k)}$ and $u_2^{(k)}$ along the axes Ox and Oy. $w^{(k)}$ is the normal displacement of the bearing layer, q^1 and q^2 are transverse tangent lines of the stress in the filler by axes *Ox* and *Oy*. The Paymushin V.N. equation system which describes the movement of the plate has the following form:

$$
\begin{gathered}
\rho_c \ddot{u}_1^c = L_{11}\left(u_1^c\right) + L_{12}\left(u_2^c\right),\ \rho_c \ddot{u}_2^c = L_{21}\left(u_1^c\right) + L_{22}\left(u_2^c\right), \\
\rho_a \ddot{u}_1^a = L_{11}\left(u_1^a\right) + L_{12}\left(u_2^a\right) + 2q^1,\ \rho_a \ddot{u}_2^a = L_{21}\left(u_1^a\right) + L_{22}\left(u_2^a\right) + 2q^2, \\
\rho_c \ddot{w}_c - \underline{m_c \Delta \ddot{w}_c} + \underline{\rho_{wq}\left(\ddot{q}_{,x}^1 + \ddot{q}_{,y}^1\right)} = -D\Delta^2 w_c + 2k_1\left(q_{,x}^1 + q_{,y}^1\right) + p_1 - p_2, \\
\rho_{aw} \ddot{w}_a - \underline{m_a \Delta \ddot{w}_a} = -D\Delta^2 w_a - 2c_3 w_a + p_1 + p_2, \\
\underline{\rho_{q1} \ddot{q}^1} - \underline{\rho_{wq1} \ddot{w}_{c,x}} = u_1^a - k_1 w_{c,x} - k_2\left(q_{,x}^1 + q_{,y}^2\right)_{,x} + k_{31} q^1, \\
\underline{\rho_{q2} \ddot{q}^2} - \underline{\rho_{wq2} \ddot{w}_{c,y}} = u_2^a - k_1 w_{c,y} - k_2\left(q_{,x}^1 + q_{,y}^2\right)_{,y} + k_{32} q^2;
\end{gathered}
\tag{3}
$$

where $u_i^c = u_i^{(1)} + u_i^{(2)}, u_i^a = u_i^{(1)} - u_i^{(2)}\ (i = 1,2), w_c = w^{(1)} + w^{(2)}, w_a = w^{(1)} - w.$

The boundary conditions correspond to a hinge edge of the plate. All functions change harmonically.

The plate's kinematic parameters are represented in the form of two-fold trigonometric series meeting the boundary conditions. The amplitudes of ingoing and passed waves are expanded into series in a similar way. The solution of an equation system results into finding the values of the kinematic parameters depending on amplitudes of wave pressure in mediums "1" and "2".

2. Equations of ground displacements and ingoing wave

A homogeneous elastic isotropic medium is used as a model of the ground [5], which equals the displacement equations (Lame equations) and the equations with respect to scalar potential φ and vector potential $\boldsymbol{\psi} = (\psi_1, \psi_2, \psi_3)$ of elastic displacements. As the area occupied by the ground is boundless, the potentials of equation solutions must satisfy the Sommerfeld radiation conditions:

To set an ingoing spherical harmonic wave, a spherical wave is considered [5] which travels along the positive direction of Oz axis.

The values of the potentials for the ingoing spherical harmonic wave are substituted into the equations of motion of the elastic medium. Taking into account that $\sigma_{33}\big|_{t=0,\ z=0} = p_*$, we will obtain the formula of amplitudes of displacements, deformations and stresses in the ingoing wave.

3. Boundary problem of interaction of harmonic wave with plate in ground

The boundary conditions with respect to the coefficients of the series depend on the conditions of contact between the plate and the ground To find the coefficients of the series corresponding to a disturbed stress-strained condition in the media, let us plug the potentials expanded into two-fold trigonometrical series. Introducing the constant values obtained from the contact conditions into the displacement expressions, we obtain the coefficients of the expansion in the series of displacements in the medium "2"Then it became possible to find the vibration acceleration module and its components.

References

[1] Umek A. Dynamic responses of building foundations to incident elastic waves.-Phd Thesis Illinois Institute of Technology, Dec.1973

[2] Kostrov B.V. Movement of rigid solid plate sealed into elastic medium affected by flat wave. PMM, 1964, V.28, issue.1 [in Russian]

[3] Rylko M.Y. [On movement of rigid rectangular inclusions in elastic medium affected by flat wave]. MTT,1977, No I [in Russian]

[4] Ivanov V.A., Paymushin V.N. Refined statement of dynamic problems of sandwich shells with transversal soft fillings and numerical analytical method of their solution. Prikladnaya mekhanika i tekhnicheskaya phisika [Applied Mechanics and Physics], 1995, V.36, No4, p. 147-151 [in Russian]

[5] Gorshkov A.G., Medvedsky A.L., Rabinsky L.N., Tarlakovsky D.V. Waves in continuum media: Textbook for Universities. Moscow, FIAMATLIT, 2004, 472 p. [in Russian]

ON THE USE OF VARIOUS FORMULATIONS OF THE EXTENDED HIGHER-ORDER SHELL THEORY IN DYNAMIC PROBLEMS FOR FUNCTIONALLY GRADED STRUCTURES

S. I. Zhavoronok

Institute of Applied Mechanics of Russian Academy of Sciences, Moscow, Russia

e-mail: Zhavoronok@iam.ras.ru

1. Introduction

Improved theories of heterogeneous shells are required as a background for the modeling of guided waves in functionally graded thin-walled structures. The finite element simulation remains the main numerical method [2] while one of the most efficient analytical approaches uses the orthogonal series expansion together with Legendre polynomials [4, 9]. At the same time the generalized shell theory [5] allows the unified variational problem formulation as well for the traditional interpretation of refined 2D shell models as for the finite element discretization across the thickness. The convergence of approximate normal wave frequencies and waveforms based such 2D solutions was analyzed in [3] for homogeneous elastic systems. An improvement of the theory consists in the accounting for the boundary conditions on the faces interpreted as constraints for the 2D variational problem [6,7]. The dynamic equations accounting for the full boundary reflection can be obtained by the Lagrange multiplier method or as extended Voronets' equations for constrained continuum system. The normal waves in power graded systems are studied here on the basis of various formulations of the shell theory [6, 7].

2. Basics of the extended higher order shell theory

A shell is interpreted as a material surface S furnished by the mechanical properties following from the variational solution of the dimensional reduction problem [5]. The shell model is defined on the 2D manifold within the configuration space $\Omega = \{u_i^{(k)}\}$, $k = 0 \dots N$, $i = 1 \dots 3$, where the field variables of the first kind are defined as biorthogonal expansion factors for the displacement vector: $u_i^{(k)} = (u_i, \mathrm{p}^{(k)})_1$, with the base system $\mathrm{p}_{(k)}(\zeta)$ depending on the thickness coordinate $\zeta \in [-1, 1]$ [5] (Legendre polynomials, trigonometric functions, or compact functions resulting in the "finite layer model"), the Lagragian density (1) and the constraints (2) [6,7]:

$$
\begin{aligned}
\mathcal{L}(u_i^{(k)}, \dot{u}_i^{(k)}, \nabla_\alpha u_i^{(k)}) = \int_S \Big[& \tfrac{1}{2}\rho_{(k)}^{(m)} \dot{u}_{(m)}^i \dot{u}_i^{(k)} - \tfrac{1}{2h}\left(\bar{C}_{(km)}^{i3j\gamma}\nabla_\gamma u_j^{(m)} + \bar{C}_{(km)}^{i3j} u_j^{(m)}\right) D_{(n\cdot)}^{(\cdot k)} u_i^{(n)} \\
& + F_{(k)}^i u_i^{(k)} - \tfrac{1}{2}\left(\bar{\bar{C}}_{(km)}^{\alpha\beta j\gamma}\nabla_\gamma u_j^{(m)} + \bar{C}_{(km)}^{\alpha\beta j} u_j^{(m)}\right)\left(\nabla_\beta u_\alpha^{(k)} + H_{\beta(n\cdot)}^{(\cdot k)} u_\alpha^{(n)} - b_{\alpha\beta} u_3^{(k)}\right) \\
& - \tfrac{1}{2}\left(\bar{\bar{C}}_{(km)}^{3\beta j\gamma}\nabla_\gamma u_j^{(m)} + \bar{C}_{(km)}^{3\beta j} u_j^{(m)}\right)\left(\nabla_\beta u_3^{(k)} + H_{\beta(n\cdot)}^{(\cdot k)} u_3^{(n)} + b_\beta^\alpha u_\alpha^{(k)}\right)\Big] dS + \int_{\partial S} q_{B(k)}^i u_i^{(k)} d\Gamma,
\end{aligned} \tag{1}
$$

$$
\begin{aligned}
& \bar{\bar{C}}_{\pm(k)}^{i\alpha\beta}\left(\nabla_\beta u_\alpha^{(k)} + H_{\beta(m\cdot)}^{(\cdot k)} u_\alpha^{(m)} - b_{\alpha\beta} u_3^{(k)}\right) + \bar{\bar{C}}_{\pm(k)}^{i\beta 3}\left(\nabla_\beta u_3^{(k)} + H_{\beta(m\cdot)}^{(\cdot k)} u_3^{(m)} + b_\beta^\alpha u_\alpha^{(k)}\right) \\
& + \bar{C}_{\pm(k)}^{i3j} h^{-1} D_{(m\cdot)}^{(\cdot k)} u_j^{(m)} - P_\pm^i = 0, \quad i,j = 1,2,3;\ \alpha,\beta,\gamma,\mu,\nu = 1,2;
\end{aligned} \tag{2}
$$

$$
\rho_{(k)}^{(m)} = \left(\rho \mathrm{p}_{(k)}, \mathrm{p}^{(m)}\right)_1, \quad \bar{\bar{C}}_{(km)}^{i\gamma j\beta} = \left(A_{\cdot\nu}^{\gamma\cdot} A_{\cdot\mu}^{\beta\cdot} C^{i\nu j\mu} \mathrm{p}_{(k)}, \mathrm{p}_{(m)}\right)_1, \quad D_{(n\cdot)}^{(\cdot k)} = \left(d\mathrm{p}_{(n)}/d\zeta, \mathrm{p}^{(k)}\right)_1, \dots
$$

$$
\bar{\bar{C}}_{\pm(k)}^{i\beta j} = \left(\bar{C}^{i3j\beta}|_{\zeta=\pm 1} + \nabla_\gamma h_\pm \bar{\bar{C}}^{i\gamma j\beta}|_{\zeta=\pm 1}\right)\mathrm{p}_{(k)}(\pm 1).
$$

Here h is the shell thickness, $b_{\alpha\beta}$ is the curvature tensor, ∇_α are covariant derivatives on the tangent bundle $T_M S$, $A_{\cdot\alpha}^{\beta\cdot}$ are parallel shifting tensors [5]. The constraints (2) follow from the boundary conditions on the shell faces $S_\pm$ [6,7], and the initial conditions closing the variational problem statement (1, 2) are written as follows:

$$
u_i^{(k)}(t = t_0) = U_i^{(k)}, \quad \dot{u}_i^{(k)}(t = t_0) = V_i^{(k)}. \tag{3}
$$

3. Spectral problems for graded shells and plates based on the Nth order theory

Let us consider a two-constituent isotropic power graded plate with Young moduli $E_{1,2}$ and mass densities $\rho_{1,2}$:

$$C^{\alpha\beta\gamma\delta}_{(km)} = \left[\lambda_1 a^{\alpha\beta} + \mu_1\left(a^{\alpha\gamma}a^{\beta\delta}+a^{\alpha\delta}a^{\beta\gamma}\right)\right]\Xi_{(km)};\ C^{3333}_{(km)} = (\lambda_1+2\mu_1)\,\Xi_{(km)};\ C^{\alpha\beta33}_{(km)} = \lambda_1 a^{\alpha\beta}\Xi_{(km)};$$
$$C^{\alpha3\beta3}_{(km)} = \mu_1 a^{\alpha\beta}\Xi_{(km)};\quad \lambda_1 = E_1\nu\left[(1-2\nu)(1+\nu)\right]^{-1};\quad 2\mu_1 = E_1(1+\nu)^{-1};\quad E_{12} = E_1/E_2; \tag{4}$$
$$\Xi_{(km)} = \left(\varphi(\zeta)\mathrm{p}_{(k)},\mathrm{p}_{(m)}\right)_1;\quad \varphi(\zeta) = f(\zeta)+(1-f(\zeta))E_{12},\quad f(\zeta) = [(1+\zeta)/2]^p,\ p\in\mathbb{R}_+\cup 0.$$

Let the waves propagate along the axis Ox_1, and let us introduce the dimensionless variables: $\tau = tc_2/h$, $\xi = x_1/h$, $\tilde{u}^{(k)}_i = u^{(k)}_i/h$. We obtain hence the dynamic equations following from (1) as Lagrange ones [5]:

$$R_{(km)}\partial^2_\tau\tilde{u}^{(m)}_1 = \eta^2\Xi_{(km)}\partial^2_\xi\tilde{u}^{(m)}_1 - D^{(\cdot n)}_{(k\cdot)}\Xi_{(ns)}\bar{D}^{(\cdot s)}_{(m\cdot)}\tilde{u}^{(m)}_1 - \left[D^{(\cdot n)}_{(k\cdot)}\Xi_{(nm)} - \left(\eta^2-2\right)\Xi_{(kn)}\bar{D}^{(\cdot n)}_{(m\cdot)}\right]\partial_\xi\tilde{u}^{(m)}_2; \tag{5}$$
$$R_{(km)}\partial^2_\tau\tilde{u}^{(m)}_2 = \Xi_{(km)}\partial^2_\xi\tilde{u}^{(m)}_2 + \eta^2 D^{(\cdot n)}_{(k\cdot)}\Xi_{(ns)}\bar{D}^{(\cdot s)}_{(m\cdot)}\tilde{u}^{(m)}_2 - \left[\left(\eta^2-2\right)D^{(\cdot n)}_{(k\cdot)}\Xi_{(nm)} - \Xi_{(kn)}\bar{D}^{(\cdot n)}_{(m\cdot)}\right]\partial_\xi\tilde{u}^{(m)}_1; \tag{6}$$
$$R_{(km)} = \left(\varrho(\zeta)\mathrm{p}_{(k)},\mathrm{p}_{(m)}\right)_1;\quad \varrho(\zeta) = f(\zeta)-(1-f(\zeta))\rho_{12};\quad \rho_{12} = \rho_1/\rho_2;\quad \eta = c_1/c_2;$$

$c_1^2 = (\lambda_1+2\mu_1)\rho_1^{-1}$, $c_2^2 = \mu_1\rho_1^{-1}$. The constraint equations (2) can be written for a graded plate as follows:

$$\left[\left(\eta^2-2\right)\partial_\xi\tilde{u}^{(k)}_1 + \eta^2\bar{D}^{(\cdot k}_{(n\cdot)}\tilde{u}^{(n)}_3\right]\mathrm{p}_{(k)}(\pm1) = 0;\quad \left(\bar{D}^{(\cdot k}_{(n\cdot)}\tilde{u}^{(n)}_1 + \partial_\xi\tilde{u}^{(k)}_3\right)\mathrm{p}_{(k)}(\pm1) = 0. \tag{7}$$

Substituting $\mathbf{u}^{(k)} = \mathbf{U}^{(k)}\exp[i(\kappa\xi-\omega\tau)]$ into (5, 6), we obtain the spectral problem for the power graded plate. The spectrum can be obtained as a solution of the constrained stationary values problem for two quadratic forms [8] accordingly to [1], by means of the Lagrange multiplier method [7], or transforming the system (5–7) to the generalized equations of Voronets type. The general formulation (5–7) is covariant, therefore it allows one to use any function system being a basis in Hilbert space over $[-1,1]$ as $\mathrm{p}_{(k)}(\zeta)$. The convergence of phase frequencies and waveforms computed for various wavenumbers and power law indices on the basis of polynomial and compact expansion functions are compared. The analogous formulation for shells, e. g. for cylindrical ones is slightly more complex; such equations are constructing using computer algebra software.

Acknowledgments This investigation is the part of the State Task for Basic Researches GP 14 (0050-2017-0001), the state register number AAAA-A17-117032010136-3, and partially supported by the RFBR under grant No. 16-01-00751-a.

References

[1] R. Underwood G. H. Golub Stationary values of the ratio of quadratic forms subject to linear constraints. *ZAMP*, 21:318–326, 1970.

[2] A. Idesman. Accurate finite-element modeling of wave propagation in composite and functionally graded materials. *Composite Structures*, 117:298–308, 2014.

[3] Ek. L. Kuznetsova, El. L. Kuznetsova, L. N. Rabinskiy, and S. I. Zhavoronok. On the equations of the analytical dynamics of the quasi-3d plate theory of I. N. Vekua type and some their solutions. *Journal of Vibroengineering*, 20(2):1108–1117, 2018.

[4] J. Yu, J. E. Lefebvre, and L. Elmaimouni. Guided waves in multilayered plates: An improved orthogonal polynomial approach. *Acta Mechanica Solida Sinica*, 27(5):542–550, 2014.

[5] S. I. Zhavoronok. A Vekua-type linear theory of thick elastic shells. *ZAMM*, 94(1-2):164–184, 2014.

[6] S. I. Zhavoronok. On the variational formulation of the extended thick anisotropic shells theory of I. N. Vekua type. *Procedia Engineering*, 111:888–895, 2015.

[7] S. I. Zhavoronok. A general higher-order shell theory based on the analytical dynamics of constrained continuum systems. In *Shell Structures: Theory and Applications*, volume 4, pages 189–192, Leiden, 2018. CRC Press / Balkema, Taylor & Francis Gr.

[8] S. I. Zhavoronok. On the use of extended plate theories of Vekua-Amosov type for wave dispersion problems. *International Journal for Computational Civil and Structural Engineering*, 14(1):36–48, 2018.

[9] M. Zheng, S. He, Y. Lu, and B. Wu. State-vector formalism and the Legendre polynomial solution for modelling guided waves in anisotropic plates. *Journal of Sound and Vibration*, 412:372–388, 2018.

A ROBUST SEMI-MIXED 4-NODE SHELL ELEMENTS WITH ASSUMED ASYMMETRIC STRAINS AND STRESS RESULTANTS

S. Burzyński[1], J.Chróścielewski[1], K. Daszkiewicz[1] and W. Witkowski[1]

[1]*Faculty of Civil and Environmental Engineering, Gdańsk University of Technology,*
e-mail: kardaszk@pg.edu.pl

1. Introduction

4-node shell finite elements are commonly used in nonlinear analysis of shell structures. Standard displacement shell elements with fully integrated matrices are prone to shear and membrane locking and the problem of spurious zero energy modes appears with reduced integration. Alternatively, hybrid mixed finite elements based on multi-field variational principles may be used. The formulation of effective shell element plays crucial role in fast and accurate analysis of complex shell structures. It was shown in papers [1,2] that mixed elements developed from the 3-field Hu-Washizu functional allow for very large load steps in comparison to other elements. The present semi-mixed elements are developed in the framework of a nonlinear 6-parameter shell theory [3], where the reference surface is formally equivalent to the Cosserat surface. Hence, the measures of strains and resultant stresses are asymmetric. Some semi-mixed shell elements with asymmetric assumed stresses were proposed in [4], yet for different shell theory. While interpolation of asymmetric strains and enhanced strains was described in [5,6]. Recently, effective mixed shell element with asymmetric independent fields of strains and stress resultants were proposed in [7,8]. Here, the preliminary results for robust 3-field semi-mixed elements are presented based on [8].

2. Element formulation

The semi-mixed elements were developed based on modified 3-field Hu-Washizu functional. In the element formulation only membrane and shear components of strains and resultant stresses were treated as independent. The components of assumed stress resultants were interpolated in the following way

(1) $\bar{N}^{11}_{\mathrm{A}} = \alpha_1 + \alpha_2\xi^*_2,\ \bar{N}^{22}_{\mathrm{A}} = \alpha_3 + \alpha_4\xi^*_1,\ \bar{N}^{12}_{\mathrm{A}} = \alpha_5,\qquad \bar{N}^{21}_{\mathrm{A}} = \alpha_6,\qquad \bar{Q}^{1}_{\mathrm{A}} = \alpha_7 + \alpha_8\xi^*_2,\ \bar{Q}^{2}_{\mathrm{A}} = \alpha_9 + \alpha_{10}\xi^*_1,$

(2) $\bar{N}^{11}_{\mathrm{B}} = \alpha_1 + \alpha_2\xi^*_2,\ \bar{N}^{22}_{\mathrm{B}} = \alpha_3 + \alpha_4\xi^*_1,\ \bar{N}^{12}_{\mathrm{B}} = \alpha_5 + \alpha_6\xi^*_2,\ \bar{N}^{21}_{\mathrm{B}} = \alpha_7 + \alpha_8\xi^*_1,\ \bar{Q}^{1}_{\mathrm{B}} = \alpha_9 + \alpha_{10}\xi^*_2,\ \bar{Q}^{2}_{\mathrm{B}} = \alpha_{11} + \alpha_{12}\xi^*_1,$

where $\xi^*_\alpha = \xi_\alpha - \bar{\xi}_\alpha$ are the so-called corrected natural coordinates, see [1]. Interpolation given by (1) was used in SMIX_A element, and by (2) in SMIX_B element. The first part of the strain field was interpolated in the same way as the stress field, while the second part according to EAS formulation, e.g. [6]. The ANS approach [9] was applied to transverse shear components of strains. The contravariant rule was used during transformation of resultant stresses and the first part of strains, while covariant rule for the second part of strains. The parameters for assumed stresses and strains were statically condensed at the element level.

3. Results

The proposed semi-mixed elements have correct rank and satisfy inf-sup condition and patch test. The performance of elements SMIX_A and SMIX_B was investigated by solving the well-known nonlinear test of pinched hemisphere with a hole. The geometry and material data are presented in Fig. 1a. Following [2] four times smaller shell thickness $h = 0.01$ was assumed to make example more prone to locking. The results for semi-mixed elements SMIX_A and SMIX_B were compared with the results for following 4-node shell elements: corresponding mixed elements MIX_A and MIX_B [7], enhanced strain element EANS4 [6] and semi-mixed element HW29 [2]. The computed nonlinear load-deflection curves are presented in Fig. 1b. The convergence rate is compared with the solutions obtained with alternative formulations in Table 1.

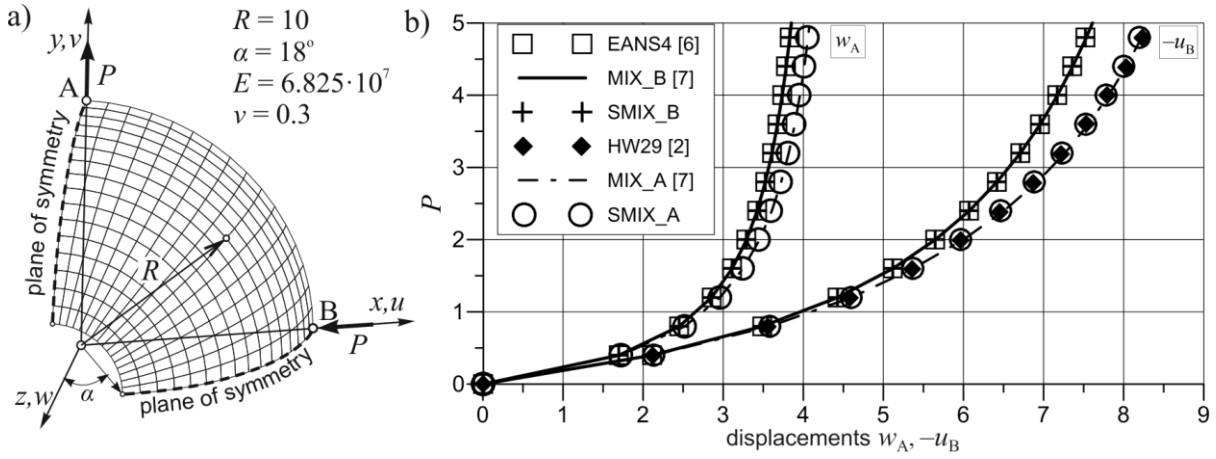

Figure 1: Pinched hemisphere with a hole, a) geometry, b) nonlinear equilibrium paths for 16×16 mesh.

Element	HW29	EANS4	MIX_A	MIX_B	SMIX_A	SMIX_B
Max ΔP	0.8	0.055	0.88	0.88	0.88	0.88
Total no. of iterations	61	518	30	38	33	36
CPU time [s]	-	856	32	40	28	31

Table 1: Comparison of maximum fixed load step ΔP, total number of iterations and process (CPU) time in nonlinear analysis for total load $P = 8.8$, 32×32 FE mesh (16×16 FE mesh for HW29).

4. Conclusions

The proposed semi-mixed shell elements require considerably less equilibrium iterations than elements EANS4 and HW29. The smaller number of independent parameters resulted in shorter CPU time than in the case of corresponding mixed elements [7]. The obtained equilibrium paths are in good agreement with the reference solutions. The element SMIX_B yield a slightly stiffer response than element SMIX_A.

Acknowledgments The research reported in this paper is supported by the National Science Centre, Poland with the grant UMO-2015/17/B/ST8/02190.

References

[1] W. Wagner and F. Gruttmann. A robust non-linear mixed hybrid quadrilateral shell element. *Int. J. Num. Meth. Eng.*, 64:635–666, 2005.
[2] K. Wisniewski and E. Turska. Four-node mixed Hu-Washizu shell element with drilling rotation. *Int. J. Num. Meth. Eng.*, 90:506-536, 2012.
[3] J. Chróścielewski, J. Makowski and W. Pietraszkiewicz. *Statics and dynamics of multifold shells: Nonlinear theory and finite element method* (in Polish), IPPT PAN Press, Warsaw, 2004.
[4] C. Sansour and H. Bednarczyk. The Cosserat surface as a shell model, theory and finite-element formulation. *Computer Methods in Applied Mechanics and Engineering*, 120:1–32, 1995.
[5] C. Sansour and J. Bocko. On hybrid stress, hybrid strain and enhanced strain finite element formulations for a geometrically exact shell theory with drilling degrees of freedom. *Int. J. Num. Meth. Eng.*, 43:175–192, 1998.
[6] W. Witkowski. 4-node combined shell element with semi-EAS-ANS strain interpolations in 6-parameter shell theories with drilling degrees of freedom. *Computational Mechanics*, 43(2):307–319, 2009.
[7] J. Chróścielewski, S. Burzyński, K. Daszkiewicz and W. Witkowski. Mixed 4-node shell element with assumed strain and stress in 6-parameter theory. *Shell Structures: Theory and Applications Vol. 4*, Pietraszkiewicz & Witkowski (eds), Taylor & Francis Group, London, 2018.
[8] K. Daszkiewicz. *A family of hybrid mixed elements in 6-parameter shell theory, geometrically nonlinear analysis of functionally graded shells*, *Doctoral Thesis* (in Polish), Gdańsk University of Technology, 2017.
[9] E. Dvorkin and K.-J. Bathe. A continuum mechanics based four node shell element for general nonlinear analysis. *Engineering Computations* 1:77–88, 1984.

ON BENDING OF A TWO-PHASE PLATE

V. A. Eremeyev[1] and V. Konopińska-Zmysłowska[1]

[1]*Gdańsk University of Technology, ul. Gabriela Narutowicza 11/12, 80-233 Gdańsk, Poland*

e-mail: eremeyev.victor@gmail.com; violetta.konopinska@pg.edu.pl

1. Introduction

Thin films made of shape memory alloys and polymers and other materials undergoing stress-induced phase transitions (PTs) constitute a new class of thin-walled structures, that is the two-phase plates and shells. For this class of shells the kinematics is complemented by additional state variables describing the phase change. Tubes, films, and plates made of martensitic materials are often used in MEMS as a basic working elements [3, 4]. Considering PTs in thin-walled structures and phase interfaces one may observe two cases of possible phase interfaces. The first case relates to the appearance and propagation of phase interfaces across the shell thickness, presented, e.g., in [8,9]. In this case the two-phase shell consists of two parts made of different phases separated by a phase interface curve. The second type of phase interfaces is that when the phase interface is almost parallel to the shell base surface, see, e.g., [11, 12]. Such two-phase shell treated as two-dimensional (2D) continuum within the so-called phase field approach as at any point both phases may exist.

For the first type of phase interfaces the phase equilibrium conditions in shells were established in [5] using variational approach within the six-parameter shell theory and were extended for thermo- and visco-elastic materials in [6, 7]. The background of the six-parameter shell model was developed in [10]. The aim of the lecture is to discuss the possible reduction techniques to the two-phase plates.

2. Equilibrium and quasistatic deformations 3D solids undergoing PTs

Following [1, 2] we briefly recall the compatibility conditions on a coherent phase interface in nonlinear elastic solids. In addition to the balances of stresses we have an additional thermodynamic condition which is required for the determination of a priori unknown phase interface $\mathcal{C}$. For statics the condition is given by

$$[\![\mathbf{n}\cdot\mathbf{Bn}]\!]=0,\quad \mathbf{B}=W\mathbf{1}-\mathbf{P}\mathbf{F}^T, \tag{1}$$

where the double brackets denote the discontinuity jump of $\mathbf{n}\cdot\mathbf{Bn}$ across the phase interface, $\mathbf{B}$ is the Eshelby tensor, W the strain energy tensor, $\mathbf{P}$ the first Piola-Kirchhoff stress tensor, $\mathbf{F}=\nabla\mathbf{x}$ the deformation gradient, $\mathbf{x}$ is the position vector in an actual configuration, $\mathbf{n}$ the unit normal to $\mathcal{C}$, and $\mathbf{1}$ is the unit tensor. For quasistatic deformations instead of (1) we use the kinetic equation that is a relation between of the velocity V of the phase interface and the jump of $\mathbf{B}$ [2]

$$V=\Upsilon\left([\![\mathbf{n}\cdot\mathbf{Bn}]\!]\right). \tag{2}$$

Here Υ is a kinetic function, $\Upsilon(0)=0$. As a result, the boundary-value problem for solids undergoing PTs includes additional equations required for the determination of the position of the phase interface, that is the vector $\mathbf{x}_C$ which is independent on $\mathbf{x}$, in general.

3. Thermodynamic compatibility conditions for shells

The 2D analogues of (1) and (2) were established in [5–7], where the sharp interface model was assumed. In other words we consider a two-phase shell as a material surface consisting of two phases separated by smooth and a priori unknown phase interface $\mathcal{L}$. As a result, the thermodynamic compatibility condition for shells has

the form (2) with new 2D Eshelby tensor $\mathbf{B}$ defined as

$$\mathbf{B} = U\mathbf{A} - \mathbf{N}^T\mathbf{F}_s^T - \mathbf{M}^T\mathbf{K}^T, \tag{3}$$

where U is the surface strain energy density, $\mathbf{N}$ and $\mathbf{M}$ are the surface stress measures of the 1st Piola-Kirchhoff type, $\mathbf{F}_s$ is the surface deformation gradient, $\mathbf{K}$ is the bending strain, and $\mathbf{A} = \mathbf{1} - \mathbf{n} \otimes \mathbf{n}$, see [5, 7] for details.

The 2D sharp interface model based on kinetic equation (2) with (3) can describe various peculiarities of PTs in thin-walled structures such as hysteresis loop [6, 7]. On the other hand for some kind of deformations of shell-like solids the new phase can appear as a layer, so instead of homogeneous shell we have layered structure, see, e.g., Fig. 1. Thus, one needs another 2D model of two-phase shells.

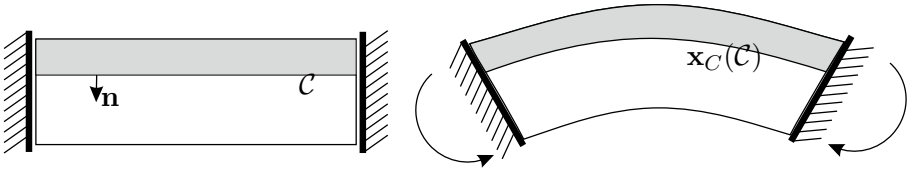

Figure 1: Deformation of a two-phase plate under bending: initial and bent configurations.

In order to describe the bending deformations of a plate undergoing PT, we utilize two approaches. The first approach is based on 3D analysis and the Eshelby tensor $(1)_2$. The position of $\mathcal{C}$ follows from the minimization of the energy functional. Then $\mathbf{N}$ and $\mathbf{M}$ have to be determined using the through-the-thickness integration. As a result, we get rather complex nonlinear problem. In particular, $\mathbf{N}$ and $\mathbf{M}$ became functionals of a priori unknown phase interface position. The second approach is based on the layer-wise model of the plate. We treat a plate undergoing bending as set of thin layers for each layer we introduce the 2D Eshelby tensor $\mathbf{B}_z$ such as given by (3). The criterion of PT is the value of $[\![\mathbf{n} \cdot \mathbf{B}_z\mathbf{n}]\!]$ in zth layer. This approach can be also more useful for multilayered films with thin layers made of different materials undergoing PTs. Few examples will be discussed during SOLMECH2018.

ACKNOWLEDGMENTS V. Konopińska-Zmysłowska is supported by the National Centre of Science of Poland with the grant DEC – 2012/05/D/ST8/02298.

References

[1] R. Abeyaratne and J. K. Knowles. *Evolution of Phase Transitions. A Continuum Theory*. Cambridge University Press, Cambridge, 2006.

[2] A. Berezovski, J. Engelbrecht, and G. A. Maugin. *Numerical Simulation of Waves and Fronts in Inhomogeneous Solids*. World Scientific, New Jersey et al., 2008.

[3] K. Bhattacharya and R. D. James. A theory of thin films of martensitic materials with applications to microactuators. *Journal of the Mechanics and Physics of Solids*, 47(3):531–576, 1999.

[4] K. Bhattacharya and R. D. James. The material is the machine. *Science*, 307(5706):53–54, 2005.

[5] V. A. Eremeyev and W. Pietraszkiewicz. The non-linear theory of elastic shells with phase transitions. *Journal of Elasticity*, 74(1):67–86, 2004.

[6] V. A. Eremeyev and W. Pietraszkiewicz. Phase transitions in thermoelastic and thermoviscoelastic shells. *Archives of Mechanics*, 61(1):41–67, 2009.

[7] V. A. Eremeyev and W. Pietraszkiewicz. Thermomechanics of shells undergoing phase transition. *Journal of the Mechanics and Physics of Solids*, 59(7):1395–1412, 2011.

[8] P. Feng and Q. P. Sun. Experimental investigation on macroscopic domain formation and evolution in polycrystalline NiTi microtubing under mechanical force. *Journal of the Mechanics and Physics of Solids*, 54(8):1568–1603, 2006.

[9] Z. Q. Li and Q. P. Sun. The initiation and growth of macroscopic martensite band in nano-grained NiTi microtube under tension. *International Journal of Plasticity*, 18(11):1481–1498, 2002.

[10] A. Libai and J. G. Simmonds. *The Nonlinear Theory of Elastic Shells*. Cambridge University Press, Cambridge, 2nd edition, 1998.

[11] A. Roytburd and J. Slutsker. Coherent phase equilibria in a bending film. *Acta Materialia*, 50(7):1809–1824, 2002.

[12] A. L. Roytburd and J. Slutsker. Theory of multilayer SMA actuators. *Materials Transactions*, 43(5):1023–1029, 2002.

ON NON-LINEAR RESULTANT THEORY OF SHELLS ACCOUNTING FOR THERMODIFFUSION

V. A. Eremeyev[1] and W. Pietraszkiewicz[1]

[1]*Gdańsk University of Technology, ul. Gabriela Narutowicza 11/12, 80-233 Gdańsk, Poland*

e-mail: eremeyev.victor@gmail.com

1. Introduction

Many different approaches to formulate thermodiffusion theories in 3D bodies have been developed in the literature, see the historical review [4]. In engineering applications to shell structures one needs a 2D model of thermodiffusion based on laws of 3D continuum thermodynamics [5, 7]. Among many important phenomena in shells to be described by such a 2D model is, for example, the transient hydrogen and heat diffusion. It embrittles the materials of shell structures used for hydrogen production, storage and distribution and significantly affects the behaviour of the structures. Another example is the moisture sorption in shell structures made of polymeric materials and composites which may considerably change the prediction of moisture transport processes in shells.

To formulate the 2D model of shell thermodiffusion we apply the direct through-the-thickness integration [1–3] of 3D laws of continuum thermodiffusion [5, 7].

2. Basic 3D relations of non-linear thermodiffusion in solids

Let P with boundary ∂P be a part of the body B in the reference placement. Then thermodiffusion phenomena in 3D bodies are governed by five integral laws of continuum thermodiffusion, which are some extension of those given in [5, 7]. These laws are: balances of body mass, of mass of diffusing medium, of linear and angular momenta, and of energy as well as the entropy imbalance. When the mass production within the body and all inertia effects are disregarded, and then influence of diffusing medium is properly accounted for, these laws in the Lagrangian description relative to the reference placement are:

$$\frac{d}{dt}\iiint\limits_P \rho\,\mathrm{d}v = 0, \quad \frac{d}{dt}\iiint\limits_P c\,\mathrm{d}v + \iint\limits_{\partial P} \mathbf{n}\cdot\mathbf{j}\,\mathrm{d}a = 0, \tag{1}$$

$$\iiint\limits_P \rho\mathbf{b}\,\mathrm{d}v + \iint\limits_{\partial P} \mathbf{P}\mathbf{n}\,\mathrm{d}a = \mathbf{0}, \quad \iiint\limits_P \mathbf{y}\times\rho\mathbf{b}\,\mathrm{d}v + \iint\limits_{\partial P} \mathbf{y}\times\mathbf{P}\mathbf{n}\,\mathrm{d}a = \mathbf{0}, \tag{2}$$

$$\frac{d}{dt}\iiint\limits_P \rho\epsilon\,\mathrm{d}v = -\iint\limits_{\partial P} \mathbf{n}\cdot\mathbf{q}\,\mathrm{d}a + \iiint\limits_P (\rho r + \mathbf{P}\bullet\mathrm{Grad}\mathbf{y})\,\mathrm{d}v, \tag{3}$$

$$\frac{d}{dt}\iiint\limits_P \rho\eta\,\mathrm{d}v \geq -\iint\limits_{\partial P} \frac{1}{\theta}\mathbf{n}\cdot\mathbf{h}\,\mathrm{d}a + \iiint\limits_P \frac{\rho r}{\theta}\,\mathrm{d}v. \tag{4}$$

In the 3D laws given above, ρ and c are the referential mass (densities) of the body and of diffusing medium, $\mathbf{b}$, ε, r and η are the body force, the internal strain energy, the heat supply and the entropy, all per unit mass of B, $\mathbf{P}$ is the Piola stress tensor field, $\mathbf{n}$ is the exterior unit normal vector of ∂P, $\mathbf{y}$ is the position vector of deformed body relative to an inertial frame, while $\mathbf{j}$, $\mathbf{q}$ and $\mathbf{h}$ are the fluxes of diffusing medium, of contact heat and of entropy through the boundary ∂P, respectively.

With standard assumptions from (1)–(4) we get the local Lagrangian balance relations. In particular, the local

diffusion equation takes the form

$$\frac{dc}{dt} + \mathrm{Div}\mathbf{j} = 0. \tag{5}$$

Hereinafter Grad and Div are Lagrangian gradient and divergence operators, respectively.

In what follows we are restricting ourselves by nonlinear thermoelastic solids. We introduce the free energy density $\psi = \epsilon - \theta\eta$ which has the form $\psi = \psi(\mathrm{Grad}\mathbf{y}, \theta, c)$. In addition we represent the energy flux $\mathbf{q}$ as follows $\mathbf{q} = \mathbf{h} + \mu\mathbf{j}$, where $\mu = \frac{\partial\psi}{\partial c}$ is the chemical potential. As a result, the global Clausius-Duhem inequality (4) transforms into the local inequality

$$(\mathrm{Grad}\mu) \cdot \mathbf{j} + \frac{1}{\theta^2}\mathbf{h} \cdot \mathrm{Grad}\theta \geq 0.$$

All local relations following from (5)–(4) should be complemented by initial and boundary conditions. In particular, for c we assume the following boundary condition $\mathbf{n} \cdot \mathbf{j} = k(c - c^0)$, where k and c^0 are the diffusion parameter and concentration in an environment of the solid.

3. Reduction of 3D problem to 2D equations of shell thermodiffusion

In the shell-like body B, the boundary surface ∂B consists of three parts: the upper M^+ and the lower M^- shell faces as well as the lateral boundary surface ∂B^*. Then the position vector $\mathbf{x}$ of B is described by $\mathbf{x} = \boldsymbol{x} + \zeta\boldsymbol{n}$, where $\boldsymbol{x}$ is the position vector of some shell base surface M, $\boldsymbol{n}$ is the unit normal vector orienting M, and $\zeta \in [-h^-, h^+]$. Each part $P(t)$ of the deformed shell-like body can be represented by a part $\mathit{\Pi}(t)$ of $M(t)$ defined by a position vector $\boldsymbol{y}(t)$. Applying the exact through-the-thickness integration [2, 6] of all 3D fields present in 3D laws of thermodiffusion given above, we can introduce uniquely the corresponding 2D fields now given entirely on M. Then following involved but straightforward transformations, all 3D laws of thermodiffusion can be reduced to their 2D representations, which can be regarded as exact implications of the 3D global laws. When 2D laws are supplemented by corresponding boundary and initial conditions, such resultant 2D initial-boundary-value problem for shell thermodiffusion becomes a direct extension of the resultant 2D model of shell thermodynamics developed in [2, 6]. As for the temperature, we introduce two surface diffusion-related fields which are related to the mean values of c and its gradient. As a result, instead of (5) we get two 2D equations for diffusion in shells.

As an example, we consider the hydrogen diffusion in pipelines in the special case of axisymmetric deformation and stress-assisted diffusion of a circular tube, [8].

References

[1] J. Chróścielewski, J. Makowski, and W. Pietraszkiewicz. *Statics and Dynamics of Multyfolded Shells: Nonlinear Theory and Finite Elelement Method (in Polish)*. Wydawnictwo IPPT PAN, Warszawa, 2004.

[2] V. A. Eremeyev and W. Pietraszkiewicz. Thermomechanics of shells undergoing phase transition. *J. Mech. Phys. Solids*, 59(7):1395–1412, 2011.

[3] A. Libai and J. G. Simmonds. *The Nonlinear Theory of Elastic Shells*. Cambridge University Press, Cambridge, 2nd edition, 1998.

[4] H. Mehrer and N. A. Stolwijk. Heroes and highlights in the history of diffusion. *Diffusion-fundamentals.org*, 11(1):1–32, 2009.

[5] W. Nowacki and Zb. Olesiak. *Thermodiffusion in Solids (in Polish)*. PWN, Warszawa, 1991.

[6] W. Pietraszkiewicz. Refined resultant thermomechanics of shells. *Int. J. Engng Sci.*, 49(10):1112–1124, 2011.

[7] Ya. S. Podstrigach and Ya. Z. Povstenko. *Introduction to Mechanics of Surface Phenomena in Deformable Solids (in Russian)*. Naukova Dumka, Kiev, 1985.

[8] Y. Weitsman. Stress assisted diffusion in elastic and viscoelastic materials. *J. Mech. Phys. Solids*, 35(1):73–93, 1987.

THE INTERRELATION OF STATICALLY EXACT AND CONVENTIONAL SHELL THEORIES

R. Winkler

Department of Mechatronics, University of Innsbruck, Technikerstrasse 13, Innsbruck, Austria

e-mail: robert.winkler@uibk.ac.at

1. Overview

The essential distinctive feature of statically exact and conventional shell theories is the existence of drill moments and drill rotations which are present in the former and absent in the latter. The present contribution immerses into the formulation of prototypical theories, addresses their individual shortcomings, and proposes related remedies in some generality. Therefore it is postulated that both theories shall lead to the same results as long as no external drill moments and no boundary conditions related to the drill rotations are applied. This postulate is supported by the observation that the drill moments can be eliminated from the statically exact balance equations to obtain a set of equations which formally coincide with the ones of the 'canonical' linear shell theory. Remarkably, these equations are obtained *without* the application of any approximate assumption. This considerations lead to a novel constitutive relation which couples the antisymmetric part of the membrane forces and the drill moment components. The parameters involved in this relation can be determined such that the non-standard strains do not produce extra strain energy, which guarantees that the initial postulate is satisfied. It is emphasized that there are no tuning parameters involved. This newly introduced coupling turns out to be essential to achieve correct results for some in-plane bending problems. Further numerical results of prominent benchmark problems confirm the general serviceability of the proposed constitutive law.

2. General

Shell theory has a long history with many doubts and discussions about the 'best' way to obtain an essentially two-dimensional description of an inherently three-dimensional (3D) structure. In particular, two well-established theories have emerged from this process, which are commonly agreed and have proved to be well-suited for the derivation of numerical procedures. In both cases, the shell balance equations are derived from the 3D balance laws giving rise to the definition of resultant shell forces $\mathbf{n}^\alpha$ and moments $\mathbf{m}^\alpha$, where the $\alpha = 1, 2$ refer to the two lateral directions $\mathbf{a}_1$ and $\mathbf{a}_2$. A *statically exact* theory is characterized by the fact that no approximations are involved in this derivation, see [1] and references therein. In contrast, 'conventional' shell theories are of the *first-order shear deformation* (FOSD) type relying on the Reissner-Mindlin kinematic assumption, see [2] for a contemporary treatment of the topic. With other words, warping of transverse material fibres is allowed in the former and prohibited in the latter case, where it gives rise to the definition of a distinguished transverse direction $\mathbf{g}_3$, not necessarily coinciding with the geometric normal direction $\mathbf{a}_3$. In the statically exact case there is no such direction other than $\mathbf{a}_3$ and so-called drill moments $m^{3\alpha} = \mathbf{a}^3 \cdot \mathbf{m}^\alpha$ naturally enter the theory, whilst the relevant transverse component $\mathbf{g}^3 \cdot \mathbf{m}^\alpha = 0$ in the FOSD case. The shell strains $\boldsymbol{\varepsilon}_\alpha$ and curvatures $\boldsymbol{\kappa}_\alpha$ are defined to be the work conjugate counterparts of $\mathbf{n}^\alpha$ and $\mathbf{m}^\alpha$, respectively. They rely on non-symmetric Biot strains in the statically exact and on symmetric Green-Lagrange strains in the FOSD case. The exact role of the kinematic variables is discussed in the presentation. It is frequently ignored that even membrane deformations come along with a warping of transverse material fibers due to the Poisson effect, as long as drill strains $\kappa_{3\alpha} = \mathbf{a}_3 \cdot \boldsymbol{\kappa}_\alpha$ occur. The primary variables are constituted of displacements and rotations. Roughly speaking, three/two rotational degrees of freedom (dofs) are required to specify the orientation of a curved/straight material fiber, respectively. In the latter case, the rotational dofs immediately refer to the orientation of the transverse material fiber indicated by $\mathbf{g}_3$. In the former case, $\mathbf{Q}$ represents an averaged rotation, which does *not* necessarily coincide with the rotation of a specific material point. This is basically the reason why the $\mathbf{g}_3$ is the only feasible choice for the transverse basis vector in FOSD theories. In contrast, for statically exact theories the geometrical normal direction $\mathbf{a}_3$ can serve as a transverse basis vector in a natural way, and the benefits of differential geometry apply. On the other hand, statically exact theories come along with practical drawbacks. In the geometrically linear case, membrane states of stress are commonly considered

to be statically determinate. This is no longer the case in the context of theories involving drill moments. Generally, the question arises which constitutive relation applies to the drill moments. Even for the simplest cases this question has remained a matter of ambiguity so far.

3. Equilibrium equations

Referring to the basis $(\mathbf{a}_\alpha, \mathbf{a}_3)$, the balance equations of the statically exact theory read

$$(1) \qquad \begin{cases} n^{\beta\alpha}|_\alpha - b^\beta_\alpha\, n^{3\alpha} + p^\beta = 0\,, & n^{3\alpha}|_\alpha + b_{\alpha\beta}\, n^{\beta\alpha} + p^3 = 0 \\ m^{\beta\alpha}|_\alpha - n^{3\beta} - \epsilon^{\beta\gamma}\, b_{\alpha\gamma}\, m^{3\alpha} + l^\beta = 0\,, & m^{3\alpha}|_\alpha - \epsilon_{\beta\gamma}\big(n^{\beta\gamma} + b^\beta_\alpha\, m^{\gamma\alpha}\big) + l^3 = 0 \end{cases}$$

with p^α, p^3 and l^α, l^3 being the distributed external forces and moments, respectively, $b_{\alpha\beta}$ and $\epsilon_{\alpha\beta}$ the components of curvature and permutation tensor referring to the deformed configuration. The common notations and conventions of Ricci calculus are applied. Introducing *effective* membrane and shear forces, $\hat{n}^{\beta\alpha} := n^{\beta\alpha} - \epsilon^{\mu\alpha}\, m^{3\beta}|_\mu$ and $\hat{n}^{3\alpha} := n^{3\alpha} + \epsilon^{\alpha\mu}\, b_{\beta\mu}\, m^{3\beta}$, respectively, the drill moments $m^{3\alpha}$ can be eliminated and the balance equations transform into

$$(2) \qquad \begin{cases} \hat{n}^{\beta\alpha}|_\alpha - b^\beta_\alpha\, \hat{n}^{3\alpha} + p^\beta = 0\,, & \hat{n}^{3\alpha}|_\alpha + b_{\beta\alpha}\, \hat{n}^{\beta\alpha} + p^3 = 0 \\ m^{\beta\alpha}|_\alpha - \hat{n}^{3\beta} + l^\beta = 0\,, & \epsilon_{\beta\alpha}\big(\hat{n}^{\beta\alpha} + b^\alpha_\mu\, m^{\beta\mu}\big) + l^3 = 0 \end{cases}$$

It is emphasized that the balance equations (2) are fully nonlinear, but formally coincide with the balance equations of the linear FOSD theory, if no external drill moments are applied, i.e. $l^3 = 0$. Note that analogous component equations can *not* be obtained from the geometrically nonlinear FOSD approach, due to the mentioned restrictions concerning the choice of the basis vectors.

4. Constitutive law

For $l^3 = 0$, the effective *pseudo* membrane forces $\hat{\tilde{n}}^{\beta\alpha} := \hat{n}^{\beta\alpha} + b^\alpha_\mu\, m^{\beta\mu}$ are symmetric. Consequently, conventional constitutive equations can be applied for the effective variables. The standard pseudo membrane forces $\tilde{n}^{\beta\alpha} := n^{\beta\alpha} + b^\alpha_\mu\, m^{\beta\mu}$ need not being symmetric any more. For a membrane state of stress and geometric linearity, the symmetric $\hat{\tilde{n}}^{\beta\alpha}$ are uniquely determined by the equilibrium equations (2) and thus coincide with the membrane forces of the conventional theory. This observation together with the definition of the $\hat{\tilde{n}}^{\beta\alpha}$ have an important impact on the possible structure of the constitutive relation from which the antisymmetric part of the membrane forces, $n^{[12]}$, and the $m^{3\alpha}$ result. The simplest possible choice is given by

$$(3) \qquad \begin{bmatrix} \tilde{n}^{[12]} \\ m^{31} \\ m^{32} \end{bmatrix} = tG \begin{bmatrix} \beta & \delta\, l_c & -\delta\, l_c \\ \delta\, l_c & \gamma\, l_c^2 & 0 \\ -\delta\, l_c & 0 & \gamma\, l_c^2 \end{bmatrix} \begin{bmatrix} \varepsilon_{[12]} \\ \kappa_{31} \\ \kappa_{32} \end{bmatrix}$$

with G being the in-plane shear modulus. The elastic energy produced by the non-standard strains $\varepsilon_{[12]} := \frac{1}{2}\,(\varepsilon_{12} - \varepsilon_{21})$ and $\kappa_{3\alpha}$ is minimum if the related stiffness matrix is nearly singular, i.e. if $\delta \approx \sqrt{\beta\gamma/2}$. The appearance of a characteristic length l_c reflects the fact that (3) is a localized form of a relation which is, in principle, non-local. The l_c can be chosen as a typical lateral dimension of the problem and is *not* related to the shell thickness t. For finite element calculations, the square root of the element area has turned out to be a feasible choice. Then, the independent, dimensionless parameters can vary in a large range without affecting the numerical results, i.e. $10^{-2} \leq \beta \leq 10^6$ and $10^{-8} \leq \gamma \leq 10^{-3}$, as long as δ obeys the relation given above. The parameter β can be interpreted as a penalty parameter enforcing the drill rotation to coincide with the in-plane material rotation, whereas γ plays the role of a (small) stabilization parameter.

References

[1] J. Chróścielewski, J. Makowski, and H. Stumpf. Genuinely resultant shell finite elements accounting for geometric and material non-linearity. *Int. J. Num. Meth. Eng.*, 35:63–94, 1992.

[2] J. C. Simo and D. D. Fox. On a stress resultant geometrically exact shell model. Part I: Formulation and optimal parameterization. *Comput. Methods Appl. Mech. Eng.*, 72:267–304, 1989.

NONLINEAR FEA OF VIBRATION CONTROL OF PIEZOELECTRIC ROD-TYPE STRUCTURAL MEMBERS

J. Chróścielewski[1], V. A. Eremeyev[1], R. Schmidt[2]

[1] *Gdańsk University of Technology, ul. Narutowicza 11/12, Gdańsk, Poland*
[2] *RWTH Aachen University, Kackertstraße 9, Aachen, Germany*

e-mail: jchrost@pg.gda.pl

1. Introduction

This lecture addresses modelling and finite element analysis of the transient large amplitude vibration response of thin rod-type structures with piezoelectric layers. We present the analysis of two problems that are the FE analyses of a clamped semicircular ring and a smart circular arch subjected to a hydrostatic pressure. The presented results are based on the paper [1].

2. Geometrically nonlinear theory of plane piezolaminated rods and numerical method

We consider the planar deformation of a naturally curved plane rod with integrated piezoelectric layers. The analysis is based on the Bernoulli theory of plane deformations of beams, which is rich enough to accommodate the longitudinal extension and flexure neglecting the transverse shear strains. In the framework of the present theory, the deformation of the rod is completely determined by two components of the displacement vector $\boldsymbol{u}(s)$ at the rod axis. Within the through-the-thickness integration we introduce the normal stress resultant N and the bending couple M, which are work-conjugate to the 2D strain measures ε and κ. We formulate the virtual work principle

$$G[\boldsymbol{u},t;\delta\boldsymbol{u}] \equiv \int_{s_b}^{s_a} (\delta\varepsilon N + \delta\kappa M)\,\mathrm{d}s - G_e + G_b = 0 \tag{1}$$

for every kinematically admissible virtual displacement field $\delta\boldsymbol{u}(s)$ and every time $t > 0$. Here G_e and G_b are the work of inertia and external forces, respectively, $s \in [s_a, s_b]$ denotes the arc length coordinate along the undeformed rod axis. In what follows Eq. (1) serves as the basis for a finite element formulation.

For numerical calculations we use the 1D 2 – node C^1-element with four degrees of freedom at each node. Using the linearization and the standard FEM approximation procedures we get the classical incremental form of the equations of motion

$$\mathbf{M}\,\Delta\ddot{\mathbf{q}} + \mathbf{C}_t\,\Delta\dot{\mathbf{q}} + [\mathbf{K}_T - \mathbf{K}_L]\Delta\mathbf{q} = \Delta\mathbf{p} + \mathbf{j}_t\,, \tag{2}$$

where, $\mathbf{K}_T(\mathbf{q}_t)$ is the tangential stiffness matrix, $\mathbf{K}_L(\mathbf{q}_t)$ is the load matrix, $\mathbf{q}^{\mathrm{T}} = \{\mathbf{u}_{(1)}\ \mathbf{u}_{(2)} \ldots \mathbf{u}_{(a)} \ldots\}$, denote the global vectors of nodal displacements, and $\Delta\mathbf{p} \equiv \mathbf{p}_{t+\Delta t} - \mathbf{p}_t$ is the vector of load increments. Eq. (2) is solved in the time domain by the Newmark method of time integration, see [1] for details.

3. Numerical Results

We discuss the static and dynamic behaviour of two thin three-layered structures: a laminated semicircular ring shell and a circular arch with piezoelectric patches within the geometrically nonlinear range of deformation, see Figure 1. Some results of the control of the ring is given in Figure 2 whereas the buckling analysis of the arch is presented in Figure 3, see [1] for more details.

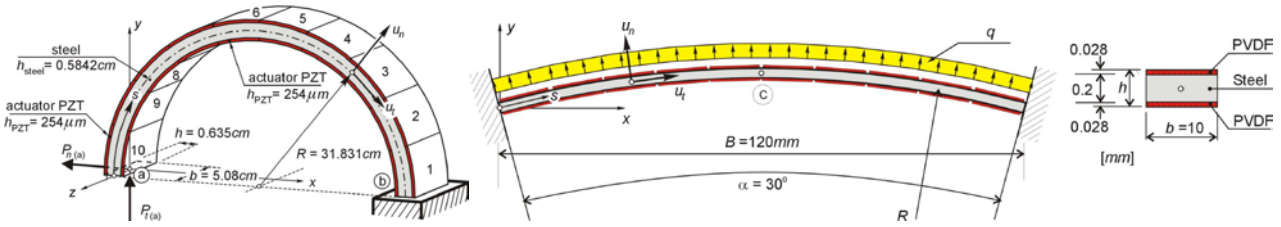

Figure 1: Laminated semicircular ring shell and circular arch with piezoelectric patches.

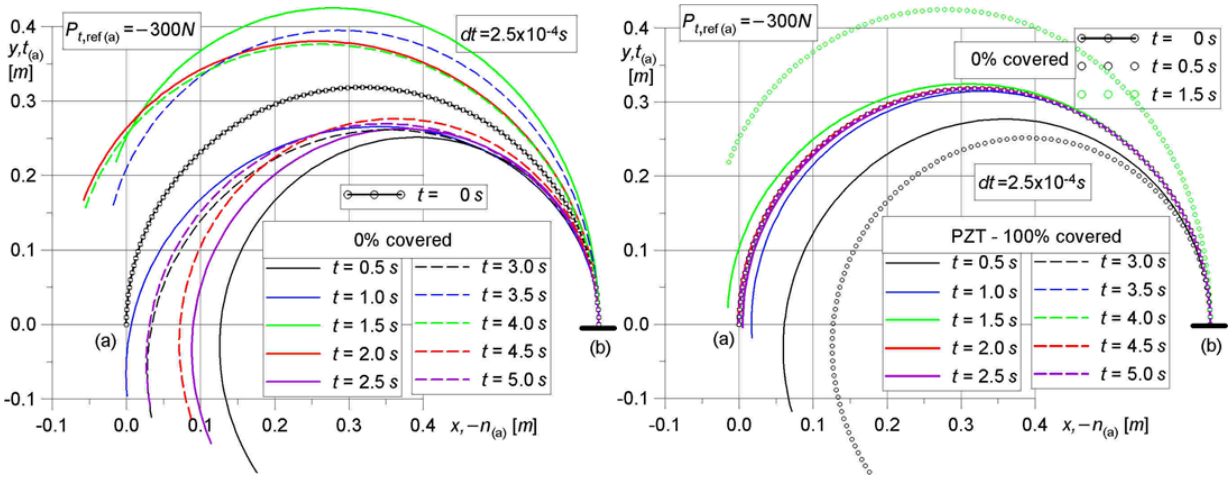

Figure 2: Uncontrolled (on the left) and controlled (on the right) responses of the ring tip, sequence of the deformed configurations.

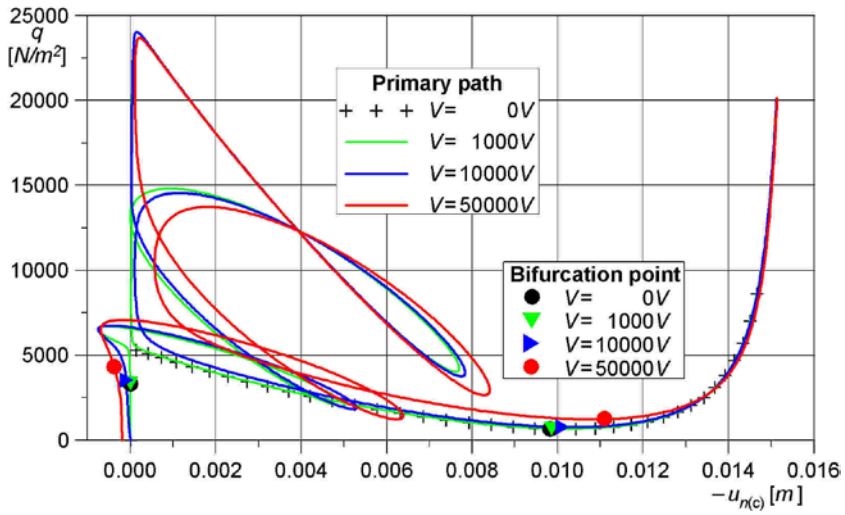

Figure 3: Load versus normal displacement in the middle point of the arch

References

[1] J. Chróścielewski, R. Schmidt, and V. A. Eremeyev. Nonlinear finite element modeling of vibration control of plane rod-type structural members with integrated piezoelectric patches. *Continuum Mechanics and Thermodynamics*. DOI: 10.1007/s00161-018-0672-4, 2018.

COMPARISON OF SOME LOW-ORDER GEOMETRICALLY EXACT SHELL FINITE ELEMENTS

M. Lavrenčič[1], B. Brank[1]

[1]*Faculty of Civil and Geodetic Engineering, University of Ljubljana, Ljubljana, Slovenia*
e-mail: marko.lavrencic@fgg.uni-lj.si

Description of the work

Low-order (e.g. 4-node) shell finite elements with nonlinear Reissner-Mindlin kinematics (that assumes one inextensible director shell field) are the basic shell finite elements of any commercial finite element code. However, there has been still research going on in order to find an optimal 4-node nonlinear shell finite element of such kind. Mixed variational principles and their modifications have been used for that purpose. In this work, we compare several 4-node large rotations finite element formulations that have been recently published in [2]-[5], [8] and [9]. The formulations are based either on Hellinger-Reissner functional, on Hu-Washizu functional, or on modified versions of Hu-Washizu functional (e.g. ANS (Assumed Natural Strain) and EAS (Enhanced Assumed Strain) concepts) for the membrane, the bending and the shearing parts of the shell response. As for the material models, the St. Venant-Kirchhoff hyperelasticity is considered and the inelastic formulations are under development. Large rotations are described in the same manner for all formulations. The comparison is done by numerical experiments, i.e. by performing an extensive set of standard shell benchmark tests and also some newly proposed tests. Numerical experiments show that some of the formulations are considerable faster than others (since they allow for much larger load increments), and some are more robust. Surprisingly, for some tests, the formulations produce quite different qualitative results for the same mesh.

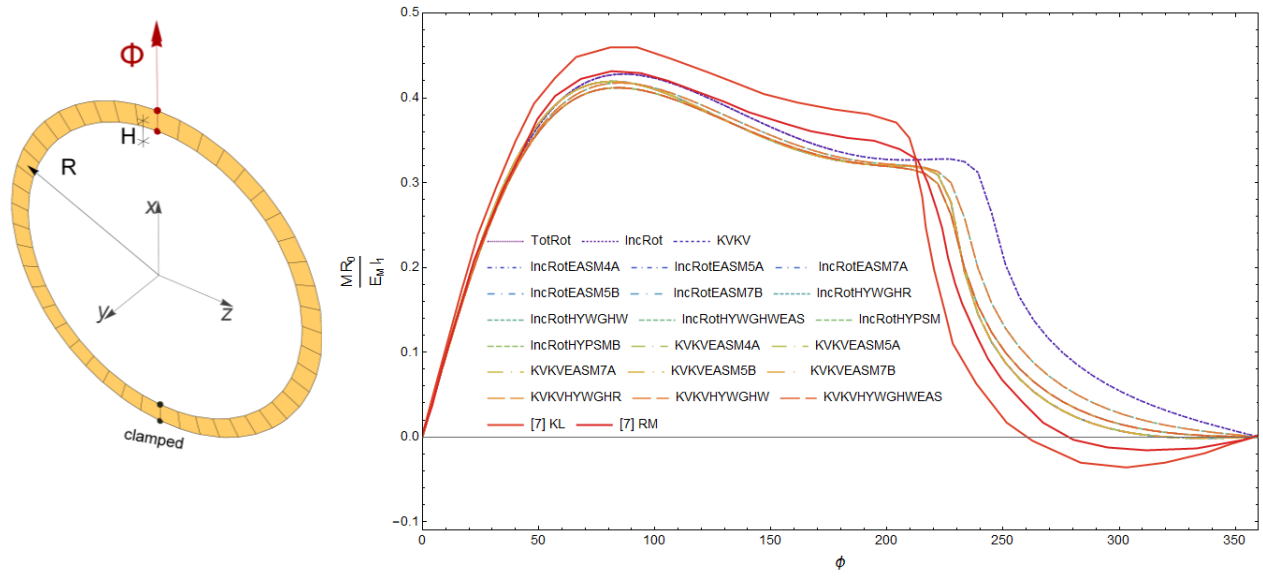

$R = 20,\ H = \frac{1}{3},$ thickness $th = 1, E = E_M = 21000, \nu = 0.2, \Phi_{final} = 2\,\pi$

Figure 1: Input data and response graph for the "snap-through of an elastic ring" example.

Finite elements

We considered the following large rotation formulations: additive update of the total rotation vector (marked as TotRot in the Figures 1 and 2), additive update of the incremental rotation vector (IncRot), and rotation update by using quaternions (KVKV). As for the 4-node elements, we considered the following formulations. (i) An EAS improvement of the membrane part with 4 (EASM4), 5 (EASM5) and 7 (EASM7) parameters [1], [2]. (ii) Hybrid Hu-Washizu formulation for membrane, bending and shear parts (HYWGHW) [4]. (iii) Hybrid

Hellinger-Reissner formulation for membrane, bending and shear parts (HYWGHR) [3]. (iv) Hybrid Hu-Washizu formulation for membrane, bending and shear parts, enhanced with EAS formulation for the membrane part (HYWGHWEAS) [5]. (v) Hybrid Hellinger-Reissner formulation with Pian-Sumihara interpolation [6] for the membrane part (HYPSM) [6]. (vi) Hybrid Hellinger-Reissner formulation with Pian-Sumihara interpolation for the membrane and bending parts (HYPSMB) [6]. (vii) MITC formulation [9]. For the interpolation of the transverse shear strains, the ANS concept [9] was applied for all formulations.

Results

In Figs. 1 and 2, we show results for two examples. It can be seen, that for these two examples, the elements produce quite different qualitative results for the same mesh.

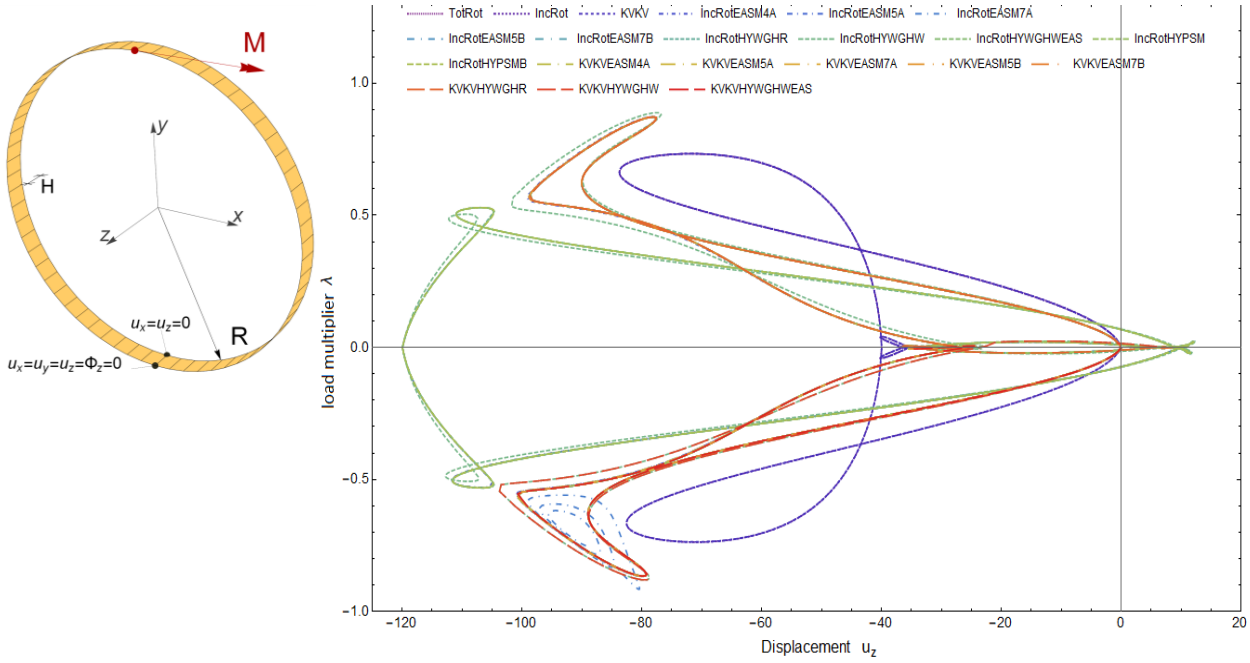

$R = 30,\ H = 1,$ thickness $th = 1\,,\ E = 21000\ \nu = 0.2, M = 250, u_z$ is displacement of node with applied moment

Figure 2: Input data and response graph for the "jumping rope" example.

References

[1] U. Andelfinger and E. Ramm, EAS-elements for two dimensional, three dimensional, plate and shell structures and their equivalence to HR-elements, *International journal for numerical methods in engineering*, 36: 1311-1337, 1993.

[2] B. Brank, Assessment of 4-node EAS-ANS shell elements for large deformation analysis, *Computational mechanics*, 42: 39-51, 2008.

[3] F. Gruttmann and W. Wagner, A linear quadrilateral shell element with fast stiffness computation, *Computer Methods in Applied Mechanics and Engineering* 194: 4279-4300, 2005.

[4] W. Wagner and F. Gruttmann, A robust non-linear mixed hybrid quadrilateral shell element, *International journal for numerical methods in engineering,* 64: 635-666, 2005.

[5] F. Gruttmann and W. Wagner, Structural analysis of composite laminates using a mixed hybrid shell element, *Comput. Mech.,* 37: 479–497, 2006.

[6] T. H. H. Pian and K. Sumihara, Rational approach for assumed stress finite elements, *International journal for numerical methods in engineering,* 20, 1685-1695, 1984.

[7] B. Oesterle, R. Sachse, E. Ramm and M. Bischoff, Hierarchic isogeometric large rotation shell elements including linearized transverse shear parametrization, *Computer Methods in Applied Mechanics and Engineering,* 321, 383-405, 2017.

[8] K. Wiśniewski, Finite Rotation Shells, Basic Equations and Finite Elements for Reissner Kinematics, *Springer Netherlands*, 2010.

[9] Y. Ko, P.-S. Lee and K.-J. Bathe, The MITC4+ shell element in geometric nonlinear analysis, *Computers and structures*, 185: 1-14, 2017.

DISCRETE AND EQUIVALENT 6-PARAMETER SHELL APPROACH TO SIMULATE MECHANICAL BEHAVIOR OF TENSEGRITY LATTICES

P. Obara[1] and W. Gilewski[2]

[1]*Kielce University of Technology, Kielce, Poland*
[2]*Warsaw University of Technology, Warsaw, Poland*

e-mail: paula@tu.kielce.pl

1. Introduction

For the purpose of this paper tensegrities are defined as cable-strut structures consisting of isolated compressed elements inside a continuous net of tensioned members [6]. Node configuration of these structures ensures occurrence of infinitesimal mechanisms that are balanced with self-stress states [1, 4]. Tensegrity lattices are complicated regarding both their geometry and mechanical properties. In order to describe their actual properties and identify features of the structure as a whole, a shell continuum model is considered within the 6-parameter theory. The shell parameters are calibrated with the use of discrete model based on algebraic equations of the problem.

2. Discrete model and 6-parameter shell theory

Discrete model of the structure is composed of *e* straight and prismatic bars of the lengths l_k, cross sections A_k and Young modulus E_k. The bars are connected in nodes in which the number of *s* nodal displacements q_j and nodal forces Q_i are defined [5]. Axial forces N_k can be expressed by the extensions of bars Δ_k in the form $N_k = E_k A_k \Delta_k / l_k$. The extensions Δ_k are a combination of nodal displacements $\Delta_k = \sum_{j=1}^{s} B_{kj} q_j$, $j = 1,2,...,s$. Additionally the self-equilibrated system of axial forces S_k which satisfy the homogeneous set of equilibrium equations $\sum_{k=1}^{e} B_{jk} S_k = 0$ is considered. If one consider equations of equilibrium in the actual configuration then moment $M_k = S_k l_k \psi_k$ is acting on each bar. Angles of bar rotations ψ_k can be expressed as a combination of nodal displacements $\psi_k = \frac{1}{l_k} \sum_{j=1}^{s} C_{kj} q_j$. The above formalism leads to the linear system of algebraic equations $\sum_{j=1}^{s} (k_{ij} + k_{ij}^G) q_j = Q_i$, in which the linear stiffness matrix k_{ij} and geometric stiffness matrix k_{ij}^G can be expressed in algebraic form $k_{ij} = \sum_{k=1}^{e} B_{ki} \frac{E_k A_k}{l_k} B_{kj}$, $k_{ij}^G = \sum_{k=1}^{e} C_{ki} \frac{S_k}{l_k} C_{kj}$ (see [5, 7] for further details). The approach is not dependent on any approximation typical for the finite element method.

Equivalent continuum model of the tensegrity shell-like structure is based on the linearized 6-parameter shell theory [3]. The subject under consideration is a shell of thickness *h*. Displacement field is described by three linear displacements u_α, w of middle surface and three rotations ϕ_α, ψ. Full description of all equations of the theory can be found in [3]. Linear constitutive relations are crucial from the point of view of the

continuum model equivalent to the discrete model:

$$N_{\alpha\beta} = B^0_{\alpha\beta\lambda\mu}\,\gamma_{\lambda\mu} + B^1_{\alpha\beta\lambda\mu}\,\kappa_{\lambda\mu},\;\; M_{\alpha\beta} = \frac{h^2}{12} B^0_{\alpha\beta\lambda\mu}\,\kappa_{\lambda\mu} + B^1_{\alpha\beta\lambda\mu}\,\gamma_{\lambda\mu},$$
$$N_{\alpha 3} = k^2 B^0_{\alpha 3\beta 3}\,\gamma_{\beta 3} + m^2 B^1_{\alpha 3\beta 3}\,\kappa_{\beta 3},\;\; M_{\alpha 3} = \frac{h^2}{12} l^2 B^0_{\alpha 3\beta 3}\,\kappa_{\beta 3} + m^2 B^1_{\alpha 3\beta 3}\,\gamma_{\beta 3}, \tag{1}$$

where: $\gamma_{\alpha\beta}$, $\kappa_{\alpha\beta}$, $\gamma_{\alpha 3}$, $\kappa_{\alpha 3}$, γ_{33} – strain components, $N_{\alpha\beta}$, $M_{\alpha\beta}$, $N_{\alpha 3}$, $M_{\alpha 3}$ – internal forces, k^2, l^2, m^2 – correction factors. The relations for tensegrity-like anisotropic shells are introduced below.

3. Mechanical behavior of tensegrity shell-like continuum

The first step of the proposed modelling is selection of a repetitive segment, which is taken out from the tensegrity shell-like structure. Then, the selected representative segment undergoes numerical homogenization [1]. By comparing the elastic strain energy from FEM truss formulation with the energy of a solid, a continuum model of the segment is obtained. The homogeneous segments are afterwards joined together to create a three-dimensional orthotropic continuum, which includes the effect of self-stress [1]. After applying the assumptions of shell theory and integration over the thickness, a two-dimensional shell model is obtained for membrane, bending and transverse shear deformations. The model includes the effect of self-stress that was initially applied to the tensegrity discrete model. For example, the selected coefficient for flat structure composed of regular extended octahedron tensegrity modules connected with additional cables can be expressed as [2]:

$$B^0_{1111} = \frac{2EA}{h}\left(1 + 1{,}52325\cdot p + 0{,}13125\cdot n + 0{,}129225\cdot\sigma\right), \tag{2}$$

with the following connection/strut/cable properties: $n = (EA)_{con} / (EA)_{str}$, $p = (EA)_{cab} / (EA)_{str}$, $(EA)_{str} = EA$ with self-stress multiplier $\sigma = S / EA$. If general shall-like tensegrity lattices are considered the mechanical behavior depends on: tensegrity module used, self-stress applied, geometry of the modules, cable/strut/connection properties and Gaussian curvature of the shell model. A separate problem is to define the values of correction factors k^2, l^2, m^2 for various tensegrity lattices. The above problems will be presented in detail and discussed during the conference.

4. References

[1] A. Al Sabouni-Zawadzka and W. Gilewski. Smart metamaterial based on the simplex tensegrity pattern. *Materials,* 11:673, 2018.

[2] A. Al Sabouni-Zawadzka, J. Kłosowska and P.Obara, W. Gilewski. Continuum model of orthotropic tensegrity plate-like structures with self-stress included. *Engng. Trans.*, 64:501-508, 2016.

[3] J. Chróścielewski, J. Makowski and W. Pietraszkiewicz. *Statics and dynamics of folded shells* (in Polish), IPPT PAN, Warsaw, 2004.

[4] K. Koohestani and S.D. Guest. A new approach to the analytical and numerical form-finding of tensegrity structures. *Int. Journ. Solids Struct.,* 50:2995-3007, 2013.

[5] T. Lewiński. On algebraic equations of elastic trusses, frames and grillages. *Journ. Theoret. Appl. Mechanics,* 39:307-322, 2001.

[6] R. Motro. *Tensegrity: structural systems for the future.* Kogan Page, London, 2003.

[7] J. Pełczyński and W. Gilewski. An extension of algebraic equations of elastic trusses with self-equilibrated system of forces. *6th European Conference on Computational Mechanics (ECCM6),* Glasgow, UK, 11-15 June 2018.

ANALYSIS OF LAMINATES WITH THE USE OF 2-D COSSERAT CONSTITUTIVE MODEL

J. Chróścielewski[1], A. Sabik[1], B. Sobczyk[1], and W. Witkowski[1]

[1]*Gdańsk University of Technology, Faculty of Civil and Environmental Engineering, Gdańsk, Poland*
e-mail: jchrost@pg.edu.pl; aqsa@pg.edu.pl; barsobcz@pg.edu.pl; wojwit@pg.edu.pl

1. Introduction

The paper presents the analysis of laminates within the framework of 6-parameter (6p) non-linear shell theory with the use of 2-D Cosserat constitutive model. This theory is specially dedicated to the modelling of irregular shells with intersections, since it takes into account the drilling rotation at material point naturally. As the direct consequence, the unsymmetrical in-plane strain and stress measures arise and reduced shell body is a Cosserat type surface [1]. The constitutive relation for such specific kinematics is non-trivial, especially if laminated fibre reinforced material is considered. Up till now the Authors have utilized the constitutive law expressed in terms of 5 independent engineering constants. In such case the drilling rotation stiffness was in a sense an arbitrary chosen quantity [2]. The approach was successfully used in the analysis of laminates undergoing large displacements [2], first-ply failure [3] and progressive failure [4]. Now a new attempt is made and the Cosserat material law is employed.

2. Cosserat law for fiber reinforced layer

According to [5], where the Cosserat material law for isotropic continuum is presented, we propose an analogical relation for a fibre reinforced layer, similarly as in [6]:

$$
(1)\qquad
\begin{Bmatrix}
\sigma_{aa}\\ \sigma_{bb}\\ \sigma_{ab}\\ \sigma_{ba}\\ \hline \sigma_{a}\\ \sigma_{b}\\ \hline m_{a}\\ m_{b}
\end{Bmatrix}
=
\left[\begin{array}{cccc|cc|cc}
\dfrac{E_a}{1-\nu_{ab}\nu_{ba}} & \dfrac{\nu_{ab}E_b}{1-\nu_{ab}\nu_{ba}} & 0 & 0 & 0 & 0 & 0 & 0\\
\dfrac{\nu_{ba}E_a}{1-\nu_{ab}\nu_{ba}} & \dfrac{E_b}{1-\nu_{ab}\nu_{ba}} & 0 & 0 & 0 & 0 & 0 & 0\\
0 & 0 & G_{ab}+G_C & G_{ab}-G_C & 0 & 0 & 0 & 0\\
0 & 0 & G_{ab}-G_C & G_{ab}+G_C & 0 & 0 & 0 & 0\\ \hline
0 & 0 & 0 & 0 & \alpha_s G_{ac} & 0 & 0 & 0\\
0 & 0 & 0 & 0 & 0 & \alpha_s G_{bc} & 0 & 0\\ \hline
0 & 0 & 0 & 0 & 0 & 0 & 2G_{ab}l^2 & 0\\
0 & 0 & 0 & 0 & 0 & 0 & 0 & 2G_{ab}l^2
\end{array}\right]
\begin{Bmatrix}
\varepsilon^{aa}\\ \varepsilon^{bb}\\ \varepsilon^{ab}\\ \varepsilon^{ba}\\ \hline \varepsilon^{a}\\ \varepsilon^{b}\\ \hline \kappa_{a}\\ \kappa_{b}
\end{Bmatrix},
$$

where σ_{ab}, ε^{ab} are, respectively, plane stress and strain components, m_j, κ_i, (j = a,b) are the coupling stresses and strains, E_a, E_b are the longitudinal and transverse Young moduli, ν_{ab} and ν_{ba} are the Poisson ratios, G_{ab} is the shear moduli; α_s is the shear correction factor, l is the characteristic length and G_c is the Cosserat shear modulus $G_c = N^2/(1-N^2)G_{ab}$ where $0 < N < 1$ is the so-called coupling number. Equation (1) is integrated in the through-the-thickness direction using equivalent single layer approach. Progressive failure analysis is performed with Hashin criterion used as the failure condition. The algorithm is based on the stiffness reduction parameter SRC as described in [4].

3. Numerical example

Consider a C-shaped column which was investigated numerically and experimentally in [7]. The scheme of the experimental setup and present FEM model is shown in Figure 1. The edges of the top cross-section are

totally fixed whereas the bottom edges are pinned. Such boundary conditions provide the best agreement with the experimental results [4]. The laminate is composed of 8 0.26 mm thick layers $[0°/-45°/+45°/90°]_s$ which are made of the material with following properties: E_1 = 38.5 GPa, E_2 = 8.1 GPa, G_{12} = 2 GPa, ν_{12} = 0.27, X_t = 792 MPa, X_c = 679 MPa, Y_t = 39 MPa, Y_c = 71 MPa, S_L = 108 MPa. The fibers orientation is measured with reference to the *y*-axis (Fig. 1). To impose the two half waves buckling mode observed during the experiment, additional imperfection forces $P_i = 0.002\,P$ are applied (Fig. 1). The column is discretized with 16 node fully integrated elements, in particular 30 elements along the column's height, 6 elements along the width of flanges and 12 elements along the web's width. The stiffness reduction parameter is taken as SRC = 0.01. All nodes along the top edge are kinematically coupled with respect to the axial displacement *v* (Fig. 1), which is chosen as the path control parameter. In the present model only the constitutive law is exchanged. In the computations the Cosserat coupling number was set as $N = \sqrt{2}/2$. This value ensures that the constitutive relation for in-plane shear components is the same as in [4]. Two values of characteristic length were chosen, i.e. l = 0.26 mm and l = 2.08 mm, which correspond to the thickness of a single layer and the total thickness of the laminate. As it can be observed in Figure 1 the obtained results are in good agreement with the previous solution [4].

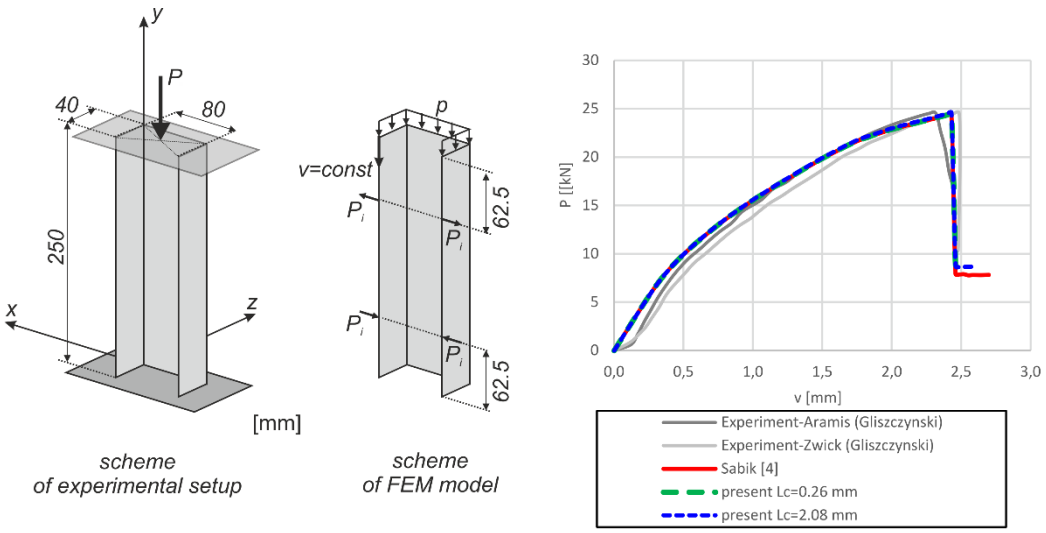

Figure 1: C-shaped column - data and results.

Acknowledgments The authors acknowledge financial support from the grant No UMO 2015/17/B/ST8/02190, financed by National Science Centre Poland.

References

[1] J. Chróścielewski, J. Makowski and H. Stumpf. Genuinely resultant shell finite elements accounting for geometric and material non-linearity. *Int. J. Num. Meth. Eng.*, 35: 63-94, 1992.

[2] J. Chróścielewski, I. Kreja, A. Sabik and W. Witkowski. Modeling of composite shells in 6-parameter nonlinear theory with drilling degree of freedom. *Mech. Adv. Mater. Struc.*, 18: 403-419, 2011.

[3] J. Chróścielewski, A. Sabik. B. Sobczyk and W. Witkowski. Nonlinear FEM 2D failure onset prediction of composite shells based on 6-parameter shell theory. *Thin Wall. Struct.*, 105: 207-219, 2016.

[4] Sabik A. Progressive failure analysis of laminates in the framework of 6-field nonlinear shell theory. *Compos. Struc.*, 200:195-203, 2018.

[5] R. De Borst. Simulation of strain localization a reappraisal of the Cosserat continuum. *Eng. Comput.*, 8: 317-332, 1991.

[6] S. Nakamura, R. Benedict and R. Lakes. Finite element method for orthotropic micropolar elasticity. *Int. J. Engng. Sci. Eng.*, 22: 319-330, 1984.

[7] A. Gliszczyński and T. Kubiak. Progressive failure analysis of thin-walled composite columns subjected to uniaxial compression. *Compos. Struct.*, 169:52–61, 2017.

MODIFIED TTO LAW FOR MATERIAL MIXTURES WITH APPLICATION TO 6-PARAMETER NONLINEAR SHELL ANALYSIS

S. Burzyński[1], J. Chróścielewski, K. Daszkiewicz, W. Witkowski

[1]*Gdańsk University of Technology, Gdańsk, Poland*
e-mail: stanislaw.burzynski@pg.edu.pl

1. Introduction

Plates and shells build from Functionally Graded Materials (FGMs) are commonly analysed in elastic and elasto-plastic range. Material mixture law must define every material parameter as a function of relative volumes of constituents. In Tamura, Tomota and Ozawa (TTO) mixture law [1] it is assumed that mixed or metallic material behaviour is elasto-plastic with linear hardening, while for pure ceramics material is elastic. This material law was enhanced to nonlinear hardening curve in paper [2], where also validation with experimental tests was conducted. Validation resulted in determining parameters for Ti/TiB mixture.

In the present research, modification of TTO law is proposed. The motivation follows from the fact that the original TTO model assumes that even the smallest inclusion of elasto-plastic metal constituent in the elastic ceramic matrix, rapidly changes material behaviour, from linear to inelastic. The proposal presented herein ensures smoothing such a rapid change and thereby introduce hyperbolic-like yield point function. The proposed form of equation is implemented within the framework of nonlinear 6-parameter shell theory with drilling rotation [3]. Specifically, an own FEM Fortran code named CAM [3] for nonlinear shell analysis is used. In formulation of the constitutive matrix for shell finite element we assume Cosserat-like plane stress at each integration point in the shell reference surface and return mapping algorithm as described in [4] for details.

2. Material law

Let (*c*) stands for ceramic and let (*m*) for metal constituent. Let the shell section is ceramic rich on the top surface $(+h^+)$ and metal rich on the bottom surface $(-h^+)$. The power law

$$V_{\mathrm{c}} = \left(\frac{z}{h}+\frac{1}{2}\right)^n, \quad V_{\mathrm{m}} = 1 - V_{\mathrm{c}}, \quad n \geq 1 \tag{1}$$

describes the changes of material constituents in the thickness direction *z*. Here *n* denotes the power-law exponent. The effective Young modulus $E(z)$, the effective Poisson ration $\nu(z)$, the ratio of stress to strain transfer q and the linear hardening modulus $H(z)$ are described by original TTO law. Since in the current theory Cosserat plane stress is assumed in each shell layer, its additional effective constants are defined as

$$l(z) = l_c V_c + l_m V_m, \quad \kappa(z) = G(z)\frac{N^2}{1-N^2}, \tag{2}$$

where $l(z)$ is characteristic length and $0 < N < 1$ is the coupling number. In this paper we propose to modify the original TTO equation for the yield stress, namely

$$\sigma_Y(z) = \left(1-k_Y\right)\sigma_{Ym}\left(V_m + \frac{q+E_m}{q+E_c}\frac{E_c}{E_m}V_c\right) + k_Y\frac{\sigma_{Ym}}{1-V_c}. \tag{3}$$

That is, we postulate the existence of the scalar k_Y such that $1 \geq k_Y > 0$. Equation (3) holds only if $V_c < 1$. When $V_c = 1$ the material is purely ceramic and does not possess the yield limit. Fig.1 displays the idea how variations of q and k_Y from equation (3) influence the stress vs. strain curve in original and modified TTO material law.

3. Numerical example

As a numerical example, equilibrium paths for axially compressed plate are shown in Fig. 2. Geometry and material data [5, 6] are: a = 200, b = 100, b/t = 40, n = 5.0, E_c = 375000, ν_c = 0.14, l_c = 0.005, E_m = 107000, ν_m = 0.34, l_m = 0.005, H_m = 4600, σ_{Ym} = 450, q = 4500, $\kappa = G$. Reference solution, obtained with original TTO law is taken from [6]. Both parametric studies reveals growth of limit load along with the rise of values of parameters. There is no major qualitative change observed in both cases.

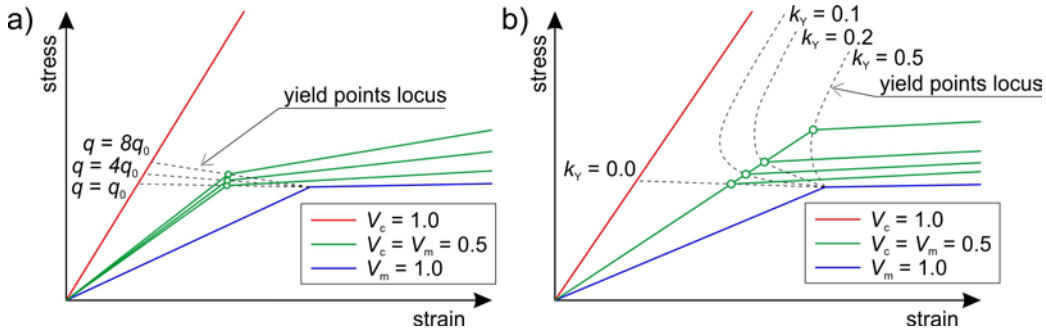

Fig. 1. Parametric analysis a) q in original TTO law b) k_Y in modified TTO law.

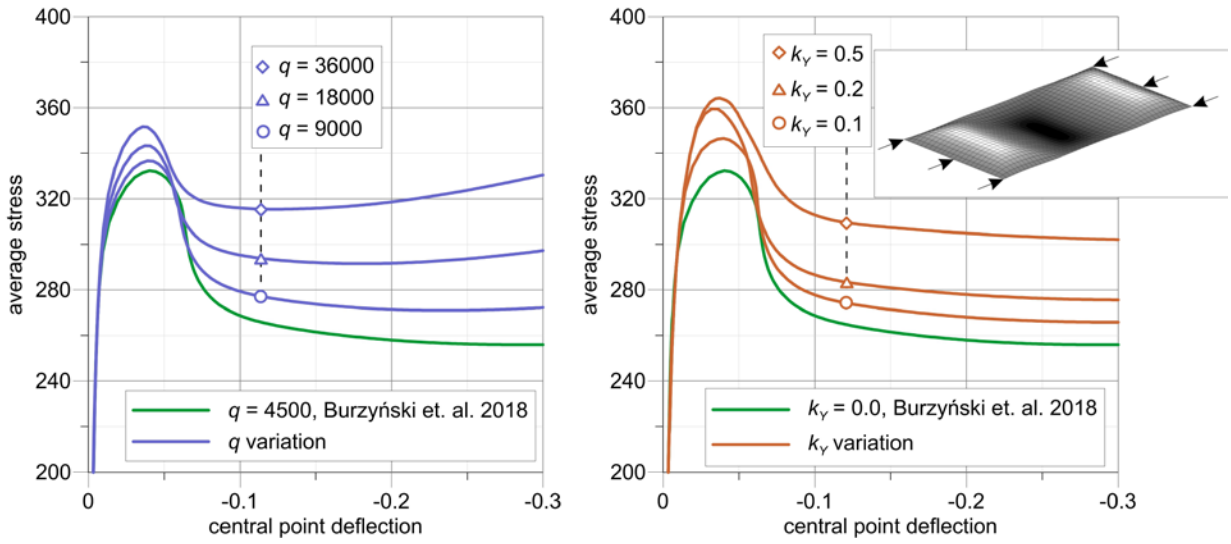

Fig. 2. Parametric analysis in compressed plate a) q variation b) k_Y variation.

Acknowledgments The authors acknowledge financial support from the grant No UMO 2015/17/B/ST8/02190, financed by National Science Centre Poland.

References

[1] I. Tamura, Y. Tomota, H. Ozawa. Strength and ductility of Fe–Ni–C alloys composed of austenite and martensite with various strength. *Proc Third Int Conf Strength Metals Alloys*, Cambridge Inst Metals 1:611–5, 1973.

[2] Z.H. Jin, G.H. Paulino, R. H. Dodds. Cohesive fracture modeling of elastic-plastic crack growth in functionally graded materials. *Eng. Fract. Mech*. 70: 1885–1912, 2003.

[3] J. Chróścielewski, J. Makowski, W. Pietraszkiewicz. *Statyka i dynamika powłok wielopłatowych Nieliniowa teoria i metoda elementów skończonych*. IPPT, PAN 2004.

[4] S. Burzyński, J. Chróścielewski, W. Witkowski. Elastoplastic law of Cosserat type in shell theory with drilling rotation. *Math. Mech. Solids*. 20: 790–805,2015.

[5] G. Xu, H. Huang, B. Chen, F. Chen. Buckling and postbuckling of elastoplastic FGM plates under inplane loads. *Compos. Struct*. 176: 225–233, 2017.

[6] S. Burzyński, J. Chróścielewski, K. Daszkiewicz, W. Witkowski. Elastoplastic nonlinear FEM analysis of FGM shells of Cosserat type. (submitted to Composites Part B), 2018.

Session S17: Stochastic mechanics

Organizers: R. Iwankiewicz (TU Hamburg), Z. Kotulski (Warsaw UT)

Dedicated to the memory of the late Professor Kazimierz Sobczyk (1939-2017)

PROBABILISTIC SOLUTIONS OF THE STRETCHED BEAM SYSTEMS FORMULATED BY FINITE DIFFERENCE SCHEME AND EXCITED BY FILTERED GAUSSIAN WHITE NOISE

Guo-Kang Er and Vai Pan Iu
University of Macau, Macau SAR, China
e-mail: gker@umac.mo

1. Abstract

The multi-degree-of-freedom (MDOF) and nonlinear stochastic dynamical (NSD) system about the nonlinear random vibration of the stretched beam is formulated by finite difference scheme. The effectiveness and efficiency of state-space-split (SSS) method [1,2] and exponential-polynomial-closure (EPC) method [3] are studied in analyzing the probability density functions of responses of the formulated systems which are excited by filtered Gaussian white noises. The Kanai-Tajimi seismic ground acceleration is adopted as the filtered Gaussian white noise in numerical analysis. Numerical results are obtained about the probabilistic solutions of the beam with pin supports at its two ends and excited by the filtered Gaussian white noise which is uniformly distributed over the beam or concentrated in the middle of the beam. The numerical analyses show that the SSS-EPC method works well for accurately and efficiently analyzing the probabilistic solutions of the stretched Euler-Bernoulli beam excited by distributed filtered Gaussian white noise when the MDOF-NSD system is formulated by finite difference scheme.

2. Nonlinear stochastic dynamical system of stretched beam

Consider the stretched beam and its finite difference discretization shown by Figure 1.

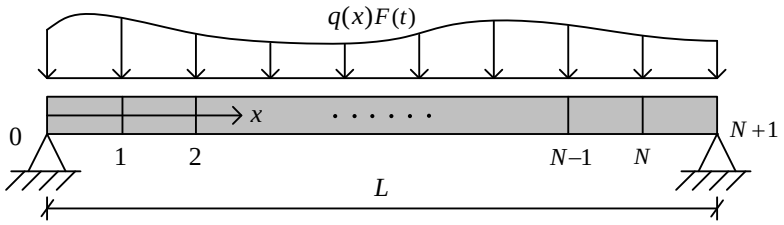

Figure 1: The stretched beam discretized by finite difference scheme

The equation of motion of the beam is

$$\rho\ddot{Y}(x,t)+c\dot{Y}(x,t)+EIY^{(4)}(x,t)-\frac{EA}{2L}Y''(x,t)\int_0^L Y'^2(x,t)dx=qF(t) \tag{1}$$

where $Y(t)$ is the deflection of beam at time t and at the location with distance x to the left-hand end of the beam; ρ is the mass density of material; c is the damping constant; E is the Young's modulus of beam material; I is the moment inertia of cross section of the beam; A is the area of cross section of the beam; L is the beam length; $q(x)F(t)$ is the distributed loading laterally applied on the beam. By finite difference scheme as shown in Figure. 1, Equation (1) can be discretized into the following system.

$$\begin{aligned}&\ddot{Y}_k+\frac{c}{\rho}\dot{Y}_k+\alpha(Y_{k+2}-4Y_{k+1}+6Y_k-4Y_{k-1}+Y_{k-2})-\beta(Y_{k+1}-2Y_k+Y_{k-1})\sum_{i=1}^{N+1}(Y_{i+1}^2+Y_i^2\\&+Y_{i-1}^2+Y_{i-2}^2+Y_{i+1}Y_i-2Y_{i+1}Y_{i-2}-Y_{i+1}Y_{i-2}-Y_iY_{i-1}-2Y_iY_{i-2}+Y_{i-1}Y_{i-2})=\frac{q_k}{\rho}F(t)\end{aligned} \tag{2}$$

$$\ddot{Z}(t)+2\varsigma\omega_0\dot{Z}(t)+\omega_0^2Z(t)=W(t) \tag{3}$$

where $k=1, 2,\ldots,N$; $F(t)=2\varsigma\omega_0\dot{Z}(t)+\omega_0^2 Z(t)$; $\alpha=EI/(h^4\rho)$; $\beta=EA/(24Lh^3\rho)$, $h=L/(N+1)$; N is the number of unknowns in finite difference scheme; Y_k is the deflection of beam at node k; q is a constant reflecting the distributed load density; ς and ω_0 are the parameters in the filter (3); $W(t)$ is the Gaussian white noise with power spectral density S.

3. Numerical results

Based on Equations (2) and (3), the probability density functions (PDFs) of deflections and velocities at the nodes are analyzed. The polynomial degree n equals 4 in EPC solution procedure. The given values of system parameters are $E=2.1\times10^{11}Pa$, $L=7m$, $A=8.61\times10^{-3}m^2$, $I=2.17\times10^{-4}m^4$, $c=10^3 Ns/m$. $\rho=7.850kg/m^3$, $\varsigma=0.3$, $\omega_0=50rad/s$, $S=0.05m^2/s$ and $q_k=50{,}000kg/m$. For $N=11$, Equations (2) and (3) formulate a 12-DOF system. In this case, the node 6 is in the middle of the beam. The PDFs and logarithm of PDFs of Y_6 obtained by SSS-EPC, Monte Carlo simulation (MCS), and equivalent linearization (EQL), respectively, are shown and compared in Figure. 2. The sample size in MCS is 10^8. In Figure 2, σ_{y_6} is the standard deviation of Y_6 obtained by EQL method. It is seen that the results obtained by SSS-EPC method are close to MCS while those obtained by EQL deviate a lot from MCS. The behaviors of the probabilistic solutions at the other nodes are similar to those at node 6. The computational time needed by MCS is about 500 times more than that needed by the SSS-EPC method for this 12-DOF system. The value of this ratio can further increase as the number of system degrees of freedom or samples in MCS increases. As the system nonlinearity increases, the required sample size and therefore the computational effort also increase with MCS.

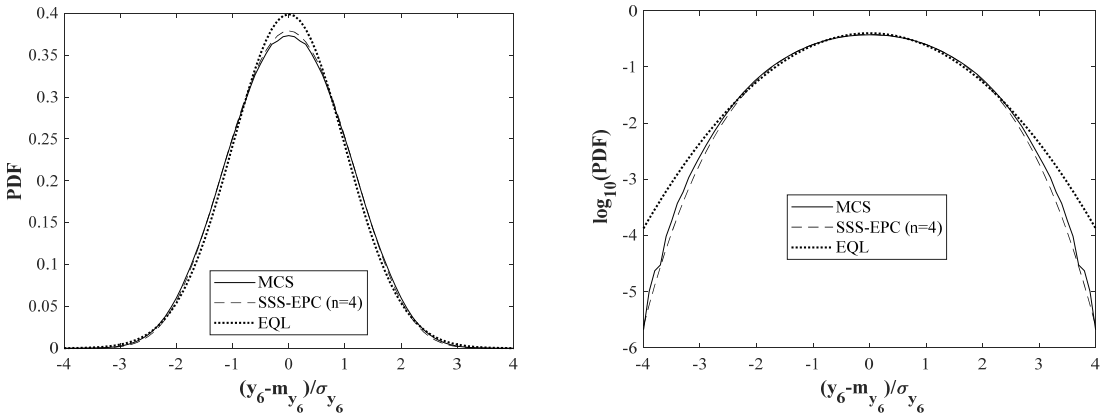

Figure 2: PDFs and logarithm of PDFs of the deflection in the middle of beam

Acknowledgement: The results presented in this paper are obtained under the project supported by the Science and Technology Development Fund of Macau (Grant No. 042/2017/A1).

References

[1] G. K. Er. Methodology for the solutions of some reduced Fokker-Planck equations in high dimensions. *Annalen der Physik*, 523(3) : 247-258, 2011.

[2] G. K. Er and V. P. Iu. A new method for the probabilistic solutions of large-scale nonlinear stochastic dynamic systems. In W.Q. Zhu ; Y.K. Lin ; G.Q. Cai (Eds.) Nonlinear Stochastic Dynamics and Control, IUTAM Book Series 29, pp. 25-34, Springer 2011.

[3] G. K. Er. An improved closure method for analysis of nonlinear stochastic systems. *Nonlinear Dynamics*, 17(3) : 285-297, 1998.

EQUIVALENT LINEARIZATION TECHNIQUE IN NONLINEAR STOCHASTIC DYNAMICS OF A CABLE-MASS SYSTEM WITH TIME-VARYING LENGTH

H.Weber[1], R.Iwankiewicz[1,2], and S.Kaczmarczyk[3]

[1]*West Pomeranian University of Technology, Szczecin, Poland*
[2]*Institute of Mechanics and Ocean Engineering, Hamburg University of Technology, Germany*
[3]*Faculty of Arts, Science and Technology, University of Northampton, UK*

e-mail: Hanna.Weber@zut.edu.pl

Abstract

In presented research a planar model of mass-cable system mounted within a host structure in a high-rise building is considered. In this type of tall slender structures the loads caused by strong wind or earthquakes induce the vibration with low frequencies and large amplitudes [1,2]. This in turn leads to excitation of structural part of the elevator equipment such as cables or ropes. Due to the nondeterministic nature of the problem both the dynamic response of the cable system and the external forces should be described by stochastic processes [3,4]. Because the problem is characterized by non-stationarity and nonlinearity it is difficult to solve it using analytical methods. Therefore the numerical techniques should be applied.

In the system considered concentrated mass M is attached at the lower end of a vertical elastic cable and moves slowly axially with the transport speed V. Therefore, the length of the cable in lifting installations varies over time $L = L(t)$ [5]. The cable longitudinal vibrations $u(x,t)$ are coupled with its lateral displacements $v(x,t)$. Cable modulus of elasticity and cross-sectional metallic area are denoted as E and A, respectively. The bending deformations of the host structure result in a sway of the structure producing harmonic motions $v_0(t)$ with frequency Ω_0 and are described by the polynomial shape function $\Psi(\eta) = 3\eta^2 + 2\eta^3$. The variable η is a ratio of coordinate measured from the ground level and height of the entire system. The longitudinal time-dependent displacement of the concentrated mass is denoted as $u_M(t)$. If slow time scale is defined as τ and the expansion of the displacements $v(x,t)$ in terms of approximating functions is used then the set of differential equations of motion is obtained as [6]

$$\ddot{q}_r(t) + 2\zeta_r\omega_r(\tau)\dot{q}_r(t) + \sum_{n=1}^{N} C_{rn}(\tau)\dot{q}_n(t) + \lambda_r^2\left\{\bar{c}^2 - V^2 + c^2\left[\frac{u_M(t)}{L(\tau)} + \frac{1}{2}\left(\frac{\Psi_L - 1}{L(\tau)}\right)^2 v_0^2(t)\right]\right\}q_r(t)$$
$$+ \sum_{n=1}^{N} K_{rn}(\tau)q_n(t) + \lambda_r^2(\tau)c^2 q_r(t)\sum_{n=1}^{N}\beta_n^2(\tau)q_n^2(t) = Q_r(t,\tau)$$

$$\ddot{u}_M(t) + 2\zeta_M\omega_M(\tau)\dot{u}_M(t) + \omega_M^2(\tau)u_M + \frac{EA}{M}\sum_{n=1}^{N}\beta_n^2(\tau)q_n^2(t) = -\frac{EA}{2M}\left(\frac{\Psi_L - 1}{L(\tau)}\right)^2 v_0^2(t)$$

where $n, r = 1, 2, ..., N$ with N denoting the number of considered terms/modes. The generalized coordinates (coefficients of expansion) $q_r(t)$ corresponding to the lateral modes vary fast over time. The expressions for the slow-varying stiffness and damping coefficients $K_{rn}(\tau)$ and $C_{rn}(\tau)$ with the modal excitation functions $Q_r(t,\tau)$ can be found in [6]. Modal damping ratios are assumed as ζ_r and ζ_M, while slowly-varying undamped natural frequencies of the system are denoted as $\omega_M = \frac{EA}{ML(\tau)}$ and $\omega_r, r = 1, 2, ..., N$. The quantity Ψ_L is equal to the ratio of the height measured from the ground level to the lower end of the cable and the height of the structure. Other constants and variables can be expressed as $\bar{c} = \sqrt{\frac{T}{m}}$, $c = \sqrt{\frac{EA}{m}}$, $\lambda_r(\tau) = \frac{r\pi}{L(\tau)}$ and $\beta_r(\tau) = \frac{1}{2}\lambda_r(\tau)$ with T and m being the mean quasi-static tension and mass per unit area of the cable, respectively.

Due to the nature of the excitation caused by, for example, the external wind load the motion $v_0(t)$ is assumed as narrow-band process mean-square comparable to the harmonic process with frequency Ω_0. The structural displacement response $v_0(t)$ must be continuous and twice differentiable. These requirements can be fulfilled by assuming $v_0(t)$ as the response of the second order auxiliary filter to the process $X(t)$, which is the response of the first-order filter to the Gaussian white noise $\xi(t)$ excitation [7]. The governing equations are assumed as

$$\ddot{v}_0(t) + 2\zeta_f \Omega_0 \dot{v}_0(t) + \Omega_0^2 v_0(t) = X(t)$$

$$\dot{X}(t) + \alpha X(t) = \alpha\sqrt{2\pi S_0}\xi(t)$$

where ζ_f, α, S_0 are the filter damping ratio defining its band width, the filter variable and constant level of the power spectrum of the white noise $\xi(t)$, respectively.

In the papers [6,8] linearised problem arises by neglecting the nonlinear terms and parametric excitation terms in the set of differential equations. In the proposed equivalent linearization technique an original system governed by non-linear differential equations with unknown solution is replaced by an equivalent system governed by linear differential equations. Using condition of the mean-square equations difference minimization the coefficients of the equivalent linear equation are evaluated and expressed in terms of the moments and of the expectations of non-linear functions of the response process. These expectations are evaluated under the assumption that the state variables of the linearised system are jointly Gaussian distributed. For an equivalent linear system the equations governing the covariance matrix of the state variables are obtained. The variance of the lateral displacement is a result of analysis presented.

The considered problem is an important issue for the high-rise buildings with elevators that are exposed to the dynamic external loads. The described phenomena correspond to the behaviour of cables that are observed in real lifting installations. The final results can be used by a designer during the computation process to set the bounds of the dynamic displacement response.

References

[1] T. Kijewski-Correa , D. Pirinia (2007). *Dynamic behavior of tall buildings under wind: insights from full-scale monitoring*, The Structural Design of Tall Special Buildings Vol. 16, 471-486.

[2] N.J. Cook. (1985). The Designer's Guide to Wind Loading of Building Structures Part 1., *London: Butterworths*.

[3] S. Kaczmarczyk, R. Iwankiewicz , Y. Terumichi (2009). *The dynamic behaviour of a nonstationary elevator compensating rope system under harmonic and stochastic excitations*, Journal of Physics.: Conference Series Vol. 181, 012047.

[4] G.F. Giaccu, B. Barbiellini, L. Caracoglia (2015). *Stochastic unilateral free vibration of an in-plane cable network*, Journal of Sound and Vibration 340, 95-111.

[5] Y. Terumichi, M. Ohtsuka, M. Yoshizawa, Y. Fukawa, Y. Tsujioka (1997). *Nonstationary vibrations of a string with time-varying length and a mass-spring system attached at the lower end*, Nonlin. Dynamics Vol. 12, 39-55.

[6] S. Kaczmarczyk, R. Iwankiewicz (2017). *On the Nonlinear Deterministic and Stochastic Dynamics of a Cable - Mass System with Time-Varying Length*, 12th Int. Conf. on Structural Safety and Reliability, Austria, 1205-1213.

[7] J.W. Larsen, R. Iwankiewicz and S.R.K. Nielsen (2007). *Probabilistic stochastic stability analysis of wind turbine wings by Monte Carlo simulations*, Probabilistic Engineering Mechanics Vol.22,181-193.

[8] S. Kaczmarczyk, R. Iwankiewicz (2017). *Gaussian and non-Gaussian stochastic response of slender continua with time-varying length deployed in tall structures*, International Journal of Mechanical Sciences Vol.134,500-510.

AN APDM+PTM APPROACH FOR EVALUATING THE RESPONSE PDF OF UNCERTAIN STRUCTURAL SYSTEMS

G. Falsone and R. Laudani

Engineering Department, University of Messina, Italy

e-mail: gfalsone@unime.it

It is known that there is no universal method suitable to solve any problem involving uncertainties in structural system characteristics. One of the oldest method for the evaluation of the response pdf of systems subjected to uncertainties is based on truncating the cumulant series expansion of the response characteristic function [1], which is the Fourier transform of the pdf. This method provides good results if the response is characterized by a relatively low non-Gaussianity. When the response is strongly non-Gaussian, the number of terms of the series may be particularly high and the convergence, that is not guaranteed, can be particularly slow. In addition, the direct evaluation of the terms of the series may not be simple.

Widely used methods are those based on the perturbation approaches, based on a Taylor series expansion in terms of a set of zero mean random variables. The perturbation approaches provide accurate results for relatively low levels of uncertainty, for which only few terms of the series are used (usually the first or the first and second order are considered). On the contrary, when the level of uncertainty of the structural parameters increases the approach loses strongly its precision and, moreover, the computational effort increases exponentially because a high number of terms of the series must be taken into account. In any case, the convergence of the approach is not guaranteed by the augmented order of the retained series terms [2].

Another important class of methods for solving uncertain structural systems is that based on the projection approaches, that is on the projection of the solution on a complete stochastic basis. Two of the most used projection approaches are those based on the Karhunen-Loève expansion and on the polynomial chaos expansion [3]. This last one is a Galerkin projection scheme based on Wiener integral representation. It requires the numerical evaluation of the series expansion terms and can be particularly onerous if the terms of the series are not limited to a relatively small number. For this reason recently several efforts has been made to improve the approach [4].

A relevant class of methods dealing with uncertain system is that related to the use of the random matrix expansion of the structural stiffness matrix in order to perform explicitly its inversion (Neumann expansion) [5]. Then, once that the explicit inverse stiffness matrix is known, it is possible to obtain the statistics of the response, or to perform a MCS to obtain the response pdf.

In 2002 Falsone and Impollonia [6,7] proposed the APDM, that belongs to the class of MCS-based methods [8]. It consists in breaking up the structural response in the base of the main deformation modes of the structure: this allows obtaining an approximation of the response, without the cost to invert the stiffness matrix of the system and enabling to reduce strongly the computational effort, the statistics of the response being obtained by the MCS directly applied on the explicit expressions of the response. In a certain sense, the method enables the evaluation of an approximated inverse stiffness matrix (as the matrix expansion methods). Nevertheless, the APDM can be considered also as a projection method, because it consists essentially in the expansion of the structural response on a particular base through a finite number of functions, depending on the uncertain parameters, strictly related to the principal deformation modes of the structural system. In any case, the coefficient of the series can be evaluated explicitly in terms of the uncertain parameters. This method is remarkably efficient, allowing the probabilistic analysis of systems with higher levels of uncertainty than that related to an efficient use of the perturbation methods.

Recently, an approach, based on a new version of the PTM, has been proposed for the study of some stochastic problems [9,10]. The method provides the basis for a new philosophy in the study of structural systems subjected to random loads, working directly in terms of input and output pdfs.

Aim of the present paper is matching the APDM with the PTM in order to give an approach able to

characterize the response of uncertain structural systems directly in terms of pdf and without using any expansive MCS. Here, a new APDM+PTM approach is proposed in order to perform the stochastic response analysis of FE modelled structural systems affected by uncertainties which are represented by random variables having any kind of joint pdf. In this way, the attempt of taking into account the virtues of both APDM and PTM is made. The result is in the definition of a very efficient approach from both the accuracy and the computational effort point of view. Moreover, it is shown that, for statically determinate structure the APDM becomes PDM, in the sense that it is able to give the exact relationships between the uncertain parameters and the structural response. As the application of the PTM can be made without introducing no more approximation, then the PDM+PTM approach is able to give the exact response pdfs of statically determinate uncertain structural systems.

References

[1] L.D. Lutes and S Sarkani. *Random Vibration Analysis of Structural and Mechanical System*. Burlingthon, 2004.
[2] M. Kaminski. Generalized perturbation-based stochastic finite element method in elastostatics, *Computer & Structures*, 85: 586, 2007.
[3] R Ghanem and P. Spanos. *Stochastic Finite Elements: A Spectral Approach*. Springer-Verlag, 1991.
[4] A. Doostan, R.G. Ghanem and J. Red-Horse. Stochastic model reduction for chaos representations, *Computer Methods in Applied Mechanics and Engineering*, 196: 3951, 2007.
[5] F. Yamazaki, M. Shinozuka and G. Dasgupta. Neumann expansion for stochastic finite element analysis, *Journal of Engineering Mechanics*, 114: 1335, 1988.
[6] G. Falsone and N. Impollonia. A new approach for the stochastic analysis of finite element modelled structures with uncertain parameters, *Computer Methods in Applied Mechanics and Engineering*, 191: 5067, 2002.
[7] G. Falsone and N. Impollonia. About the accuracy of a novel response surface method for the analysis of finite element modelled uncertain structures, *Probabilistic Engineering Mechanics*, 19:53, 2004.
[8] J.E. Hurtado and A.H. Barbat, Monte Carlo techniques in computational stochastic mechanics, *Archives of Computational Methods in Engineering*, 5: 3-29, 1998.
[9] G, Falsone and D. Settineri. Explicit solutions for the response probability density function of linear systems subjected to random static loads, *Probabilistic Engineering Mechanics*, 33: 86, 2013.
[10] G. Falsone and D. Settineri. Explicit solutions for the response probability density function of nonlinear transformations of static random inputs, *Probabilistic Engineering Mechanics*, 33: 79, 2013. .

RESEARCH ACTIVITY OF THE LATE PROFESSOR KAZIMIERZ SOBCZYK (1939-2017)

R. Iwankiewicz[1,2], Z. Kotulski[3]

[1]*West Pomeranian University of Technology, Szczecin, Poland*
[2]*Institute of Mechanics and Ocean Engineering, Hamburg University of Technology, Germany*
[3]*Warsaw University of technology, Warsaw, Poland*
e-mail: iwankiewicz@tu-harburg.de

Stochastic mechanics is subject area concerning modeling mechanical problems by using random variables and stochastic processes to reflect all model uncertainties. It started extensive development at early sixties of the twentieth century, which coincided with the beginning of research activity of the late Prof. Kazimierz Sobczyk. During next decades Prof. Kazimierz Sobczyk made research in various areas of stochastic mechanics including: stochastic dynamical systems, stochastic wave propagation, modeling of random materials, fracture mechanics, micromechanics, information-theory based methods and many others. A complete list of his publications can be found in the Preface [34] to the special issue of Probabilistic Engineering Mechanics which was dedicated to Prof. Kazimierz Sobczyk on the occasion of his 70th birthday, containing post-conference papers of the Int. Conf. ''Stochastic Methods in Mechanics: Status and Challenges'' held in Warsaw, on Sept. 28–30, 2009. In the following sections we briefly present main topics of scientific interests and research achievements of Prof. Kazimierz Sobczyk with representative references.

Stochastic dynamics: Contributions made by Professor Kazimierz Sobczyk to the subject area of stochastic dynamics (random vibrations theory) were often of pioneering nature. Such was e.g. the paper dealing with free vibrations of an elastic plate with random stiffness (which lead to the random eigenvalue problem [2]. The paper [4] was one of the first contributions to the problem of random vibrations of composite plates. Also an important issue of non-Gaussianity of response of vibratory systems was dealt with by Professor Kazimierz Sobczyk [5-8]. Of original nature were also the applications of maximum entropy principle [9-12]. Book [1] presents most fundamental methods known in stochastic dynamics at the time.

Stochastic waves: The first problem undertaken by Professor Kazimierz Sobczyk in the area of stochastic wave propagation was scattering of elastic waves at randomly rough surfaces [14]. A plane harmonic elastic wave incident at the random surface separating two different elastic half-space was considered and the probabilistic structure of the scattered field at some observation point was determined. Next he considered scattering of elastic surface (Rayleigh) waves at a random boundary of an elastic body [15]. Studies in this subject area were continued and the findings published in a number of papers and collected in a book [13].

Stochastic differential equations: The book [16] provides an account of basic results of the theory of stochastic differential equations. It also covers most important concepts and results of stochastic processes and stochastic calculus theory. Some of most effective methods of solution of stochastic differential equations as well as examples of applications to vibration problems are given.

Stochastic approach to fatigue: Professor Kazimierz Sobczyk made a contribution to problems of stochastic modeling of fatigue phenomena through his innovative approaches, such as e.g. modeling of fatigue accumulation in terms of Markov chains [18], or modeling of fatigue crack growth as a cumulative jump process (driven by a random counting process) [19-23]. He also developed some stochastic models of stiffness degradation of vibratory systems [24-26]. The book [17] presents most important methods of stochastic modelling of fatigue fracture of engineering materials.

Stochastic modelling of microstructures: Research done in the area of micromechanics was focused on reconstruction of random grain structure from incomplete empirical information [29], characterization of crack growth in elastic material with a random array of small defects [30] and characterization of random microstructural stresses and fracture estimation [31]. Most important methods of stochastic modelling of microstructures were collected in the book [27].

Stochastic information-theoretic modelling: Professor Kazimierz Sobczyk also developed a theoretic information approach (based on the concept of entropy) to identification, signal processing and dynamics of

stochastic systems [32], [33].

References:

[1] K. Sobczyk, *Methods of Statistical Dynamics* (in Polish), Polish Scientific Publishers, Warsaw, 1973.
[2] K . Sobczyk, Free vibrations of elastic plate with random properties - the eigenvalue problem*, Journal of Sound and Vibration,* 22(1) 33-39, 1972.
[3] K. Sobczyk, D.B. Macvean, J.D. Robson, Response to profile-imposed excitation with randomly varying traversal velocity*, Journal of Sound and Vibration*, 52 (1) 37-49, 1977.
[4] M. Witt, K. Sobczyk, Dynamic response of laminated plate to random loading, *Int. J. Solids and Structures*, 16(2) 231-238, 1980.
[5] Z. Kotulski, K. Sobczyk, Linear systems and normality, *Journal of Statistical Physics,* 24(2) 359-373, 1981.
[6] R. Iwankiewicz, K. Sobczyk, Dynamic response of linear structures to correlated random impulses, *Journal of Sound and Vibration*, 86(3) 303-317, 1983.
[7] Z. Kotulski, K. Sobczyk, Characteristic functionals of randomly excited physical systems, *Physica* A, 123(1) 261-278, 1984.
[8] Z. Kotulski, K. Sobczyk, Effects of parameter uncertainty on the response of vibratory systems to random excitation, *Journal of Sound and Vibrations*, 119(1) 159-171, 1987.
[9] K. Sobczyk, J. Trębicki, Maximum entropy principle in stochastic dynamics, *Prob. Eng. Mech.,* 5(3) 102-110, 1990.
[10] K. Sobczyk, J. Trębicki, Maximum entropy principle and nonlinear stochastic oscillators, *Physica A,* 193(3-4) 448-468, 1993.
[11] J. Trębicki, K.Sobczyk, Maximum entropy principle and non-stationary distributions of stochastic systems, *Probabilistic Engineering Mechanics*, 11(1) 169-178, 1996.
[12] K. Sobczyk, J. Trębicki, Approximate probability distributions for stochastic systems: maximum entropy method, *Computer Methods in Applied Mechanics and Engineering*, 168(1-4) 91-111, 1999.
[13] K. Sobczyk, *Stochastic Wave Propagation, Elsevier, Amsterdam, 1985.*
[14] K. Sobczyk, Scattering of plane wave at a random surface, *Proc. Vibr. Problems*, 6(1) 99-109, 1965.
[15] K. Sobczyk, Scattering of Rayleigh waves at a random boundary of an elastic body, *Proc. Vibr. Problems,* 7(4) 363-374, 1966.
[16] K. Sobczyk, *Stochastic Differential Equations with Applications to Physics and Engineering,* Kluwer, 1991.
[17] K. Sobczyk, B.F. Spencer. Jr., *"Random Fatigue: From Data to Theory",* Academic Press, Boston, 1992.
[18] K. Sobczyk, On the Markovian models for fatigue accumulation, *J. Mec. Theor. et Appl.,* N. spec., 147-160, 1982.
[19] K. Sobczyk, Stochastic models for fatigue damage of materials, *Adv. Appl. Probability,* 19(3) 652-673, 1987.
[20] O. Ditlevsen. K. Sobczyk, Random fatigue crack growth with retardation, *Eng. Frac. Mech.*, 24(6) 861-878, 1986.
[21] K. Sobczyk, J. Trębicki, Modelling of random fatigue by cumulative jump processes, *Eng. Frac. Mech.*, 34(2) 477-493, 1989.
[22] K.Sobczyk, J.Trębicki, Cumulative jump-correlated model for random fatigue, *Eng. Frac. Mech.,* 40(1) 201-210, 1991.
[23] K. Sobczyk, J. Trębicki, B.F. Spencer, Modelling of curvilinear fatigue crack growth, *Eng. Frac. Mech.*, 52(4) 703-715, 1995.
[24] K. Sobczyk, J. Trębicki, Stochastic dynamics with fatigue-induced stiffness degradation, *Prob. Eng. Mech.,* 15(1) 91-99, 2000.
[25] J. Trębicki, K. Sobczyk, On nonlinear stochastic vibratory systems with stiffness degradation, *Acta Mechanica*, 195(1-4) 203-214, 2008.
[26] K. Sobczyk, K. Perros, C. Papadimitriou, Fatigue reliability of multi-dimensional vibratory degrading systems under random loading, *ASCE Journal of Engineering Mechanics*, 136(2) 179-188, 2010.
[27] K. Sobczyk, D.J. Kirkner, *Stochastic Modelling of Microstructures,* Birkhauser, Boston, 2001.
[28] K. Sobczyk, (Ed.), *Random Material Microstructures: Modelling and Mechanical Behaviour,* IPPT PAN, Warszawa, 2004.
[29] K. Sobczyk, Reconstruction of random material microstructures; patterns of maximum entropy, *Prob. Eng. Mech.*, 18(4) 279-287, 2003.
[30] K. Sobczyk, J. Trębicki, A.B. Movchan, Crack path in an elastic material with a random array of small defects, *Intern. J. of Fracture*, 125(1-2) 103-123, 2004.
[31] K. Sobczyk, J. Trębicki, A.B. Movchan, Characterization of random microstructural stresses and fracture estimation, *European J. of Mech./A-Solids*, 25(1) 573-591, 2007.
[32] K. Sobczyk, Information Dynamics: Premises, Challenges and Results, *Mech. Systems & Signal Processing*, 15(3) 475-498, 2001.
[33] K. Sobczyk, P. Hołobut, Information-theoretic approach to dynamics of stochastic systems, *Prob. Eng. Mech.,* 27(1) 47-56, 2012.
[34] R. Iwankiewicz, Z. Kotulski, Preface to Special Issue: Stochastic Methods in Mechanics -Status and Challenges, *Probabilistic Engineering Mechanics,* 26(1) 1-4, January 2011. https://doi.org/10.1016/j.probengmech.2010.07.004

Session S18: Composite Materials and Structures

Organizers: B. Brank (U Ljubljana), J. Hohe (IWM Freiburg), I. Kreja (Gdansk UT)

BOUNDARY ELEMENT ANALYSIS FOR UNSYMMETRIC COMPOSITE LAMINATES WITH ELASTIC INCLUSIONS

Chia-Wen Hsu and Chyanbin Hwu

Institute of Aeronautics and Astronautics, National Cheng Kung University, Tainan, Taiwan, R.O.C.

1. Introduction

For unsymmetric composite laminates, the material properties are not symmetric with respect to the middle plane, and the deformation in stretching and bending will be coupled together. This coupling effect would then make the analysis complicated, and the methods in analyses for pure stretching or pure bending in metallic plates or symmetric laminates, are infeasible for unsymmetric laminates. Fortunately, the Stroh-like formalism has been developed to cope with the coupled deformation [1]. Since the mathematical form of Stroh-like formalism is identical to Stroh formalism for two-dimensional linear anisotropic elasticity, almost all the techniques and identities developed for the two-dimensional problems can be employed here. With this advantage, several Green's functions for unsymmetric laminates have been derived. In addition, the boundary element method (BEM) for the coupled deformation have also been successfully implemented by taking the Green's function for the infinite unsymmetric laminates as the fundamental solution [2]. With this success, in this paper we consider to develop a special boundary element by using the fundamental solution for the infinite unsymmetric laminates with elastic inclusions. Although its associated Green's function has been derived one decade ago, after numerical computation we found that some physical quantities calculated from the existing solution become discontinuous across the inclusion or on some other unexpected locations, which contradicts the assumption of continuum model and has not been noticed in the literature. Most of the discontinuities are raised by the terms containing the multi-valued complex logarithmic function [3], and some others are due to the misfit of the rigid body motion of matrix and inclusion. Additionally, in Stroh-like formalism only the values of in-plane displacements and rotation angles (with respect to x_1- or x_2- axis) are provided, the calculation of deflection requires the integral via rotation angles. Although the integration can be done analytically or numerically, to get a continuous deflection some integral constants cannot be arbitrarily neglected and should be treated carefully.

After the above proper treatment, the Green's function obtained in the literature [1] can be corrected and converted into the fundamental solution required by BEM for coupled stretching-bending analysis (which is simply named as CBEM). The analyses for unsymmetric laminates with inclusions can then be carried out, which is expected to be much more efficient and accurate than the conventional boundary element. To verify the correctness of CBEM, a symmetric laminate with elastic inclusion under in-plane loading is served as a special case whose results can be compared by BEM for two-dimensional analysis (named as 2D-BEM).

2. Numerical Examples

Consider a graphite/epoxy fiber-reinforced composite laminate with isotropic steel inclusion subjected to a uniform tensile stress $\sigma^{\infty}=1$ MPa as shown in Fig. 1. To start our verification process, a symmetric laminate [45/0/0/45] is considered in the present example. The geometry of the laminate and inclusion can be represented by a/L=0.2, b/L=0.1, L=1 m, and $h_1-h_0=h_2-h_1=h_3-h_2=h_4-h_3=1$ mm. The material properties of each lamina are $E_L=138$ GPa, $E_T=9$ GPa, $G_{LT}=6.9$ GPa, $\nu_{LT}=0.3$, whereas the properties of steel are $E=210$ GPa, $\nu=0.3$. Here, E, G and ν are, respectively, Young's modulus, shear modulus, and Poisson's ratio, while the subscripts L and T represent the fiber and transverse directions. Forty linear elements and 44 nodes are used in the present example for both of CBEM and 2D-BEM. The hoop stresses σ_{ss} along the interface of the inclusion are shown in Table 1 where φ is a parameter representing the point along the inclusion boundary ($x_1=a\cos\varphi$, $x_2=b\sin\varphi$). The superscripts (1) and (2) denote, respectively, the values in the side of matrix and inclusion. Table 1 shows that the numerical results of CBEM are quite close to 2D-BEM analysis. Through the verification by the special case of symmetric laminate, we are now confident with the feasibility of the proposed CBEM for the general cases of coupled stretching-bending

deformation. And hence, several examples of *unsymmetric laminates* subjected to in-plane forces, bending or twisting moments, or transverse loads will then be presented in this conference.

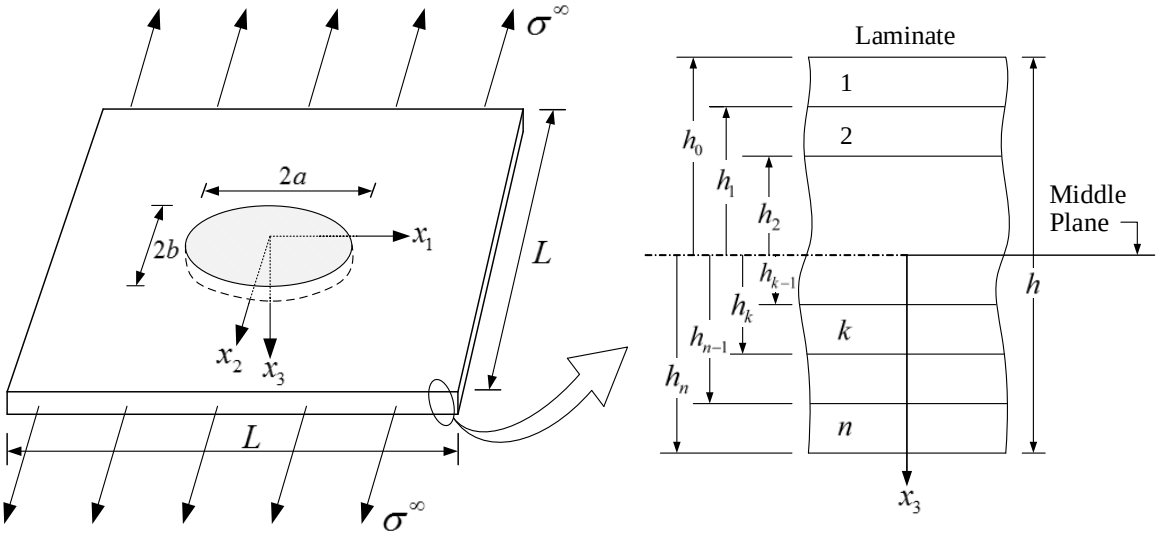

Fig. 1: A laminate with inclusion subjected to a tensile stress σ^∞.

φ (degree)	$\sigma_{ss}^{(1)}/\sigma^\infty$		$\sigma_{ss}^{(2)}/\sigma^\infty$	
	2D-BEM	CBEM	2D-BEM	CBEM
0	0.0145	0.0146	1.32	1.32
30	-0.409	-0.409	0.818	0.818
60	-0.805	-0.805	0.373	0.373
90	0.253	0.253	0.169	0.169
120	1.37	1.37	0.148	0.147
150	0.485	0.485	0.517	0.517
180	0.0145	0.0146	1.32	1.32

Table 1: Hoop stresses along the interface of the inclusion.

Acknowledgments The authors would like to thank Ministry of Science and Technology, TAIWAN, R.O.C for support through Grants MOST 104-2221-E-006-138-MY3.

References

[1] C. Hwu. *Anisotropic elastic plates*, Springer, New York, 2010.
[2] C. Hwu. Boundary element formulation for the coupled stretching-bending analysis of thin laminated plates. *Engineering Analysis with Boundary Elements*, Vol. 36, pp. 1027-1039, 2012.
[3] C. Hwu, C. L. Hsu and W. R. Chen. Corrective evaluation of multi-valued complex functions for anisotropic elasticity. *Mathematics and Mechanics of Solids*, DOI: 10.1177/1081286517728542, 2017.

INVESTIGATION OF SHOCK WAVE COMPRESSIBILITY OF TEXTOLITE FOR EXPERIMENTS AT PRIOR

V. Mochalova[1,2], A. Utkin[1], M. Endres[3], and D.H.H. Hoffmann[3]

[1]*Institute of Problems of Chemical Physics RAS, Chernogolovka, Russia*
[2]*FSBI "SSC RF ITEP" of NRC "Kurchatov Institute", Moscow, Russia*
[3]*Technical University Darmstadt, Darmstadt, Germany*

e-mail: roxete20000@gmail.com

1. Introduction

Using a laser interferometer VISAR with nanosecond time resolution, the experiments on developing of targets, investigation of the shock wave structure and spall strength and also the determination of Hugoniot data were carried out with samples of textolite with longitudinal and transverse direction of the fibers. The goal of this study is development of targets for experiments at a novel diagnostic system proton microscope (PRIOR) at the TU Darmstadt. Textolite is a composite anisotropic material with a low specific weight, consisting of interwoven fabric fibers and a binder - epoxy resin. The density of the investigated material is 1.265 g/cm^3. The thickness of the samples in the experiments varied from 3 to 10 mm, the diameter from 25 to 50 mm. The measured sound speed along the fibers is C_l = 7.1 km/s, transverse - C_l = 2.45 km/s.

2. Scheme of experiments

To study the shock wave compressibility of textolite under high pressure, the explosive propellant charges were used to provide a flat throw of aluminum flyer plates with diameter of 70-100 mm and thickness of 2-10 mm. Their velocity W varied from 0.7 to 2.5 km/s. The scheme of experiments is shown in Figure 1. Shock waves in the investigated samples (3) were created by the collision of an aluminum flyer plate (1) with the metal plate (2). The velocity of the sample-water (4) boundary was recorded by VISAR interferometer. To determine the absolute value of the velocity, two interferometers with velocity fringe constants of 280 m/s and 1280 m/s were used simultaneously. A laser beam was reflected from an aluminum foil which was glued onto the sample (5). In each experiment, the piezoelectric gauge (6) recorded the entry time into the sample of the shock wave, which allowed us to determine the average value of the shock wave velocity *D* using interferometric data.

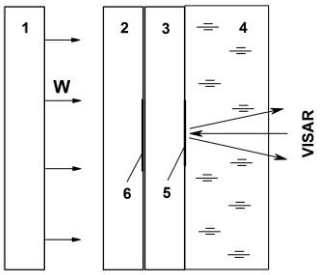

Figure 1: Scheme of experiments.

3. Experimental results

Particle velocity profiles on the textolite/water boundary at high pressure are shown in Fig. 2. The experimental setup parameters are indicated in the figure descriptions. On the velocity profile for a textolite with transverse direction of the fibers, after the shock jump, oscillations are observed due to the porosity of the investigated material (Fig. 2, left). Unlike the textolite with transverse orientation of the fibers, in the case when a shock wave propagates along the fibers (Fig. 2, right), a two-wave configuration is recorded (precursor and shock wave), which is due to the anisotropic structure of material. The amplitude of the

precursor is about 150 m/s. The velocity of the perturbations propagation along the fibers can be several times higher than the shock wave velocity, what results in the formation of the precursor. Since the amplitude of forward-running perturbations attenuates, the front of the first wave degenerates into a sound pulse, so its propagation velocity is close to 7.1 km/s, measured by the ultrasonic method.

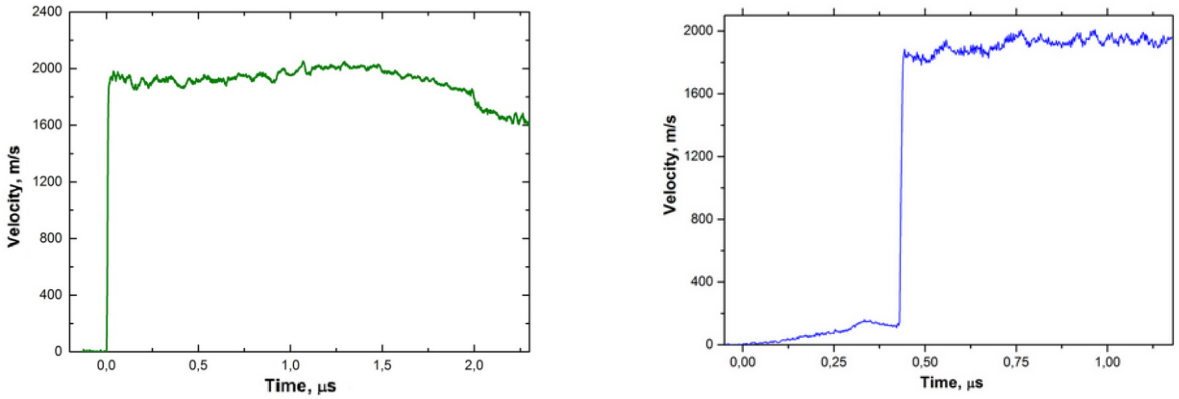

Figure 2. Particle velocity profiles on the textolite/water boundary. Aluminum projectile of 10 mm, W=2.5 km/s; aluminum plate of 4 mm: left - transverse orientation of the fibers, right – parallel.

As a result of the processing of the experimental data, Hugoniot parameters of textolite in the coordinates of shock wave D – particle velocity u were plotted (Fig. 3) at the wave propagation along (red filled circles) and across the fibers (black filled circles). The solid lines represent a linear approximation of the experimental data: $D = 1.50 + 2.00*u$, km/s for parallel orientation of the fibers, $D = 2.17 + 1.45*u$, km/s – for transverse.

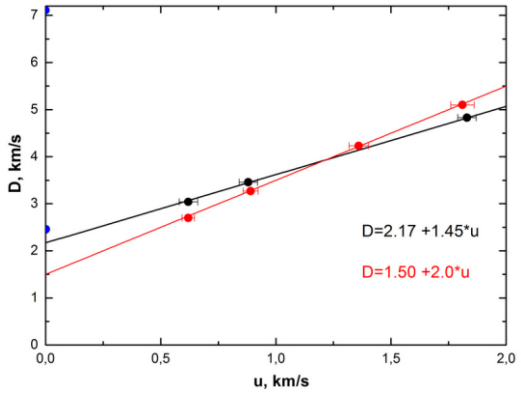

Figure 3. Hugoniot parameters of textolite.

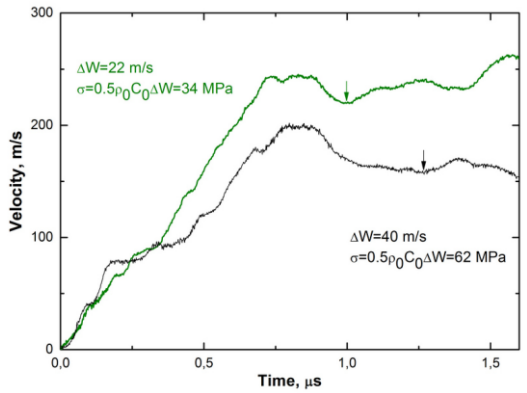

Figure 4. Particle velocity profiles of free surface for textolite.

Also a study of spall strength for textolite was conducted. The measured particle velocity profiles of free surface of textolite for parallel (black profile) and perpendicular (green profile) orientation of the fibers are shown in fig.4. The exit of the shock wave on the free surface causes an increase in the velocity of the surface up to the maximum value. A rarefaction wave propagates inside the sample, which, interacting with the incident unloading wave, results in an internal fracture - a spall. The spall strength σ, which characterizes the maximum tensile stress in the sample, is determined by the equation: $\sigma=0.5\ \rho_0 C_0\ \Delta W$, where ΔW - the velocity difference between its maximum and value at the moment of arrival of spall pulse (shown by arrow), C_0 – the sound speed at zero pressure, ρ_0 – the initial density of the sample.
It was found that the spall strength value of textolite with parallel orientation of the fibers is almost twice higher than that for perpendicular orientation.
Thus, it was found that shock wave properties of textolite were strongly dependent on the fibers orientation.

Acknowledgments The work is carried out with the financial support of FAIR-Russia Research Center.

A FATIGUE DAMAGE DEGRADATION MODEL FOR CFRP MATERIALS

J. Hohe[1], M. Gall[1], and Z.M. Abdul Hamid[1,2]

[1]*Fraunhofer IWM, Wöhlerstr. 11 79108 Freiburg Germany*

[2]*Karlsruhe Institute of Technology. Institute for Applied Materials, Straße am Forum 7, 76131 Karlsruhe, Germany*

e-mail: joerg.hohe@iwm.fraunhofer.de

1. Introduction

Carbon fiber reinforced plastics (CFRP) are common materials in all fields of lightweight construction. In addition to the classical field of aerospace, CFRP materials nowadays are widely used in automotive industry and other fields of the transport sector, the naval industry, in the wind energy industry as well as in nonclassical fields of lightweight construction such as civil engineering. A major concern under cyclic loading is the fatigue resistance. A special feature for fiber reinforced materials is the initial stiffness degradation at low cycle numbers followed by a region of nearly vanishing degradation until a progressive material degradation till failure occurs towards the end of the fatigue lifetime. Objective of the present study is the formulation, implementation and validation of an anisotropic continuum damage model for CFRP materials accounting for these effects.

2. Formulation

Using a generalization of an earlier approach (Gauch [1], Hohe et al. [2]), the model is based on the following basic assumptions:

- except for damage effects, the material response is linear elastic as described by Hooke's law,
- the anisotropic damage mechanism is the formation, growth and coalescence of microcracks oriented towards the three main spatial directions,
- the damage evolution is controlled by the dissipation of microplastic work below the overall yield limit of the material.

Considering these basic assumptions and employing a Kachanov-Lemaitre type damage approach

$$\bar{\sigma} = (1-D)\sigma \tag{1}$$

by scaling of the stress σ determined from the material constitutive equation with a damage variable D, defined with respect to the different spatial directions, the constitutive equation

$$\begin{pmatrix} \bar{\varepsilon}_{11} \\ \bar{\varepsilon}_{22} \\ \bar{\varepsilon}_{33} \\ 2\bar{\varepsilon}_{23} \\ 2\bar{\varepsilon}_{13} \\ 2\bar{\varepsilon}_{12} \end{pmatrix} = \begin{pmatrix} \frac{1}{(1-D_1)E_1} & -\frac{\bar{\nu}_{21}}{E_2} & -\frac{\bar{\nu}_{31}}{E_3} & 0 & 0 & 0 \\ -\frac{\bar{\nu}_{12}}{E_1} & \frac{1}{(1-D_2)E_2} & -\frac{\bar{\nu}_{32}}{E_3} & 0 & 0 & 0 \\ -\frac{\bar{\nu}_{13}}{E_1} & -\frac{\bar{\nu}_{23}}{E_2} & \frac{1}{(1-D_3)E_3} & 0 & 0 & 0 \\ 0 & 0 & 0 & \frac{1}{(1-D_2)(1-D_3)G_{23}} & 0 & 0 \\ 0 & 0 & 0 & 0 & \frac{1}{(1-D_1)(1-D_3)G_{13}} & 0 \\ 0 & 0 & 0 & 0 & 0 & \frac{1}{(1-D_1)(1-D_2)G_{12}} \end{pmatrix} \begin{pmatrix} \bar{\sigma}_{11} \\ \bar{\sigma}_{22} \\ \bar{\sigma}_{33} \\ \bar{\sigma}_{23} \\ \bar{\sigma}_{13} \\ \bar{\sigma}_{12} \end{pmatrix} \tag{2}$$

is obtained, where E_i, G_{ij} and ν_{ij} are the anisotropic elastic constants whereas D_i are the anisotropic damage variables. Estimating the microplastic work from the elastic stresses and strains assuming a Ramberg-Osgood type plasticity law for the microplastic strains and introducing the material parameters A and n as well as the damage warping function ω, the one-dimensional damage evolution equation

(3) $$\mathrm{d}D = \begin{cases} A\, w(D)\, |\,\bar{\sigma}\,|^{n}\, \mathrm{d}\sigma & \text{for:} \quad \mathrm{d}\bar{\sigma} > 0 \\ 0 & \text{for:} \quad \mathrm{d}\bar{\sigma} \le 0 \end{cases}$$

is obtained. Subsequently, this equation is re-written to a fully three-dimensional form and the model is implemented as a user-defined material model into a commercial finite element program. Full details on the formulation and finite element implementation can be found in an oncoming contribution (Hohe et al. [3]).

3. Example

For validation, the proposed fatigue damage model is applied to an experimental data base on a filament wound carbon epoxy material. Exemplary results for the obtained S-N-curves are presented in Figure 1. In all three cases considered, the numerical prediction is found in a good agreement with the experimental data. Especially the linear shape of the S-N- (Wöhler-) curve in the double logarithmic representation of the fatigue diagrams is recalled in a perfect manner. Despite the distinct scatter of the experimental data, a good quantitative prediction of the fatigue strength is obtained.

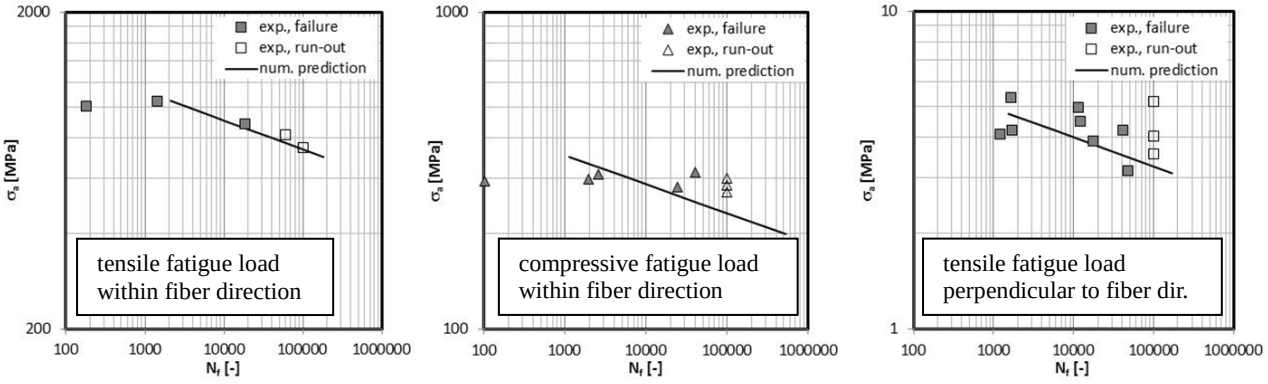

Figure 1: Numerical example.

4. Conclusions

The present contribution is concerned with the definition and implementation of a continuum damage mechanics model for fatigue degradation of CFRP materials. The model is based on a linear elastic base formulation in conjunction with anisotropic damage based on three independent damage variables. The damage evolution is assumed to be controlled by microplastic effects below the overall yield limit of the material. In an application to an experimental data base, the model proves to provide an accurate prediction of the S-N-curves obtained in different testing directions and loading modes.

Acknowledgments The present work has been funded by the German Federal Department of Economic Affairs and Energy (BMWi) under grant no. 03ET6013F. The authors are fully responsible for the contents of this contribution.

References

[1] H. Gauch: *Implementation and validation of a fatigue degradation model for carbon fiber reinforced plastics*, Master Thesis, Karlsruhe Institute of Technology and Fraunhofer IWM, Freiburg 2015, in German.
[2] Hohe, J., Gall, M., Gauch, H., Fliegener, S. and binti Abdul Hamid, Z.M.: A material model for prediction of fatigue damage and degradation of CFRP materials, *Key Eng. Mat.* 742 (2017) 740-744.
[3] J. Hohe, M. Gall, S. Fliegener and Z.M. Abdul Hamid: A continuum damage mechanics model for fatigue degradation of fiber reinforced materials, *submitted*.

EFFECTIVE PROPERTIES OF MATERIALS WITH PERIODIC THIN WALLED CUBIC MICROSTRUCTURE

G. Mejak[1]

[1] *Faculty of Mathematics and Physics, University of Ljubljana, Ljubljana, Slovenia*

e-mail: george.mejak@fmf.uni-lj.si

1. Introduction

In this paper we study effective elastic properties of composites with a periodic microstructure that have a unit cell with geometrical cubic symmetry and such that one of its material phases builds up of thin plates. It is further assumed that the unit cell is made of two isotropic materials. An important example of such materials are foams. Certain microstructures, such as cubic–octet microstructure [1], give materials with the theoretical limit of elastic stiffness.

It is found in [2] that the homogeneous eigenstrain approximation to the equivalent eigenstrain principle gives an accurate prediction to the effective properties for certain thin walled structures. Among them are cubic, octet and cubic–octet microstructures. In fact, the approximation gives a closed form solution

$$\kappa_{\mathrm{e}} = 1 - \frac{3f(1-\kappa_{\mathrm{r}})(1-\nu)}{3(1-\nu)-(1+\nu)(1-\kappa_{\mathrm{r}})(1-f)}, \tag{1}$$

$$\mu_{\mathrm{e}} = 1 - \frac{3f^2(1-\mu_{\mathrm{r}})(1-\nu)}{\Delta_1}, \tag{2}$$

$$\hat{\mu}_{\mathrm{e}} = \frac{6f^2(1-\mu_{\mathrm{r}})^2(\nu-1)(5\beta(f)+(f-1)f)}{\Delta_1\Delta_2}, \tag{3}$$

where

$$\Delta_1 = 2\beta(f)(1-\mu_{\mathrm{r}}) + 2f^2(1-\mu_{\mathrm{r}})(1-\nu) + f(2\mu_{\mathrm{r}}+1)(1-\nu),$$
$$\Delta_2 = -3\beta(f)(1-\mu_{\mathrm{r}}) + f^2(1-\mu_{\mathrm{r}})(1-2\nu) + f(\mu_{\mathrm{r}}(1-2\nu)-\nu+2).$$

Here κ_{r} and μ_{r} are the quotients of elastic moduli of material phases of the unit cell, ν is the Poisson ratio of the walls and f is the volume ratio between the materials of the unit cell with f near 1 for thin walled structures. Coefficient $\beta(f)$ which is obtained by solving the equivalent eigenstrain equation by the Fourier method is given by the series

$$\beta(f) = \sum_{\underline{m}\neq\underline{0}} \frac{c_0(\underline{m})^2\left(m_1^2m_2^2 + m_1^2m_3^2 + m_2^2m_3^2\right)}{\left|\underline{m}\right|^4}. \tag{4}$$

Here $c_0(\underline{m})$ is $\underline{m}$-nth Fourier coefficient of the compliment of the walls within the unit cell. It follows from (1-3) that the structural dependence of effective elastic properties depends only upon the function $\beta(f)$.

2. Elastic performance of composites

The elastic energy of composite subjected to the homogeneous macro strain : $\underline{\underline{\epsilon}}_0$ is given by the Hill–Mandel formula $\frac{1}{2}\underline{\underline{\epsilon}}_0 : \underline{\underline{C}}^{\mathrm{eff}} : \underline{\underline{\epsilon}}_0$. The elastic performance of the composite is measured by the amount of the elastic energy it can store. The amount is given by volume of the 6 dimensional ellipsoid with semi axes which are the

eigenvalues of $\underline{\underline{C}}^{\text{eff}}$. They are $\lambda_1 = C^{\text{eff}}_{1212}$, $\lambda_2 = C^{\text{eff}}_{1111} - C^{\text{eff}}_{1122}$ $\lambda_3 = C^{\text{eff}}_{1111} + 2C^{\text{eff}}_{1122}$ with multiplicities 3, 2 and 1. The volume $\mathcal{V}$ is proportional to $\lambda_1^3\lambda_2^2\lambda_1$. Formulae (1-3) allow to express $\mathcal{V}$ as a function of ν, κ_r, μ_r, f and β. Regarding $\mathcal{V}$ as a function of β it is found that $\mathcal{V}(\beta)$ is stationary at five values of β. However, only one of them, namely $\beta = \frac{1}{5}(1-f)f$ depends solely on f, others depend also on ν and μ_r. It follows from (3) that at this value $\hat{\mu}_e = 0$. Therefore, the stiffness thin walled microstructure is isotropic.

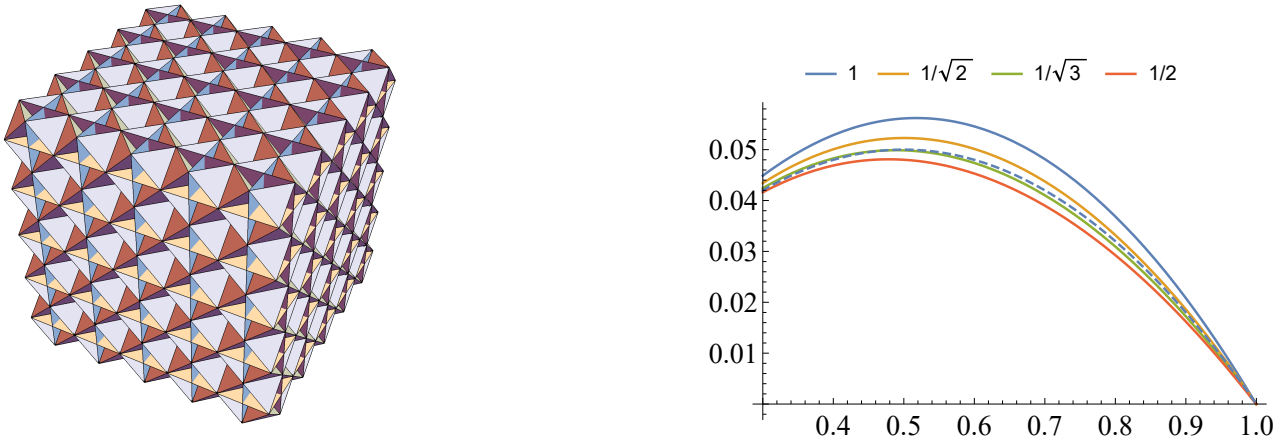

Figure 1: Cubic–octet foam and $\beta(f)$ for various ratios α of octet to coordinate walls thicknesses; from the bottom curve $\alpha = 1/2$ to the top curve with $\alpha = 2$. A dashed line is $\beta = \frac{1}{5}(1-f)f$.

It was shown in [1] by another method that the cubic–octet foam (see Figure 1), which is combination of the cubic and the octet structure, is for the ratio $1/\sqrt{3}$ of the octet to coordinate walls thicknesses isotropic. This is confirmed by the present results in Figure 1. Moreover, not only cubic–octet foam but any composite with thin walls of the cubic–octet structure is macroscopically isotropic. Of course, function $\beta(f)$ does not unequally determines shape of the unit cell. It is aim of the further research to identify other thin walled structures that are isotropic. On the other hand, dependence of elastic moduli upon β allows also to formulate conditions on β for other extremal elastic properties such as extremal values of the Poisson's or Zener ratios.

References

[1] J. B. Berger, H. N. G. Wadley, R. M., and McMeeging. Mechanical metamaterials at the theoretical limit of isotropic elastic stiffness. *Nature*, 543:533–537, 2017.

[2] G. Mejak. High concentration ratio approximation of linear effective properties of materials with cubic inclusions. *Coupled Systems Mechanics*, 7:61–77, 02 2018.

TRANSIENT THERMAL STRESSES IN A FUNCTIONALLY GRADED CYLINDER BY PSEUDOSPECTRAL CHEBYSHEV METHOD

Durmus Yarimpabuc[1], **Mehmet Eker**[2], **Kerimcan Celebi**[3], and **Ali Yildirim**[2]

[1]*Osmaniye Korkut Ata University, Department of Mathematics, Osmaniye, Turkey*
[2]*Osmaniye Korkut Ata University, Department of Mechanical Engineering, Osmaniye, Turkey*
[3]*Cukurova University, Ceyhan Engineering Faculty, Department of Mechanical Engineering, Adana, Turkey*

e-mail: durmusyarimpabuc@osmaniye.edu.tr

Introduction

Functionally graded material (FGM) can be categorized as advanced engineering material that is able to survive in a severe working environment by preserving its properties during service. They are designed with varying properties that include changing chemical, mechanical, magnetic, thermal, and electrical properties [1]. FGMs are used in many applications exposed to high temperature such as; energy conservation system, aerospace and nuclear energy applications, heat engine component. The temperature gradient on the material give rise to thermal stress due to different amount of expansions, thus transient stresses are the maximum thermal stress on the material. If the thermal shock is severe enough, crack initiation-propagation and creep may occur. Therefore, it is important to analyze the internal thermal stresses in FGMs and to evaluate their resistance to thermal loading such as thermal shock [2].

Transient thermoelastic analysis of a FG cylinder under thermal loading was studied. The cylinder material is considered to be graded along the radial direction, where an exponentially varying distribution is assumed. The cylinder is subjected to a constant temperature at the surface. The governing equation of the cylinder transformed into the Laplace space and then solved numerically by Chebyshev pseudospectral approach in radial direction for transient condition. Pseudospectral Chebyshev method is a global method and converges at a rate that is faster than that of conventional methods. It can be achieved a great accuracy for coarse grid points. Solutions were transformed from Laplace domain to the time domain by applying modified Durbin's procedure. The time dependent temperature, radial displacement and stress distributions are examined for a FG cylinder consists of ceramic ZrO_2 and alloy $Ti-6Al-4V$. The method is validated with the literature.

Basic Equations

Heat Conduction

The transient temperature distribution in a FG circular cylinder is considered under prescribed thermal boundary conditions. The material properties are assumed to change in radial direction. The heat conduction equation in axisymmetric cylindrical coordinates-to solve at first- without heat generation,

$$\frac{\partial^2 T}{\partial r^2}+\frac{\partial T}{\partial r}\left(\frac{1}{r}+\frac{1}{k(r)}\frac{dk}{dr}\right)=\frac{\rho(r)c_p(r)}{k(r)}\frac{\partial T}{\partial t} \tag{1}$$

where $T(r,t)$ is the time dependent temperature field and k, ρ, c_p and t are thermal conductivity, density, specific heat at constant pressure and time, respectively.

Thermal Stress

A long FGM cylinder of an isotropic material is investigated. In this case, the deformation of the cylinder is expressed through the radial stress σ_r, the hoop stress σ_ϕ, and the axial stress σ_z. So the thermoelastic stress-

strain relations are given as follows:

$$\begin{aligned}\sigma_r &= c_{11}\epsilon_r + c_{12}\epsilon_\phi - (c_{11}+2c_{12})\alpha\Delta T \\ \sigma_\phi &= c_{12}\epsilon_r + c_{11}\epsilon_\phi - (c_{11}+2c_{12})\alpha\Delta T \\ \sigma_z &= c_{12}(\epsilon_r+\epsilon_\phi) - (c_{11}+2c_{12})\alpha\Delta T\end{aligned} \tag{2}$$

where c_{ij} and α are the elastic constants and thermal expansion coefficient, respectively. $\Delta T = T - T_\infty$ is the temperature difference with the ambiant temperature T_∞. Equation of stress equilibrium is

$$\frac{\partial \sigma_r}{\partial r} + \frac{\sigma_r - \sigma_\phi}{r} = \rho \frac{\partial^2 u}{\partial t^2} \tag{3}$$

By inserting elastic constant and strain components ($\epsilon_r = du/dr,\ \ \epsilon_\phi = u/r$) into Eqs. (2) and then into Eq. (3), the dynamic equation of motion for the displacement u can be obtained as

$$\begin{aligned}\frac{\partial^2 u}{\partial r^2} + \frac{\partial u}{\partial r}\left[\frac{1}{r} + \frac{1}{E}\frac{dE}{dr}\right] + \frac{u}{r}\left[\frac{\nu}{1-\nu}\frac{1}{E}\frac{dE}{dr} - \frac{1}{r}\right] = \\ \frac{1+\nu}{1-\nu}\left[\frac{\partial}{\partial r}(\alpha\Delta T) + \alpha\Delta T\frac{1}{E}\frac{dE}{dr}\right] + \frac{(1+\nu)(1-2\nu)}{(1-\nu)}\frac{\rho}{E}\frac{\partial^2 u}{\partial t^2}.\end{aligned} \tag{4}$$

When the solution of u is known from Eq. (4), the stresses and strains can be determined from Eqs. (2). Since the stresses at the center are expected to be to be finite, the displacement u must vanish at $r = 0$. And, the cylinder is assumed to be free of surface tractions at the outer surface.

Pseudospectral Chebyshev Model

Pseudospectral Chebyshev Model used to perform transient thermal stress analysis of FG cylinder by referring to the study of Gottlieb [3] that depends on discretization the governing equations (1-4) with respect to the radial variable using pseudospectral Chebyshev method. With regard to collocation points, the first order $(n+1)\times(n+1)$ Chebyshev differentiation matrix

$$0 = r_0 < r_1 \cdots < r_n,\ \ with\ \ r_j = \frac{1}{2}[1 - \cos(j\pi/n)] \tag{5}$$

$(j = 0, 1, \cdots, n)$ will be denoted by D. First-order Chebyshev differentiation matrix D provides highly precise approximation to $u^{'}(r_j), u^{''}(r_j), ...$, simply by multiplication differential matrix with vector data $u^{'}(r_j) = (D\,u)_j,\ u^{''}(r_j) = (D^2 u)_j$, suchlike where $u = [u_0, \ldots, u_n]^T$ discrete vector data at positions r_j.

The computation procedure of the Chebyshev differentiation matrix and codes as m-file can be found in notable references, see e.g., Trefethen [4], where the collocation points x_i are numbered from right to left and defined in $[-1, 1]$. With a small revision, differentiation matrix D can be implemented to the any interval.

References

[1] R. M. Mahamood and E. T. Akinlabi. *Functionally Graded Materials*, Springer International Publishing, Switzerland, 2013.

[2] B. L. Wang, Y. W. Mai and X. H. Zhang. Thermal shock resistance of functionally graded materials, *Acta Materialia*, 17:52, 4961-4972, 2004.

[3] D. Gottlieb. The Stability of Pseudospectral-Chebyshev Methods, *Mathematics of Computation*, 36:153, 107-118, 1981.

[4] L.N. Trefethen. *Spectral Methods in Matlab*, SIAM, Philadelphia, PA, 2000.

[5] F. Durbin. Numerical Inversion of Laplace Transforms: An Efficient Improvement to Dubner and Abrate's Method, *Computer Journal*, 17, 371-376, 1974.

AN EFFICIENT NONLOCAL MODEL FOR PRELIMINARY DESIGN OF SANDWICH RECTANGULAR PLATE WITH LAMINATED FACINGS

S. Karczmarzyk

Institute of Vehicles, Faculty of Automotive and Construction Machinery Engineering, Warsaw University of Technology, Warsaw, Poland

e-mail: karczmarzyk_st@poczta.onet.pl

1. Introduction

Layered surface girders (plates and shells) can be divided into two groups: laminate and sandwich. The sandwich constructions are usually composed of three layers, with different thicknesses h_k, $k = 1,2,3$, fulfilling the condition that the ratio h_2/h_k, $k = 1,3$, is much greater than one. Usually $h_2 / h_k \in (20-100)$. The second indicator characteristic of these sandwich constructions is the ratio of Young's modules of adjacent layers , ie E_k/E_2, $k = 1,3$. Usually $E_k / E_2 \in (100-10000)$. As it results from the above values of the ratios, the sandwich constructions are physically and geometrically inhomogeneous with abruptly variable parameters. If we take into account that the outer layers of the sandwich girders can be laminated, it is obvious that the exact elastic mathematical models of these girders are usually very complex.

The sandwich plates have been attractive to many researchers interested in the structural aspects of engineering constructions. Elastic models of sandwich plates can be divided into two groups: non-local and local. The local models are presented, for example, in the following papers [1-2]. As far as the author knows, all the previous local models are limited to rectangular simply supported plates. The non-local models are much more frequently published in the literature and therefore their exact classification is not very easy because of the large number of scientific papers devoted to them. Here, non-local models are divided into two groups: the equivalent single layer (ESL) models and individual-layer (I-L) models. Below there are mentioned some exemplary works containing the ESL and I-L models (theories). A simple ESL theory of sandwich plate one can find in [3]. In paper [4] an ESL refined theory for the sandwich plate with laminated facings was presented. Also in paper [5] an ESL refined theory has been presented in detail. In paper [6] an I - L theory of sandwich plate was outlined.

This presentation concerns an I-L model for the rectangular sandwich plate composed of laminated outer layers (facings) and an orthotropic middle layer (core). The plate is symmetric about the middle plane.

2. Outline of the present individual-layer model of sandwich plate with laminated facings

Displacements vector $\underline{u}_k$ occuring within k^{th} layer, $k = 1\text{-}3$, as well as the corresponding stresses within this model satisfy the compatibility equations between the adjacent layers, i.e.

(1) $$\underline{u}_1 = \underline{u}_2 \ , \qquad \underline{u}_1 = \underline{u}_2 \ , \qquad \underline{u}_k = \left[u_{xk} \ \ u_{yk} \ \ u_{zk}\right]^T ,$$

(2) $$\underline{\sigma}_1 = \underline{\sigma}_2 \ , \qquad \underline{\sigma}_1 = \underline{\sigma}_2 \ , \qquad \underline{\sigma}_k = \left[\sigma_{zx} \ \ \sigma_{zy} \ \ \sigma_{zz}\right]_k^T .$$

Of course, the cross-sectional boundary conditions, for the first and third layer, have also been satisfied. The local constitutive equations applicable in k^{th} layer are consistent with the kinematic model for the layer.

To obtain displacement vectors $\underline{u}_k$ the following equations, for each k^{th} layer separately, have been applied,

(3) $$\int_{z_{1k}}^{z_{2k}} \left(\frac{\partial (\sigma_{xx})_k}{\partial x} \right) z dz + \int_{z_{1k}}^{z_{2k}} \left(\frac{\partial (\sigma_{xy})_k}{\partial x} \right) z dz + \int_{z_{1k}}^{z_{2k}} \left(\frac{\partial (\sigma_{xz})_k}{\partial x} \right) z dz = \int_{z_{1k}}^{z_{2k}} \left(\frac{\partial^2 (u_x)_k}{\partial t^2} \right) z dz,$$

$$\int_{z_{1k}}^{z_{2k}}\left(\frac{\partial(\sigma_{yx})_k}{\partial x}\right)zdz+\int_{z_{1k}}^{z_{2k}}\left(\frac{\partial(\sigma_{yy})_k}{\partial x}\right)zdz+\int_{z_{1k}}^{z_{2k}}\left(\frac{\partial(\sigma_{yz})_k}{\partial x}\right)zdz=\int_{z_{1k}}^{z_{2k}}\left(\frac{\partial^2(u_y)_k}{\partial t^2}\right)zdz, \tag{4}$$

$$\int_{z_{1k}}^{z_{2k}}\left(\frac{\partial(\sigma_{zx})_k}{\partial x}\right)dz+\int_{z_{1k}}^{z_{2k}}\left(\frac{\partial(\sigma_{zy})_k}{\partial x}\right)dz+\int_{z_{1k}}^{z_{2k}}\left(\frac{\partial(\sigma_{zz})_k}{\partial x}\right)dz=\int_{z_{1k}}^{z_{2k}}\left(\frac{\partial^2(u_z)_k}{\partial t^2}\right)dz. \tag{5}$$

Finally, equations (3) are summed up for *k = 1 - 3*, ie through the entire thickness of the plate. The same applies to equations (4) and (5).These final equations, derived after the summations, make it possible to determine the functions of $\underline{u_k}$. To obtain complete statement of the boundary problem the edge boundary conditions have to be satisfied. For example, for a plate with fixed edges these conditions are as follows,

$$\begin{aligned} x=0,a \quad &\Rightarrow \quad u_{zk}=0, \quad \frac{\partial u_{zk}}{\partial x}-\frac{T_{zx}}{S_{zx}}=0, \\ y=0,b \quad &\Rightarrow \quad u_{zk}=0, \quad \frac{\partial u_{zk}}{\partial y}-\frac{T_{yz}}{S_{yz}}=0. \end{aligned} \tag{6}$$

Symbols T_{yz}, T_{zx}, denote the transverse edge shear forces, S_{yz}, S_{zx}, are the shear stiffnesses of the plate, while symbols a, b denote dimensions of the plate.

3. Local model for cellular core

The middle layer (core) of the sandwich panel can be of continuous or cellular material. There are many "continuum" models in the literature for the cellular core which simplify modelling of the sandwich plate. For instance, in [7] the following formulas for the Young's and shear modulus of the cellular core are given,

$$E_c=E_s\left(\frac{\rho_c}{\rho_s}\right)^2, \qquad G_c=\frac{3}{8}E_s\left(\frac{\rho_c}{\rho_s}\right)^2. \tag{7}$$

Symbols E_c, G_c, ρ_c, in expressions (7), denote equivalent Young's modulus, shear modulus and density, respectively, of the "isotropic" cellular core while E_s, G_s, ρ_s, are the same parameters of the solid material from which the core is made. It is noted that directly from (7) we have the Poisson's ratio value, $v_c = 1/3$. It is noted that many other formulas analogous to (7) can be found in the literature.

The I-L model of a rectangular sandwich plate commented here is much simpler in comparison with other I - L models existing in the literature. Therefore, it is useful for the preliminary design of the plate eg to analyse the influence of type and arrangement of reinforcements in laminate layers on stiffness of the plate.

References

[1] S. Srinivas, A.K. Rao. Bending, vibration and buckling of simply supported thick orthotropic rectangular plates and laminates. *Int. J. Solids & Struct.*, 6: 1463-1481, 1970.

[2] A.T. Jones. Exact natural frequencies and modal functions for a thick of-axis lamina. *J. Comp. Mat.*, 5: 504, 1971.

[3] D. Zenkert. *An introduction to sandwich construction*. EMAS Publishing, 1995.

[4] T. Kant, K. Swaminathan. Analytical solutions for the static analysis of laminated and composite sandwich plates based on a higher order plate theory. *Composite Structures*, 56: 329-732, 2002.

[5] M. A-A. Meziane, H. H. Abdelaziz and A. Tounsi. An efficient and simple refined theory for buckling and free vibration of exponentially graded sandwich plates under various boundary conditions. *J. Sandwich Struct. and Materials*, 293-318, 2014.

[6] K. Malekzadeh and A. Sayyidmousavi. Free vibration analysis of sandwich plates with a uniformly distributed attached mass, flexible core, and different boundary conditions. *J. Sandwich Struct. and Materials*, 709-732, 2010.

[7] J. B. Min, L. J. Ghosen and B. A. Lerch. A study for stainless steel fan blade design with metal foam core. *Journal of Sandwich Struct. and Materials*, 56-73, 2015.

WRINKLING PATTERN TRANSITION OF AXIALLY COMPRESSED BILAYERED CYLINDRICAL COMPOSITES

M. Lavrenčič[1], B. Brank[1] and M. Brojan[2]

[1]*Faculty of Civil and Geodetic Engineering, University of Ljubljana, Ljubljana, Slovenia*
[2]*Faculty of Mechanical Engineering, University of Ljubljana, Ljubljana, Slovenia*
e-mail: marko.lavrencic@fgg.uni-lj.si

Problem description

Surface wrinkling is observed in diverse composite systems, ranging from biology to engineering. Wrinkling usually develops due to the loss of system's stability. Traditionally, it has been understood as a sign of failure. In recent years, however, it is exploited to achieve advanced functionality or superior physical properties of a composite system, e.g. [1]. A systematic understanding of the process of development and evolution of the wrinkling pattern calls for extensive numerical analyses. In this respect, it turns out that accurate numerical solutions related to wrinkling simulations are difficult to attain. Specialized numerical formulations have been developed.

In this work, we study wrinkling of the stiff shell-soft core cylindrical systems. The elastic cylinder is resting on elastic substrate with no inside cavity. It is exposed to axial compression as shown in Fig. 1.

Experimental, theoretical and numerical investigation of a system on Fig. 1 was reported in [2] and [3]. The authors showed that regardless of the system characteristics, the first wrinkling mode is always axisymmetric. They also observed wrinkling pattern transition from the axisymmetric to the diamond-like pattern for some configurations. They proposed a coefficient C_S with the critical value $C_{S,crit} \approx 0.88$, see Eq. (1), where E_F and E_S are elastic moduli of film and substrate, respectively. They showed that for $C_S < C_{S,crit}$, only the axisymmetric wrinkling mode occurs, whereas for $C_S > C_{S,crit}$, the transition from the axisymmetric to the diamond-like wrinkling mode is expected.

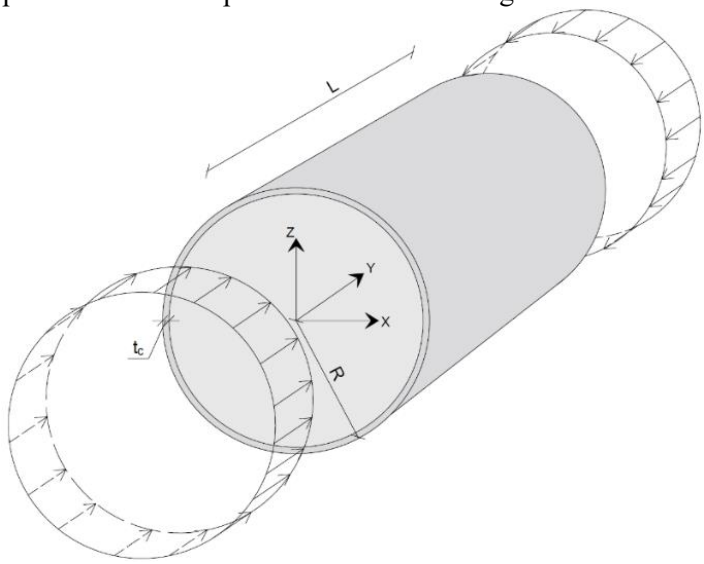

Figure 1: Problem description

$$C_S = \frac{E_S}{E_F}\left(\frac{R}{t_c}\right)^{\frac{3}{2}} \tag{1}$$

Solution methods

In [2] and [3], numerical solutions of the Fig.1 problem were obtained by rather complex 3d solid and composed 3d solid and shell models. We recomputed the problem by a simpler and faster numerical formulation. The shell was modelled by 6-parameter stress-resultant extensible-director shell quadrilateral finite element, enhanced by ANS (Assumed Natural Strain) concept. The substrate was modelled as a set of linear springs, with stiffness K_S. As a solution method, implicit dynamics was chosen. We used three implicit time-stepping schemes with controllable numerical damping of high-frequency modes and little numerical dissipation in the low-frequency range: generalized α scheme [4], JHW scheme [5], and Energy-Momentum-Decaying scheme [6].

Results

In Fig. 2 some results are shown that were computed with generalized α method (GAM). The transition from axisymmetric wrinkling pattern to the diamond-like pattern was nicely captured.

$R = 0.3$ mm
$L = 0.3$ mm
$t_c = 10^{-3}$mm

$E_F = 2.16 \cdot 10^4$MPa
$E_F/E_S = 12000$
$K_S = 75.2 \frac{\text{kN}}{\text{mm}^2}$
$\nu_F = 0.4$
$\nu_S = 0.48$
$\rho_F = 10^{-3} \frac{\text{g}}{\text{mm}^3}$
$C_S = 0.43$

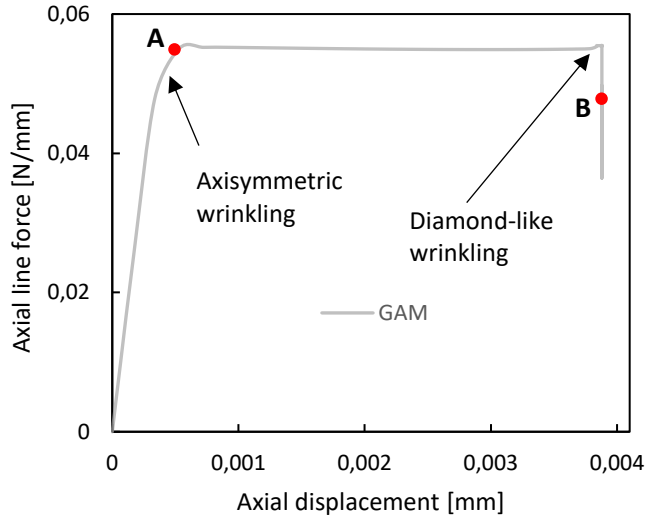

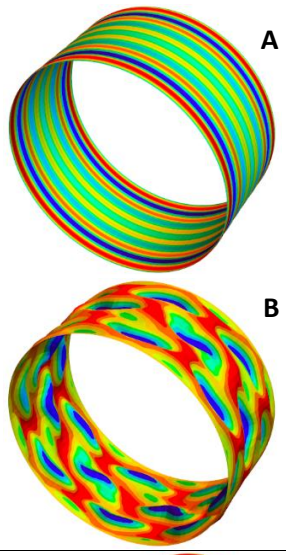

$R = 0.113$ mm
$L = 0.3$ mm
$t_c = 10^{-3}$mm

$E_F = 2.16 \cdot 10^5$MPa
$E_F/E_S = 120000$
$K_S = 35.2 \frac{\text{kN}}{\text{mm}^2}$
$\nu_F = 0.4$
$\nu_S = 0.48$
$\rho_F = 10^{-3} \frac{\text{g}}{\text{mm}^3}$
$C_S = 0.01$

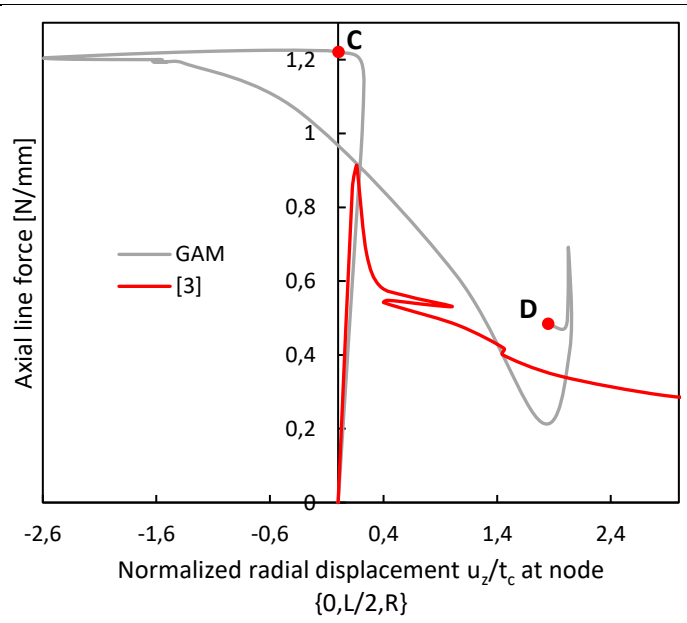

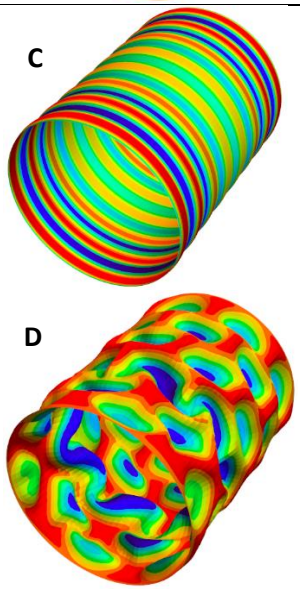

Figure 2: Two sets of input data (left), response graphs (middle) and wrinkling patterns (right)

References

[1] D. Terwagne, M. Brojan and P. M. Reis, Smart morphable surfaces for aerodynamic drag control, *Advanced Materials,* 26(38): 6608-6611, 2014.

[2] Y. Zhao, Y. P. Cao, X. Q. Feng and K. Ma, Axial compression-induced wrinkles on a core-shell soft cylinder: Theoretical analysis, simulations and experiments, *Journal of the Mechanics and Physics of Solids*, 73: 212-227, 2014.

[3] F. Xu and M. Potier-Ferry, On axisymmetric/diamond-like mode transitions in axially compressed core-shell cylinders, *Journal of the Mechanics and Physics of Solids*, 94: 68-87, 2016.

[4] D. Kuhl and E. Ramm, Generalized energy–momentum method for non-linear adaptive shell dynamics, *Computer Methods in Applied Mechanics and Engineering*, 178: 343-366, 1999.

[5] K. E. Jansen, C. H. Whiting and G. M. Hulbert, A generalized-α method for integrating filtered Navier-Stokes equations with a stabilized finite element method, *Comput. Methods Appl. Mech. Eng*., 190: 305–319, 2000.

[6] B. Brank, J. Korelc and A. Ibrahimbegović, Dynamics and time-stepping schemes for elastic shells undergoing finite rotations, *Computers and Structures*, 81: 1193-1210, 2003.

FEM MODELING OF FGM THERMO-MECHANICAL CYLINDER

D. Szubartowski, S. Hernik, and A. Ganczarski

Institute of Applied Mechanics, Cracow University of Technology, Kraków, Poland

e-mail: dszubartowski@pk.edu.pl, hernik@mech.pk.edu.pl, artur.ganczarski@pk.edu.pl

1. Introduction

Functionally graded materials (FGMs) provide thermal insulation and mechanical toughness at high temperature by varying the composition of thermal conductivity coefficient, thermal expansion coefficient and Young's modulus from high temperature side to low temperature side continuously and simultaneously by removing the discontinuity of layered structures.

When the classical FEM based on homogeneous elements is used for FGMs, the material properties stay the same for all integration points belonging to one finite element. This means that material properties may vary in a piecewise continuous manner, from one element to the other and a unique possibility to model FGM structure is approximation by use of appropriately fine mesh. On the other hand, a too coarse mesh may lead to unrealistic stresses at the interface between the subsequent sub-layers. To overcome this difficulty a special graded element has been introduced by Kim and Paulino [3] to discretize FGM properties. The material properties at Gauss quadrature points are interpolated there from the nodal material properties by the use of isoparametric interpolation functions. Contrary to the classical FEM formulation, the stiffness matrix of an element is expressed by the integral in which constitutive matrix is a function of the coordinates.

2. Formulation of FGM thermo-elastic cylinder

The system of equations of uncoupled thermo-elasticity expressed by stress function formulation [6] is as follows

$$\begin{aligned} &\mathcal{F}_1[\theta(\rho)] = \theta'' + (\tfrac{\lambda'}{\lambda} + \tfrac{1}{\rho})\theta' = 0 \\ &\mathcal{F}_2[F(\rho)] = F'' + (\tfrac{1}{\rho} - \tfrac{E'}{E})F' + (\tfrac{\nu}{1-\nu}\tfrac{E'}{E} - \tfrac{1}{\rho})\tfrac{F}{\rho} = -\tfrac{AE}{1-\nu}(\alpha\theta)' \end{aligned} \tag{1}$$

where: θ stands for increment of temperature, F denotes stress function, λ, E, α are coefficient of thermal conductivity, Young's modulus and coefficient of thermal expansion, respectively, whereas format of constant A depends on plane strain state type according to following scheme: in case of plane strain state imposed on both mechanical and thermal deformation $A = 1$, whereas in case of plane strain state imposed on mechanical deformation only $A = \frac{1}{1+\nu}$. The Poisson ratio ν is not subjected to any change.

All thermo-mechanical properties of the FGM such as α, λ and E are arbitrary functions of radius ρ, subsequent global approximations of which are presented in Table 1.

Voigt [5]	$f_{\mathrm{V}} = (f_{\mathrm{m}} - f_{\mathrm{c}})\frac{\rho - r_1}{r_{\mathrm{f}} - r_1} + f_{\mathrm{c}}$
Reuss [5]	$f_{\mathrm{R}} = \dfrac{f_{\mathrm{m}} f_{\mathrm{c}}}{f_{\mathrm{m}}(1 - \frac{\rho - r_1}{r_{\mathrm{f}} - r_1}) + f_{\mathrm{c}}\frac{\rho - r_1}{r_{\mathrm{f}} - r_1}}$
Hashin-Shtrikman $\zeta = \frac{1+\nu}{3(1-\nu)}$ [1, 2]	$f^{+}_{\mathrm{HS}} = \dfrac{3f_{\mathrm{m}}f_{\mathrm{c}} + 2f_{\mathrm{m}}(f_{\mathrm{m}} - f_{\mathrm{c}})\frac{\rho - r_1}{r_{\mathrm{f}} - r_1}}{3f_{\mathrm{m}} + (f_{\mathrm{c}} - f_{\mathrm{m}})\frac{\rho - r_1}{r_{\mathrm{f}} - r_1}}$ $\quad$ $f^{-}_{\mathrm{HS}} = \dfrac{f_{\mathrm{m}}f_{\mathrm{c}} + 2f_{\mathrm{c}}^2 + 2f_{\mathrm{m}}(f_{\mathrm{m}} - f_{\mathrm{c}})\frac{\rho - r_1}{r_{\mathrm{f}} - r_1}}{2f_{\mathrm{c}} + f_{\mathrm{m}} + (f_{\mathrm{c}} - f_{\mathrm{m}})\frac{\rho - r_1}{r_{\mathrm{f}} - r_1}}$ $E^{+}_{\mathrm{HS}} = E_{\mathrm{c}} + \dfrac{(E_{\mathrm{m}} - E_{\mathrm{c}})\frac{\rho - r_1}{r_{\mathrm{f}} - r_1}}{1 + \zeta(1 - \frac{\rho - r_1}{r_{\mathrm{f}} - r_1})(\frac{E_{\mathrm{m}}}{E_{\mathrm{c}}} - 1)}$ $\quad$ $E^{-}_{\mathrm{HS}} = E_{\mathrm{m}} + \dfrac{(E_{\mathrm{c}} - E_{\mathrm{m}})(1 - \frac{\rho - r_1}{r_{\mathrm{f}} - r_1})}{1 + \zeta\frac{\rho - r_1}{r_{\mathrm{f}} - r_1}(\frac{E_{\mathrm{c}}}{E_{\mathrm{m}}} - 1)}$

Table 1: Approximations functions of thermo-mechanical properties α, λ and E.

3. FEM formulation

From the FEM point of view both the Fourier equation (1_1) and the mechanical state equation (1_2) are treated as differential equations of variable coefficients describing isotropic material which inhomogeneity is subjected to smooth change form one element to other due to the global FGM approximation functions shown in Table 1). In order to save Euler's type of both equations (1) the following material inhomogeneity shape functions, that approximate the global FGM functions presented in Table 1 at a level of element, are assumed

$$\lambda^{(\mathrm{e})} = \lambda_0 \rho^n \qquad E^{(\mathrm{e})} = E_0 \rho^m \qquad \alpha^{(\mathrm{e})} = \alpha_0 \rho^s \tag{2}$$

Transformation of Eq. (1) to FEM form is done by discretization, use of the Galerkin weighted residual process [3,4,7]

$$\int_{\Gamma} [\mathcal{F}_{1,2}(\phi) + Q] W d\rho = 0 \tag{3}$$

and approximation of unknown function by N_i global shape functions $\phi = \sum_{i=1}^{n} N_i \phi_i$. The weighting functions W_i corresponding to node i are conveniently chosen such that $W_i = N_i$, hence substituting for ϕ and W in Eq. (3) and assembling all elements results in $H_{ij}\Phi_j + Q_i = 0$, in which typical element components of the element stiffness matrices $h_{ij}^{(\mathrm{e})}$ and the element nodal force vectors $q_i^{(\mathrm{e})}$ are

$$\begin{aligned}
h_{ij}^{(\mathrm{e})} &= \frac{\lambda_0}{n+2} \frac{r_{k+1}^{n+2} - r_k^{n+2}}{R^2} \begin{bmatrix} 1 & -1 \\ -1 & 1 \end{bmatrix} \qquad q_i^{(\mathrm{e})} = \lambda_0 \begin{bmatrix} -r_k^{n+1}\theta'(r_k) \\ r_{k+1}^{n+1}\theta'(r_{k+1}) \end{bmatrix} \\
h_{ij}^{(\mathrm{e})} &= \begin{bmatrix} \left(1 - \frac{m\nu}{1-\nu}\right)\frac{R}{3\overline{r}} + \frac{\overline{r}}{R} - \frac{m}{2} & \left(1 - \frac{m\nu}{1-\nu}\right)\frac{R}{\overline{r}}\left(\frac{1}{6} - \frac{r_k r_{k+1}}{R^2}\right) - \frac{\overline{r}}{R} + \frac{m}{2} \\ \left(1 - \frac{m\nu}{1-\nu}\right)\frac{R}{\overline{r}}\left(\frac{1}{6} - \frac{r_k r_{k+1}}{R^2}\right) - \frac{\overline{r}}{R} - \frac{m}{2} & \left(1 - \frac{m\nu}{1-\nu}\right)\frac{R}{3\overline{r}} + \frac{\overline{r}}{R} + \frac{m}{2} \end{bmatrix} \\
q_i^{(\mathrm{e})} &= \begin{bmatrix} -r_k F'(r_k) - A\frac{\alpha_0 E_0}{1-\nu}\left(\frac{r_{k+1}^{m+s+3} - r_k^{m+s+3}}{m+s+3} - r_{k+1}\frac{r_{k+1}^{m+s+2} - r_k^{m+s+2}}{m+s+2}\right)\frac{\theta_{k+1}-\theta_k}{R^2} \\ r_{k+1}F'(r_{k+1}) + A\frac{\alpha_0 E_0}{1-\nu}\left(\frac{r_{k+1}^{m+s+3} - r_k^{m+s+3}}{m+s+3} - r_k\frac{r_{k+1}^{m+s+2} - r_k^{m+s+2}}{m+s+2}\right)\frac{\theta_{k+1}-\theta_k}{R^2} \end{bmatrix}
\end{aligned} \tag{4}$$

for thermal and mechanical problems, respectively, and $\overline{r}$ stands for mid radius of an element. For the case of a two-node element with a linear variation of ϕ the shape functions are $N_1^{(\mathrm{e})} = (r_{k+1} - \rho)/R$ and $N_2^{(\mathrm{e})} = (\rho - r_k)/R$, where R is the length of an element. Symbols r_k and r_{k+1} refer to the radii of first and second node of an element, respectively.

References

[1] J. Aboudi and S.M. Arnold, and B.A. Bednarcyk Micromechanics of Composite Materials, Elsevier, Amsterdam, 2013.

[2] C. Calvo-Jurado and W.J. Parnell. Hashin-Shtrikman bounds on the effective thermal conductivity of a transversely isotropic two-phase composite material, J. Math. Chem., 53, 828-843, 2015.

[3] J.H. Kim and G.H. Paulino. Isoparametric graded finite elements for non-homogeneous isotropic and orthotropic materials, *ASME J. Appl. Mech*., 69, 502-514, 2002.

[4] D.R.J. Owen and E. Hinton. Finite Elements in Plasticity: Theory and Practice, Pineridge Press, 1980.

[5] J.J. Skrzypek and A.W. Ganczarski. Mechanics of Anisotropic Materials, Springer, Heidelberg, 2015.

[6] D. Szubartowski and A. Ganczarski. Problem of FGM TBC coated cylinder, *Computer Methods in Mechanics (CMM2017)*, AIP Conf. Proc. 1922, 120002-1–120002-8, https://doi.org/10.1063/1.5019117, 2017.

[7] O.C. Zienkiewicz and R.L. Taylor. The Finite Element Method, Butterworth, Oxford. 2000.

DIFFERENCES IN COMPRESSIVE AND TENSILE PROPERTIES OF CORE AND FACINGS IN SANDWICH PANELS

Ł. Smakosz[1], and I. Kreja[2]

[1,2]*Faculty of Civil and Environmental Engineering, Gdańsk University of Technology, Gdańsk, Poland*
e-mail: [1]luksmako@pg.edu.pl, [2]ikreja@pg.edu.pl

1. Introduction

Sandwich panels are widely used in civil engineering due to their advantageous properties such as high strength to weight ratio, good thermal insulation and ease of transport and assembly. The idea of a sandwich structure allows the use of diverse core and facing material combinations to obtain a composite with properties customized for a specific application. However, the intrinsic difference in stiffness of facing and core layers makes predicting the panel's failure mode a difficult task. Depending on materials used, the panel's geometry, and the type of loading, failure might be caused by local facing buckling, global panel buckling or reaching a limit stress in any of the panel's layers [1, 2].

Accurate assessment of material parameter values for core and facings is essential in sandwich panel design. The current research concentrates on taking into account differences in property values caused by material response dependence on the stress state. The panel under consideration is composed of expanded polystyrene (EPS) core and magnesium-oxide (MgO) board facings and is classified as a composite structural insulated panel (CSIP) [3, 4]. Presented material property values for both constituents are based on own experimental research [5] and literature. Pertaining computational analysis consists of two stages: (1) numerical replication of small-scale bending tests on CSIP beams and (2) numerical simulation of flexure tests for full-scale panels [6]. FEA is performed using commercial Abaqus software [7] and a self-created user procedure.

2. Component material properties

Common core materials used in sandwich panels are structural foams, such as EPS, which have a complex microstructure that behaves differently in different loading conditions. As one can observe the microstructure's struts buckle quite easily in compression while in tension they typically stretch until fracture. In consequence effective material properties in macro-scale depend on the stress state in micro-scale [5, 8]. Such phenomena should be taken into account in cases where localised loads are involved. MgO board is a composite consisting of MgO cement mixture matrix and a glass-fibre mesh reinforcement on its top and bottom surfaces [3]. Reinforcement meshes carry loads in tension but are inactive in compression, which causes the difference in effective property values. Main material parameter values for both constituents in different loading conditions are presented in Table 1. EPS parameters given for three different densities (in kg/m^3) are provided as mean values, whereas MgO board properties are shown as extremes.

	MgO min	MgO max	EPS 15	EPS 19	EPS 21
E^c [MPa]	2430	3886	5.0	5.4	6.8
E^t [MPa]	5750	8040	7.2	9.2	10.5
ν [-]	0.18	0.18	0.09	0.11	0.12
σ_y^c [MPa]	5.0	18.2	0.07	0.09	0.10
σ_y^t [MPa]	4.8	6.1	0.12	0.15	0.16

Table 1: Material properties of MgO board and EPS; E – elasticity modulus, ν – Poisson number, σ_y – yield stress, c – compression, t – tension.

3. Numerical analysis

Commercial Abaqus software [7] has been used to perform a numerical recreation of CSIP beam bending tests. Beams of three different lengths have been tested (Figure 1) under two types of loading conditions (12 samples in total). A half of the tests has been carried out as three-point bending (3PB) and a half as third span four-point bending (4PB) [5]. In FEA samples have been modelled with a dense mesh of plane stress 4-node reduced integration elements. Since no debonding has been observed in laboratory tests a perfect bond between adjacent constituents has been assumed. Supports and loads have been realized with rigid body objects. Geometrical nonlinearity has been taken into account as well as material nonlinearity for both core and facings. Drucker-Prager material model has been applied in all layers.

The most challenging part was associated with an automatic change of material parameters in accordance with changes of stress state. In order to do so, a user defined procedure has been created. The procedure generates an additional variable in every integration point, its value ranging from -1 to 1 and being updated with each increment. Material data for elastic, inelastic and failure states have been then linked with this variable in such a way, that compression values have been used for -1, tension values for 1 and linear interpolation has been used for intermediate states. Numerical results obtained were in a reasonably good agreement with the test data (Figure 1).

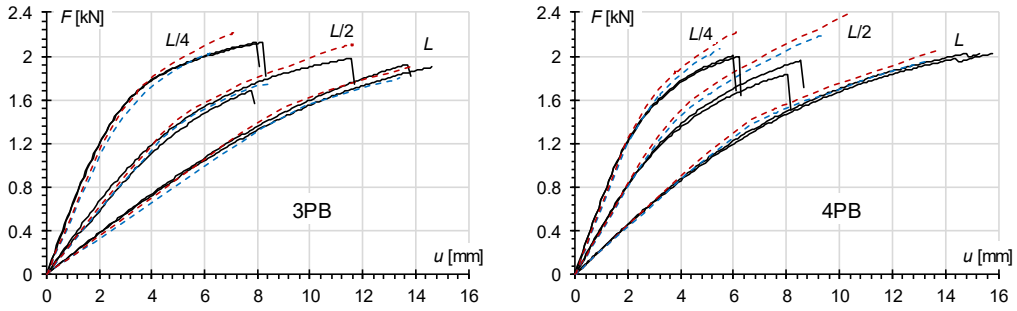

Figure 1: Comparison of FEA results (dashed lines) with test data (continuous lines) for 3- and 4-point bending; red – MgO max, blue – MgO min, *L* – CSIP beam length.

The final stage of this research will comprise of numerical experiments performed on full-scale panels of varying length to core thickness ratios. This analysis will aim to determine how sensitive to core crushing are the CSIPs in question and when it is necessary to take the advanced material phenomena into account.

Acknowledgments The authors acknowledge the access to computational software provided by the Centre of Informatics - Tricity Academic Supercomputer & networK (CI TASK).

References

[1] H. G. Allen. *Analysis and Design of Structural Sandwich Panels*. Pergamon Press, 1969.
[2] Z. Pozorski. *Sandwich panels in civil engineering – theory, testing and design*. The Publishing House of Poznan University of Technology, 2016.
[3] A. Manalo. Structural behaviour of a prefabricated composite wall system made from rigid polyurethane foam and Magnesium Oxide board. *Construction and Building Materials*. 41:642, 2013.
[4] M. A. Mousa and N. Uddin. Flexural Behavior of Full-Scale Composite Structural Insulated Floor Panels. *Advanced Composite Materials*. 20:547, 2011.
[5] Ł. Smakosz and J. Tejchman. Evaluation of strength, deformability and failure mode of composite structural insulated panels. *Materials and Design*. 54:1068, 2014.
[6] Ł. Smakosz and I. Kreja. Experimental and numerical evaluation of mechanical behaviour of composite structural insulated panels. *Recent Advances in Computational Mechanics*. CRC Press-Taylor & Francis Group, 2014.
[7] *Abaqus Analysis User's Manual*. Dassault Systèmes, 2016.
[8] M. F. Ashby. The mechanical properties of cellular solids. *Metallurgical Transactions A*, 14A:1755, 1983.

FINITE ELEMENT BASED ON A REDUCED KIRCHHOFF-LOVE SHELL MODEL FOR SIMULATION OF SOFT BILAYERS

M. Brojan[1], T. Veldin[1], and B. Brank[2]

[1]*University of Ljubljana, Faculty of Mechanical Engineering, Ljubljana, Slovenia*
[2]*University of Ljubljana, Faculty of Civil and Geodetic Engineering, Ljubljana, Slovenia*

e-mail: miha.brojan@fs.uni-lj.si

1. Background

Depending on geometrical and material properties thin-film/soft-substrate bilayers may, when subjected to compressive loading, loose its stability and bifurcate from a homogeneous state of compression to either global or local deformation modes. In the case of a stiff and thin surface, bonded to a thick and compliant substrate, several wrinkling modes (e.g. dimple, labyrinthine or hybrid) are the modes preferred over the global buckling in early post-critical regime. Further increase in the load pushes the structure deeper into the post-critical regime and typically induces secondary instabilities, showing that these types of structures are often multi-stable. Several interesting phenomena can be observed, such as pattern switching, wrinkle-to-fold transitions, creasing, etc., which make this problem worth exploring, especially in search for advanced functionalities. As such, researchers used surface wrinkling as a platform to study tuneable adhesion [1], wetting to attain hydro-phobicity/hydro-philicity [2], for fabrication of micro-lens arrays [3], micro-gears [4], etc.

It turns out that theoretical solutions of this problem are very difficult to find due to the strong non-linearities (large deformations, discrete material distribution, multi-stable states, etc.). With the exception of a few studies (see e.g. Xu and Potier-Ferry [5,6]), no efficient (fast and reliable) numerical procedures are available. Here, we present our attempt to develop such procedure based on a finite element method and a reduced model of the Kirchhoff-Love shell.

2. Finite element based on a reduced Kirchhoff-Love shell model

The derivation of the finite element procedure we show in this contribution is based on the Kirchhoff-Love kinematics. Moreover, we apply a reduced Kirchhoff-Love kinematic model, similar to that used in [7], where the tangential components of the displacement vector were considered to be small when compared to the normal component. The simplification calls for the use of the classical treatment of the shell displacement field (with the displacement components resolved with respect to the curvilinear covariant basis in the finite element formulation). By neglecting the tangential strains, the standard Kirchhoff-Love shell Green-Lagrange strain tensor is significantly simplified. As for the material model, we use the St. Venant-Kirchhoff shell hyperelastic model. The substrate is modelled as a linear spring, with constant stiffness k in units of $\mathrm{N/m^2}$.

We derived quadrilateral and triangle finite elements, denoted as DKQ-4 and DKT-3, respectively. In order to approximate the Kirchhoff-Love shell kinematic constraint, three degrees of freedom, w, $\partial w/\partial x$ and $\partial w/\partial y$, were introduced at each node, where w is normal displacement and x, y are orthogonal coordinates in the tangent plane at the node. By using linked interpolation of w and its derivatives, similar to the one applied in discrete Kirchhoff (DK) quadrilateral (Q) and tringle (T) plate elements [8], the Kirchhoff kinematic constraint becomes fulfilled along the edge of each element in the direction of the edge.

The results shown in the next section were computed by either standard Newton-Raphson iterative procedure or by the path-following methods presented in [9]. We note that the problems presented in the next section, computed by DKQ-4 and DKT-3, were too difficult for standard Assumed Natural Strain (ANS) quadrilateral with Reissner-Mindlin kinematics (both static analysis with enhanced path-following method and implicit dynamics analysis failed).

4. Results

Figure 1 shows deformed configurations of a spherical and cylindrical shell on elastic substrates. Material and geometrical parameters are as follows: thickness $t = 0.48$ mm, radius $R = 20.0$ mm, elastic modulus $E = 2$ MPa, $k = 0.22$, Poisson's ratio $\nu = 0.48$ for both shells, height $h = 10$ mm for cylindrical shell.

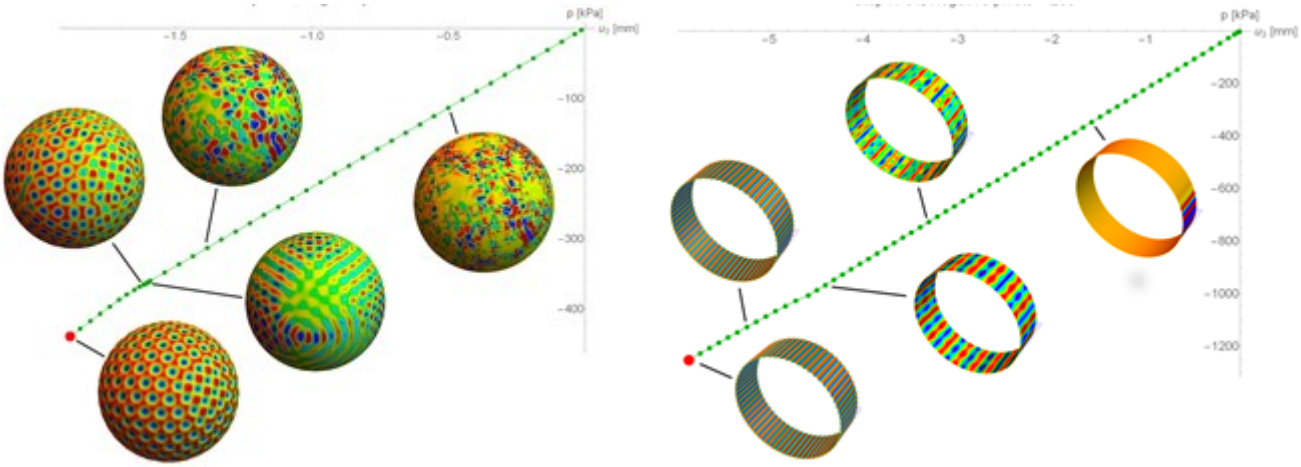

Figure 1: Deformed configurations of a spherical (left) and cylindrical (right) shell.

The solution procedure converged within 10 mins on an average laptop. The drawback of the current setup is that the solution is only valid for moderate displacements. Generalization of the procedure is underway.

References

[1] Lin P. C., Vajpayee S., Jagota A., and Hui C. Y. Mechanically tuneable dry adhesive from wrinkled elastomers. *Soft Matter*, 4:1830-1835, 2008.

[2] Chung J. Y., Youngblood J. P., and Stafford C. M. Anisotropic wetting on tunable micro-wrinkled surfaces. *Soft Matter*, 3:1163-1169, 2007.

[3] Chan E. P. and Crosby A. J. Fabricating microlens arrays by surface wrinkling. *Advanced Materials*, 18(24):3238-3242, 2006.

[4] Yin J., Bar-Kochba E., and Chen X. Mechanical self-assembly fabrication of gears. *Soft Matter*, 5:3469-3474, 2009.

[5]] F. Xu, M. Potier-Ferry. A multi-scale modeling framework for instabilities of film/substrate systems. *Journal of the Mechanics and Physics of Solids*, 86:150-172, 2016.

[6] [6] F. Xu and M. Potier-Ferry. On axisymmetric/diamond-like mode transitions in axially compressed core-shell cylinders, *Journal of the Mechanics and Physics of Solids*, 94: 68-87, 2016.

[7] Stoop N., Lagrange R., Terwagne D., Reis P. M., and Dunkel J. Curvature-induced symmetry breaking determines elastic surface patterns. *Nature Materials*, 14:337-342, 2015.

[8] Bohinc U., Brank, B., Ibrahimbegovic A. Discretization error for the Discrete Kirchhoff plate finite element approximation. *Computer Methods in Applied Mechanics and Engineering*, 269:415-436, 2014.

[9] Stanić A., Brank B., Korelc J. On path-following methods for structural failure problems. *Computational Mechanics*, 58:281-306, 2016.

Poster session

FUNCTOR-ORIENTED FINITE ELEMENT PROGRAMMING WITH APPLICATION TO STRUCTURAL TOPOLOGY OPTIMIZATION

P. Tauzowski[1], B. Blachowski[1], and J. Logo[2]

[1]*Institute of Fundamental Technological Research, Polish Academy of Sciences, Warsaw, Poland*
[2]*Budapest University of Technology and Economics, Budapest, Hungary*

e-mail: ptauzow@ippt.pan.pl

1. Problem statement

The subject of this study is an efficient approach to the development of a finite element framework, which is intended to be used for solving a variety of problems in computational solid mechanics. One of such problems, recently becoming an active field of research, is topology optimization of structures made of elastic-plastic materials. For finding the optimal topology of real, practical and complex structures the knowledge of a number of numerical algorithms is required, to mention a few: modification of finite element meshes, aggregation of tangent stiffness matrices, or direct and iterative solvers.

The classical computer implementation of the original Classical Optimality Criteria method (COC) of the topology optimization problem given by Bendsoe and Sigmund [1] is relatively simple and contains 99 lines of code in the MATLAB language. However, it assumes that there exists only a single loading case, single displacement (compliance) constraint, the material is linearly elastic and the optimal topology can be found using the so-called Solid Isotropic Material with Penalization (SIMP) algorithm, which is based on the original COC method. In reality, engineers face a slightly different problem. They need to find the topology of a minimum weight structure subjected to multiple loading cases, made of an elasto-plastic material, and with a limit on stresses. The above mentioned SIMP approach may not lead to an optimal solution [2].

To avoid this obstacle in this study we reformulate the minimum compliance problem so that we look for a minimum weight structure subjected to multiple loading under stress constraints instead of volume fraction constraint. In this way several local constraints are used instead of a single global one.

Mathematically, we can express our approach for topology optimization in the following form

$$\begin{aligned} &\text{Find minimum of} && V(\rho) = \int_V \, dV \\ &\text{Subject to} && \int_V \, \sigma_{ij}\delta\varepsilon_{ij} \, dV - \int_{\partial V} f_i \delta u_i \, d\Gamma = 0 \\ & && |\sigma_{red}| \leq \sigma_0 \\ & && \rho_{min} \leq \rho \leq \rho_{max} \end{aligned}$$

where V is the volume of the structure, σ_{ij} is the stress tensor, $\delta\varepsilon_{ij}$ is the virtual strain, f_i represents surface loading, δu_i is the virtual displacement, σ_{red} is the von Mises stress, σ_0 denotes the yield limit and finally ρ represents the density of the material distribution.

In computational mechanics the above formulation is usually discretized using the finite element method. Then, the structural topology optimization investigated in this study can be expressed in the following form

$$\begin{aligned} &\text{Find minimum of} && V(\boldsymbol{\rho}) = \textstyle\sum_e V_e \\ &\text{Subject to} && \mathbf{K}\mathbf{u} - \mathbf{f} = \mathbf{0} \\ & && |\boldsymbol{\sigma}_{red}| \leq \sigma_0 \mathbf{I}_\rho \\ & && \rho_{min}\mathbf{I}_\rho \leq \boldsymbol{\rho} \leq \rho_{max}\mathbf{I}_\rho \end{aligned}$$

where $\mathbf{K}$ is the tangent stiffness matrix, $\mathbf{u}$ is the vector of displacement, $\boldsymbol{\rho}$ is the vector of material distribution density, and $\mathbf{I}_\rho$ is the identity vector.

To find the optimal structural topology using the above formulation a large number of iterations and finite element analyses are required. To compensate this great demand on computational power we propose an effective architecture of our FE code, which is based on the functor-oriented programming paradigm [3].

2. Functor based finite element programming

The classical formulation of finite elements usually contains a class called finite element whose purpose is not only to approximate some fields (displacements, temperature or own geometry) but also to define matrices necessary for a particular analysis (Listing 1). It often leads to a sophisticated class hierarchy of finite elements.

Listing 1.

```
class FiniteElement
{
     vector<Node> nodes;
     Material *mat
public:
...
  virtual Vector getX( Vector ksi)  = 0;
  virtual Matrix getStifnessMatrix()= 0;
  virtual Matrix getMassMatrix()    = 0;
  virtual Matrix getTangentMatrix() = 0;
...
};
```

In our approach matrices necessary for an analysis (tangent matrix, mass matrix) are in separate classes. The hierarchy of these classes can be developed almost separately from finite elements. Also the finite elements hierarchy is much smaller. Because each class represents one kind of matrix computed in the analysis, the best (in our opinion) kind of object to use in this case is a functor. A functor represents one subroutine and it can also be called as a function: `functor(FiniteElement)`. (Listing 2). By contrast, in the classical approach each matrix function in a finite element has its own unique name. It makes aggregation process more complex. The connection of the functor with the finite element is only accomplished through the call parameter. In the other words, the finite element is the parameter of the functor. Another advantage of our approach is the use of templates. This allows us to avoid the overhead associated with virtual function call in those places of the code, where it is especially important (e.g. calculations at Gauss points).

Listing 2.

```
template <class T>
class TElemFunctor
{
public:
  TElemFunctor( const DTvec &dv):m_dofs( dv){ }
  virtual TElemFunctor* Clone() const = 0;
  const T& GetValue() const { return m_value; }
  virtual const T& operator()
       (  const CFEInstance &ielem  ) = 0;
protected:
    T m_value;
};
```

3. Topology optimization under stress constraints

The effectiveness of functor-oriented programming in optimal design has been demonstrated on several examples including benchmark problems like cantilever or simply supported beam (Figure 1).

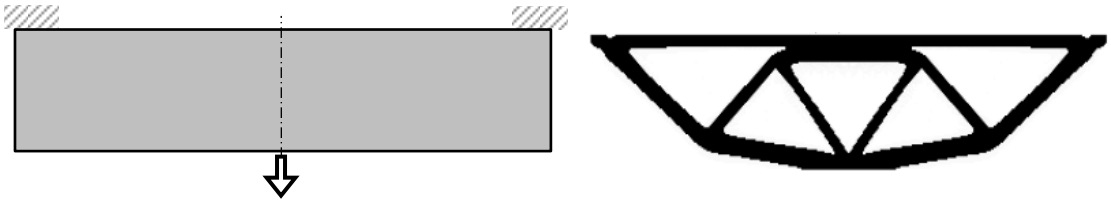

a) Design domain b) Optimal solution

Figure 1. Optimal topology of the simple supported beam.

Acknowledgments The Authors are grateful for financial support provided by the National Research, Development and Innovation Office (grant K 119440) - Joint grant of the Hungarian and the Polish Academy of Sciences.

References

[1] M. P. Bendsoe, O. Sigmund, *Topology Optimization: Theory, Methods, and Applications*, Springer-Verlag, 2004.
[2] K. Mela, J. Koski, *On the equivalence of minimum compliance and stress-constrained minimum weight design of trusses under multiple loading conditions*, Struct Multidisc Optim, 46: 679, 2012.
[3] D. Vandevoorde, N. M. Josuttis, D. Gregor, *C++ Templates - The Complete Guide*, 2nd ed., Addison-Wesley, 2017.

A NOVEL APPROACH FOR MEASUREMENT OF ELASTIC MODULUS OF TRABECULAR BONE IN MANDIBLE

Y. Dohi[1], Y. Othuka[1], M. Inose[2], N. Suda[1] and S. Arikawa[3]

[1] Division of Orthodontics, Department of Human Development and Fostering Meikai University School of Dentistry
[2] Graduate School of Science and Technology, Meiji University
[3] Department of Mechanical Engineering Informatics, Meiji University

e-mail: yosuke.dohi@dent.meikai.ac.jp

1. Introduction

Stress analysis of cortical bone and trabecular bone in the jaws is very important for not only basic science but also accurate diagnosis and effective treatment in clinical dentistry. Currently, finite element method (FEM) is widely used for such stress analysis. FEM is a numerical analysis, that is, the analysis result largely depends on the substituted material properties. However, characteristic of material properties in the mandible with complicated anatomical structure has not been elucidated. Especially, the property of trabecular bone is still unknown and the properties of the femur and vertebra have been used as substitution values. The reason why it is hard to analyze the material property of trabecular bone in the mandible can be ascribed to the difficulty in obtaining specimen from trabecular bone, and also to the mechanical anisotropy of bone.
Therefore, we tried to apply a method of linear rule of mixtures for mesurement of elastic modulus of mandibular trabecular bone. The linear rule of mixtures is known as an effective method for analysing composite materials in the engineering field. This approach is a procedure of calculating the material properties of a whole composite material from a prediction formula based on product of numbers in each volume fraction and material property in a composite material. By applying this method, it is possible to measure the elastic modulus of trabecular bone without extracting only trabecular bone. In this study, we measured the elastic modulus of the trabecular bone of porcine mandible using linear rule of mixtures.

2. Material and method

Cortical bone and trabecular bone were cut out from the center of the 6 months old pig's mandibular ramus in one piece. For the purpose of repeating the compression test using the linear rule of mixtures, the specimen was precisely trimmed in a rectangular shape. Measurement of the elastic modulus was evaluated by displacement analysis in a compression test using a laser displacement meter (Panasonic, HL-G1) with a specimen placed in the precision universal testing machine (SHIMADZU, AG-250kNplus) at the center of the compression jig. In the experiment, first, the end portion of the specimen was cut and removed repeatedly to arbitrarily reduce its shape, and the elastic modulus of the specimen was measured at each cutting. Then, by using the prediction equation of linear rule of mixtures shown below (1), the elastic modulus of the resected bone was calculated by finding the difference between consecutive data. E_f is the modulus of elasticity of the part cut and removed, E_c is the elastic modulus before cutting and removal, E_m is the elastic modulus after cutting and removal, V_m is the volume fraction after cutting removal, and the following equation (1) was obtained by transforming linear rule of mixtures.

$$E_f = \frac{E_c - V_m E_m}{1 - V_m}. \tag{1}$$

In experiment 1, trabecular bone with cortical bone at both ends of the specimen was used. In experiments 2

and 3, trabecular bone with cortical bone only at one end of the specimen was used, and modulus of such different bones structure were measured. As for the measurement error due to the deformation of the jig of the precision universal testing machine, we calculated the correction value from the basic experiment using the aluminium alloy (JIS A 2017) and corrected the result of experiments 1, 2, and 3.

3. Result

The elastic modulus of Experiment 1 in which specimen was cut three times were 11.9 GPa for bone including cortical bone and 3.8 GPa and 6.2 GPa for bone with only trabecular bone in order from lingual side. The elastic modulus of Experiment 2 in which specimen was cut twice were 1.2 GPa and 1.9 GPa in order from the lingual side. The elastic modulus of experiment 3 in which specimen was cut four times to obtain narrow range data of the trabecular bone were 5.0 GPa, 3.9 GPa, 3.6 GPa and 8.3 GPa in order from the lingual side.

4. Discussion

From the finding of experiment 1, since elastic modulus was low high and low in cortical bone and trabecular bone respectively, it was suggested that linear rule of mixtures was useful to determine the elastic modulus. From experiments 2 and 3, it was found that the elastic modulus of trabecular bone greatly varies depending on the excised site. From all these findings, elastic modulus could be calculated without extracting trabecular bone solely. The modulus was determined at any arbitrary site having cortical and trabecular bones. By utilizing more accurate elastic modulus distribution of bone, it is expected to clarify the correct mechanical properties of trabecular bone.

References

[1] E. Lakatos, L. Magyar and Imre Bojtar. Material Properties of the Mandibular Trabecular Bone. *Journal of Medical Engineering,* 2014;2014:470539, doi:10.1155//2014/470539. Epub 2014 Oct 29. https://www.hindawi.com/journals/jme/2014/470539

[2] M. Sakamoto, K. Sato, K. Kobayashi, J. Sakai, E. Takano and T. Hara. Measurements of Mechanical Properties of Cortical Bone Using Nanoindentation Tests. *Japanese Journal of Clinical Biomechanics*, 24: 1-5, 2003.

[3] J. Takayanagi. Mechanical effect of bite force at different occlusal regions on mandible and temporomandibular joint : Using the three-dimensional finite element method models. *Orthod Waves.Jpn Ed*, 65(1): 11~23, 2006

[4] M. Kohara. A dynamic study of multi-bracket appliance using a digital image correlation method combined with three-dimensional finite element analysis : stress distribution in the root surroundings during maxillary anterior retraction. *Orthod Waves.Jpn Ed* 69(1): 141~155, 2010

STUDY OF THE DISTRIBUTION OF NORMAL CONTACT PRESSURE BETWEEN ELEMENTS JOINED IN A MULTI-BOLTED SYSTEM UNDER OPERATIONAL LOADS

R. Grzejda[1]

[1]*West Pomeranian University of Technology, Szczecin, Poland*

e-mail: rafal.grzejda@zut.edu.pl

1. Introduction

In a multi-bolted connection treated as a system [1], it is possible to distinguish, among others, the contact layer at the interface of the joined elements. This contact layer can be replaced with both nonlinear and linear elastic foundation models.

Assuming that the load of the joined elements acts on the direction perpendicular to the surface of their contact, the contact layer can be modelled using the Winkler model [2]. Then contact phenomena between the joined elements can be sufficiently modelled using the normal characteristics of the connection. Such characteristics can be represented with a good approximation by an exponential function [3, 4]. However, the contact layer at the interface of the elements joined in the multi-bolted connection is usually operated after the preload, when the normal characteristics of the connection from nonlinear become close to linear. Therefore, in addition to the application of nonlinear contact characteristics, it is also appropriate in this case to use linearised courses of these characteristics.

In the paper a multi-bolted system model with the Winkler type contact layer between the joined elements is presented, on the basis of which it is possible to include for each element of the contact layer (for each nonlinear or linear spring, depending on the model) normal mechanical characteristics, for example obtained from experimental tests. The aim of the paper is to study the distribution of normal contact pressure between the elements joined in a multi-bolted system under operational loads for selected models of this system.

2. Structure of the system

The structure of the multi-bolted system is based on the model of four subsystems shown schematically in Figure 1.

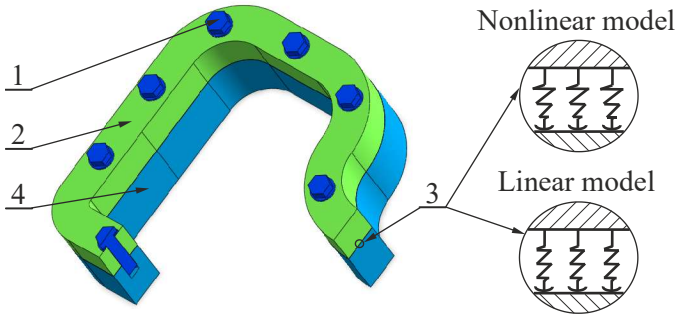

Figure 1: Multi-bolted system (1 – subsystem **B**, a set of the bolts, 2 – subsystem **F**, the flexible flange element, 3 – subsystem **C**, the contact layer, 4 – subsystem **S**, the flexible support).

The set of equations of equilibrium of such a multi-bolted system can be written in the following matrix notation

$$(1) \qquad \begin{bmatrix} \boldsymbol{K}_{BB} & \boldsymbol{K}_{BF} & \boldsymbol{0} & \boldsymbol{K}_{BS} \\ \boldsymbol{K}_{FB} & \boldsymbol{K}_{FF} & \boldsymbol{K}_{FC} & \boldsymbol{0} \\ \boldsymbol{0} & \boldsymbol{K}_{CF} & \boldsymbol{K}_{CC} & \boldsymbol{K}_{CS} \\ \boldsymbol{K}_{SB} & \boldsymbol{0} & \boldsymbol{K}_{SC} & \boldsymbol{K}_{SS} \end{bmatrix} \cdot \begin{bmatrix} \boldsymbol{q}_B \\ \boldsymbol{q}_F \\ \boldsymbol{q}_C \\ \boldsymbol{q}_S \end{bmatrix} = \begin{bmatrix} \boldsymbol{p}_B \\ \boldsymbol{p}_F \\ \boldsymbol{p}_C \\ \boldsymbol{p}_S \end{bmatrix},$$

where: $\boldsymbol{K}_{BB}$, $\boldsymbol{K}_{FF}$, $\boldsymbol{K}_{CC}$, $\boldsymbol{K}_{SS}$ – stiffness matrices of individual subsystems, $\boldsymbol{K}_{BF}$, $\boldsymbol{K}_{FB}$, $\boldsymbol{K}_{BS}$, $\boldsymbol{K}_{SB}$, $\boldsymbol{K}_{FC}$, $\boldsymbol{K}_{CF}$, $\boldsymbol{K}_{CS}$, $\boldsymbol{K}_{SC}$ – matrices of elastic couplings between separated subsystems, $\boldsymbol{q}_i$ – displacements vector of the i-th subsystem, $\boldsymbol{p}_i$ – loads vector of the i-th subsystem (i – symbol of the subsystem, $i \in \{B, F, C, S\}$).

3. Results of calculations

Sample calculations were performed for a selected asymmetrical multi-bolted system shown in Figure 2a. The thickness of the joined flanges is equal to 20 mm. The connection is fastened by means of seven M10 bolts with the preload F_m equal to 20 kN. The set of bolts is built from the spider bolt models. The preloaded multi-bolted system is subjected to an external normal force F_e equal to 30 kN and applied in the manner shown in Figure 2a. The location of nodes adopted to describe the normal contact pressure distribution is depicted in Figure 2b. The distribution of normal contact pressure at the interface of the elements joined in the multi-bolted system loaded externally by the force F_e is illustrated in Figure 2c.

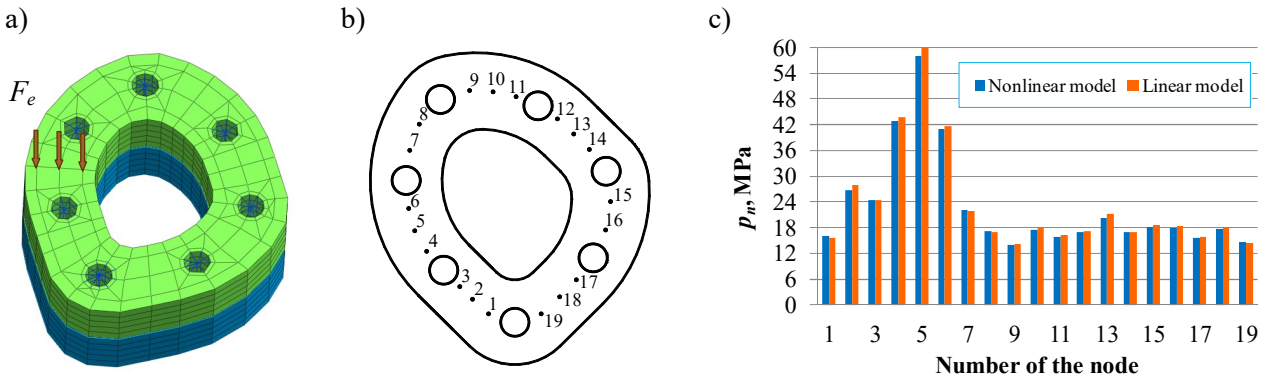

Figure 2: Example of calculations: a) FEM-based model of the multi-bolted system, b) nodes adopted to describe the normal contact pressure distribution, c) distribution of normal contact pressure at the interface of the elements joined in the multi-bolted system loaded externally.

4. Conclusions

In the paper a general systemic approach to modelling and calculations of arbitrary multi-bolted systems is presented. It can be implemented in the operational state of the system adopted for various bolt models.

References

[1] R. Grzejda. Modelling nonlinear preloaded multi-bolted systems on the operational state. *Engng. Trans.*, 64:525, 2016.

[2] O. H. Mahrenholtz. Beam on viscoelastic foundation: an extension of Winkler's model. *Arch. Appl. Mech.*, 80:93, 2010.

[3] K. Grudziński and R. Kostek. An analysis of nonlinear normal contact microvibrations excited by a harmonic force. *Nonlinear Dynam.*, 50:809, 2007.

[4] A. Misra and S. Huang. Effect of loading induced anisotropy on the shear behavior of rough interfaces. *Tribol. Int.*, 44:627, 2011.

EQUATIONS OF MOTION AND VIBRATION A SWITCH POINT - A CURVED BEAM WITH A VARIABLE CROSS-SECTION

J. Kisilowski[1],R. Kowalik[2],

[1]*University Of Technology And Humanities, Radom, Poland*
[2]*Polish Air Force Academy, Dęblin, Poland*
e-mail: jerzy@kisilowscy.waw.pl, r.kowalik@wsosp.pl

1. Abstract

The article presents mathematical considerations describing the dynamics of the springing switch point, which is an element of the railway turnout. Stages of mathematical analysis due to the structure of the switch point were divided into two stages. The first phase refers to the analysis of the dynamics of the switch point as a beam with variable rectilinear stiffness to which three forces are applied (coming from three closures of switch drives) placed in the initial section of the switch point. The next stage of the analysis concerns the same beam, but curved with a variable cross-section. In both cases, the normal force reflecting forces from the rail vehicle will act on the beam. The calculations will refer to a switch point with a length of 230 [m] and a radius of curvature R = 1200 [m]. The analysis of the switch point in the first stage will refer to the case of movement of the rail vehicle on the straight rail, and in the second stage it will concern the movement of the rail vehicle on the closure rail.

2. Mathematical model of a curved switch point

Considering the switch point as a trapezoidal curved beam described by the width b (Fig. 1), lying on a continuous elastic substrate and subjected to vertical load, which passes through its neutral axis, let F be the shear force in the cross-section of the beam, located at a distance x from the beginning of the coordinates, and by M the moment of external forces relative to this cross-section. If by F we will understand the sum of all vertical forces acting on the beam from the side of the cross-section on which the origin of the coordinates is located. In the literature [1], [2] and [3], one can find mathematical models describing the dynamics of a beam with a variable cross-section except that they lack the impulse of forces acting on the surface in the vertical direction (wheel pressure on the switch point) and horizontal (force holding a railway turnout drive).

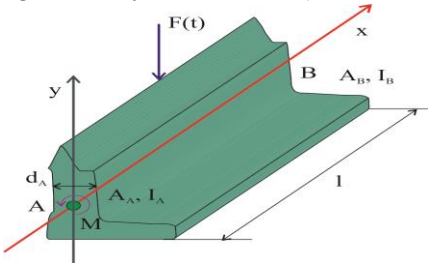

Fig. 1 Parameters characterizing the switch point

At the beginning, assumptions were made, which simplify the process of describing by differential equations the movement of a curved beam with a variable cross-section, which is an element of a beam associated with two degrees of freedom. Thus, one rotary movement and one progressive movement takes place at both ends of the beam. The action of force F causes deformations (displacements) in the direction x of the narrower part of the switch point. In the drawing by A, the beginning of the switch point was marked, the end by B. In turn, the cross section of the beam with a variable cross-section was determined by d_a and d_b. The length of the beam was determined by the quantity of l.

For the switch point - trapezoidal beam, the cross-section area can be written by the relationship:

$$A_x = A_A \cdot \left[1 + \left(\frac{d_B}{d_A} - 1\right) \cdot \frac{x}{l}\right]^m . \tag{1}$$

The change of the moment of inertia for the analyzed section of the beam cross-section around the deflection axis was defined as:

$$I_x = I_A \cdot \left[1 + \left(\frac{d_B}{d_A} - 1\right) \cdot \frac{x}{l}\right]^n . \tag{2}$$

by A_A and I_A the cross-sectional area and the moment of inertia at the beginning of the switch point were denoted respectively, with the subscript *B* defined the above-mentioned values at the end of the beam. Parameters *m* and *n* refer to the shape factor, which depends on the section and dimension of the beam with a variable cross-section.

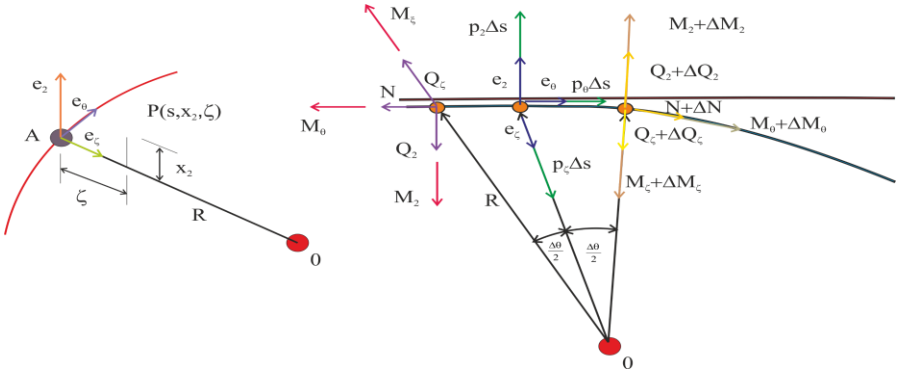

Fig. 2 Nominal model of the switch point - determination of forces

Based on the presented nominal models, mathematical models were determined and calculations were made for the beam, which is in fact a turnout switch point with a radius of 1200 [m], and the forces that arise when the rail vehicle travels through the turnout on straight and closure rail were taken into account. The results of simulation tests performed in the software.

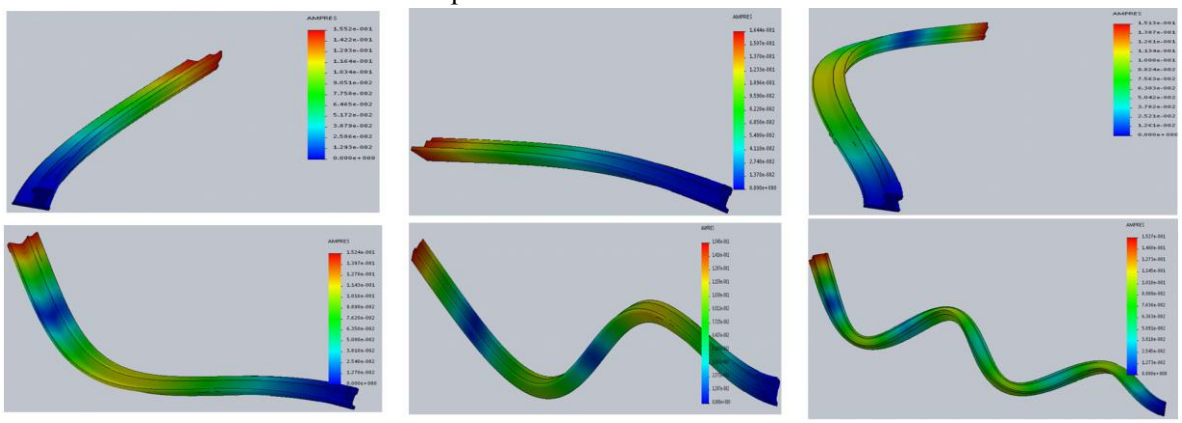

Fig. 3 The own vibrations of the beam with a variable cross-section (from the first harmonic to the sixth - from the left)

References

[1] J.-P. Blaizot and G. Ripka. *Quantum theory of finite systems*. MIT Press, 1985.
[2] Kaliski S., *Drgania i fale*, PWN, Warszawa 1966, s. 161-163.
[3] O. C. Zienkiewicz and J. Z. Zu. A simple error estimator and adaptive procedure for practical engineering analysis. *Int. J. Num. Meth. Eng.*, 24:334, 1987.

EXPERIMENTAL AND NUMERICAL INVESTIGATION OF MODE I FRACTURE IN PLATE PMMA SAMPLES WITH NOTCHES

E. Bura[1], A. Seweryn[1]
[1]*Bialystok University of Technology, Bialystok, Poland*

e-mail: e.bura@doktoranci.pb.edu.pl

1. Introduction

A shape, loading and operating conditions, a type of material are only few of many factors which are having influence on the fracture process. Experimental studies allow to get to know the nature of the phenomenon and to build numerical models for cracking process predictions. Many papers show results of experimental studies, in which polymethyl methacrylate (PMMA) samples were often used. This thermoplastic polymer is highly sensitive to temperature changes and deformation speed. It manifests typically brittle properties during dynamic tests or at low temperatures [1]. Experimental fracture investigations were carried out in different conditions. Flat elements usually were tested under tension [2] and compression [3], less often under torsion [4]. Samples had form of: discs, semi-circular discs, blocks, beams et cetera. Researchers used sharp or small radius rounded notches, so they always received linear stress-strain curves. Strong stress concentrators, accelerate the fracture process (below the yield point). During experimental studies, authors determined basic cracking parameters: the critical load value, the initiation angle and the initiation place.

Based on the empirical results, numerical analysis were conducted. In most of them, the finite element method or the boundary element method were used. Most of numerical models consist of 2D elements, assuming the plane stress. Any analysis of stress and strain distributions on a sample thickness, do not existed. Calculations simplified using a linearly elastic material model. Distribution of stress and strain fields and their variability is important during the construction and the verification of fracture criteria.

2. Experimental study

Transparent PMMA samples were used. Flat elements had two thicknesses (9.7 and 18 mm) and they were weakened by two types of edge-notches: a rounded V-notch with a root radius 0.5 mm and a U-notch with a radius 10 mm. Monotonic tensile tests were conducted at room temperature under displacement control (0.02 mm/s), which was measured by the axial extensometer INSTRON 2620.601 with 25 mm of a gauge. The dynamic biaxial MTS 809.10 test machine was used. Load-displacement curves were recorded. They are close to linear for V-notched specimens but for U-notched they are strongly nonlinear. The critical value of load was measured. The initiation place was indicated on the fracture surface. It always appears in the notch tip and near to the middle of sample thickness. The fracture process was recorded by high-speed camera PHANTOM v1610/96 (recording speed: 200 000 frames per second). These photos were helpful to measure the initiation angle (Fig. 1).

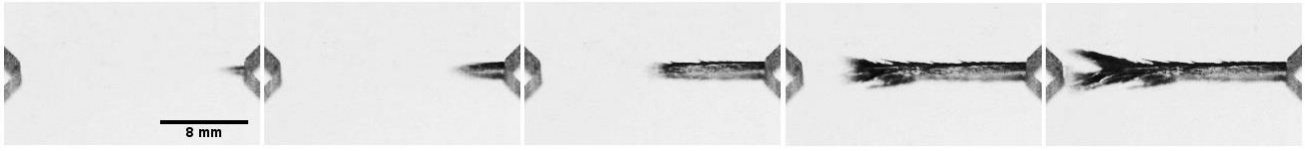

Fig. 1. Crack evolution in V-notched samples with thickness 9.7 mm (recording angle -15°).

Firstly, the increase of crack length at time was estimated. Next a crack propagation velocity was described. The maximum value of velocity was 850 m/s for V-notched and 1120 m/s for U-notched specimens. Definitely, the fracture process was faster in samples weakened by U-notches. In thick elements crack tip had lower velocities.

3. Numerical study

In order to describe the stress and strain fields distribution, the finite element method was used (MSC. MARC). Numerical models consisted of three-dimensional isoparametric elements (HEX8). Based on a geometry and load symmetry, only 1/8 of the sample was used. A material was described by elastic-plastic model with isotropic hardening (Huber-von Mises condition of plasticity). The good agreement of numerical and experimental data was obtained. As a results of MES analysis Authors got stress and strain field distributions under critical loading conditions. The influence of notch shape and sample thickness was investigated. The maximum principal stress, equivalent stress, maximum principal plastic strain and equivalent plastic strain were presented in distance from the notch tip and sample thickness functions. New form of fracture criterion for PMMA was proposed. It was build on stress-strain relationship [5,6].

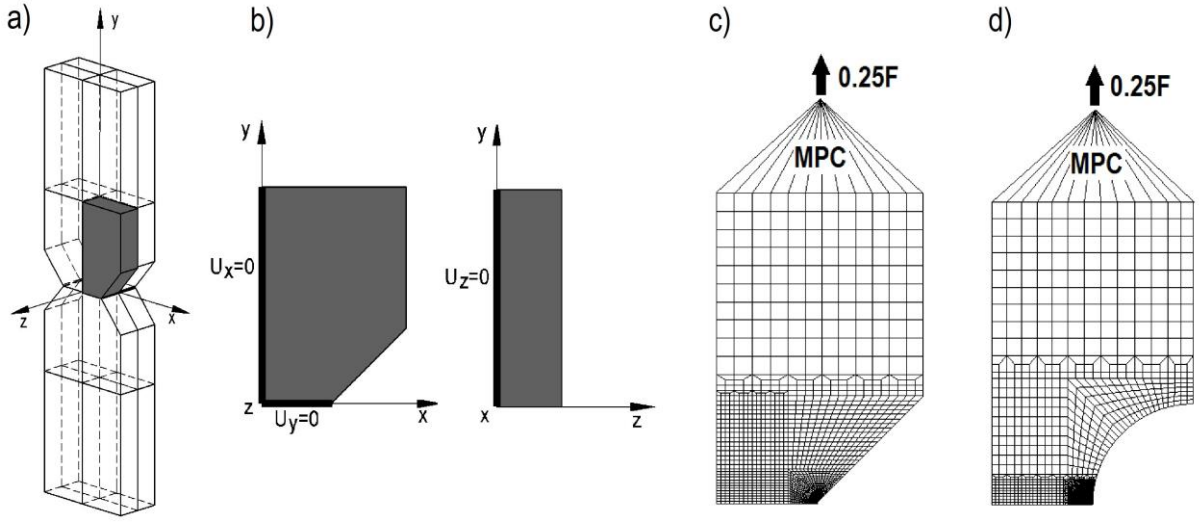

Fig. 2. Boundary conditions and loading a) b); finite element meshes c) d).

4. References

[1] Wenjun Hu, Hui Guo, Yonhmei Chen, Ruoze Xie, Hua Jing, Peng He, Experimental investigation and modeling of the rate-dependent deformation behavior of PMMA at different temperatures, *Eur. Polym. J.*, 85:313-32, 2016.

[2] M.R. Ayatollahi, M.R. Moghaddam, S.M.J. Razavi, F. Berto, Geometry effect on fracture trajectory of PMMA samples under pure mode I loading, *Eng. Fract. Mech.*, 163:449-461, 2016.

[3] A.R. Torabi, M. Firoozabadi, M.R. Ayatollahi, Brittle fracture analysis of blunt V-notches under compression, *Int. J. Solids Struct.*, 67-68:21-230, 2015.

[4] M.R. Ayatollahi, B. Saboori, A new fixture for fracture test under mixed mode I/III loading, *Eur. J. Mech. A-Solid*., 51:67-76, 2016.

[5] Ł. Derpeński, A. Seweryn, Ductile fracture of EN-AW 2024 aluminum alloy specimens with notches under biaxial loading. Part-2 Numerical research and ductile fracture criterion, *Theor. Appl. Fract. Mech*., 84:203-214, 2016.

[6] Ł. Derpeński, A. Seweryn, Ductile fracture criterion for specimens with notches made of aluminum ally EN-AW 2024, *J. Theor. Appl. Mech*., 54:1079-1093, 2016.

SENSITIVITY ANALYSIS OF BIOLOGICAL TISSUE DAMAGE WITH RESPECT TO THE PARAMETERS OF THE HYPERTHERMIA PROCESS

M. Paruch

Institute of Computational Mechanics and Engineering
Silesian University of Technology, Konarskiego 18A, 44-100 Gliwice, Poland
e-mail: marek.paruch@polsl.pl

1. Introduction

Hyperthermia in addition to radiotherapy and chemotherapy, plays an important and significant role in modern oncology. The essence of this method of treatment focuses on the thermal sensitivity of living cells. In a certain temperature range, between 40 and 45°C, healthy cells remain untouched, while pathological cells are destroyed. However, exceeding the temperature of 45°C (temperature above 45°C is known as thermoablative) may cause irreversible changes, both in healthy and cancerous tissues [1]. Therefore, a very important problem during hyperthermia treatment is to predict and accurately control the temperature in the target area and the time of heating, in order to minimize the possibility of overheating and damage the healthy tissues. From the point of view of the possibility of supporting thermotherapeutic techniques, it is important to examine the impact of individual parameters occurring in the mathematical model on the degree of tissue destruction. Therefore, it is necessary to estimate, based on the sensitivity analysis methods, which parameter has the greatest effect on the computations results.

2. Method of solution

The mathematical model describing the process of biological tissue destruction primarily involves the equation of the bioheat transfer (the Pennes equation), tissue destruction model (the Arrhenius scheme), internal source functions (the source component related to perfusion or metabolism) and external source function (resulting from the interaction of the electric field).
The heat transfer process in biological tissue is described by a system of Pennes equations [2]

$$X \in \Omega_e: \quad c_e \rho_e \frac{\partial T_e(X)}{\partial t} = \lambda_e \nabla^2 T_e(X) + k_e \left[T_B - T_e(X) \right] + Q_{met\,e} + Q_e^E \tag{1}$$

where e=1, 2 denotes the healthy tissue and tumor, respectively, $X=\{x_1, x_2, x_3\}$ are the spatial co-ordinates, t denotes time, ρ_e [kg/m^3] is the density, c_e [J/(kgK)] is the specific heat, λ_e [W/(mK)] is the thermal conductivity, T_e [K] is the temperature, k_e [W/(m^{3}K)] is the perfusion rate, T_B is the supplying arterial blood temperature, $Q_{met\,e}$ [W/m^3] is the metabolic heat source and Q_e^E is an external heat source due to the electric heating.
Using the quasi-static formulation, the electric field intensity **E** (V/m) inside the tissue for 3D problem can be calculated as follows [3, 4] (φ_e [V] is an electric potential)

$$\mathbf{E}_e(X) = -\nabla \varphi_e(X) \tag{2}$$

The heat generation Q_e^E due to the electric heating is defined as follows

$$Q_e^E(X) = \frac{\sigma_e}{2} \left| \mathbf{E}_e(X) \right|^2 \tag{3}$$

where σ_e [S/m] is an electrical conductivity.
To estimate the degree of tissue destruction the Arrhenius integral, which describes the relationship between temperature and tissue damage, is used [5]

$$Arr(X, t^f) = \int_0^{t^f} A \exp\left[-\frac{\Delta E}{RT(X, t)} \right] dt \tag{4}$$

where R [J/(molK)] is the universal gas constant (R=8.3143), ΔE [J/mol] is the activation energy, A [1/s] is the pre-exponential factor, $T(X, t)$ denotes a temperature at the point considered, while $[0, t^f]$ is the time interval considered. It is assumed that the thermal tissue damage is irreversible and total when $Arr(X, t^f) \geq 1$. In this case the probability of the cell's damage is equal to 63%. If the Arrhenius integral value exceeds 4.63 the probability of cell destruction is equal to 99%

The task was solved by means of finite element method using the MSC Marc/Mentat software.

4. Results of computations

The 3D domain of biological tissue (approx. by cylinder) with tumor (approx. by sphere) which is located at the center of healthy tissue has been considered (c.f. Figure 1a). Figure 1b presents the distribution of Arrhenius integral after 2400 seconds (electric potential U=17[V], time step Δt=1s). In fact, this figure should be treated as an illustration of the shape of the thermal damage of tissue. The sensitivity analysis of the temperature field and the degree of tissue destruction will be performed due to the geometric and physical parameters of the analyzed process.

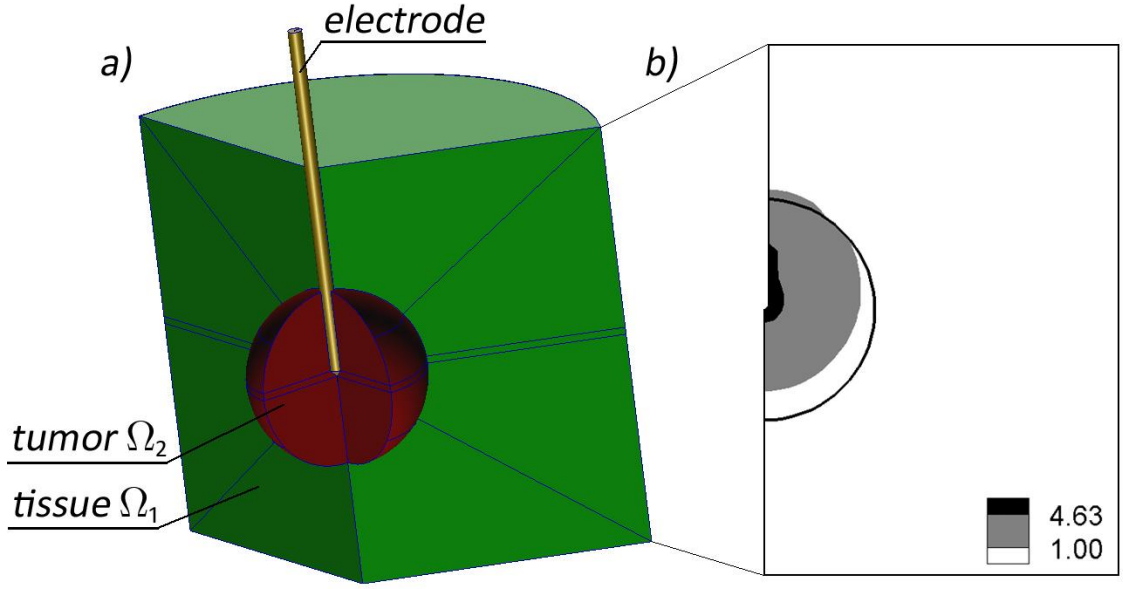

Fig. 1. a) The healthy and tumor tissues with the internal electrode b) Arrhenius integral distribution

Acknowledgments The paper and research were financed within the project 2017/01/X/ST8/01859 sponsored by the National Science Centre, Poland.

References

[1] E. van Sonnenberg, W.N. McNullen and L. Solbiati. *Tumor Ablation. Principles and Practice*. Springer, USA, 2005.

[2] H.H. Pennes. Analysis of tissue and arterial blood temperature in the resting human. *J. Appl. Physiol.*, 1:93-122, 1948.

[3] D. Andreuccetti and N. Zoppetti. Quasi-static electromagnetic dosimetry: from basic principles to examples of applications. *Int. J. Occup. Saf. Ergon.*, 12:201-215, 2006.

[4] M. Paruch. Identification of the cancer ablation parameters during RF hyperthermia using gradient, evolutionary and hybrid algorithms. *Int. J. Num. Meth. Heat Fluid Flow.*, 27(3):674-697, 2017.

[5] M. Paruch and Ł. Turchan. Mathematical modelling of the destruction degree of cancer under the influence of a RF hyperthermia. *AIP Conference Proceedings.*, 1922(060003):1-10, 2018.

WIRE REINFORCED COMPOSITE MATERIAL FOR ADDITIVE MANUFACTURING

T. Tateno[1], K. Takeuchi[1], and Y. Yaguchi[2]

[1]*Meiji University, 1-1-1 Higashimita, Tama-ku, Kawasaki, Kanagawa, 214-8571, Japan*
[2]*Tamagawa University, 6-1-1 Tamagawagakuen, Machida, Tokyo 194-8610, Japan*

e-mail: tateno@meiji.ac.jp

1. Introduction

Fused Filament Manufacturing (FFM) is one method of Additive Manufacturing (AM) called 3D printing. This method is expected as an innovative manufacturing technology to create materials by composing several materials and fabricate an object by allocating several materials. Additionally, the composition and allocation of different materials can be operated by a computer program. In conventional FFM, the fabricated parts were difficult to be used as mechanical parts because the material was limited in thermoplastics. However, currently, some FFM machines that treat Carbon Fiber Reinforced Plastics (CFRP) using long carbon fiber have been commercialized. The strength of the fabricated parts by these machines has similar strength with Aluminium. Therefore, FFM has high potential to treat high performance materials. In this study, a new FFM method, in which wire is extruded together with plastic, is proposed. This method can treat any kinds of materials for reinforcement. The mechanical property of the composite material fabricated by this method are tested.

2. Wire reinforced material extrusion

FFM is a method to extrude fused plastic and deposit it appropriate place according to computer program. Then, the material used in FFM must be based on thermoplastics. However, if the thermoplastic is used as a composite material with a reinforcement material, the strength can be reinforced. Carbon Fiber Reinforced Plastics (CFRP) is a famous composite material, which has similar tensile strength with metal parts. Some FFM machines for using CFRP are commercialized. There are two methods to use carbon fiber in FFM. One is to use a filament containing carbon fiber like pellets used in injection molding [1]. Another one is use carbon cloth or string laid on the thermoplastics [2].
In the proposed method, the latter type is expanded to use arbitral materials. Figure 1 shows the concept of the method. The reinforcement material is prepared as string shape, and it is supplied with fused thermoplastics in FFM process. The extruded thermoplastic is condensed with the reinforcement wire.

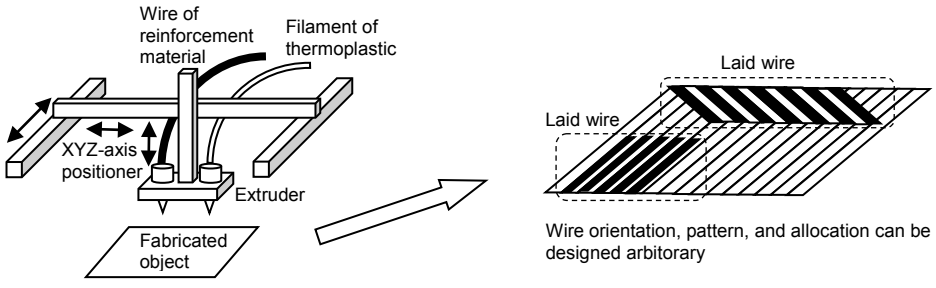

Figure 1 Concept of FFM machine that can extrude a wire reinforced composite material

There are two important merits of this method.

- *Arbitral material can be used as reinforcement material if it can be shaped as string*
- *Arbitral wire alignment and allocation can be designed and controlled by computer program*

3. Reinforcement materials

The most considerable material for reinforcement is carbon fiber string, which is similar with the commercialized machine. Beside the CFRP, a metal wire can be used. Most metal AM machines currently used in industry are the powder-bed fusion type, which uses metal powder as material and a laser or electron beam power is used to melt it and form an object. In general, it takes high costs. If FFM can fabricate a high strength object with low costs, it will become a competitive method with the powder-bed fusion type AM.

4. Wire alignment and allocation design

The proposed method enables us to design the wire alignment and allocation by programming FFM process. As well as carbon fiber orientation is important factor of the strength, the design of wire orientation decides the mechanical property of the object fabricated by the proposed method. However, the design method has not been established. The authors are working on the development of design method.
The design problem is categorized into following two issues.

- *Wire alignment: How the wire should be set with orientation and pattern.*
- *Wire allocation: Where and what kind of wire should be supplied.*

5. Test of the wire reinforced composite material

A prototype machine was developed and one line deposition using a carbon string with nylon was realized. The machine will be improved to deposit multi layers and fabricate test specimens. The wire reinforced composite will have strong anisotropic property in strength. Through the tests using many kinds of specimens that have different orientation and pattern, the mechanical properties of the wire reinforced composite material are discussed.

Acknowledgments This study is supported by JSPS KAKENHI Grant Number 17K06126.

References

[1] H.L.Tekinalp, et.al. “Highly oriented carbon fiber-polymer composites via additive manufacturing”, Composites Science and Technology, 105: 144-150, 2014.
[2] N. Li, Y. Li, S. Liu, ”Rapid prototyping of continuous carbon fiber reinforced polylactic acid composites by 3D printing”, Journal of Materials Processing Technology, 238: 218-225, 2016.

METHOD FOR MEASURING CRITICAL BUCKLING LOAD OF CANTILEVER COLUMNS

B. Blostotsky[1] and E. Efraim[1]

[1]*Department of Civil Engineering, Ariel University, Ariel, Israel*

e-mail: efraime@ariel.ac.il

1. Introduction

The critical sway buckling load is the upper limit of the allowed vertical columns loading. This load is defined by the columns configuration, cross-sections of the columns as well as configuration and stiffness of the end connections. Motivation to determine accurate value of critical force is caused by its using as follow:
- critical load is maximal allowable load for given configuration of columns and can be used as criterion of perfection or efficiency of the structure;
- it is used in calculation prescribed by standards for design of structural elements under combined action of compression and bending [1];
- it is used for verification of theoretical analysis of stability at various end conditions of columns [2].

There are two types of non-destructive testing of frames for critical load: dynamic [3] and static. In static method the lateral deformation of frame caused by compression forces in columns due to their initial imperfection is measured [4]. Load acting on a column is limited by plastic deformations and it is always lower than critical load. At columns and frames testing in sway mode the vertical loading is performed by using of additional weights [5], directly via a lever system [6] or using special mechanism as gravity load simulator [7]. To determine a critical load, the extrapolation is performed using Southwell's diagram or other applications [8]. The accuracy of the method depends on closeness of initial imperfect form with buckling mode shape.

The aim of the present work is developing of more exact non-destructive experimental method for determination of critical load of frame in sway mode. Increasing in accuracy is achieved by conducting experiments in diapason of vertical loads includes the critical load as well as by using of loading system without friction. The method allows performing measurements during the tests under loads that exceeds the frame critical loads without losing its stability. Technological advantage of this method is the ability to create loading correspond to critical loads of real full-size columns.

2. The idea and brief description of the method

Figure 1 presents the setup scheme for testing of cantilever column (A) fully restrained at the base and unbraced upper end. The traction element (B) (cable) has a pinned connection to the free end and includes the traction device (C) or additional weights for producing of tension force. In the initial position, the cable is positioned at an angle γ_0 to the column. Under the action of force P in the cable the column bends and the cable turns. At a certain value of traction force, the cable holds a vertical position and the force in the cable is equal to the critical force of the column. This statement is proved by the analysis of deformation of the column-cable system from which follows that at $\gamma = 0$ the force is equal to the critical force of cantilever column in sway mode

$$P = P_{sw} = \frac{\pi^2 EI}{4L^2}. \tag{1}$$

The problem of determination of critical force for the system column-traction element with initially inclination of cable at at $\gamma = 0$ has been considered by Timoshenko [9]. A similar result can be obtained in case of a column of variable cross-section and a column with initial curvature, provided that $y << \gamma d$, where y

is a deviation of the free end of the column relative to the base due to initial curvature. In this case, the angle of deflection of the cable should be reckoned relatively to the line connecting a column base to its free end at unloaded state.

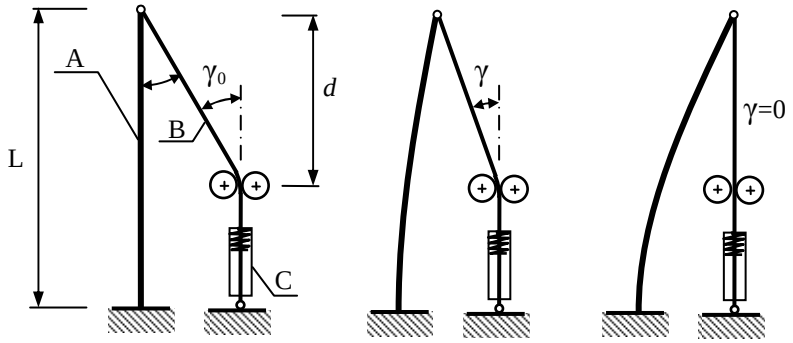

Figure 1: Setup scheme for testing of sway column: (a) - the initial position without traction force; (b) - intermediate state at any traction force; (c) - the state of system includes a column with lost lateral stiffness.

The physical meaning of the coincidence of the force in the traction cable with the column's critical buckling load is that for γ=0 the loading and the deflection form of the column correspond to loading and shape of the cantilever prismatic rod with loss of stability in sway mode. Using as a criterion of loss of stability in sway mode the condition of equality to zero of lateral stiffness [10], it can be asserted that a condition γ=0 corresponds to this criterion. At the same time the general stability remains as force P is less than critical force of column-cable system.

The advantages of the proposal method are:
- possibility of testing a column at a critical load for sway mode and also exceeding this load;
- elimination of friction influence in the loading system caused by the movement of the column's loaded end.

The efficiency and reliability of the method is confirmed by laboratory studies of column models. The results of the study are recommended for use in laboratory and industrial testing of columns and sway frames.

References

[1] European Committee for Standardization (CEN), *Eurocode 3: Design of steel structures – Part 1.1: General rules and rules for buildings* (European standard EN 1993-1-1:2005:E), Brussels; 2005

[2] L.Tomski, J. Przybylski, M. Golebiowska-Rozanow, J. Szmidla, Stability and vibration of a two-member frame under generalized load, *Proceedings of European Session of International Colloquium "Stability of Steel Structures"*, Budapest, I/409-I/416, 1995

[3] B. Blostotsky, E. Efraim, Dynamic method for measuring critical buckling load of sway frames, *Proceedings of the 9th International Conference on Structural Dynamics, EURODYN 2014*,Porto, Portugal, 30 June - 2 July 2014

[4] L.H. Donnell, *On the application of Southwell's method for the analysis of buckling tests*. Stephen Timoshenko 60th Anniversary Volume, MWGraw-Hill Book Company, 1938, pp. 27-38.

[5] B. Blostotsky, E. Efraim, Y. Ribakov, Improving the Reliability of Measuring Critical Buckling Load in Sway Mode Frames, *Experimental Mechanics*, 56:311–321, 2016, DOI 10.1007/s11340-015-0098-x

[6] Y.C. Yen, L.W. Lu, G. C. Jr. Driscoll, *Tests on the stability of welded steel frames*, Welding Research Bulletin, No. 81,p12, September 1962, Reprint No. 206 (62-10), Fritz Laboratory Reports. Paper 1767, 1961.

[7] E. Yarimci, J.A. Pura, L.W. Lu, Techniques for testing structures permitted to sway, *Experimental Mechanics*, Vol. 7 (8), pp. 321-331, 1967

[8] S. T. Ariaratnam, The Southwell method for predicting critical loads on elastic structures, *The Quarterly Journal of Mechanics and Applied Mathematics*, Vol.14 (2), pp. 137-154, 1961, doi:10.1093/qjmam/14.2.137

[9] Timoshenko, S. P. and Gere J. M., *Theory of Elastic Stability*, 2nd ed., McGraw-Jill, New York, 1962.

[10] Y. Liu and L. Xu, Storey-Based Stability Analysis of Multi-Storey Unbraced Frames, *Structural Engineering and Mechanics – An International Journal*, 19(6), 679-705, 2005.

TOPOLOGY OPTIMIZATION OF AUXETIC MATERIALS

E. Idczak[1], T. Stręk[1]

[1] *Institute of Applied Mechanics, Poznan University of Technology*
e-mail: eligiusz.j.idczak@doctorate.put.poznan.pl

1. Introduction

Mechanical metamaterials are material which properties are depended on their macroscopic structure. These properties can be mechanical, optical, acoustic or electrostatic. One of groups of mechanical metamaterials are so-called auxetic materials – which have negative Poisson's ratio. The Poisson's ratio for the homogenous, isotropic elastic solid material is the negative ratio of transverse to longitudinal strain at every point in a body under longitudinal loading. Isotropic materials have Poisson's ratio greater than -1 and less than 0.5. Anisotropic materials haven't these boundaries. To obtain the maximal value of Poisson's ratio are used methods of topology optimization and Finite Element Method. In this paper will be presented the results of topology optimization by means of various methods and the comparison between them.

2. Subject of optimization

The subject of optimization is an area limited by various shapes with boundary conditions: on the top – loading force, on the bottom and left side: roller condition and on the left side – free condition. In the Fig. 1 and Fig. 2 are presented two examples of optimized area.

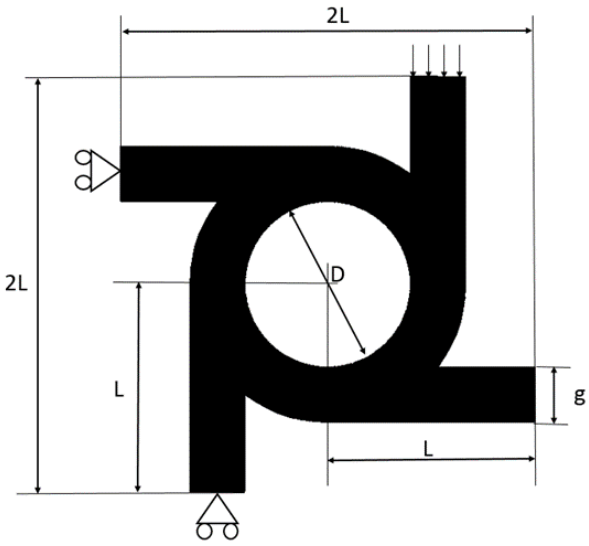

Fig. 1. Anti-tetra-chiral optimized shape

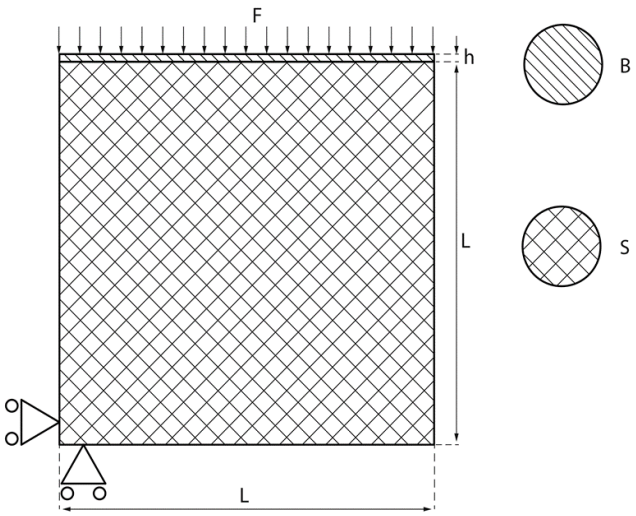

Fig. 2. Optimized square as a core of composite

3. Results

The results of optimizations are found by filling the shape with two materials with positive initial values of Poisson's ratios. Initial parameter of optimization is also the percentage of the first material in the whole shape. In the Fi. 3 and Fig. 4. are shown the examples of results – final shapes built by two materials with minimal effective Poisson's (the colours mean the two materials).

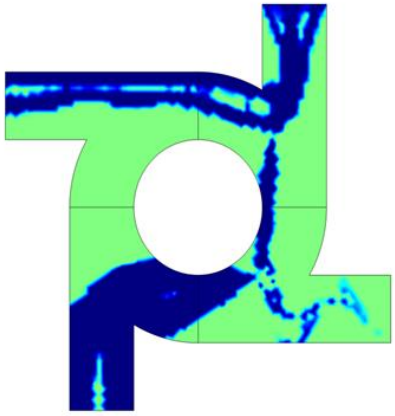

Fig. 3. Optimized anti-tetra-chiral shape

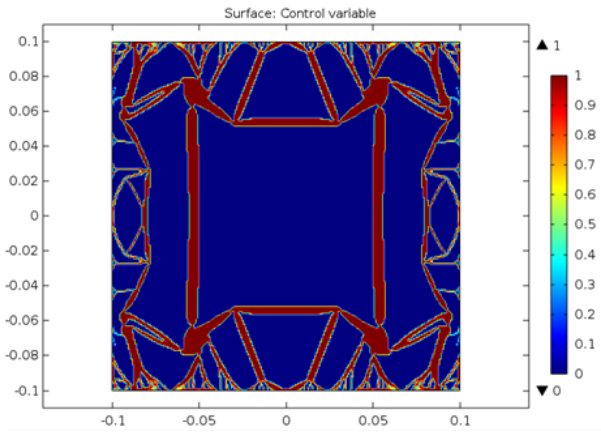

Fig. 4. Optimized square with two materials

4. Summary

The results show that the topology optimization method can lead to obtain the negative Poisson's ratio in the earlier defined geometry. The domain is filled by two materials with initial positive Poisson's ratio. The result can be less than -1.

5. References

Acknowledgments This work was supported by grants of the Ministry of Science and Higher Education in Poland: 02/21/DS PB/3493/2017 and 02/21/DSMK/3498/2017. The simulations have been carried out at the Institute of Applied Mechanics, Poznan University of Technology.

References

[1] M. P. Bendsøe and O. Sigmund. *Topology optimization. Theory, Methods and Applications*. Springer Verlag, Berlin, Germany, ISBN: 3-540-42992-1, 2003.
[2] E. Idczak and T. Strek. *Minimization of Poisson's ratio in anti-tetra-chiral two-phase structure*. IOP Conf. Series: Materials Science and Engineering, 248, 012006, 2017.
[3] T. Strek, H. Jopek, E. Idczak and K.W. Wojciechowski. *Computational modelling of structures with non-intuitive behaviour.* Materials: Auxetic materials 2017 ISSN 1996-1944, 2017.
[4] T. Strek, H. Jopek and E. Idczak. *Computational design two-phase auxetic structures*. Phys. Status Solidi B 253, 1387–1394, 2016.
[5] R. Kutyłowski. *Optymalizacja topologii kontinuum materialnego*. Oficyna Wydawnicza Politechniki Wrocławskiej, Wrocław, Polska, 2004.
[6] M. Ameen. *Computational elasticity*, Alpha Science, UK, 2005.
[7] B. Lautrup. *Physics of Continuous Matter, Exotic and Everyday Phenomena in the Macroscopic World*, IOP, Bristol, 2005.
[8] R.S Lakes. *Foam structures with a negative Poisson's ratio* Science 235 pp. 1038-1040. 1987.
[9] K.E. Evans. *Auxetic polymers: a new range of materials*. Endeavour, 15(4), 170-174. 1991.
[10] D. Prall and R. S. Lakes *Properties of a chiral honeycomb with a Poisson's ratio of –1*. International Journal of Mechanical Sciences, vol. 39, no. 3, p. 305-314, 1997.
[11] Y.J. Chen, F. Scarpa, Y.J Liu and J.S. Leng. *Elasticity of anti-tetrachiral anisotropic lattices.* International Journal of Solids and Structures, vol. 50, no. 6, p. 996-1004, 2013.
[12] M. Nowak. *Projektowanie konstrukcji o wysokiej sztywności z zastosowaniem optymalizacji strukturalnej.* Wydawnictwo Politechniki Poznańskiej, 2016.

BIOMECHANICAL INVESTIGATION OF INTACT AND INFLAMMATION OF THE NEW ZELAND WHITE RABBITS URETHRA

A. Mackiewicz[1], A. Kaczmarek-Pawelska[1], M. Malinowski[1], A. Noszczyk-Nowak[2], J. Skonieczna[2], J.P.Madej[2], and R. Bedzinski[1]

[1]*University of Zielona Góra, Zielona Góra, Poland*
[2] *Wroclaw University of Environmental and Life Sciences, Wroclaw, Poland*

e-mail: a.mackiewicz@ibem.uz.zgora.pl

1. Introduction

The aim of the study was to determine the mechanical characteristics of samples originating from a physiologically normal urethra from New Zealand White Rabbits and with induced inflammation during a tensile test in the radial and axial direction on a testing machine and determining a mathematical material model for urethral tissue in nonlinear condition. The structure and mechanical properties of the urethra should be performed to determine the parameters for the construction of new urethra stent models. Urethral strictures are common in male patents, it is rarely a congenital disease, in most of the cases it is acquired. In the USA the percentage of the patients with urethral stricture is 0.3% for men below 55 years old, and increase in the group above 55 years of age to 0.6% [5]. Between 1992 and 2000, more than 1.5 million office visits were made for male urethral strictures, and the cost of surgical treatment of one patient is 18 thousand dollars [1]. There are several techniques for the treatment of urethral strictures, but they do not guarantee satisfactory results. Most often a surgical treatment is carried out, which consists in the mechanical or surgical enlargement of the urethra lumen with dilators, catheters or a resection of the fibrosis and autogenic transplantation of the tissue. Implantation of relatively stiff stents into the urethra lumen, due to its arched shape, may be a cause of stent migration or sudden loss of the mechanical properties (breakage or bending of the stent) which leads to urinary retention.

2. Material and Methods

The test material consisted of 14 male New Zealand White Rabbits with a body weight of 2.1-3.0 kg. This animal model was chosen because of the histological and functional similarity between the human and the rabbit urethra [2,8]. During the tests the rabbits were divided into two groups of 7 specimens: the control group and the group with the irritated epithelium urethra. In both stages, fresh urethral specimens were used, for which the time from the moment of euthanasia to the end of the endurance test did not exceed 8 hours. In order to verify the condition of the urethra (intact, fibrosis or inflammation), histological examination was also performed using hematoxylin and eosin staining (H&E stain) [4]. The quasi-static tensile test of urethras were performed using the Zwick / Roell EPZ 005 testing machine. Curves of force-streching obtained from the tensile test were the basis for further research. Knowing the cross reaction and longitudinal dimensions of the samples, the obtained data was converted into stress and strain values in Microsoft EXCEL software. In STATISTICA 12 Software developed curves of the stress-strain curves of the regression parameter, and Young's Modulus for the different range of deformation.

3. Results

The urethra tissue samples from control group was subjected to histological verification which did not show pathological abnormalities of connective and muscular tissue structure as well as discontinuities of the multi-row layer epithelial. The histological analysis of inflammation urethra samples revealed changes in lamina

propria of mucous membrane. The congestion and in some cases concomitant hemorrhages were present, as well as edema and mononuclear cells infiltration.

4. Discussion

Based on the results obtained during the quasi-static tensile test, it can be noticed that the obtained results are similar to the experimental examination results published by other researchers (Table 1). It should be noted, that species variation (species, size, sex, living conditions, etc.) has a strong influence on the mechanical properties of the urethra.

Author's research (2018)	New Zealand White Rabbits	**Intact urethra** E=0.37-0.98MPa **Inflammation urethra** E=0.01-0.028MPa
Feng (2010) [3]	New Zealand White Rabbits	E=0.5 MPa
Zhang (2017) [8]	New Zealand White Rabbits	E=0.25 MPa
Natali (2016) [6]	Horse	E= 0.0058-0.0156 MPa
Nava (2004) [7]	Human	E=0.1-0.2MPa

Table 1: Mechanical properties of the urethra

The mechanical properties of the urethra with the occurrence of inflammation showed a significant, almost 10-fold reduction in the strength properties of the tissue compared to the control. Based on stress-strain curves for the axial and the radial directions, a comparison was made with non-linear material models. The best fit was found in the hyperelastic 9-parameter Mooney-Rivlin model [9].

Acknowledgments This investigation was supported by a research grant, as a part of the project DEC-2016/21/B/ST8/01972 financed by The National Science Centre. The protocol of the study was approved by the Local Ethics Committee in Wroclaw (decision No. 7/2012).

References

[1] S.B. Brandes, *Epidemiology, Etiology, Histology, Classification, and Economic Impact of Urethral Stricture Disease*, in *Urethral Reconstructive Surgery*, Brandes S.B. (ed.), Humana Press, 2008.
[2] G. Faydaci, F. Tarhan, M. Tuncer, B. Eryildirim, O. Celik, S.H. Keser, A. Ozgül. Comparison of two experimental models for urethral stricture in the anterior urethra of the male rabbit. *Urology*, 80:1, 2012.
[3] Ch. Feng, Y-M. Xu, Q. Fu, W-D. Zhu, L. Cui, J. Chen, Evaluation of the biocompatibility and mechanical properties of naturally derived and synthetic scaffolds for urethral reconstruction, *J Biomed Mater Res A.*, Jul;94(1):317-235, 2010
[4] W. Jia, H. Tang, J. Wu, X. Hou, B. Chen, W. Chen, Y. Zhao, C. Shi, F. Zhou, W. Yu, S. Huang, G. Ye, J. Dai. Urethral tissue regeneration using collagen scaffold modified with collagen binding VEGF in a beagle model, *Biomaterials*, 69, 2015.
[5] M. Lazzeri, S. Sansalone, G. Guazzani, G. Barbagli. Incidence, Causes, and Complications of Urethral Stricture Disease, *Eur. Urol. Suppl.* 15:2, 2016.
[6] A.N. Natali, E.L. Carniel, A. Frigo, P.G. Pavan, S. Todros, P. Pachera, C.G. Fontanella, A. Rubini, L. Cavicchioli, Y. Avital, G.M. De Benedictis. Experimental investigation of the biomechanics of urethral tissues and structures. *Exp Physiol*. 101:5, 2016.
[7] A. Nava, E. Mazza, F. Kleinermann, N.J. Avis, J. McClure, J., Bajka, M. Evaluation of the mechanical properties of human liver and kidney through aspiration experiments. *Technology and Health Care*.;12:269–280, 2004.
[8] K. Zhang, Q. Fu, J. Yoo, X. Chen, P. Chandra, X. Mo, L. Song, A. Atala, W. Zhao, 3D bioprinting of urethra with PCL/PLCL blend and dual autologous cells in fibrin hydrogel: An in vitro evaluation of biomimetic mechanical property and cell growth environment, *Acta Biomater*., Mar 1;50:154-164, 2017
[9] N. Kumar, V.V. Rao. Hyperelastic Mooney-Rivlin Model: Determination and Physical Interpretation of Material Constants, *MIT Internat. J. Mech. Eng.* 6:1, 2016.

Cyclic softening of P91 steel during thermomechanical low-cycle fatigue tests

P. Sulich H. Egner and W. Egner

Institute of Applied Mechanics,
Faculty of Mechanical Engineering,
Cracow University of Technology,
31-864 Kraków Al. Jana Pawła II 37, Poland.
e-mail: piotrjansulich@gmail.com
wladyslaw.egner@pk.edu.pl
wladyslaw.egner@pk.edu.pl

1. General

Thermomechanical low cycle fatigue is one of the dominant failure modes in high temperature structural components, such as electric power boilers, boiler pipes, engine elements etc. Many studies show the complexity of the cyclic elasto-visco-plastic-damage behaviour, such as effect of non-proportional loading, cyclic softening/hardening behaviour dependent on the strain amplitude and on the loading path, plastic strain range memorization effect or damage [1,2].

2. Experimental background and results

Experimental tests were performed on P91 steel specimens. The chemical composition of steel was 0.197 C, 0.442 Si, 0.489 Mn, 0.017P, 0.005 S, 8,82 Cr, 0.971 Mo, 0.307 Ni, 0.012 Al, 0.017 Co, 0.036 Cu, 0.074 Nb, 0.004 Ti, 0.201 V and 0.02 W. Low-cycle fatigue tests were strain controlled, with constant total strain amplitude (where frequency of loading 0,2 Hz) and constant temperature in each test. Five levels of total strain amplitude (0.25%, 0.30%, 0.35%, 0.50%, 0.60%) and three levels of temperature (20^0C, 400^0C and 600^0C) were applied. Experiments were performed on testing machine Instron 8502, equipped with heating chamber.

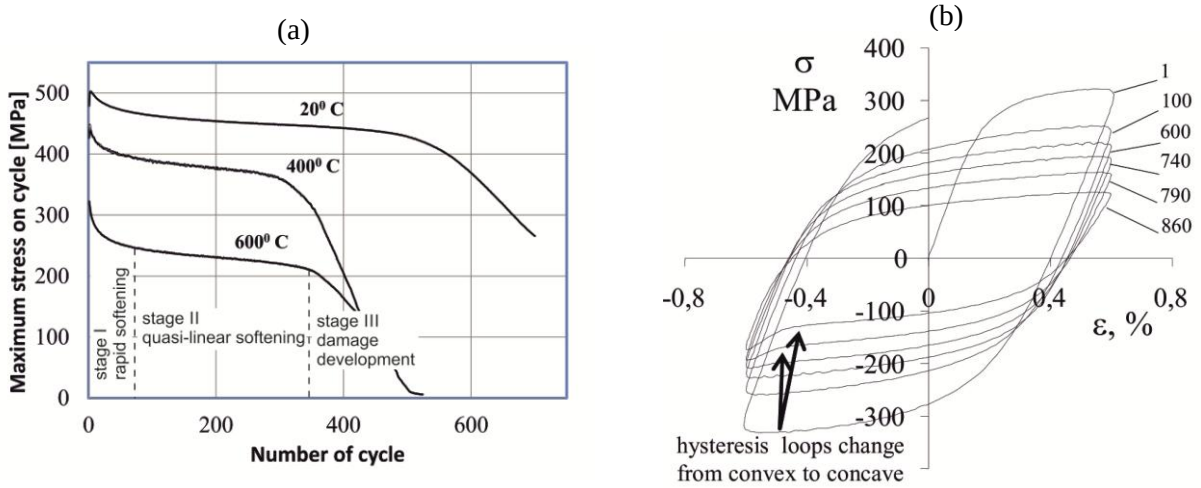

Fig. 1. (a) Maximum stress on cycle versus number of cycle for chosen test temperatures; (b) chosen hysteresis loops for fatigue test performed at 600^0C.

Tested steel exhibits cyclic softening, regardless of the testing temperature (half-stress amplitude decreases with increasing cumulated plastic strain. This softening could be divided into three phases, which are: the rapid softening phase during the initial up to a hundred cycles, followed by a slow quasi-linear softening phase, and finally again fast softening till rupture (see Fig. 1). The first phase is generally explained by the

rapid change of dislocation density inherited from the quench treatment, the second is related to the formation of dislocation sub-structure and carbide coarsening under the action of time, temperature and cyclic load, while the third phase is a consequence of micro-damage development in the material that ultimately causes failure of the tested sample.

3. Modelling

The dimension of the elasticity domain can be controlled with a law of the type:

(1) $$R = Q(\theta)(1-e^{-b(\theta)r})$$

where $b(\theta)$ and $Q(\theta)$ are two coefficients that are material and temperature dependent. However, such description leads to a typical saturation , therefore it is not suitable for steels that soften continuously without a saturation period. To take into account the non-saturating cyclic softening observed experimentally in the case of P91 steel, the drag stress R can be divided into two parts, R_1 and R_2 ([3]):

(2) $$R_1 = Q(\theta)(1-e^{-b(\theta)r}),\ R_2 = H^R(\theta)r$$

The first part, R_1 corresponds to the initial strong softening, while the second one, R_2 allows to reflect the continuous softening. Due to quasi-linear character of the second stage of softening drag stress R_2 was here adopted in a linear form, where $H^R(\theta)$ (see Fig. 2b) reflects the slope of the second stage of cyclic softening (see Fig. 2a).

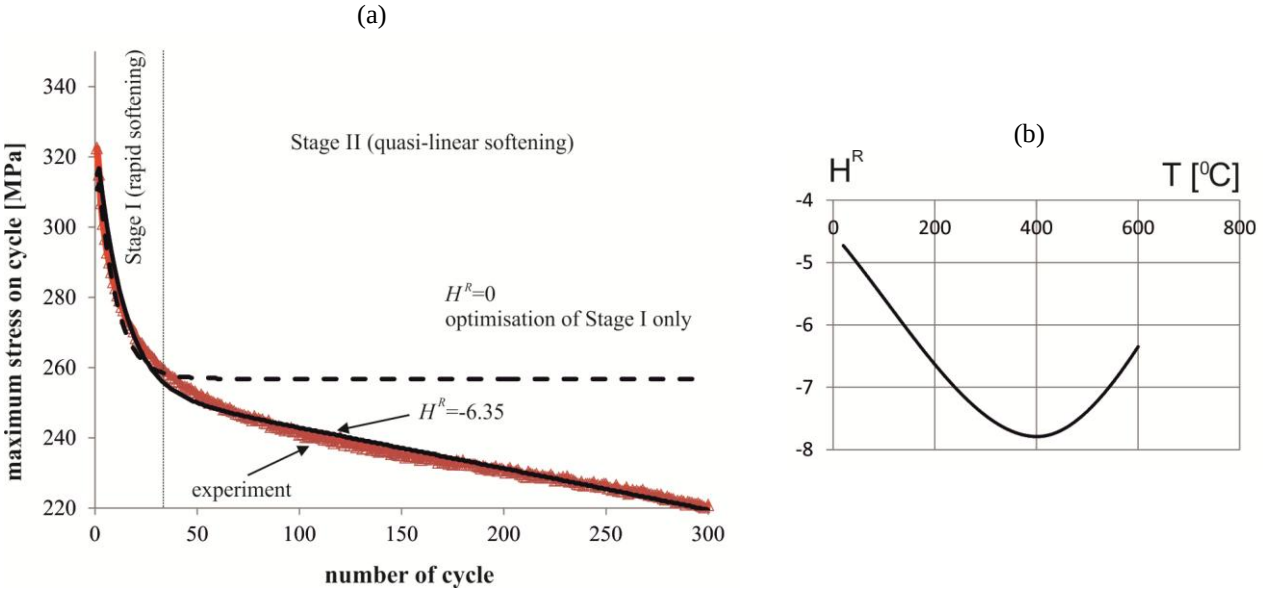

Fig.2 (a) Influence of linear part of isotropic softening (isothermal fatigue test at a temperature of 600^{0}C); (b) H^R versus temperature (T denotes temperature in Celsius scale)

Acknowledgments This work was supported by the National Science Centre of Poland through the Grant No. 2017/25/B/ST8/02256.

References

1. W. Egner, E. Egner, Thermo-mechanical coupling in constitutive modeling of dissipative materials, Int J. Solids Struct. 91, 78-88 (2016).
2. G. Golański, S. Mroziński, Low cycle fatigue and cyclic softening behavior of martensitic cast steel, Eng. Fail. Anal. 35, 692-702 (2013).
3. P. Sulich, W. Egner, S. Mroziński, H. Egner, Modeling of cyclic thermo-elastic-plastic behaviour of P91 steel. Journal of Theoretical and Applied Mechanics 55, 2, 595-606 (2017).

DEVELOPMENT OF NON-CONTACT FATIGUE CRACK PROPAGATION MONITORING METHOD USING AIR-COUPLED ACOUSTIC EMISSION SYSTEM

T. Matsuo[1], and D. Hatanaka[1]

[1]*School of Science and Engineering, Meiji University, Kanagawa, Japan*
e-mail: matsuo@meiji.ac.jp

1. Introduction

The acoustic emission (AE) method is the efficient monitoring technique, and it can be used to assess the integrity of the equipment during operation. Especially, AE method enables to observed fatigue crack propagation by investigating the AE analysis and predicts fatigue life [1]. However, the fatigue monitoring of rotating components during operation is difficult because attaching the sensor to the surface of the rotating component is difficult. In order to overcome this problem, a non-contact AE monitoring system was developed and used for the fatigue monitoring of rotating components [2]. Even though, the AE signals were detected immediately before fracture, the AE signals from crack initiation and propagation at an early stage were not detected. The purpose of this study is to develop the method for fatigue crack monitoring of AE. We first clarified the relationship between sensor sensitivity and surface condition of the specimen. Next, AE signals from bending fatigue test in rotating component was monitored using modified specimen.

2. Relationship between surface condition of the specimen and sensitivity of the system

The relationship between the sensitivity of the AE signals detected by the system and the configuration of the specimen during the test was first investigated. The amplitude of the artificial AE signals propagated in the arc and flat surface specimen were compared. The arc surface specimen was a rod of diameter 18 mm. The flat surface specimen was machined by milling a cylinder of diameter 18 mm on the upper side at a depth of 4 mm and length of 25 mm. The air coupled ultrasonic sensor for detecting AE signal was set over the surface at a distance of 20 mm. The artificial AE was generated by a pulse YAG laser at 8.0 mJ on the end surface of the specimen. Figure 1 shows the waveforms generated by the pulse YAG laser on (a) the arc specimen and the (b) flat surface. The SN ratio of the signals in the arc and the flat surface were 26.3 dB and 38.4 dB, respectively. This result indicated that the SN ratio of AE signals was dependent on the configuration of the specimen. It was necessary to consider the configuration of the specimen used in the rotary bending fatigue test to detect the AE signals at an early stage.

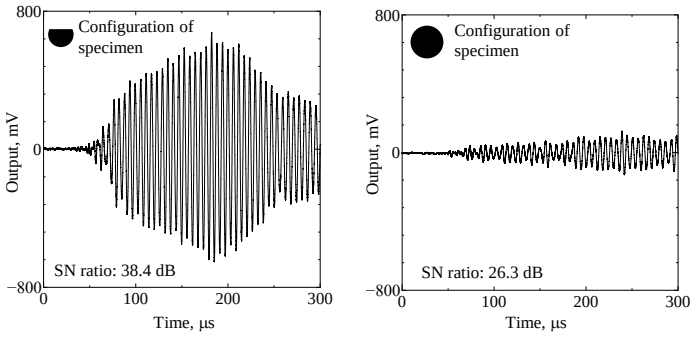

Figure 1: Waveforms detected by air-coupled ultrasonic sensor in arc (left) and flat (right) surface specimen.

3. AE monitoring during the rotary bending fatigue test using the circular bar specimen with flat surfaces

The result in Fig.1 indicated that the plane surface shape was higher efficiency than the arc surface shape using the air-coupled ultrasonic sensor. Therefore, the circular bar specimen with flat surface for rotary bending fatigue

test was machined and utilized for fatigue monitoring. Figure 2 shows the specimen configuration and experimental setup. The specimen was an aluminum alloy (A2024) with 18 mm diameter and 120 mm length. The flat surface was made by milling a cylinder of diameter 18 mm on the upper and under side at a depth of 4 mm and length of 25 mm. The slit with 0.5 mm depth and 1 mm width was made on the end of the flat surface in order to limit the locations of crack initiation. This specimen was mirror finished surface because it was easy to observe the fatigue cracks. The fatigue crack length on the surface of this specimen measured by the replica method. The loading frequency was 3 Hz and the load was 294 N. The air-coupled ultrasonic sensor was set over the surface of specimen. The AE signals detected were amplified by 60 dB using a pre-amplifier. The passband was from 150 to 250 kHz and the trigger level was 7 mV. The resonant frequency of the air-coupled ultrasonic sensor was 200 kHz.

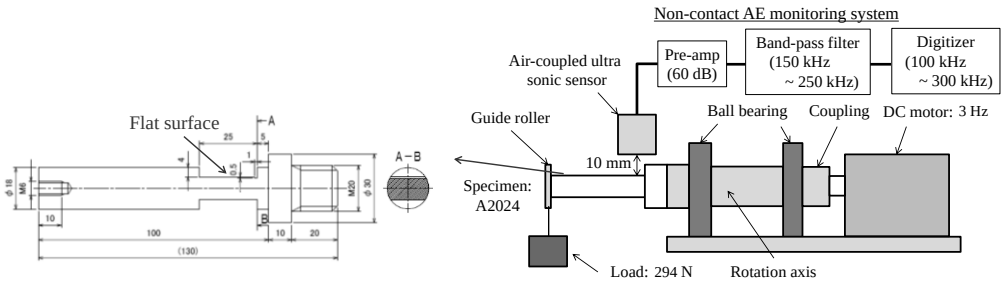

Figure 2: Configuration of fatigue specimen with flat surface (left) and experimental setup for monitoring AE signals during rotary bending fatigue test (right).

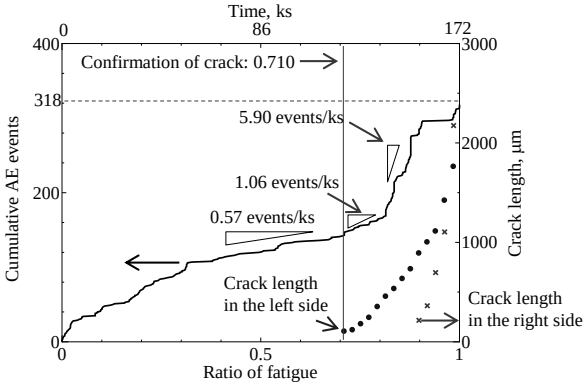

Figure 3:Cumulative AE events and crack length in both side of the specimen.

Figure 3 shows cumulative AE events during the test and crack length in the specimen. The fatigue crack was confirmed at 0.710 of fatigue life on the left side and cracks exponentially increased during the rotary bending fatigue test. From the test initiation, the AE signals were continuously generated. It was indicated that these AE signals before the confirmation of cracks were noise generated by the test machine. From 0.815 to 0.919 of fatigue life, the AE generation rate rapidly increased. It is indicated that fatigue cracks propagation was corresponding to the AE generation rate. Additionally, detection of fatigue crack in rotary component at an early stage can be possible by non-contact AE system.

4. Conclusion

A non-contact AE monitoring system was used to detect AE signals during rotary bending fatigue tests. The AE signals were detected at an early stage of fatigue during the test. It is possibility that detection of fatigue crack at an early stage can be possible by non-contact AE system.

References

[1] T. M. Roberts and M. Talebzadeh, *J. Constr. Steel. Res.*, 59, 2003, pp. 679-694.
[2] Y.Ota, T.Matsuo and H.Cho, *Proc. the 2012 M&M Symposium for Young Researchers*, (2012), pp.127-132.

RESEARCH ON INFLUENCE OF TiSi(N) REFLECTIVE COATING THERMAL RESISTANCE ON ENERGY ABSORPTION OF FIREPROOF TEXTILE COUPLED WITH AUXETIC FABRIC

D. Miedzińska[1*], M. Stankiewicz[1], R. Gieleta[1] and K. Marszałek[2]

[1]*Military University of Technology, Faculty of Mechanical Engineering, Urbanowicza 2 St., Warsaw, Poland*
[2]*AGH University of Science and Technology, Al. Mickiewicza 30, Krakow, Poland*

** corresponding author, e-mail: danuta.miedzinska@wat.edu.pl*

1. Introduction – aim of research

Textile science is a very wide and still developed part of knowledge. In the presented study the special interest is directed to fireproof textiles improvement. Fireproof textiles are a kind of fabrics more resistant to fire or heat than others through chemical treatment or specially manufactured fibres.
Such fibres could be classified into three categories. The first one are inherently heat and flame retardant fibres (e.g. aramid [1], modacrylic [2], polybenzimidazole (PBI) [3], Panox (oxidised acrylic) [4] or semicarbon, phenolic, asbestos, ceramic [5]). The second cathegory are chemically modified fibres and fabrics, in which one can find flame retardant cotton, wool and viscose [6] and synthetic fibres [7], produced by incorporating special additives in the spinning dope before extrusion. The last cathegory of a fireproof textiles are currently developed [8, 8] fibres coated with reflective nanolayer with the use of sputtering method.
In the paper the thermal resistance improvement is based on the TiSi(N) nanocoating application with the use of sputtering technology.
Additionally it must be noticed that fireproof textiles are not designed to improve the protection against for example gas impact, the possible situation during fire of houses or flats. For this improvement the auxetic textile coupled with fireproof one was proposed. Auxetics are new materials which fibre diameter widens on stretching it whereas normal textiles flat (Fig. 1).

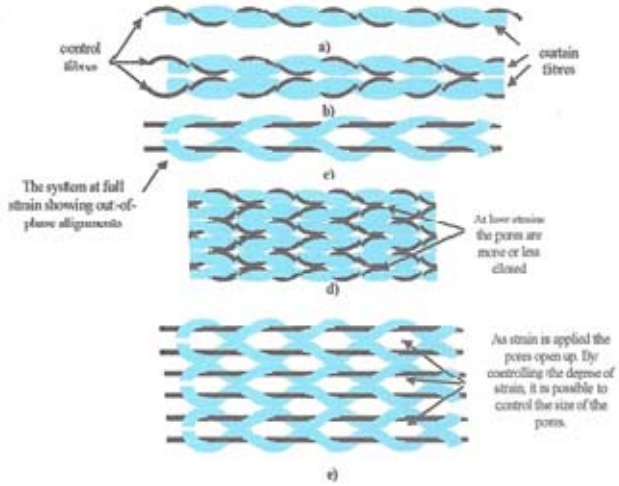

Fig. 1. Basic concept of auxetic textile: a) base textile unit – thin yarn winded around thick core, b) two base units aligned in opposite to each other, c) fully tensiled pair of unit yarns, d) partially tensiled textile, e) fully tensiled textile [10]

There are two main disadvantages of auxetics implementation in such constructions as firemen protective clothes. Firstly, they must be stretched during loading to gain the negative Poisson ratio effect. Secondly, the auxetic effect decreases in higher temperatures [11]. Those properties can be a problem when the textile is used for firemen suits. The best application can be a kind of a protective panel.
So the material construction of fireproof textile, additionally coated with reflective nanocoating, and auxetic

one can improve both mechanical and thermal protection. The fireproof textile will protect the user against the high temperature and will protect the auxetic textile allowing to use its energy absorption abilities in the most effective way. This phenomenon is studied in the paper.

2. Researched materials and metchodology

For the purpose of proposed research PROTON fireproof textile was selected. PROTON is made of paraaramid 58%, PBI 40%, antistatic 2%. The applied auxetic fabric is composed of elastomer core and Kevlar braid.
Two kinds of tests were carried out:

- comparative study on PROTON thermal resistance with and without TiSi(N) coating,
- comparative study on PROTON and PROTON – auxetic structure gas impact resistance.

Special testing stands were built to achieve those aims. It must be mentioned that there is no influence of coating on PROTON gas impact resistance, what was shown in [12].

3. Results and conclusions

As it was shown in [11] the temperature increase from 20 to 180°C causes the decrease in auxetic effect of even 13.2%.
The results of thermal resistance of coated and not coated PROTON shown that the application of such structure can decrease the temperature acting behind the textile from 180 to 100°C (45%).
The next tests shown that the application of the auxetic textile can increase the PROTON resistance to gas impact of 18.2 %.
Finally on the base of achieved results it can be concluded that using both improvement: TiSi(N) nanocoating and auxetic fabric can improve energy absorption and thermal resistance of fireproof textile.

Acknowledgments The research presented in the paper was supported by a grant No DOB-BIO6/04/104/2014 financed in the years 2014-2018 by The National Centre for Research and Development, Poland..

References

[1] Teijin Ltd.. Super FR cloth. *Textile Horizons*, 9:31, 1989.
[2] A. R. Harrocks, S. C. Anand. *Handbook of Technical Textiles*. Woodhead Publishing Limited, Cambridge, 2000.
[3] D. T. Ward. High Tech. Fibres featured at Frankfurt show. *International Fibre Journal*, 6:89, 1991.
[4] N. Saville, M. Squires. *Multiplex panotex textiles*. International Conference Industrial and Technical Textiles, University of Huddersfield, UK, 6-7 July 1993.
[5] P. Lennox – Kerr. Friction spinning creates hybrid yarns for improved thermal protection. *Technical Textiles International*, 6:18, 1977.
[6] S. Heidari, A. Paren, P. Nousianinen. The mechanism of fire resistance in viscose/silicic acid hybrid fibres. *Journal of Society of Dyers and Colourists*, 109:201, 1993.
[7] Z. Ma, W. Zhao, Y. Liu, J. Shi. Synthesis and properties of intumescent phosphorus-containing flameretardant polyesters. *Journal of Applied Polymer Science*, 63:1511, 1997.
[8] E. Małek, D. Miedzińska, M. Stankiewicz. Heat Resistance Research and Surface Analysis of Fireproof Textiles with Titanum Silicide Coating. *Procedia Structural Integrity*, 5:508, 2017.
[9] K. Marszałek, R. Mania. *The Nanocomposite TiN-Si3N4 coatings on textiles*. 9-th Symposium on Vacuum Based Science and Technology, Kołobrzeg, Poland, 16-18 November 2015,.
[10] J. R. Wright, K. E. Evans and M. K. Burns. *Auxetic Blast Protection Textiles – Crime Feasibility Study, Final Report– EP/D036690/1*. University of Exeter, 2007.
[11] M. Klasztorny, P. Szurgott, T. Niezgoda, D. Miedzińska, A. Kiczko. Preliminary Comparative Static Identification Research on Selected Commercial Auxetic Fabrics. *Composites Theory and Practice*, 17:59, 2017.
[12] D. Miedzińska, R. Gieleta, E. Małek, D. Zasada, M. Stankiewicz, K. Marszałek. Experimental research on influence of gas impact on thermal and mechanical properties of auxetic material covered with titanium silicide coating. *Bulletin of the Polish Academy of Sciences - Technical Sciences*, BPASTS-00464-2017-01, in press, 2018.

NUMERICAL COMPARATIVE ANALYSIS OF STRESS DISTRIBUTION FOR DIFFERENT SHAPES OF SPREAD FOOTING FOUNDATIONS

M. Major[1], I. Major[1], and K. Kuliński[1]

[1]*Faculty of Civil Engineering, Czestochowa University of Technology, Częstochowa, Poland*
e-mail: mmajor@bud.pcz.czest.pl

1. Introduction

In Polish national standard [1, 2] spread footing calculations are limited only to the basic shapes of foundations. Also in the literature [3, 4] there are discussed basic shapes only, however authors mention that different shapes may be calculated via appropriate software. Despite that there is a very small number of articles concerning the spread footing shape optimization. This paper concerns comparative analysis of stress distribution for different shapes of spread footing foundation with the utilization of finite element method (FEM) based software. In order to perform numerical analysis SolidWorks FEM based software has been chosen.

2. Model geometry and results

For the numerical analysis purposes six different shapes of spread footing have been adopted. Two different shapes of foundation bottom surface have been analysed – circular and rectangular pattern. For the circular shape of foundation base, diameter of 2.50 m has been assumed, whereas for the rectangular shape – square with side edge equal 2.50 m has been assumed, respectively. Height of each foundation has been set to 1.40 m, which is the maximum ground frost depth value in Poland on the basis of Polish national standard.
Following spread footing foundation shapes have been adopted: simple, sloped and stepped column footing. In the simple column footing, circular and square foundation base surface have been extracted vertically by 1.40 m. In sloped column footing, rectangular foundation base has been extracted vertically by 0.60 m, then by 0.80 m sloped by 45 degrees to the centre, whereas for the circular plate vertical extraction has been adopted as 0.30 m, and then 1.10 m sloped by 40 degrees to the body revolution axis. In stepped column footing, two steps were created: for the square and circular foundation base, the first step has been extracted by 0.60 m, whereas second step, located in the centre of former step has been extracted by 0.80 m.
For square shape foundation the second step dimensions have been adopted as: 1.00 × 1.00 × 0.80 m (width; depth; height), whereas in the circular shape the second step has diameter 1.30 m. In each case, the column has been placed onto the top surface of foundation and longitudinal axis of column has coincided with the centre point of foundation top surface. For the square shape foundations, square shape column has been adopted with following dimensions: 0.40 × 0.40 × 1.00 m, whereas for the circular shape foundation circular columns with 0.40 m diameter and 1.00 m height have been adopted, respectively. To reflect footing located onto the ground, each analysed foundation had on its whole bottom surface vertical displacement boundary condition fixed and in the centre of that surface all displacements had also been fixed to provide model stability. It should be noted that ground weight located onto the foundation, ground friction and subsidence have been neglected in the analysis. In order to compare obtained results constant static concentrated force have been adopted equal 500 kN, which has been evenly distributed onto the top of each column surface.
For the foundations and columns isotropic concrete material model has been assumed, which correspond to the C25/30 concrete class. According to the fact that stress results concerning only concrete material had been the subject of interest, reinforced steel has been neglected in the analysis.
Hence, on the basis of stress isolines in concrete optimal foundation shape could be determined. Exemplary stress results for the circular pattern of sloped column footing has been presented in Fig. 1. Moreover, in paper obtained maximum stress results from the connection between footing-column and from the centre point of bottom foundations surfaces have been compared.

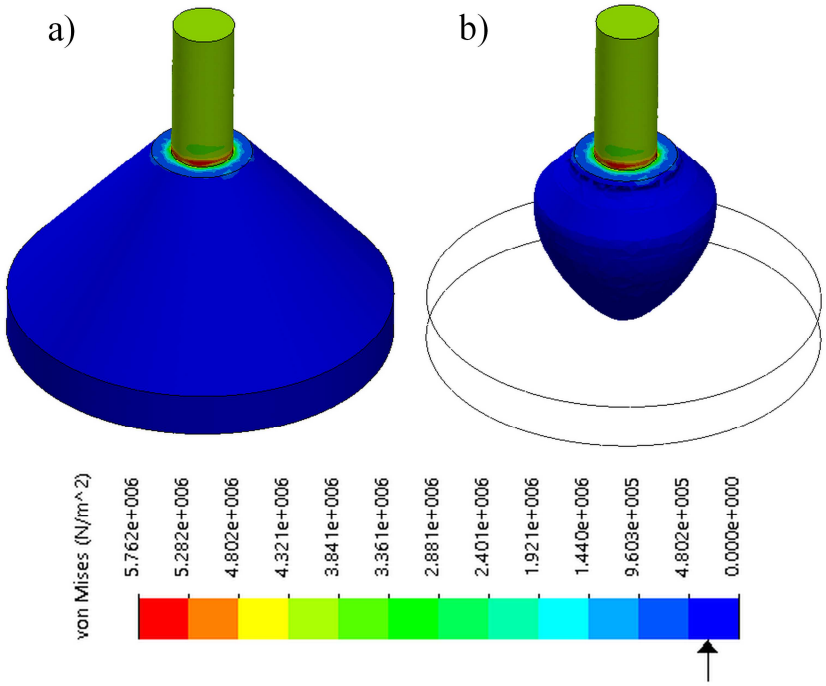

Fig 1: Misses stress distribution in circular sloped column footing: a) stress distribution in the whole numerical model, b) minimum Misses stress limited to the range of 0.30 MPa.

3. Conclusion

Through the numerical analysis performed it has been shown that the dimensions and even assumed shape of spread footing foundation subjected to the pure axial loading may be furtherly optimized. In [3, 4] has been shown the procedure of spread footing calculations concerning only basic shapes. Thus with the utilization of FEM method it is possible to propose another shape, which correspond to the stress distribution in any spread footing and with any boundary and loading conditions.

References

[1] PN-EN 1997-1:2008/NA:2011, Eurocode 7: Geotechnical design Part 1: Fundamental rules, PKN, Warszawa, 2011. (In Polish).
[2] PN-EN 1997-2:2009, Eurocode 7: Geotechnical design Part 2: Recognition and examination of the ground substrate, PKN, Warszawa, 2009. (In Polish).
[3] O. Puła, Design of direct foundations on the basis of Eurocode 7, Extended 3rd Edition, Dolnośląskie Wydawnictwo Edukacyjne, p. 142, 2014. (In Polish).
[4] Group work under the redaction of L. Lichołai, General Building Engineering. Volume 3: Building elements and design fundamentals, Arkady, Warszawa, 2015. (In Polish).

THE INFLUENCE OF HIGH TENSILE BOLTS STIFFENING ON COUPLED CONNECTION BEHAVIOR

I. Major[1], M. Major[1], and K. Kuliński[1]

[1]*Faculty of Civil Engineering, Czestochowa University of Technology, Częstochowa, Poland*
e-mail: imajor@bud.pcz.czest.pl

1. Introduction

Utilization of bolts have such a long history; it is believed that first wooden bolts were used in the water rising devices around 240 B.C. in the ancient Greece. Some experts differ in opinion, if bolts were not developed even earlier, in the ancient Egypt before the Archimedes. On the basis of their considerations first wooden bolts were used for land irrigation and to bilge the water from ships [1]. In the XV century bolts and screws were used by Gutenberg in his printing devices, whereas at fall of XV/XVI century first draft designs of screw-cutting machine were drawn.

The most intense development of thread bolts and screws fall over last one hundred years. Both classic mathematical methods and experimental studies were carried out to determine bolts load bearing capacity. Mentioned test concerned different materials, bolt head shape, thread shape etc. Further, world technological development lead to boundary problem solving with Finite Element Method (FEM) approach. Hu et al. [2] performed numerical simulation with the use of finite element method and experimental tests of high-strength bolts under tension. Through the analysis it was shown some discrepancy in load-displacement relationship and also failure mechanism could be observed. Bolts failure mechanism with the FEM utilization was also the subject of interest of Grimsmo et al. [3], who showed that nut location has significant influence on failure mode. Fire conditions and their influence on high-strength bolts was studied by Guo et al. [4]. It was stated that preload has insignificant effect of endplate in the fire conditions.

In this paper the static behavior of high tensile bolt in a coupled connection has been discussed. Section of steel tubes at coupled connection with introduced high tensile bolts has been adopted. Two different parameters have been taken into considerations i.e. coupled connection and single bolt deformation/stress – both under introduced tightening torque and torsion momentums. Stated problem has been solved with the utilization of SolidWorks software.

2. Model geometry and results

For the model geometry an assemblage of two steel tubes with ϕ305 external diameter and length of 200 mm have been adopted. Thickness of each tube has been assumed as 10 mm. Connection have been realized via end-plate welded to the host tube, for which external diameter of ϕ505 mm, thickness of 24 mm and internal circular cut with diameter of ϕ285 mm have been adopted, respectively. Eight M24 10.9 grade bolts have been introduced into connection. In order to increase the rigidity of connection special ribs from metal sheet have been provided. Overall connection shape and dimensions of adopted section of structure have been presented in Fig. 1.

For the analysis purposes of single static bolt behaviour under applied compressive preload, geometry of M24 high-strength bolt have been adopted on the basis of DIN 931 standard, assuming that the length of the bolt is equal 100 mm.

Two different loads have been investigated – bolts preload and torsion momentum applied to the tubes section. Single bolt deformations and stress results under applied maximum allowable preload force has been presented in Fig. 2.

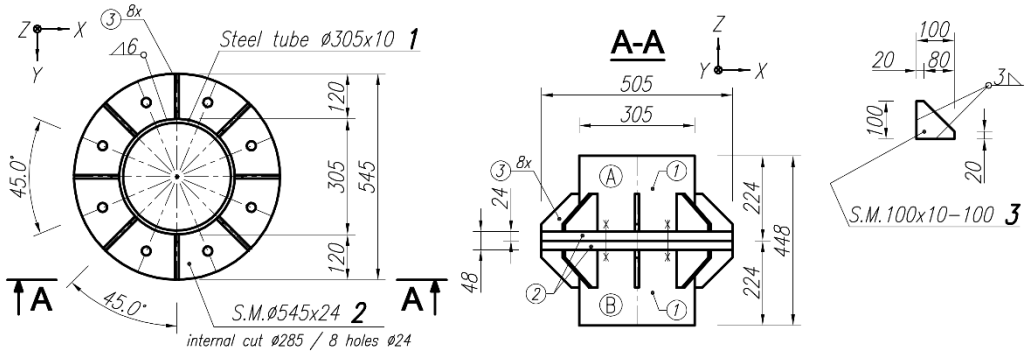

Fig 1: Planar view of steel column structure.

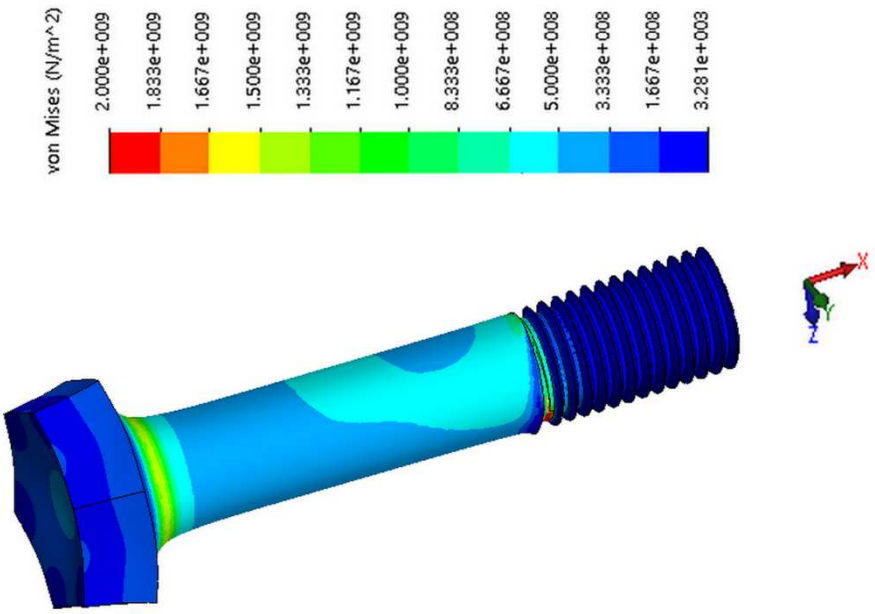

Fig 2: Deformation and Misses stress in the metric M24 high tensile bolt subjected to the stiffening force.

3. Conclusion

Through the numerical analysis performed in SolidWorks software deformations and stresses could be observed in both: high-strength bolt and coupled connection. Moreover, it was shown that for the analyzed coupled connection configuration applied value of torsion momentum had only small effect onto stress distribution in bolts and under the bolt head. Mentioned small effect of torsion momentum has been the result of circular shape of endplate, tubes utilized as columns as well as additional metal ribs welded between endplate and tube to increase the connection rigidity.

References

[1] http://www.nord-lock.com/pl/bolted/the-history-of-the-bolt/
[2] Y. Hu, L. Shen, S. Nie, B. Yang and W. Sha, FE simulation and experimental tests of high-strength structural bolts under tension, *Journal of Constructional Steel Research*, 126, 2016.
[3] E.L. Grimsmo, A. Aalberg, M. Langseth and A. H. Clausen, Failure modes of bolt and nut assemblies under tensile loading, *Journal of Constructional Steel Research*, 126, 2016.
[4] Z. Guo, N. Lu, F. Zhu and R. Gao, Effect of preloading in high-strength bolts on bolted-connections exposed to fire, *Fire Safety Journal*, 90, 2017.

MODELLING OF THE PHENOMENON OF AN EXPLOSION UNDER THE INNER WHEEL ARCH OF THE LIGHT ARMOURED VEHICLE

G. Sławiński[1], M. Świerczewski[1] and P. Malesa[1]

[1]*Military University of Technology, Gen. Witolda Urbanowicza 2 Street, 00-908 Warsaw, Poland*
e-mail: grzegorz.slawinski@wat.edu.pl

1. Introduction

Over many years of fights in Afghanistan, due to significant dominance of the forces of the North Atlantic Treaty Organisation (NATO), the partisan hit squads of that country have developed an effective and very cheap method of destroying the vehicles of the NATO forces, namely Improvised Explosive Devices (IED). The use of IEDs in fights against armies which are well-equipped with conventional weapons and armoured vehicles has been named an asymmetrical conflict. IEDs have become a main threat for military transports and patrols which keep stability in a given region. The level of dynamic loads results from the amount of an explosive detonated under a vehicle or within its area. Due to significant diversity of threats and different mass of explosives, the values of forces, moments and acceleration which may occur in the case of the detonation of normalised explosives are strictly defined for a given level of protection against mines in Annex B of the STANAG 4569 standardisation agreement and in Volume 2 of the AEP-55 test procedure entitled: "Procedures for evaluating the protection level of armoured vehicle" volume 2, "Mine threat".

2. Materials and methods

This study concerns the tests of the effects of the shock wave on the vehicle's construction loaded with the wave of pressure coming from the detonation of an explosive under the front inner wheel arch. Multi-variant numerical analyses have been conducted based on a validated model and on the basis of the results of experimental tests. The numerical model of the hull of the light armoured vehicle has been selected for numerical analyses and subjected to the effects of the shock wave coming from the detonation of TNT explosives of various mass. Numerical simulations have been conducted using the LS-Dyna calculation code. The detonation and loading with the shock wave have been conducted by using the built-in CONWEP option.

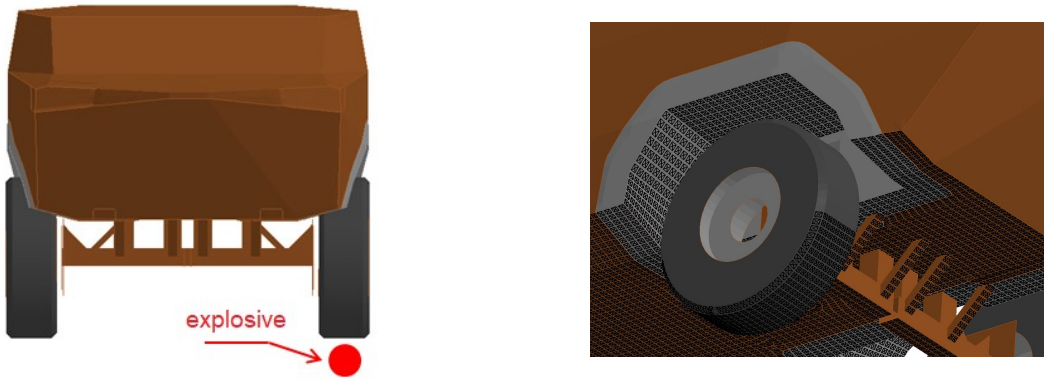

Fig. 1. The location of an explosive in relation to the vehicle (a) together with the place of loading the vehicle's construction (b)

The aim of using the FEM numerical method was to render it possible to correctly test the effects of an explosion on the vehicle's construction. The conducted numerical analyses have rendered it possible to learn about the consequences of those effects on the elements of the hull and also to select weak points in the construction.

3. Results

The results of the numerical calculations regarding the displacement of the inner wheel arch, measured using a comb, have been depicted in Table 1. The displacement of the inner wheel arch has been presented within a range. The distance of the comb's leaf which has been deformed constitutes the lower limit, whereas the distance of the leaf which has not been deformed as a result of the contact between the wheel and the comb constitutes the upper limit. The permanent deformations of combs have been depicted in Fig. 2.

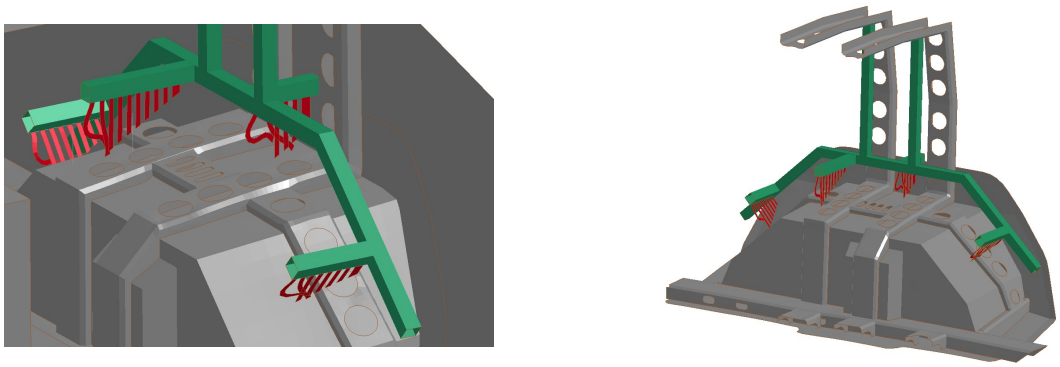

Fig. 2. The view of the deformed leaves of the combs

Left inner wheel arch, version A – numerical calculations				
Comb No.	L1	L2	L3	L4
Displacement within the range	20.7-37.69	19,55- 31.7	18.99-31.39	7.89-21.28

Table 1. The results of the total deformations of inner wheel arches obtained using the comb method – the results of the numerical calculations

3. Summary

The FEM model of the light armoured vehicle has been developed as a result of the conducted analyses and then, the model has been validated on the basis of the results of experimental test. Satisfactory consistency of the results of the numerical simulations and the experimental tests has been obtained. The stress-strain of the material in the vehicle's inner wheel arch has been assessed and the weak points of the vehicle's construction have been indicated. Those weak points should be modified or secured by additional protection systems, i.e. energy-absorbing panels.

As part of the conducted tests, also the impact of those additional energy-absorbing systems has been tested on the validated FEM model. The aim of the energy-absorbing panel was to decrease the acceleration affecting the vehicle and thus its occupants. The obtained results constitute the basis for further advanced numerical analyses.

6. References

[1] AEP-55, Vol. 1, Edn. 1, Procedures for Evaluating the Protection Levels of Logistic and Light Armoured Vehicles for KE and Artillery Threats, NATO/PFP Unclassified, 2005.

[2] AEP-55, Vol. 2, Edn. 1, Procedures for Evaluating the Protection Levels of Logistic and Light Armoured Vehicle Occupants for Grenade and Blast Mine Threats Level, NATO/PFP Unclassified, 2005.

Acknowledgments The research was done within project no. DOBR-BIO4/022/13149/2013 'Improving the Safety and Protection of Soldiers on Missions Through Research and Development in Military Medical and Technical Areas', supported and co-financed by NCR&D, Poland.

THE EFFECT OF HALL-PETCH RELATIONSHIP ON MULTI-SCALE NUMERICAL SIMULATION OF MECHANICAL BEHAVIOUR OF TI-6AL-4V POLYCRYSTALLINE

F. Benmessaoud[1], V. Velay[1], M. Cheikh[1, 2], V. Vidal[1], C. Boher[1] and F. Rézaï-Aria[1]

[1]*Institut Clément Ader, Université de Toulouse; CNRS, IMT Mines Albi, Campus Jarlard, F-81013 Albi Cedex 09, France*

[2]*Université Toulouse II, IUT Figeac F-46100 Figeac, France*

e-mail: fbenmess@mines-albi.fr

1- Context

Mechanical behaviour of an equiaxed polycrystalline alpha-beta Ti-6Al-4V alloy is investigated by an elasto-viscoplastic constitutive law developed based on crystal plasticity and finite element approach. Effects of the material parameters are investigated considering the Hall-Petch relationship.

2- Finite element modeling

The effect of grain size is investigated basing on local elasto-viscoplastic constitutive equations proposed by Méric-Cailletaud and Hall Petch relationship [1-3] with consideration of small strain assumption. The model parameters are founded in [4-5]. The microstructure features and crystallographic texture are modeled using Voronoi tessellations.

Four Representative Volume Element (RVE) with different Ti-6Al-4V microstructural features are reported in table 1. The role of five textures is studied (see table 2).

REV (120x120x120μm^3)	Microstructure	Average grain size μm	Number of grains within RVE
1	Homogenous	3	1900
2		14	700
3	Heterogeneous	3	1900
4		14	700

Table 1: REVs and microstructural aspects investigated

Texture	Tx1	Tx2	Tx3	Tx4	Tx5
Macrozone	No	Intermediate	Strong (0,0,0)	Strong (90,90,0)	Strong (45,45,45)

Table 2: Different textures investigated

3- Results

The evolutions of local yield stress and plastic strain are shown respectively in figures 1 and 2 as a function of the scattering of gain size. For heterogeneous morphology with no or intermediate macrozones, a strong heterogeneity of plastic strain is found. Coarse grains present more plastic straining compared to small grains. This is linked to the motion of dislocations, which is limited in the small grains since the grain boundaries limit the distance for free sliding of the mobile dislocations compared to the more coarsened grains. The interaction of the dislocation and grain boundaries induce in consequence more hardening of small grains and therefore enhance their yield strengths. This interaction is implicitly integrated through the Hall-Pech relationship that was added to the model

of Meric-Cailletaud. However, when the Ti-6Al-4V grains are strongly textured along particular orientations (Tx3, Tx4 and Tx5), the plastic strain is more homogeneous Figure 2 and the yield stresses are comparable whatever their sizes. A very small variation is observed when the texture is Tx5, Figure 1. For this highly textured microstructure, the Hall-Petch relationship has no more a drastic effect.

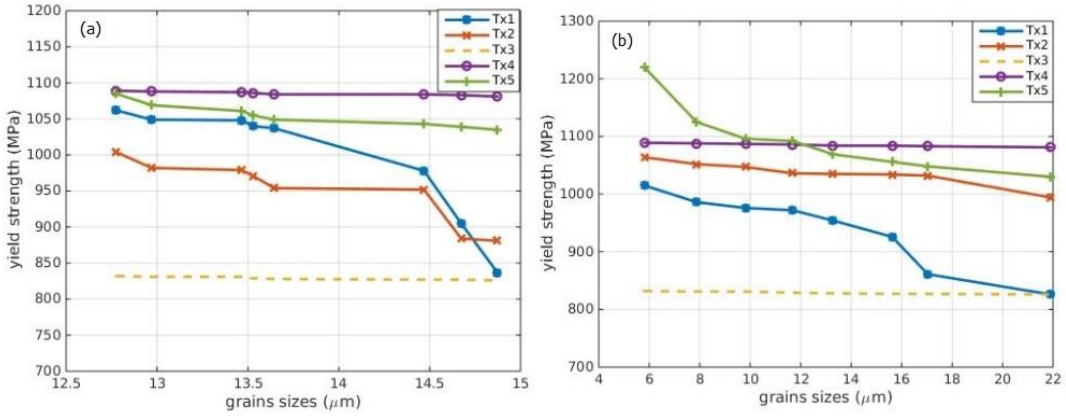

Figure, 1: Evolution of local yield strength of a Ti-6Al-4V modelled with an average grain size of 14 µm and small grain size scattering morphology (homogeneous microstructure) in (a) and large grain size scattering (heterogeneous microstructure) in (b)

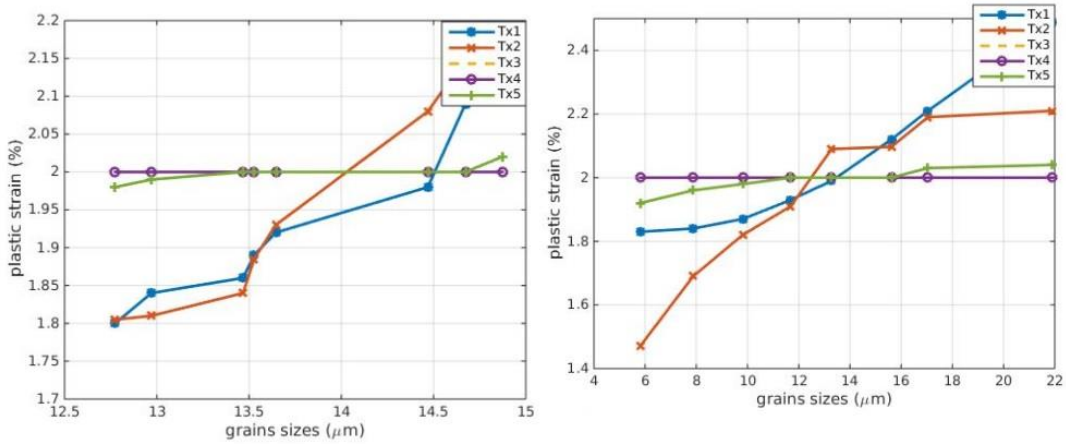

Figure 02: Evolution of local plastic strain of a Ti-6Al-4V modelled with average grain size of 14 µm and small grain size scattering morphology (homogeneous textured microstructure) in a and large grain size scattering heterogeneous textured microstructure in b

References:

[1]: L. Méric, P. Poubanne and G. Cailletaud, Single Crystal Modeling for Structural Calculations: Part 1- Model Presentation, *Int. J. Eng and Mat Tech* 113, 162-170, 1991.

[2]: E.O. Hall, The Deformation and Ageing of Mild Steel: III Discussion of Results, *Int. J. Proc of the Phy*, 64, 747–753, 1951.

[3]: N.J. Petch, The Cleavage Strength of Polycrystals, *Int. J.of the Iron and Steel Institute*, 174, 25-28, 1953.

[4]: J.R. Mayeur, D.L. McDowell, A three-dimensional crystal plasticity model for duplex Ti–6Al–4V, *Int, J. of Plasticity* 23, 1457-1485, 2007.

[5]: T. Dick and G. Cailletaud , Fretting modelling with a crystal plasticity model of Ti6Al4V, *Int. J. Comp Mat Science* 38, 113–125, 2006.

CHARACTERIZATION OF THE STRESS FIELDS NEAR CRACK TIP FOR COMPACT SPECIMEN FOR ELASTIC-PLASTIC MATERIALS IN PLANE STRAIN STATE DOMINATION

M. Graba[1]

[1] *Kielce University and Technology, Faculty of Mechatronics and Mechanical Engineering, Department of Manufacturing Engineering and Metrology, Al. 1000-lecia PP 7, 25-314 Kielce, POLAND*

e-mail: mgraba@tu.kielce.pl

1. Introduction

One of many basic specimens used in fracture mechanics is a compact specimen, designated by C(T). It appears in the ASTM standards [1],or even the norm that is still in force in Poland in the didactic or research process [2]. In 2012, Zhu and Joyce [3] presented an overview of methods for determining fracture toughness using C(T), SEN(B) and CC(T) specimens, indicating the need to consider the influence of geometric constraints in formulas approximating the equations of the J-R curves. The parameters of geometrical constraints mentioned in the paper [3] include the Q-stress (Q-parameter) defined by O'Dowd et al. and the A_2 parameter (described also as A_2 aplitude) discussed by Yang et al.. It should be remembered, however, that both parameters – Q and A_2 are determined by numerical calculations with the assumption of small deformations and displacements, which leads to obtaining singular stress distributions near the crack tip. It can be said that both parameters are a correction of the HRR solution presented in 1968 and improve the description of stress fields near the crack tip taking into account the influence of the other parts of the asymptotic solution.

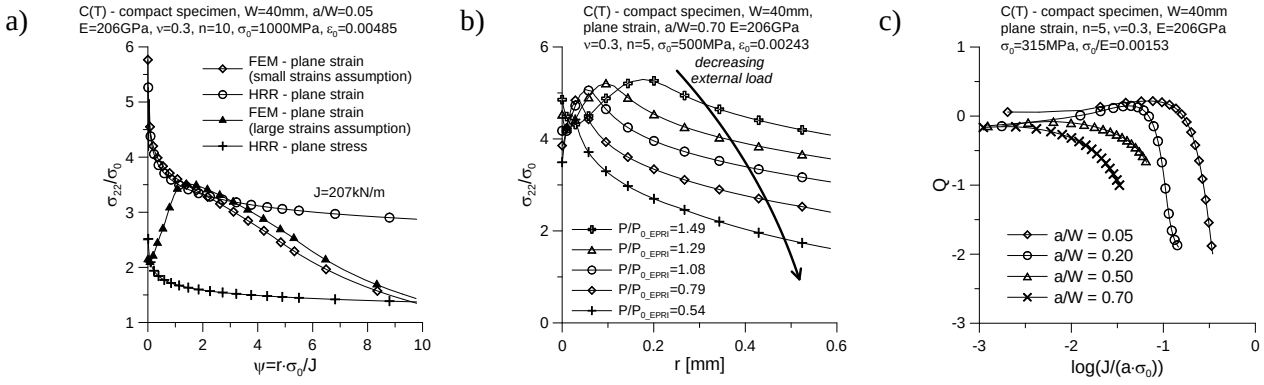

Fig. 1. a) The stress distribution near the crack tip for C(T); b) The influence of the external load on the maximum crack opening stress (normalized by yield stress) for C(T) specimens; c)The influence of the crack length on the Q=f(log(J/(a·σ_0)) trajectories for C(T) specimens.

As it is known, in the real structural element, the stresses in front of the crack tip are finite - such a distribution in numerical calculations is obtained by assuming large strains and large displacements, which in the case of stress distribution leads to reach a Maximum of the crack Opening Stress (MOS) at a specific distance from the crack tip [4] - Figure 1a. The value of this maximum as well as its position near the crack tip was used in [4] in the proposal of a modified crack criterion based on the RKR hypothesis. It should be noted that the level of MOS and their position near the crack tip depends on the material characteristics, geometry and external load (Figure 1b), which is also shown in [4]. The same applies to the Q-parameter, commonly referred to as Q-stresses (Figure 1c).

The applications of the fracture mechanics to solving practical engineering problems require knowledge of the Q-parameter or the MOS and their position in front of the fracture tip. In addition, these parameters, generally referred to as in-plane constraints, are determined by carrying out comprehensive numerical calculations, the

results of which are subject to detailed analysis (postprocessing). The development of a numerical model allowing to estimate the measures of in-plane constraints is not a trivial problem, as shown in [5]. Based on previous achievements [6-9], the author of this article presents a catalog of numerical solutions and their approximations, which for compact specimens allow to estimate the values of selected measurements of in-plane constraints depending on external load, crack length or material characteristics.

2. Highlights, some results and summary

All calculations were made using the ADINA program, using the analysis schemes developed over the years. In addition to the ready solution catalog, the influence of material characteristics and the relative crack length on selected measures of in-plane constraints were discussed, also taking into account the influence of external load expressed by J-integral (which may be accepted as a crack driving force).
The numerical analysis was showed, that in the range of low external loads, it is noticed that C(T) specimens characterized by high level of in-plane constraints. The increase in the relative crack length causes an increase in the value of Q-stresses – the in-plane constraints increase. The increase in external load results in decreasing of the level of in-plane constraints expressed by Q-stress. The C(T) specimens characterized by a lower yield point, faster reach a lower level of in-plane constraints. The lower level of in-plane constraints is also characterized by C(T) specimens made of a strongly hardening material.
Based on the FEM analysis, assume large deformations, it can be noted, that the level of MOS increases with the increasing external load, and then reaches the saturation state. The weak influence of the crack length should on the level of MOS is observed. The same conclusions may be apply to the normalized position of the MOS near the crack tip. A very pronounced effect of the yield point on the level of MOS of the fracture surfaces was observed - the smaller the yield point, the greater the values of the MOS. The MOS of the fracture surfaces and their normalized position near the crack tip are clearly influenced by the degree of material hardening – the stronger material, the greater value of the MOS and the smaller the value of their normalized position relative to the crack tip.
Some details of the numerical models, the specific numerical results presented in the graphical form, their approximation using simple mathematical formulas (formulas, tables with coefficients, comparison with numerical results) and right conclusions will be presented on the conference poster on August 2018.

Acknowledgments The research reported herein was supported by a grant from the Faculty of Mechatronics and Machine Design at Kielce University of Technology (project No. 01.0.09.00/2.01.01.01.0027 MNSP.MKTM.17.002).

References

[1] *ASTM E 1820-05 Standard Test Method for Measurement of Fracture Toughness*. American Society for Testing and Materials, 2005.
[2] PN-87/H-4335, *Metals – Test method for measurement of the fracture toughness for plane strain conditions*, 1987.
[3] X.-K. Zhu and J.A. Joyce. Review of fracture toughness (G, K, J, CTOD, CTOA) testing and standardization, *Engineering Fracture Mechanics* 85 (2012) 1–46, doi:10.1016/j.engfracmech.2012.02.001
[4] A. Neimitz, M. Graba and J. Gałkiewicz. An alternative formulation of the Ritchie-Knott-Rice local fracture criterion. *Engineering Fracture Mechanics*, vol.74, pp.1308-1322, 2007.
[5] M. Graba and J. Gałkiewicz. Influence of the crack tip model on results of the finite element method. *Journal of Theoretical and Applied Mechanics*, Warsaw, vol.45, No.2, pp.225-237, 2007.
[6] M. Graba M. The influence of material properties and crack length on the Q-stress value near the crack tip for elastic-plastic materials for single edge notch plate in tension. *Archives of Civil and Mechanical Engineering*, vol.XI, No. 2, pp. 301-319, 2011.
[7] M. Graba. The influence of material properties and crack length on the Q-stress value near the crack tip for elastic-plastic materials for centrally cracked plate in tension. *J. Theor. Appl. Mech.*, vol.50, No.1, pp.23-46, 2011.
[8] M. Graba. The influence of material properties on the Q-stress value near the crack tip for elastic-plastic materials. *Journal of Theoretical and Applied Mechanics*, vol.46, No.2, pp.269-290, 2008.
[9] M. Graba. Catalogue of the numerical solutions for SEN(B) specimen assuming the large strain formulation and plane strain condition. *Archives of Civil and Mechanical Engineering*, Published by Elsevier, vol.12, No.1, pp.29-40, 2012.

SELECTED TRIBOLOGICAL CHARACTERISTICS OF A390.0 ALLOY AT ELEVATED TEMPERATURE UNDER DRY FRICTION CONDITIONS

J. Kozuba, R. Wieszała

Siesian University of Technology, *Faculty of Transport, Gliwice, Poland*
E-Mail: Jaroslaw.Kozuba@polsl.pl, Robert.Wieszala@polsl.pl;

The article presents the tests determining the coefficient of friction μ and the amount of wear for the A390.0 alloy combined with EN GJL-350 cast iron at elevated temperature of up to 200ºC under dry friction conditions. It also presents the results of research concerning mechanical properties (HB, HV, Rm) and yield properties ($R_{0,2}$, A_5, Z) of the alloy examined. The A390.0 alloy is used for manufacturing pistons for spark-ignition internal combustion engines, therefore the research parameters were selected so as to correspond to the conditions inside a spark-ignition turbocharged internal combustion engine with the power of up to 100 kW. The research was conducted in order to determine whether the alloy analyzed meets excessive wear resistance requirements, which are imposed on piston materials to be used in modern spark-ignition turbocharged internal combustion engines.

The A390.0 alloy belongs to AlSi casting alloys. The properties of these alloys are determined by the state of their structure, i.e. mainly the size, the distribution of intermetallic phases in the metallic matrix, and the morphology of eutectics. As the silicon content approaches hypereutectic composition, the influence of the refinement of grains containing solid solution dendrite families decreases, and the significance of the morphology of primary silicon crystals and their uniform distribution in the matrix increases. The most frequently occurring forms of primary silicon in hypereutectic silumins are: star-shaped, polyhedral, dendritic (at rapid cooling), and ornament. They are precipitations assuming the structures of i.a. radial plates, needles, polyhedrons, long-pointed stars – unfavorable from the perspective of performance and machinability of hypereutectic silumins Such an unfavorable structure may be transformed i.a. as a result of modifications with, for instance, individual or combined phosphorus-, titanium-, and boron-based master alloys.

The objective of such modifications is to increase the density of heterogeneous bases and to hinder nucleation of silicon crystals, and, what it involves, to limit their growth. However, it should be noted that the refinement of silicon crystals alone is insufficient. It is also necessary to obtain the proper shapes of silicon crystals being close to spheroidization. As an example of that may serve modified fine-grained silicon crystals with sharp edges having an adverse effect on e.g. tribological properties. Consequently, it is necessary to develop manufacturing processes enabling multidirectional optimization. The research concerned the A390.0 alloy, whose chemical composition is given in Table 1, modified with phosphorus (0.05% by wt. of the alloy) using the CuP10 master alloy. The alloy was refined using Rafglin-3 preparation (0.3% by wt.)

Alloy	Chemical composition, mass %						
	Si	Fe	Cu	Mn	Mg	Zn	Al.
A390.0	16.8	0.573	4.95	0.189	1.001	0.145	remainder

Table 1. Chemical composition of the A390.0 alloy

The tests were performed in a pin-on-disc system, according to the ASTM G 99 standard. This means that the coefficient of friction may be determined after grinding-in, i.e. when the whole surface of the pin exhibits traces of wear. Otherwise, the test should be repeated. In the tests conducted, the pin was made of the A390.0 alloy, and the disc of the EN GJL-350 cast iron. The tests were carried out for technically dry friction, under a load of 1.3 MPa, a velocity v = 1.2m/s, at variable temperatures of 100ºC, 125ºC, and 150ºC. The path of friction was 1000m. The parameters were selected so as to correspond to the conditions inside a turbocharged spark-ignition internal combustion engine with a power of 150kW and a direct fuel injection. Because of the high load, in all cases the whole surface of the pin showed traces of wear. In total, 12 tests were performed. The mass decrement of the mating pin and disc elements was measured with a Radwag AS 220/C/2 balance whose precision was 0.1mg. The observations of the surface after friction were performed with an Olympus SZX9/8X stereoscopic microscope and a Hitachi S-3400N scanning electron microscope.

Fig.1 presents the surface of the disc and the pin after applying friction at 125ºC. Fig. 2 shows the scale of material wear of the disc and the pin in the tribo-pair analyzed, while Table 2 presents the results of friction coefficient.

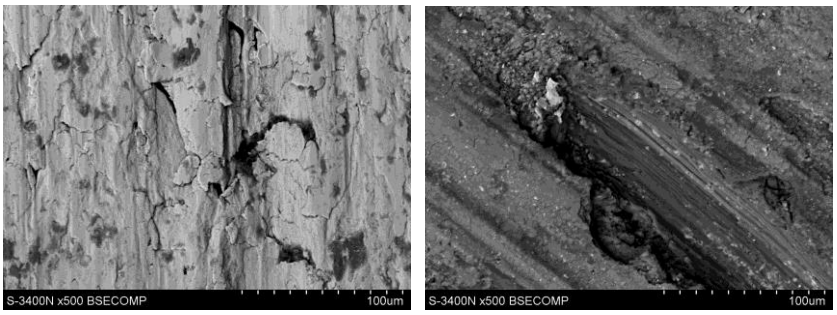

a) b)

Fig. 1. The surface after friction at 125ºC: a) disc (EN GJL-350), b) pin (A390.0)

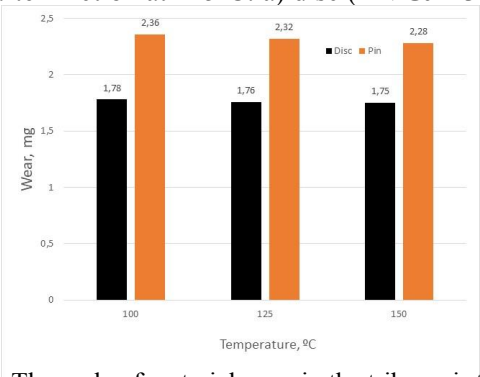

Fig. 3. The scale of material wear in the tribo-pair tested

Alloy examined: A390.0	Temperature, ºC	μ	σ_μ
Sample No. 1	100	0.33	0.008
Sample No. 2	125	0.33	0.005
Sample No. 3	150	0.32	0.002

where: μ – friction coefficient, σ_μ – standard deviation of friction coefficient

Table 2. The results of the A390.0/EN GJL-350 tribo-pair tests

The highest coefficient of friction μ = 0,33 was obtained for two temperatures examined, 100ºC and 125ºC, whereas the lowest, μ = 0,32, was obtained for the highest temperature, 150ºC. It is worth noting, however, that for 100ºC the standard deviation was 0.008 whereas for 125ºC it was at the 0.005 level. For the temperature of 100°C the wear was 1.78mg for the disc (EN GJL-350) and 2.36mg for the pin (A390.0). For the temperature of 125°C the respective wear was 1.76mg for the disc and 2.32mg for the pin. For the highest temperature, 150ºC, the wear was at the level of 2.28mg for the pin and 1.75mg for the disc.

The application of air supercharging (turbo charger), particularly in spark-ignition engines, and the installation of direct injection systems changed the characteristics of loads present during the operation of a car-engine piston to such extent that it became necessary to test the already-existing materials under new operating conditions. On the basis of the tests performed, it may be concluded that the A390.0 material modified with the CuP master alloy without additional modifications does not fulfill the requirements characterizing operating conditions of modern internal combustion engines. Values of the friction coefficient for all tested loads exceeded the level of 0.33. The research studies were deliberately conducted at elevated temperatures in order to most accurately reproduce the actual conditions of engine operation. The aforementioned studies indicate a necessity to search for new material solutions, and they prove that the materials in use so far have ceased to meet the design requirements of new engine technologies

References

[1] Ch. Tomastik, M. Jech, T. Wopelka, F. Franek. *Surface analysis of cylinder liners from tribological model experiments and internal combustion engines*. Surface and Interface Analysis 42(6-7): 1357-1360, 2010.

[2] F. Grun, F. Summer, K. Pondicherry. *Tribological functionality of aluminium sliding materials with hard phases under lubricated conditions.* Wear 298-299(1): 127-134, 2013.

[3] R. Wieszała, J. Piątkowski. *Selected tribological properties of A390.0 alloy.* Archives of Foundry Engineering 17(1): 175-178, 2017.

[4] P. Kumar, M.F. Wani. *Friction and wear behaviour of hypereutectic Al-Si alloy/steel tribopair under dry and lubricated conditions.* J. Tribologi 15: 21-49, 2017.

RELIABILITY ANALYSIS OF RETAINING WALL USING SEISMIC CONE TEST DATA

I. Bagińska[1], M. Wyjadłowski[1]

[1] *Wroclaw University of Science and Technology, Wrocław, Poland*

e-mail: marek.wyjadlowski@pwr.edu.pl

The aim of this paper is to examine the influence of geotechnical uncertainties on the reliability retaining wall. The results from seismic piezocone tests (SCPTu) are shown to be applicable for providing all the necessary input parameters to drive the computations and calculate displacements of retaining wall. Reliability sensitivity analysis was conducted using MCS (Monte Carlo simulations).

The physical uncertainties of action, the inherent variability of soil and model error were assessed by experimental in situ standard penetration test (SCPTu). The approach involves a combination of finite element analysis, random field theory and Monte Carlo simulations. Small-strain stiffness is mostly found to be manifold of stiffness obtained in classical laboratory testing. Therefore, not accounting for it in geotechnical analyses may result in overestimating retaining wall deflections.

The overall reliability of numerical displacements analysis is considerably increased. In this calculation HS-small input parameter soil stiffness G_o [1], [2] (in program PLAXIS [3] parameter: G_{oref}) is derived from SCPTu testing. The stiffness of the surrounding soil is represented by a shear modulus G. The initial fundamental small-strain shear modulus of the ground is obtained from the shear wave velocity measurements:

$$Go = \rho \cdot Vs^2 \tag{1}$$

where

ρ- total mass density of the soil.

This small-strain stiffness is within the true elastic region of soil corresponding to nondestructive loading. To approximately account for nonlinearity of the stress-strain-strength behaviour of soils, a modified hyperbola is adopted [4]:

$$G = Go \cdot [1 - (P/P_{ult})g] \tag{2}$$

Where:

P - applied force,

P_{ult} - axial capacity of the pile segment, and the exponent "g" is a fitting parameter.

Thus when P = 0, initially $G = G_o$ and at all higher load levels the shear modulus reduces accordingly. In the analysis of the retaining wall displacement the soil parameter has been expected as a random variable: G shearing module and parameters entered for model HS-small : G_{oref} (shear stiffness at very small levels).

The value is described in a one-dimensional random field with a average value μ_x, standard deviation σ_x , and Markov's correlation structure. In the random finite element method (RFEM) in first place a random field that represents the parameters of the analysed ground foundation has been generated. Next the field is discretised to a net of finite-elements and for this a method of random variables. is used. The next step is the calculation method where the Finite element method is used in order to calculate the response of structure[5]. Multiple repeating for the consecutive field realization leads to reaching set results. Because of the difficulties in showing the systems answer in a functional way Monte Carlo simulation method was used. The number of simulations n must be chosen in order to provide stability of the solution during simulations. For the considered task a stable answer was reached after about 100000 simulations. The task shows usefulness of the used modelling tools with the help non-linear ground model and ground parameters based on SPTU [6] sounding.

References

[1] T. Benz. Small-strain stiffness of soils and its numerical consequences. Ph.D. Thesis. Institut für Geotechnik, Universität Stuttgart, 2006.

[2] T. Schanz, T., P.A.Vermeer, P.G. Bonnier. The hardening soil model: Formulation and verification. *Beyond 2000 in computational geotechnics*. Balkema, Rotterdam, 281-290, 1999.

[3] R. Brinkgreve et al. *Plaxis Material Model Manual*. Plaxis bv, Delft, Netherland, 2011.

[4] M. Fahey. Shear modulus of cohesionless soil: variation with stress and strain level. *Canadian Geotechnical Journal* Vol. 29, No. 1, 157-161, 1992.

[5] M. Lloret-Cabot, G.A. Fenton, M.A. Hicks. On the estimation of scale of fluctuation in geostatistics. *Georisk: Assessment and Management of Risk for Engineered Systems and Geohazards*. 8(2), 129–140, 2014.

[6] P.K. Robertson. Soil classification using the cone penetration test. *Canadian Geotechnical Journal*. 27(1), 151– 158, 1990

STRAIN SOFTENING COSSERAT PLASTICITY FOR FGM SHELLS IN NONLINEAR 6-PARAMETER SHELL THEORY

S. Burzyński[1]

[1]*Gdańsk University of Technology, Gdańsk, Poland*
e-mail: stanislaw.burzynski@pg.edu.pl

1. Introduction

Decreasing of strength during growing deformation in solids in known as strain softening phenomena, which can occur in materials like concrete, rock, ceramics etc. [1]. Strain softening plasticity, along with brittle damage, are two possible ways to predict ultimate behaviour of enlisted materials. Plates and shells made of Functionally Graded Materials (FGM) are usually composed from ceramics and metal constituents. During extreme loading, some cracks may occur in ceramics layer, then ductile metal constituent is responsible for stopping their development into structure depth. While a lot of research was done in the topic of elastic behaviour of FGM plates and shells investigations to cover materially nonlinear FGM shell structures deformations are limited. As a rule the TTO mixture model was applied (e.g. [2,3,4]), which assumes elasto-plastic material law with linear hardening and ceramics is considered as perfectly elastic constituent, without any limit stress defined to enrich its material law. In this study, the elasto-plastic model with strain softening attributed to ceramic constituent is proposed, as a possible way to simulate brittle behaviour. Since strain softening exhibits strong mesh dependence in numerical calculations with classic FEM codes, it is reasonable and appropriate to implement present idea in code based on Cosserat type kinematics, where drilling rotation and its' stiffness expressed by the characteristic length l have influence on regularization (reduction of mesh dependence) of result [5,6]. All present calculations are carried out in authors own FEM code named CAM, written in Fortran language.

2. Material law

It is assumed that shell is built from two constituents: the first is ceramic and the second metallic type. Material mixture proportions vary through the thickness of the shell with well-known power law. At each point of the shell reference surface Cosserat plane stress is assumed

$$(1)\qquad \begin{Bmatrix} \sigma_{aa} \\ \sigma_{bb} \\ \sigma_{ab} \\ \sigma_{ba} \\ m_a \\ m_b \end{Bmatrix} = \left[\begin{array}{cccc:cc} Ea_1 & Ea_2 & 0 & 0 & 0 & 0 \\ Ea_2 & Ea_1 & 0 & 0 & 0 & 0 \\ 0 & 0 & G+k & G-k & 0 & 0 \\ 0 & 0 & G-k & G+k & 0 & 0 \\ \hdashline 0 & 0 & 0 & 0 & 2Gl^2 & 0 \\ 0 & 0 & 0 & 0 & 0 & 2Gl^2 \end{array}\right] \begin{Bmatrix} \varepsilon^{aa} \\ \varepsilon^{bb} \\ \varepsilon^{ab} \\ \varepsilon^{ba} \\ \kappa_a \\ \kappa_b \end{Bmatrix}, \quad a_1 = \frac{1}{1-\nu^2}, \quad a_2 = \nu a_1, \quad a,b = 1,2$$

with $k = N^2/(1-N^2)G$ where $0 < N < 1$ is the so-called coupling number. All material parameters in through-the-thickness direction follow simple rule of mixture $X = V_c X_c + V_m X_m$, where V_i denotes constituents relative volume in shell layer, subscripts c and m refer to ceramic and metal parameters. Each of materials is assumed to be elasto-plastic with piece-wise linear hardening (m) or softening rule (c). Plastic flow theory, based on J_2 plasticity extended to Cosserat continua is applied [5]. Closest Point Projection Method is used to numerical integration of plasticity equations at single integration point.

3. Numerical example

Consider FGM plate with initial imperfect geometry. Parametric study of similar plate was conducted in [3] with TTO mixture model. Dimensions of the plate are defined as $a = 111.125$, $b = 127$, $h = 3.175$. In Fig. 1. geometry, load, mesh (division into 16-node CAM finite elements) is shown. In present study double

symmetry is taken into account. Here, metal constituent is assumed to be perfectly elasto-plastic, with material data $E_m = 206200$, $\nu_m = 0.3$, $l_m = 0.0001$, $H_m = 0$, $\sigma_{Ym} = 250$. Ceramics is assumed as strain softening elasto-plastic with $E_c = 340000$, $\nu_c = 0.25$, $l_c = 0.0001$ or $l_c = 0.01$. Softening curve, defined as pairs of parameters (σ_Y, ε_{eff}) with ε_{eff} as the effective plastic strain, is displayed in Fig 1. When $\varepsilon_{eff} \geq 0.02$, yield stress remains constant $\sigma_Y = 50$. Thickness integration is performed with 7 point Gauss-Lobatto rule. Graph in Fig. 1 shows equilibrium paths. Values on vertical axis are an average compression stress normalized with $S_Y = \sigma_Y$ while on horizontal axis displacement of loaded edge is shown. Equilibrium paths reveal that mesh refinement do not affect limit load, differences however are visible in global softening curves after limit point is passed. There is a small effect of ceramics characteristic length visible in the finest mesh. Contour plot of effective plastic strain shows localization phenomena, typical for strain softening, in which plastified zones are narrow and divide structure into elastic subregions.

Example proves capability of the author's CAM code to analyze deformations in FGM structures with novel strain softening ceramics behaviour description. Limit load and further course of deformation could be investigated, with characteristic for strain softening localization phenomena.

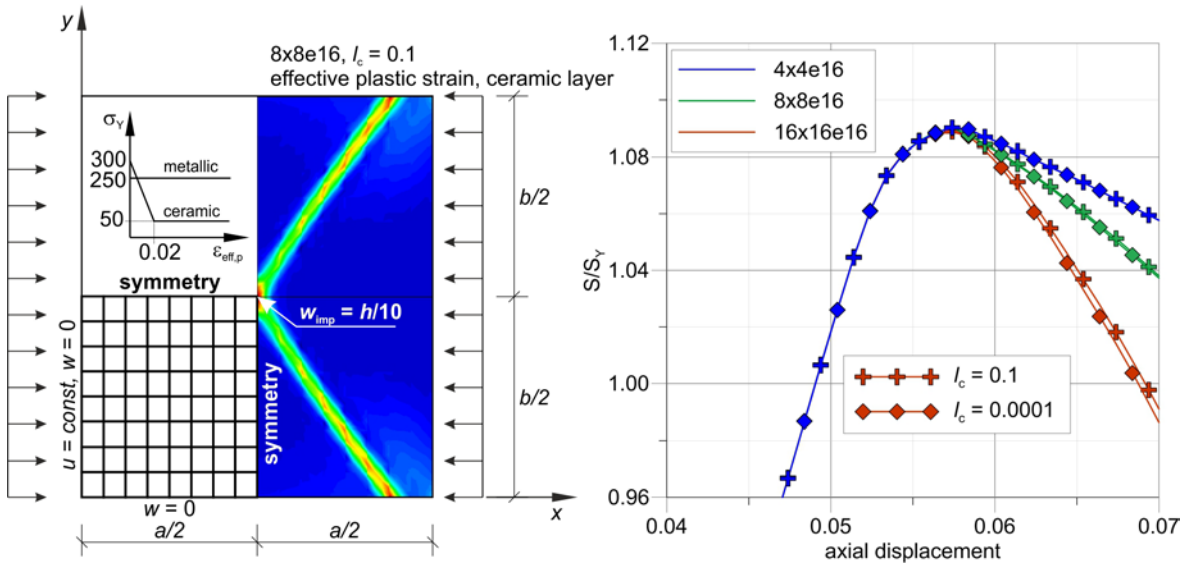

Fig. 1. FGM plate under in-plane load: geometry, discretization, equilibrium paths.

Acknowledgments The authors acknowledge financial support from the grant No UMO 2015/17/B/ST8/02190, financed by National Science Centre Poland.

References

[1] J. Lubliner. *Plasticity Theory*. Pearson Education, Inc., 2006
[2] G. Xu, H. Huang, B. Chen, F. Chen. Buckling and postbuckling of elastoplastic FGM plates under inplane loads. *Compos. Struct.* 176: 225–233, 2017.
[3] M. Kleiber, M. Taczała, R. Buczkowski. Elasto-Plastic Response of Thick Plates Built in Functionally Graded Material Using the Third Order Plate Theory. *In: Advances in Computational Plasticity*, 185–199, 2018.
[4] S. Burzyński, J. Chróścielewski, K. Daszkiewicz, W. Witkowski. Elastoplastic nonlinear FEM analysis of FGM shells of Cosserat type. (submitted to Composites Part B), 2018.
[5] R. de Borst. Simulation of strain localization: a reappraisal of the Cosserat continuum. *Eng. Comput*. 8: 317–332, 1991.
[6] S. Burzyński. O zbieżności rozwiązań w nieliniowym mikropolarnym ośrodku sprężysto-plastycznym - zastosowanie elementów skończonych wyższego rzędu. *Inżynieria Morska i Geotech*. 2: 125–134, 2013.

Author index

Institute of Fundamental Technological Research
Polish Academy of Sciences (IPPT PAN)
Pawińskiego 5b, 02-106 Warszawa, POLAND
http://solmech2018.ippt.pan.pl

ISBN 978-83-65550-13-2